Proceedings of the
25th Seismic Research Review --
Nuclear Explosion Monitoring:
Building the Knowledge Base

September 23-25, 2003

Tucson, Arizona

Volume I

Theme Paper
Seismic Regional Characterization and Wave Propagation
Seismic Event Detection and Location
Seismic Identification and Source Characterization

Approved for Public Release; further dissemination unlimited.

National Nuclear Security Administration

LA-UR-03-6029

Proceedings of the 25th Seismic Research Review -- Nuclear Explosion Monitoring:
Building the Knowledge Base

To view these Proceedings online, visit
https://www.nemre.nnsa.doe.gov/review2003.

Vol. I

Acknowledgements

The National Nuclear Security Administration (NNSA) and the Air Force Research Laboratory (AFRL) gratefully acknowledge the important contributions of the following people for their work on the ***Proceedings of the 25th Seismic Research Review – Nuclear Explosion Monitoring: Building the Knowledge Base.***

Authors of papers for excellent research, good technical content and willing cooperation in electronic submission.

Dr. Anton M. Dainty, Air Force Research Laboratory (AFRL)/Defense Threat Reduction Agency (DTRA), for review and clearance of abstracts and papers related to AFRL and DTRA contracts.

Dr. Frederick R. Schult, Air Force Technical Applications Center (AFTAC)/AFRL, for review and clearance of abstracts and papers related to AFTAC contracts.

Dr. Stanley D. Ruppert, Lawrence Livermore National Laboratory (LLNL), for burning, labeling, jacketing, and delivering the CD ROMs.

Ms. Francesca C. Chavez, Los Alamos National Laboratory (LANL), for technical editing of abstracts and papers.

Ms. E. Louise Mendius, LANL, for technical editing of abstracts and papers.

Mr. Michael C. Pankratz, LANL, for classification review of compiled papers.

Ms. Ruth N. Robichaud, LANL, for design and artwork of the CD label.

Ms. Leslie A Casey, NNSA, for review and clearance of abstracts and papers related to NNSA contracts and for providing financial support for the Proceedings.

Mr. Marvin D. Denny, NNSA, for technical review of abstracts and papers.

Dr. Christine M. Wehlburg, NNSA, for technical review of abstracts and papers.

Dr. Joseph C. Wehlburg, NNSA, for technical review of abstracts and papers.

Mr. William L. Andre, Space and Missile Defense Command (SMDC), for review and clearance of abstracts and papers related to SMDC contracts.

Ms. Mary L. Girven, Sandia National Laboratories (SNL), for making everyone's job easier with web-based technology for abstract and paper submission, on-line review and approval tools, and creation of the master files for the hardcopy and CD versions of the Proceedings.

Ms. Guadalupe (Lupe) Massoth, SNL, for providing assistance to Mary Girven on troubleshooting web related problems.

Dr. David B. Harris, LLNL; ***Dr. John J. Zucca,*** LLNL; ***Dr. CL Edwards,*** LANL; ***Dr. Steven R. Taylor,*** LANL; ***Dr. Dale N. Anderson***, Pacific Northwest National Laboratory (PNNL); ***Dr. Harry S. Miley,*** PNNL; ***Mr. J. Mark Harris,*** SNL; ***Mr. Preston B. Herrington,*** SNL; for a myriad of internal management and technical reviews of NNSA abstracts and papers.

Table of Contents - Volume I

1. Theme Paper 1

1-01 **Young, C., P. Herrington, J. Harris, C. Edwards, S. Taylor, J. Zucca, D. Harris, D. Anderson, H. Miley, M. Woods, and L. Casey**
Building the Knowledge Base: Transitioning Science from Research to Operations 3

2. Seismic Regional Characterization and Wave Propagation 15

2-01 **Ammon, C., G. Randall, J. Julia, R. Herrmann, E. Arias, and T. Diehl**
Systematic Inversion of Receiver Functions & Surface-Wave Dispersion for Crustal Structure in Central Asia 17

2-02 **Ammon, C., G. Randall, and J. Julia**
Improving Estimates of Depth, Magnitude, and Faulting Parameters of Earthquakes in Central Asia 24

2-03 **Ammon, C., R. Herrmann, M. Pasyanos, W. Walter, and M. Kosarian**
Simultaneous Inversion of Receiver Functions, Multi-Mode Dispersion, and Travel-Time Tomography for Lithospheric Structure Beneath the Middle East and North Africa 34

2-04 **Brown, W., T. VanDeMark, D. Doser, G. Keller, and A. Velasco**
An Integrated Geophysical Study of the Lithospheric Structure Beneath Libya 43

2-05 **Harris, D., F. Ringdal, E. Kremenetskaya, S. Mykkeltveit, J. Schweitzer, T. Hauk, V. Asming, D. Rock, and J. Lewis**
Ground-Truth Collection for Mining Explosions in Northern Fennoscandia and Russia 54

2-06 **Jiao, W. and W. Chan**
Broadband Seismic Experiments in Southwest and Northeast China 63

2-07 **Mackey, K., K. Fujita, H. Hartse, and L. Steck**
Seismic Regionalization in Eastern Russia 73

2-08 **Mooney, W., I. Artemieva, S. Detweiler, M. Billien, and J. Leveque**
Supplementing Ground Truth Data with Shear Wave Velocity, Seismic Attenuation, and Thermal Structure of the Continental Lithosphere 83

2-09 **Morozov, I., E. Morozova, S. Smithson, and L. Solodilov**
Deep Seismic Sounding Datasets for Seismic Calibration of Northern Eurasia 98

2-10 **Morozov, I., H. Li, J. Duenow, and S. Smithson**
Analyzing Peaceful Nuclear Explosion Arrival Codas for Crustal Properties 105

2-11 **Myers, S., J. Wagner, S. Larsen, A. Rodgers, K. Mayeda, K. Smith, and W. Walter**
Simulation of Regional Explosion S-phases (SiRES) Project 117

2-12 **Pasyanos, M., W. Walter, and M. Flanagan**
Geophysical Models for Nuclear Explosion Monitoring 125

2-13 **Priestley, K., S. Russell, V. Gaur, J. Lewkowicz, S. Mitra, and A. Maggi**
Broadband Seismic Studies in Southern Asia 135

2-14 **Rodgers, A., H. Tkalcic, and A. Al-Amri**
Data Collection in the Arabian Peninsula for Nuclear Explosion Monitoring 145

2-15 **Stevens, J., D. Adams, and M. Eneva**
Improved Surface Wave Dispersion Models and Amplitude Measurements 152

2-16 **Toksoz, M., S. Kuleli, C. Gurbuz, D. Kalafat, T. Bekler, E. Zor, M. Yilmazer, Z. Ogutcu, C. Schultz, and D. Harris**
Calibration of Regional Seismic Stations in the Middle East with Shots in Turkey 162

2-17 **Wu, R., X. Xie, Z. Ge, X. Wu, and T. Lay**
Quantifying Source Excitation and Path Effects for High Frequency Regional Waves 172

2-18 **Xie, J.**
Pn Q Under Tibet and Tienshan with Practical and Scientific Implications 182

3. Seismic Event Detection and Location 191

3-01 **Ballard, S.**
Seismic Event Location: Dealing with Multi-Dimensional Uncertainty, Model Non-Linearity and Local Minima 193

3-02 **Brazier, R., Y. Park, A. Nyblade, and M. Pasyanos**
Ground-Truth Events from Northeastern Africa 203

3-03 **Britton, J., D. Harris, I. Tibuleac, and J. Bonner**
Detection of Mining Explosions for a Southern Asia Seismic Database 211

3-04 **Erickson, J., D. Carlson, A. Ortiz, K. Hutchenson, L. Owiesny, G. Kraft, D. Anderson, and M. Tinker**
Station Correction Uncertainty in Multiple Event Location Algorithms and the Effect on Error Ellipses 220

3-05 **Kohl, B., H. Israelsson, and M. Fisk**
Advanced Concepts for Nuclear Explosion Monitoring Applied to Regional Events in the Artic Region 227

3-06 **Leidig, M., D. Reiter, J. Bonner, S. Johnson, I. Tibuleac, A. Rodgers, and H. Hooper**
Development of SSLOC3D: A Tool for Single-Station Locations of Small Seismic Events Using Regional 3D Velocity Models 237

3-07 **Minaya, E., P. Aliaga, G. Avila, C. Condori, and A. Cordova**
Neural Network and Wavelets Model in Seismic Location for the Central Andes of Bolivia 248

3-08 **Myers, S., D. Harris, M. Anderson, W. Rodi, W. Walter, M. Flanagan, and F. Ryall**
Relative Location Accuracy and Waveform Subspace Detector 259

3-09 **Pinsky, V., Y. Gitterman, A. Shapira, M. Ergin, and C. Gurbuz**
Improvements in Monitoring of Small Regional Events Based on Ground Truth Data in Turkey and Israel 269

3-10 **Richards, P., J. Armbruster, V. Burlacu, V. Cormier, M. Fisk, V. Khalturin, W. Kim, I. Morozov, E. Morozova, C. Saikia, D. Schaff, A. Stroujkova, and F. Waldhauser**
Seismic Location Calibration for 30 International Monitoring System Stations in Eastern Asia: Final Results 280

3-11 **Ringdal, F., T. Kvaerna, E. Kremenetskaya, V. Asming, S. Mykkeltveit, S. Gibbons, and J. Schweitzer**
Research in Regional Seismic Monitoring 291

3-12 **Rodi, W. and M. Toksoz**
Confidence Regions on Seismic Event Locations Based on Multiple-Event Analysis 301

3-13 **Rodi, W., S. Myers, and C. Schultz**
Grid-Search Location Methods for Ground-Truth Collection from Local and Regional Seismic Networks 311

3-14 **Rosca, A.**
Improved Regional Seismic Event Depth Estimation 320

3-15 **Saikia, C., R. Lohman, G. Ichinose, and M. Simons**
Ground-Truth Location Using a Synergy Between InSAR and Seismic Methods 324

3-16 **Steck, L., G. Randall, M. Begnaud, C. Rowe, and A. Velasco**
Karatau, Makanchi, and Location in Western China 334

3-17 **Thurber, C., W. Du, H. Zhang, and W. Lutter**
Methods for Improving Seismic Event Location Processing 342

3-18 **Tibuleac, I., E. Herrin, J. Britton, R. Shumway, and A. Rosca**
Automatic Secondary Seismic Phase Picking using Wavelet Transforms 352

4. Seismic Identification and Source Characterization 361

4-01 **Bonner, J., B. Stump, W. Walter, D. Pearson, C. Hayward, A. Velasco, D. Baker, C. Edwards, J. Lewkowicz, S. Harder, T. Wallace, S. Russell, M. Leidig, and S. Myers**
Planning Source Phenomenology Experiments in Arizona 363

4-02 **Bonner, J., D. Harkrider, M. Leidig, G. Herrin, B. Shumway, S. Russell, I. Tibuleac, and D. Reiter**
Estimating Ms From Short-Period (< 10 sec) Rayleigh Waves 373

4-03 **Bonner, J., H. Patton, A. Rosca, H. Hooper, J. Orrey, M. Leidig, and I. Gupta**
Aspects of Rg and Lg Generation from the Shagan Depth of Burial Explosions 384

4-04 **Bungum, H., T. Kvaerna, S. Mykkeltveit, M. Roth, K. Astebol, D. Harris, and S. Larsen**
Energy Partitioning for Seismic Events in Fennoscandia and NW Russia 394

4-05 **Jiao, W., W. Chan, R. Herrmann, and R. Wagner**
Discrimination Studies in the Yunnan Region, Southwest China 405

4-06 **Mayeda, K., T. Eken, A. Hofstetter, N. Turkelli, J. O'Boyle, G. Orgulu, and R. Gok**
Moment Magnitude Calibration for the Eastern Mediterranean Region from Broadband Regional Coda Envelopes 420

4-07 **Murphy, J., B. Barker, and W. Rodi**
Improved Focal Depth Determination for Use in Nuclear Explosion Monitoring 428

4-08 **Phillips, W., H. Patton, C. Aprea, H. Hartse, G. Randall, and S. Taylor**
Automated Broad Area Calibration for Coda Based Magnitude and Yield 437

4-09 **Richardson, E., A. Nyblade, W. Walter, and A. Rodgers**
Seismic Source Characterization and Energy Partitioning From In-Mine and Regional Broadband Data in South Africa 445

4-10 **Sammis, C.**
Scaling Laws for Secondary Seismic Radiation Generated by Fracture Damage 450

4-11 **Stevens, J., G. Baker, H. Xu, J. Bennett, N. Rimer, and S. Day**
The Physical Basis of Lg Generation by Explosion Sources 456

4-12 **Stevens, J., N. Rimer, H. Xu, G. Baker, J. Murphy, B. Barker, C. Lindholm, F. Ringdal, S. Gibbons, T. Kvaerna, and I. Kitov**
Analysis and Simulation of Cavity-Decoupled Chemical Explosions 466

4-13 **Taylor, S., X. Yang, W. Phillips, H. Patton, M. Maceira, H. Hartse, and G. Randall**
Regional Event Identification Research in Eastern Asia 476

4-14 **Walter, W., K. Smith, J. O'Boyle, T. Hauk, F. Ryall, S. Ruppert, S. Myers, M. Anderson, and D. Dodge**
Improving the Fundamental Understanding of Regional Seismic Signal Processing with a Unique Western United States Dataset 486

4-15 **Walter, W., M. Pasyanos, A. Rodgers, K. Mayeda, and A. Sicherman**
Regional Body-Wave Corrections and Surface-Wave Tomography Models to Improve Discrimination 495

4-16 **Zhou, R., B. Stump, Y. Chen, C. Hayward, Z. Yang, M. Templeton, X. Yu, S. Bai, and X. Xu**
Network Installation in the Yanqing-Huailai Basin and Preliminary Study of Natural and Man-Induced Events 504

Theme Paper

BUILDING THE KNOWLEDGE BASE: TRANSITIONING SCIENCE FROM RESEARCH TO OPERATIONS

Christopher J. Young,[1] Preston B. Herrington,[1] J. Mark Harris,[1] C. L. Edwards,[2] Steven R. Taylor,[2] John J. Zucca,[3] David B. Harris,[3] Dale N. Anderson,[4] Harry S. Miley,[4] Mark T. Woods,[5] and Leslie A. Casey[6]

Sandia National Laboratories,[1] Los Alamos National Laboratory,[2]
Lawrence Livermore National Laboratory,[3] Pacific Northwest National Laboratory,[4]
Air Force Technical Applications Center,[5] and National Nuclear Security Administration[6]

Sponsored by National Nuclear Security Administration
Office of Nonproliferation Research and Engineering
Office of Defense Nuclear Nonproliferation

Contracts No. DE-AC04-94AL85000, W-7405-ENG-36, W-7405-ENG-48, DE-AC06-76RLO1830

ABSTRACT

Nuclear explosion monitoring depends upon the accurate, continuous, and immediate processing of a vast amount of data to support the needs of decision makers. The Air Force Technical Applications Center (AFTAC) operates highly automated data collection and processing systems to support this mission. This data processing system requires extensive knowledge (e.g., station calibration and tuning parameters) to effectively monitor the earth for signs of nuclear explosions.

The National Nuclear Security Administration (NNSA) Ground-Based Nuclear Explosion Monitoring Research & Engineering (GNEM R&E) program has developed the process, infrastructure, and tools needed to manage the movement of research results into the NNSA Knowledge Base for evaluation and potential use by AFTAC. When possible, information in the NNSA Knowledge Base is put into a form used by the operational software. Thus, AFTAC can readily incorporate this information into its testbed for validation and appropriate baseline inclusion into operational pipeline processing. The NNSA Knowledge Base also facilitates use of information in an analyst-driven, special event-processing mode, in some cases by providing software tools included in the NNSA Knowledge Base itself.

This paper describes the life of a scientific data product from its conception as a research effort and development at a research institution, through its inclusion in a NNSA laboratory information product to its integration into the NNSA Knowledge Base, where after delivery it is tested and evaluated by AFTAC for use in the automated processing system or by event analysis staff.

Introduction

In this paper we describe the process that NNSA has developed to integrate research products into an NNSA Knowledge Base release. This process produces a well-integrated, scientifically validated, fully documented NNSA Knowledge Base that is fully compatible with AFTAC's procedures and software and that will help them with their monitoring mission. It is essential not only that the NNSA Knowledge Base be effective, but also that it be easy to use. Despite the tremendous size and complexity of the NNSA Knowledge Base, we seek to deliver a product that is as close as possible to "plug-and-play" when it is delivered to AFTAC for evaluation.

AFTAC's Treaty Monitoring Mission

AFTAC is the US agency tasked with monitoring of the earth environment in the context of international nuclear treaties. AFTAC accomplishes this monitoring mission by acquiring various types of sensor data (seismic, atmospheric and space, hydroacoustic, infrasonic, and radionuclide) from the field environments, and then processing it to look for possible nuclear events.

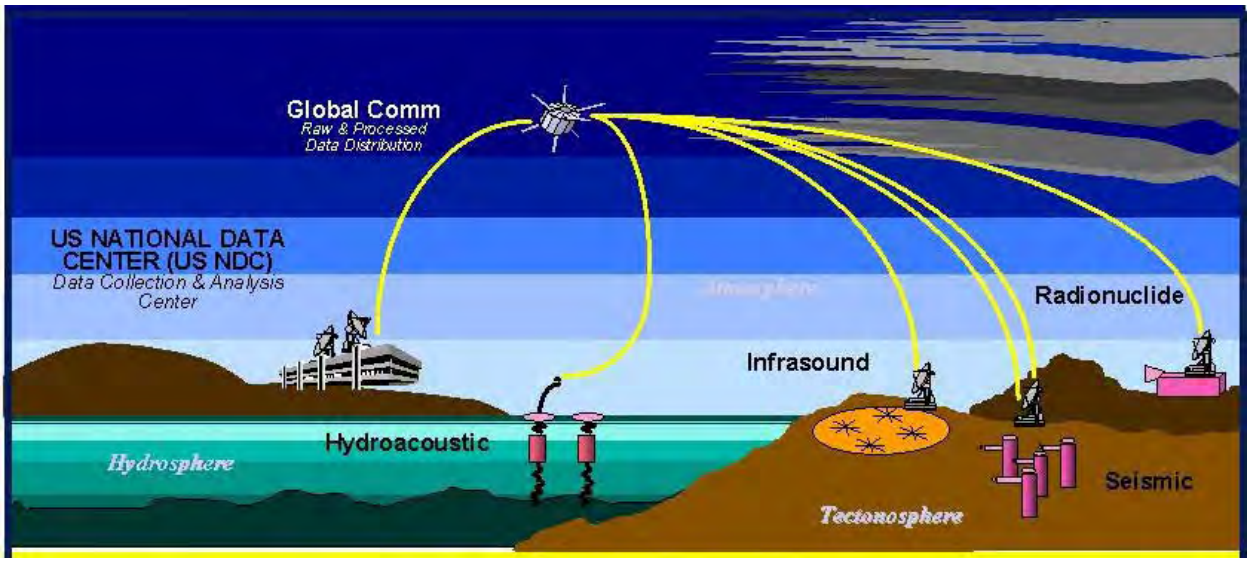


Figure 1. USNDC ground-based sensor data collection and transmission (from USNDC web site: http://www.tt.aftac.gov/overview.html).

The computer systems used to process the ground-based sensor data are in the United States National Data Center (USNDC) at AFTAC. The USNDC supports automated processing as well as interactive analyst review, and thus is the prime customer for any relevant monitoring research.

To better understand what types of research products might be of use for the USNDC, it is helpful to know a little about how the USNDC works. The core of the USNDC is an automatic data processing pipeline that feeds raw sensor data in at one end and produces a list of possible nuclear events at the other. To accomplish this, the data is processed through a series of steps that we briefly describe here in conjunction with Figure 2. Note that these steps hold for seismic, hydroacoustic, and infrasound data; processing for radionuclide data and data from satellite-based sensors is somewhat different.

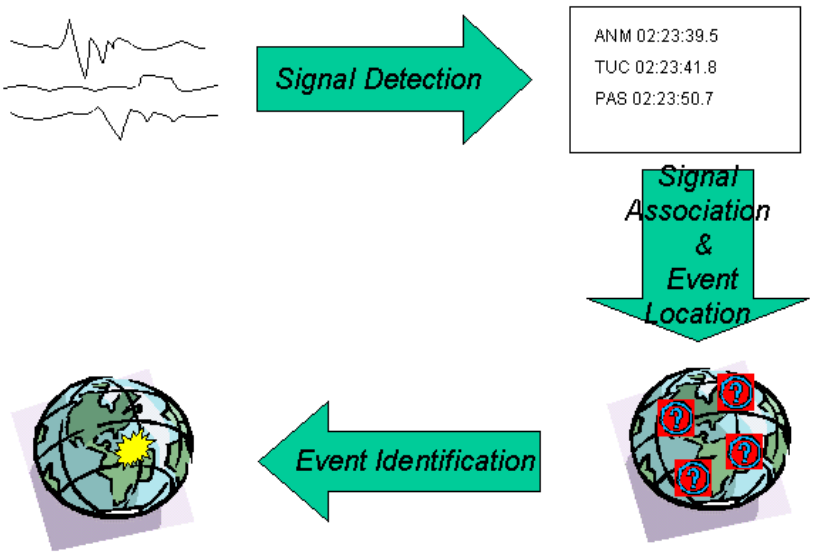


Figure 2. A simplified conceptual diagram of the USNDC pipeline processing tasks.

First, raw sensor data are processed to look for detections that might come from nuclear events. This analysis is a critical step because if no detections are found for an event, then regardless of the following steps, the event itself will not be found by the automatic processing. The next step is to group detections from the same event together. This grouping is known as association, and this step is closely related to the next step, event location, wherein the latitude, longitude, depth/elevation, and time of the event are determined. Once an event has been properly located, it can be categorized both by size (magnitude or yield) as well by event type (i.e., definite explosion, possible explosion, possible earthquake). The end result of processing data through these steps for a given time period is a list of well-located events with source types identified. Analysts then review these automatic event lists.

Every processing step is important, so improving any of them can have a significant impact on the quality of AFTAC's monitoring. Though the algorithms and procedures taken as a whole are diverse and complex, virtually all of them involve minimizing the difference between some observed quantity (i.e., raw or processed sensor data) and the corresponding predicted value (e.g., an arrival time of a seismic phase). Thus, to improve monitoring capability, one should seek either to improve the quality of the observations (e.g., more or better stations, better instrumentation, improved detection algorithms) or to improve the quality of the predictions (i.e., improved Earth models). NEM R&E includes both types of work, but the most voluminous contributions have focused on improving Earth models compiled in the NNSA Knowledge Base. Virtually any type of research product that can aid in modeling ground-based sensor data is of potential use for the NNSA Knowledge Base—i.e., 1-D travel time models, 3-D tomographic models, ground-truth event sets, topography maps, etc. There is no set list of types of products that do or do not belong in the NNSA Knowledge Base; if a research product can either directly or indirectly improve AFTAC's monitoring capability, then it should be considered for inclusion in the NNSA Knowledge Base.

The Role of the NNSA Knowledge Base

AFTAC requires an integrated, well-indexed, thoroughly validated NNSA Knowledge Base that is completely compatible with their methods and software. Conversely, most researchers' work is done in a developmental environment so they can focus on the important scientific issues, which are not generally dependent on specific data formats and operational algorithms. This gap between what AFTAC needs and what most researchers produce has historically resulted in a relatively small number of research products being utilized by AFTAC, despite the obvious potential relevance of many of them. AFTAC, as an operational user, does not have the resources to do the many things required to utilize these research products.

The NNSA GNEM R&E program has been very successful at bridging this gap. NNSA personnel are actively involved in monitoring research, so they are knowledgeable about the state of the art research. They are also familiar with the details of AFTAC's mission, so they can look for good matches between research products and operational

use. In addition, they have an excellent support infrastructure they can draw on to help them transition products from research to operations. Besides geophysicists, NNSA personnel include experts on nuclear phenomenology, databases, data formats, data integration, metadata, etc. The NNSA Knowledge Base provides a mechanism to get research products used at AFTAC so that the research investment achieves the intended national security enhancement.

Integration of Research Products

The NNSA Knowledge Base integration process is documented in a report by Gallegos et al. (2002). A summary diagram is shown below.

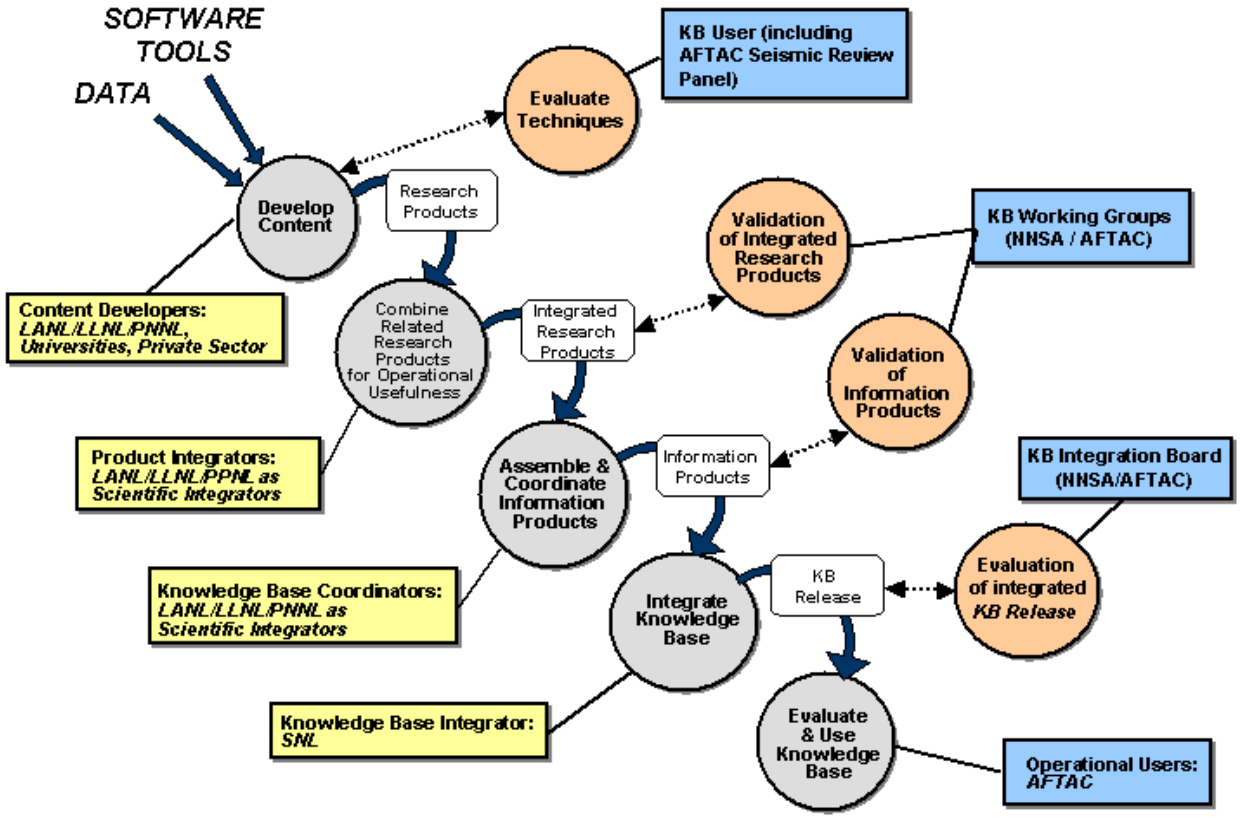


Figure 3. The NNSA Knowledge Base integration process

The process is complex and is outlined in the following 8 steps.

1. Develop Content

The first "step" in our process is really an ongoing process: scientists (*Content Developers*) constantly perform monitoring research and develop *Research Products* that have potential operational use at AFTAC. The necessary screening, reformatting, integration, and validation that enable these products to achieve their operational potential are performed in steps 2–8 of the NNSA Knowledge Base integration process.

2. Information Product Proposal and Approval

The next step in the process, the first real integration step, is to propose and plan the integration of *Research Products* into *Integrated Research Products* which are an aggregation and packaging of a suite of research products into an operationally useful form. *Integrated Research Products* then are further integrated into *Information Products* for the coming NNSA Knowledge Base release. An *Information Product* is a group of related *Integrated*

Research Products that address one of AFTAC's basic monitoring tasks (e.g., Detection, Association, and Location is one; Event Identification is another). The design of each of the Information Products is assigned to one of eight NNSA Knowledge Base *Working Groups* that are composed of researchers from the GNEM R&E labs and AFTAC. There is one Working Group per Information Product, and hence per AFTAC monitoring task. The *Integration Board*, comprised of NNSA and AFTAC program leaders evaluates each proposed *Integrated Research Product* for incorporation into the proposed NNSA Knowledge Base. The objective of the integration board is to assure that AFTAC's needs are addressed. They may reject an *Integrated Research Product* if it does not address an AFTAC need or suggest new products to fill unmet requirements.

3. Integrated Research Product Assembly

Once an *Integrated Research Product* proposal has been approved, the *Product Integrator* executes the plan to build it. The *Product Integrator* may solicit datasets or algorithms from the original contributor as part of the plan, and may refer the contributor to the NNSA Knowledge Base Contributor's Guide (Carr, 2002a) that guides him or her through the process of preparing datasets for transfer. For certain types of datasets, specific formats are required (e.g., Carr, 2002b), but often the formatting is done by the *Product Integrator* after receiving the *Research Product* from a contributor. The *Product Integrator* may ask the contributor for metadata, which help provide an audit trail for construction of the dataset or algorithm.

As part of product assembly, the *Product Integrator* will reformat data or recode algorithms to be compatible with AFTAC software. Extensive testing of the finished product follows to assure proper operational use. The *Product Integrator* creates extensive *Integrated Research Product* documentation (which includes any metadata), product installation procedures and tests, following NNSA templates.

4. Information Product Integration and Validation

By specified deadlines for each release, the *Integrated Research Products* (content and documentation) must be presented by the Scientific Integrator to Sandia National Laboratories (SNL), as the NNSA Knowledge Base Integrator, for integration in conjunction with the appropriate Working Groups into *Information Products*. SNL validators check product contents against documentation, and attempt to run installation tests. The validators iterate with *Product Integrators* to resolve any problems encountered.

In parallel with the integration and testing of the content of the *Information Product* at SNL, an *Information Product* document is created by one of the *Information Product Editors* based at Los Alamos National Laboratory (LANL) and Lawrence Livermore National Laboratory (LLNL) from component *Integrated Research Product Documents* sent to the *Editors* by *Knowledge Base Coordinators* at each laboratory. When each *Information Product* document is complete, it is sent to the *Knowledge Base Integrator* for assembly into comprehensive documentation for the entire NNSA Knowledge Base.

5. NNSA Knowledge Base Integration and Testing

Once the *Integrated Research Product* components of the *Information Products* have been put in place and unit level tested, the proposed NNSA Knowledge Base is assembled. A graphical interface to the proposed NNSA Knowledge Base is built using a new NNSA tool known as the Knowledge Base Navigator. The Navigator provides a simple "point-and-click" style interface that allows users rapid and intuitive access to the vast holdings of the Knowledge Base.

The tool combines a hierarchical file browser with a map that can be used to show the spatial extents for *Integrated Research Products* or to find *Integrated Research Products* by specifying a spatial location (e.g., the border of a given country). The Navigator also can launch all of the software tools delivered with the NNSA Knowledge Base. Working Group correlated *Information Products* are organized as folders within the Navigator interface; constituent *Integrated Research Products* are found in subfolders. Within the *Integrated Research Product* subfolders are additional folders that hold product components and automatically launch the installation tests for the product. Folder contents can be associated with keywords such as "group velocity model" and "phase match filtering" so that they can be found using Navigator's keyword search capability. Contents also can be linked with a geographic polygonal region showing the area of coverage, enabling the product to be found by a geographic search.

6. Integration Board Approval

The *Integration Board* reviews individual *Integrated Research Products*, and assesses the quality of the proposed NNSA Knowledge Base as a whole, aided by the Navigator and the now complete documentation in the accompanying *Information Product* document. This review can result in deferral of products to later releases to allow more development or redirection of products based primarily on optimizing operational usefulness. The *Board* assures that products pass all integration crosschecks, that all content has been delivered, and that validation testing has been passed. It also verifies proper integration of product documentation.

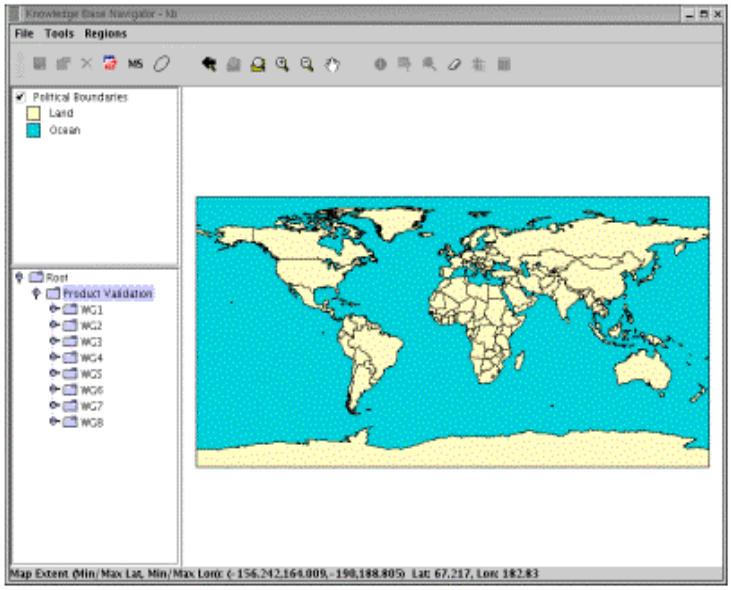


Figure 4. A fictional KB as presented through the KB Navigator

7. NNSA Knowledge Base Delivery and Demonstrations

The approved NNSA Knowledge Base is delivered to AFTAC, which involves more than a simple transfer of files. Some re-configuration must be done on-site to account for any system differences between the NNSA Knowledge Base development test area at SNL and the AFTAC target system. Products are re-tested to assure that nothing has been broken during delivery. The fully tested NNSA Knowledge Base delivery is demonstrated to AFTAC by teams of NNSA researchers who travel to AFTAC, describe the use of the products and provide hands-on training.

8. AFTAC Evaluation of the NNSA Knowledge Base

AFTAC personnel critically evaluate the NNSA Knowledge Base. Generally NNSA Knowledge Base calibration products and tools are evaluated on AFTAC data to test effectiveness for various monitoring tasks. Performance is the most important criterion, but organization, ease of use, and completeness of metadata are also factors. Detailed feedback for each product is provided to NNSA *Product Integrators*, which guide product updates and new product development. Following evaluation, AFTAC chooses suitable parts of the NNSA Knowledge Base for implementation and invoke their internal configuration control procedures.

List of Data Types Integrated

Table 1 lists data types that have been, or are expected to be, integrated by the NNSA program. The table lists also the type of scientific integration performed (second column) and the end use or product developed (third column). The table makes clear that the NNSA program seeks a very wide range of data, models, and algorithms for integration into the NNSA Knowledge Base. We make no attempt to describe the details of this table here, but present two representative examples of integration.

Table 1. Data types integrated by the NNSA program, integration performed, and end products

Data Type	Integration Performed	End Uses / Products
Catalogs, bulletins • Event descriptions • Picks • Aftershock studies	Reconciliation of all catalogs into a unified master catalog Ground-truth event collection and validation Travel-time tomography and other model construction Kriged travel-time correction surface generation	Driver for event waveform segment extraction Travel-time model validation Velocity models Phase travel-time correction surfaces
Waveform data, from: • Major providers: AFTAC, IRIS, USGS • PASSCAL deployments • Joint BAA/ROA deployments • Local network data • Other sources	Event waveform segment extraction – waveform database construction Phase arrival time and amplitude measurement integration into unified catalog Full-waveform modeling to estimate source parameters and velocity models Source phenomenology studies Coda shape calibration	Phase amplitude correction surfaces MDAC amplitude correction models Source models Discriminants Coda magnitude calibrations Base velocity models
Source ground-truth information • Earthquake mechanisms, depths, moments • Explosion yields, shot configuration data, emplacement data	Coda parameter estimation MDAC parameter estimation Discriminant calibration Source phenomenology studies	Coda magnitude calibration and yield estimation MDAC amplitude correction models Explosion models Discriminants
Geophysical information • Velocity models • Surface wave slowness maps • Attenuation maps • Geologic maps • Contextual data	Validation on AFTAC and NNSA test data Travel-time ray tracing MDAC parameter estimation Unified geophysical model construction	Base geophysical models Travel-time models MDAC amplitude correction models Contextual database for analysts Ms phase-match calibrations
Derived Measurements • Surface wave dispersion	Surface wave dispersion and attenuation tomography	Surface wave dispersion maps and models Moment tensor estimation Ms phase-match calibrations
Algorithms • Signal processing • Array • Location and discrimination • Error propagation • Inversion	Validation on AFTAC and NNSA test data Assessment for calibration potential Recoding to use AFTAC / KB pipeline software libraries	Pipeline detection, global association, location and identification functions Analyst event review/reanalysis Calibration methods Error assessment

Representative Integration Examples

Our first example is the construction of a surface wave dispersion map useful in phase-match filtering to estimate Ms and potentially full-waveform moment tensor inversions. A very high-quality, five-degree, global surface wave model is available from Stevens and McLaughlin (1997), which the NNSA labs are using as a baseline (Figure 5, where the top panel shows the 20-second Rayleigh velocity map). We are developing complementary, two-degree, high-resolution regional maps to be embedded into the Stevens-McLaughlin background model. Results of this embedding process are illustrated in the middle and lower panels of Figure 5. The middle panel shows the same model overlayed by an NNSA-developed, high-resolution Western Eurasia and North Africa (WENA) tomography model. Slow velocities from sedimentary basins like the Caspian Sea and Persian Gulf are more clearly delineated in the regional model. Finally, the bottom panel shows the blending of the WENA models with the Stevens and McLaughlin model, providing global coverage.

To build the WENA high-resolution regional velocity model, we systematically measured Rayleigh and Love wave group velocities (Pasyanos et al., 2001) and integrated measurements from a number of other research groups. In the WENA region we examined more than 25,000 seismograms and made more than 15,500 Rayleigh wave measurements and 10,000 Love wave measurements at periods from 8–150 seconds. We exchanged group velocity curves with other research groups and incorporated more than 3,000 path measurements from the University of Colorado (Ritzwoller, written communication) and SAIC/Maxwell (Stevens, written communication).

Our second example illustrates the extension of the 3-degree Eurasian coda Q map for 1 Hz Lg of Mitchell *et al.* (1997) with a 2-degree inset attenuation tomography map (Figure 6, white outline). The high-resolution regional map was developed using a set of 1,651 events recorded at 12 stations. For central Asian events, this high-resolution map provides a variance reduction of 27% over the prior model of Mitchell *et al.,* (1997) and 67% over an initial constant Q model of 418 (the average of the Mitchell *et al.,* 1997 model).

We have been investigating the utility of Bayesian methods as a way to incorporate and refine tomographic maps as part of the integration process. By using a Bayesian approach, tomographic maps provided to the NNSA laboratories can be used as prior background models in order to produce high-resolution refined maps in critical areas. The resulting refined tomographic models smoothly blend into the prior background models. Moreover, the uncertainties are well established in a Bayesian framework. We have been using Bayesian tomography for regional phase attenuation models (Taylor *et al.,* 2003), surface wave slowness models (Maceira and Taylor, 2003), and surface wave attenuation models (Yang *et al.,* 2003).

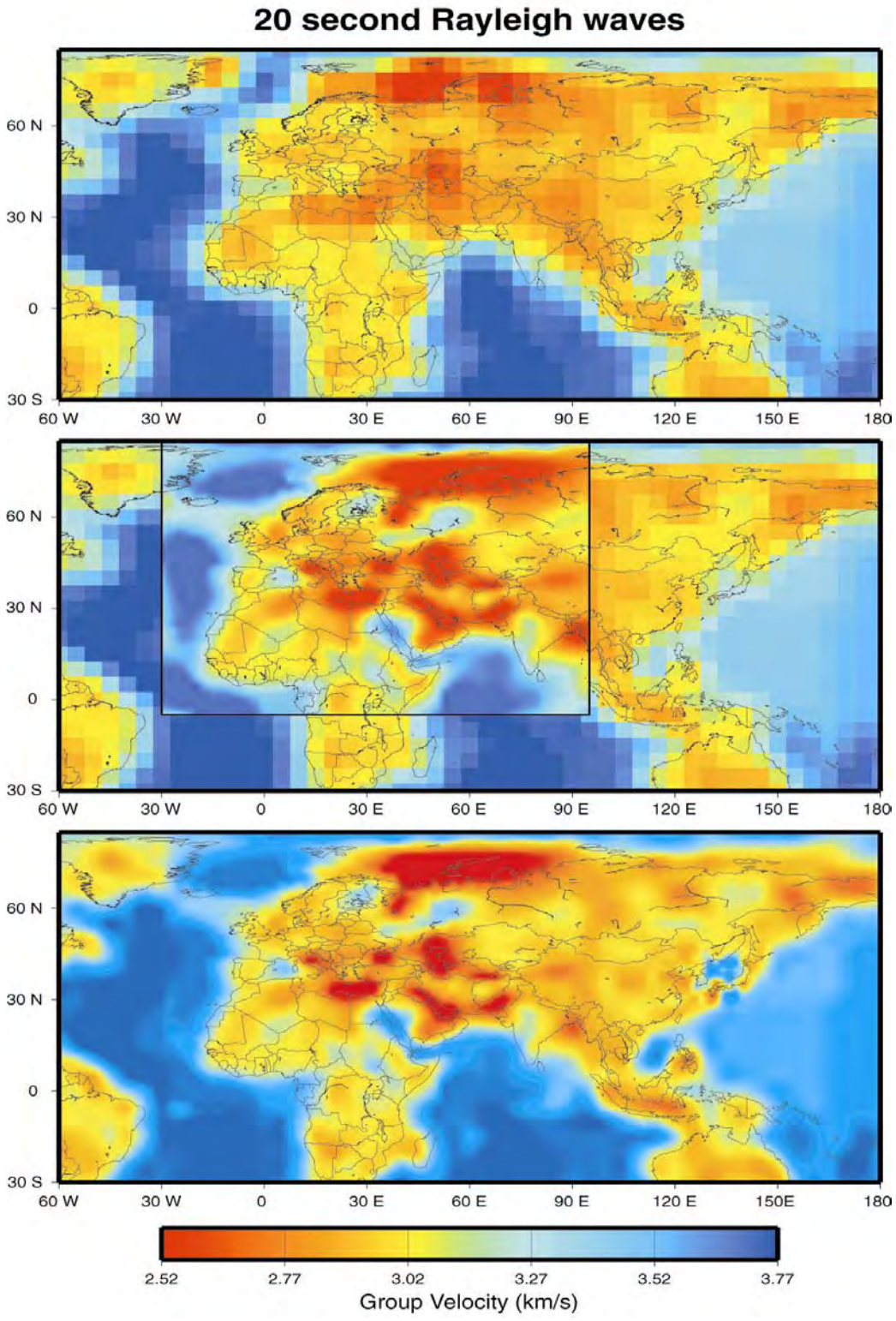


Figure 5 Example of blending two-degree regional surface wave tomography maps into a five-degree global baseline map. Original 20-second Rayleigh wave group velocity map (top) of Stevens and McLaughlin (1997). High-resolution inserts superimposed (middle). Blended map with global coverage (bottom). The five-degree background map has been interpolated to the higher-resolution grid.

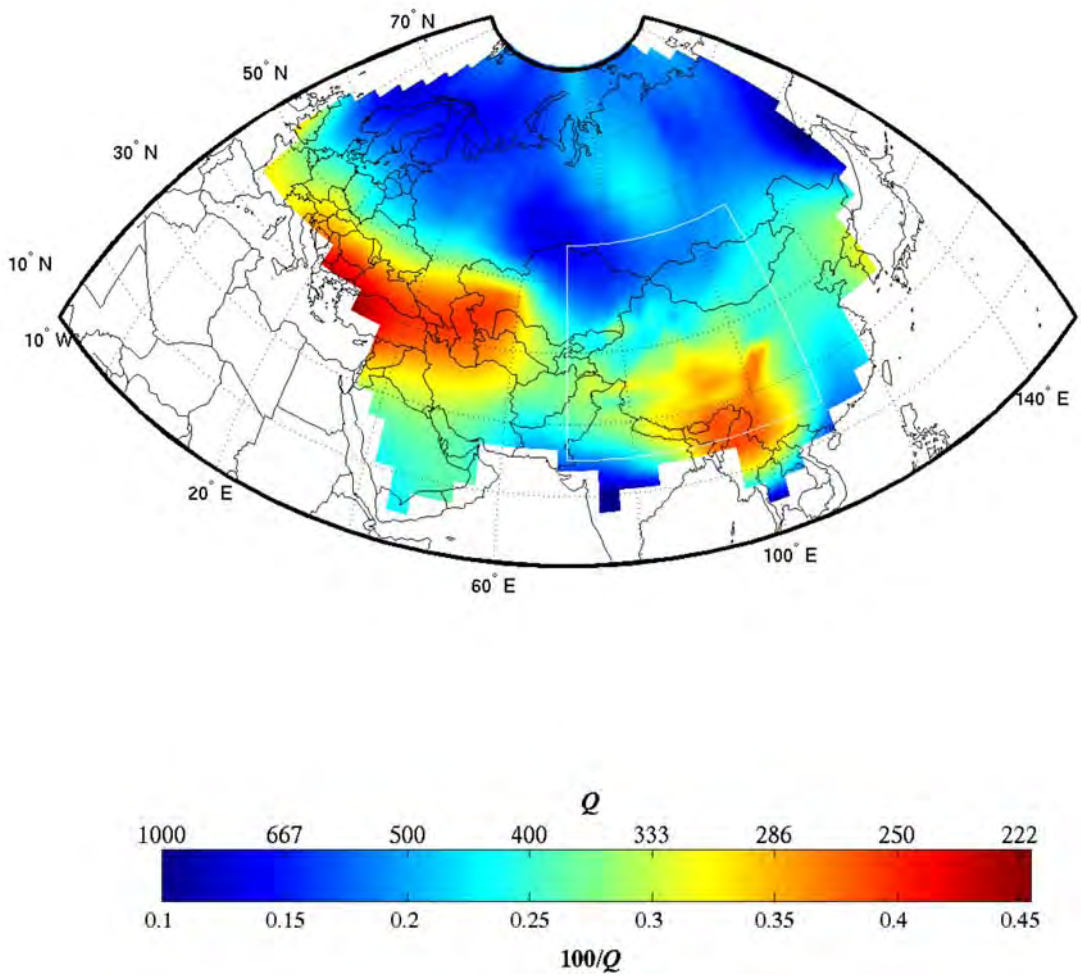


Figure 6. Two-degree attenuation tomography map for 1 Hz Lg of Figure 2 (white outline) blending into 3 degree Lg coda Q map of Mitchell et al. (1997).

SUMMARY

The valuable *Research Products* from relevant nuclear explosion monitoring research (largely represented at this Seismic Research Review) must be put into an operationally useful form to effectively improve national security. The NNSA GNEM R&E program has developed the process, infrastructure, and tools needed to manage the movement of nuclear monitoring research results into the NNSA Knowledge Base for evaluation and use by AFTAC for their nuclear treaty monitoring mission. The NNSA Knowledge Base integration process has greatly increased the number of research products that reach operational usefulness at AFTAC. The process exploits unique NNSA resources (personnel and support infrastructure) to bridge the gap between the disparate worlds of nuclear monitoring research and nuclear monitoring operations, thereby greatly benefiting both AFTAC and the research community by making optimum use of government resources.

REFERENCES

Carr, D. B. (2002a), National Nuclear Administration Security Knowledge Base Contributor's Guide, Sandia National Laboratories Report SAND2002-2771 (Revised, available at https://www.nemre.nnsa.doe.gov/cgi-bin/prod/nemre/index.cgi?Page=Knowledge+Base).

Carr, D. B. (2002b), National Nuclear Security Administration Knowledge Base Core Table Schema Document, Sandia National Laboratories Report SAND2002-3055 (available at https://www.nemre.nnsa.doe.gov/cgi-bin/prod/nemre/index.cgi?Page=Knowledge+Base).

Carr, D. B (2003), Assembling the NNSA Knowledge Base, 25th Seismic Research Review - *Nuclear Explosion Monitoring: Building the Knowledge Base*.

Gallegos, D. P., D. B. Carr, P. B. Herrington, J. M. Harris, C. L. Edwards, S. R. Taylor, J. J. Zucca, D. B. Harris, N. A. Wogman, D. N. Anderson, and L. A. Casey (2002), The Integration Process for Incorporating Nuclear Explosion Monitoring Research Results into the National Nuclear Security Administration Knowledge Base, Sandia National Laboratories Report SAND2002-2772 (available at https://www.nemre.nnsa.doe.gov/cgi-bin/prod/nemre/index.cgi?Page=Knowledge+Base).

Maceira, M. and S.R. Taylor (2003), Short-period surface-wave tomography in central Asia and its application to seismic discrimination, *Seism. Res. Lett*., 74, 212.

Mitchell, B.J., Y. Pan, J. Xie, and L. Cong (1997), Lg coda Q variation across Eurasia and its relation to crustal evolution, *J. Geophys. Res.*, 102, 22,767-22,779.

Pasyanos, M. E., W. R. Walter and S. E. Hazler (2001). A surface wave dispersion study of the Middle East and North Africa for monitoring the comprehensive nuclear-test-ban treaty, *Pure. Appl. Geophys*., 158, 1145-1474.

Stevens, J.L., and K.L. McLaughlin (1997), Improved methods for regionalized surface wave analysis, Phillips Laboratory Report PL-TR-97-2135, 26 pp.

Taylor, S.R., X. Yang, and W. S. Phillips (2003), Bayesian Lg attenuation tomography applied to eastern Asia, *Bull. Seism. Soc. Am.*, 93 795-803.

Yang, X., H.J. Patton, and S.R. Taylor (2003), 20-sec Rayleigh-wave attenuation tomography in central Asia, *Seism. Res. Lett.*, 74, 213.

Seismic Regional Characterization and Wave Propagation

SYSTEMATIC INVERSION OF RECEIVER FUNCTIONS & SURFACE-WAVE DISPERSION FOR CRUSTAL STRUCTURE IN CENTRAL ASIA

Charles J. Ammon,[1] George E. Randall,[2] Jordi Julia,[1] Robert B. Herrmann,[3] Eliana Arias,[1] and Theresa Diehl[1]

Penn State University,[1] Los Alamos National Laboratory,[2] Saint Louis University[3]

Sponsored by National Nuclear Security Administration
Office of Nonproliferation Research and Engineering
Office of Defense Nuclear Nonproliferation

Contract No. DE-FC03-02SF22498

ABSTRACT

We report on our investigations into the seismic structure of the lithosphere in central Asia using surface waves and receiver functions. We are relying on global and regional tomographic analyses for long-period surface-wave dispersion constraints on the structure, which we supplement with short-period observations measured directly from regional signals (when available). We will present an overview of receiver function complexity across the region using results from previous studies and receiver functions from many of the permanent stations. We have completed short-period tomographic imaging of the central and eastern Tibetan Plateau using Love and Rayleigh-waves with periods between 10 and 40 seconds period. The short period information is critical to tight constraints on shallow shear-wave velocity structure, but the measurements are sensitive to source location and origin time uncertainties. We have also surveyed receiver functions from the INDEPTH III experiment and estimated Poisson's ratio variations across the south-central Plateau. We will illustrate the combined inversion of surface-waves and receiver functions using a variety of model constraints focusing on select stations including WMQ, MAK. Our initial efforts have focused on permanent stations and temporary stations for which data are already in hand.

OBJECTIVES

Our objectives are the construction of shear-velocity profiles for regions surrounding broad-band seismic stations throughout central Asia. Application of the technique in the region provides an opportunity to revise models of the crust and upper mantle structure throughout the region and to exploit the global and regional work of previous seismic verification research (*e.g.* Pasyanos et al., 2001; Ritzwoller & Levshin, 1998, Larson and Ekstrom, 2001, Stevens and McLaughlin, 2001). The resulting shear-velocity models provide a single structure consistent with a range of observations and which can be tested as a tool for the construction of mode isolation filters that can help improve surface-wave magnitude estimated. We also plan to explore the possibility of adding additional data to our inversions of receiver functions, surface-wave dispersion. The diverse seismic activity throughout the region will facilitate cross-validation of the mode isolation filters with simple empirical filters constructed using larger events with adequate signal-to-noise ratios.

Background

Much of the background for this project is identical to that found in “Simultaneous Inversion of Receiver Functions, Multi-Mode Dispersion, and Travel-Time Tomography for Lithospheric Structure Beneath the Middle East and North Africa”, by Ammon *et al.*, which appears elsewhere in these proceedings. We refer the reader to this other work for additional background information.

The Joint Inversion of Receiver Functions and Surface-Wave Dispersion Curves

The receiver function is sensitive to velocity transitions and vertical travel times, surface-wave dispersion measurements are sensitive to aver-ages of the velocities, and relatively insensitive to sharp velocity contrasts. The complementary nature of the signals makes them ideal selections for joint study because they can fill in resolution gaps of each dataset. Ammon and Zandt (1993) pointed this out in a study of the Landers region of southern California (although for their specific case, available observations were unsuitable to resolve subtle features in the lower crust) and Ozalaybey et al. (1997) and Last et al. (1997) have performed complementary analyses of surface-wave dispersion and receiver functions and Du and Foulger (1999) and Julia et al. (2000) implemented joint inversions of these data types. The mechanics of the inversion are relatively simple since partial derivatives of dispersion observations (Herrmann, 1995) and receiver functions waveforms *(e.g.*, Randall, 1989, Ammon et. al, 1990) can be calculated quickly and accurately. For more details on the method, we refer the reader to Ammon et al. (these Proceedings).

RESEARCH ACCOMPLISHED

Surface-Wave Group-Velocity Imaging of Central Tibet

A critical aspect of constructing an accurate shear-velocity model of the upper crust is the availability of short-period surface-wave observations. Global (Larson and Ekstrom, 2001) and broad regional (Ritzwoller and Levshin, 1998) studies provide very good coverage of the longer period dispersion. In some areas we have relatively closely spaced stations that can allow improvements to these studies on much small scales. Tibet is an area that has drawn much attention due to its tectonic importance. Several field experiments have produced data that can be used to supplement existing studies and improve resolution. As part of our lithospheric imaging efforts, we have combined data recorded within Tibet during the last 13 years for small-to-moderate size earthquakes in an effort to refine group velocity maps of the plateau. Specifically, we gathered waveforms from 190 events located predominantly within the Plateau and recorded on 29 stations that at one time have been deployed within, or immediately adjacent to the Plateau. Although we made measurements for periods from 6 to 45 seconds, periods less than 10 seconds contained sparse measure-ments and we were not able to perform a useful tomography at these shortest periods.

Sample results for 10 seconds period are shown in Figure 1. To interpret the maps it is necessary to know where the resolution is sufficient. We tested the maximum resolution using checkerboard tests with noise-free numerical “data” computed using the same distribution as the actual observations and inverted using the same smoothness and damping weights that were employed in the inversion. The test results are shown in Figure 2 and indicate that a small

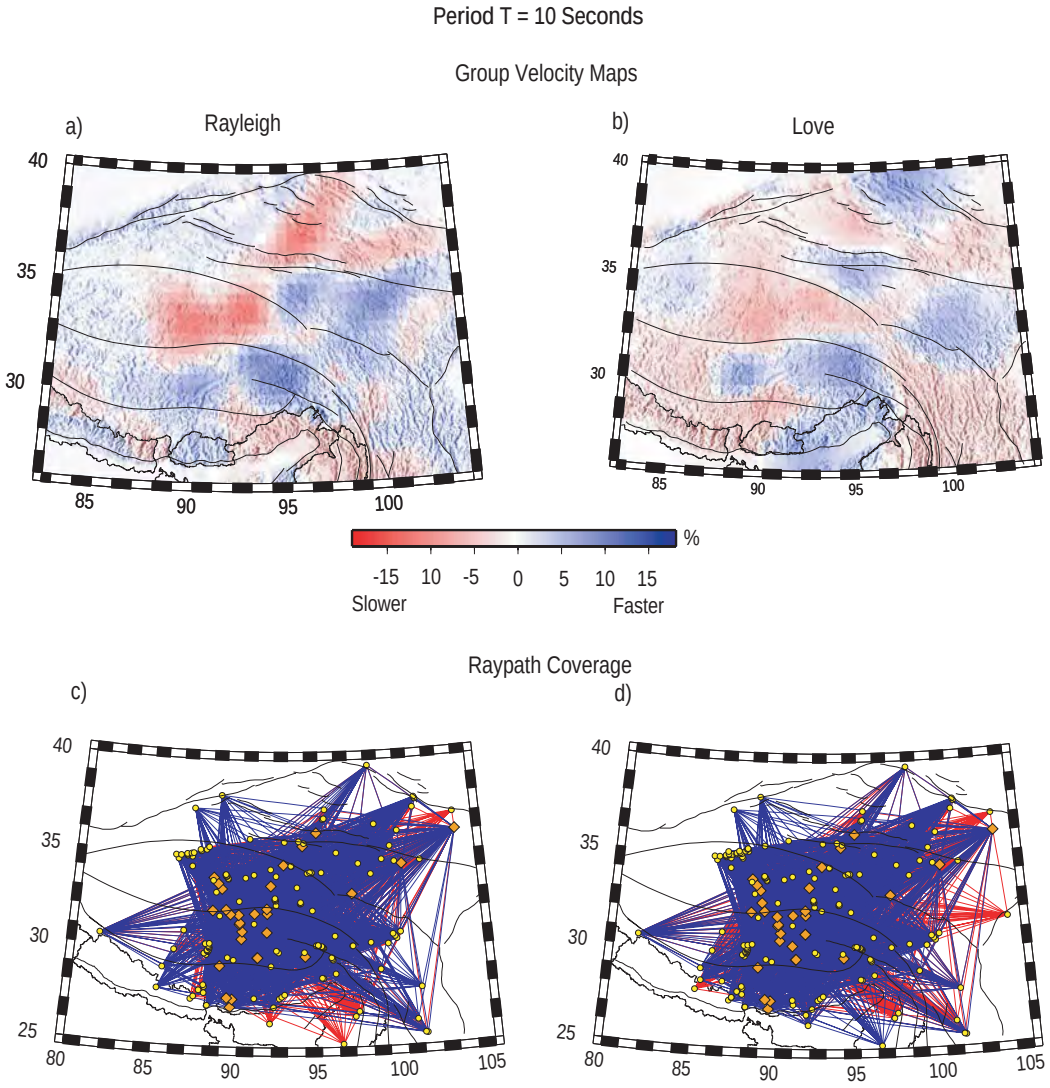


Figure 1. Tomographic results for Rayleigh and Love waves for a period of 10 seconds. The symbols in the lower panels indicate events (yellow circles) and stations (orange diamonds). Not all the stations were operating simultaneously. Paths shown as blue are faster than average, paths shows as red are slower than average.

region near the center of the model is the only area where the spatial resolution is sufficient, although even in the adjacent regions broad averages are constrained by the data. In the region of good resolution, the heterogeneity follows the terrain boundaries. At 10 seconds, the Qiangtang terrain appears to be relatively slow compared with the Lhasa terrain. The boundary between these anomalies nicely follows the suture separating the two terrains.

Our plan is to combine these group velocity information with receiver functions across the region to improve our estimates of the subsurface shear velocity. At present we are experimenting with relocating the events using the group delays to reduce the scatter in the measurements (which is substantial since most paths are short).

Receiver Function Computation

Our focus on receiver function analysis so far is on permanent stations and temporary networks that have completed their monitoring. Data that we have begun to process at the time this report was written are shown in Figure 3. Our

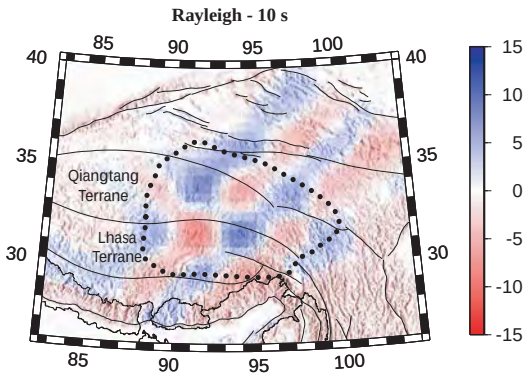


Figure 2. Results of a resolution test for 10-second Rayleigh waves. The target pattern was a checkerboard pattern with ±2.5% slowness variations and a spatial variation of 2.5°. Smoothness prohibits us from recovering sharp features, but the resolution near the center of the model is ideally reasonable. The dotted curve outlines the area of reasonable resolution.

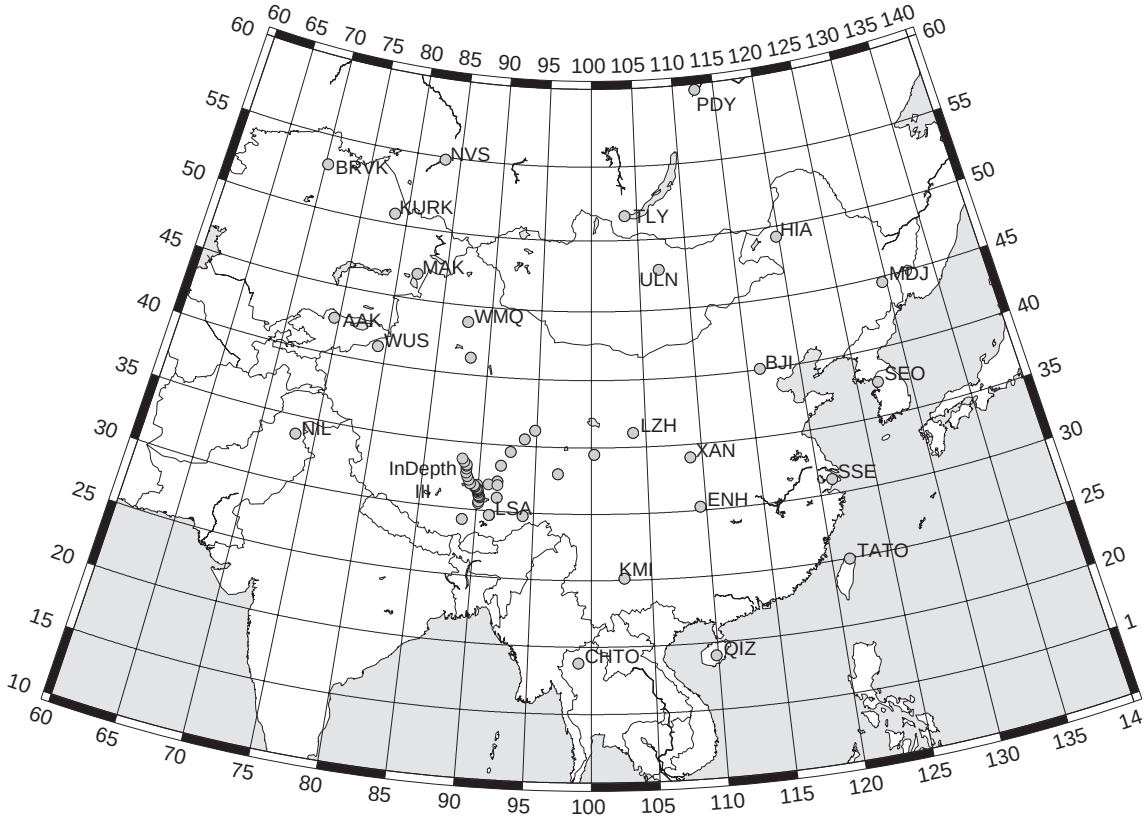


Figure 3. Open stations that we have targeted for analysis as part of this project. The stations are located in a range of environments and most have some regional activity nearby that we can use to add short-period dispersion measurements and to test the resulting shear-velocity models.

approach is relatively simple, we select the station, gather teleseismic P-waveforms for events greater than magnitude 5.5, compute receiver functions using an iterative time-domain approach (Ligorria and Ammon, 1999), and then select the best receiver functions for analysis. Depending on the station, we may cluster the receiver functions as a

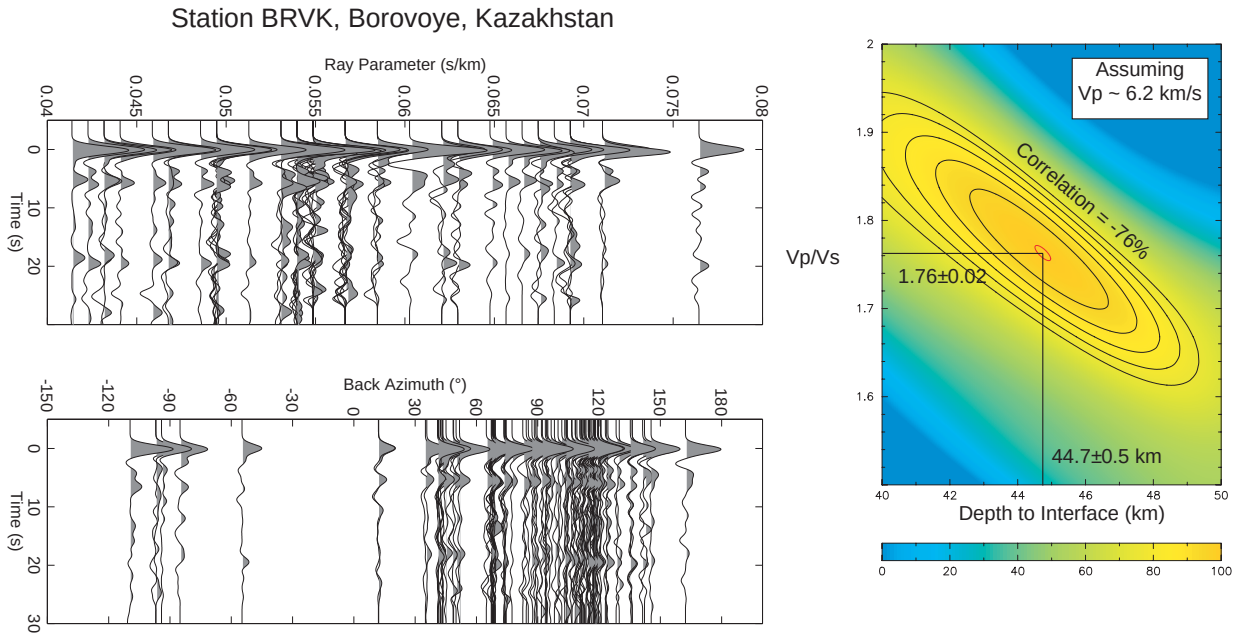


Figure 4. Sample receiver function observations and a limited analysis of Poisson's ratio and crustal thickness (assuming Vp ~ 6.2 km/s). The observed receiver functions are shown as a function of ray parameters (sin of the P-wave incident angle) and as a function of back azimuth. The data do not sample the azimuthal structure uniformly as teleseisms are predominantly observed from western-Pacific subduction zones. The ray parameter sampling is good, and identifiable conversions and multiples are seen clearly for a range of incident angles. The image on the right shows the results of stacking all waveforms to identify the crust-mantle transition. Uncertainties were estimated using a jack-knifing technique. These uncertainties are conservative since they also depend on the assumed P-velocity of the crust. As a result of azimuthal sampling, the results are most reflective of the structure to the east of the station.

function of back azimuth and ray parameter (the amount of data determines the feasibility of this approach). Our analysis usually begins with a relatively simple stacking procedure that allows the estimation of the Vp/Vs ration (or Poisson's ratio) and crustal thickness (Zhu and Kanamori, 2000). The analysis produces relatively good estimates when the simple assumptions (relatively flat crust-mantle boundary) are satisfied. Example receiver functions for station BRVK in central Asia are shown in Figure 4. Receiver functions generally vary with azimuth and ray parameter and so we summarize our observations in two profiles to show the variation with each. As a first order approximation of the structure, we've ignored azimuthal variation and performed a stacking procedure to use the waveforms to estimate the thickness and Poisson's ratio of the crust (assuming that Vp ~ 6.2 km/s) using the method of Zhu and Kanamori (2000). The resulting fits are reasonable, with a thickness value of about 45 km and a Poisson's ratio of 0.26. We will perform similar analyses and inversions for each station with suitable data.

We have examined a subset of the InDepth III broadband seismic profile located in central Tibet (Figure 3). We have estimated receiver functions and performed the waveform stacking procedure to estimate the crustal thickness and Poisson's ratio along the roughly north-south profile (Diehl, 2003). The results from "A" and "B" quality stations are shown in Figure 5. The crustal thickness shows thicker sections to the south, consistent with earlier results. The Poisson's ratio values are more variable and hard to interpret. The complications may be reflective of the relatively simple assumptions of the method which include a relatively flat crust-mantle boundary and isotropy. We have not recovered any evidence that favors a region of high Poisson's ratio between 30.5°N and 32.5°N, which was suggested by Kind et al. (2002). More work is needed to complete the imaging of the entire profile before a final assessment can be made.

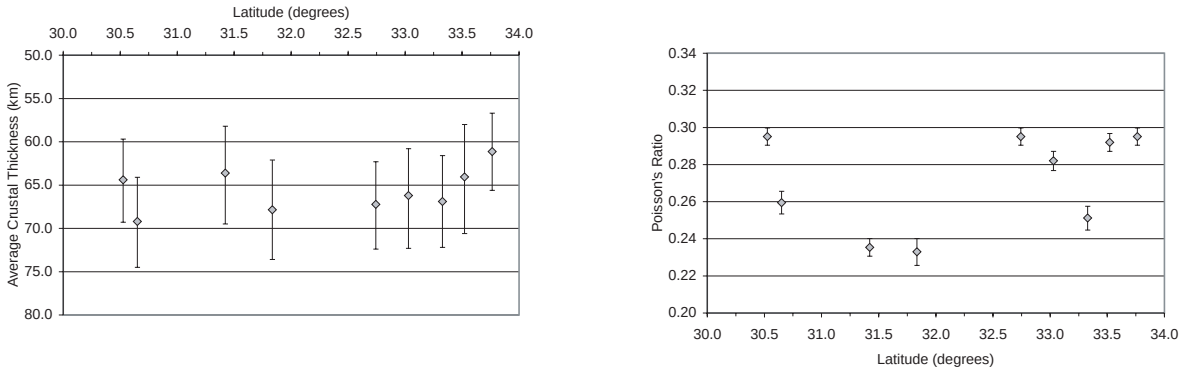


Figure 5. Quality results from an analysis of the inDepth III profile receiver functions using the Vp/Vs crustal thickness tacking method of Zhu and Kanamori (2000). The left panel shows a general thinning of the crust from south-to-north. Poisson's ratio's are more variable. Most of the quality values are between 0.26 and 0.29. The low values near the center of the profile are hard to justify geologically. Our results differ from those of an earlier study.

CONCLUSIONS AND RECOMMENDATIONS

Obviously, our next step is to begin combining our surface-wave and receiver functions into joint shear-velocity inversions. Sharing the group velocity measurements with other groups involved in tomography is also part of our plan, although larger-scale tomographic studies with heavy smoothing may oversimplify the details necessary for imaging variations in shallow crustal structure.

ACKNOWLEDGEMENTS

We thank the P. Wessel and W. H. F. Smith, the authors of GMT for producing easy-to-use, quality software for making maps and charts.

REFERENCES

Ammon, C.J., G.E. Randall, and G. Zandt (1990), On the non-uniqueness of receiver function inversions, *J. Geophys. Res.*, 95, 15303-15318.

Ammon, C. J., and G. Zandt (1993), The receiver structure beneath the southern Mojave Block, *Bull. Seism. Soc. Am.*, 83, 737-755.

Diehl, T. M., Determining Crustal Structure Beneath the Tibetan Plateau Using Receiver Functions, *B. S. Thesis*, Penn State University, University Park, PA, 2003.

Du, Z.J. and G.R. Foulger (1999), The crustal structure beneath the northwest fjords, Iceland, from receiver functions and surface waves, *Geophys. J. Int.*, 139, 419-432.

Herrmann, R. B., *Computer Programs in Seismology, 1995*, Saint Louis University, St. Louis, MO, USA.

Jackson, D.D., Interpretation of inaccurate, insufficient, and inconsistent data (1972), *Geophys. J. R. Astron. Soc.*, 28, 97-109.

Julia, J., C. J. Ammon, R. B. Herrmann, and A. M. Correig (2000), Joint Inversion of receiver function and surface-wave dispersion observations, *Geophys. J. Int.* 143, 99-112.

Kind, R., J. Yuan, J. Saul, D. Nelson, S.V. Sobolev, J. Mechie, W. Zhao, G. Kosarev, J. Ni, U. Achauer, and M. Jiang, Seismic Images of Crust and Upper Mantle Beneath Tibet: Evidence for Eurasian Plate Subduction, *Science*, 298, 1219-1221, 2002.

Larson, E. W. F. and G. Ekström (2001), Global Models of Group Velocity, *Pure and Applied Geophys.*, 158, 1377-1399.

Last, R. J., A. A. Nyblade, C. A. Langston and T. J. Owens (1997), Crustal structure of the East African Plateau from receiver functions and Rayleigh wave phase velocities, *J. Geophys. Res.*, 102, 24,469-24,483.

Ligorria, J.P., and C.J. Ammon, Iterative deconvolution of teleseismic seismograms and receiver function estimation, Bull. Seism. Soc. Am., 89, 1395-1400, 1999.

Özalaybey, S., M.K. Savage, A.F. Sheehan, J.N. Louie, and J.N. Brune (1997), Shear-wave velocity structure in the northern Basin and Range Province from the combined analysis of receiver functions and surface waves, *Bull. Seismol. Soc. Am.*, 87, 183-199.

Pasyanos, M.E., W.R. Walter, and S.E. Hazler (2001), A surface wave dispersion study of the Middle East and North Africa for monitoring the Comprehensive Nuclear-Test-Ban Treaty, *Pure and Applied Geophys*, 158, 1445-1474.

Randall, G. E. (1989), Efficient calculation of differential seismograms for lithospheric receiver functions, *Geophys. J. Int.*, 99, 469-481.

Ritzwoller, M. H. and A. L. Levshin (1998), Eurasian surface wave tomography: Group velocities, *J. Geophys. Res.*, *103*, 1839-1878.

Stevens, J. L. and K. L. McLaughlin (2001), Optimization of Surface Wave Identification and Measurement, *Pure and Applied Geophys*., 158, 1547-1582

Zhu, L., and H. Kanamori (2000), Moho depth variation in Southern California from teleseismic receiver functions, *J. Geophys. Res.*, 105 (2), 2969-2980.

IMPROVING ESTIMATES OF DEPTH, MAGNITUDE, AND FAULTING PARAMETERS OF EARTHQUAKES IN CENTRAL ASIA

Charles J. Ammon,[1] George E. Randall,[2] and Jordi Julia[1]

Penn State University,[1] Los Alamos National Laboratory[2]

Sponsored by National Nuclear Security Administration
Office of Nonproliferation Research and Engineering
Office of Defense Nuclear Nonproliferation

Contract No. DE-FC04-00AL67668

ABSTRACT

Accurate and stable seismic source parameters for small-to-moderate size events are essential for many aspects of regional nuclear explosion monitoring. For example, magnitude and distance amplitude corrections (MDAC) have been developed for regional discrimination, but they rely on stable moment estimates. We develop a catalog of regional earthquakes in eastern Asia with estimated seismic moments, source mechanisms, and depths using regional seismic data. A significant challenge of modeling small-to-moderate-size seismic sources is the necessity of relying on short-period signals with long travel paths that have substantial sensitivity to earth structure along the path. When the path effects are unknown or difficult to account for, we must rely on components of seismic signals that are minimally dependent on the structure. Although regional surface-wave phases are strongly influenced by structure, surface-wave amplitude spectra can be modeled adequately with relatively simple earth models, and these spectra carry valuable information on source character. Our efforts build on existing seismic source analysis techniques. We directly model regional seismograms where possible but combine those with surface-wave amplitude spectra observed at more distant stations. The inversion is performed using a grid search for strike, dip, rake, moment, and depth. When available, we also include long-period body-wave trains, which can be modeled reliably using simple stratified earth models. The use of spectra and long-period signals is ideal for estimating the moment and faulting geometry of signals but simple least-squares norms based on these signals do not often provide satisfactory resolution of source depth (when the source is shallow). However, in cases where the long-period mechanism is relatively stable as a function of depth, we can overcome this limitation by exploiting signals more diagnostic of source depth such as teleseismic body-waveforms, broad-band Pn waveforms, or select short-period Rayleigh wave spectra. We use an L1 norm for all the modeling, scaling each signal's misfit by the signal power. Once the best mechanism is identified we search for a weighted L1 optimal seismic moment with confidence intervals.

OBJECTIVE

Estimating the source type or faulting geometry of small seismic events located hundreds of kilometers from the nearest seismometer can be difficult. Typically one of two classes of modeling approaches are adopted: Spectral or time-domain. Spectral techniques use the observed variation in surface-wave spectra as a function of azimuth to match the radiation pattern of the source (*e.g.* Patton, 1976, 1980, 1998; Herrmann, 1976, 1979; Romanowicz, 1982; Patton and Zandt, 1992; Herrmann and Ammon, 1997, and many others). Time-domain methods are straight-forward matches to the observed seismograms and include both amplitude and phase information (*e.g.* Langston, 1981; Dreger and Helmberger, 1991, 1992, 1993; Lay et al., 1994; Randall et al., 1995; Ghose et al, 1998; Ammon et al., 1998, and others). Spectral methods can be designed to include amplitude only, or amplitude and phase information, while time-domain methods include both. Phase information provides valuable constraints on the source mechanism and depth, but the observed phase is often sensitive to details in Earth structure along the propagation path. Time-domain source inversion methods are usually applied to large events with good long-period signals or short-period signals of small events that have minimal distortion from Earth structure (such as teleseismic P and SH waves) or local and close-regional (less than a few hundred *km*) signals. To use phase in surface-wave spectral analyses works best with a good estimate of the surface-wave phase velocity variations between the source and receiver.

If we consider the problem addressed in nuclear explosion monitoring, the best signals from a shallow small event are most likely to be short-period surface waves. But directly fitting the phase of short-period Rayleigh waves (probably the best regionally observed, deterministic signal from a small, shallow event) is challenging because these waves are sensitive to shallow, variable structure along the propagation path. Rayleigh-wave spectral amplitudes are less sensitive to structure variations than the corresponding signal phase, and contain valuable information on the source depth. Thus it is desirable to combine the part of distant signals that is less sensitive to structure with the amplitude and phase information from the closer stations.

Simultaneous Spectral and Time-domain Seismic Source Modeling

To achieve this, we combine surface-wave spectral amplitude modeling and time-domain waveform fitting in a grid-search algorithm to estimate the source mechanism (systematically check strike, dip, rake, and depth, & include an isotropic source for comparison). The procedure includes surface-wave amplitude information for all stations and includes both amplitude and phase information from the closer observations (either complete three components or Pnl) and teleseismic body waves if the event is large enough for these to be observed (Figure 1). Incorporating observations from more distant stations makes a significant contribution to seismic source studies in two important ways: First, the azimuthal coverage of radiation patterns is improved and second, Rayleigh wave amplitude spectra contain information on the source depth. For shallow events, improved resolution of the depth requires short-period information because the information on shallow depths are contained in the short-period signals. Herrmann (1979) exploited information in intermediate-period surface waves to estimate the faulting geometry and depth of earthquakes in the east and central North America from old analog records. He observed signals out to distances of thousands of kilometers and extracted spectral amplitudes suitable for constraining the earthquake parameters. Our experience suggests that observations from such large distances in central Asia are not as simple or robust as those in the stable part of North America (*e.g.* Levshin et al.,1990). The signal amplitudes are complicated due to scattering and intrinsic attenuation, but generally well observed for larger events (Mw ~ 5). However, signals from small events may be isolated from background noise and extracted using phase-match filtering exploiting dispersion observations from larger events.

RESEARCH ACCOMPLISHED

The goal of estimating source depth with some precision requires a combination of observations. Particularly valuable in constraining earthquake depth are short-period Rayleigh waves, which may contain a spectral notch indicative of source depth (e.g. Herrmann, 1979) but often shown systematic amplitude variations that vary with depth. Short-period surface waves can be tricky and when analyzing the signals some form of mode isolation can help simplify their interpretation. Currently we use group velocity windows with spectral smoothing to simplify the seismic signals, but preliminary studies of the impact of mode isolation indicates that it is often not necessary for

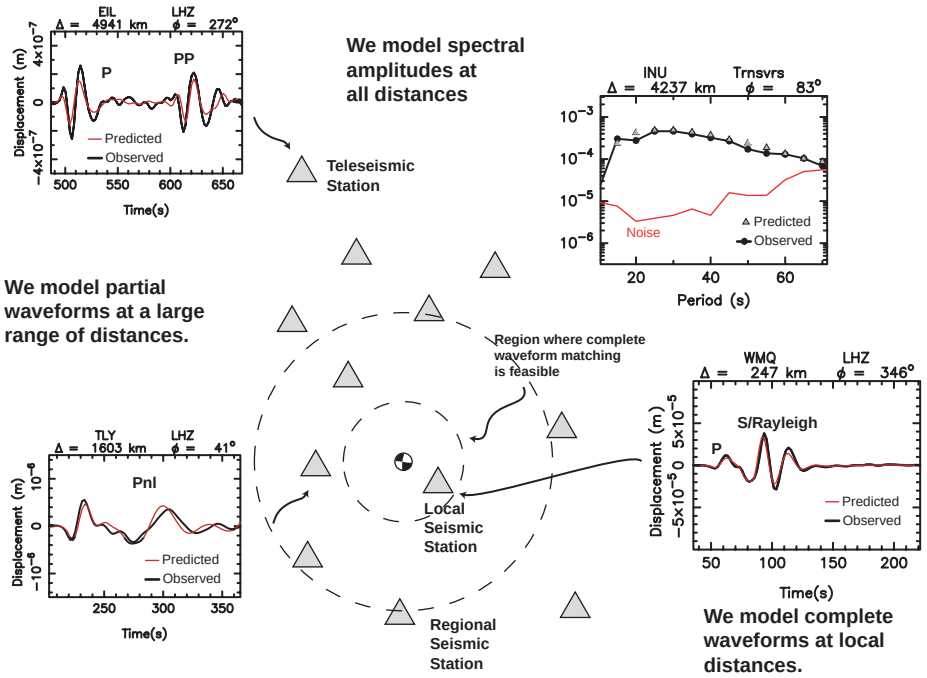


Figure 1. Schematic illustration of the joint source parameter inversion scheme. The triangles represent seismic stations, the focal mechanism represents the source location. The basic idea is to combine observations with a minimal sensitivity to earth structure to produce more accurate estimates of the event mechanism and depth. Since most observations are too far for direct short-period waveform modeling we sacrifice the phase information and use only the more robust spectral amplitudes at those sites. Phase information is included from seismograms recorded at nearby stations, teleseismic P-waves, or regional *Pnl* arrivals. Sample observations and predictions are shown around the margins.

larger events - or it adds little improvement. That may not be the case when event signals are small and separation from background noise requires some form of signal enhancement.

Our primary control on the source mechanism arises from the azimuthal variation of Rayleigh and Love wave spectra. Nearby time-domain signals provide the required phase information as well as additional information on the mechanism and often the most sensitivity to depth. All spectra are estimated using a windowed autocorrelation function which produces smoother and statistically more reliable spectral amplitudes. This procedure requires substantially more time than using the FFT amplitude spectrum since the smoothing requires that we incorporate periods adjacent to those used in the misfit norm. However, the smooth, statistically-better measures should be more valuable for analyses of path effects and systematic variations in signals at particulate stations. The seismic moment for each mechanism tested in the grid search is estimated using an L1 fit to the logarithm of spectral amplitudes of all the signals. Green's functions are computed using a generic model of a slightly thicker than average (46 km) continent resting on an earth-flattening transformed version of the isotropic Preliminary Reference Earth Model (PREM).

Our early inversions revealed that many of the data available from the global seismic networks are noisy or contain other problems that render them unsuitable for use in an inversion. To identify a problem, we visually inspect all the data in the bandwidth from 100 to 20 seconds period to identify signals with grossly inadequate signal-to-noise ratios. To insure that we rely more heavily on the best observations, we weight each spectral observation by the inverse of the ambient seismic noise at the same period. The ambient noise is estimated using the pre-P-wave signal. Each signal's spectrum is also weighted relative to all other spectra using the mean of spectral amplitude of the noise in the period range of interest. Distant stations are down-weighted using a simple one-over-distance measure. This is strictly a pragmatic approach designed to include our *a priori* assumption that the model we are using is probably best suited

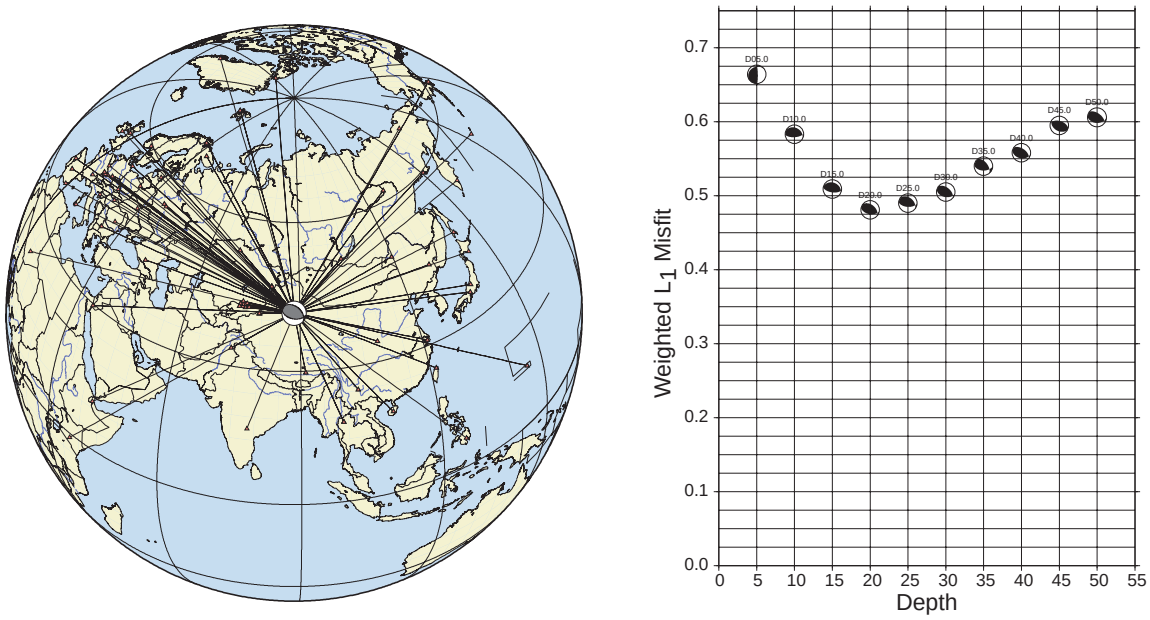


Figure 2. Sample inversion results for event with Harvard ID B013099A. The paths from the source to the station are shown on the left, the mechanisms on the right are plotted on the right. The best depth is 20 km but solutions at 25 km are also acceptable. Sample observed-predicted fits were used to illustrate the inversion ideas in Figure 1.

for short paths. Interestingly, we have found little correlation of misfits with distance, suggesting that we are able to fit the most distant observations with the same fidelity that we fit the intermediate distance observations. Azimuthal bias in station coverage is moderated by weighting observations by the number of other signals within 15° azimuthal range of the particular observation. In other words, a signal separated from all others by a gap of more than 15° has an azimuthal weight of 1.0 and a signal with 4 other signals within 15° has an azimuthal weight of 0.2 (1/5, including the observation). Automating the weights substantially reduces the time needed to adjust the parameters during an inversion. Observation weights reflect our attempts to cope with the problems of driving an inversion with a single-number norm.

Although each event is different, the combination of these observations can produce good depth, mechanism, and seismic moment constraints. Data coverage and results for an example inversion are shown in Figure 2. The event was located in Southern Xinjiang, China and occurred on 1999 01/30 03:51:5.00. This inversion included 123 signals, including 3 complete seismograms recorded at nearby station WMQ, 10 vertical component P-waveforms, 2 radial component Pnl waveforms, 71 Rayleigh-wave spectra, and 37 Love-wave spectra. We fit just over 50% of the power in the weighted signals (visually the fits are very good). The estimated depth is 20 km, the seismic moment is 1.02e24 (M_W = 5.3), and the mechanism corresponds to roughly north-south compression with a near-vertical tension axis. The variation in the complete norm shown in Figure 2 does not necessarily reflect the variation in fit to just the time-domain signals. To identify such instances we track 8 norms: vertical-radial complete- and partial-waveform seismogram misfits, Rayleigh-wave spectral misfits, transverse component complete seismogram misfit and Love-wave spectral misfit, and the combination of all misfits (that was used in Figure 2).

Uncertainties

We have investigated two approaches to quantifying uncertainties. For seismic moment uncertainty, we estimate the weighted L1 misfit optimal moment using a grid search employing the best fitting dislocation. A by product of the grid search is a moment versus misfit curve (Figure 3). Note the strong asymmetry in the misfit versus moment curve.

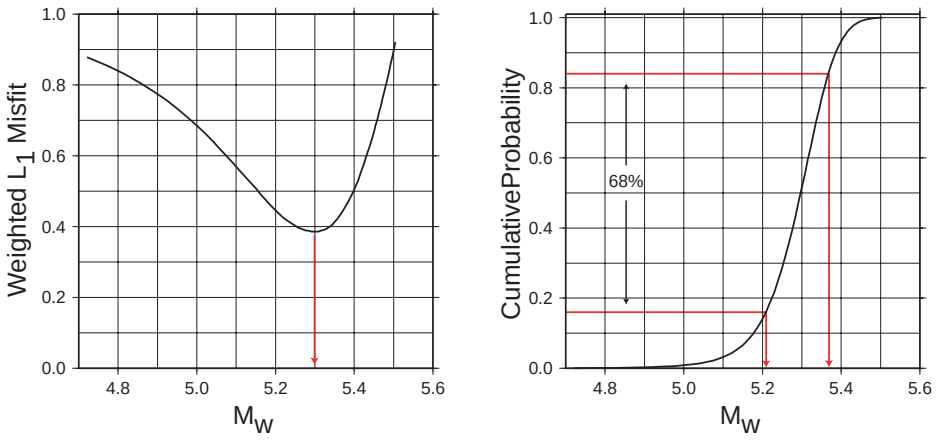


Figure 3. Moment versus weight, L1 misfit is shown on the left and a cumulative probability distribution derived from the misfit curve is shown on the right. The red lines indicate the range containing 68% of the probability around the best fitting solution (the same area associated with one standard deviation). The asymmetry in the misfit curve is reflected in asymmetry in the confidence range.

This is a consequence of misfit arising from a number of non-simple sources, including Green's function inadequacy, background seismic noise, *etc.* We can estimate a confidence interval using the misfit curve if we can estimate the equivalent of a standard deviation in the observations. Based on experience with different velocity models, propagation geometries, etc., we assumed a value of 0.1 for an effective absolute deviation width normalization constant (an equivalent of a "standard deviation"). With this value defined, we can map the misfits into an exponential likelihood function, which we can integrate as shown on the right in Figure 3.

We can identify various likelihood values on the curve and estimate ranges for different confidence intervals. For the example event (optimal M_W = 5.3), we found a 68% confidence range in M_W was 5.20 to 5.36; a 95% confidence range of 5.07 to 5.43; and a 99% confidence range of 4.82 to 5.48. The single-standard deviation equivalent range of 0.1 lower and 0.06 higher is relatively good and equivalent to errors calculated from large-size Harvard CMT solutions. The larger values on the more demanding confidence intervals grow to the point where you can see differences in all of the observed-predicted comparisons. We believe that these numbers include the effects of assuming what different models would have on the results, this scales the misfit by 0.1 when mapping into a likelihood function.

To estimate uncertainties in the dislocation parameters, we explore the variation in individual misfit measure such as vertical, radial, transverse seismograms and vertical and transverse spectra, into separate norms. We use a multiple-objective optimization (MOO) approach to identify the solutions optimal for each of our tracked misfit norms. The MOO framework allows the identification of solutions that bound the region of feasible solutions (Ammon, 2003). A two-dimensional example is illustrated in Figure 4 and 5. Figure 4 is a map of dislocation misfits for the case of seismograms and spectral split into two separate norms. A search for solutions that are not dominated by other solutions (no other solution has a lower misfit in at least one of the two norms for the solutions). The non-dominated solutions form the boundary surrounding the range of feasible solutions. They are shown in red in Figure 4. The mechanisms associated with the non-dominated solution are shown in Figure 5. Most solutions are roughly east-west reverse fault with one exception. The exception corresponds to the best fitting solution for amplitude spectra only. The inclusion of any information on time-domain signals eliminates this solution from serious consideration, but the example illustrates the short-comings of inversions without phase information. Formally, this solution produces amplitude spectra very similar to those of the other mechanisms. The lack of phase information allows a 90° rotation of the tension axis with little change in the amplitude spectra. The Pareto solutions span a depth range of 15-25 km, but the range narrows to 20-25 km as soon as we consider seismogram misfits. The moment magnitude for all the solutions is 5.3 and the estimated uncertainties were discussed earlier. Our preferred solution is that closest to the ideal solution (shown in blue in Figure 4). This is the dislocation is the closest to best fitting both data sets which we

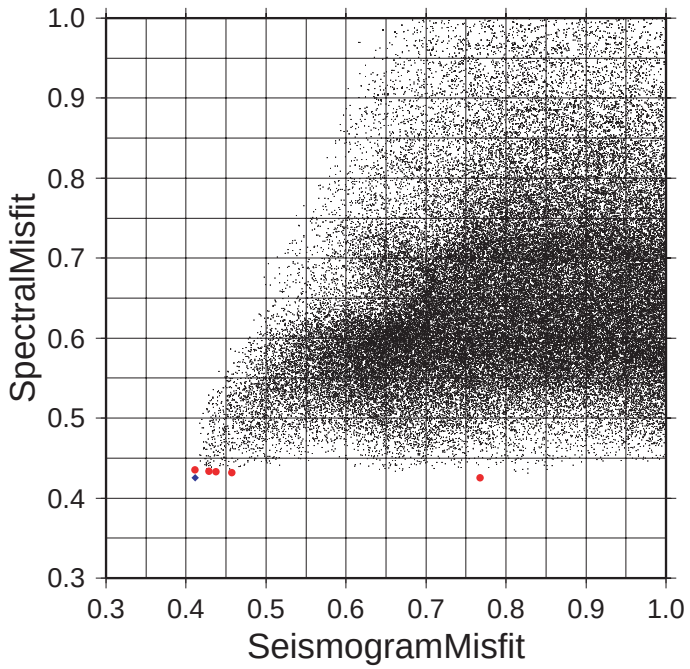


Figure 4. Two-dimensional objective space created by combining all of our time-domain misfits and our spectral amplitude misfits into two norms. The misfits associated with each dislocation are shown as black points. The blue point identifies the ideal solution (the ideal solution identified with the lowest value in each norm). The red points show the Pareto set, solutions not dominated by any other solutions. The Pareto solution far to the right is associated with the best norm for the amplitude spectra, but does not fit the seismograms.

can fit either independently. In this case the solution has a strike, dip, and rake of 310, 40, 120, respectively, and a depth of 20 km.

Joint Amplitude-Spectra/Seismogram Grid-Search Inversion Results

Preliminary grid-search results are shown in Figure 6. In general our results agree with the Harvard mechanisms, although often some rotation of the mechanisms is required by our data and occasionally we appear to have less control on the mechanism. Perhaps the most interesting difference is the dependence of the seismic moment difference between Harvard and our analyses on seismic moment. For moderate-size events ($M_W > 5.5$) our moments agree well with Harvard's, for events near the threshold of the CMT method, more often than not the Harvard CMT moment is larger than the moments derived by us (Figure 7). No doubt some of the difference arises from the different models used in each method and our moment is really a fit of the spectrum from 80 to 20 seconds, for the smaller events, Harvard's moment is generally more appropriate near 40 seconds period (when only body waves are used). Most interesting is the character of the discrepancy which suggests a systematic difference as a function of moment. For the smaller magnitude events, the misfit is substantial when inspecting the time-domain signals. All events with a grid-search moment magnitude less than 5.0 are produce positive residual magnitudes (which indicates overestimation by Harvard or underestimation by us). Such differences may reflect the excitation functions for the different velocity structures assumed in each method, and while they cannot be resolved completely (moment depends on the assumed structure), the differences can be important are worth noting.The moment-magnitudes obtained from the two waveform modeling techniques agree better than either does with Ms. A comparison of the grid-search M_W and the USGS Ms is shown in Figure 7. For simplicity, we've assumed the same uncertainty in grid search M_W as exists in the Harvard CMT solution. Here the trend is the opposite with M_S for smaller events under-predicting their size. The trend is unchanged if you use the Harvard CMT moments - the differences are larger.

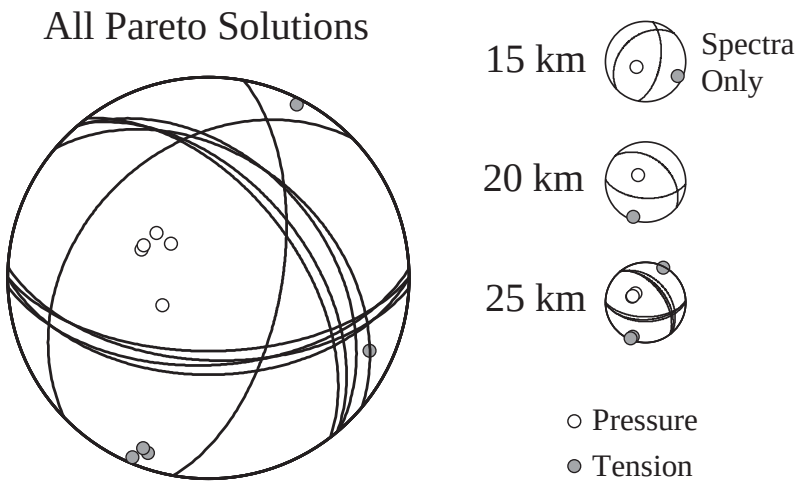


Figure 5. Pareto solutions for the example inversion. The mechanisms cluster tightly with one exception. The "outlier" solution corresponds to the lowest amplitude spectral misfit. The lack of phase information allows a 90° rotation of the T axis and still produces a good fit. The other solutions include amplitude and phase information and correspond to the preferred solution.

CONCLUSIONS AND RECOMMENDATIONS

The addition of teleseismic body waves directly into the inversion will also help refine the depths of the larger events for which the body-wave signals are adequate. It may be possible to simply use the teleseismic to estimate depth, fixing the moment and mechanism from the spectra and regional seismograms. Then a relatively easy-to-implement cross-correlation misfit norm, which requires little effort on aligning the signals, could be used to estimate the depth. For the shallowest events, inspection of short-period surface waves from nearby stations may help confirm source depth and add important confidence to the grid-search results. Such additional information is subjective but there may be no likely way to avoid classifying solution quality without some fuzziness. Seismic signals are complex and their sensitivity to different aspects of the source are difficult to quantify with easily computed misfit norms.

ACKNOWLEDGEMENTS

We thank the P. Wessel and W. H. F. Smith, the authors of GMT for producing easy-to-use, quality software for making maps and charts and T. J. Pearson, author of PGPLOT library, for producing a robust, flexible, well-documented graphics library.

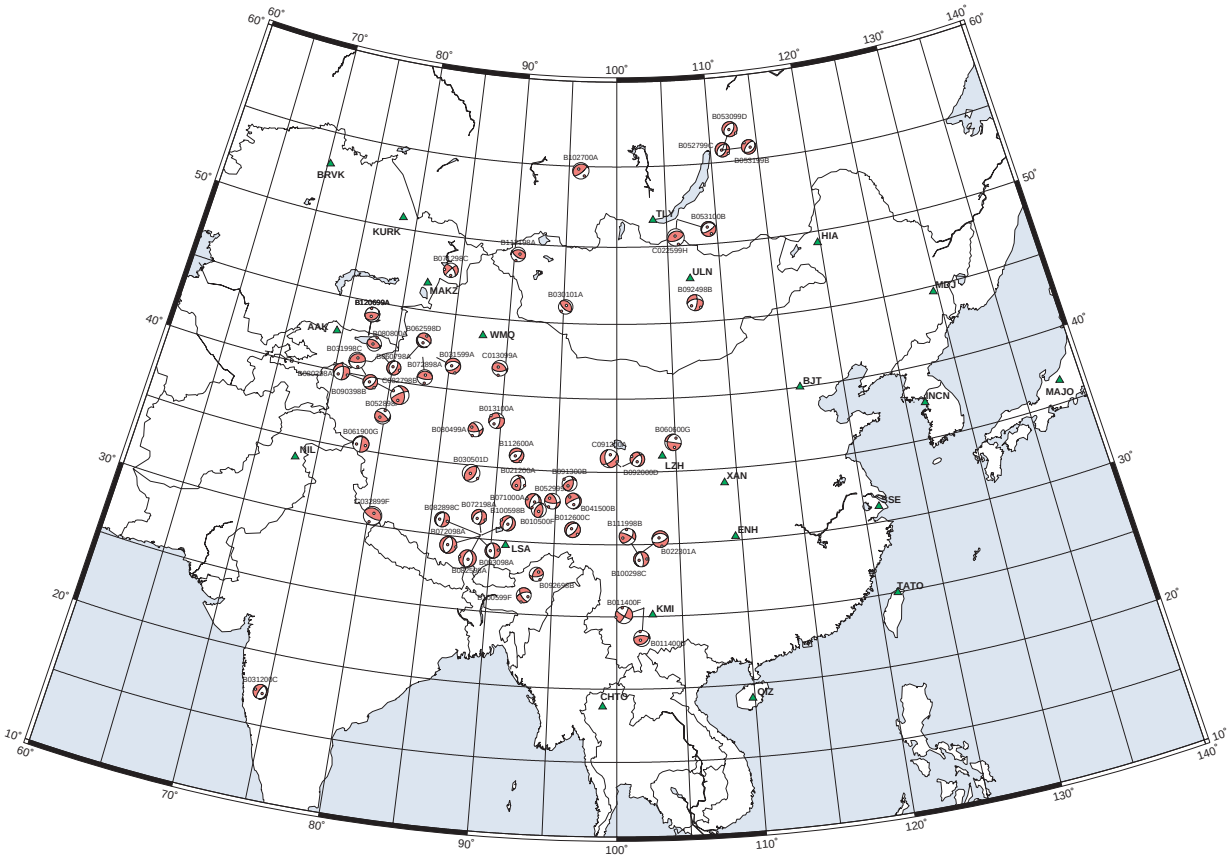


Figure 6. The map above shows the results of inversions using the waveforms and spectra for 30 events in the Harvard CMT Catalog. The results are generally consistent although some of our mechanisms have significant rotations relative to the CMT solutions (and what you might expect from tectonics). We believe that part of the problem with our preliminary results lies in the use of small-amplitude signals. Our seismic moments (or Mw) are less sensitive to variations in structure and noisy traces (for these inversions we used the L1 norm and the median values to compute an optimal moment in the period range from 65 to 20 s). For some events, no nearby waveforms are available and the results are ambiguous (but constrained) - for example, the rake can be changed by $\pm\pi$.

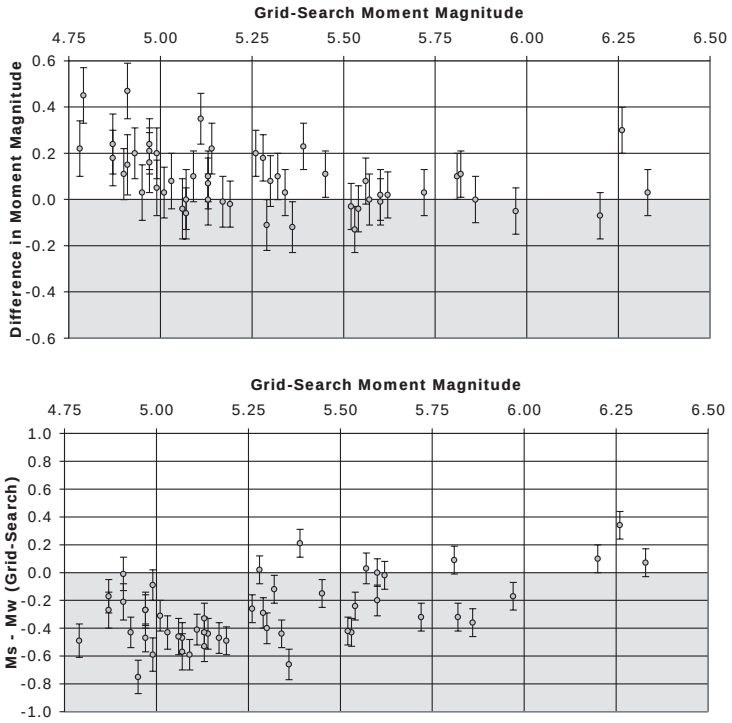


Figure 7. (Top) Comparison of the moment from grid searches and the Harvard CMT moment. Vertical axis shows the (Harvard Mw) – (Grid-Search Mw). Since the two approaches use different velocity structures and fit the data over different, finite bandwidths, the agreement should not be perfect. The CMT method tends to over-predict (or our method under-predicts) the moment for small events. Uncertainties were computed for the Harvard CMT using a Monte-Carlo method. The outlier at Mw 6.25 is a result of our failure to incorporate a time function for this larger event (Mw > 6.5). (Bottom) Comparison of the moment magnitude from grid searches and the USGS Ms estimate. Vertical axis shows the (Ms) – (Grid-Search Mw). Uncertainties were computed for the grid-search were computed using a Monte-Carlo method on the CMT moments (an approximation).

REFERENCES

Ammon, C. J., Seismic Source Inversion as a Multiple Objective Optimization Problem, submitted to Geophysical Journal International (under revision), 2003.

Ammon, C. J., R. B. Herrmann, C. A. Langston and H. Benz (1996), Source parameters of the January 16, 1994 Wyomissing Hills, Pennsylvania earthquakes, Seism. Res. Letters, 69, 261-269.

Dreger, D. S., and D. V. Helmberger (1990), Complex faulting deduced from broadband modeling of the 28 February 1990 Upland Earthquake, Bull. Seism. Soc. Am., 81, 1129-1144.

Dreger, D. S., and D. V. Helmberger (1991), Source Parameters of the Sierra Madre earthquake from regional and local body waves, Geophys. Res. Letters, 18, 2015-2018.

Dreger, D. S., and D. V. Helmberger (1993), Determination of source parameters at regional distances with three-component sparse network data, J. Geophys. Res., 98, 8107-8125.

Ghose, S., M. W. Hamburger and C. J. Ammon (1998), Source parameters of moderate-size earthquakes in the Tien Shan, central Asia from regional moment tensor inversion, Geophys. Res. Letters, 25, 3181-3184.

Herrmann, R. B. (1979), Surface wave focal mechanisms for eastern North American Earthquakes with tectonic implications, J. Geophys. Res., 84, 3543-3552.

Herrmann, R. B. (1986), Surface-Wave studies of some South Carolina earthquakes, Bull. Seism. Soc. Am., 76, 111-121.

Langston, C. A. (1981), Source inversion of seismic waveforms: the Koyna, India, Earthquakes of 13 September, 1967, Bull. Seism. Soc. Am., 71, 1-24.

Lay, T., C. J. Ammon, A. A. Velasco, J. Ritsema, T. C. Wallace and H. J. Patton (1994), Near-real time seismology: Rapid analysis of earthquake faulting, GSA Today, 4, 129,132-134.

Levshin, A., L. Ratnikova and J. Berger (1992), Peculiarities of surface-wave propagation across central Asia, Bull. Seism. Soc. Am., 82, 2464-2493.

Patton, H. (1976), A note on the source mechanism of the southeastern Missouri earthquake of October 21, 1965, J. Geophys. Res., 81, 1483-1486.

Patton, H. (1980), Reference point equalization method for determining the source and path effects of surface waves, J. Geophys. Res., 85, 821-848.

Patton, H. J. (1998), Bias in the centroid moment tensor for central Asian earthquakes: Evidence from regional surface wave data, J. Geophys. Res., 103, 26,963-26,974.

Patton, H. J., and G. Zandt (1992), Seismic moment tensors for western U. S. earthquakes and implications for the tectonic stress field, J. Geophys. Res., 96, 18,245-18,259.

Randall, G. R., C. J. Ammon and T. J. Owens (1995), Moment-tensor estimation using regional seismograms from a Tibetan Plateau portable network deployment, Geophys. Res. Letters, 22, 1665-1668.

Romanowicz, B. A. (1982), Moment tensor inversion of long-period Rayleigh Waves: A new approach, J. Geophys. Res., 87, 5395-5407.

SIMULTANEOUS INVERSION OF RECEIVER FUNCTIONS, MULTI-MODE DISPERSION, AND TRAVEL-TIME TOMOGRAPHY FOR LITHOSPHERIC STRUCTURE BENEATH THE MIDDLE EAST AND NORTH AFRICA

Charles J. Ammon,[1] Robert B. Herrmann,[2] Michael E. Pasyanos,[3] William R. Walter,[3] Minoo Kosarian[1]

Penn State University,[1] Saint Louis University,[2] Lawrence Livermore National Laboratory[3]

Sponsored by Defense Threat Reduction Agency and
National Nuclear Security Administration
Office of Nonproliferation Research and Engineering
Office of Defense Nuclear Nonproliferation

Contract No. DTRA01-02-C-0038[1,2] and W-7405-ENG-48[3]

ABSTRACT

We report on our initial investigations into the seismic structure of the lithosphere in the Middle East and North Africa (MENA) using surface waves and receiver functions. We have initiated the collection of prior work in the region and computing receiver functions for use in the joint inversion. Critical to the joint inversion is surface-wave dispersion information localized to approximately the same region sampled by receiver functions. We continue to improve our surface wave dispersion model of Western Eurasia and North Africa. We have developed group velocity maps at 2 degree resolution for both Love and Rayleigh waves from 10-100 seconds period. The model shows excellent relationship to tectonic structure and group velocity variations correlate well with orogenic zones, cratons, sedimentary basins, and rift zones. We have recently implemented a variable-resolution tomography and have pushed the resolution of the model down to 1 degree in areas with sufficient density sampling. We plan to present information on the complexity of receiver structure at many permanent sites in the region and several illustrative inversions for lithospheric structure. We have examined receiver functions at over 40 MENA stations and have inverted a number using dispersion measurements from global tomographic models. We will present a comparison of crustal thickness and Poisson's ratio estimates for the crust beneath these stations. Other work on the combination of additional observations (body-wave travel times, higher-mode observations, surface-wave polarization information) is planned for the future stages of the project, but we include illustrations outlining our ideas for the use of these data to help further constrain the seismic structure of the lithosphere.

OBJECTIVES

Our objectives are the construction of shear-velocity profiles for regions surrounding broad-band seismic stations throughout the Middle East, central and north Africa, and parts of western Europe. Application of the technique in the MENA region provides an opportunity to revise models of the crust and upper mantle structure throughout the region and to exploit the global and regional work of previous seismic verification research (*e.g.* Pasyanos *et al.*, 2001; Ritzwoller & Levshin, 1998, Larson *et al.*, 2001). The resulting shear-velocity models provide a single structure consistent with a range of observations that can be tested as a tool for the construction of mode isolation filters to help improve surface-wave magnitude estimates. We also plan to explore the possibility of adding additional data to our inversions of receiver functions and surface-wave dispersion estimates. The diverse seismic activity throughout the region will facilitate cross-validation of the mode isolation filters with simple empirical filters constructed using larger events with adequate signal-to-noise ratios.

Estimating Subsurface Shear Velocities

Subsurface geology generally has a broad “wavenumber” spectrum containing sharp, or high-wavenumber, changes in velocity near Earth’s major geologic boundaries and smooth low-wavenumber variations in regions of relatively uniform geologic structure. Access to the full spectrum of earth structure requires that we exploit signals that span a wide frequency range and that are sensitive to the entire spectrum of heterogeneity. Surface-waves, travel times, and direct-wave amplitudes, for example, are sensitive to smooth variations in earth structure; reflected and converted waves are sensitive to velocity contrasts. Combining seismic data in joint inversions is an obvious approach to improve estimates of earth structure. To successfully combine data in an inversion, we must insure that all the data are sensitive to the same (or related) physical quantities and that they sample or average structure over comparable length scales. Recent advances in surface-wave tomography have provided an opportunity to combine localized surface-wave dispersion estimates with other data such as P- and S-wave receiver functions. Ammon and Zandt (1993) used surface-wave dispersion observations to try and distinguish between competing models of the Mojave desert, but Ozalaybey *et al.*, (1997) pioneered a formal, joint inversion of these data. They nicely illustrated the value of even a limited band of dispersion values to help reduce the trade-off between crustal thickness and velocity inherent in receiver function analyses. Specifically, they used Rayleigh-wave phase velocities in the 20-25 second period range to help produce stable estimates of crustal thickness in the northern and central Basin & Range. The limited bandwidth did not permit resolution of details in the crust and they limited their inversion (or at least their interpretation) to depths above 40 km. More recent authors have exercised the approach and combined the data with additional *a priori* model constraints (Du and Foulger, 1999; Julia *et al.*, 2000). Recent accomplishments in global and regional tomography now provide a more complete band of dispersion measurements to combine with receiver functions that allow us to improve the resolution of earlier works.

Surface-wave dispersion measurements are sensitive to broad averages, or low wavenumber components of earth structure. They provide valuable information on the absolute seismic shear velocity but are relatively insensitive to sharp, high-wavenumber velocity changes. Generally surface-wave inversions must be constrained using a particular layer parameterization (*e.g.* near-surface, upper-crust, lower crust, mantle lid, deep mantle), resemble an *a priori* model, or substantially smoothed to stabilize earth-structure estimation. Despite these drawbacks, surface-wave dispersion values contain important constraints on the subsurface structure, and the general increase in depth sensitivity with depth allows an intuitive understanding of their constraints on structure. Additionally, modeling dispersion values facilitates a broadband inversion by reducing the dominance of airy phases, which pose problems when constructing broad-band misfit norms to model seismograms directly. Perhaps most important for our application is the ability to localize Earth’s dispersion properties using seismic tomography. The idea is now well established and global dispersion models exist for a broad range of frequencies (*e.g.* Larson and Ekstrom, 2001; Stevens *et al.*, 2001). The localization of dispersion allows us to isolate the variations in properties spatially and global models of surface-wave dispersion exist and are readily available for application to other studies such as the proposed work.

Receiver functions are time series computed from three-component body-wave seismograms, that show the relative response of Earth structure near the receiver (*e.g.* Langston, 1979). Source, near-source structure, and mantle propagation effects are removed from the seismograms using a deconvolution that sacrifices P-wave information for

the isolation of near-receiver effects (Langston, 1979; Owens *et al.*, 1984; Ammon, 1991; Cassidy, 1992). Receiver function waveforms are a composite of P-to-S (or S-to-P) converted waves that reverberate within the structure near the seismometer. Modeling the amplitude and timing of those reverberating waves can supply valuable constraints on the underlying geology. In general, the receiver functions sample the structure over a range of 10's of kilometers from the station in the direction of wave approach (the specific sample width depends on the depth of the deepest contrast). Stations sited near geologic boundaries can produce different responses for different directions. Recent innovations in receiver function analysis include more detailed modeling of receiver function arrivals from sedimentary basin structures (*e.g.* Clitheroe *et al.*, 2000), anisotropic structures (*e.g.* Levin and Park, 1997; Savage 1998), estimation of Poisson's ratio (*e.g.* Zandt *et al.*, 1995; Zandt and Ammon, 1995; Zhu and Kanamori, 2000, Ligorría, 2000), reflection-like processing of array receiver functions (*e.g.* Chevrot and Girardin, 2000; Ryberg and Weber, 2000) and joint inversions (*e.g.* Ozalaybey *et al.*, 1997; Du and Foulger, 1999; Julia *et al.*, 2000).

Our joint inversion method is similar to that of Ozalaybey *et al.* (1997) except that we use jumping, smoothness, and constraints to include as much *a priori* information into the inversion as is available. We combine the receiver function and surface-wave observations into a single algebraic equation and account for their different physical units and equalize their importance in the misfit norm by weighting each dataset by an estimate of the uncertainty in the observations and the number of data. We also append smoothness constraints and *a priori* model constraints on the deepest part of the model. Although we cannot resolve fine details in the deep upper mantle, these regions can impact our results since surface-wave dispersion values at intermediate and longer periods are somewhat sensitive to this deeper structure. We believe that it is important to have a reasonable basement structure so that our results are more consistent with global models. We extend our models to about 500-700 km to insure this consistency. The resulting inversion equations are

$$\begin{bmatrix} \sqrt{\frac{\mathbf{p}}{\mathbf{w}_s^2}}\mathbf{D}_s \\ \sqrt{\frac{\mathbf{q}}{\mathbf{w}_r^2}}\mathbf{D}_r \\ \sigma\Delta \\ \mathbf{W} \end{bmatrix} \cdot \mathbf{m}_{i+1} = \begin{bmatrix} \sqrt{\frac{\mathbf{p}}{\mathbf{w}_s^2}}\mathbf{r}_s \\ \sqrt{\frac{\mathbf{q}}{\mathbf{w}_r^2}}\mathbf{r}_r \\ 0 \\ 0 \end{bmatrix} + \begin{bmatrix} \sqrt{\frac{\mathbf{p}}{\mathbf{w}_s^2}}\mathbf{D}_s \\ \sqrt{\frac{\mathbf{q}}{\mathbf{w}_r^2}}\mathbf{D}_r \\ 0 \\ 0 \end{bmatrix} \cdot \mathbf{m}_i + \begin{bmatrix} 0 \\ 0 \\ 0 \\ \mathbf{W} \end{bmatrix} \cdot \mathbf{m}_a \qquad (1)$$

where $\mathbf{p}$, $\mathbf{q} = 1 - \mathbf{p}$, σ, and $\mathbf{W}$ are weights that control the relative importance of receiver functions, dispersion values, smoothness, and *a priori* model constraints in the norm minimized during the inversion. The data comprise the vectors $\mathbf{r}_s$ and $\mathbf{r}_r$, and the partial derivatives fill the matrices $\mathbf{D}_r$ and $\mathbf{Ds}$. The matrix Δ is a finite-difference stencil that "computes" model roughness, and the matrix $\mathbf{W}$ is a layer-dependent weight that is used to insure the model blends smoothly into the *a priori* model, $\mathbf{m}_a$, at depth. The values of $\mathbf{w}_s$ and $\mathbf{w}_r$ are equal to the product of the number of points in the dispersion curve and receiver functions and the variance of the observations.The second term on the right is added to create the "jumping" inversion scheme (*e.g.* Constable *et al.*, 1987; Ammon *et al.*, 1990) and allows us to solve for (and constrain) the shear-velocity models as opposed to shear-velocity correction vectors. Equation (1) is solved in a least-squares sense for the model, $\mathbf{m}_{i+1}$, starting with an initial model $\mathbf{m}_0$. The procedure generally converges in a few iterations.

Estimating Receiver Functions

When the data are high-quality and the receiver structure is not too complex, the choice of a deconvolution procedure does not make much difference. However, when the noise in the seismograms is substantial, or the receiver structure is complex, different deconvolution approaches have strengths and weaknesses. We will compute receiver functions using the iterative time-domain deconvolution procedure described by Ligorría and Ammon (1999). We prefer the iterative approach, which is based on the Kikuchi and Kanamori (1982) source-time function estimation algorithm, for several reasons. First, in the iterative approach the receiver function is constructed by a sum of Gaussian pulses which produces a flat spectrum at the longest periods. The flat long-period spectrum can be viewed as *a priori*

information that helps reduce side-lobes that may result of spectral or singular-value truncation stabilization procedures. The reduction of side-lobes eases the interpretation and helps stabilize "low-frequency" receiver functions. Second, the iterative approach constructs a causal receiver function, which is what we expect in all cases of reasonable earth structure. This is a subtle difference from spectral techniques (*e.g.* Langston, 1979; Park and Levin, 2000) which can always introduce a component to the signal before the P-wave. The acausal component of the spectral signal may be small, but still important to the satisfaction of the convolutional model that defines a receiver function, *i.e.:*

$$\mathbf{R}(\mathbf{t}) = \mathbf{Z}(\mathbf{t}) * \mathbf{E_R}(\mathbf{t}). \quad (2)$$

In equation (2), $\mathbf{R}(\mathbf{t})$ and $\mathbf{Z}(\mathbf{t})$ are the radial and vertical seismograms, and $\mathbf{E_R}(\mathbf{t})$ is the radial receiver function (a similar equation holds for the transverse component). The point is that even when the receiver function estimation is unstable, spectral deconvolutions may satisfy (2) quite well. The iterative time-domain approach, which can be restricted to produce the best *causal* solution, may not always satisfy (2). Experienced modelers have always been able to identify failed receiver functions, but the misfit to (2) available from iterative deconvolutions provides quantitative information that can be used when stacking signals, or in extreme cases, to discard obviously failed deconvolutions. In our case we find using a threshold cut-off of 80-90% of the radial power fit allows us to quickly discard poorly constrained deconvolution results, enabling an efficient and objective select of the data to include in further analysis.

RESEARCH ACCOMPLISHED

Receiver Function Computation

The first step in the project is the selection of target stations and the computation of receiver functions at those stations. To begin, we have a selected a subset of permanent stations that have relatively long recording histories and thus will have substantial data already available. More recently installed stations and operating temporary stations will be added later in the project. Data processed at the time this report was written are shown in Figure 1. We plan to include all available temporary and permanent stations within central and norther Africa, the Middle East, and parts of Europe. So far we have investigated 69 stations, 36 in Africa, 34 in the Middle East, and 24 stations in southern Europe.

Poisson's Ratio and Crustal Thickness Estimation

As a first step in the receiver function analysis we use the receiver function stacking method of Zhu and Kanamori (2000) to estimate the crustal thickness and Vp/Vs velocity ratio (or Poisson's ratio). The stacking method makes a rather limiting assumption of a uniform crust but the analysis provides good estimates of these quantities when the structure is relatively simple. The estimated values of Poisson's ratios can be used in subsequent inversions which require some assumed value of bulk crustal Poisson's ratio. We summarize the results so far in Figure 2. If a station is shown twice, that indicates that we observed significant azimuthal variations (which may indicate a likely failure of this simple imaging approach). Ignoring obvious outliers, we see an overall trend suggesting a decrease in Poisson's ratio (Vp/Vs) with increasing crustal thickness. The trend is primarily cause by results for stations in southwestern Asia and the trend is absent in results for stations sampling Africa and southern Europe. The fact that two of three geographic clusters do not show the feature suggest it is not an artifact of the method. The pattern may still be "coincidence" since the data from southwestern Asia span a large and the lowest values are unusually low, perhaps a result of lateral heterogeneity unaccounted for in the method. Still, all are located in the zone of plateaus and collision-related uplifts and more analysis is need to investigate the trend's validity and its potential explanations. Crustal thickness agree in general with the global crustal model 2.0, but at times the differences are significant (greater than 5 km). The median difference between the global model and our results is 0 km, the median absolute difference is 3 km. The numbers agree more closely when we rank our estimates using the complexity of the observed receiver functions.

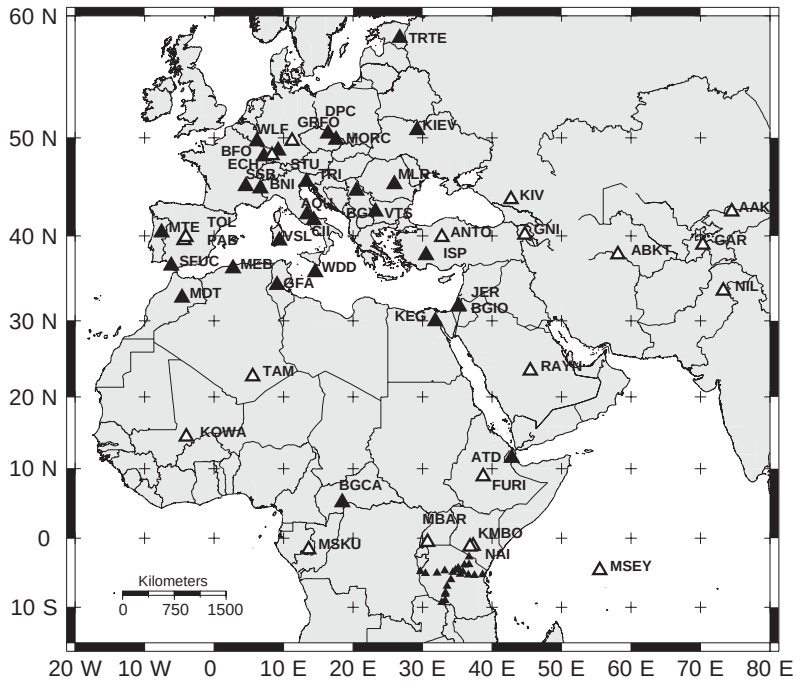


Figure 1. Stations for which we have computed receiver functions (as of the date of this report). The eventual target stations include all available permanent and temporary three-component seismic stations. Shaded symbols indicate stations analyzed since the last review.

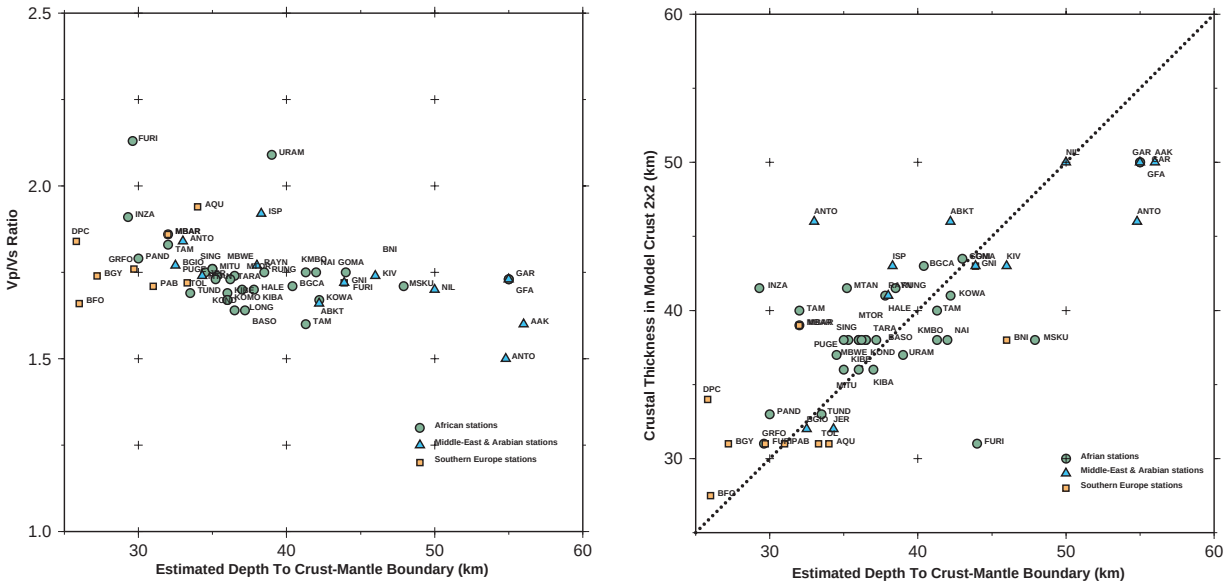


Figure 2. Variation of Vp/Vs ratio with crustal thickness and comparison of crustal thickness estimated with receiver functions versus values from crustal model 2.0.

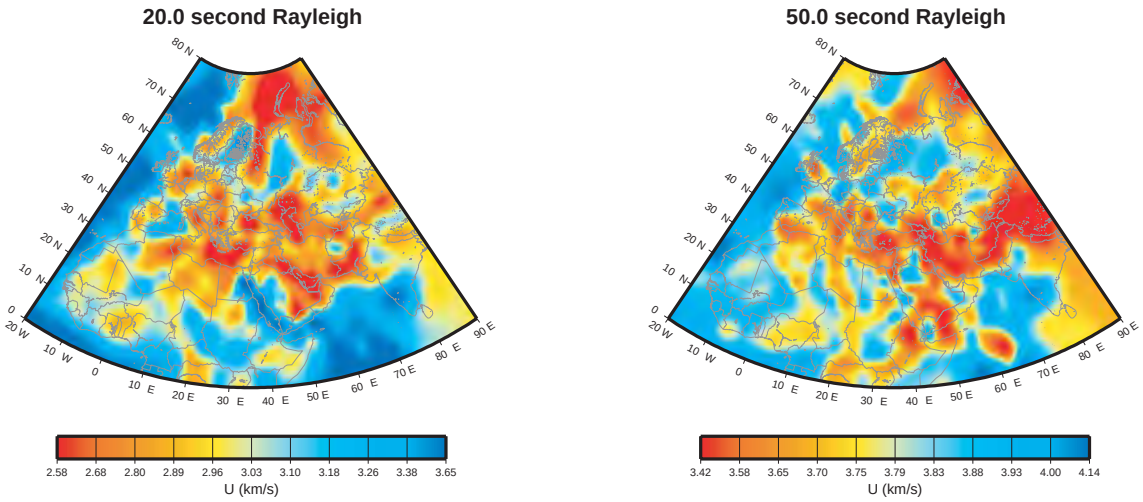


Figure 3. Tomographic imaging results for the Middle-East, North Africa, and western Europe. The upper diagram shows the lateral group velocity variations in 20-second period Rayleigh waves, the lower 50-second period Rayleigh waves.

Tomographic Imaging of Group-Velocity Variations

We have performed a large-scale study of surface wave group velocity dispersion across Western Eurasia and North Africa (Pasyanos, 2002). This study expands the coverage area northwards relative to previous work (Pasyanos *et al.*, 2001), which covered only North Africa and the Middle East. As a result, we have increased by about 50% the number of seismograms examined and group velocity measurements made. We have now made good quality dispersion measurements for about 10,000 Rayleigh wave and 6,000 Love wave paths, and have incorporated measurements from several other researchers into the study. We use a conjugate gradient method to perform a group velocity tomography.

We have improved our inversion from the previous study by adopting a variable smoothness (Pasyanos, 2002). This technique allows us to go to higher resolution where the data allow without producing artifacts. Our current results include both Love and Rayleigh wave inversions across the region for periods from 10-100 seconds. Figure 3 shows inversion results for Rayleigh waves at periods of 20 and 50 seconds. Short period group velocities are sensitive to slow velocities associated with large sedimentary features such as the Russian Platform, Mediterranean Sea, and Persian Gulf. Intermediate periods are sensitive to differences in crustal thickness, such as those between oceanic and continental crust or along orogenic zones. At longer periods, we find fast velocities beneath cratons and slow upper mantle velocities along rift systems and the Tethys Belt.

An Example Combined Inversion, Station PUGE, Tanzania

We illustrate the ideas with an example. In Figure 4 we present the results of the inversion of PUGE receiver functions with the Rayleigh-wave group-velocity dispersion values from Pasyanos and Walter (2002) combined with phase velocities digitized from Weeraratne *et al* (2003). The fit to the Pasyanos and Walter (2002) dispersion curve is very good and the general fit to the phase-velocities is good. The phase velocities are slightly under-predicted for the shorter periods and over-predicted for the longest periods. The long-period over-prediction is a result of our constraints that the deepest part of the model match that of PREM. Relaxing that assumption would allow the low velocities to extend deeper that 220 km and reduce the deepest average shear-velocity to match the phase velocity. The difference at the shorter periods represents a fundamental difference between the group and phase-velocities. One explanation may be the smoothing of the group velocities has resulted in an artificially lower estimate - very slightly inconsistent with the phase velocities. The receiver functions are very well modeled and produce the relatively smooth crust-mantle transition and crustal thickness (provided with the absolute velocity information from

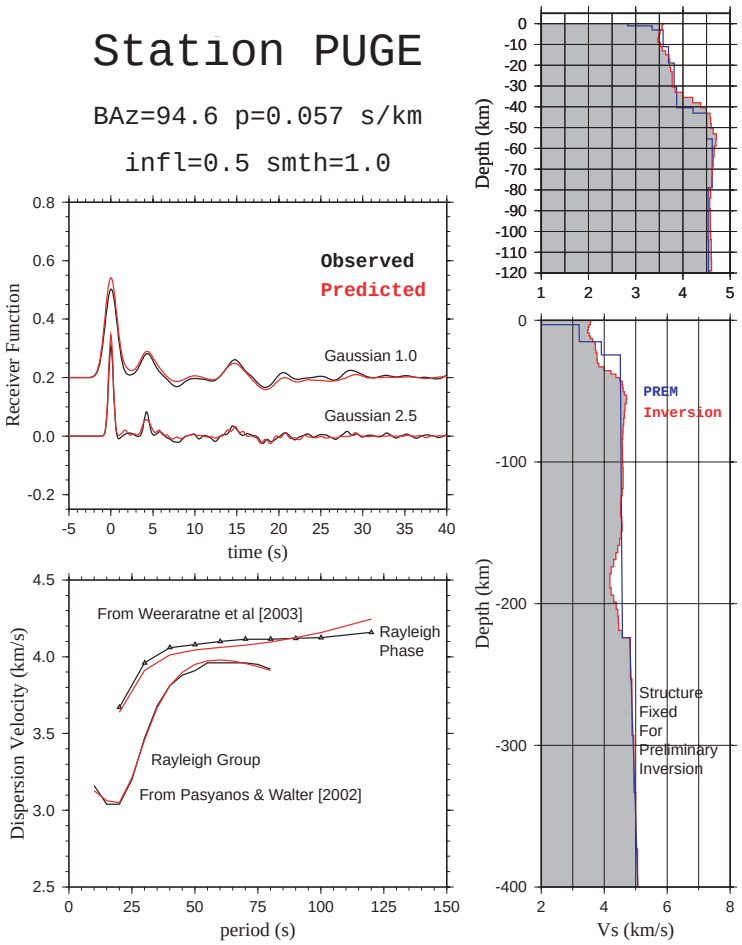


Figure 4. Inversion results for station PUGE using dispersion curves from Pasyanos and Walter (2002) & Weereratne et al., (2003). The back azimuth and ray parameter of the incoming P-wave are shown at the top. The influence parameter was 0.5, which balances the weight between the receiver functions and dispersion values, and the smoothness weight was 1.0. The observed and predicted receiver functions in two bandwidths are shown in the upper left, the observed and predicted dispersion curves in the lower left, and the resulting models are shown on the right. The deep structure is constrained to transition smoothly into the PREM - the data have little sensitivity for detailed absolute velocities below approximately 100-150 km. These velocities are earth-flattened by default since we use flat-earth codes to perform the analyses.

the surface-wave information).The model has a relatively simple crust, consistent with earlier results, and the crust-mantle transition about 7.5 km thick (this could be an intermediate layer at the base of the crust). The mantle structure includes a lid with a thickness of approximately 100 km underlain by a region of low velocities. These velocities are low compared with other shields - consistent with the results of Weeraratne et al (2003). Although the lid is fast at shallow depths, consistent with regional propagation (e.g. Nyblade and Brazier, 2002; Langston et al., 2002) the model lid is also thinner than usual for an Archean shield.

CONCLUSIONS AND RECOMMENDATIONS

Our work is proceeding nicely and most of the permanent stations have been imaged. We are also working with other groups to secure and image structures beneath several more sites in northeastern Africa. We have a few more permanent stations to analyze. We are moving from the initial data collection and preliminary analysis phase into a more expansive interpretation and assessment stage.

ACKNOWLEDGEMENTS

We thank the P. Wessel and W. H. F. Smith (1990), the authors of GMT for producing easy-to-use, quality software for making maps and charts.

REFERENCES

Ammon, C.J., G.E. Randall, and G. Zandt (1990), On the non-uniqueness of receiver function inversions, *J. Geophys. Res.*, 95, 15303-15318.

Ammon, C.J. (1991), The isolation of receiver effects from teleseismic P waveforms, *Bull. Seism. Soc. Am.*, 81, 2504-2510.

Ammon, C. J., and G. Zandt (1993), The receiver structure beneath the southern Mojave Block, *Bull. Seism. Soc. Am.*, 83, 737-755.

Cassidy, J.F., Numerical experiments in broadband receiver function analysis, *Bull. Seismol. Soc. Am.*, 82, 1453-1474, 1992.

Chevrot, S., and N. Girardin (2000), On the detection and identification of converted and reflected phases from receiver functions, *Geophys. J. Int.*, 141 (3), 801-808.

Clitheroe, G., O. Gudmundsson, and B.L.N. Kennett (2000), Sedimentary and upper crustal structure of Australia from receiver functions, *Australian Journal of Earth Sciences*, 47 (2), 209-216.

Constable, S.C., R.L. Parker, and C.G. Constable (1987), Occam's inversion: A practical algorithm for generating smooth models from electromagnetic sounding data, *Geophysics*, 52, 289-300.

Du, Z.J. and G.R. Foulger (1999), The crustal structure beneath the northwest fjords, Iceland, from receiver functions and surface waves, *Geophys. J. Int.*, 139, 419-432.

Julia, J., C. J. Ammon, R. B. Herrmann, and A. M. Correig (2000), Joint Inversion of receiver function and surface-wave dispersion observations, *Geophys. J. Int.* 143, 99-112.

Kikuchi, M., and H. Kanamori, Inversion of complex body waves (1982), *Bull. Seism. Soc. Am.*, 72, 491-506, 1982.

Langston, C.A. (1979), Structure under Mount Rainier, Washington, inferred from teleseismic body waves, *J. Geophys. Res.*, 84, 4749-4762.

Larson, E. W. F. and G. Ekstrom (2001), Global Models of Group Velocity, *Pure and Applied Geophys.*, 158, 1377-1399.

Levin, V., and J. Park (1997), Crustal anisotropy in the Ural Mountains from teleseismic receiver functions, *Geophysical Research Letters*, 24 (11), 1283-1286.

Ligorría, J.P. (2000), An Investigation of the Crust-Mantle Transition Beneath North America and the Bulk Composition of the North American Crust, *Ph.D. Thesis, Saint Louis University*, 261 pages.

Ligorría, J.P. and C. J. Ammon (1999), Iterative deconvolution and receiver function estimation, *Bull. Seismol. Soc. Am.*, 89, 1395-1400.

Myers, S.C., and S.L. Beck (1994), Evidence for a local crustal root beneath the Santa Catalina metamorphic core complex, Arizona, *Geology*, 22, 223-226.

Owens, T.J., G. Zandt, and S.R. Taylor (1984), Seismic evidence for an ancient rift beneath the Cumberland Plateau, Tennessee: A detailed analysis of broadband teleseismic P waveforms, *J. Geophys. Res.*, 89, 7783-7795.

Ozalaybey, S., M.K. Savage, A.F. Sheehan, J.N. Louie, and J.N. Brune (1997), Shear-wave velocity structure in the northern Basin and Range Province from the combined analysis of receiver functions and surface waves, *Bull. Seismol. Soc. Am.*, 87, 183-199.

Park, J., and V. Levin (2000), Receiver functions from multiple-taper spectral correlation estimates, *Bull. Seismol. Soc. Am.*, 90 (6), 1507-1520.

Pasyanos, M.E., W.R. Walter, and S.E. Hazler (2001), A Surface wave dispersion study of the Middle East and North Africa for Monitoring the Comprehensive Nuclear-Test-Ban Treaty, *Pure and Applied Geophys*, 158, 1445-1474.

Pasyanos, M.E., and W.R. Walter, Crust and upper-mantle structure of North Africa, Europe and the Middle East from inversion of surface waves, Geophys. J. Int., 149, 463-481, 2002.

Pasyanos, M.E. (2002), A Variable-resolution Surface Wave Dispersion Study of Western Eurasia and North Africa, submitted to *Journal of Geophysical Research*.

Ritzwoller, M. H. and A. L. Levshin (1998), Eurasian surface wave tomography: Group velocities, *J. Geophys. Res., 103*, 1839-1878.

Ryberg, T., and M. Weber (2000), Receiver function arrays; a reflection seismic approach, *Geophys. J. Int.*, 141 (1), 1-11.

Sandvol, E., D. Seber, A. Calvert, M. Barazangi (1998), Grid search modeling of receiver functions: Implications for crustal structure in the Middle East and North Africa, *J. Geophys. Res.*,103, 26,899-26,917.

Savage, M.K. (1998), Lower crustal anisotropy or dipping boundaries? Effects on receiver functions and a case study in New Zealand, *J. Geophys. Res.*, 103 (7), 15,069-15,087, 1998.

Stevens, J. L. and K. L. McLaughlin (2001), Optimization of Surface Wave Identification and Measurement, *Pure and Applied Geophys*., 158, 1547-1582

Su, W., R. L. Woodward, and A. M. Dziewonski (1994), Degree 12 model of shear velocity heterogeneity in the mantle, *Nature*, 99, 6945-6980.

Weeraratne, D.S., D.W. Forsyth, K.M. Fischer, and A.A. Nyblade, Evidence for an upper mantle plume beneath the Tanzanian craton from Rayleigh wave tomography, *J. Geophys. Res.*, 2002JB002273R, 2003.

Zandt, G., and C. J. Ammon (1995), Continental Crustal composition constrained by measurements of crustal Poisson's ratio, *Nature*, 374, 152-154.

Zandt, G., S.C. Myers, and T.C. Wallace (1995), Crust and mantle structure across the Basin and Range-Colorado Plateau boundary at 37 degrees N latitude and implications for Cenozoic extensional mechanism, *J. Geophys. Res.*, 100 (6), 10,529-10,548.

Zhu, L., and H. Kanamori (2000), Moho depth variation in Southern California from teleseismic receiver functions, *J. Geophys. Res.*, 105 (2), 2969-2980.

AN INTEGRATED GEOPHYSICAL STUDY OF THE LITHOSPHERIC STRUCTURE BENEATH LIBYA

Wesley A. Brown, Tom F. VanDeMark, Diane I. Doser, G. Randy Keller, Aaron A. Velasco

University of Texas at El Paso

Sponsored by Air Force Research Laboratory

Contract No. DTRA01-01-C-0058

ABSTRACT

The tectonic evolution of Libya has yielded a complex crustal structure and is composed of a series of basins and uplifts. In order to constrain this complex crustal structure, we have complied and reduced over 16000 gravity measurements in conjunction with other geologic and geophysical data to construct a 3-D model of density/geology for northern Libya and surrounding regions. The 3-D model is developed by calculating contributions from various crustal layers, including the Mesozoic surface as the elevation, the top of the Precambrian, the Moho, etc. The 3-D model will then be used to develop a regional velocity model that can be verified/modified by analysis of regional waveform data that we are collecting from earthquakes occurring within northern Libya.

Northern Libya is the most seismologically active and highly faulted portion of the country. For this reason, we have collected thirteen Landsat 5 satellite images covering the most seismically active and structurally significant regions of northeast and northwest Libya. The satellite images have been mosaicked using a seamless mosaicking technology based on ENVI's cutline feathering approach. The resulting mosaicked figures were then overlain with the previously mapped faults analyzed to identify the more recent faults.

We have examined regional waveforms from 30 Libyan earthquakes that occurred from January 1990 to May 2000. We used regional stations GFA, IDI, KEG, and WDD, which are all broadband digital stations and all members of the Mediterranean Network (MEDNET). Event magnitudes ranged from 3.7 to 5.2, and all were shallow events. The great majority of events originated in the northeastern section of Libya bordering the Cyrenaica uplift. We find significant *Lg* blockage across the Mediterranean Sea, thus limiting any discrimination techniques that rely on *Lg*. We thus investigate the utility of *P*-wave cross spectral ratios and *Pn*/*Sn* phase ratios, recognizing our preliminary results lack explosion data.

OBJECTIVE

Our objective is to improve upon the existing crustal velocity model for Libya. We are building a 3-D density/geology model using a wealth of geophysical data. We will validate the models through the use of regional waveforms.

RESEARCH ACCOMPLISHED

3-D Gravity Analysis

Over 16000 gravity data points covering northern Libya and the southern portion of the Mediterranean Sea have been compiled and reduced. These gravity points were collected from a number of databases, about a half of which were collected from the worldwide gravity database maintained by the National Imagery and Mapping Agency (NIMA). The other points were gathered from our local database here at the University of Texas at El Paso (UTEP). Figure 1 shows the gravity points covering an area extending from 8°E, 35°N to 26°E, 19°N. These data have been gridded at three-minute intervals using a minimum curvature gridding technique.

The program "SURFGRAV" is a general-purpose 3-D gravity-modeling program that is being used to construct the 3-D gravity model of the study area. The computation is based on representing the Earth's surface as a gridded Digital Elevation Model (DEM) with an associated grid derived from mapped geologic units. This software is designed for conventional single-density terrain correction, variable geology/density terrain corrections, as well as general purpose modeling of subsurface structures. The software program is equipped to handle irregularly spaced gravity stations at arbitrary elevations, common to land surveys. For this computation, the geologic map of Libya (Figure 2) has been digitized, gridded and will be used in conjunction with the DEM of the study area (Figure 3a). The output computed gravity (a kernel file) is presented as a matrix or spreadsheet dataset with each row a gravity station, and the columns containing unit-density gravity contributions for each of the geologic units in the area of computation. Spreadsheet, Matlab or other specialized software can then combine these kernel files to give terrain-corrections, regional/local contributions, tests of forward models at different densities, or the Jacobian for use in inverse algorithms (Baker 2001).

Figure 2 is a generalized geologic map of Libya showing polygons bordering individual geologic outcrops. These polygons have been assigned their various densities from the rock description obtained from a 1:2,000,000 scaled geologic map of the Kingdom of Libya, compiled by Constant *et al*. (1964). Neighboring polygons that were found to vary by less than 0.02g/cc were merged to form a single polygon as a tradeoff for processing time. The nearest neighbor gridding technique was used to produce the grid map shown as Figure 4. In all other cases, the Kriging technique was used to produce various grids. A gridded map of the surface of Libya as well as a contour map of the study areas are shown in Figures 3a and 3b. These two grids (DEM and geology/density) along with a file containing the gravity readings are fed into SURFGRAV and the gravity contribution of each polygon is calculated at infinite depth. The same process is repeated for subsequent layers: the Paleozoic layer that has been assigned a uniform density of 2.55g/cc (Figure 5), the Precambrian with a uniform density of 2.7g/cc (Figure 6), the lower crust with a uniform density of 3.0g/cc and from the Moho down to a depth of approximately 50 km was assigned a uniform density of 3.3g/cc.

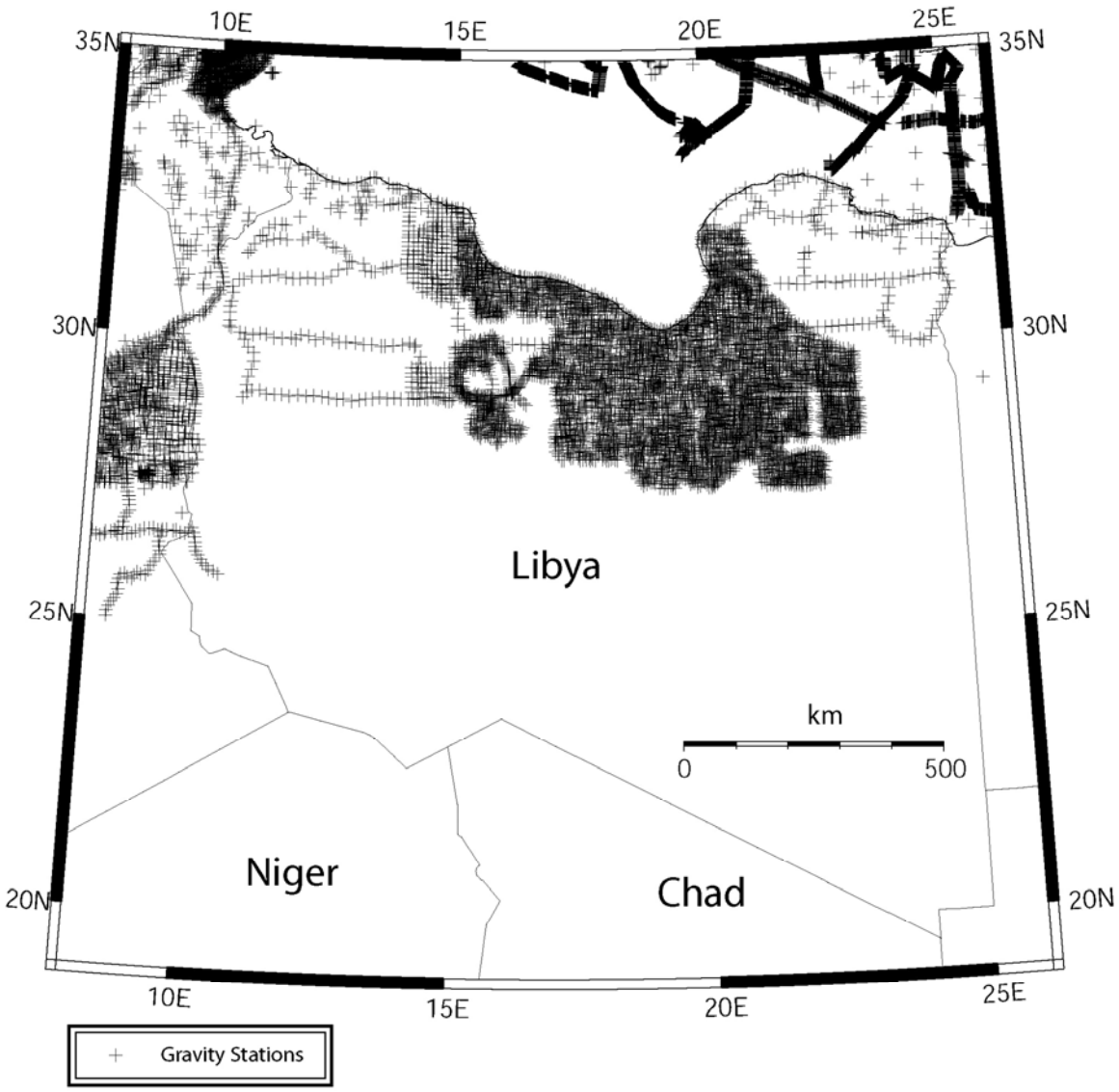


Figure 1. Map of Libya showing the locations of gravity stations that have been reduced and are being used in the gravity-modeling portion of this study.

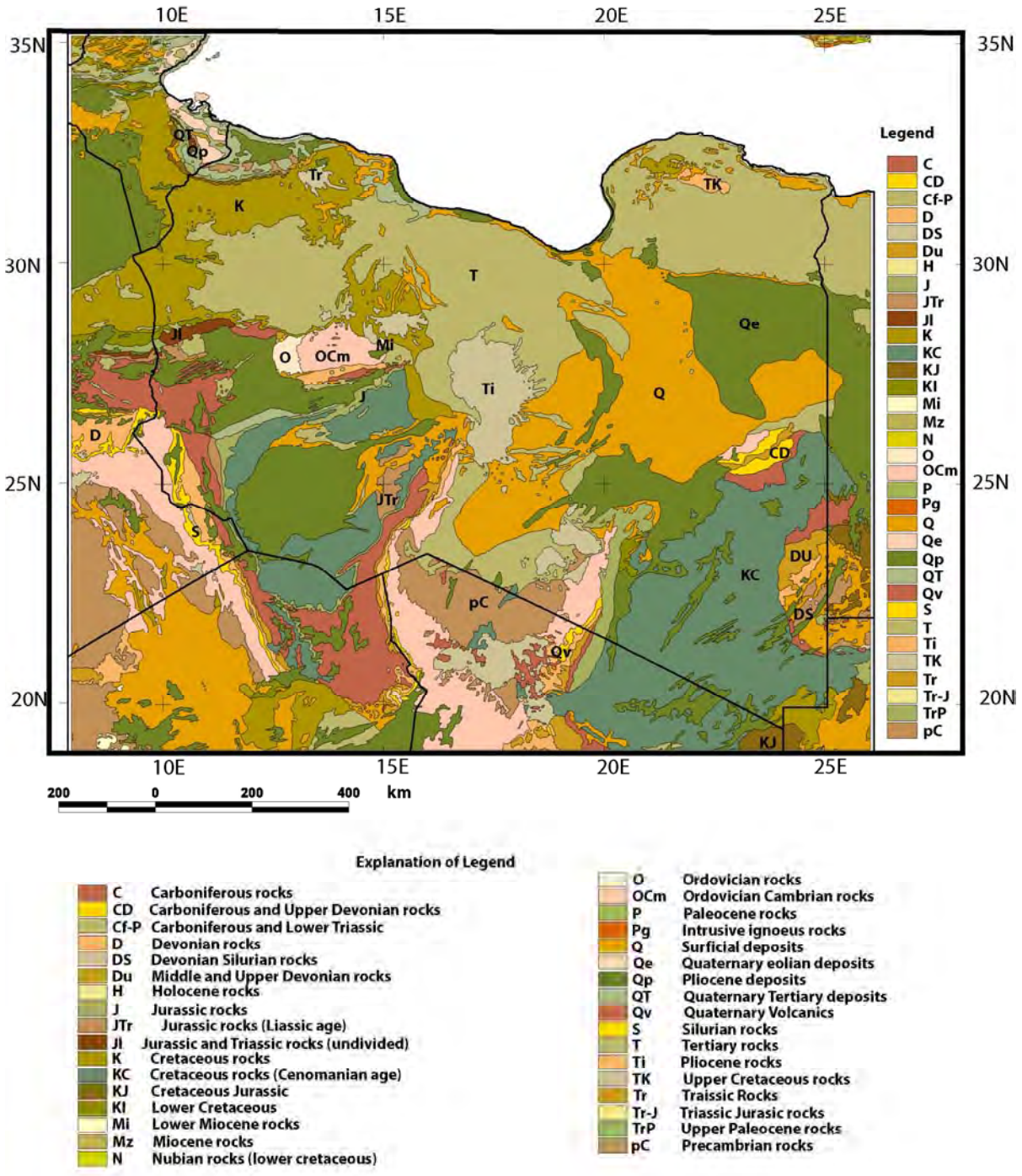


Figure 2. Generalized geologic map of Libya and adjacent areas (modified from Hearn, 2001)

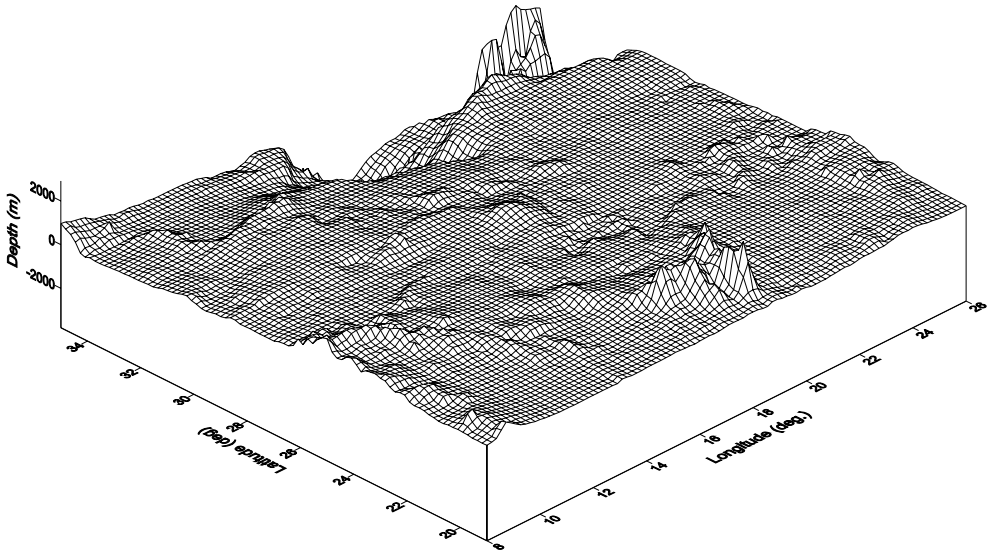


Figure 3a Vertically exaggerated gridded DEM for the topographic surface of Libya. Libya is a generally flat country, except for the Tibesti Mountains in the south there is not much topography. The gridding interval used for the SURFGRAV software is at a 3 minute interval but has been reduced for ease of display in this figure.

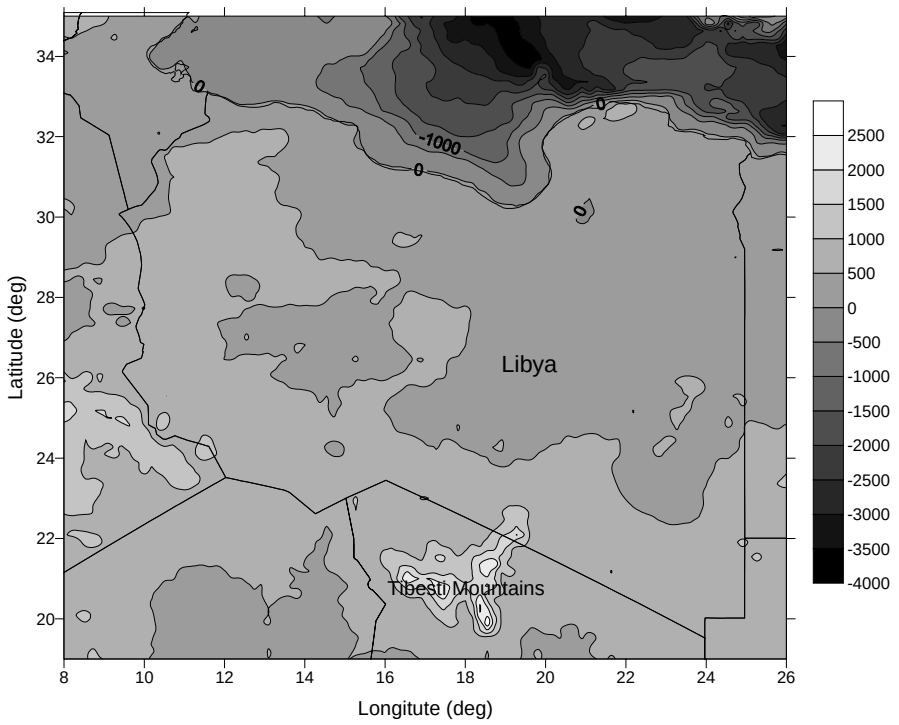


Figure 3b. Contour map of the Libya region. Contour lines are drawn at intervals of 500m.

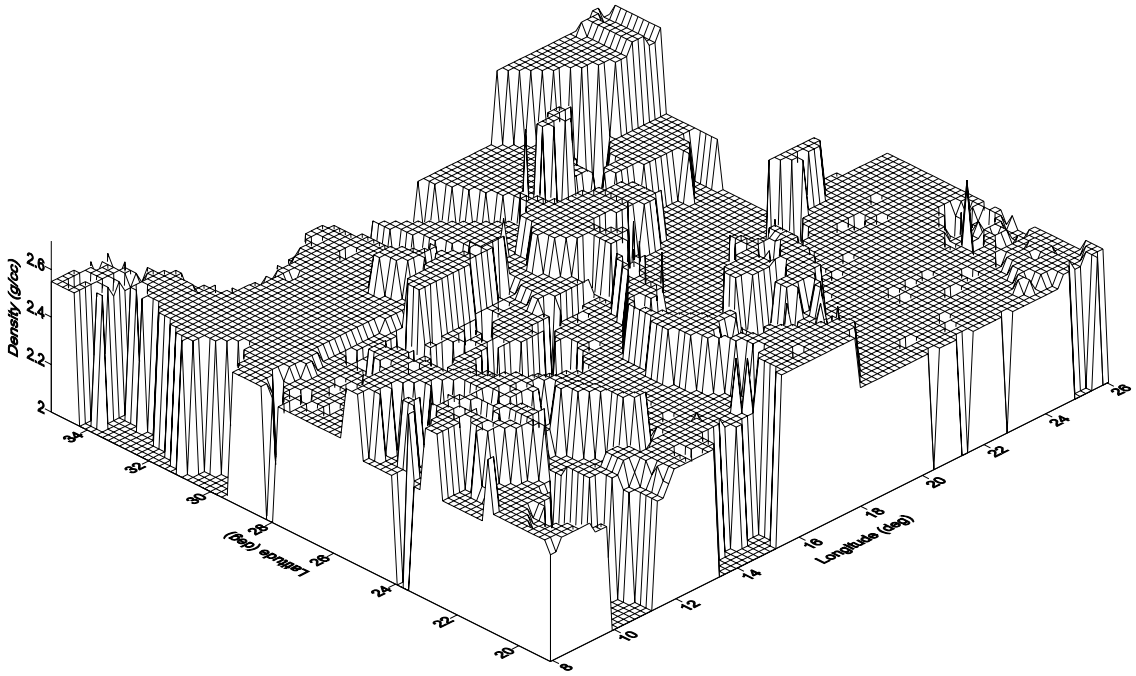


Figure 4. Representation the gridded surface geology/density of the study area. The nearest neighbor technique is used to do the gridding so that the sharp changes in geology/densities can be more accurately represented.

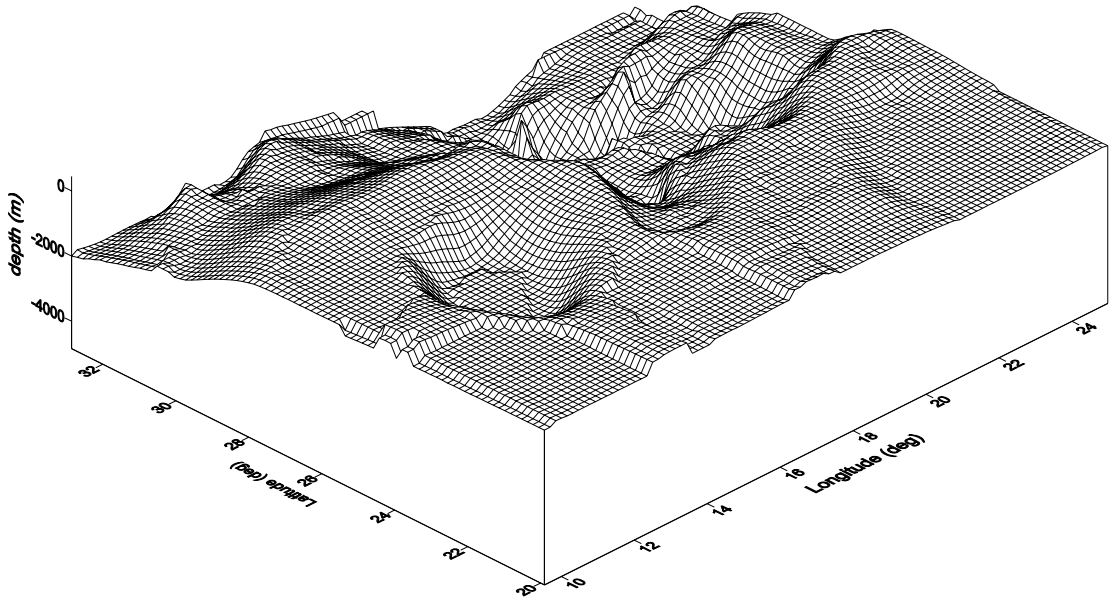


Figure 5. Gridded surface of the top Paleozoic Layer. These data were digitized from a preliminary structure-contour map of the Libyan Arab Republic and adjacent areas compiled by Goudarzi *et al.* (1978). The scale of the structure contour map is 1:2,000,000.

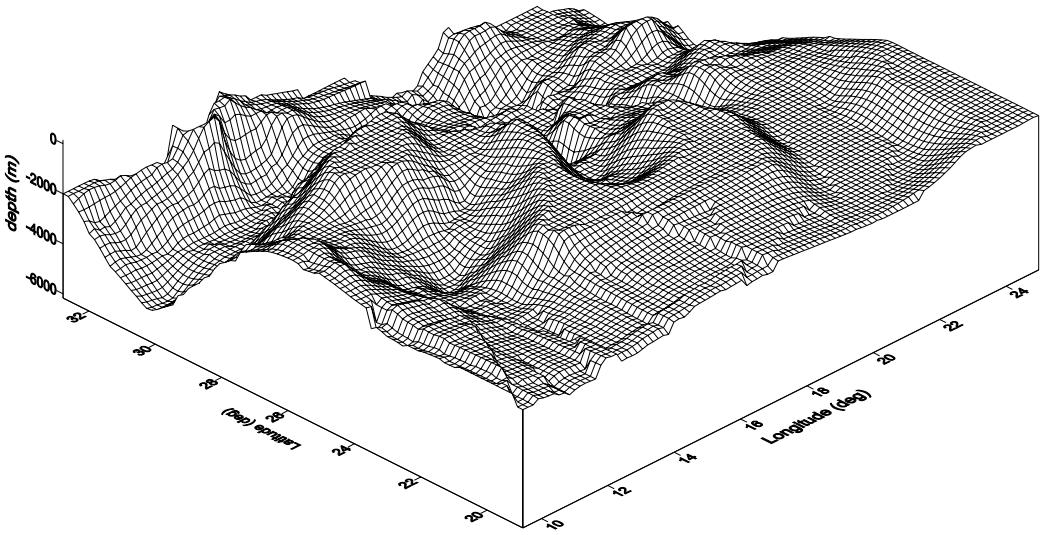


Figure 6. Gridded surface of the top Precambrian strata. These data were digitized from a structure-contour map of the Libyan Arab Republic and adjacent areas compiled by Goudarzi *et al*. (1978). The scale of the structure contour map is 1:2,000,000.

The surficial layer was grouped with the Cenozoic and Mesozoic layers and considered one layer since there is not enough data available to make the distinction between these layers. Below this layer is the Paleozoic layer which was hand digitized from the structure contour map of Goudarzi *et al*. (1978). Next layer is the Precambrian layer, which was extracted from the same source in a similar manner. The base of the Precambrian layer forms the top of the lower crust. The lower crust is assumed to terminate at a depth of approximately 19 km. The top of the Moho was digitized from Dial (1998) and was extended to an arbitrary depth of 50 km.

Preliminary Waveform Analysis

We have found that regional seismic data is difficult to obtain due to the lack of instrumentation at regional distances around Libya. The dataset consists of thirty Libyan earthquake events that occurred from January 1990 to May 2000. Event magnitudes ranged from 3.7 to 5.2 Mb and all were shallow events. A majority of the events originated in the vicinity of the Cyrenaica uplift in the northeast section of Libya. The stations used for this study are Gafsa, Tunisia (GFA), Anoyia, Crete (IDI), Kottamia, Egypt (KEG), and Wield Dalam, Malta (WDD), which are all broadband digital stations of the Mediterranean Network (MEDNET). Our strategy is to gather as many events as possible within regional distances and to produce usable seismic records for the purpose of discrimination. Records are then being cataloged and seismic phases are being picked to best identify which phases and discriminatory methods will work best in now and in the future.

Component velocity seismograms were corrected for instrument response, tapered, and band passed with a Butterworth filter at five different frequency bands: 0.5-1 Hz, 1-2Hz, 2-4Hz, 4-6Hz, and 6-8 Hz. Signal to noise ratios (SNR) were then measured and evaluated. We chose an SNR of two for our analysis. We calculated theoretical phase arrival times, picked arrival times, and measured the largest amplitude within three seconds of the predicted arrival time.

We find significant *Lg* blockage across the Mediterranean Sea, making any use of *Lg* for discrimination difficult. Thus, we must rely on *Pn* cross-spectral ratios and/or *Pn*/*Sn* phase ratios for discrimination. *Sn* is present in some of the records; but not sufficiently to construct a *Pn*/*Sn* phase ratio diagram. Since we do not have identified explosions in our dataset, we cannot make any conclusion about the effectiveness of phase and cross-spectral ratios for

discrimination. However, we find good signal to noise for *Pn* 1-2/ 6-8 Hz spectral ratios as well as *Pn*/*Sn* phase ratios at 6-8 Hz (Figure 7). The earthquake events plotted on the *Pn* 1-2/6-8 Hz spectral ratio give similar results as previous work conducted with Nevada Test Site (NTS) data (e.g., Walter et al., 1995; Figure 2). This demonstrates that *Pn* maybe a useful discriminatory phase as more events and data become available.

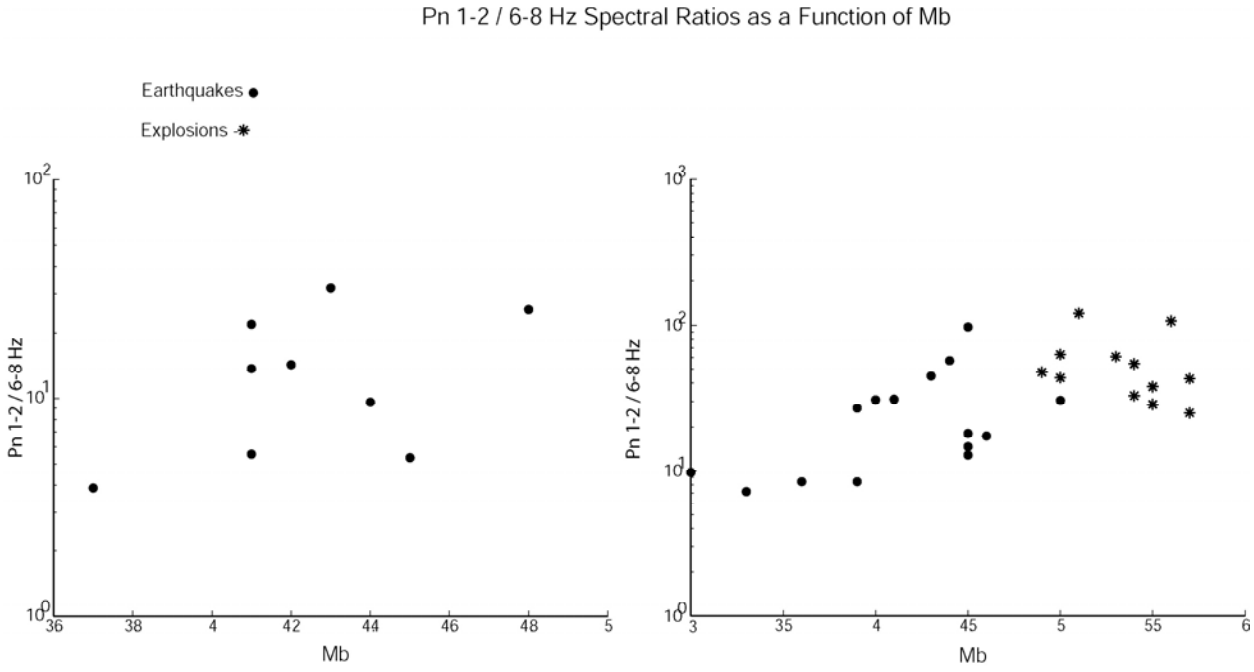


Figure 7. Comparison of Libyan spectral ratio diagram (left), compared to NTS spectral ratio diagram (right).

Remote Sensing Data

Remote sensing data were used to identify major geologic features and spatial correlations between various datasets. Thirteen remotely sensed images covering two different regions of Northern Libya were carefully selected. Four images covered a segment of northeastern Libya, which is the most seismically active portion of the country. The surface geology of this area is composed primarily of Triassic rocks and Quaternary surficial deposits. A few major basement faults are located in the area but the faulting style found in this area is that of thrust faulting which is different from those seen in the northwestern portion of the country. Nine of the remotely sensed images were collected for the northwestern portion of the country, which is the second most seismically active and is also the site of recent seismic activity. This area is highly faulted, much more geologically complex, and contains a portion of the Hun Graben and other prominent geological features in Libya. The faulting style exhibited in this region is that of strike-slip and normal faulting with a general northwesterly trend. Analyzing these images will help in identifying more recently active faults and may even help in identifying previously unmapped faults.

The first step in processing the remotely sense images was to create a mosaic of the two areas. We applied a seamless mosaicking technology that employs histogram matching, cutline feathering, and careful selection of the order in which images are overlain for the cuts. The images collected for the northeastern portion of Libya were Landsat 4 (path/Row): 182/38, 183/38, 184/38 and 183/37. These images were already georeferenced to UTM zone 34. Landsat 4 images are composed of 7 bands, and for the initial phase of our analysis, bands 3, 2, and 1 (in that order) were selected for processing as these bands best represent the natural color. The final mosaicked image is shown in Figure 8.

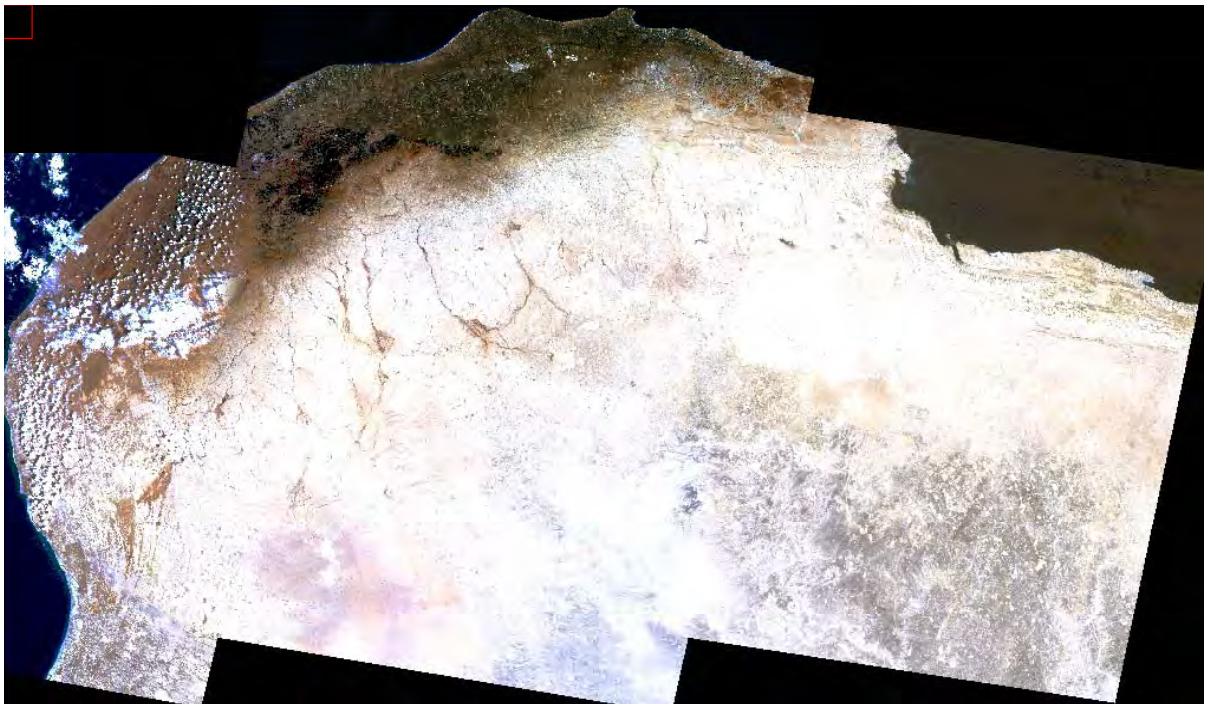


Figure 8. Final mosaicked image for the northeastern portion of Libya.

Figure 9 shows some of the mapped faults in Libya overlaid on the two mosaicked images. There seems to be a correlation of the location of the faults with changes in vegetation, geology and drainage. It is noteworthy, however, that the images depict surface reflectance that is not always related to vegetation. Having the faults overlaid on the images helps in identifying the appearance of faults on the image. This will later help us in identifying suspect or unmapped faults, and we may be able associate an age with some of the previously undated faults. Since the faulting styles exhibited in the Cerenaica uplift and the Hün Graben area are so different, we may even be able to identify the styles of some of the unmapped faults based purely on the satellite images. We are constructing another overlay that includes the location of seismic events and will enable us to associate the events with the faults on which they occur.

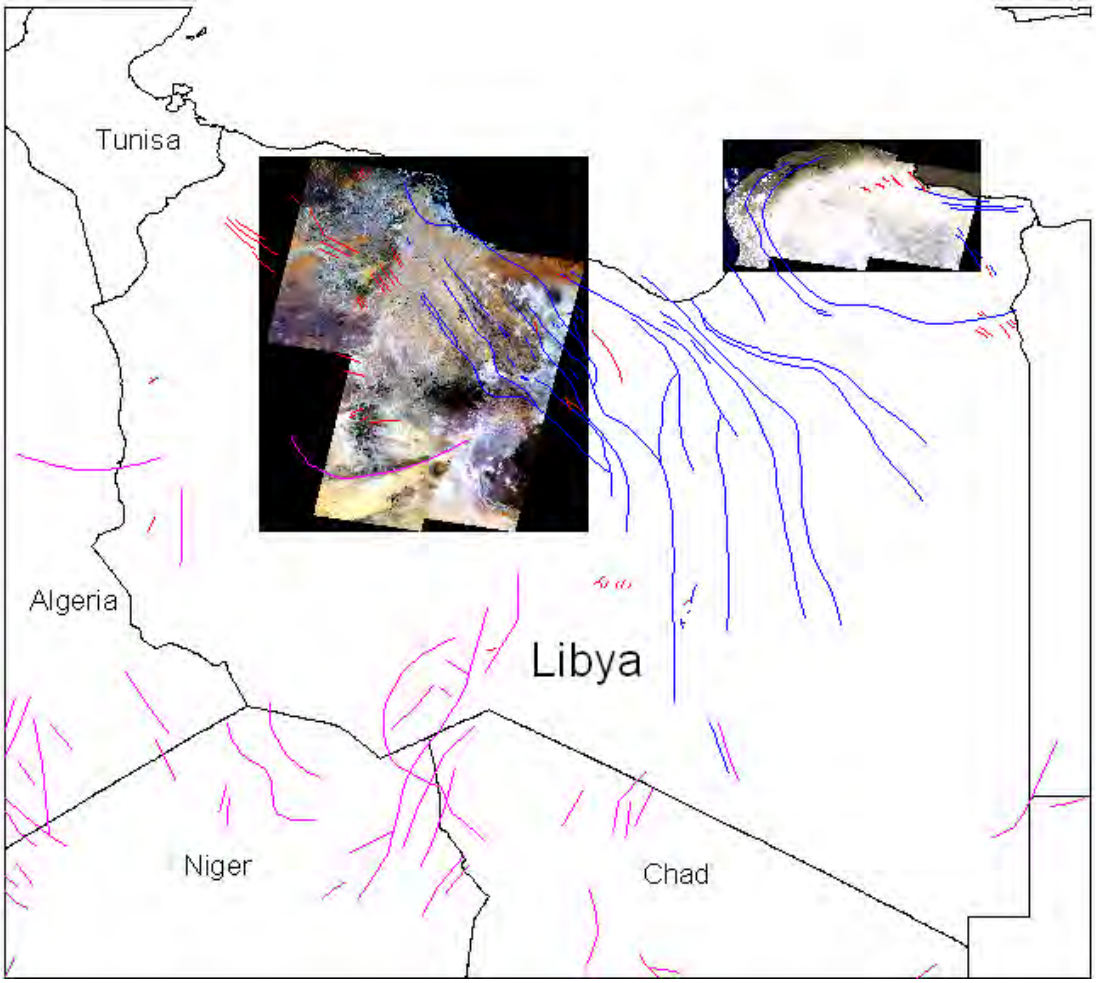


Figure 9. Two mosaicked areas overlain by mapped faults in Libya. The blue faults are faults cutting basement and younger rocks, the red faults cut only Mesozoic and younger rocks, and the magenta faults are other mapped faults in the region

CONCLUSIONS

We are in the process of calculating the gravity attraction of each layer in our 3-D model. This model will be a comprehensive model of the Libyan lithosphere. We will validate our 3-D model with regional waveforms. At this time the seismic data on hand presents no solid conclusion except that a couple possible discriminatory methods may be helpful in future verification work. The collection of more regional data is of key importance at this point. There are regional networks in Algeria and Egypt that could offer abundant records, however obtaining this data is difficult. On completion, we believe that our integrated analysis will be the most comprehensive study of the Libyan lithosphere ever undertaken and will provide significant insight on the tectonics and wave propagation in the area.

REFERENCES

Baker, M. R., and D. I. Doser, 1988, Joint inversion of regional and teleseismic earthquake waveforms, *J. Geophys. Res.* 93, 2037-2045.

Dial, P., 1998, An integrated geophysical study of North Africa and Mediterranean lithospheric structure, *PhD. Dissertation*, p.1-38.

Goudarzi, G.H, and Smith J.P., 1978, Preliminary-structure contour map of the Libyan Arab Republic and other adjacent areas, *USGS.*

Hearn, P. Jr., et Al, 2001, Global GIS Database: Digital Atlas of Africa, *USGS. Digital Data Series (DDS-62-B).*

Lay, T., Wallace, T. C., Modern Global Seismology, 1995, *Academic Press*, p. 310-430.

Philips, W.S., Hartse, H.E. Taylor, S.R. and Velasco, A.A., Application of regional phase amplitude tomography to seismic verification,

Walter, W. R, K. M Mayeda, and H. J. Patton, 1995, Phase and spectral ratio discrimination between NTS earthquakes and explosions; Part I, Empirical observation, *Bull. Seism. Soc. Am., 85*, 1050-1067.

Wessel, P., and Smith, W. H. F., 1995, New version of the generic mapping tools released, *EOS Trans. Amer. Geophys. U.*, 76, 329.

GROUND-TRUTH COLLECTION FOR MINING EXPLOSIONS IN NORTHERN FENNOSCANDIA AND RUSSIA

David B. Harris,[1] Frode Ringdal,[2] Elena O. Kremenetskaya,[3] Svein Mykkeltveit,[2] Johannes Schweitzer,[2] Teresa F. Hauk,[1] Vladimir E. Asming,[3] Donald W. Rock,[1] Jon P. Lewis[1]

Lawrence Livermore National Laboratory,[1] NORSAR,[2] Kola Regional Seismological Center[3]

Sponsored by National Nuclear Security Administration
Office of Nonproliferation Research and Engineering
Office of Defense Nuclear Nonproliferation

Contract No. W-7405-ENG-48[1] and DE-FC03-01SF22420[2,3]

ABSTRACT

This project is providing ground-truth information on explosions conducted at the principal mines within 500 kilometers of the ARCES station, and is assembling a seismic waveform database for these events from local and regional stations. The principal mines of interest are in northwest Russia (Khibiny Massif, Olenogorsk, Zapolyarny, and Kovdor groups) and Sweden (Malmberget, Kiruna). These mines form a natural laboratory for examining the variation of mining explosion observations with source type, since they include colocated surface and underground mines and mines conducting a variety of different shot types. In September 2002 we deployed two lines of temporary stations from the Khibiny Massif through and to the north of the ARCES station. This deployment is producing data that will allow researchers to examine the variation of discriminants caused by varying source-receiver distance and the diversity of explosion types.

To date, we have collected ground-truth information on 1,118 explosions in the Kola Peninsula, and have assembled waveform data for approximately 700 of these. The database includes waveforms from instruments temporarily deployed in the Khibiny Massif mines, from the Apatity network just outside of the Massif, from LVZ, KEV and ARCES, and from the stations deployed along the two lines into northern Norway. In this paper we present representative waveforms for several types of shots recorded at various regional distances.

We have conducted a preliminary study of the variation of phase ratios as a function of source type. This study shows significant differences in Pn/Sn and Pn/Lg ratios for two types of mining explosions: surface ripple-fired explosions and compact underground explosions. Compact explosions are, typically, underground explosions of a few tons with only one or two short delays, and are the closest approximation to single, well-tamped explosions available in the Khibiny mines. The surface shots typically are much larger (ranging up to hundreds of tons), with many delays. The surface mine that we present results for typically also conducts several distinct shots across the mine nearly simultaneously (with a few seconds or tens of seconds). Measured phase ratios are more consistent for compact underground explosions. This consistency is an expected result given the smaller scope for shot variation in these smaller events. In addition, Pn/Lg ratios appear more stable than Pn/Sn ratios for both types of events. The most interesting result is that the compact underground explosions are richer in shear energy (i.e. having smaller P/S ratios) than their surface ripple-fired counterparts.

We continue to work on an approach for identifying the principal mines to be targeted for screening at a particular station. Often, routine industrial blasts constitute a large proportion of events detected by monitoring stations close to major mining districts. Many mines may be present, and it may be a problem to determine which subset of mines is responsible for the majority of the events, and should be prime candidates for the deployment of ground-truth collection resources. Our solution to this problem entails several steps. The first is to find geographic clusters of events that may correspond to major groups of mines. For this step, we use event density maps generated from existing network catalogs. This year we examined some of the tradeoffs in generating event density maps: use of automated bulletins to produce maps vs. analyst-reviewed bulletins, and the amount of time required to produce stables maps which can be used to identify significant mines.

OBJECTIVES

This year the project has had five principal objectives:

1. Collect ground-truth information for a large number of explosions in a diverse set of mines in the Kola Peninsula.
2. Assemble a database of waveform observations of these events from principal monitoring stations of the region.
3. Deploy additional stations in the region to fill range gaps in the set of observations.
4. Perform preliminary analysis of the variation of standard discriminants with source-receiver range and source type.
5. Examine strategies for allocating ground-truth resources in complex mining regions.

RESEARCH ACCOMPLISHED

Ground-truth Collection and Database Construction

KRSC has collected ground-truth information on mining explosions in the Kola Peninsula for the period September 2001 through June 2003. Information provided by the operators of ten mines in northwest Russia (Figure 1) includes shot location (i.e. which mine), the type of each shot (underground, surface, ripple-fired, compact), the yield, and the number of shots (where several are nearly simultaneous). KRSC estimates the origin times of all explosions using its local and near regional seismic network. In addition, KRSC has deployed two temporary stations (RASV, GFR) within the Khibiny Massif complex (Figure 2) and another station near the Olenogorsk group (MON). Waveform data are available from the in-mine sensors typically for about one third of all the shots.

The GT catalogs provided by KRSC are being processed into an Oracle database and are being used to extract waveforms from continuous data. To date, information on 1,118 events has been loaded to the database (through March 2003). We have extracted event segment waveform data for over 700 of these events (from the ARCES array, the Apatity stations and in-mine stations).

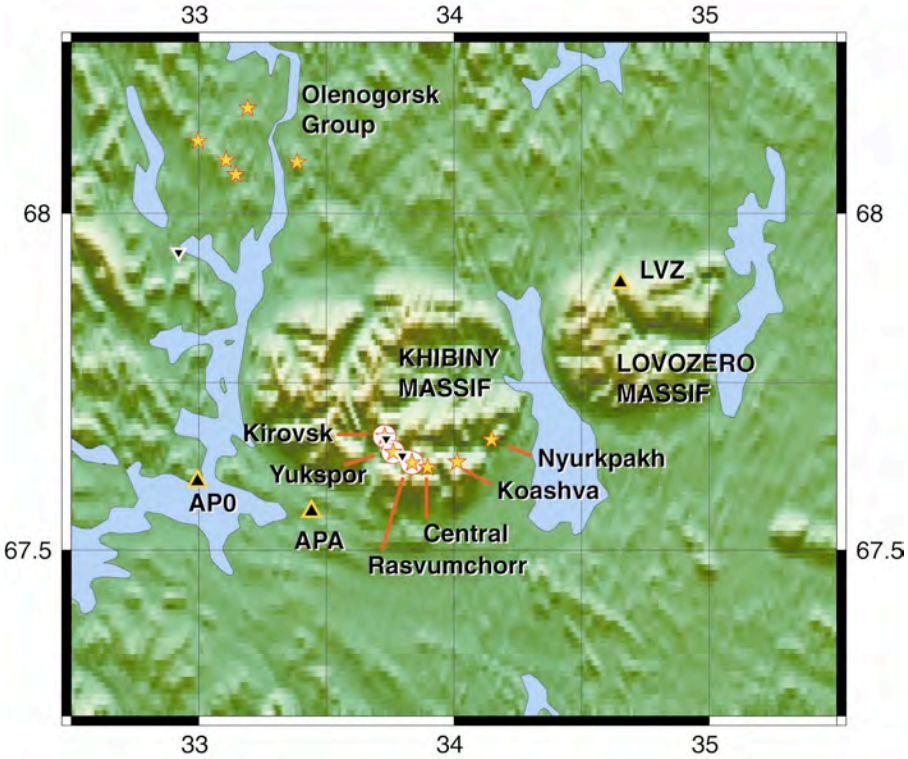


Figure 1. Locations of the mines (stars; circles indicate mines with both underground and surface facilities), permanent stations (triangles) and temporary stations (inverted triangles) in the vicinity of the Khibiny Massif included in this study. The local stations provide origin times for the explosions.

Temporary Sensor Deployment

To enable studies of the behavior of discriminants over a range of source-receiver distances and source types, we deployed an additional eight stations in northern Finland, Norway and Russia. Six GS-13 three-component stations with Reftek recorders were deployed in late August / early September 2002 (Harris, et al., 2002) to sites in northern Norway and Finland. Subsequently a broadband station with a Reftek recorder was deployed at the Zapolyarny deep borehole site in Russia. A significant sample of data has been collected from these sites, allowing preliminary analysis. Continued operation of these stations until late summer 2004 is planned.

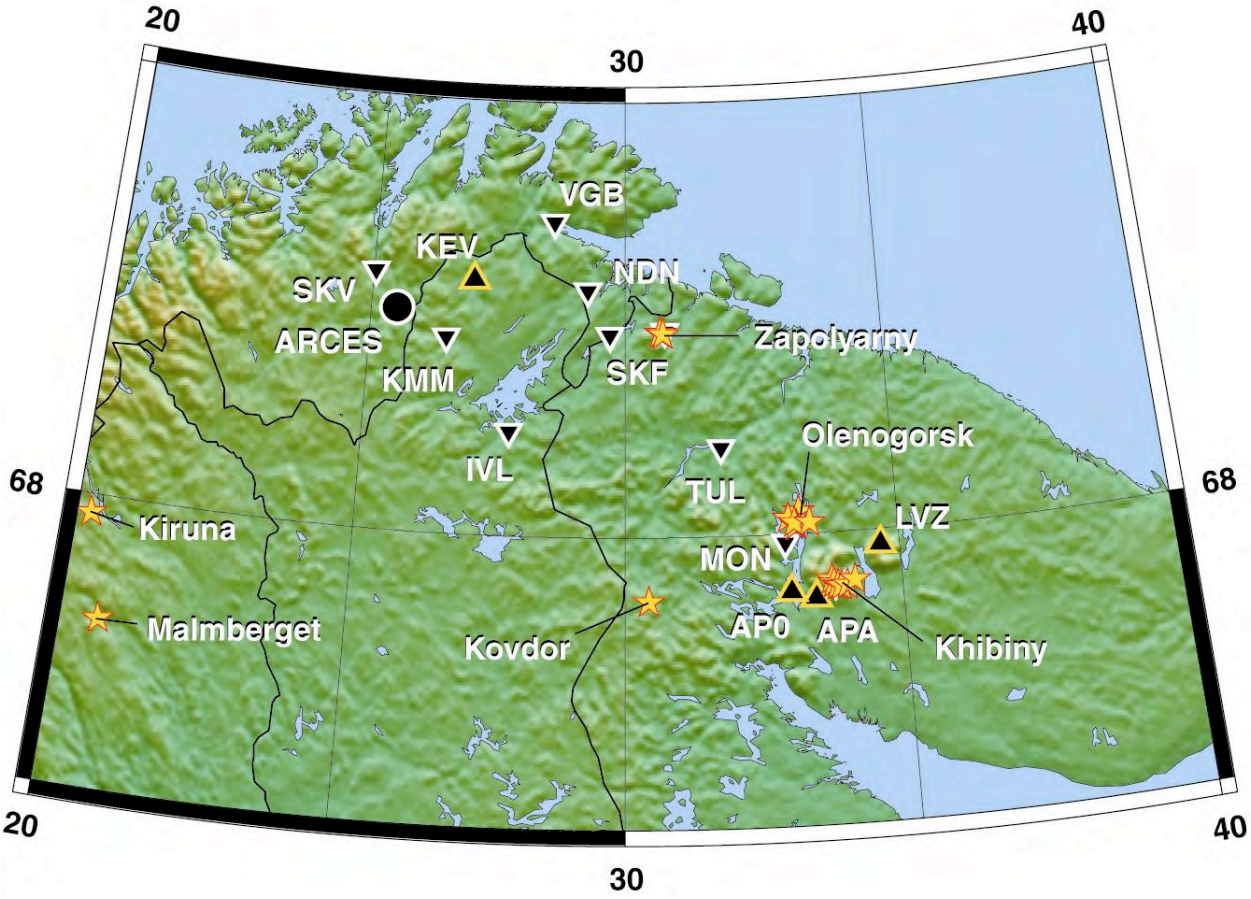


Figure 2. Sites of temporary seismometer deployments (inverted triangles), major mines or mine groups (stars) and permanent stations (triangles and filled circle for IMS primary) included in the regional-scale portion of this study.

Preliminary Examination of Data and Discriminant Behavior

A preliminary examination of the data from the ARCES array and stations along the southern line deployed in Finland and Norway show significant differences in the character of seismic signals from different types of mining explosions. In particular, compact underground explosions at the Kirovsk mine and surface ripple-fired explosions at the Central mine (Khibiny Massif, Figure 1) produce signals with markedly different variability. The compact underground explosions are small shots typically in the 2-5 ton range conducted with only a few delays. The surface shots at the Central mine typically are much larger, ranging up to several hundred tons in the aggregate and with many delays. In addition, the Central open-pit shots are usually conducted in several separate groups and dispersed over the 2-3 kilometer aperture of the mine. These separate shots are typically detonated within a few seconds or tens of seconds of each other.

The signals from the Kirovsk compact underground shots are relatively uniform and consistent with their simplicity. Figure 3 shows a typical Kirovsk compact shot filtered into a succession of 4-Hz bands. At left in the figure are the

observations from our temporary station at IVL that show a relatively flat distribution of energy across all frequency bands at a source-receiver range of 271 kilometers. This type of energy distribution is consistent for compact underground shots.

By contrast, the open-pit ripple-fired explosions conducted at the Central mine are relatively inconsistent. Figure 4 shows three examples of surface explosions from that mine. The event in Figure 4a has a very similar pattern to the compact explosion of Figure 3. The event of Figure 4b displays a marked decline in signal energy as a function of frequency (more normal by most analyst's expectations). Figure 4c shows an event where the energy actually increases as a function of frequency. This large range in spectral characteristics undoubtedly is a function of the differences in detail of the delays applied in the shots, as well as the complex interactions among the several groups of shots that comprise each of these explosions.

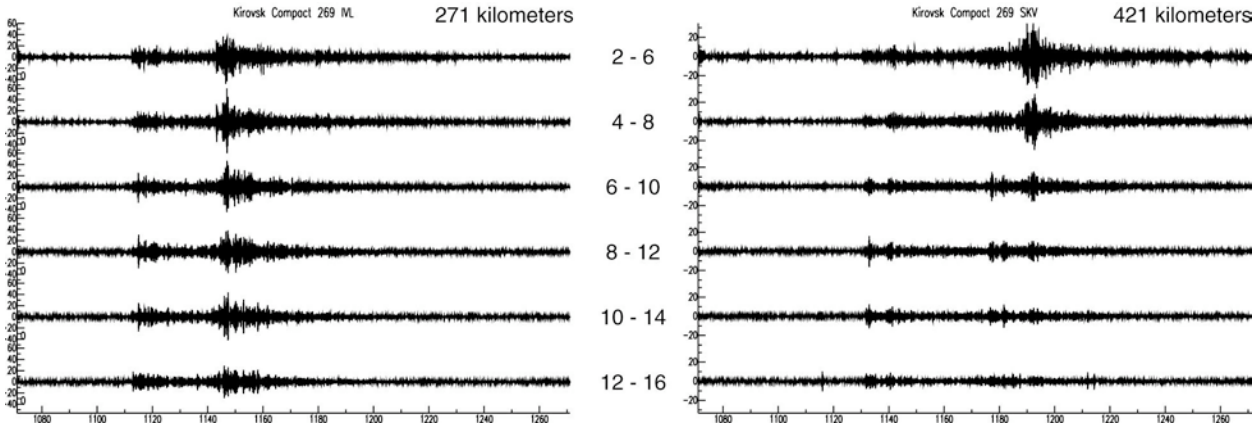


Figure 3. Compact underground explosions conducted at the Kirovsk mine show fairly uniform broadband excitation when observed at IVL (left; 271 kilometer range). These plots display waveforms filtered into overlapping bands of 4 Hz width (2-6 Hz, 4-8 Hz, etc.). This uniform pattern of excitation is consistent for shots of this type. At SKV (right; 421 kilometer range) the larger shear attenuation results in the extinction of the shear phases, Sn and Lg, above 10 Hz.

The behavior of P/S discriminants is consistent with these simple waveform observations. P/S ratios for the compact underground explosions exhibit less scatter than corresponding ratios for the surface ripple-fired explosions. We computed P/S ratios for a selection of Kirovsk and Central events recorded with good signal-to-noise ratios at our temporary stations IVL and SKV (Figure 5). The compact explosions P/S ratios exhibit substantial less scatter, particular when observed at the more distant station (SKV). It is more remarkable that there appears to be a distinct bias between the two types of events. The compact shots have noticeably lower P/S ratios than their open-pit counterparts. This observation is at variance with expectations that smaller underground shots with few delays might be a better approximation of single shots such as nuclear explosions (which should have higher P/S ratios). It is possible that this unexpected behavior is due to the fact that the compact underground shots are typically designed to drop the ceilings of tunnels. Consequently, they are not well contained (despite being underground), and they may have large secondary energy releases from the mass of the falling ceiling.

Note that the P/S ratios increase with increasing frequency, which is consistent with the frequent observation that P/S ratios discriminate earthquakes and explosions more reliably at higher frequencies. Pn is the more suitable P phase to measure, given its lower increase in attenuation rate with increasing frequency, as has been noted previously (Kvaerna, et al., 2002). Similarly, Sn is more likely than Lg to be observed at greater distances and higher frequencies (Kvaerna, et al., 2002).

These measurements were repeated with larger numbers of event observations available at ARCES, with the same results. From the database we have been constructing, we selected 66 Central open-pit explosions (with good SNR at ARCES) and 185 Kirovsk compact underground explosions. The P/S ratios in two frequency bands are shown in

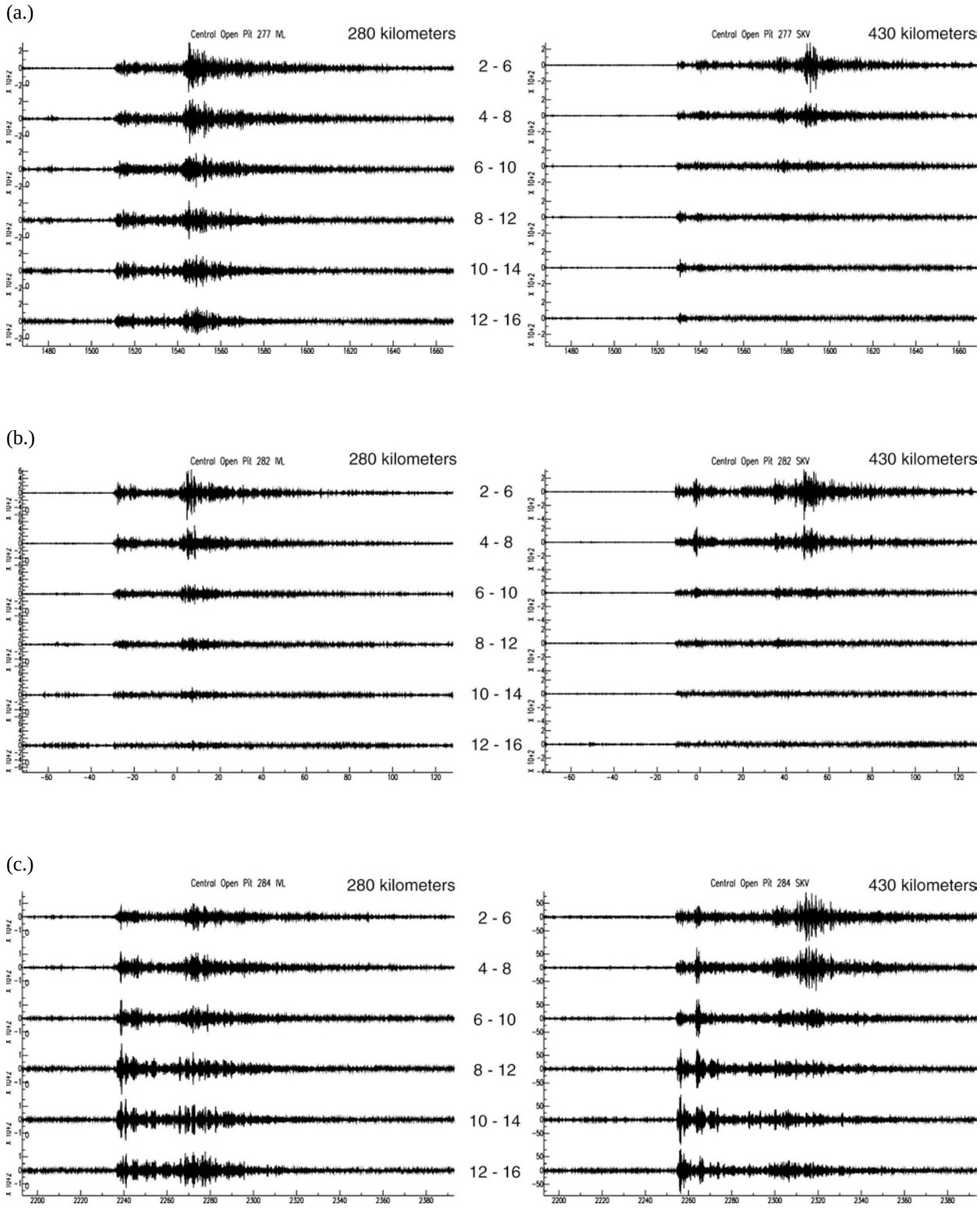


Figure 4. Larger ripple-fired explosions at the Central open-pit mine of the Khibiny Massif exhibit large variations in spectral content consistent with their greater complexity. Signals energy content may be flat (a.) with frequency, or may decrease (b.), or increase (c.) as observed at station IVL (left). The variations are even more pronounced for P phases observed at SKV (right).

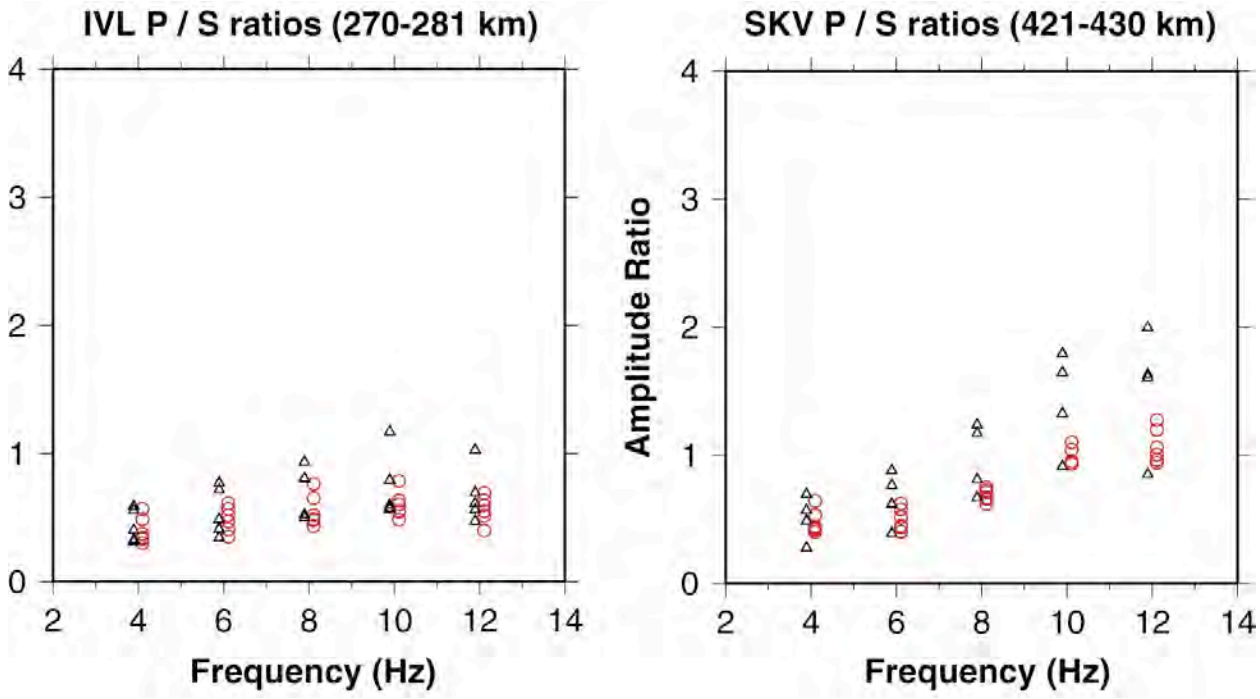


Figure 5. P/S ratios for open-pit explosions (triangles) show more scatter than P/S ratios for compact underground explosions (circles). Ratios for the compact underground shots are biased lower than their open-pit counterparts. These effects are more pronounced at greater source-receiver distances.

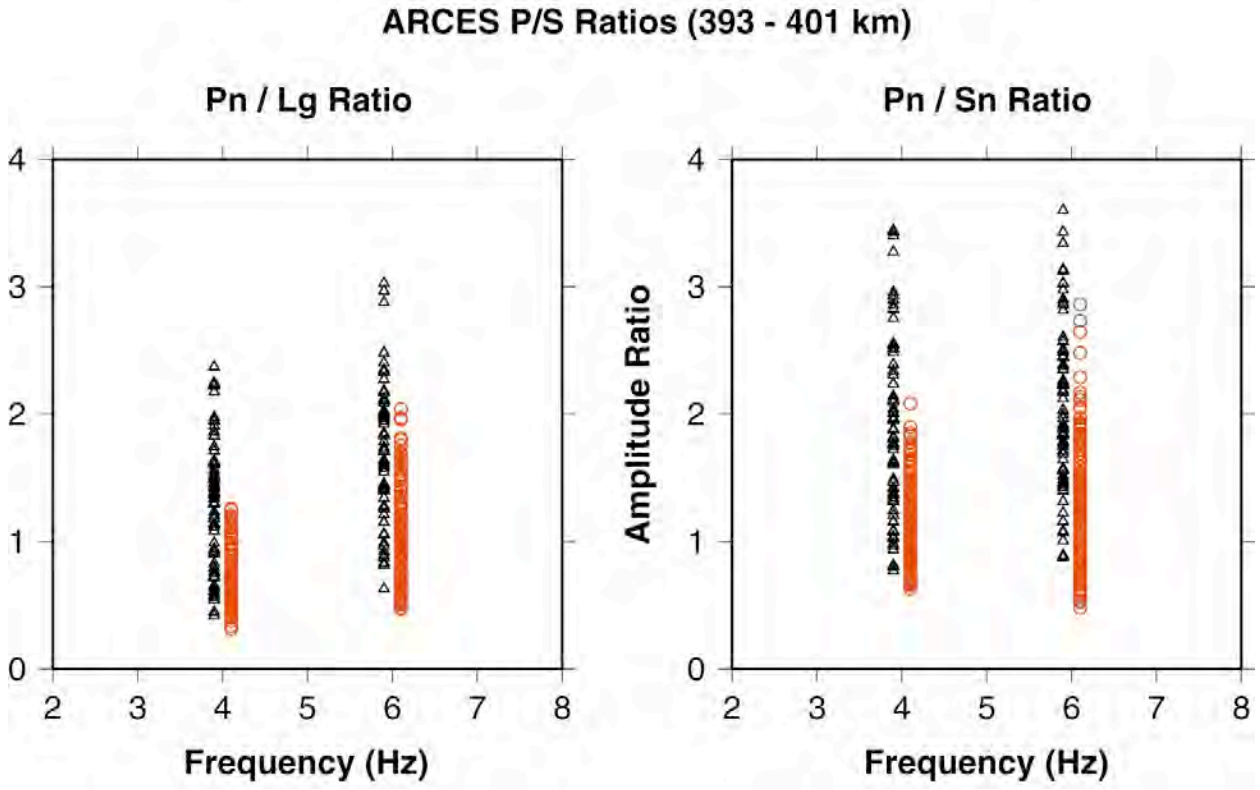


Figure 6. Plots of larger populations of compact underground (185, circles) and open-pit (66, triangles) P/S ratios show the same trends at ARCES as at the temporary stations. The Pn/Lg ratio (left) is more stable than the Pn/Sn ratio (right).

Figure 6, this time separated by shear phase type (the Figure 5 measurements used a shear window that encompassed both Sn and Lg). For these measurements, we used one of the short-period array elements, so that measurements could be conducted only in the two lowest frequency bands (2-6 and 4-8 Hz). Note that the Pn/Lg ratios have lower variance than the Pn/Sn ratios.

Strategies for Ground-truth Allocation

One approach to allocating ground-truth resources is to determine which mines or mining districts are most visible seismically. Maps of seismic event density, constructed from catalogs, provide one method for determining the hot spots requiring calibration attention. This year we examined several tradeoffs in the construction of event density maps: use of single-station catalogs vs. network catalogs, use of automated catalogs vs. analyst-reviewed catalogs, and use of catalogs constructed over short time durations vs. long time durations. In the last case, we seek to answer the question "How much data is enough?"

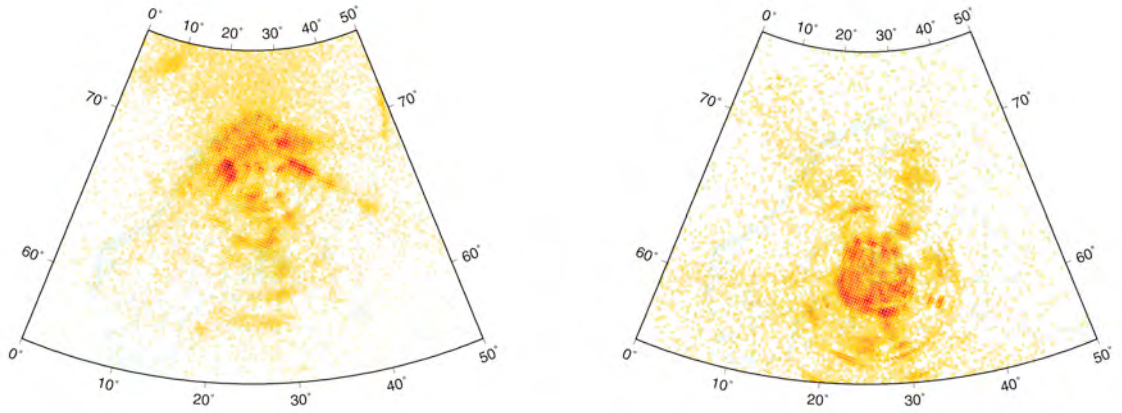


Figure 7. Event density maps constructed from automatically-generated single-station catalogs of about one decade duration. The event density map at left is constructed from an ARCES catalog, and the one at right is constructed from a FINES catalog. These maps have a high degree of clutter and poorly resolved geographic clusters, but do serve to identify some of the major mining regions. Areas of greatest event density are red (dark), grading to yellow (light) for intermediate density, then white for low event density.

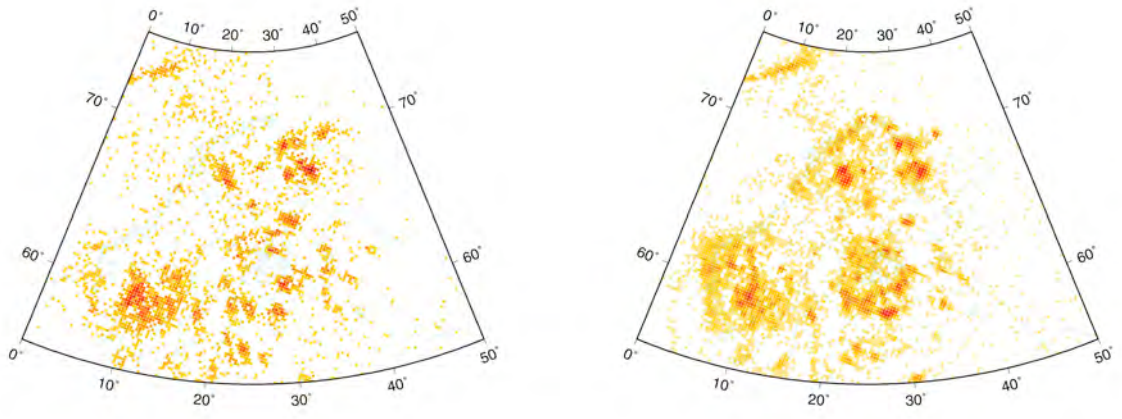


Figure 8. Event density maps derived from network catalogs are far better resolved with less clutter than maps constructed from individual station catalogs. At left is a map derived from the automated NORSAR global beamforming catalog; at right is the map developed from the analyst-reviewed EPX bulletin. The latter bulletin spans a decade.

Figure 7 shows event density maps constructed from automatically generated bulletins for individual stations, ARCES at left and FINES at right. These maps are poorly resolved with a large amount of background clutter. They might suffice to identify the very largest mining districts within 300 or 400 kilometers of the station. A much more satisfactory solution is to use event density maps generated from network catalogs. We show two such maps in Figure 8. At left is an event density map derived from the NORSAR automatically-generated global beamforming bulletin. This map has excellent delineation of large mining districts (Khibiny, Olenogorsk, the two Swedish iron mines, etc.), but still a moderate amount of background clutter. The map at right was produced from the highest-quality analyst-reviewed NORSAR bulletin and has even better resolution and further reductions in clutter. Clearly network bulletins are required to produce adequate maps for identifying high-interest mines or mining districts, and analyst-reviewed bulletins are desirable.

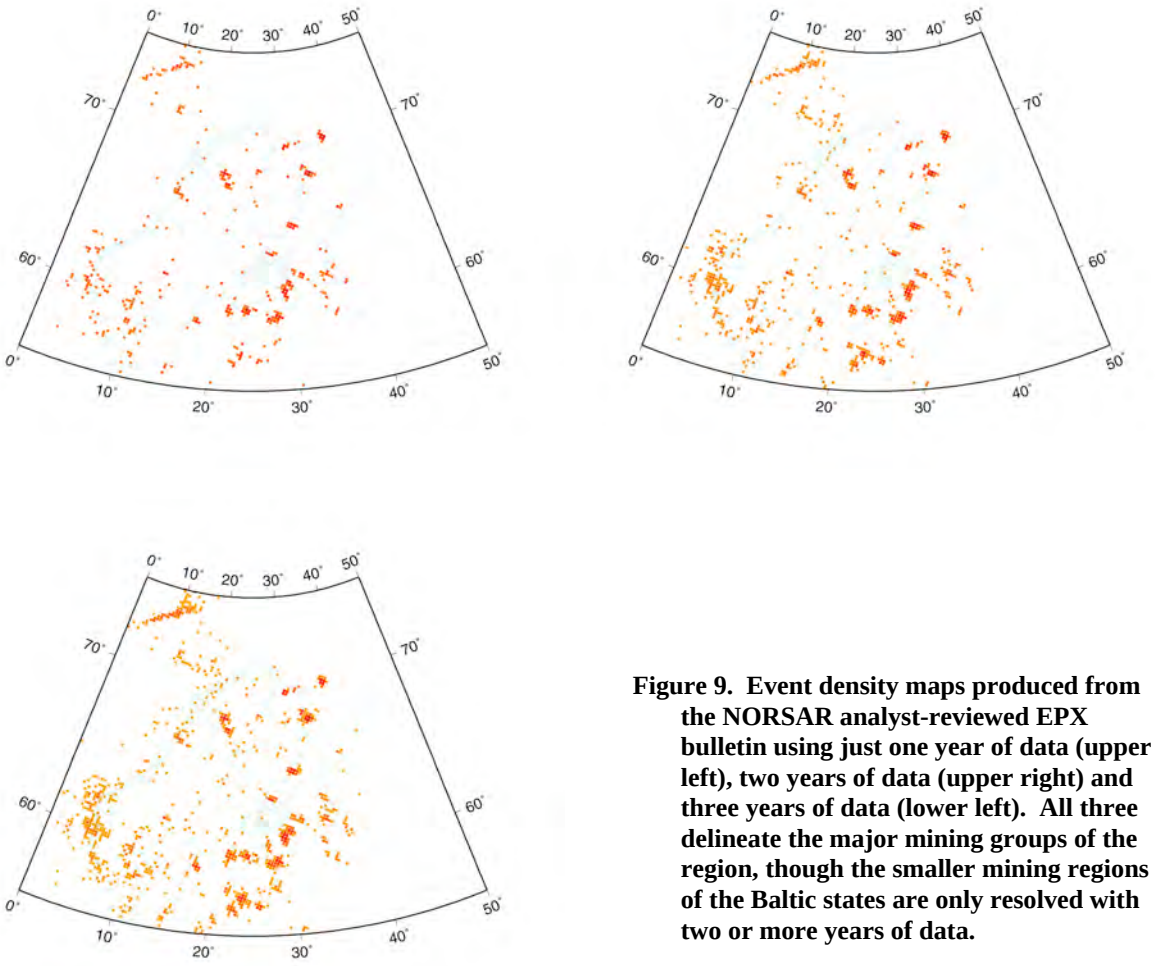


Figure 9. Event density maps produced from the NORSAR analyst-reviewed EPX bulletin using just one year of data (upper left), two years of data (upper right) and three years of data (lower left). All three delineate the major mining groups of the region, though the smaller mining regions of the Baltic states are only resolved with two or more years of data.

Figure 9 provides some insight on how much data is required to delineate significant mining areas. The figure shows three maps constructed from one, two and three years of the NORSAR analyst-reviewed network bulletin. The major mining groups are delineated with just one year of data, though many of the smaller mining districts require two or more years to be resolved from background clutter.

CONCLUSIONS AND RECOMMENDATIONS

The bias in spectral ratios between compact underground explosions and open-pit ripple-fired explosions has potential operational and source phenomenology implications. P/S discriminants that lump all mining explosions together may have higher variance than a collection of discriminants designed to sort the different types of shots.

The potential reduction in variance may become more significant as P/S discriminants are adapted to higher frequency signals. The fact that compact underground shots appear relatively richer in S energy than surface rippled shots may shed light on source physics, especially the generation of S phases. Not only is there a clear observational difference in the relative generation of P and S phases in these two populations of mining explosions, but we also have information on how these two shot types are conducted.

Our first recommendation for continued research is to check the reproducibility of the P/S bias observation for other mines. The Rasvumchorr mine conducts compact underground explosions, and the Koashva mine conducts large ripple-fired surface shots. Kirovsk occasionally conducts small surface explosions. The Olenogorsk mines and Kovdor conduct larger ripple-fired surface explosions. Our database contains many examples of these other explosions that can be used to check reproducibility. In addition, a later phase of the project will provide data from the Swedish iron mines at Kiruna and Malmberget, both of which conduct compact underground shots.

Our second recommendation is to determine why the compact underground shots appear relatively richer in S energy. Does it have anything to do with the fact that these shots are subterranean? Is it a function of the fewer delays (i.e. does the large pattern of delays in the surface shots preferentially suppress shear energy)? Is it a secondary mass transfer effect? Many of the smaller underground shots are designed to drop the roof of a tunnel. Some of the data we are collecting will help answer these questions. The Khibiny mines conduct occasional large ripple-fired explosions underground. A combination of observations and modeling probably will be required to understand the source physics. Results from this summer's source phenomenology experiments in Arizona should be particularly useful.

ACKNOWLEDGEMENTS

The authors would like to thank Bill Walter for helpful suggestions regarding the analysis of P/S discriminants.

REFERENCES

Harris, D., F. Ringdal, E. Kremenetskaya, S. Mykkeltveit, D. Rock, and J. Schweitzer (2002), "Ground-truth Collection for Mining Explosions in Northern Fennoscandia and Russia," *Proceedings of the 24th Seismic Research Review - Nuclear Explosion Monitoring: Innovation and Integration*, Los Alamos National Laboratory, *LA-UR-02-5048*, Ponte Vedra, FL, Sept. 17-19, 2002.

Kvaerna, T., E. Hicks, J. Schweitzer, and F. Ringdal (2002), "Regional Seismic Threshold Monitoring," *Proceedings of the 24th Seismic Research Review - Nuclear Explosion Monitoring: Innovation and Integration*, Los Alamos National Laboratory, *LA-UR-02-5048*, Ponte Vedra, FL, Sept. 17-19, 2002.

BROADBAND SEISMIC EXPERIMENTS IN SOUTHWEST AND NORTHEAST CHINA

Wenjie Jiao and Winston Chan

Multimax Inc.

Sponsored by Defense Threat Reduction Agency

Contract No. DTRA01-00-C-0081

ABSTRACT

Since August 2001, we have conducted two broadband portable seismic experiments in China to collect seismic data for advanced studies on regional crustal and mantle structures, earthquake prediction, characteristics of wave propagation, and earthquake and explosion sources. The first one is in Yunnan province, southwest China, while the second experiment is in Jilin and Heilongjiang provinces, northeast China. The experiment region in southwest China is situated in a transitional tectonic region between the uplifted Tibetan plateau to the west and the Yangtze continental platform to the east. The region displays varying crustal thickness from 35 km to over 60 km with seismic activity strongly associated with the mapped active faults. The portable seismic network, consisting of nine stations equipped with STS-2 seismometers and RefTek data loggers, and 10 stations with Chinese broadband instruments, is deployed in the region of 98-105°E, 21-29°N. There are also 23 permanent digital broadband seismic stations recording in the region. Yunnan has the strongest intra-plate seismic activities in China. Moreover, Yunnan is a very interesting area considering its position relative to several strong seismic zones in China, such as Tibet, Xinjiang, Sichuan, and North China, as well as those in Burma, India-Pakistan, Tonga-Fiji, Japan, and the west coast of South and North America. The experiment region in northeast China lies near the China-North Korean border, in the region of 124-130°E, 41-48°N. The region is characterized by volcanic activities accompanied with low-level seismicity. Other active seismic zones are the Haicheng area in Liaoning province as well as those in the Korean Peninsula. The northeast portable network consists of 10 broadband instruments.

This is the third year of this project. All the waveforms have been converted into Seismic Analysis Code (SAC) formats, and are ready for delivery. A final report is in preparation. This paper is a brief summary of the three years' deployment work. During the experiments we recorded several moderate (M=4.5-6) local earthquakes, including one located only 100 km north from the auxiliary International Monitoring System (IMS) station KMI. These moderate earthquakes are well surveyed by the provincial Yunnan Seismological Bureau and yield high quality ground-truth information. The rare, $M_W = 7.3$ deep earthquake (depth 581.5 km) in northeast China was also recorded. A large number of local events are routinely recorded among which many are believed to be industrial explosions. Moderate to large earthquakes in other parts of China, as well as large events worldwide, are also routinely recorded, including the November 14, 2001, Ms=8.0 Qinghai earthquake; December 18, 2001, Ms=7.3 Taiwan earthquake; September 11, 2001, Ms=6.4 Iran earthquake; October 12, 2001, Ms=7.3 Mariana earthquake; January 2, 2002, Ms=7.6 Vanuatu Islands earthquake; March 3, 2002, Ms=7.2 Hindu-Kush earthquake; June 22, 2002, west Iran earthquake; August 19, 2002, $M_W = 7.7$ Fiji earthquake; September 8, 2002, Ms=7.8 Papua coast earthquake; October 10, 2002, Ms=7.7 Irian Jaya, Indonesia earthquake; and November 3, 2002, Ms=8.3 central Alaska earthquake. More over, the June 28, 2002, $M_W = 7.3$ deep earthquake (depth = 581.5km) was recorded locally, which provided invaluable waveform data for studies on regional structure and the mechanism of deep earthquake. In conclusion, this project provides a very good database for studies on the source, path and site terms of regional seismology.

OBJECTIVE

The major purpose of this project is to collect fundamental ground-truth data for advanced studies on regional crustal and mantle structures, earthquake prediction, and regional characteristics of wave propagation and seismic sources in southwest and northeast China, by deploying a broadband portable seismic network in the two areas. The region in southwest China is situated in an evolving tectonic region transitioning between the uplifted Tibetan plateau to the west and the Yangtze continental platform to the east. The region displays varying crustal thickness from 35 km to over 60 km, and seismic activity strongly associated with the mapped active faults. Figure 1 shows the topography of the Yunnan province and the layout of our broadband network. The red triangles are STS-2 seismometers from the US, while the red circles are Chinese broadband instruments (the long-period corner at 20 s) from our Chinese collaborators. Yunnan has the strongest intra-plate seismic activities in China. There are several strong seismic zones in its surrounding areas, such as Tibet, Sichuan, Burma, and India. There is also an abundance of mining activity in this area. Moreover, the distances from the Yunnan area to many of the strongest seismic zones in the world, such as the Tonga-Fiji, the east coast of North and South America, and the Japan-Kuril region, make the Yunnan area an ideal location for tectonic and structure studies recording various seismic phases. Therefore, the strong seismicity and the intense mining activity in Yunnan and its surrounding areas, as well as its unique position relative to many strongest seismic zones in the world, provide the foundation for the success of this deployment. The deployment region in northeast China is in Jilin and Heilongjiang provinces, across the border between China and N. Korea. The region is characterized by a large plain with the exception of the Changbai Mountain alone the China-N. Korea border (Figure 2). Although the seismic activity in northeast China is not as strong as that in the southwest, there are some moderate seismic zones to the south in Liaoning province and in North Korea (Figure 3). Moreover, there is some volcanic activity present in the Changbai Mountain area that generates significant seismological research interest in the area. The important position of northeast China allows our deployment in the region to provide valuable information on the regional seismology of the Northeast China Plain and North Korea.

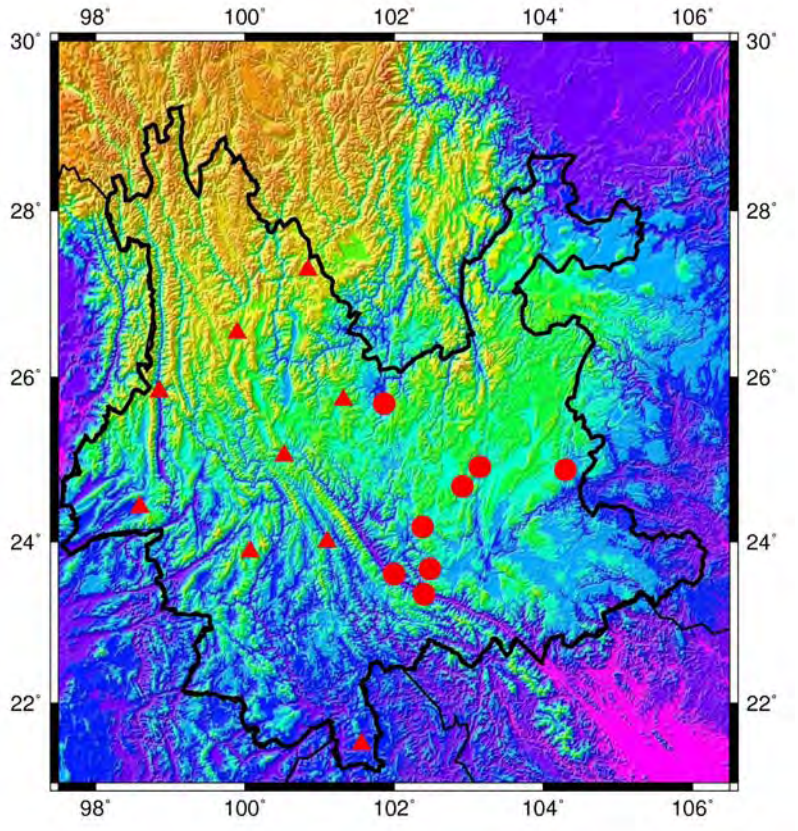


Figure 1. The topography of the Yunnan province and the layout of our broadband network. The red triangles are STS-2 seismometers, while the red circles are Chinese broadband instruments (the long period corner at 20s).

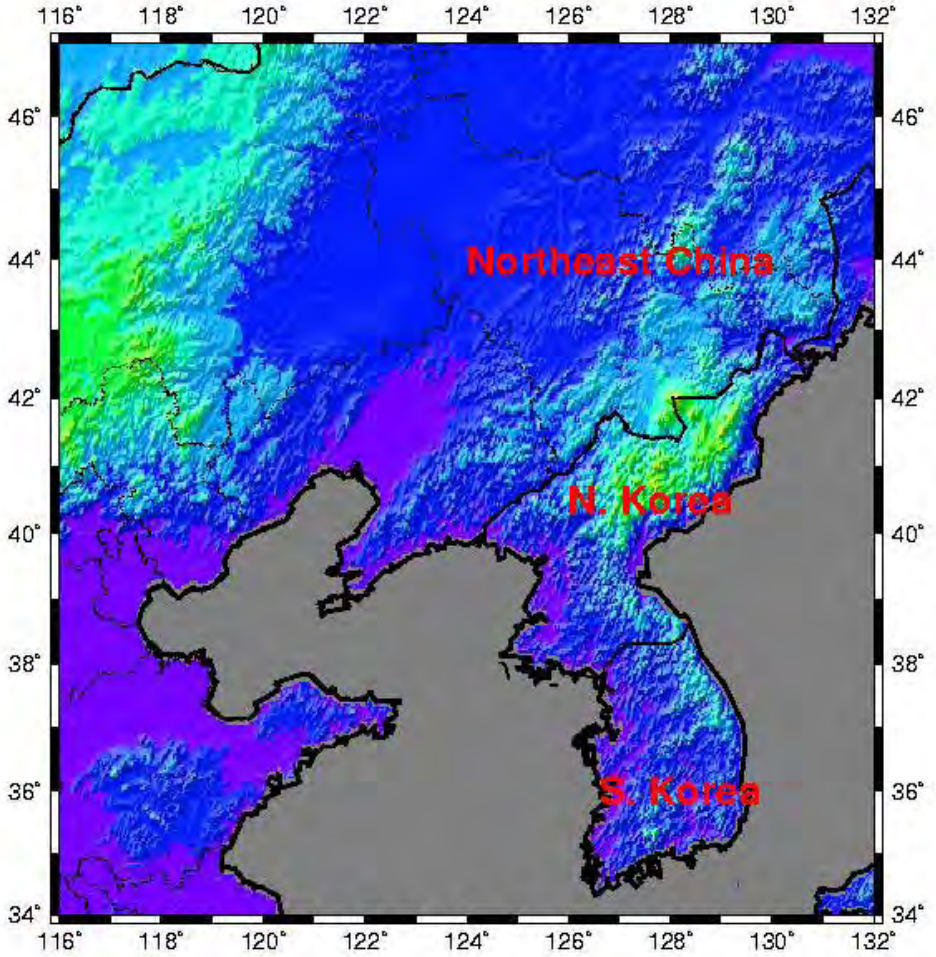


Figure 2. The topography of northeast China and the Korean peninsular. The northeast China region is characterized by a large plain with the exception of the Changbai Mountain alone the China-N. Korea border.

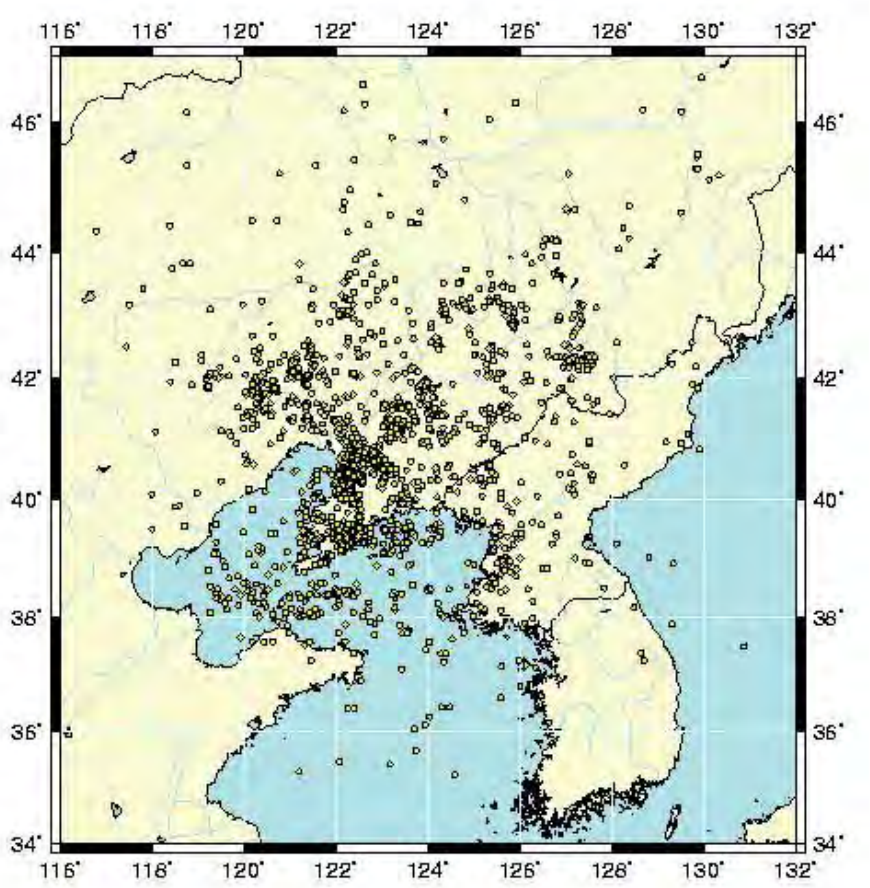


Figure 3. The seismicity of northeast China and North Korea during the past two years.

RESEARCH ACCOMPLISHED

This is the third year of the project. All the waveforms have been converted into Seismic Analysis Code (SAC) formats and are ready for delivery. A final report is in preparation. This paper is a brief summary of the three years' deployment work. Except for one station, all the instruments are deployed alongside the existing short-period analog seismic stations operated by the provincial seismological bureaus in southwest and northeast China. The instruments are installed in vaults that are typically 30-m deep extending horizontally into the hillside. Since these piers were normally professionally built to seismological standard, the data quality of this deployment is on average very high. The local provincial bureaus provide the support in the security and maintenance of the instruments.

The data have been routinely processed. Our analysts have screened a large number of recorded waveforms recorded and constructed a waveform database. Basically, the database includes three kinds of events: the small to moderate local-regional earthquakes, the industrial explosions, and the moderate to large earthquakes at teleseismic distances.

Local Earthquakes

Several moderate local earthquakes occurred during our experiment. After such an event, the provincial seismological bureaus usually dispatch exploration teams to perform on-site geological and geophysical surveys. Therefore, they provide excellent ground-truth information. Figure 4 is the vertical waveform recorded across our network for an M=5 earthquake at Jinggu on September 4, 2001. The epicentral distances to the stations in our network are from 50–400 km.

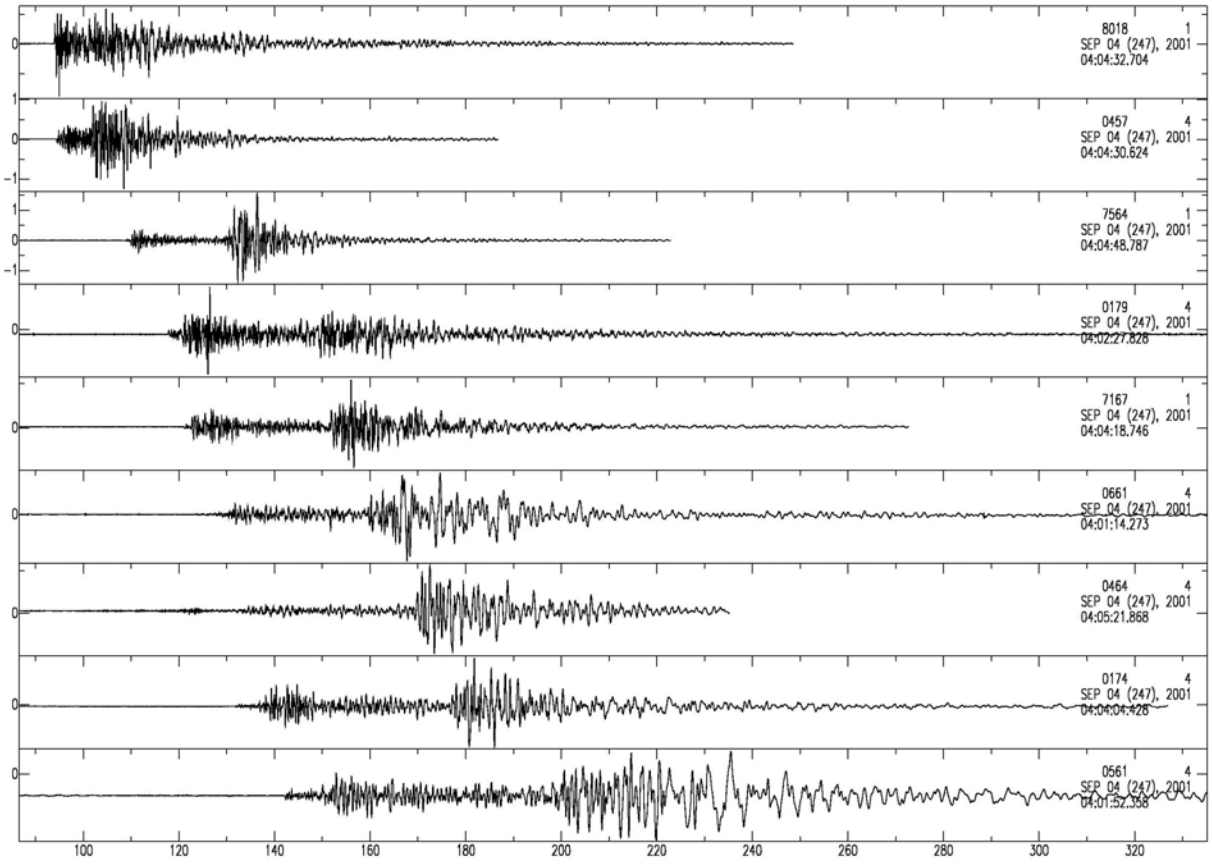


Figure 4. The vertical component of the waveforms of the September 4, 2001 Jinggu earthquake recorded across the Yunnan network. The epicentral distances to the stations in our network are from 50 km (Lincang, the top trace, to 400 km, Ninglang, the bottom trace).

Screening of Industrial Explosions

The provincial earthquake catalogs, compiled from recordings generated by the high-density, short-period analog seismic network in the deployment regions and some provincial digital seismic networks, are a complete list of all the earthquakes in the deployment regions. Of all the waveforms we have processed, many could neither be associated with any earthquakes in the catalog nor be associated with any other events in the global PDE catalog. Figure 5 and 6 show two examples of such waveforms. These events are most likely the local and regional industrial explosions that need to be studied further.

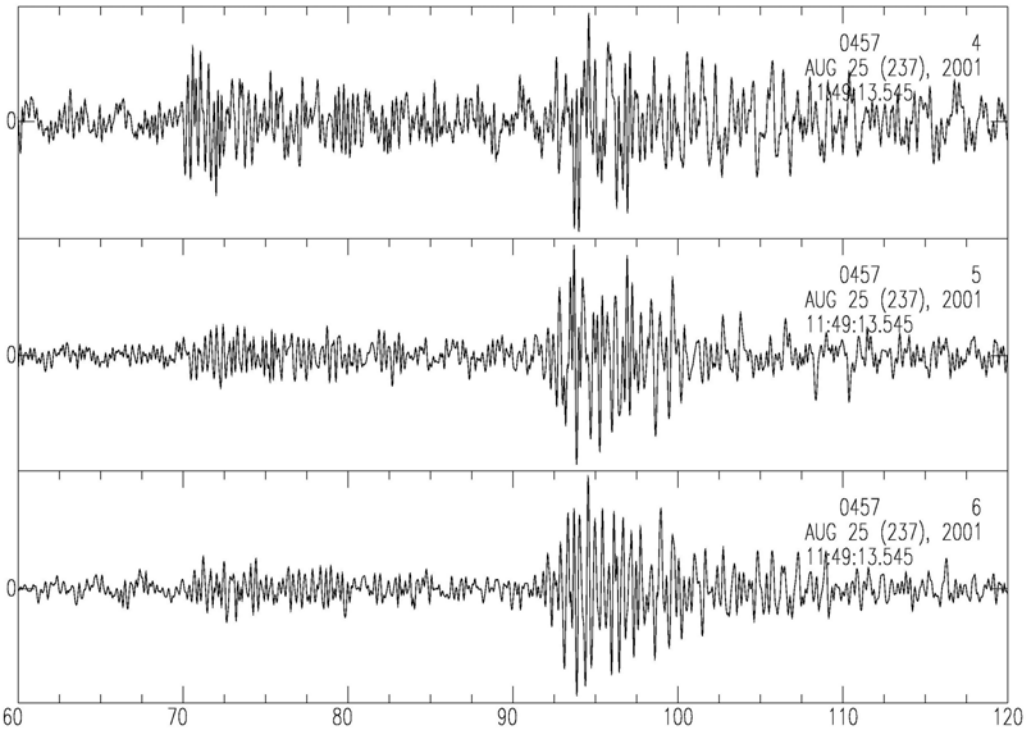


Figure 5. An example of waveforms of a potential industrial explosion recorded at station Zhenyuan, Yunnan province.

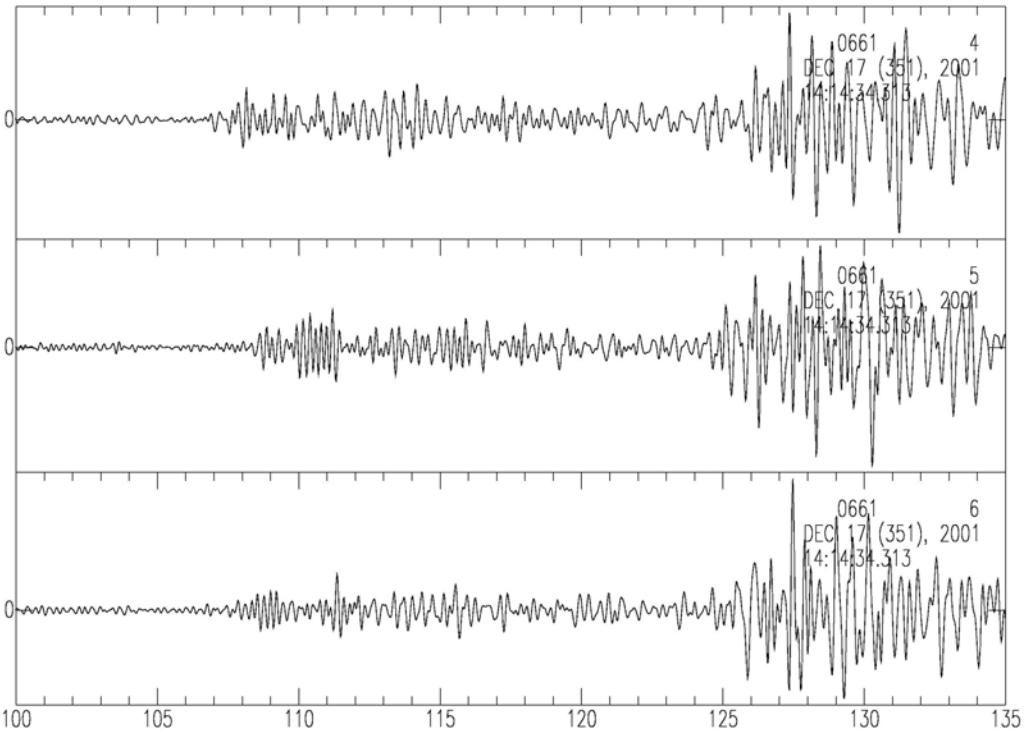


Figure 6. An example of waveforms of a potential industrial explosion recorded at station Mengla, Yunnan network.

Moderate to Large Earthquakes at Teleseismic Distances

The world's moderate to large earthquakes are routinely recorded, including the Nov. 14, 2001, Ms=8.0 Qinghai, China, earthquake, December 18, 2001, Ms=7.3 Taiwan earthquake, September 11, 2001, Ms=6.4 Iran earthquake, October 12, 2001, Ms=7.3 Mariana earthquake, January 2, 2002, Ms=7.6 Vanuatu Islands earthquake, and March 3, 2002, Ms=7.2 Hindu-Kush earthquake, etc. The waveforms from these records are valuable for studying the wave propagation along the paths from Southwest China to many interesting regions in the world, as well as for studying the source mechanism of large earthquakes. Figure 7 shows the waveforms of the October 12, 2001, Ms=7.3 Mariana earthquake recorded at the network.

The June 28, 2002 M_W=7.3 Deep Earthquake in Northeast China

On June 28, 2002, a rare, large, deep earthquake occurred in northeast China. The hypocenter was at 130.45E, 43.74N, depth=581.5 km. Our local network recorded this event, with the epicentral distances ranging from 1.7º to 6.5º. Figures 8 and 9 show the velocity and displacement waveforms of this event. Some interesting properties from these waveforms are shown, such as the sharp contrast of the frequency components of P and S waves, as well as a possible "slab phase." Such recordings are extremely valuable for studies on the regional structure, tectonics, and the mechanism of deep earthquakes.

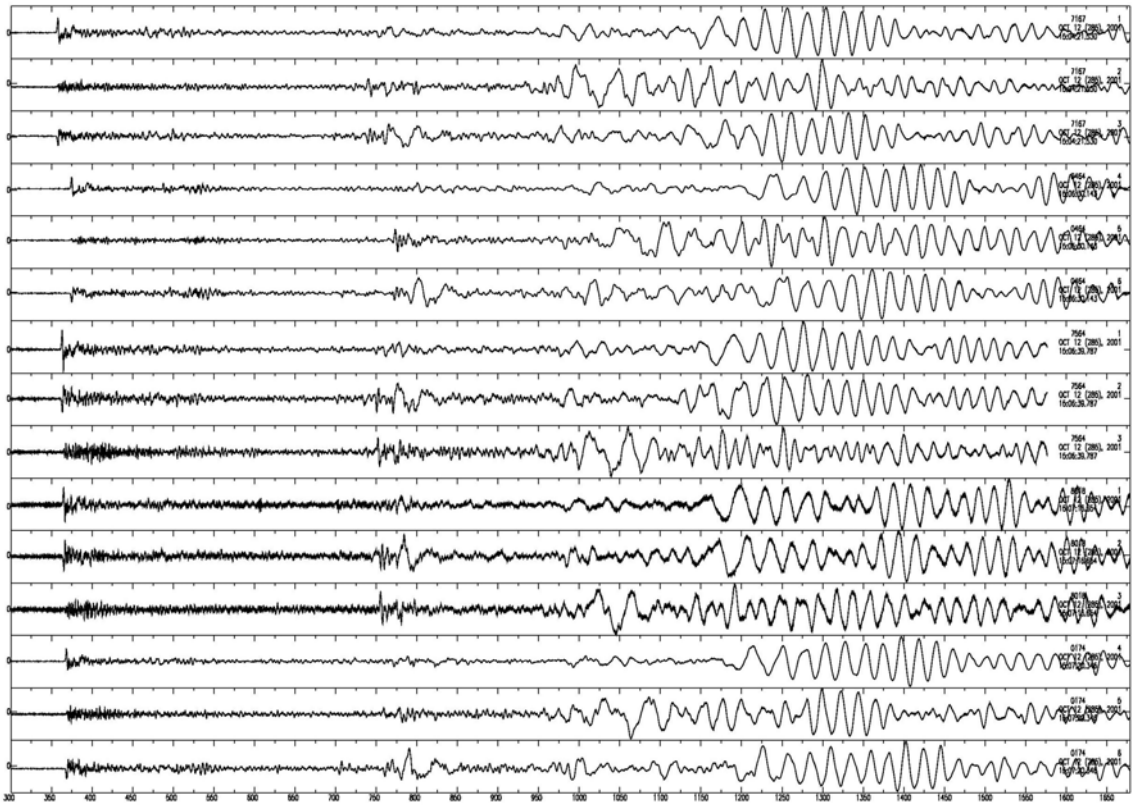


Figure 7. The waveforms of the October 12, 2001 Mariana earthquake recorded at the Yunnan network.

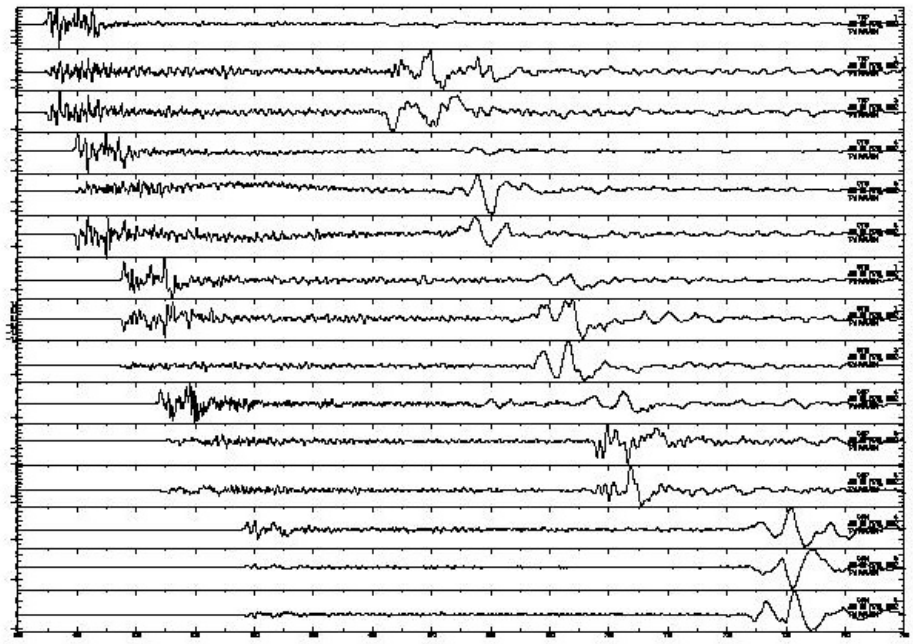


Figure 8. The velocity waveforms of the June 28, 2002, M_W=7.3 deep earthquake recorded at the northeast China network.

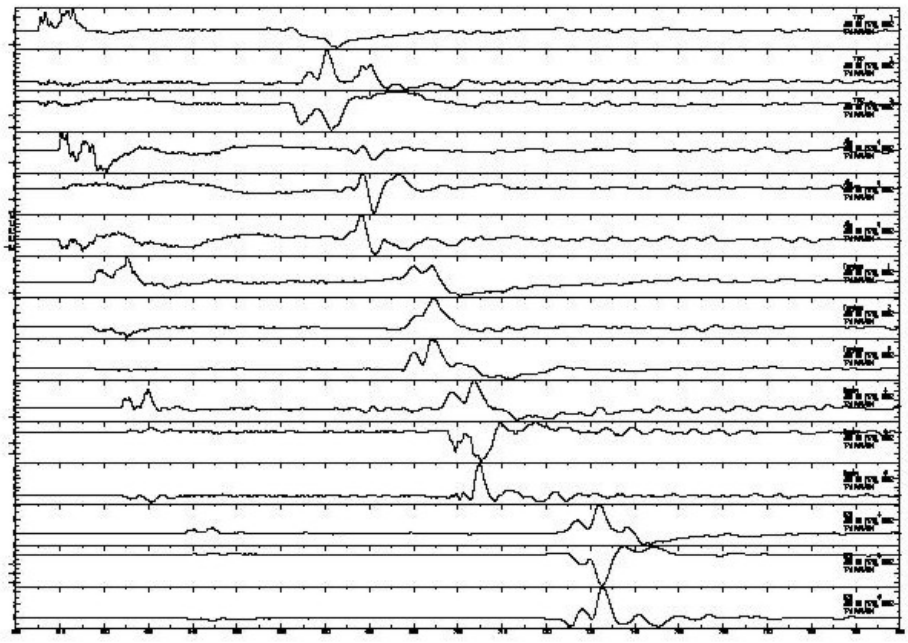


Figure 9. The displacement waveforms of the June 28, 2002, M_W=7.3 deep earthquake recorded at the northeast China network.

CONCLUSIONS AND RECOMMENDATIONS

The two broadband seismic experiments conducted in southwest and northeast China are very successful. A high-quality, unique database of waveforms recorded in the experiments is being established. In the database, there are basically waveforms of three kinds of events: the small to moderate local-regional earthquakes, the industrial explosions, and the moderate to large earthquakes at teleseismic distances. A screening of the waveforms shows that more than 15% of events are potential industrial explosions. This database includes tremendous ground-truth information and provides excellent opportunities for studying regional wave propagation, seismic source discriminants, and active tectonics in the experiment areas.

ACKNOWLEDGEMENTS

We thank Peter Goldstein at Lawrence Livermore National Laboratory for providing us the SAC program under Linux for field use. We also thank IRIS/PASSCAL instrument center, as well as Refraction Technology Inc., for providing many technical help.

REFERENCES

Aki, K. (1980), Attenuation of shear waves in the lithosphere for frequencies from 0.05 to 25 Hz, *Phys. Earth Planet. Inter*., 21, 50-60.

Chen, P. S., F. T. Liu, Q. Li, and J. Z. Qin (1991), The lateral inhomogeneity in Yunnan province. China, *Science in China (Series B),* 34 (5), 630-640.

Cui, Z. Z., D. Y. Du, J. P. Chen, Z. Y. Zhang, and L. Y. Huang (1987), The Deep Structure and Tectonic Features of the Crust in Panxi Area, *Chinese J. Geophy*., 30(6): 566-580 (in Chinese).

Ge, B. R., and K. Y. Yang (1990), Mesozoic-Cenozoic Tectonic Features in Panzhihua-Xichang Area, *Chinese J. Geophy.*, 33(1): 64-69 (in Chinese).

Herrmann, R. B., and C. J. Ammon (1997). Faulting parameters of earthquakes in the New Madrid, Missouri region, *Engineering Geology* 46**,** 299-311.

Hu, H. X., et al. (1986), Explosion Investigation of the Crustal Structure in Western Yunnan Province. *Chinese J. Geophy*., 29(2), 133-144 (in Chinese).

Hu, H. X., Z. Y. Lin, Y. J. Bian, C. Y. Wang and L. B. Zhu (1996), Study on the Characteristics of Crust-Mantle Transition Zone in Western Yunnan Province, *Acta Seismologica Sinica*, 18 (4): 444-450 (in Chinese).

Lin, Z., et al. (1993), The Preliminary Interpretation of Deep Seismic Sounding in Western Yunnan, Acta Seismologica Sinica, 15 (4): 427-440 (in Chinese).

Liu, R. F., P. S. Chen, and Q. Li (1993), Three-Dimensional Velocity Images in Yunnan and Its Neibouring District, *Acta Seismologica Sinica*, 15 (1): 61-67 (in Chinese).

Liu, Z., R. B. Herrmann, J. Xie, and E. D. Cranswick (1991), Waveform characteristics and focal mechanisms of five aftershocks of the 1983 Goodnow, New York, earthquake by polarization analysis and waveform modeling, *Seism. Res. Letters*, 62, 123-133.

Malagnini, L. (1999), Ground Motion Scaling in Italy and Germany, *Ph. D. Dissertation*.

National Research Council (1997), Research Required to Support Comprehensive Test Ban Treaty Monitoring, National Academy Press, Washington, D.C.

Qin, J. Z., and R. J. Kan (1986), Q Values and Seismic Moments Estimates Using the Coda Waves of Near Earthquakes in the Kunming and Surrounding Regions, *Chinese J. Geophy*., 29(2): 145-155 (in Chinese).

Raoof, M., R. B. Herrmann, and L. Malagnini (1999), Attenuation and excitation of three-component ground motion in Southern California, *Bull. Seism. Soc. Am.* 89, (Aug. 99) preprint.

Rodgers, A. and W. Walter (1997), Regionalization and calibration of seismic discriminants, path effects, and signal-to-noise for station ABKT, *Proc. 19th Annual Seismic Research Symposium on Monitoring a Comprehensive Test Ban Treaty* (Editors: M. J. Shore, R. S. Jih, A. Dainty, and J. Erwin), Defense Special Weapons Agency, Alexandria, 143-151.

Sun, K. Z., J. W. Teng, D. M. Jin, and Y. Zheng(1987), Q-Value and Its Lateral Variations in Pan-xi Tectonic Belt, *Chinese J. Geophy*., 30(1): 101-104 (in Chinese).

Wang, C. Y., X. L. Wang, and Q. Z. Yan (1994), Tree Dimensional Velocity Structure Beneath the Kunming Telemetered Seismic Network. Acta Seismologica Sinica, 1994, 16 (2): 167-175 (in Chinese).

Xiong, S. B., J. W. Teng, Z. X. Yin, M. H. Lai , and Y. P. Huang (1986), Explosion Seismological Study of the Structure of the Crust and Upper Mantle at Southern Part of the Panxi Tectonic, Belt, *Chinese J. Geophy*., 29(3), 235-244 (in Chinese).

Xiong, S. B., et al. (1993), The 2-D Structure and Its Tectonic Implications of the Crust in the Lijiang£-Panzhihua£-Zhehai Region, *Chinese J. Geophy*., 36(4), 434-444 (in Chinese).

Yazd, M. R. S. (1993), Ground motion studies in the Southern Great Basin of Nevada and California, *Ph. D. Dissertation*, Saint Louis University, 189p.

Zhu, P. D., Y. M. Li, L. M. Zhang, P. Y. Shu and S. H. Liang (1986), On the Study of the Seismic Telemetry Network in South Sichuan and North Yunnan Provinces, *Chinese J. Geophy*., 29(3), 245-254 (in Chinese).

Carr, D., S. Moore, H. Armstrong, L. Wilkening, M. Chown, E. Shepherd, T. Edwards, R. Keyser, C. Young, A. Cogbill, J. Aguilar-Chang, A. Velasco, and S. Ruppert (2/00), Knowledge Base Contributor's Guide, Sandia National Laboratories report SAND2000-0442 (available at http://www.nemre.nn.doe.gov).

Firbas, P., K. Fuchs, and W. Mooney (1998), Calibration of Seismograph Network May Meet Test Ban Treaty's Monitoring Needs, *Eos Trans. Am. Geophys. Union*, 79, 413, 421.

Leith, W. and L. Kluchko (1998), Seismic Experiments, Nuclear Dismantlement Go Hand in Hand in Kazakhstan, *Eos Trans. Am. Geophys. Union*, 79, 437, 433-444.

Moore, S., H. Armstrong, D. Carr, R. Keyser, E. Shepherd, L. Wilkening, C. Young, M. McCornack, J. Aguilar-Chang, A. Velasco, S. Ruppert, T. Hauk, and C. Schultz (5/3/00), The Integration Process Design for Incorporating *Information Products* into the Department of Energy *Knowledge Base*, Sandia National Laboratories report SAND2000-0597 (available at http://www.nemre.nn.doe.gov/).

Myers, S. and C. Schultz (2000), Improving Sparse-Network Seismic Location with Bayesian Kriging and Teleseismically Constrained Calibration Events, *Bull. Seism. Soc. Am*., 90, 199-211.

PrepCom 9 (8/30/99), Draft Guidelines and Reporting Formats for the Implementation of Confidence-Building Measures, CTBT/PC-9/1/Annex II, Appendix IV, pp. 26-43, (available at http://www.ctbto.org/).

Schultz, C., S. Myers, J. Hipp, and C. Young (1998), Nonstationary Bayesian Kriging: Application of Spatial Corrections to Improve Seismic Detection, Location and Identification, *Bull. Seism. Soc. Am*., 1275-1288.

Sweeney, J. (1998), Criteria for Selecting Accurate Event Locations from NEIC and ISC Bulletins, Lawrence Livermore National Laboratory report UCRL-JC-130655.

SEISMIC REGIONALIZATION IN EASTERN RUSSIA

Kevin G. Mackey,[1] Kazuya Fujita,[1] Hans E. Harste,[2] and Lee K. Steck[2]

Michigan State University;[1] Los Alamos National Laboratory[2]

Sponsored by National Nuclear Security Administration
Office of Nonproliferation Research and Engineering
Office of Defense Nuclear Nonproliferation

Contract No. DE-FC03-02SF22490[1] and W-7405-ENG-36[2]

ABSTRACT

In an effort to characterize seismicity in support of nuclear explosion monitoring for the continental regions of eastern Russia, we have been analyzing information obtained from regional seismic network operators. Our goal is to merge catalog, bulletin, waveform, and other ground truth data from several regional networks into a comprehensive data set that we will use for various seismic research projects. To date we have compiled a bulletin from published and unpublished event data of over 280,000 events, 1,300,000 arrival times, and 580,000 waveform amplitudes. We have also now parsed several regional bulletins into database tables. After parsing into database tables we merged event, arrival, and amplitude information that was originally contained in the different bulletins.

With this merged data set we have been improving and expanding upon crustal velocity models. Preliminary results from the Sakhalin region indicate slow Pg velocities on the order of 5.75 to 5.80 km/s with Sg velocities around 3.35 to 3.37 km/s. We are also estimating velocity models for the Irkutsk region. Crustal velocities in the Irkutsk region are highest in the northwest, with Pg and Sg approaching 6.200 to 6.225 km/s and 3.59 to 3.61 km/s respectively. Velocities in the southeast portion of the Irkutsk region, along the Chinese border, are lower with Pg about 6.05 km/s and Sg around 3.53 km/s. The general velocity gradients observed are consistent with the large-scale regional geology, as well as previously determined velocities for adjacent regions. Our event re-location work to date emphasizes selection of well-recorded events appropriate for estimating source specific station corrections.

We continue deployment of a network of digital stations in northeast Russia to aid in our calibration efforts. We have been obtaining digital waveforms from older stations of this deployment for several years. We have started explosion identification efforts by assembling waveforms based on those explosions that have already been identified by network operators. Using these ground-truth explosion waveforms, we will test discriminants based on body-wave amplitude measurements and cross-correlation analysis, and rank ground-truth events for calibration of far-regional and teleseismic stations.

OBJECTIVES

The objective of our research is to improve event location and identification capability in eastern Russia in support of nuclear explosion monitoring. We plan to reach our objectives through (1) collection, analysis, and merging of historic regional catalogs and bulletins, (2) deployment of additional digital seismic stations in northeast Russia, (3) improving travel-time curves, relocating events, and estimating appropriate correction surfaces for improved locations, and (4) analysis of waveform characteristics to identify effective regional event discriminants.

RESEARCH ACCOMPLISHED

Historic Database for Eastern Russia

Considerable effort has gone into development of a comprehensive historic database for all of eastern Russia. Data sources and the development effort have been previously summarized (Mackey, 1999; Mackey and Fujita, 1999, 2000; Mackey et al., 2002), and a significant amount of new data has been recently added. Our goal is to merge catalog, bulletin, waveform, and other ground-truth data from several regional networks into a comprehensive data set that we will use for various seismic research projects. To date we have compiled a bulletin from published and unpublished event data of over 280,000 events, 1,300,000 arrival times, and 580,000 waveform amplitudes, essentially tripling the amount of data in the past year. We have now parsed over 86,000 events and associated arrival times and waveform amplitudes from several regional bulletins into database tables. After parsing into database tables, we have merged event, arrival, and amplitude information that were originally contained in the different bulletins.

Crustal Velocity Model

A small subset of this database was used to recalculate a crustal velocity model for eastern Russia using a grid search method with a moving window to determine best fit Pg and Sg (Lg onset, but hereafter referred to as Sg) crustal velocities to well located events. The method is the same as that outlined in Mackey (1999) and Mackey and Fujita (2000) except that a moving window of 2.5 x 5° using increments of 0.5°in latitude and 1.0° in longitude was applied to the entire study area to obtain more details on the variation of velocities and avoid artificially sharp discontinuities. Cells calculated using only one event were removed to reduce edge effects. In addition to recalculating velocities for northeast Russia using this improved method, we added the Baikal, Chita, and Sakhalin regions to this analysis using additional phases for Sakhalin, Amur, and the Baikal regions that have recently been added to the database from the “Materials on the Seismicity of Siberia” and the “Seismological Bulletin for the Far East.” The model was calculated using 1,708 events that were well recorded by local networks between 1984 and 1996. The results obtained for Pg velocities in northeastern Russia (Figure 1) are generally similar to those discussed in our earlier paper (Mackey and Fujita, 2000); the Siberian platform is generally fast, there are slower velocities along the extension of the Arctic Mid-Ocean Ridge in the southern Laptev Sea and in areas affected by a Pliocene rifting episode, and are average elsewhere. Sg velocities (Figure 2) are also low in regions of rifting, both in and south of the Laptev Sea, as well as along the northern coast of the Sea of Okhotsk where Worrall et al. (1996) have suggested the existence of pull-apart basins as a far-field effect of the India-Eurasia collision. Below, we discuss our new results for southeastern Russia and compare them to velocities obtained from Russian studies.

Velocity Structure of Southeastern Russia

Examination of the results for Pg and Sg show three general velocity regions: 1) very high velocities in the southern Aldan shield; 2) elevated velocities in the Baikal rift and adjacent regions; and 3) very low velocities in Sakhalin. The region has several local travel-time studies and been criss-crossed by a large number of Russian long- and short-range refraction lines, allowing us to compare our results to independently obtained data.

Southern Aldan Shield. Pg velocities of 6.2–6.3 km/sec and Sg velocities of 3.5–3.7 km/sec are observed in the southern Aldan shield. These values are consistent with Pg and Sg values of 6.3 and 3.64 km/sec observed in local surveys in the southern Siberian platform (Suvorov et al., 1999), and the 6.3 km/sec Pg velocity obtained both from PNE-based long-range profiles that sampled the Aldan shield (Egorkin et al., 1987; Pavlenkova and Romanyuk,

1991) and from local earthquake studies (Suvorov and Kornilova, 1985). These high velocities also extend to the coast of the Sea of Okhotsk. All of these results are consistent with a thick, old, Precambrian platform.

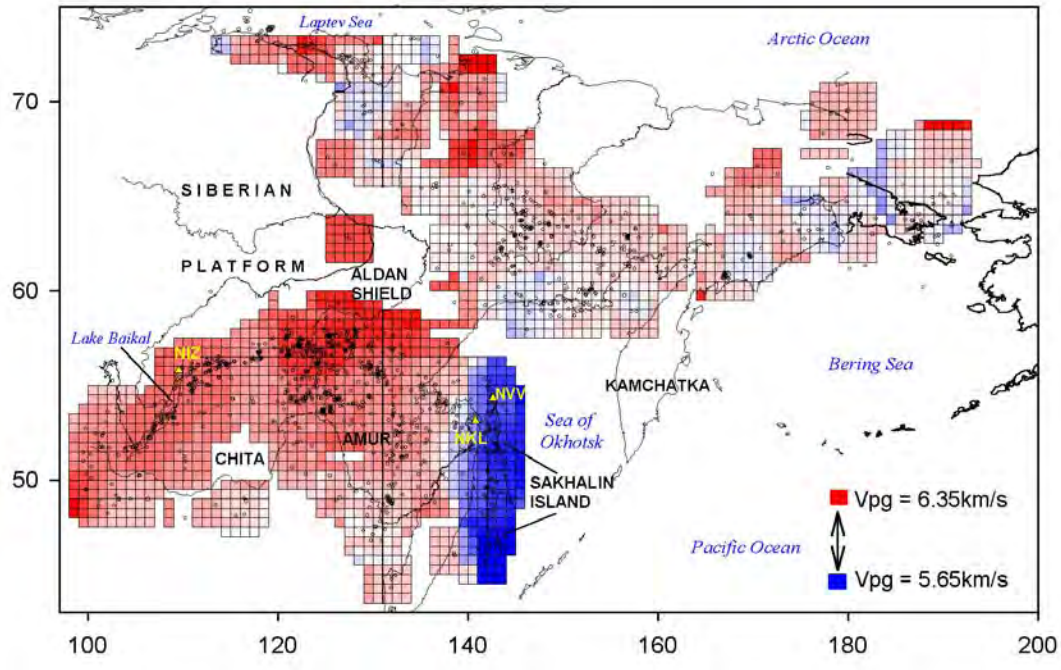


Figure 1. Pg velocity model determined in this study. Events used shown as circles.

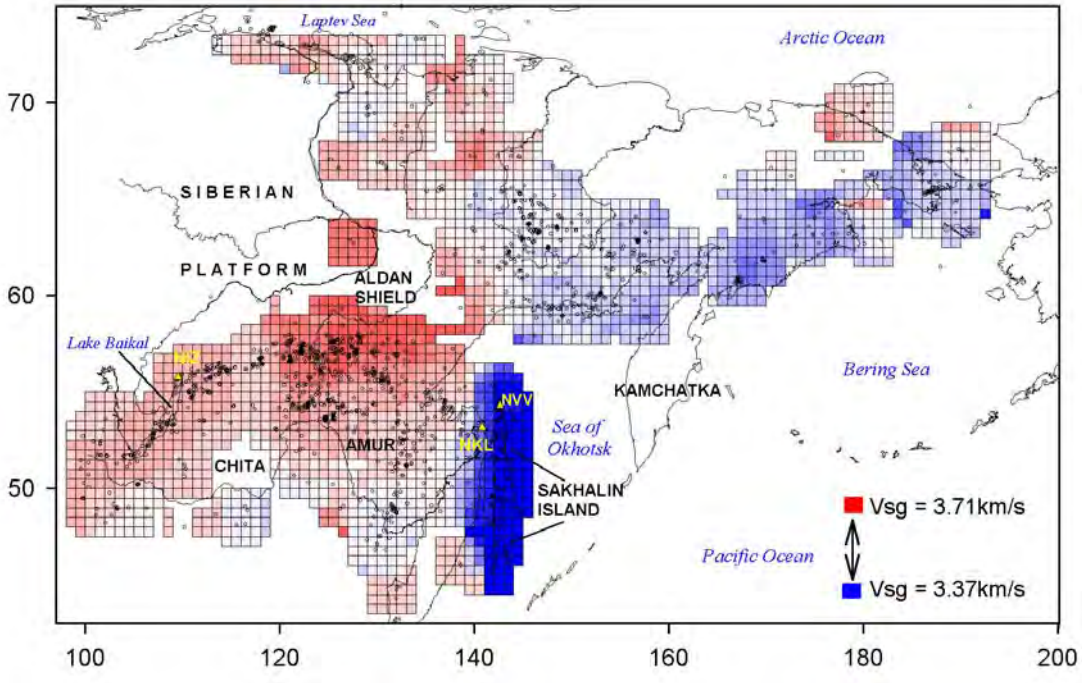


Figure 2. Sg (Lg onset) velocity model determined in this study. Events used shown as circles.

Baikal, Buryatia and Chita Regions. Pg velocities along the Baikal rift zone and to the southwest, towards Lake Khosgobul, are about 6.2 km/sec. In the northeastern extension of the Baikal rift, in the Upper Angara, Muya-Kaunda, and Chara basins, velocities are slightly lower, 6.10–6.15 km/sec. To the southeast of Baikal, in eastern Buryatia and the Chita regions, Pg velocities decrease to about 6.1 km/sec, with a band of slightly lower velocities between 116° and 120°E. There are insufficient data to the northwest, in the Angara shield, to be meaningful.

It is interesting to note that velocities along the Baikal rift are slightly higher (Pg 6.20–6.28 km/sec, average 6.222 km/sec; Sg 3.59–3.61 km/sec) than in adjacent regions (Pg 6.125–6.175 km/sec, average 6.137 km/sec; Sg 3.55–3.57 km/sec). This difference is confirmed by travel-time curves calculated for arrivals at Nizhne Angarsk for events along the axis of the lake and from the east. Statistically, the curves are independent (Figure 3).

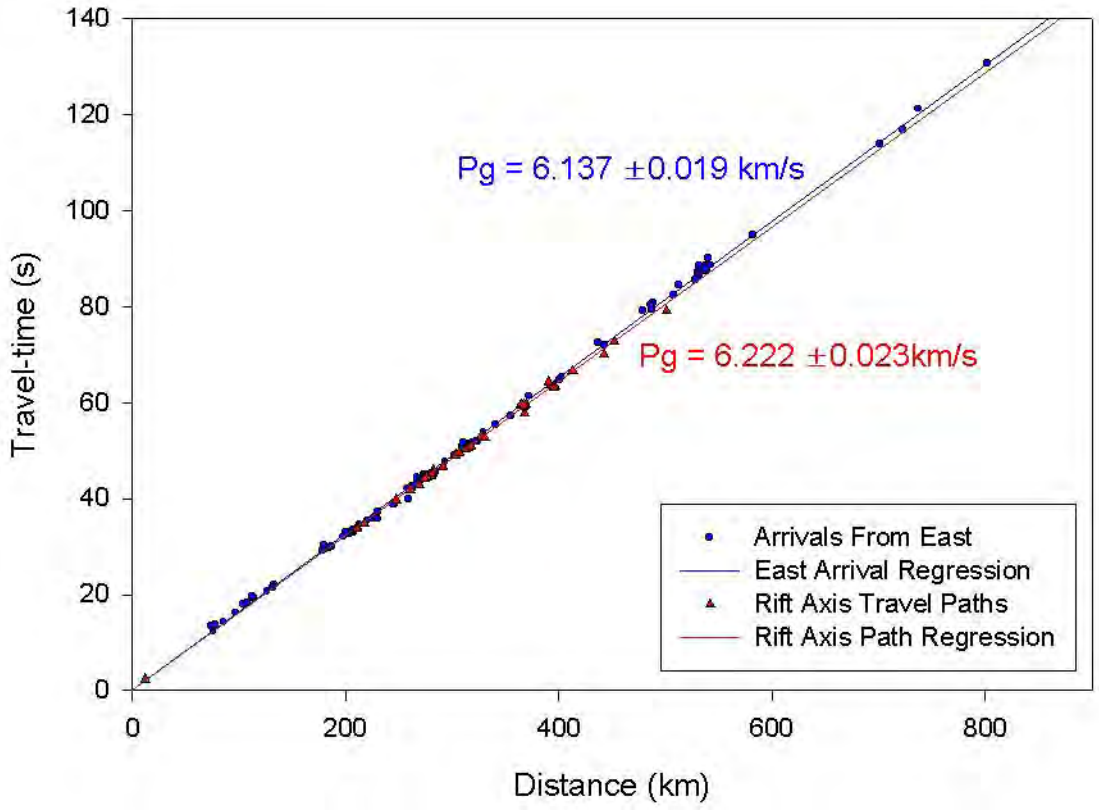


Figure 3. Pg Travel-time curve for Nizhne Angarsk (NIZ) showing a slightly faster velocity for arrivals traveling along the rift axis (red triangles) and a slower velocity for arrivals from the east (blue circles). Regression determined velocities noted on figure.

Russian refraction lines within Lake Baikal obtained a value of 6.2 ± 0.2 km/sec (Puzyrev, 1993, p. 149) for the top of the consolidated crust. The Ust'-Uda– and Ulan-Ude–Chita profiles yielded an average velocity for the upper crust (0–20 km) of 6.2 km/sec in the rift, decreasing to 6.1 km/sec to the southeast (Krylov et al., 1972; Suvorov et al., 2002); this profile shows an increase to 6.3 km/sec to then northwest in the Angara shield; however, we have insufficient data in that region. Long-range profiles using PNEs suggest similar results; data from the southern end of the RIFT profile indicate that the upper crustal velocities in the Baikal rift zone are similar to those in the Siberian craton, 6.2–6.3 km/sec (Pavlenkova et al., 2002). Travel-time curves for Pg and Sg based on Russian regional stations yield velocities of 6.17 ± 0.01 and 3.56 ± 0.02 km/sec, respectively (Golenetsky et al., 1978)—very much in agreement with our results.

Although upper mantle velocities in the Baikal rift show reduced seismic velocities as a result of hotter asthenosphere at shallower depths (Krylov and Duchkov, 1996), and there is a thick layer of low-velocity sediments near the surface (Krylov et al., 1972), our results, and those of the previous Russian studies, suggest that the upper crust is relatively unaffected seismically by the rifting process. This outcome may be a result of the narrowness of the rift and therefore its lack of resolution on our grid and on refraction profiles, or a result of mafic intrusions into the upper crust that increase the seismic velocity slightly.

To the southwest of Baikal, near Lake Khosgobul, Soviet refraction studies obtained upper crustal velocities of 6.3 km/sec (Zorin et al., 1993). Our data show 6.2 km/sec Pg velocities with a few cells having reaching 6.30–6.35 km/sec within northern Mongolia.

Northeast of Lake Baikal are a series of depressions that represent an extension of the Baikal rift system. We obtain Pg and Sg velocities in the region of these basins of 6.10–6.15 km/sec and 3.55–3.59 km/sec, respectively. Russian refraction studies indicate upper crustal Pg velocities in this region of about 6.1–6.2 km/sec (Puzyrev and Mandelbaum, 1984; Suvorov et al., 2002) and are calculated at 6.09-6.16 km/sec based on local earthquakes (Golonetsky et al., 1975). Suvorov and Kornilova (1985) obtained a slightly lower velocity of 6.0 km/sec for Pg in this region. Sg velocities from local earthquakes are 3.53–3.59 km/sec (Golonetsky et al., 1975). These velocities are slightly lower than in Lake Baikal proper and may be because of the fact that the rift is less well developed here. All studies show the increase in velocities near the Olekma River at the east end of the rift and the transition into the Aldan shield.

Southeast of Lake Baikal, in eastern Buryatia and the Chita region, we obtain Pg and Sg velocities of 6.08–6.15 km/sec and 3.55–3.57 km/sec, respectively. These velocities are slightly lower than in Lake Baikal or its northeastern extension. A thicker, low-velocity, upper crust is also obtained by Soviet refraction studies (e.g., Krylov et al., 1972; Krylov and Dychkov, 1996; Sun Youngsheng et al., 1996) and in mean velocity calculations for the upper crust (Suvorov et al., 2002). Average upper crustal Pg velocities as low as 5.9 km/sec are reported near Chita by Puzyrev and Mandelbaum (1984). Our results indicate that velocities are lowest slightly farther east, along 118–120°E, decreasing to 6.0–6.1 km/sec in Mongolia and near Hailar, China. Song et al. (1996) also obtain apparent velocities of about 6.12 km/sec near Hailar.

Amur District. We obtain slightly elevated velocities in the Amur district with Pg ranging from 6.0–6.2 km/sec and Sg values of 3.53–3.59 km/sec; these velocities are similar to those previously presented for this region in Mackey and Fujita (2000). One Soviet refraction line (Zeya—Bureya) crosses through the central Amur district, along a region where we obtain Pg values of 6.175–6.225 km/sec. The Soviet profile obtains upper crustal refraction velocities ranging from 5.8 to 6.4 km/sec with an upper crustal average velocity of 6.1 km/sec (Mishenkin et al., 1987).

Sakhalin Island. The velocities obtained for Sakhalin Island are very low, with Pg ranging from 5.65–5.85 km/sec and Sg between 3.3 and 3.47 km/sec. Travel-time curves for Nyvrovo (Figure 4), located on the north end of the island, for paths from the south, along the axis of Sakhalin, confirm this (Pg velocity of 5.70 km/sec). There is a sharp step in velocity with respect to the eastern Amur region where Pg velocities exceed 6.0 km/sec. Examination of travel-time curves from Nikolaevsk-na-Amur, located approximately on the boundary between the high- and low-velocity regions (Figure 5) also shows a clear difference with faster velocities (6.14 km/sec) to the west—in Amur.

A large number of refraction studies were conducted by the Soviet Union in Sakhalin and in the adjacent Sea of Okhotsk. These studies, however, do not indicate reduced velocities. The results of most of the Soviet surveys are summarized in Suvorov (1975), and include some contradictory interpretations. Two of the profiles run parallel to the island, profile 18 to the west of Sakhalin in the Tatar Strait, and profile 20 to the east, just offshore. Profile 20 yielded upper crustal velocities of 5.8 to 6.5 km/sec, with the lowest velocities near Hokkaido, Japan, while Profile 18, show highly variable refraction velocities for the upper crust ranging from 5.8 to 6.7 km/sec (Suvorov, 1975, p. 55, 67). Other cross-island profiles gave results of 6.1–6.8 km/sec. Volvovsky (1973) cites a velocity of 6.2 km/sec for northern Sakhalin, while Belyaevsky (1974) cites values of 6.0–6.1 km/sec for Sakhalin as a whole. These Russian studies all yield velocities higher than we obtain. The only exception is a profile shown by Gnibidenko (1979, p.42) that indicates a refractor with a velocity of 5.8–6.0 km/sec beneath northern Sakhalin.

On the other hand, Russian studies of travel times using local earthquakes consistently give velocities closer to that obtained in this study. Solovev et al. (1967) noted that travel times along the axis of Sakhalin fit closely to the 1939 Jeffreys-Bullen travel-time curve based on a 5.6 km/sec upper crustal velocity. A velocity model with a 5.6 km/sec upper crust derived from Maki (1983) is used in Sakhalin today. Additional studies using local earthquakes in Sakhalin by Nagornykh et al. (1988) yielded a Pg velocity of 5.73 ± 0.19 km/sec and an Sg velocity of 3.38 ± 0.09 km/sec, very close to our values presented above. Thus in Sakhalin there appears to be a difference between the Pg propagation velocity and what are considered upper crustal velocities observed on refraction lines. The reason for the low Pg velocities is unclear; much of Sakhalin is composed of sediments from the forearc of the Mesozoic Sikhote-Alin arc (e.g., Natalin and Parfenov, 1983) that became a zone of transpression resulting from the accretion of the Sea of Okhotsk (Jolivet et al., 1992). This accretion may have produced a thickened low velocity upper crust.

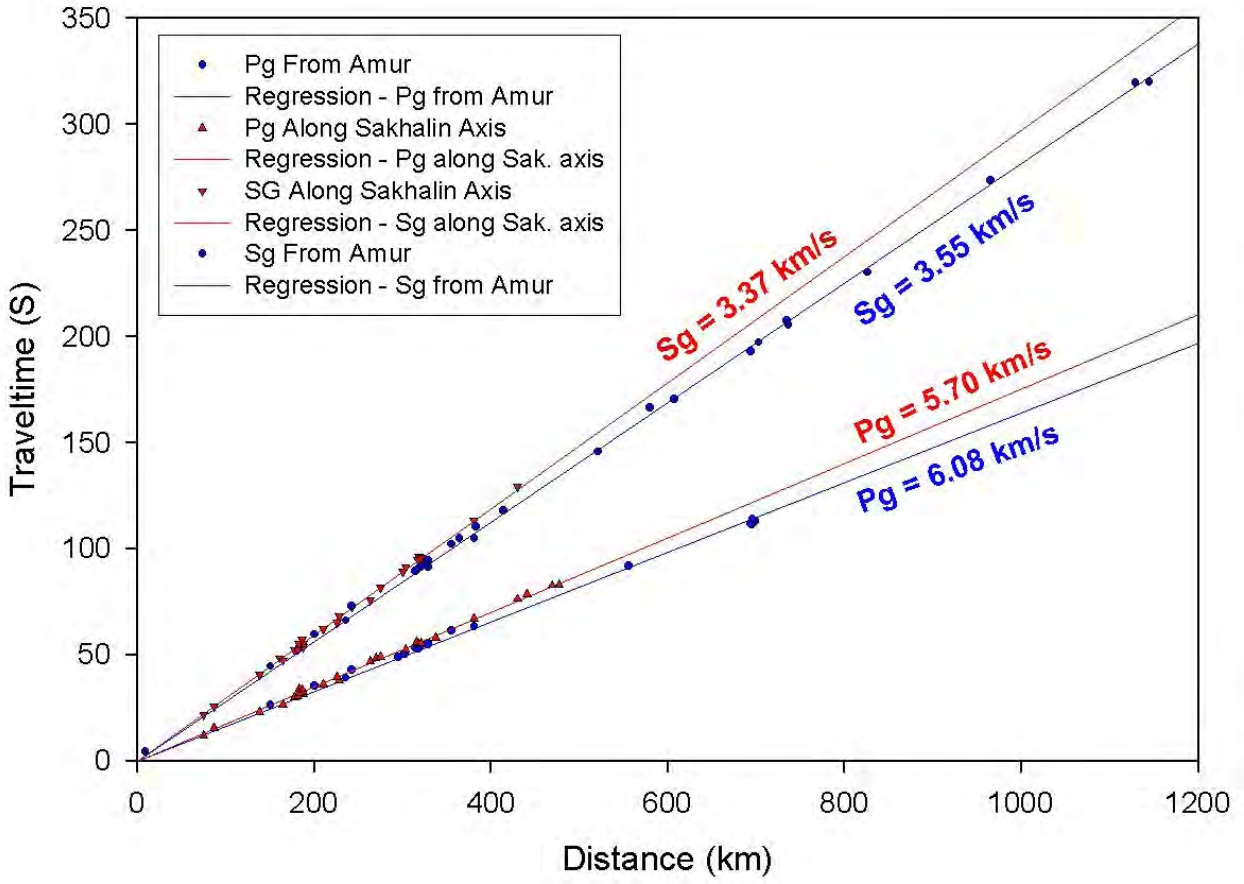


Figure 4. Station Nyvrovo (NVV) Pg and Sg travel-time curves comparing velocities for paths along Sakhalin Island axis (slow) and arrivals coming from the west (fast). Regression values are noted on figure.

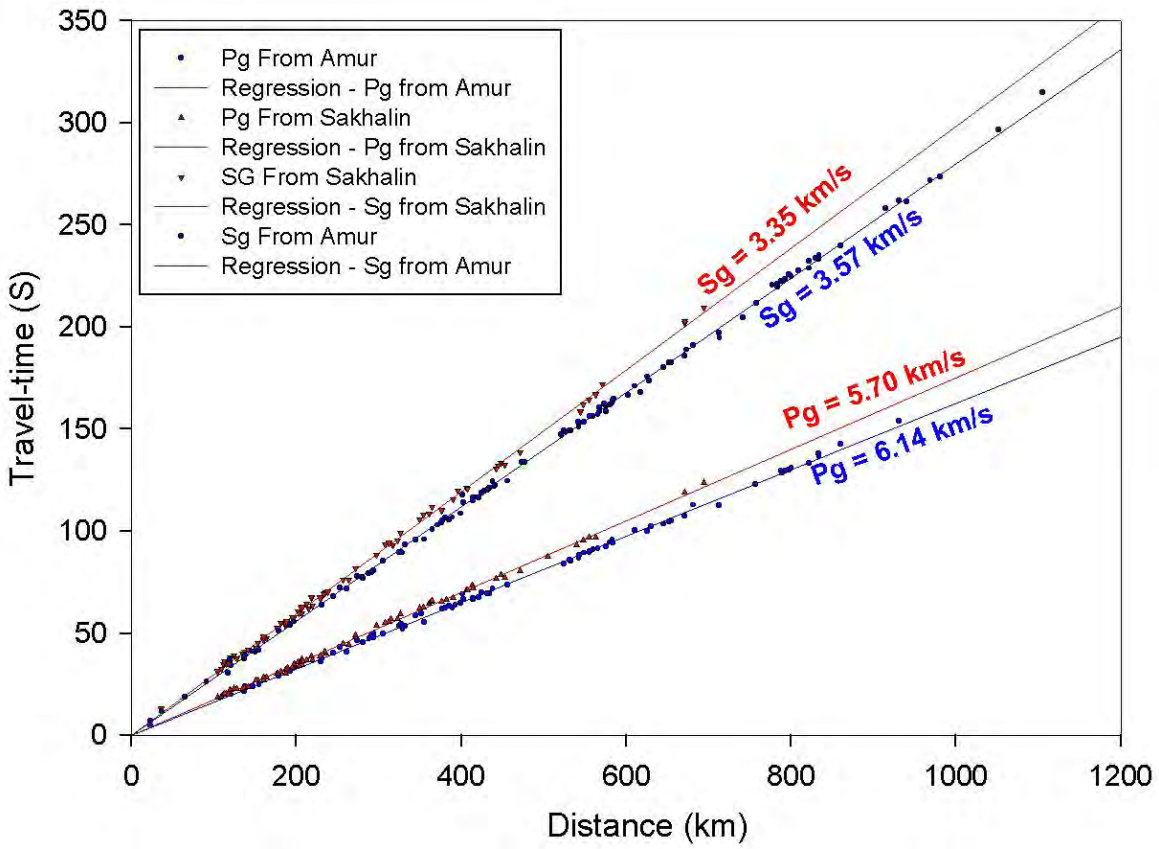


Figure 5. Station Nikolaevsk-na-Amur (NKL) Pg/Sg travel-time curves comparing velocities for paths from Sakhalin Island (slow) and arrivals coming from the west (Amur; fast). Regression values are noted on figure.

Figure 6 shows a summary of all phases identified as Pg, P*, and Pn (and corresponding S-phases) for Sakhalin as a function of epicentral distance. This figure shows a clear P* arrival at 6.39 km/sec between the Pg (5.72 km/sec) and Pn (7.88 km/sec) curves and suggests that what is identified as P* is the strong refractor observed in the refraction studies noted above.

The low-velocity region associated with Sakhalin appears to extend to the northern coast of the Sea of Okhotsk, where lower seismic velocities are also noted, especially for Sg.

Maritime Provinces. We have a limited amount of data from a cluster of earthquakes south of Lake Khaki that give velocities of about 6.1 km/sec. Russian refraction data here indicate a refractor with a velocity of 6.2 km/sec and an average upper crustal velocity of 5.8 km/sec (Argentov et al., 1976).

Based on the general consistency between the Pg values we have calculated and the refraction or average velocities in the upper crust obtained by Russian workers (except for Sakhalin), we conclude that the Pg phase reported by the regional networks is a phase that is sampling the upper continental crust, generally corresponding to velocities prevailing between 5 and 20 km depth. In Sakhalin, the Pg velocities are slower than the major refractor derived from deep seismic sounding studies; the latter appears to correspond to P*.

Event relocations

In conjunction with determining a new crustal velocity model, events used were simultaneously relocated. Relative to Russian network determinations, our relocations form tighter clusters and better defined fault lineations, suggestive of improved locations. Throughout the study area, events often move 5–15 km upon relocation, with the

exception of hypocenter determinations from the Irkutsk (Baikal) network. Relocations of Irkutsk network events generally move less than 5 km, indicating event locations determined by the Irkutsk network are probably better than locations provided by local networks in other regions of eastern Russia, possibly as a result of the denser regional network or use of a better-calibrated travel-time curve.

Digital station deployments

We continue development of our digital station network in northeastern Russia to improve epicenter locations and develop seismic discriminants in support of nuclear explosion monitoring by digitally recording local explosions and earthquakes. Deployment of these stations began under a previous project (Mackey et al., 2002). At present, we have twelve permanent stations deployed in and operated in conjunction with the Magadan Yakutsk, and Irkutsk networks of northeast Russia, four of which have opened this year. Several additional stations will open by fall of 2003. We also maintain three portable stations for explosion ground-truth acquisition and rapid deployment for aftershock sequence studies.

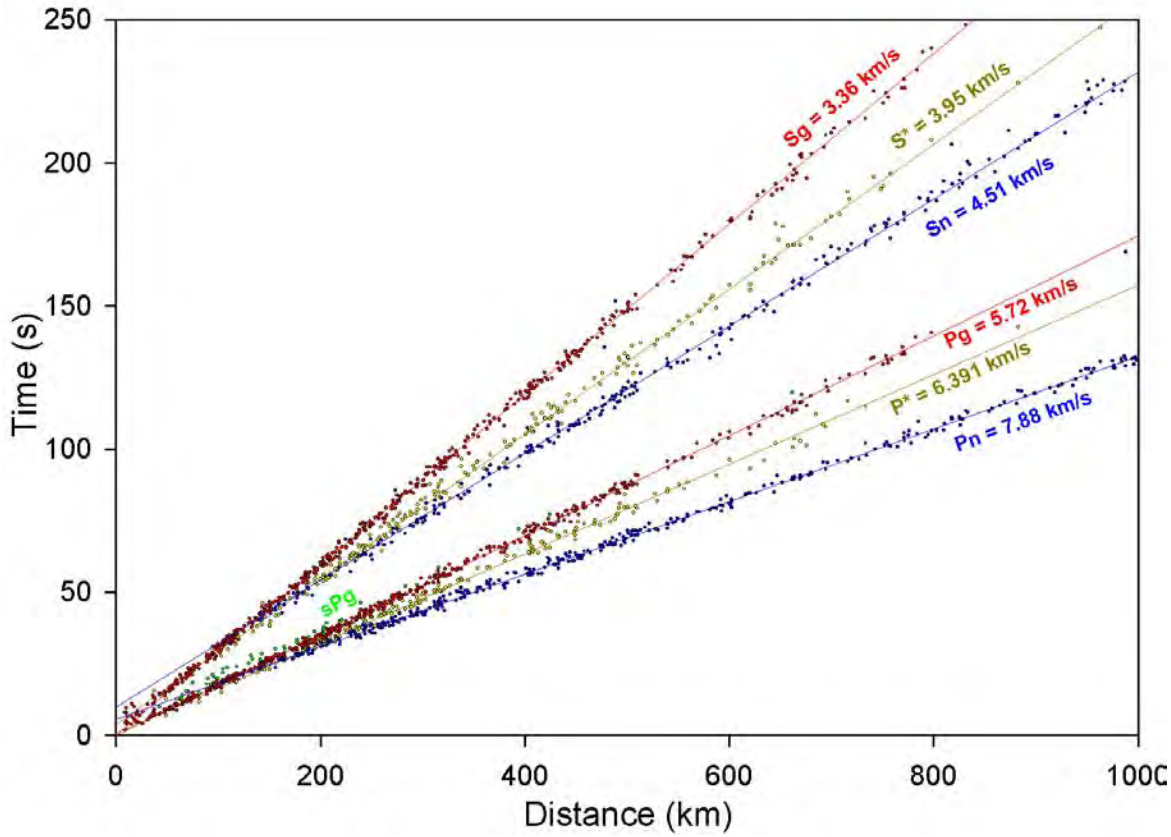


Figure 6. Composite travel time and regressions for Pg, P*, Pn, Sg, S*, and Sn phases reported from 92 Sakhalin earthquakes used in this study. Sakhalin data also include a significant number of additional local and regional phases, such as the sPg phase data plotted in green (others not shown).

CONCLUSIONS

We have now obtained a relatively detailed one-layer crustal velocity model for all of continental Siberia east of Lake Baikal. Pg and Sg velocities correspond to upper crustal velocities throughout the region and agree well with a wide variety of Russian studies, most of which are in the Baikal-Amur-Sakhalin regions. This agreement with smaller localized studies that exist in portions of our study lends support to our model for the remainder of the study area, particularly the Russian Far East. The analysis needs to be expanded into Kamchatka and, with the utilization

of additional events, may be extendable into less seismically active regions of continental eastern Siberia. A good understanding of Pg and Sg velocities is essential to improving hypocenter location abilities in eastern Russia as they are the dominant phases observed at local and regional distances out to about 600km.

ACKNOWLEDGEMENTS

We gratefully acknowledge the assistance of V. Khalturin and T. Rautian for help in our literature review.

REFERENCES

Argentov, V. V., Gnibidenko, G. S., Popov, A. A., and Potapev, S. V. (1975), *Deep Structure of Pri-Amuria*:, Nauka, Moscow, 88 pp. (in Russian)

Belyaevsky, N. A. (1974), *The Earth's Crust Within the Territory of the USSR*, Nauka, Moscow, 278 pp. (in Russian)

Egorkin, A. V., Zuganov, S. K., Pavlenkova, N. A., and Chernyshev, N. M. (1987), Results of lithospheric studies from long-range profiles in Siberia, *Tectonophysics*, **140**, 29-47.

Gnibidenko, G. S. (1979), *Tectonics of the Marginal Seas of the Far East*, Nauka, Moscow, 160 pp.

Golonetsky, S. I., Novomeiskaya, F. V., and Perevalova, G. I. (1975), Travel-time curves of seismic waves and thickness of the Earth's crust in northeast near-Baikal, in Solonenko, V. P., ed., *Seismotectonics, Deep Structure, and Seismicity of the Northeastern Baikal Rift Zone*, Nauka, Novosibirsk, 40-53. (in Russian)

Golenetsky, S.I., Kruglyakov, M. I., and Perevalova, G. I. (1978), Travel-time curves of seismic waves of the earthquakes of the near-Baikal, in *Seismicity and Deep Structure of Near-Baikal*, Nauka, Novosibirsk, 30-38.

Jolivet, L., Fournier, M., Huchon, P., Rozhdestvenskiy, V. S., Sergeyev, K. F., and Oscorbin, L. S. (1992), Cenozoic intracontinental dextral motion in the Okhotsk-Japan Sea region, *Tectonics*, **11**, 968-977.

Krylov, S. V., and Duchkov, A. D. (1996), Deep strain-strength regionalization of the Earth's crust (on the example of the Altai-Sayan and Baikal seismic zones), *Geologiya i Geofizika*, **37**(9), 56-65. (in Russian)

Krylov, S. V., Mishenkin, B.P., and Petrik, G. V. (1972), On the study of the upper mantle using the DSS method in the Baikal rift zone, in Gaisky, V. N., and Treskov, A. A., eds., *Problems of the Seismicity of Siberia, part 1, Structure of the Earth's Crust and Upper Mantle, Dynamics of Seismic Waves*, Academy of Sciences of the USSR, Institute of Geology and Geophysics, Novosibirsk, 5-15. (in Russian)

Mackey, K.G. (1999), *Seismological studies in northeast Russia*, Ph.D. Dissertation, Michigan State University, East Lansing, xxiii + 346 pp.

Mackey, K. G., and Fujita, K. (1999), The northeast Russia seismicity database and explosion contamination of the Russian earthquake catalog, in *Proceedings of the 21st Seismic Research Symposium: Technologies for Monitoring the Comprehensive Nuclear-Test-Ban Treaty*, **1**, US Department of Defense, Arlington, LA-UR-99-4700, 151-161.

Mackey, K. G., and Fujita, K. (2000), Event relocations and seismic calibration in northeast Russia, in *22nd Annual DoD/DoE Seismic Research Symposium Proceedings*, **2**, US Department of Defense, Dulles, 223-232.

Mackey, K. G., Fujita, K., Steck, L. K., and Hartse, H. E. (2002), Seismic regionalization in northeast Russia, in *Proceedings of the 24th Seismic Research Review*, **1**, US Department of Defense, Dulles, LA-UR-02-5048, 107-116.

Maki, T. (1983), Extended travel-time tables for the JMA standard model of the crust and upper mantle structure beneath the Japanese Islands, *Bulletin of the Earthquake research Institute*, **58**, 311-383.

Mishenkin, B. P., Mishenkina, Z. R., and Annenkov, V. V. (1987), Deep seismic sounding in the Bureya massif, *Geologiya i Geofizika*, **28** (10), 98-107. (in Russian)

Nagornykh, T. V., Bobkov, A. O., and Poplavskaya, L. N. (1988), Results of the adaptation of the "Amur" automated system to the Sakhalin Island region (abstract), in *Development of Seismological and Geophysical Investigations in Siberia and the Far East (in Memory of A. A. Treskov)*, Institute of the Earth's Crust, Academy of Sciences of the USSR, Irkutsk, 21.

Natalin, B. A., and Parfenov, L. M. (1983), Accretional and collisional eugeosynclinal folded systems of the northwestern Pacific rim, in Hashimoto, M., and Uyeda, S., eds., *Accretion Tectonics in the Circum-Pacific Regions*, Terra Scientific Publishing Co., Tokyo, 59-68.

Pavlenkova, G. A., Priestley, K., and Cipar, J. (2002), 2D model of the crust and uppermost mantle along RIFT profile, Siberian craton, *Tectonophysics*, **355**, 171-186.

Pavlenkova, N. I., and Romanyuk, T. V. (1991), Combined geophysical models of Siberian lithosphere, *Soviet Geology and Geophysics*, **32**(5), 85-93.

Puzyrev, N. N., editor (1993), *Detailed seismic investigations of the lithosphere using P and S waves*, Nauka, Novosibirsk, 197 pp. (in Russian)

Puzyrev, N. N., and Mandelbaum, M. M., eds. (1984), *Geology and Seismicity of the BAM Zone – Deep Structure*, Nauka, Novosibirsk, 171 pp.

Solovev, S. L., Oskorbin, L. S., and Ferchev, M. D. (1967), *Earthquakes of Sakhalin*, Nauka, Moscow, 178 pp. (in Russian)

Suvorov, A. A., (1975), *Deep Structure of the Earth's Crust in the South Okhotsk Sector According to Seismic Data*, Nauka, Novosibirsk, 101 pp. (in Russian)

Suvorov, V. D., and Kornilova, Z. A. (1985), Deep structure of the Aldan shield according to near earthquake data: *Soviet Geology and Geophysics*, **26**(2), 79-84.

Suvorov, V. D., Parasotka, B. S., and Chernyl, S. D. (1999), Deep seismic sounding studies in Yakutia, *Izvestiya, Physics of the Solid Earth*, **35**, 612-629.

Suvorov, V. D., Mishenkina, Z.M., Petrick, G. V., Sheludko, I. F., Sleznev, V. S., and Solovyov, V. M. (2002), Structure of the crust in the Baikal rift zone and adjacent areas from Deep Seismic Sounding data, *Tectonophysics*, **351**, 61-74.

Volvovsky, I. S. (1973), *Seismic Investigations of the Earth's Crust of the USSR*, Nedra, Moscow, 207 pp. (in Russian)

Worrall, D.M., Kruglyak, V., Kunst, F., and Kuznetsov, V. (1996), Tertiary tectonics of the Sea of Okhotsk, Russia: Far-field effects of the India-Eurasia collision, *Tectonics*, **15**, 813-826.

Zorin, Y. Z., Belichenko, V. G., Turutanov, Y. K., and Kozhevnikov, V. M. (1993), The Central Siberia – Mongolia transect, *Geotectonics*, **27**, 103-117.

SUPPLEMENTING GROUND TRUTH DATA WITH SHEAR WAVE VELOCITY, SEISMIC ATTENUATION, AND THERMAL STRUCTURE OF THE CONTINENTAL LITHOSPHERE

Walter D. Mooney,[1] Irina Artemieva,[1,2] Shane T. Detweiler,[1] Magali Billien,[2] Jean-Jacques Leveque[2]

United States Geological Survey,[1] Ecole et Observatoire de Sciences de la Terre[2]

Sponsored by National Nuclear Security Administration
Office of Nonproliferation Research and Engineering
Office of Defense Nuclear Nonproliferation

Contract No. DE-A104-98AL79758

ABSTRACT

Ground truth data provide the opportunity to calibrate regional seismic velocity and Q (inverse attenuation) models. However, in many cases, available wave propagation data are too sparse to characterize seismic velocities and Q everywhere. It is therefore of interest to examine on a global basis the relationship between regional geology and heat flow versus the seismic properties (Vs and Qs) of the upper mantle. To better understand the propagation of seismic waves caused by nuclear explosions, we have developed new, theoretical models of the dissipation of energy in the crystalline rocks typical for the Earth's mantle. Using laboratory results, we suggest a temperature dependence of attenuation through the activation energy. We therefore compare maps of the thermal structure of the continental lithosphere with the inverse attenuation of seismic shear waves Qs and seismic velocity Vs as determined from surface wave dispersion and amplitudes. Our study is based on recently available global databases. We compare the values of Qs, Vs, and temperature T at the depths of 50, 100, and 150 km in the continental lithosphere. We find that qualitatively (by the sign of the anomaly) the maps of Qs closely correlate with lithospheric temperatures. The best correlation is observed for the depth of 100 km, where the resolution of the attenuation model is the highest. At this depth, the contour of zero attenuation anomaly approximately corresponds to the 1000^{o}C contour of lithospheric temperature, in agreement with laboratory data on a sharp change in seismic attenuation and shear velocities in upper mantle rocks at 900-1000^{o}C. The correlation between Vs and two other parameters (T and Qs), though present, is less distinct. We find that most cratonic regions show high lithospheric Vs, Qs and low T. Several prominent low Qs regions correlate with high lithospheric temperatures. We calculate that even if temperature variations in the lithosphere are the main cause of seismic velocity and attenuation variations, the relation between temperature and seismic properties is non-linear.

OBJECTIVE

It is widely accepted that a significant part of seismic velocity and attenuation anomalies in the mantle can be attributed to temperature variations. For the purposes of nuclear test monitoring at teleseismic distances, a knowledge of these anomalies is highly desirable. Ground truth data provide the opportunity to calibrate available regional seismic velocity and Q (inverse attenuation) models. However, in regions of interest such as Iran, India and China, wave propagation data are too sparse to adequately characterize seismic velocities and Q. It is therefore necessary that we examine on a global basis the correlations between seismic shear-wave velocities (V_s), inverse attenuation (Q_s), and temperature (T) in order to distinguish compositional and thermal origins of the attenuation anomalies in the upper mantle.

RESEARCH ACCOMPLISHED

Numerous seismic and laboratory studies have addressed the question of the correlation between seismic elastic and anelastic properties, and temperatures. (1) A global anelastic tomography study (Romanowicz, 1995) as well as regional seismic studies for the oceans (Sheehan and Solomon, 1992; Roth *et al,* 2000; Tsumura *et al,* 2000) found that **seismic velocity and attenuation** are correlated. (2) The strong effect of **temperature on seismic velocity** and elastic moduli was demonstrated by laboratory measurements (e.g., Berckhemer *et al,* 1982; Sato *et al,* 1989; Jackson *et al,* 1992; Jackson, 1993), implying that shear-wave velocity perturbations in the uppermost mantle can be caused by temperature variations. (3) The strong effect of **temperature on seismic attenuation** has been measured in a number of experimental studies. Laboratory measurements of seismic wave attenuation in ultramafic upper mantle rocks were carried out for a wide range of pressures and temperatures at ultrasonic frequencies (60-900 KHz) on dry peridotite (Sato *et al,* 1989) and at seismic frequencies (0.01-1 Hz) on dry dunite (Berckhemer *et al,* 1982; Jackson *et al,* 1992) and on synthetic polycrystalline olivine (Tan *et al,* 1997; Gribb and Cooper, 1998; Jackson, 2000). They show that at seismic frequencies attenuation, Q^{-1}, in mantle rocks at subsolidus temperatures follows the Arrhenius law and exponentially increases with temperature T:

$$Q^{-1} = T_o^{\alpha} \exp(-\alpha E^*/RT), \quad (1)$$

where E^* is the activation energy, R is the gas constant, T_o is the oscillation period, and the exponent α is about 0.15-0.30 as determined from seismic studies and laboratory measurements on the upper mantle rocks (e.g., Jackson *et al,* 1992).

Laboratory measurements with the temperature dependence of seismic attenuation were used in a number of studies where mantle geotherms were calculated from seismic attenuation (e.g., Kampfmann and Berckhemer, 1985; Sato *et al,* 1988; Sato and Sacks, 1989; Karato, 1990). The high sensitivity of seismic attenuation to temperatures, revealed in laboratory measurements, was used recently to correlate seismic attenuation anomalies in the mantle with temperature variations (e.g., Bodri *et al,* 1991; Durek *et al,* 1993; Mitchell, 1995; Romanowicz, 1994, 1995). Romanowicz (1995) found that in the depth interval from 100 to 300 km shear-wave attenuation Q_s^{-1} calculated from the amplitudes of low-frequency Rayleigh waves on a 10°x10° grid (the QR19 model) correlates with the surface heat flow values (the correlation coefficient r is in the range 0.20 to 0.35 with the correlation peak at z~200 km); while at depths of z>200 km Q^{-1} correlates with the hot spot distribution, with the strongest correlation (r~0.35–0.38) at z~300–660 km.

On the continents, low seismic attenuation in the upper mantle has been reported beneath western Australia, western Africa, and the Himalayas in a number of recent anelastic tomographic models (e.g. Romanowicz, 1994, Bhattacharyya *et al.,* 1996), supporting the idea of the thermal origin of most of the upper mantle Q_s anomalies. Seismic studies of shear-wave attenuation also revealed a qualitative correlation between regional attenuation anomalies in the crust and upper mantle and tectonic provinces (e.g., Nakanishi, 1978; Canas and Mitchell, 1978; Roult, 1982; Dziewonski and Steim, 1983; Chan and Der, 1988; Mitchell *et al,* 1997; Sarker and Abers, 1998).

Few studies have been carried out thus far to analyze: (a) the correlations between all three parameters (V_s, Q_s, and T) and (b) the global correlation between seismic attenuation and temperatures. We particularly know very little about regions where clandestine nuclear testing may be taking place. Here we present maps of V_s, Q_s, and T distributions at the depths of 50, 100, and 150 km and compare shear-wave velocities and attenuation at different depths in the upper mantle with temperature estimates in order to evaluate the influence of T on V_s and Q_s.

In the present study we use a subset of the 3-D V_s and Q_s models for the upper mantle produced by Billien (1999).

The models are based on the inversion of broadband seismological data of fundamental mode surface waves. The data used are amplitude and frequency spectra at periods between 40 s and 150 s for the direct path Rayleigh wave data (the first orbit) only, which is a subset of the extensive phase and amplitude data set measured and selected by Trampert and Woodhouse (2000). For a detailed description of the automatic measurement technique and implementation of the strict data rejection criteria, see Trampert and Woodhouse (1995).

V_s and Q_s calculations are based on a two-step inversion (for details see Billien, 1999; Billien *et al,* 2000). First, from phase (Φ) and amplitude (A) measurements, we made a simultaneous regionalization at several periods of the phase velocity (c_R) and the surface wave attenuation factor ($q_R=Q^{-1}_R$) (Billien *et al,* 2000):

$$A_i(\omega), \Phi_i(\omega) \Rightarrow c_R(\omega, \theta, \phi), q_R(\omega, \theta, \phi) . \quad (2)$$

A depth inversion of the phase velocity and surface wave attenuation maps at different frequencies provides a 3D model of the shear-wave velocity V_s and the shear-wave attenuation factor q_s ($q_s=Q_s^{-1}$) *(*Billien, 1999):

$$q_R(\omega, \theta, \phi) \Rightarrow q_s(z, \theta, \phi). \quad (3)$$

$$c_R(\omega, \theta, \phi) \Rightarrow V_s(z, \theta, \phi) \quad (4)$$

The classical inversion method of Tarantola and Valette (1982) is used at this stage. It employs a least-square method and includes information on the expected model in the form of: (1) an *a priori* model and (2) an *a priori* covariance of the model. Billien (1999) use a layered version of PREM with 50 km thick layers in the depth range 25 to 825 km as the *a priori* velocity and attenuation models. The upper 25 km ("the crustal layer") are fixed to the PREM value and are never updated in the inversion process. In the globally spherical PREM model (Dziewonski and Anderson, 1981) the radial average Q_s has a value of 600 at depths between 40 km and 80 km, and Q_s=80 between 80 km and 220 km. Similar to the attenuation model, the velocity value in the "crustal layer" is not allowed to change in the inversion, since the phase velocity maps are corrected at all periods for the crustal effects calculated from the CRUST5.1 model (Mooney *et al,* 1998). These corrected maps as a function of period are then inverted to obtain the 3D *S*-velocity model.

The *a priori* covariance of the attenuation model is described by *a priori* standard deviations as a function of depth. In order to allow larger Q_s variation in the lithosphere, which is believed to be more heterogeneous than the asthenosphere, a standard deviation on the *a priori* model σ_m was chosen to be twice as large in the lithosphere as in the asthenosphere.

The results for Q_R, and hence for Q_s, account for the effect of focusing (due to velocity heterogeneities) on the wave amplitude. More precisely, a linear approximation (Woodhouse and Wong, 1986) is used to include the focusing effect in the inversion. Amplitude variations due to scattering are not separately modeled. Thus the attenuation factor derived in this study includes both anelastic and scattering effects.

In the regionalization, smooth models were favored over rough models. This is achieved by use of a cost function based on the norm of the Lagrangian (second derivatives) of the model (Billien *et al,* 2000) rather than a classical damped least square method based on the norm of the model (e.g., Tarantola and Valette, 1982). In our model, phase velocity and attenuation maps, and then V_s and Q_s maps, are represented by spherical harmonics up to degree l=20. However, the effective degree of the computed maps is only 12 to 13, due to the damping used in the regionalization that progressively shut off the highest degree terms. This effective degree corresponds to a ~3000 km wavelength of attenuation and velocity lateral variations.

The depth resolution matrix shows that the best resolved layer for Q_s is at a depth of 100±25 km. The tuning of the cost function in the first step of the inversion largely influences the absolute values of Q_R variations (Billien *et al*, 2000) and thus the values of Q_s, but the sign of the variations and the sharpness of the contrasts are less sensitive to this tuning. Moreover, due to large perturbations found for attenuation, the numerical values are sensitive to the choice of the displayed parameters, $\Delta Q_s/Q_s$ or $-\Delta Q_s^{-1}/Q_s^{-1}$. For instance, our choice to display $-\Delta Q_s^{-1}/Q_s^{-1}$ anomalies (Figures 1-3) leads to perturbation values in the range between -250% and +100%. Plotting $\Delta Q_s /Q_s$ anomalies would lead to the same figure, but with perturbations ranging from -71% to 0. Since Billien (1999) and Billien *et al* (2000) use a damped inversion, the value of Q_s variations at each depth layer within the lithosphere is probably underestimated. On the whole, the vertical resolution of V_s and Q_s models is ~50 km.

Two global studies of the thermal regime of the continental lithosphere are available at present. The model of Pollack and Chapman (1977) is based on a degree-12, spherical harmonic representation of global surface heat flow and provides a rather generalized estimate of lithospheric thickness. Since that study numerous new heat flow measurements have become available. Here we use a more recent global model of the thermal state of the continental lithosphere (Artemieva and Mooney, 2001), hereafter referred to as the AM01 model. The model is based on global heat flow database (Pollack *et al,* 1993) updated for more recent heat flow measurements reported since 1993, and crustal structure database (Mooney *et al,* 1998, 2002). Estimates of the thermal regime of the stable continental lithosphere are based on the solution of the steady-state thermal conductivity equation:

$$\nabla^2 T = - A/k \qquad (5)$$

with the boundary conditions at the surface given by:

$$T \big|_{z=0} = 0 \qquad (6)$$

$$q_0 = - k \, \partial T/\partial z \qquad (7)$$

where q_0 is the near-surface heat flow, T is temperature, $k = k(z)$ and $A = A(z)$ are thermal conductivity and the heat production as functions of depth. The solution of Eqs. (5)–(7) permits the calculation of temperatures within the crust and lithospheric mantle, constrained by borehole heat flow measurements, q_0, (Pollack *et al,* 1993) and the distribution of thermal parameters with depth.

The strong effect of temperature on seismic velocities is known from laboratory studies (e.g. Berckhemer *et al,* 1982; Kampfmann and Berckhemer, 1985; Sato *et al,* 1989). A number of studies where upper mantle temperatures are estimated from seismic velocities (e.g. Sobolev *et al,* 1996; Goes *et al,* 2000; Goes and van der Lee, 2002) assume the existence of a strong correlation between these parameters. However, for the maps presented in Figures 1, 2, and 3, a statistical analysis of the correlation (r) between V_s and T in the lithospheric mantle of the continents suggests that even though there is the expected negative correlation between the two parameters (r=-0.38 at z=100 km and r=-0.42 at z=150 km) (Table 1), the conversion of seismic velocities into temperatures (or visa versa) is subject to considerable uncertainty. For a depth of 100 km, the range of possible temperatures corresponding to any given velocity value is at least $\pm 250^o$ C. At shallower depth (50 km) almost no correlation exists between V_s and T due to a large scatter in both of the parameters.

A qualitative correlation between seismic attenuation and velocities that has been observed in regional (e.g., Sheehan and Solomon (1992) and Tsumura *et al* (2000)) and global studies (Romanowicz, 1995), suggests to relate these two parameters quantitatively. Such an attempt was recently made by Roth *et al* (2000) for the Fiji-Tonga region, which assumed that anomalies of both attenuation and velocities have a similar thermal origin. They find that, at depths greater than 100 km, velocity and attenuation anomalies are strongly correlated and can be fit by an exponential equation; at shallower depths their data show a high degree of scattering.

Roth *et al* (2000) also examined the correlation between attenuation and shear-wave velocity anomalies derived from global seismic tomography studies (Su *et al,* 1994; Romanowicz, 1995) and concluded that the strong correlation between Q_s and V_s, observed in the Tonga subduction zone is more a regional phenomenon than a general rule. The statistical analysis of a global Q_s -V_s dataset for the continents presented here (Table 1) supports this conclusion. However, the correlation between Q_s and V_s varies with tectonic provinces. In accord with the results of Roth *et al* (2000), we do observe poor correlation (r=0.38) between Q_s and V_s in shallow (50 km) lithosphere of the continents, probably because crustal effects have the greatest influence on calculated Q_s and V_s at 50 km depth. However, the correlation remains low at 100-150 km depth, even though in this depth interval scattering has a lesser effect on Q_s.

The influence of temperature on seismic attenuation was examined in a number of laboratory experiments, where an exponential law for the correlation of two parameters was found (Berckhemer *et al,* 1982; Kampfmann and Berckhemer, 1985; Sato *et al,* 1989; Jackson *et al,* 1992; Gribb and Cooper, 1998). The only attempt to calculate temperatures from seismic attenuation data that we are aware of is presented by Sarker and Abers (1999) for the crust of southern and central Eurasia. Though regional seismic data show the existence of a correlation between deep temperatures and attenuation (e.g. Bodri *et al,* 1991), statistical analysis (Table 1) shows that in reality the coefficient of correlation is, in general, weak (r=-0.34 at z=150 km).; at shallower depths no significant correlation is observed on the global scale (r~0.2).

A poor correlation between Q_s and T suggest that effects other than temperature (e.g., composition, fluids, partial melt) play an important role in producing attenuation anomalies in the upper mantle. For example, in stable continental regions one would expect that compositional variations could play a dominant role in smearing the correlation between Q_s and T; for example, at 100 km depth, temperatures of 800-900^o C can exist in both Paleozoic and Precambrian platforms (Artemieva and Mooney, 2001). At the same time, petrological studies (e.g. Boyd, 1989) indicate that subcrustal lithosphere of the Precambrian cratons is chemically depleted compared to oceanic lithosphere and younger platforms and has higher Mg/Fe ratio. No experimental studies have examined how depletion can influence seismic attenuation. However, recent laboratory measurements of attenuation in MgO (Getting *et al*, 1997) suggest that variations in Mg in the subcrustal lithosphere of the cratons and Paleozoic platforms could affect seismic attenuation values.

We next qualitatively compare maps of seismic and temperature anomalies in the upper mantle to examine if there is a qualitative agreement between the parameters and to check if the quantitative correlation does not hold due to high amplitude variations of seismic anomalies at near-solidus temperatures. The maps of shear-wave velocity V_s, shear-wave quality factor Q_s, and temperature T are plotted at three depths (Figures 1-3). Due to the vertical resolution of V_s and Q_s models, the velocity and attenuation maps refer to depth intervals of 50±25 km, 100±25 km, and 150±25 km.

We emphasize a comparison of V_s, Q_s, and T maps only for the continental regions where an acceptable resolution is achieved for all three parameters. In this section we discuss only the qualitative correlations of the anomalies, and Figures 1-3 reveal the existence of a strong overall qualitative correlation between the signs of V_s, Q_s, and T anomalies for most of the continental lithosphere at depths of 50-150 km (see also Table 2). At first look, there is less correlation between the three maps for a depth of 150 km. The eye catches strong positive seismic anomalies over North America and Eurasia, while temperature anomalies appears to be much weaker there. However, a more careful comparison of the maps reveals a good qualitative correlation between the signs of the anomalies at this depth as well (see Table 2 for summary). The correlation (in terms of the sign of the anomalies) between the T and Q_s for most of the continents suggests that the anelasticity anomalies in the continental lithosphere are primarily caused by thermal effects.

Table 2 gives a summary of the qualitative comparison of shear-wave velocity, inverse shear-wave attenuation and temperature anomalies for the continents. It shows that in most tectonic provinces the signs of all three anomalies are well correlated; however in some regions only two types of the anomalies correlate.

There are two types of regions where all three anomalies correlate. “Cold” regions include most of the Precambrian cratons; “hot” regions include continental rifts, Cenozoic orogens and, unexpectedly, the Sino-Korean craton. A correlation between the signs of all three anomalies is observed within both of the groups throughout the entire lithosphere and suggests a thermal origin of most of the seismic anomalies.

“Hot” (red) anomalies (low V_s, low Q_s, and high T) are found in all three maps (Figure 1) for many tectonically active regions of the continents, that includes western North America (which is largely composed of young accreted terrains), the Andes, Cenozoic eastern Australia, the Red Sea rift, and Phanerozoic western Europe. However, some active tectonic regions show a non-correlated behavior of the anomalies, which will be discussed below.

At all depths, blue, “cold” anomalies with high V_s, high Q_s, and low T dominate in cratonic regions (see Table 2 for a summary). This includes the Canadian shield, the Siberian craton, the Baltic shield and the East European platform, the Precambrian Western Australia, and the Indian craton. It is possible that Greenland is also characterized by the “cold” set of V_s, Q_s and T anomalies; however, the velocity and attenuation anomalies are smeared due to the proximity of the Icelandic plume. The Brazilian shield of South America shows a correlation of high V_s with high Q_s, but T estimates are absent there, except for the Saõ-Francisco craton, which is characterized by low T typical for the cratonic lithosphere.

On the whole, we find a better agreement between T and Q_s for large cratons than for small ones. Large cratons (the Canadian shield, the Baltic shield, the East European platform, and the Siberian craton) have lower attenuation and lower temperature down to at least 200-250 km depth (and even deeper for attenuation anomalies *(*Billien, 1999)), implying that cold, thick lithosphere beneath these Precambrian cratons is present to at least this depth (c.f., Jordan,

1988; Nyblade and Pollack, 1993; Artemieva and Mooney, 2001). Since T and Q_s are so well correlated, we suggest that attenuation maps can provide a first order estimate of lithospheric temperatures in regions where the heat flow measurements are sparse.

A strong correlation between all three anomalies, V_s, Q_s, and T, is observed at 100 km depth beneath most of Eurasia, with the strongest anomalies beneath the Baltic shield and East European platform and beneath the Siberian craton, which are separated by a "hot" high-temperature and high-attenuation anomaly beneath the much younger West Siberian basin. However, at 150 km depth, a pronounced "cold" attenuation anomaly in the West Siberian basin (Figure 3b) is not correlated with high temperature anomaly (Figures 3c). At 150 km depth, northern Eurasia is another large region with poorly correlated temperature and attenuation anomalies, though it displays a somewhat better correlation between shear velocities and temperatures.

The nuclear test monitoring community has a number of regions of potential interest. We examine one, China, in detail here. The Early Proterozoic Sino-Korean craton, which has undergone intensive tectonic reworking since the late Mesozoic, shows near-zero anomalies in the three maps at 100 km depth and "hot" anomalies in the maps for 150 km. Surface heat flow data suggest that the lithosphere there is atypically thin (120-150 km, Artemieva and Mooney, 2001) compared to other cratons and lithospheric temperatures are intermediate between other Precambrian cratons and tectonically active Cenozoic regions. Xenolith studies (Griffin et al, 1998) provide evidence that the composition of the lithosphere of the Sino-Korean craton has been significantly modified by Mesozoic-Cenozoic tectonic and magmatic activity, and that its lower part (below 80-140 km depth) has been largely or even completely removed and replaced by more fertile Phanerozoic material (Xu *et al*, 2000). Thus, a part of V_s and Q_s variations there may probably have a non-thermal origin.

The Tibet-Himalayan orogen is consistently evident only in the map of T. However, temperature estimates in the lithosphere of this region are not calculated from the surface heat flow data, but were derived from petrological and non-steady state model constraints (e.g., Henry *et al*, 1997), and thus should be interpreted with caution. Moreover, the existence of a large time delay in the upward propagation of a thermal anomaly also implies that the correlation between seismic models and geotherms derived from surface heat flow data should be the best in stable regions that did not undergo tectonic or magmatic activity over a long geological time. The cratonic regions are the best examples of such structures and, as discussed above, indeed show a strong correlation between seismic parameters, on one hand, and the thermal state, on the other hand. Though orogenic regions like the Himalayas are not expected to closely follow the same rule, we cannot identify any region where seismic anomalies are clearly of a non-thermal origin.

The regions with non-correlated seismic anomalies in the lithosphere deserve special attention, as both V_s or Q_s anomalies used in this study were derived in a joint inversion of one data set (Billien, 1999; Billien *et al*, 2000). However, according to experimental studies on polycrystalline olivine at seismic frequencies (e.g. Jackson, 2000), attenuation in shallow lithosphere needs not correlate with temperature and shear-wave velocities, because at low T ($<600^o$ C) typical for shallow cratonic lithosphere the upper mantle rocks exhibit an almost elastic behavior, while the values of Q^{-1} are essentially scattered.

The Alpine-Himalayas zone, which extends from the Alps through the Asia Minor to the Tibetan Plateau, clearly appears in Figures 1b and 1c as a hot and highly attenuating zone. However, the V_s anomaly is close to zero at all depths, rather than showing the expected negative anomaly. Other regions where neither Q_s nor T anomalies correlate with V_s anomalies in the deep lithosphere (z~100-150 km) include the West Siberia basin and the Arabian shield. However, the lateral dimensions of the Arabian shield are too small to be resolved by the seismic models used in the present study. In the West Siberia basin, the disagreement between Q_s and T may also be apparent due to a very high amplitude of attenuation anomaly beneath the Siberian craton in East Siberia, which may possibly "overprint" attenuation anomaly in the basin (~2000 km from east to west compared to the lateral resolution of the seismic models of ~3000 km).

On the other hand, laboratory and theoretical studies (e.g., Berckhemer *et al*, 1982; Karato and Spetzler, 1990; Jackson *et al*, 1992) indicate that seismic attenuation is considerably more sensitive to temperature variations than elastic velocities, while seismic velocities are to a larger degree affected by compositional variations (e.g., Bina and Silver, 1997; Deschamps *et al*, 2002). We, therefore, favor a compositional origin of the velocity anomalies beneath the West Siberia basin. This conclusion is supported by the results of the recent study of Kaban *et al* (2002), in

which lithospheric gravity anomalies were corrected for temperatures in order to discriminate between compositional and thermal effects. One of the conclusions of that study is that there are large compositional differences between the Precambrian lithospheres of the East European platform and the Siberian craton, on one hand, and the Paleozoic West Siberian basin, on the other hand. As seismic attenuation in the cratonic lithosphere seem to have purely thermal origin, a compositional origin of seismic anomalies in the lithosphere of West Siberian basin cannot be ruled out.

CONCLUSIONS AND RECOMMENDATIONS

We examine the correlations among seismic shear-wave velocity, Q_s, and temperature in order to distinguish the attenuation anomalies in the upper mantle of thermal origin. Our analysis is based on the shear-wave velocity and shear-wave attenuation anomalies in the lithosphere, calculated for the whole Earth from the broad-band seismological data of the fundamental mode surface waves at periods 40 to 150 sec (Billien, 1999; Billien *et al*, 2000), and on the data on lithospheric temperatures beneath continents (Artemieva and Mooney, 2001).

1. We present a qualitative comparison of V_s, Q_s, and T lithospheric anomalies based on the visual comparison of the maps for 50, 100, and 150 km. A weak visual correlation at 50 km depth between seismic parameters and temperature can be attributed to the low resolution of V_s and Q_s at shallow depth due to the sensitivity to the corrections for crustal effects.

At depths of 100 and 150 km, high V_s, high Q_s, and low T correlate with cratons, except for the South America and South Africa, where seismic anomalies may be artifacts produced by smearing of offshore anomalies. We propose that positive seismic anomalies in the cratonic lithosphere are primarily of the (low-T) thermal origin. Correlation between attenuation and temperature anomalies in the cratonic lithosphere can be used to estimate lithosphere thickness in the regions where heat flow measurements are absent.

Similarly, we find the expected inverse correlations (low V_s, low Q_s, and high T) for many tectonically active regions. We hypothesize that fluids, partial melts, or compositional anomalies can have an essential effect on anelastic and elastic seismic properties of the continental lithosphere.

2. Comparison of the attenuation values calculated from seismic inversion with theoretical estimates based on temperatures and analytical equations derived in laboratory studies (Sato and Sacks, 1989; Jackson *et al*, 1992) suggests that attenuation can be considered as an indicator of tectonic processes only in the upper 100 km of the lithosphere.

3. This study shows that even if temperature variations in the lithosphere are the main cause of seismic velocity and attenuation variations, the relation between temperature and seismic properties is non-linear and the hypothesis of compositionally homogeneous lithospheric roots is invalid. Rather, the lithospheric mantle appears to have a complex deep structure, analogous to the crust. These compositional and structural variations contribute to the observed anomalies in seismic properties.

For the purposes of nuclear test monitoring, we believe that we have developed a new method for supplementing ground truth data by providing calibrations of regional seismic velocity and Q (inverse attenuation) for regions of interest. Additional wave propagation data where data are currently sparse would be useful as a check of this new method. However, results indicate that our models are very useful for detection and monitoring of the propagation of seismic waves caused by nuclear explosions. We recommend that further implementation of this technique be considered.

Table 1. Correlation coefficients between temperature, seismic velocity, and attenuation for different upper mantle depths

Depth	T vs Q_s	T vs V_s	V_s vs Q_s
50 km	-0.19	-0.19	0.38
100 km	-0.23	-0.38	0.41
150 km	-0.34	-0.42	0.41
200 km	-0.23	-0.26	0.25

Table 2. Qualitative correlations between Vs, Qs and T for different tectonic provinces

Depth	V_s, Q_s and T correlate	V_s and Q_s do not correlate with T	V_s and T do not correlate with Q_s	Q_s and T do not correlate with V_s
50 km	<u>cratons, Ar-ePt ("cold"):</u> 1. Canadian shield 2. Baltic shield 3. East European Platf. 4. Siberian craton 5. Western Australia 6. Indian shield 7. Greenland ? 8. Amazonian craton? <u>Active regions, Cz-Pz ("hot"):</u> 1. Western North America 2. the Andes 3. Eastern Australia 4. Western Europe 5. Alpine-Himalayan belt (V_s anomaly weak)	1. East African Rift, Cz (hot T, cold V_s and Q_s) 2. Sino-Korean craton, ePt/Mz (hot V_s and Q_s, cold T)	1. West African craton, Ar-ePt (cold V_s and T, Q_s~*0*) 2. South Africa, Ar-ePt (cold V_s and T, hot Q_s)	1. West Siberian basin, Pz (hot Q_s and T, cold V_s) 2. Arabian shield, m-lPt (cold Q_s and T, hot V_s)
100 km	<u>cratons, Ar-ePt ("cold"):</u> 1. Canadian shield 2. West African craton 3. Baltic shield 4. East European Platf. 5. Siberian craton 6. Western Australia 7. Greenland ? 8. Amazonian craton ? 9. Congo craton ? <u>Active regions, Cz-Pz ("hot"):</u> 1. Western North America 2. the Andes 3. Eastern Australia 4. Western Europe 5. Alpine-Himalayan belt (V_s anomaly weak) <u>Intermediate anomalies:</u> 1. Sino-Korean craton, ePt/Mz (V_s~0, Q_s and T variable)	1. East African Rift, Cz (hot T, cold V_s and Q_s)	1. South Africa, Ar-ePt (cold V_s and T, hot Q_s) 2. Indian shield, Ar-ePt (cold V_s and T, hot Q_s)	1. West Siberian basin, Pz (hot Q_s and T, cold V_s) 2. Arabian shield, m-lPt (cold Q_s and T, V_s ~0) 3. Amazonian craton, Ar-ePt (hot Q_s and T, cold V_s)
150 km	<u>cratons, Ar-Pt ("cold"):</u> 1. Canadian shield	1. Tibet and Himalayas, ePt-Cz	1. Baltic shield, Ar-Pt (cold V_s and T, Q_s ~*0*)	1. East African Rift, Cz (hot Q_s and T,

	2. East European Platf. 3. Siberian craton 4. West African craton 5. Western Australia 6. Arabian shield 7. Greenland ? <u>cratons, Ar-ePt (zero anomalies):</u> 1. Indian shield 2. Amazonian craton? <u>Active regions, Cz-Pz ("hot"):</u> 1. Western North America 2. the Andes 3. Eastern Australia 4. Western Europe 5. Sino-Korean craton, ePt/Mz 6. Red Sea rift and Afar	(hot T, cold V_s and Q_s) 2. West Siberian basin, Pz (all three parameters poorly correlate: hot T, cold Q_s, and V_s ~0)	2. South Africa, Ar-ePt (cold V_s and T, hot Q_s)	cold V_s)

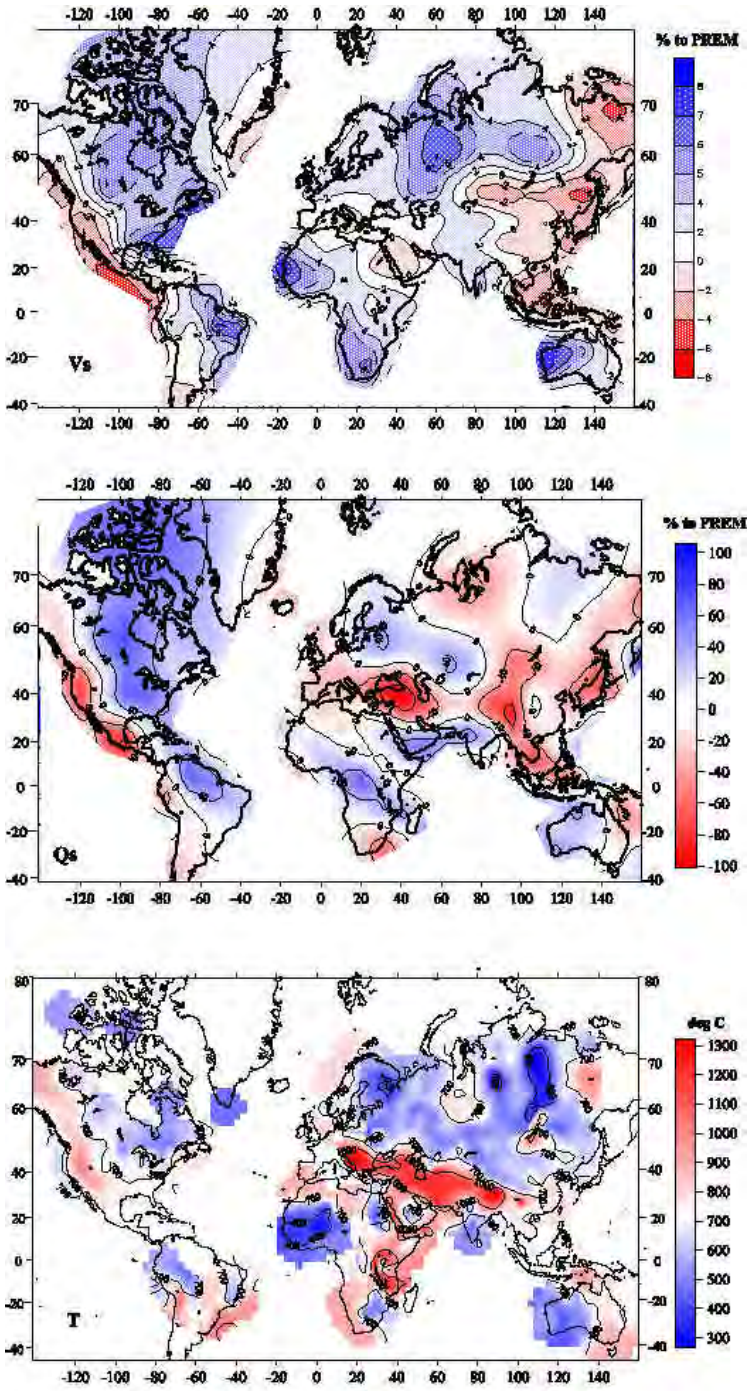


Figure 1. Map of shear-wave velocity V_s (as variation in % to PREM), inverse attenuation Q_s (as variation in % to PREM, $-\Delta Q_s^{-1}/Q_s^{-1}$), and temperature T (in deg C) for continental lithosphere at a depth of 50 km. Blue colors correspond to high V_s, high Q_s, and low T. Red colors correspond to low V_s, low Q_s, and high T. The dominant pattern on all three maps is the correlation of blue colors with stable Precambrian cratons and red colors with tectonically active Phanerozoic regions. The maps show a correlation in blue regions in the Canadian, Baltic, Siberian, West African, and Australian cratons. Red regions that correlate include western North America, Europe, the Middle East, eastern China and eastern Australia.

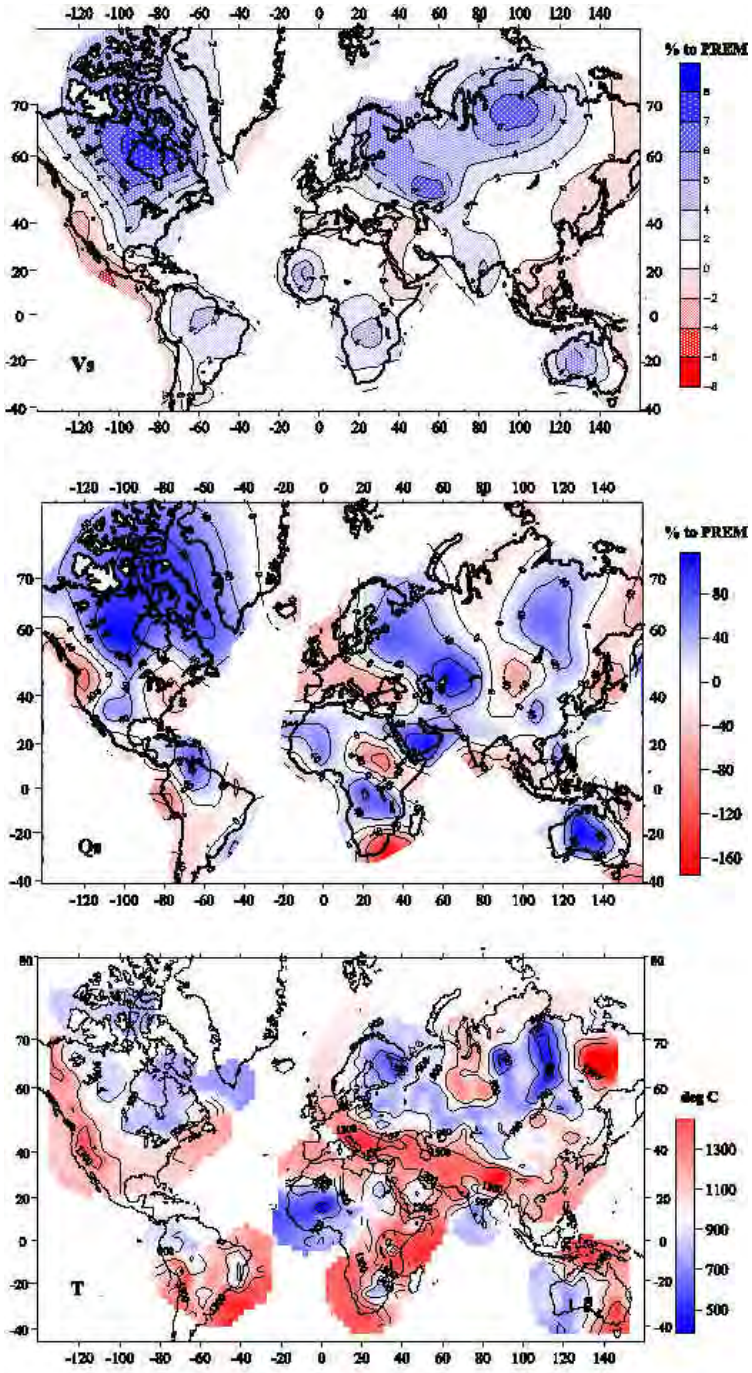


Figure 2. Map of shear-wave velocity V_s (as variation in % to PREM), inverse attenuation Q_s (as variation in % to PREM), and temperature T (in deg C) for continental lithosphere at a depth of 100 km. Presentation as in Figure 1. There is a close correspondence in the anomaly patterns for most of the Precambrian cratons and the Cenozoic regions, especially for the Precambrian Eurasia, West Africa, northern Canada, western North America and central Australia. This correspondence indicates that temperature plays the dominant role in determining the strength of V_s and Q_s anomalies at this depth in the lithosphere.

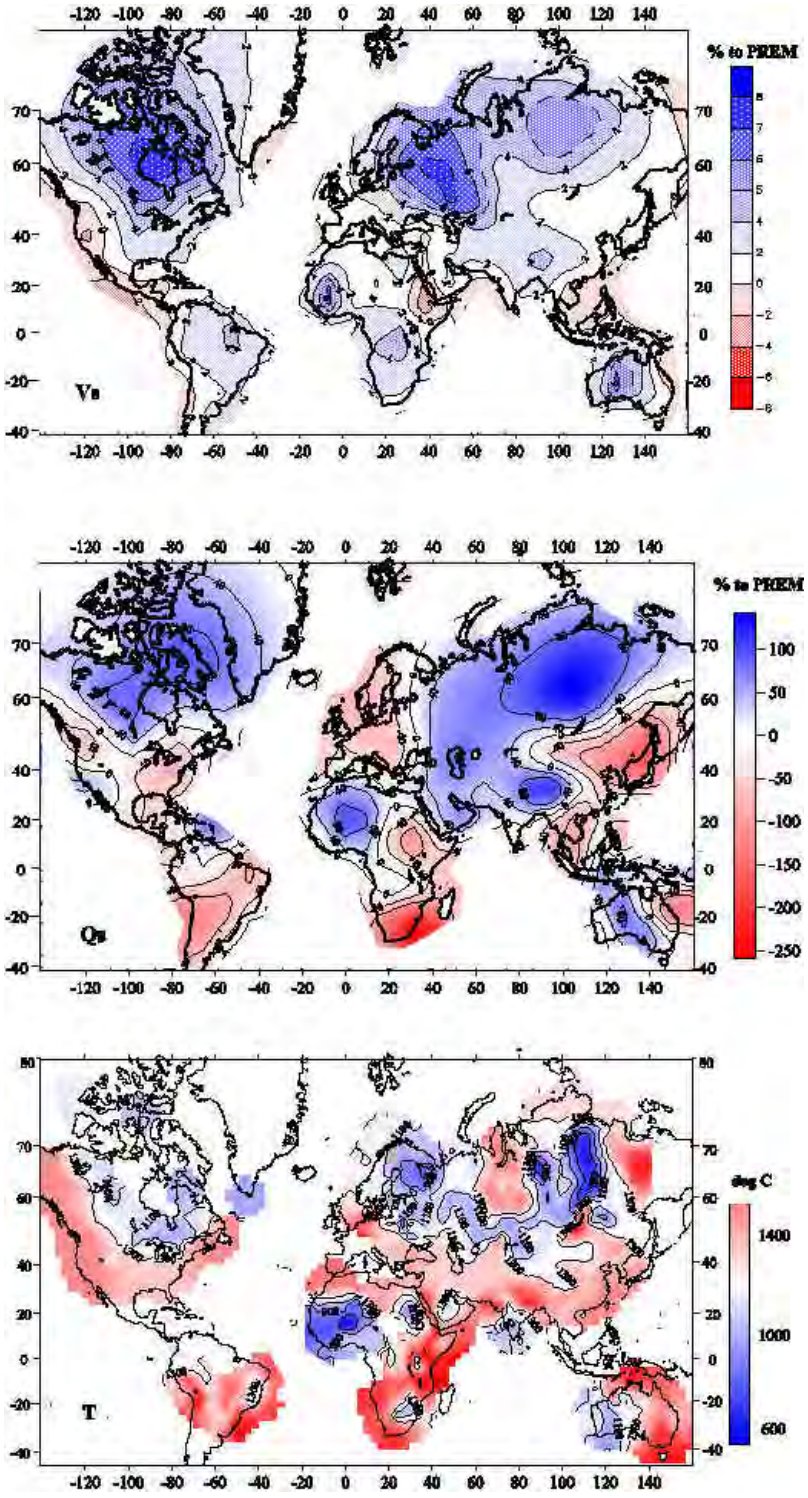


Figure 3. Map of shear-wave velocity V_s (as variation in % to PREM), inverse attenuation Q_s (as variation in % to PREM), and temperature T (in deg C) for continental lithosphere at a depth of 150 km. Presentation as in Figure 1. All low temperatures (lower panel) correspond to stable cratons. In contrast, high V_s and high Q_s anomalies include these same stable cratons plus some regions of active tectonics, such as the southern Eurasia suture zone extending from the Alps to the Tibetan plateau. This may indicate the presence of cold subducted lithosphere beneath the southern European suture zone.

REFERENCES

Artemieva I.M. and Mooney W.D., 2001. Thermal structure and evolution of Precambrian lithosphere: A global study. *J. Geophys. Res,* 106, 16387-16414.

Berckhemer H., Kapfmann W., Aulbach E., and Schmeling H., 1982. Shear modulus and Q of forsterite and dunite near partial melting from forced oscillation experiments. *Phys. Earth Planet. Interiors,* 29, 30-41.

Bhattacharyya J.G., Masters G., and Shearer P.,1996. Global lateral variations of shear attenuation in the upper mantle. *J. Geophys. Res.,* 101, 22273-22290.

Billien M., 1999. Hétérogénéités de vitesse et d'attenuation du manteau superior à l'echelle globale par modelisation du mode fundamental des ondes de surface. *PhD Thesis*, EOST-IPG, Strasbourg.

Billien M., Lévêque J.-J., and Trampert J., 2000. Global maps of Rayleigh wave attenuation for periods between 40 and 150 seconds. *Geophys. Res. Lett*., 27, 3619-3622.

Bina C.R. and Silver P.G., 1997. Bulk sound travel times and implications for mantle composition and outer core heterogeneity. *Geophys. Res. Lett*., 24, 499-502.

Bodri B., Iizuka S. and Hayakawa M., 1991. Relations between deep temperatures and other geophysical characteristics in central Honshu, Japan. *Tectonophys.*, 194, 325-336.

Boyd F.R., 1989. Compositional distinction between oceanic and cratonic lithosphere. *Earth Planet. Sci. Lett.,* 96, 15-26.

Canas J.A. and Mitchell B.J., 1978. Lateral variation of surface wave anelastic attenuation across the Pacific. *Nature*, 328, 236-238.

Chan W.W. and Der Z.A., 1988. Attenuation of multiple ScS in various parts of the world. Geo*phys. J*., 92, 303-314.

Deschamps F., Trampert J., and Snieder R., 2002. Anomalies of temperature and iron in the uppermost mantle inferred from gravity data and tomographic models. *Phys. Earth Planet. Inter*., 129, 245-264.

Durek J.J., Ritzwoller M.H. and Woodhouse J.H., 1993. Constraining upper mantle anelasticity using surface wave amplitude anomalies. *Geophys. J. Int.,* 114, 249-272.

Dziewonski A. and Steim J., 1983. Dispersion and attenuation of mantle waves through waveform inversion. *Geophys. J. Roy. Astron. Soc*., 70, 503-527.

Dziewonski A.M. and Anderson D.L., 1981. Preliminary reference Earth model. *Phys. Earth Planet. Inter.*, 2, 297-356.

Getting I.C., Dutton S.J., Burnley P.C., Karato S. and Spetzler H.A., 1997. Shear attenuation in and dispersion in MgO. *Phys. Earth Planet. Inter.*, 99, 249-257.

Goes S., Govers R., and Vacher P., 2000. Shallow mantle temperatures under Europe from P and S wave tomography. *J. Geophys. Res.,* 105, 11153-11169.

Goes S. and van der Lee S., 2002. Thermal structure of the North American uppermost mantle inferred from seismic tomography. *J. Geophys. Res.,* 107(B3).

Gribb T.T. and Cooper R.F., 1998. Low-frequency shear-attenuation in polycrystalline olivine: Grain boundary diffusion and the physical significance of the Andrade model for viscoelastic rheology. *J. Geophys. Res.,* 103, 27267-27279.

Griffin W.L., Zhang A., O'Reilly S.Y., and Ryan C.G., 1998. Phanerozoic evolution of the lithosphere beneath the Sino-Korean craton. In: Flower M. et al. (Eds.), Mantle dynamics and plate interactions in East Asia. Washington, D.C., *AGU Geodynam. Monogr*. 27, 107-126.

Henry P., Le Pichon X., and Goffe B., 1997. Kinematic, thermal and petrological model of the Himalayas: constraints related to metamorphism within the underthrust Indian crust and topographic elevation. *Tectonophys*., 273, 31-56.

Jackson I., 1993. Progress in the experimental study of seismic wave attenuation. *Ann. Rev. Earth Planet. Sci.,* 21, 375-406.

Jackson I., Paterson M.S., Fitz Gerald J.D., 1992. Seismic wave dispersion and attenuation in Åheim dunite: an experimental study. *Geophys. J. Int.*, 108, 517-534.

Jackson I., 2000. Laboratory measurement of seismic wave dispersion and attenuation: recent progress. *Geophysical Monograph*, 117, 265-289.

Jordan, T.H., 1988. Structure and formation of the continental tectosphere. *J. Petrology*, 29, 11-37.

Kaban M.K., Schwintzer P., Artemieva I.M., and Mooney W.D., 2002. Density of continental roots: compositional and thermal effects. *Earth Planet. Sci. Lett.(submitted).*

Kampfmann W. and Berckhemer H., 1985. High temperature experiments on the elastic and anelastic behaviour of magmatic rocks. *Phys. Earth Planet. Inter.*, 40, 223-247.

Karato S.-I., 1990. Low Q zone at the base of the mantle: Evidence for lower mantle convection? *Phys. Earth Planet. Inter*., 22, 155-161.

Karato S.I. and Spetzler H.A., 1990. Effect of microdynamics in minerals and solid-state mechanisms of seismic wave attenuation and velocity dispersion in the mantle. *Rev. Geophys.*, 28, 399-421.

Mitchell B.J., 1995. Anelastic structure and evolution of the continental crust and upper mantle from seismic surface wave attenuation. *Rev. Geophys.*, 33, 441-462.

Mitchell B.J., Pan Y., Xie J. and Cong L., 1997. Lg coda Q variation across Eurasia and its relation to crustal evolution. *J. Geophys. Res.*, 102, 22767-22779.

Mooney W.D., Laske G., and Masters T.G., 1998. CRUST 5.1: A global crustal model at 5^{o}x5^{o}. *J. Geophys. Res.*, 103, 727-747.

Mooney, W.D., Prodehl, C., and Pavlenkova, N.I., 2002. Seismic velocity structure of the continental lithosphere from controlled source data. In: H. Kanamori, P. Jennings, and W.H.K. Lee (Eds.): *IASPEI Handbook on Earthquake and Engineering Seismology*, Academic Press, San Francisco, p. 887-910.

Nakanishi I., 1978. Regional difference in the phase velocity and the quality factor Q of mantle Rayleigh waves. *Science*, 200, 1379-1381.

Nyblade A.A. and Pollack H.N., 1993. A global analysis of heat flow from Precambrian terrains: Implications for the thermal structure of Archean and Proterozoic lithosphere. *J. Geophys. Res*., 98, 12207-12218.

Pollack H.N. and Chapman D.S., 1977. On the regional variation of heat flow, geotherms and lithospheric thickness. *Tectonophys*., 38, 279-296.

Pollack H.N., Hurter, S.J., and Johnson, J.R., 1993, Heat flow from the Earth's interior: analysis of the global data set. *Rev. Geophysics*, 31, 267-280.

Romanowicz B., 1994. Anelastic tomography: a new perspective on upper-mantle thermal structure. *Earth Planet. Sci. Lett.*, 128, 113-121.

Romanowicz B., 1995. A global tomographic model of shear attenuation in the upper mantle. *J. Geophys. Res*., 100, 12375-12394.

Roth E.G., Wiens D.A. and Zhao D., 2000. An empirical relationship between seismic attenuation and velocity anomalies in the upper mantle. *Geophys. Res. Lett., 27*, 601-604.

Roult G., 1982. The effect of young oceanic regions on the periods and damping of free oscillations of the Earth. *J. Geophys.*, 51, 38-43.

Sarker G. and Abers G.A, 1998. Deep structures along the boundary of a collisional belt: attenuation tomography of P and S waves in the Greater Caucasus. *Geophys. J. Int.*, 133, 326-340.

Sarker G. and Abers G.A., 1999. Lithospheric temperature estimates from seismic attenuation across range fronts in southern and central Eurasia. *Geology*, 27, 427-430.

Sato H.I., Sacks E., Takahashi E., and Scarfe C.M., 1988. Geotherms in the Pacific Ocean from laboratory and seismic attenuation studies. Nature, 336, 154-156.

Sato H., Sacks I.S., 1989. Anelasticity and thermal structure of the oceanic mantle: Temperature calibration with heat flow data. *J. Geophys. Res.*, 94, 5705-5715.

Sato H., Sacks I.S., Murase T., Muncill G., and Fukuyama H., 1989. Q_p-melting temperature relation in peridotite at high pressure and temperature: Attenuation mechanism and implications for the mechanical properties of the upper mantle. *J. Geophys. Res.*, 94, 10647-10661.

Sheehan A.F. and Solomon S.C., 1992. Differential shear wave attenuation and its lateral variation in the North Atlantic region. *J. Geophys. Res.*, 97, 15,339-15,350.

Sobolev S.V., Zeyen H., Stoll G., Werling F., Altherr R. and Fuchs K., 1996. Upper mantle temperatures from teleseismic tomography of French Massif Central including effects of composition, mineral reactions, anharmonicity, anelasticity and partial melt. *Earth Planet. Sci. Lett.*, 139, 147-163.

Su W.-J., Woodward R.L., and Dziewonski A.M., 1994. Degree-12 model of shear velocity heterogeneity in the mantle. *J. Geophys. Res*., 99, 6945-6980.

Tan B.H., Jackson I., and Fitz Gerald J.D., 1997. Shear wave dispersion and attenuation in fine-grained synthetic olivine aggregates: preliminary results. *Geophys. Res. Lett.*, 24, 1055-1058.

Tarantola A. and Valette B., 1982. Generalized nonlinear inverse problems solved using the least squares inversion. *Rev. Geophys.*, 20, 219-232.

Trampert J. and Woodhouse J.H., 1995. Global phase velocity maps of Love and Rayleigh waves between 40 and 150 s. *Geophys. J. Int.*, 122, 675-690.

Trampert J. and Woodhouse J.H., 2000. Assessment of global phase velocity models. *Geophys. J. Int*. 142, 67-73.

Tsumura N., Matsumoto S., Horiuchi S. and Hasegawa A., 2000. Three-dimensional attenuation structure beneath the northeastern Japan arc estimated from spectra of small earthquakes. *Tectonophys.*, 319, 241-260.

Woodhouse J.H. and Wong Y.K., 1986. Amplitude, phase and path anomalies of mantle waves. *Geophys. J. R. Astron. Soc*., 87, 753-773.

Xu X., O'Reilly S.Y., Griffin W.L., and Zhou X., 2000. Genesis of young lithospheric mantle in southeastern China; an LAM-ICPMS trace element study. *J. Petrology*, 41, 111-148.

DEEP SEISMIC SOUNDING DATASETS FOR SEISMIC CALIBRATION OF NORTHERN EURASIA

Igor B. Morozov,[1, 2] Elena A. Morozova,[2] Scott B. Smithson,[2] and Leonid N. Solodilov[3]

University of Saskatchewan;[1] University of Wyoming;[2] Center GEON[3]

Sponsored by Air Force Research Laboratory

Contract No. DTRA01-01-C-0081

ABSTRACT

The University of Wyoming, in cooperation with the Center GEON in Moscow, Russia, is preprocessing and transferring data to the Incorporated Research Institutions for Seismology (IRIS) and the Space and Missile Defense Center Monitoring Research (SMDCMR) facility. This data consists of digital seismic recordings from several unique long-range Deep Seismic Sounding (DSS) profiles using Peaceful Nuclear Explosions (PNEs). As a result of this four-year effort, seismic data from nine major DSS projects using 22 PNEs, several hundred chemical explosions, and recordings of natural seismicity in Northern Eurasia will become broadly available for seismological and nuclear test monitoring research. To date, complete sets of records from the projects QUARTZ, CRATON, KIMBERLITE, and RIFT were delivered to IRIS and SMDCMR, and the data from two RUBY profiles will be delivered October 2003.

DSS PNE profiles were recorded by the Center GEON (the Special Geophysical Expedition at the time) from the early 1970's through late 1980's using 200-400 three-component analog instruments deployed in a grid of lines traversing most of the territory of the Former USSR. Each profile recorded 2-4 PNEs and several dozens of chemical explosions at the same receiver locations. Listening times of up to ~600 sec (after the first arrival) allowed recording of the secondary phases (*S*, *Lg*, *Pg*, *Rg*) critical for nuclear test monitoring. The energies of the PNEs (m_b >5) were sufficient for reliable recordings beyond 3000 km, including consistent reflections from the mantle transition zone and several reflections from the core-mantle boundary. Chemical explosions of 5-12 tons yielded reflections from ~100-km depths and were recorded to 300-600-km distance.

DSS PNE data represents an unparalleled source of seismic information about the detailed structure of the upper mantle down to 400-800 km depth. The core PNE data sets cover an intermediate distance range (between 0-3200 km) and bridge the gap between conventional controlled-source seismology and nuclear explosion monitoring seismology. Dense, linear systems of DSS/PNEs observations lead to unusually detailed models of the crust and uppermost mantle over 4000-km long geotraverses. For regional seismic calibration, these datasets provide virtually the only dense three-component recordings of regional phases in aseismic regions of Northern Eurasia.

Numerous publications (primarily by GEON, the Russian Academy of Sciences, the Universities of Wyoming and Saskatchewan, and the Potsdam/Karlsruhe and Copenhagen groups) have presented velocity, reflectivity, attenuation, scattering, and receiver function models inspired by these profiles. As the ongoing discussion of the short-scale heterogeneity of the uppermost mantle shows, PNE waveforms still contain a wealth of information that needs to be recovered by modern numerical analysis. When made broadly accessible for nuclear test monitoring research, the datasets should become very important for seismic calibration and for the development of transportable seismic discriminants in Asia. From a broader scientific perspective, the digitized DSS recordings and models of the upper mantle could provide ideal reference and calibration data sets for the detailed structure of the upper mantle targeted by the recently funded USArray program.

OBJECTIVE

Over the past three decades, Russian scientists acquired a network of dense, linear, long-range, three-component Deep Seismic Sounding (DSS) profiles using conventional and Peaceful Nuclear Explosions (PNEs) over a large territory of Northern Eurasia. These historic data provide unique opportunities to calibrate seismic nuclear discrimination techniques by studying regional wave propagation through complex continental lithospheric structures.

The objective of this four-year effort is to digitize, verify, edit, and make broadly available through IRIS and SMD CMR data repositories a significant part of the unique collection of DSS PNE datasets currently stored on analogue magnetic tapes at Center GEON. The data processed and transferred to IRIS over this project's four years will include 22 PNEs recorded by nine major seismic projects (Figure 1). As a result of this work, we will deliver to the seismological and seismic Comprehensive Nuclear-Test-Ban Treaty (CTBT) monitoring community a set of unparalleled recordings of a large number of nuclear explosions recorded across a grid of propagation paths to the distances of ~3,000 km across the Northern Eurasia.

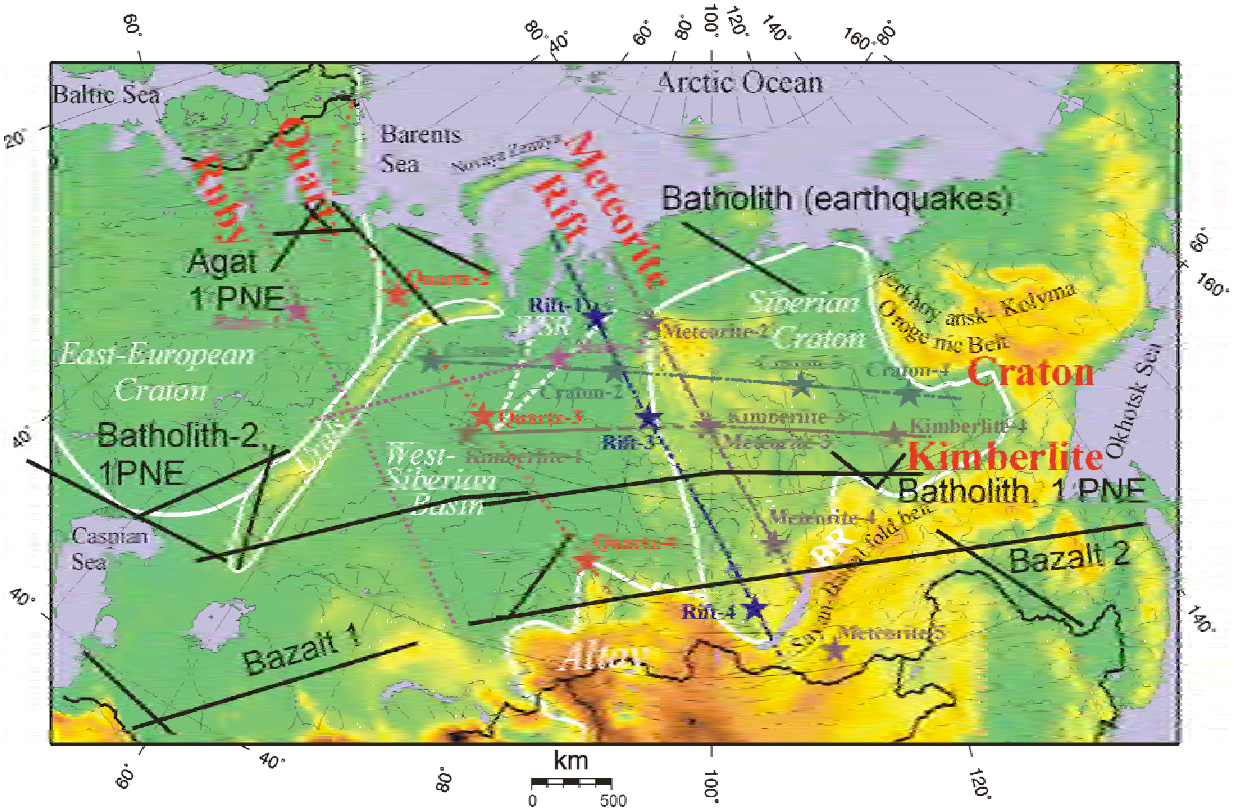


Figure 1 Nine DSS PNE projects to be delivered to IRIS as a result of this project. The data from profile QUARTZ and the PNEs from profile CRATON have already been delivered to IRIS. Colored lines and stars indicate the profiles and PNEs that have been digitized previously, black lines are the profiles to be digitized in this work. The coordinates and other parameters of the PNEs were reported by Sultanov et al. (1999), and the PNEs were also recorded by numerous permanent and temporary seismographic stations worldwide. Major tectonic units are indicated. Note the extent of systematic, continuous profiling, with PNEs detonated at the nodes of a 2-D recording grid. Note that the profiles cover a vast asiesmic area that would be difficult to calibrate by other means.

RESEARCH ACCOMPLISHED

This is an update of our last year's report (Smithson et al., 2002) on a four-year project for digitization and transcribing a significant part of the DSS PNE datasets from the Former Soviet Union. DSS PNE data have been widely recognized as a still unparalleled source of seismic information about the detailed structure of the upper mantle down to 400- to 800-km depth and in some cases to the Earth's core. The PNE data sets of the DSS program cover an intermediate distance range between 0–3,200 km bridging the gap between the conventional controlled source, earthquake, and nuclear–explosion-monitoring seismology. The dense, linear systems of PNEs and chemical explosions allow obtaining unusually detailed models of the crust and uppermost mantle over 4,000-km long geotraverses. Because the Northern Eurasia is largely aseismic, these datasets provide virtually the only dense three-component recordings of regional phases in aseismic regions of Northern Eurasia.

PNE yields were between 7–23 kton providing reliable seismic recording throughout the full recording ranges (Figure 1). Continuous and often reversed PNE recordings allow observations of seismic phases diving to depths of ~800 km (e.g., Egorkin et al, 1987; Ryaboy, 1989; Kozlovsky, 1990; Morozova et al., 1999). On a typical PNE profile, 3–4 nuclear explosions were recorded at up to 400 of three-component seismograph stations with nominal spacing of 10 to 15 km. About 50–80 chemical explosions (typically, each 3,000–5,000 kg) per profile were also recorded to enable interpretation of crustal and uppermost mantle structures. The locations, depths, yields, times of the PNEs, and characterizations of the source conditions were recently reported by Sultanov et al., (1999). The data are being digitized at Center GEON, Moscow, and preprocessed and edited at the University of Wyoming.

DSS profiles cross a variety of contrasting tectonic structures in Northern Eurasia and their studies have resulted in detailed images of the crust and uppermost mantle (Yegorkin, 1992). Some of the recent interpretations were performed by Egorkin and Mikhaltsev (1990), Mechie et al. (1993, 1997), Cipar et al. (1993), Priestley et al., (1994), Ryberg et. al. (1995, 1996), Schueller et al. (1997), Lorenz et al. (1997), Morozov et al. (1998a), and Morozova et al. (1999). The interpretations of the profile QUARTZ (Figure 2) by the University of Wyoming utilized the full spectrum of seismic data, including refractions and reflections from all 51 explosions of the dataset, lithospheric multiples, crustal-guided phases, seismic attenuation (Morozov et al., 1998b), coda amplitude decay (Morozov and Smithson, 2000), receiver functions (Morozov et al, in press), and empirical travel-time regionalization (Morozov et al., in final preparation). Using travel time, amplitude, and attenuation data, this study resulted in unusually well constrained images of crustal and mantle heterogeneity (Schueller et al., 1997; Morozov et al. 1998a, 1998b; Morozova et al., 1999). PNE data served as a basis for a new class of stochastic models of the uppermost mantle (e.g., Ryberg et al., 1995; Enderle et al., 1997), which, however, also resulted in a significant controversy (Morozov et al., 1998a; Morozov, 2001) and are being actively debated at present. The datasets contain spectacular and nearly continuous, 3-component recordings of regional phases (Figure 3) that still hold great potential for nuclear test monitoring research (Morozov et al., 2003).

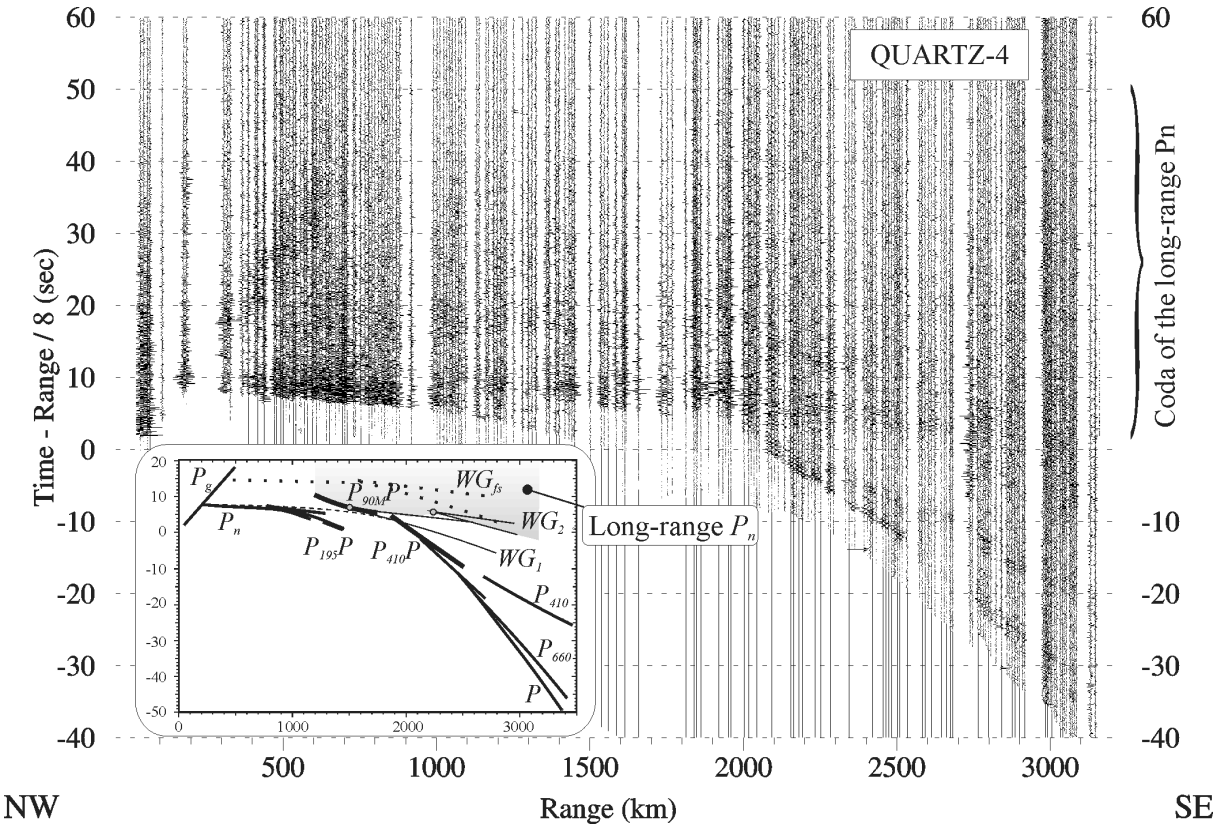


Figure 2. Vertical component record from PNE QUARTZ-4 (Figure 1). Inset shows a sketch of seismic phases identified in the wavefield. Note the free-surface and Moho *P*-wave multiples (*PP*, or whispering-gallery modes) labeled *WGfs* and *WG*, respectively. These phases were interpreted as caused by strong scattering within the uppermost mantle (Ryberg et al., 1995); however, in another interpretation, they may be a result of a strong velocity gradient and mantle layering beneath the East European platform and the southern part of the West Siberian Basin (Morozov, 2001). Both of these inferences might have significant implications for nuclear test monitoring along the critical NW-SE paths across the East European Platform.

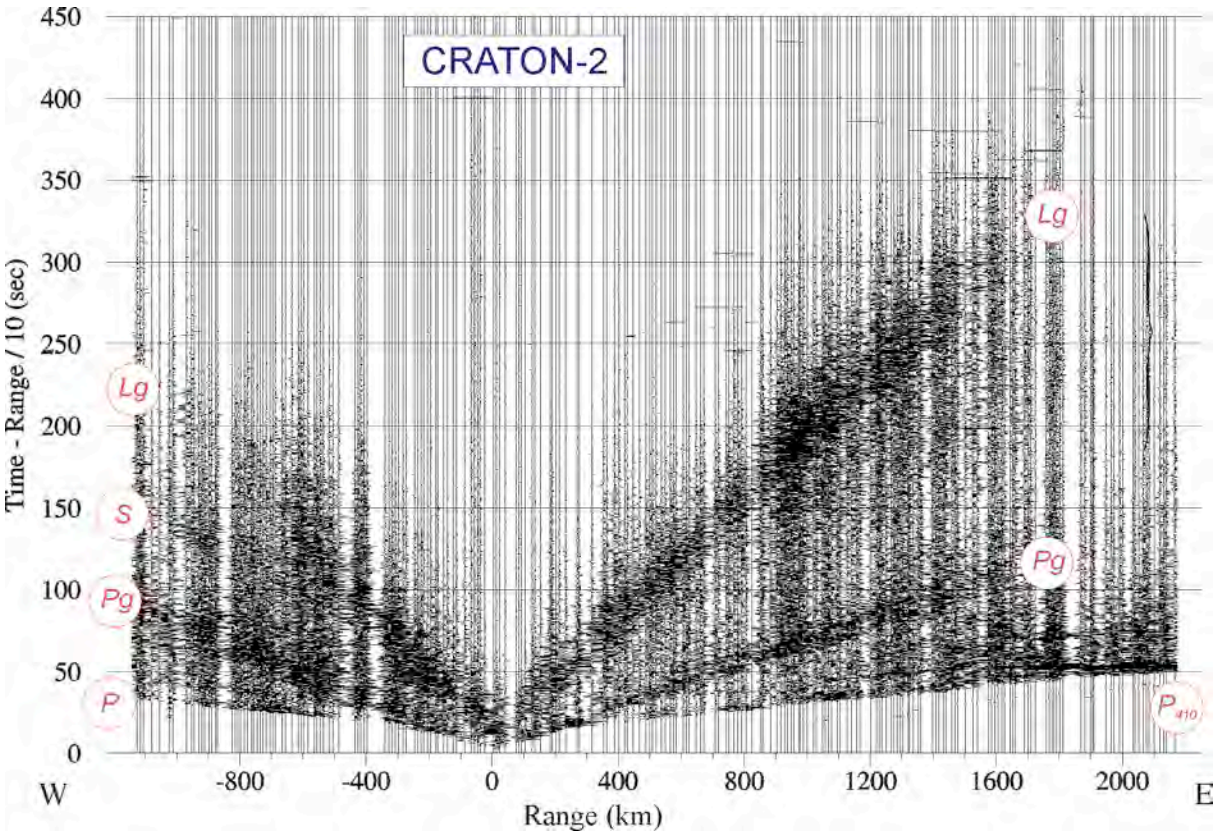


Figure3. Vertical-component record from PNE CRATON-2 (Figure 1). Note the continuity of arrivals extending to the transition zone discontinuities. Also note the strong *Lg* and *Pg* propagating to the ranges exceeding 1600 – 1700 km, and the differences between the character of *S* wave and *Lg* in two directions from the PNE. *Lg* is very strong east of the shot point (under the Siberian Craton) whereas the mantle *S*-wave propagates efficiently to the west, under the West Siberian basin (Figure 1).

To date, we have delivered to IRIS and SMD CMR the digitized seismic data from profiles QUARTZ, CRATON, KIMBERLITE, and RIFT (Figure 1). At the early stages of the project, we experienced delays in chemical shot data deliveries from the Center GEON; however, at present, we are back on schedule, and GEON event provided us with the data from AGATE ahead of schedule (see the table below). On request from Center GEON, we also changed the order of processing of the projects by moving the profile METERORITE to the end of the project and advancing the delivery dates for the new datasets (AGATE, BATHOLITH, and BAZALT). The updated schedule for current and further planned data deliveries is given in Table 1 below.

Table 1. Revised planned and actual data deliveries as of July 2003.

#	Data set	Raw data delivery from GEON to UWyo (months)		Edited and reduced data delivered to IRIS DMS (months)	
		planned	*actual*	*planned*	*actual*
1	QUARTZ	Already delivered	-	12/2001	12/2002
2	CRATON	02/2002	10/2002	08/2002	11/2002
3	KIMBERLITE	05/2002	11/2002	11/2002	11/2002
4	RIFT	08/2002	11/2002	05/2003	07/2003
5	RUBY	02/2003*	02/2003	10/2003	
6	AGATE (5 profiles)	08/2003	06/2003	05/2004	
7	BATHOLITH-1,2	04/2004		11/2004	
8	BAZALT-1,2	11/2004		06/2005	
9	METEORITE	03/2005*		11/2005	

*Only chemical explosion data sets need to be delivered to UWYO

CONCLUSIONS AND RECOMMENDATIONS

Preliminary examination of the newly obtained Russian PNE records from the DSS PNE profiles demonstrates that the data provide valuable information for the analysis of the propagation of L_g and other phases for their use in nuclear test monitoring and calibration studies. When made broadly accessible for nuclear test monitoring research, the datasets will boost research on seismic calibration of the region and on transportable seismic discriminants in Asia. Greater availability of the unique PNE recordings would foster current research on several DoD-sponsored projects and facilitate extension of such research in the future. From a broader scientific perspective, the digitized DSS recordings and models of the upper mantle could also provide ideal reference and calibration data sets for the detailed structure of the upper mantle targeted by the recently funded by the NSF Earthscope program.

REFERENCES

Cipar., J., K. F. Priestley, A. V. Egorkin, and N. I. Pavlenkova (1993). The Yamal Peninsula-Lake Baikal deep seismic sounding profile, Geophys. Res. Lett., 20 (15), 1631-1634.

Egorkin, A. V. and A. V. Mikhaltsev (1990). The Results of Seismic Investigations along Geotraverses, in Super-Deep Continental Drilling and Deep Geophysical Sounding, K. Fuchs, Y. A. Kozlovsky, A. I. Krivtsov and M. D. Zoback (Editors), Super-Deep Continental Drilling and Deep Geophysical Sounding, Springer, Berlin, 111-119.

Enderle, U., M. Tittgemeyer, M. Itzin, C. Prodehl, and K. Fuchs (1997). Scales of structure in the lithosphere - Images of processes, Tectonophysics, 275, 165-198.

Kozlovsky, Y. A. (1990). The USSR Integrated Program of Continental Crust Investigations and Studies of the Earth's Deep Structure under the Globus Project, in Super-Deep Continental Drilling and Deep Geophysical Sounding, Fuchs K., Kozlovsky Y. A., Krivtsov A. I. and Zoback M. D. (Editors), Springer, Berlin, 90-103.

Lorenz, F., F. Wenzel, and J. Mechie (1997). Lateral heterogeneity implications from 2-D nuclear-seismic travel-time inversion, in: Fuchs, K. (Ed.) Upper mantle heterogeneities from active and passive seismology, pp. 237-248, Kluwer Academic Publ., Dordrecht.

Mechie, J., A. V. Egorkin, K. Fuchs, T. Ryberg, L. Solodilov, and F. Wenzel (1993). P-wave velocity structure beneath northern Eurasia from long-range recordings along the profile Quartz, Phys. Earth Planet Inter., 79, 269-286.

Mechie, J., A. V. Egorkin, L. Solodilov, K. Fuchs, F. Lorenz, and F. Wenzel (1997). Major features of the mantle velocity structure beneath northern Eurasia from long-range seismic recordings of peaceful nuclear explosions, in: Fuchs, K. (Ed.) Upper mantle heterogeneities from active and passive seismology, pp. 33-50, Kluwer Academic Publ., Dordrecht.

Morozov, I. B., and S. B. Smithson (2000). Coda of long-range arrivals from nuclear explosions, Bull. Seism. Soc. Am., 90, 929-939.

I. B. Morozov, H. Li, J. N. Duenow, and S. B. Smithson (2004). Analyzing Peaceful Nuclear Explosion Arrival Codas for Crustal Properties, this volume.

Morozov, I. B., E. A. Morozova, and S. B. Smithson, (1998a). On the nature of the teleseismic Pn phase observed in the recordings from the ultra-long range profile "Quartz", Russia, Bull. Seism. Soc. Am, 88 (1), 62-73.

Morozov, I. B., E. A. Morozova, S. B. Smithson, and L. N. Solodilov. (1998b). 2-D image of seismic attenuation beneath the Deep Seismic Sounding profile "Quartz", Russia, Pure and Applied Geoph., 153, 311-348.

Morozov, I. B., S. B. Smithson, and L. N. Solodilov, Imaging crustal structure along refraction profiles using multicomponent recordings of first-arrival coda, Bull. Seism. Soc. Am., in press.

Morozova, E. A., I. B. Morozov, S. B. Smithson, and L. N Solodilov (1999). Heterogeneity of the uppermost mantle beneath the ultra-long range profile "Quartz," Russian Eurasia, *J. Geophys. Res.*, 104 (B9), 20,329-20,348.

Priestley, K. F., J. Cipar, A. Egorkin, and N. I. Pavlenkova (1994). Upper-mantle velocity structure beneath the Siberian Platform, Geophysical Journal International, 118 (2), 369-378.

Ryaboy, V. (1989). Upper mantle structure studies by explosion seismology in the USSR, Delphic Associates, 138 pp.

Ryberg, T., F. Wenzel, J. Mechie, A. Egorkin, K. Fuchs, and L. Solodilov (1996). Two-dimensional velocity structure beneath Northern Eurasia derived from the super long-range seismic profile Quartz, Bull. Seismol. Soc. Am., 86, 857-867.

Ryberg, T., K. Fuchs, A. V. Egorkin, and L. Solodilov (1995). Observations of high-frequency teleseismic Pn on the long-range Quartz profile across northern Eurasia, J. Geophys. Res., 100, 18151-18163.

Schueller, W., I. B. Morozov, and S. B. Smithson (1997). Crustal and uppermost mantle velocity structure of northern Eurasia along the profile Quartz, Bull. Seismol. Soc. Am., 87, 414-426.

Smithson, S. B., I. B. Morozov, E. A. Morozova, and L. N. Solodilov (2002). Deep Seismic Sounding Data Sets for Seismic Calibration Of Northern Eurasia, 24th Seismic Research Review – Nuclear Explosion Monitoring: Innovation and Integration.

Sultanov, D. D., J. R. Murphy, and Kh. D. Rubinstein (1999). A seismic source summary for Soviet Peaceful Nuclear Explosions, Bull. Seism. Soc. Am., 89, 640-647.

Yegorkin, A. V. (1992). Crustal structure along seismic geotraverses, International Geology Review, 34 (4), 345-362.

ANALYZING PEACEFUL NUCLEAR EXPLOSION ARRIVAL CODAS FOR CRUSTAL PROPERTIES

Igor B. Morozov,[1] Hongyan Li,[2] Joel N. Duenow,[2] and Scott B. Smithson[2]

University of Saskatchewan;[1] University of Wyoming[2]

Sponsored by Air Force Research Laboratory

Contract No. DTRA01-01-C-0057

ABSTRACT

Coda amplitude decay of regional arrivals from Peaceful Nuclear Explosions (PNEs) could be used for characterization of crustal properties critical for seismic monitoring. In particular, as coda waves at 0.5–10 Hz are believed to consist predominantly of scattered shear waves, coda analysis could provide information about *Lg* attenuation and scattering from crustal heterogeneities. Digital recordings of 21 reversed PNEs—recorded by 200–400 three-component instruments within 0–3,000 km range in Northern Eurasia—enable coda amplitude measurements to provide valuable information for understanding *Lg* propagation in the region. In this project, we focus on the analysis of the spectral properties of *Lg*, crustal attenuation using the spectral and coda decay information extracted from the PNE records, and on modeling these characteristics.

Measurements of PNE phase amplitudes show that *Lg*/*Sn* and *Lg*/Pg_{coda} RMS (root mean square) amplitude ratios significantly constrain variations of crustal structure. *Lg* coda *Q* computed using spectral ratio methods shows poor stability resulting from high noise and the narrow (1-5 Hz) frequency band; however, time-domain *Lg* coda *Q* estimates are stable and reflect variations of crustal structure. *Lg* arrivals are subdivided into shorter (~40-s) range-independent early parts, followed by longer codas with distinct exponential amplitude decay and with time durations increasing with range. Sediment thickness appears to be the most important factor affecting *Lg* coda attenuation, with lower *Lg* coda *Q* observed within sedimentary basins. We present a map of *Lg* coda *Q* values measured from PNE profiles, with potential areas of "*Lg* blockage" identified.

Our modeling effort targets realistic, three-component codas produced by a distant PNE source. Since three-dimensional (3-D) simulations are required for a correct description of short-period coda of PNE arrivals, we perform our modeling in 3-D by employing a single-scattering (Born) approximation. Reflectivity synthetics based on velocity models of different crustal and upper mantle properties are used as the Green's functions. The full seismic response is calculated using numerical integration in time and a 2D surface integral over uniformly distributed Monte-Carlo-sampled surface points. Coda *Q* values are measured on modeled records based on a range of intrinsic crustal *Q*'s to determine an empirical relationship of $Q_{coda}(Q_{crust})$. This relation, approximated as a power law, is further inverted to obtain Q_{crust} estimates for PNE data from the observed coda *Q* values.

Using the reflectivity synthetics in velocity models of greater crustal complexity leads to greater dependence of Q_{coda} on Q_{crust}. For the teleseismic *P* coda at 0.3 Hz, measurements of synthetic coda created using the Quartz-4 velocity model, gives $Q_{coda} = 16 \cdot Q_{crust}^{0.47}$ at 0.3 Hz and $Q_{coda} = 28 \cdot Q_{crust}^{0.43}$ at 0.7 Hz. The IASP-91 model, with a simpler 2-layer crust and mantle, gives a much weaker dependence, $Q_{coda} = 75 \cdot Q_{crust}^{0.06}$ at 0.3 Hz and $Q_{coda} = 75 \cdot Q_{crust}^{0.14}$ at 0.7 Hz. Our modeling suggests that the crust, and not the mantle, plays the most significant role in determining the $Q_{coda}(Q_{crust})$ dependence. Based on the empirical relationships above, we improve our previous measurements of the bulk crustal *Q* from Quartz PNE data, with the resulting Q_{crust} ranging from ~50 at 1.5 Hz to ~170 at 5 Hz.

Further research will include: (1) inversion of the amplitude and spectral decay parameters for variations in the regional crustal attenuation structure and correlation with tectonics; and (2) modeling of *Lg* propagation using an extension of the above technique. These studies should result in an improved model of the crustal properties and a comprehensive modeling capability that could be utilized for interpretation of both the average and the region-specific character of regional wave propagation in Northern Eurasia.

OBJECTIVE

Regional phases used in the Comprehensive Nuclear-Test-Ban Treaty (CTBT) monitoring (*Lg*, *Pg*, *Pn*, *Sn*) travel through the crust and the upper mantle, which are highly heterogeneous, and therefore amplitude and travel-time calibration of these phases requires understanding of their relation to the tectonic and geologic environment. This study focuses on

1) gathering of empirical data on amplitude and spectral ratio characteristics of regional phases from nuclear explosions of the Russian Deep Seismic sounding program, and

2) using numerical modeling to establish semi-empirical relationships between the *in situ* crustal properties and the observed wavefield characteristics. Among these characteristics, we are particularly interested in the quality factor, *Q*, describing attenuation of seismic waves.

RESEARCH ACCOMPLISHED

Of all the regional phases, the *Lg* is often the most prominent and robust regional phase in continental regions. It has been widely used to determine regional variation of crustal attenuation properties and to differentiate nuclear explosion from other sources. It depends on the rock type and the degree of heterogeneity and therefore could be correlated with the geological structure. *Lg* amplitude ratios, such as *Lg*/*Sn* (Sandvol, et al., 2001), *Pg*/*Lg* (Philips, et al., 2001), Lg/Pg_{coda} (McNamara and Walter, 2001) are used for seismic source discrimination in different tectonic areas. Also, according to Walter, et al. (1995) and Koch (2002), *Lg* spectral ratios *Lg*(1–2Hz)/*Lg*(6–8Hz) or Lg_{coda}(1–2Hz)/Lg_{coda}(6–8Hz) provide good differentiation of nuclear explosions from earthquakes.

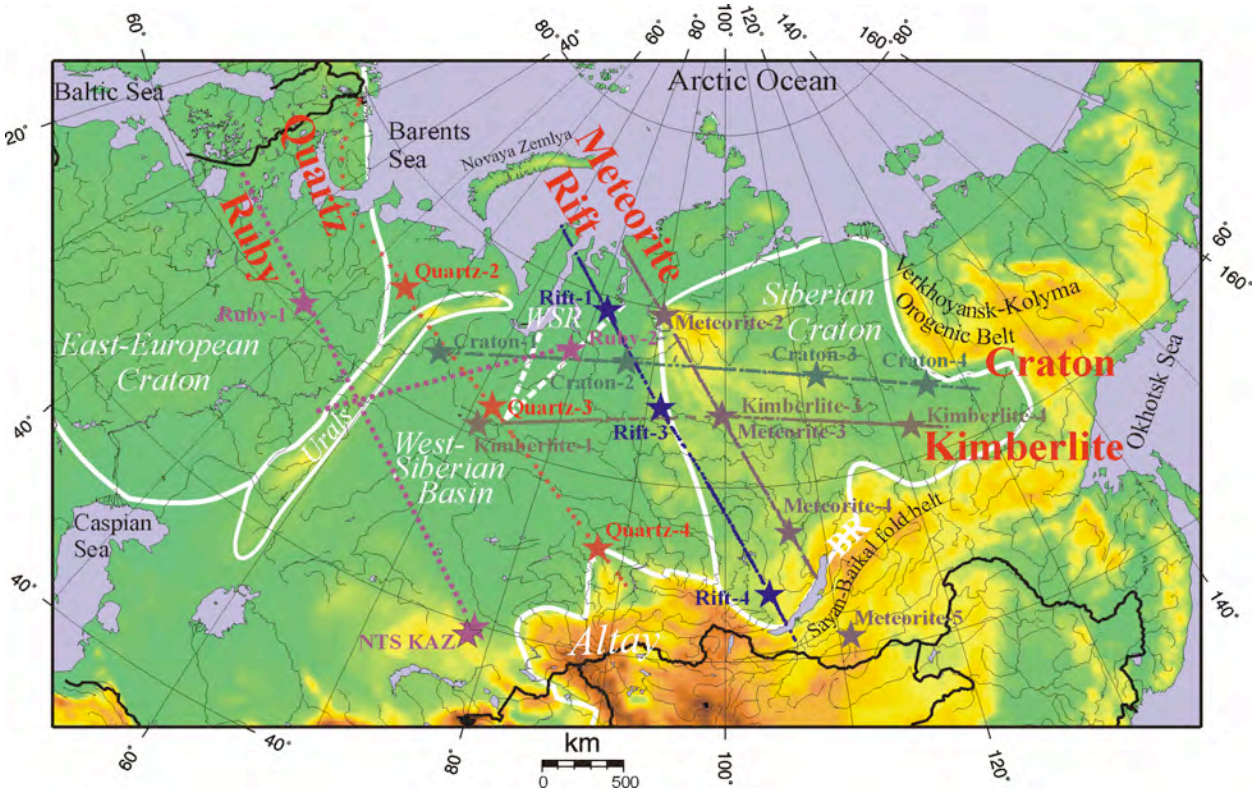


Figure 1. Location of PNE profiles and major tectonic boundaries. Large labeled stars indicate nuclear explosion locations, small stars are the chemical explosions. For profile Quartz, small dots show the chemical explosions; for other profiles - individual station locations. White lines show major tectonic features (WSR – West Siberian Rift, BR – Baikal Rift) and color represents the topography (Zonenshain, 1990).

Since at regional distances the *Lg* phase could be highly attenuated or even blocked with abrupt change in the crustal structure, it is crucial to gather information about *Lg* propagation across a variety of continental tectonic structures. However, Northern Eurasia is largely aseismic, and the regional recordings of natural sources are very limited. Also, path calibration of regional seismic phases is strongly dependent on the accuracy of hypo-central locations of calibration events (Saikia, 2001), and for earthquake data, especially for small events, this information is difficult to obtain. However, from the mid 1960s through late 1980s, Russian scientists acquired a network of dense, linear, long-range, three-component Deep Seismic Sounding (DSS) profiles using conventional and Peaceful Nuclear Explosions (PNEs) over almost all Northern Eurasia. At the University of Wyoming, we obtained records from seven PNE profiles and 19 PNEs of this program (Figure 1), and are analyzing them in order to extract ground truth and develop calibration techniques for CTBT monitoring.

Recent studies included: study the main factors that affect the *Lg* phase propagation characteristics, calibrate the detailed crustal structure in Northern Eurasia, study the attenuation properties quantitatively in Northern Eurasia, and try to find the better ways to differentiate nuclear explosions from earthquakes.

Correlation of the spectral ratios and *Lg* coda *Q* with the variations of the crustal structure. In order to study the effects of crustal structure on *Lg* phase propagation and calibrate the detailed in Northern Eurasia, we computed *Lg*/*Sn* and *Lg*/Pg_{coda} RMS amplitude ratio. In addition, we measured the *Lg* coda *Q* to constrain crustal attenuation.

Figure 2summarizes some of the attributes extracted from the records from PNE Craton-3. *Lg* coda *Q* was measured in a 120-s at 40 s after the picked *Lg* onset. The 40-s lag was chosen so that the early, steeper *Lg* coda was not included in the measurements. The frequency band was 1 to 2.5 Hz and the radial-component recordings were used in RMS estimates. A commonly used amplitude decay relation is:

$$A(f,t) = G(r)R(f)S(f)e^{-\pi f t / Q(f)}, \qquad (1)$$

where, *G* is the geometric spreading factor, *R* and *S* are receiver and source response functions, respectively; *f* is the frequency; *t* is the travel time; and *Q* is the quality factor.

Logarithm of the amplitude ratio (1) at two times, t_1 and t_2, yields:

$$\log\left[A(f,t_1)/A(f,t_2)\right] = -\frac{\pi f (t_1 - t_2)}{Q(f)} \qquad (2)$$

Therefore, *Q* can be measured by 1) the change of the log*A*(*f*) slope with time; and 2) by measuring the log*A*(*t*) slope using band-pass filtered records. Thus the second (time-domain) method proves advantageous because of the greater stability of the resulting 1/*Q* values, and also because it allows using individual traces for estimation of *Lg* coda *Q*.

In comparing the resulting attributes (amplitude ratios and *Lg* coda *Q*) with geology, we are particularly interested in a possible correlation with the sedimentary basins. We profile the Craton across three major sedimentary basins: the Patom-Viluy Basin, the Tunguss Basin, and the West SiberianBasin (Figure 2a). The Patom-Viluy Basin is covered with very thick sediments (deeper than 15 km) and shallower Moho underneath; the sediments of Tunguss Basin are also deep (>10 km), but the velocity of the sediments is high (5.5 km/s), and the velocity of the lower crust is low (6.8 km/s). The sediment thickness in West-Siberian Basin reaches 8 km, and the velocities are low (3.5km/s). Note that there is a low-velocity zone identified within the uppermost mantle under the West-Siberian Basin (Pavlenkova, 1996). The heat flow is high (~70 mWm^{-2} in the West Siberian and Viluy Basins, and low at other locations (Pavlenkova, 1996).

Both the *Lg*/*Sn* and *Lg*/Pg_{coda} amplitude ratios and particularly the *Lg* coda *Q* show correlation with the sedimentary basins crossed by the profile (Figure 2). Note that in Figure 2b, for the west branch, *Lg*/*Sn* increases from offset ~300km to ~600km, then decreases until offset ~800km (within the Tunguss Basin), then increases again until offset ~1,200km, then the ratio decreases quickly as the waves enter the West Siberian Basin. To the east, *Lg*/*Sn* increases slowly until offset ~600km, and then the ratio decreases rapidly, again within the Patum-Viluy basin. *Lg* coda *Q* shows similar behavior (Figure 2d). West of the PNE, the *Lg* coda *Q* first decreases until offsets of ~600km, then increases until to ~1,200km, and then decreases strongly within the West Siberian basin. To the east, *Lg* coda *Q* values stay nearly constant until offsets of ~600km, at Q^{a} 450. For the western branch, the minimum Q value is ~300, and the maximum is ~400km. The scatter in *Lg* coda *Q* values west of the PNE is large, which may be a result

of the variations in the *Lg* amplitudes, as suggested by the increased scatter in the *Lg*/*Sn* and *Lg*/Pg_{coda} RMS amplitude ratios.

The fact that the short-period *Lg* decreases in amplitude when recorded within a sedimentary basin and tends to rebound on its opposite side suggests that the *Lg* is attenuated by the sediments; yet significant *Lg* energy bypasses the basin through the mid- and lower-crust and "heal" the *Lg* amplitude afterwards. Increased *Lg* coda attenuation (lower *Q*) within the basins also corroborates this observation. It appears that the coda is formed primarily by *Lg* scattering near the receiver, within the upper crust of the basins. Indeed, localized anomalies of high-coda attenuation imply a source of strong scattering close to the receivers.

This interpretation of *Lg* coda *Q* is somewhat different from the model by Mitchell et al. (1997), in which they assumed that the coda could equally likely originate from *Lg*Æ*Lg* scattering on points distributed on system of ellipses having the source and receiver as their common foci. In their model, scattering amplitudes are assumed to be constant and independent on the scattering angles, and *Lg* coda 1/*Q* is formed as an areal average of Lg 1/*Q* values. However, scattering is likely to increase within the sedimentary basins, and to include other than *Lg*Æ*Lg*

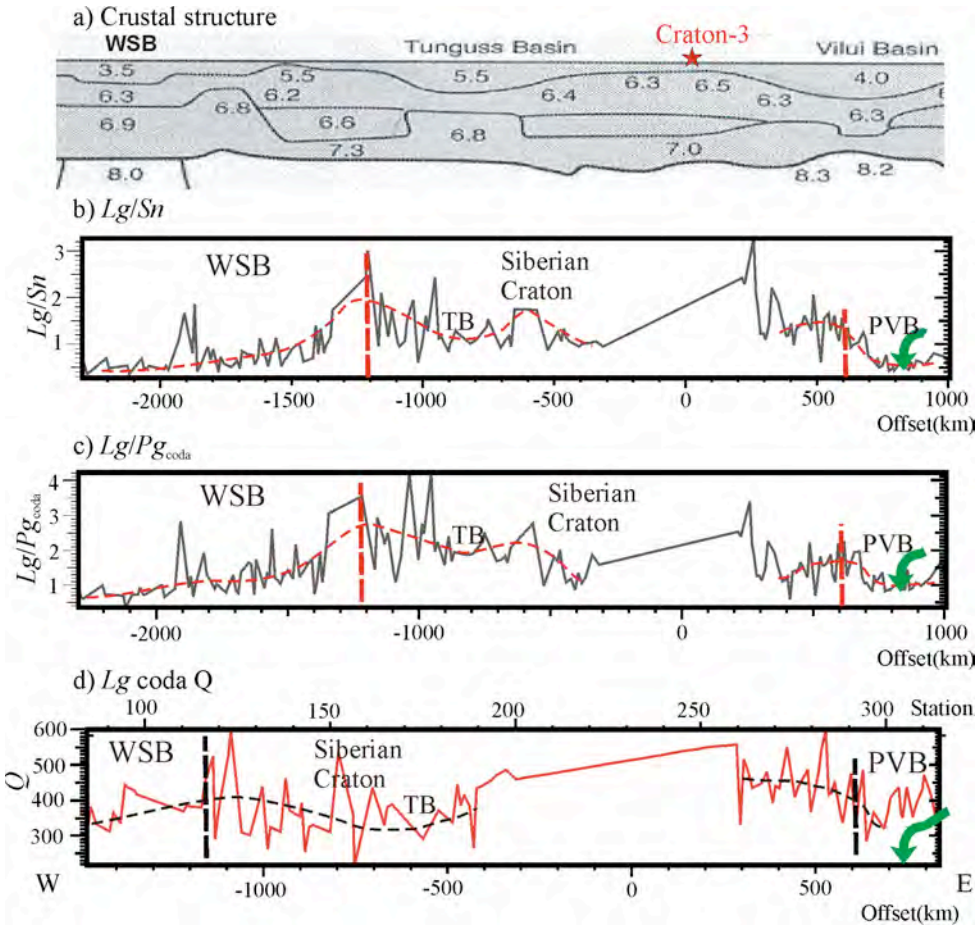


Figure 2. Regional phase attributes from PNE Craton-3: (a) crustal velocity model from Pavlenkova (1996), with P-wave velocity values labelled; (b) *Lg*/*Sn* RMS amplitude ratio; (c) *Lg*/Pg_{coda} RMS amplitude ratio; (d) time-domain *Lg* coda *Q*. In (a), we see that *Lg* phase is the strongest phase, and can travel to far offset. In (a) and (b), west of the shot, the ratios increase first until~600km, then decrease until ~800km, and then increase again until ~1,200km. They then decrease quite fast; for the right branch, and the ratios increase slowly until ~600km, where they decrease rapidly. Since the Lg phase can only be formed after ~300 km offset, we don't consider the ratio within a 300 km offset. In (d), Lg coda Q is high (~450) for the right branch with offset ~300km – ~600km; Q is lower (~300) at Tunguss basin, and decreases in West-Siberian Basin. (WSB – West Siberian Basin; TB - Tunguss Basin; PVB - Patom-Viluy Basin).

modes. Therefore, it is not clear to what extent the resulting *Lg Q* maps may actually represent spatial gradients of the scattering amplitude.

Scatter in coda *Q* values. Figure 3 shows the logarithm amplitude of Lg coda vs. time for three adjacent traces. The general trend of the three curves is to decrease linearly, but there is local variation, and the local variation for different traces is different. Moreover, there are many low-value spikes in every trace, and there could be data dropouts, and clipping. These problems could seriously contaminate any data analysis results, especially at high-frequencies (Murphy, et el., 2001). So, the local variation of the amplitude and the low-value spikes could be the main reason for the variation of the *Lg* coda *Q*.

Dependence of *Lg* coda *Q* on the time gate and frequency. Figure 3 shows the measured *Lg* coda *Q* values vs. station numbers on the Kimberlite profile for different frequency bands. Despite significant scatter in the values, it is clear that *Lg* coda *Q* increases with frequency. Also, from the figure we can see that a different frequency band has a different response to the variation of the crustal structure. This difference could be a result of the narrow frequency band of the Lg phase.

The discrimination ability of *Lg*(1-2Hz)/*Lg*(6-8Hz). According to Walter et al. (1995), nuclear explosions could be discriminated from earthquakes using spectral ratios *Lg*(1–2Hz)/*Lg*(6–8Hz) or Lg_{coda}(1–2Hz)/*Lg*(6–8Hz) (Figure 4). For nuclear explosions, these ratios are higher compared to earthquakes, with separation clear above magnitude 3 and increasing with magnitude (Figure 4). Figure 5 shows the *Lg*(1–2Hz)/*Lg*(6–8Hz) RMS amplitude ratio measured from PNEs Craton-3, Kimberlite-3, and Quartz-323. For the PNEs *Lg*(1–2Hz)/*Lg*(6–8Hz) is generally higher than 2, in agreement with the result by Walter et al. (1995).. Also, at offsets of ~500km to ~1,000km, the ratio increases with offset, and thus this could be the best discrimination range.

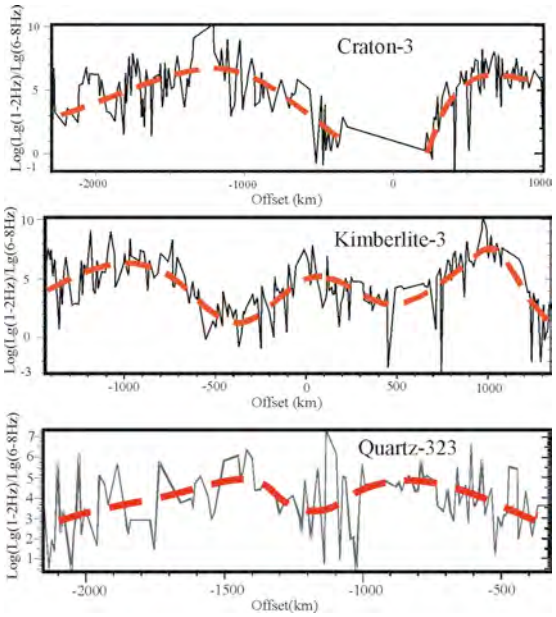


Figure 3. Log(*Lg*(1–2Hz) /*Lg*(6–8Hz) from three PNEs, as labelled. Measured values are shown in the thin black line, and the dashed red line is the interpreted smoothed variations. The log-ratios are usually >2, with significant variations with offset or crustal structure. Near ~1,000 km, the values are generally higher, suggesting that this range could be most efficient for discrimination (see Figure 4).

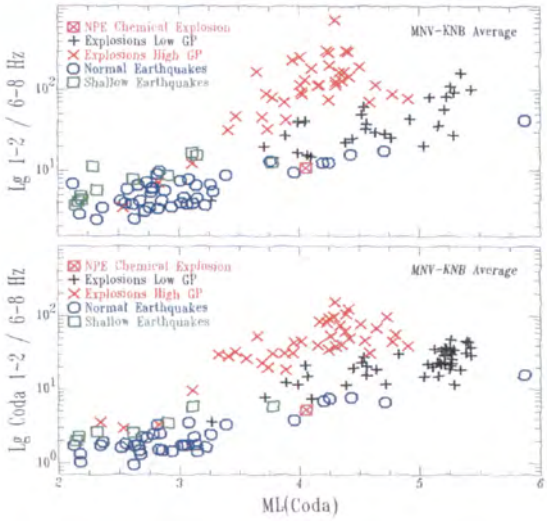


Figure 4. (From Walter et al, 1995) Two-station average (1–2Hz)/(6–8Hz) S wave spectral ratios for (a) *Lg* and (b) *Lg* coda as a function of magnitude. *Lg*(1–2Hz)/*Lg*(6–8Hz) for nuclear explosion is usually higher than from earthquakes with magnitudes >3.

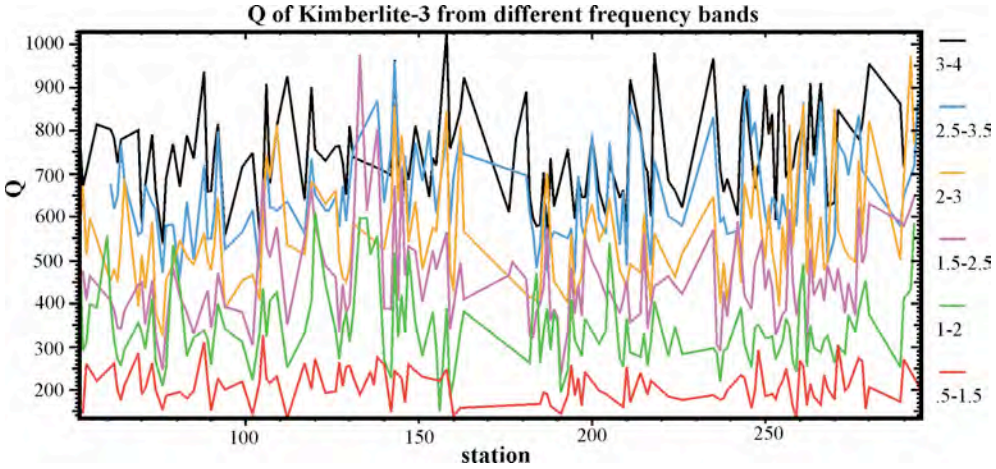


Figure 5. *Lg* coda *Q* of PNE Kimberlite-3 from in frequency bands (labelled on the right). The *Lg* coda *Q* increases with frequency. Note that at higher frequencies, the dependence of *Lg* coda *Q* on frequency decreases.

Regional variations of *Lg*/*Sn* and *Lg*/Pg_{coda}, and the *Lg* coda *Q* within the Siberian Craton. To date, we have analyzed four profiles crossing the Siberian Craton: Craton, Kimberlite, Meteorite, and Rift. Figure 6 shows a summary of the observed characteristics from the four profiles, correlated with the tectonic unites of Northern Eurasia.

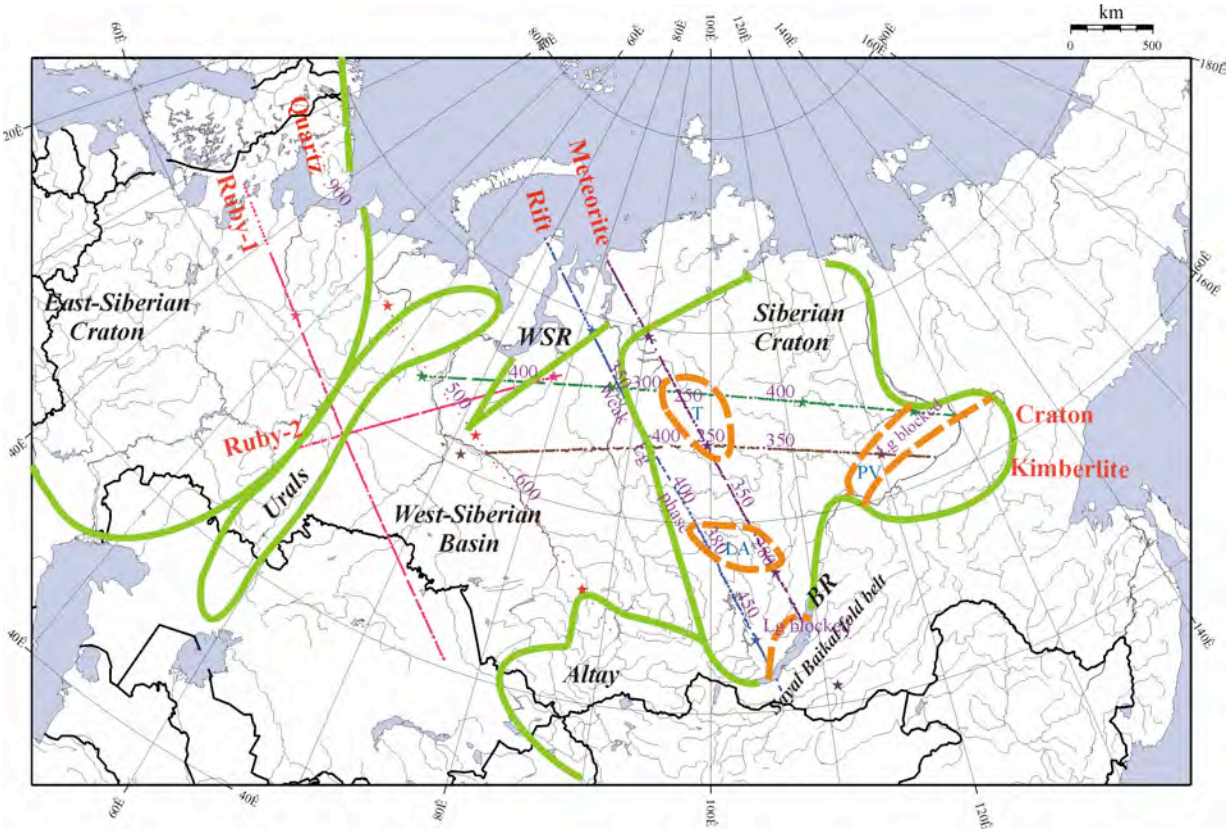


Figure 6. Sketch of the tectonic boundaries of Northern Eurasia (green line), and distribution of the *Lg* coda *Q* and the *Lg* phase propagation characteristics. (Green lines show tectonic boundaries, Orange lines indicate areas where *Lg* is blocked or highly attenuated areas. WSR indicates the West Siberian Rift, BR – Baikal Rift, T– Tunguss Basin, and PV is the Patom-Viluy basin.

Numerical coda model. In order to study the relationship between the observed coda *Q* from the *Lg* (and also other phases) and the *in situ P*- and *S*-wave crustal *Q*, we performed numerical simulations of the coda (Duenow, 2003). Morozov and Smithson (2000) argued that for a teleseismic *P*-wave arrival, the coda originates from elliptical areas surrounding the source and receiver, with the upper crust causing most of such scattering. Our scattering model thus represents crustal heterogeneities as scatterers are distributed within the Earth's crust. The resultant scattered coda energy *U* recorded at a receiver at time *t* is an integral over scattering volume *V*:

$$U(\vec{r},t) = \int dt_s \iiint_V d^3\vec{r}_s \, \Upsilon(\vec{r}_s) U_{source}(\vec{r}_s,t_s) G(\vec{r}_s,t_s;\vec{r},t) \,, \tag{3}$$

where t_s is the time of the direct arrival at the scatterer, $\vec{r}_s$ represents scatterer positions, Υ is the scattering potential describing the amount of energy reflected at the scatterer, and U_{source} is the seismic source function describing energy arriving at the scatterer from the source explosion. *G* is the scattering from Green's function describing the propagation of scattered energy from scatterer to receiver. For simplicity, because the upper crust is assumed to be the primary contributor to the seismic coda, this volume integral is replaced with a surface integral (Figure 7):

$$U(\vec{r},t) = \int dt_s \iint_S d^2\vec{r}_s \, \Upsilon(\vec{r}_s) U_{source}(\vec{r}_s,t_s) G(\vec{r}_s,t_s;\vec{r},t) \,. \tag{4}$$

The Green's function is approximated as translationally invariant in time and space:

$$G(\vec{r}_s,t_s;\vec{r},t) = G(\vec{r} - \vec{r}_s, t - t_s) \,.$$

Synthetic seismic sections created using the reflectivity method (Fuchs and Müller 1971) were used as source and Green's functions in the model (3-4) (Figure 8).

Note that for a constant scattering potential, the scattering area increases with time after the primary arrival, it will compensate the geometric spreading of the Green's function, and therefore, with no intrinsic attenuation, coda energy would not decay. The observed coda *Q* was thus thought indicative of the average crustal *Q* (Morozov and Smithson, 2000).

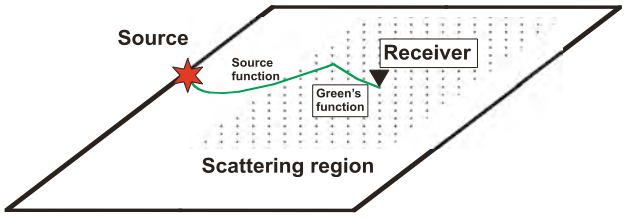


Figure 7. Surface scattering model. Seismic energy originates at source, scatters from uniformly distributed Monte-Carlo-sampled surface points, and is detected at receiver. Source and Green's functions describe propagation of seismic energy.

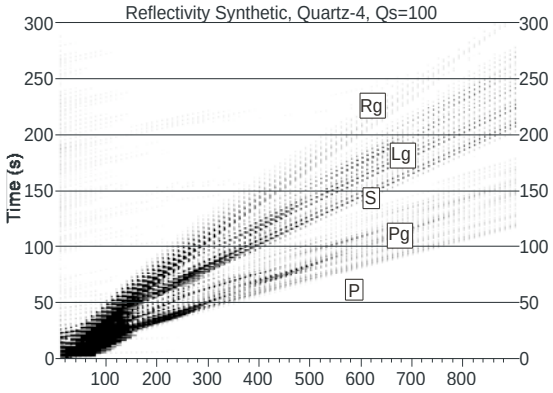


Figure 8. Reflection synthetic seismograms used as the source and Green's functions (Figure 7), created using the Quartz-4 velocity model (Morozova et al., 1999). Note that multiple modes contribute to the scattered coda wavefield.

However, the values of Q_{crust} and Q_{coda} may differ. For example, $Q_{coda} < Q_{crust}$ would indicate that seismic energy is leaking into the mantle and does not return to the surface, whereas. $Q_{coda} > Q_{crust}$ would correspond to mantle phases contributing to the recorded seismic energy. These mechanisms may also be frequency-dependent, causing frequency dependence of the $Q_{coda}(Q_{crust})$ relation.

In our numerical experiments, therefore, we sought an empirical relationship between the observed time-domain log-amplitude coda slope and crustal quality factor:

$$k_{coda} \equiv \frac{f}{Q_{coda}} = k(f) Q_{crust}^{g} \ , \quad (5)$$

where f is the frequency, k_{coda} is the observed coda attenuation factor, and $k(f)$ and g are constants. A power-law relation is used because it is general, asymptotes are well-behaved, and it has been commonly used when determining Q as a function of f in previous studies.

We performed measurements on teleseismic P and L_g codas for four types of velocity models with varying crustal and mantle complexity (of which the preferred the Quartz-4 model, derived using the PNE data; Morozova et al., 1999). Synthetic codas for the Quartz-4 velocity model at f = 0.3 Hz are shown in Figure 9. A delay in the onset of coda amplitude is evident between the direct teleseismic P arrival and the strong part of the coda (Figure 9 top and middle) resulting from the low energy of arrivals at the small offset in the Green's functions before the onset of the L_g phase. Since the Green's function is of lower energy at precritical distances (<100–200 km), the coda builds up only after the radius of the scattering ellipse expands beyond this distance.

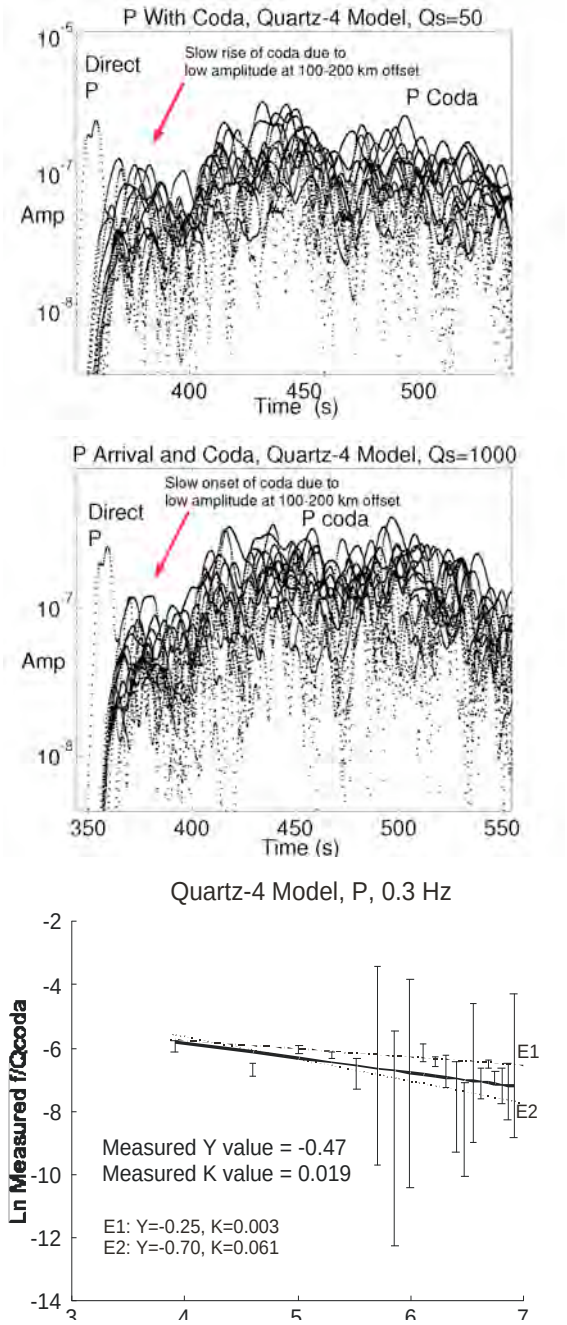


Figure 9. Quartz-4 model results at f=0.3 Hz. *Top and middle:* Teleseismic *P* direct arrival with coda for Q_{crust}=50 and 1000, respectively. Note the noticeably flatter slope for high Q_{crust}. *Bottom*: Slope fitting of $\ln(f/Q_{coda})$ vs. $\ln(Q_{crust})$ to determine parameters of Q_{coda}-Q_{crust} relation. Note the slow onset of coda energy after the direct arrival (red arrows).

Synthetics were filtered to center frequencies of 0.3, 0.7, and 1.3 Hz to examine the coda amplitude slopes (5) as a function of frequency. By summarizing the observed measurements (Table 1), we derived an empirical frequency dependence of the parameter k(f) in expression (5).

Estimation of *in-situ* Q_{crust} from *Lg* coda *Q*. Estimates of Q_{crust} for Quartz PNE data were made using the inverse relation of the parameterization (5):

Table 1. Coefficients and exponents of $Q_{coda}(Q_{crust})$ relation. Coefficient is the ratio of f/k, exponent is $-g$, according to Equation (5).

Model, Coda	0.3 Hz		0.7 Hz		1.3 Hz	
	Coeff.	Exp.	Coeff.	Exp.	Coeff.	Exp.
Quartz-4, *P*	16	0.47	28	0.43	-	-
IASP-91, *P*	75	0.06	75	0.14	-	-
IASP-Quartz, *P*	49	0.14	37	0.42	-	-
Complex Crust, *P*	2	0.98	25	0.58	-	-
Quartz-4, L_g	18	0.40	63	0.24	65	0.50
Complex Crust, L_g	6	0.78	88	0.22	217	0.07

$$Q_{crust} = \left(\frac{1}{k(f)} \frac{f}{Q_{coda}} \right)^{1/g}, \qquad (6)$$

where f/Q_{coda} is measured from the coda envelope slope, $k(f)$ is determined from a power law (5), and g is obtained from the parameterization (Table 1). By interpolating the $k(f)$ values (again using a power law) between the imaged points, we obtained an empirical relation mapping the observed Q_{coda} onto crustal Q_{crust} (Figure 10). A surprising observation not well understood at present is the significantly higher *P* coda *Q* values as compared to the intrinsic *Q* of the crust. Apparently the only "physical" explanation of this result is that significant energy propagates through the mantle thereby bypassing the crust (with lower *Q*) and increasing the overall duration of the coda.

Unfortunately, the modeling program did not allow modeling at high frequencies for the sufficiently long-signal durations necessary to simulate the coda. The primary frequencies of the Quartz data are between 1 Hz and 10 Hz, whereas we were able to model only up to ~2 Hz, and therefore significant extrapolation of the frequency dependencies (5–6) had to be performed. This extrapolation is a major limitation of this approach that may have contributed to the above difficulty and will need to be overcome in the future.

By using the *P*-wave coda measurements by Morozov and Smithson (2000), combined with several additional frequency points, we obtained revised crustal *Q* estimates (Figure 11). Crustal *Q* values increase with frequency, as suggested by Morozov and Smithson (2000); however the resulting values of Q_{crust} are somewhat surprisingly low, ranging between ~60–150. Such low values arise from the anomalously high-modeled coda *Q* value mentioned above.

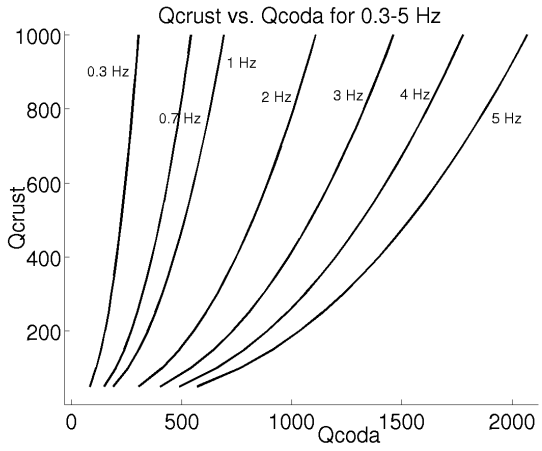


Figure 10. Empirical inverse $Q_{crust}(Q_{coda},f)$ dependence of Quartz-4 model derived for *P*-wave coda from our numerical simulations.

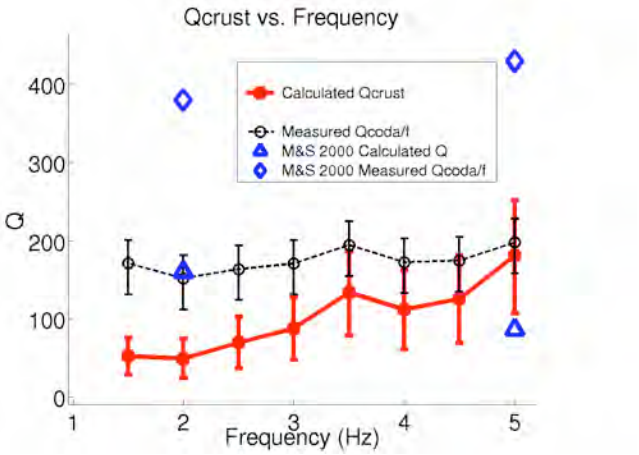


Figure 11. *Q* values as a function of frequency, from Quartz-323 coda measurements. Circles with black line are measured Q_{coda}/f values. Error bars were chosen as 30 above and 40 below the measured value. Squares with red line are the Q_{crust} values computed using Equation (6) to determine relation as a function of frequency. Q_{crust} values appear to generally increase with increasing frequency. Error bars are propagated from those on the Q_{coda}/f values. For comparison, blue triangles at 2 Hz and 5 Hz represent values of Q_{coda}/f by Morozov and Smithson (2000), with corresponding estimates of Q_{crust} shown by blue diamonds.

CONCLUSIONS AND RECOMMENDATIONS

Lg/*Sn* and *Lg*/Pg_{coda} amplitude ratios show significant correlation with crustal thickness; in particular, these ratios decrease sharply within thick sedimentary basins. The *Lg* coda *Q* appears to correlate with tectonic types, but also with the variations of the crustal structures, such as the sediment and crustal thickness. The two effects are not easy to differentiate, because deep basins are usually associated with shallowing Moho resulting from isostatic effects.

In the Siberian Craton, the *Lg* coda *Q* is highly variable. The attenuation is much higher (*Q* is ~280–350) within the deep sedimentary basins, and Q ª 400–450 in areas with thinner sedimentary covers.

Lg(1–2Hz)/*Lg*(6–8Hz) ratios measured using DSS PNE records fall within the explosion population. Variation of these ratios with offsets suggest that distances of ~1,000 km could be the best used as the discriminant in Northern Eurasia.

Numerical modeling of the *P*- and *Lg*-arrival coda from PNEs suggests that the observed coda *Q* may be higher than the intrinsic *Q* of the crust. This difference could be because of the contribution of mantle-guided phases into the coda. As a consequence of this result, the crustal *Q* values may be overestimated when judged by the observed *Lg* coda *Q*.

Teleseismic *P* Q_{coda} values measured from the envelope of a set of Quartz PNE traces gave Q_{crust} values of 50 at 2 Hz, increasing to 175 at 5 Hz, for the East European Platform. These crustal values are commensurate with others obtained previously in other regions. The Quartz-4 L_g parameterization at 1.3 Hz gave a Q_{crust} estimate of 21 for the West Siberian Basin using the PNE Quartz L_g coda, which we expected to be lower since the trace was recorded in a region of thick sediments.

REFERENCES

Campillo, M., and J. L. Plantet (1991). Frequency dependence and spatial distribution of seismic attenuation in France: experimental results and possible interpretations. Physics of the Earth & Planetary Interiors, 67: 48-64.

Duenow, J. N. (2003). Surface Scattering as a Source of Teleseismic Arrival Coda, M.S. thesis., University of Wyoming, Laramie, WY.

Mitchell, B. J., Y. Pan, J. Xie, and L. Cong (1997) Lg coda Q variation across Eurasia and its relation to crustal evolution. Journal of Geophysical Research, 102(B10): 22767-22779.

Mooney, W.D. (2002). Crustal and upper mantle seismic velocity structure of the former USSR. 21st Seismic Research Symposium, 162-171.

Morozov, I.B. and Smithson, S.B., 2000. Coda of Long-Range Arrivals from Nuclear Explosions, Bull. Seis. Soc. Am. 90, 929-939.

Morozova, E.A., I. B. Morozov, S. B. Smithson, and L. N. Solodilov (1999). Heterogeneity of the uppermost mantle beneath Russian Eurasia from the ultra-long profile QUARTZ, J. Geophys. Res. 104, no. B9, 20329-20348.

Murphy, J.R., I. O. Kitov, B. W. Barker, and D. D. Sultanov (2001). Seismic source characteristics of Soviet peaceful nuclear explosions. Pure and Applied Geophysics, 158: 2077-2101.

Pavlenkova, N.I. (1996). Crust and upper mantle structure in Northern Eurasia from seismic data. Advances in Geophysics, 37: 1-333.

Pavlenkova, G.A., K. Priestley, and J. Cipar (2002). 2D model of the crust and uppermost mantle along rift profile, Siberian Craton. Tectonophysics, 355: 171-186.

Sandvol, E., K. Al-Damegh., A. Calvert, D. Seber,M. Barazangi, R. Mohamad, R. Gök, N. Türkelli, and C. Gürbüz (2001). Tomographic imaging of Lg and Sn propagation in the Middle East. Pure and Applied Geophysics, 158: 1121-1163.

Walter, W.R.,K. M. Mayeda, and H. J. Patton (1995). Phase and spectral ratio discrimination between NTS earthquakes and explosions. Part I: empirical observations. Bulletin of the Seismological Society of Americas, 85: 1050-1067.

Zonenshain L.P., M. I. Kuzmin, and B. M. Natapov (1990). Geology of the USSR: a plate tectonic synthesis. American Geophysical Union, Washington, D.C.

SIMULATION OF REGIONAL EXPLOSION S-PHASES (SIRES) PROJECT

Stephen C. Myers,[1] Jeffrey Wagoner,[1] Shawn Larsen,[1] Arthur Rodgers,[1] Kevin Mayeda,[1] Kenneth Smith,[2] and William Walter[1]

Lawrence Livermore National Laboratory;[1] University of Nevada, Reno[2]

Sponsored by National Nuclear Security Administration
Office of Nonproliferation Research and Engineering
Office of Defense Nuclear Nonproliferation

Contract No. W-7405-ENG-48[1] and DE-FC03-02SF22656[2]

ABSTRACT

Seismic monitoring aims to locate and identify all events that generate elastic waves in the solid earth. Amplitudes and arrival-times of seismic phases are commonly exploited to accomplish these goals. For large events that produce strong body and surface waves out to 90 degrees, events can be accurately located and the Ms/m_b discriminant can be used to distinguish earthquakes from explosions. As event yield/magnitude decreases, the probability of detecting signals at distant stations diminishes, and monitoring relies heavily on regional-distance stations (between about 2 and 13 degrees). Many regional discriminant and magnitude methods make use of S-phase amplitude measurements, which are expected to diminish for explosion sources. Despite the general success of regional monitoring methods there remain instances when explosions produce anomalously large S-phases that confound regional discriminants. The 2-year Simulation of Regional Explosion S-phases (SiRES) project explores the phenomenology of regional S-phase generation through numerical simulation. In the first year of this study we construct a 3-dimensional model of the Nevada Test Site (NTS) and the surrounding region. Extensive databases of geologic information, including existing 3-dimensional models developed under past and ongoing NTS programs, are used to construct the regional model. In addition to deterministic geologic structure and topography we introduce stochastic variability within geologic units and along boundaries. The stochastic variability provides a more realistic simulation of the regional wave field, which is known to largely consist of scattered energy. Here we introduce the project and report on the first few months of progress.

OBJECTIVE

Regional monitoring relies heavily on S-phases. Discriminants commonly use P- and S-wave amplitude ratios (Pomeroy et al., 1982; Walter et al., 1995). Widely used methods of determining magnitude make use of Lg and Lg coda amplitudes (e.g., Nuttli, 1986; Mayeda and Walter, 1996; Patton, 2001), and regional S-phases often add important arrival-time observations to limited, small-magnitude datasets used for location (PNE volume, 1994, Mayeda and Walter, 1996 , Myers et al. 1999).

Despite pervasive use of S-phases in seismic monitoring, generation of regional S-waves from explosive (P-wave) sources is not well understood. Most investigators agree that appreciable energy from explosion sources is converted to S-waves near the source, but the dominant P-to-S transfer mechanism is not agreed upon. Several physically reasonable transfer mechanisms are proposed, including P-to-S conversion at the free surface, spall, scattering of short-period surface waves, tectonic release, and rock-damage (e.g., Vogfjord, 1997; Day and Mclaughlin, 1991; Gupta et al., 1992; Wallace et al., 1985; Johnson and Sammis, 2001). With the exception of surface-wave scattering, supporters of each mechanism describe them analytically, and each mechanism can be used to fit a subset of observations. However, surface-wave scattering—the only mechanism without an adequate analytical representation, offers an explanation for some of the most intriguing regional S-wave observations (see below).

RESEARCH ACCOMPLISHED

The importance of Rg scattering was first proposed to explain teleseismic P-coda amplitudes (e.g., Dainty, 1990). Gupta et al. (1992) proposed Rg-to-S scattering to explain frequency-dependent variations in regional P/Lg ratios at the Kazakh and Nevada Test Sites (NTS), where the P/Lg spectra for explosions increases in the ~1–10 Hz band. The minimum in the P/Lg spectra was found to be coincident with expected spectral peaking in Rg excitation, suggesting a link between Rg and regional S-wave energy. In an in-depth analysis of NTS explosion spectra, Patton and Taylor (1995) also found evidence for Rg-to-S scattering. An expected notch in the Rg spectrum from a compensated linear vector dipole (CLVD) source, which the authors attribute to spall, matched spectral characteristics of the Lg phase. Gupta et al. (1997) confirmed these observations using an expanded data set.

Myers et al. (1999) found further evidence to support the importance of Rg-to-S conversion for regional seismic phases. In 1997 at the former Soviet test site at Balapan, Kazakhstan (Glenn and Myers, 1997), three 25-ton chemical explosions where detonated at nominal depths of 50 m, 300 m, and 550 m. Regional distance recordings of the explosions exhibit increased S-wave excitation for the shallow shots in the 1–5 Hz band relative to P-wave amplitudes (Figure 1). Above 5 Hz, S-wave excitation scales with P-wave amplitude, and P/S ratios are relatively constant for the three shots. Likewise, regional Lg coda amplitudes for the shallow shots are peaked in the 1–5 Hz band in comparison to the deepest shot. The Kazakhstan experiment stands out because local recordings of the shots are also available, and near-source Rg amplitudes can be measured. For the 1997 Kazakh explosions Rg is 1) peaked in the 1–5 Hz band, 2) greater in amplitude for the shallow shots, and 3) rapidly attenuates ($Q_{Rg}(f)\mu f$ and $Q^{a}10$ at 1 Hz) (Figure 2). The extreme attenuation and frequency dependence is interpreted to result from scattering. In summary, Rg rapidly looses energy in the 1–5 Hz band and regional S-waves correspondingly gain energy in the 1–5 Hz band. Also, both Rg and regional S-phase amplitudes increase for the shallow shots. Taken as a whole, these observations point towards Rg-to-S scattering as an important mechanism for generation of regional S-energy.

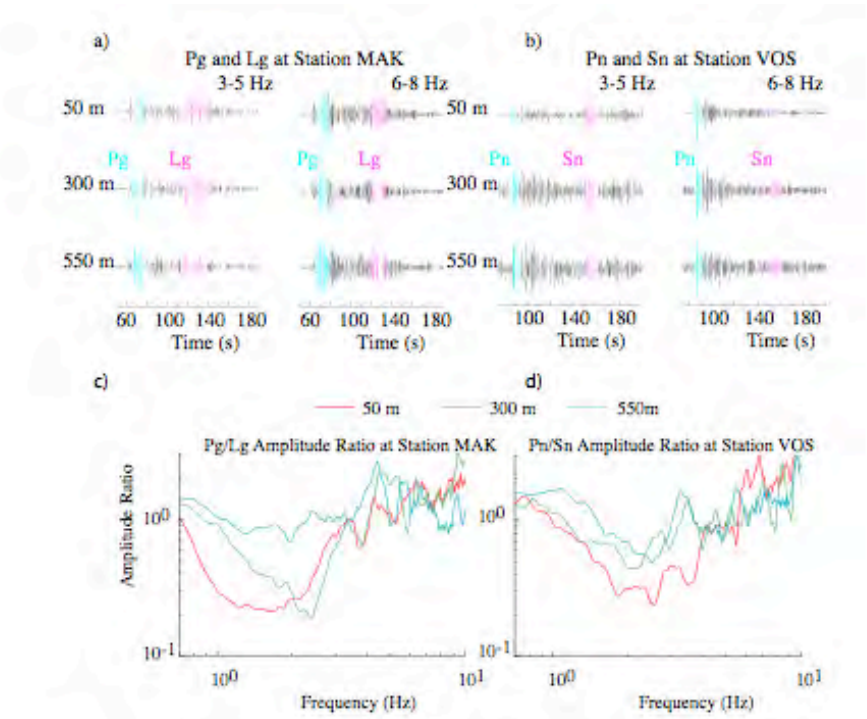


Figure 1. Observations of the 1997 Depth Of Burial (DOB) experiment (Myers et al., 1999). a) Bandpass seismograms (3–5 Hz and 6–8 Hz) at station MAK. Highlighted Pg and Lg phases show enhanced Lg amplitude for the shallower shot in the 3–5 Hz band pass. b) The same band passes as a) but with Pn and Sn phases highlighted at station VOS. Again, the S-phase (Sn) amplitude is enhanced in the 3–5 Hz pass band for the shallow shots. Spectral ratios for c) Pg/Lg and d) Pn/Sn show the frequency dependence of the P/S energy partitioning. The frequency band with lower P/S ratios is coincident with the peaking of the Rg phase.

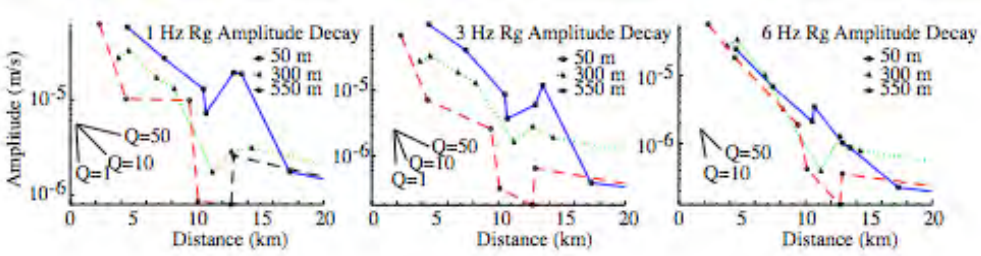


Figure 2. DOB Rg amplitude as a function of distance is shown in 3 frequency bands. These observations suggest rapid, frequency-dependent attenuation of Rg.

Currently the Rg-to-S mechanism is represented by an empirical transfer function (e.g., Gupta et al., 1992; Patton, 2001). Because analytical representation of the Rg-to-S mechanism is, at best, cumbersome for complex geologic structure, a transfer function is a practical representation. Although Jih (1995) used numerical simulation and simple 2-D models to show the plausibility of Rg scattering into regional phases, application of the transfer function would be bolstered by a more detailed understanding of the physical mechanism in more realistic geology. In particular, a better understanding of the effects that geologic and source emplacement conditions have on transfer function parameters is needed.

NPE Case Study

We fashion the seismic simulations around the 1993 Non-Proliferation Experiment (NPE) (see reference in Denny and Stull, 1994). The NPE was a chemical explosion with nominal yield of 1 kiloton. Knowledge of the source

location, origin time, emplacement conditions, and near source geology are unparalleled, providing an excellent data set for modeling.

The NPE was well instrumented both locally and regionally (Figure 3), including two temporary deployments extending to regional distance. One deployment forms a line to the northwest and the other forms a line to east, where the shot was well recorded with high signal to noise ratio. Each of these deployments is anchored by a permanent station (Elko and Kanab, respectively) with historic recordings of nuclear tests. Perhaps most importantly, regional NPE seismograms are near replicas of nearby nuclear explosions (Walter et al., 1994), so our simulations are directly applicable nuclear test monitoring. Local stations surround the NPE out to about 20 km (Figure 3). Local recordings provide crucial validation of the near-source model and propagation effects.

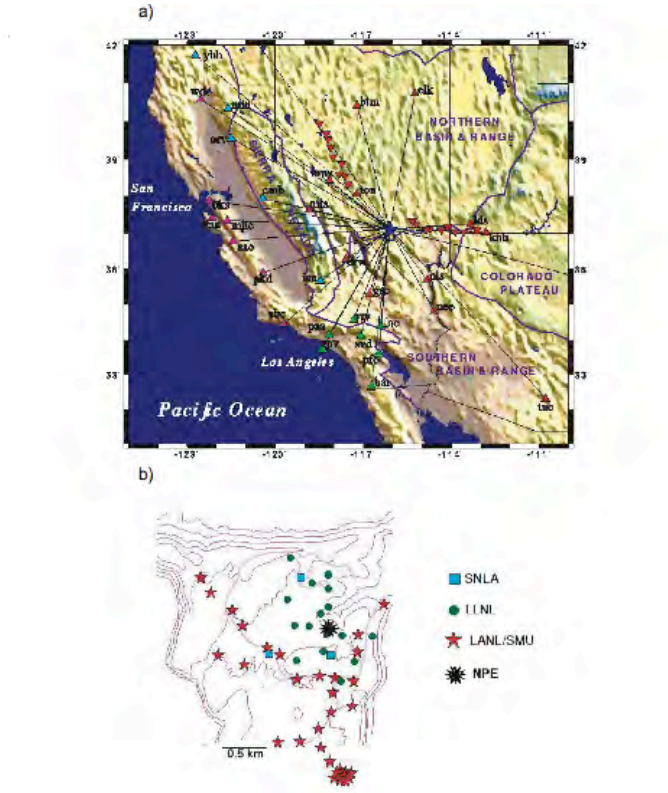


Figure 3. a) Regional and b) local networks recording the NPE shot. The local and regional recordings of the NPE provide validation data for simulations.

Seismic Simulation

E3D Finite-Difference computer code

Computational simulations in this study are performed with E3D, a state-of-the-art finite-difference seismic wave propagation code developed at Lawrence Livermore National Laboratory (LLNL) (e.g., Larsen and Schultz, 1995; Larsen and Grieger, 1998). E3D is based on the elastodynamic formulation of the full wave equation on a staggered grid [e.g., Levander, 1988]. It is 4th-order accurate in space and 2nd-order accurate in time. E3D can be used to simulate the propagation of elastic waves (compressional and shear energy) in a complex and fully heterogeneous 3-D geologic environment (Figure 4).

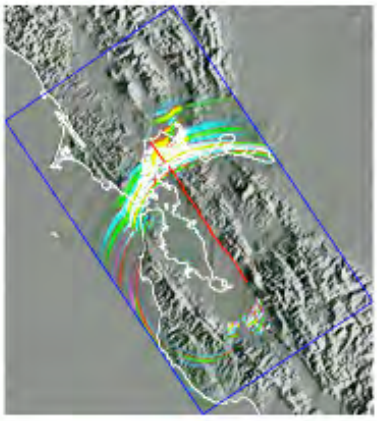


Figure 4. Example of full elastic simulation using the e3d finite difference code. The E3D code can accommodate topography and 3-D geology to produce a more realistic simulation of seismic wave propagation.

E3D contains several advanced features that make it particularly well suited to our study. Physics-based enhancements include fully 3-D elastic wave propagation, 3-D viscoelastic propagation (attenuation, Q), 3-D topography, and multiple source representations, including explosions. Computational enhancements include propagating grids, and parallelization. Of particular interest to this study is the advanced-graphic run-time visualization, which can be used to visually evaluate wave propagation phenomenology.

Our simulations require world-class computational facilities, like those available at LLNL. A 3-D elastic simulation at a source frequency of 4 Hz propagated through typical regional geology out to 300 km will require approximately 12 hours of run time using 1 Terabyte of computer memory and 1,000 CPU's in a parallel computing environment. Simulations in the presence of topography or viscoelastic attenuation will be more intensive.

Geological Simulation

Explosions are detonated and Rg propagates in the top few kilometers of the crust, which is typified by fault-bounded geologic units that comprise a highly heterogeneous medium. This patchwork of complex, nonstationary units may not be adequately represented by either homogeneous, fault-bounded units, or by continuous stochastic models. Hybrid models may be necessary. From the 1997 Kazahk experiment (described above), we know that near-source Rg attenuation is strong and highly frequency dependant. Although narrow-band scattering attenuation may be simulated with any number geologic realizations, frequency-dependent broadband scattering attenuation requires realistic geologic structure. To better simulate the close-in NPE wave field, we have collected geologic information near the NPE shot and constructed a deterministic model. We are also working to characterize the stochastic properties of the geologic media to create a realistic model that extends for local to regional distance.

Deterministic structure

Geologic structure close to the NPE source is likely to control Rg scattering. Numerous studies of geologic structure at the NTS allow construction of a detailed model that will enable us to credibly evaluate whether Rg scattering contributes appreciably to regional S-phases. Geologic mapping at fine scales, ten of thousands of borings, and geophysical imaging have all been conducted in and around NTS. We have compiled this information to construct of a detailed deterministic model near the NPE shot (Figure 5). The detailed model extends 20 km from the NPE shot and to a depth of 6 km. A 10-meter digital elevation model forms the topographic surface, and the following stratigraphic units are specified: Quaternary alluvium, Tertiary volcanics, Mesozoic intrusive granites, Paleozoic sedimentary and metasedimentary rocks, and upper-crustal crystalline rocks.

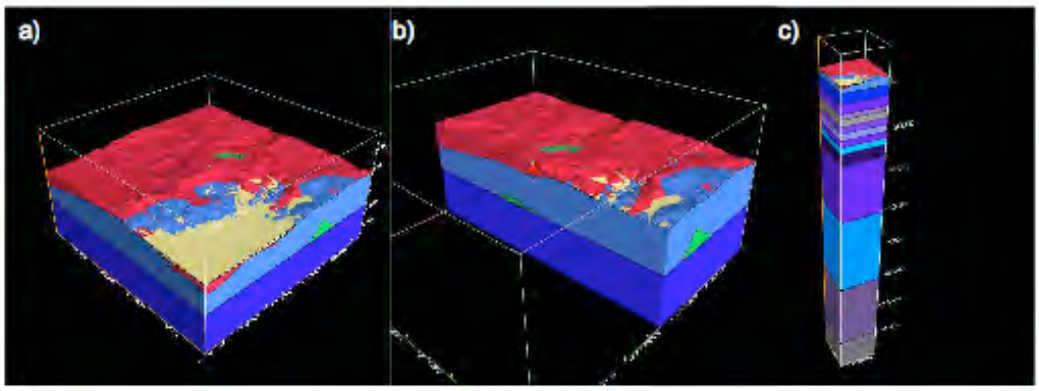


Figure 5. Local model around NPE shot determined from detailed geologic and geophysical studies. a) The entire local model. b) Cross section through the NPE shot. c) Local model merged into a lithospheric velocity stack.

The surfaces of these units are defined primarily by geologic mapping and borehole data. As an example, we show the top of the Paleozoic (Figure 6a,b), which is constrained by numerous borehole data points. Two other examples are the intrusive granites (Gold Meadows stock and Climax stock; green in Figure 5), which are locally exposed at the surface, penetrated by several boreholes and further constrained by gravity modeling (Healey and Miller, 1963; USGS OFR, 1983).

Simulated structure

Although we are taking great measures to incorporate as much deterministic structure as possible, it is impossible to construct a model with sufficient detail without a major 3-dimensional imaging campaign. In order to better simulate the earth, we are using geostatistical simulation techniques to perturb geologic boundaries and elastic parameters within geologic units. Statistical characteristics are gleaned from densely sampled data sets, and these characteristics are then used to "roughen" the model in areas with few data constraints.

Figure 6 is an example of a conditional simulation of the upper contact of Paleozoic (Pz) sedimentary rocks near Rainier Mesa. The top of the Pz is one of the first major seismic contrasts encountered by the NPE wavefield. Therefore, proper simulation of this contact is critical for realistic evaluation of seismic scattering. Numerous boreholes define the Pz contact in the southeast portion of the model area. Elsewhere, only the general dip and depth of the Pz contact are constrained. If conventional interpolation is used to construct the Pz surface, then the surface is quite smooth in areas with sparse borehole sampling (Figure 6a,b). Figure 6c,d shows that a more realistic Pz surface can be constructed through conditional simulation. The new surface will scatter high-frequency energy more readily than a smooth surface and may help to explain the frequency dependence of Rg attenuation.

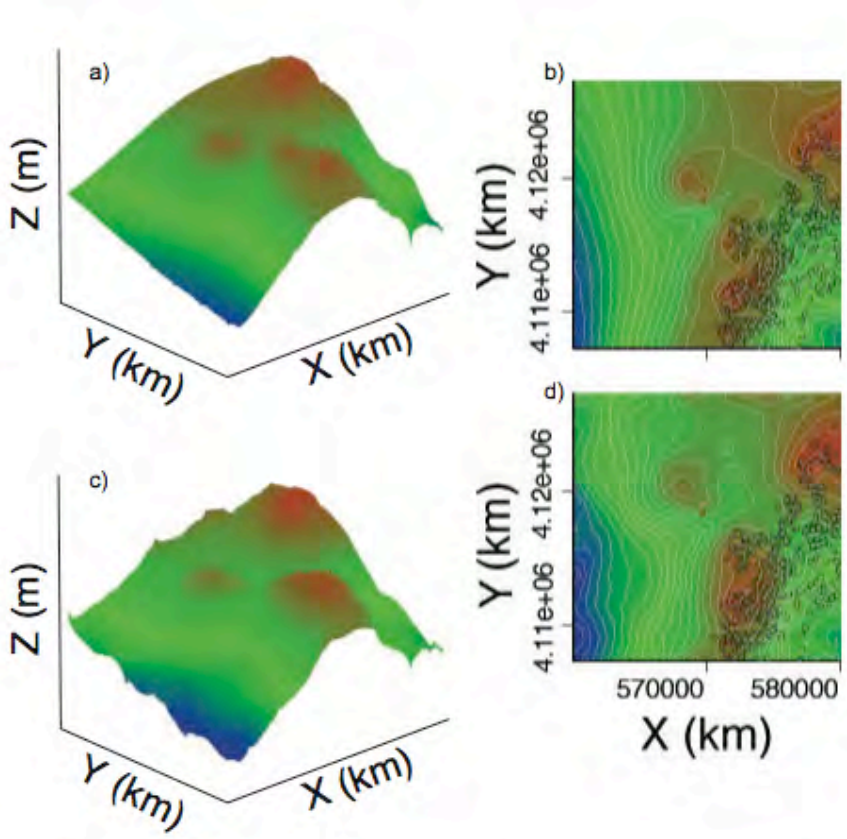


Figure 6. Conditional simulation of the upper contact for Paleozoic (Pz) rocks. a) Surface determined using borehole data, which are concentrated in the southeast portion of the model area, and a simple interpolation algorithm. b) plan view of a) showing borehole data (circles colored in accordance with borehole observation). Note the difference in the roughness of the surface between areas with and without borehole data. c) Conditional simulation of upper Pz surface using statistical characterization of surface roughness and constraints from borehole observations. d) Plan view of c) showing borehole observations and consistent surface roughness in areas with and without observations.

CONCLUSIONS AND RECOMMENDATIONS

We review the first three months of progress on the Simulation of Regional Explosion S-phases (SiRES) project. During this period we made use of geologic and geophysical studies at NTS to construct a detailed earth model within 20km of the NPE shot. We use geostatistical simulation to make geologic contacts and elastic parameters within geologic units as realistic as possible. This level of local model detail is needed to evaluate the Rg-to-S transfer function.

Our next step is to imbed the local, detailed model in a regional model (out to ~400 km). The regional model draws on previous studies of crustal scale structure. Like the local model, conditional geostatistical simulation will be used to produce a realistic model at relevant wavelengths. Seismic simulation will be used for validation during model construction and will culminate in a Tera-Scale, 3-D simulation.

REFERENCES

Dainty, A. M., Studies of coda using array and three-component processing, *Pageoph*, **132**, 221-244,1990.

Denny, M.D., S.P. Stull, Proceedings of the Symposium on The Non-Proliferation Experiment (NPE): Results and Implications for Test Ban Treaties, Rockville Maryland; Lawrence Livermore National Laboratory,1994.

Glenn L. and S. Myers (1997). Depth of Burial Experiment at Balapan, *Proceeding of the International Symposium on Monitoring and Discrimination of Underground Nuclear Explosions and Earthquakes*, Moscow, Russia, November 17-21, 1997 (229-235); see also LLNL UCRL-JC-128313.

Gupta, I.N., T.R. Zhang, R.A. Wagner, Low frequency Lg from NTS and Kazakh Nuclear Explosions – observations and interpretations, *Bull., Seismol. Soc. Am.*, **87**, 1115-1125, 1997.

Healey, D. L. and Miller, C. H., 1963. Gravity survey of the Gold Meadows Stock, Nevada Test Site, Nye County, Nevada. USGS Technical Letter NTS-40.

Jih, R.S., Numerical investigation of relative contribution of Rg scattering and incomplete dissipation to Lg excitation, Proceedings of the 17th Seismic Research Symposium on Monitoring a Comprehensive Test Ban Treaty, PL-TR-95-2108, 1995.

Johnson, L.R., and C.G. Sammis, Effects of rock damage on seismic waves generated by explosions, *Pageoph*, **158**, 1869-1908, 2001.

Larsen, S. C., and C. A. Schultz, ELAS3D: 2D/3D elastic finite-difference wave propagation code, LLNL internal report, 18 p., 1995.

Larsen, S., and J. Grieger, Elastic modeling initiative, Part III: 3-D computational modeling, Soc. Expl. Geophys. Confer. Proceed., 68,1803-1806, 1998.

Levander, A. R., Fourth-order finite-difference P-SV seismograms, Geophysics, 53, 1425-1436, 1988.

Myers, S.C., W.R. Walter, K. Mayeda, L. Glenn, Observations in support of Rg scattering as a source for explosion S waves: regional and local recordings of the 1997 Kazakhstan depth of burial experiment, *Bull. Seismol. Soc. Am.*, **89**, 544-549, 1999.

Nuttli, O.W., Yield estimates of Nevada Test Site explosions obtained from seismic Lg waves, *J. Geophys. Res.*, **91**, 2137-2151, 1986.

Patton, H.J., Regional magnitude scaling, transportability, and Ms:mb discrimination at small magnitudes, *Pageoph*, **158**, 1951-2015, 2001.

USGS, 1983. Geologic and geophysical investigations of Climax Stock Intrusive, Nevada. USGS Open-file Report 83-377.

Walter, W.R., K. Mayeda, and H.J. Patton, Regional seismic observations of the Non-Proliferation Experiment at the Livermore NTS network, in *Proceedings of the Symposium on The Non-Proliferation Experiment (NPE): Results and Implications for Test Ban Treaties*, Denny and Stull eds., 1994.

Whitney, J. W., W.R. Keefer, Geologic and geophysical characterization studies of Yucca Mountain, Nevada, a potential high-level radioactive-waste repository, USGS Digital Data Series 58, 2001

GEOPHYSICAL MODELS FOR NUCLEAR EXPLOSION MONITORING

Michael E. Pasyanos, William R. Walter, Megan P. Flanagan

Lawrence Livermore National Laboratory

Sponsored by National Nuclear Security Administration
Office of Nonproliferation Research and Engineering
Office of Defense Nuclear Nonproliferation

Contract No. W-7405-ENG-48

ABSTRACT

Geophysical models are increasingly recognized as an important component of regional calibrations for seismic monitoring. The models can be used to predict geophysical measurements, such as body wave travel times, and can be derived from direct regional studies or even by geophysical analogy. While empirical measurements of these geophysical parameters might be preferred, in aseismic regions or regions without seismic stations, this data might not exist. In these cases, models represent a “best guess” of the seismic properties in a region, which improves on global models such as the PREM (Preliminary Reference Earth Model) or the IASPEI (International Association of Seismology and Physics of the Earth's Interior) models. The model-based predictions can also serve as a useful background for the empirical measurements by removing trends in the data. To this end, Lawrence Livermore National Laboratory (LLNL) has developed the WENA model for Western Eurasia and North Africa. This model is constructed using a regionalization of several dozen lithospheric (crust and uppermost mantle) models, combined with the Laske sediment model and 3SMAC upper mantle. We have evaluated this model using a number of data sets, including travel times, surface waves, receiver functions, and waveform analysis. Similarly, Los Alamos National Laboratory (LANL) has developed a geophysical model for East Asia, allowing LLNL/LANL to construct a model for all of Eurasia and North Africa. These models continue to evolve as new and updated datasets are used to critically assess the predictive powers of the model. Research results from this meeting and other reports and papers can be used to update and refine the regional boundaries and regional models. A number of other groups involved in monitoring have also developed geophysical models. As these become available, we will be assessing the models and their constitutive components for their suitability for inclusion in the National Nuclear Security Administration (NNSA) Knowledge Base (KB).

OBJECTIVE

The objective of regional-scale geophysical models is to improve predictions for location and identification of regional seismic events by improving the resolution compared to global-scale models. As such, we wish to provide the highest resolution model possible that can be used to reliably derive parameters such as body wave travel times, group velocity dispersion, waveforms, etc. In addition, the models should also convey proper uncertainty estimates which can be mapped into uncertainties in the derived products.

Geophysical models can serve as background values for correction surfaces and other derived parameters. This can be particularly important in aseismic regions, which might only have a limited number of empirical measurements. Additionally, models can provide guidance on spatial parameters, such as tectonic boundaries and correlation lengths. Furthermore, models can be used to evaluate new stations before they are installed and special events, such as dedicated shots, before they occur. Finally, models can serve as an integrated geophysical repository for research community results.

RESEARCH ACCOMPLISHED

WENA Construction

We have constructed an *a priori* 3-D geophysical model for Western Eurasia and North Africa (WENA). Details of the construction and validation of the model can be found in Pasyanos et al., 2003. The WENA model is constructed from separate sediment, crust, and upper mantle models. Sediments are taken from Laske and Masters (1997), a 1º 3-layer sediment model based on the 1985 Exxon map. Crustal regionalizations and velocity profiles are taken from a series of Lawrence Livermore National Laboratory (LLNL) reports (Walter et al., 2000; Bhattacharyya et al., 2000; Sweeney et al., 1998) and based on CRUST 5.1, Exxon, and many published studies. Our regionalizations are shown in Figure 1. The crustal regionalizations also include velocities in the uppermost mantle layer. We use the 3SMAC model (Nataf and Ricard, 1996) for the remainder of the WENA model upper mantle, extending down to 660 km depth. 3SMAC is an *a priori* model based on tectonics, heat flow, and geophysical knowledge.

Until now, the WENA model has exclusively been an *a priori* geophysical model. While we will continue to maintain this model by correcting any newly discovered problems, updating the model with new information as it becomes available, and integrating results from the research community, we now shift our focus to data driven models. These new models will use the *a priori* model as a starting model, but will be driven by data from several different types of geophysical measurements, which are sensitive to different portions of our model.

WENA Validation

The WENA model has been validated using many different types of geophysical data, including body wave travel times, gravity, surface wave group velocities, receiver functions, and waveform modeling (Pasyanos et al., 2003). We will focus on several of the validations here. The first is the travel-time validation test that assesses how well the WENA model does in predicting P and Pn travel times. Figure 2a shows a P-wave correction surface for station ARU in Russia. To compute model-based correction surfaces we subtract the iasp91 (Montagner and Kennett, 1996) predicted time from the WENA predicted time along a regular grid in latitude, longitude and at a depth of 10 km. Blue indicates fast regions and red indicates slow. Each correction surface provides station-specific travel time corrections for regional to near-teleseismic distances, which can be used to improve location capability. We find travel time differences of up to 6 seconds relative to iasp91, most in areas of very thick crust or sediment. The (observed-iasp91) P-wave residuals are plotted on top of the correction surfaces. To test the predictive power of the model we compute the median residuals between the observed arrival times at each station and those predicted by both the WENA model and iasp91. We use *P* and *Pn* travel times from a global dataset of relocated events (Engdahl et al., 1998), which have been further processed with a declustering algorithm. To compute these residuals we interpolate between grid nodes to calculate the predicted travel time for an exact source-station path. This is done for both the WENA travel time volume and the iasp91 travel time volume computed with the FD code. These residuals (observed - predicted time) are shown as histograms in Figure 2. Note the reduction in the SMAD (scaled median average deviation) produced by the WENA model over iasp91.

Another way of validating the model was to compare the surface wave group velocities predicted from the model against a tomography model of the same data. Figure 2b shows a comparison of 20 second Rayleigh wave group velocities between the WENA model and a surface wave tomography (Pasyanos et al., 2001). At this period, surface waves are sensitive to the top 20 km and illustrate crustal thickness variations between oceanic and continental crust, as well as the effect of deep sedimentary basins. There is good agreement between the two figures, with both well-outlining oceanic and continental crust in addition to large sedimentary basins.

Access Tools

Working with Sandia National Laboratories (SNL), we have created a utility designed to view and extract geophysical models. VEXtool (or Viewing and EXtraction tool) allows users to extract 1-D profiles (boreholes), 2-D profiles (cross-sections), and 3-D profiles (volumes) from the models. These portions of the model can either be viewed graphically or exported into a series of export formats, including those for the TauP travel time generator (Crotwell et al., 1999), Randall's reflectivity codes (based on Kennett, 1985), or Herrmann's surface wave package SURF (based on Russell, 1988). For example, one could select a point and generate Love and Rayleigh group and phase velocities from the profile (Figure 3a), or select a cross-section and generate body wave travel times from an average velocity structure along the profile (Figure 3b), or generate reflectivity synthetics (Figure 3c). Finally, one can export the 3-D model and port the results to a finite difference code, which can be used to trace rays through the model and compute travel times.

Other Geophysical Models

There are a number of other geophysical models that have been developed in the context of improved regional monitoring. Los Alamos National Laboratory (LANL) has created the CEA model that covers China and East Asia. This effort has paralleled some of LLNL's work on geophysical models in Western Eurasia and North Africa. We have worked with LANL to insure that the regionalizations of the two individual models are consistent, allowing us to build a unified model for the broader region.

Other such models have been developed completely independently of the LLNL geophysical modeling effort. Examples covering portions of Western Eurasia and North Africa include CRUST 5.1, WINPAK3D, CUB, and EurID. CRUST 5.1 is a global crust (and uppermost mantle) model at 5˚ resolution (Mooney et al., 1998), now updated to CRUST 2.0 (Laske and Masters, written communication). WINPAK3D is a model for India and Pakistan that was developed by Weston Geophysical (Johnson and Vincent, 2002). Another model is the CUB model, a global mantle model developed by the University of Colorado at Boulder and their Group 2 consortium partners (Shapiro and Ritzwoller, 2002). The EurID model (Du et al., 1998) is a model covering Europe. Other models, such as those from the Group 1 consortia, cover regions of Eastern Eurasia.

In each case, when the selected models are made available, they will be converted into a format accessible by VEXtool, so that the model can be viewed and portions of the model extracted for further analysis. The models can then be validated using many data types, similar to those performed for the WENA model, and independently assessed. Once the models have been evaluated, the model or portions of the model can be integrated into the National Nuclear Security Administration (NNSA) Knowledge Base (KB). Potential issues related to integration of research include: how to handle multiple inconsistent models, and how best to quantify and validate model uncertainty.

Model Evaluation

We have been working with researchers Gabi Laske, Guy Masters, and Christine Reif from the University of California, San Diego (UCSD) Scripps on reviewing the literature for geophysical parameters, such as crustal thickness (Figure 4a). These points can be used to assess or build models. Alternatively, this data can be used to understand some of the fundamental quantities of these parameters, such as uncertainty and correlation length. For example, in Figure 4b, we plot the variogram of crustal thicknesses in Europe, Asia, and North Africa, which provides the spatial statistics for kriging. The sill is the background variance of the data, the range is the distance at which correlation between data points is zero, and the nugget is the covariance of co-located points. From this analysis, we find that the uncertainty on individual point is about 1.5 km, the correlation length of crustal thickness is about 15 degrees, and that uncorrelated points have a variance of about 10 km. Figure 4c shows the kriged

surface of crustal thickness data for Europe, Asia, and North Africa. This surface is interpolated at 2˚ resolution using the kriging algorithm and the variogram statistics specified above.

We are currently assessing the travel-time prediction uncertainty of our WENA model in a region-specific framework (i.e., 3D). Figure 5 shows variograms of travel time residuals at station ARU for both the WENA and iasp91 velocity models. Triangles are the data variogram values in 1.0 degree bins; solid lines are the model variograms determined by curve fitting. Note the variograms do not approach zero for points that are closely co-located (i.e., data are not perfectly correlated) due to errors associated with determining travel time residuals. However, it is apparent that the variograms reach minima (correlation is maximum) for points close together, and the variograms increase (correlation decreases) as points become separated by greater distance. Travel time prediction uncertainty for the WENA model compares favorably to iasp91. Not only is the overall variance reduced (from s^2=3.5 to s^2=2.5), but the travel time residuals are more stationary for the 3-D model. Three-dimensional models reduce the dimensionality of the uncertainties by accounting for the non-stationary component.

CONCLUSIONS AND RECOMMENDATIONS

In conclusion, we have developed a 3-D geophysical model for Western Eurasia and North Africa, along with sophisticated access tools, which are directly usable for generating a number of geophysical parameters of interest. Geophysical models are an important way of calibrating regions in the absence of direct measurements. In addition to providing a background for measurements, geophysical models also improve our interpolation by reducing the non-stationarity of the uncertainties. We will be evaluating a number of geophysical models for inclusion in the NNSA Knowledge Base.

Models can be a repository for a vast array of geological and geophysical datasets of all types - receiver functions, refraction profiles, tomographic inversions, travel time models, etc. This product integrates results from many contractors and can be used to integrate future results.

ACKNOWLEDGEMENT

We wish to thank Lee A. Jensen and Christopher J. Young at Sandia National Laboratories for their work on VEXtool. We thank William Hanley from Lawrence Livermore National Laboratory for his declustering algorithm.

REFERENCES

Bhattacharyya, J., W. Walter, M. Flanagan, J. O'Boyle and M. Pasyanos (2000), Preliminary definition of geophysical regions in Western Eurasia, UCRL-ID-138402, LLNL (http://www.llnl.gov/tid/lof/documents/pdf/237980.pdf).

Crotwell, H.P., T.J. Owens, and J. Ritsema (1999), The TauP ToolKit: Flexible seismic travel-time and raypath utilities, Seism. Res. Lett., 70, 154-160.

Du, Z.J, A. Michelini, G.F. Panza (1998), EurID: a regionalized 3-D seismological model of Europe, Phys. Earth Planet. Int, 141, 31-62.

Engdahl, E.R., R. van der Hilst, and R. Buland (1998), Global teleseismic earthquake relocation with improved travel times and procedures for depth determination, *Bull. Seismol.. Soc. Am., 88*, 722-743.

Johnson, M. and C. Vincent (2002). Development and testing of a 3-D velocity model for improved event location: a case study for the India-Pakistan region, Bull. Seism. Soc. Amer., 92, 2893-2910.

Kennett, B.L.N. (1985), Seismic wave propagation in stratified media, 342 pp., Cambridge University Press, Cambridge, England

Laske, G. and T.G. Masters (1997), A global digital map of sediment thickness, EOS Trans. AGU, 78, F483.

Montanger, J.–P. and B. L. N. Kennett (1996), How to reconcile body-wave and normal-mode reference earth models, Geophys. J. Int., 125, 229-248.

Mooney, W. D., G. Laske, and T. G. Masters (1998), CRUST 5.1: A global crustal model at 5° x 5°: Journal of Geophysical Research, 103, 727-747.

Nataf, H.C., and Y. Ricard (1996), 3SMAC: an a priori tomographic model of the upper mantle based on geophysical modeling, Physics of the Earth and Planetary Interiors, 95, 101-122.

Pasyanos, M. E., W. R. Walter, S. E. Hazler (2001), A surface wave dispersion study of the Middle East and North Africa for monitoring the Comprehensive nuclear-test-ban Treaty, Pure and Applied Geophysics, 158, 1445-1474.

Pasyanos, M. E., W. R. Walter, M. P. Flanagan, P. Goldstein and J. Bhattacharyya (2003), Building and testing an a priori geophysical model for western Eurasia and North Africa, Pure and Applied Geophysics.

Russell, D.R. (1988), Multichannel processing of dispersed surface waves, Ph.D. Dissertation, St. Louis University, St. Louis, MO.

Shapiro, N.M. and M.H. Ritzwoller (2002), Monte-Carlo inversion for a global shear velocity model of the crust and upper mantle, Geophys. J. Int., 151, 88-105.

Sweeney, J. and W. R. Walter (1998), Preliminary definition of geophysical regions for the Middle East and North Africa, UCRL-ID-132899, LLNL (http://www.llnl.gov/tid/lof/documents/pdf/235042.pdf).

Walter, W.R., M.E. Pasyanos, J. Bhattacharyya and J. O'Boyle (2000), MENA 1.1 - An updated geophysical regionalization of the Middle East and North Africa, UCRL-ID-138079, LLNL (http://www.llnl.gov/tid/lof/documents/pdf/237521.pdf).

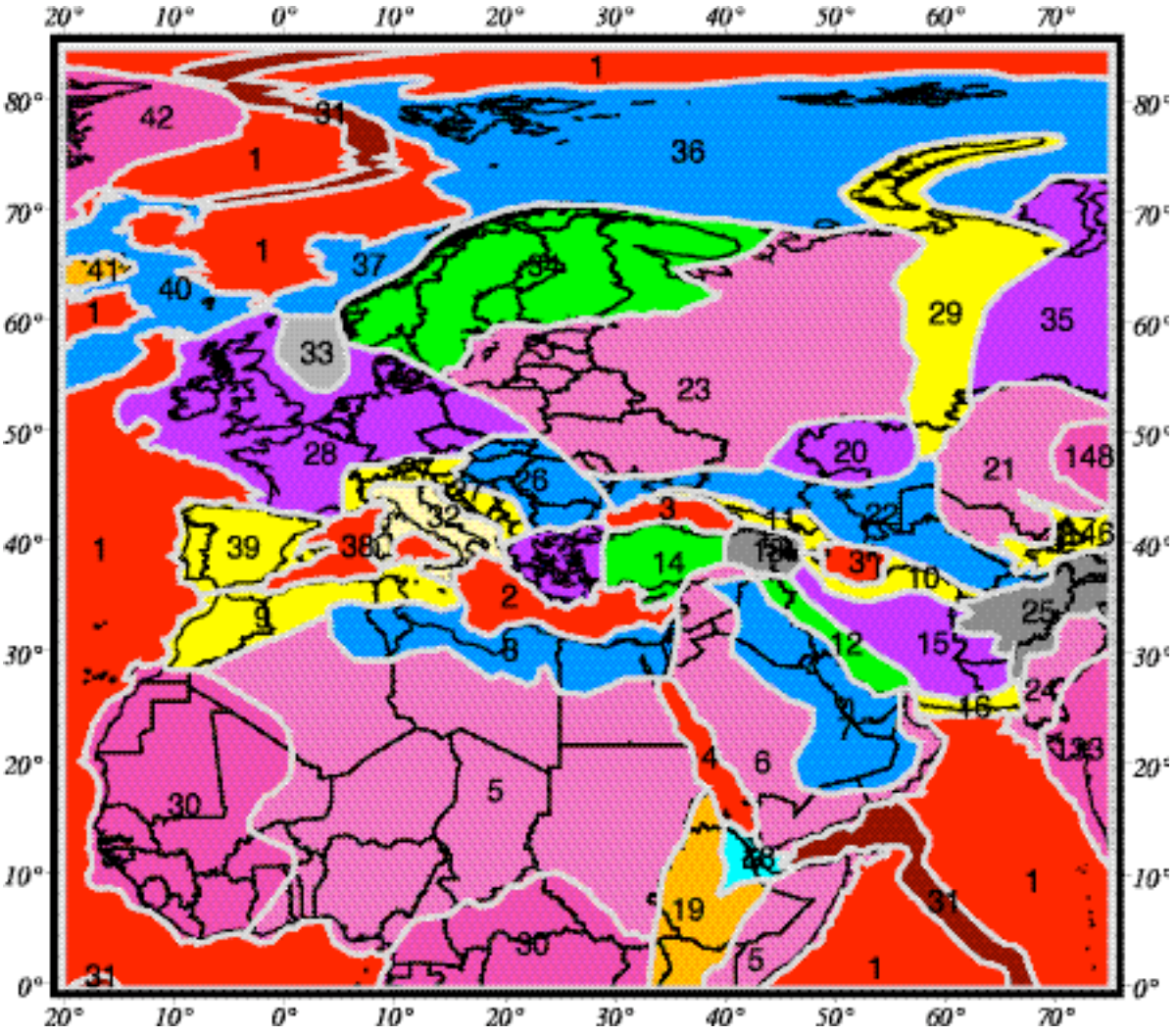


Figure 1. Regionalization of the crust and upper mantle in the WENA model.

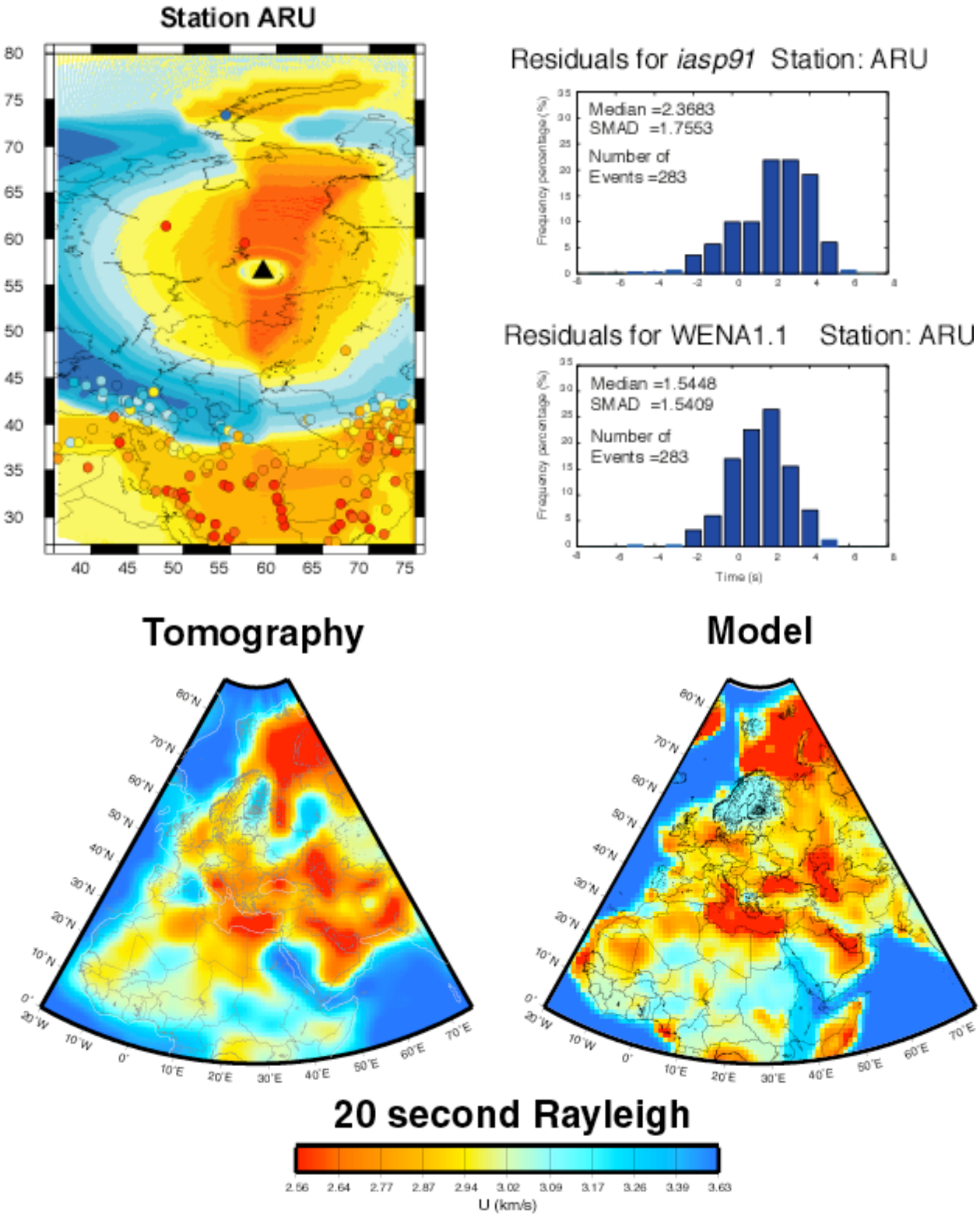


Figure 2. WENA model validations using surface wave group velocities and P-wave travel times

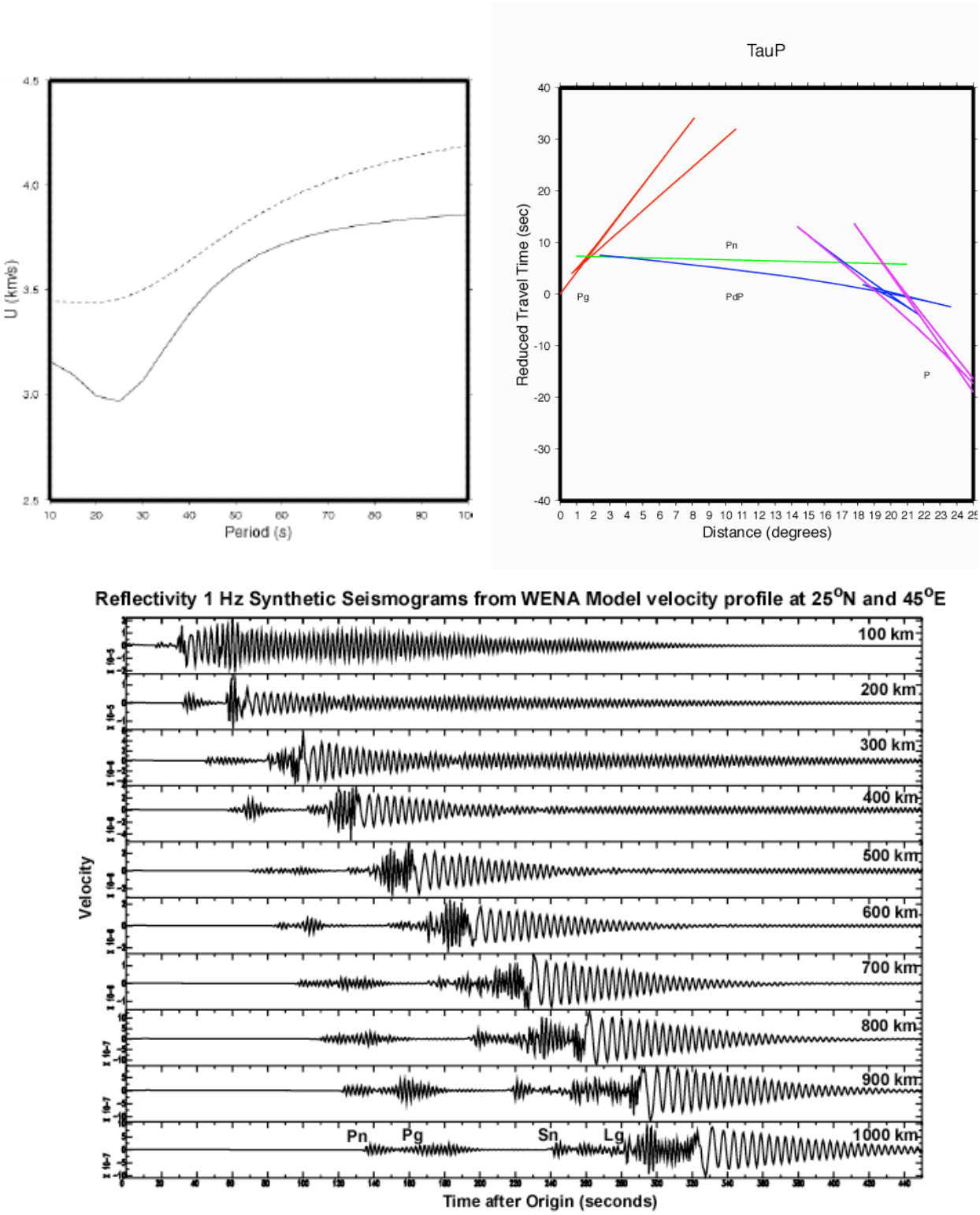
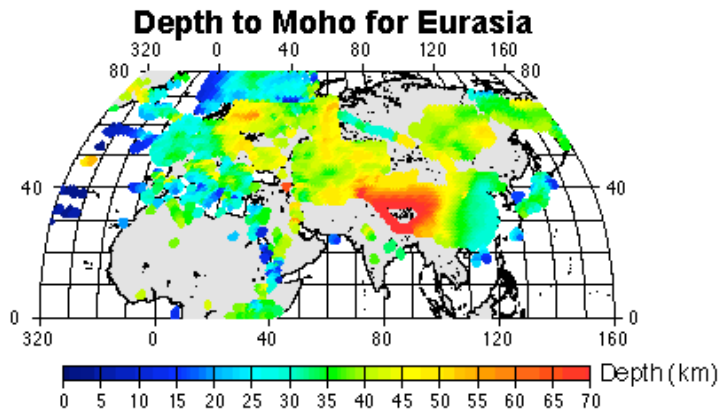
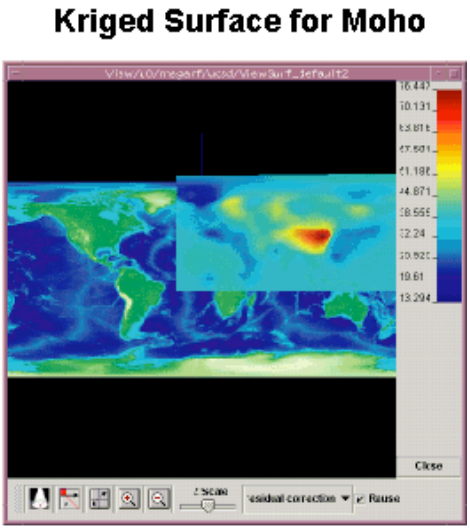


Figure 3. The WENA model can be accessed to predict surface wave dispersion values, body wave travel times, and reflectivity synthetics.





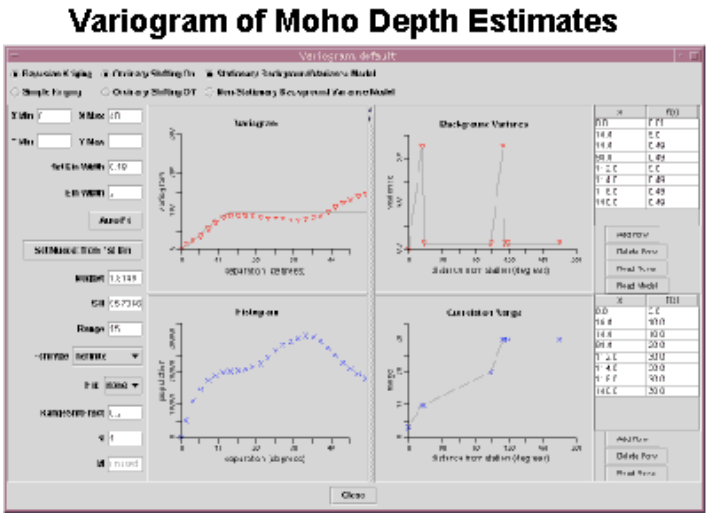


Figure 4. Variogram modeling of crustal thickness data showing a) individual data points, b) crustal thickness variogram, and c) kriged surface.

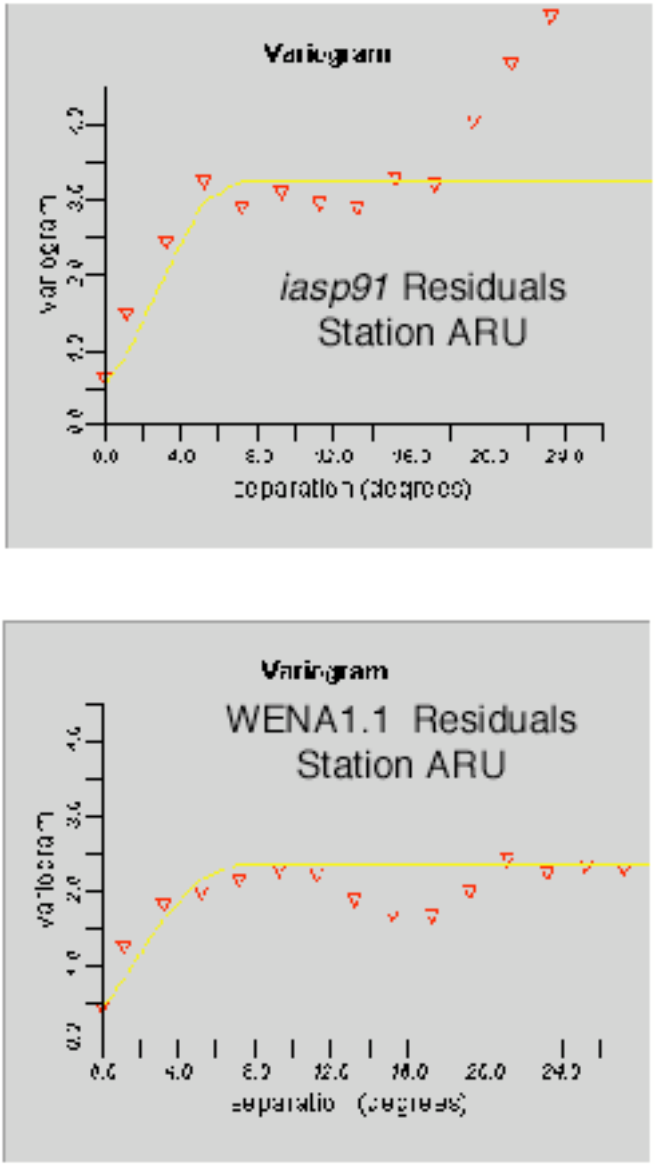


Figure 5. Variograms of P-wave travel time residuals for a 1-D model (iasp91) and a 3-D model (WENA).

BROADBAND SEISMIC STUDIES IN SOUTHERN ASIA

Keith F. Priestley,[1] Sara Russell,[2] Vinod Gaur,[3] James F. Lewkowicz,[2] Supriyo Mitra,[1] and Alessia Maggi[1]

Cambridge University,[1] Weston Geophysical Corporation,[2] Indian Institute of Astrophysics[3]

Sponsored by the Defense Threat Reduction Agency

Contract No. DTRA01-00-C-0028

ABSTRACT

Weston Geophysical Corporation (WGC), Cambridge University (CAM), and the India Institute of Astrophysics (IIA) formed a consortium in 2000 to deploy a network of eight high-quality broadband seismometers distributed across India. This network began operation in April 2001 and is now fully operational providing important data for studies focusing on the characterization of the structure and propagation of seismic waves throughout Southern Asia. Each station consists of a Guralp CMG-3TD digital output seismometer plus a Storage and Acquisition Module (SAM) data logger. The sensors have a broadband velocity response between 0.008 and 50 Hz, continuously record at 100 samples/second, and are time-stamped using a GPS receiver. The data are archived on 9 or 18 GB disks, which are changed at intervals of approximately six months. We experienced various difficulties with the instrument design and the operating environment during the first 18 months of deployment, and these problems spurred modifications to the instrument by Guralp, Ltd. and a change in some of our operating practices. To simplify maintenance of the network we have designed and constructed an interface for the stations allowing dial-up modem or Internet access to the CMG-3TD + SAM, which will provide monitoring and rapid troubleshooting capabilities for the network. We have collected a significant database that has already provided several noteworthy results. For example, an understanding of the regional attenuation structure of India is critical to evaluating phase propagation for determination of source magnitude, moment and yield estimates. We have explored the attenuation characteristics of the India and Pakistan crust through analysis of the frequency dependence of *Lg* spectral decay with epicentral distance. We measured *Lg* amplitudes at varying frequencies to compute *Q*, the quality factor, and its frequency dependence in order to place constraints on the regional attenuation structure [Mitra *et al.*, 2002]. We have also used receiver function analysis *Rai et al.* [2002] to examine the velocity and anisotropy structure of the Neoproterozoic south Indian granulite terrane and compared these with the velocity and anisotropy structure beneath Bangalore on the Dharwar craton. Also, *Gupta et al.* [2002, 2003ab] used a receiver function stacking procedure to estimate crustal thickness and Poisson's ratio from receiver function analysis at 32 sites on the Archaean and Proterozoic terrains of South India. In addition to the January 26, 2001 Bhuj earthquake (Mw = 7.6) mainshock, we recorded numerous Bhuj aftershocks. We have determined source parameters for the aftershocks from the regional seismic data [Gaur *et al.*, 2001]. Results from these and additional published studies using this new dataset will be presented.

OBJECTIVE

The objective of this project was to deploy broadband seismic stations in India in order to acquire new data needed to improve the knowledge of regional seismic wave propagation in this complex region.

RESEARCH ACCOMPLISHED

The Indian Institute of Astrophysics, the National Geophysical Research Institute, and Cambridge University have now operated the broadband seismographs on the Indian Shield since 1997. We initially concentrated on the seismic structure of the shield in southern India but now have operated seismographs over much of the peninsula and in the Himalayas. In this report we summarize our recent efforts in determining the seismic structure of India.

Crustal Structure from Teleseismic Receiver Function Analysis

We present crustal thickness and Poisson's ratio determinations from the receiver function analyzed at 32 sites on the Achaean and Proterozoic terrains of south India (Figure 1). The crustal thickness in the late Achaean (2.5 Ga) eastern

Dharwar craton varies from 34-39 km. Similar crustal thickness is observed beneath the Deccan Volcanic Province and the Cuddapah basin. The most unexpected result is the anomalous present-day crustal thickness of 42-51 km beneath the mid-Achaean (3.4-3.0 Ga) segment of the Western Dharwar Craton. Since the amphibolite-grade metamorphic mineral assemblages (5-7 Kbar paleopressures) in this part of the western Dharwar craton equilibrated at depths of 15-20 km, our observations suggest the existence of an exceptionally thick (57-70 km) crust 3.0 Ga ago. Beneath the exhumed granulite terrain in southernmost India, the crustal thickness varies between 42-60 km (Figure 2). The

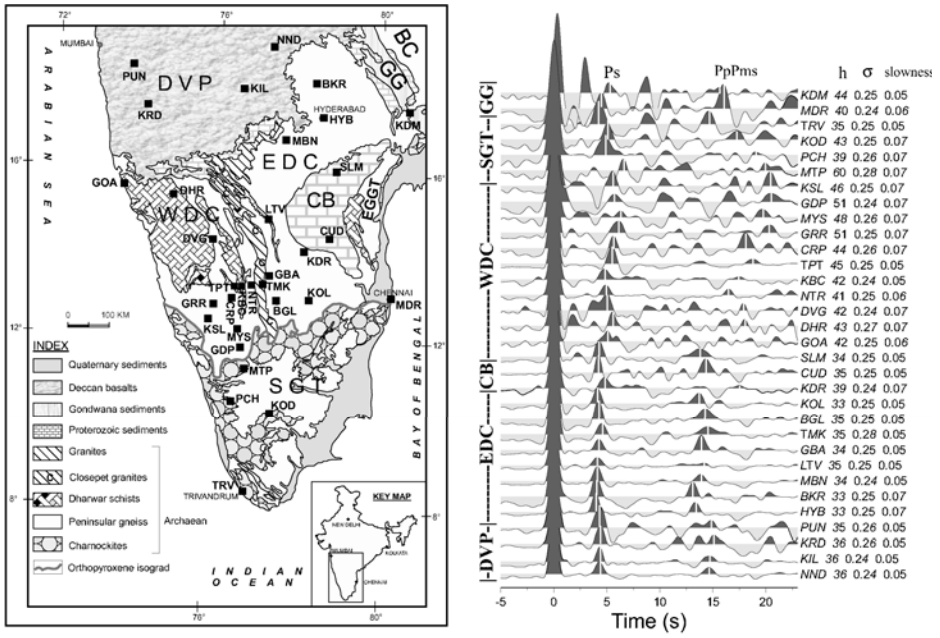


Figure 1. Left - Generalized geotectonic map of south India. Important geological blocks include EDC - Eastern Dharwar Craton, WDC - Western Dharwar craton, DVP - Deccan Volcanic Provinces, SGT - Southern Granulite Terrain, CB - Cuddapah Basin, GG - Godavari Graben, EGGT - Eastern Ghat Granulite Terrain and BC - Bastar Craton. Locations of broadband seismic stations are indicated by filled squares. Right -- Stacked radial receiver functions organized according to geological provinces. The Moho conversion and reverberations are indicated on the receiver functions. The geological provinces are denoted to the left of the receiver functions and the crustal thickness, the average Poisson's ratio, and average slowness for the stack are given to the right of the receiver function. A clear time shift in the *Ps* phase is visible for stations in the WDC and SGT compared to stations in the EDC. (From Gupta et al, 2003)}

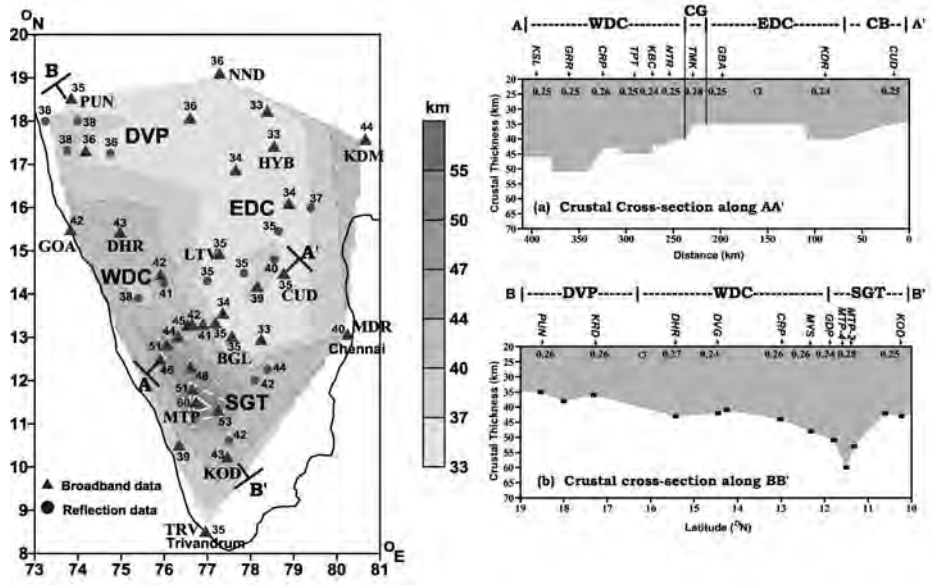


Figure 2. Left -- Crustal thickness map for South India derived from the receiver function analysis and published reflection/refraction results. Numbers denote Moho depth. The locations of the two crustal cross-sections (AA', BB') are indicated. Right -- Cross-section depicting Crustal thickness and Poisson's ratio variation across: (a) SW--NE profile across the Western Dharwar craton (WDC), the Closepth granite (CG), the Eastern Dharwar craton (EDC) and the Cuddapah Basin (CB), (b) NW--SE profile across the Deccan Volcanic Province (DVP), the Western Dharwar craton (WDC) and the Southern Granulite Terrain (SGT). In cross-section AA' the crustal thickness is projected at depth with horizontal offset in the direction of the earthquakes. The azimuth ranges used are SW-W, NE-E and the entire 360° azimuthal sector. (From Gupta et al, 2003)

Poisson's ratio ranges between 0.24-0.28 beneath the Precambrian terrains, indicating the presence of intermediate rock type in the lower crust. These observations of thickened crust suggest significant crustal shortening in south India during the Achaean. We have begun a study of the anisotropic properties of the crust. Shear wave splitting observed in P-to-S converted phases from the Moho indicates velocity anisotropy in the crust. A 0.2 s splitting with the fast-axis oriented NS is observed on the Dharwar craton (BGL, KIL - Figure 3) and a 0.2 s splitting with the fast-axis oriented EW are obtained for stations in the granulite terrane in southern India (KOD, PALK - Figure 3).

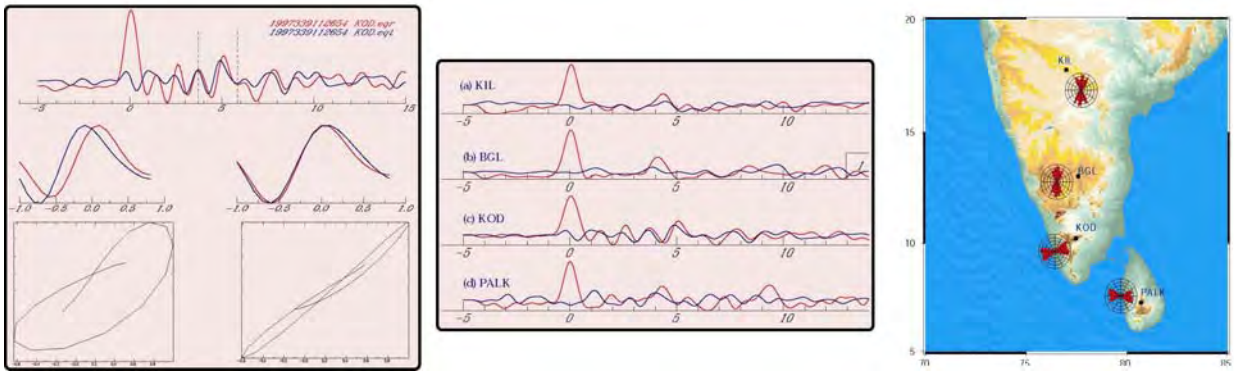


Figure 3. Left - Processing of *Ps* splitting observed at KOD. Center - Examples of splitting of the Moho converted *Ps* phases for South-Indian stations (BGL, KOD and PALK). The fast-axis polarization direction of crustal components of anisotropy for Dharwar craton (BGL) and Granulite terrain (KOD and PALK). The fast direction is oriented N-S with a split time of 0.15 s for low-grade terrain and E-W with a split time of 0.2 s for high-grade terrain. (From Rai et al (2003).

We use broadband teleseismic data recorded at seven sites along a 250 km NS profile from stations in NE India to determine the crustal structure along a profile extending from the Shillong Plateau to the Lesser Himalaya (Figure 4). The analysis shows that the crustal thickness beneath the Shillong Plateau varies from 35-40 km, and that the site on the southern edge of this plateau has an azimuthal variation in crustal thickness. The depth to the Moho obtained by modeling the receiver functions for arrivals sampling the Bengal Basin indicates a very thick crust (66 ±2 km), while the events from the north show a comparatively thinner crust (38 ± 2 km), comparable to that observed in the central part of the plateau. Further north along the profile in the Brahmaputra Valley, the crust is 40-44 km thick and the Moho appears to dip gently northward, reaching a depth of about 48 km beneath the Lesser Himalaya several kilometers north of the Main Boundary thrust and a few kilometers south of the Main Himalayan Central thrust in the region. These Moho depths are compared with Moho depths beneath the southern Tibetan Plateau where the crust thickens from about 65 km just north of the high Himalayas to about 85 km beneath Lhasa.

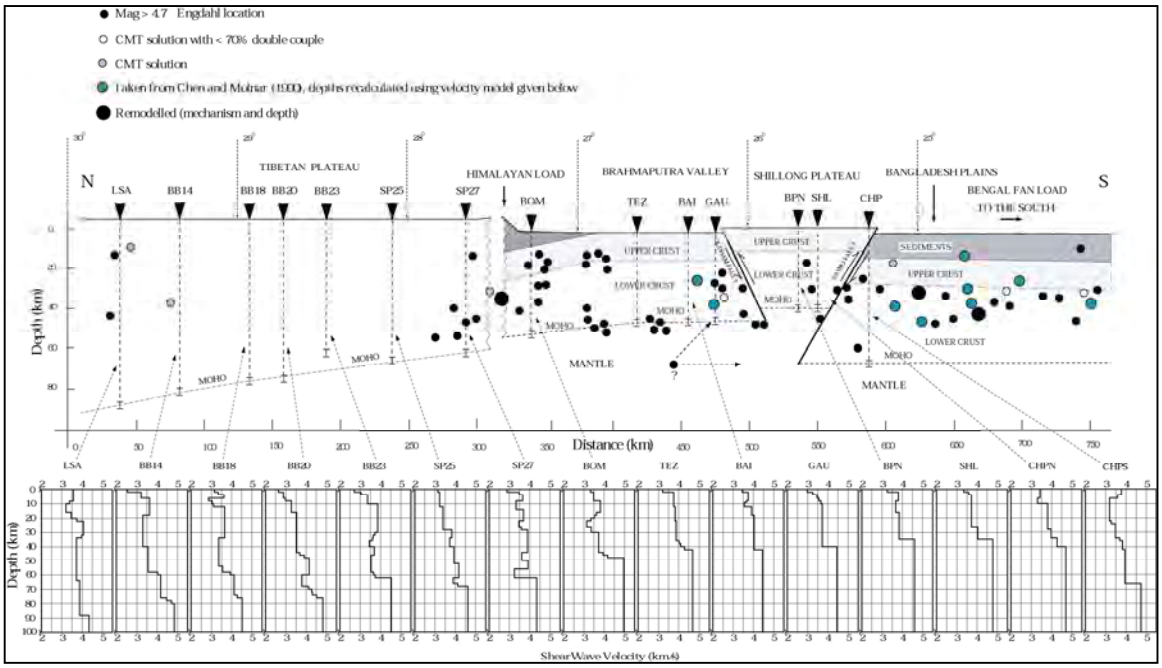


Figure 4. Schematic N-S profile from the Southern Tibetan plateau to the Bengal basin. The stations are marked with inverted triangles and the depth to the Moho at the 7 sites being used as a guide to interpolate the northward dip and pop-up of the Shillong plateau. (From Mitra et al, 2003)

Seismic structure of India from regional waveform matching

We use regional seismic waveforms to determine the velocity structure using a neighborhood algorithm adaptive grid search procedure and reflectivity synthetics to model seismograms from regional earthquakes recorded on these seismographs, FSDN seismographs, and seismographs operated by the Indian Meteorological Department (Figure 5). This procedure results in 1-D path average crust and upper mantle velocity and attenuation models whose propagation characteristics closely match that of the real Earth.

We use an adaptive forward modeling approach, which efficiently samples the entire data space of Earth parameters we wish to model, and closes in on the minimum-misfit solution. This approach is similar to the neighborhood algorithm of Sambridge (1999) (Figure 6). The number of Earth parameters modeled, and the ranges within which they are allowed to vary, depend strongly on the sensitivity of the data itself. We have created an Earth Model Framework (EMF) which allows us to specify our model as a set of uniform or gradient layers with interfaces that can be fixed or mobile (Figure 7). Furthermore, we allow any subset of Earth parameters to be defined for each layer, and calculate the undefined parameters using standard relationships. Any parameter that has been explicitly set may be used by the

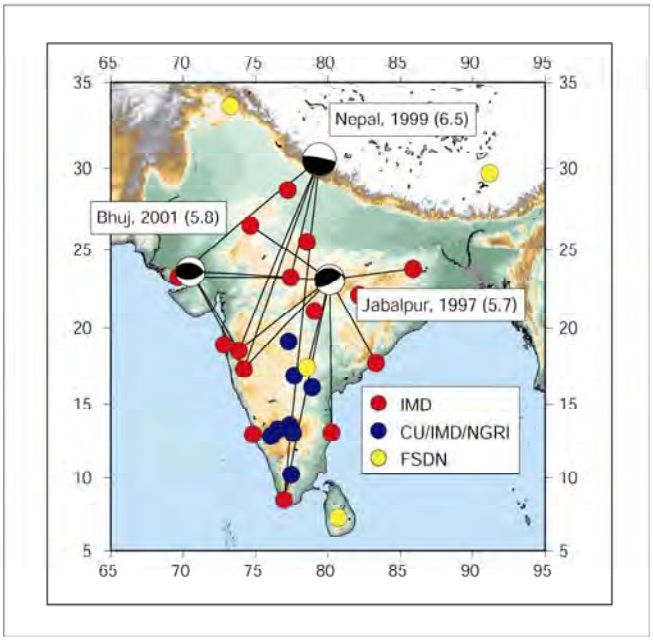


Figure 5. Topographic map of India with earthquakes studied and seismograph stations used. Stations are color coded according to network. Focal mechanisms for earthquakes from Harvard CMT. The paths modeled in this study are shown in black. (From Maggi et al, 2002).

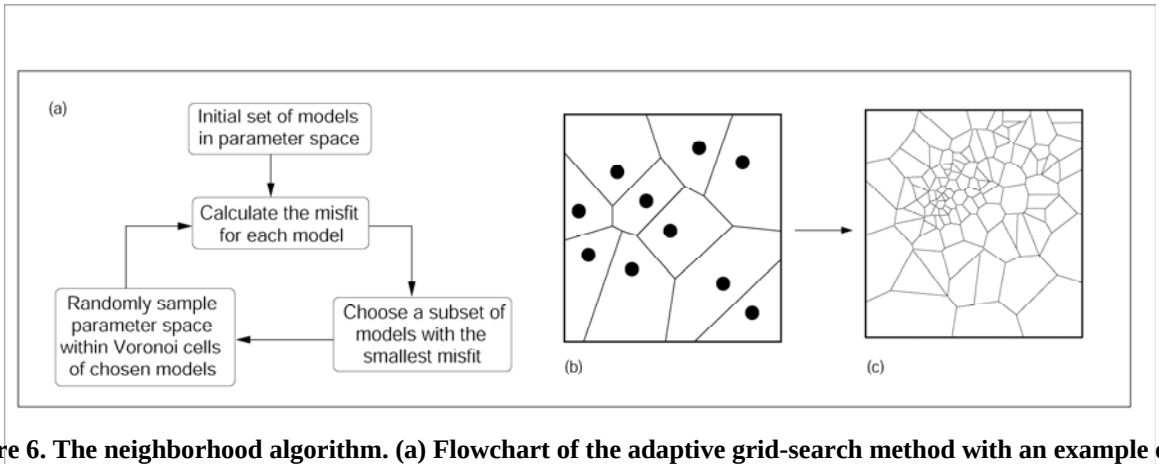


Figure 6. The neighborhood algorithm. (a) Flowchart of the adaptive grid-search method with an example of (b) an initial and (c) final distribution within a parameter space. (b) and (c) are reproduced from Sambridge (1999). (From Maggi et al, 2002).

neighborhood algorithm (NA). Any dependent parameter will be recalculated for each sample. To stop a dependent parameter being used by the NA, we set the upper and lower bounds on that parameter to be identical. The EMF ensures full flexibility of Earth parameter constraints, but also self-consistency within a single Earth model

The portions of the regional waveform that are most influenced by shallow crust and upper mantle Earth structure are the P_nl and the 20-100 s period surface waves. We perform simple synthetic tests (Figure 8) to determine the smallest number of parameters for which it was possible to obtain a good fit to the seismograms, and also to quantify the influence of the resulting 1-D Earth models of error in the earthquake source parameters. P_nl and 50-100 s surface waves do not allow us to differentiate between a two-layer crust and a gradient (Figure 8). Note that large errors in origin time (and by extension epicentral location) can substantially affect the resulting 1-D Earth model. For each path we simultaneously fit vertical component P_nl and surface waves. We choose the time and frequency window individually for each seismogram (Figure 9). Figure 10 depicts the 1-D Earth models we obtained by adaptive grid searching. We searched for models with a gradient crust over a uniform mantle for all paths, and parameterized both Vs and Moho depth. Most paths are well-modeled by a gradient crust over a half-space. The integrated crustal thickness over the path varies from close to 50 km for northern India to 35-40 km for central and southern India (Figure 11).

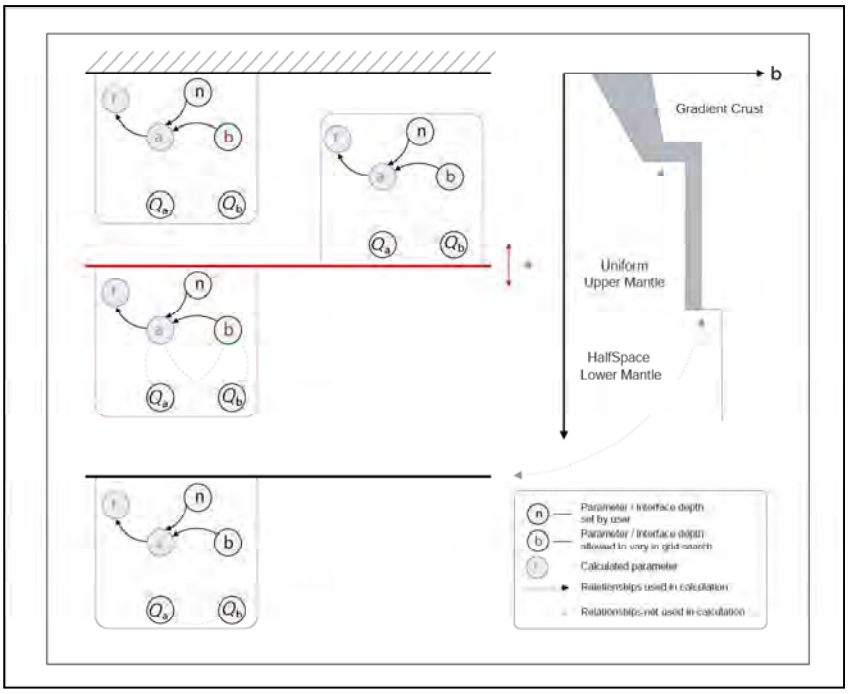


Figure 7. The Earth Model Framework (EMF). The Earth model is made up of horizontal layers that can have uniform parameters (in the example the upper and lower mantle), or gradients in parameters (the crust), and that can have fixed or mobile interfaces (the Moho). Relationships between parameters are shown by faint grey lines, or by thick black lines if they are used in the calculation of dependent parameters. (From Maggi et al, 2002).

We find that the structure of the Indian shield is both simple and uniform, and that both $P_n l$ and the surface wave portions of most of the regional seismograms are well-matched by reflectivity synthetics for a half-space mantle (β ~ 4.65 km/s) overlain by a crust with a linear gradient in shear wave velocity between 3.0-3.6 km/s at the surface and 3.8-4.2 km/s at the Moho at 35 to 40 km depth. The two, circled models in figure 10 above seem to have too large a crustal thickness compares to other models. Their two paths are both for a large proportion of their length within the sediment-filled foreland deep of the Himalayas. Therefore, it is possible that a gradient crust is no longer a good approximation to the 1-D structure, and a two-layer crust is required.

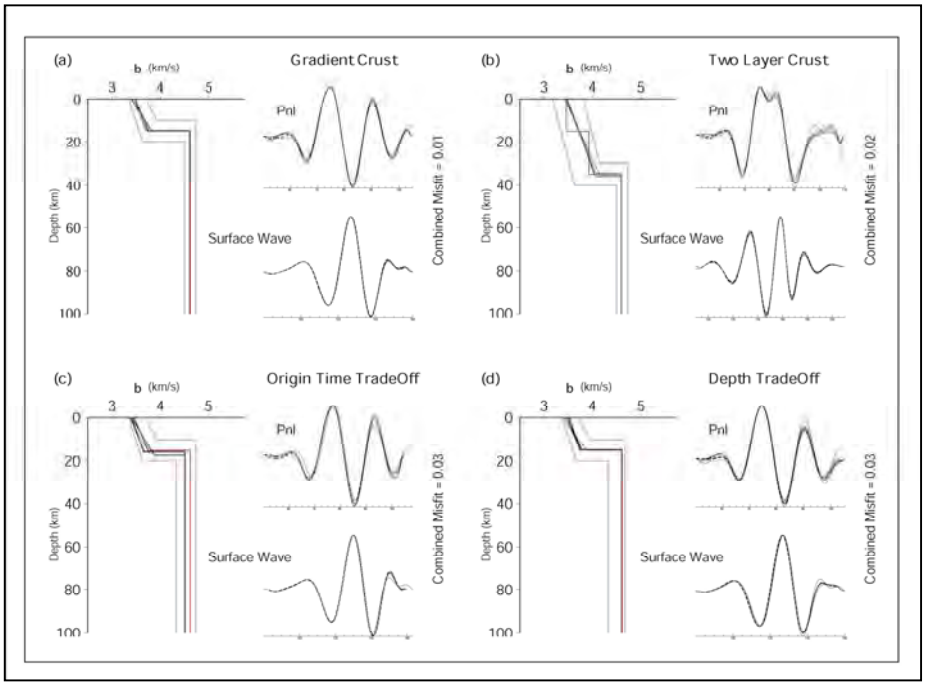


Figure 8. Synthetic test. (a) Retrieval of a gradient crust starting model assuming a gradient crust. (b) Fitting synthetics created using a two-layer crust model with a gradient crust model. (c) Trade-of test for origin time (dt = 3 sec). (d) Trade-off test for depth (dh = 10 km). (From Maggi et al, 2002)

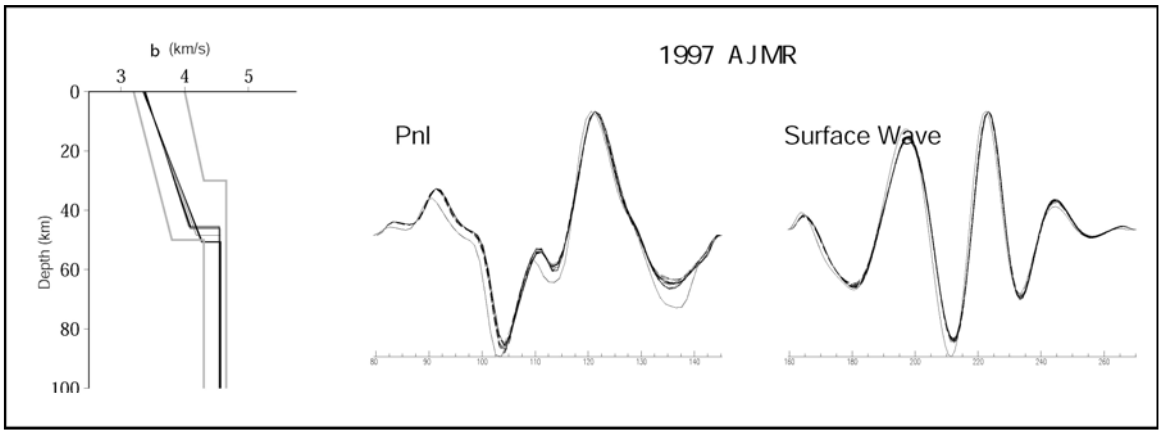


Figure 9. Example result. The Earth model panel shows all models whose misfit is within 5% of the best misfit. Similarly, the best 5\% seismograms fits are shown for the P_nl and surface wave. (From Maggi et al, 2002).

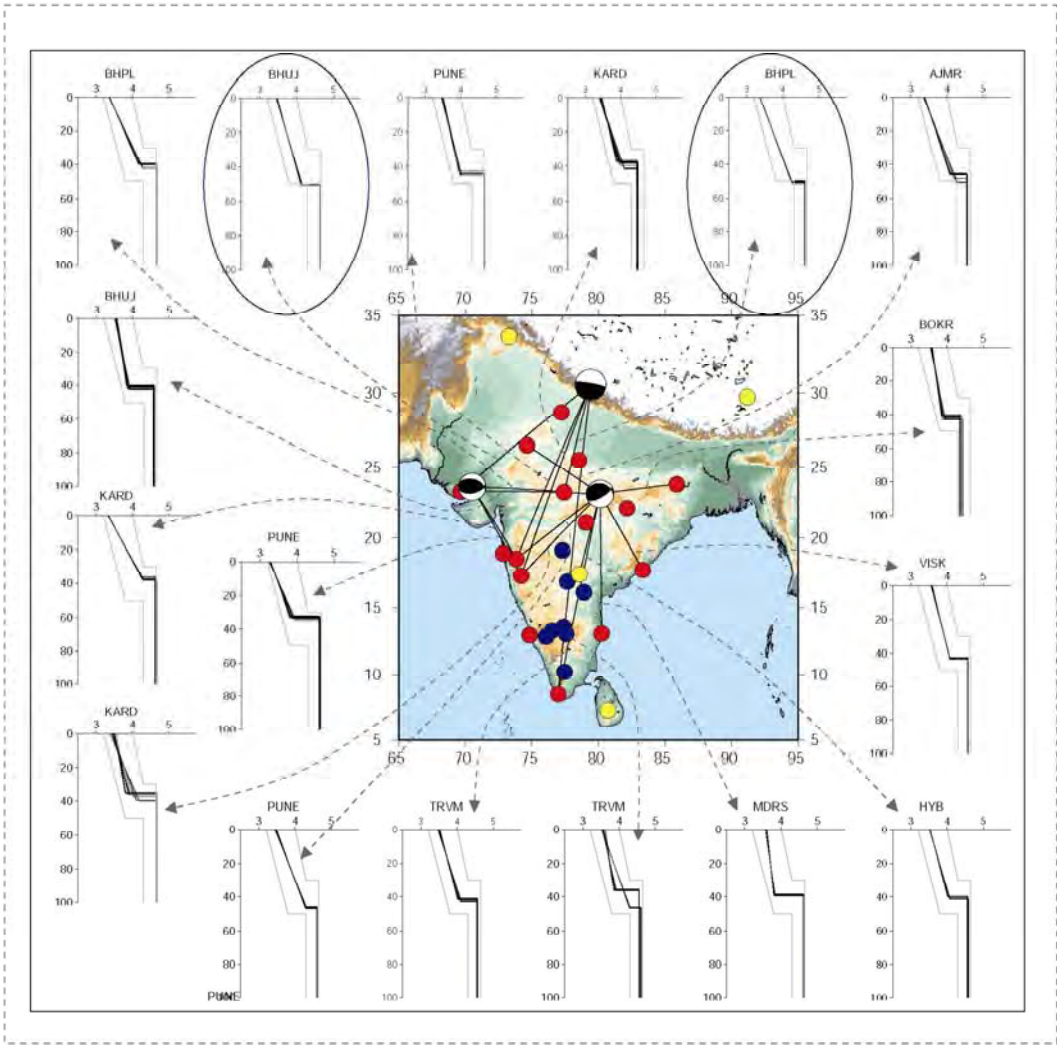


Figure 10. 1-D results. All 1-D profiles show shear wave velocity Vs (km/sec) against depth (km). (From Maggi et al, 2002).

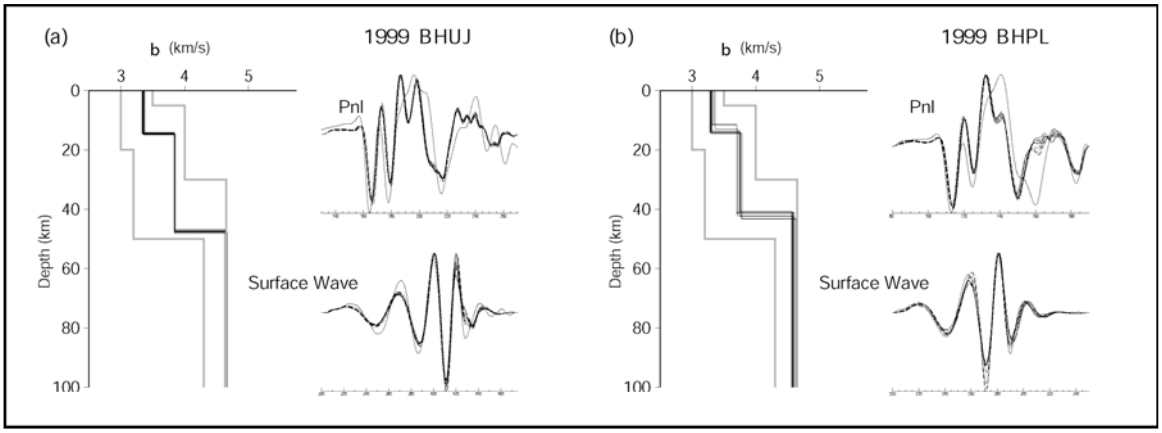


Figure 11. Two layer crust adaptive grid-search for (a) the 1999 - BHUJ and (b) the 1999 - BHPL paths. (From Maggi et al, 2002).

Measurements of frequency dependent *Lg* attenuation in India

We measure the spatial decay of spectral amplitudes of the higher-mode seismic surface wave train *Lg* for the Indian Peninsula. The shield area can be sub-divided into three main Archean cratons- Dharwar, Singhbhum, and Aravali (Figure 12). There is an essential coherence of the entire shield since Late Archean or early Proterozoic. Geophysical studies have confirmed that most of the Indian peninsula has normal crustal thickness (35-40 km), with very small velocity variations in the crust (Kharechko, 1981). The crustal characteristics of the Indian shield are broadly typical of other shield areas in the world.

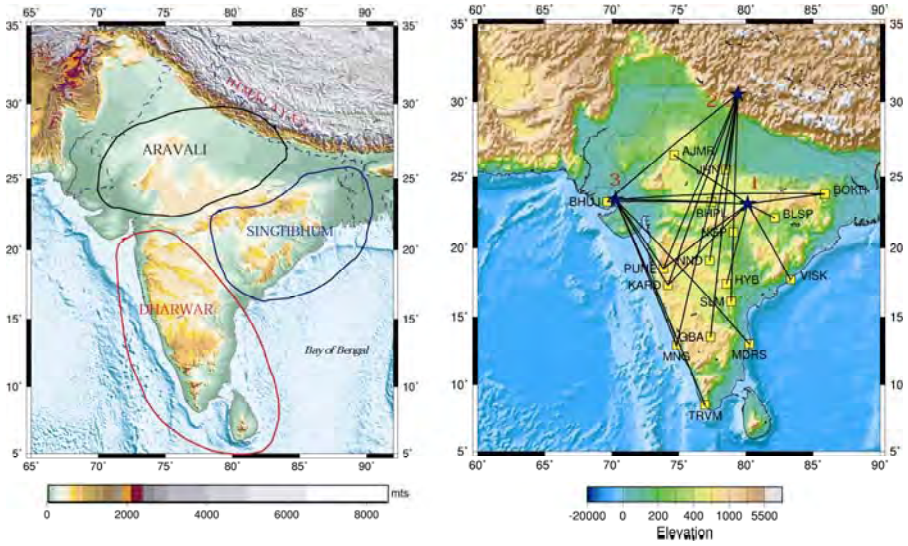


Figure 12. (a) Figure showing the 3 major Archean cratons of the Indian sub-continent, Aravali, Singhbhum and Dharwar. (b) Shows the locations of the earthquakes (1-1997,2-1999,3-2001), seismic stations, and the travel path between them. (From Mitra et al, 2002).

The earthquake data set for this study consists of regional, digital seismograms of 3 earthquakes; one in the Himalayas and two in the Indian sub-continent. The data were recorded at several stations operated by NGRI, Cambridge University, Indian Institute of Astrophysics and the Indian Meteorological Department in the sub-continent (Figure 12). We selected events that were recorded by at least three of the stations and covered a large range of epicentral distances. The travel paths provided a good sampling of the Indian sub-continental crust.

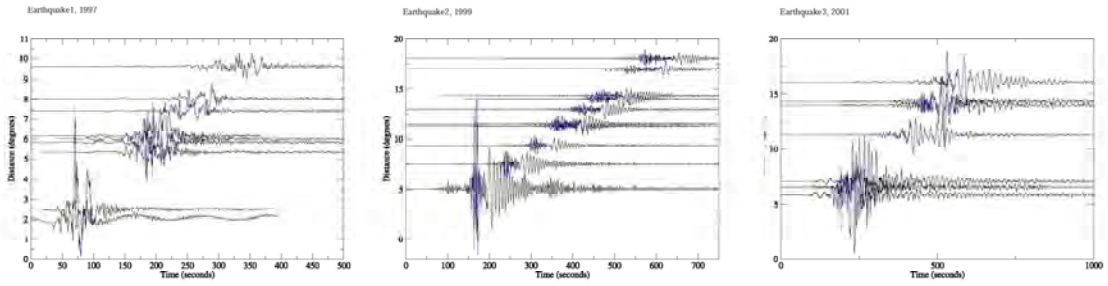


Figure 13. Record section plots of the 3 earthquakes used for the analysis. The velocity window between 3.6-2.8 km/s is colored blue on the seismograms. (From Maggi et al, 2002).

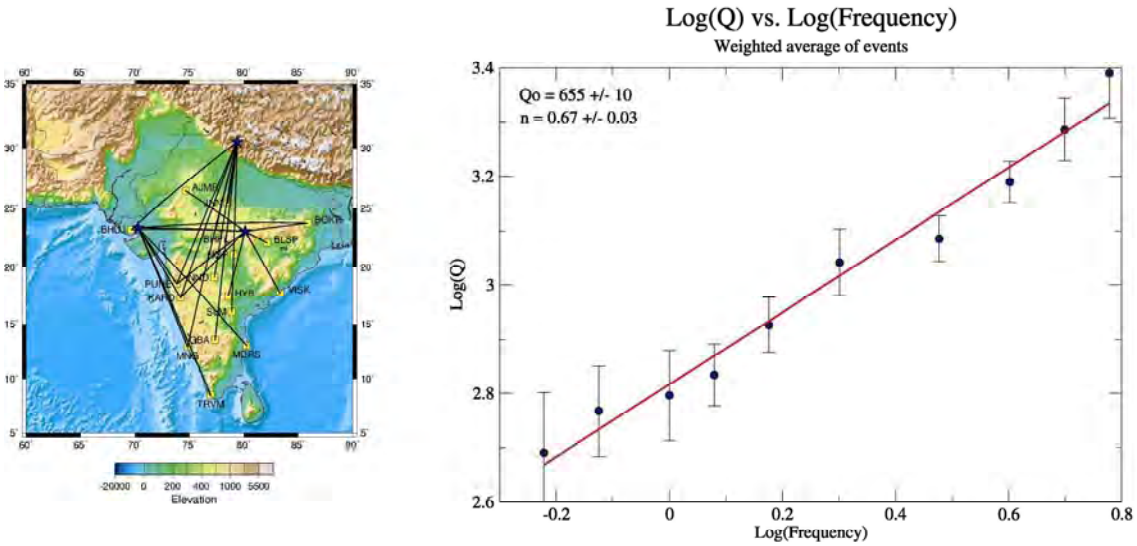


Figure 14. Left-travel paths for all three events. Right-Plot of weighted Average Log Q vs. Log f. (From Maggi et al, 2002).

We determine shear wave attenuation structure of the southern and central Indian shield region through spectral amplitude measurements of *Lg*. *Lg* in vertical component is extracted using a velocity window 3.6-2.8 km/s (Figure 13). Spectral amplitudes of *Lg* are measured on the vertical component in the frequency range 0.6-6 Hz. Amplitude as a function of frequency (*f*) and epicentral distance (*R*) of *Lg* can be expressed as:

$$A(R, f) = \frac{S(f)}{G(R)} * e^{\frac{-\pi f R}{vQ}} \qquad (1)$$

where *S(f)* is the source term, *G(R)* the geometrical spreading, $\sqrt{R}$, v the average velocity, 3.5 km/s, and *Q* is the attenuation quality factor. We take $\log_{10}$ of the amplitude equation yielding:

$$\log_{10} A + 0.5 \log_{10} R = \log_{10} S - \frac{\log_{10} e \pi f}{vQ} R \qquad (2)$$

For each earthquake, we plot $\log_{10}A + 0.5 \log_{10}R$ versus R and perform a linear regression to find Q at each frequency. We assume frequency dependent Q of the form:

$$Q(f) = Q_0 f^n \tag{3}$$

or

$$\log_{10} Q = \log_{10} Q_0 + n \log_{10} f \tag{4}$$

where Q_o is Q at f = 1 Hz. Linear regression of $\log_{10}Q$ versus f yields values for Q_o and n.

We measure *Lg* spectral attenuation for paths from three large Indian earthquakes sampling the shield structure of India. For the overall Indian shield region, we find an average value of $Q_o = 655 \pm 10$ and $n = 0.67 \pm 0.03$ (Figure 14).

This value is consistent with previous results obtained by Singh et al. (1999) ($Q_o = 508$, $n = 0.48$) for the same region and is similar to the *Lg* attenuation results observed in eastern North America. There was variability in attenuation values for the individual earthquakes, however, we are unable to constrain spatial variations without additional measurements to more precisely determine regional Q_o and n. Future work will focus on analyzing more earthquakes recorded at the IMD and NGRI/IIA/CAM broadband networks.

CONCLUSIONS AND RECOMMENDATIONS

The goal of this project was to deploy a temporary network of seismic stations. The network is now fully operational and a number of important research results have been produced based on the data. It is recommended that this deployment be continued and stations be deployed in other sub-regions of India, in order to acquire a more comprehensive database.

ACKNOWLEDGEMENTS

The authors thank Anca C. Rosca, Jessie L. Bonner, Heather J. Hooper and Delaine T. Reiter for their efforts in completing this project.

REFERENCES

Chavez D.E., and Priestley K.F., 1986,Measurement of frequency dependent Lg attenuation in the great basin; *Geophys. Res. Lett.* Vol-13, (6), 551-554

Kharechko G.E., 1981, Velocity irregularities in the upper crust beneath the Indian shield.; *Geophys. J.* 3(4), 574-579.

Singh et al., 1999, A spectral analysis of the 21 May 1997, Jabalpur, India, earthquake (Mw=5.8) and estimation of ground motion from future earthquakes in the Indian Shield region; *Bull. Seis. Soc. Am.*, 89(6) 1620-1630.

Naqvi S.M. and Rogers J.J.W., The Precambrian Geology of India; Oxford University Press Inc, USA.

DATA COLLECTION IN THE ARABIAN PENINSULA FOR NUCLEAR EXPLOSION MONITORING

Arthur J. Rodgers,[1] Hrvoje Tkalcic,[1] and Abdullah M. S. Al-Amri[2]

Lawrence Livermore National Laboratory[1] and King Saud University[2]

Sponsored by National Nuclear Security Administration
Office of Nonproliferation Research and Engineering
Office of Defense Nuclear Nonproliferation

Contract No. W-7405-Eng-48[1] and DE-FC03-01SF22418[2]

ABSTRACT

We report results from the second year of our project (ROA01-35) to collect seismic event and waveform data recorded in and around the Arabian Peninsula. This effort involves several elements. We have a temporary broadband seismic station operating near the International Monitoring System primary array site in central Saudi Arabia. We recently installed two temporary broadband stations in the United Arab Emirates, which are funded by the National Nuclear Security Administration (NNSA) Office of Nonproliferation and International Security (NA-241). We are working with King Abdulaziz City for Science and Technology to collect and analyze data from the Saudi National Seismic Network, which consists of 37 digital three-component stations (26 broadband and 11 short-period).

We will present results of these efforts including integration of the raw data into the NNSA/LLNL Seismic Research Database and preliminary analysis of event locations and source parameters and inference of earth structure.

OBJECTIVE

The objective of this project is to collect raw waveform and event parameter data for calibration of the Arabian Peninsula and surrounding regions for seismic monitoring. This effort involves several components described below. These include deployment of Lawrence Livermore National Laboratory (LLNL) equipment to the region and collaboration with seismological institutions in the region.

RESEARCH ACCOMPLISHED

During the last year we have made progress toward collecting the raw materials for seismic calibration of the Arabian Peninsula. The scope of this project covers the data collection effort and preliminary analysis. These data are integrated into the LLNL Seismic Research Database (O'Boyle et al., this Proceedings). Currently, we are not funded to analyze the data in this project though some preliminary analysis is being done for quality control. Figure 1 shows our study area and seismic stations considered. The various elements of our project are described below.

Broadband Deployment at IMS Array Site PS38

A broadband three-component seismic station was deployed near the site of the International Monitoring System (IMS) primary array site near Halban, central Saudi Arabia (PS38). LLNL and King Saud University (KSU) jointly deployed the station in January 2002 (Rodgers et al., 2001). KSU serviced the station every 6-8 weeks. Data from this site could be used as surrogate data for the IMS array. Currently the IMS array is not operating, however it is expected that testing will start later this year.

Broadband Deployment in the United Arab Emirates (UAE)

In May 2003 we deployed two broadband three-component seismic stations in the United Arab Emirates (UAE) as part of a joint research project on seismology. This project is funded by NNSA/NA-241. The stations are located near Al-Ain and Fujairah. Figure 2 shows the station locations and map of the UAE and surrounding region. The stations were deployed jointly by LLNL and UAE University in May 2003 (Rodgers et al., 2003).

Each station consists of a Guralp CMG-3T broadband seismometer and Geotech DL24 seismograph recorder. The Guralp CMG-3T seismometers have a broadband response that can sense ground motions from periods between 0.01 Hz (120 sec) and 50 Hz. We set-up the systems to record ground motion at 40 samples/sec. An anti-aliasing filter reduces the useful high frequency pass-band of the system to 16 Hz. Data are written to a 1 Gigabyte microdrive at 30 minute records. Microdrives are collected every 4-6 weeks by UAEU and a copy is sent to LLNL for archival.

Cooperation with KACST

The Saudi Arabian National Seismic Network is operated by King Abdulaziz City for Science and Technology KACST), based in Riyadh. This network features 26 broadband and 11 short-period three-component seismometers (Figure 1). We are working with KACST to improve velocity models for routine local and regional event locations. Velocity models are being developed for the main geologic/tectonic regions of the Kingdom: the Arabian Shield, Arabian Platform and the Gulf of Aqaba.

Waveform data from the KACST and Kuwait (see below) networks can be used to estimate regional velocity structure and source parameters. Figure 3 shows an example of the utility of these data for source parameter estimation. A moderate sized earthquake occurred in March of 2002 on the Musandam Peninsula in the northern UAE. Earthquakes are quite rare in this area and this event provides an opportunity to understand the seismotectonics and structure of the region.

Cooperation with KISR

The Kuwait National Seismic Network is operated by the Kuwait Institute for Scientific Research (KISR). This network consists of 1 broadband and 7 short-period stations (Figure 4). Currently we have a small collection of local, regional and teleseismic events for this network. Local events are typically small, mb < 3.0. However a moderately large event occurred in southern Kuwait on December 30, 1997.

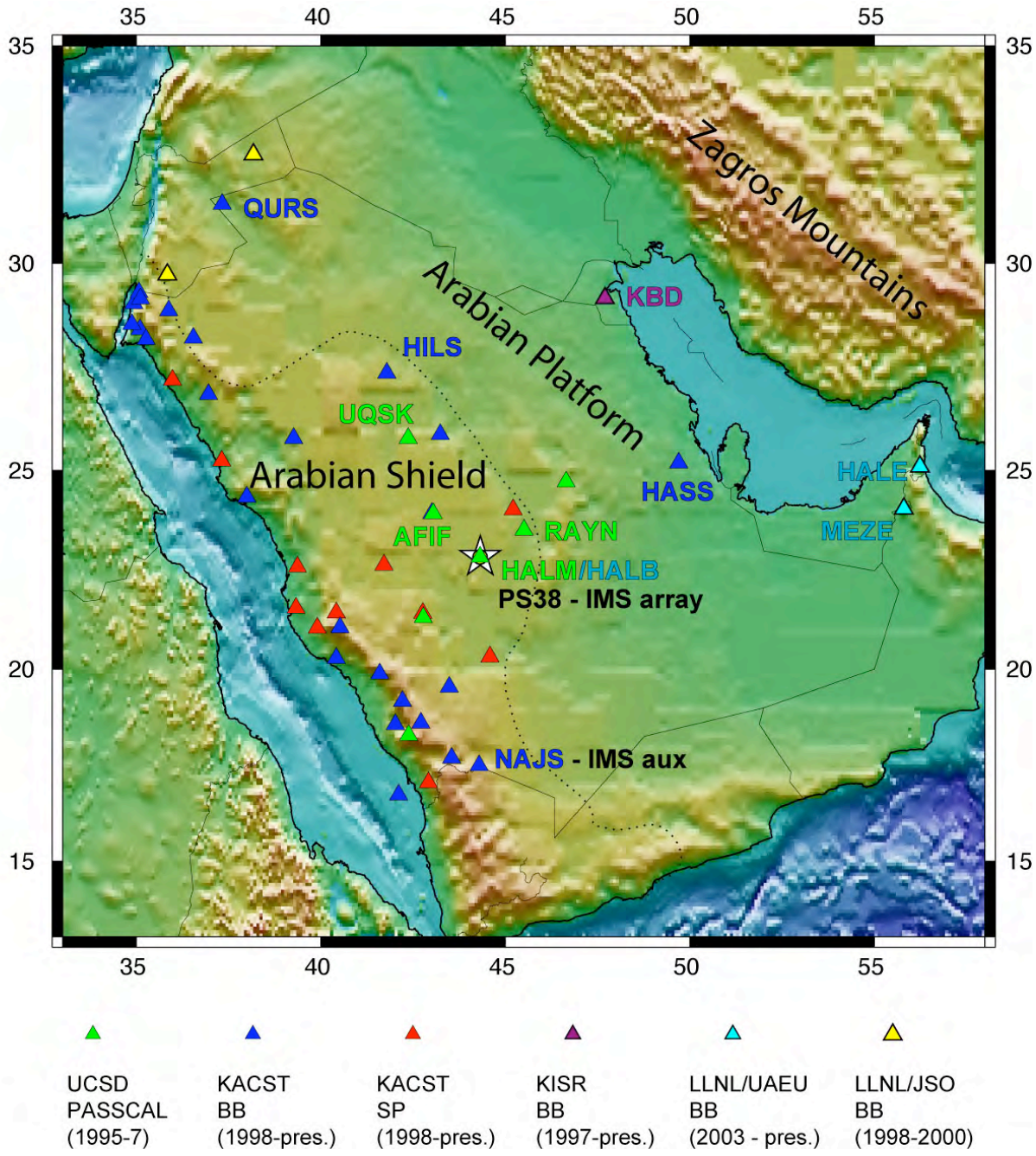


Figure 1. Map of the Arabian Peninsula showing seismic stations considered in this study.

Workshop on Reference Events on/near the Dead Sea Rift

A workshop was help in Paris France October 7-9, 2002 to bring together seismologists from many institutions in Middle East with the specific goal of advancing data exchange and analysis of events along the Gulf of Aqaba and Dead Sea Rift. Participants came from Cyprus, Egypt, France, Israel, Jordan, Lebanon, Saudi Arabia, Turkey, the United Kingdom and the United States. A set of forty-six events was selected before the meeting and data from each participating institution were requested (raw waveform, arrival, event locations, magnitudes, etc…). A map of the events and stations is shown in Figure 5.

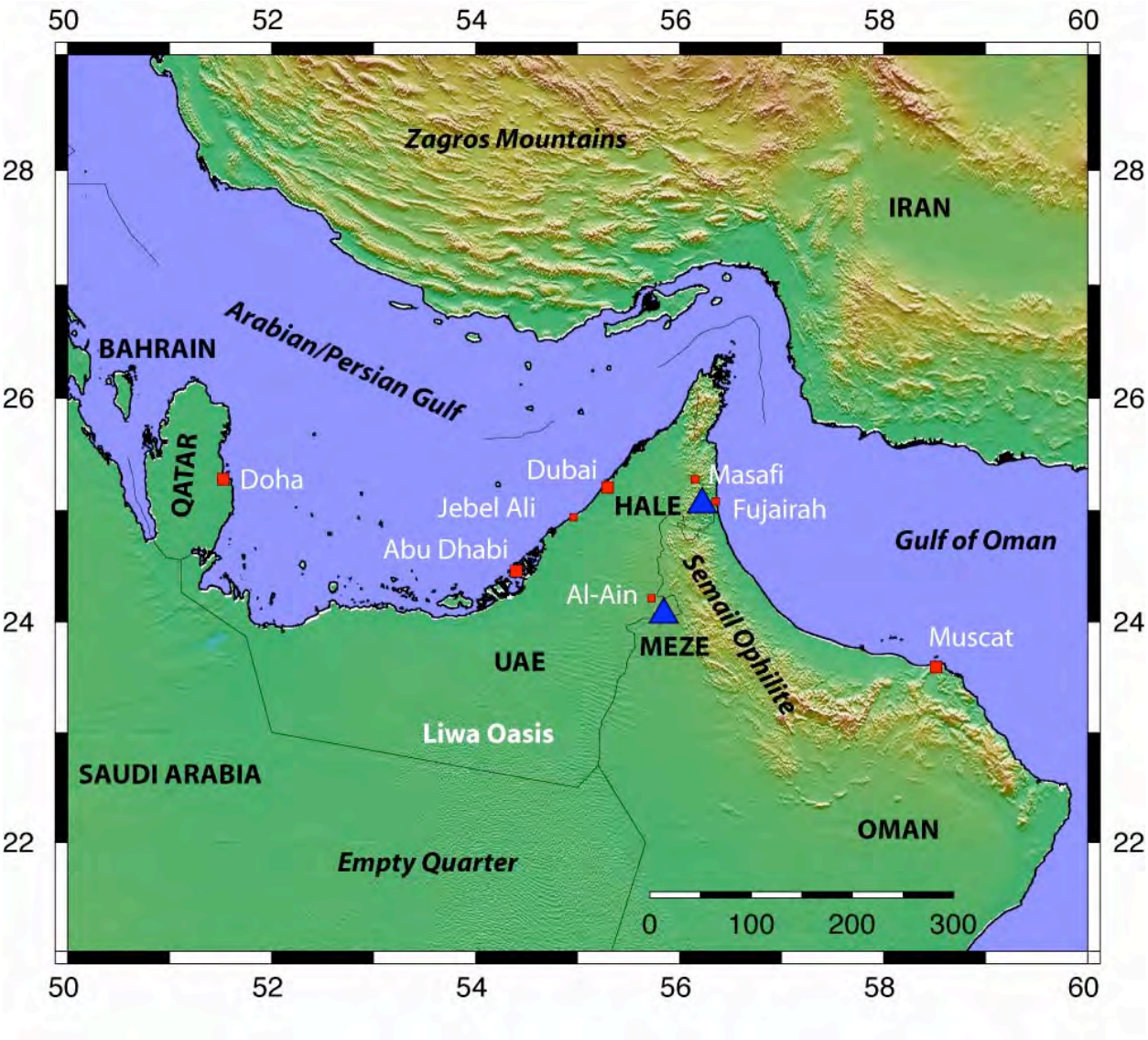


Figure 2. Map showing the locations of the two LLNL-UAEU broadband seismic stations (MEZE and HALE) in the UAE.

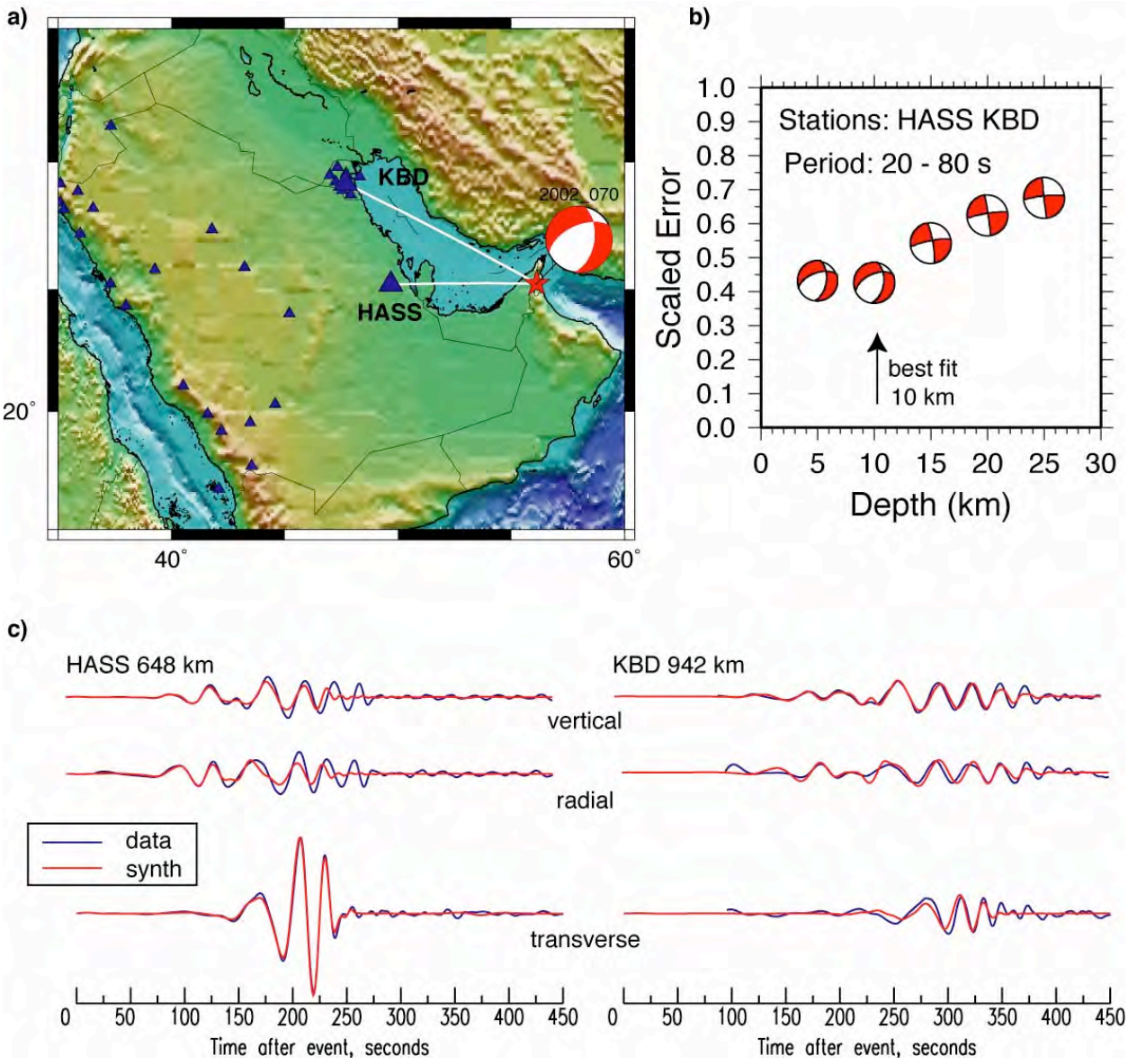


Figure 3. Analysis of the March 11, 2002 Musadam Peninsula earthquake. (a) Map showing the event location (star) from the USGS-PDE. Stations used in the source parameter estimation are shown as large triangles. Also shown are stations from the KACST network for which we have waveform data (small triangles). (b) Depth-focal mechanism-misfit curve estimated from broadband complete waveform modeling using stations HASS (eastern Saudi Arabia) and KDB (Kuwait). The best-fitting depth is 10 km. (c) Observed and synthetic waveforms for the best-fitting source model at stations HASS and KBD. Data and synthetic were filtered between 20-80 seconds.

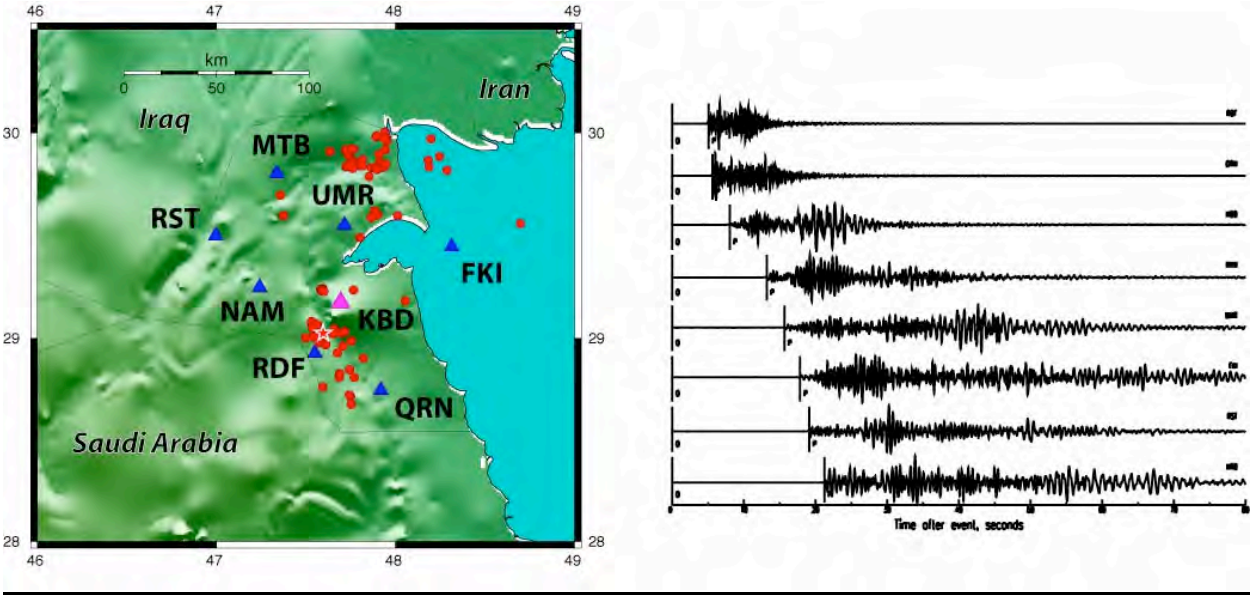


Figure 4. (left) Kuwait National Seismic Network stations (triangles). The broadband station, KBD is shown in magenta. Also shown are local events and the M 4.3 Minagaish event (Dec. 30, 1997). (right) Vertical component waveforms (unfiltered) for the Minagish event, sorted by distance.

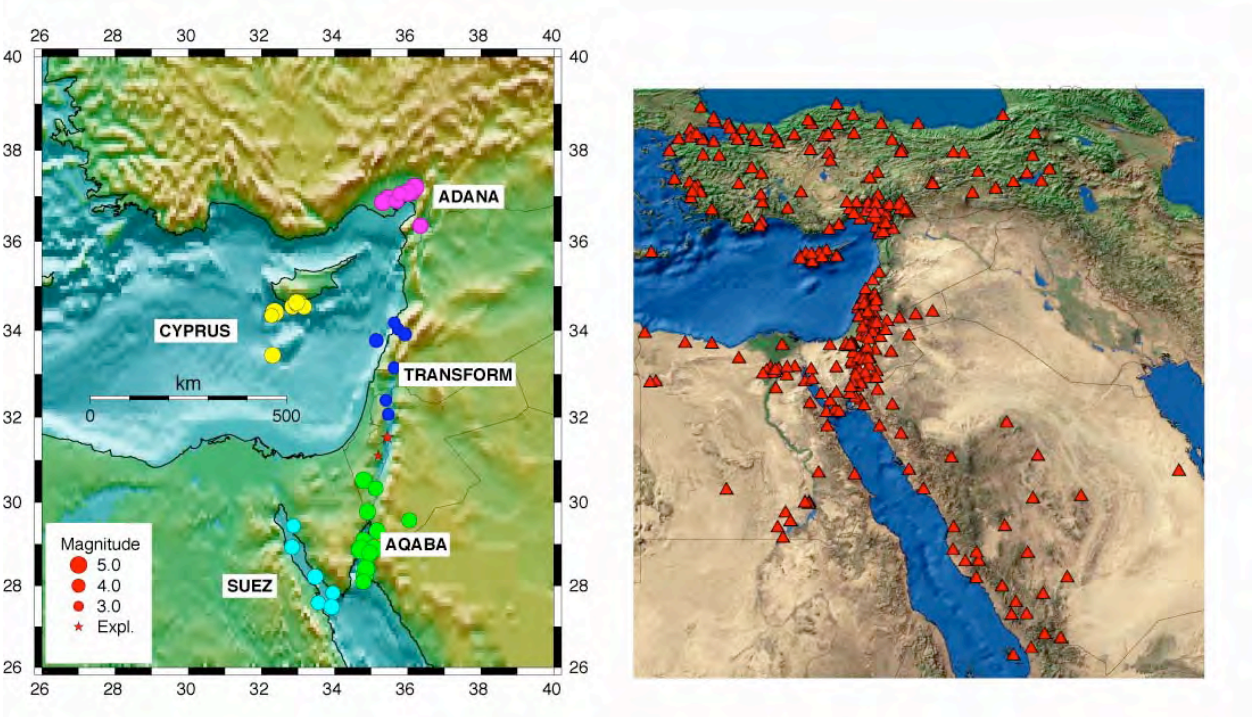


Figure 5. (left) Events selected for the Paris Workshop. (right) Stations that contributed waveform, arrival and/or location data for the Paris Workshop.

CONCLUSIONS AND RECOMMENDATIONS

Data collected in the Arabian Peninsula is a valuable resource. This region is vast yet has only a few seismic stations openly distributing data. Many studies have demonstrated the complex propagation characteristics of high-frequency regional phases, suggesting additional data will deepen understanding of regional phase behavior Rodgers et al., 1997; Mellors et al., 1999). Models exists for sediment and crustal thickness (Sandvol et al., 1998; Rodgers et al., 1999), however little broadband data has been available for evaluation of these models.

ACKNOWLEDGEMENTS

Data was integrated into the LLNL Seismic Research Database by Stanley D. Ruppert, Jennifer L. O'Boyle, Teresa (Terri) F. Hauk and Douglas A. Dodge. Keith K. Nakanishi and Cindy Lersten assisted in the planning of the UAE Deployment. Pat Lewis traveled to the UAE to deployed the two broadband stations. Donald W. Rock prepared the Lawrence Livermore seismic equipment and facilitated the loan agreements.

REFERENCES

Al-Amri, A. M. S. (1999b). The crustal and upper-mantle structure of the interior Arabian platform, *Geophys. J. Int*., **136**, 421-430.

Mellors, R., F. Vernon, V. Camp, A, Al-Amri, A. Gharib and M. Al-Dial (1999). Regional waveform propagation in the Saudi Arabian Peninsula, *J. Geophys. Res*.

O'Boyle, J., S. Ruppert, T. Hauk, D. Dodge, M. Ganzberger and F. Ryall, Middle East, North Africa and Western Eurasia Seismic Research Database, *Proceedings of the 25th Seismic Research Review*, Tucson, AZ.

Rodgers, A., J. Ni and T. Hearn (1997). Propagation characteristics of short-period Sn and Lg in the Middle East, *Bull. Seism. Soc. Am*., **87**, 396-413.

Rodgers, A., W. Walter, R. Mellors, A. Al-Amri and Y. Zhang (1999). Lithospheric structure of the Arabian Shield and Platform from complete regional waveform modeling and surface wave group velocities, *Geophys. J Int*., **138**, 871-878.

Rodgers, A., J. P. Lewis and A. M. S. Al-Amri (2002). Broadband seismic station deployment at Hadabat Al-Mahri, Halban Saudi Arabia. Lawrence Livermore National Laboratory Informal Document, UCRL-ID-147211.

Rodgers, A., J. P. Lewis and A. R. Fowler (2003). A Broadband Seismic Deployment in the United Arab Emirates, Lawrence Livermore National Laboratory Informal Document, UCRL-ID-153713.

Sandvol, E., D. Seber, A. Calvert and M. Barazangi (1998). Grid search modeling of receiver functions: Implications for crustal structure in the Middle East and North Africa, *J. Geophys. Res.*, **103**, 26,899-26917.

IMPROVED SURFACE WAVE DISPERSION MODELS AND AMPLITUDE MEASUREMENTS

Jeffry L. Stevens, David A. Adams, and Mariana G. Eneva

Science Applications International Corporation

Sponsored by Air Force Research Laboratory

Contract No. DTRA01-01-C-0082

ABSTRACT

Surface waves are of primary importance for nuclear monitoring because the M_s:m_b discriminant and its regional variants are among the most reliable means of determining whether an event is an earthquake or an explosion. The primary goal of this project is to reduce the magnitude threshold for which surface waves can be identified and measured reliably and to improve the accuracy of surface wave measurement using phase-matched filtering and global regionalized earth and dispersion models.

Global regionalized earth and dispersion models are being developed by inversion of a very large data set of phase and group velocity dispersion measurements. The complete data set now contains over one million dispersion data points. The dispersion measurements are inverted for earth structure, and the earth structure is then used to generate dispersion predictions. This is accomplished in the following way. The inversion is performed for approximately 600 distinct base structures, which were originally derived from the Crust 2.0 models over the AK135 mantle model. The Moho depth, bathymetry, and sediment depths vary on a one-degree grid. Moho depths are derived from Crust 2.0, sediment depths from the Laske and Masters sediment maps, and bathymetry from ETOPO5. Moho depth, bathymetry, and sediment properties are fixed in the inversion, while crust and upper mantle velocities are allowed to vary in the base models. Phase and group velocity dispersion curves are calculated for each of 64,800 models on the one-degree grid. The phase velocity dispersion curves are then used to calculate phase-matched filters to improve detection.

One of the difficulties of performing such a large, heterogeneous inversion is finding optimum values for smoothing and damping (regularizing) parameters. This is important because too much smoothing/damping will increase data misfit, and too little will produce unrealistic earth models. In this case, smoothing minimizes the gradient of each structure between specified discontinuities, while damping minimizes the difference between the model and the starting model. Discontinuities occur at the Moho and at the base of the surface sediments. In a few cases where there is sufficient high frequency information to resolve shallower structure, inversion is performed for deeper sediments, which introduces another discontinuity. A significant improvement in the inversion procedure over the past year has been the introduction of the capability to vary damping and smoothing parameters for each model. This allows us to improve the data fit for many models, while still retaining realistic earth models in all areas. We are performing 2D inversions (inversion of dispersion at discrete frequencies to form spatial dispersion maps) to identify regions where additional parameterization is needed in the 3D inversions. The additional parameterization takes the form of introduction of new base structures, merging of base structures, or adjustments to boundaries between base structures.

In addition to improving earth and dispersion models, we have implemented and tested procedures for measuring surface wave amplitudes at short periods (5-15 seconds) and at regional distances. We are identifying optimum procedures for measuring path corrected spectral magnitudes and then comparing the results with other procedures, such as Marshall-Basham amplitude corrections, which were designed to correct time domain amplitudes for frequency and structure dependence. Path corrected spectral magnitudes should be independent of distance and only weakly dependent on frequency for shallow events. At higher frequencies and longer distances the amplitude correction depends on having accurate Q models. We find that the best procedure is to measure surface wave amplitudes at periods greater than 14 seconds at all distance ranges for three reasons: 1) earthquake spectra tend to decrease with frequency, degrading discrimination; 2) unlike time domain measurements, spectral measurements can be made accurately at lower frequencies at close distances; and 3) S/N remains higher at periods greater than 14 seconds even for very close distances.

OBJECTIVE

The goal of this project is to reduce the magnitude threshold for which surface waves can be identified and measured reliably, and to improve the accuracy of surface wave measurement, using phase-matched filtering, development of global regionalized earth and dispersion models, and other techniques.

RESEARCH ACCOMPLISHED

During the second year of this project, we have focused on two topics: improvements to global earth models and dispersion maps, and improved techniques for measuring surface wave amplitudes. During the first year we completed work on implementation and testing of azimuth estimation techniques at three component stations based on polarization analysis (Stevens et al, 2002).

Global Earth Models and Surface Wave Dispersion Maps

To improve the detection (e.g. by phase matched filtering) and measurement of surface waves it is important to make good predictions of their dispersion. In our work, surface wave dispersion predictions are based on dispersion measurements for ray paths from all over the globe. We make these predictions via models of the earth. Alternate methods could be developed which would depend on interpolation schemes, such as kriging and which would not make use of earth models. An important advantage gained from using earth models is that we can include information from other studies leading to physically reasonable constraints on dispersion. For our earth models this information consists of the boundaries between geologic zones, bathymetry of oceans, thicknesses of sediments and ice, Moho depths, and prior estimates of seismic velocities derived from Crust 2.0 and AK 135 earth models. These constraints are especially important for filling in the gaps found in the path coverage of our data set and they enable prediction along paths unlike any of the paths in the data set. We perform by non-linear least squares inversion of the dispersion data for two types of models. First are 3D earth models where the adjustable parameters are the shear wave velocities of layers. Second are 2D group velocity models determined by inverting dispersion measurements made in narrow frequency bands. The 2D models are used as a guide in the parameterization of the 3D earth model.

Description of 3D earth model

The 3D earth model is described briefly here and in greater detail in Stevens et al. (2002). It consists of 1ºx1º blocks and is made up of layers of ice, water, sediments, crust and upper mantle. Currently this model depends on 8918 free parameters, which are adjusted by least squares fitting to Rayleigh wave dispersion data. The free parameters are the S-wave velocities of layers of 572 different model types. Other constrained parameters in the model are P wave velocities, densities and Q. The model types are based on the Crust 2.0 2ºx2º crustal types (Bassin et al., 2000 and Laske et al. 2001) and also on ocean ages (Stevens and Adams, 2000). The top few km of the model (consisting of water, ice and/or sediments) are fixed and match data from one degree bathymetry maps made by averaging Etopo5 five minute measurements of topography, and Laske and Masters (1997) 1 degree maps of sediments. There is an explicit discontinuity between the bottom of the sediments and the crust. There are three or more crustal layers. The Crust 2.0 models, which were the starting point for these structures have three crustal layers, but we found it necessary to add more layers in regions of thick crust. There is another explicit discontinuity at the Crust/Mantle boundary. The Moho depth is derived from Crust 2.0 and varies on a 2º grid. The mantle starting model is derived from AK135 (Kennett, et al, 1995). With these constraints, the inversion is performed for the shear velocity of the crust and upper mantle to a depth of 300 km. Below 300 km the earth structure is fixed, and the inversion model is required to be continuous with the mantle structure at the base of the inversion. In broad ocean areas, we replace the Crust 2.0 model with models distinct for each ocean and subdivided by ocean age. We also separate into distinct models Crust 2.0 models that are geographically separated. So, for example, if Crust 2.0 has the same model type in North America and in Asia, we use the same starting model for each, but treat them as separate models in the inversion.

Surface wave dispersion data set

During the second year of our project we added three new sets of dispersion data and improved one already existing set bringing the total number of Rayleigh wave dispersion measurements with frequencies greater than or equal to .01 Hz to more than 1,000,000. One new set comes from Los Alamos National Laboratory (Yang et al, 2002) consisting of more than 37,000 dispersion measurements (2009 individual paths) from Central Asia ranging between 0.05 Hz and 0.23 Hz. One other set, not yet reviewed by us, comes from Huang et al (2003) and consists of more than 285,000 data points (9730 paths) from China and another consists of nearly 14,000 our own measurements

from Eurasia. Pre-existing data coming from University of Colorado (Levshin et al, 2002) was improved by relocating events to the hypocenters in Engdahl et al (1998) where possible. Other data already in the data set are described in Stevens et al (2001a,b and 2002). Figure 1 shows the frequency distribution of group velocity measurements in our data set. Phase velocity measurements are dominated by a set coming from the global phase velocity model of Ekstrom et al. (1996), and there are fewer phase velocity measurements at high frequencies.

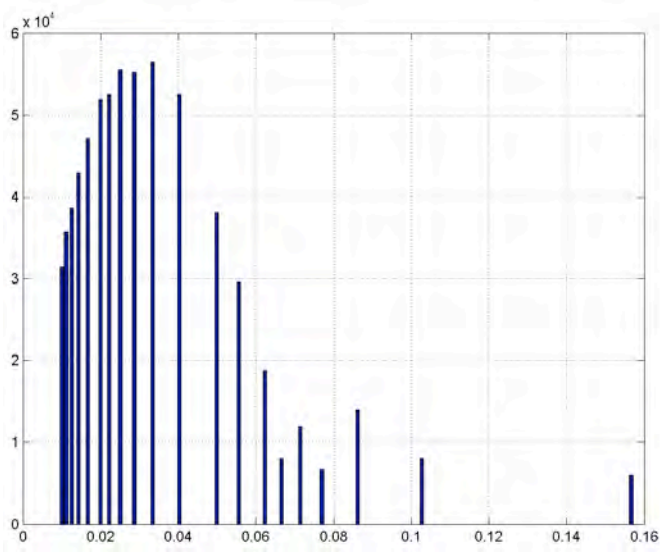


Figure 1. Bar graph of the number of group velocity measurements in each frequency band for all data currently used in the tomographic inversions

The inversion procedure for the 3D earth model

The relationship between dispersion and the shear wave velocities of the layers in the earth model is non-linear, so the shear wave velocities are estimated by non-linear least squares. At each step a system of tomographic equations is formed, augmented by additional equations of constraint and then solved by the LSQR algorithm. The equations solved are

$$\begin{pmatrix} A \\ sH \\ lI \end{pmatrix} \vec{x} = \begin{pmatrix} \vec{l} \\ -sH\vec{x}_0 \\ -l\vec{x}_0 \end{pmatrix} + \vec{e} \quad ,$$

where **x** is the vector of slowness adjustments to the shear wave slownesses of layers in each of the 572 model types. **l** is the vector of slowness differences between predicted and observed dispersion measurements. **e** is the vector of residuals that remain after inversion (the inversion minimizes |**e**|). $\mathbf{x_o}$ is the vector of slownesses estimated in the last iteration. The elements of the matrix **A** consist of partial derivatives of dispersion predictions with respect to shear wave slownesses in each layer. **H** is a difference operator that applies to vertically neighboring layers and has the effect of constraining the vertical smoothness of velocity profile. **s** is the weighting of the importance of the smoothness constraint and can be a diagonal matrix (for variably weighted smoothing) or a scalar (constant smoothing). We have implemented variable smoothing so that a different smoothing parameter can be selected for each model type. Lateral smoothing, which is usually applied in tomography studies, is executed indirectly in our study through selection of the model types. **I** is the identity matrix and **l** weights the damping that constrains the norm of the difference between final slownesses and constraining model slownesses (in our work usually the Crust 2.0 values). **l** can be a scalar for constant damping, or a diagonal matrix for variable damping. As for smoothing, variable damping is implemented so that a different parameter can be selected for each model type.

Regularization and predictions

Choosing regularizing parameters is an essential part of finding a model which best predicts dispersion, since regularization acts both to control the influence of data noise on the estimation of model parameters and to constrain parts of the model that are poorly constrained by data. Too much regularization will make the model too smooth and too little regularization will allow noise to be projected into the model, making it rough. In this study the damping and smoothing constraints and their associated weighting parameters are used to regularize the solution. Techniques for optimization of regularization parameters are not yet mature, especially for large-scale problems such as this. The methods most often described (e.g. Hansen, 1998) are the L-curve, generalized cross validation, and discrepancy principle. In the literature the first two methods are usually applied to smaller scale problems than ours and with only one regularizing parameter, whereas we have at least 2 and possibly many more. The last method mentioned requires a reliable independent estimate of data noise and works by selecting the regularization resulting in the residual based estimate of noise being the same as the independent one. We have experimented with several of these techniques for our inversion problem, but have not found any reliable enough to replace analyst review of the inversion results.

Techniques for evolving earth models

The selection of model types and regularizing parameters are interrelated. For example making a parameterization finer (i.e. adding new model types) without increasing data coverage increases the need for regularization. Our approach for finding a best predictive model has been to start with a small number of model types and increase this number gradually as new data become available or when we detect systematic data misfit. Once a new parameterization is determined, the regularizing parameters are adjusted.

To determine whether there are enough model types, we carry out 2D inversions of group velocity residuals in at least 12 narrow frequency bands to determine group velocity adjustment maps at 1-degree resolution. Each 2D inversion of group velocity residuals is regularized with a damping parameter, which constrains the norm of the group velocity adjustment, and a smoothing parameter which weights a first difference operator that constrains lateral smoothness of the estimated group velocity (i.e. v+dv). We vary these two parameters for each frequency band to find the smoothest looking map that still reduces data misfit reasonably. The resulting maps are examined to find areas of similar adjustment common to most frequency bands, which are then used to delineate new model types.

After the model types are selected the damping and smoothing parameters (scalars, or diagonal matrices) **l** and **s** are adjusted to find a reasonable looking model that still fits the data adequately. Currently we are experimenting with spatially variable regularization using diagonal matrices rather than scalars. We find that the sensitivity of slowness adjustments to scalar regularization parameter settings is not uniform and depends on model type. In other words when comparing adjustments for different combinations of scalar pairs (s, l), there is much less variation for some model types than others (see for example Figure 2). The strategy we are now developing is to relax regularization for those types that are relatively insensitive to regularization, and to increase it for those model types that are too sensitive to it.

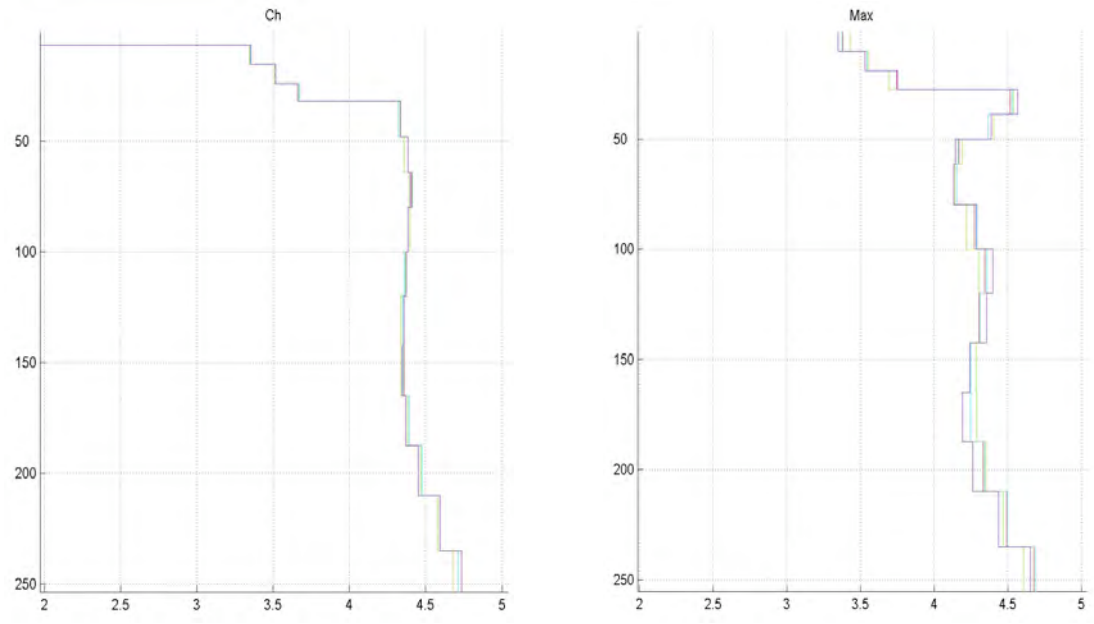


Figure 2. Shear velocity profiles for two model types: less sensitive to regularization on the left and more sensitive on the right. Ch is from the Yellow Sea and Max is from North East of Mexico. The different structures correspond to different combinations of the scalar regularization parameters s and l.

Data statistics for best current 3D earth model

The means and standard deviations of normalized group velocity residuals, $1-v_o/v_p$, where v_o and v_p are observed and model predicted group velocities, were calculated for narrow frequency bands and are shown in Figure 3. Solid is

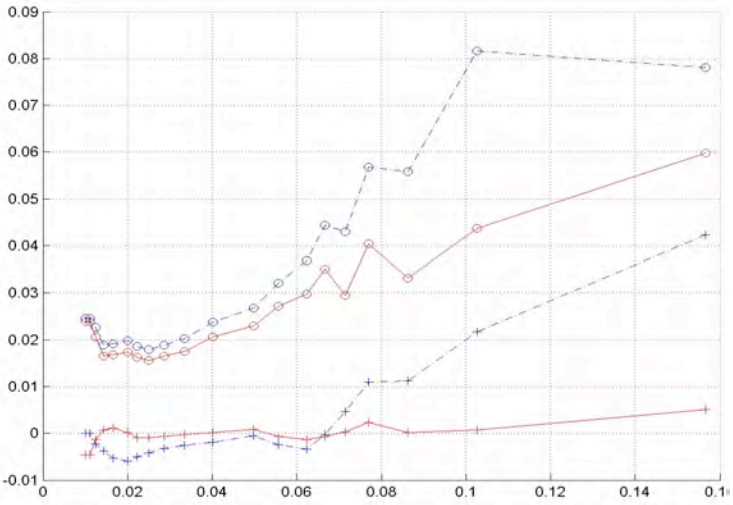


Figure 3. Standard deviations (o) and means (+) of normalized group velocity residuals are plotted against frequency for 1degree earth model (solid red) and 5-degree earth model (dashed blue).

for our best 1-degree model, and dashed is for the best 5-degree model (e.g. Stevens and Adams, 2000) based on Crust 5.1 (Mooney, et al., 1998). Figure 3 shows the value of the 1-degree model, especially for high frequencies.

Optimization of Surface Wave Amplitude Measurements

Surface wave measurements traditionally are accomplished by measuring a time domain amplitude at a period near 20 seconds. This procedure is problematic at regional distances because the surface wave is not well dispersed and a distinct 20-second arrival may not be present. It is possible to measure time domain amplitudes at higher frequencies with corrections (e.g. Marshall and Basham, 1972), however measurements may be inaccurate due to differences in dispersion caused by differences in earth structure. Stevens and McLaughlin (2001) suggested as an alternative replacing time domain measurements with a path corrected spectral magnitude. The path corrected spectral magnitude is calculated by dividing the observed surface wave spectrum by the Green's function for an explosion of unit moment. The path corrected spectral magnitude is the logarithm of this ratio, and can be estimated over any desired frequency band. This path corrected spectral magnitude is denoted by $\log M_0$.

The advantages of using $\log M_0$ instead of the traditional surface wave magnitude M_s are that $\log M_0$ is insensitive to dispersion, independent of distance, works well at regional distances, and is inherently regionalizeable. Regionalized path corrected spectral magnitudes incorporate geographic variations in source excitation and attenuation. Furthermore, as discussed below, it can in principle be measured over different frequency bands to optimize the signal-to-noise ratio. M_s and $\log M_0$ share some limitations: spectra from earthquakes vary due to source mechanism and depth, and errors can occur if the measurement is made in a spectral dip or at high frequencies for a deep event. Azimuthal variations in amplitude caused by focal mechanism also affect the amplitudes of both $\log M_0$ and M_s.

The test cases discussed by Stevens and McLaughlin (2001) used a frequency band of 0.02-0.05 Hz (50-20 s) to estimate the spectral magnitudes. They estimated that on average, the time domain and spectral magnitudes are related as $\log M_0 = M_s + 11.25$. Most of the waveforms in that work were recorded at distances exceeding 8^0. Due to the relatively flat spectra over the 0.02-0.05 Hz band for most data, this choice worked quite well. The authors noted, however, that higher frequencies might be required for shorter paths. An important observation was that the $\log M_0$ residuals are independent of distance, despite the simple Q models used in the earth structures.

In the present work we focus on the utility of higher frequencies in estimating spectral magnitudes of smaller events, recorded at smaller distances. The purpose is to optimize the spectral magnitude estimates, to test their distance and frequency independence, and to identify any measurement problems or pitfalls. For large amplitude signals we can expect the lower frequencies to be better in general, particularly at larger distances due to greater attenuation at higher frequencies. Our hypothesis at the initiation of this study was that using higher frequencies for measuring spectral magnitudes at shorter distances would optimize signal to noise ratio and therefore be better for measuring surface waves at regional distances, however as discussed below this is only true to a limited extent.

To optimize the measurement procedures and examine the performance of the path corrected spectral magnitude at regional distances, we use 584 spectra from 76 earthquakes and 11 explosions in the Lop Nor area (Figure 4). Additional spectra are available from these events, but only the above spectra were deemed to be of good quality. This means that they passed the dispersion test described by Stevens and McLaughlin (2001) and were checked for certain anomalies such as incorrect instrument calibrations. Approximately 11% of the spectra used for the $\log M_0$ estimates originate from records at source-station distances of 5^0 or less, and another 11% at distances of 30^0 or greater. Thus the bulk of the data comes from intermediate distances. Figure 5 shows examples of explosion and earthquake

path corrected spectra from Lop Nor at various distances. The tendency of the explosion spectra to be relatively flat over more extended frequency bands compared with earthquake spectra is evident. This is expected because 1) the spectra are corrected by an explosion Green's function that flattens earthquake spectra imperfectly, and 2) the earthquake spectra have frequency variations caused by source mechanism and depth.

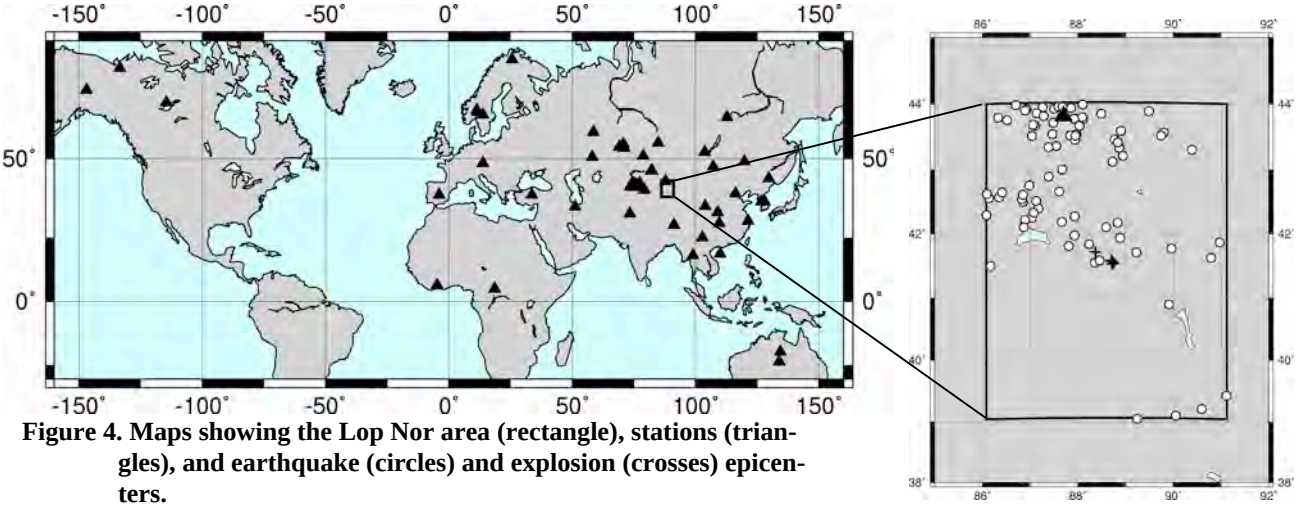


Figure 4. Maps showing the Lop Nor area (rectangle), stations (triangles), and earthquake (circles) and explosion (crosses) epicenters.

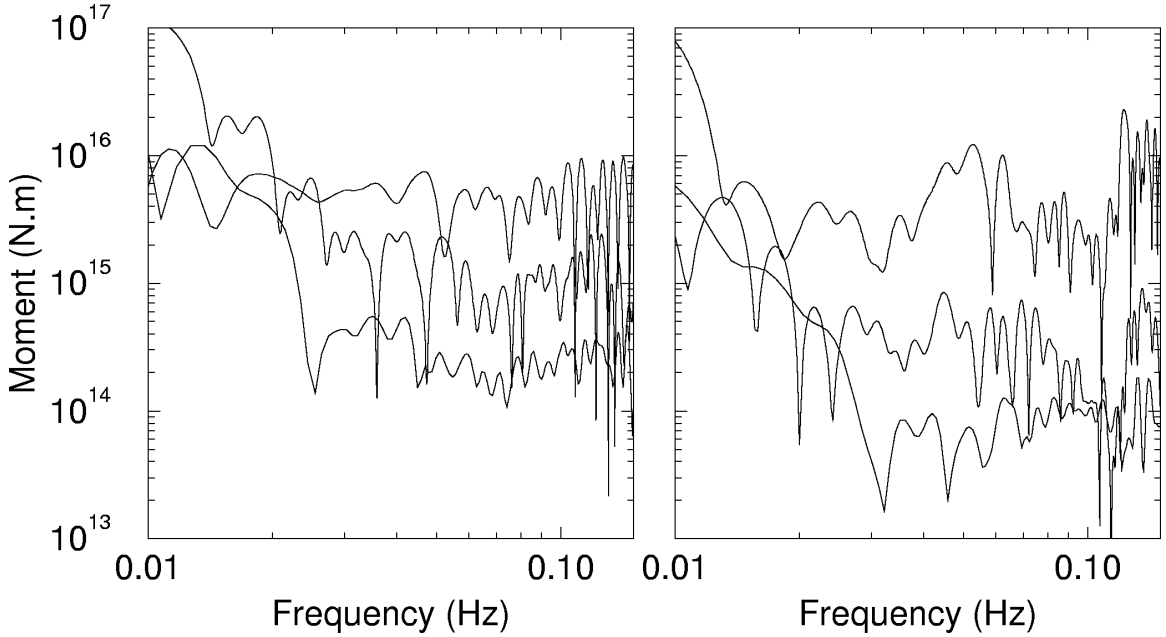


Figure 5. Examples of path corrected spectra used in this work: (a) Lop Nor explosions recorded at distances of 2°, 7° and 67° (left); (b) Lop Nor earthquakes recorded at distances of 0.4°, 22° and 65° (right). See examples of station logM_0 estimates in Table 1. S/N is good at all but the highest frequencies. Instrument responses are uncertain below 0.02 Hz.

We calculated individual spectral magnitudes (i.e., several station magnitudes per event) over all possible frequency bands between 0.02 Hz (50 s) and 0.15 Hz (~7s), with bandwidths of 0.03 Hz, 0.04 Hz, etc., up to 0.13 Hz for the 0.02-0.15 Hz band. This procedure provided 153 bands to examine from each spectrum. In the search for the most robust spectral magnitude estimate, four different methods were used as follows.

1. Calculating a "simple" mean of the logarithms of all path corrected amplitude measurements made in a given frequency band. This is comparable to Stevens and McLaughlin's (2001) estimates in the 0.02-0.05 Hz band.

2. Iteratively calculating a "robust" mean, by rejecting outliers outside two standard deviations from the mean calculated at each step. The procedure ends when all measurements remain within two standard deviations or when half of the amplitude measurements in a frequency band are rejected, whichever occurs first. Thus the spectral magnitude estimates are much less affected adversely by the tendency of some spectra to sharply vary in amplitude over some frequencies, with most outliers marking anomalously low amplitudes (see Figure 5 above). Figure 6 compares the individual (station) logM_0 estimates from (1) and (2). Standard deviations from the robust-mean method are predictably lower than those in the simple-mean method, as the insets in Figure 6 show.
3. Calculating logM_0 at the center frequency of a least-squares straight line fit to the spectrum over a given frequency band.
4. Same as (3), but the straight line is "robust", minimizing the absolute deviations of the logarithms of the amplitudes from the line.

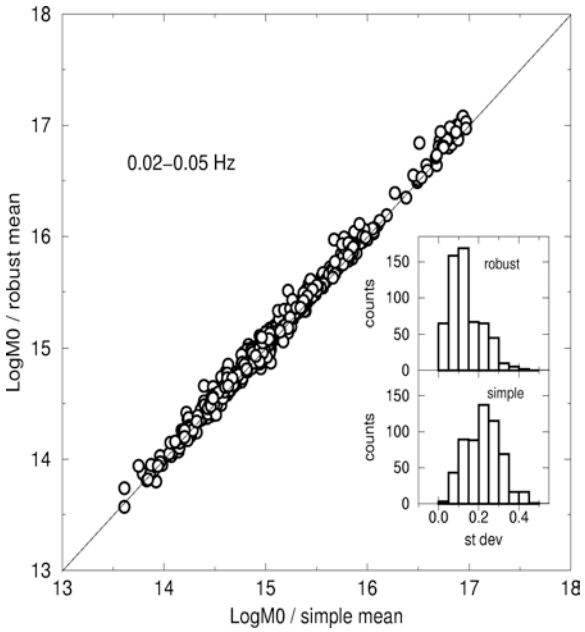


Figure 6. Comparison of station spectral magnitudes calculated with two different methods. Insets show standard deviations as indicated. See text for details.

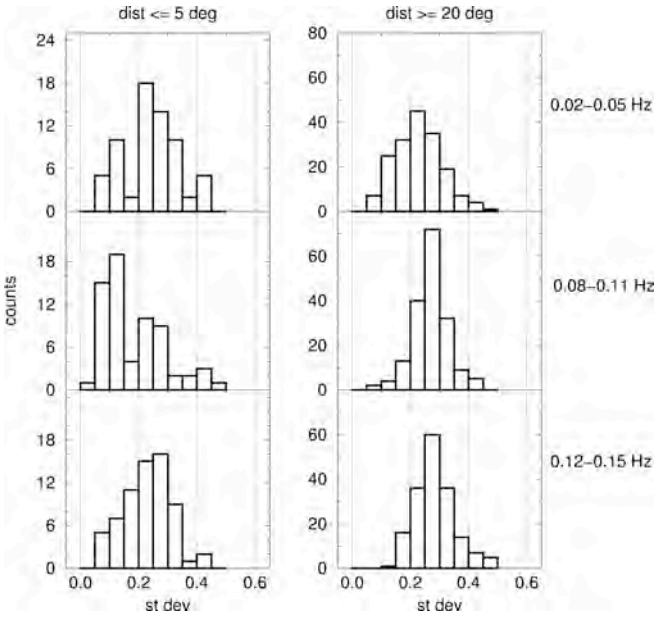


Figure 7. Histograms of standard deviations of the mean station logM_0 estimated in three frequency bands (shown on right), for small and larger distances (shown on top).

The above estimates were compared in order to select the most suitable frequency bands, possibly varying with distance. Ideally, the corrected spectra would be flat over an extended band of frequencies. Flatness is particularly expected for explosions, as supported (within limits) by the explosion examples in Figure 5 above. The magnitude spectra estimated over any reasonable band would be then consistent. In reality, truly flat spectra over extended frequency bands are rare, so we need to choose bands small enough not to include too many variable features of the spectra, yet large enough not to reflect only local, possibly spurious, characteristics.

In view of the above, the two main desirable properties of a spectrum over a given frequency band are small standard deviations and flatness. For this reason, in our search for optimum frequency bands we used two criteria. First, small standard deviations from (1) above represent one measure of the suitability of a frequency band. Figure 7 indicates that for small distances, the 0.08-0.11 Hz frequency band may be preferable (the largest number of small standard deviations) to either 0.02-0.05 Hz, or 0.12-0.15 Hz. Larger distances do not present a clear picture, but it is still evident that relatively more small standard deviations are found in the 0.02-0.05 Hz frequency band, compared with the higher frequencies. We note that at this stage we do not use the standard deviations from (2), since they are designed to greatly diminish the presence of outliers and are thus not representative enough of the quality of the estimates in the different frequency bands. However, once a suitable frequency band is chosen, the robust mean is the

most reliable estimate of logM_0. Spectral flatness as measured with the slopes of the "robust" lines in (4) above provides a second measure of the quality of frequency band; the smaller the slope, the flatter the spectra. Table 1 shows examples of selected estimates, over one specific frequency band out of 153 (0.05-0.1 Hz), for the explosion and earthquake spectra shown in Figure 5. Smaller slopes (flatter spectra) are evident for explosions compared with earthquakes. On the other hand, increasing absolute values of slopes and standard deviations are seen for earthquakes with increasing distance. This is to be expected, as the relatively high-frequency band in the example is less suitable as distance increases.

Table 1. Station LogM_0 estimates in 0.05-0.10 Hz from the spectra in Figure 5

Event Type	*ID.station*	*Distance, degrees*	*Station logM_0 (simple)*	*Station logM_0 (robust)*	*Station slope/logM_0*	m_b
Explosions	21450528.WMQ	2.2	14.31+0.10	14.33+0.08	+1.02/14.31	4.5
	21450535.MAK	7.1	15.60+0.15	15.67+0.05	+0.41/15.64	5.8
	21450534.ESDC	66.8	14.95+0.22	15.02+0.09	+1.62/14.97	5.4
Earthquakes	21456615.WMQ	0.4	13.92+0.14	14.01+0.05	+3.64/13.93	3.2
	21456712.ARU	22.2	14.44+0.25	14.44+0.24	-8.70/14.48	3.8
	21457058.ILAR	65.3	15.55+0.27	15.45+0.10	-11.18/15.59	4.3

Next, we examined the consistency of spectral magnitude estimates in different frequency bands. Figure 8 shows examples of such estimates in several frequency bands (marked along the plot axes). These results indicate that although measurements are generally consistent when measured in different frequency bands, some individual measurements do change significantly. Also, there is a tendency for measurements to be smaller at higher frequencies (points lie slightly to the right of the lines in Figure 8). These results indicate that spectral magnitudes can be measured in different frequency bands, but with some caution and attention to spectral shape variations.

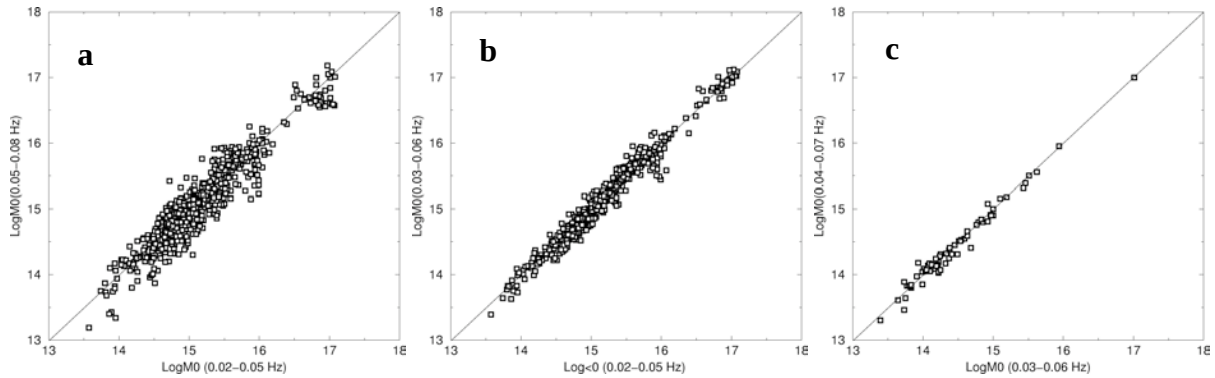


Figure 8. Comparison of station spectral magnitudes in different frequency bands: (a) adjacent bands, all distances; (b) overlapping bands, all distances; (c) overlapping bands, distances ≤5^o.

Finally, we examine which frequency bands perform best for discrimination between small earthquakes and explosions. That is, we want to find out if any set of variable frequencies would perform better in terms of discrimination than a single frequency band applied at all distances. Figure 9 shows logM_0:m_b plots using a set of variable frequencies (0.02-0.05 Hz for distances exceeding 25^0, 0.06-0.09 Hz for 10^0 to 250, and 0.08-0.11 Hz for distances below 10^0) and the 0.03-0.07 Hz frequency band for all distances. The plot on the left, where higher frequencies are used at small distances (and hence for the smallest earthquakes) apparently has a lower discriminating power for small events than when 0.03-0.07 Hz magnitudes are used. The reason is that the spectral magnitudes of smaller events (logM_0 14 to 15; i.e., M_s 2.2 to 3.2), recorded predominantly at regional distances, are generally smaller than the estimates at lower frequencies. We examined the logM_0:m_b ratio for a number of frequency bands and established that the 0.03-0.07 Hz interval performs best in discriminating between earthquakes and explosions for the Lop Nor

data set. The performance of the time domain M_s:m_b discriminant for these events (not shown), is similar to that of the variable frequency measurement (Figure 9, left), although the comparison is complicated by the fact that there is not a standard procedure for measuring time domain *Ms* in the regional distance range.

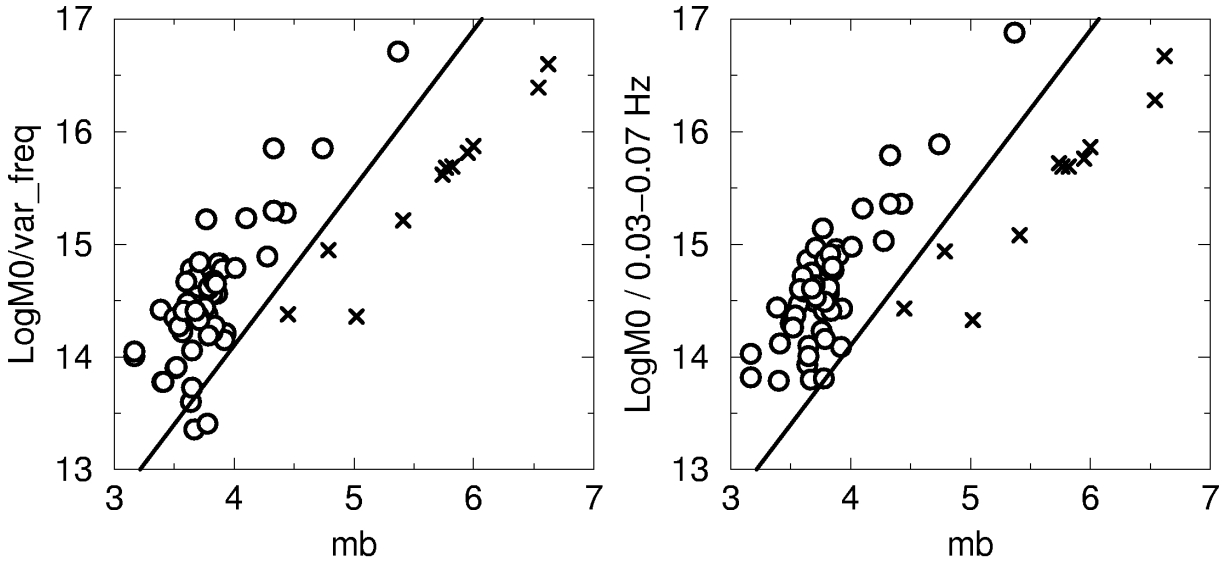


Figure 9. LogM_0:m_b plots showing event spectral magnitudes for earthquakes (O) and explosions (X) in Lop Nor. Station spectral magnitudes were calculated using frequencies increasing with distance (left) and the 0.03-0.07 Hz frequency band for all distances (right). Bold lines mark the empirical discrimination relationship of Stevens and McLaughlin (2001).

CONCLUSIONS AND RECOMMENDATIONS

Improvements to surface wave dispersion models are being accomplished by: 1) continuing addition of new data with good quality control and particular attention to regions with gaps in data coverage; 2) removal of poor quality data in the data set (poor quality data becomes more apparent as the data set increases and the model quality improves); 3) addition of model types where the data requires them; 4) improvement in constraints on sediments and Moho thickness; 5) improvement to the regularization techniques, which can now be defined on a model by model basis, allowing improved data fit while achieving realistic earth models.

Improved methods for surface wave measurement are being implemented and tested. Surface wave spectra are derived from phase-matched filtered data, and the phase-matched filters are derived from the regionalized dispersion models. Path corrected spectral magnitudes are derived by dividing the observed spectra by an explosion Green's function, where the Green's functions are calculated from the global earth models. Thus we use the earth and dispersion models to optimize spectral measurements and regionalize surface wave excitation and attenuation. In this paper, we have described a detailed study of procedures for optimizing measurement of path corrected spectral magnitudes. A significant advantage of logM_0 over M_s is that it can be measured at any distance range without the anomalies caused by variations in dispersion that affect M_s. In principle, logM_0 can be measured over any frequency band and optimized by choosing the band with maximum S/N. However, we found that logM_0 for earthquakes is frequently significantly lower at higher frequencies, which degrades discrimination, and that furthermore the S/N for lower frequencies is good even for very short distances. We therefore recommend that surface wave measurements be made at lower frequencies even at short distances. We are in the process of determining the optimum frequency band for measurement, and our current recommendation is to use a frequency band of 0.03-0.07 Hz consistently for all data. We are continuing to evaluate this recommendation for a larger data set with more types of earth structure.

ACKNOWLEDGEMENTS

We would like to thank Mike Ritzwoller, Anatoli Levshin and Nikolai Shapiro of the University of Colorado, Bob Herrmann of St. Louis University, and other researchers who have allowed us to use their data in this project.

REFERENCES

Bassin, C., G. Laske, and G. Masters (2000), The Current Limits of Resolution for Surface Wave Tomography in North America, *EOS Trans AGU* 81, F897.

Ekstrom, G., A. M. Dziewonski, G. P. Smith, and W. Su (1996), Elastic and Inelastic Structure Beneath Eurasia, in *Proceedings of the 18th Annual Seismic Research Symposium on Monitoring a Comprehensive Test Ban Treaty, 4-6 September, 1996*, Phillips Laboratory Report PL-TR-96-2153, July, ADA313692, 309-318.

Engdahl, E. R., R. van der Hilst, and R. Buland (1998), Global Teleseismic Earthquake Relocation with Improved Travel Time and Procedures for Depth Determination, *Bull. Seismol. Soc. Am.* 88, 722 - 743.

Hansen, P. C. (1998), Rank-Deficient and Discrete Ill-Posed Problems, SIAM, Philadelphia, 1998.

Huang, Z., W. Su, Y. Peng, Y. Zheng, and H. Li (2003), Rayleigh Wave Tomography of China and Adjacent Regions. *J. Geophys. Res.* 108(B3), 2073, doi: 10.1029/2001JB001696.

Kennett, B. L. N. E. R. Engdahl, and R. Buland (1995), Constraints on Seismic Velocities in the Earth from Travel Times, *Geophys. J. Int.* 122**,** 108-124.

Laske, G. and G. Masters (1997), A Global Digital Map of Sediment Thickness, *EOS Trans. AGU* 78, F483.

Laske, G., G. Masters, and C. Reif, Crust 2.0 (2001): A New Global Crustal Model at 2x2 Degrees, http://mahi.ucsd.edu/Gabi/rem.html.

Levshin, A., J. L. Stevens, M. H. Ritzwoller, and D. A. Adams (2002), Short Period (7s-15s) Group Velocity Measurements and Maps in Central Asia, in *Proceedings of 24th Seismic Research Review - Nuclear Explosion Monitoring: Innovation and Integration, 17-19 September 2002*, 97-106.

Marshall, P. D. and P. W. Basham (1972), Discrimination Between Earthquakes and Underground Nuclear Explosions Employing an Improved M_s Scale, *Geophys. J. R. astr. Soc.* 28, 431-458.

Mooney, W., G. Laske, and G. Masters (1998), Crust 5.1: A Global Crustal Model at 5x5 Degrees, *J. Geophys. Res.* 103, 727-747.

Stevens, J. L. and D.A. Adams (2000), Improved Surface Wave Detection and Measurement Using Phase-Matched Filtering and Improved Regionalized Models, in *Proceedings of the 23rd Seismic Research Review: Worldwide Monitoring of Nuclear Explosions, 12-15 September 2000*, 145-154.

Stevens, J. L., D.A. Adams, and G. E. Baker (2001a), Improved Surface Wave Detection and Measurement Using Phase-Matched Filtering with a Global One Degree Dispersion Model, in *Proceedings of the 23rd Annual DOD/DOE Seismic Research Symposium, 1-5 October 2001*, 420-430.

Stevens, J. L., D. A. Adams, and E. Baker (2001b), *Surface Wave Detection and Measurement Using a One Degree Global Dispersion Grid*, SAIC Final Report to Defense Threat Reduction Agency, SAIC-01/1084, December.

Stevens, J. L., D. A. Adams, and E. Baker (2002), Improved Surface Wave Dispersion Models and Azimuth Estimation Techniques, in *Proceedings of 24th Seismic Research Review - Nuclear Explosion Monitoring: Innovation and Integration, 17-19 September 2002*, 552-561.

Stevens, J. L. and K. L. McLaughlin (2001), Optimization of Surface Wave Identification and Measurement, *Pure Appl. Geophs.* 158, 1547-1582.

Yang, X., S. R. Taylor, H. J. Patton, M. Maceira, and A. A. Velasco (2002), Evaluation of Intermediate-Period (10- to 30-sec) Rayleigh-Wave Group Velocity Maps for Central Asia, in *Proceedings of 24th Seismic Research Review - Nuclear Explosion Monitoring: Innovation and Integration, 17-19 September 2002*, 609-617.

CALIBRATION OF REGIONAL SEISMIC STATIONS IN THE MIDDLE EAST WITH SHOTS IN TURKEY

M. Nafi Toksoz,[1] Sadi Kuleli,[1] Cemil Gurbüz,[3] Dogan Kalafat,[3] Tolga Bekler,[3] Ekrem Zor,[3] Mehmet Yilmazer,[3] Zafer Ogutcu,[3] Craig A. Schultz,[2] and David B. Harris[2]

Massachusetts Institute of Technology;[1] Lawrence Livermore National Laboratory;[2] Bogazici University[3]

Sponsored by National Nuclear Security Administration
Office of Nonproliferation Research and Engineering
Office of Defense Nuclear Nonproliferation

Contract No. DE-FC03-01SF22398[1,3] and W-7405-ENG-48[2]

ABSTRACT

The objective of this project is to calibrate regional travel-times and propagation characteristics of seismic waves in Turkey and surrounding areas in the Middle East in order to enhance detection and location capabilities in the region. Important data for the project will be obtained by large calibration shots in central and eastern Turkey.

The first, a two-ton shot, was fired in boreholes near Keskin in central Anatolia on 23 November 2002. The explosives were placed in 14 holes, each 80 m deep, arranged in concentric circular arrays. Ninety temporary seismic stations were deployed within a 300 km radius around the shot. The permanent stations of the Turkish National Seismic Network provided a good azimuthal coverage as well as three radial traverses. Most stations within a radius of 200 km recorded the shot. Travel-time data have been analyzed to obtain a detailed crustal model under the shot and along the profiles. The model gives a 35-km thick crust, characterized by two layers with velocities of 5.0 and 6.4 km/s. The P_n velocity was found to be 7.8 km/s. The crustal thickness decreases to the north where the profile crosses the North Anatolian fault. There is a slight increase in crustal velocities, but no change in crustal thickness to the west. Data analysis effort is continuing to refine the regional velocity models and to obtain station corrections.

OBJECTIVES

The Eastern Mediterranean, Caucasus, and many parts of the Middle East are characterized by complex tectonics, and lateral variations of crust/upper mantle structures and seismic velocities. These complexities affect the detection, location, and characterization of seismic events. The primary objective of this project is to improve event location capabilities in the Middle East using calibration shots in Turkey. Specific objectives are: (1) calibrate regional travel-times and propagation characteristics of seismic waves across the Middle East and Eastern Mediterranean; (2) calibrate local and regional models for specific International Monitoring System (IMS) stations in Turkey; (3) conduct reciprocity experiments where feasible; and (4) provide data and models to enhance IMS detection and location capabilities in the region. The calibration data will be generated by two shots in Turkey, one in central Anatolia, and another in eastern Turkey.

RESEARCH ACCOMPLISHED

The first calibration shot was fired in central Turkey near Keskin in November 2002. The explosives (dynamite) were loaded into 14 holes, each drilled to a depth of 80 m, in granite outcrop. Shot holes were located in two concentric circles with radii of 4 m and 9 m, respectively. Two tons of dynamite, about 143 kg per hole, was loaded into the boreholes. Figure 1 shows the location of the shot on a map of Turkey, regional geology, and the geometry of the drill holes. The coordinates of the shot point are: 49°43'29.9"N and 33°38'08.0"E. Elevation is 1425 m. The explosion took place in two steps. First, two holes containing 280 kg of explosives, were detonated on November 23, 2002, at 22:47:33.40 UT. The main shot was fired a day later on November 24, 2002, at 21:10:04.80. It consisted of about 1,720 kg explosives in 12 holes. All holes were detonated at the same time with zero time delay. The shots were fired around midnight local time in order to minimize seismic noise due to cultural activities and atmospheric effects.

Eighty new (temporary) seismic stations were installed to monitor the shot. These complemented about 30 permanent seismic stations, within 500 km of the shot point, operated by the Kandilli Observatory and Earthquake Research Institute (KOERI). Twenty-three of the temporary stations (10 broadband and 13 three-component short period) were shipped from the United States. All others were provided by KOERI and cooperating institutions in Turkey. The distribution of seismic stations is shown in Figure 2. Two linear arrays of short period instruments were deployed to the north and to the southeast of the shot point. A third, less regular profile, was deployed to the southwest. The linear arrays were designed for crustal structure studies and for potential reciprocity experiments. The other stations, especially the broadband instruments, were deployed to provide good azimuthal coverage around the shot.

Unfortunately, there was a strong storm affecting most of Turkey at the time of the experiment. Before the explosion, heavy rains and snow in some areas made the checking and servicing of 80 temporary stations especially difficult. In spite of the weather, all but eight of the stations operated normally and large amounts of good quality seismic data were acquired. Although the retrieval of data from a variety of seismic instruments used in the experiment was a time-consuming task, this task was completed and a database was generated.

The analysis of the shot data is continuing. In this report we describe the initial results concerning crustal structure.

Crustal Structure

The three seismic arrays shown in Figure 2 provide the first opportunity to obtain a well-constrained crustal structure profile in central Turkey. The crustal structure and P_n velocities of the Anatolian plateau have been studied by various methods (Canitez and Toksöz, 1980; Gurbüz and Evans, 1991; Hearn and Ni, 1994; Turkelli et al., 1996; Mangino and Priestly, 1998; Gok et al., 2000; Laske et al., 2001). These studies found crustal thicknesses ranging from about 35–40 km, P_n velocities between 7.6 and 7.9 km/sec, and crustal velocities quite different from each other. None of these studies included long refraction lines.

The travel-time data (three profiles) provide the first opportunity to determine crustal structure and upper mantle velocities for P-waves in the Anatolian plateau. For each profile, velocity models are obtained by fitting the travel-times with a two-dimensional (2-D), laterally varying velocity model. The starting model is generated using a one-dimensional layered model. These models are revised to improve fit to observed travel times. A 2-D ray-tracing

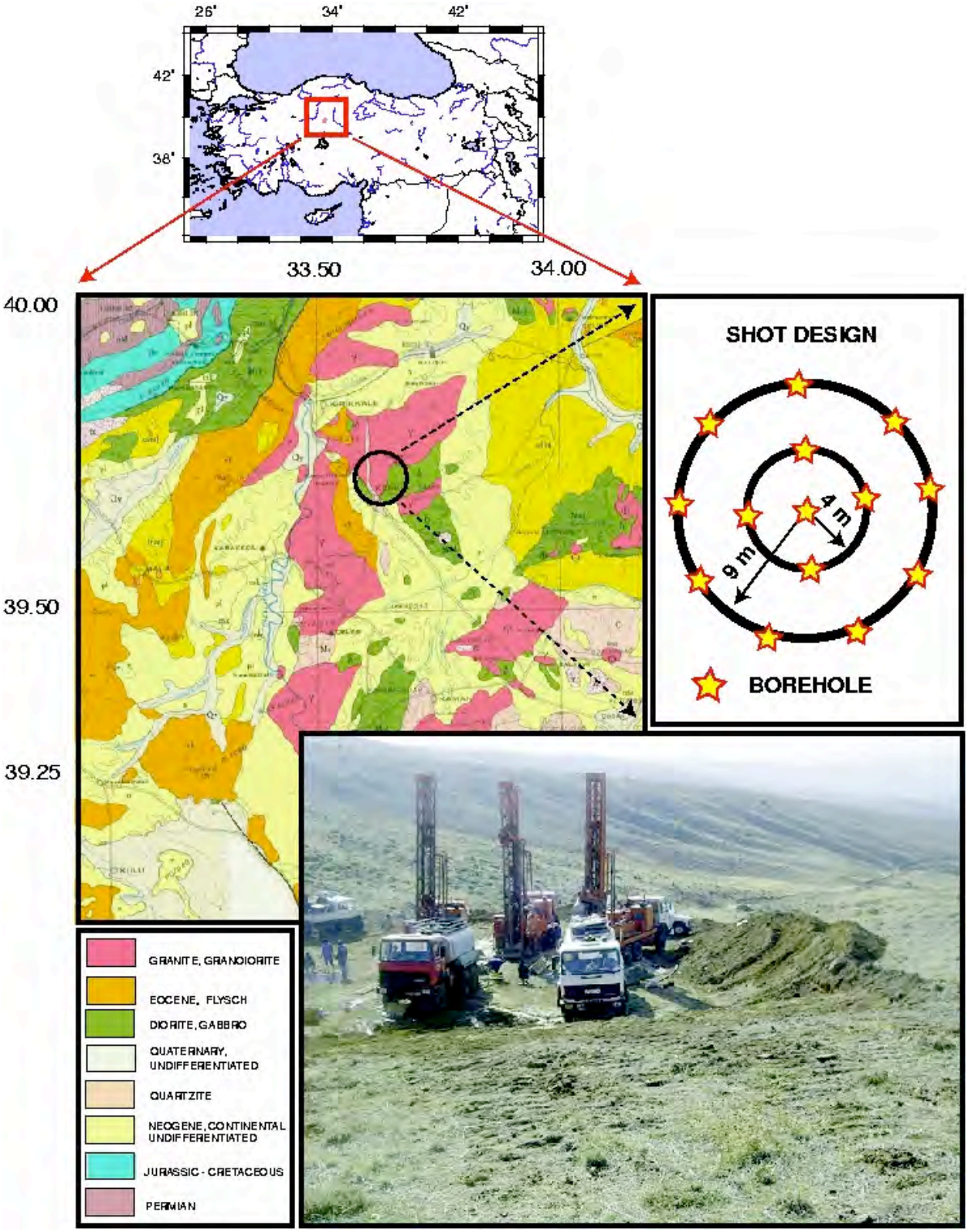


Figure 1: The shot point. Counterclockwise from top: (a) Location of shot point. (b) Geology of shot point vicinity. (c) Drilling of boreholes. (d) Geometry of shot holes.

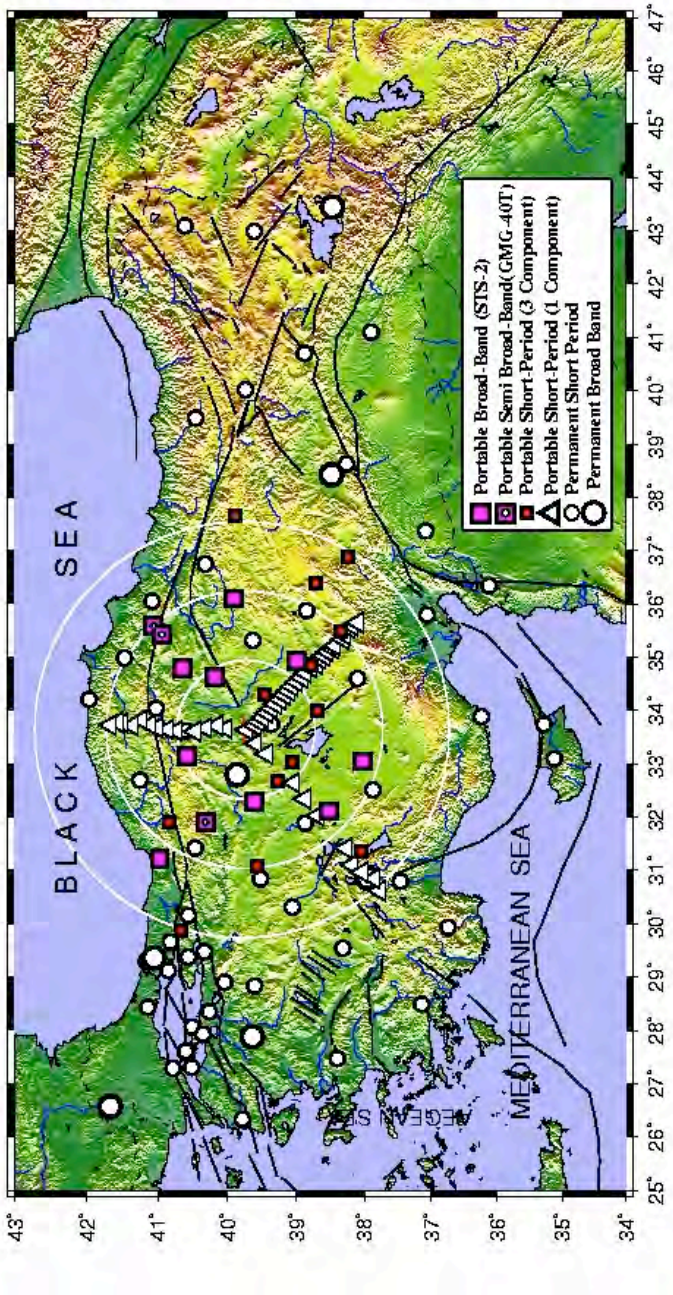


Figure 2: Distribution of seismic stations around the shotpoint. Circles are of 1°, 2°, and 3° radii. Symbols designate station types. Three refraction profiles going north, southeast, and southwest are shown by high density station arrays (triangles). Major faults are also shown.

program is used for calculating travel-times. Velocity gradients, which are included in modeling, are adjusted to improve fit both to travel-times and amplitudes. All structured information obtained is based on forward modeling only.

Figures 3, 4, and 5 display the seismograms (i.e., record section), the travel-times and 2-D velocity models for the north, southeast, and southwest profiles. The seismograms are filtered with a 4–10 Hz bandpass filter to reduce the noise. Signal-to-noise ratio is good up to about 180 km in all profiles with the exception of a few noisy stations. Beyond a distance of 200 km, identifying the first arrivals becomes more challenging. We used different pass-band filters, based on the noise characteristics, at different stations to improve the signal-to-noise ratio. Frequency changes associated with the signals were helpful in identifying the arrivals.

Northern profile. The velocity model for the northern profile (Figure 3) shows a crust with two prominent layers. There is an increase of velocity with depth in the thicker crustal layer, but no evidence of a prominent discontinuity. The average velocity in the top layer is about 5 km/sec and the lower layer about 6.4 km/sec. The uppermost mantle velocity is 7.8 km/sec to 7.9 km/sec. The crustal thickness is 36 km under the shot. There is a prominent change in crustal thickness 120 km north of the shot. There is also an anomaly in the top crustal layer. This anomaly corresponds to the trace North Anatolian fault. The seismic profile crosses the fault 120 km north of the shot point. There is a prominent Bouger gravity anomaly associated with the fault. The 5-km crustal thinning across the fault is consistent with the Bouger anomaly.

Southeastern profile. The record section, travel-times, crustal structure, and velocities are shown in Figure 4. The crustal model shows some prominent features. The thickening of the uppermost layer at 100 km distance is quite well-constrained. It seems to correspond to a little known Gumuskent fault. The noisy station at 100 km may have been situated in the fault zone. The anomaly at about 170 km that affects both the upper layer and the crustal thickness corresponds to the Ecemis fault. This fault is mapped. It has little seismic activity. It is not as prominent as the North Anatolian fault that crosses the northern profile. The crustal thickness along this profile is 36 km, possibly thinning slightly toward the southwest.

Southwestern profile. This profile, shown in Figure 5, has the fewest stations. The quality of the data is excellent. Because of the sparse coverage, the crustal model shown should be considered "tentative." We will try to test this model by calculating fully elastic synthetic seismograms to match the observed records.

Location of the Shot

To locate the shot we used the P-wave arrival times from a well-distributed subset of our seismic stations. The stations used for this study are shown in Figure 6. For the location we used a 1-D velocity model and hypoinverse.

Three velocity models were used for the location. These included AK 135, the model used by KOERI, and a simplified 1-D velocity model derived from the average of three velocity profiles described in the previous section. The velocity models are shown in Figure 6b. The results are summarized in Table 1. All models give good locations, including accurate depths and origin times. The MIT model, based on a new velocity model, does the best.

Table 1: Shot location, and the errors, using P-wave times and three velocity models.

	AK135	KOERI	MIT
Epicenter	39.722N, 33.657E	39.720N, 33.662E	39.724N, 33.650E
Error (m)	1,894	2,351	1,209
Depth (km)	h = 0.02	h = 0.01	h = 0.01
Origin Time	21:10:04.93	21:10:03.65	21:10:04.11
Error (sec)	+0.13	-1.15	-0.69

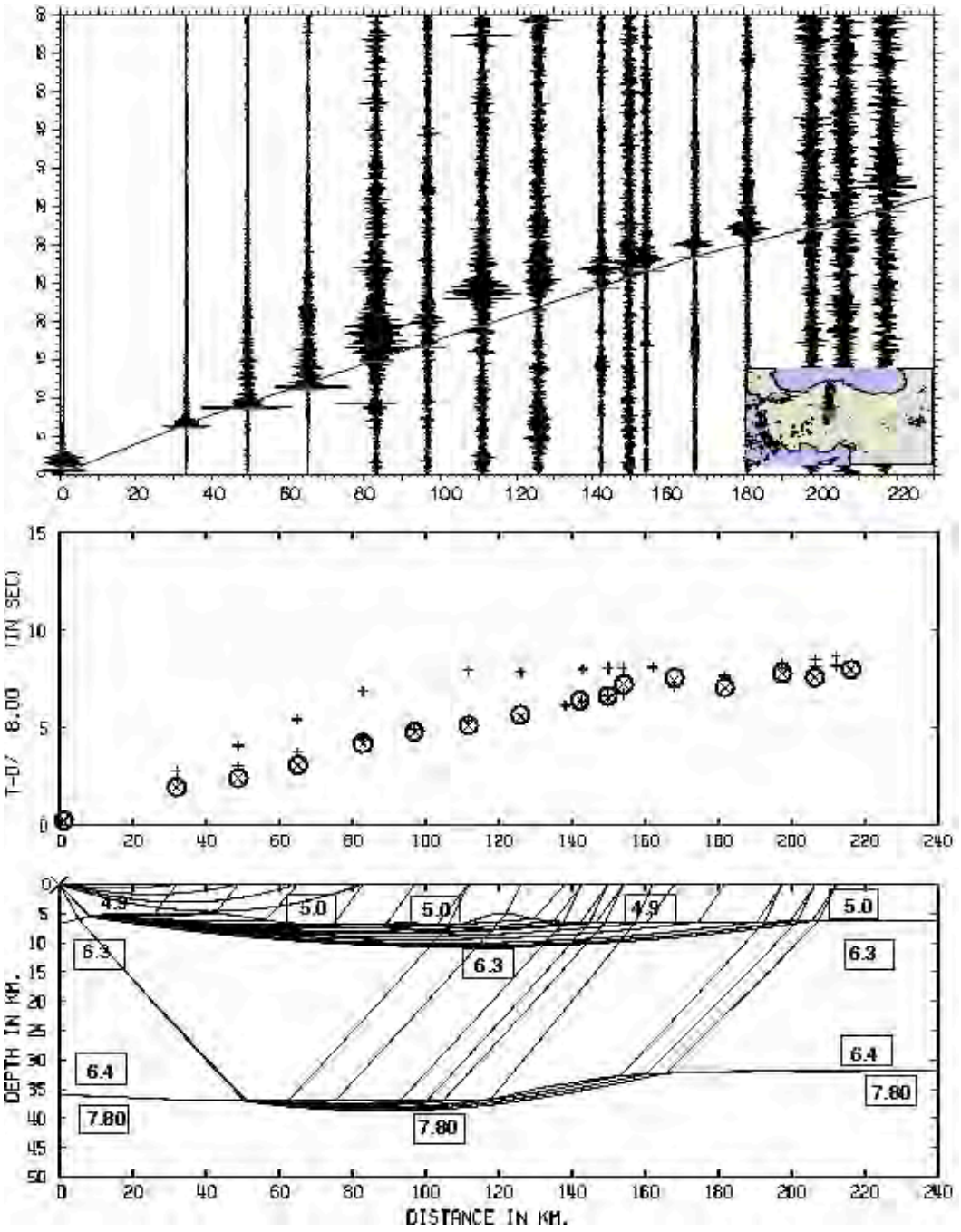


Figure 3: Seismograms and crustal model for the north profile shown in the inset. Top: Record section. Middle: Observed (circles) and calculated (crosses) travel-times. Bottom: Crustal structure and P-wave velocities. Ray paths are also shown. The North Anatolian fault crosses the profile at 170 km distance. Note the crustal thinning across the fault.

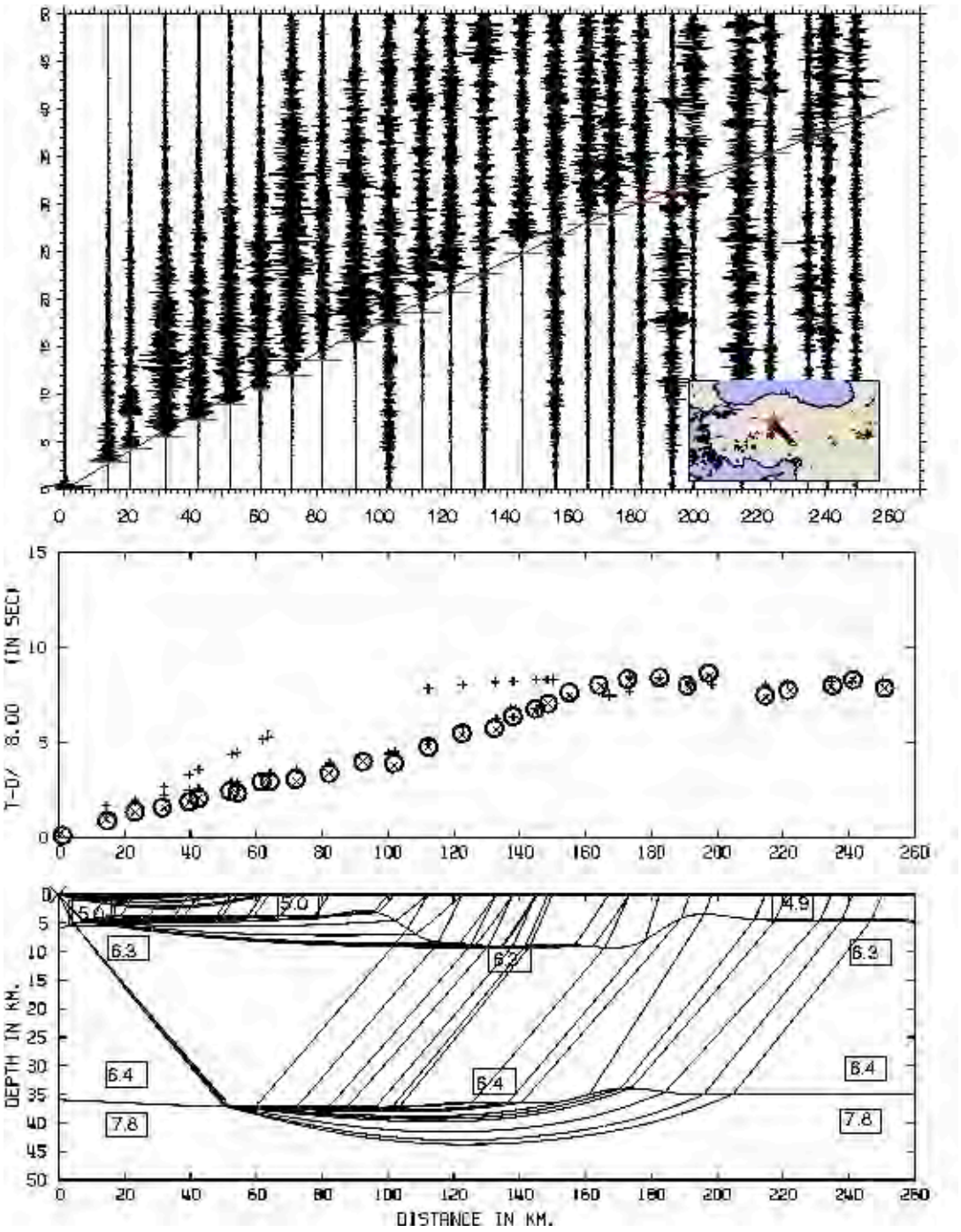


Figure 4: Seismograms and crustal model for the southeast profile shown in the inset. Panels and symbols are the same as in Figure 3. Two fault zones cross this profile at distances of about 100 and 160 km. Note the noisy traces near the fault zones.

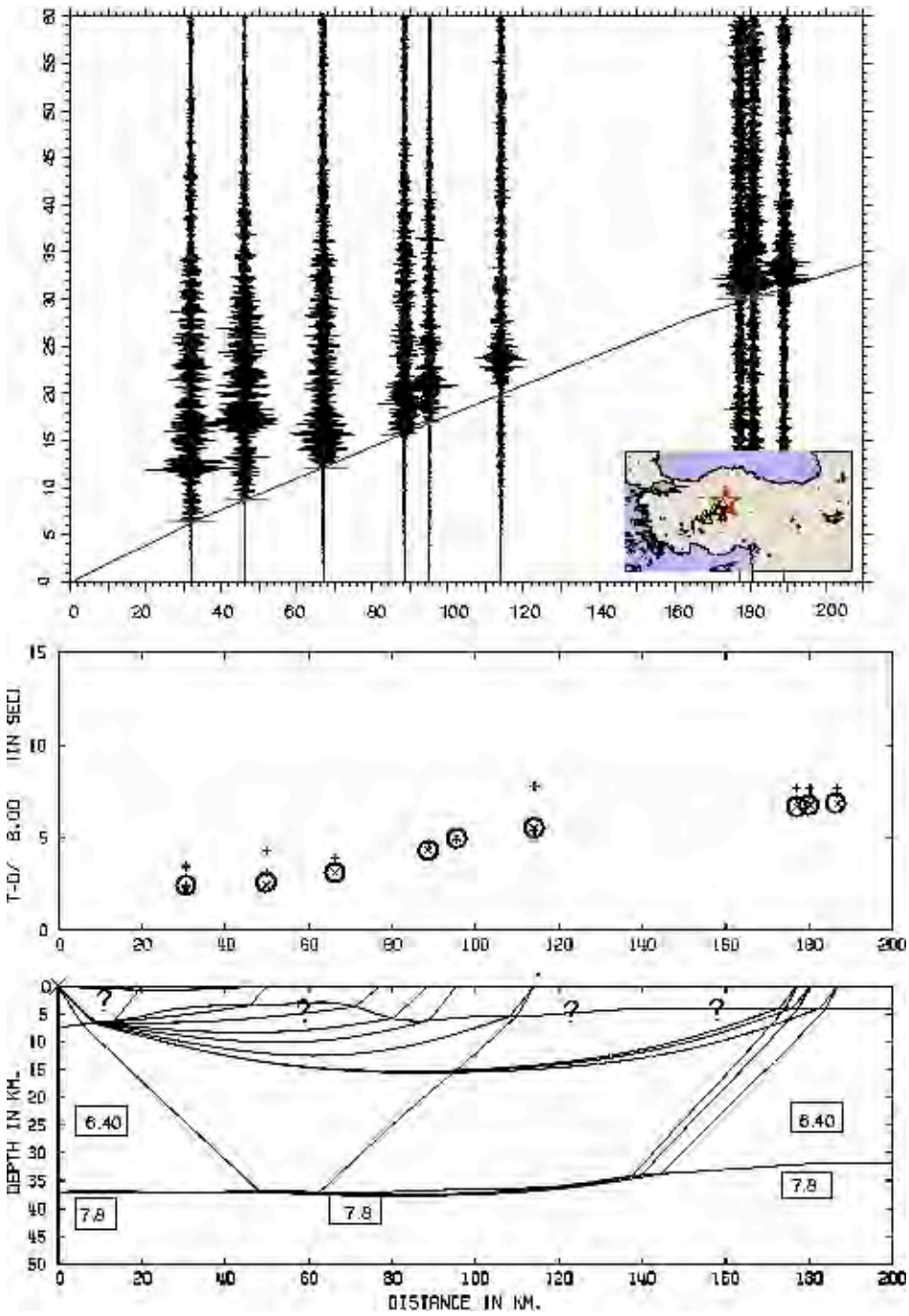


Figure 5: Seismograms and crustal model for the southwest profile shown in the inset. Because of limited data, crustal structure and velocity models are tentative and uncertain.

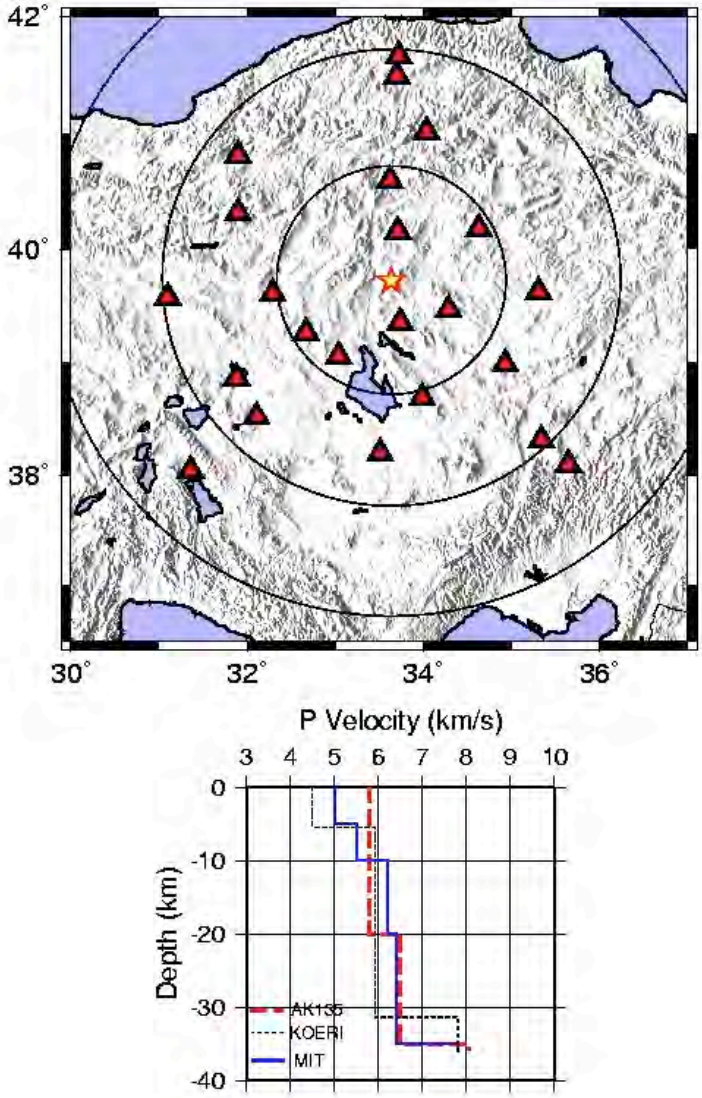


Figure 6: Location of the shot from observed P-wave travel-times. Top: Stations whose arrival times are used. Circles are 1°, 2°, and 3° distances from the shot. Bottom: Three velocity models used for location: AD135; KOERI; and MIT, which is the average of velocities shown in Figures 3, 4, and 5.

Because of good coverage in both azimuthal and distance, all velocity models give accurate locations. However, the velocity model specific to the site gives the best results.

CONCLUSIONS AND RECOMMENDATIONS

The calibration shot at Keskin produced valuable data for obtaining crustal structure and velocities for central Anatolia. The models are the first ever derived from an explosion in central Turkey. The models show that the crust is 36-km thick under Keskin. It can be modeled with two layers, each with velocity gradients. The top layer is about 5–10-km thick, an average velocity of 5 km/sec. The thick lower layer has an average velocity of 6.4 km/sec. The average P_n velocity is 7.8 km/sec.

There are lateral variations in crustal structure and velocities. There is a prominent lateral discontinuity at the North Anatolian fault where the crustal thickness decreases by 5 km from south to north across the fault. There are less prominent structural changes across the Erciyas-Ecemis fault zone. At present, the preliminary crustal models are being refined by calculating synthetic seismograms to match the amplitudes of the first and later arrivals that are observed on the data.

The Keskin shot provided much valuable field experience for deploying and maintaining a large number of portable stations in the field. This experience will help with the planning of field operations for the two large shots to be conducted in Phase II of this project.

REFERENCES

Canitez, N. and M.N. Toksöz (1980). Crustal structure beneath Turkey, *Eos Trans Am. Geophys. Un., 61*, 290.

Gok, R., N. Turkelli, E. Sandvol, D. Seber, and M. Barazangi, (2000). Regional wave propagation in Turkey and surrounding regions, *Geophys. Res. Lett., 27*, 429-432.

Gürbüz, C. and J.R. Evans (1991). A seismic refraction study of the western Tuz Golu basin, central Turkey, *Geophys. J. Int., 106*, 239-251.

Hearn, T.M. and J. F. Ni (1994). Pn velocities beneath continental collision zones: The Turkish-Iranian plateau, *Geophys. J. Int., 117*, 273-283.

Laske, G., G. Masters and Reif (2001). CRUST 2.0: A new global crustal model at 2x2 degrees, http://mahi.ucsd.edu/Gabi/rem.html.

Mangino, S. and K. Priestley (1998). The crustal structure of the southern Caspian region, *Geophys. J. Int., 133*, 640-648.

Turkelli, N., G. Horasan, H.S. Kuleli, and D. Reiter, (1996). Preliminary results of velocity distribution study in eastern Turkey, *Eos, Trans. Am. Geophys. 77*, 46, F477.

QUANTIFYING SOURCE EXCITATION AND PATH EFFECTS FOR HIGH FREQUENCY REGIONAL WAVES

Ru-Shan Wu, Xiao-Bi Xie, Zengxi Ge, Xianyun Wu, and Thorne Lay

University of California, Santa Cruz

Sponsored by Air Force Research Laboratory

Contract No. DTRA01-01-C-0076

ABSTRACT

A finite-difference modeling plus slowness analysis method is developed for predicting the Lg-wave energy. The method allows us to investigate near source energy partitioning in multiple domains including frequency, slowness and time. The main advantage of this method is that it can be applied at close range, well before Lg is actually formed at larger distance. To test the method, a large model is used in the calculation. The short distance array measurements can be directly compared with the long distance surface measurements. The two types of results show the consistency that verifies the validity of the analysis method.

We have extended the boundary element method from 2D SH case to the P-SV case. The method allows us to accurately handle the wave propagation in models with irregular topography. The validity and accuracy of the method have been checked by comparing the results with other numerical results. We also developed a connecting technique to reduce the cost of the boundary element method when calculating long distance forward propagations. Although the boundary element method is less efficient, it provides an accurate solution that can be used to calibrate other fast numerical methods with approximations. We also used the boundary element method to investigate the effect of the near source topography on the Rg-Lg coupling.

The half-space screen method has been further improved to model Lg-wave propagation in the complex crustal waveguides. Many crustal waveguide characteristics that potentially contribute to the Lg-wave attenuation have been built into the propagator. Results from the propagator provides a useful tool for investigating the relationship between the Lg wave attenuation and crustal waveguide properties. The half-space screen method has been extended to the P-SV case including the Rayleigh wave. Preliminary results are obtained and compared to the 2D elastic finite-different result.

OBJECTIVE

The regional seismic phase Lg is one of the most useful phases for event discrimination and magnitude estimation associated with monitoring a CTBT. The characteristics of Lg are strongly affected by the excitation conditions in the source region and by path effects controlled by waveguide structures of different scales. To obtain a comprehensive understanding of Lg signals, it is crucial to do research on both the excitation and propagation of Lg for realistic crustal models. The Regional Wave Synthetic Seismogram program, a branch of the Institute of Geophysics and Planetary Physics (IGPP) at the University of California, Santa Cruz (UCSC) has done extensive work on the excitation and propagation of regional phases, and has developed the theory and methods for the investigation of these problems.

Currently, there are three research directions under this project. (i) A finite-difference modeling plus slowness analysis method developed for predicting the Lg-wave energy development. This method allows us to investigate near source energy partitioning in the multiple domains including frequency, slowness, and time. The main advantage of this method is that it can be applied at a close range, which is well before the Lg is actually formed at greater distance. This year we used a larger crustal model in the calculation. The short distance array measurements are directly compared with the long distance surface measurements. The two types of results show consistency that verifies the validity of the analysis method. (ii) We extended the boundary element method from 2D SH case to the P-SV case. The accuracy of the method has been carefully checked. Although the boundary element method is not an efficient solution, it provides a flexible and accurate way to solve the wave propagation problems in crustal models with irregular free surfaces. There are two motivations to introduce the boundary element method into the Lg wave analysis. First, we need an accurate solution to calibrate other fast approximations. Second, we will use the boundary element method to investigate the effect of near source topography on the couplings between the Pg, Rg and Lg waves. (iii) We are continually working on the high efficiency generalized screen propagator (GSP) for Lg propagation (Wu et al., 2000a,b; Wu and Wu, 2001). This year we applied the elastic screen propagator to investigate the Lg wave path effects. More realistic crustal models including the heterogeneities of different scales and intrinsic attenuations are being used in the numerical simulation. At the same time, we are working on the coupling issues between the body waves and the surface waves for the P-SV propagator.

RESEARCH ACCOMPLISHED

Rg-Lg Coupling, Pg-Lg Coupling and the Lg-Wave Energy Partitioning

Lg is predominantly comprised of shear wave energy trapped in the crust. Explosions are not efficient sources to generate shear energy. Although several mechanisms have been proposed to convert P-wave energy into Lg waves, e.g., spall, tectonic release, S*-wave, free surface reflection pS, etc., they often require certain environmental conditions that do not exist. Compared to deeper earthquake sources, shallow explosions generate relatively large Rg phases, which is readily disrupted by crustal heterogeneities. Rg energy may scatter into trapped crustal S-waves near the source region and contribute to a low-frequency Lg-wave (Gupta et al., 1991, 1992). In this project we develop a method, based on the finite-difference simulation and slowness analysis, to investigate the contributions of Rg-Lg and Pg-Lg couplings relative to the explosion of energy partitioning. To investigate these mechanisms it requires very fine near source velocity models, however in order to obtain well-developed Lg phases, the waves need be propagated up to very long distances. To overcome this difficulty, Xie and Lay (1994) proposed a slowness analysis method. With this method, fine velocity structures are used in the near source region, which provide coupling conditions between Pg, Rg and Lg waves. The finite-difference method is used to propagate the seismic waves in the crustal waveguide. In the intermediate distances, energy flux in the waveguide is calculated from synthetic seismograms using the array technique. The energy that will contribute to the Lg wave can be measured and used as an indicator of Lg wave energy at a longer distance. The slowness analysis can be conducted well before the Lg-wave is fully formed. The entire system requires only a compact sized model and it provides an efficient tool for investigating different near source Lg-wave excitation mechanisms.

In the previous year, we tested this method and obtained some preliminary results. Further simulations are being conducted this year. Figure 1 shows the configuration of the model used to calculate the Lg wave propagation. The explosion source is located at a depth of 750 m. A 2D elastic finite-difference code (Xie and Lay, 1994) is used to generate the synthetic seismograms. A Gaussian derivative source time function is used and the effective frequency band is roughly 0 to 5 Hz.

Synthetic seismograms are collected from two receiver arrays for different investigations. The first is a 50x40 array with 1 km spacing located 150 km from the epicenter and is used for short distance slowness analysis. The second receiver array is located on the surface, 450 km from the epicenter, which simulates conventional Lg wave observations. The energy partitioning obtained from the shorter distance is compared to the surface Lg observations at the longer distance.

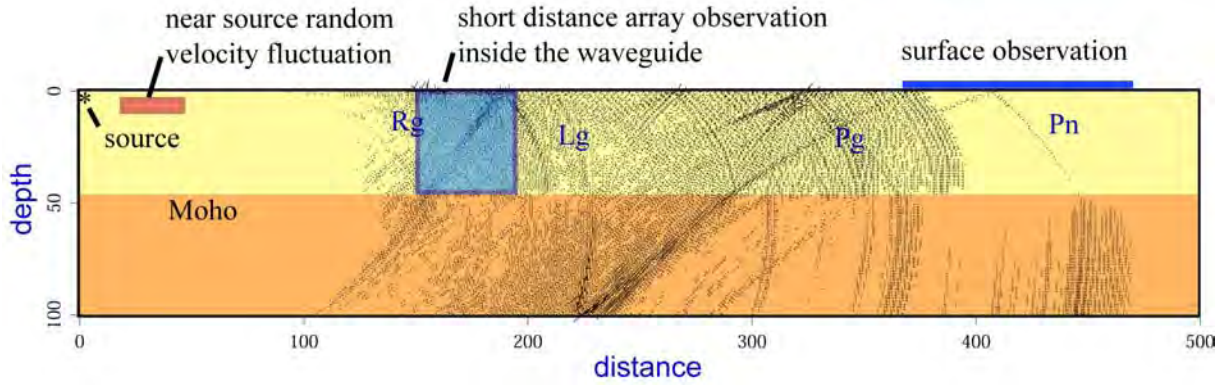


Figure 1. Cartoon showing the process of FD simulation and slowness analysis. The FD method is used to generate synthetic seismograms within the crustal waveguide. Near source random velocity fluctuations are added to the background velocity to generate Pg to Lg and Rg to Lg couplings. Energy flux at a short distance is calculated using an array technique then analyzed based on the slowness, frequency, and travel-times. The energy that will contribute to the Lg can be measured and used as an indicator of Lg wave energy at a longer distance.

We use a layered velocity structure that resembles the east Kazakh crust as the background model. This is a typical high-velocity crust where the upper crust P-wave velocity is larger than the upper mantle S-wave velocity. For such a velocity structure, very little energy generated from an explosion source can be trapped in the waveguide to form the Lg-wave. To investigate the near source Rg to Lg and Pg to Lg couplings, we add some small random velocity patches near the source region. These random patches are 10 km wide, 2.5 km thick, located at the epicenter a distance of 5-15 km and at different depths. The RMS velocity fluctuation for these patches is 10 % with a 1 km correlation length for both vertical and horizontal directions. Synthetic seismograms computed at the receiver arrays are used for the slowness analysis. The size of the sub-array for slowness analysis is 10x10.

Figure 2 shows the slowness analysis results at 180 km in the crustal waveguide. The data is processed in three frequency bands. The left, middle and right columns are for 0.3-1.5 Hz, 0.8-2.0 Hz and 2.0-5.0 Hz pass bands, respectively. In each panel, the vertical axis is the horizontal phase velocity. The horizontal axis is time. The group velocity is also marked on the top of each panel. The dashed line marks the upper mantle S-wave velocity. The solid circles are energy picked from the slowness domain and summed up for the entire cross section. The top row is for the background velocity model. Little Lg energy can be observed, which is typical for such a high velocity crustal waveguide. The following rows are for crust models with near source random velocity perturbations. We first focus on the low frequency results (left panel). From the top panel we can see a strong Rg-wave. However, there is little energy within the Lg wave window. In the second panel, a random velocity patch located at a depth of 0.0-2.5 km is added to the background model. Compared with the background model, considerable energy is transferred from the Rg-wave to the Lg-wave through scattering. Panels 3 to 5 are similar to panel 2, except that random patches are located at depths of 2.5-5.0 km, 5.0-7.5 km, and 10.0-12.5 km, respectively. Similar to the case in the second panel, energy is transferred from Rg to Lg. The tendency is: the shallower the random patch the more energy is scattered from Rg to Lg. This also provides additional evidence that the low frequency Lg energy comes from the Rg-wave, since the Rg energy is mostly concentrated at the shallow depth.

In the high frequency results (right panel), from the top panel we can see a strong Pg-wave. There is some energy fall into the Lg group velocity window. However, these energy have a high horizontal phase velocity implying they are coming from Pg-wave through Pg to Sg reflections on a flat free surface or Moho discontinuity. As a result of the steep incident angles the energy will gradually leak to the upper mantle and cannot form the Lg-wave. In the

following panels, after adding random velocity perturbations in the near source region, part of the Pg energy transfer to the Lg window, i.e., scattered energy falls into the proper slowness window. In general, the Rg-Lg coupling takes place at a lower frequency and the Pg-Lg coupling at a higher frequency.

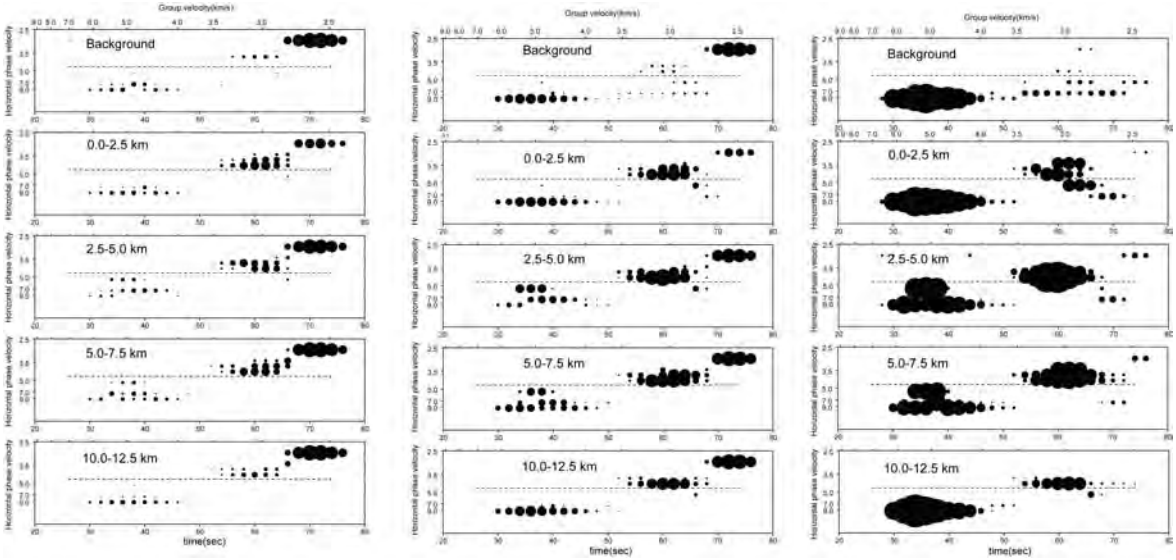


Figure 2. Examples of slowness analysis. From left to right are for 0.3-1.5 Hz, 0.8-2.0 Hz, and 2.0-5.0 Hz frequency bands. The top row is for the background velocity model without any randomness, and the following rows are for models with random patches at different depths. Random velocity patches extend from a distance of 5-15 km and are located at depths from 0 to 15 km.

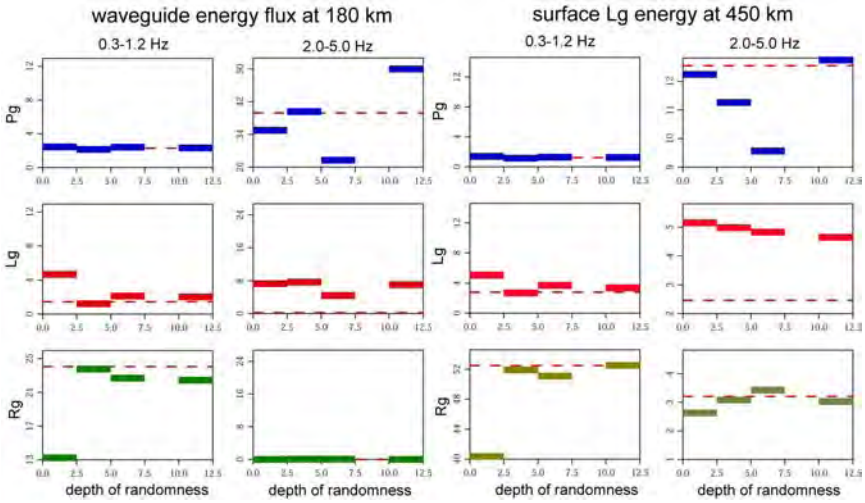


Figure 3. Comparison between the waveguide energy flux at 180 km (left two panels) and the wave energy on the surface at 450 km (right two panels). Shown in each small panel is relative energy, the horizontal axis is the depth of the random patches, and the vertical axis is the energy. Dashed line indicates the energy level for the background velocity model. Short bars indicate the energy changes as a result of the random velocity fluctuations.

The two left columns in Figure 3 give the relationships between the energy of different wave types and the depth of the random velocity perturbations. Column 1 is for low frequency and column 2 is for high frequency. As comparisons, the two right columns (3 and 4) give the energy from the surface array at a distance of 450 km from the epicenter. The surface observations are obtained by calculating the RMS amplitudes in different group velocity windows, which is similar to the conventional Lg-wave observations. The relative energy is shown in each small

panel. The horizontal axis is the depth of the random patches, and the vertical axis is the energy. The dashed line indicates the energy level for the background velocity model. The short bars indicate the energy changes due to the random velocity fluctuations. By comparing columns 1 and 3, we see that at a lower frequency, energy exchange mainly occurs between the Rg and Lg waves. There is almost no Pg energy. Since Rg energy is more concentrated in the shallow depth, the Rg-Lg coupling is more sensitive to the shallow velocity perturbations. The slowness analysis at a short epicenter distance correctly predicts the Lg surface wave energy observed at a greater distance. By comparing columns 2 and 4, we see that at a higher frequency, energy exchange occurs between the Pg and Lg waves. The Pg-Lg coupling is less sensitive to the depth of the randomness. For Lg waves, the slowness analysis result is consistent with the surface Lg observation at the greater distance. For Pg waves, there is a discrepancy between the two measurements. Since the Pg-wave is not a trapped wave, the result suggests that part of the Pg energy leaks to the upper mantle before it reaches the greater distance. These comparisons verify that the current analysis method can be used to investigate the near source Lg excitation and energy partitioning mechanisms such as Pg-Lg and Rg-Lg couplings.

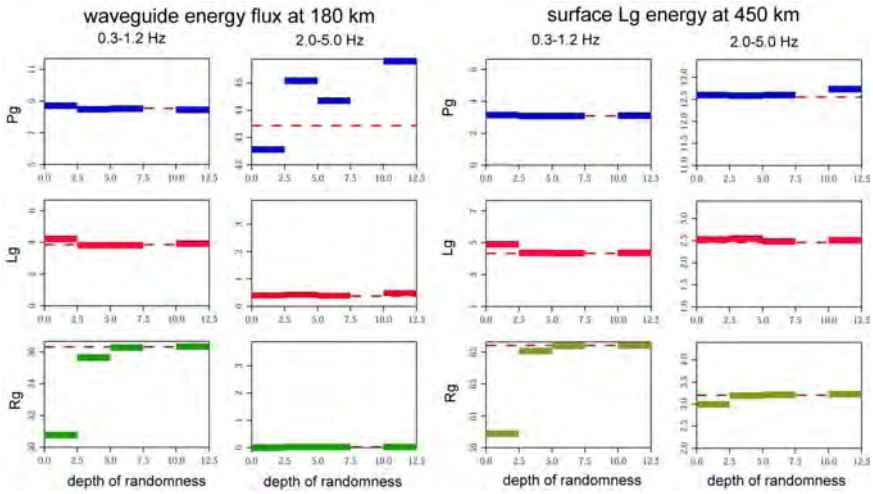


Figure 4. Comparison between waveguide energy flux at 180 km (left panel) and the wave energy on the free surface at 450 km (right panel). This figure is similar to the Figure 3, except the random velocity patches are located between 45 km and 55 km. Because the random patches are located farther away from the source, the coupling between the Rg and Lg is weaker.

Figure 4 is similar to the Figure 3, except that the random velocity perturbations are between 45 km and 55 km from the epicenter. Once again, the low frequency energy flux at a shorter distance correctly predicts the surface Lg wave observations at a larger distance. Because the random velocity perturbations are located farther away from the source, the coupling between the Rg and Lg waves are weaker compared to the near source velocity perturbations. However, if there are velocity perturbations along the entire propagation path, their accumulated effects may still generate considerable Lg energy.

Boundary Element Modeling of P-SV Wave Scattering from the Irregular Topography

Summary of the boundary element method

The Lg wave is composed of multiple reflected shear waves between the free surface and the MOHO discontinuity. Surface topography has an important effect on the Lg-wave excitation and propagation. Although the boundary element method is not an efficient method, it provides a flexible and accurate solution for wave propagation in the models with irregular free surfaces. There are two goals of introducing the boundary element method in the Lg wave analysis. First, we will use an accurate boundary element result to calibrate other fast approximations. Second, we will use the boundary element method to investigate the effect of near source topography on the coupling between the Pg, Rg, and Lg waves. Fu and Wu (2001) applied the boundary element method for calculating the SH-wave propagation. We extend the frequency-domain direct boundary element method to the P-SV case for models with irregular topographies.

Considering the 2-D P-SV wave propagation in a homogeneous region *V* bounded by surface *S*, the displacement **u**(**r**) at location **r** can be calculated by representation integrals (e.g., Aki and Richards, 1980)

$$\mathbf{C}(\mathbf{r})\mathbf{u}(\mathbf{r}) + \int_S \mathbf{\Sigma}(\mathbf{r},\mathbf{r}')\mathbf{u}(\mathbf{r}')\mathbf{d}S = \int_S \mathbf{G}(\mathbf{r},\mathbf{r}')\mathbf{t}(\mathbf{r}')\mathbf{d}S + \int_V \mathbf{G}(\mathbf{r},\mathbf{r}')\mathbf{f}(\mathbf{r}')\mathbf{d}V \tag{1}$$

where **f** is the body force, **G**(**r**,**r**') and **Σ**(**r**,**r**') are Green's functions of the displacement and traction, **t(r)** is the traction, **C**(**r**) is the coefficient matrix, which can be expressed as

$$\mathbf{C}(\mathbf{r}) = \begin{cases} \mathbf{I} & \mathbf{r} \in V \\ \dot{\mathbf{C}}(\mathbf{r}) & \mathbf{r} \in S \\ \mathbf{0} & \mathbf{r} \notin V \end{cases} \tag{2}$$

and

$$\dot{\mathbf{C}}(\mathbf{r}) = \frac{1}{4\pi(1+\mu)} \begin{pmatrix} 2(1-\nu)(\theta_1-\theta_2) + \frac{1}{2}(\sin 2\theta_1 - \sin 2\theta_2) & (\sin^2\theta_1 - \sin^2\theta_2) \\ (\sin^2\theta_1 - \sin^2\theta_2) & 2(1-\nu)(\theta_1-\theta_2) - \frac{1}{2}(\sin 2\theta_1 - \sin 2\theta_2) \end{pmatrix} \tag{3}$$

where μ is the shear module and ν is the Poisson's ratio. Note that the matrix $\dot{\mathbf{C}}$ depends on θ_1, θ_2 and the orientation of the side of the angle in the global coordinate. For simplicity, let **r**' = **0**. In an unbounded homogeneous isotropic elastic medium, the Green's functions for 2-D P-SV case can be expressed as

$$G_{ij}(\mathbf{r}) = \frac{1}{2\pi\rho\beta^2}\left[\psi\delta_{ij} - \phi r_{,i} r_{,j}\right]$$

$$\Sigma_{ij}(\mathbf{r}) = \frac{1}{2\pi}\left[\left(\frac{\partial\psi}{\partial r} - \frac{\phi}{r}\right)\left(\delta_{ij} r_{,k} n_k + r_{,j} n_i\right) - \frac{2\phi}{r}\left(r_{,i} n_j - r_{,i} r_{,j} r_{,k} n_k\right)\right]$$

$$- 2\frac{\partial\phi}{\partial r} r_{,i} r_{,j} r_{,k} n_k + \left(\frac{\alpha^2}{\beta^2} - 2\right)\left(\frac{\partial\psi}{\partial r} - \frac{\partial\phi}{\partial r} - \frac{\phi}{r}\right) r_{,i} n_j$$

where $r = |\mathbf{r}|$, **n** is the normal vector of *S* and pointing outside. "$,i$"and "$, j$" denote $\partial / \partial x_i$ and $\partial / \partial x_j$, α and β are P- and S-wave velocities, and

$$\psi = \frac{i\pi}{2}\left[H_0^{(1)}(k_s r) - \frac{1}{\beta r}\left(H_1^{(1)}(k_s r) - \frac{\beta}{\alpha} H_1^{(1)}(k_p r)\right)\right]$$

$$\phi = \frac{i\pi}{2}\left[\frac{\beta^2}{\alpha^2} H_1^{(1)}(k_p r) - H_1^{(1)}(k_s r)\right]$$

where $H^{(1)}(.)$ is the Hankel function of the first kind, k_p and k_s are P and S wavenumbers, respectively. In the frequency-domain, equation (1) can be discretized along the boundary *S*, which may include irregular topography. Assuming **u**(**r**) and **t**(**r**) are located on the surface *S* and linear over each of the *N* boundary elements, we have the system of linear equations

$$\mathbf{C}(\mathbf{r}^l)\mathbf{u}(\mathbf{r}^l) + \sum_{m=1}^{N}\left\{\left[\mathbf{\Sigma}(\mathbf{r}^l,\mathbf{r}^m)\mathbf{u}(\mathbf{r}^m)\right] - \left[\mathbf{G}(\mathbf{r}^l,\mathbf{r}^m)\mathbf{t}(\mathbf{r}^m)\right]\right\} = \mathbf{u}^0(\mathbf{r}^l) \tag{4}$$

Here *l* and *m* denote the indexes of elements. For free surface, **t**(**r**) =**0**. For internal interfaces, continuity conditions of displacements and stresses should be satisfied. By solving the linear equations, the displacements and stresses at all boundary elements can be obtained. Using the integral representation, the wavefield everywhere inside the volume can then be obtained.

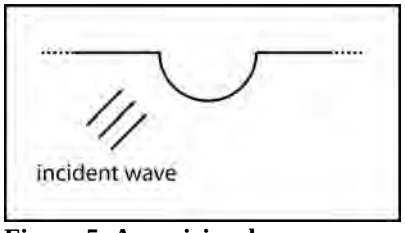


Figure 5. A semicircular canyon model.

Numerical tests. To test the accuracy of the method, we conducted a series of calculations using our boundary element method and compared the results with those calculated from other methods. The first model is a semicircular canyon on a homogeneous half-space with a Poisson's ratio of 1/3 (Figure 5). The plane waves with incident angles of 0 degree and 30 degrees are incident on the free surface. This problem has been studied by many authors for

example: Kawase, 1988; Sanchez-Sesma and Rosenbluth, 1979; and Sanchez-Sesma and Campillo, 1991. Their results were in agreement with each other. Here we compare our results to that of Sanchez-Sesma and Campillo (1991) and calculated them using an indirect boundary integral method. The results of plane P and SV waves with incident angles 0 and 30 degrees are shown in Figure 6. Normalized frequencies $\eta = \omega a/\pi\beta$ = 1.0, 1.5, and 2.0 are used in the calculation. The results show good agreement with the previous authors.

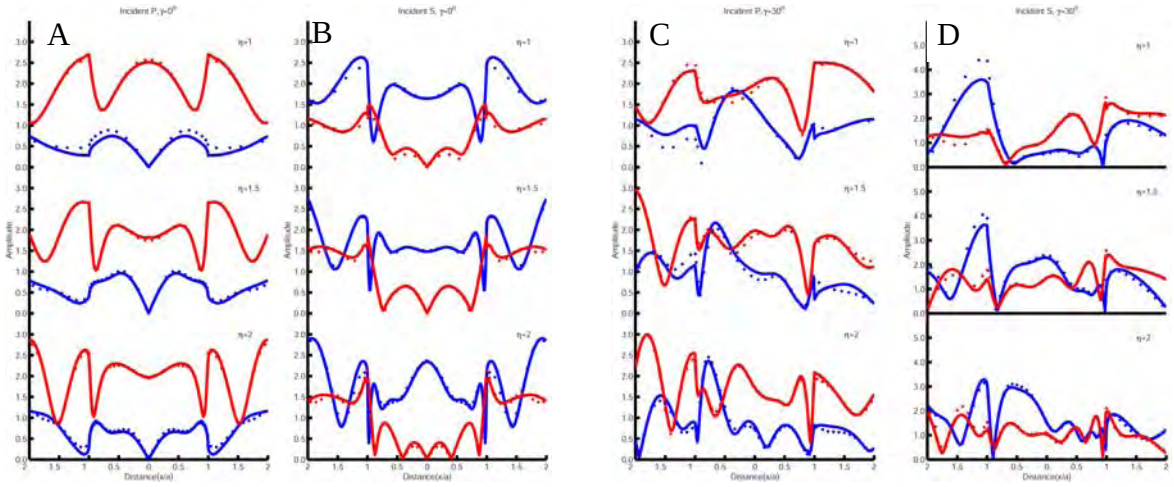


Figure 6. The comparison between our results and Sanchez-Sesma's results for a semicircular canyon model. A: vertical P-wave incidence, B: vertical SV-wave incidence, C: 30 degree P-wave incidence and D: 30 degree SV-wave incidence. From upper to bottom are for normalized frequencies 1.0, 1.5 and 2.0. The solid lines denote our results and the dotted lines denote Sanchez-Sesma's results.

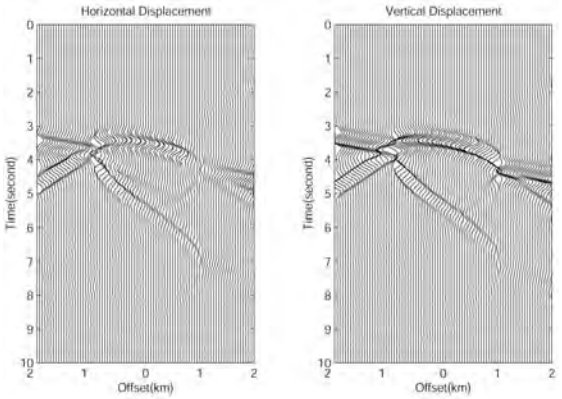


Figure 7. Synthetic seismograms at the free surface of a semicircular canyon. A 30 degree P-wave is incident on the surface. On the left and right are horizontal and vertical components.

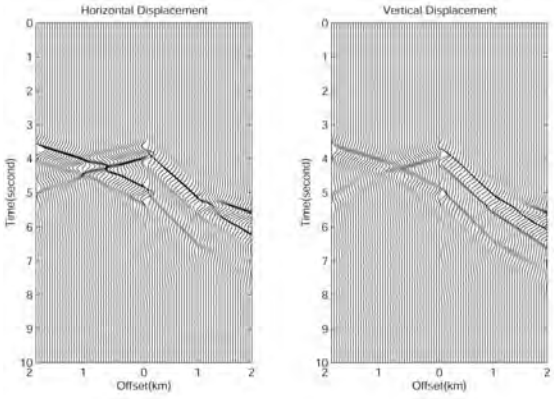


Figure 8. Synthetic seismograms at the free surface of a triangular canyon. A 30 degree SV-wave is incident on the surface. On the left and right are horizontal and vertical components.

Shown in Figure 7 are synthetic seismograms on the free surface of a semicircular canyon. A 30 degree P-wave is incident on the surface. The receivers are located along the surface from -2 to 2 km. The reflected P-wave can be clearly seen along the left wall of the canyon. We can also see the creeping Rayleigh waves that propagate along the surface of the canyon. Similarly, Figure 8 shows the response of a triangular canyon to a 30 degree SV-wave incidence. Reflected P waves and diffracted Rayleigh waves from the edges of the canyon can be identified in the synthetic seismograms.

To reduce the computation cost, especially for long propagation distances, we designed a connection technique. To avoid solving a huge matrix, the entire waveguide is divided into several sections. Artificial interfaces are

introduced between the adjacent sections. Assuming that the Lg wave does not produce multiple scattering between different sections, a transparent boundary condition can be adopted at these artificial boundaries. The output from one section can be used as the input of the next section. The entire matrix can be divided into several small matrixes and fit into conventional computer memories. Figure 9 gives a simple example on how this technique works. The waveguide is composed of a flat one-layer crust over the upper mantle. The solid lines are synthetic seismograms calculated directly from the source to the receivers. The dotted lines are synthetic seismograms calculated using the connection technique. The two results are consistent with each other.

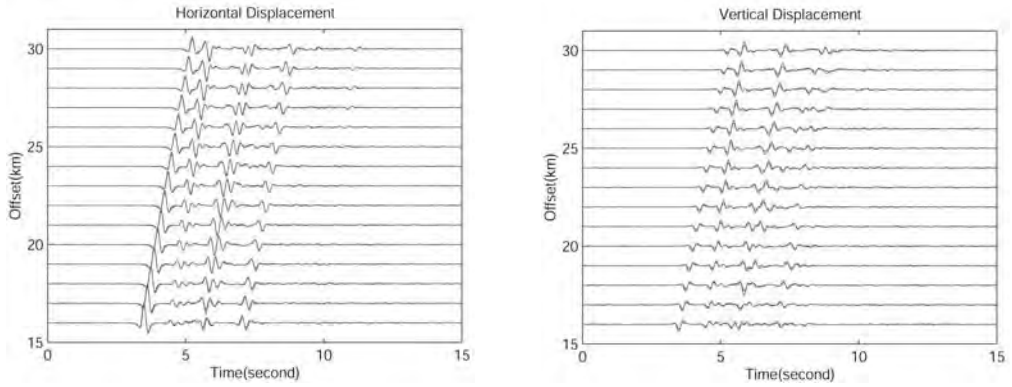


Figure 9. Comparison of synthetic seismograms calculated using the connection technique (dotted lines) and those directly calculated from the source to receivers (Solid lines). On the left is the horizontal component and on the right is the vertical component.

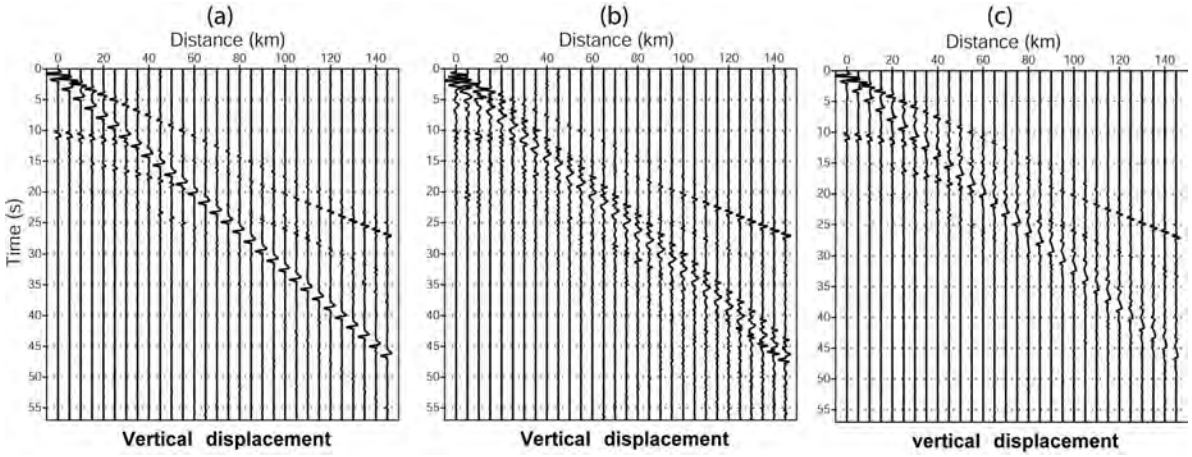


Figure 10. Scattering of Rg waves due to irregular free surface: (a) reference model with a flat free surface, (b) model with a near source irregular free surface, and (c) model with mild irregular free surface along the entire path.

Rg wave scattering on the irregular topography

To investigate the effect of irregular topography on the Rg scattering, we calculated the synthetic seismograms for crustal waveguide models with and without irregular topographies. In Figure 10 we show the vertical component of a synthetic seismograms for different velocity models. Figure 10a is the reference model, which is a two-layer model composed of a flat crust and a homogeneous upper mantle. The depth of the Moho discontiniuity is 32 km. The P- and S-wave velocities for the crust are 6 km/s and 3.4 km/s, and 8.0 km/s and 4.6 km/s, respectively, for the upper mantle. In Figure 10b, a section of a near source irregular topography is added to the reference model between 0 and 20 km. Its RMS value is 0.6 km and the correlation length is 1 km. In Figure 10c, the model has an irregular topography along the entire free surface. Its RMS value is 0.3 km and the correlation length is 5 km. Both irregular topographies provide the Rg-wave scatterings although their appearances are different. Detailed characteristics of

these scatterings and their contributions to the explosion source energy partitioning will be investigated in the furture.

Simulation of Lg Wave Propagation and Blockage Using the Elastic Screen Method

Many observations reveal that the attenuation of the regional phase Lg relates to the waveguide structures of all scales. Both elastic and anelastic properties contribute to the attenuation. However, the mechanism of the Lg wave attenuation has not been fully understood. The numerical simulation is still one of the most important ways to investigate the Lg wave attenuation mechanisms. We continue to investigate the path effects using the elastic screen propagators. More realistic crustal models including heterogeneities of different scales and intrinsic attenuations are used in the numerical simulations. Two numerical examples are presented here to show how this method works.

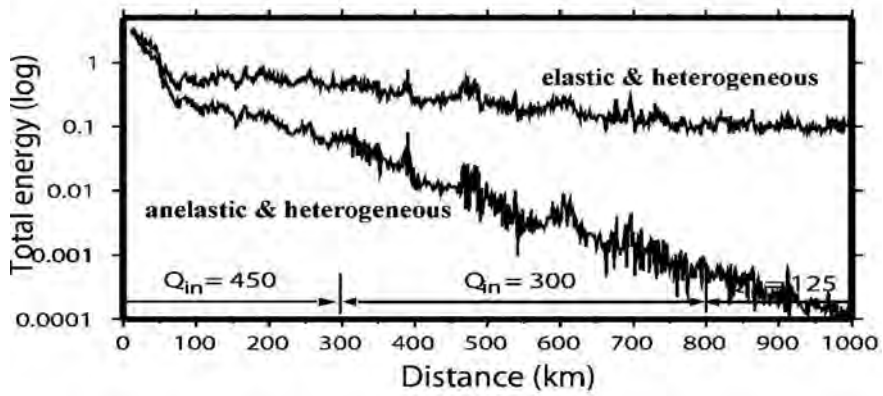


Figure 11. Synthetic SH Lg wave attenuation curves for Tibetan Plateau. Compared to the elastic case, the anelastic crust gives much higher Lg energy attenuation.

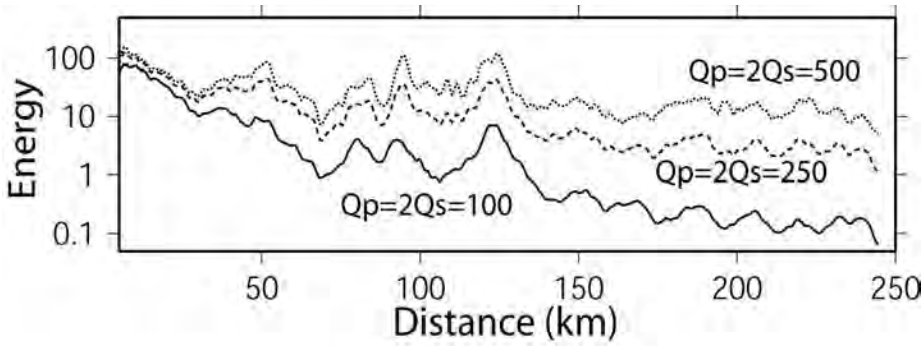


Figure 12. Synthetic P-SV Lg wave attenuation curves for the Flora-Asnes crust model. The intrinsic attenuation in the crust plays an important role for Lg energy attenuation.

SH Lg simulation for the Tibetan Plateau model.

Regional phase Lg has been widely observed across Asia. However, for the propagation paths crossing the Tibetan Plateau, little energy can be observed. It has been demonstrated that the Lg-wave undergoes an abnormally strong attenuation in this region. For the SH case, a waveguide model based on the actual topography and the depth of the Moho discontinuity is designed for the simulation. In addition to the large-scale crustal structures, random velocity fluctuation is added to the crustal waveguide. The horizontal and vertical correlation lengths of the random fluctuation are 10 km and 5 km. The RMS velocity perturbation is 10%. The source is located at a depth of 16 km and its dominant frequency is 2 Hz. Both elastic and anelastic models are used in the calculation. For the anelastic case, a laterally varying intrinsic attenuation is added to the model. Figure 11 gives the Lg energy attenuation curves along a 1000 km path. Even with the proper heterogeneities, the elastic model fails to explain the observed strong Lg attenuation and its regional distribution. On the other hand, after the intrinsic attenuation is introduced, the Lg energy dropped three orders of magnitude compared with the elastic model. The results are compatible with the observations in the region.

P-SV Lg-wave propagation in the Flora-Asnes crust model

For the P-SV wave case, we are continually working to improve the stability of our complex screen propagator for long distance propagation. At the same time, we are working on the couplings between the body waves and the surface wave. Figure 12 shows the P-SV Lg wave attenuation versus distance. The 1-D background model is the Flora-Asnes crust model in the NORSAR region. A random velocity fluctuation with a 10% RMS value and correlation lengths similar to the SH wave case is added to the background model. Three sets of P- and S-wave quality factors are used in the calculation. The results show that the intrinsic attenuation plays an important role in the Lg wave energy decay.

CONCLUSIONS AND RECOMMENDATIONS

The purpose of the project is to develop computationally viable techniques for investigating the excitation and path effects of high frequency regional waves. Currently there are three research directions under this project. First, a finite-difference modeling plus slowness analysis method is developed for predicting the Lg-wave energy. This work is essential for both discriminating explosions and earthquakes, and for understanding Lg wave energy partitioning. Second, the boundary element method for both SH and P-SV cases are developed and tested. Although the boundary element method is not an efficient solution, we can use it to calibrate other fast approximations and investigate the effect of near source topography on the Rg-Lg coupling. Third, We are continually working on the high efficiency GSP propagators for both SH and P-SV Lg-wave simulations. In general, we are trying to build computational tools that can handle more realistic crust models and use these tools to investigate the excitation and propagation of Lg-waves in different geological structures.

REFERENCES

Aki, K. and P.G., Richard (1980), Quantitative seismology, W. H. Freeman, San Francisco.

Fu, L.Y. and R.S., Wu (2001), A hybrid BE-GS method for modeling regional wave propagation, *Pure and Apply Geophysics*, 158, 1251-1277.

Gupta, I.N., W.W. Chan, and R.A. Wagner (1992), A comparison of regional phases from underground nuclear explosions at east Kazakh and Nevada test sites, *Bull. Seism. Soc. Am*., 82, 352-382.

Gupta, I.N., T.W. McElfresh, and R.A. Wagner (1991), Near source scattering of Rayleigh to P in teleseismic arrivals from Pahute Mesa (NTS) shots, in *Explosion Source Phenomenology*, edited by, Taylor, S.R., Patton, H.J. and Richards, P.G., American Geophysical Union, Washington, DC.

Kawase, H. (1988), Time domain response of a semicircular canyon for incident SV, P, and Rayleigh waves calculated by the discrete wavenumber boundary element method, *Bull. Seism. Soc. Am.* 78, 1415-1437.

Sanchez-Sesma, F.J. and M., Campillo (1991), Diffraction of P, SV and Rayleigh waves by topographic features: A boundary integral formulation, *Bull. Seism. Soc. Am.*, 81, 2234-2253.

Sanchez-Sesma, F. J. and E., Rosenblueth (1979), Ground motion at canyons of arbitrary shape under incident SH waves, *Intl. J. Earthq. Eng. Struct. Dyn*., 7, 4441-4450.

Wu, R.S., S. Jin, X.B. Xie (2000a), Seismic wave propagation and scattering in heterogeneous crustal waveguides using screen propagators: I SH waves, *Bull. Seis. Soc. Am*., 90, 401-413.

Wu, R.S., S. Jin, X.B. Xie (2000b), Energy partition and attenuation of Lg waves by numerical simulations using screen propagators, *Phys. Earth and Planet. Inter*., 120, 227-244.

Wu, X.Y. and R.S. Wu (2001), Lg-wave simulation in heterogeneous waveguides with surface topography suing screen propagators, *Geophys. J. Int*., 146, 670-678.

Xie, X.B. and T. Lay (1994), The excitation of Lg waves by explosions: A finite-difference investigation, *Bull. Seism. Soc. Am*., 84, 324-342.

Pn Q UNDER TIBET AND TIENSHAN WITH PRACTICAL AND SCIENTIFIC IMPLICATIONS

Jiakang Xie

Lamont-Doherty Earth Observatory, Columbia University

Sponsored by Defense Threat Reduction Agency

Contract No. DTRA01-00-C-0048

ABSTRACT

Pn waves from three near-co-located seismic events in the eastern Tarim Basin are well recorded by seismic arrays in Kyrghistan and the central and southern portions of the Tibetan Plateau. These events include two underground nuclear explosions from 1994 and one nearby earthquake from 1999, all with similar magnitudes (~5.9). Pn waves recorded at the Kyrghistan and Tibetan (INDEPTH) arrays sample the uppermost mantle under the Tienshan and Tibetan plateaus, respectively, and have similar distance ranges of ~1,000 km. Pn wave arrival times are used to estimate high-apparent velocities of 8.3– 8.4 km/s under the Kyrghistan and southern Tibetan arrays, and low-apparent velocities of about 7.6 km/s under the north central Tibet array. Pn amplitudes are highly variable across the Kyrghistan array (by a factor of ~19). When stacked across the arrays, the average Pn wave amplitude over the Tienshan and Tibetan paths have very similar levels at low frequencies (~0.3 Hz). With increasing frequency, the average amplitudes over the Tibetan paths become lower and lower as compared to those over the Tienshan paths. At 4 Hz the average amplitudes over the Tibetan paths drop to a factor of 40, lower than those over Tienshan paths. The Pn wave source spectra can be successfully modeled by the modified Mueller-Murphy (MMM) and Brune source models for the explosions and the earthquake, respectively. A spectral overshoot near the corner frequencies (between 1-2 Hz) in the MMM source model is required to fit the explosion spectra. Pn attenuation can be modeled by a Pn Q that follows a power-law frequency dependence. We estimated the Pn Q_0 (Pn Q at 1 Hz) to be 30% higher over the Tienshan paths than over the Tibetan paths. We found the most striking difference is the power-law exponent η values; η is ~0.5 over the Tienshan paths and is ~0 over the Tibetan paths.

A practical implication of our result is that when we attempt to identify explosions with seismic data over paths with an Lg blockage, we may take advantage of the spectral overshoot that is present in the explosion Pn source spectra but absent in the earthquake source spectra. Array data is highly desirable owing to the inherent instability of Pn wave amplitudes. A scientific implication is that a melt-bearing uppermost mantle, such as that under Tibet, may have a frequency-independent P wave Q. This frequency independence is in direct contrast with the normal, “dry” uppermost mantle in which P wave Q is moderately dependent on frequency.

OBJECTIVE

The primary objective of this research is to quantify propagation and attenuation of high-frequency regional waves in and around the Tibetan plateau. We wish to measure the laterally-variable Pn and Lg Q and the travel times of Pn waves from events in the southern and central Tarim Basin of Tibet. Additionally, we wish to invert fundamental-mode surface waves to obtain depth variations of crustal Q in localized regions inside the plateau, such as the regions behind the vast Himalayas where Lg blockage appears to take place.

This research provides important data for the worldwide monitoring of nuclear explosions. The Q and travel times can be used for estimating source spectral characteristics and locations of any future seismic events to infer their nature and size. A comparison of the source spectra of explosions and earthquakes, estimated using the Pn over Tibetan paths, allows us to test the possibility of identifying the source type using the Pn alone when the Lg and Sn waves are blocked. Details of the lateral variations of Q will also enable us to search for a physical mechanism, such as a molten crust or upper mantle, that is responsible for the severe attenuations of regional waves in complex, low-Q regions of the world.

RESEARCH ACCOMPLISHED

Data Processing

We collected Pn waveforms from three nearby co-located seismic events in the eastern Tarim Basin. These events include two underground explosions on June 10 and October 7, 1994 with an mb of 5.7 and 5.9, respectively; and an earthquake on January 30, 1999 with an mb of 5.9 (Figure 1). The two explosions were recorded by multiple portable stations deployed in southern Tibet during the 1994 INDEPTH II PASSCAL experiment. The earthquake was recorded by stations deployed in the central and southern regions of Tibet during the 1999 INDEPTH III experiment. All three events were also recorded at the Kyrghistan network (KNET), which is located to the west of the events and consists of eleven broadband stations. As shown in Figure 1, Pn to the INDEPTH stations travels southward, mainly sampling the uppermost mantle under Tibet. By contrast, Pn to the KNET stations travels westward, sampling the mantle under Tienshan. The distances in ranges to the INDEPTH and the KNET arrays are similar (roughly 1,100±200 km). In this study, only vertical-component seismograms are used. Figure 2 shows examples of the record sections that contain Pn. On each record Pn arrival times are read. The Fourier amplitude spectra of Pn and early Pn coda are obtained by using multiple windows of 4.5 s with a 50% overlap (Xie and Patton, 1999). These spectra are then averaged to yield a stable spectral estimate of Pn and early Pn coda. From here on we will refer to the averaged spectra of Pn and early Pn coda as “Pn spectra”.

Apparent Pn Velocities Under Tibet and Tienshan

The Pn arrival times at the KNET and INDEPTH arrays are used to fit the apparent Pn velocities v_{app}, under these arrays (Figure 3). The values of v_{app} under the KNET are high (8.3 km/s or higher). Values of v_{app} under the INDEPTH II and the southern half of the INDEPTH III arrays, south of the Bangong-Niujiang Suture (BNS), in Figure 1) are also high (about 8.3–8.4 km/s). On the other hand, the value of v_{app} under the northern half of the INDEPTH III array is low (about 7.7 km/s). This value is consistent with the previous discovery that the upper 100–150 km of the mantle under northern Tibet has slow P velocities (Zhao and Xie, 1993; McNamara et al., 1997).

Pn Amplitude Variability Across the Arrays

In the top panel of Figure 2, the time domain Pn amplitude varies by a factor of 19 across the KNET from the October 7 explosion. This instability of Pn amplitudes had been noticed before. Xie (1996) has explored extensively the origin of this instability and concluded that a Moho topography near the KNET is the most likely reason for this instability. Figure 4 shows a calculated ray pattern in the model that contains a Moho thinning, which might occur on the eastern side of the KNET as a deep signature of Lake Issyk-Kul. The ray focusing/defocusing in Figure 4 gives rise to an amplitude variability that is qualitatively similar to that observed in the top of Figure 2. The Moho thinning model in Figure 4 is 2-D and we anticipate even stronger focusing/defocusing if the Moho thinning has a more realistic 3-D shape.

Differences in Pn Attenuation Under Tibet and Tienshan

Figure 5 shows the Pn spectra from the October 7 explosion and the January 30 earthquake, both with an mb of 5.9. Similar to the time domain amplitude variability discussed earlier, the Pn spectra vary drastically by a factor of up to 10 for the INDEPTH and 20 for the KNET arrays, respectively, across each array. However, the array-average spectra (thick curves) start at similar levels at the lowest frequencies of about 0.3 Hz for different arrays recording the same event. Since the recording distances of the different arrays are similar (Figures 1 through 3), these similar low-frequency amplitudes of the array average mean that the uppermost mantle under Tibet and Tienshan have similar Pn attenuation rates. With increasing frequency the array-averages become more and more different than those from the INDEPTH arrays and lower than those from KNET. This difference means that the Tibetan mantle becomes increasingly more attenuated (compared to the Tienshan mantle) as the frequency increases. At 4 Hz in Figure 5, the INDEPTH array-average of Pn spectra is about 40 times lower than the KNET average. Another interesting phenomenon is that the explosion Pn spectra contains overshoot between 1–2 Hz, which is absent in the earthquake Pn spectra.

Following Xie and Patton (1999) we can quantify the above difference in Pn attenuation by assuming (1) a stochastic model of Pn spectra, (2) the modified Mueller-Murphy and Brune model for explosion and earthquake source spectra, respectively; and (3) a power-law frequency dependence of Pn Q:

$$Q_{Pn}(f) = Q_0 f^{\eta}$$

Using a Bayesian inverse method Xie and Patton (1999) estimated the moments and corner frequencies of Pn source spectra from the 1994 explosions; they also estimated Pn Q to the KNET stations from the explosion site (Lop Nor). In this study, we use these estimates as *a priori* knowledge to estimate the Pn Q to the INDEPTH arrays. The following Pn Q models are obtained:

$$Q_{Pn}(f) = (284 \pm 60) f^{(-0.1 \pm 0.2)}$$

from Lop Nor to INDEPTH II

$$Q_{Pn}(f) = (266 \pm 65) f^{(0.1 \pm 0.2)}$$

from Lop Nor to INDEPTH III, and

$$Q_{Pn}(f) = 364 f^{0.5}$$

from Lop Nor to KNET.

The 1-Hz Pn Q (Q_0) differs by about 30% under Tienshan and Tibet from the above equations. But Q_0 is not a good measure of how Pn Q differs under Tibet and Tienshan. This conclusion is so because in Figure 5 we see that Pn attenuation, or Q, should be roughly the same at the lowest frequencies of about 0.3 Hz. With increasing frequency, Pn Q under Tienshan and Tibet becomes more and more different. At 1 Hz the difference is minor compared to the difference at the higher frequencies. Fundamentally it is the frequency dependence, η, that characterizes the difference of Pn Q under Tibet and Tienshan; η is virtually 0 under the former and is moderate (about 0.5) under the latter. Previously, much of the Tibetan mantle traversed by Pn waves recorded at the INDEPTH arrays has been inferred to be partially molten based on studies of Pn velocity and Sn attenuation. By contrast, the Tienshan mantle is not a melt-bearing.

Practical and Scientific Implications

A practical implication of results of this study is that where regional S waves (e.g., Lg and Sn) are blocked, Pn spectra may be useful in event identification since explosion sources do, but earthquake sources do not, exhibit the spectral overshoot. Array data seem to be necessary in such a possible event identification to suppress the P-wave amplitude variability. Also, knowledge of Pn Q will be helpful because removing the path affect may enhance the source spectral signatures.

A scientific implication is that a melt-bearing mantle such as that under north and central Tibet may have an inherent physical property—that is, its bulk Q is nearly invariant between frequencies of a fraction of 1 Hz and a few Hz. This invariance contrasts with a dry mantle such as that under Tienshan in which bulk Q is moderately dependent on frequency. Recently Faul at el (2003) have conducted laboratory measurements of shear Q in olivine at seismic frequencies and upper mantle temperatures and pressures. They found that that a small fraction (<3%) of melt could produce a broad peak over which shear Q is independent of frequency. They infer that melt-bearing grain-boundary

gliding and diffusion may be the primary mechanisms for the shear wave energy loss. These microscopic mechanisms may be at work for bulk Q, as well.

CONCLUSIONS AND RECOMMENDATIONS

Pn waves from two explosions and a nearby earthquake in the eastern Tarim Basin have been recorded by arrays in Kyrghistan and central and southern Tibet. The respective Pn paths sample the uppermost mantle under the Tienshan and the Tibetan plateaus, respectively, at similar distances (around 1,000 km). Pn arrival times yield estimates of high-apparent velocities of 8.3–8.4 km/s under the Kyrghistan and southern Tibetan arrays, and low-apparent velocities of about 7.6 km/s under north central Tibet. Pn amplitudes are highly variable across each array (by factors of 10–20). When stacked over the arrays, the average Pn amplitudes over the Tienshan and Tibetan paths have very similar levels at low frequencies (~0.3 Hz). With increasingly higher frequencies, the average amplitudes over the Tibetan paths become increasingly lower as compared to those over the Tienshan paths. At 4 Hz the average amplitudes over the Tibetan paths drop to 40 times lower than those over Tienshan paths. The modified Mueller-Murphy and Brune source models can be used to successfully model the Pn source spectra for the explosions and earthquake. A spectral overshoot near the corner frequencies (between 1–2 Hz) is required to fit the explosion spectra. Pn Q is assumed to follow a power-law frequency dependence. We estimated Pn Q_0 (Pn Q at 1 Hz) to be 30% higher over the Tienshan paths than over the Tibetan paths. The most striking difference is found in η values; η is ~0.5 over the Tienshan paths and ~0 over the Tibetan paths.

Our results have both a practical implication in source identification using P waves and a scientific implication on an inherent frequency-independent bulk Q of the melt-bearing uppermost mantle. These implications lead to two recommended future works: (1) an exploration of whether it is feasible to use Pn or mantle P waves, recorded by arrays, to detect explosions which seem to exhibit spectral overshoots—such a use of P wave spectra for event identification may be necessary over paths of Lg and Sn blockage; and (2) measurements of bulk Q in the uppermost mantle in other regions not only to enhance our monitoring capability, but also to explore if an frequency-independent Q is a general, intrinsic property of the melt-bearing upper mantle.

REFERENCES

Faul, U.H., J.D. Fitz Gerald and I. Jackson (2003), Shear-wave attenuation and dispersion in melt-bearing olivine polycrystals II. Microstructural interpretation and seismological implications**,** *J. Geophys. Res*., submitted.

McNamara, D., W.R. Walter, T.J. Owens, and C.J. Ammon (1997), Upper mantle velocity structure beneath the Tibetan Plateau from Pn travel time tomography, *J. Geophys. Res*., **102**, 493-505.

Roecker, S.W., T.M. Sabitova, L.P. Vinnik, Y.A. Burmakov, M.I. Golyanov, R. Mamatkanova, and L. Munirova (1993), Three-dimensional elastic wave structure of the western and central Tien Shan, *J. Geophys. Res*., **98**, 15779-15795.

Xie, J. (1996), Synthetic and observational study of Pn excitation and propagation in central Asia, *Phillips Laboratory Scientific Report No. 1*, PL-TR-96-2270, 24 pp.

Xie, J. and H. Patton (1999), Regional Phase Excitation and Propagation in the Lop Nor Region of Central Asia and Implications for the Physical Basis of P/Lg Discriminants, *J. Geophys. Res*., **104**, 941-954.

Zhao, L.S. and J. Xie (1993), Lateral variations in compressional velocities beneath the Tibetan Plateau from Pn travel time tomography, *Geophys. J. Int*., **115**, 1970-1084.

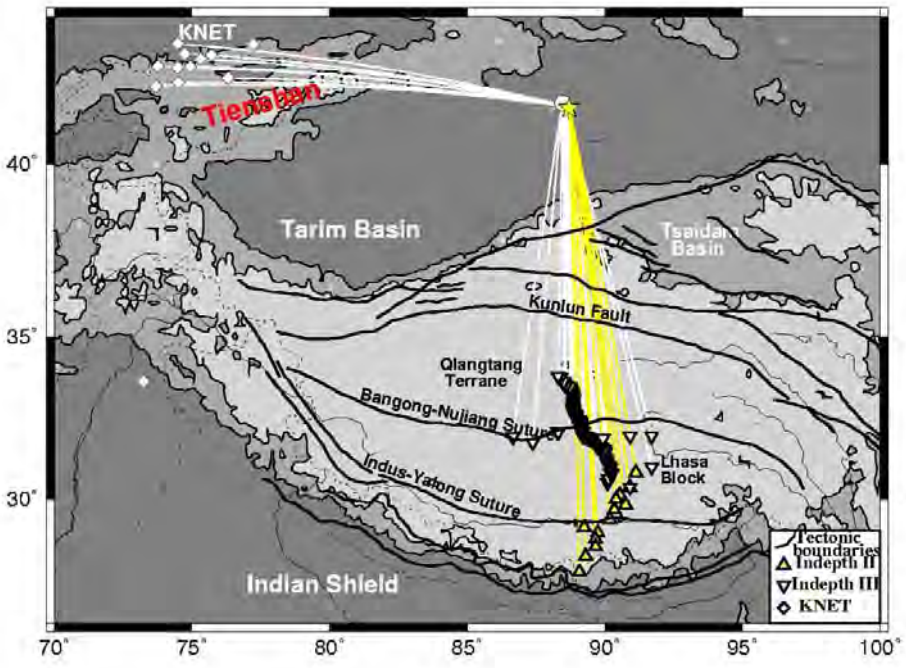


Figure 1. Map showing the tectonic and geographic features of the study area of the 1994 explosions (stars), the 1999 earthquake (circle), and KNET and INDEPTH stations (see legend), and the PN paths used.

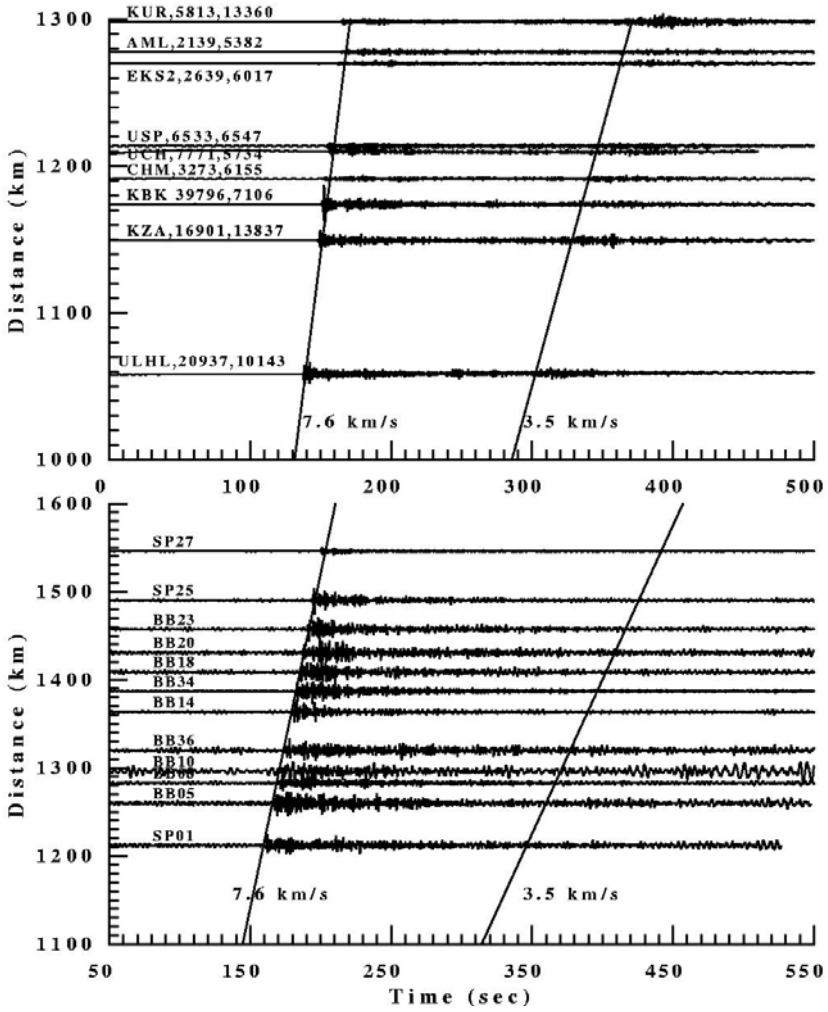


Figure 2. (Top) Record section from the October 7, 1994 explosion (mb=5.9) across the KNET. Station names, maximum Pn and Lg amplitudes in digital counts are written near the traces. The instrument gains are unified. The maximum Pn amplitude at KBK is about 19 times greater than that at AML. (Bottom) Record section from the same explosion but across the INDEPTH II array. Note the Lg is blocked.

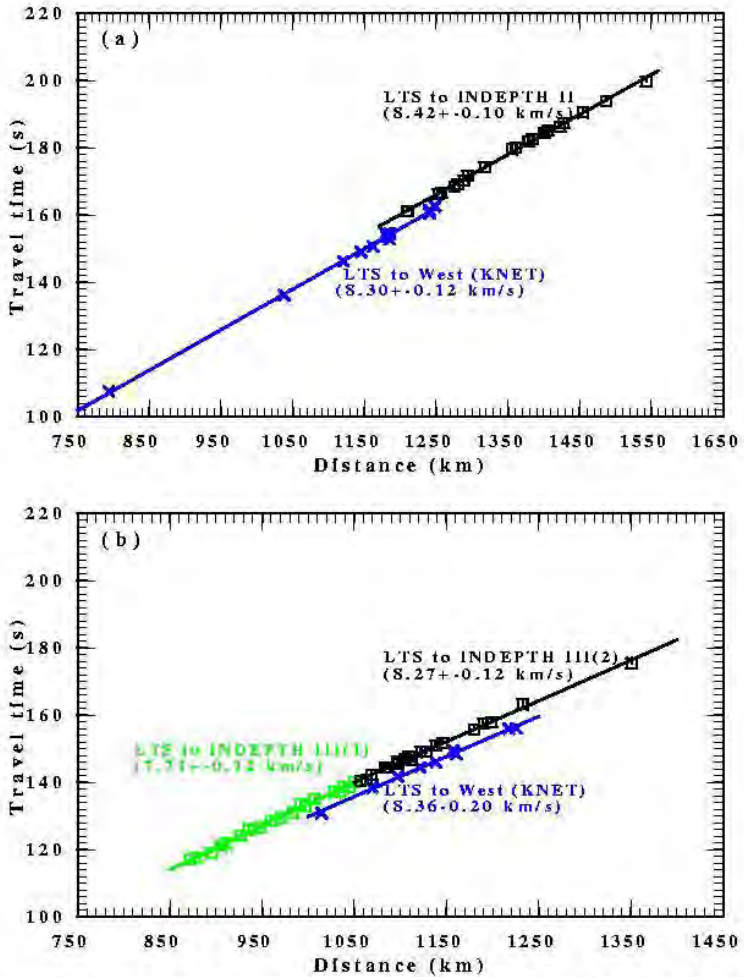


Figure 3. (a) Pn travel times from the October 7 Lop Nor Test Site (LTS) explosion to the INDEPTH II array (squares) and the KNET stations (crosses). Straight lines are linear regression fit for apparent Pn velocities. (b) Pn travel times from the January 30 LTS earthquake to the INDEPTH III sub-arrays (1) and (2) that are composed of stations north and south of the BNS (see Figure 1), plotted as squares (crosses). Straight lines are linear regression fit for apparent Pn velocities.

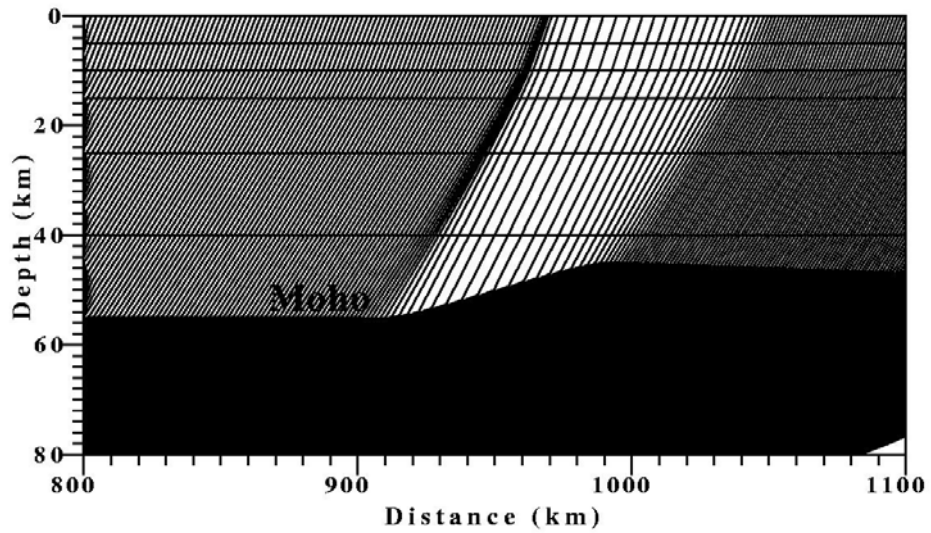


Figure 4. Pn ray pattern in a model for Tienshan by Rocker et al. (1993) that is modified from the Model M1 by adding a 2-D Moho topography. The ray tracing is conducted to simulate the focusing/defocusing effect by a Moho thinning under Lake Issyk-Kul and may be more complex (3-D) producing a more pronounced focusing/defocusing to Pn. We consider such Moho thinning the most likely cause of the large variability in Pn amplitude across the KNET.

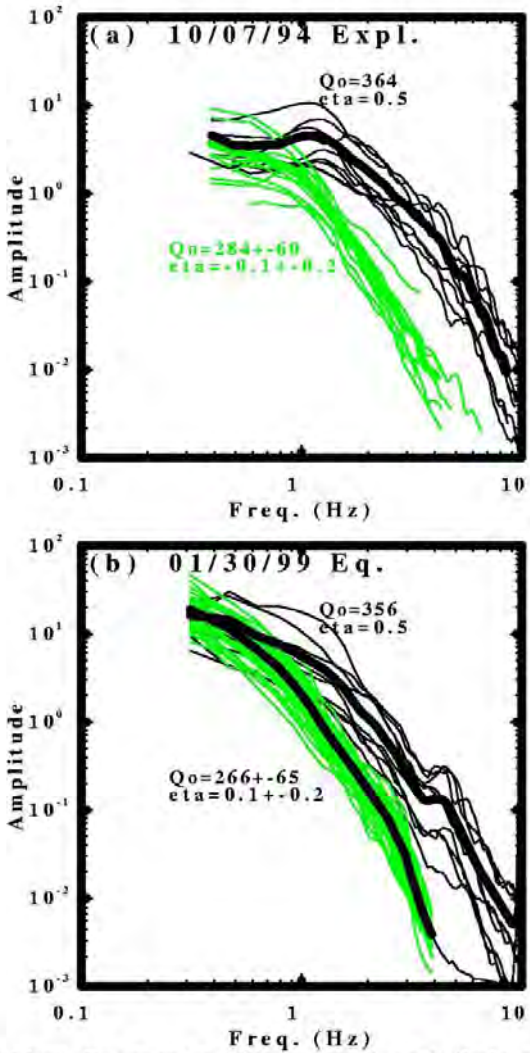


Figure 5. Individual Pn spectra (thin curves) and their array-average (thick curves). Panels (a) and (b) are spectra from the October 7, 1994 explosion and the January 30, 1999 earthquake, respectively. Black curves are for paths to the west (KNET array). Green curves are for the paths to the south (the INDEPTH II and III arrays in panels (a) and (b), respectively. Average Pn Q0 and η to the west and south are written near the curves. Note the apparent spectral overshoot in the curves in (a).

Seismic Event Detection and Location

SEISMIC EVENT LOCATION: DEALING WITH MULTI-DIMENSIONAL UNCERTAINTY, MODEL NON-LINEARITY AND LOCAL MINIMA

Sanford Ballard

Sandia National Laboratories

Sponsored by National Nuclear Security Administration
Office of Nonproliferation Research and Engineering
Office of Defense Nuclear Nonproliferation

Contract No. DE-AC04-94-AL85000

ABSTRACT

Seismic event location is made challenging by the difficulty of describing event location uncertainty in multi-dimensions, by the non-linearity of the Earth models used as input to the location algorithm, and by the presence of local minima which can prevent a location code from finding the global minimum. Techniques to deal with these issues will be described. Since some of these techniques are computationally expensive or require more analysis by human analysts, users need a flexible location code that allows them to select from a variety of solutions that span a range of computational efficiency and simplicity of interpretation. A new location code, LocOO, has been developed to deal with these issues.

A seismic event location is comprised of a point in 4-dimensional (4D) space-time, surrounded by a 4D uncertainty boundary. The point location is useless without the uncertainty that accompanies it. While it is mathematically straightforward to reduce the dimensionality of the 4D uncertainty limits, the number of dimensions that should be retained depends on the dimensionality of the location to which the calculated event location is to be compared. In nuclear explosion monitoring, when an event is to be compared to a known or suspected test site location, the three spatial components of the test site and event location are to be compared and 3 dimensional uncertainty boundaries should be considered. With LocOO, users can specify a location to which the calculated seismic event location is to be compared and the dimensionality of the uncertainty is tailored to that of the location specified by the user. The code also calculates the probability that the two locations in fact coincide.

The non-linear travel time curves that constrain calculated event locations present two basic difficulties. The first is that the non-linearity can cause least squares inversion techniques to fail to converge. LocOO implements a non-linear Levenberg-Marquardt least squares inversion technique that is guaranteed to converge in a finite number of iterations for tractable problems. The second difficulty is that a high degree of non-linearity causes the uncertainty boundaries around the event location to deviate significantly from elliptical shapes. LocOO can optionally calculate and display non-elliptical uncertainty boundaries at the cost of a minimal increase in computation time and complexity of interpretation.

All location codes are plagued by the possibility of having local minima obscuring the single global minimum. No code can guarantee that it will find the global minimum in a finite number of computations. Grid search algorithms have been developed to deal with this problem, but have a high computational cost. In order to improve the likelihood of finding the global minimum in a timely manner, LocOO implements a hybrid least squares-grid search algorithm. Essentially, many least squares solutions are computed starting from a user-specified number of initial locations; and the solution with the smallest sum squared weighted residual is assumed to be the optimal location. For events of particular interest, analysts can display contour plots of gridded residuals in a selected region around the best-fit location, improving the probability that the global minimum will not be missed and also providing much greater insight into the character and quality of the calculated solution.

OBJECTIVE

Introduction

The objective of this study is to improve our ability to locate seismic events relative to current techniques. The main areas where current practice can be improved includes the addition of capability to report 3D and 4D uncertainty information, improved handling of non-linear Earth model effects, and increasing the probability of finding global as opposed to local minima when seeking the seismic event location that best fits the available data. In addition, a new method of calculating the uncertainty ellipses around fixed-depth event location solutions is also described.

Multidimensional Uncertainty Boundaries.

The linear least squares seismic event location algorithm returns two fundamental objects, examples of which are:

```
Final location:

  latitude longitude     depth     origin_time
   27.4255   71.4839    37.456   894881631.266

4D space-time uncertainty hyper_ellipse:

  Principal axes:
  North:  -5.13552111E-01   3.60035966E-01   3.74867000E-01   9.32939723E-01
  East:   -6.33040235E-02  -9.32938424E-01   9.25246750E-01   3.60032600E-01
  Depth:  -8.46798394E-01  -4.79448998E-08  -8.38960340E-03   2.72955198E-08
  Time:   -1.23244918E-01   3.04267339E-07   5.76437276E-02  -2.87875086E-07
  Length:  3.47029259E+01   2.08530626E+01   1.24056628E+01   4.84719957E+00
```

The first object is the seismic event location that consists of the latitude, longitude, depth and origin time that yields the smallest sum squared weighted difference, in a least squares sense, between observed and predicted seismic parameters. The second object is the uncertainty in the location, which consists of a 4D hyper-ellipse that surrounds the best-fit seismic event location. In this example, the uncertainty hyper-ellipse is represented by a 5 x 4 matrix. Each of the 4 columns of this matrix describes one of the 4 principal axes of the uncertainty hyper-ellipse. The first four elements of each column describe a 4 dimensional unit vector in Cartesian coordinates while the last element in each column describes the length of the vector in 4D space-time. The length represents the distance from the best-fit event location (the center of the hyper-ellipse) to the contour in 4D location space where the sum squared weighted residuals is greater than the sum squared weighted residuals that characterizes the best-fit location by a value of 1.

While this depiction of the uncertainty hyper-ellipse is complete, it is not particularly useful in terms of providing significant insight into the level of confidence we might have in our best-fit event location. There are two problems with it. The first is that a contour in location space where $\Delta c^2 = 1$ is difficult to interpret. Fortunately, there are statistical formulas that tell us how to scale the dimensions of the hyper-ellipse such that it encompasses some desired percentage, *p*, of the total probability distribution (Jordan and Sverdrup, 1981; Bratt and Bache, 1988; Wilcock and Toomey, 1971, Press et al., 2002). We can point to the scaled uncertainty hyper-ellipse and state, with confidence *p*, that "the true location of the seismic event that generated the observations is located within this hyper-ellipse".

The second difficulty with the uncertainty hyper-ellipse is that it is difficult to visualize and interpret a 4 dimensional surface. The key to overcoming this difficulty is careful examination of the question that is being addressed with the seismic event location and its associated uncertainty. Typically, we wish to compare our calculated event location to some other location, **X**, in time and/or space and would like to know "did the event occur at location **X**". If location **X** has fewer than 4 dimensions, then there are components of our solution that are not relevant and those components should be ignored. The correct way to remove from consideration components of the problem that are not relevant is to project the 4D uncertainty probability distribution onto planes in location space that correspond to the irrelevant components. A detailed description of how to accomplish this mathematically is described in Press, et al. (2002).

In nuclear explosion monitoring, a frequently encountered scenario is that a seismic event is detected in general proximity to a known nuclear test site and we wish to determine whether or not the event could have occurred at the

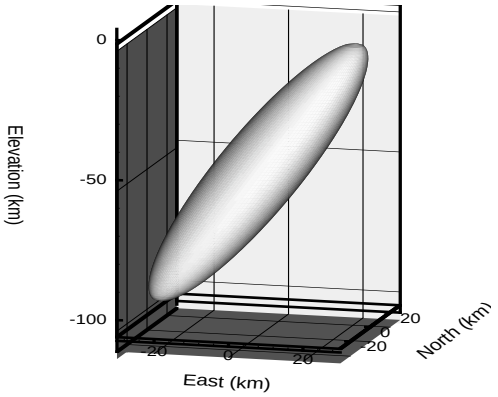


Figure 1. A 3D uncertainty ellipsoid for a seismic event that occurred on October 25, 2002 in the Sea of Japan, viewed from the SE. The major axis of the ellipsoid plunges steeply to the W/SW, and the ellipsoid does not intersect the surface.

test site, at some specified probability level. This is a 3 dimensional problem. The geographic coordinates and depth of the seismic event are important but the origin time of the event is not of interest. In this case, the question being asked is "does the 3D location of the test site fall within the 3D uncertainty interval centered on the seismic event location?" It is critical that all 3 components of the event and test site locations be considered jointly because the statistical analysis depends on the number of free parameters in the location comparison (Jordan and Sverdrup, 1981; Bratt and Bache, 1988). The 4D uncertainty hyper-ellipsoid returned by the least squares location algorithm should be projected onto a plane of constant time, resulting in a 3D ellipsoidal uncertainty boundary. An example of such an ellipsoid for an event that occurred in the Sea of Japan on October 25, 2002 is shown in Figure 1.

After reducing the dimensionality of the uncertainty bounds, it is useful to define a statistical index that can assist in determining the degree to which a seismic event location is co-located with a second location such as the location of a nuclear test site. To this end, a statistic called the *co-location index* is introduced that represents the percentage of the total probability density distribution that lies outside of a surface with the shape of the uncertainty surface but scaled to pass exactly through the location of interest. If the calculated location and the location of interest coincide perfectly, then 100% of the probability density distribution lies outside of the surface and that is the value of the co-location index. If the separation between the calculated location and the location of interest is large compared to the dimensions of the uncertainty surface, the co-location index is very small. If the location of interest lies directly on the *p%* confidence boundary, then the co-location index will be 100–*p*. Note that the co-location index will be a number between 0 and 100 and will differ depending on the number of dimensions that characterize the uncertainty bound. It is appropriate to refer to the "*n-dimensional co-location index*", where *n* ranges from one to four.

Non-Linear Earth Models

The least squares algorithm that is at the heart of many commonly used seismic event location codes assumes that the Earth model used to generate predictions of seismic events is linear, implying that seismic travel time curves are straight lines. This is, of course, not the case and the iterative scheme originally proposed by Geiger (1910) overcomes this limitation in cases where the non-linearity is not severe. This allows the iterative least squares algorithm to find the point in 4D location space characterized by the minimum sum squared weighted residuals, in most cases. The linearity assumption also permits the calculation of the hyper-elliptical uncertainty boundaries, as discussed in the previous section. In practice, however, it frequently occurs that the non-linearity is sufficiently severe that its effects cannot be ignored. This can manifest itself in two ways: the algorithm may fail to converge, and the actual uncertainty boundaries may deviate significantly from elliptical shapes.

Figure 2 illustrates a location situation where the non-linear effects cause the least squares algorithm to fail to converge. Note that the contours of constant root mean squared weighted residuals indicated by the colors in Figure 2 are not elliptical in shape. This results from significant non-linearity of the Earth model across the Moho at a depth of 30 km. If nothing is done to prevent it, the iterative least squares algorithm will oscillate infinitely between two non-optimal solutions indicated by the purple lines and circles. The step length weighting algorithm implemented in libloc, illustrated on the right, fails to find the minimum sum squared weighted residuals after 30 iterations. The Lenvenberg-Marquardt algorithm implemented by LocOO (Marquardt, 1963; Levenberg, 1944; Ballard, 2002) is illustrated on the left of Figure 2. It successfully deals with the non-linearity in the following manner: for each proposed step that will result in an increase in the sum squared weighted residuals, the step length is shortened and the direction of the step is rotated such that the step moves more in the direction of steepest descent. It is guaranteed to converge in a finite number of iterations, for tractable problems.

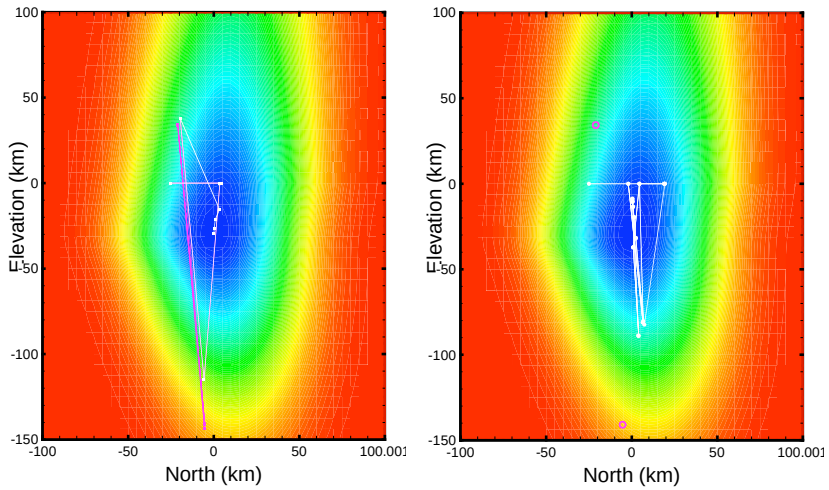


Figure 2. Comparison of the Levenberg-Marquardt damping algorithm implemented by LocOO (left) and the step-length weighting damping algorithm implemented by libloc (right). Colors represent RMS weighted residuals at each point on a vertical slice through the hypocenter, decreasing from red to blue. White symbols connected by lines indicate the solution location trajectory followed by each algorithm. The purple lines and symbols represent the cyclical solution trajectory followed by the iterative least-squares algorithm in the case where no damping algorithm is implemented.

The other negative impact of significant non-linearity is that the calculated uncertainty boundaries that surround the best fit calculated seismic event location may deviate significantly from an elliptical shape. This can be handled using a gridded residuals approach to calculating uncertainties (Willcock and Toomey, 1991). Basically, the approach involves generating a regularly spaced grid of points surrounding the best-fit location found with the least-squares inversion technique and, at each of these points, using a 1D minimization algorithm to find the origin time which yields the smallest sum squared weighted residual between observed and predicted seismic parameters, c^2, at that location. c^2_{min} is known to us from the least squares algorithm so we can compute $Dc^2 = c^2 - c^2_{min}$. Contours of constant Dc^2 correspond to confidence intervals so from the gridded residuals, we can find the non-linear 95% confidence interval and compare it to the elliptically shaped, linear 95% confidence bounds deduced with the least squares algorithm.

Note that this technique only removes the assumption that the Earth model is linear. The assumption that the data errors are normally distributed remains. To remove this assumption as well will require a full-blown grid search algorithm such as the one developed by Rodi and Toksoz (2001). The advantage of the technique described here is that it does not require computationally expensive Monte Carlo procedures to generate the uncertainty information. While the full grid-search algorithm may take many hours to complete, the grids shown in this paper require at most a couple of minutes to compute. Furthermore, for problems characterized by a single, well defined minimum, the least squares algorithm will find the same c^2_{min} value, at the same location in space, as the minimum c^2 on the grid. This means that we don't have to use the grid to find the best-fit event location, we can leave that to the very efficient least squares algorithm. The grid is used only to characterize the spatial distribution of Dc^2 surrounding the best fit location. Furthermore, it is not necessary to compute residuals on a full 3D grid in order to illuminate the geometry of the 3D uncertainty distribution. It is frequently sufficient to generate the residuals on 3 mutually orthogonal planes, thereby reducing the computational burden from $O(n^3)$ to $O(n^2)$.

Figure 3 illustrates the gridded residual uncertainty boundaries surrounding the October 25, 2002 Sea of Japan event that was described in an earlier section of this paper. The three plots illustrate the gridded residuals on 2 vertical and 1 horizontal plane, all of which have their origins at the epicenter of the event. In the figure in the upper left, note the substantial difference between the linear (white) and non-linear (black) 95% confidence limits around the best fit event location. In particular notice that while the linear uncertainty ellipoid does not intersect the Earth's surface,

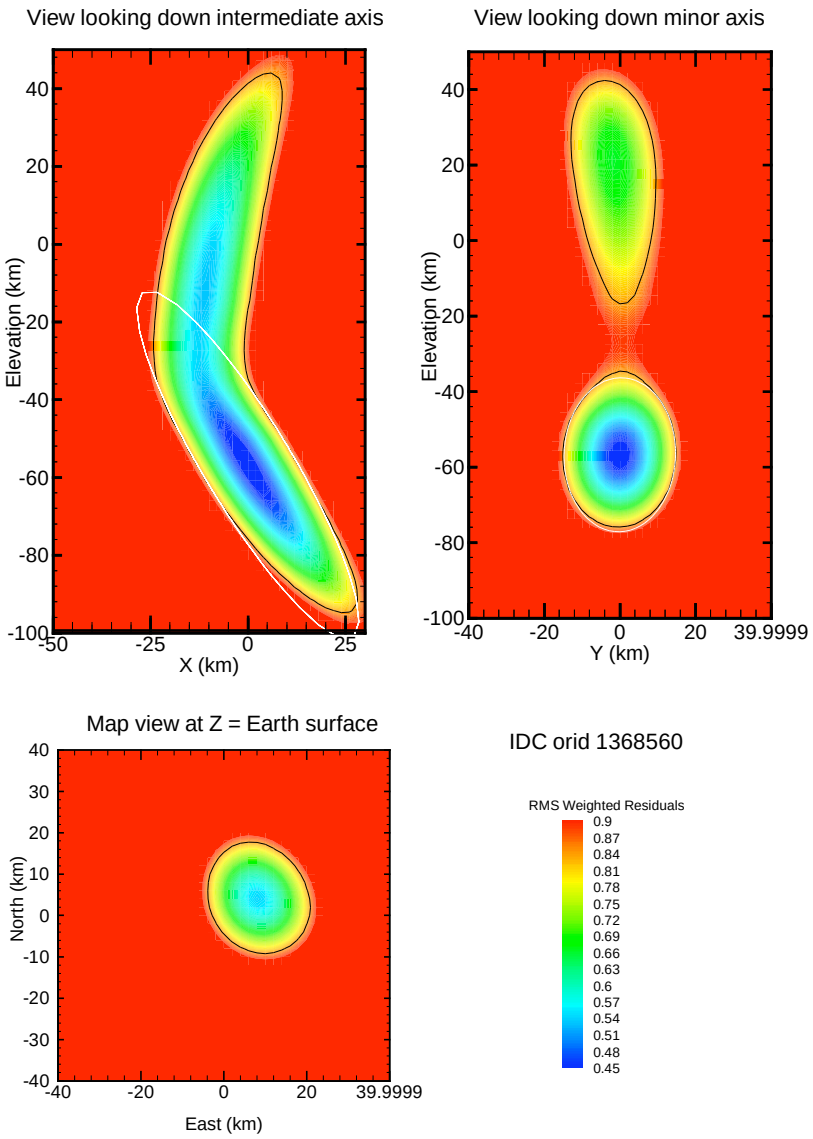


Figure 3. Gridded residual uncertainties surrounding the October 25, 2002 Sea of Japan event. Colors represent the root mean squared weighted residuals at each point in the figure. The black curve illustrates the non-linear 95% confidence limits surrounding the best fit location, deduced from the gridded residuals. The white curve represents the intersection of the plane of the figure with the linear 3D uncertainty ellipsoid illustrated in Figure 1. The origin of the plots coincides with the epicenter of the event.

the non-linear uncertainty boundary most decidedly does. In a nuclear monitoring situation, failure to observe the non-linear uncertainty limits would lead investigators to an incorrect conclusion as to whether or not this event could have occurred at the surface. Once again, the non-linearity is most pronounced at the Moho at a depth of 30 km.

Local Minima

Another challenge in locating seismic events is dealing with the possibility that several local minima may exist in the sum squared weighted residuals. The iterative least squares algorithm can be misled in its quest for the global minimum if the initial guessed starting location for the algorithm lies upgradient from a local rather than the global minimum. While grid search algorithms have a higher probability of finding the global minimum than a simple least

squares algorithm, no algorithm can guarantee with 100% confidence that it will locate the global minimum in a finite number of computations.

LocOO can optionally implement a hybrid least squares – grid search algorithm to improve the probability of finding the global minimum rather than a local minimum. The approach is to specify a number of depths at which the location should be started. The locator performs a fixed depth location at each of the specified depths and then seeks a free depth solution starting at the fixed depth location that provided the lowest sum squared weighted residuals. Then starting from the free depth solution, the locator steps out horizontally a user-specified distance in a number of equally spaced azimuthal directions and repeats the free depth solution. The location found in this manner that has the lowest sum squared weighted residual is accepted as the final best fit location.

By way of an example, the Sea of Japan event that has already been used as an example several times in this paper exhibits a local minimum at a depth of 14 km. For some initial starting locations, this local minimum location is found instead of the presumed global minimum location at 57 km depth. The hybrid least squares – grid search algorithm described above dramatically improves the probability of finding the 57 km depth solution.

Fixed Depth Solutions

The 2D linear uncertainty ellipses that surround fixed depth seismic event locations bear some reconsideration. When designing a solution to a seismic event location problem (or any problem for that matter) it is crucial to first very clearly state the problem that the solution is designed to address. The question that fixed depth solutions address is "if the seismic event occurred at the a particular depth *Z*, where in 2D location space did it occur, and what is the uncertainty associated with that location?"

At first this may appear to be a two-dimensional question since only the 2 horizontal components of the event location are explicitly sought. More careful reading of the question reveals, however, that there is at least a suggestion of a third dimension to the question. The first phrase, "If the event occurred at depth Z, …", acknowledges that the event may not have occurred at depth *Z*. We are not asserting, with infinite confidence that the event actually occurred at depth *Z*. In addition, when we ask "… and what is the uncertainty associated with that location?", we do not necessarily intend to limit the uncertainty to just the 2 horizontal dimensions. The question would be clearer if it were stated as "If the event occurred at depth *Z*, where in 2D horizontal space did it occur and with what probability did it occur there, as opposed to some other position in 3D space?" Current practice answers the question "Given that the event is known with zero uncertainty to have occurred at depth *Z*, where in 2D horizontal space did it occur and with what probability did it occur there, as opposed to some other position in 2D horizontal space?"

What is actually desired is a 2 dimensional location at the specified depth, but with uncertainty that considers the vertical dimension as well. This can be accomplished by calculating Δc^2 using the F-statistic with three free parameters instead of two and by scaling the dimensions of the uncertainty ellipse to reference the global minimum sum squared weighted residuals, $c^2_{3D,min}$ instead of $c^2_{2D,min}$.

When a fixed-depth solution is requested, the least-squares algorithm returns an uncertainty ellipse with the equation

$$c_0 x^2 + c_1 xy + c_2 y^2 = 1 \qquad (1)$$

where x is north in km, y is east in km, and the coefficients c_i define the shape of the ellipse. Equation 1 defines the distance from the point in parameter space where $c^2 = c^2_{2D,min}$ to the elliptical contour in parameter space where $c^2 = c^2_{2D,min} + 1$, or, $\Delta c^2 = 1$. This ellipse is then scaled with two parameters. The first is s_s^2, the data variance scale factor, which is a constant described by Jordan and Sverdrup (1981) and Bratt and Bache (1988). The second is the F-statistic, $M' F[M', N, p]$, where M' is the number of free parameters in the uncertainty analysis, N is the number of degrees of freedom (number of observations minus number of free parameters in the location calculation) and p is the desired confidence level. Note that the number of free parameters in a fixed-depth location calculation is 3, one for each horizontal component of the location and one for the origin time. M' is the number of free parameters in the uncertainty calculation. In current practice, when calculating the 2D spatial uncertainty ellipses, M' is set to 2,

one for each of the horizontal coordinates of the location. This implies perfect confidence in the depth of the solution. In current practice, the uncertainty ellipse is given by

$$c_0 x^2 + c_1 xy + c_2 y^2 = s_s^2 2F[2, N, p] \tag{2}$$

which yields an elliptical contour in *x*, *y* space where

$$c^2 = s_s^2 2F[2, N, p] + c_{2D,\min}^2 \tag{3}$$

To obtain an ellipse scaled to include 3D uncertainty information, we wish find the contour where

$$c^2 = s_s^2 3F[3, N, p] + c_{3D,\min}^2 \tag{4}$$

To find this contour centered on $c^2_{2D,\min}$ we subtract $c^2_{2D,\min}$ from both sides to obtain

$$\Delta c^2 = c^2 - c_{2D,\min}^2 = s_s^2 3F[3, N, p] + c_{3D,\min}^2 - c_{2D,\min}^2 \tag{5}$$

So, to rescale the uncertainty ellipse to three free parameters centered on $c^2_{2D,\min}$, the ellipse should be

$$c_0 x^2 + c_1 xy + c_2 y^2 = s_s^2 3F[3, N, p] + c_{3D,\min}^2 - c_{2D,\min}^2 \tag{6}$$

Example

Let us compare these approaches by applying them to a sample problem. The location problem that we will address is the India nuclear test of May 11, 1998. Of the 60 travel time observations available for the event, only the 27 observations from stations located in an azimuthal window 45° wide, located to the north of the event have been used. Figure 4a is a vertical cross section through the hypocenter of the event, oriented perpendicular to the trend of the intermediate axis of the 3D hypocentral uncertainty ellipsoid. Figure 4b is a horizontal slice through the epicenter of the event, which is located 40 km above the hypocenter. The colors represent contours of Δc^2 measured relative to $c^2_{3D,\min}$. The black contour lines represent the 3D, non-linear 95% confidence intervals calculated directly from the gridded residuals. The white ellipses represent the intersections of the 3D, linear 95% hypocentral uncertainty ellipsoid with the plane of the figure. In Figure 4b, the unmodified (Equation 2) and modified (Equation 6) fixed-depth uncertainty ellipses are also illustrated.

Of all the confidence intervals plotted in Figure 4b, the gridded-residuals confidence intervals is the one that best captures the real 3D uncertainty in the event location (assuming that it occurred at the surface). This is because it does not assume that the Earth model used to locate the event is linear. This confidence interval is the only one that is not an ellipse. While it is the best, it is also the most expensive to compute (~ 3 minutes) and the most difficult to process. It is difficult to process because it is not an ellipse and therefore cannot be expressed conveniently in text format but rather must be viewed graphically.

The modified fixed-depth confidence ellipse coincides almost perfectly with the gridded-residuals confidence interval but does not suffer from the disadvantages of the latter. It is quick to compute (~ 1 second) and convenient to process. It is more accurate than the 3D hypocentral ellipsoid intersection because the latter fails to account for non-linearity in the Earth model. The hypocenter of this event was calculated to be at a depth of 40 km, which is below the base of the crust in the IASP91 Earth model. Figure 4a illustrates quite clearly that, while the ellipsoid captures the uncertainty in the mantle with reasonable accuracy, it deviates significantly from the gridded-residuals confidence interval above the crust-mantle boundary where the seismic velocities differ substantially from the velocities in the vicinity of the hypocenter. The modified fixed-depth confidence ellipse reflects conditions at the Earth's surface and hence is not as susceptible to disruption from non-linear effects as is the ellipsoid intersection. If the Earth model were perfectly linear, the ellipsoid intersection ellipse and the modified fixed-depth confidence ellipse would coincide exactly.

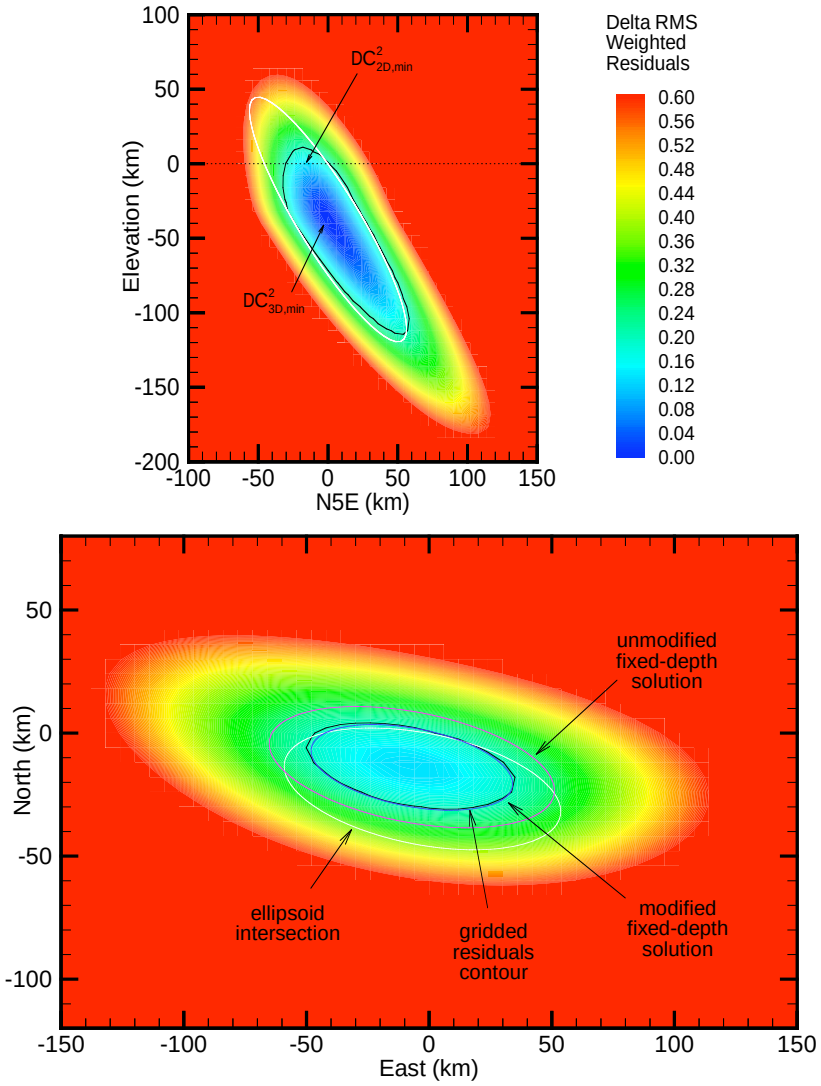


Figure 4. Uncertainty of fixed depth solutions.

The unmodified fixed-depth ellipse, like the modified fixed-depth ellipse and the gridded-residuals contour, is centered on $c^2_{2D,min}$. Its confidence ellipse is substantially larger than the modified fixed-depth ellipse since the unmodified fixed-depth solution is attempting to provide an answer to a different question than is the modified fixed-depth solution. The unmodified fixed-depth ellipse will not always be larger than the modified fixed-depth ellipse. Figure 5 compares the areas of the 3 elliptical confidence intervals as a function of the depth at which the depth is fixed. At depths near the hypocenter, the unmodified fixed-depth ellipse has linear dimensions that are approximately 12% smaller than the modified fixed-depth ellipse reflecting the fact that the F-statistic with 2 free parameters is substantially smaller than the F-statistic with 3 free parameters. While the size of the modified fixed-depth ellipse decreases rapidly with distance from the depth of the hypocenter, the size of the unmodified fixed-depth ellipse remains relatively unchanged, reflecting the fact that the former is centered on $c^2_{3D,min}$ while the latter is centered on $c^2_{2D,min}$.

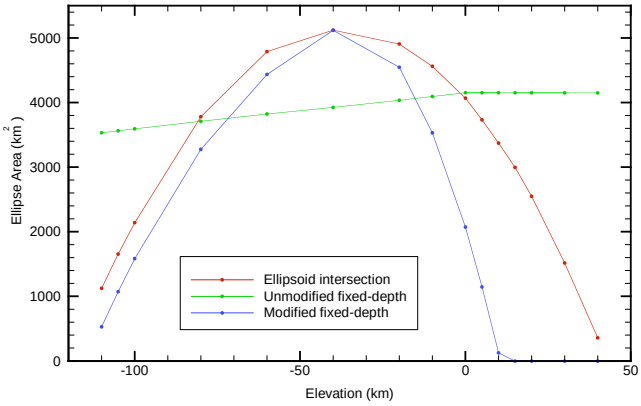


Figure 5. Comparison of the areas of the 3 elliptical confidence intervals as a function of the depth at which the depth is fixed.

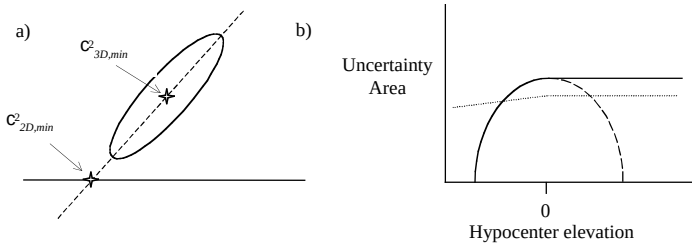


Figure 6. Sketch illustrating airquake scenarios. In b, the solid curve represents the modified fixed-depth uncertainty ellipse altered to impose the constraint that the event must have occurred below the Earth's surface. The dashed curve represents the modified fixed-depth ellipse not altered to deal with airquakes, and the dotted curve represents the unmodified fixed-depth ellipse.

Airquakes

What happens when the hypocenter of the free-depth solution has a negative depth, implying that the event occurred above the surface of the Earth? For the free-depth solution, the unrealistic location and associated uncertainty should be reported as is so that the analyst can gain whatever insight into the problem that they may be able to glean. If the 3D uncertainty limits intersect the surface of the Earth, the results are still useful.

For a fixed-depth solution however, $c^2_{3D,min}$ now occurs at a location in space that is not possible and it is desirable to mitigate its impact. Figure 6a illustrates an extreme example where even the 3D uncertainty limits of the hypocenter do not intersect the surface. Without further modification, the area of the modified fixed-depth uncertainty ellipse would be zero in this case. This seems unreasonable, because we know that airquakes cannot happen. The event must have occurred somewhere at or below the surface of the Earth, with the most likely location being close to the Earth's surface since this would require the smallest deviation from the best-fit 3D calculated location.

The proposed remedy is based on the premise that the calculated value of $c^2_{3D,min}$ could not be achieved in reality and hence should not be used to rescale the fixed-depth uncertainty ellipse. Instead, $c^2_{3D,min}$ should be replaced in Equation 6 with the closest reasonable alternative, which would be $c^2_{2D,min,0}$, the minimum value of c^2 found at the Earth's surface. In Figure 6a, this is tantamount to shifting the uncertainty ellipsoid along its major axis until the hypocenter coincides with the Earth's surface. If depth in the fixed-depth solution was fixed at the Earth's surface, this yields an ellipse scale factor of $s_s\ 3F[3, N, p]$ rather than $s_s\ 3F[3, N, p] + c^2_{3D,min} - c^2_{2D,min}$, regardless of the elevation of the hypocenter above the Earth's surface. Figure 6b illustrates how the ellipse area of a fixed-depth

solution with depth fixed at the surface would change as a function of hypocentral elevation. For airquakes, the modified fixed-depth solution maintains a constant uncertainty ellipse area regardless of the elevation of the hypocenter above the Earth's surface.

To summarize, the modified fixed-depth uncertainty ellipse equation is

$$\begin{aligned} c_0x^2 + c_1xy + c_2y^2 &= s_s^2\,3F[3, N, p] + c_{3D,\min}^2 - c_{2D,\min}^2 \qquad Z_{hypo} \le 0 \\ c_0x^2 + c_1xy + c_2y^2 &= s_s^2\,3F[3, N, p] + c_{2D,\min,0}^2 - c_{2D,\min}^2 \qquad Z_{hypo} > 0 \end{aligned} \tag{7}$$

where Z_{hypo} is the elevation of the event hypocenter above the Earth's surface.

CONCLUSIONS AND RECOMMENDATIONS

A number of improvements to current seismic event location capabilities have been described. These include: a) the addition of the ability to compute multidimensional uncertainty boundaries, b) alternative methods of dealing with non-linear Earth models, which improve the convergence behavior of the least squares algorithm and which give greater insight into the non-linear uncertainty in the computed location, c) addition of optional algorithms for improving the probability that the global, rather than local minima are found, and d) an alternative method for scaling the dimensions of 2D fixed-depth uncertainty intervals such that they reflect uncertainty in depth as well as horizontal components. All of these capabilities are available in a new location code called LocOO.

REFERENCES

Ballard, S., 2002, Seismic Event Location Using Levenberg-Marquardt Least Squares Inversion, Sandia National Laboratories Report, SAND2002-3083.

Bratt, S. R. and T. C. Bache (1988), Locating Events with a Sparse Network of Regional Arrays, Bull. Seis. Soc. Am., v. 78, pp. 780-798.

Geiger, L. (1910), Herdbestimmung bei erdbeden ans den ankunftzeiten, K. Gessel. Wiss. Goett. v. 4, pp. 331-349.

Jordan, T. H. and K. A. Sverdrup ,1981, Teleseismic Location Techniques and their Application to Earthquake Clusters in the South-Central Pacific, Bull. Seis. Soc. Am., v. 71, pp. 1105-1130.

Levenberg, K., 1944, A method for the solution of certain non-linear problems in least squares, Quart. Appl. Math., v. 2, pp. 164-168.

Marquardt, D. W., 1963, Journal of the Society for Industrial and Applied Mathematics, v. 11, pp. 431-441.

Press, W. H., S. A. Teukolsky, W. T. Vetterling and B. P. Flannery, 2002, *Numerical Recipes in C++, The Art of Scientific Computing*, 2nd Edition, Cambridge University Press.

Rodi, W. and M. Toksoz, 2001, Uncertainty Analysis in Seismic Event Location, Proceedings of the 23rd Seismic Research Review, pp. 324-332.

Wilcock, W. S. D. and D. R. Toomey, 1971, Estimating Hypocentral Uncertainties for Marine Microearthquake Surveys: A Comparison of generalized inverse and grid search methods, Marine Geophysical Researches, v. 13, 161-171.

GROUND-TRUTH EVENTS FROM NORTHEASTERN AFRICA

Richard A. Brazier,[1] Yongcheol Park,[1] Andrew A. Nyblade,[1] and Michael E. Pasyanos[2]

Penn State University,[1] Lawrence Livermore National Laboratory[2]

Sponsored by National Nuclear Security Administration
Office of Nonproliferation Research and Engineering
Office of Defense Nuclear Nonproliferation

Contract No. DE-FC03-02SF22500[1] and W-7405-ENG-48[2]

ABSTRACT

Determining accurate seismic locations with representative uncertainty estimates is of fundamental importance to ground-based nuclear explosion monitoring. In this project, we are developing a catalog of reference events (ground-truth [GT]) in the northeast African area where reference event coverage is exceptionally poor due to the limited station coverage by historic networks. The results of this project will enable the seismic monitoring community to enhance their operational capability to monitor for nuclear tests in North Africa and the Middle East by increasing their ability to accurately locate and identify seismic events in these regions.

The collection of GT events for northeastern Africa is being achieved using state-of-the-art event location methods applied to broadband seismic data from regional networks in Ethiopia, Kenya and Tanzania, as well as to broadband data from primary and auxiliary International Monitoring System (IMS) stations in the region. The GT catalog is being assembled by determining origin time, focal mechanism and hypocenters for many events that lie within close proximity of recording stations or are well-recorded teleseismically.

Accurate event locations for fourteen M>3 events in northeastern Africa have been obtained so far using data from the Tanzania Broadband Seismic Experiment and the Ethiopia Broadband Seismic Experiment. Hypocenters have been constrained by using P and S arrival times, pP-P and sP-P times, and waveform modeling. Focal mechanisms for a subset of these events have also been obtained by modeling P and SH polarities and amplitude ratios in a grid search method.

INTRODUCTION

Determining accurate seismic locations with representative uncertainty estimates is of fundamental importance to ground-based nuclear explosion monitoring. In this project, we are developing a catalog of reference events (ground-truth[GT]) in northeast Africa where reference event coverage is exceptionally poor due to the limited station coverage by historic networks. We are developing a catalog of accurately located hypocenters within a range of GT levels, origin times, and focal mechanisms for several tens of earthquakes with magnitudes > 3. The catalog will enable the seismic monitoring community to enhance their operational capability to monitor for nuclear tests in North Africa and the Middle East by increasing their ability to accurately locate and identify seismic events in these regions.

Earthquakes in northeastern Africa provide a principal source of GT for North Africa and the Middle East. The earthquakes of interest are associated with the northern and central portions of the East African Rift System (Figure 1). Since there are very few earthquakes within North Africa proper or within large parts of the Middle East that can be used to develop a set of GT, naturally occurring events in northeastern Africa take on an added importance for improving nuclear explosion monitoring capabilities in the region.

The development of GT for North Africa and the Middle East has in the past been limited not only by the lack of appreciable seismicity but also by a dearth of seismic stations throughout most of Africa. This situation is now changing. We operated regional seismic networks in Ethiopia and Kenya comprised of 27 and 11 broadband stations, respectively, between 2000 and 2002, and several years ago (1994-1995) we operated a similar network of 20 broadband seismic stations in Tanzania. The broadband waveforms recorded by these networks, together with waveforms from primary and auxiliary IMS stations in the region, provide a rich dataset that can be used to accurately locate earthquakes and determine their origin times and source mechanisms.

The GT catalog is being assembled by (1) determining origin time, focal mechanism and hypocenters for many events that lie within close proximity of recording stations or are well recorded teleseismically; (2) using these events to construct regional travel time correction surfaces using a Bayesian kriging technique, and (3) using the travel time correction surfaces to obtain origin times and epicenters for numerous other events. Robust estimates of the uncertainties in the locations and origin times will also be determined.

Here we present improved locations for 11 events within Tanzania with M>4 and 3 events from Ethiopia with M > 3.5 constrained by P and S arrival times and pP, sP and Pmp depth phases recorded by the regional broadband networks in Tanzania and Ethiopia. We begin by providing background information about the geology of the region and on the broadband seismic experiments. This is followed by a discussion of our event locations and uncertainties, and we conclude with a brief description of future work.

Background Information

The locations of the broadband seismic experiments, together with the geology and topography of East Africa, are shown in Figure 1. The geology of the region is comprised of an Archean craton (the Tanzania Craton, Figure 1) surrounded Proterozoic mobile belts. The rift faults of the Cenozoic East African rift system have developed mainly within the Proterozoic mobile belts, forming a rift system with two branches (Western rift and Eastern rift).

The broadband seismic experiment in Tanzania was conducted in 1994 and 1995 and consisted of 20 seismic stations deployed for a year in two skewed arrays, one oriented more or less east-west, and the other northeast-southwest. The experiment was designed so that structure beneath the Archean Tanzania Craton and the terminus of the Eastern Rift in northern Tanzania could be imaged with seismic data from local, regional and teleseismic earthquakes. Information about the station configuration, recording parameters and other details of the field deployment has been reported by Nyblade et al. (1996).

In the other broadband seismic experiments, seismic stations consisting of broadband sensors, 24-bit data loggers, 4 Gbyte hard disks, and GPS clocks were deployed in regions of Ethiopia and Kenya that were safe for traveling (Figure 1). The stations were spaced 50 to 200 km apart and were located to optimize the recording of teleseismic body and surface waves that sample upper mantle structure beneath the Eastern Rift. For East Africa, the major source regions for teleseismic earthquakes are the Hindu Kush/Pamir region to the northeast and the Fiji/Tonga

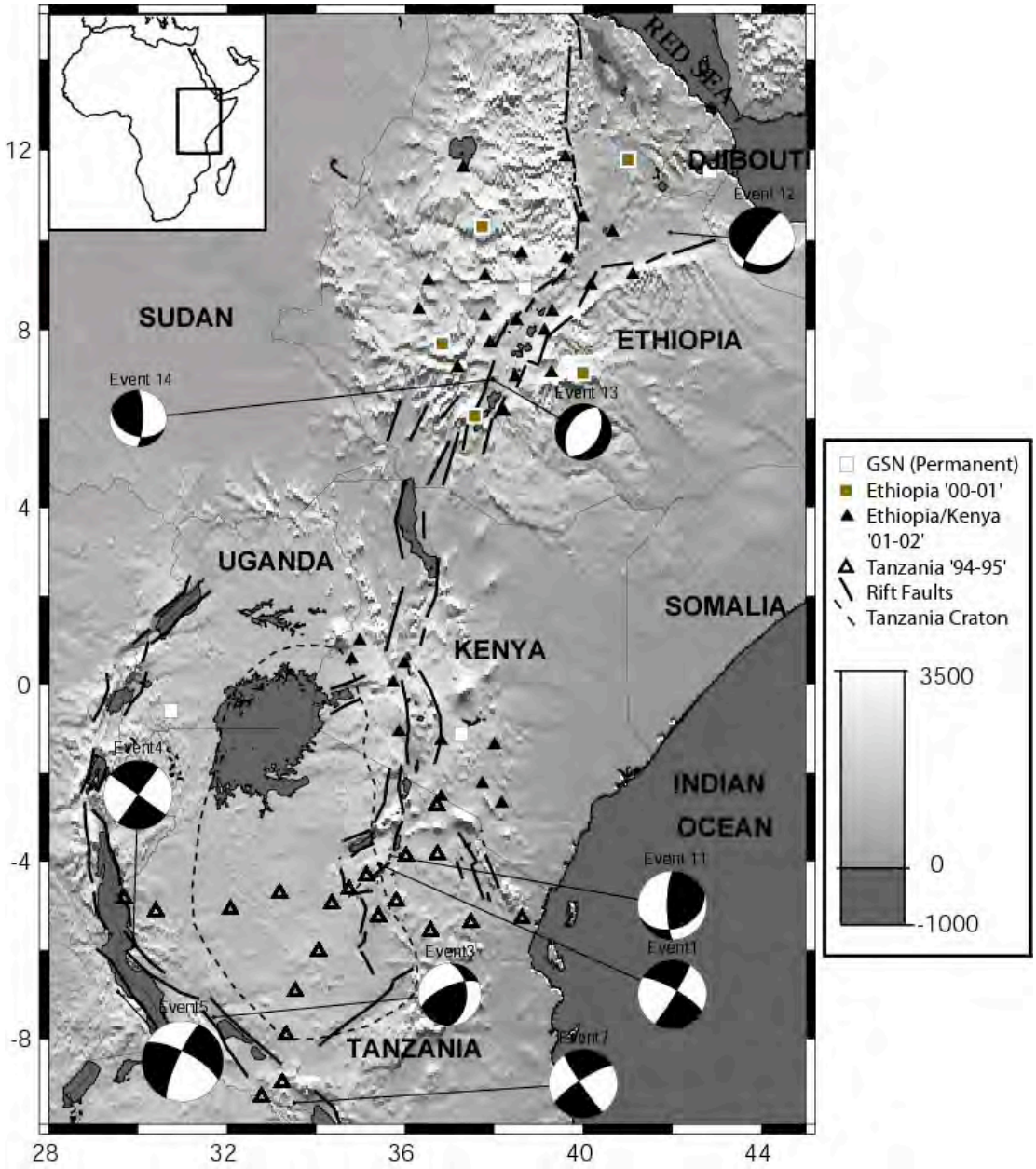


Figure 1. Topographic map of East Africa showing the Ethiopian and East African plateaus (regions with > 1000 m elevation), the outline of the Archean Tanzania craton, the major rift faults of the East African rift system, focal mechanisms for our events, and the location of broadband seismic stations.

subduction zones to the east. Additional criteria used for site selection included access to bedrock, security, and year-round road conditions.

Installation of the Ethiopian stations was completed in two phases. During March 2000, five stations were installed around the periphery of the network, and then one year later (March 2001) an additional 20 stations were installed to densify the network (Figure 1). All 25 stations were removed from the field in March 2002. Installation of the Kenyan stations took place during July and August 2001, and all 10 of the stations were removed in July 2002. Two data streams were recorded; a 1-sample/sec continuous stream and a 20 sample/sec continuous stream, yielding a data volume of 21 Mbytes per station per day.

Event Locations

Event locations have been obtained for several events in Tanzania with magnitudes $\geq$ 4 and in Ethiopia with magnitudes > 3.5 that were well recorded by the Tanzania and Ethiopia regional networks. The locations were obtained using P and S arrival times, a regional velocity model for both the crust and upper mantle constrained by a number of previous studies, and the event location code HYPOELLIPSE (Lahr, 1993). The P and S onset times were individually handpicked to within 0.1 seconds. The velocity models in Table 1 were used in the event location code for each respective region. The crust and uppermost mantle in East Africa have been studied in detail by many authors using refraction surveys, receiver functions, surface waves, regional waveforms and Pn tomography. From these studies, it is clear that Tanzania's crustal and uppermost mantle structure is fairly uniform in the Precambrian terrains away from the rift valleys proper (Last et al., 1997; Brazier et al., 2000; Nyblade, 2002; Langston et al., 2002; Fuchs et al. 1997 and references therein). Only minor differences in crustal thickness (2-5 km), mean crustal velocity (0.1-0.2 km/s), and uppermost mantle P velocities (0.1 – 0.2 km/s) are found between the various stations of the Tanzania network, and these differences introduce very small uncertainties in the event locations.

Table 1. Crust and uppermost mantle seismic structure for Tanzania and Ethiopia, East Africa.

	V1 (km/s)	V2 (km/s)	Poisson's Ratio	Moho Depth (km)	Mean crustal Vp (km/s)	Pn (km/s)
Tanzania	5.84	7.09	0.25	38	6.5	8.3
Ethiopia	6.2	6.99	0.25	44	6.4	8.0

V1= uppermost crustal velocity; V2=lowermost crustal velocity

Table 2 summarizes the event origin times and locations, and the uncertainties associated with the locations. All of the events are well recorded on at least 11 stations in Tanzania and 6 in Ethiopia. A number of the events are within a few tens of kilometers of a station and none are more than a few hundred kilometers from a station. The magnitude estimates for these events derive from using the maximum P wave amplitude within the first 5 seconds and the local magnitude scale for East Africa determined by Langston et al. (1998). Standard statistical measures at the 68% confidence interval in the error ellipse indicate that the hypocenters appear to be constrained to within a few kilometers. However, a detailed study of several of these events using regional waveform modeling (Langston et al., 2002) indicates that while the P and S arrival times do a fairly good job at constraining epicentral location, they do not provide tight constraints on source depth. Source depth for the events studied by Langston et al. (2002) are shown in Table 2. The source depth obtained from the P and S arrival times for these events differed from the source depths in Table 2 by 10 or more kilometers.

Focal mechanisms have been determined using polarities and amplitude ratios of local and regional P and S phases using the grid-search technique by Snoke (1984) and are plotted in Figure 1 and in Table 3. The focal mechanisms are then used with a wavenumber integration algorithm (Kennett, 1983) to compute full synthetic seismograms for several stations at several depths. The synthetics are compared against the data and regional depth phases such as pPn, sPn and PmP are used to constrain the source depths. In Figure 2, we show the P wave train from the vertical component for the Lake Tanganyika event of November 12th 1994 (event 5), from two stations, RUNG at 402 km and KIBA at 766 km from the source. These traces are reduced to the Pn velocity. The depth phase sPn aligns best with the data and synthetics for a 18 km source depth. Fixing the depth of this event at 18 km, and then relocating using the arrival times, gives a more accurate location overall.

For comparison, we also show in Table 2 the locations and origin times for several of the events taken from the ISC catalog and earlier locations obtained without using depth phases to constrain focal depths. Locations for two events were also determined using data from stations outside of our networks in East Africa. The comparison shows discrepancies in origin times of several seconds in most cases, and differences in event location of many tens of kilometers for some events. In addition, no catalog listings were found for several of the events.

Future Work

In future work, we will focus on obtaining more accurate hypocenters for the regionally recorded events in Tanzania and Ethiopia. Preliminary locations using P travel times for several events in Ethiopia are given in Table 4.

In all of these steps it is crucial to have good velocity models for the crust and upper mantle. We will use analyses of receiver functions, surface waves and seismic refraction profiles to provide independent estimates of crustal and

Table 2. Locations for earthquakes in East Africa with M > 4 from July 1994 – June 1995 recorded by the Tanzania Broadband Seismic Experiments and from April 2000 - March 2002 recorded by the Ethiopia Broadband Seismic Experiment.

Event:source	yr:mo:day:hr:min:sec	Lat.	Lon.	Dep	M	N	Gap	RMS	Smaj	Az	Smin	Sez
1:Traveltimes	94:07:20:11:32:04.30	-4.080	35.440	42	4.5	19	141	0.44	0.25	-106	0.45	1.7
1:ISC	94:07:20:11:31:58.49	-4.171	35.185	0	3.8			1.26	10.4	90	6.6	
1:Fixed Depth	94:07:20:11:32:02.79	-4.251	35.585	15+	4.5	19	132	2.34	0.22	-108	0.35	0.49
2: Fixed Depth	94:08:18:00:45:48.80	-7.440	31.770	25*	5.9+	17	167	1.77	0.35	-34	0.48	2*
2: ISC	94:08:18:00:45:52.70	-7.650	31.830	25	5.9			0.69	2.20	90	2.20	
3: Traveltimes	94:09:05:04:08:56.04	-7.508	31.700	?	4.1	15	174	0.43	0.41	-59	0.70	?
3: ISC	94:09:05:04:08:50.41	-7.738	30.882	4	4.6			1.38	10.9	90	6.3	
3. Fixed Depth	94:09:05:04:08:54.83	-7.502	31.700	18+	4.1	18	174	0.54	0.38	-50	0.55	2*
4: Traveltimes	94:09:30:01:36:53.14	-5.920	29.890	26	4.5	16	229	1.13	0.55	-40	1.18	1.4
4: ISC	94:09:30:01:36:47.62	-8.426	37.261	0	4.4			1.78	15.6	90	8.6	
4: Fixed Depth	94:09:30:01:36:55.54	-5.876	30.202	11	4.5	16	210	1.50	0.82	-4	1.03	2.1
5: Traveltimes	94:11:12:12:18:00.00	-6.950	29.920	30*	5.3	16	179	0.55	0.42	-24	0.89	2*
5: ISC	94:11:12:12:18:01.33	-6.777	29.821	22	4.6			1.05	6.3	90	4.5	
5. Fixed Depth	94:11:12:12:18:00.88	-6.708	30.111	18+	5.3	16	179	0.95	0.39	-26	0.74	2+
5. Fixed Depth plus additional data	94:11:12:12:17:57.73	-6.939	29.552	18+	5.3	23	94	2.13	0.31	-40	0.36	2+
6: Traveltimes	94:11:12:20:16:59.37	-6.617	30.016	?	4.7	17	223	0.88	0.45	-33	0.96	?
6: ISC	94:11:12:20:16:49.66	-6.834	29.946	0	4.6			1.15	8.4	90	5.5	
6. Fixed Depth	94:11:12:20:16:58.59	-6.652	30.135	8+	4.7	20	211	1.29	0.39	-26	0.73	2+
7: Traveltimes	94:11:16:01:08:11.20	-9.070	33.330	8*	4.5	17	193	0.80	0.48	-129	0.66	2*
7: ISC	94:11:16:01:08:09.07	-9.179	33.273	10	5.0			1.64	7.8	90	6.8	
7: Fixed Depth	94:11:16:01:08:10:21	-9.145	33.454	7+	4.5	17	204	0.86	0.51	-112	0.73	2+
7: Fixed Depth plus additional data	94:11:16:01:08:05.78	-9.424	33.513	7+	4.5	20	150	3.6	0.29	-52	0.54	0.97
8: Traveltimes	94:11:27:04:20:51.65	-3.568	35.827	30	4.0	15	213	0.51	0.36	-93	0.95	0.7
8: ISC	94:11:27:04:20:44.27	-3.954	35.722	10	4.0			0.12	22.4	90	10.1	
9: Traveltimes	94:12:25:04:25:27.44	-5.113	29.752	21	4.2	11	301	0.59	0.81	19	6.42	1.9
9: ISC	No listing											
10: Traveltimes	95:01:29:00:23:35.02	-5.419	35.909	13	4.1	11	128	0.37	0.34	-107	0.51	1.0
10: ISC	No listing											
11: Traveltimes	95:02:12:16:37:30.00	-3.960	35.830	32*	4.5	20	?					2*
11: ISC	No listing											
11: Fixed Depth	95:02:12:16:37:33.85	-3.879	35.670	34+	4.5	13	215	0.56	0.36		0.96	2+
12: ISC	00:05:16:20:47:51.93	10.10	41.23	10	4.4							
12: Fixed Depth	00:05:16:20:47:51.27	10.17	41.95	7+	4.4	6	166	1.72	0.49	-120	1.25	3.45
13: Traveltimes	01:03:11:00:42:43.58	6.91	38.01	0.02	3.7	13	78	1.57	0.26	-64	0.3	0.87
13: Fixed Depth	01:03:11:00:42:41.88	6.88	37.96	4+	3.7	7	92	0.41	0.35	-69	0.37	2.91
14: Traveltimes	01:03:12:16:40:08.92	6.78	37.98	0	3.7	9	128	2.79	0.31	-82	0.42	0.94
14: Fixed Depth	01:03:12:16:40:07.23	6.88	37.97	5+	3.7	7	92	0.40	0.35	-74	0.37	1.09

D = depth in km. * = depth was determined from regional depth phases (Langston et al., 2002). Otherwise depths were determined from only P and S arrival times.

M = magnitude. Magnitudes in this study are based on the ML scale from Langston et al. (1998). ISC magnitudes are a mixture of different types.

N = number of stations used in the event location.

Gap = azimuth range in stations.

RMS = Rms error in arrival times.

Smaj, Smin, Sez, Az = dimensions (in kms) and orientation of the error ellipse. For this study, the numbers in the table are for a 68% confidence level. * on Sez numbers indicates that the depth uncertainty was obtained from modeling regional depth phases (Langston et al., 2002).

mantle velocities. In addition, we will make surface wave dispersion measurements of data from the three regional networks in the area. We are measuring both Love and Rayleigh surface wave group velocities using a multiple narrow-band filter technique. Combined with thousands of other measurements made in the broader regional area (Pasyanos et al., 2001), we will conduct a high-resolution group velocity tomography of northeastern Africa. Using near-regional data will enable us to make more accurate short-period (5-15 seconds) measurements that will allow us to constrain velocities in the uppermost crust. We will use the surface wave work, along with receiver functions and other data, to improve the velocity model of the crust and upper mantle and in turn improve the event locations.

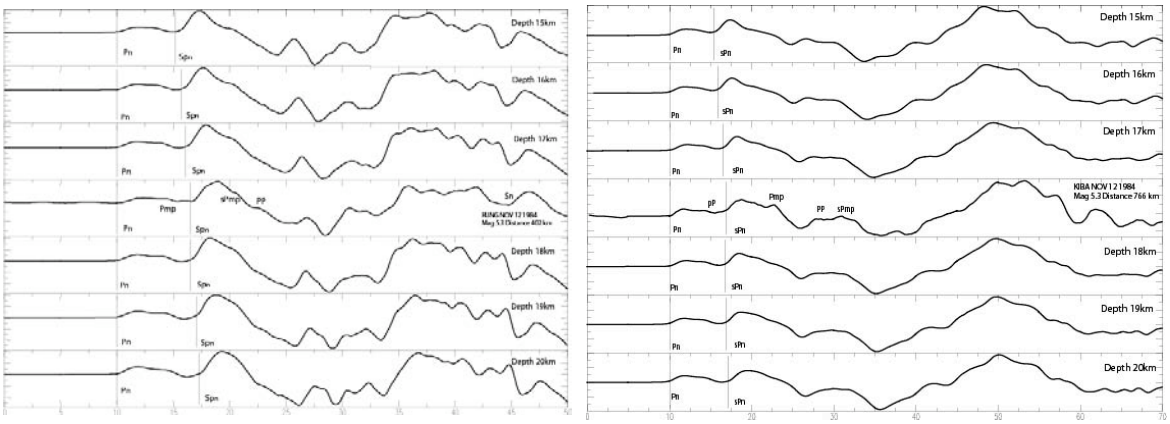


Figure 2. Data from November 12th 1994 Tanganika event recorded at (a) RUNG and synthetics for source depths 15 –20 km, and (b) Data from November 12th 1994 Tanganika event recorded at KIBA and synthetics for depths at 15 –20 km

Table 3. Focal mechanisms for events in Table 2.

	Strike (deg)	Dip (deg)	Rake (deg)
Event 1	300	77	-5
Event 3	0	45	32
Event 4	36	335	-10
Event 5	204	79	-19
Event 7	146	85	-11
Event 11	180	77	59
Event 12	102	26	-25
Event 13	210	45	-90
Event 14	109	38	22

To expand the catalog of events in northeastern Africa, we will take the events located using the approach described above and use them as calibration events to construct travel-time correction surfaces using the kriging method of Schultz et al., (1998, 1999) and Myers and Schultz (2000). The travel-time correction surfaces will then be used with local and regional P arrivals to determine epicenters and origin times for numerous other events in the Ethiopia, Kenya and Tanzania datasets. Based on the expected proximity of many of these events to recording stations, we anticipate that there will be many events whose epicenters will be determined to within 10 km.

The travel-time correction surfaces will be constructed following the approach outlined by Myers and Schultz (2000). For the regional networks, we will calculate travel-time residuals for the calibration events relative to a regional velocity model. The travel-time residuals will be assigned to the respective calibration epicenter and form a set of spatially varying travel-time correction points. This set of points will then be declustered to reduce the dimensions of the observations, and this refined set of calibration points will be used with Bayesian kriging to form continuous travel-time surfaces that will provide source-specific corrections for each station in the regional networks. In locating epicenters, a standard location algorithm will be used with the kriging corrections applied. A

Table 4. Locations for earthquakes in Ethiopia with M > 2 from April 2000 to March 2002.

Event:source	yr:mo:day:hr:min:sec	Lat.	Lon.	Dep	M	N	Gap	RMS	Smaj	Az	Smin	Sez
1:Traveltimes	01:04:03:17:40:27.84	15.008	40.990	?	3.9	18	286	5.74	21.08	-70	4.29	?
2: Traveltimes	01:04:04:01:00:21.84	13.534	39.913	?	3.2	22	276	1.76	3.72	-78	0.92	4.22
3: Traveltimes	01:04:05:12:50:14.29	11.848	40.856	15	3.3	9	190	6.08	6.65	-89	1.28	1.12
4: Traveltimes	01:04:06:16:36:30.99	11.403	39.659	?	3.6	23	82	2.06	2.10	-51	0.72	4.97
5: Traveltimes	01:04:09:10:49:52.44	7.565	38.843	15	2.8	4	139	0.73	?	-25	0.83	?
6: Traveltimes	01:04:11:20:33:49.85	12.15	39.683	15	3.0	10	258	9.06	12.6	-54	3.38	2.53
7: Traveltimes	01:04:12:11:50:57.28	6.65	38.067	15	2.9	6	135	1.97	9.52	-43	0.53	15.1
8: Traveltimes	01:04:14:23:40:27.86	8.979	39.95	15	2.9	19	101	7.94	1.3	-49	0.77	3.1
9: Traveltimes	01:04:20:06:16:40.62	9.589	39.641	15	2.4	4	193	0.44	28.79	-60	1.68	18.0
10: Traveltimes	01:04:20:19:02:0073	5.593	37.187	15	2.8	7	288	0.91	13.8	-52	1.34	8.51
11: Traveltimes	01:04:21:20:41:37.81	11.213	42.617	15	2.7	8	177	4.21	19.06	-16	3.62	?
12: Traveltimes	01:04:24:01:58:35.01	14.218	40.912	15	3.3	16	272	5.92	12.03	-85	3.4	?
13: Traveltimes	01:04:24:21:56:28.42	10.122	42.867	15	3.2	14	224	2.33	12.74	0	2.57	15.4
14: Traveltimes	01:04:25:19:26:19.86	11.575	40.964	15	3.2	14	89	2.52	2.84	-100	0.9	3.88
15: Traveltimes	01:04:25:21:12:25.76	7.553	44.198	15	4.1	17	276	8.62	2.16	24	0.55	?
16: Traveltimes	01:04:27:22:43:44.46	6.203	37.684	15	2.1	8	144	2.27	7.1	-47	2.18	3.85
17: Traveltimes	01:04:27:17:39:12.21	6.067	37.556	15	2.5	3	252	?	?	4	2.19	?
18: Traveltimes	01:05:03:13:39:55.53	13.847	41.076	10	3.8	17	265	2.98	2.00	-78	0.60	?
19: Traveltimes	01:05:04:17:26:22.00	12.786	41.239	10	3.7	10	236	2.47	1.37	-82	0.56	1.63
20: Traveltimes	01:05:07:00:16:12.46	7.010	45.689	10		6	360	0	10.03	-133	1.12	99
21: Traveltimes	01:05:07:10:32:49.81	0.795	41.022	10		3	360	0	9.44	30	0.85	99
22: Traveltimes	01:05:12:01:44:16.07	9.508	39.691	0.02	3.6	11	123	2.32	0.46	-34	0.35	0.86
23: Traveltimes	01:05:17:07:24:01.24	11.410	42.942	0	3.6	11	252	6.72	4.48	-24	0.77	3.47
24: Traveltimes	01:05:17:09:24:55.33	11.770	42.893	10	3.6	8	279	5.46	5.21	-27	0.85	1.18
25: Traveltimes	01:05:18:18:07:55.44	5.539	36.081	10	4.0	18	143	6.23	0.66	22	0.34	?
26: Traveltimes	01:05:19:17:54:28.67	8.629	39.504	325	4.4	21	119	5.13	0.76	31	0.43	2.05
27: Traveltimes	01:05:19:18:49:18.28	11.773	43.200	10	3.7	15	308	7.29	5.27	-25	0.82	1.9
28: Traveltimes	01:05:22:09:20:52.26	7.586	45.386	10	4.1	13	256	13.5	1.82	2	0.56	?
29: Traveltimes	01:05:23:01:16:12.76	2.639	49.772	10	4.1	24	60	2.81	0.29	-132	0.21	0.63
30: Traveltimes	01:05:25:05:14:29.10	21.059	39.799	10	4.4	14	291	5.60	3.81	18	0.86	?

D = depth in km.

M = magnitude. Magnitudes in this study are based on the ML scale from Langston et al. (1998).

N = number of stations used in the event location.

Gap = azimuth range in stations.

RMS = Rms error in arrival times.

Smaj, Smin, Sez, Az = dimensions (in kms) and orientation of the error ellipse. For this study, the numbers in the table are for a 68% confidence level.

conservative uncertainty estimate for the kriging correction will be used to characterize the travel-time-prediction error, according to the procedure followed by Myers and Schultz (2000). This conservative estimate will be developed using rigorous statistical modeling with available seismic data. Cross-validations will be provided to ensure that the estimates are accurate. In general, these statistics will be used as input to generate chi-squared values for robustly determining the final reference event error ellipses.

REFERENCES

Brazier, R., A.A. Nyblade, C. A. Langston, and T.J. Owens, Pn velocities beneath the Tanzania Craton and adjacent rifted mobile belts, East Africa, *Geophys. Res. Lett.*, 27, 2365-2368, 2000.

Fuchs, K., Altherr, B., Muller, B., and Prodehl, C., Structure and dynamic processes in the lithosphere of the Afro-Arabian rift system: *Tectonophysics, 278*, 1-352, 1997.

Kennett, B.N.L., Seismic wave propagation in stratified media, *Cambridge University Press*, 1983.

Lahr, J.C., Hypoellipse, a computer program for determining local earthquake hypocentral parameters, magnitude and first motion pattern, U.S. Geological Survey Open File Report 89-116, 1993.

Langston, C.A., R. Brazier, A.A. Nyblade and T. J. Owens, Local magnitude scale and seismicity rate for Tanzania, East Africa, *Bull. Seis. Soc. Am., 88*, 712-721, 1998.

Langston, C.A., A.A. Nyblade, and T.J. Owens, Regional wave propagation in Tanzania, East Africa, *J. Geophys. Res.*, 107, 10.1029, 2002.

Last, R., A.A. Nyblade, C.A. Langston, and T.J. Owens, Crustal structure of the East African plateau from receiver functions and Rayleigh wave phase velocities, *J. Geophys. Res., 102*, 24469-24483, 1997.

Myers, S., and C. Schultz, Improving sparse network seismic location with Bayesian kriging and teleseismically constrained calibration events, *Bull. Seis. Soc. Am., 90*, 199-211, 2000.

Nyblade, A.A., C. Birt, C. A. Langston, T.J. Owens, and R. J. Last, Seismic experiment reveals rifting of craton in Tanzania, *Eos Trans. AGU, 77*, 517-521, 1996.

Nyblade, A.A., Crust and upper mantle structure in East Africa and the origin of Cenozoic extension, magmatism and plateau uplift, in *Magmatic Rifted Margins*, edited by M. Menzies, C. Ebinger and S. Klemperer, Geological Society of America special paper 362-0, in press, 2002.

Pasyanos, M.E., W.R. Walter, and S.E. Hazler, A surface wave dispersion study of the Middle East and North for monitoring the Comprehensive Nuclear-Test-Ban Treaty, *Pure and Applied Geophysics*, 2001.

Schultz, C., S. Myers, J. Hipp, and C. Young, Nonstationary Bayesian kriging: a predictive technique to generate spatial corrections for seismic detection, location and identification, *Phys. Earth. Planet. Int., 113*, 321-338, 1999.

Schultz, C., S. Myers, J. Hipp, and C. Young, Nonstationary Bayesian kriging: a predictive technique to generate spatial corrections for seismic detection, location and identification, *Bull. Seis. Soc. Am., 88*, 1275-1288, 1998.

Snoke, J.A., Munsey, J W; Teague, Alan G; Bollinger, G A. A program for focal mechanism determination by combined use of polarity and SV-P amplitude ratio data, *Seismological Society of America, Eastern Section, 56th annual meeting, Earthquake Notes, vol.55, no.3, pp.15, Sep* 1984.

DETECTION OF MINING EXPLOSIONS FOR A SOUTHERN ASIA SEISMIC DATABASE

James M. Britton,[1] David B. Harris,[2] Ileana M. Tibuleac,[1] and Jessie L. Bonner[1]

Weston Geophysical Corporation[1] and Lawrence Livermore National Laboratory[2]

Sponsored by National Nuclear Security Administration
Office of Nonproliferation Research and Engineering
Office of Defense Nuclear Nonproliferation

Contract No. DE-FG02-01-ER83341[1] and W-7405-ENG-48[2]

ABSTRACT

Weston Geophysical maintains a high-quality seismic research database for southern Asia consisting of detailed mining information together with seismograms recorded from mine blasts in India, Pakistan, Iran, and the surrounding regions. This digital mining database contains data on more than 240 mines and mineral deposits in southern Asia, including information on location, geology, commodities, production, mineralogy, references, operator, and mining explosion resources. The waveform data include seismograms from several stations in southern Asia including NIL, ABKT, HYB, and GBA, in addition to data from proprietary stations.

In the past year, we have employed different techniques to detect probable mining explosions. First, we have applied the waveform correlation method (Harris, 1991) to several months of data from each station of interest. Clusters of mining events were detected near stations in south and central India. Mining clusters were also detected near zinc mines in northwestern India. No mining clusters, however, were detected near station ABKT in southern Turkmenistan. An additional tool currently being developed to aid in the detection of mining events is a short-period Rayleigh wave (*Rg*) detector. Analysis of the waveform data was initiated employing a three-component detector to highlight *Rg* arrivals, which are often seen on mine-blast/shallow source, near-regional seismograms. The detector was modeled after the Chael (1997) automatic teleseismic Rayleigh-wave detection method; however we have modified the detector for regional distance and short-period (< 3 sec) applications. The modifications in the initial detection stage include: 1) application of a zero phase Butterworth filter between 0.4 and 1.3 Hz; 2) calculation of the covariance matrix for rotated waveforms; 3) estimation of the constants for the STA and LTA recursive filters; and 4) addition of two new weights of the detection function for planarity verification. We have observed that proper pre-filtering is essential for accuracy in back azimuth estimation. Therefore, once a detection has been declared, a Meyer Continuous Wavelet Transform at the estimated *Rg* frequency was applied as an alternative pre-filtering method, improving the backazimuth estimates. We have tested the detector on well-located clusters of mine events from central India.

Events detected by either of these two methods are located using single-station location techniques (Leidig *et al*., 2003). We obtained satellite imagery for the areas covering the locations of the mining clusters. These images show the location of open-pit mines in close proximity (in most cases less than 10 km) from the centers of mining cluster epicenters. The imagery, event locations, station locations, and information on the mines are stored in an ArcView 8.3 geographic information system (GIS) database in which the digital seismic waveform data are linked. The database is updated as more mining clusters are detected and supplemental information (satellite imagery, mining information) is received.

OBJECTIVES

The objectives of this research are to catalog the mining resources of Iran, India, and Pakistan and to compile mine information together with mining explosion waveforms into a single, digital database.

RESEARCH ACCOMPLISHED

Mine Database

Continuous broadband waveform data have been obtained from the Incorporated Research Institutions for Seismology/International Deployment of Accelerometers (IRIS/IDA) stations ABKT, NIL, and PALK. The HYB waveforms were obtained from the Geoscope Network, and the GBA waveforms were obtained through the Atomic Weapons Exchange (AWE) in the United Kingdom. Table 1 shows the dates of some continuous data segments. Locations of these stations are shown in Figure 1, with proprietary stations indicated by P1 and P2 on the map and in this paper.

In addition to obtaining continuous waveform data at these stations, information on the mines and mining districts surrounding these stations is being compiled. Supplemental information, such as satellite imagery, is imported into the database to aid in determining ground truth for the locations of the detected mine blasts.

Table 1. Stations for which continuous data have been obtained

Station	Network	Dates	Segment Length [days]	Lat	Lon
ABKT	IRIS/IDA	4/9/02 – 10/22/02	196	37.9304	58.1189
NIL	IRIS/IDA	7/2/98 – 3/3/99	244	33.6500	73.2517
HYB	GEOSCOPE	4/21/99 – 5/20/99	30	17.4169	78.5531

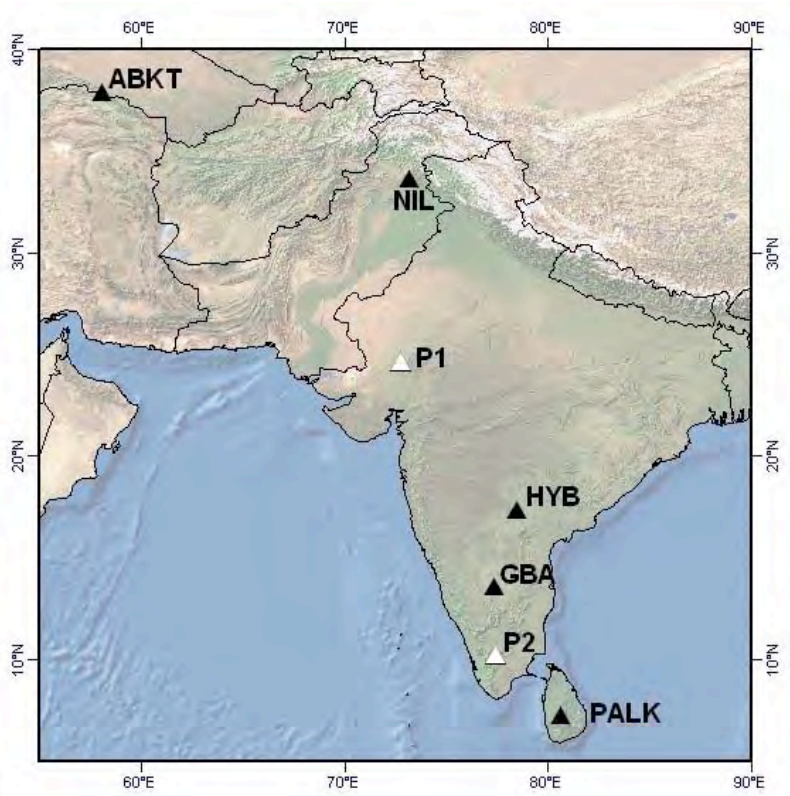


Figure 1. Location of IRIS/IDA stations, Geoscope station HYB, GBA, formerly operated by the Atomic Weapons Establishment (AWE) at Blacknest, and proprietary stations P1 and P2.

Detection of Mining Events from Continuous Data Using Waveform Correlation Techniques

Two methods for detecting mine blasts are employed in this research. The first is the waveform correlation method (Harris, 1991). This procedure involves the application of a simple STA/LTA detector to a month or more of continuous data. Detections are correlated to a certain threshold and assigned to clusters of events. Events in these clusters are examined by eye, and if the events appear to be mine blasts (based on the presence of the *Rg* phase or repeated occurrence during daylight hours) then the events in the cluster are located. The waveform correlation method has been the primary method for the detection of mine blasts in this research. This method has been used on data from HYB, ABKT, GBA, and the proprietary stations.

As an example of this application, a simple STA/LTA detector was applied to the first 40 days of continuous data from proprietary station P2 as an initialization for the waveform correlation. Two hundred and thirteen detections were made and the detected waveforms were correlated to a threshold of 0.4 into clusters of 2 or more events each. We developed subspace detectors for the two largest clusters, and these detectors were used to reprocess the entire P2 dataset for additional events in the two clusters.

Cluster 1, the largest cluster, contained 17 events upon initial inspection (33 events after further analysis). All of the events detected occurred between 1 April 2001 and 21 July 2001, with all but two events occurring between 1 April 2001 and 3 May 2001. The events occurred between 0500 and 0700 UTC (10:30 AM to 12:30 PM local time). Cluster 5, the second largest cluster, contained 11 events. These events occurred between the hours of 1000 and 1100 UTC (3:30 PM to 4:30 PM local time) from 5 April 2001 to 2 August 2001. Given the long durations of these sequences (111 days for Cluster 1; 119 days for Cluster 5) and the consistency of the origin times, the sources appear to be mines. Events from Cluster 5 also exhibit an *Rg* phases, which are consistent with shallow sources such as open-pit mine blasts. Figure 2 shows the locations of the clusters relative to P2 and nearby stations GBA and PALK. None of the events in either cluster were observed in the PALK dataset and no data from GBA are available after 1996. Figure 3 shows the detections, sorted by time of day, for a 4-month period.

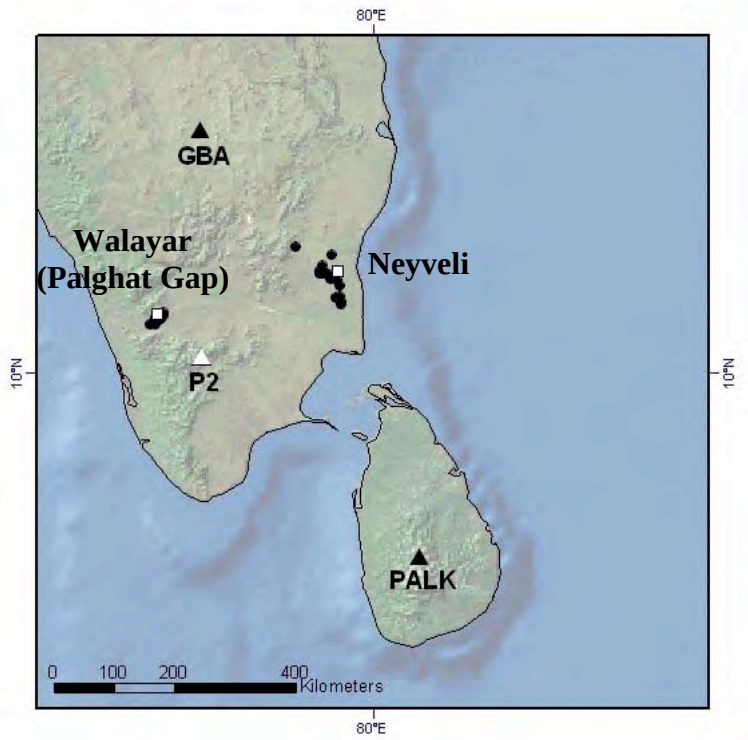


Figure 2. Location of the events from the two largest subspace detection clusters recorded at P2. Suspected mine blasts are plotted as dark circles. White squares represent locations of open-mine pits.

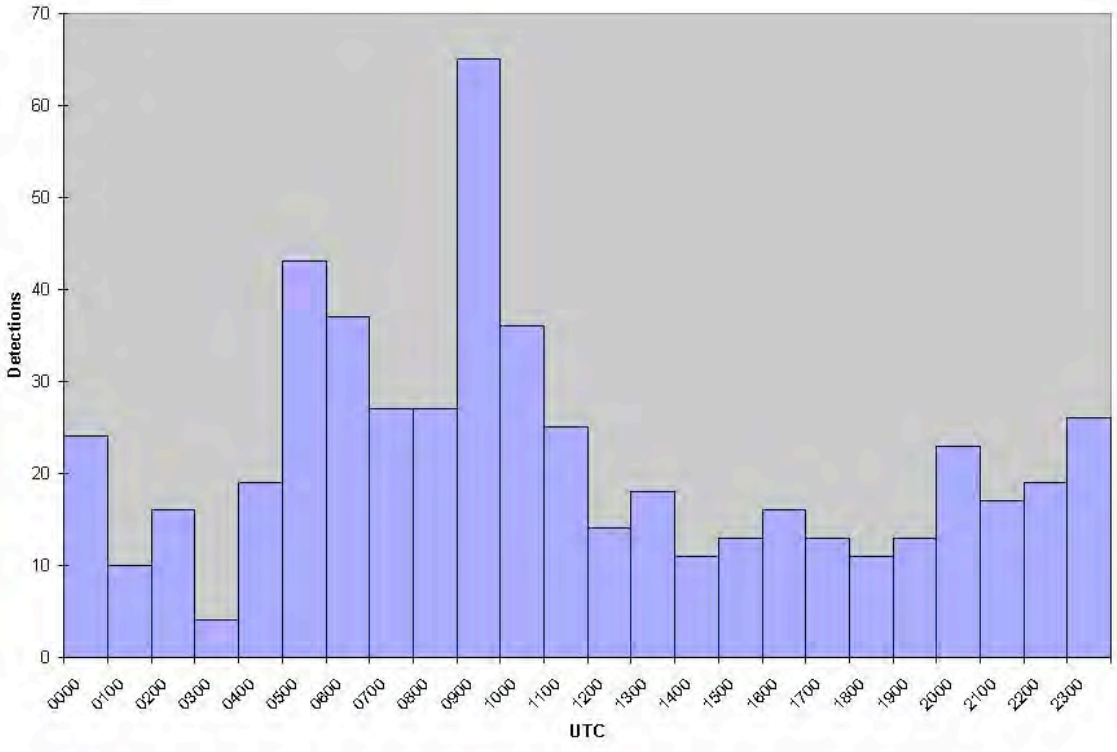


Figure 3. Event detections at station P2 between 29 March 2001 and 8 August 2001, sorted by time of day. Local time equals UTC plus 5.5 hours.

Detection of Possible Mining Events from Continuous Data using an Automated *Rg* Detector

The presence of *Rg* on waveforms indicates shallow source depth and, when detected repeatedly during daytime hours, it is often an indication of mining operations. Thus, the second method used to detect shallow events (possible mine blasts) is an automatic *Rg* detector. The *Rg* detector code has been tested on clusters of well-located events and we have developed routines necessary for automatic analysis of continuous data, as described below.

We modified the Chael (1997) detection method, which was developed for intermediate-period Rayleigh wave arrivals (17 to 22 sec), to account for the shorter periods (< 3 sec) characteristic of the *Rg* phase. The modifications included: 1) pre-filtering the waveforms between 0.4 and 1.3 Hz using a zero-phase, 3-pole Butterworth filter, 2) calculating the covariance matrix for rotated waveforms, 3) estimating the optimal constants for the STA and LTA recursive filters (Allen, 1982), and 4) using two additional weights of the detection function for planarity verification. The algorithm is coded in Matlab and will eventually be incorporated as a Matseis module (Young, 1997).

The *Rg* detector was applied to the data in two steps:

Step 1. Preliminary detection using Fourier techniques. First, the data was filtered between 0.4 – 1.3 Hz. Then, the algorithm was applied to the three components (Z, N, E) of the data in a moving time window with a step size of 0.5 seconds, over a swath of backazimuth ranging between 0 and 355 degrees. Detections were declared when the maximum value of the detection function was larger than an empirical threshold, which was calculated for each station.

Step 2. Back azimuth estimation. After detection was declared, values larger than 10% of the detection function's maximum value (see the lower plots in Figure 5) were plotted as a function of time and back azimuth. An initial back azimuth (bazF), corresponding to the largest values of the detection function, was estimated from the plot. All

the back azimuths in this study were calculated with a procedure described as the direction of the center of mass (Mardia, 1972), using the squared values of the detection function as weights.

We have observed that wavelet pre-filtering significantly improved the signal-to-noise ratio (*SNR*) of the *Rg* arrivals. Therefore, we decided to apply pre-filtering using a Meyer wavelet, once detection was declared, to assess whether it would improve the back azimuth estimates. The Meyer wavelet scale was calculated to correspond to the *Rg* period chosen by the analyst. A back azimuth was estimated for each *Rg* period. When using additional *Rg* periods (a total of three in this study), the final back azimuth (bazW) was calculated as the mean of the estimated back azimuths, using the *SNR* values for each scale as weights. We calculated *SNR* in the propagation plane as the ratio between the maximum amplitude and twice the standard deviation of the noise (Der and Shumway, 1999). We prefer this formula for *SNR* calculation to the classical ratio of six-second signal-to-noise *rms* because it accounts for the short duration (< 3 sec) of the *Rg* phase and for several seconds of possibly large S arrivals immediately preceding *Rg*.

The *Rg* detector was tested on 6 clusters (more than 60 events) recorded at stations in central and southern India. Unlike teleseismic Rayleigh waves, *Rg* has periods of less than 3 seconds. The frequency range of the Step 1 filter is very important for *Rg* detection and is specific to the event's epicentral distance. For the detector to be implemented for local and regional data processing, choosing the appropriate frequency range will be the key for successful detections.

Results for 24 central India events recorded at HYB are presented in Figure 4. These events belong to four clusters: 2, 10, 12 (GT20) and Cluster 9 (GT5).

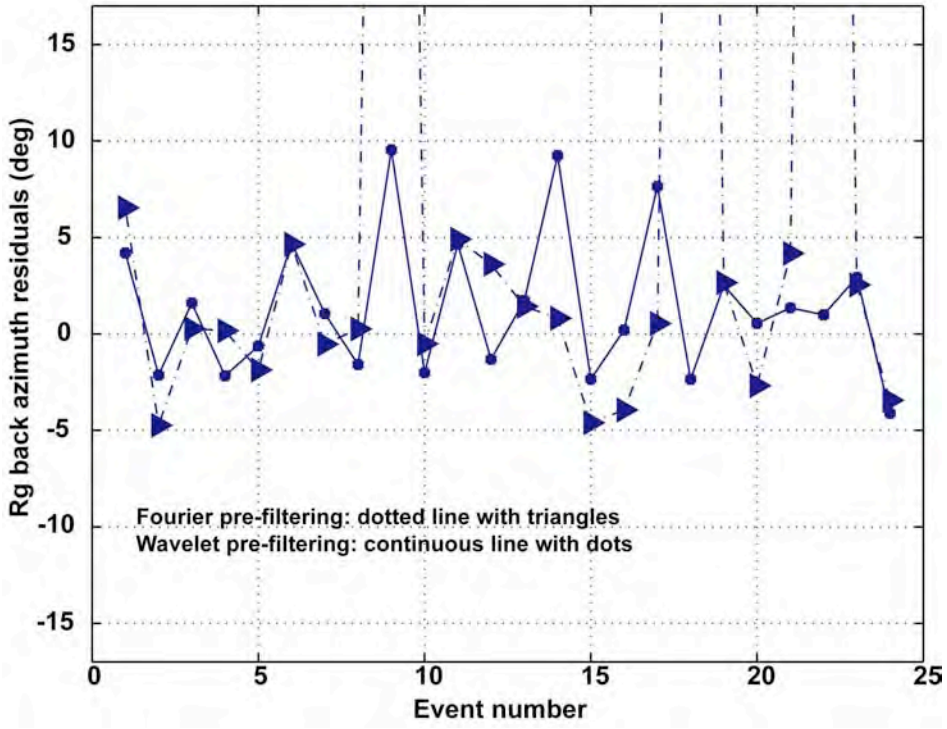


Figure 4. Back azimuth residuals estimated using Fourier pre-filtering (dotted line with triangles) and using wavelet pre-filtering (continuous line with dots). The residuals are relative to each cluster ground truth (GT) back azimuth. Events 1 and 2 are from Cluster 2, events 3 to 5 are from Cluster 9, events 6 to 9 are from Cluster 10 and events 10 to 24 are from Cluster 12.

Whereas *Rg* was detected as the most probable arrival in all 24 events using wavelet pre-filtering, it was detected as the most probable arrival in only 21 of 24 (87%) events using Fourier pre-filtering. Below we examine the three low *SNR* events that were not correctly detected using Fourier methods. For the event No. 18, 1999/11/29 09:39:03, from

Cluster 12, *Rg* is detected as one of three possible arrivals. The lower left plot of Figure 5 shows that the *Rg* arrival was detected with the correct backazimuth (40 degrees) at about 104 sec. However, the arrival that corresponds to the largest value of the detection function after Fourier pre-filtering was not the *Rg*. It was another Rayleigh-type arrival at ~107 sec, with a period of ~ 2.5 seconds and a back azimuth of 155 degrees (see Figure 4). In the right plots in Figure 5 we show that Meyer wavelet pre-filtering (scale 14, corresponding to 1.1 sec period) increased the *Rg SNR* dramatically.

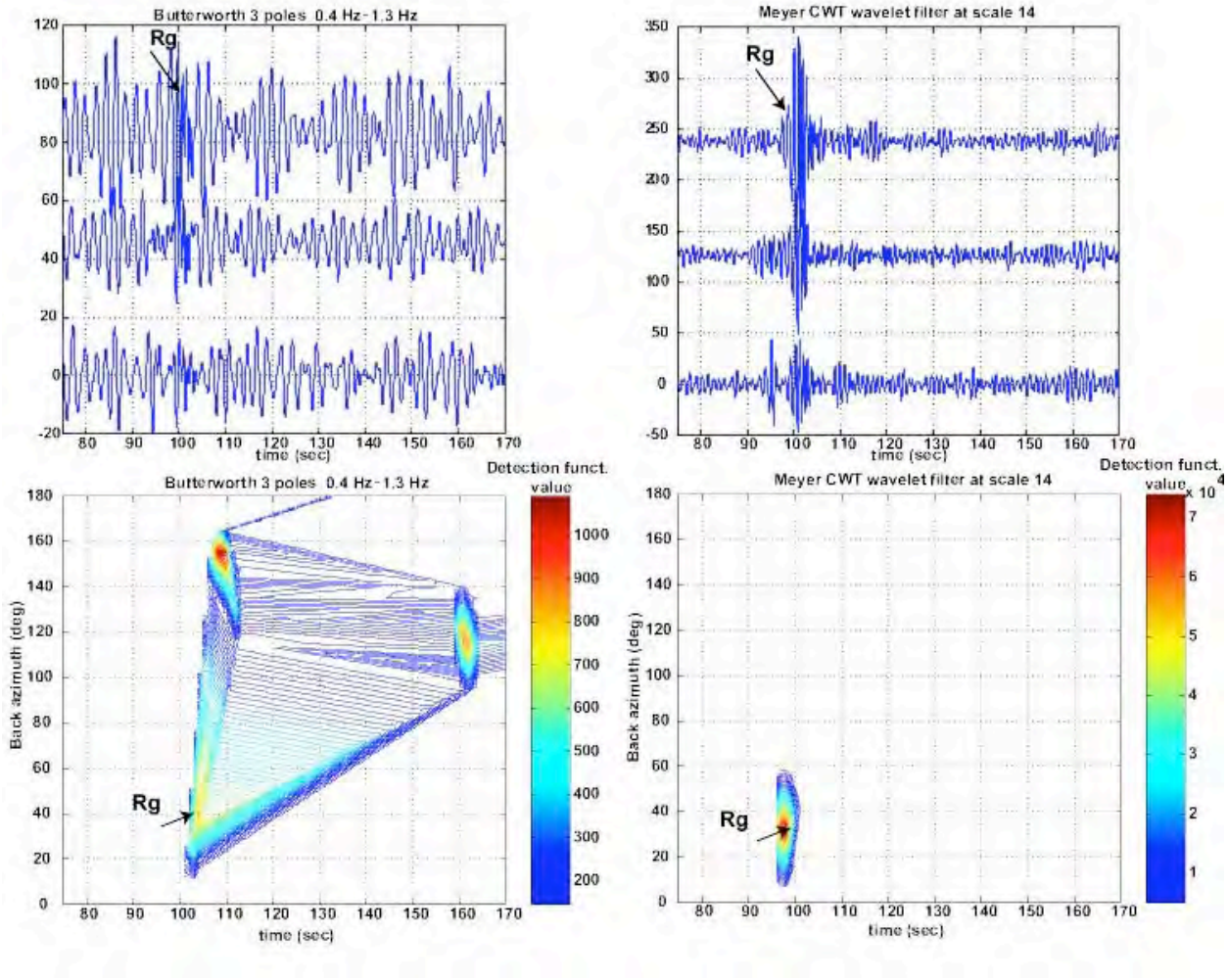


Figure 5. Top: Fourier and wavelet pre-filtered data of the 1999/11/29 09:39:03 event from Cluster 12, designated No. 18. Bottom: Detection function value as a function of time and back azimuth. As shown in the lower right plot, *Rg* is clearly detected in after wavelet pre-filtering. However, as shown in the lower left plot, *Rg* is only the third choice of the detector, based on the detection function value, after Fourier pre-filtering. The empirical detection threshold calculated for Fourier pre-filtering at HYB was 670.

The other two events not detected by Fourier pre-filtering were 9 and 22. For these two events the maximum of the detection function was below the empirical threshold value of 670 calculated at HYB. Wavelet pre-filtering improved the detection results for these events as well (see Figure 4).

The total estimated back azimuth sample standard deviation for the 24 events near HYB, using wavelet pre-filtering, was 3.7 degrees, equivalent to a maximum location error between 11 km (Clusters 2, 10, 12) and 12 km (Cluster 9). This result was better than the estimates using Fourier pre-filtering value and was comparable to the standard

deviation of the first arrival back azimuth residuals (3.8 degrees) calculated using data from a single station. Considering the location error (GT5 to GT20) for these 24 events, we consider the results encouraging. The *Rg* periods for this distance range were between 0.8 and 1.7 seconds.

Two clusters of events were analyzed at station P2. Cluster 1 (GT15) contained 33 events. Of these events, only one larger *SNR* event had a clear *Rg* arrival detected after data was Fourier pre-filtered between 0.6 and 4.5 Hz. No detections were found by the analyst, in several frequency intervals, for the other 32 events. For the one detected event, the GT back azimuth was 56.6 degrees and the first arrival back azimuth was estimated to be 67.1 degrees. Applying the *Rg* detector, we estimated the back azimuth as 66.2 degrees using Fourier pre-filtering and 59.9 degrees using wavelet pre-filtering. An empirical detection threshold of 650 was calculated for these events, for a frequency range of 0.4 – 1.3 Hz. Locations determined for the Cluster 1 events suggest the source is over 250 km northeast of the station. We attributed the strong attenuation of short period *Rg* from these events to the large event-station distance and to a propagation path with considerable topography.

Cluster 5 (GT2) contained 11 events located about 95 km distance from the station P2 at 317.2 degrees back azimuth. A frequency range of 0.6 – 4.5 Hz was used when searching for *Rg* in this cluster. Only four events, all detected, had visible *Rg*. The estimated back azimuth for the Fourier pre-filtering, as well as for the wavelet pre-filtering, differed by 30 degrees from the GT back azimuth for three of the events, and by 20 degrees for the fourth event. The largest first arrival back azimuth difference between events in this cluster was 13 degrees. There is considerable topography on the path from the station to the source for Cluster 5. Thus, the lack of *Rg* arrivals for this cluster suggests that either *Rg* is highly attenuated for this path or the events were too deep for *Rg* generation. However, the latter explanation is unlikely, as subsequent sections will show that the events are located very near open-pit mines as determined from satellite imagery. Further tests of the method are ongoing.

Our tests show that the *Rg* detector performs better when using wavelet pre-filtering and offers the advantage of improved back azimuth estimates. As wavelet decomposition considerably improves the performance of the detector, we will investigate using it as the primary pre-filtering mechanism. The *Rg* detector is currently being tested in automated mode and applied to continuous data from station HYB. Results from this analysis, as well as a comparison to the waveform correlation method, will be presented in the poster associated with this paper.

Location of Mining Events

During the past year, we have implemented SSLOC3D (Leidig *et al*., 2003) to form single-station locations for the clusters determined from waveform correlation. SSLOC3D includes a polarization technique (Jurkevics, 1988) to determine back azimuths. A pilot study (Leidig *et al*., 2003) showed that the polarization technique reduced the measurement error in determining back azimuths when compared to the three-component *f-k* technique in Matseis (Young, 1997). SSLOC3D also estimates epicentral distances based on matching observed *Lg-P* times with travel time differences estimated using 3D velocity models. Prior to SSLOC3D implementation, we were using a single 1D *P*-wave velocity profile for central India to locate events at HYB, P1, and P2. The profile was based on the WINPAK3D *P*-wave velocities (Reiter *et al*., 2001) beneath the HYB station. We determined that using the 3D *P*-wave travel-time grids, based on WINPAK3D, and an *Lg* travel-time grid based on a constant velocity of 3.6 km/sec could decrease the mislocation for most of the clusters in the database. The mislocations for P1 and HYB were decreased between 4 and 12 km through the use of SSLOC3D. An example of this improvement is shown in Figure 6, which compares 1D and SSLOC3D locations for mine events recorded at HYB. For SSLOC3D, 50% of the locations fall within the box drawn around the Ramagnundan mine complex as compared to none of the 1D locations. We do note that our mislocation errors for mines near P2 were slightly increased (< 3 km) using SSLOC3D as compared to 1D techniques. We note that these locations are model dependent and will improve as we develop better knowledge of the regional velocity structure.

Events from P2 Cluster 1 have been located near the large township of Neyveli in the southern Indian state of Tamil Nadu. Neyveli Lignite Corporation (NLC) Limited operates two open-cast mines (Mine I and Mine II) just south of Neyveli. The NLC website (http://www.nlcindia.co.in/) states that the mines are the largest mechanized lignite mines in India. Mine I and Mine II are located approximately 5 km apart. The mine locations were obtained from a map produced by Sinha and Sridharan (1999) in their noise level study of the Neyveli mines. Figure 7A shows the location of the Cluster 1 events relative to the township of Neyveli and the lignite mines. The orange cross in Figure 7A represents the average latitude and longitude of the cluster.

Cluster 5 events (Figure 7B) are centered near the town of Walayar in the state of Kerala near the Tamil Nadu border. Limestone mining is common in the Walayar area. Satellite imagery of the area has revealed two quarries, or open-pit mines, within 10 km of the centers of Cluster 5 and Cluster 3.

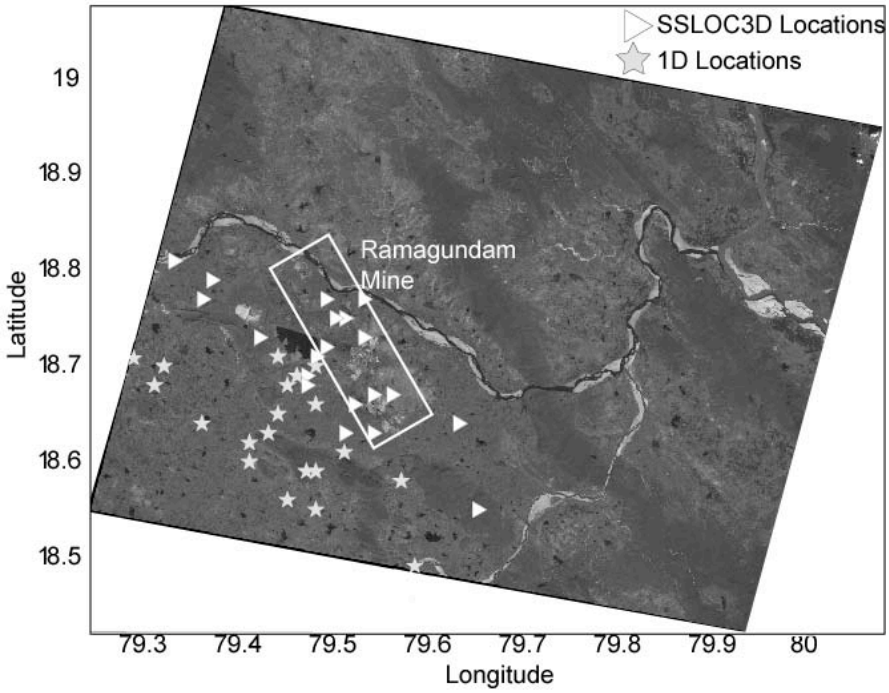


Figure 6. Epicenters determined from SSLOC3D (triangles) and 1D location techniques (stars) in relation to a large coal mining complex in central India.

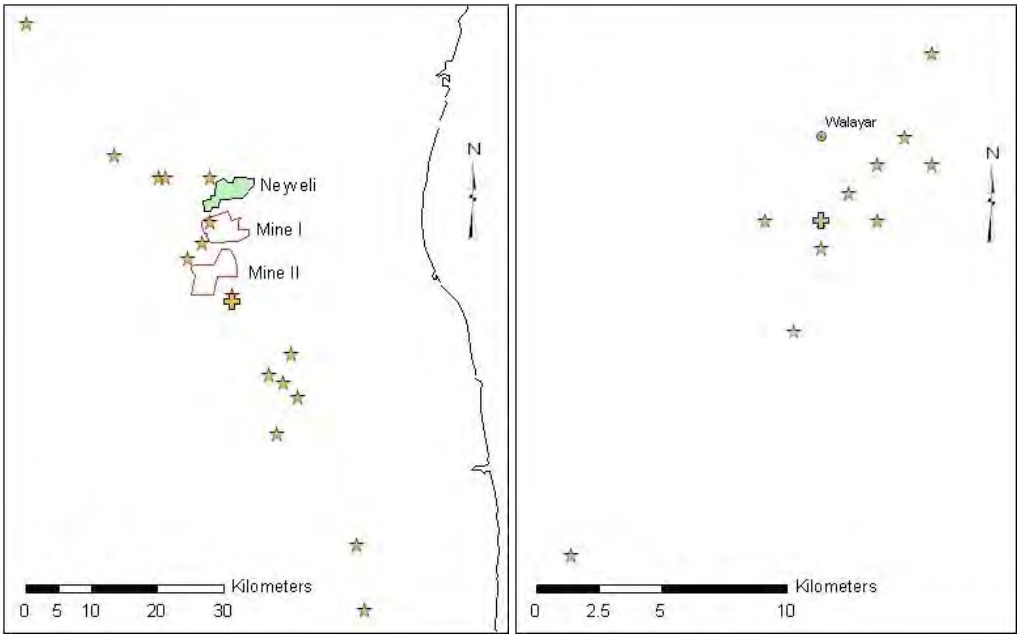


Figure 7. Single-station locations for suspected mine events. The figure on the left (Figure 7A) shows the events of Cluster 1. The figure on the right (Figure 7B) shows the events of Cluster 5. Centers of clusters are denoted by a cross.

CONCLUSIONS AND RECOMMENDATIONS

Information on mining activity around seismic stations in southern Asia is continually being compiled and updated. Continuous data for these stations have been analyzed by the waveform correlation method to detect events associated with nearby mines and mining districts. Waveform correlation has been the primary tool for detecting local mine blasts.

We have developed and tested a semi-automatic *Rg* detector. For 24 well-located events clustered near HYB, *Rg* is always detected after wavelet pre-filtering. Using Fourier pre-filtering between 0.4 and 1.3 Hz, *Rg* is detected as the most probable arrival for the 21 largest *SNR* events of the 24 (87%). The estimated *Rg* back azimuth sample standard deviation was 3.7 degrees, comparable to the standard deviation of the first arrival back azimuth residuals (3.8 degrees). Based on these results we will investigate the possibility of using wavelet pre-filtering in the initial detection stage instead of Fourier methods. For other events clustered near station P2, *Rg* was detected in all cases when it was visible on the seismogram. We plan to evaluate the detector on more GT data in India. Additionally, we are focused on making the whole procedure automatic. We consider the *Rg* detector tool a useful addition to the crosscorrelation method. The *Rg* detector offers the advantage of supplementary back azimuth estimates and therefore information on *Rg* propagation path characteristics, while the crosscorrelation method has the advantage of detecting mining events without visible *Rg*.

Detected waveforms from the clusters mentioned in this paper, along with other clusters detected in southern Asia by these techniques, are located using the SSLOC3D method (Leidig *et al*., 2003). These waveforms are linked to an ArcView 8.3 geographic information system (GIS) database containing information on event location, satellite imagery, regional geology, station information, and mine information.

ACKNOWLEDGMENTS

We express our gratitude to Heather Hooper, Mark Leidig, and Delaine Reiter for their fruitful discussions and help on this project.

REFERENCES

Allen, R. (1982), Automatic phase pickers: their present use and future prospects, *Bull. Seis. Soc. Am*, **72**, S225-S242.

Chael, E. P., (1997), An automated Rayleigh wave detection algorithm, *Bull. Seis. Soc. Am*., 157-163.

Der, Z. A, and R. H. Shumway, (1999), Phase onset time estimation at regional distances using the CUMSUM algorithm, *Phys. Earth Planet. Int*., **113**, 227 –246.

Harris, D.B. (1991). A waveform correlation method for identifying quarry explosions, *Bull. Seism. Soc. Am.*, **81**, 2395-2419.

Jurkevics, A. (1988). Polarization analysis of three-component array data, *Bull. Seism. Soc. Am.*, **78**, 1725-1743.

Leidig, M., D.T. Reiter, J. L. Bonner, and A. Rodgers, (in review). Applicability of 3D modeling techniques in creating single-station locations: a test case in southern Asia. Submitted to *Bull. Seism. Soc. Am.*

Mardia, K. V. (1972), Statistics of directional data, Academic Press, New York

Reiter, D. T., M. Johnson, A. Rosca, C. Vincent, (2001). Development of a regional 3D velocity model of the Pakistan region for improved seismic event location. Final Report, Weston Geophysical, 27 p.

Sinha, S. and P.V. Sridharan (1999). Present and future assessment of noise level in the Neyveli region, *Journal of Environmental Studies and Policy*, 2(1): 1-13.

Young, C., (1997). Matseis: a seismic toolbox for MATLAB, *Proceedings of the 18th Annual DoD/DOE Seismic Research Symposium.*

STATION CORRECTION UNCERTAINTY IN MULTIPLE EVENT LOCATION ALGORITHMS AND THE EFFECT ON ERROR ELLIPSES

Jason P. Erickson,[1] Deborah K. Carlson,[2] Anne M. Ortiz,[1] Kevin D. Hutchenson.[1] Linda J. Owiesny,[1] Gordon D. Kraft[1], Dale N. Anderson,[2] Mark A. Tinker[1]

Quantum Technology Services, Inc.,[1] Pacific Northwest National Laboratory[2]

Sponsored by Air Force Technical Applications Center

Contract No. F08650-01-C-0063

ABSTRACT

Accurate location of seismic events is crucial for nuclear explosion monitoring. Of equal importance is an accurate representation of the location uncertainty, as this determines the area, to a certain confidence level, within which the event may be located.

There are many sources of error present in the location process, including measurement error and model bias. In a multiple event process error sources expand to include uncertainty in the station corrections and uncertainty in the location of calibration events. In order to generate meaningful error ellipses, all of these sources of error must be taken into account.

Most location algorithms calculate ellipses using some combination of *a priori* knowledge of the data variance, signal-to-noise weighting, and *a posteriori* measurement of the data residuals. Multiple event algorithms can calculate, and kriged station correction surfaces include, an estimate of the station correction uncertainty. We seek a unified general method for combining the station corrections and uncertainties from different sources and calculating an accurate error ellipse. Furthermore, in some situations it may be desirable to utilize calibration events that are known with a varying degree of accuracy, and in this case the influence of the calibration events should be weighted relative to the confidence in their locations.

We have derived the full covariance matrix for a multiple event location using Fisher's information theory (Lehman, 1983). This formulation of the covariance matrix is generally not used in seismic location, but is common theory for maximum likelihood estimation. The information theory covariance matrix gives complete control over the variance of all of the model parameters. This allows for station corrections from many approaches to be included in the location model and for calibration events with different confidence levels to be given different weighting. We examine the behavior of error ellipses calculated with this covariance with known sources of error. Progressive Multiple Event Location (PMEL, Pavlis and Booker, 1983) is used as a maximum likelihood estimate solver, and is also used to demonstrate the construction of a covariance matrix with the PMEL estimates.

OBJECTIVE

Error ellipses describe the area, to a given confidence level, within which an event is likely to have occurred. There are numerous methods for determining the size of an ellipse, but the shape and orientation are always calculated from the covariance matrix of the model parameters. The purpose of this research is to develop an alternate method of calculating the location covariance matrix. This method is intended to generalize the error ellipse construction by using a formulation of the covariance matrix that allows for any source of error or uncertainty to be incorporated into the location model.

RESEARCH ACCOMPLISHED

Introduction - PMEL

Traditional location methods seek to find a hypocenter or, in the case of multiple event algorithms, a set of hypocenters that minimize the difference between the observed and predicted arrival times (the travel-time residual). A common model for the predicted arrival time is (unweighted):

$$t_{ij} = t_i + T(x_i, y_i, z_i, R_j) + S_j + e_{ij}, \qquad e_{ij} \overset{iid}{\sim} N(0, s^2) \tag{1}$$

where

t_{ij} is the arrival time of the ith event recorded at the jth station,

t_i is the origin time of the ith event,

x_i, y_i and z_i are the longitude, latitude, and depth, respectively, of event i,

R_j is the location of station j,

$T(\mathbf{x}_i, y_i, z_i, R_j)$ is the travel time from event i to station j through an arbitrary earth model,

S_j is the correction for the jth station, and

e_{ij} is the measurement error of the ith event at the jth station.

As Equation (1) is non-linear with respect to the hypocenter, the problem is usually linearized by taking a Taylor series expansion and dropping a second order and higher terms. The residual for a given observation then becomes approximately equal to:

$$r_{ij} = dt_i + \left.\frac{dT}{dx}\right|_{x_i} dx + \left.\frac{dT}{dy}\right|_{y_i} dy + \left.\frac{dT}{dz}\right|_{z_i} dz + dS_j, \tag{2}$$

and the residuals for all of the observations can be written in matrix form as:

$$\mathbf{r} = \mathbf{A}\Delta\mathbf{x} + \mathbf{S}\Delta\mathbf{s}. \tag{3}$$

PMEL (Pavlis and Booker, 1983) solves for the hypocenter parameters and the station corrections separately through two least squares inversions. In the first inversion, hypocenters are calculated while the station corrections are held constant. The hypocenter term in Equation (3) is then removed using an annulling transformation, resulting in a set of equations relating station corrections to a set of annulled data. The station corrections are then calculated via the second least squares inversion. These station corrections are then substituted into the hypocenter inversion, and the process repeats until the convergence criteria have been met.

The covariance matrix for PMEL is given by:

$$\mathbf{Cov} = \begin{bmatrix} \mathbf{HH}^T + \mathbf{HSC}_S\mathbf{S}^T\mathbf{H}^T & -\mathbf{HSC}_S \\ -\mathbf{C}_S\mathbf{S}^T\mathbf{H}^T & \mathbf{C}_S \end{bmatrix} \quad (4)$$

where

H is the generalized inverse of the **A** matrix in Equation (3),

S is the matrix of station correction partial derivatives, and

$\mathbf{C}_s$ is the covariance matrix of the station corrections.

Information Theory Covariance Matrix

If we rewrite Equation (1) in terms of the errors:

$$e_{ij} = t_{ij} - t_i - T(x_i, y_i, z_i, r_j) - S_j, \quad (5)$$

the resulting density function of the model is:

$$f_e = \frac{1}{s\sqrt{2p}} \exp\left[-\frac{1}{2s^2} e^2_{ij}\right]. \quad (6)$$

The joint density is the product of the individual densities:

$$j = \prod f_e(e_{ij}) \quad (7)$$

and the log-likelihood function is:

$$l = -N\ln(s) - \frac{N}{2}\ln(2p) - \frac{1}{2s^2}\sum e^2_{ij}, \quad (8)$$

where N is the total number of observations. Maximum likelihood estimates are values of s, t_i, x_i, y_i, z_i, and S_i that maximize equation (8).

The information matrix is defined as the expectation matrix of negative second partial derivatives of the log-likelihood function with respect to each model parameter pair (Lehmann, 1983):

$$\mathbf{I}(q)_{pq} = -E\left[\frac{\partial^2 l}{\partial q_p \partial q_q}\right] \quad p = 1,2,...k; q = 1,2,...k \quad (9)$$

where $\mathbf{q}$ is the vector of all model parameters (of length k), including the hypocenter parameters for all events and the station corrections.

And finally, the covariance matrix is the inverse of the information matrix:

$$Var(\hat{q}) = \left[I(q)\right]^{-1}. \quad (10)$$

In practice, parameter values in I(q) are replaced with the maximum likelihood estimates. This matrix contains the variance and covariance of all of the model parameters and its construction provides the framework for the development of covariance matrices when enhancements are made to the fundamental travel time model. Using this

covariance matrix it is then possible to calculate confidence ellipses (Flinn, 1965), coverage ellipses (Evernden, 1969), or K-weighted ellipses (Bratt and Bache, 1988). In this report, we demonstrate only coverage ellipses.

Data

Results of each method are demonstrated using two different data sets. The first is a synthetic data set that has had normally distributed random measurement error and model bias added to all of the arrivals. The stations associated with these data are azimuthally distributed at increments of 45 degrees. Four of the stations are located at a distance of 20 degrees from the events, while the other four are at a distance of 35 degrees (Figure 1). Each of the nine events is located at a distance of 0.2 degrees from the adjacent events, and all events were "recorded" by every station (Figure 2). These data will be used to demonstrate the behavior of the ellipses under idealized conditions with known errors.

Ellipses are also shown for a set of mining explosions (Table 1) from the Powder River region in Wyoming. While ground-truth for these regionally recorded events was unavailable, arrivals at a local station provided high confidence correlation of each explosion to a unique mine site.

In order to simulate a sparse network configuration that could be available in a low-yield nuclear monitoring situation, a subset of three stations was used for the locations and ellipse calculations (Figure 3). These stations were located at distances of 3 degrees (PDAR), 4 degrees (ISCO), and 11 degrees (FLAR). The phases used in the locations were Pn and Sn for PDAR, and Pn for ISCO and FLAR. To reduce the variability of the measurement error, the picks were made after the waveforms had been correlated.

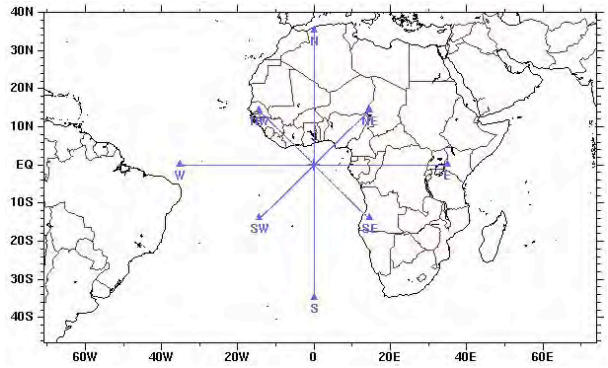


Figure 1. Station configuration of synthetic data.

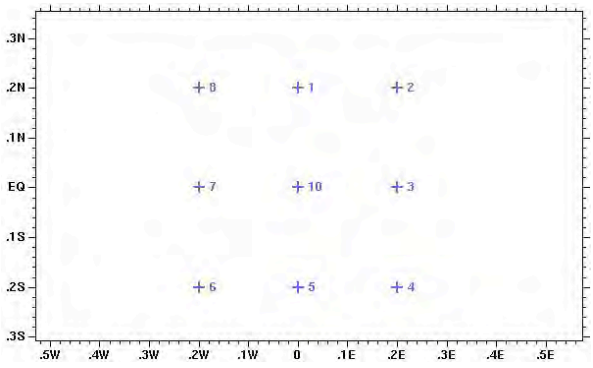


Figure 2. Event configuration of synthetic data.

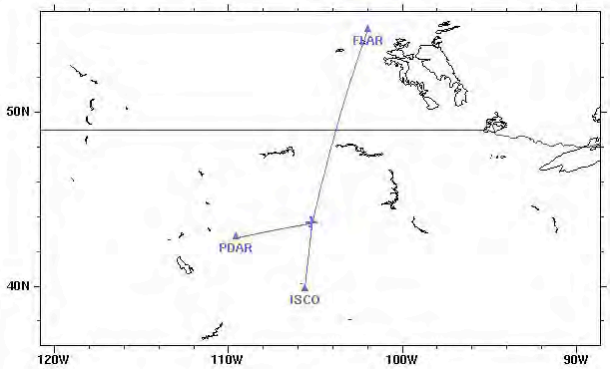


Figure 3. Stations used to calculate locations and ellipses for Powder River mining events.

Table 1. Powder River mining event origin information.

Date	Origin Time	Latitude (N)	Longitude (W)	Depth	M_b
11/30/02	20:00:01.775	43.9796	105.3221	0	3.46
12/06/02	19:07:50.251	43.6259	105.1642	0	3.78
12/09/02	21:19:45.498	43.9870	105.3221	0	3.16
12/13/02	22:09:44.746	43.6386	105.1989	0	3.60
12/14/02	21:06:33.249	43.6246	105.1828	0	3.72
12/20/02	19:17:18.226	43.6224	105.2024	0	3.78

Results

Locations and their corresponding ellipses were calculated with all of the synthetic data having a measurement error variance of 0.3 seconds and with full station coverage (Fig. 4). In this case, both methods give nearly identical results. The only difference is that the information theory derived ellipses are marginally smaller.

A similar set of locations and ellipses were calculated, with the exception that the measurement error for arrivals recorded at stations N, NE, S, and SW was increased to a variance of 0.9 seconds, while those for E, SE, W and NW remained at 0.3. The two methods again produce nearly identical ellipses, all of which are nearly circular (Figure 5), despite the fact that the station corrections to the north, northeast, south, and southwest are generated with data that have a much greater variability than the other stations.

Ellipses have also been calculated using data from mining events located in the Powder River area of Wyoming (Figure 6). With a small number of observations, ellipse calculations can become unstable, sometimes resulting in unreasonably large error regions (as is the case for one of the ellipses in Figure 6). The information theory derived covariance matrix will likely increase the stability of ellipse calculations in the sparse data case providing a more accurate representation of the location uncertainty.

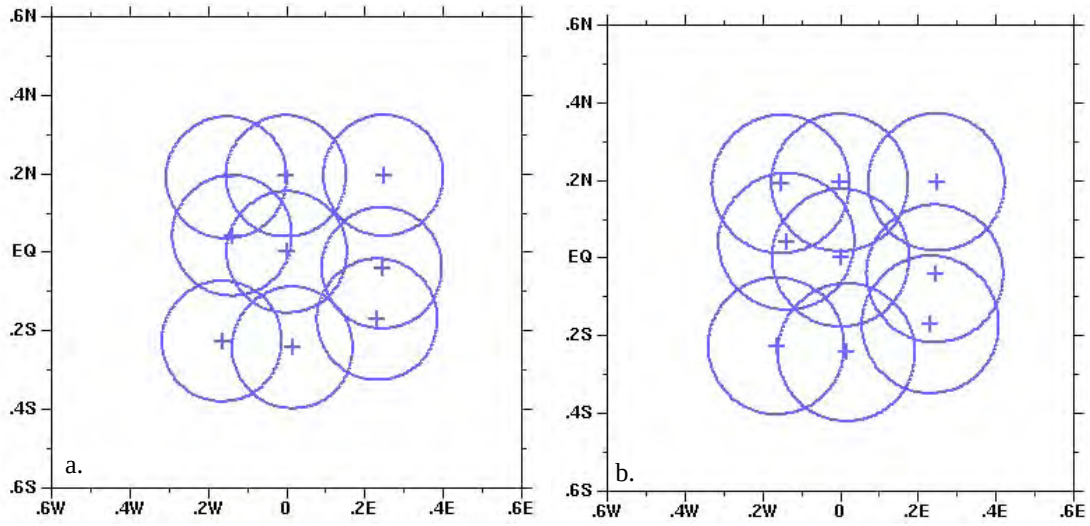


Figure 4. Coverage ellipses with full station coverage and equal random error at all stations using PMEL (a) and information theory (b).

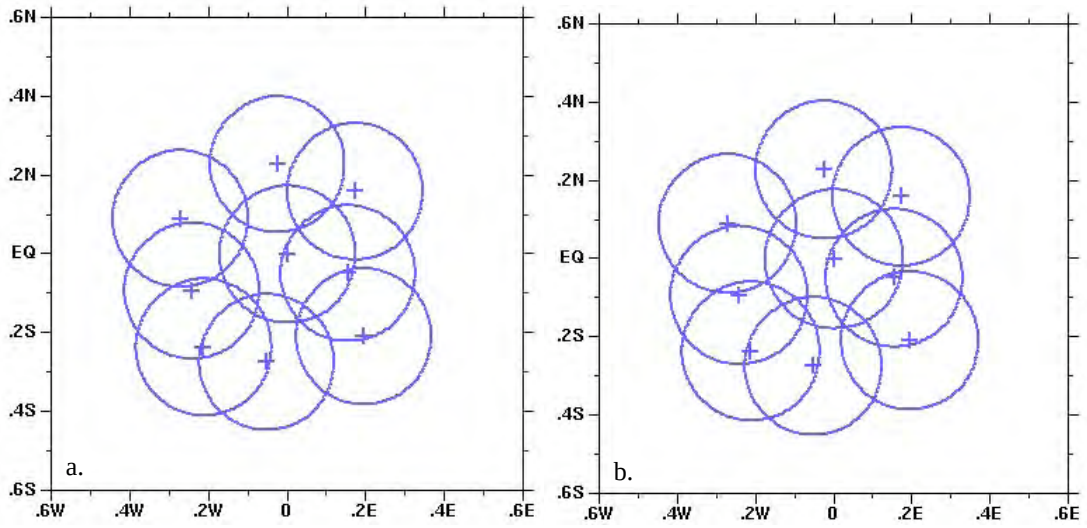


Figure 5. Locations and error ellipses from PMEL (a) and information theory (b). The stations to the north, northeast, south, and southwest all have random error with a variance of 0.9 seconds, while the others have random error with a variance of 0.3 seconds. Despite the difference in this error, both methods result in circular ellipses.

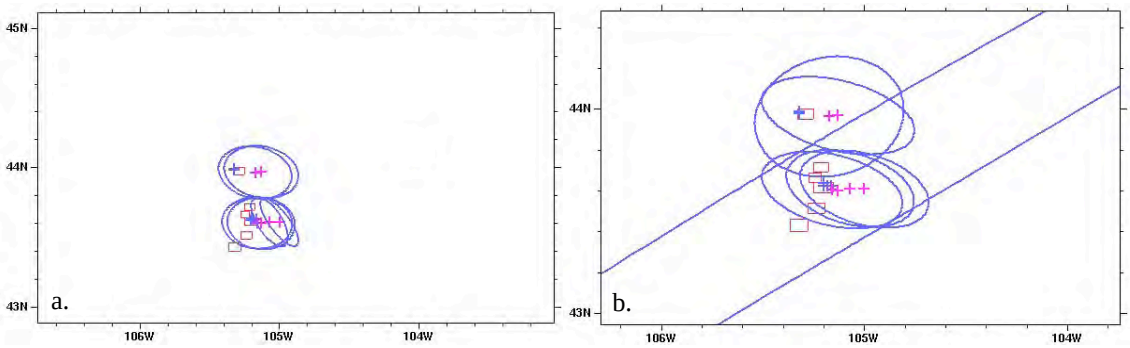


Figure 6. Locations and ellipses for six Powder River mining explosions (seed location – stars, PMEL locations – crosses). The events were located using a calibration event and four arrivals for each event. Due to the small amount of data and limited azimuthal coverage, the resultant error ellipses from PMEL (a) are unstable, while those computed with the information theory (b) covariance matrix are all of similar size.

Discussion

The information theory formulation of a covariance matrix allows for enhanced flexibility in the way that error ellipses are calculated. This work is progressing to more sophisticated formulations of the travel time model.

Information theory covariance construction provides the ability to incorporate a number of enhancements, including station corrections that are not constant, but rather are a function of other parameters. Presently, station corrections are held constant for all events in an inversion. This is based on the assumption that clustered events share the same path to the receiver, and thus the same velocity model deficiencies. As the distance between events increases, this assumption becomes less valid. Allowing station corrections to vary spatially according to some function would allow for a more realistic representation of station corrections and would allow for more distant events to be included in the inversion.

It is also possible to have the station correction variability directly affect the size and shape of the ellipse. Currently, the station correction covariance matrix (C_s from Equation 4) is solely a function of azimuthal coverage and the number of events recorded by a given station. This matrix is unaffected by how well the data are fit by the station corrections, and hence the error ellipses do not adequately represent the fact that some station corrections may be known to a higher degree of confidence than others. This explains why the ellipses in Figure 4 are circular, despite the fact that there is considerably more uncertainty in the stations corrections to the northwest and southeast of the event cluster. By adjusting the hypocenter variances and covariances to account for this uncertainty, a more accurate error region can be obtained.

The information theory covariance matrix provides the ability to use station corrections from different sources (*i.e.* PMEL and kriged correction surfaces) and include their respective uncertainties. There may be instances where a station or stations cannot be included in multiple event processing due to an insufficient number of observations. It may still be desirable to include these arrivals, particularly if they provide additional azimuthal or distance coverage to the network. As currently coded, PMEL allows for the use of observations recorded at stations that do not have corrections. The information theory covariance matrix will allow for station corrections from other sources to be applied to these observations, and will allow for the uncertainties associated with these corrections to be incorporated into the error ellipses, and

Finally, it will be possible to use calibration events with different degrees of confidence (*i.e.* GT5, GT10), and have the error ellipses reflect that uncertainty. This ability would be of particular value in locations where no previous nuclear testing had occurred, and only earthquakes were available for calibration.

CONCLUSIONS AND RECOMMENDATIONS

The information theory covariance matrix has been derived for the basic location model with station corrections and used to calculate error ellipses around seismic locations. This will provide the framework for determining the covariance matrix for a more complicated travel time model and will allow additional information to be incorporated into the uncertainty ellipses, thereby improving their accuracy.

ACKNOWLEDGEMENTS

The authors thank Drs. Gary Pavlis, David Russell, and Terry Wallace for their helpful discussion.

REFERENCES

Bratt, S. R. and T.C. Bache (1988), Locating Events with a Sparse Network of Regional Arrays, *Bull. Seism. Soc. Am.*, 78, 780-798.

Evernden, J. F. (1969), Precision of Epicenters Obtained by Small Numbers of World-Wide Stations, *Bull. Seism. Soc. Am.*, 59, 1365-1398.

Flinn, E. A. (1965), Confidence Regions and Error Determination for Seismic Event Location, *Reviews of Geophysics*, 3, 157-185.

Lehmann, E. L. (1983), Theory of Point Estimation, John Wiley & Sons, Inc., New York.

Pavlis, G. and J. Booker (1983), Progressive Multiple Event Location, *Bull. Seism. Soc. Am.*, 73, 1753-1777.

ADVANCED CONCEPTS FOR NUCLEAR EXPLOSION MONITORING APPLIED TO REGIONAL EVENTS IN THE ARCTIC REGION

Benjamin Kohl,[1] Hans Israelsson,[1] and Mark Fisk[2]

Science Applications International Corporation,[1] Mission Research Corporation[2]

Sponsored by Army Space and Missile Defense Command

Contract No. DASG60-03-C-0009

ABSTRACT

A number of innovative data processing algorithms and analysis techniques were developed to demonstrate improved capability for nuclear explosion monitoring. The focus was on techniques to address the challenges unique to the detection, location and characterization of events in the Arctic region using regional seismic array data. This research and development project was built upon the techniques and algorithms of others (e.g. as developed by NORSAR) and involved the development of new processing techniques and integration into a demonstration prototype system.

In support of the research and development activities, and as a test dataset to demonstrate improvements in capability, a comprehensive dataset of seismic recordings was assembled from historical regional events. The dataset included waveform segments from 40 different seismic stations recording historical nuclear and chemical explosions, earthquakes, and in-water explosions. In addition to the segmented datasets, 12 continuous days of waveform data, from key stations, were assembled into a fixed dataset that was used amongst other purposes, to assess noise characteristics and detection false alarm rates.

The above datasets were supplemented by theoretically scaling historical nuclear explosion waveform recordings down to levels allowing assessment of techniques applicable to low signal-to-noise ratios situations. The scaled waveforms were embedded in representative background noise and integrated into a database suitable for processing using both standard systems and new and improved algorithms. The embedded scaled events were used to conduct a detector fly-off experiment that systematically compared the performance of a new implementation of the adaptive beamforming (ABF) technique, the F-statistic detector, and a number of different recipes and configurations of the standard sta/lta detector running against conventional coherent and incoherent beams.

Detection comparison tests involving key regional seismic arrays (ARCES, SPITS) running against much broader and varied time windows, have the objective of better quantifying the performance of the ABF and F-stat detectors, and confirm that significant improvements in detection are achievable.

OBJECTIVES

Regional event detection, location and characterization have been areas of considerable interest and focus of nuclear explosion monitoring research and development for many years. This research and development project emphasized improved processing techniques. The scope of the project included signal detection of low SNR events, improved location particularly in the area of uncertainty error estimation and reference waveform utilization, and new techniques for event characterization.

RESEARCH ACCOMPLISHMENTS

In the following subsections we present many of the key results of the research. It should be noted that several key accomplishments were achieved and are summarized in bulleted form here, and are not described further in this paper.

- Developed a test and evaluation dataset of seismic recordings assembled from historical events recorded at the regional seismic arrays ARCES, FINES and SPITS
- Assembled 12 continuous days of waveform data from key stations into at fixed dataset
- Theoretically scaled historical nuclear explosion waveform recordings down to low SNR levels
- Developed a non-Gaussian error estimation and visualization tool
- Developed a scrolling-FK visualization tool to facilitate continuous review of array data in FK-space
- Applied phase-match filtering and spectral surface wave magnitude to enhance detection and reliable measurement of Ms for use with the Ms:mb discriminant.

The key research accomplishments are presented below.

Adaptive Beamforming and Detector Comparison Experiments

Noise at small regional arrays like ARCES is often partially coherent across the array and therefore not attenuated by conventional beamforming (CBF). At low frequencies (< 3Hz) coherent noise is often dominated by microseisms. Above 3 Hz, anthropogenic continuous narrow-band clutter is often from machinery and/or aircraft. Adaptive beamforming (ABF) updates a prediction error filter for each channel based on past noise to match the conventional beam directed at a specified slowness and azimuth. Consequently, ABF provides a distortionless response directed at the target beam while rejecting organized noise from other beams. ABF has the potential to remove coherent noise to reduce detection thresholds, increase bandwidth, increase signal-to-noise of weak onsets, and reduce false alarms.

ABF was tested against CBF using the prototype *Matlab* code to analyze noise windows (~1 hour) before and after small events recorded at ARCES and SPITS. Figure 1 compares the ABF and CBF Pn spectrograms recorded at ARCES. At the time, ARCES suffered from severe winter microseisms and anthropogenic clutter at several frequencies. Clutter from an aircraft is also seen. ABF attenuated microseisms below 3 Hz by 3-9 DB and narrow-band signals by 10-20 DB. A 3.1 Hz line associated to clutter was attenuated by ~30 DB.

ABF was coded in DFX (Detection and Feature eXtraction) and installed in a processing pipeline. The DFX installation of ABF is stable and adds only modest computational overhead compared to CBF. ABF output was configured for standard DFX STA/LTA detection. ABF was run for 24 hours on selected Pn and Sn beams optimized for signals at ARCES, NORES, FINES, and SPITS. Scaled explosion waveforms were embedded in the noise. STA/LTA detections from ABF and CBF output were compared. SNR were estimated from STA/LTA ratios of the embedded explosions.

The relative performance of four detectors was compared for one day, February 23, 2002. Scaled waveforms of a historical nuclear explosion were embedded in the data for three of the arrays, ARCES, FINES, and NORES. To assess detector performance at low SNRs, the waveforms were scaled and embedded at many different levels. The detector comparison or “fly-off” test included, as a baseline, the conventional detector with two different sets of recipes, one provided by NORSAR and employed in its operational processing (here labeled NORSAR) and another with a broad coverage of the Arctic region was composed for the test (labeled CBF below). The F-statistic detector

(FSTAT) was included in the "fly-off", although this detector is often considered less effective at regional than at teleseismic distances.

The embedded explosions were detected by all four detectors - NORSAR, CBF, ABF, and FSTAT - down to the same lowest scaled magnitude. The top panel in Figure 2 compares the SNR of the detecting beams of the NORSAR and the ABF detectors with CBF as a reference. The average SNR is generally higher for the ABF detector than for the two conventional beam sets (NORSAR & CBF). The SNR of the FSTAT cannot be directly compared with those of the other detectors as its STA/LTA ratio is based on an F-statistic and not a signal beam.

Some of the detections could be associated with known events in the IDC REB and other bulletins. The ABF detector triggered on a clearly larger number of associated detections (REB data not available for NORES and SPITS association) than had other detectors. Unassociated detections are an indication of the false alarm rate. Unassociated detections vs. threshold vary among the detectors and from station to station, but the FSTAT detector generally had the smallest number of unassociated detections (bottom panel of Figure 2). The modest number of unassociated detections (per day) suggests that it is possible to lower the detection threshold in some instances by selective threshold tuning.

All detectors detected scaled explosions down to the same low-magnitude levels. The ABF provided higher SNR and association rates than the conventional detectors with similar unassociated detection rates. The FSTAT detector provided robust detection capability with the lowest unassociated rates among the detectors. Results suggest that using an F-statistic detector on the ABF output may provide both higher SNRs and lower false alarm rates. The "fly-off" test demonstrated the usefulness of scaled signals for detector assessment. The ABF and FSTAT show promise in lowering thresholds and lower false alarm rates and warrants further investigation.

Elevation Corrections and Data Resampling

The large elevation difference among elements of the SPITS array (0.140 km) compared with the horizontal aperture of the array (0.9 km) limits the performance of processing based on a horizontal planar array. Time delays used in beamforming only approximate actual time delays at array elements, resulting in reduced SNR and estimates of slowness and azimuth, based on FK analysis that may be biased.

To account for elevation differences and improve spatial coherence, 3D FK processing and beamforming were implemented in DFX. The vertical slowness for a given beam is defined from the horizontal slowness of the beam and the local P and S wave velocity at the array. A local average P velocity of 4.6 km/s for the SPITS array was estimated from teleseismic P waves recorded from about 100 broadly-distributed large events. The estimated value is in close agreement with estimates based on local data (Kremenetskaya et. al., 2001). The estimate was obtained by fitting values of horizontal slowness, azimuth, and vertical slowness of a plane wave across the array to pairs of time delays among array elements obtained from cross-correlation analysis.

Signals of small events recorded at the arrays SPITS and ARCES often contain significant energy above 10 Hz. Resampling of waveform data to a higher sampling rate further improves the alignment of element traces for the array beam. Improvements in SNR with resampling and elevation corrections are illustrated in Figure 3.

Elevation correction and data resampling of SPITS waveform data reduce bias in azimuth and slowness estimates. Elevation corrections and data resampling can also provide some SNR improvement. A consistent improvement was obtained for small events recorded at ARCES and SPITS. A 5 dB improvement was demonstrated for high frequency signals recorded at SPITS.

Phase Dependent Measurement Errors

In standard practice, location uncertainties are represented by the 90% coverage ellipse, which assumes that the data uncertainties are known *a priori* (IDC Doc. 5.2.1, 1998). If the *a priori* errors are independent and Gaussian, the confidence coefficient (or coverage parameter) follows a c^2-distribution with 2 degrees of freedom. The *a priori* errors are further divided into measurement and model errors, the former representing reading errors, the latter the uncertainties in the predicted travel-times. The actual coverage of the 90% error ellipse (i.e. the percent of true locations covered by the error ellipse 90% of the time) clearly depends on the reliability of the *a priori* error

estimates. Location calibration deals primarily with improved travel-time predictions and model errors. The primary focus of this study was the better estimation of measurement errors.

Currently, measurement errors are calculated from the signal-to-noise ratio (SNR) of the detection (Israelsson et. al., 1997). The linear relationship was derived from teleseismic P phases, but applied to all other phases. Therefore the measurement errors can be under-estimated for regional and secondary phases. While retaining the linear dependency on the SNR we have now derived coefficients for teleseismic and regional P, S, and Lg phases using REB readings for some 200 GT0-5 mining events and explosions in Fennoscandia and the Eastern European platform (Bondár et. al. 2002).

To test the phase-dependent measurement errors, we relocated the ground-truth events first using the current IDC error model, then the new measurement errors. In both cases IASPEI travel-time tables and model errors were applied. Finally, the events were located using the new measurement errors and path-dependent travel-time corrections with their corresponding model errors.

In conclusion, the enlarged phase-dependent measurement errors result in larger but more realistic error ellipses thus leading to significant improvements in coverage statistics. The actual coverage of the 90% error ellipse increased from 65% to 75%, when using the IASPEI velocity model, indicating that the IASPEI model errors are still underestimated. Phase-dependent measurement errors combined with calibrated travel-time predictions and model errors generate error ellipses close to 90% actual coverage.

Ground-Truth Through Use of Satellite Imagery and Terrain Elevation Data

In the development of the test and evaluation datasets, a number of published sources (Izdat, 2000, Richards, 2000 amongst others) were reviewed in order to select ground-truth events for testing and evaluating event location techniques. Given that there were inconsistencies between the published sources (e.g. the Oct. 24, 1990 nuclear explosion) and the importance of GT locations, we reexamined the waveform data for the historical nuclear explosions along with satellite imagery and terrain elevation data to assess GT attributions.

Standard imagery analysis techniques were applied to a series of 1m resolution commercial satellite images taken in 2000 to determine all known man-made features on the images, with a particular emphasis on identifying adits. Based on estimated yields, consequent overburden requirements and possible adit locations we were able to map out those portions of the test site that could realistically contain the largest of the nuclear explosions recorded since 1984. Figure 4 shows a map of the Matochkin Shar test site area, showing that the generally accepted location (Richards, 2000) for the Oct. 24, 1990 event appears to be slightly mislocated. A relocation of the event using a combined waveform cross-correlation, master event location technique also points to the event being about 1-2 km farther west than described by Richards, 2000.

Cepstral Analysis of Seismic Recordings of In-water Events

In-water explosions that do not breach the surface produce bubble pulses. In-water and shallow underground events can also produce water column reverberations. Both effects cause interference of the signals that are observed as modulations (or scalloping) in spectra and peaks in cepstra at corresponding delay times. Because these are near source effects, scalloping is generally present in all seismic phases at stations with adequate SNR over a sufficient bandwidth.

Spectral analysis is often advantageous in cases of limited bandwidth, which can obscure valid cepstral peaks and introduce false alarms. However, it is not clear how to quantify the significance of spectral scalloping. Thus, we use cepstral peak measurements because their significance can be quantified (Bonner et. al. 2000), and we apply a stringent significance level and physical constraints, based on local bathymetry and source yield, to eliminate spurious peaks.

The significance of a cepstral peak at a delay time, *td*, is quantified by defining $F2,2(N-1)(td) = Nx(td)2/var(td)$, where N is the number of cepstra computed for each seismic phase, $x(td)$ and $var(td)$ are the mean and variance of the cepstra at td. Under the hypothesis that the peak is zero, this quantity has an F-distribution with 2 and $2(N-1)$ degrees of freedom. This hypothesis is rejected if $F2,2(N-1)(td)$ is greater that the percentile of the F-distribution at a

given significance level, which we set at 0.005. Figure 5 shows an example of this analysis for the main *Kursk* explosion on 12 August 2000.

Physical interpretation of cepstra is modeled by exponential time functions for the primary pressure wave and bubble pulses, convolved with ocean surface and bottom reflections for a given water depth, event depth, and yield (Baumgardt and Der, 1998). The cepstrum of this theoretical time function is computed and peaks in the model and data cepstra are compared to estimate the source depth and yield that provide the best fit (Figure 5). For the Kursk explosion, the estimated source depth and yield are approximately 104 meters and 5.5 tons, respectively.

Regional 3-C Pn/Sn Spectral Ratio Discriminant

Pn/Sn amplitude ratios are corrected for attenuation that is modeled by: log(Pn/Sn) = $a + bD$, where D is the epicentral distance (in degrees), and the coefficients a and b are estimated by combining earthquake data from ARCES, KEV, and NORES. Estimated coefficients for Pn/Sn(6-8 Hz) are a = -0.890 and b = 0.056. Similar distance dependence is estimated using explosion data, supporting applicability of the attenuation corrections for both explosions and earthquakes.

Spatial variations of Pn/Sn are treated by kriging (Bottone et. al, 2002) station-averaged, distance-corrected log(Pn/Sn) data for earthquakes, assuming a constant offset between explosions and earthquakes. Kriging station-averaged data, versus individual station data, provides slightly more robust corrections by reducing random variations. Kriging requires a correlation length and residual and calibration variances as input parameters. The residual variance is estimated from a cluster of 20 earthquakes near Steigen, Norway to be 0.108. The total variance of the station-averaged, distance-corrected log(Pn/Sn) data for the regional earthquakes is 0.142. The difference of these variances yields an estimated calibration variance of 0.092. For kriging, the residual and calibration variances are set conservatively at 0.11. A correlation length of 5 degrees is used, typical of estimates in previous studies (Bottone et. al, 2002). The leave-one-out procedure is used to compute the corrected data values.

Figure 6 shows the correction and uncertainty grids and corrected data values. All of the markers for the explosions are black circles, corresponding to values above the local earthquake mean. The correction grid exhibits systematic spatial variations, which range from about -0.10 to +0.09. The grid of the posterior calibration standard deviation approaches the prior calibration standard deviation of 0.11 far from data, and is reduced to about 0.035 near the clusters of events in the Barents Sea south of Spitzbergen and near Steigen, Norway.

The Pn/Sn criteria treat the fact that each event has a different calibration uncertainty associated with the kriged corrections. Let R denote station-averaged, distance-corrected log (Pn/Sn(6-8 Hz)]. An event is rejected as an earthquake if:

$$\frac{R - \mu_{eq}(x_0)}{\sqrt{\sigma^2_{r,eq} + \tilde{\sigma}^2_{c,eq}(x_0)}} > z_a,$$

where $\mu_{eq}(x_0)$ is the posterior mean (kriged correction term) and the denominator includes the residual and posterior calibration variances, estimated at the location, x_0, of the event being tested. Similarly, an event is rejected as an explosion if:

$$\frac{R - \mu_{eq}(x_0) - \Delta\mu}{\sqrt{\sigma^2_{r,ex} + \tilde{\sigma}^2_{c,eq}(x_0)}} < -z_a,$$

where $\Delta\mu = 0.64$ is the mean difference of $R - \mu_{eq}(x_0)$ for explosions and earthquakes and $\sigma_{r,ex}$ is the residual standard deviation for explosions, estimated from nuclear explosion data to be 0.11. In the preceding criteria, z_a is the (1-a)-percentile of the standard normal distribution with zero mean and unit variance. For 0.005 significance level, z_a = 2.576.

REFERENCES

Baumgardt, D. and Z. Der, "Identification of presumed underwater chemical explosions using land-based regional arrays," *Bull. Seism. Soc. Am.*, **88**, 581-595, 1998.

Bondár, I., K. McLaughlin, X. Yang, J. Bhattacharyya, "Assessing location improvements without ground truth data," *Seism. Res. Let.*, **73**, 227, 2002.

Bondár, I., S. Myers, R. Engdahl, E. Bergman, "Epicenter accuracy based on seismic network criteria", submitted to *Geophys. J. Int.*, 2002.

Bonner, J., D. Reiter, and B. Shumway, "Application of a Cepstral F-statistic for Improved Depth Estimation", *22nd Annual DoD/DOE Seismic Research Symposium Proceedings*, v. 2, 02-07, 2000.

Bottone, S., M. Fisk and G. McCartor (2002). Regional seismic event characterization using a Bayesian formulation of simple kriging, *Bull. Seism. Soc. Am*., **92**, 2277-2296.

Engdahl, E.R., R. van der Hilst, R. Buland, "Global teleseismic earthquake relocation with improved travel times and procedures for depth determination," *Bull. Seism. Soc. Am.*, **88**, 724-743, 1998.

Grant, L., J. Coyne, and F. Ryall, "CSS Ground-Truth Database: Version 1 Handbook," Center for Seismic Studies Technical Report, C93/05, 1993.

Hanson, J., R. Bowman, and G. Beall, "An Advanced Concept Demonstration for Monitoring the Indian Ocean," *24th Annual DoD/DOE Seismic Research Review Proceedings*, 04-02, 2002.

IDC Processing of Seismic, Hydroacoustic and Infrasonic Data, *IDC Documentation 5.2.1*., 1998.

Israelsson, H., G. Beall, H. Swanger, Independent modeling of time measurement and model errors, *Center for Monitoring Research*, CCB-PRO-97/24, 1997.

Izdat, USSR Nuclear tests. Novaya Zemlya Test Site: Ensuring general and radiation safety (in Russian), Eds. N. P. Voloshin, G. E. Zolotukhin, G. A. Krasilov, V. A. Logachev, A. M. Matushenko, G. A. Mikhailikhina, A. K. Tchernyshev, and O. E. Shamov. Izdat publishing office, Moscow, 2000

Kremenetskaya, E, S. Baranov, Y. Filatov, V.E. Asming, F. Ringdal, "Study of seismic activity near Barenetsburg mine," in NORSAR Scientific Technical Report No.1-2001, Kjeller, July, 2001.

Kremenetskaya, E., Private communication, April 2000.

Mueller, R. A., and J. R. Murphy, "Seismic characteristics of underground nuclear detonations. Part I: Seismic Spectrum Scaling," *Bull. Seism. Soc. Am*., **61**, 1675-1692, 1971.

Nicholson, T. M. Sambridge, O. Gudmundsson, "On entropy and clustering in earthquake hypocentre distribution," *Geophys. J. Int*, **142**, 37-51, 2000.

NORSAR, Waveforms from selected events in the European Arctic, DE-AC04-99AL66001, 1999.

Richards, P. G., Accurate estimates of the absolute location of underground nuclear tests at the northern Novaya Zemlya test Site, Second workshop in IMS location Calibration, Oslo, 2000

Ringdal, F., and J. Fyen, "RMS Lg Analysis of Novaya Zemlya Explosion Recordings," in NORSAR Semiannual Technical Summary, 1 October 90 – 31 March 1991, NORSAR Scientific Report 2-90/91, 53-67, 1991.

Ringdal, F., Study of low-magnitude seismic events near the Novaya Zemlya nuclear test site, *Bull. Seismol. Soc. Am.*, **87**, 1563-1575, 1997.

Stevens, J. L. and J. R. Murphy, "Yield Estimation from surface wave amplitudes," *Pure and Applied Geophysics*, **158**, 2227-2251, 2001.

Sultanov, D. D., J. R. Murphy, and Kh. D. Rubinstein, "A seismic source summary for Soviet peaceful nuclear explosions," *Bull. Seism. Soc. Am*., **89**, 640-647,1999.

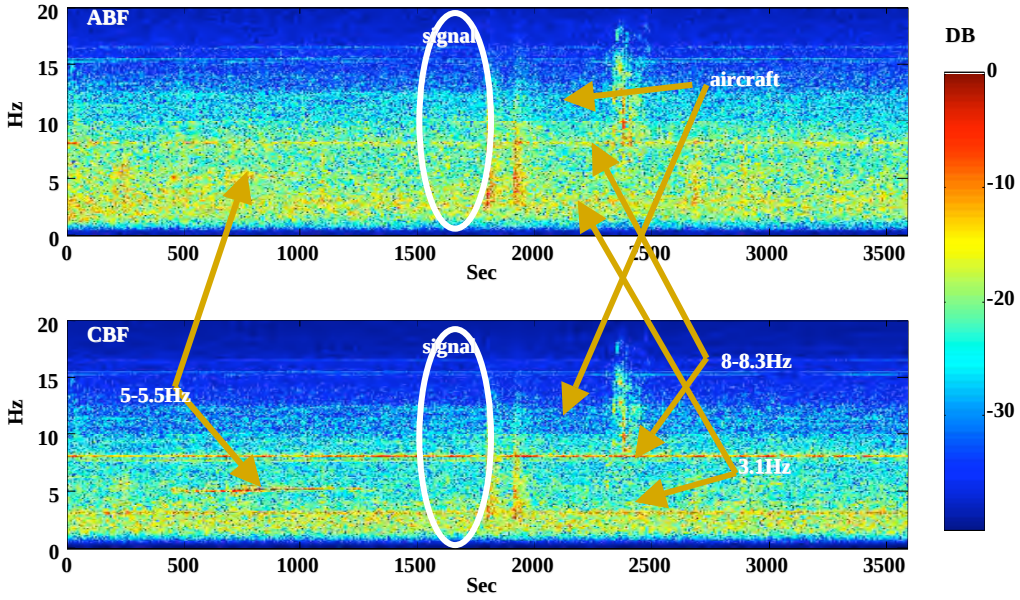


Figure 1: Pn beam ABF and CBF spectrograms for the 1996/01/13 event recorded at ARCES (DB w.r.t. max). Low frequency microseisms (<3 Hz), narrowband clutter (at 3.1, 5-5.5 and 8-8.3 Hz), and aircraft noise are attenuated, improving low frequency signal bandwidth and initial Pn arrival SNR.

SNR Ratio for Embedded Signals (dB)		
	NORSAR/CBF	ABF/CBF
ARCES	1.0+/-0.5	3.4+/-1.7
FINES	1.7+/-0.3	5.5+/-0.2
NORES	0.7+/-0.5	3.9+/-0.7

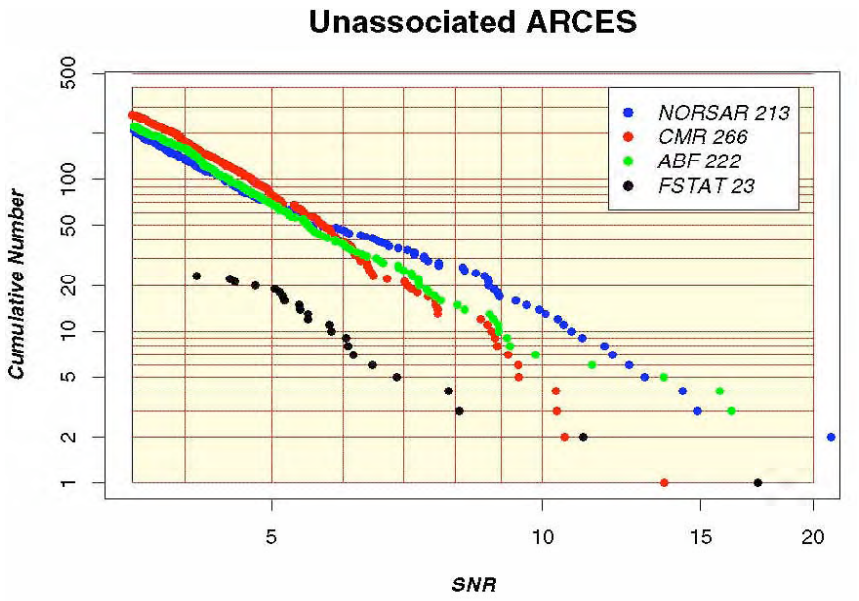


Figure 2: SNR and false alarm rate results of detector comparison experiment. The top panel shows relative SNR gain achieved by the ABF detector. The bottom panel shows the cumulative number of unassociated detections at the ARCES array versus SNR = STA/LTA ratio or Fstat. ABF and conventional beams show similar false alarms per day.

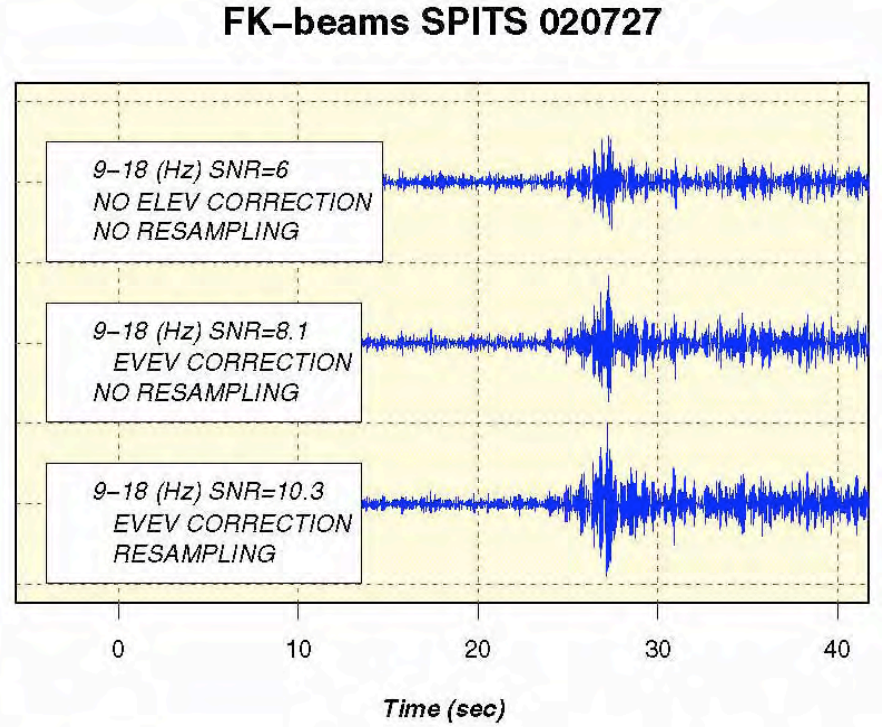


Figure 3: SNR of FK-beams improve by almost a factor of 2 at SPITS as a result of elevation corrections and resampling for small magnitude event (July 27, 2002).

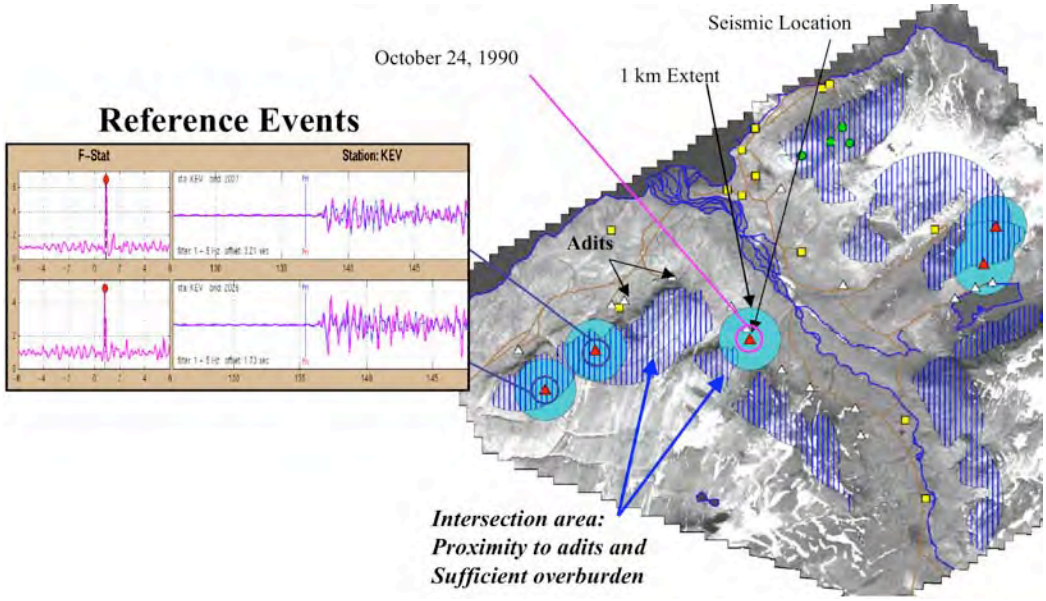


Figure 4: Map of the Matochkin Shar test site area showing visible adits (white triangles), other man-made artifacts (yellow squares) and seismic locations (red triangles) for the five largest nuclear explosions since 1984. The hatched area represents all those areas with at least 200 meter overburden and within 2 km of an adit, or with 3 km of any other visible man-made artifact. The fact that the seismic location of the Oct. 24, 1990 event falls outside the hatched area brings into question the designation of this event as GT1.

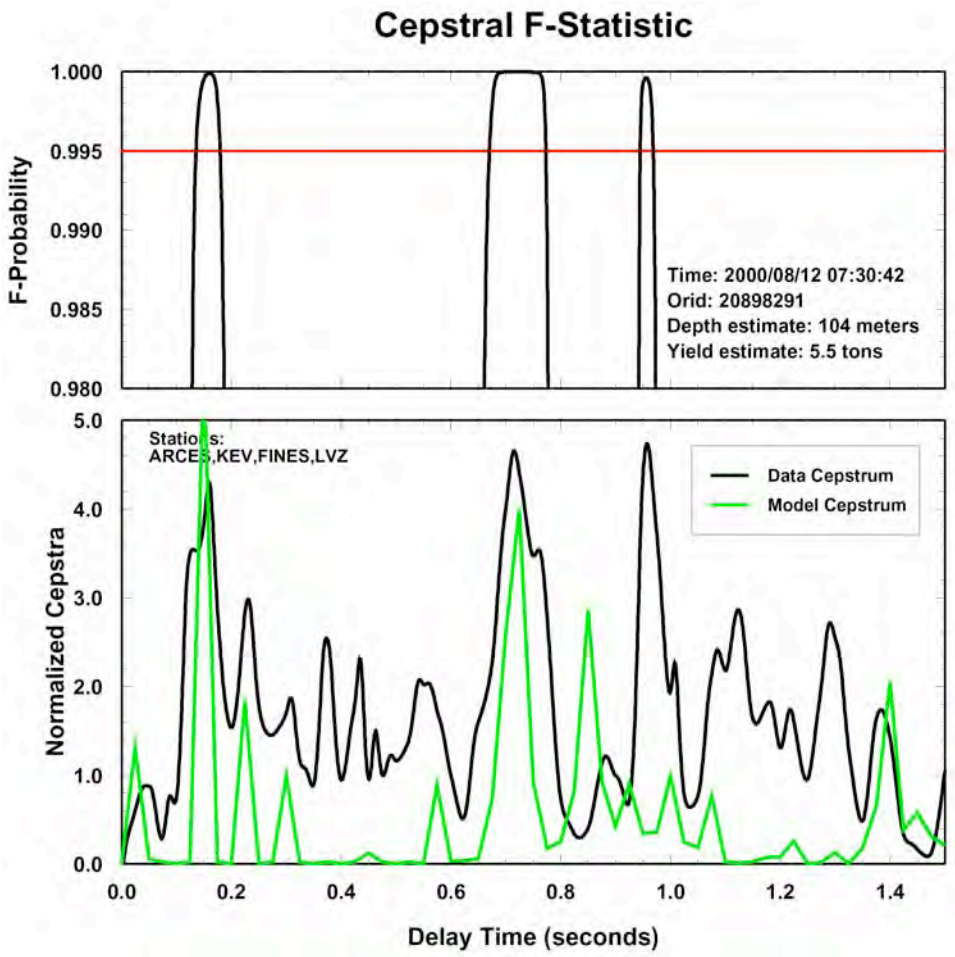


Figure 5: The lower frame shows the combined data cepstrum, using cepstra of regional phases at ARCES, KEV, FINES and LVZ for the August 12, 2000 Kursk explosion (black curve) and model cepstrum (green curve) that fits the main peaks of the data cepstrum. The upper frame shows the F-probability trace and threshold at a 0.005 significance level.

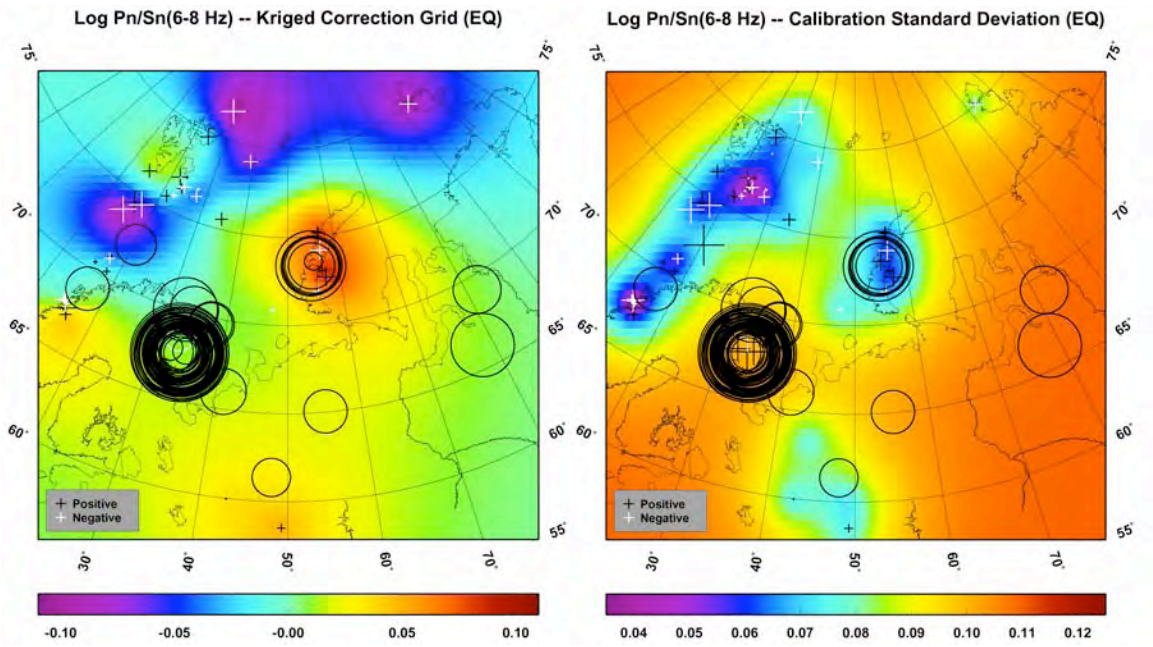


Figure 6: Correction (lower left) and uncertainty (lower right) grids for station-averaged, distance-corrected log(Pn/Sn) in the 6-8 Hz band using earthquake data. Circles and crosses represent explosions and earthquakes, respectively, with the size of the marker proportional to the corrected log (Pn/Sn) value.

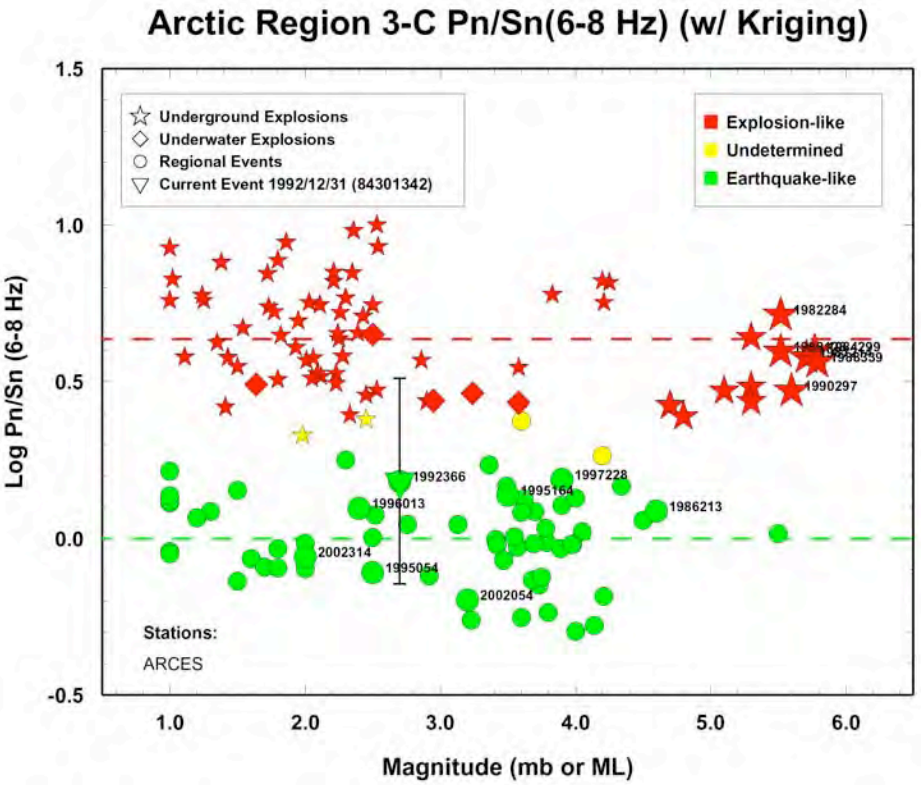


Figure 7: Station-averaged, distance-corrected log[Pn/Sn(6-8 Hz)]. Marker colors indicate the classification results.

DEVELOPMENT OF SSLOC3D: A TOOL FOR SINGLE-STATION LOCATIONS OF SMALL SEISMIC EVENTS USING REGIONAL 3D VELOCITY MODELS

Mark Leidig,[1] Delaine T. Reiter,[1] Jessie L. Bonner,[1] Shelly Johnson,[1] Ileana Tibuleac,[1] Arthur J. Rodgers,[2] and Heather Hooper[1]

Weston Geophysical Corporation,[1] Lawrence Livermore National Laboratory[2]

Sponsored by National Nuclear Security Administration
Office of Nonproliferation Research and Engineering
Office of Defense Nuclear Nonproliferation

Contract No. DE-FG02-02ER83572[1] and W-7405-ENG-48[2]

ABSTRACT

Regional monitoring of low-yield nuclear explosions requires detection, location, and discrimination of small seismic events. Locating accurate epicenters for these small-to-intermediate magnitude ($2.5 < m_b < 4.5$) seismic events with traditional network location techniques can be problematic because only one or a few stations may record the event. To facilitate the monitoring of low-yield nuclear explosions, we developed SSLOC3D, a prototype system for determining single three-component (3C) station epicenter locations using epicentral distance estimates and back-azimuth corrections determined from 3D velocity models. Software components developed for SSLOC3D include a polarization analysis tool for 3C back-azimuth estimation, *Lg* phase picking tools to improve analyst picks, travel-time grids for *P*-, *S*-, and *Lg*-waves, station-dependent back-azimuth corrections, and calibrated error analyses used to generate confidence ellipses. SSLOC3D compares observed travel time differences for secondary and primary phases (e.g., *Lg* - *P*) with modeled travel time differences generated from regional and global velocity models. The models tested include the 1D-IASP91 global model, the WINPAK3D regional model (developed by Weston Geophysical), and the CRUST2.0 3D global model. Currently, we have developed travel time grids, back-azimuth corrections, and error analyses for stations NIL (Nilore, Pakistan) and HYB (Hyderabad, India). In the future, we plan to calibrate more stations and incorporate arrays, which have been shown to provide more reliable estimates of back-azimuth by using techniques such as beam-forming and cross-correlation.

We used SSLOC3D to determine single-station locations for 39 events in southern Asia classified as GT15 or better. The events include 38 earthquakes occurring in four separate clusters and a nuclear explosion at the Pokhran Test Site, India. For single-station locations performed using observed regional *S-P* travel times, the use of the CRUST2.0 model to generate travel times for both phases resulted in an average of 14 km less distance error than IASP91. The results for *Lg-P* show a 5 km improvement in the distance error when using 3D models in contrast to the 1D-IASP91 model. For the nuclear explosion and two of the four clusters, SSLOC3D locations have approximately 20 km or less average total mislocation and compare favorably with traditional network locations. The remaining two clusters have large back-azimuth errors that cause larger total mislocations. Back-azimuth error is the largest source of total mislocation in all four clusters, and results show that the application of 3D model-based back-azimuth corrections was only partially successful at improving these locations. We anticipate reducing the back-azimuth errors in the future with the use of arrays. The results indicate the need for additional development of phase modeling tools such as 3D modeling of *Lg* velocities. Our findings also suggest that empirical calibrations of both travel-times and back-azimuths can further improve the SSLOC3D methodology.

OBJECTIVE

In order to monitor low-yield nuclear explosions at regional distances, the detection, location, and discrimination of small seismic events recorded only at regional distance seismic stations or arrays is required. Prior to classifying a small, regionally recorded seismic event as a nuclear explosion, the event must be located and the spectral characteristics of the signal must be evaluated for discrimination purposes. Location of the event on or near a known nuclear test facility plays an important role in determining the processing steps used to discriminate the event. Thus, the accurate location of small seismic events in both space and time plays a vital role in nuclear monitoring efforts.

For global network locations, such as those computed by the United States National Data Center (USNDC), the United States Geological Survey (USGS) National Earthquake Information Center (NEIC), and the International Data Center (IDC), as well as the International Seismological Centre (ISC), the preferred solution is to have multiple observations (at numerous seismic stations around the globe) of relatively few of these recorded phases (i.e., only the *P* waves). In regions with relatively few seismic stations and small-to-intermediate ($2.5 < m_b < 4.5$) magnitude events, the traditional location methods cannot always satisfy the location accuracy requirements for monitoring because only one or a few stations may record the event. We addressed this problem by developing and testing a model-based prototype single-station location software system, known as SSLOC3D (**S**ingle-**S**tation **LOC**ations determined from **3D** velocity models), for achieving accurate epicentral estimates based on observations made at single seismic stations or arrays. This system is an innovative and practical approach to determining locations for small-to-intermediate magnitude seismic events using three-component (3C) single-station data.

RESEARCH ACCOMPLISHED

Introduction

To locate an event with a single seismic station or array, the slowness vector for the various seismic phases recorded (e.g., *Pn*, *Pg*) must be estimated. For a single three-component (3C) station, the horizontal projection of the slowness vector is the back-azimuth, and the vertical projection gives the angle of incidence that can be converted to an apparent phase velocity if a crustal velocity near the station is known. In contrast to typical location routines for moderately sized events that use a single scalar observable for one component of ground motion, this method incorporates the important information contained on all three components of the ground motion. Our method consists of complete three-dimensional (3D) ray tracing through regional 3D velocity models to determine off-azimuth propagation and travel time differences between secondary phases, such as *Lg*, *Sn*, and *Rg*, and primary phases, including *Pn* and *Pg*. These predicted arrival times are compared with travel time differences observed on three-component seismic stations or arrays in order to determine the epicentral distance. Back-azimuth estimates for the primary and secondary phases are determined with polarization techniques (3C) or waveform crosscorrelation methods (arrays) and corrected for off-azimuth propagation determined by 3D ray tracing and empirical calibration. Using the back-azimuth and distance estimates, an epicentral location is estimated using standard geometrical formulae and appropriate error distributions are used to define confidence regions around the epicenter. A schematic of the system is presented in Figure 1, which shows the software input requirements from two components. The first component consists of travel-time grids and azimuth corrections derived from 3D velocity models. A database of observed data, consisting of regional phase picks (e.g., *Lg*, *Sn*, and *Pn*) and back-azimuth estimates form the second component of the system. The two components are then combined to determine a single-station location and an error ellipse estimate for each event in the database. To develop the prototype SSLOC3D system, we:

- Compiled a waveform database of regional seismic events in southern Asia recorded at NIL (Nilore, Pakistan) and HYB (Hyderabad, India) with varying ground truth classifications.
- Examined different methodologies for phase picking and back-azimuth estimation using 3C stations.
- Tested various 2D and 3D ray tracing methods of estimating regional phase (*P*, *S*, and *Lg*) travel times.
- Calculated theoretical back-azimuth corrections.

- Developed a 3D seismic velocity model-based single-station location algorithm.
- Completed testing of the algorithm using various 3D and 1D velocity models and events in our ground truth database.

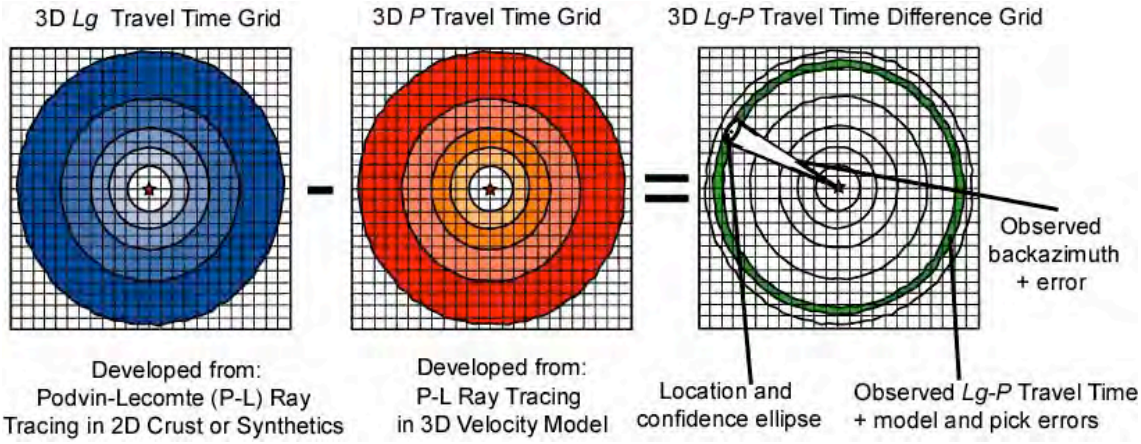


Figure 1. Schematic showing the processing components for locations formed with *Lg* and *P* phases using SSLOC3D. The procedure can also be modified with 3D travel time grids for *S* replacing the *Lg* results.

Database Development

To develop and test our location software we compiled a database of events with the most accurate ground truth locations for our study region of southern Asia, downloaded regional waveforms for these events at the 3C stations NIL and HYB, and picked the regional phases observed on the seismograms. The database consists of 85 events with location accuracy characterized by GT1 (4 events), GT5 (31), GT10 (7), GT15 (17), and GT25 (23). The sources for the catalog data included the GROUP2 reference event list (REL) (McLaughlin *et al.*, 2002), the EHB bulletin (Engdahl *et al.*, 1998), and the Center for Monitoring Research's Reference Event Data Base (CMR REDB; Yang *et al.*, 2000). Data from NIL and HYB were downloaded from the Incorporated Research Institutions in Seismology (IRIS) Data Management Center (DMC), and the locations of the stations and events are shown in Figure 2. Figure 2 also marks the locations of the Koyna, Bhuj, Jiashi, and Chamoli earthquake clusters, which together with the Indian nuclear test at the Pokhran Test Site (PTS) of 11 May 1998 were all GT15 accuracy or better and the focus of the study.

3C Station Phase Picking and Back-azimuth Estimation

The next stage consisted of an analyst picking all regional phases observed on each waveform and creating an arrival database that includes *Pn*, *Pg*, *Sn*, and *Lg* onset times. While onset determination for *Pn*, *Pg*, and *Sn* is relatively straightforward for our study region of southern Asia, the onset of *Lg* varies from simple, impulsive arrivals in the shield regions of India to complex, emergent arrivals in tectonic regions such as the Himalayas. In order to verify the accuracy of the analyst *Lg* picks, we extended the Jurkevics (1988) phase detection method, which calculates the ratio of the radial component to the vertical and transverse components, to include spectral analyses. Abrupt changes in these ratios, together with changes in the frequency content of the signal, are often associated with *Lg* arrivals (Figure 3). We also verified the analyst *Lg* picks using the WAVELET detector of Tibuleac *et al.* (2003). The analyst results were typically within 2 seconds of the picks suggested from the Jurkevics (1988) and WAVELET methods. In a couple cases, the two techniques helped highlight an analyst error resulting in a re-picking of the phase.

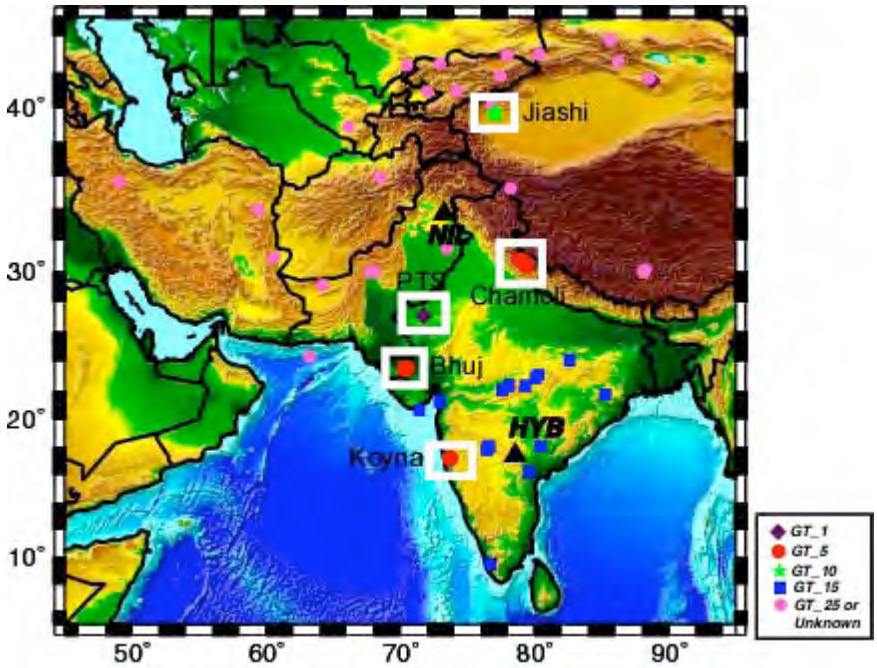


Figure 2. Events and stations (triangles) of the database used for SSLOC3D development.

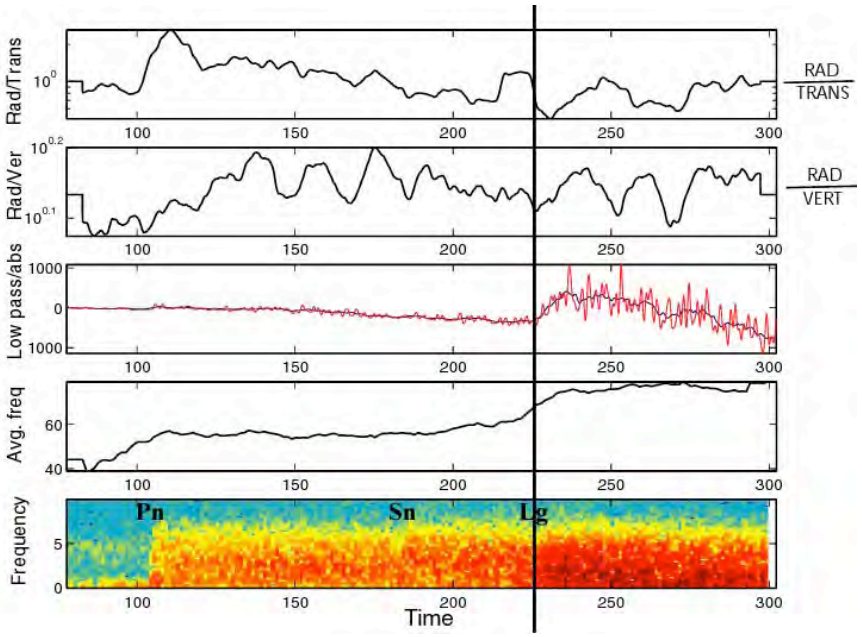


Figure 3. SSLOC3D technique for picking *Lg* arrivals using a modified version of the Jurkevics (1988) method. Jurkevics noted that the *Lg* arrival is often associated with abrupt changes in the ratio of the radial component to the vertical and transverse components. We note similar results when applying the technique to data recorded at HYB as shown in the upper two subplots. The final subplot shows the change in frequency content associated with the *Lg* arrival, the solid vertical line at 226 seconds in the plot.

We determine the back-azimuth of the *P*-wave arrival by using a polarization technique developed by Jurkevics (1988). Using this technique, we developed a polarization module for SSLOC3D that calculates the back-azimuth and rectilinearity for overlapping windows of three-component seismic data. An example of the analysis is shown in Figure 4. We search for the largest value of the rectilinearity within the *P*-wave

arrival window, and we determine the mean back-azimuth in a one-half second window following the time of the maximum rectilinearity. When compared to another method of three-component back-azimuth estimation, the frequency-wave number method as coded in MatSeis (Young, 1997), we find the polarization technique is computationally faster and offers more accurate back-azimuths for the events from our study region with location accuracy better than GT15. Thus, the polarization technique was the preferred method to estimate back-azimuths for all events in our database.

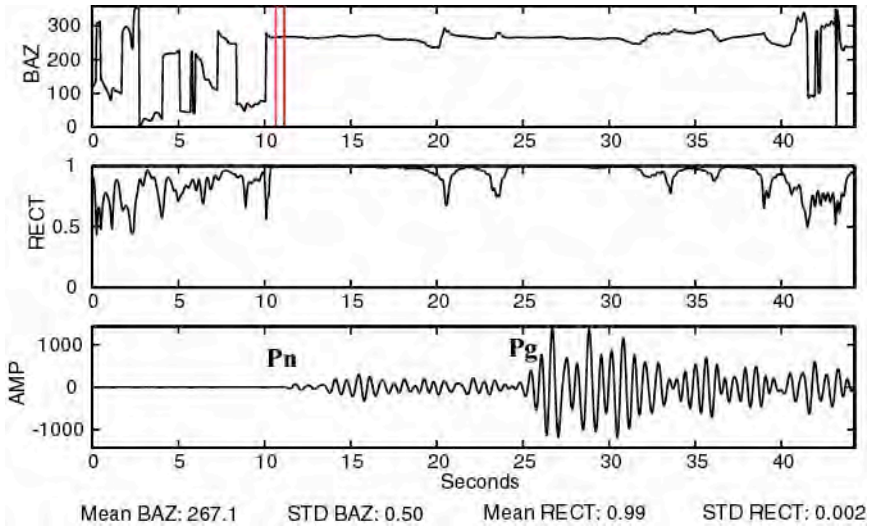


Figure 4. SSLOC3D polarization analysis for an event recorded at HYB. The upper subplot presents the back-azimuth calculated while the middle subplot displays the rectilinearity. The *Pn* and *Pg* arrivals are shown in the bottom subplot. The mean back-azimuth was determined to be 267.1° with one standard deviation equal to 0.5°.

Regional Phase Travel Time Estimation

We calculated theoretical travel times to a single station in complex 3D models for the regional phases *P*, *S*, and *Lg*. The resulting 3D travel time grids are differenced (e.g., *Lg*-*P*) and compared to observational data using SSLOC3D. We were required to determine the appropriate 3D velocity models, parameterize these models, and perform the ray tracing for the phases.

WINPAK3D. Weston Geophysical Corporation compiled a detailed initial 3D velocity model through synthesis of pertinent data from approximately 69 published references on the velocity structure, geology, and tectonics throughout the region of southern Asia (Reiter *et al.*, 2001). The model is referenced as WINPAK3D for its coverage of INdia and PAKistan, however the extents also include Afghanistan and sections of Iran. The references utilized to develop the model included data such as seismic refraction and reflection studies, interpretations of gravity data, surface wave studies, and receiver function analyses. Reiter *et al.* (2001) completed a fully 3D tomographic update of the *P*-wave model and subsequently converted the model into an *S*-wave model using a depth-dependent Poisson's ratio equivalent to that in the IASP91 (Kennett and Engdahl, 1991) model. The fact that the *P*-wave velocity model was developed using GT data from southern Asia (Reiter *et al.*, 2001) was an advantage for using WINPAK3D. However, we also examined the performance of a global model, CRUST2.0.

CRUST2.0. The global 3D model chosen for evaluation, CRUST2.0, was developed by Bassin *et al.* (2000) from an extension of CRUST5.1 (Mooney *et al.*, 1998). CRUST2.0 is a prototype 2-degree crustal model developed using large databases of crustal and sedimentary basin structure, compressional wave and shear wave velocities, and densities determined from field and laboratory studies. Rigorous statistical methods were used to predict crustal structure in regions without data. In addition to global coverage, the advantages to using this model are that it has more detailed crustal structure than WINPAK3D; however, the disadvantage is that the mantle lid velocities are not updated by a tomographic inversion using data in our study region.

Body Wave Travel Time Grid Calculation. To determine the values of the travel time grid for *P*-waves and *S*-waves, we applied the Podvin-Lecomte (P-L) finite-difference travel time algorithm (Lomax, 1999; Podvin and Lecomte, 1991) to the earth models using the location of the station as the source in the calculation. The Podvin-Lecomte method solves the eikonal equation in a 3D medium using a finite-difference approximation. It can accurately model different propagation modes, such as transmitted and diffracted body waves or head waves. It estimates accurate travel times in the presence of severe, arbitrarily shaped velocity contrasts, as those occurring across the Moho discontinuity. This is an improvement over similar methods (Vidale, 1988; Moser, 1991), which can encounter serious difficulties in the presence of sharp, first-order velocity contrasts. The model is discretized on an equally spaced grid composed of constant velocity cells. Multiple arrivals (transmitted, diffracted, and head waves) are calculated at each grid node and the first arrival time is chosen. This computation produces a complete grid of travel times considerably faster than two-point ray tracing, while allowing the sources and receivers to be located anywhere within the model. The P-L computations are then output in the form of a 3D travel time grid for the *P*- and *S*-phases at the station of interest.

Lg Travel Time Grid Calculation. Before theoretical *Lg* travel-times could be estimated, we first examined the published definitions of this important phase. The phase was first described by Press and Ewing (1952) as a transverse impulsive phase traveling across the North American continent with average crustal *S*-wave velocities. Since then, *Lg* has been described as refracted and reflected *S*-waves within the crust (Bouchon, 1982; Olsen and Braile, 1983) as well as higher-mode surface wave propagation (Oliver and Ewing, 1957; Kovach and Anderson, 1964). We have used these definitions to determine the theoretical travel-times for the phase in southern Asia, and the results of using each method in SSLOC3D will be shown in the location results section.

Masked *S*-Wave Models. We have examined the effects of constraining the *S*-wave model velocities to small values at depths below the lower and mid-crustal levels. We refer to this concept as "masking" the *S*-wave model. For this method, we calculated travel-times through the masked models using the P-L ray tracing technique. This concept tests the hypothesis that *Lg* travel-times can be modeled as *S*-waves refracted within the crust at different depths.

Crustal-Averaged 2D *Lg* Grids. Another technique we developed for modeling *Lg* travel-times involved computing the average of the *S*-wave velocities in the upper 30 km of the crust for the WINPAK3D and CRUST2.0 *S*-wave models. We chose 30 km because displacement eigenfunctions for 1 Hz higher-mode Rayleigh-waves are normally confined to the upper 30 km of crust. For regions where the crustal thickness was less than 30 km, the averaging was completed for the layers above the Moho. The averaged velocity at each model node was then used as the input to a 2D extension of the P-L ray tracing method, and the *Lg* travel times were estimated. Figure 5 shows the results for this methodology at station NIL.

Constant *Lg* Velocities. We generated modal summation synthetics (Herrmann, 2002) for the first five (5) Rayleigh-wave higher modes using the WINPAK3D velocity profile beneath each of the stations NIL and HYB. The results are shown in Figure 6. After fitting a straight line to the higher-mode onsets, we determined *Lg* velocities of approximately 3.5 km/sec and 3.6 km/sec for NIL and HYB, respectively. We used these constant velocities to generate the *Lg* travel time grids at NIL and HYB. This modeling tests the assumption that *Lg* can be modeled as higher-mode Rayleigh-wave propagation, and we are currently proposing to extend this technique to 2D and 3D models using synthetic data from the Generalized Fourier Method.

Back-azimuth Correction Estimation

Our technique for deriving back-azimuth corrections was designed by Bill Rodi (MIT) and is again based on the P-L finite difference method, which we use for our travel time calculations. Using reciprocity, travel times are calculated between a particular station location and all points in a 3D grid of event locations. The slowness and azimuth observed at a station from a given event are the length and direction of the slowness vector defined by taking the gradient of travel time with respect to the station location. Our approach is to approximate this gradient by subtracting travel times computed for the actual station location from travel times calculated for perturbed station locations. Specifically, we compute travel times to each point in a 3D grid, using the P-L algorithm, from three different "station" locations: (1) at the proper station location, (2) displaced from the station by one node to the north, and (3) displaced from the station by one node to the east. We have chosen one-node displacement (5 km) for initial testing of this technique, but we are exploring varying the displacement amplitude for accuracy. Slowness is

calculated in seconds/km and then converted to seconds/degree. Note that with this approach we obtain the slowness vector for each point in the 3D grid. To determine the slowness corrections at each node, we subtract the back-azimuth values based on the theoretical back-azimuth from those predicted for the 3D model.

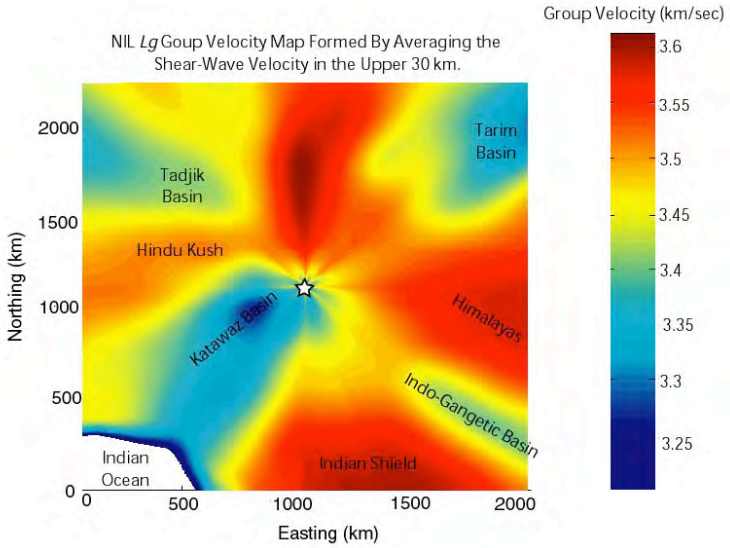


Figure 5. *Lg* group velocity map for station NIL (star) developed by averaging the CRUST2.0 *S*-wave velocities in the upper 30 km and ray-tracing through the resulting 2D model. Features to note include increased theoretical *Lg* velocities in the Indian Shield and the Himalayas with reduced *Lg* velocities associated with basin structures.

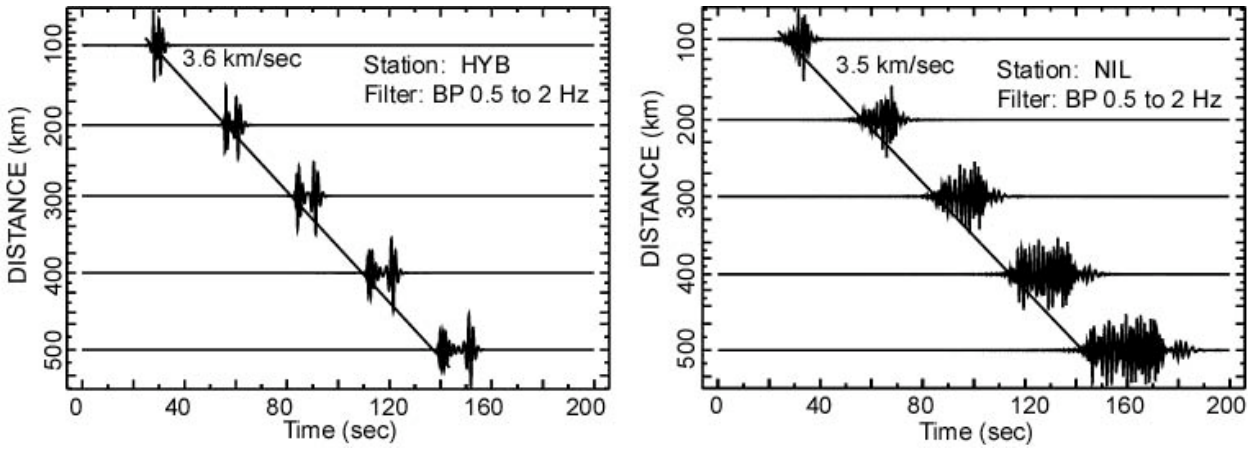


Figure 6. Modal summation synthetics for velocity profiles extracted from WINPAK3D at the HYB and NIL station locations. The fundamental mode and the first five higher modes were filtered between 0.5 and 2 Hz and plotted. The resulting *Lg* group velocities were measured at the onset time of the higher modes as approximately 3.6 km/sec and 3.5 km/sec for HYB and NIL, respectively.

Single-Station Location Methodology

The objective of the single station location program, SSLOC3D, is to locate events recorded at only a single station and to provide realistic error ellipses. It requires an observed back-azimuth and differential phase arrival time, such as *Lg-P*. The program utilizes theoretical 3D modeled travel time grids, described earlier, to determine the epicentral distance and uses 3D modeled back-azimuth grids to apply a correction to account for structural effects on the observed back-azimuth. SSLOC3D combines the estimated distance with the corrected back-azimuth to locate the

event. Then the *P* travel time is determined from the 3D travel time models and an origin time is obtained. Finally, SSLOC3D calculates the 95% confidence interval for the location error ellipse.

The prototype SSLOC3D program was designed to work with HYB and NIL and uses custom models and parameters for these stations. The next generation of the program will be expanded to additional stations/arrays. The travel time grids, back-azimuth corrections, and error uncertainty bounds must be calculated and calibrated using any available ground truth data for each station. The 11 May 1998 Indian nuclear test and 38 GT15 or better events from four clusters were used to calibrate and test SSLOC3D for stations HYB and NIL. With the ground-truth data, mislocations were calculated for each 3D model to determine the most appropriate model. These mislocations allow quantification of the errors that are used when locating non-GT events.

For each SSLOC3D location, we define a 95% confidence interval in the form of an ellipse empirically determined from back-azimuth and distance errors. First, the back-azimuth error is defined as the difference between the theoretical (station to ground truth location) and observed back-azimuth. Thus, our back-azimuth error includes both the measurement error in the polarization technique as well as off azimuth propagation caused by structural complexities. This error varies as a function of back-azimuth and some clusters have larger errors than others do. HYB shows the smallest back-azimuth errors for the clustered events near Koyna and larger errors at Bhuj, while NIL has smaller errors at Jiashi and PTS than at the Chamoli cluster. In order to determine the 95% confidence interval, two standard deviations of back-azimuth error are calculated for HYB and NIL using all clustered events (Figure 2) recorded at those stations and determined to be 6.2 degrees and 17.5 degrees for HYB and NIL, respectively.

The epicentral distance error is more complicated and is a function of incorrect phase picks and model error. Rather than assume values for the model and pick errors, we chose to empirically determine the distance error. Thus, the observed back-azimuth for every event in the database was fixed to the true back-azimuth and the event was relocated. The mislocation due only to distance errors is a combined function of the pick errors in both *Lg* (or *S*) and *P* and model uncertainty. For CRUST2.0, two standard deviations of the distance errors were 42.22 km and 63.05 km at HYB and NIL, respectively. We have also calculated the distance errors (model + pick) for all other models considered during the study.

Location Results in Southern Asia

We examined the performance of our single-station location methodology on the 11 May 1998 Indian nuclear test and 38 GT15 or better events located from four clusters (Koyna, Bhuj, Jiashi, and Chamoli; Figure 2). The resulting mislocations were determined as the difference in distance between the station and ground truth locations, and the best results are compiled in Table 1. We present two mislocations in Table 1; the first is the total mislocation in km due to both back-azimuth and distance errors, while the second mislocation is due to distance error only. One standard deviation of the mislocation is presented in the parentheses.

The Koyna region of west-central India is well known for the clustered seismic activity that started in 1962 after the impoundment of the Koyna reservoir. We formed single-station locations for 10 events from this region ranging from $4.2 < m_b < 4.9$ using HYB data. Nine of the ten events were listed as GT5 in the GROUP2 Reference Event List (REL) (McLaughlin *et al.*, 2002) while the remaining event was listed at GT15 in the EHB bulletin. For the Koyna events, the best locations (Table 1) were determined from the WINPAK3D *P*-wave model and the 2D WINPAK3D averaged *Lg* travel times. For these models, we observed an average of 9.4 km of total mislocation, which is less than 2% of the total travel path.

The Republic Day earthquake of 26 January 2001 was the mainshock for the Bhuj earthquake cluster. We formed single-station locations for 8 events from this cluster ranging from $4.5 < m_b < 6.9$, and the cluster mislocations are presented in Table 1. Data from station HYB, which is approximately 1080 km southeast of the cluster, were used for these locations, and the events were listed as GT5 in the GROUP2 REL. For the Bhuj events, the best locations were created using the constant velocity *Lg* travel times and *P*-wave travel times determined from the WINPAK3D model. For these models, we averaged 49.6 km of total mislocation, which is less than 5% of the total travel path. Most of the mislocation is due to back-azimuth error as only 11.2 km, 1% of the total travel path, is caused by distance error.

We created a single-station location for the Indian nuclear test of 11 May 1998 as recorded at NIL (Table 1). NIL is 743 km north-northeast of the Pokhran Test Site (Figure 4), and the event is listed as GT1 in the GROUP2 REL. For this event, the best location was obtained for the CRUST2.0 *P*-wave and crustal-averaged *Lg* (2D CRUST *Lg*) travel-times. For this combination, we observed 0.6 km of total mislocation, which is less than 1% of the total travel path. There was essentially no mislocation due to back-azimuth error for this event.

The Jiashi cluster in northwest China had twin mainshocks occurring on 21 January 1997 with M_s magnitudes of 6.2 and 6.5. We created single-station locations for 6 aftershocks with $3.7 < m_b < 5.4$ using regional seismograms from NIL (Table 1). NIL is 740 km southwest of the Jiashi cluster, and the events are listed as GT10 in the GROUP2 REL. For this cluster, the best locations were created from the CRUST2.0 *P*-wave and crustal-averaged *Lg* travel times (2D CRUST *Lg*). For this combination, we have 22.5 km of total mislocation, which is approximately 3% of the total travel path. Of this mislocation, only 9.4 km was due to distance error. We note that the *S-P* results for this cluster were significantly worse than those determined using the observed *Lg-P* data.

The Chamoli mainshock was a magnitude 6.8 earthquake that occurred in northern India on 29 March 1999 (Figure 4). We created single-station locations for 14 aftershocks with $3.8 < m_b < 5.1$ using regional seismograms from NIL (Table 1). NIL is approximately 670 km northwest of the Chamoli cluster, and the events are listed as GT5 in the GROUP2 REL. For this cluster, the best locations were created for the CRUST2.0 *P*-wave and masked *Lg* travel times. For this combination, we have 101 km of total mislocation, which is approximately 15% of the total travel path. Most of this mislocation is due to error in the observed back-azimuths as 33.9 km, 5% of the total travel path, is due to error in the epicentral distance.

Table 1. Best model combinations and associated errors for the nuclear test and each cluster.

Cluster	*P*-wave Model	Secondary Phase	Secondary Phase Model	BAZ Correction Applied	Total Mislocation Error in km (Distance+BAZ) Mean (STD)	Mislocation Error in km (Distance only) Mean (STD)
KOYNA (HYB)	WINPAK3D	*Lg*	2D WINPAK3D Lg Average	Y	9.4 (5.7)	4.4 (4.5)
BHUJ (HYB)	WINPAK3D	*Lg*	Constant Lg Velocity	Y	49.6 (31.9)	11.2 (8.5)
PTS (NIL)	CRUST2.0	*Lg*	2D CRUST2.0 Lg Average	N	0.6	0.6
JIASHI (NIL)	CRUST2.0	*Lg*	2D CRUST2.0 Lg Average	Y	22.5 (15.8)	9.4 (8.7)
CHAMOLI (NIL)	CRUST2.0	*Lg*	CRUST2.0 Lg Mask	N	101.0 (55.2)	33.9 (16.3)

CONCLUSIONS AND RECOMMENDATIONS

We used SSLOC3D to form single-station locations for 39 events in southern Asia classified as GT15 or better. For single-station locations performed using observed regional *S-P* travel times, the use of the CRUST2.0 model to generate travel times for both phases resulted in 14 km less distance error than IASP91. The results for *Lg-P* show 5 km improvement in the distance error when using 3D models as opposed to the 1D IASP91 model. WINPAK3D performed the best for clusters recorded at HYB while CRUST2.0 performed better at clusters recorded at NIL. Further work needs to be done to understand which regions of each model give the most accurate locations and use that information to develop new models.

It is clear from Table 1 that back-azimuth error is still the largest source of the total mislocation error, and results show that the application of 3D model-based back-azimuth corrections were not consistently successful at improving these locations. Only 3 of the 5 region mislocations improved with the use of back-azimuth corrections (Table 1). We examined the effects of empirical calibration of the back-azimuth error by fitting an experimental cosine curve to the observed NIL back-azimuths following a method similar to Tibuleac and Herrin (1997). Using this technique, we reduced the mean residual (theoretical-observed) back-azimuth from 3.0 to 0.1 degrees and reduced the standard error from 7.1 km to 6.9 km. Application of the empirical corrections to the Chamoli cluster

reduced the total mislocation from 101 km to 82 km. We plan to further examine additional azimuthal calibration techniques.

The single station location system used in this project yields locations that compare favorably with results from traditional multi-station location techniques but with the added benefit of being able to locate events recorded at only a single station. Single-station mislocations for four of the five event regions studied were less than 6% of the total epicentral distance. In addition, while many of the nuclear test sites have calibrated single-station location formulae, our single-station method improves location capability in broad and/or aseismic regions where little or no calibration data exists. The current *Lg* models, crustal averaged, "masked", and constant velocity, performed equally well. Yet, the results indicate that the development of additional phase modeling tools, such as 3D modeling of *Lg* travel times, and empirical calibration of both 3D travel-time grids and back-azimuth correction grids should further improve the methodology. We note that these locations are model dependent and will improve as we develop better knowledge of the regional velocity structure.

REFERENCES

Bassin, C., G. Laske, and G. Masters, (2000), Current limits of resolution for surface wave tomography in North America, *EOS Trans AGU*, 81, p F897.

Bouchon, M. (1982), The complete synthesis of seismic crustal phases at regional distances. *J. Geophys. Res.*, 87, 1735-1741.

Engdahl, E.R., and R. van der Hilst, and R. Buland, (1998). Global teleseismic earthquake relocation with improved travel times and procedure for depth determination, *Bull. Seism. Soc. Am.*, 88, 722-743.

Herrmann, R., (2002), *Computer Programs in Seismology Version 3.15*, St. Louis University.

Jurkevics, A. (1988), Polarization analysis of three-component array data, *Bull. Seism. Soc. Am.*, 78, 1725-1743.

Kennett, B.L.N., and E.R. Engdahl, (1991), Travel times for global earthquake location and phase identification, *Geophys. J. Int.* 105, 429-465.

Kovach, R.L. and D.L. Anderson, (1964). Higher mode surface waves and their bearing on the structure of the earth's mantle, *Bull. Seism. Soc. Am.* 54, 161-182.

Lomax, A. (1999), Probabilistic, non-linear earthquake location in 3D media (An online guide to software), http://www.iapetus.unice.fr/~lomax/nlloc.

McLaughlin, K., I. Bondár, X. Yang, J. Bhattacharyya, H. Israelsson, R. North, V. Kirichenko, E.R. Engdahl, M. Ritzwoller, A. Levshin, N. Shapiro, M. Antolik, A. Dziewonski, G. Ekström, H. Ghalib, I. Gupta, R. Wagner, W. Chan, W. Rivers, A. Hofstetter, A. Shapira, and G. Laske, (2002), Seismic Location Calibration in the Mediterranean, North Africa, Middle East and Western Eurasia, 24th Seismic Research Review, Ponte Vedra Beach, FL, September 17-19.

Mooney, W., G. Laske, and G. Masters, (1998), Crust 5.1: a global crustal model at 5x5 degrees, *J. Geophys. Res.*, 103, 727-747.

Moser, T.J. (1991), Shortest path calculation of seismic rays, *Geophys*, 56, 59-57.

Oliver, J. and M. Ewing, (1957), Higher modes of continental Rayleigh waves, *Bull. Seism. Soc. Am*. 47, 187-204.

Olsen, K. H. and L.W. Braile, (1983), Modeling short-period crustal phases (*P*, *Lg*) for long-range refraction profiles, *Phys. of the Earth Planet Interiors*.

Podvin, P. and I. Lecomte, (1991), Finite difference computation of travel times in very contrasted velocity models: a massively parallel approach and its associated tools, *Geophys. J. Int.* 105, 271-284.

Press, F. and M. Ewing, (1952). Two slow surface waves across North America. *Bull. Seism. Soc. Am.*, 42, 219-228.

Reiter, D. T., M. Johnson, A. Rosca, C. Vincent, (2001), Development of a regional 3D velocity model of the Pakistan region for improved seismic event location. Final Report, Weston Geophysical, 27 p.

Tibuleac, I.M, E. T. Herrin, J. Britton, R. Shumway and A. Rosca, (2003), Automatic detection of secondary seismic phases using wavelet transforms, submitted to *Seismological Research Letters*.

Vidale, J. (1988), Finite difference calculations of travel times, *Bull. Seism. Soc. Am.*, 78, 521-526.

Yang, X., I. Bondar, and K. McLaughlin, (2000). PIDC Reference Event Database (REDB), Center for Monitoring Research CMR-00/17.

Young, C. (1997), Matseis: a seismic toolbox for MATLAB, *Proceedings of the 18th Annual DoD/DOE Seismic Research Symposium*, Annapolis, MD.

NEURAL NETWORK AND WAVELETS MODEL IN SEISMIC LOCATION FOR THE CENTRAL ANDES OF BOLIVIA

Estela Minaya, Percy Aliaga, Guido Avila, Cristina Condori, and Alejandro Córdova

Observatorio San Calixto

Sponsored by Army Space Defense and Missile Command

Contract No. F49620-97-1-0214

ABSTRACT

The location of seismic events in the Central Andes of Bolivia frequently displays differences between the reports by international agencies such as the International Data Center (IDC) or the Preliminary Determination of Epicenters (PDE) and those obtained from the National network. Also observed is an instability for different algorithms of location. The main cause of this instability is the dispersed azimuth distribution and the small number of seismic stations that are used to locate the events. Other factors that can cause this instability are marked attenuation of the S phase in earthquakes located in the south zone of Bolivia, or phases recorded as a consequence of the complex crustal structure that includes several refracting layers causing abrupt changes of period and amplitude.

In our first stage of investigation, we proposed to develop an artificial and automatic method that accomplishes localization using a Neural Network on Radial Bases Functions (NNRBF) by applying a Gaussian function to the coda of the seismic signal and its location parameters. Our results show that the NNRBF requires a better approximation of the training parameters with the activating functions.

In our second stage of investigation, we used a wavelet method instead of a Gaussian function to try to retain the maximum information recorded in the seismic signal when we applied the filters. This procedure applies the discrete wavelet transform to decompose the seismic noise, based on the Haar wavelet (or first Debauchies decomposition) with an alternating introduction in the NNRBF algorithm. Initially this methodology was tested with earthquakes in the central zone of Bolivia where the occurrence of seismic events is frequent and waveforms are less complex than in the rest of the region.

The 23 earthquakes tested that occurred in 2000 and consisting of magnitudes (Ml) greater than 3 were analyzed with a success rate of 83%. This first result leads us to consider using this technique as a solution for the problem involving a small number of stations and the dispersed azimuth distribution, thus increasing the database of seismic events and identifying mislocated events as 17% of the data analyzed. We will continue our investigations to determine the limitations of this method by testing it in the remaining zones of Bolivia.

OBJECTIVE

The objective of this research was to find a model (or method) for automatic localization that allows improvement in the localization of seismic events occurring in zones of complex crust structure, with few seismic stations and a disperse azimuthal distribution across them. The model would use Artificial Intelligence (AI) based on a Neuronal Networks on Radial Bases Functions (NNRBF) and the Wavelets method for treatment of seismic signals.

RESEARCH ACCOMPLISHED

One of the most concrete problems of localization precision has been the 1998 earthquake that occurred in the central region of Bolivia. Differences in localization, (Avila, 2000), reported by international agencies (IDC, PDE, ISC) and those obtained from the Bolivian National Network are clear and stated below on both Table 1 and Figure 1.

Table 1. Locations for the earthquake occurred on May 22, 1998 in the central region of Bolivia.

Source	Time	Latitude	Longitude	Depth
IDC	04 48 48.2	17.54	65.14	34
PDE o NEIC	04 48 50.4	17.73	65.43	24
ISC	04 41 50.5	17.85	65.53	24
Harvard CMT	04 49 02.5	17.60	65.20	15
3DGRIDLOC	04 48 46.2	17.81	65.10	1
3DGRIDLOC, 5km	04 48 45.2	17.92	65.18	1
OSC, French	04 48 44.8	17.88	65.05	9
OSC, Lienert	04 48 43.6	17.80	65.057	13
Isoseismals		17.85	65.16	11

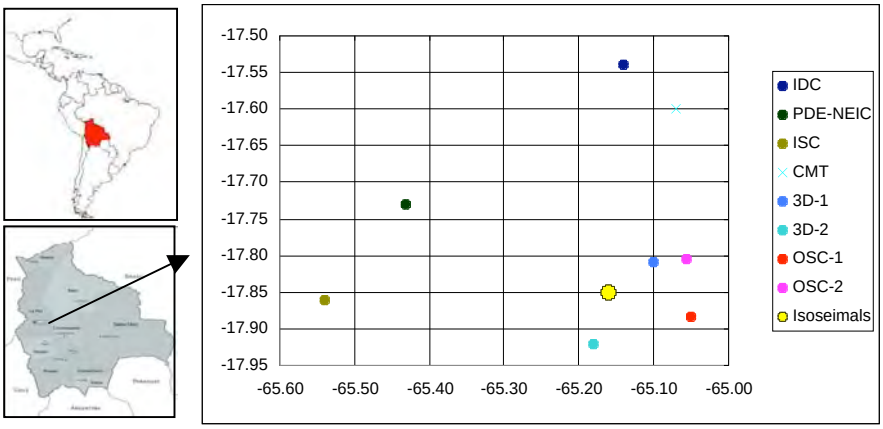


Figure 1. Map showing the locations of Table 1.

As the earthquake of May 22, 1998, there are many other events with the same problem, and the necessity for an automatic seismic localization model became imperious and was mainly based on the following premise: “A model is the explicit interpretation of what is understood from a situation or the idea about that situation. It may be expressed in mathematical or symbolic terms, or in words; but in essence it is a description of entities, processes, attributes and the relationship between them”, Pressman (1993).

METHODOLOGY

The seismic location model, proposed by Aliaga (2002), is composed of the elements shown in Figure 2. The task of the neuronal network was to classify a signal from an existing signal. It asks for signals previously localized with standard methods to be stored for training and searching. In order to obtain the results, an approximation of the maximum and minimum variations between training signals and the entry signal (or signal to be located) is used, and is determined by the Mean Squared Error (MSE or bias). The epicenters of the training signal (obtained by standard or traditional methods) are considered as provisional or previous localization for the entry signal. Once the neural network selection is concluded, the event is located using the Geiger method.

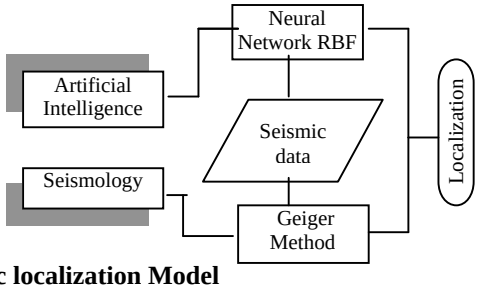


Figure 2. Components of the seismic localization Model

The following example shows this process. There is an entry signal of a seismic event that will be classified in relation to the training signals A and B. The entry signal is similar to the training signal A shown in Figure 3. Consequently the provisional epicenter of the entry signal is training signal A. However we fully acknowledge that there will always be a variation between the entry signal and the result because of the fact that no two seismic signals are identical.

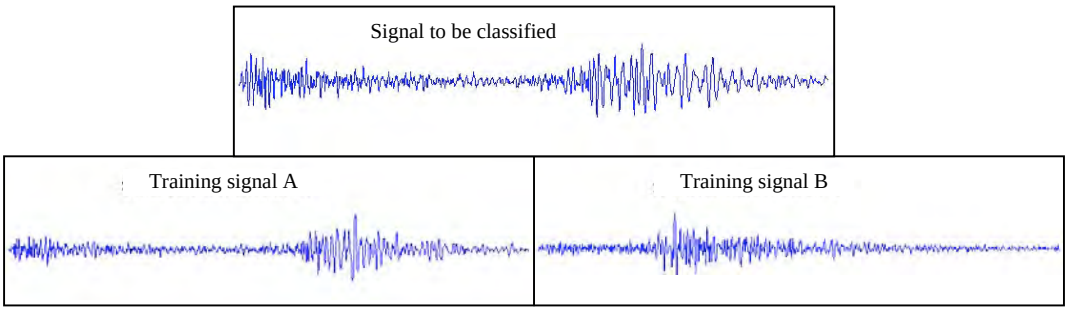
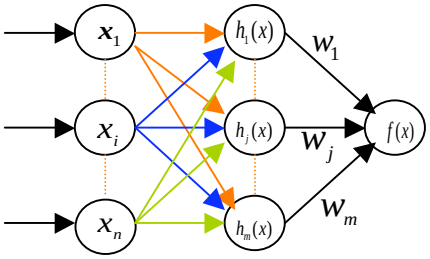


Figure 3. Example of an entry signal to be classification with the NNFRB.

In the final stage, seismic localization is obtained with the Geiger method, which employs localization parameters obtained in the neuronal network process as its requirement.

Theoretical analysis

The Neural Network on Radial Bases Functions is built with activation functions. In the beginning, several models were employed (linear or non-linear) as well as several network groups (for a single layer or multi layer). However the Neural Network on Radial Bases Functions (NNRBF) has been traditionally associated to a single layer network (Figure 4).



$$MSE = s = \sum_{i=1}^{p} (\ddot{y}_i - f(x_i))^2 \qquad \text{[Equation 1]}$$

$$f(x) = \sum_{j=1}^{m} w_j h_j(x) \qquad \text{[Equation 2]}$$

$$T = \left\{ x_i, \ddot{y}_i \right\}_{i=1}^{p} \qquad \text{[Equation 3]}$$

$\ddot{y}_i$ *is the* exit *f(x)* of the neuronal network plus an amount of noise.

Figure 4. The *n* components of the entry vector *x* and the activation base function h_j are lineally combined with the weight wj for the network exit *f(x)*.

The NNRBF is nonlinear, if the base functions are enabled for movement, change their size, or if there is more than one hidden layer. The NNRBF is linear when it is a single-layer and connects to a network with functions fixed in position as well as in size. Nonlinear optimization (Orr, 1996) is used only for regularization parameters in the ridge regression and in the optimal base function subgroup within the unidirectional selection.

The Mean Squared Error (MSE, Equation 1) is applied in the linear model of directed learning. Mean squares lead to the beginning of an optimization problem. Error is minimized applied equation 2 and 3.
If a weight (Figure 4) is adjusted to Equation 1, the error is added, as in the case of the ridge regression; then the regularization function Equation 4 is minimized plus the Equation 1.

$$C = \sum_{i=1}^{p} (\ddot{y}_i - f(x_i))^2 + \sum_{j=1}^{m} \lambda_j w_j^2, \qquad \text{[Equation 4]}$$

where λ_j is the regularization parameter; "j" is an index from 1 to m; m is the number of signals; and p is the signal window.

Wavelets

The Wavelets are function families of the type:

$$\Psi_{a,b}(x) = \frac{1}{\sqrt{|a|}} \Psi\left(\frac{x-b}{a}\right) \qquad \text{[Equation 5]}$$

where *a* equals expansion; *b* equals translation; and *x* equals sequence of signal points. The Wavelet is transformed from a signal and is represented by the following expression:

$$WT(f(x)) = f(x) * \Psi = \frac{1}{a} \int_{-\infty}^{\infty} f(t) \Psi\left(\frac{x-t}{a}\right) dt \qquad \text{[Equation 6]}$$

Discreet analysis of a continued signal in time defines the parameters *a* and *b* with: $a = 2^j, b = k2^j, (j,k) \in Z^2$, and is named dyadic Wavelet. Later the Discreet Rapid Transformed Wavelet (DRTW) is used.

The transformed Wavelets are applied to the signal filters of high-pass filters, detail and low-pass filters, or approximation. The number of times the signal is filtered is determined by the decomposition level. To reduce the signal noise, the main idea eliminates components obtained in the transformed Wavelet that are under a certain threshold, or multiplies them by a certain pondering value before performing the inverse transformation. The most significant differences are found within the threshold or pondering value.

For noise reduction a nonlinear (proposed by Donoho, 1995) procedure is used called soft-thresholding, where only those coefficients of details under a certain threshold will be eliminated; the rest is pondered. The threshold calculation is obtained with statistical procedures (Novak et al, 2000) beginning with detail coefficients obtained by the transformed Wavelet. For natural noise reduction, it is necessary to consider a signal s(n):

$$s(n) = f(n) + \eta\, e(n) \qquad \text{[Equation 7]}$$

where n is equally spaced, $f(n)$ represents noiseless signal, $e(n)$ is natural noise for our case, and η means noise level.

The main noise reduction procedure is summarized in three fundamental steps:

1. Decomposition—a Wavelet is selected, an N level is chosen which will be the decomposition level, and the Wavelet decomposition calculations on an s signal are made on a N level.
2. Threshold Detail Coefficients (high pass)—for each level from 1 to N, a threshold is selected and applied to the soft-thresholding of detail coefficients.
3. Reconstruction—an inverse transformed Wavelet is calculated by using the original approximation coefficients of level N and a modified detail coefficients of level 1 to N.

The transformed Wavelet is used to obtain signal details at different levels by applying the threshold

$$C_\delta(i,j) = \begin{cases} 0, si\,|C(i,j)\cdot\delta| \\ \text{por otro}, (C(i,j))(|C(i,j)| - \delta), si\,|C(i,j) \geq \delta| \end{cases} \qquad \delta = \sqrt{2\log(N)}\hat{s} \qquad \text{[Equation 8]}$$

To perform noise reduction in a nonlinear manner by employing soft-thresholding, the inverse transformed Wavelet is calculated to obtain the resulting signal. Ci,j represents coefficients of details obtained through the transformed Wavelet. The value of $\hat{s}$ used for this threshold is given by the expression:

$$\hat{s} = media\left(|C(i,j)|\right)/0.6745 \qquad \text{[Equation 9]}$$

The final equation of the transformed Wavelet is defined by the sum of the last approximation and the sum of all the decompositions.

$$S = A_J + \hat{A}_{j\pounds J} D_j \qquad \text{[Equation 10]}$$

Model Development

Data

In order to perform the initial tests, 36 seismic events were selected from the region of Cochabamba, Bolivia, for the year 2000 The coordinates of these events were –16° to –17° 5 latitude south and –64° to 67°.9 longitude west, and the events had magnitudes Ml greater than 3.0 (Table 2).

Model Scheme

The scheme in Figure 5 shows the information, procedure, and function flows used in the NNRBF first stage seismic localization model .

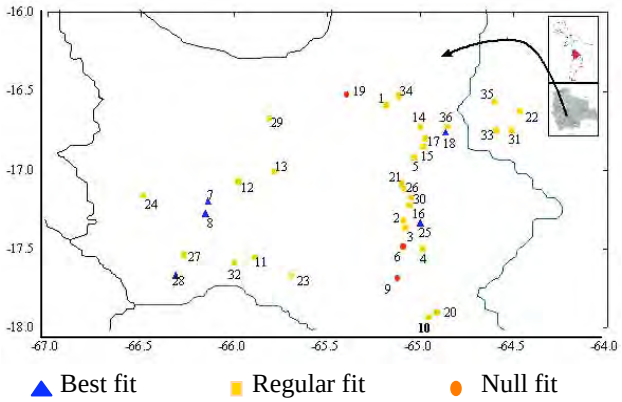
The initial stage is developed in the neural network environment, and introduces parameters for each of the 36 seismic events performed under directed training. Each event consists of up to 12,000 points (increased in some cases and reduced in others, as we should have uniform-sized samples.

To validate the NNRBF, test localization parameters for 35 seismic events were used as well as an independent event as an entry signal. Consequently the training matrix for this case is in the order of 12,000 x 35 (H, design matrix), and the event to be localized is outside the matrix. Once the test validation is concluded, more H matrix events may be incorporated, which increases the training group. The seismic events analyzed were registered in the national network (consisting of six stations), but in the first stage only data from the station closest to epicenters was used. This station also had a lower noise percentage.

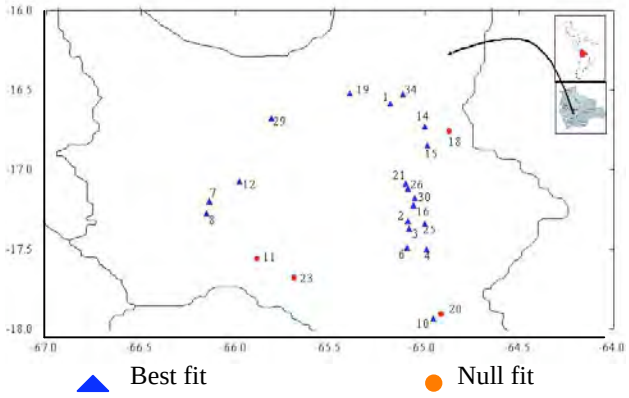
NNFRB application

W weights (Figure 3) are adjusted so that the best solution between training signals and the entry signal ˆy may be found and a mean squared error (MSE) obtained. With the weight adjustment, a minimum or a maximum is obtained for each event (Table 2). These adjustments are selected by the MSE result obtained. For instance, event Nº8 (Table 2) renders a minimum of –0.1444 and a maximum of 0.1745, which are related to events Nº7 and 12, respectively, (Figure 6). The MSE value is lower for event Nº8 than it is for event Nº12, therefore provisional localization of event Nº8 is assumed for event Nº7. The process is performed for all 35 remaining events (Figure 6a).

Once all events were relocated (Geiger Method), the proposed model was evaluated. An optimal response of 13.9% was obtained, and a 77.8% regular result—a guide of the uncertainty in localization—plus a null result of 8.3% were obtained in relation to the 36th signal sample.



Map 1. Results obtained with NNFRB model.



Map 2. Results with Neural Networks and Wavelet

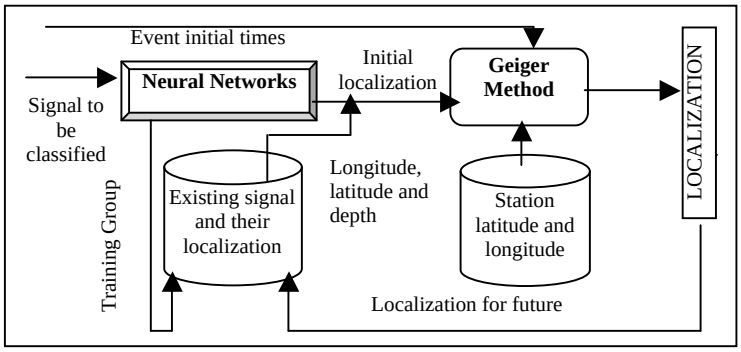


Figure 5. Schema of seismic localization model.

Table 2. Seismic events used in initial test the last column show the result obtained.

No.	Date	Time	Lat	Lon	Depth	MI	Best	Regular	Null	Result
1	16/01/00	10:55:11.775	-16.588	-65.183	65.00	3.32		MINIMUM		35
2	20/01/00	23:05:39.860	-17.323	-65.091	65.00	4.13		MINIMUM		21
3	21/01/00	03:35:16.869	-17.369	-65.083	65.00	4.19		MAXIMUM		16
4	21/01/00	05:34:56.200	-17.502	-64.990	16.06	3.14		MINIMUM		16
5	24/02/00	23:28:59.762	-16.921	-65.032	15.00	3.48		MAXIMUM		31
6	25/02/00	11:02:57.937	-17.489	-65.093	45.00	3.51			x	7
7	07/03/00	03:57:30.910	-17.197	-66.140	16.95	3.71	MINIMUM			8
8	07/03/00	03:59:36.234	-17.275	-66.154	40.00	3.57	MINIMUM			7
9	21/03/00	00:22:12.273	-17.687	-65.125	65.00	3.52			x	18
10	22/03/00	19:47:53.374	-17.907	-64.913	30.00	3.18		MAXIMUM		9
11	29/03/00	21:50:00.221	-17.559	-65.887	20.00	3.14		MAXIMUM		7
12	04/04/00	06:31:32.980	-17.076	-65.978	50.00	3.76		MAXIMUM		8
13	25/04/00	23:21:28.667	-17.013	-65.786	42.00	3.71		MAXIMUM		8
14	03/05/00	11:19:09.060	-16.730	-65.000	10.00	3.10		MINIMUM		34
15	03/05/00	15:44:17.249	-16.851	-64.985	31.00	3.28		MINIMUM		35
16	05/05/00	01:41:16.831	-17.224	-65.060	30.00	3.69		MINIMUM		9
17	07/05/00	07:43:58.882	-16.803	-64.978	8.00	4.16		MAXIMUM		34
18	24/05/00	09:16:37.859	-16.761	-64.869	10.00	3.75	MAXIMUM			36
19	03/06/00	15:36:49.793	-16.523	-65.397	25.00	3.20			x	4
20	14/07/00	01:06:52.358	-17.936	-64.956	30.00	3.61		MAXIMUM		9
21	28/07/00	18:57:09.935	-17.089	-65.102	15.00	3.56		MAXIMUM		16
22	29/07/00	13:30:02.771	-16.628	-64.468	10.00	3.13		MINIMUM		5
23	16/08/00	13:33:06.738	-17.680	-65.692	65.00	3.09		MAXIMUM		7
24	22/08/00	19:52:28.232	-17.165	-66.485	51.00	3.02		MINIMUM		27
25	25/08/00	19:43:32.564	-17.338	-65.001	40.00	3.08	MAXIMUM			2
26	08/09/00	05:23:24.860	-17.118	-65.090	15.00	3.06		MAXIMUM		9
27	15/09/00	19:38:23.284	-17.542	-66.267	21.00	3.81		MINIMUM		8
28	20/09/00	04:47:15.985	-17.669	-66.314	65.00	3.40	MAXIMUM			27
29	21/09/00	05:06:07.212	-16.676	-65.810	23.99	3.31		MINIMUM		12
30	27/09/00	03:06:03.683	-17.178	-65.052	35.00	3.26		MINIMUM		2
31	01/10/00	09:34:52.154	-16.750	-64.512	50.00	3.70		MINIMUM		21
32	03/10/00	15:00:43.571	-17.592	-65.997	65.00	3.35		MINIMUM		29
33	03/10/00	17:46:26.885	-16.750	-64.593	65.00	3.19		MAXIMUM		36
34	12/11/00	05:44:50.738	-16.529	-65.115	20.00	3.26		MINIMUM		18
35	30/11/00	15:44:54.595	-16.570	-64.604	65.00	3.83		MINIMUM		11
36	04/12/00	06:30:10.883	-16.724	-64.856	30.00	3.05		MINIMUM		31

We could not validate the localization obtained with the Geiger method and starting from results obtained with the NNRBF because the approximation between the entry signal and the training signals were inconsistent as a result of the signal variation in the first the coda phase.

Such an unexpected result drove us to seek the causes that render this NNRBF model inoperative. We performed a visual analysis of the coda signal and the type of phase, as well as measured the exactness of the first arrival reading (see Figure 7) and applied filters. Our results of this stage are conclusive and the main factor is each complex waveform that is affected by the crust structure under the central Andes and that, in some cases, leads to a wrong localization.

The visual analysis result indicated a signal association, which does not necessarily have the same localization but is in the same zone. For instance, as shown in Figure 8, this situation repeats itself throughout the analyzed region and allows a new analysis of 23 signals by introducing the Wavelet methodology.

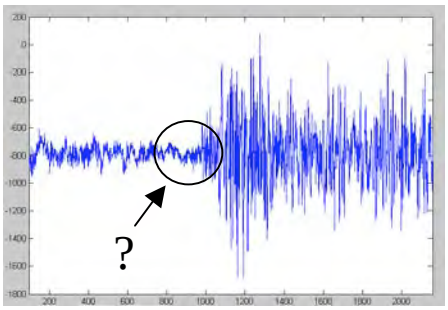


Figure 6. Unclear first arrival of event No 33, original signal

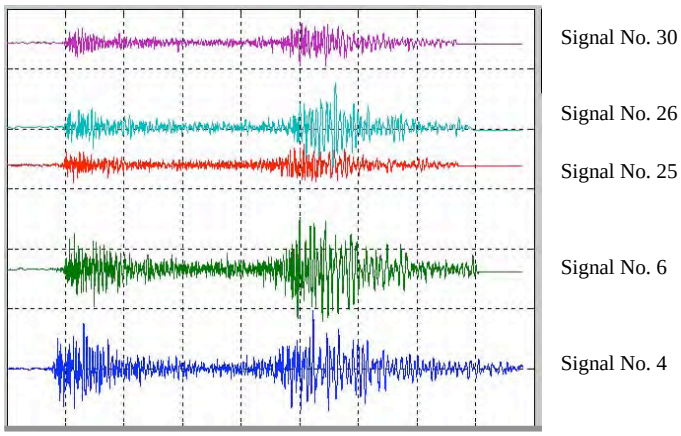


Figure 7. Similarities in five seismic events showing association among them as shown on Map 1.

Development with the Neural Networks and Wavelets

To optimize results, especially in the entry signals of the neural network, we introduce the Wavelet methodology and incorporate it in the localization model. We then proceed to transform the time domain entry signal without losing information. See Figure 9.

The process is performed with all 23 seismic events, Figure 6b that will be the database and entry to the neural network without considering the function of radial base. With the Wavelet method, we seek to obtain a representative model of each signal and we achieved this representation with the Haar family Wavelet.

In the Harr family Υ is the Wavelet; x is entry points and f is the scale of wavelet function.

$$\begin{cases} \psi(x) = 1, & x \in [0, 0.5[\\ \psi(x) = -1, & x \in [0.5, 1[\\ \psi(x) = 0, & x \notin [0, 1[\\ \\ \phi(x) = 1, & x \in [0, 1] \\ \phi(x) = 0, & x \notin [0, 1] \end{cases}$$

The Wden (MatLab) tool is applied in the Wavelet equations in order to reduce noise. Syntax of this function follows:

xd = wden(x,'sqtwolog','min',5,'Haar');

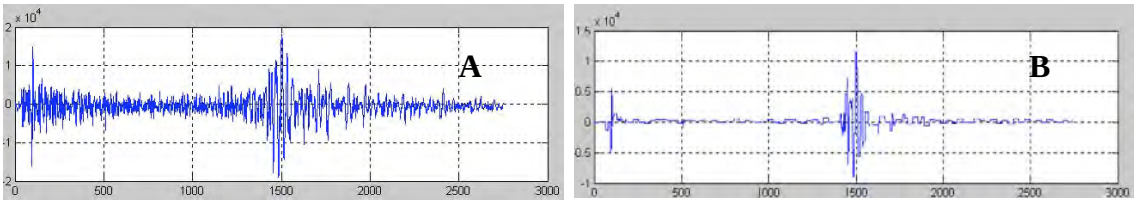


Figure 9. Signal no. 15, A) original signal B) transformed signal

where x is the entry signal to transform with the defined function 'sqtwolog' as the parameter that calculates each of the detail coefficients (high pass)' threshold; 's' is soft - thresholding (a noise reduction process); 'min' is the

parameter that does not refer to Gaussian noise and is used in the decomposition level that depends on the noise level; the '5' function value relates to the decomposition level,; and "Haar" refers to the Wavelet Haar family. The transformed signal is defined as xd, which is the entry parameter of the neuronal network.

The results featured in Table 3 reflect the scale conversion process of the entry signal. Later the Wavelet transformation is performed and finally the signal is classified in the neural network, finding a MSE for each of the events. These steps are performed for each one of the iterations (1^{st}, 2^{nd}, 3^{rd}, 4^{th}) independently.

Table 3. Results applying Wavelets and neural networks to 23 earthquakes

Nº	1 st	2 nd	3 rd	4 th	MSE	Result
1	19	18	25	6	8.207 EXP(-6)	1
2	21	3	21	21	11.545 EXP(-4)	1
3	2	2	26	2	11.444 EXP(-4)	1
4	21	12	30	21	9.936 EXP(-6)	1
6	21	7	25	1	10.350 EXP(-6)	1
7	8	8	8	8	14.187 EXP(-5)	1
8	7	7	7	7	7.658 EXP(-5)	1
10	4	7	30	20	4.197 EXP(-6)	1
11	20	18	30	30	2.650 EXP(-6)	0
12	8	7	29	8	19.297 EXP(-5)	1
14	15	18	15	15	26.475 EXP(-7)	1
15	14	18	14	14	24.991 EXP(-7)	1
16	18	21	26	6	40.788 EXP(-5)	1
18	1	23	30	30	56.556 EXP(-6)	0
19	1	18	30	25	10.082 EXP(-6)	1
20	18	18	30	30	5.730 EXP(-6)	0
21	18	16	4	4	16.598 EXP(-5)	1
23	1	18	30	30	6.655 EXP(-6)	0
25	1	18	30	26	20.594 EXP(-7)	1
26	1	7	25	25	46.925 EXP(-7)	1
29	12	12	30	11	19.463 EXP(-6)	1
30	18	8	25	15	18.040 EXP(-7)	1
34	18	23	30	1	30.501 EXP(-6)	1

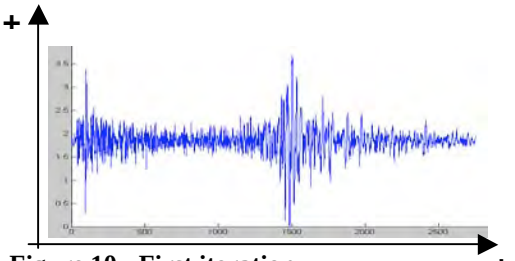


Figure 10. -First iteration

In the first iteration (Figure 10), the scale is changed and seismic amplitudes are converted to positive values. This result is obtained by finding the highest negative values, inverting their sign, and adding them to each of the signal points. Next the Wavelet transformation is performed and finally the result are obtained after the signal is classified with the neural network

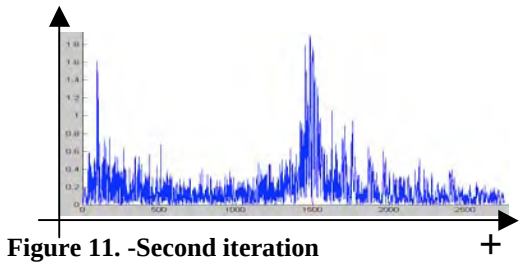


Figure 11. -Second iteration

In the 2^{nd} iteration (Figure 11), some amplitudes of the seismic event are converted into a positive. The negative values of the signal are inverted. Next the Wavelet transformation is performed, and finally the results are obtained after the signal is classified with the neural network

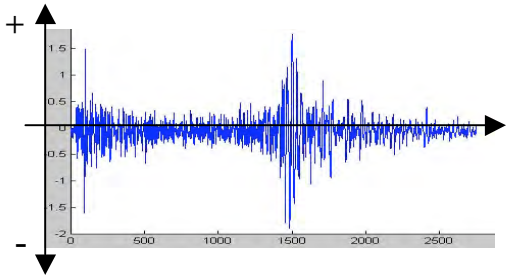


Figure 12. -Third iteration

In the 3rd iteration (Figure 12), the scale is changed in the positive and negative values; but the first value of the seismic event's amplitude begins at ZERO. The same values is added or subtracted from the first. Next the Wavelet transformation is performed, and finally the result are obtained after the signal is classified with the neural network

In the 4th iteration the same scale changes are performed as in the 1st iteration, with the sole difference being that when Wavelets are applied, decomposition is not a level 5 (as in the case of previous iterations), but a level 1. Next the Wavelet transformation is performed and finally the results are obtained after the signal is classified with the neural network

The first four columns in Table 3 indicate the identification of the event to be localized. These columns are responses to each of the iterations related to identification of the event associated with the entry signal. For instance, event Nº8 is similar to the 1st iteration of Nº15. We note that the remaining iterations provide us with the same event number, thus ensuring a very dependable localization. By contrast, the opposite happened with event Nº34 because of the fact that its optimal localization is found in the 4th iteration. We also note that results for event N 34 are different in the previous iterations. Optimal result choice is based on the MSE calculated by the neural network. The example has a MSE of 30.501 10^{-6}, which is lower if related to the other iterations' results.

The number "1" in the last column of Table 3 means an optimal result is related with the previous localization. A total of 83% functionality and 17% of bad previous localization was obtained from the entire study sample as a result of the association of events that were more localized in their epicenters.

CONCLUSIONS AND RECOMMENDATIONS

A first model (or method) for automatic localization, based on a Neuronal Networks on Radial Bases Functions (NNRBF) could not be validated as the approximation between the entry signal and the training signals are inconsistent resulting from the signal variation in the first stage coda. The first test was performed with 36 seismic events taken from the year 2000 and located in the region of Cochabamba - Bolivia (magnitudes greater than 3), and the results were an optimal response of 13.9%, a 77.8% regular result, and a null result of 8.3%

After a visual analysis of the coda signal characteristic in each event, a second model proposed based on neural networks and wavelets using three main steps: Decomposition; Threshold Detail Coefficients, and Reconstruction. These steps are performed by four independent iterations. Results reflected 83% functionality and 17% show a bad response.

We recommend continuing to improve the Wavelet model proposed by introducing other traditional location methodsand applying other Wavelets families. It will be necessary to use the wavelet methodology in order to identify the phases in the p code; this information will be introduced in the final model. Once the model is validated, we will apply it in other regions of Bolivia and other sites.

REFERENCES

Aliaga, H. P. (2002), Modelo de Localización Sísmica con Parámetros Sismológicos Aplicando la Red Neuronal con Funciones de Base Radial y la Metodología de Geiger, *Tesis Universidad Católica Boliviana*, La Paz –Bolivia.

Avila, G. (2000), Métodos de Localización Aplicados a Sismos Ocurridos en Bolivia, *Tesis universidad Técnica de Oruro*, Oruro- Bolivia.

Bitmead, R. (1993), Introducción a las Redes Neuronales, *Grupo de Tratamiento Avanzado de Señales, Universidad de Cantabria.*

Donoho, D. L. (1995), De-noising by Soft-thresholding, *IEEE Trans. Information Theory*, vol. 41, num. 3, pp.612-617.

Hilera, J. R. y V. J. Martínez (1995), Redes Neuronales Artificiales.

Kohonen, T. (1984), Neuro Computación, *Escuela Técnica Superior de Ingenieria Informatica, Universidad de Granada*, España.

Kung, S. Y. (1993), Digital Neural Networks.

Misiti M. y et al (1997-2000), Wavelet Toolbox for Use with MatLab, *The MathWorks Inc.*, ver 2.

Novák, D. y et al (2000), Denoising Electrocardiogram Signal Using Adaptive Wavelets, *Proceeding of the 15th Biennial Eurasip Conference BIOSIGNAL*, pp 18-20.

Orr, M. J. L. (1996), Introducción a las Redes con Funciones de Base Radial, *Universidad de Edimburgo*, Escocia.

Pressman, R. S. (1993), Ingeniería de Software, 3ra. Ed.

Rumbaug, M. y et al (1996), Modelado y Diseño Orientado Objetos OMT, España.

Wallace, T. C. (1996), Modern Global Seismology, pp 217-231.

RELATIVE LOCATION ACCURACY AND WAVEFORM SUBSPACE DETECTOR

Stephen C. Myers,[1] David B. Harris,[1] Megan L. Anderson,[1] William Rodi,[2]
William R. Walter,[1] Megan P. Flanagan,[1] and Flori Ryall[1]

Lawrence Livermore National Laboratory[1], Massachusetts Institute of Technology[2]

Sponsored by National Nuclear Security Administration
Office of Nonproliferation Research and Engineering
Office of Defense Nuclear Nonproliferation

Contract No. W-7405-ENG-48

ABSTRACT

We present two Lawrence Livermore National Laboratory (LLNL) research projects in the topical areas of location and detection. The first project assesses epicenter accuracy using a multiple-event location algorithm, and the second project employs waveform subspace correlation to detect and identify events at Fennoscandian mines.

Accurately located seismic events are the bases of location calibration. A well-characterized set of calibration events enables new Earth model development, empirical calibration, and validation of models. In a recent study, Bondar et al. (2003) develop network coverage criteria for assessing the accuracy of event locations that are determined using single-event, linearized inversion methods. These criteria are conservative and are meant for application to large bulletins where emphasis is on catalog completeness and any given event location may be improved through detailed analysis or application of advanced algorithms. Relative event location techniques are touted as advancements that may improve absolute location accuracy by 1) ensuring an internally consistent dataset, 2) constraining a subset of events to known locations, and 3) taking advantage of station and event correlation structure. Here we present the preliminary phase of this work in which we use Nevada Test Site (NTS) nuclear explosions, with known locations, to test the effect of travel-time model accuracy on relative location accuracy. Like previous studies, we find that the reference velocity-model and relative-location accuracy are highly correlated. We also find that metrics based on travel-time residual of relocated events are not a reliable for assessing either velocity-model or relative-location accuracy.

In the topical area of detection, we develop specialized correlation (subspace) detectors for the principal mines surrounding the ARCES station located in the European Arctic. Our objective is to provide efficient screens for explosions occurring in the mines of the Kola Peninsula (Kovdor, Zapolyarny, Olenogorsk, Khibiny) and the major iron mines of northern Sweden (Malmberget, Kiruna). In excess of 90% of the events detected by the ARCES station are mining explosions, and a significant fraction are from these northern mining groups. The primary challenge in developing waveform correlation detectors is the degree of variation in the source time histories of the shots, which can result in poor correlation among events even in close proximity. Our approach to solving this problem is to use lagged subspace correlation detectors, which offer some prospect of compensating for variation and uncertainty in source time functions.

OBJECTIVE

One of the most important and challenging aspects in seismic calibration is assessment of location accuracy for candidate reference events. Location accuracy criteria based on network coverage has been developed for routine bulletins (e.g. Bondar et al., 2003), where single-event algorithms make use of contributed phase picks. These objective criteria allow efficient assessment of large volumes of bulletin data. However, there is an increasing trend towards the application of multiple-event algorithms combined with careful analyst review to develop reference-event bulletins (Armbruster et al., 2002; Engdahl et al., 2002). The currently accepted criteria (Bondar et al., 2003) are not applicable to – and probably over estimate – location errors determined by using multiple-event algorithms. One of the primary benefits of multiple-event locations is the determination of station corrections based on the best-located events; in effect, diminishing the importance of reference velocity model accuracy. Here we present preliminary results for seismic location accuracy studies using the Nevada Test Site (NTS) nuclear explosions with known locations. To test the importance of the velocity model accuracy, 74 events are relocated using 4 distinct travel-time models.

In the second part of this study we examine the use of waveform subspace detectors in Fennoscandia. The National Nuclear Security Administration (NNSA) Ground-Based Nuclear Explosion Monitoring Research and Engineering (GNEM R&E) Program at Lawrence Livermore National Laboratory (LLNL) is conducting research on subspace (i.e. generalized correlation) detectors for use in mine-event screening. Regional mining explosions dominate detections at some seismic monitoring stations. This is particularly true of the ARCES array, where the large mining districts of the Khibiny Massif, Zapolyarny, Olenogorsk, Kovdor and northern Sweden (iron mines Malmberget and Kiruna) constitute up to 90 percent of detections. Here, we present initial efforts to develop screening detectors for application to the mines of the Khibiny Massif.

RESEARCH ACCOMPLISHED

Location Accuracy

Dataset

We make use of the NTS dataset (Walter et al., this Proceedings), with known event locations, to study the accuracy of relative seismic locations. The 74 explosions and 61 regional stations used in this study are shown in Figure 1. An individual LLNL analyst re-picked these events to produce a high-quality dataset. The 1577 LLNL phase arrivals, with best-fit regressions, are shown in Figure 2. National Earthquake Information Center (NEIC) phase picks augment the LLNL dataset in some of our relocations, but only picks whose residuals are within three standard deviations of the empirical curves are kept. The number of picks outside the three standard deviation bound far exceeds statistical expectations (including the LLNL picks). In large part, transient clock errors are thought to account for the “heavy tails” in the residual distribution in this dataset (Walter et al., this Proceedings).

Travel-time models

Events are re-located using four travel-time models. The first model consists of linear, empirical fits to LLNL phase picks (Figure 2): two other models are derived from regional surface-wave modeling (Patton and Taylor, 1984 and Priestly and Brune, 1978). Finally, we test IASPEI91 for comparison with a global average. The Pn arrivals reduced by predictions from the four models are shown in Figure 2b. The regression model fits best, followed by Patton & Taylor, Priestly & Brune, and IASPEI91. Ordered ranking of model fit to Pg and Lg arrivals (not shown) is the same as for Pn, and we use this order when assessing the importance of the travel-time model accuracy for multiple-event location accuracy.



Figure 1. NTS explosions (red cluster of stars near the southern Nevada boarder) and regional stations used for relocation (blue cluster of stars shown near the northern region of Utah).

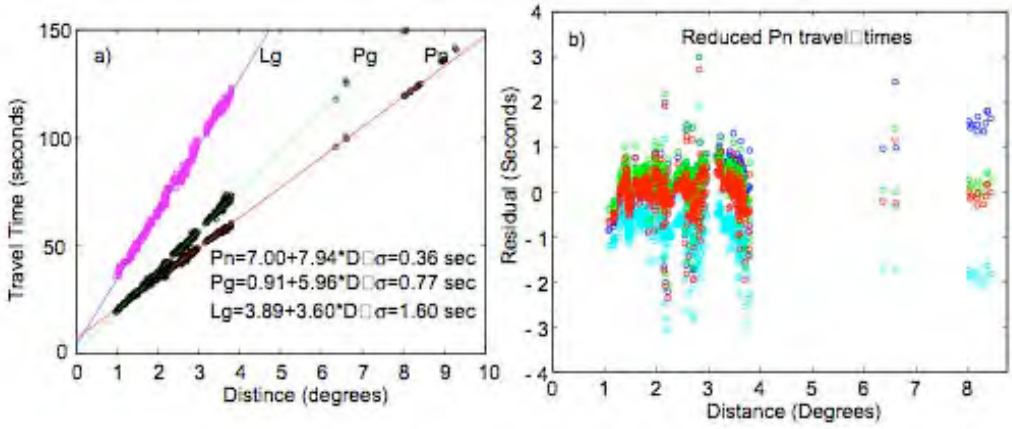


Figure 2. a) Empirical travel time curves for NTS explosions with travel-time models from linear regression. b) Pn arrival times reduced using IASPEI91 (blue), Priestly & Brune (cyan), Patton & Taylor (green) and a new LLNL model (red).

Location algorithm

We use the Grid-search Multiple Event Location (GMEL) algorithm (Rodi et al., this Proceeding) and briefly note its highlights here. GMEL is formulated within a maximum likelihood estimation framework and implemented numerically with grid search and Monte Carlo techniques; it does not rely on the usual assumption of local linearity

of the forward problem. Station-specific travel-time corrections are determined using residuals from grid-search locations. This process is iterated to convergence. One of the relevant features of GMEL is the ability to constrain any number of events to the known location, therefore, supplementary information (e.g. satellite images) may be used to improve accuracy of an event cluster.

Location experiments

We simultaneously relocate 74 NTS nuclear explosions with known hypocenters using the GMEL locator. New locations are determined using each of the four travel-time models described above. All hypocenters are unconstrained during inversion. We do, however, remove outlier arrival-time data, as identified using known hypocenter information, in an attempt to isolate model error. Figure 3 shows mislocations in map-view with corresponding mislocation histograms plotted in Figure 4. It is apparent that locations derived from the empirical travel-time curves are most accurate, with mean mislocation of 3.3 km and 95% of the locations within 6 km of the known epicenter. Considering the careful review of each phase arrival and the empirical nature of the travel-time curves, this degree of accuracy (~GT6) is likely to approach the lower bound of regional location accuracy for this dataset. We acknowledge that waveform correlation, which is not used for any of our arrival times, could reduce the uncertainty of arrival times, and thus location error.

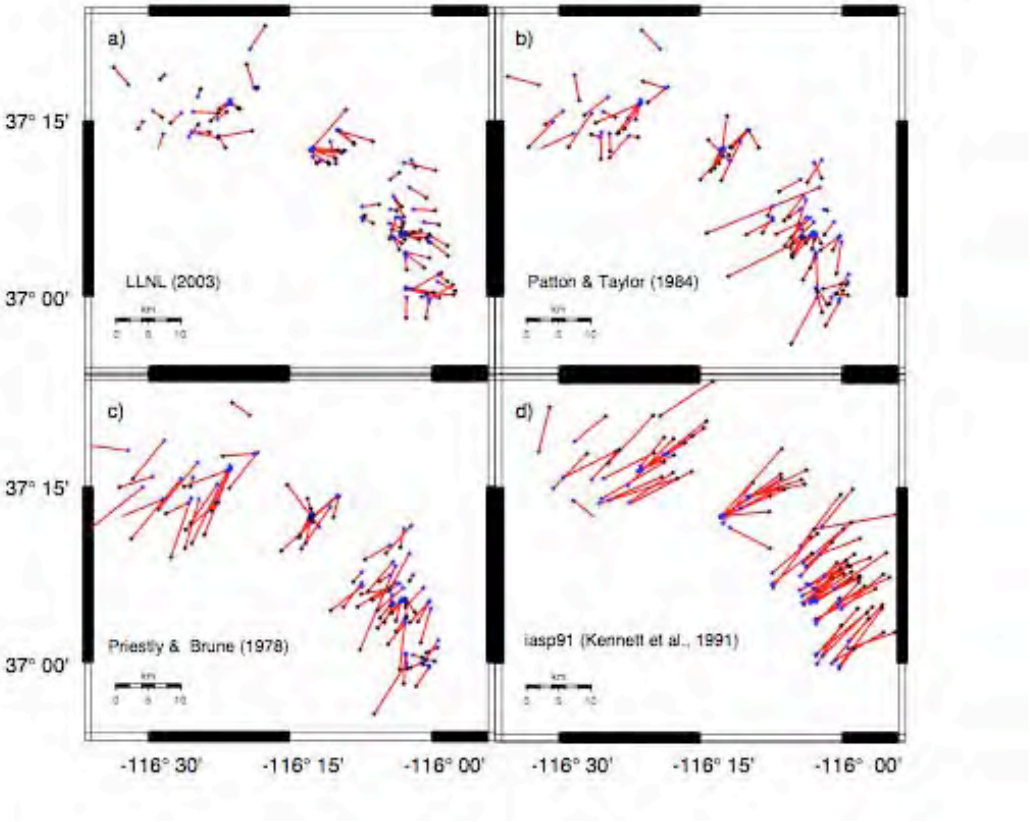


Figure 3. Multiple-event location epicenter errors for 4 models a) LLNL empirical curves, b) Patton & Taylor, c) Priestly & Brune, and d) IASPEI91. Blue stars and black dots are known and estimated locations, respectively. Note how each model imparts a distinct vector bias.

Similar to previous studies, we find that model error can contribute significantly to multiple-event mislocation, and this is apparent in Figures 3 and 4, parts b, c, and d. For the most part, increased error is manifested as a bias, with each model producing a distinct vector shift in the locations. The mean location accuracy of the Patton and Taylor, Priestly and Brune, and IASPEI91 models is 4.5 km, 5.6 km, and 9.9 km, respectively; the 95% bound on location accuracy is 8.7 km, 12.8 km, and 13.3 km, respectively. Using the error from the empirical curves as a baseline, we deduce that the model component of error is between 1.2 (Patton and Taylor) and 6.6 km (IASPEI91) in this study.

We note that in other parts of the world, observed regional IASPEI91 residuals can be more than twice that observed in the Basin and Range of Nevada. Therefore, regional application of a global model is probably unwise, even when using a multiple location algorithm and groomed dataset.

The correlation between travel-time prediction and epicenter error is shown in Figure 5. Epicenter error is plotted against "known" and estimated travel-time prediction errors. "Known" errors are determined using known hypocenter parameters, and estimated travel-time errors are derived from GMEL posteriori residuals. It is apparent that epicenter and known travel-time prediction errors are highly correlated, and that model-based, travel-time prediction error remains significant even when using a multiple-event algorithm. Perhaps more important is the lack of reliability in the correlation between estimated model error and location accuracy. Although the first three models suggest a weak correlation between estimated model error and location accuracy, the IASPEI91 point significantly deviates from this trend. We conclude, therefore, that travel-time residuals should not be used to access location accuracy. This conclusion is consistent with previous studies (e.g. Myers and Schultz, 2000; Bondar et al., 2003), where confidence ellipses (based on posteriori residual distributions) significantly underestimate true location error.

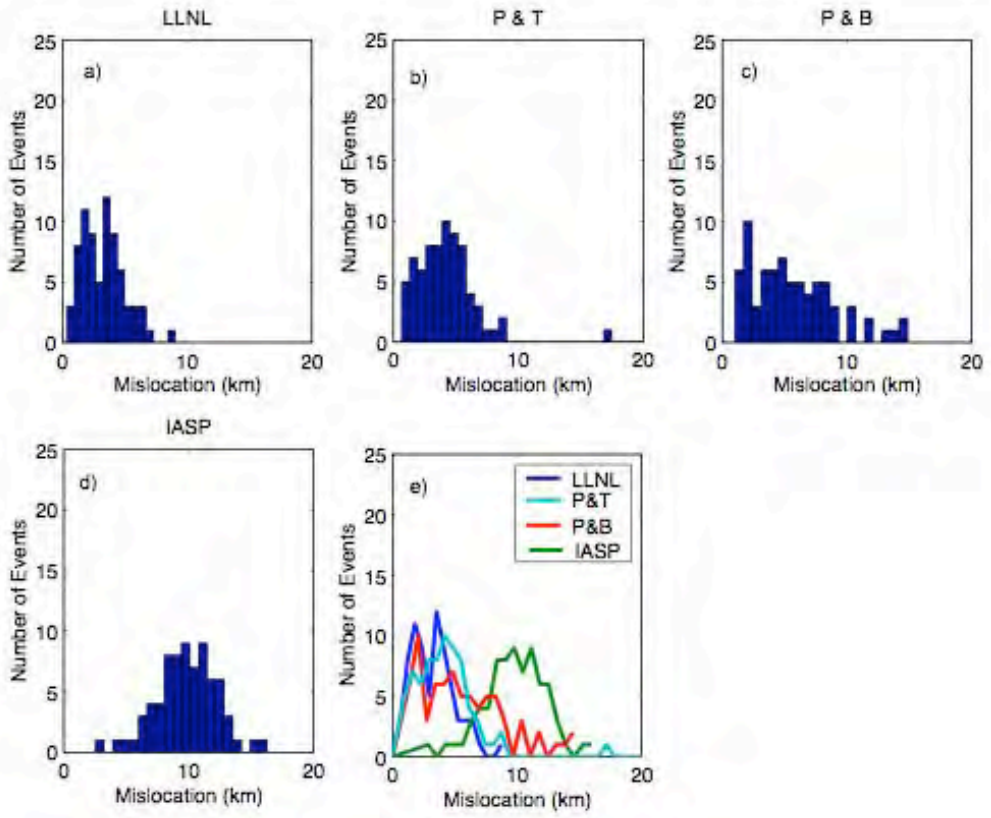


Figure 4. Histograms of epicenter error for the 4 velocity models. a) LLNL empirical travel-time curves. b) Patton and Taylor (1994). c) Priestly and Brune (1978). d) IASPEI91. and e) is a composite of parts a through d for comparison.

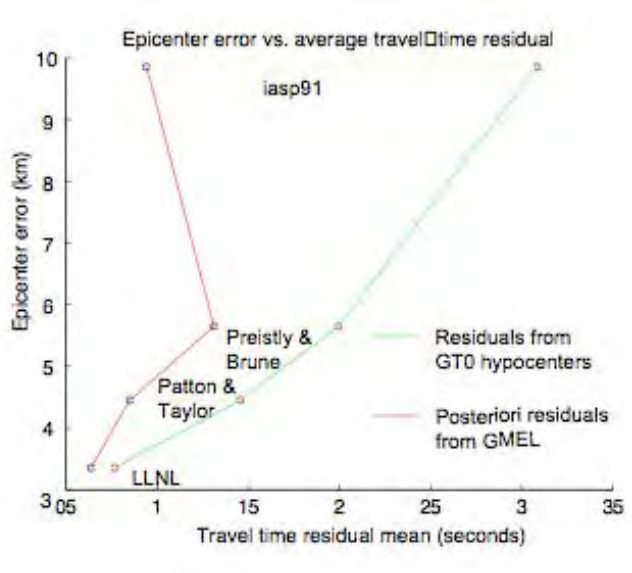


Figure 5. Mean epicenter error is plotted against mean absolute deviation (MAD) of travel-time prediction error for each of the 4 models. All phases are used for location (Pn, Pg, and Lg). The green line connects points determined using "known" travel-time errors (i.e., determined using known hypocenters). The red line connects points determined using relocation posteriori residuals. The green line shows a clear correlation between locations and "known" travel-time error, however, the correlation is not as clear when posteriori residuals – which are necessarily used in earthquake studies – are used to assess travel-time prediction error.

Lastly, our regional results suggest better location accuracy than the broader study of Bondar et al. (2003). Bondar et al., (2003) conclude that regional events with good azimuthal coverage (secondary azimuthal gap<120°) are accurate to within 20 km at 95% confidence. In the present study we find that IASPEI91 produces locations with accuracy of ~13km at 95% confidence. The discrepancy is probably due to a combination of factors, including: the use of analyst-reviewed arrival times; the use of the multiple-event location algorithm, which reduces errors attributable to 3-dimensional Earth structure; and IASPEI91 is better suited to the Basin and Range than many other regions of the world.

Subspace Detector

The master-event waveforms from the 40-event cluster were decomposed into time-series basis functions. A subset of the basis is used as the signal representation in the subspace detector. The size (dimension) of the subset is chosen to maximize the probability of detection and minimize false alarms. Figure 8 shows one of the diagnostics used to determine the size of the basis subset. It displays the energy capture, i.e. the fraction of waveform energy contained in the basis (least-square) representation of the waveforms as a function of the selected dimension of the representation. The figure displays 40 separate curves in blue to represent the energy capture for each of the 40 master event waveforms. The single red curve represents the average energy capture for the suite of events. A significant number of the signals are not well represented except at very large subset dimension (approaching 40); this fact suggests a high degree of diversity among the signals generated by this mine and potentially poor correlation detector performance.

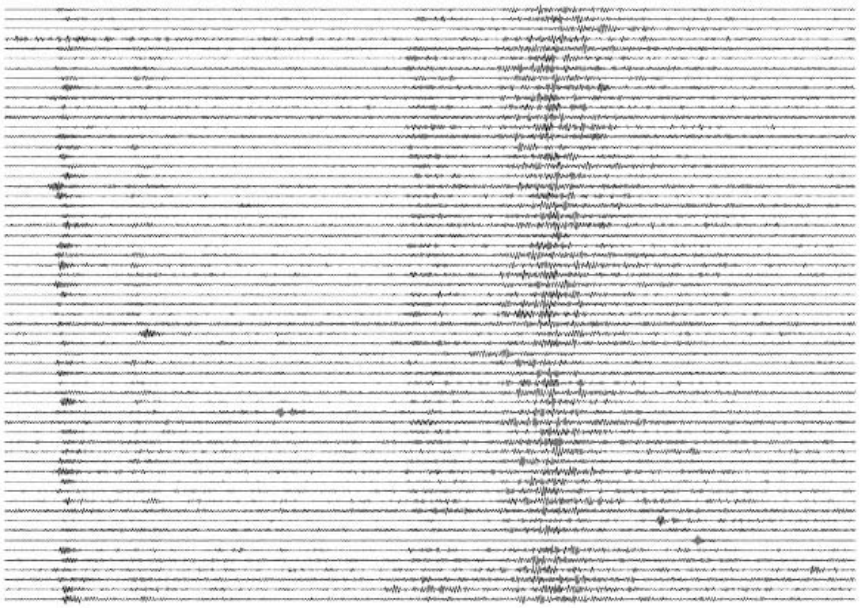


Figure 6. Master waveforms for the 61 event of the Kirovsk mine recorded at ARCES.

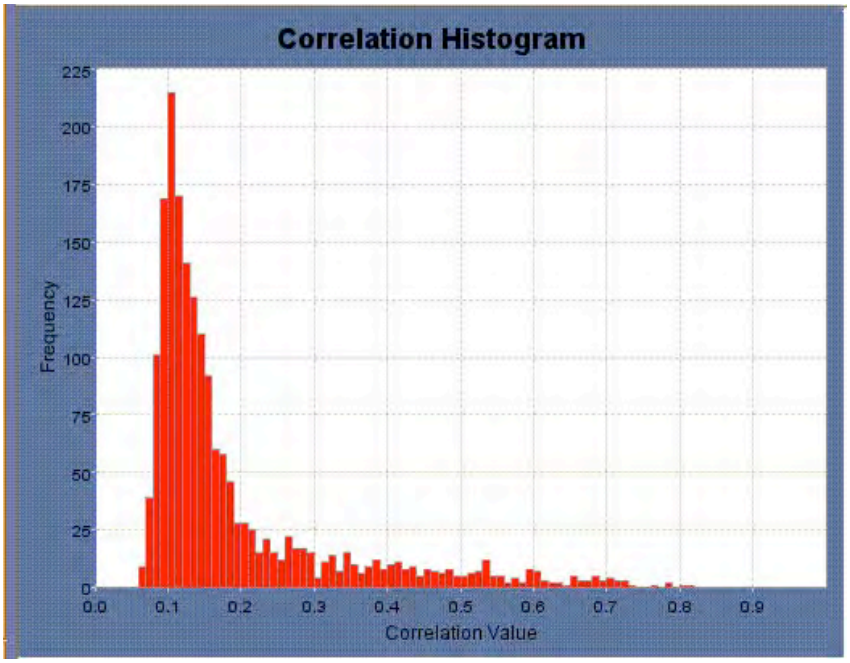


Figure 7. Histogram of correlation values for the 61 master events. Despite our efforts to select events with similar firing practice, waveform correlation tends to be low. The subspace detector makes use of the disparate waveforms to span the possible waveform characteristics for a particular mine.

The master-event waveforms from the 40-event cluster were decomposed into time-series basis functions. A subset of the basis is used as the signal representation in the subspace detector. The size (dimension) of the subset is chosen to maximize the probability of detection and minimize false alarms. Figure 8 shows one of the diagnostics used to determine the size of the basis subset. It displays the energy capture, i.e. the fraction of waveform energy contained in the basis (least-square) representation of the waveforms as a function of the selected dimension of the representation. The figure displays 40 separate curves in blue to represent the energy capture for each of the 40 master event waveforms. The single red curve represents the average energy capture for the suite of events. A

significant number of the signals are not well represented except at very large subset dimension (approaching 40); this fact suggests a high degree of diversity among the signals generated by this mine and potentially poor correlation detector performance.

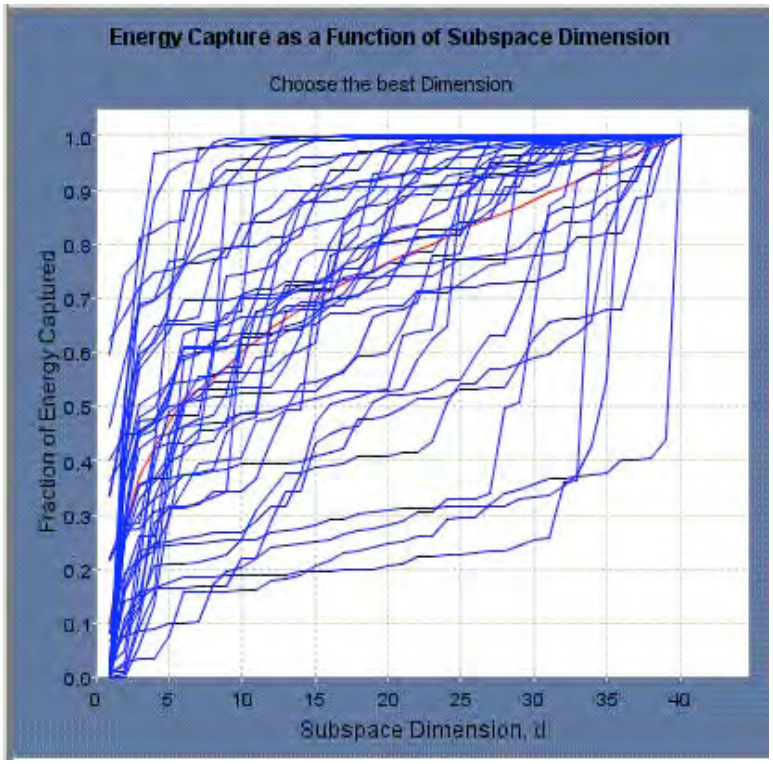


Figure 8. Fraction of energy captured for each of the master-event waveforms is plotted against a trial subspace detector with varying dimension. This analysis is used to select detector subspace dimension (see text).

A theoretical probability of detection can be calculated for a subspace detector constructed with a basis of given dimension. The operating assumption is that the detector conducts a binary hypothesis test on the presence of white Gaussian noise (the null hypothesis) in a detection window, or on noise plus a signal represented as a linear combination of the basis functions (the alternate hypothesis). Figure 9 shows a suite of theoretical probability of detection curves, one for each possible choice of subspace dimension. The single curve highlighted in red shows the probability of detection for a subspace detector of dimension 15 generated from the 40 master event waveforms, for a fixed threshold (0.4). The probability of detection curve actually is a hybrid, consisting of the average probability of detection for the collection of 40 events assuming all were equally likely. At the selected threshold, the probability of a false alarm is vanishingly small.

This detector was run on a data window consisting of the first 40 days of 2003 for a limited number of ARCES elements. The detector made nine detections for this time interval, missing 19 events that are known to have occurred at the Kirovsk mine during this interval. The false alarm rate was zero, as expected. Our result suggests that for the Kirovsk mine, the variability of firing practice and geographic distribution of sources produces an exceedingly diverse set of waveforms. It is possible that a master-event set drawn from a longer time window is needed to capture the full waveform variability.

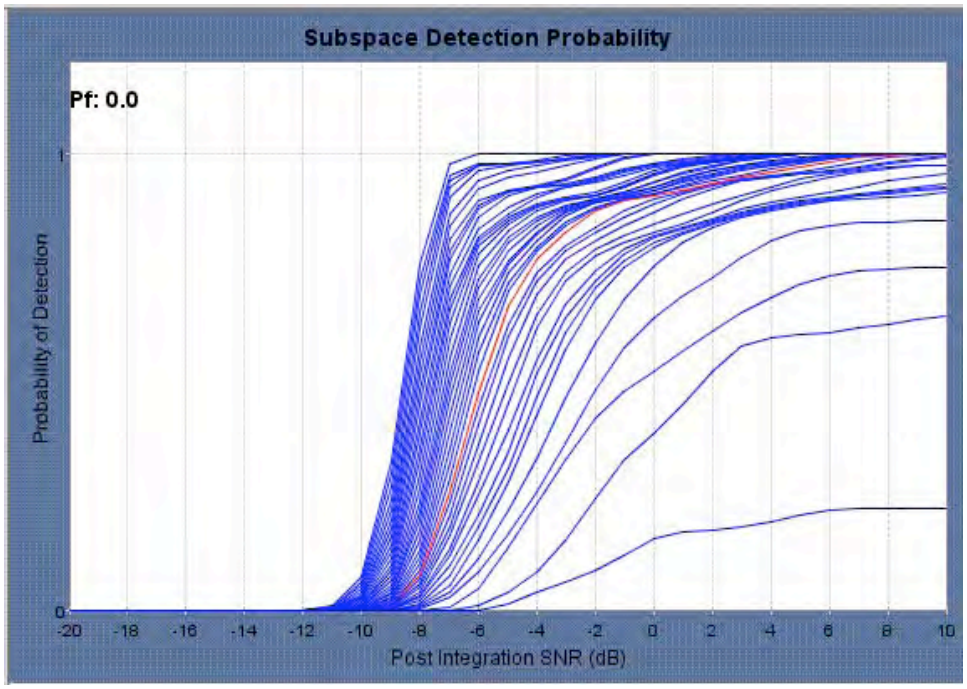


Figure 9. The probability of detection for subspace detectors is a function of the order of the detector. A subspace detector designed from 50 master event waveforms can have an order ranging anywhere from 1 to 40. This suite of curves displays the theoretical probability of detection for each possible detector order. The red curve corresponds to the order 15 detector actually used in our attempt to detect Kirovsk compact underground mining events.

CONCLUSIONS AND RECOMMENDATIONS

NTS Regional-Network Location Study:

1) For our groomed dataset, empirical travel-time curves (derived using the known NTS hypocenters) produce GT6 locations. (Note: our dataset does not include correlation picks, which– where applicable – may further improve location accuracy).

2) Two other Basin and Range models (based on surface-wave modeling) produce GT9 and GT13 locations. The IASPEI91 model produces GT14 locations.

3) Epicenter and "known" travel-time prediction accuracy (derived from known NTS-explosion hypocenters) are well correlated. However, the correlation between epicenter and estimated travel-time prediction (multiple-location posteriori residuals) is not reliable. Therefore, assessment of location accuracy based on travel-time fit is also not reliable.

Subspace Detector

1) Subspace detection is a valuable tool for detecting and screening on-going, mine-related seismicity.

2) For our case example (Kirovsk mine) the false alarm rate is zero but detection rate is currently about one third.

3) For the Kirovsk mine a master-event set spanning a long time window (current set is from a 3-month period) may be needed to improve the detections rate.

ACKNOWLEDGEMENTS

We continue to enjoy a dialog on seismic location research with William (Bill) Rodi, who also provided the GMEL location codes. Much of the NTS dataset was developed in cooperation with Kenneth D. Smith at University of Nevada, Reno.

REFERENCES

Armbruster, J., V. Burlacu, M. Fisk, V. I Khalturin, W.Y. Kim, I. Morozov, E. Morozova, P. G. Richards, D. Schaff, and F. Waldhauser, Seismic Location Calibration For Thirty International Monitoring System Stations In Eastern Asia, *"Proceedings of the 24th Seismic Research Review: Nuclear Explosion Monitoring: Innovation and Integration", 2002,* Los Alamos National Laboratory *LA-UR-02-5048*, pp 231-241. Ponte Verde, FL.

Bondar, I., S.C. Myers, E.R. Engdahl, E. Bergman, Epicenter accuracy based on seismic network criteria, *Geophys. Jour. Int*., In Press, 2003.

Engdahl, E. R., E. A. Bergman, M. H. Ritzwoller, N. M. Shapiro and A. L. Levshin, A Reference Data Set For Validating 3-D Models, *"Proceedings of the 24th Seismic Research Review: Nuclear Explosion Monitoring: Innovation and Integration", 2002,* Los Alamos National Laboratory *LA-UR-02-5048*, pp 261-270, Ponte Verde, FL.

Myers, S. and C. Schultz, Improving Sparse-Network Seismic Location with Bayesian Kriging and Teleseismically Constrained Calibration Events, *Bull. Seism. Soc. Am*., 90, 199-211, 2000.Patton, H.R., S.R. Taylor, Q-Structure of the Basin and Range from Surface-Waves, Jour. Geophys. Res., 89 (NB8): 6929-6940 1984.

Priestley K.F., J. N. Brune**,** Surface-Wave Dispersion In Great Basin Of Nevada And Western Utah, Eos T Am Geophys Un 57 (12): 951-951, 1976

Rodi, W, C. A. Schultz, W. G. Hanley, S. Sarkar, and H. S. Kuleli, Grid-Search Location Methods For Ground-Truth Collection From Local And Regional Seismic Networks, *"Proceedings of the 24th Seismic Research Review: Nuclear Explosion Monitoring: Innovation and Integration", 2002,* Los Alamos National Laboratory *LA-UR-02-5048*, pp 394-402, Ponte Verde, FL.

Schultz, C., S. Myers, J. Hipp, and C. Young (1998), Nonstationary Bayesian Kriging: Application of Spatial Corrections to Improve Seismic Detection, Location and Identification, *Bull. Seism. Soc. Am*., 1275-1288.

Walter, W.R., K. D. Smith, J. L. O'Boyle, T. F. Hauk, F. Ryall, S.D. Ruppert, S.C. Myers, M. Anderson, and D.A. Dodge, Improving The Fundamental Understanding Of Regional Seismic Signal Processing With A Unique Western United States Dataset, *Proceedings of the 25th Seismic Research Review: Nuclear Explosion Monitoring: Building the Knowledge Base*, Tucson, AZ, 2003.

IMPROVEMENTS IN MONITORING OF SMALL REGIONAL EVENTS BASED ON GROUND TRUTH DATA IN TURKEY AND ISRAEL

Vladimir Pinsky,[1] Yefim Gitterman,[1] Avi Shapira,[1] Mehmet Ergin,[2] and Cemil Gurbuz[3]

Geophysical Institute of Israel (GII);[1] TUBITAK Marmara Research Center;[2]
Bogazici University, Kandilli Observatory and Earthquake Research Institute (KOERI)[3]

Sponsored by Defense Threat Reduction Agency

Contract No. DTRA01-00-C-0119

ABSTRACT

To upgrade local crust models and estimate site-specific station corrections (SSSCS) for more accurate hypocenter location, a number of controlled quarry blasts (GT0) were recently conducted in the Marmara Sea region, close to the Izmit earthquake (17 August 1999). Both the blasts and well-constrained aftershocks (GT5) were recorded by the KOERI network and TUBITAK stations in Turkey. The blasts were located using arrival times and two 1-D crustal models: 1) the KOERI model for regional location; 2) a modified model from refraction profiles. Improvement was achieved by using model 2 and VELEST, an optimization procedure. The improved models were used to relocate selected Izmit aftershocks. Relocation experiments, including calculation of the hypocenter ellipsoid and Monte-Carlo simulation, were performed to verify accuracy and reliability of new hypocenter estimations.

We continued the program of calibration explosions in Israel, conducting a series of controlled quarry blasts to the North of the Sea of Galilee, including a 25-ton shot to complement the 2002 Rotem explosion in the Negev desert, providing better signal observations in Cyprus, Lebanon, Syria and Turkey. The closely spaced (~50 km) 1999 Dead Sea and 25-ton Rotem calibration explosions were recorded at the same stations in Israel, Jordan, Cyprus and Saudi Arabia, providing observations for similar propagation paths. The data enabled an analysis of the influence of different sources on amplitudes, waveform and spectral content of regional phases. The calibration explosions, located in the Dead Sea fault zone, provided a variety of results in the context of nuclear test monitoring: a) accurate travel time corrections for regional phases relative to IASPEI91 and GII models at stations of local networks and the International Monitoring System (IMS), b) verification and improvement of velocity models, c) estimation of attenuation and magnitude-yield relations, d) characterization of new seismic sources and local mining practices, and multi-station discrimination analysis.

We provided a pilot performance analysis for a new IMS array on Mt. Meron, Israel (MMAI or AS49), operational in January 2003. The 16-element small aperture array is equipped with broadband Gurlap seismometers placed in deep (50 –100 m) boreholes. The MMAI detectability and signal parameter estimation was analyzed by the standard and adaptive beamforming techniques using data from the recent controlled quarry explosion series in Israel and regional GT5 earthquakes. New robust beamforming techniques have been developed and applied to the array data, showing promising results for enhancing monitoring capabilities in the region.

The 2Dtracerdn software was used to compute SSSCs of the Pg, Pn, P, Sg, Sn, S phases for the eight stations: EIL, MRNI, BRAR, DAVOS, KVAR, MLR, GERESS and OBN, using the 3D velocity model CUB1.0. For stations EIL, MRNI and BRAR we have computed SSSCs in the direction of small areas in Cyprus and Turkey (Izmit, Duzce and Adana), containing selected Ground Truth (GT0-GT5) sources. The results have been compared to the observed deviations between the measured and IASPEI91 travel times from the ground-truth (GT) events.

OBJECTIVE

The main objective is to characterize and enhance the nuclear explosion monitoring potential in the eastern Mediterranean area through building a regional knowledge base, including upgrading local crust models, and estimating site-specific station corrections for more accurate hypocenter locations, using ground-truth events.

RESEARCH ACCOMPLISHED

Marmara Controlled GT0 Blasts and Location Analysis

To upgrade local crust models and estimate site-specific station corrections for more accurate hypocenter locations, a number of controlled quarry blasts (GT0) were recently conducted in the Marmara Sea region.

Numerous seismic events in the Istanbul area (east and southeast of the Marmara Sea) were recorded at KOERI and TUBITAK stations during the past two years (Figure 1a). The data analysis shows that not all of them are earthquakes, because the distribution of events does not follow the known fault systems. A survey of the area revealed quarries conducting regular production blasts (Figure 1b). Most of these quarries are located to the east of Istanbul.

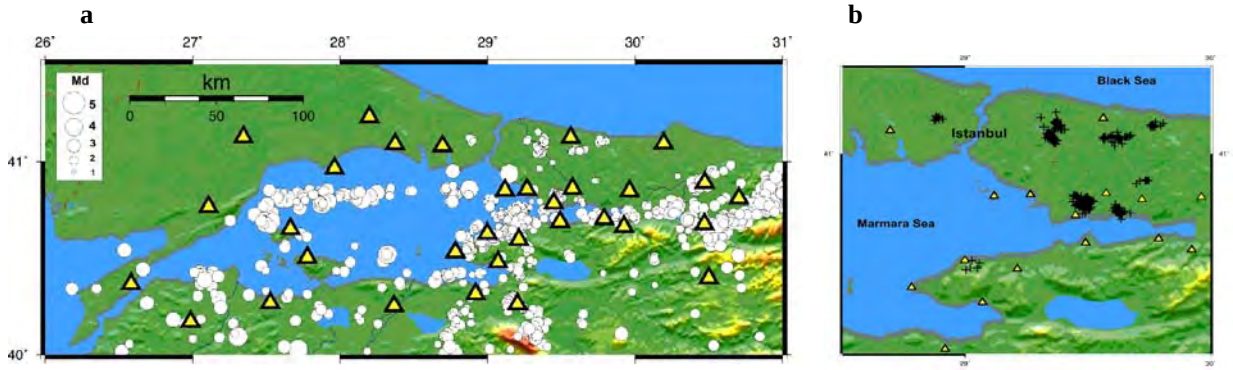
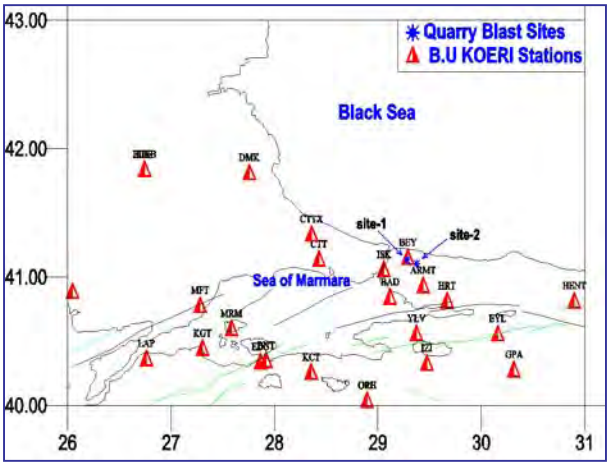


Figure 1. Epicenter distribution in the Marmara Region (2001-2002) (a), and explosion clusters near Istanbul (b).



The KOERI project team visited some of the areas and found that large explosions were conducted in two locations (Figure 2). We measured the coordinates, recorded origin times and collected blast design parameters (see Table 1). First arrival times were measured with seismic sensors (equipped with GPS) placed near (50–100 m) the blast site, providing relatively accurate estimates of origin (detonation) time.

Because the blasts are single-fired there is no delay between holes. Several blasts with ground-truth (GT0) information were recorded at distances up to 80 km from the shot point by the KOERI seismic network stations (Figure 3). We used this data to perform the location analysis.

Figure 2. Map of quarry blast sites and local recording stations.

The quarry site location was estimated based on the arrival times and three crustal models for the study area (Table 2): 1) the KOERI starting model 1 which is used in the Kandilli laboratory to locate earthquakes in and around Turkey; 2) the

KOERI modified model obtained from ray-tracing modeling of refraction studies in the region; and 3) the TUBITAK crustal model.

Table 1. Parameters of the controlled Marmara quarry blasts.

#	Quarry site	Date	Origin time	Closest station, km	Charge, kg	Hole depth,m	Number of holes
1	#1-Soyak 41.102N 29.375E	31.07.2002	12:50:01.79	~4(BEY)	1030	7	14
2		05.08.2002	13:38:41.80	0.1	1300	8	16
3	#2-Lafarge 41.116N 29.295E	14.08.2002	10:15:40.55	~4(BEY)	735	8	41
4		14.08.2002	10:24:17.70	~4(BEY)	800?	-	-
5		16.08.2002	09:15:11.55	0.05	210	8	15
6		26.08.2002	09:28:33.20	~4(BEY)	900?	-	-

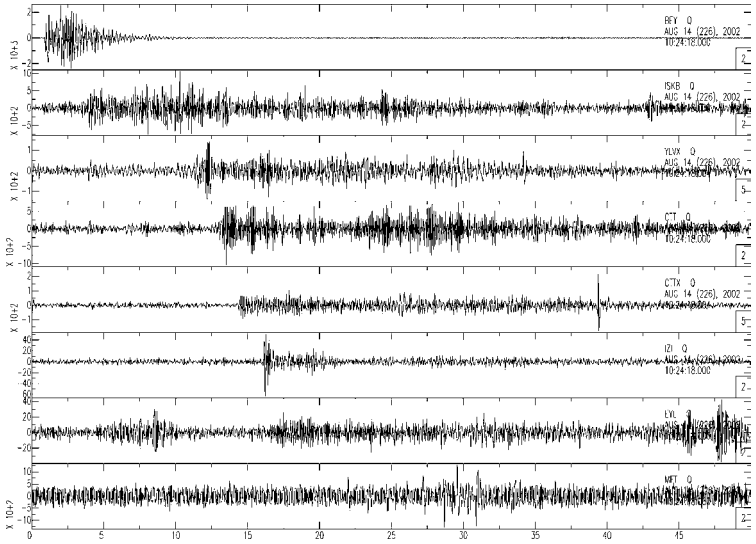


Figure 3. Seismograms of the Marmara blast No.4 (14.08.2002) recorded at KOERI stations used for the location analysis.

Table 2. Crustal models used for the Marmara blasts location analysis.

Vp,km/sec	Depth, km
KOERI starting model 1	
4.500	0.000
5.910	5.400
7.800	31.600
8.300	89.200
KOERI modified model 2	
3.800	0.000
5.700	2.100
6.100	4.000
6.800	25.000
7.800	31.600
8.300	89.200
TUBITAK crustal model 3	
2.25	0
5.70	1.0
6.10	6.0
6.80	20.0
8.05	33.0
8.07	40.0

We found a significant improvement in location and origin time estimation by applying the corrected crustal structure model 2 for the area (Table 3). The error estimation was made based on the ground-truth location and origin time of the blasts.

Table 3. Location analysis of the Marmara blast No.4, 14.08.2002 (Hypo71 results).

Type	Origin Time	OT error	Lat.	Lat. error	Long.	Long. error	Depth, km	Depth error	RMS	N of stations
GT data	10:24:17.7	-	41.116	-	29.295	-	0	-	-	-
Model 1	10:24:17.13	0.57	41.1541	0.038	29.2711	0.024	5.0	5.0	0.21	8
Model 2	10:24:18.02	0.32	41.1337	0.018	29.2827	0.012	0.2	0.2	0.1	8

An additional location calibration study, based on the Marmara GT0 blasts, was performed to estimate the accuracy of the seismic event locations and to reduce the size of error ellipses. The KOERI, TUBITAK, and ISTANBUL municipality stations, all within a distance of 100 km, were used. The existing KOERI velocity model was improved by examining the residuals of well-recorded events. A new velocity model 3 (Table 2) was obtained that reduced the error.



Three velocity models (Table 2) were used to calculate travel time residuals using the HYPOCENTER earthquake location software.

We compared the models using location errors and error ellipses (Figure 4). For event N1 the location obtained using model 1 (red) was shifted 3 km southwest with respect to the ground-truth location and is much larger than it is for models 2 and 3. The largest error ellipse was also obtained for model 1. The model 2 error ellipses are relatively small but biased and do not include the true location. Both small ellipses and unbiased locations are obtained with model 3 which should be used for earthquake location in this area.

Figure 4. Horizontal error ellipses of the Marmara quarry blasts, obtained from the three models.

Israel Calibration Explosions

The closely spaced (~50 km) Dead Sea and 25-ton Rotem calibration explosions (Gitterman et al., 2002) were recorded at the same stations in Israel, Jordan, Cyprus, and Saudi Arabia (Figure 5) and provide observations for similar propagation paths; thus, allowing a comparison of source properties such as amplitudes, waveform, and spectral content of regional phases. In order to quantify the differences between these two calibration events, we examined the Power Spectral Density (PSD). For each component, 2 time windows were defined that corresponded to P- and S-waves. The windows begin at the P, S wave onsets and end 20 sec later.

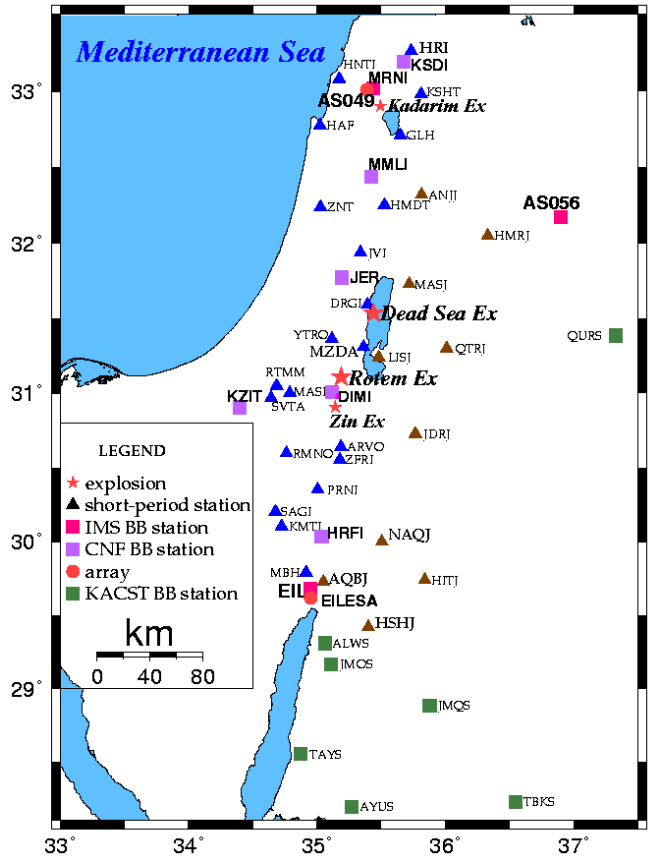
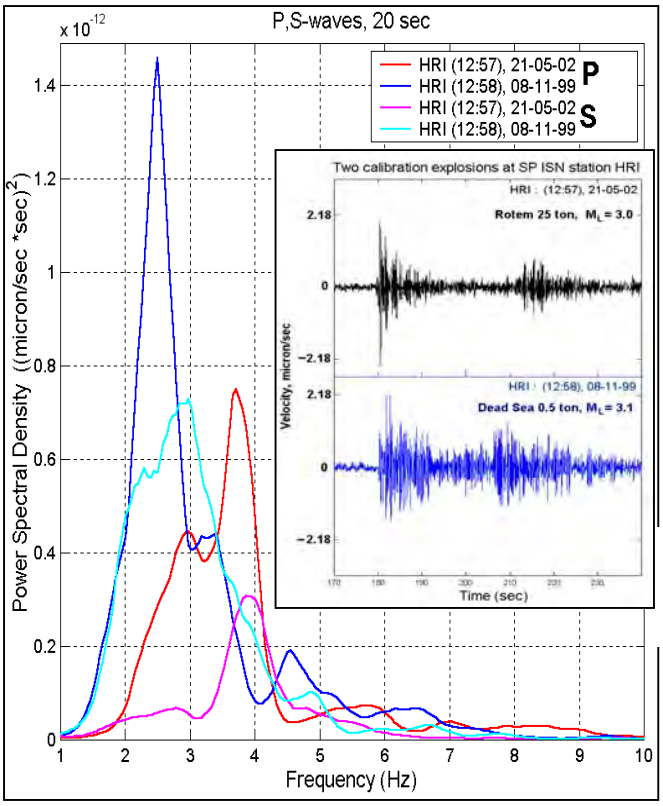


Figure 5. Calibration explosions in Israel and observing stations.

The spectra in Figure 6 exhibit higher power of P-waves (compared to S-waves) for both explosions. Spectral energy of both P and S waves for the land Rotem 25 ton blast is lower, compared to the underwater Dead Sea 0.5-ton shot, and shifted (by 1–1.5 Hz) to higher frequencies. However, the Rotem blast, which has a smaller local magnitude (M_L=3.0) than the Dead Sea shot (M_L= 3.1), shows stronger P-wave amplitudes and better quality of the first arrival (though recorded at a larger distance).

The 25-ton Rotem blast records at several Saudi Arabia stations of the KACST network were recently obtained at the RELEMR workshop in Paris in October 2002. Clear signals were observed up to 346 km away (station TBKS, see Figure 7), but stations located at range >700 km did not show a signal. At three stations (QURS, ALWS, and TBKS) we have records of the Dead Sea 2-ton explosion, M_L=3.6 (data for the 0.5-ton shot are not available). We also compared waveforms and spectral content of P and S-waves.

The P-wave spectra for ALWS station (Figure 8) shows lower energy for the Rotem blast than the 2-ton Dead Sea explosion in the range 1–6 Hz, and similar power at higher frequencies. It is noteworthy that spectral curves for the land blast show similar peaks and troughs to the underwater explosion, believed caused by the bubble pulse (Gitterman and Shapira, 2001). The reason for this is not clear.



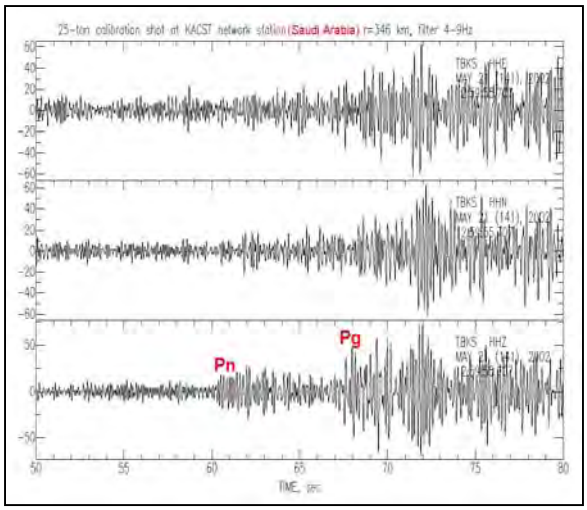


Figure 7. Clear regional phases P, Pg were found at BB station TBKS (Saudi Arabia) after narrow band-pass filtration (4-9 Hz).

Figure 6. Seismograms and PSD of P and S waves at vertical short-period station HRI at distances 194 km from the Dead Sea 0.5 ton shot (08-11-99) and 245 km from the Rotem 25-ton shot (21-05-02).

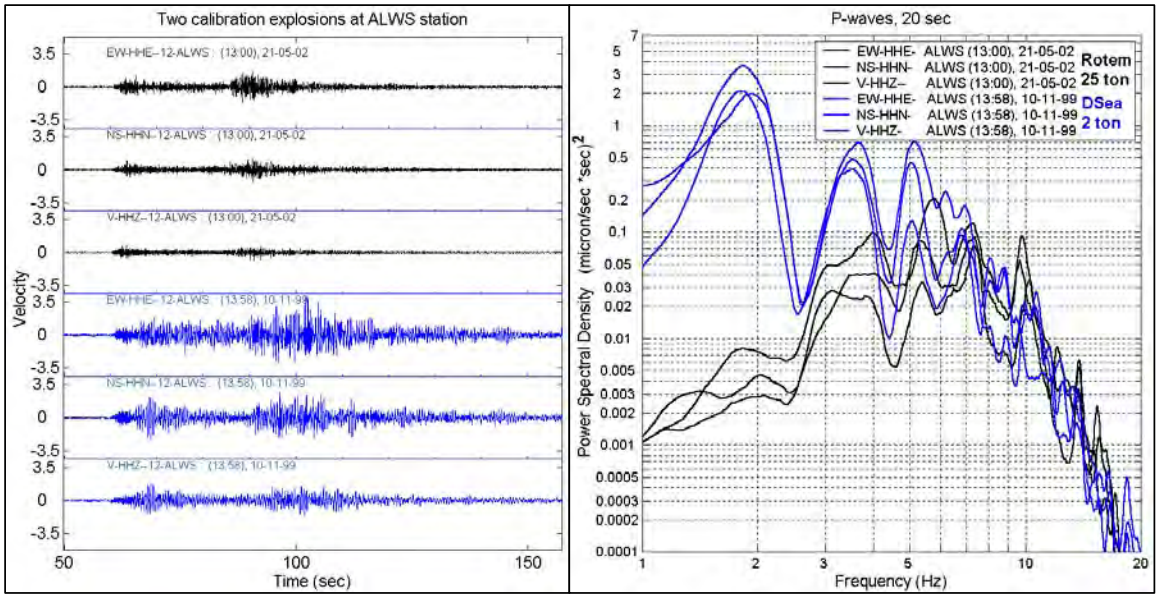


Figure 8. Seismograms and PSD of P waves at BB station ALWS (Saudi Arabia) at distances of 248 km from the 2-ton Dead Sea explosion (10-11-99) and 200 km from the 25-ton Rotem blast (21-05-02).

During the preparation of the second 25-ton calibration explosion in northern Israel, we conducted a number of controlled (GT0) test blasts at the Kadarim quarry (see Figure 5). The goals were: 1) ensuring the safety of nearby buildings in this densely populated area by measuring blast ground motions near the buildings and comparing them to predicted values from an empirical relationship and a code safety threshold; and 2) determining capability of the planned 25-ton explosion to provide the desired magnitude M_L=2.8-3.0. Data from these blasts will also be used to estimate attenuation, magnitude-yield relations, characterization of new seismic sources and local mining practices, and multi-station discrimination analysis.

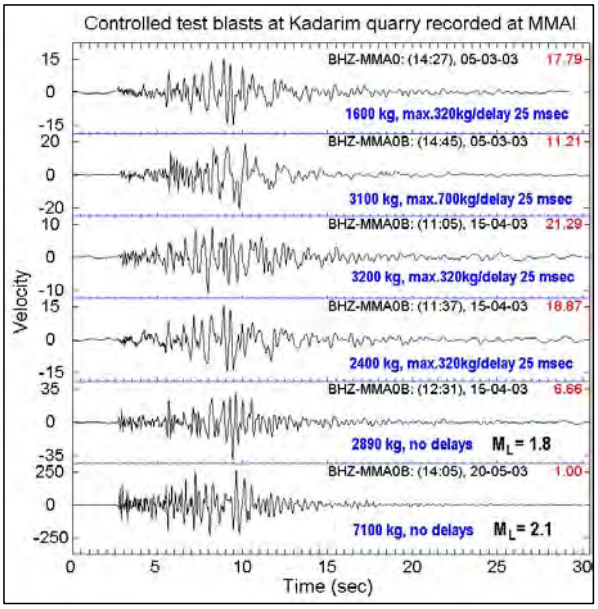


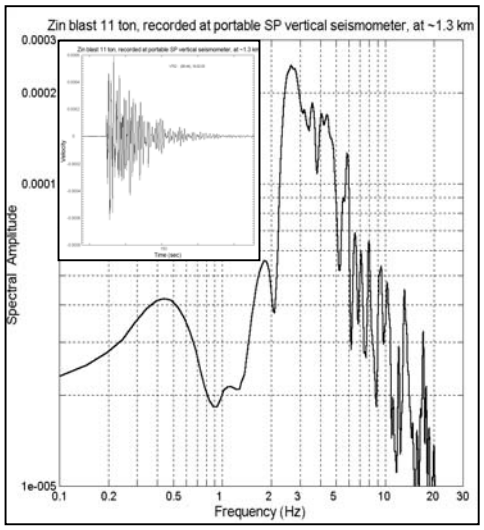
Figure 9. Records of controlled ripple-fired and instantaneous quarry blasts at central BB vertical element of the IMS array MMAI at Mt. Meron.

For the strongest blast the magnitude value was lower (2.1) than expected (2.4-2.5) for an instantaneous blast (Gitterman, 1998). Blast energy loss was caused by the small separation between the first hole and the bench face (2-3 m); this needs to be increased for the big calibration explosion.

We collected records of these blasts at the new IMS array MMAI (AS049) that started operation at Mt. Meron in early 2003 (Figure 9 {A: where is the Figure 8 callout?}). The blasts discussed above are located a short distance (r = 12.5 km) from the array. We also conducted a controlled (routine) 11-ton blast (16.02.2003) in the Zin quarry, Negev (Figure 5), at r=237 km. This first dataset of GT0 events at MMAI array can be used for regional calibration of this IMS station.

The Zin blast record at a close-in (~1.3 km) portable seismometer (see inset on Figure 10a) can be considered an approximation of the source spectrum, showing most of the energy in the range 2-6 Hz (Figure 10a). Background noise records at MMAI have most energy at lower frequencies (0.1-1 Hz). Band-pass filtration in the 2 – 10 Hz band provides significant improvement of the signal-to-noise ratio and reveals clear P and S waves for the 11-ton blast (see inset on Figure 10b).

a



b

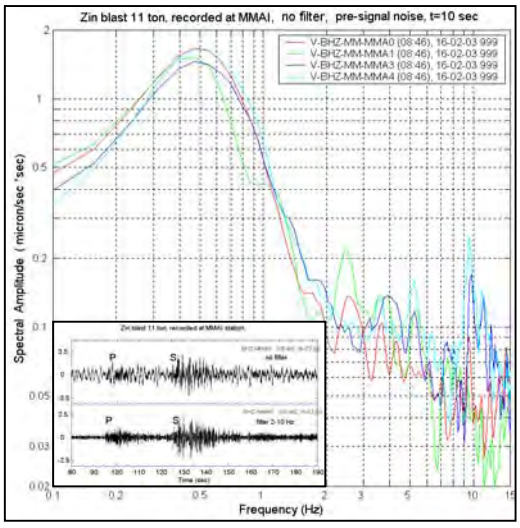


Figure 10. Spectral analysis of the near-source record of the Zin blast (a) and pre-signal noise (b) was used to improve SNR at MMAI records.

Travel Time Evaluation

First arrival (P/Pn) travel time deviations relative to the IASPEI91 and local GII velocity models for the Rotem and Dead Sea calibration explosions were calculated and are presented in Figure 11. Travel time deviations for P waves relative the IASPEI91 and GII models are plotted on a map where color of the station symbol (triangle) corresponds to a delay value based on the palette.

The deviations show that at small distances (up to 90 km) the difference between observed and IASPEI91 travel time can be corrected by using the local (GII) velocity model. However, at the northern stations AS049 (212 km, IMS surrogate station), KSDI (235.3 km), and HRI (245 km) there is still a delay of ~1 sec. For the southern stations EIL and HRFI (120 km, 160 km) and the IMS station AS056 in Jordan, the respective negative delay was also observed. In general, for distances R > 125 km, the difference between the two model travel times and the observations diminishes.

A difference ~1 sec is found in travel time corrections (relative to IASPEI91) for some Saudi Arabia stations (ALWS, TBKS, BDAS/TAYS) obtained from the closely spaced (~50 km) calibration shots: in the Rotem quarry (Figure 11 a) and in the Dead Sea (Figure 11 c). Note the Rotem quarry is in the Negev desert while the Dead Sea is in the Dead Sea fault zone, a different geological setting.

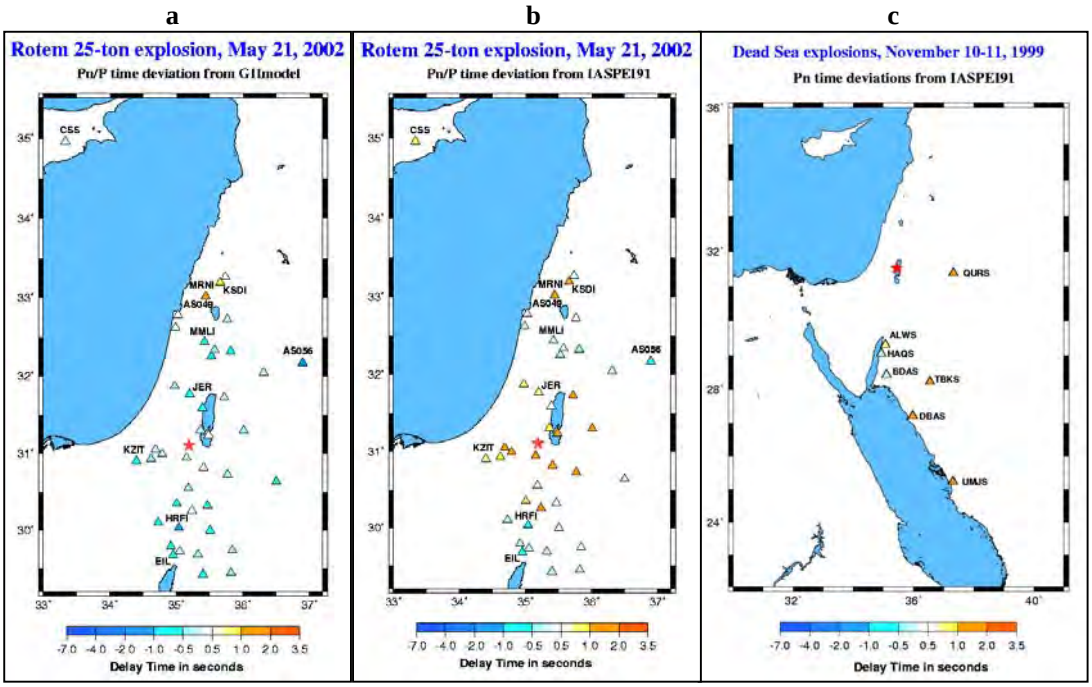


Figure 11. Discrete regional map of Pn/Pg travel-time deviations for the Rotem (a, b) and Dead Sea (c) calibration explosions recorded at local network stations.

Computation of SSSCs for the Middle East-East Mediterranean Region

To improve the IMS event location in the region, we investigated Pn travel times calculated with the best existing 3-D velocity models compared to measured values from the GT events database. For this investigation we installed at GII the crust and mantle 3-D CUB1.0 velocity model, developed by the Geophysics Group of Colorado University (CU) Physics Department (Ritzwoller and Levshin, 1998), and the 2Dtracerdn software (Barmin et al., 2001). The CU 3-D model was obtained from inversion of broadband surface-wave dispersion data on a 2°×2° grid and the application of a simple scaling relationship $d(\ln V_P) = 0.5d(\ln V_S)$. The rays and travel times (SSSCs) have been calculated up to 2,000 km distance for stations EIL, MRNI, and BRAR (see Figure 12).

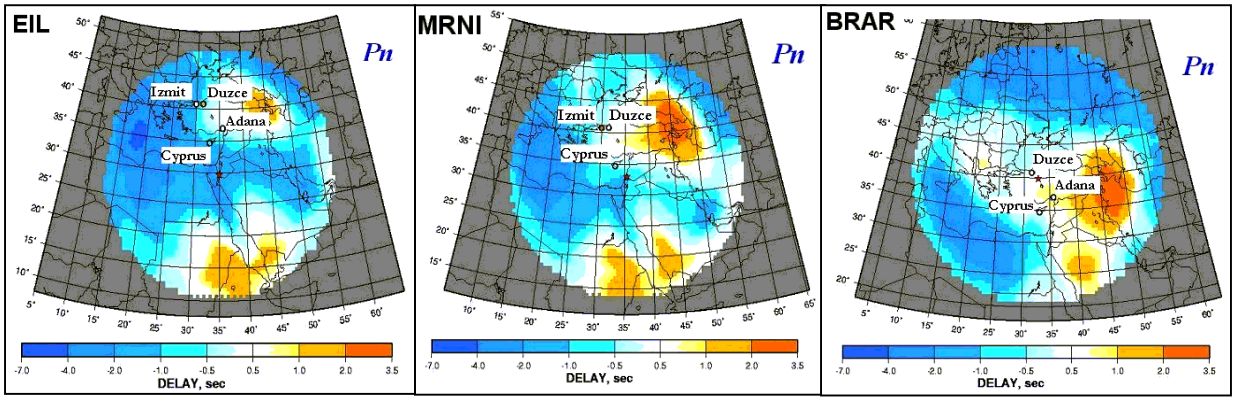


Figure 12. SSSCs for Pn relative to IASPEI91, depth H=10 km, for the three IMS stations.

The model-based travel time computations were compared to those obtained from arrival time measurements and hypocenter estimation of the GT events collected in the areas of Duzce, Izmit, Adana (Turkey), and Cyprus. The measured time delays for different GT events were calculated as: $dM=TT-TT_{IASP91}$, where $TT=AT-OT$ - travel time, determined by the measured arrival time AT at the IMS stations EIL, MRNI, and BRAR with GT origin parameters OT, Lat, $Long$, and depth H, taken from the results of the relocation experiment (Pinsky et al, 2001). For calculation of the TT_{IASP91} we used the *ttimes* program (Kennett and Engdahl, 1991).

The dM values are averaged according to $EdM = \Sigma\, k_j\, dM_i / \Sigma k_j$, where weights k_j are determined by the SNR, and are depicted in Figure 12 as colored circles plotted on the contoured SSSCs from CUB 1.0, which are computed for the source depth H=10 km.

Match of a circle and the background color indicates coincidence of the measured and CUB1.0 predicted travel times. For many cases we have good agreement between the measured and calculated SSSCs. However, there are a number of large discrepancies at various sites (see, for example, Duzce for EIL, Izmit for MRNI).

Pilot Performance Analysis for New IMS Array on Mt. Meron and a New Robust Beamformer

The 16-element modern array AS049 (MMAI) has the potential to notably increase the nuclear test monitoring capability in the region (see Figure 13a). The array geometry (3.1-km long, 2.3-km wide) is shown in Figure 13b. Although this site is regarded as the best suited for this purpose in Israel and the array seismometers are deployed in deep boreholes for noise abatement, there is a significant level of noise generated by a number of technological sources in the area. Sporadic bursts are often seen on only one or several of the array channels, causing a non-stationary noise process. As a result of the mountainous character of the landscape, the geology around the array is very heterogeneous—leading to waveform distortions and random delays. Therefore, we immediately confronted a deficiency of signal coherency at mutually remote stations leading to both reduced detection capability and location accuracy.

To solve the problem we started to develop a new robust beamforming technique. In the frequency domain beamforming is equivalent to the calculation at each discrete frequency f a scalar product $w=\boldsymbol{H}^*\boldsymbol{X}$, where $\boldsymbol{X}$ is a DFT vector of observations: $\boldsymbol{X}^{\mathrm{T}}=(x_1,x_2,\ldots,x_M)$, and $\boldsymbol{H}$ is a vector of DFT plane wave delays: $\boldsymbol{h}_m(k)=exp(-i2\pi f\tau_m)$, where plane wave time delay $\tau_m=(d1_m, k)$. For an ideal array without noise and signal distortion and an ideal plane wave coming with wave number vector k_0, vector $\boldsymbol{X} = x_1 H(k_0)$, and, thus, $w = M\, x_1$.

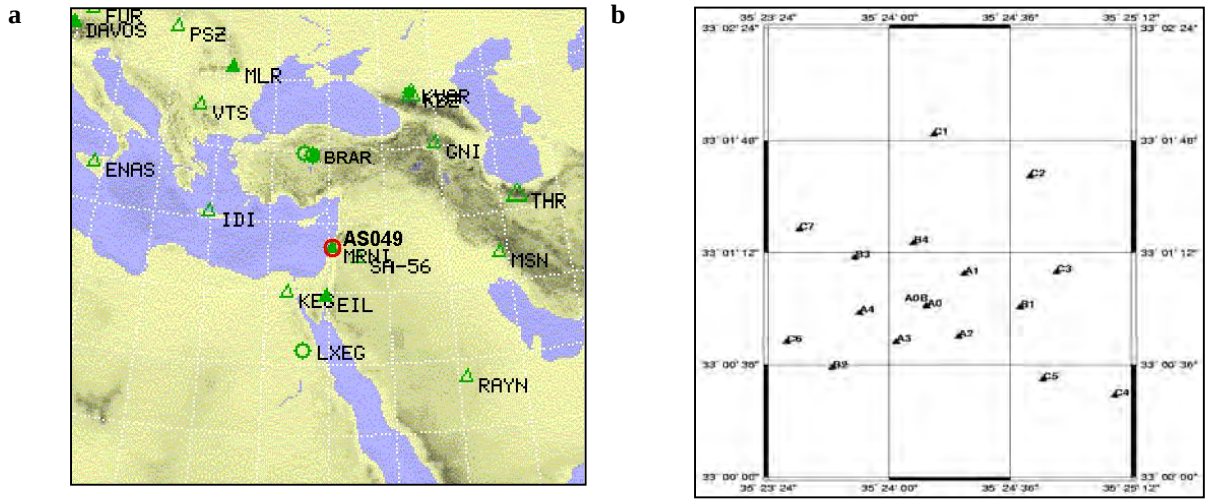


Figure 13. Location (a) and configuration (b) of the AS049 array, Mt. Meron, Israel

The wave number vector k_0 is estimated by maximization of $|w|^2$. In fact, the assumption as stated above is rarely valid for all the array stations, thus reducing beamforming effectiveness, however, it may remain so for a subnetwork. Let us introduce a bell-shape function $y=\varphi(t)$: $\{\varphi(0)=1,\ \varphi(t) \to 0 \text{ when } t \to \infty\}$ and compute the statistic:

$$v = \max_{\theta\in(0,2\pi],k\in K,f\in\Phi} \sum_{m=1}^{M} \varphi[\arg(h_m^* x_m) - \theta], \quad (1)$$

where K- slowness range, Φ- frequency range. In the ideal case v=M. In the adaptive beamforming case

$$W = H^* * F^{-1} X \ \ /(H^* F^{-1} H), \quad (2)$$

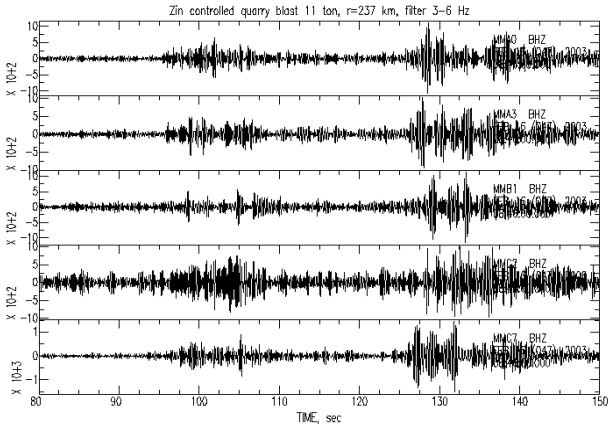


Figure 14. Five BP-filtered (3–6 Hz) channels of the *AS049 array

where $\boldsymbol{F}$ is a noise spectral density matrix $\boldsymbol{F} = \mathbf{E}\boldsymbol{N}\boldsymbol{N}^*$. Since the denominator in (2) is a real number, then for computation statistic equivalent to (1) we should substitute x_m by components y_m of the vector $\boldsymbol{Y} = \boldsymbol{F}^{-1}\boldsymbol{X}$, where $\boldsymbol{F}^{-1}$ is inverse or pseudo-inverse of matrix $\boldsymbol{F}$. Thus, finally the target statistic is

$$u = \max_{\theta\in(0,2\pi],k\in K,f\in\Phi} \sum_{m=1}^{M} \varphi[\arg(h_m^* y_m) - \theta] \quad (3)$$

We performed a pilot study of the robust beamforming based on observations of the controlled explosions at the Israel quarries mentioned above. An example of the analysis for the Zin quarry blast (ground truth azimuth 186.5°) is presented in Figures 14 and 15.

Low SNR (~1) is observed at the array records, and first Pn arrivals can hardly be seen even after heavy BP filtering in the 3–6 Hz frequency band (see Figure 14). However, estimates of the azimuth Az and apparent velocity V, shown in the F-K diagram (Figure 15) at frequency F=1.9 Hz, correspond well to the ground-truth values for both the conventional (Az=195°, V=6.4 km/s) and "robust" beamforming (1) (Az=184.7, V=8.3 km/s) (see Figure 15 a, b). To demonstrate the stability of the "robust" beamforming, the channel B2 was distorted. The conventional beam failed, however, the "robust" beamforming result remained almost unchanged (see Figure 15 c, d).

CONCLUSIONS AND RECOMMENDATIONS

Controlled quarry blasts are a relatively cheap and useful tool to deliver information needed for underground nuclear test monitoring, such as velocity models, travel time and azimuth corrections, characterization of the influence of propagation path and source on waveforms, and spectral contents, magnitudes, etc. Using data from controlled quarry blasts we improved the velocity model and event location in the Marmara region, Turkey, and provided calibration information for the IMS stations EIL and AS049 in Israel. The Kadarim quarry test blast series provided data for conducting a second large 25-ton calibration explosion in Northern Israel. Two calibration explosion sites, the Dead Sea shot point and the Rotem quarry, were close enough to assume different propagation paths for the close stations and similar propagation paths for the remote stations, allowing evaluation of source and path effects.

Spectral estimates of the signal from the Zin quarry explosion, Negev, at a close-in portable station and the AS049 array provided information to estimate the path effect of a 237-km segment along the Dead Sea fault. The explosion data were also used for apparent velocity and azimuth calibration and tuning of a new robust beamforming algorithm at the array. This pilot research revealed the high potential of the array to extract weak signals from noisy seismograms and showed the effectiveness of a robust approach in location of small events under difficult conditions of heterogeneity and impulsive cultural noise. The new technique showed promise; however, it is relatively time consuming and must contend with large stationary and mutually correlated noise. Further investigation will be devoted to calibrating azimuth and apparent velocity estimations around the array, development of the adaptive robust beamformer, and tuning of its parameters. A large statistical experiment is planned to estimate the effectiveness of the new technique under various conditions.

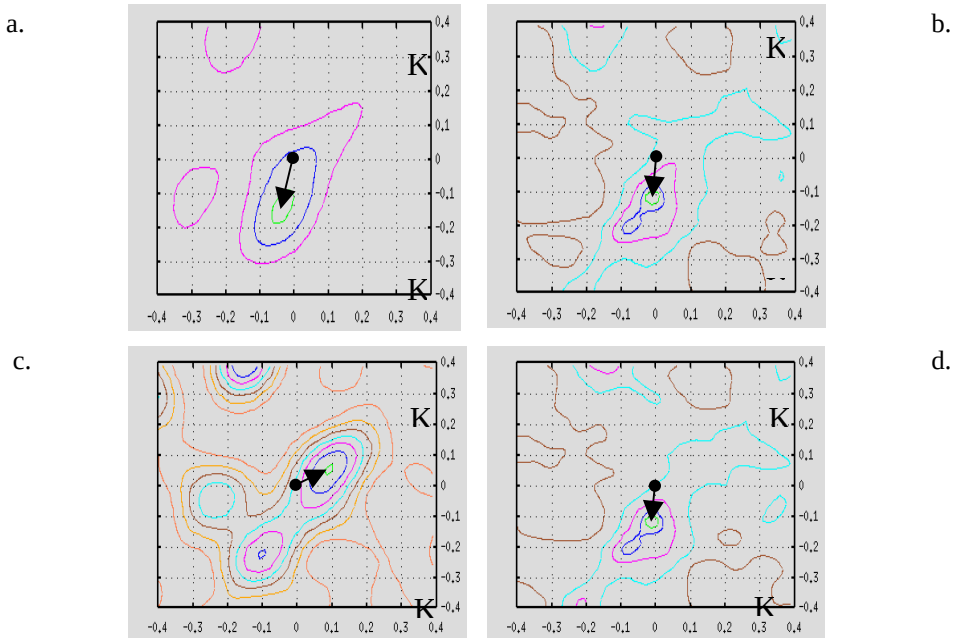


Figure 15. Comparison of conventional (a, c) and robust (b, d) beamforming in the F-K domain, applied to the Zin explosion (Az=186.5, V=7.9 km/s) at a time point t=92 sec, time window length l=3.2 sec, frequency 1.9 Hz, before (a, b) and after (c, d) the distortion of the B2 channel signal.

REFERENCES

Barmin, M.P., M.H. Ritzwoller, and A.L. Levshin (2001), A fast and reliable method for surface wave tomography, *Pure and Appl. Geophys.*, Volume 158, Issue 8, 1351-1375.

Gitterman, Y., V. Pinsky, A. Shapira, M. Ergin, D. Kalafat, G. Gurbuz, K. Solomi (2002), "Improvement in detection, location and identification of small events through joint data analysis by seismic stations in the Middle East/Eastern Mediterranean region," *Proceedings of the 24th Seismic Research Review – Nuclear Explosion Monitoring: Innovation and Integration*, 17-19 September 2002, Ponte Vedra Beach, Florida, pp. 271-282.

Gitterman, Y. and A. Shapira (2001), Dead Sea Seismic Calibration Experiment contributes to CTBT Monitoring, *Seismological Research Letters*, Vol. 72, Num. 2, March/April 2001, 159-170.

Gitterman, Y. (1998), Magnitude yield correlation and amplitude attenuation of chemical explosions in the Middle East, Proceedings of the 20th Annual Seismic Research Symposium on Monitoring a Comprehensive Nuclear Test Ban Treaty, Santa Fe, Sept.21-23, 1998, 302-311.

Kennett, B.L.N. and E.R. Engdahl (1991), Travel times for global earthquake location and phase identification, *Geophys. J. Int.*, 105, 469 - 465.

Pinsky, V., Gitterman, Y., Goldshmidt, V., Shapira, A. (2001). Collection of regional calibration data within the area around the Israel Seismic Network. CTBTO Calibration Program - Phase 1. Annual Report on Contract 00/20/5024. November 2001, GIIRep. 571/155/01(2), 105 p.

Ritzwoller, M.H., and A.L. Levshin (1998). Eurasian surface wave tomography: Group velocities, *J. Geophys. Res.*, 103, 4839 - 4878.

SEISMIC LOCATION CALIBRATION FOR 30 INTERNATIONAL MONITORING SYSTEM STATIONS IN EASTERN ASIA: FINAL RESULTS

Paul G. Richards,[1] John Armbruster,[1] Valeriu Burlacu,[2] Vernon F. Cormier,[4] Mark D. Fisk,[2]
Vitaly I. Khalturin,[1] Won-Young Kim,[1] Igor B. Morozov,[3] Elena A. Morozova,[3]
Chandan K. Saikia,[5] David Schaff,[1] Anastasia Stroujkova,[4] and Felix Waldhauser[1]

Lamont-Doherty Earth Observatory of Columbia University,[1] Mission Research Corporation,[2]
University of Wyoming,[3] University of Connecticut,[4] URS Group[5]

Sponsored by Defense Threat Reduction Agency

Contract No. DTRA01-00-C-0029,[4] DTRA01-00-C-0031,[1,2,3] DTRA01-00-C-0033[5]

ABSTRACT

We have completed a three-year consortium effort to improve the capability to locate seismic events based on data acquired by 30 International Monitoring System (IMS) stations in East Asia.

We have developed and tested Source Specific Station Corrections (SSSCs) for Pn and Sn travel times at these 30 IMS stations (or suitable surrogates), and for 127 other stations used for validation testing. The SSSCs were initially computed by the method of Bondár (1999), using regionalized 1-D travel-time curves established after extensive review of published studies including many from the Russian literature. Subsequently we developed a 3-D model of the P-wave velocity for East Asia (using a set of 36 different regions in each of which we obtained velocity as a function of depth), and used 3-D ray tracing in the latter model to compute SSSCs. These model-based SSSCs were refined empirically by applying a kriging algorithm to travel-time residuals for ground-truth (GT) events. Off-line validation tests were performed by evaluating travel-time residuals and by relocating GT events, with and without using SSSCs. To test the validity of the model directly, relocation tests were first performed using model-based SSSCs without kriging. Tests were then performed to evaluate the kriged SSSCs, using a leave-one-out approach so that events were not simultaneously used to both compute and test the SSSCs.

Nuclear explosions dominated our ground-truth datasets in the first two years of this project. In particular we used source parameters for Soviet-era Peaceful Nuclear Explosions (PNEs). But this approach, while quite satisfactory for calibrating stations in much of Russia and Central Asia (which made up approximately half the IMS stations we studied) could not be extended to the remaining stations, for which it was necessary to develop GT information on significant numbers of earthquakes. By use of the double-difference method and detailed fault maps, we obtained 64 GT5 earthquakes by re-analyzing the Annual Bulletin of Chinese Earthquakes (ABCE) for a 15-year period (1985 to 1999). It contains phase picks for approximately 1000 earthquakes in and near China, each year. A preliminary examination of digital waveforms for about 14,000 events, in and near China, shows that approximately 9% of them (1301 events) have the property that any one event has almost the same Lg waveform as at least one other event. These events are grouped into 494 sets of events, each of which has essentially the same short-period waveform and thus the events of each set must be within about 1 km of each other. These event sets provide a good method for assessing the quality of standard event catalogs. When combined with other information, they can provide high-quality absolute locations.

Using Pn and Sn arrival times for our GT data sets, we relocated 525 events recorded by various combinations of 140 regional stations. Mislocations were reduced for 66% of the events using the model-based SSSCs, and for 85% of the events using model-based SSSCs refined by kriging. Median mislocation improved from 16.9 km to 11.4 km and 6.5 km, respectively. Median error ellipse area was reduced from 2,616 km^2 to 1,633 km^2 and 722 km^2, respectively. Error ellipse coverage (percentage of GT locations within 90% error ellipses) was 89% without using SSSCs, 91% using model-based SSSCs, and 92% using kriged SSSCs. These results were obtained for source locations, stations, and paths that sample very extensive and diverse geological provinces throughout much of Asia. The SSSCs are expected to perform, on average, as well as the test results using the model-based SSSCs, and substantially better for areas where GT calibration data were utilized to refine the SSSCs.

OBJECTIVE

The goal of this project has been to improve the accuracy of estimates of the location of seismic events — and to reduce the uncertainty of such estimates — on the basis of an interpretation of the arrival times of regional seismic waves observed at 30 stations of the International Monitoring System (IMS) located in Eastern Asia.

RESEARCH ACCOMPLISHED

Introduction

Our project began as a three-year effort in March 2000 and has now been completed. It has been a collaborative academic-industry research project led by Lamont and involving a consortium of five institutions. We developed a structural model of East Asia built up from 36 sub-regions, shown in Figure 1, and we also developed the capability to compute travel times in this model by 3D ray tracing. We developed a set of 525 ground-truth events (almost all them of GT5 quality or better), and their associated phase picks. In addition to calibrating 30 IMS stations we calibrated another 110 stations in East Asia. The total set of 140 stations and GT locations, and the Pn paths between them, are shown in Figure 2. We derived a set of model-based Source-Specific Station Corrections (SSSCs) for Pn and Sn from 3D ray tracing in our regionalized model, and we then used empirical arrival times and GT information to refine the model-based SSSCs by kriging. In this paper, we emphasize the end-to-end validation of our claims of significant location improvement when our SSSCs are applied to relocate seismic events in East Asia.

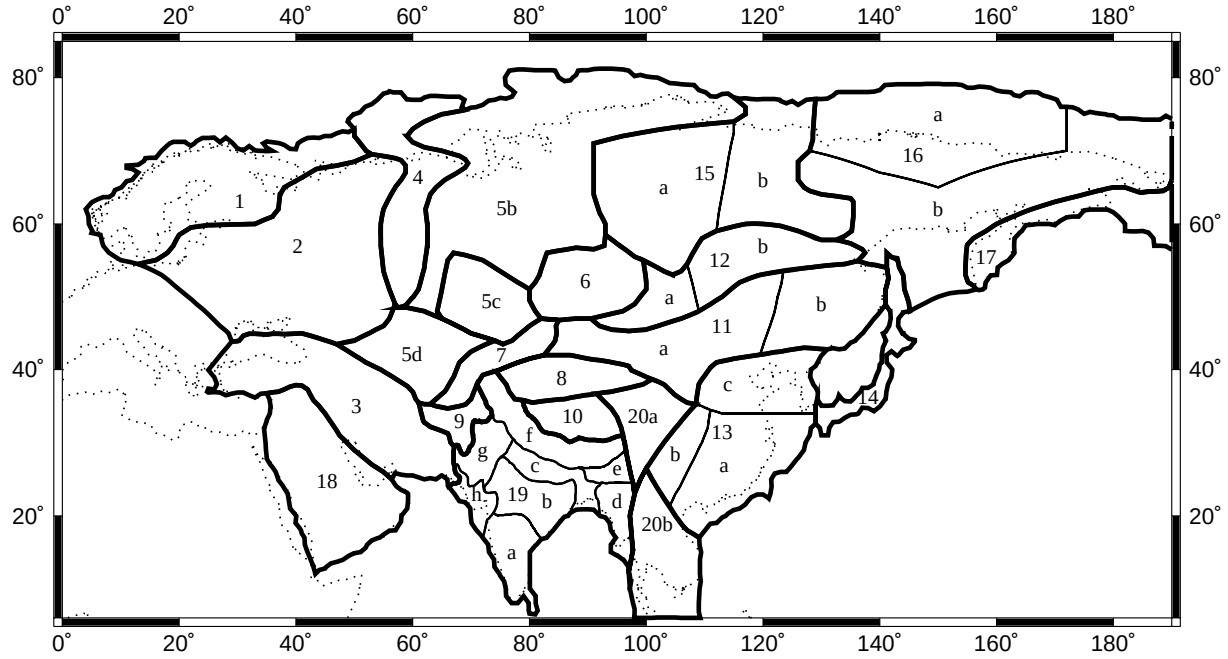


Figure 1. The region boundaries and numbering system used for 36 1D regions in East Asia and surrounding areas, which together make up the 3D velocity model in which 3D ray tracing was used to give our model-based SSSCs.

Further details of our work, including much information on how we obtained our regionalized model and numerous new GT events in East Asia (mostly, in and near China), are contained in Fisk (2002), Waldhauser and Richards (2003ab), Schaff and Richards (2003ab), Yang et al. (2003), and Burlacu et al. (2003). A CD has been prepared with our main final report (Burlacu et al., 2003) and 1871 additional files giving our data, including details of our 3D model, our GT events (including phase picks in CSS 3.0 format), and our model-based and kriged SSSCs. Our work has also been described in 11 papers presented at four Oslo workshops on location calibration organized by NORSAR from 1999 to 2003 (and appearing in the proceedings of those workshops), eight presentations at meetings

of the American Geophysical Union, the Seismological Society of America, and the International Association of Seismology and Physics of the Earth's Interior, and in Seismic Research Review meetings of 2000, 2001, and 2002.

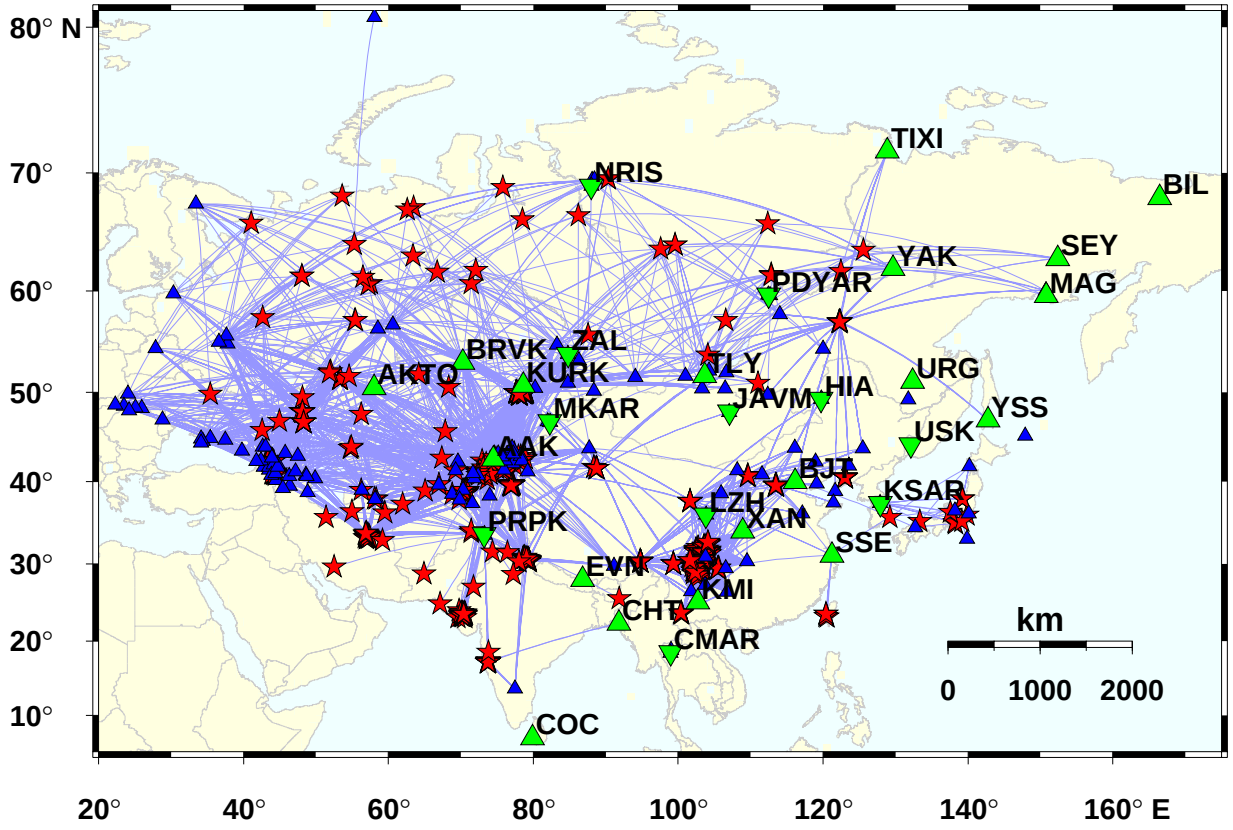


Figure 2. Map of events (red stars) and recording seismic stations (blue triangles) of the data set used for model validation. The green triangles represent the 30 IMS stations that our consortium was tasked to calibrate. Also shown are great circle Pn paths between events and stations.

Table 1. Mean and standard deviation of Pn and Sn travel-time residuals, in seconds, for all the stations that recorded at least 3 GT events.

Case	IASP91		Model-Based SSSCs		Model + Kriged SSSCs	
	$\mu_{\Delta T}$(s)	$\sigma_{\Delta T}$(s)	$\mu_{\Delta T}$(s)	$\sigma_{\Delta T}$(s)	$\mu_{\Delta T}$(s)	$\sigma_{\Delta T}$(s)
Pn	1.89	1.77	1.33	1.48	0.22	1.01
Sn	6.08	4.24	3.08	3.76	1.34	3.76

The tables and figures in this paper contain descriptions of our claims of location improvement, which have been the subject of a successful integration test conducted in May 2003 by the Research and Development Support System staff of the group then known as the Center for Monitoring Research.

As an overall indication of how well our SSSCs reduce the misfit between observed and calculated arrival times, Table 1 shows RMS values for the mean and standard deviation of the Pn and Sn travel-time residuals for all the stations that recorded at least 3 GT events. The kriged results were obtained via a leave-one-out approach in the generation of SSSCs, so that the arrival times from any one event were not used to provide the location estimate in that case. From this Table, we see that a very significant reduction of residuals is obtained by kriging.

In sections that follow, we describe a discovery concerning broad area seismicity of China which proved useful in generating ground truth reference events and which points the way to a future in which seismicity will be located by making use of waveforms rather than being based on phase picks. We then describe our model validation, and end-to-end validation of our kriged SSSCs, before giving our conclusions and recommendations.

A discovery concerning broad-area seismicity

As part of our work to generate ground-truth reference events in East Asia, we found that whole waveforms of regional signals, from a few seconds prior to the P arrival and running to several tens of seconds after the Lg arrival, were very similar for certain clusters of events. This result was first obtained for events (foreshocks, aftershocks) associated with a magnitude 5.9 earthquake in 1999 in the Xiuyan region of Liaoning Province, China (Schaff and Richards, 2003a). The correlation coefficient was above 0.9, for a time window of a few hundred seconds (recorded in the band from 0.5 to 5 Hz for stations several hundred km distant from the events). Because it was possible to measure relative arrival times with precision of a few milliseconds (about three orders of magnitude better than traditional Lg phase picks), relative locations accurate to about 150 m could be obtained.

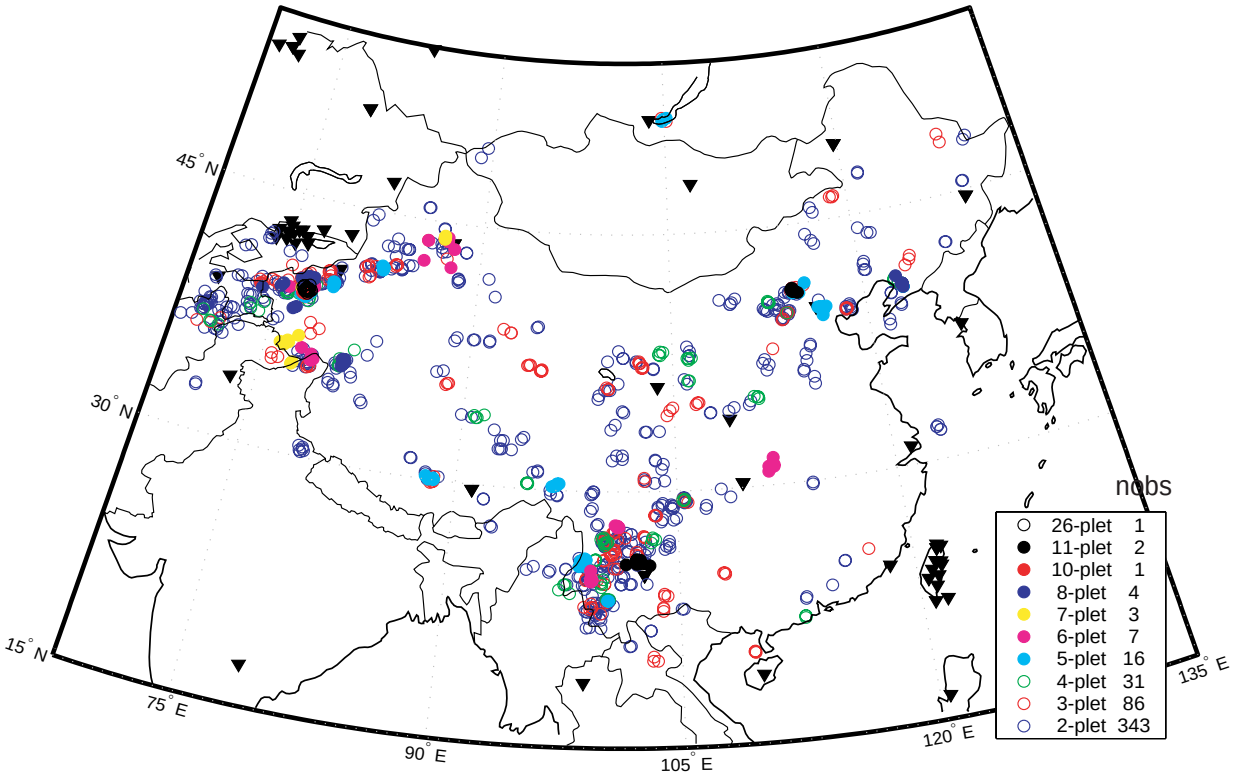


Figure 3. The location of 494 multiplets, totaling 1301 seismic events (9% of the ABCE). For each multiplet, the cross-correlation is greater than or equal to 0.8 for a window running from 4 s before the P arrival, to 40 s after the Lg arrival, and passed in the band from 0.5 to 5 Hz.

Our studies of Chinese seismicity for the years 1985 to 1999 included analysis of about 15,000 events reported in the Annual Bulletin of Chinese Earthquakes (ABCE), and allowed us to derive 64 GT5 quality events as documented by Waldhauser and Richards (2003a). Knowing the approximate location of these 15,000 events, we made a major data request to the IRIS (Incorporated Research Institutes for Seismology) Data Management Center for the regional waveforms of about 14,000 events in and near China, as recorded by all digital stations within 20° for each event (a total of 115 stations). When this dataset (about 12 Gbytes) was searched for repeating waveforms, it was found that a set of 1301 events had the property that each event had almost exactly the same seismograms as at least one other event. These 1301 events, about 9% of the ABCE, were composed of 494 subsets of repeating signals (Schaff and Richards, 2003b). Each subset (in most cases composed of just a pair of events, i.e. a doublet) must consist of events that were within 1 km of each other, given the time window and bandwidth of the signals that were cross-correlated.

Numerous different uses may be made of our discovery that a significant fraction of seismicity in a broad region is made up of repeat events. Excellent relative locations may be obtained for the events within a cluster. The clusters may in some cases be located in an absolute sense (enabling their use as GT events). And the fact that each cluster is so small in size (less than 1 km across) enables a simple evaluation of the precision of event catalogs that locate the events one-at-a-time (Schaff and Richards, 2003b).

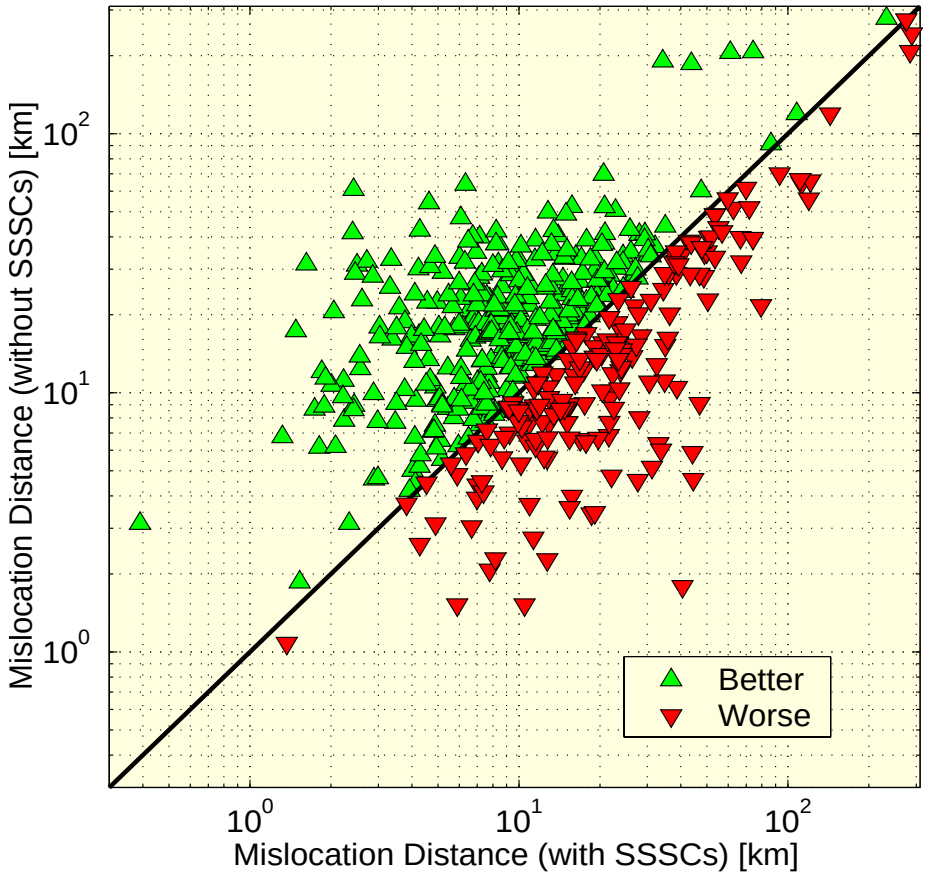


Figure 4. Mislocation distances with and without using model-based SSSCs with respect to corresponding GT locations. The green symbols show the events for which the mislocation error is smaller using SSSCs than without. Red symbols show the events for which the mislocation errors are smaller without using SSSCs. The bisecting line corresponds to equivalent mislocation errors for the two solutions (with and without SSSCs).

Evaluation of our travel time model

For model validation we use 525 events recorded at 140 stations. The test consists of relocating these events using Pn (5677 picks) and Sn (1586 picks) arrivals. All the relocations are performed with depth fixed at the surface. Figure 2 shows the distributions of events and seismographic stations used in this analysis. Also shown in Figure 2 are great circle Pn paths between events and stations. The relocation procedure is first applied using the IASP91 travel-time tables, without any SSSCs. This is followed by relocating the same events using the SSSCs. Executing EvLoc with and without SSSCs resulted in 525 events with location estimates that converged.

First we look at the mislocations, then at the travel time residuals, and then at the size of the error ellipses and their coverage, when using our model-based SSSCs.

Mislocation is expressed as the difference in distance between the GT location and the location obtained by EvLoc. Of the 525 events, the locations using SSSCs improved for 348 events (66%) and deteriorated for 177 events (34%). The median mislocation was reduced from 16.9 km to 11.4km. For 276 events (53%) the solutions improved by more than 20%, while for 140 events (27%) the deterioration is more than 20%. Figure 4 shows the mislocation results. The green symbols represent the events for which the relocation with SSSCs is closer to the GT location than without SSSCs. The red symbols show the events for which the mislocation without SSSCs is smaller than with SSSCs.

The standard error of observations, a measure of the fit that depends on the root-mean-squared (rms) travel-time residuals, shows improvement for 304 solutions (58%) and deterioration for 221 solutions (42%). 186 solutions (35%) are improved by more than 20% and 147 solutions (28%) deteriorated by more than 20%.

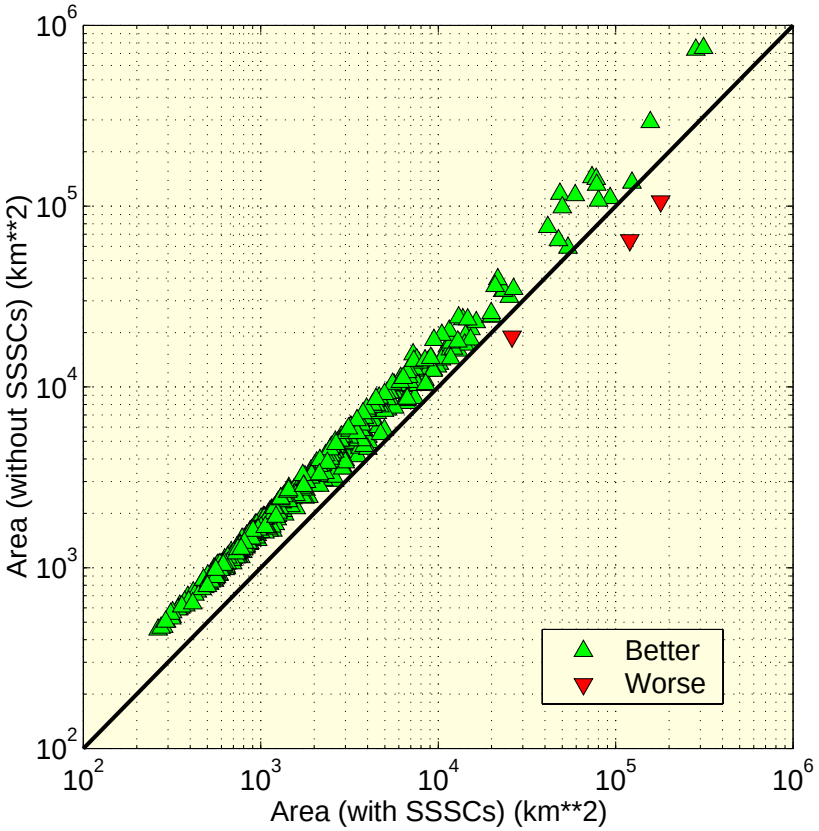


Figure 5. Scatter plot of error ellipse areas computed with (x-axis) and without (y-axis) using model-based SSSCs. Green symbols represent error ellipse areas that are smaller when using the SSSCs than without.

Our SSSCs lead in general to smaller error ellipses. Thus, using model-based SSSCs, error ellipse area is reduced for 522 of 525 solutions (99%), 498 of which (95%) are improved by more than 20%. Only 3 solutions (1%) do not have smaller error ellipses. The decrease in the median error ellipse area is 953 km^2 (from 2,616 km^2 to 1,633 km^2). Figure 5 shows the scatter plot of error ellipse areas computed with and without SSSCs.

Error ellipse coverage is defined as the percentage of GT event locations that fall within the corresponding 90%-confidence error ellipse. For relocation solutions without using SSSCs, 466 events (89%) have 90%-confidence ellipses that contain the GT locations. Using SSSCs, 476 events (91%) have 90%-confidence ellipses that contain the GT locations. In both cases the coverage is near the target of 90%, while the median area of the error ellipses is reduced significantly when relocating with SSSCs.

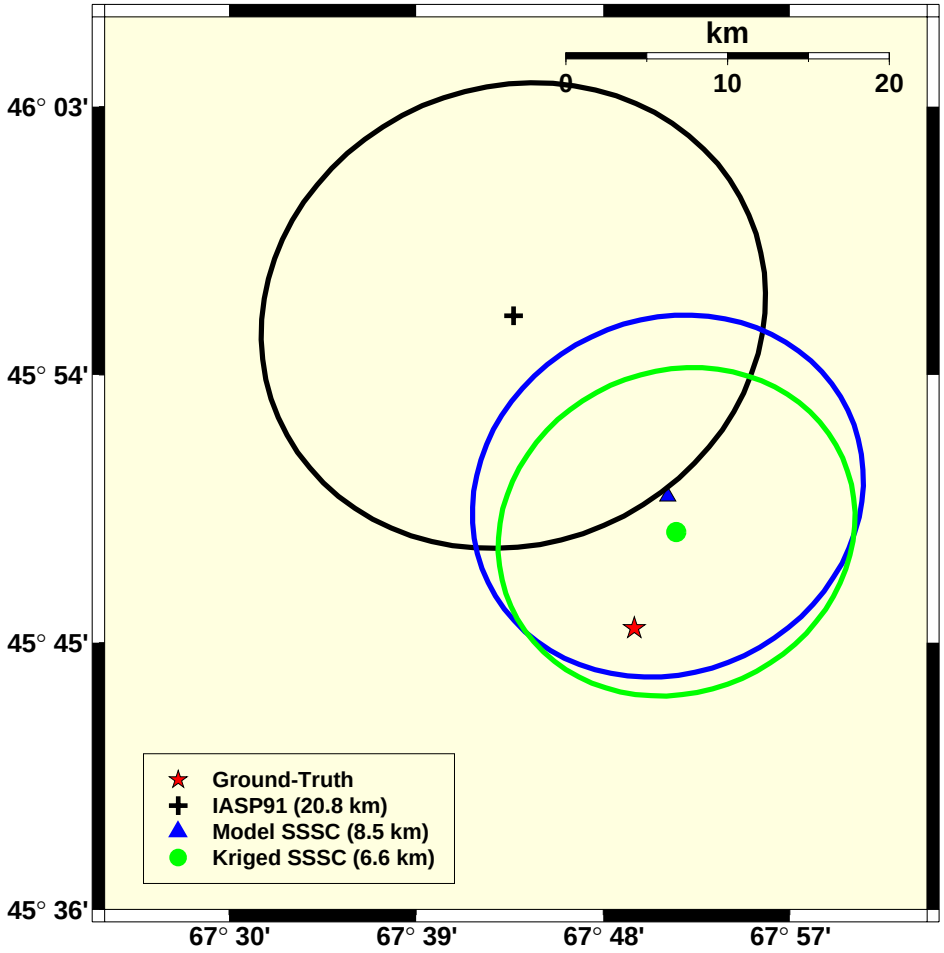


Figure 6. Relocation results, with and without using SSSCs, for a PNE (Meridian-2) in the Former Soviet Union on 19 September 1973. Mislocation errors relative to the ground-truth location are 20.8 km without using SSSCs, 8.5 km using model-based SSSCs, and 6.6 km using kriged SSSCs. The error ellipse areas are 710 km^2 without using SSSCs, 425 km^2 using model-based SSSCs, and 357 km^2 using kriged SSSCs.

Evaluation of our kriged SSSCs

We evaluated location performance using the kriged SSSCs. At locations near calibration data, the kriged corrections converge to the mean of the nearby data values and the uncertainty converges to the residual (i.e., local) variance. For grid points far from calibration data, the correction surface approaches the model-based SSSC, with larger uncertainty that is the sum of the calibration and residual variances. Thus, the kriged SSSCs should perform at least as well as the model-based SSSCs, and much better for locations close to calibration points. In this analysis, we used a computationally intensive but necessary "leave-one out" procedure in which the event to be relocated was

excluded from the kriging calculation of the SSSCs. We then relocated each of the 525 events with kriged SSSCs that are re-computed for each event so that we do not use the same data to both compute and test the SSSCs.

As an example, Figure 6 shows relocation results without SSSCs, with model-based SSSCs, and with kriged SSSCs for a PNE, Meridian-2, which was detonated on 19 September 1973 in the Former Soviet Union. The kriged SSSCs reduce the mislocation error from 20.8 km to 6.6 km and reduce the error ellipse area from 710 km^2 to 357 km^2. For this event, the relocation results do not differ significantly when using the model-based or kriged SSSCs. Note that

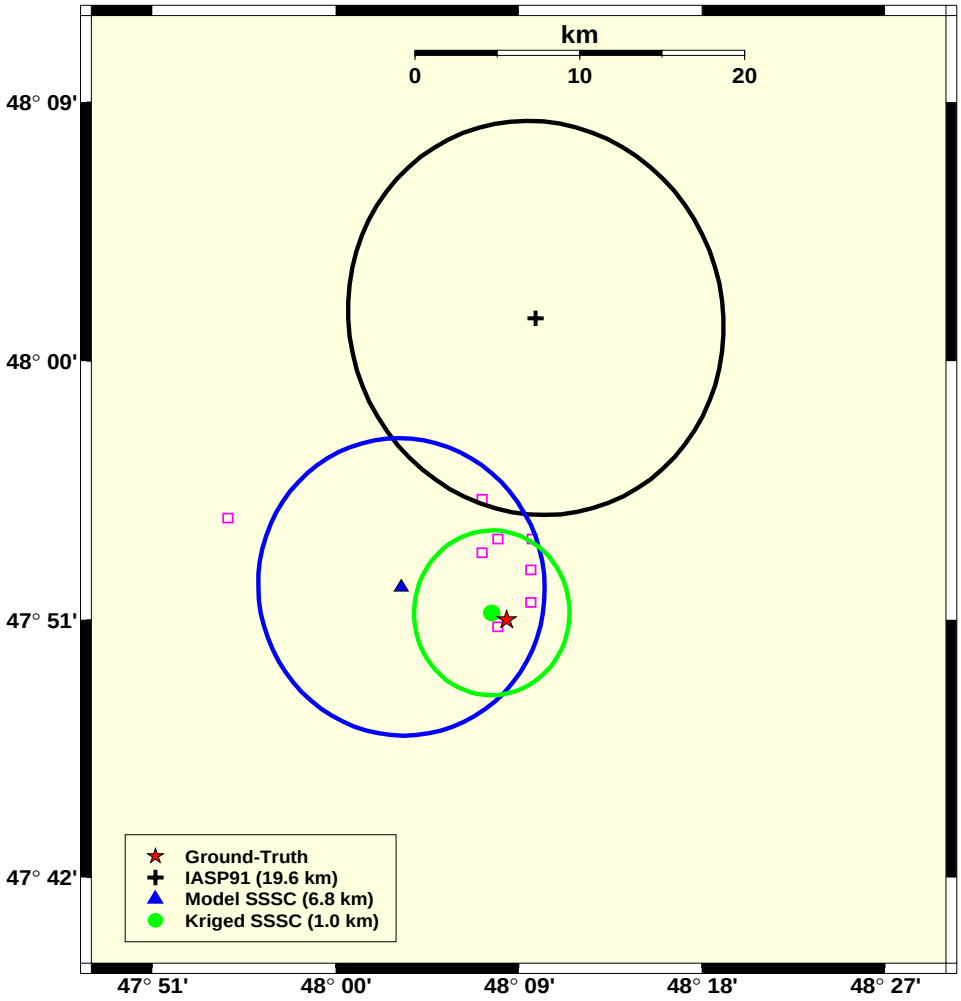


Figure 7. Relocation results, with and without using SSSCs, for a PNE (Azgir-10) in the Former Soviet Union on 24 October 1979. Mislocation errors relative to the ground-truth location are 19.6 km without using SSSCs, 6.8 km using model-based SSSCs, and 1.0 km using kriged SSSCs. Magenta square markers represent calibration points. The error ellipse areas are 455 km^2 without using SSSCs, 264 km^2 using model-based SSSCs, and 79 km^2 using kriged SSSCs.

the error ellipses are smaller when using either version of the SSSCs, and contain the GT location, unlike the error ellipse based on IASP91 without SSSCs. Another case, depicted in Figure 7, shows that kriging, when calibration points are near the event to be located, can have a significant impact. In this case again, the error ellipse based on IASP91 without SSSCs does not include the GT location. What is different in this case is that there are 23 GT events inside a 4° radius around the Azgir-10 PNE and only one in the previous case (Meridian-2). With magenta squares we display in Figure 7 the nearby GT reference events. The residuals of the 23 GT events are being used in the kriging process. The kriged SSSCs, used in relocation, contribute to a solution that is 1 km distance from the GT location compared to 6.8 km when model-based SSSCs are used in the relocation process. The improvement of

results shown in Figure 7, compared to the results in Figure 6, is an indication of the effectiveness of empirical data, in a situation where such data are available.

Next we look at the mislocations in general, then at the size of the error ellipses and their coverage, when using our model-based SSSCs refined by kriging.

Of the 525 GT events, 445 solutions (85%) have smaller mislocation errors using kriged SSSCs than those obtained using just the IASP91 travel-time tables. Of these, 410 events (78%) have mislocation errors that are reduced by more than 20%. Only 80 solutions (15%) deteriorated and 53 solutions (10%) deteriorated by more than 20%. The median mislocation is reduced from 16.9km to 6.5 km when kriged SSSCs are used. Figure 8 shows a scatter plot of the mislocation distances, relative to the GT locations, obtained with (x-axis) and without (y-axis) using the SSSCs.

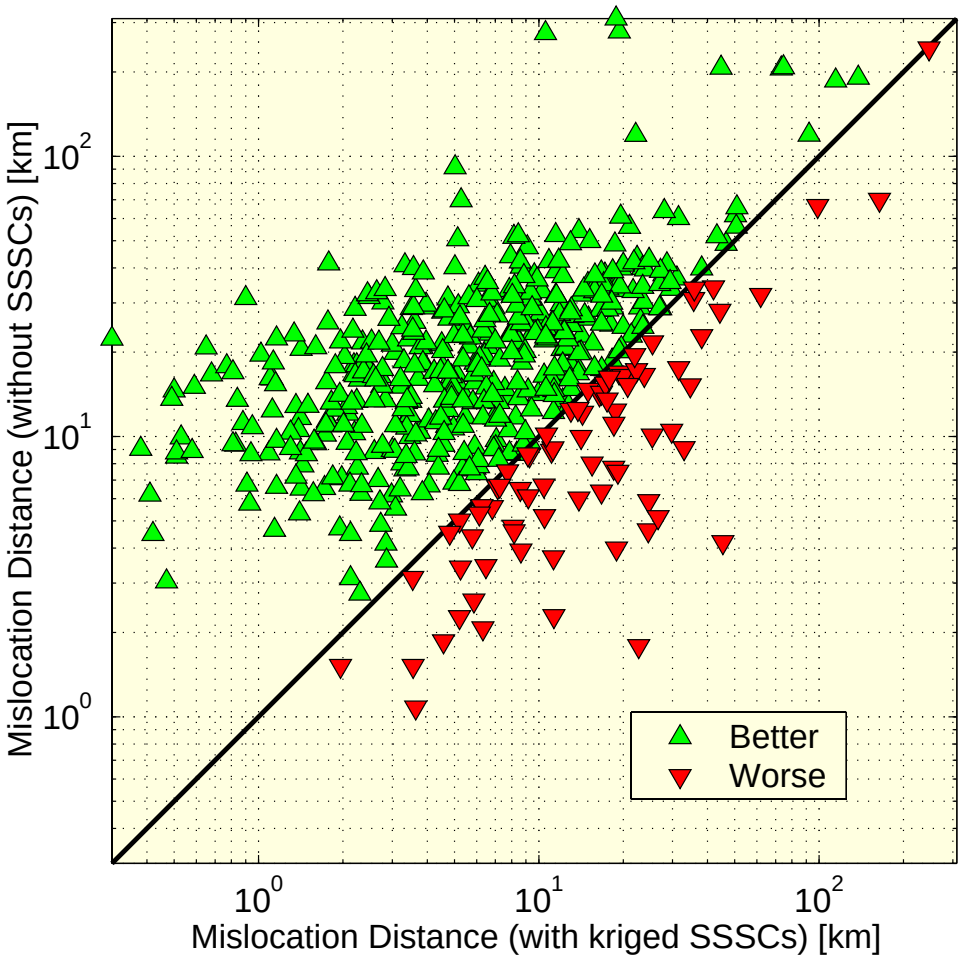


Figure 8. Mislocation distances with and without using kriged SSSCs with respect to corresponding GT locations. Markers and the line are defined as in Figure 4.

As in Figure 4, the green symbols represent events for which location estimates using the kriged SSSCs are closer to the GT locations, while the red symbols show solutions that are better without using SSSCs. Using kriged SSSCs, error ellipse area is reduced for all the 525 solutions (100%), 523 of which (99.6%) are improved by more than 20%. The median ellipse area is reduced from 2,616 km^2 to 722 km^2. The results are shown in Figure 9. Error ellipse coverage, computed as the percentage of GT event locations contained within the 90%-confidence error ellipses, is 92% (483 GT events) when using the kriged SSSCs, as compared to 89% (466 GT events) without using SSSCs (i.e., using IASP91 only).

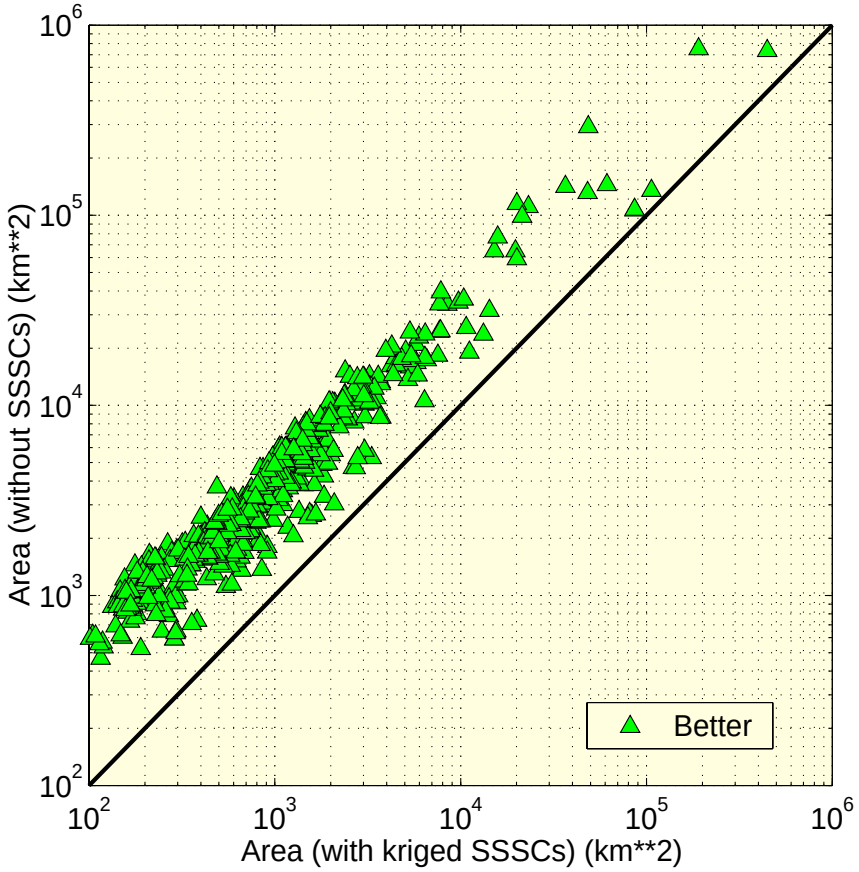


Figure 9. Scatter plot of error ellipse areas computed with (x-axis) and without (y-axis) using kriged SSSCs. Markers are defined as in Figure 5.

CONCLUSIONS AND RECOMMENDATIONS

In this paper we have briefly presented results validating our regionalized travel-time model of East Asia and evaluating the effectiveness of the regional Pn and Sn SSSCs developed by the Lamont Consortium for Group 1 IMS stations. In Table 2 we summarize the main location performance metrics when Pn and Sn arrivals were used with and without SSSCs. More extensive documentation is available.

We believe the results indicate the general validity of the model and the resulting SSSCs for this region. In all cases, the results demonstrate that the regionalization and travel-times curves, developed by the Lamont Consortium for Group 1 stations, along with the computational methods of 3D ray tracing and kriging, developed by the Consortium, have produced Pn and Sn SSSCs and modeling errors that improve the performance of location and uncertainty estimates in East Asia. We expect that these SSSCs will perform, on average, as well as indicated by the validation test results for the model-based SSSCs, and substantially better for regions surrounding the Lop Nor, Semipalatinsk, Indian and Pakistani nuclear test sites, where high-quality calibration data have been utilized.

We note that the degree of location improvement using our SSSCs significantly exceeds the criteria developed at Location Workshops held in 1999, 2000, 2001, 2002, and 2003 in Oslo, Norway (see for example CTBT/WGB/TL-2/18 for 1999). In part, this is a reflection of the fact that the IASP91 travel times are a poor representation of regional travel times in much of the region we have studied. We therefore recommend that any users of regional signals recorded by the 140 stations that we have calibrated consider our SSSCs for seismic event location in East Asia. In particular, we recommend that our SSSCs be considered for use in operational systems that interpret seismic arrival-time data from these stations. Finally, we note that our overall method (of first obtaining model travel times and then kriging with empirical data) is well suited to calibration of any stations in East Asia that have a significant archive of reliably measured arrival times.

Table 2. Location performance metrics for Pn and Sn.

Case	IASP91	Model-Based SSSCs	Model + Kriged SSSCs
Median mislocation (km)	16.9	11.4	6.5
Events with reduced mislocation		66%	85%
Median error ellipse area (km^2)	2,616	1,663	722
Events with smaller ellipses		99%	100%
90% coverage	89%	91%	92%

REFERENCES

Bondár, I (1999), Combining 1-D models for Regional Calibration, in *Proceedings of a Workshop on IMS Location Calibration*, Oslo, January 1999.

Burlacu, V., M. Fisk, J. Armbruster, V. Khalturin, W.-Y. Kim, P. Richards, D. Schaff, F. Waldhauser, M. West, I. Morozov, E. Morozova, V. Cormier, A. Stroujkova, and C. Saikia (2003), Development and Validation Testing of a Regionalized Travel-Time Model, and Source-Specific Station Corrections for Thirty IMS Stations and Other Stations in East Asia, 300 page draft Technical Report to DTRA.

Fisk, M. (2002), Accurate locations of nuclear explosions at the Lop Nor Test Site using alignment of seismograms and IKONOS satellite imagery, *Bull. Seism. Soc. Amer.*, 92, 2911-2925.

Schaff , D., and P. Richards (2003a), Lg-wave cross correlation and double-difference location: application to the 1999 Xiuyan, China, sequence, submitted for publication June 25, *Bull. Seism. Soc. Amer.*

Schaff, D., and P. Richards (2003b), High precision location of seismic activity across China, ms in preparation for SCIENCE.

Waldhauser, F., and P. Richards (2003a), Reference events and empirical Source Specific Station Corrections for regional phases at IMS stations in China, submitted for publication June 9, *Bull. Seism. Soc. Amer.*

Waldhauser, F., and P.. Richards (2003b), Location of underground nuclear explosions at the Lop Nor Test Site, 1969 to 1996, in preparation for submission to *Bull. Seism. Soc. Amer.*

Yang, Z.-Y., F. Waldhauser, Y.-T. Chen, and P. Richards (2003), Relocation of earthquakes in central-western China using the double-difference earthquake location algorithm, submitted for publication, *Journal of Seismology*.

RESEARCH IN REGIONAL SEISMIC MONITORING

Frode Ringdal,[1] Tormod Kvaerna,[1] Elena O. Kremenetskaya,[2] Vladimir Asming,[2]
Svein Mykkeltveit,[1] Steven J. Gibbons,[1] and Johannes Schweitzer[1]

NORSAR;[1] Kola Regional Seismological Center[2]

Sponsored by Defense Threat Reduction Agency

Contract No. F08650-01-C-0055

ABSTRACT

This project represents a continuing effort aiming at three main topics: (a) to carry out research in regional monitoring of the European Arctic, (b) to apply experimental methods such as the site-specific threshold monitoring to target areas of interest and assess the results and (c) to contribute to the global location calibration effort currently being under taken in Vienna, Austria by Working Group B of the Preparatory Commission (PrepCom).

We have used data from the regional networks operated by NORSAR and the Kola Regional Seismological Centre (KRSC) to assess the seismicity and characteristics of regional phases of the European Arctic. Recently, seismic instrumentation has been installed inside the mines in the Khibiny Massif of the Kola peninsula in order to provide origin times of the seismic events as well as to contribute to additional validation of the location accuracy. These recordings supplement the ground truth information that is routinely obtained by KRSC for mining explosions in the Kola Peninsula. Some interesting results are emerging from comparing underground and surface explosions. For example, two explosions, one underground and one at the surface occurred in the Rasvumchorr mine in Khibiny on 16 November 2002. These explosions were only 300 m apart, so that differences in path effects at the more distant stations can be ignored. Nevertheless, the recorded signals at stations in our network (up to 400 km distance) were remarkably different: At lower frequencies (2-4 Hz), the underground explosion was stronger by a factor of 10 in amplitude, whereas above 10Hz, the surface explosion had by far the stronger signals.

We have made some significant progress in automating the detection and location of seismic events from selected mining areas. For example, an experimental on-line detection and location system, using the ARCES array, has been implemented for the Kovdor mine in Kola, and the automatic process has been compared to the regular analyst reported bulletin. It turns out that the automated process, with appropriate calibration, can match or exceed the performance of the analyst in terms of location precision. The main reasons for this performance is the application of optimized, fixed frequency band filters together with careful application of automatic autoregressive onset estimation techniques.

We have continued our efforts to develop and improve the site-specific threshold monitoring system for the Novaya Zemlya test site in Russia. We have also developed a site-specific generalized beamforming procedure, which has proved able to detect small events at this site with a very low false alarm rate. In addition, we are attempting to optimize the automatic detector performance for Novaya Zemlya and adjacent regions by adjusting the beam set, adding specially designed filters and correcting for plane-wave anomalies in the beamforming.

A workshop was held in Oslo, Norway, during 4-9 May 2003 in support of the global seismic event location calibration effort currently being undertaken by PrepCom's Working Group B in Vienna. The workshop, which was chaired by Dr. Frode Ringdal, was attended by 54 scientists from 10 countries and the Provisional Technical Secretariat of the CTBTO. The workshop recommendations will be reported to Working Group B.

OBJECTIVE

This work represents a continued effort in seismic monitoring, with emphasis on studying earthquakes and explosions in the Barents/Kara Sea region, which includes the former Russian nuclear test site at Novaya Zemlya. The overall objective is to characterize the seismicity of this region, to investigate the detection and location capability of regional seismic networks and to study various methods for screening and identifying seismic events in order to improve monitoring of the Comprehensive Nuclear-Test-Ban Treaty (CTBT). Another objective is to apply advanced site-specific seismic monitoring methods to other sites of special interest, in particular known nuclear test sites. A third objective is to support the international effort to provide regional location calibration of the International Monitoring System.

RESEARCH ACCOMPLISHED

Introduction

NORSAR and the Kola Regional Seismological Centre (KRSC) of the Russian Academy of Sciences have for many years cooperated in the continuous monitoring of seismic events in northwest Russia and its adjacent sea areas. The research is based on data from a network of sensitive regional arrays which was installed in northern Europe during the last decade in preparation for the CTBT monitoring network. This regional network, which comprises stations in Fennoscandia, Spitsbergen and NW Russia provides a detection capability for the Barents/Kara Sea region that is close to $m_b = 2.5$ (Ringdal, 1997).

The research carried out as part of this effort is documented, in detail, in several contributions contained in the NORSAR Semiannual Technical Summaries. In this paper we will limit the discussions to recent results of interest in the general context of regional monitoring of seismic events in the European Arctic. In particular our studies have focused on mining explosions in the Kola Peninsula, using data from stations shown in Figure 1. This figure also shows some of the most active mining areas. We also briefly review the location calibration effort currently underway for the International Monitoring System (IMS).

Khibiny Mine Explosions

We have continued our research on rockbursts and mining explosions in the mining areas of NW Russia, in particular the Khibiny Massif region. Seismic instrumentation was recently installed inside the mines in the Khibiny Massif region of the Kola Peninsula in order to provide origin times for seismic events as well as to contribute to additional validation of the location accuracy. These recordings supplement the ground-truth information that is routinely obtained by KRSC for mining explosions. We are also cooperating with Lawrence Livermore National Laboratory (LLNL) to carry out more detailed studies of the characteristics of recordings from mining events in northern Fennoscandia and western Russia. The project includes the installation of additional seismometers along profiles in Norway, Finland, and the Kola Peninsula, that will be used for recording over a period of one year. The station Ivalo (IVL) in Figure 1 is one of these temporary stations.

Some interesting results are emerging from comparing underground and surface explosions. For example, two explosions, one underground and one at the surface occurred in the Rasvumchorr mine in Khibiny on 16 November 2002. As illustrated in Figure 2, the underground explosion was a ripple-fired explosion of 257 tons; whereas the open-pit explosion, comprised four separate ripple-fired explosions, was set off with approximately a 1 second separation between each group of explosions from south to north. The surface and underground explosions were only 300 m apart, so that differences in path effects at the more distant stations can be ignored. Nevertheless, the recorded signals, e.g. at the temporary station in Ivalo, Finland at 300 km distance, were remarkably different: The vertical component of these recordings is shown in Figure 3 in different filter bands. At lower frequencies (2-4 Hz), the underground explosion was stronger by a factor of 10 in amplitude, whereas above 10 Hz, the surface explosion had by far the stronger signals. A similar spectral difference between open-pit and underground explosions has been observed also in other cases.

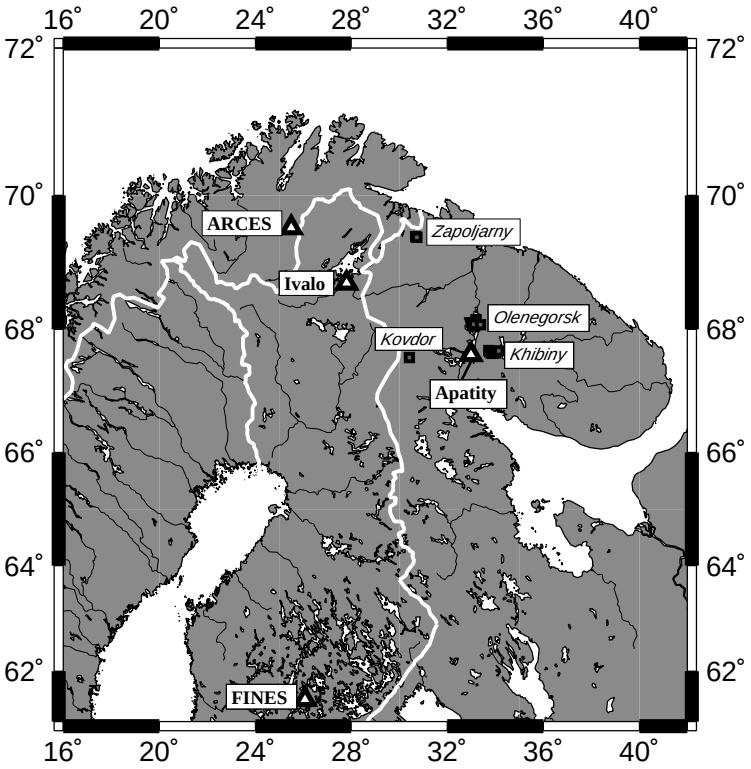


Figure 1. Seismic stations (triangles) used in our studies of mine explosions in Kola Peninsula. The main mining sites are marked as squares.

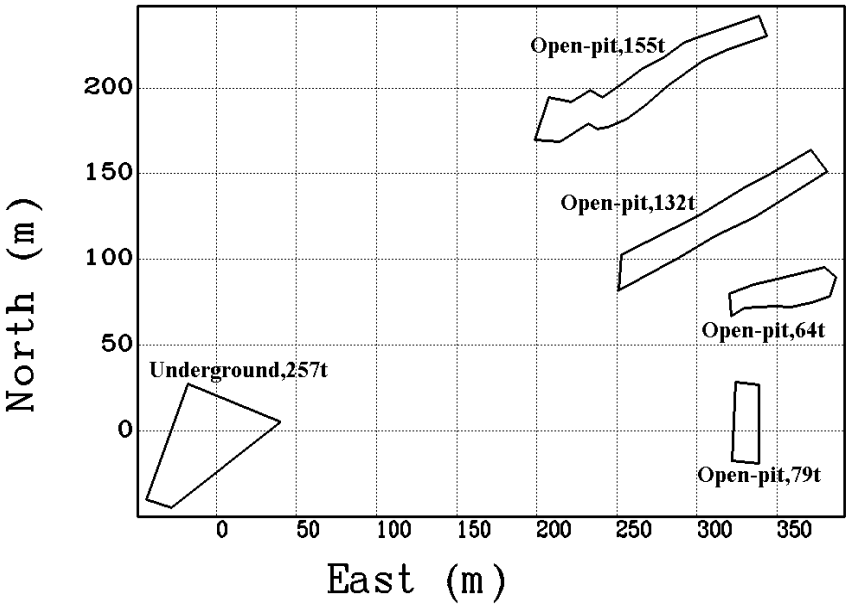


Figure 2. Schematic view of the shot configuration for the two explosions in Khibiny on 16 November 2002. Geographical coordinates of the point (0,0) are 67.6322N 33.8565E. See text for details.

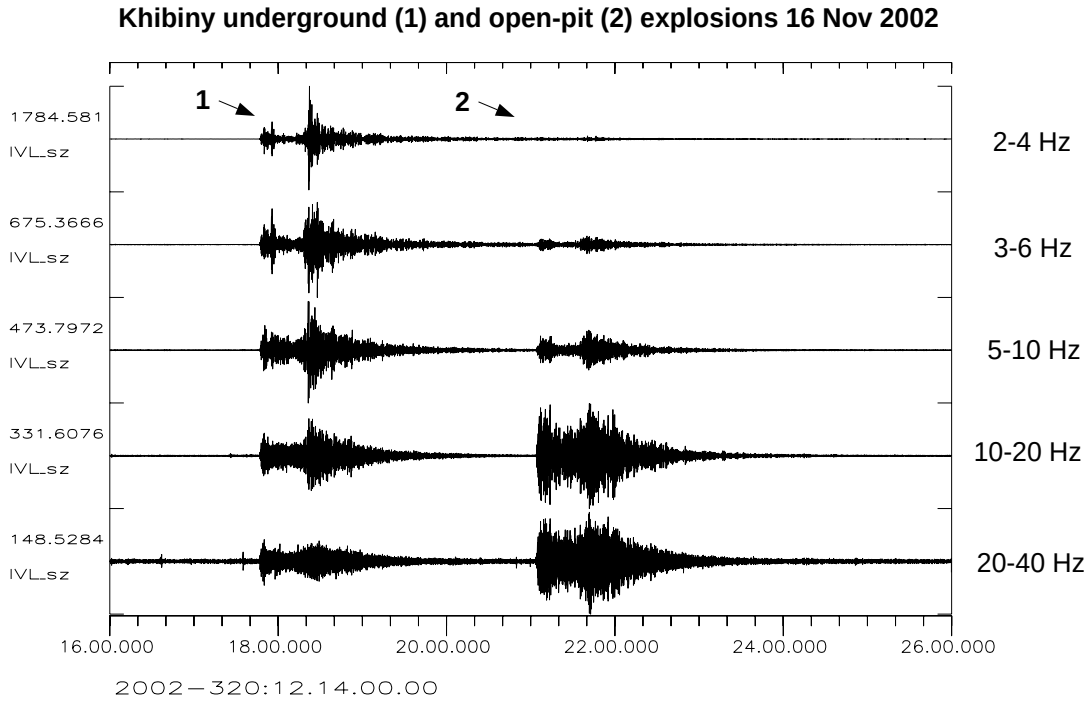


Figure 3. Recorded SPZ waveforms at station Ivalo (northern Finland) for the two explosions in Khibiny on 16 November 2002. The data have been filtered in five different frequency bands. Note the significant difference in relative size of the two events as a function of frequency.

Kovdor Mine: A Single-Array Location Study

The goal of this work is to use a single regional seismic array (ARCES) to characterize seismic signals resulting from explosions that are known to have occurred at the Kovdor open cast mine in Russia (67.557 N, 30.425 E) and use these observations to determine whether other events recorded at ARCES are the result of operations at this mine. Wherever possible, events which are deemed to be likely candidates for Kovdor events are located to the best possible accuracy. A total of 38 events within a testing period have been located in this way and the location error has been compared with that of the analyst reviewed network locations. For details, we refer to Gibbons et. al. (2003).

Figure 1 shows the location of the Kovdor mine relative to ARCES together with the Zapoljarny, Olenegorsk and Khibiny mining regions on the Kola Peninsula. The distance between ARA0, the central seismometer of the ARCES array, and Kovdor is 298 kilometers with a receiver to source backazimuth of 135 degrees.

Ground-truth information for events at the mines indicated in Figure 1 has been provided by the Kola Regional Seismological Centre (KRSC) and has been used to assemble yield information and approximate origin times for explosions at the Kovdor mine between October 6, 2001, and July 13, 2002.

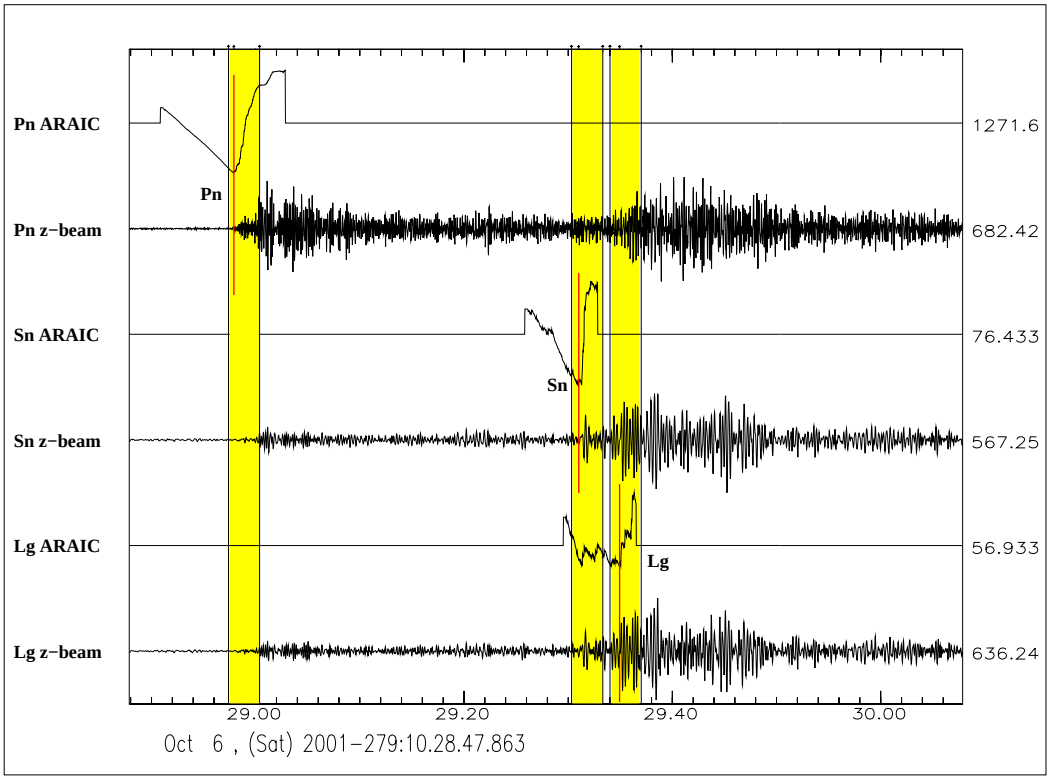


Figure 4. Illustration of the automatic processing of a Kovdor event 2001-079 recorded at ARCES. The Pn, Sn and Lg onset picks have been made applying the autoregressive ARAIC method of Akaike (1974). We have used fixed time windows positioned relative to the Pn onset and fixed filter bands for fk-analysis of each of these phases.

We have developed a stepwise, fully automatic algorithm for identifying, processing, and locating events from the Kovdor mine, using only data from the ARCES array. Using results from the analysis of confirmed Kovdor events, we have developed a set of criteria to help determine whether or not detections from ARCES result from events at Kovdor. A detection is considered very likely to result from a Kovdor event if it passes the following three tests:

1. The automatic ARCES detection list gives velocity and azimuth values within appropriate ranges, determined from confirmed Kovdor events.
2. Velocity and azimuth values obtained from a fixed frequency band fk-analysis are consistent with a Pn-arrival from a Kovdor event.
3. There is evidence of a secondary phase (appropriate velocity and azimuth from fixed frequency band fk-analysis within a time window at a fixed delay after the first P-arrival).

The automatic process was run on ARCES data from January 1, 2002 to July 27, 2002.

- A total of 6,176 detections passed test 1.
- Seventy-two detections were still considered likely candidates after test 2.
- Forty-eight detections were still considered likely following test 3, of which only one was found to correspond to an event located at a different site.
- All of the events confirmed by KRSC to have originated at Kovdor were successfully identified by these three tests.

Of the events which are successfully identified as likely Kovdor candidates, those satisfying a fourth condition - that at least one secondary phase has been assigned a satisfactory arrival time - may be located within the automatic process. A total of 38 events were located in this way with an error comparable to or better than that of the analyst reviewed network locations. The event locations are displayed in Figure 5 and the statistics of these locations are given in Table 1.

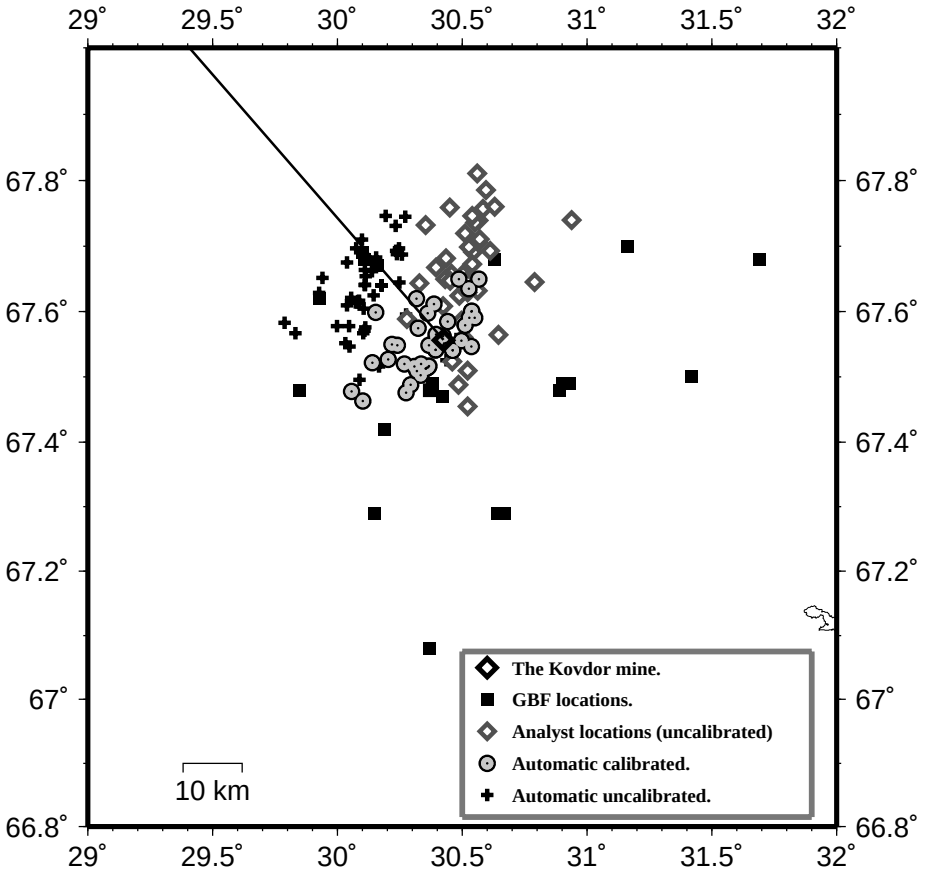


Figure 5. Comparison of event locations by various methods for Kovdor events. The line shows the direction towards ARCES, and the true mine location is marked at the end of the line.

The results of the Kovdor study are quite encouraging. We started out with the ARCES automatic detection lists for a processing period of 208 days. During this period, we identified 6176 ARCES detections that potentially corresponded to events from Kovdor. By sophisticated automatic processing, we were able to reduce this number to 48 event candidates, out of which 47 were correct and only 1 was a false alarm. The 47 events included all of the 28 Kovdor mining explosions originally reported by KRSC during the time period, plus a number of secondary events in "double" explosions.

Our single-array location procedure, with adjustment for systematic bias, provided locations for the 38 events with detected P and S phases with a median error of only 5.8 km. This is significantly better than the median error (12.1 km) obtained in our regular analyst-reviewed network bulletin for the same event set. We should note that this excellent performance of the automatic processing is due to the application of consistent, fixed filter frequency bands and sophisticated onset time analysis, as well as calibration by comparison to ground-truth locations.

Table 1: Statistics of event locations

Location type	Number of events	Location difference (km)			
		90%	95%	Median	Maximum
Automatic network locations (GBF method)	36	32.1	42.9	20.3	102.7
ARCES one-array locations without bias corrections	38	22.7	23.3	16.6	27.3
ARCES one-array locations with bias corrections	38	12.0	12.8	5.8	18.0
Analyst reviewed network locations[a]	40	21.7	24.3	11.0	28.9

a.Note that the analyst reviewed locations did not apply any bias corrections.

Development of site-specific GBF

In the two preceding NORSAR Semiannual Technical Summaries we have reported on our developments concerned with monitoring the Lop Nor test site in China (Lindholm et. al., 2002; Kværna et. al., 2002a). Using data from the global arrays and single stations having the best detection capability for the area, we developed and tested both an optimized Site-Specific Threshold Monitoring (SSTM) and a Site-Specific Generalized Beamforming (SSGBF) system for the Lop Nor test site.

We have now carried out a study of experimental SSGBF applied to the Novaya Zemlya former nuclear test site (see Kværna et. al., 2003 for details). We have used data from the regional arrays ARCES, SPITS, FINES and NORES, with calibration based on available data for the Novaya Zemlya region. We present some preliminary results in applying SSGBF to the test site, using a 24-hour data set for performance testing. The data set covers the day of 23 February 2002, when a seismic event near the test site occurred.

The Generalized Beamforming (GBF) technique, originally developed by Ringdal and Kværna (1989), is now widely accepted as the most efficient method for associating seismic phases from a global or regional network. In a typical implementation, a large number of generalized “beams” are steered to the points in a global or regional grid. An automatic detector is applied to each station or array in the network, and a set of “box-car” or “triangular” functions is generated for each station, such that the non-zero parts of these functions correspond to a time interval around a detection. By summing these functions with appropriate weights and with time delays corresponding to the particular phase-station-grid point combination, one obtains a “beam” that may then be subjected to a detector algorithm.

When monitoring a particular site it is possible to optimize the parameter settings to ensure the best possible detection probability for the target site. This idea was first tested by Ringdal and Kværna (1993) to monitor the aftershocks of a large earthquake sequence occurring in Western Caucasus during the GSETT-2 experiment. They concluded that the approach showed a superior performance compared with the association procedures being employed at the four experimental international data centers operating during GSETT-2. In the present paper we elaborate further on this site-specific approach to monitoring the Novaya Zemlya test site.

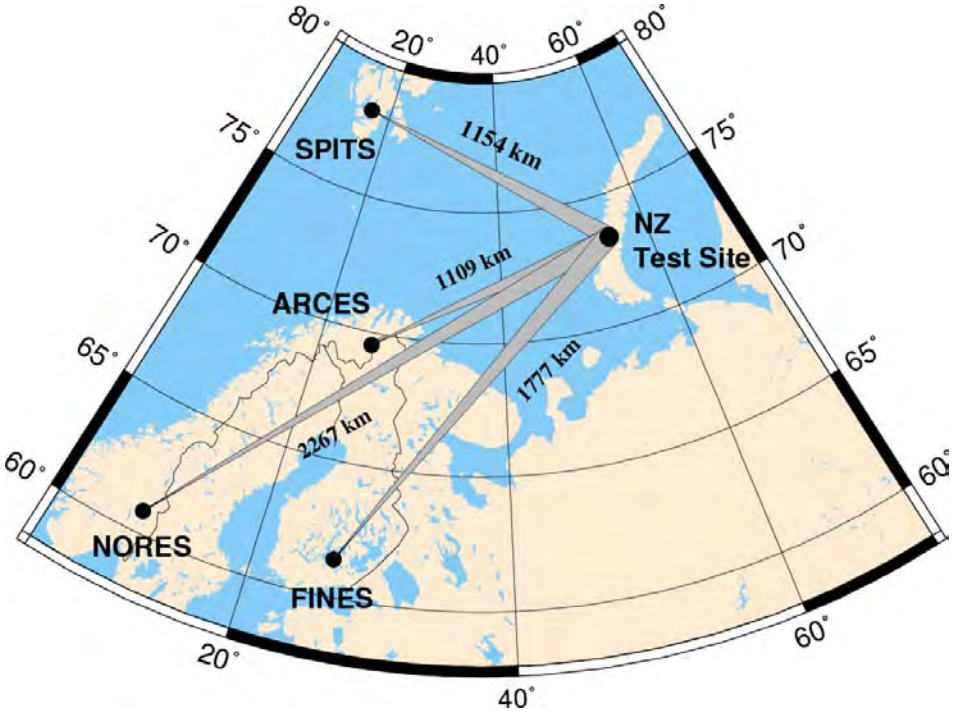


Figure 6. Map showing the arrays used for both site-specific Threshold Monitoring and site-specific Generalized Beamforming of the former Novaya Zemlya test site.

Array network and analysis procedure

The 4-array network displayed in Figure 6 has been shown to provide a monitoring capability for the NZ test site down to mb 2.0 for most time intervals (Kværna et. al., 2002b). Similarly, we have in the implementation of the SSGBF processing used the same 4-array network, and the processing parameters have been derived from the same events in the Novaya Zemlya region as have been used for the tuning of the SSTM process (Kværna et. al., 2002b). The beamforming procedure follows the GBF standard, except that only one generalized beam is formed in the site-specific case. The main steps are:

- Applying an automatic detector at each of the stations/arrays in the network
- Summing “boxcar” or “triangular” weight functions representing the detector outputs with the appropriate restrictions on travel time, azimuth and slowness
- Applying a thresholding procedure on the resulting generalized beam

We have used “triangular” functions centered at the expected arrival time for the beamforming in our NZ analysis. Experiments have shown that the effect of sidelobes is reduced when compared with using “boxcar” functions, while still retaining a high sensitivity for detecting events in the target area.

Example: 23 February 2002

An example of SSGBF processing is shown in the left part of Figure 7. The plots cover the day of 23 February 2002. At 01:21:12.1 GMT on that day there was an event with a magnitude of about 3.2, located about 100 km northeast of the former nuclear test site. The SSGBF traces for each phase considered are shown together with the network trace on top. To align the detections we have subtracted the phase travel-time from NZ to the respective arrays. The network trace on top is calculated by adding “triangular” functions surrounding each detection, using P and S from ARCES and SPITS, and P from NORES and FINES.

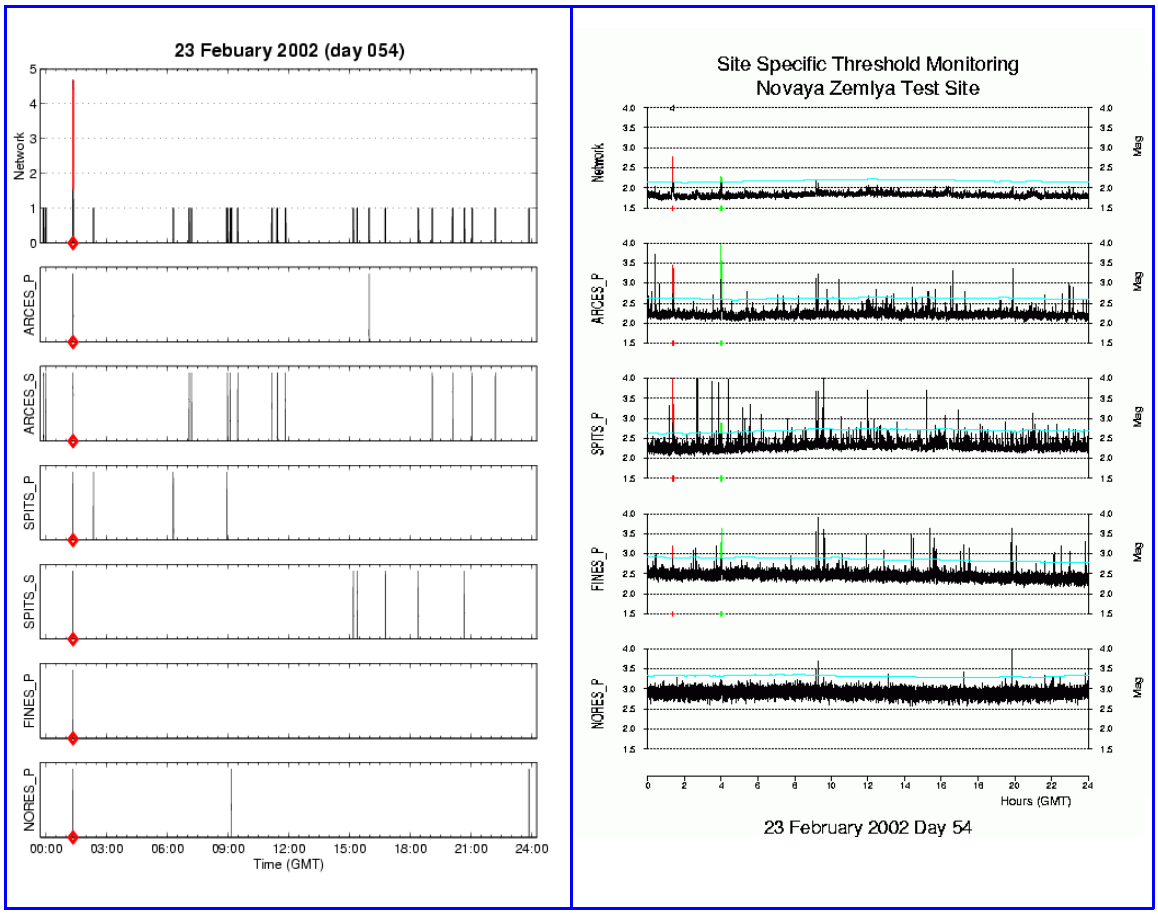


Figure 7. SSGBF traces for 23 February 2002 are shown in the left part of the figure. The corresponding SSTM traces are shown in the right part of the figure. For detailed information on SSTM we refer to Kværna et. al., 2002b.

From the SSGBF traces of Figure 7 we find that during 23 February 2002 there is only one significant event trigger, and this trigger corresponds to the NZ event. By summing the "triangular" weight functions of the six detected phases we obtained a network SSGBF value of about 4.7 for the NZ event. No other peak exceeds 1 for this day. The detector performance and false alarm statistics will continue to be evaluated.

Location Calibration

Oslo Workshop on location calibration

A workshop was held in Oslo, Norway, 4-9 May 2003 in support of the global seismic event location calibration effort currently being undertaken by PrepCom's Working Group B in Vienna. The workshop, which was chaired by Dr. Frode Ringdal, was attended by 54 scientists from 10 countries and the Provisional Technical Secretariat of the CTBTO. The workshop recommendations will be reported to Working Group B.

CONCLUSIONS AND RECOMMENDATIONS

The analysis of mining explosions in the Kola Peninsula shows significant spectral differences between surface and open-pit explosions. We recommend pursuing this work as ground-truth data from mining events is collected and a larger database of recordings from near-field stations becomes available.

The automatic processing results from the Kovdor experiments shows that, at a distance of 300 km, a single array, with application of optimized processing, can locate seismic events with an accuracy comparable to or better than that of an experienced analyst, even when the analyst uses a regional network. Such performance cannot be expected at greater distances, but the possibilities and limitations of this method applied in a more general way should be investigated. Extension of the method to network processing should be considered.

The combination of the SSTM and the SSGBF methods provide a convenient tool for day-to-day monitoring of the Novaya Zemlya test site. The SSTM technique has as its main strength the ability to display the real seismic field, regardless of “station detector performance”. The SSGBF technique takes advantage of the individual station detector outputs, and uses this combined information to narrow down the number of possible candidates for events in the target area. We recommend further development of this concept.

The location calibration effort will continue to be an important part of our work. The recommendations provided at the Oslo workshop should be followed up by the international community, and the progress of this work will be reviewed in future meetings.

REFERENCES

Akaike, H. (1974): Markovian representation of stochastic processes and its application to the analysis of autoregressive moving average processes. *Ann. Inst. Stat. Math.* 26, 363-387.

Gibbons, S., T. Kværna and F. Ringdal (2003): Single array analysis and processing of events from the Kovdor mine, Kola, NW Russia. *Semiannual Technical Summary 1 January - 30 June 2002*, NORSAR Sci. Rep. 1-2003, Kjeller, Norway.

Kværna, T., E. Hicks and F. Ringdal (2002a): Site-Specific Generalized Beamforming (SSGBF) applied to the Lop Nor test site. *Semiannual Technical Summary 1 January - 30 June 2002*, NORSAR Sci. Rep. 2-2002, Kjeller, Norway.

Kværna, T., F. Ringdal, J. Schweitzer, and L. Taylor (2002b): Optimized Seismic Threshold Monitoring – Part 1: Regional Processing. *Pure Appl. Geophys.*, 159, 969-987.

Kværna, T., E. Hicks and F. Ringdal (2003): Site-Specific GBF monitoring of the Novaya Zemlya test site. *Semiannual Technical Summary 1 July - 31 December 2002*, NORSAR Sci. Rep. 1-2003, Kjeller, Norway.

Lindholm, C., T. Kværna and J. Schweitzer(2002): Site-Specific Threshold Monitoring (SSTM) applied to the Lop Nor test site. *Semiannual Technical Summary 1 July - 31 December 2001*, NORSAR Sci. Rep. 1-2002, Kjeller, Norway.

Ringdal, F. (1997): Study of low-magnitude seismic events near the Novaya Zemlya nuclear test site, *Bull. Seism. Soc. Am. 87 No. 6*, 1563-1575.

Ringdal, F. and T. Kværna (1989). A multichannel processing approach to real time network detection, phase association and threshold monitoring, *Bull. Seism. Soc. Am., 79*, 1927-1940.

Ringdal, F. and T. Kværna (1993): Generalized Beamforming as a tool in IDC processing of large earthquake sequences, *Semiannual Technical Summary, 1 April - 30 September 1993*, NORSAR Sci. Rep. 1-93/94, Norway

CONFIDENCE REGIONS ON SEISMIC EVENT LOCATIONS BASED ON MULTIPLE-EVENT ANALYSIS

William L. Rodi and M. Nafi Toksöz

Massachusetts Institute of Technology

Sponsored by Defense Threat Reduction Agency

Contract No. DTRA01-00-C-0102

ABSTRACT

We have developed a new approach to analyzing seismic event location uncertainty. The approach is based on a maximum-likelihood statistical framework and implemented with numerical techniques such as grid search and Monte Carlo simulation. It determines confidence regions on event locations under a general class of picking error models (Gaussian and non-Gaussian) and taking the nonlinear dependence of travel-time on event location into account. Non-Gaussian error distributions and nonlinear analysis lead to confidence regions that depart significantly from the elliptically shaped confidence regions obtained with the conventional Gaussian/linear approach, especially in the case of sparsely recorded events. Our recent focus has been on how errors in travel-time tables ("modeling" errors) affect event location uncertainty. Such errors are usually accommodated through an augmentation of the error model assumed in the uncertainty analysis, using an appropriate probability distribution for modeling errors determined from the analysis of calibration data from ground-truth (GT) events. This conventional approach, however, presents severe difficulties such as accounting for errors in GT event locations and parameterizing the dependence of the modeling error distribution on event location. We have adopted an alternative approach in which location uncertainty is analyzed in conjunction with a calibration analysis, i.e. performing the uncertainty analysis in the context of the multiple-event location problem in which the location parameters of a set of events are determined jointly with travel-time corrections associated with the paths between the events and recording stations. Uncertainty analysis in this joint inverse problem considers the trade-offs between location parameters and travel-time corrections, and thus the location confidence regions inferred for individual events implicitly account for the effect of calibration uncertainty (errors in path corrections). We have implemented this approach on the small-cluster multiple-event location problem, where path corrections are assumed to be station-dependent but event-independent, by extending our grid search/Monte Carlo algorithm for single-event location. We are testing our new approach to location uncertainty on regional and teleseismic arrival time data from the 1999 Izmit and Duzce earthquake clusters.

OBJECTIVE

The objective of this work is to develop a methodology for seismic event location that provides reliable estimates of location uncertainty needed in nuclear event monitoring. In previous work (Rodi and Toksöz, 2000, 2001) we have formulated a theoretical approach to event location uncertainty in terms of likelihood functions and hypothesis testing and implemented the approach with grid-search and Monte Carlo techniques. The resulting algorithm computes confidence regions on event locations that account for such complexities as nonlinearity of the forward travel-time problem and non-Gaussian distributions of observational (picking) errors. A major objective of our project has been to also incorporate a rigorous treatment of the errors in travel-time models (modeling errors) into our uncertainty analysis. Toward this goal, we have linked our uncertainty analysis to the process of seismic travel-time calibration, recognizing that modeling errors are due to the uncertainty in calibration parameters such as path corrections and tomographic velocity models. Therefore, we have extended our formulation to the multiple-event location problem, i.e., whereby data from multiple events and stations are used to simultaneously infer the locations of the events and calibration parameters. The trade-offs and correlations among the unknowns of this joint inverse problem affect an implicit account of modeling errors. Our first step in implementing this formulation was to extend our single-event grid-search location algorithm (known as GSEL) to a multiple-event one (GMEL). Currently, GMEL only solves the basic multiple-event location problem, applicable to event clusters of small spatial aperture, in which calibration parameters comprise an event-independent travel-time correction for each station. This algorithm is described in Rodi et al. (2002), where it is also compared to some other multiple-event location algorithms. In the present paper, we describe our formulation of multiple-event location uncertainty and our efforts to implement it in an extended version of GMEL.

RESEARCH ACCOMPLISHED

Formulation

We state our formulation of the joint location/calibration inverse problem for the special case of a data set comprising only seismic arrival times, with at most one seismic phase observed for each event-station pair. If there are m seismic events ($i = 1, \ldots, m$) and n seismic stations ($j = 1, \ldots, n$), the inverse problem can be written as

$$d_{ij} = t_i + T_j(\mathbf{x}_i) + c_{ij} + e_{ij} \qquad (1)$$

where d_{ij} is the observed arrival time for the (i,j)th path; t_i and $\mathbf{x}_i$ are origin parameters (time and hypocenter, respectively) of the ith event; T_j is a model-based travel-time function for the jth station; c_{ij} is a correction to this function; and e_{ij} is an observational error in d_{ij}. This equation holds for the station/event pairs for which data have been observed. The unknown parameters of this joint calibration/location inverse problem are the event hypocenters and origin times ($\mathbf{x}_i$ t_i, $i = 1, \ldots, m$) and the path correction c_{ij}.

The exact nature of the inverse problem depends on how the path corrections c_{ij} are parameterized, and what prior constraints are imposed on them and the event origin parameters. On the latter issue, the problem is purely one of calibration when the event parameters are assumed known, and purely one of location when the path corrections are known. In practice, neither set of parameters is completely known or unknown. Two difficult problems in nuclear discrimination, in fact, are the same problem in this formulation. The first is how to account for uncertainty in a seismic calibration (errors in estimates of c_{ij}) when the calibration events have imperfectly known locations, i.e. ground-truth (GT) levels greater than 0. The second, which is the focus of this project, is how the location error of any particular event is affected by imperfect knowledge of the path corrections. These are two aspects of a complete uncertainty analysis in the joint calibration/location problem.

Parameterization of Path Corrections

The multiple-event inverse problem is hopelessly ill posed if the path corrections are not constrained via prior information or a parameterization that reduces the number of independent unknowns, or both. In the basic multiple-event location problem, relevant to small event clusters, the path corrections are assumed to be event-independent, i.e.

$$c_{ij} = a_j. \qquad (2)$$

The calibration parameters comprise a time term, a_j, for each station. Our work on uncertainty analysis to date has focused on this basic problem. However, our formulation pertains to other ways of parameterizing path corrections, such as with correction functions (or surfaces):

$$c_{ij} = a_j (\mathbf{x}_i). \tag{3}$$

Here, there is an unknown function, a_j (**x**) assigned to each station. It also pertains to the universal parameter functions described by Rodi et al. (2003). When spatial functions are used to parameterize travel-time corrections, however, it is necessary to provide additional prior information on their smoothness, such as with geo-statistical constraints (e.g. Schultz et al., 1998).

Maximum-Likelihood Formulation

Our approach to inverse problems and uncertainty analysis is based on likelihood functions. A likelihood function is a function of the unknown parameters whose purpose is to quantify how well any given values for the parameters agree with the observed data. An optimal estimate of the unknown parameters is taken to be those values that maximize the likelihood function (the *maximum-likelihood* estimate). A confidence region on the parameters is the collection of parameter values whose likelihood is within some tolerance of the maximum likelihood.

A given assumption about the probability distribution of the data errors defines a particular likelihood function for the parameters. In our location algorithms GSEL and GMEL, we currently assume that the picking errors, e_{ij}, are statistically independent and that each has a *generalized Gaussian* probability distribution of order p. The probability density function (p.d.f.) of this distribution is given by (Billings et al., 1994)

$$f[e_{ij}] = \frac{\text{const}}{\sigma_{ij}} \exp\left[-\frac{1}{p} \left| \frac{e_{ij}}{\sigma_{ij}} \right|^p \right] \tag{4}$$

where σ_{ij} is the assigned standard error. For $p = 1$, the p.d.f. is a Laplace distribution (two-sided exponential) and for $p = 2$ it is Gaussian. For the small-cluster problem ($c_{ij} = a_j$), this error model implies a likelihood function, L, given by

$$-\log L = \text{const} + \sum_{ij} \log \sigma_{ij} + \frac{1}{p} \sum_{ij} \frac{1}{(\sigma_{ij})^p} \left| d_{ij} - t_i - T_j (\mathbf{x}_i) - a_j \right|^p . \tag{5}$$

We comment that, with the generalized Gaussian distribution, the negative logarithm of the likelihood function is an L_p norm (to the pth power) of the data residuals. In the Gaussian case it is an L_2 norm, and maximization of the likelihood function with respect to the problem unknowns becomes a least-squares problem.

When correction functions, instead of correction terms, are used to parameterize path corrections, an additional term can be added to L in order to invoke geo-statistical constraints (see Rodi et al., 2003).

Single-Event Confidence Regions

We briefly describe our uncertainty approach to location error in the single-event location problem and refer the reader to Rodi and Toksöz (2001) for further detail. To define the single-event problem in our notation we can drop the event index i in equation (1). To simplify this discussion, let us also set path corrections to zero, yielding

$$d_j = t + T_j(\mathbf{x}) + e_j. \tag{6}$$

Our current single-event algorithm (GSEL) assumes that the data standard errors are known within a constant factor, i.e.

$$\sigma_j = \sigma \eta_j \tag{7}$$

with the n_j being known weights and with σ the unknown standard error across all the data. The problem unknowns are then the event parameters, **x** and *t*, and σ. The log likelihood function from equation (5) becomes

$$-\log L(\mathbf{x},t,\sigma;\mathbf{d}) = \text{const} + n\log\sigma + \frac{1}{p\sigma^p}\sum_i \frac{1}{(u_j)^p}\left|d_j - t - T_j(\mathbf{x})\right|^p . \qquad (8)$$

Here, **d** denotes the arrival time data (d_j) collectively as an *n*-component vector.

Our single-event location algorithm uses a grid-search technique to maximize *L* with respect to the event hypocenter **x**. For each hypocenter in a 3-D grid, the algorithm computes a reduced likelihood function, i.e. maximized with respect to *t* and σ with **x** fixed. The maximization over σ and *t* is performed with analytic and root-finding techniques. The hypocenter grid is constructed dynamically through a process of successive refinement, along the lines of Sambridge's (1999) neighborhood algorithm. The search finds the hypocenter that yields the largest reduced likelihood among all grid nodes tested. To incorporate hard bounds on the event hypocenter (GT constraints), one simply eliminates grid nodes violating the bounds from the search.

Flinn (1965), Evernden (1969) and Jordan and Sverdrup (1981) developed the methodology for hypocentral confidence regions for the case of Gaussian data errors ($p = 2$) and using a linear approximation to the travel-time functions, T_j. Their methods can be formulated in terms of hypothesis testing using a likelihood ratio as the test statistic. Doing so allows us to define confidence regions under less restrictive assumptions.

Confidence regions can be found on all four location parameters simultaneously (including origin time) or on any subset of parameters. For a 3-D, hypocentral confidence region on **x**, the relevant test statistic is

$$\tau(\mathbf{x},\mathbf{d}) = \log\left[\frac{\max_{x,t,\sigma} L(\mathbf{x},t,\sigma;\mathbf{d})}{\max_{t,\sigma} L(\mathbf{x},t,\sigma;\mathbf{d})}\right] . \qquad (9)$$

This statistic compares the value of *L* achieved by maximizing it over all unknown parameters to the value of *L* when maximized over only *t* and σ, with the hypocenter fixed to any given **x**. Given a confidence level β, we can reject **x** at that level if $\tau(\mathbf{x},\mathbf{d})$ is greater than some critical value, τ_β. This critical value is determined by the probability distribution of $\tau(\mathbf{x},\mathbf{d})$, as induced by the errors in **d**. If **x** is *not* rejected, it is *inside* the confidence region for the specified confidence level. That is, the confidence region comprises the hypocenters **x** satisfying

$$\tau(\mathbf{x},\mathbf{d}) \le \tau_\beta . \qquad (10)$$

Under Flinn's assumptions, τ is F-distributed and τ_β can be found directly from the F cumulative distribution function (c.d.f.). The locus of points **x** satisfying equation (10) fills an ellipsoid whose axis lengths and orientations are easily found.

With our more general assumptions, τ does not necessarily have a well-known probability distribution and the geometry of the confidence region cannot be found with analytic formulas. Therefore, we use numerical techniques to find τ_β and the values of **x** that satisfy equation (10). Our confidence region method becomes a two-step procedure:

1. Sample $\tau(\mathbf{x},\mathbf{d})$ at points **x** on a dense 3-D hypocenter grid. This entails maximizing *L* with respect to origin time and σ for each point on the grid, and comparing each such value to the maximum *L* over all parameters (i.e. the maximum likelihood solution).

2. Perform a Monte Carlo simulation to find τ_β for various β. This entails computing $\tau(\mathbf{x}^{tru},\mathbf{d}^{syn})$ for an assumed "true" hypocenter $\mathbf{x}^{tru}$ and many realizations of synthetic data, $\mathbf{d}^{syn}$. Each realization $\mathbf{d}^{syn}$ is constructed by adding a realization of pseudo-random errors to arrival times calculated for $\mathbf{x}^{tru}$. The random noise is generated according to the assumed error distribution using an assumed "true" value of σ.

Both steps of this procedure can be computationally intensive. The first step (likelihood sampling) requires maximizing L for all hypocenters on a 3-D grid, but only for the real data. The second step (Monte Carlo simulation) entails maximizing L twice, with $\mathbf{x}$ fixed and free, for each of many realizations of synthetic data. We have found that about 200–300 realizations of synthetic data yield stable results.

Confidence regions on other event parameters are obtained in an analogous manner, and share some of the calculations needed for hypocentral regions. For epicenter confidence regions, for example, one changes the likelihood-ratio statistic in equation (9) to include maximization with respect to event depth, z, in addition to t and s.

Examples

An example of our approach, which demonstrates the importance of accounting for travel-time nonlinearity, is shown in Figure 1. This figure displays confidence regions for an earthquake in Honshu, Japan, as determined from mostly first-arrival, teleseismic data obtained by the International Monitoring System (IMS) seismic network. Each figure shows the 2-D confidence region of the event epicenter (at varying confidence levels) and cross-sections through the 3-D confidence region on the event hypocenter. The IASP91 travel-time tables were used in these computations, and the best-fitting location of the event is in the mantle of the IASP91 model (depth = 44 km). The epicenter confidence region for each confidence level (right of figure) is nearly elliptical in shape. The corresponding hypocentral confidence region, however, is quite non-ellipsoidal and extends upward into the crust (left and middle frames). This is an effect of nonlinearity that is not accounted for with the conventional Gaussian/linear formulas. The cause of it is the velocity difference, and consequent difference in the sensitivity of travel-time to event depth (dT/dz), across the Moho. The conventional confidence ellipsoid formulas in this case would assume the mantle dT/dz holds everywhere, precluding the asymmetry seen in Figure 1. This example illustrates only one simple nonlinear phenomenon that can occur even with well-recorded events, 1-D Earth models, and Gaussian data errors (our computations used a Gaussian error model).

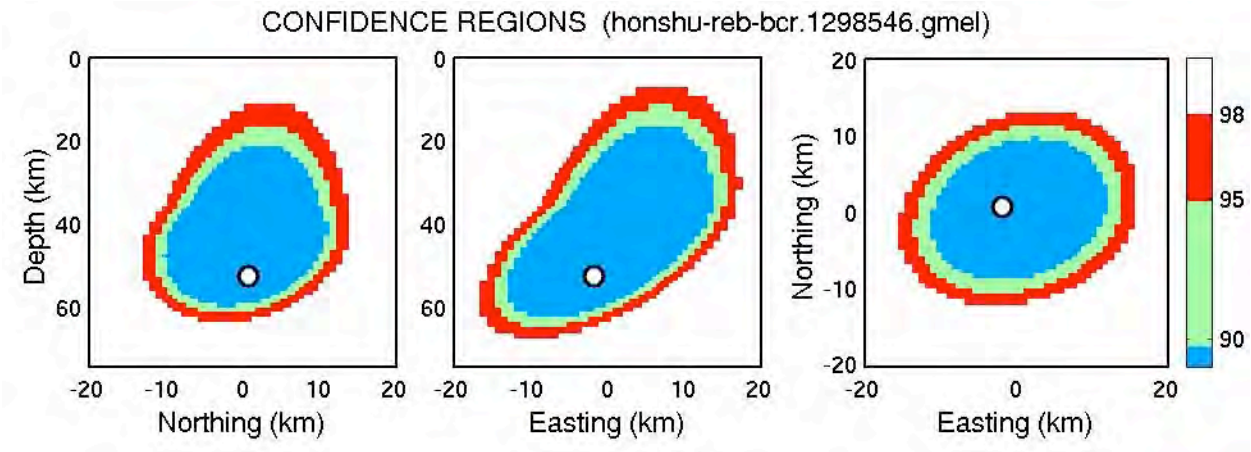


Figure 1: Confidence regions for a 1998 earthquake in Honshu determined using 23 REB arrival time data (2 Pn, 1 Sn, 18 P, 1 S and 1 PKP). Confidence regions at three confidence levels are displayed: 90% (inner (blue) shaded area), 95% (combined inner and central (blue and green) shaded areas), and 98% (inner, central and outer (blue, green and red) shaded areas). *Left and middle frames*: cross-sections through 3-D confidence regions on the event hypocenter. *Right frame*: 2-D confidence regions on the event epicenter. The circle marks the event location reported in the REB.

A second example of Monte Carlo confidence regions is shown in Figure 2. These are for an event (no. 91135030) from the 1991 Racha, Georgia earthquake sequence, studied by Myers and Schultz (2000). The data set comprised P wave arrival times from six stations, obtained from ISC and supplemented with picks made by F. Ryall of LLNL. The stations cover an epicentral distance range of 6° to 22°.

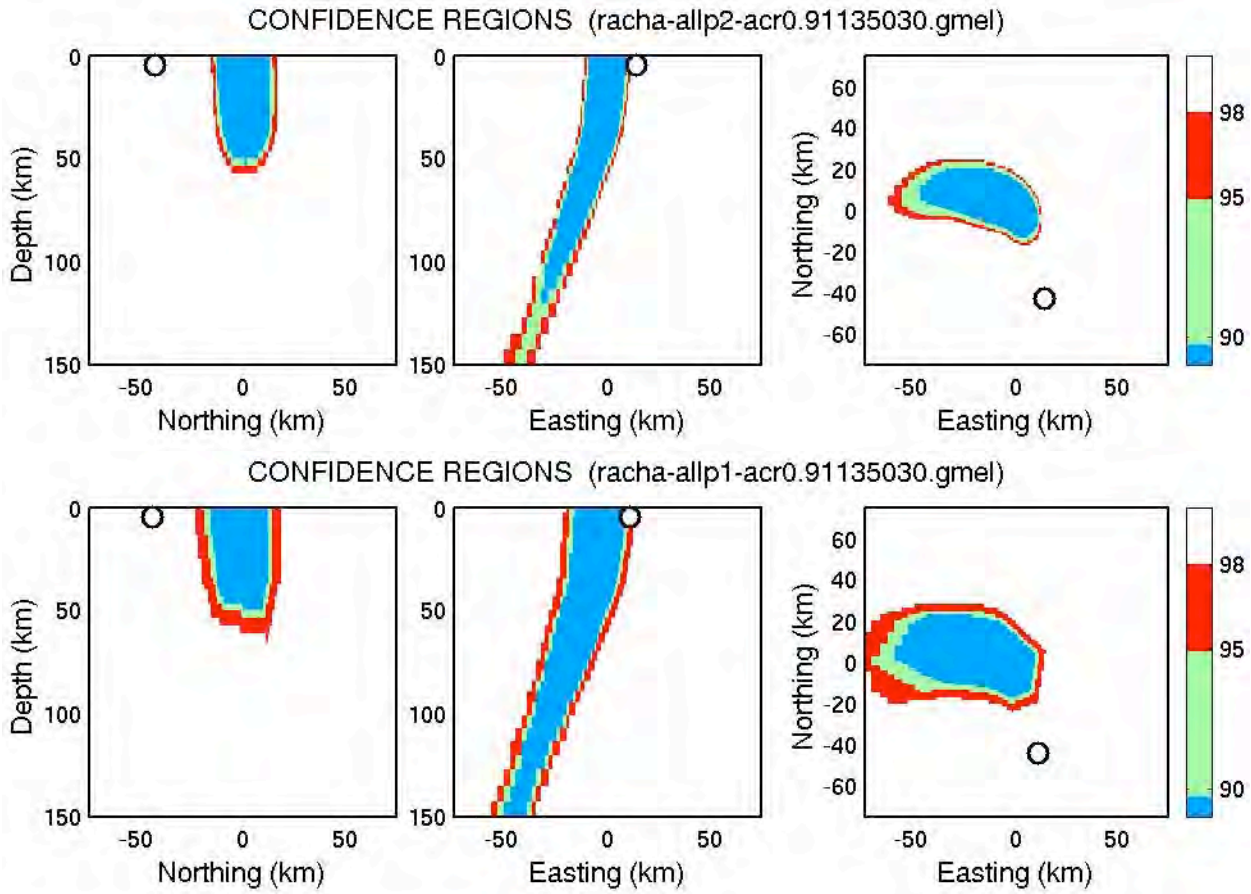


Figure 2: Confidence regions (at 90, 95 and 98%) for an event from the 1991 Racha earthquake sequence. The data set used comprised first-arrival P wave times at six regional stations, with epicentral distances varying from 6 to 22°. The top frames are based on the assumption of Gaussian picking errors (p = 2). The bottom frames assume the errors are from a Laplace (two-sided exponential) (p = 1). *Left and middle*: Cross-sections of 3-D confidence regions on the event hypocenter, taken through the maximum-likelihood location. *Right*: Confidence regions on epicenter. The circle in each plot marks the local network location for the event reported by Myers and Schultz (2000). The maximum-likelihood epicenter is at zero northing and zero easting.

We computed confidence regions using two different assumptions about the probability distribution of picking errors. The top frames of Figure 2 assumed a Gaussian distribution (p = 2) while the bottom frames assumed a Laplace distribution (p = 1). Even in the Gaussian case we see that the confidence regions are blatantly non-elliptical, especially the epicentral confidence regions (rightmost frames). As with the Honshu events, a big contributor to non-ellipticity is the nonlinearity of the travel-times with respect to event depth. This factor is even more significant in this example because the event depth is so poorly constrained by the sparse network available. We also see that Laplace-error confidence regions (bottom frames of Figure 2) are blockier and larger than Gaussian-error ones, which can be attributed to the differing properties of L_1 and L_2 error norms.

We note that the confidence regions in Figure 2 do not cover the GT location inferred by Myers and Schultz (the circles in each frame), and our maximum-likelihood location is biased by about 30 km. This is because we did not apply travel-time corrections to the data, or attempt to account for them as modeling errors in the computation of the confidence regions.

Multiple-Event Location Confidence Regions

Our multiple-event location algorithm (GMEL) solves jointly for the location parameters, x_i and t_i, of m events, and the travel-time correction terms, a_j, for n stations. It finds maximum-likelihood solutions for these unknown parameters, using the multiple-event, multiple-station version of the likelihood function in equation (5) Like its single-event predecessor, GMEL implements the generalized Gaussian error model, this time allowing unknown station-specific scale factors, s_j, on the standard errors, i.e.

$$s_{ij} = s_j n_{ij} \tag{11}$$

where the n_{ij} are specified weights. Hard bounds on all the unknown parameters, including upper and lower bounds on the a_j, are allowed. GMEL finds the maximum-likelihood solutions for the parameters by iterating over alternating loops over events, to update event locations with station terms fixed, and over stations, to update the station terms and station scale factors, with the event locations fixed. Grid-search is used to find the optimal event locations (see Rodi et al., 2002).

To define confidence regions on one of the m events in the multiple-event location problem, we have adapted our location uncertainty approach as follows. Let us denote the likelihood function for the multiple-event location problem as $L(\mathbf{x}_1, t_1, \mathbf{x}_2, t_2, \ldots, \mathbf{x}_m, t_m, a_1, s_1, a_2, s_2 \ldots, a_n, s_n; \mathbf{d})$, where the vector $\mathbf{d}$ now contains the data for all events and stations. Let us arbitrarily identify the event of interest to be the first (i =1). To define a confidence region on its hypocenter, $\mathbf{x}_1$, our uncertainty paradigm tells us to define a test-statistic, $t(\mathbf{x}_1, \mathbf{d})$ that compares two values of the likelihood function. The first is the value achieved by maximizing L over all event and station parameters: $\mathbf{x}_1, t_1, \mathbf{x}_2, t_2, \ldots, \mathbf{x}_m, t_m$ and $a_1, s_1, a_2, s_2, \ldots, a_n, s_n$. The second value of L is that achieved by maximizing L over all the parameters except $\mathbf{x}_1$, which is held fixed. Maximization of L in both cases is performed subject to available GT constraints on any of the event locations. We will not write the formula for $t(\mathbf{x}_1, \mathbf{d})$ but it is analogous to equation (9).

Given this, our method for computing a confidence region on $\mathbf{x}_1$ is a two-step process analogous to the single-event case:

1. Sample $t(\mathbf{x}_1, \mathbf{d})$ for values of $\mathbf{x}_1$ on a dense grid.

2. Compute Monte Carlo realizations of $t(\mathbf{x}_1^{\text{tru}}, \mathbf{d}^{\text{syn}})$ for many random realizations of (multiple-event) synthetic data, $\mathbf{d}^{\text{syn}}$.

Each computation of t, whether for real or synthetic data, now entails computing the solution to a multiple-event inverse problem involving the data and parameters for all events and stations.

This approach to location confidence regions implicitly accounts for the uncertainty in $\mathbf{x}_1$ induced by its trade-off with the travel-time corrections, a_j, as they are constrained by the multiple-event data set and GT information on the other events. It avoids the need for an explicit uncertainty model for the station terms, which would then be treated as modeling errors added to the picking errors. This implicit approach takes into account correlations and the finite accuracy of GT events, and handles nonlinearity and non-Gaussian data errors.

Example from the Izmit Earthquake Sequence

We show some preliminary results of our multiple-event uncertainty approach applied to the 17 August 1999 Izmit, Turkey, earthquake and 32 of its aftershocks. The data set contains approximately 3500 Pn and teleseismic P arrival times from 640 stations from National Earthquake Information Center (NEIC), which we obtained courtesy of R. Engdahl and the IASPEI Working Group on Multiple-Event Location. Previously, Engdahl and Bergman (2001) applied the hypocentroidal decomposition (HDC) method to this cluster and a similar cluster from the 12 November 1999 Duzce earthquake sequence. We show confidence regions that we have computed for one of the events in the Izmit cluster.

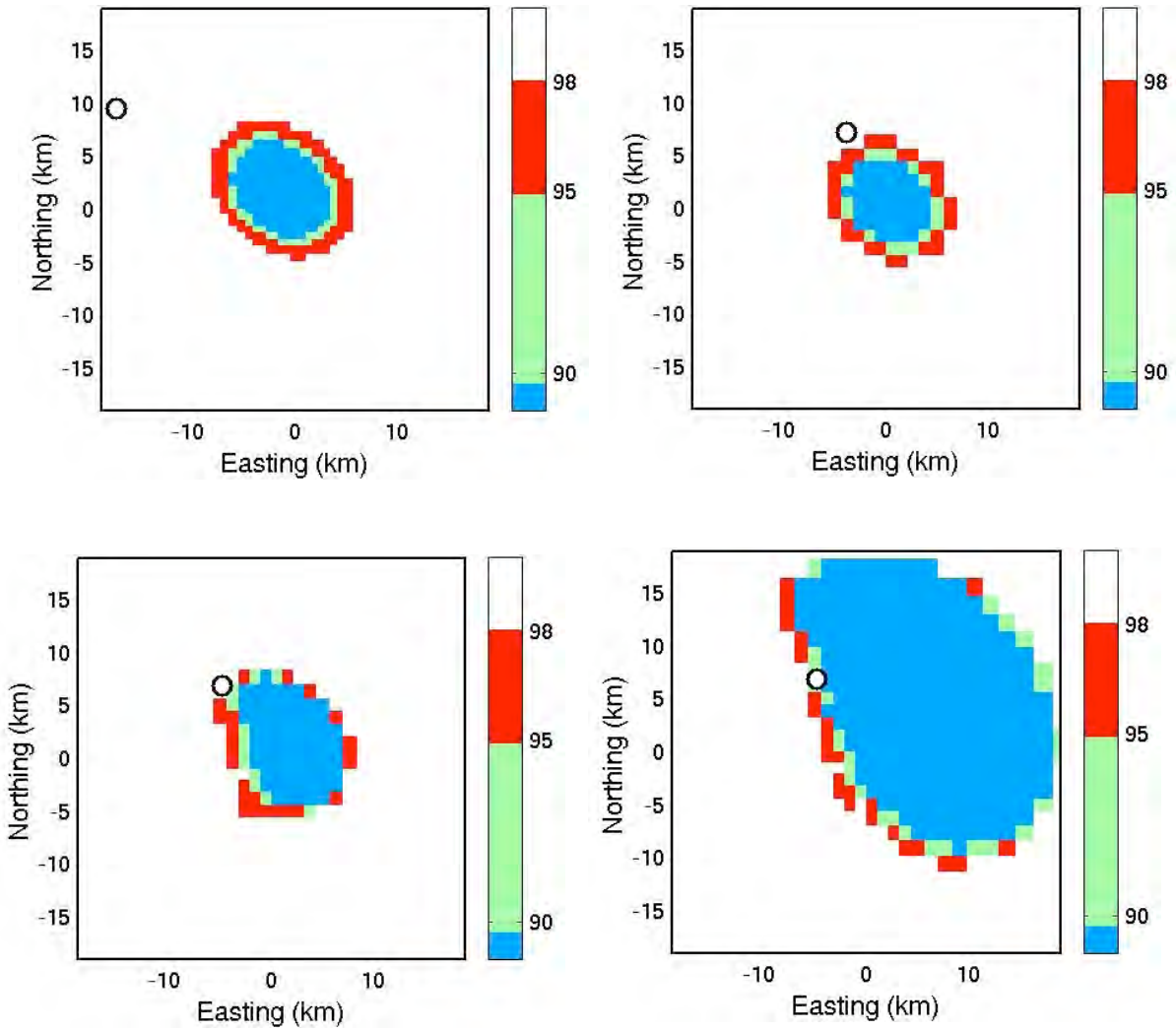


Figure 3: ***Top left*****: Single-event epicentral confidence regions (at 90, 95 and 98% confidence) for a well-recorded aftershock of the 1999 Izmit, Turkey earthquake. Station travel-time corrections were assumed to be zero.** ***Top right and bottom*****: Multiple-event confidence regions for the same event.** ***Top right*****: computed with the Izmit mainshock constrained as a GT0 event.** ***Bottom left*****: computed with the Izmit mainshock constrained as a GT5 event.** ***Bottom right*****: computed using no GT constraints on any events. In each frame, the circle marks the ground-truth (GT5) epicenter for the aftershock.**

The event we consider is a well-recorded aftershock occurring on 31 August 1999, and has 138 defining phases in the data set (compared to 388 defining phases for the Izmit mainshock). The top/left frame of Figure 3 shows the single-event, epicentral confidence region for this event, computed independently of the other events and with zero travel-time corrections at the stations ($a_j = 0$). Gaussian data errors were assumed and the depth of the event was fixed. The circle marks a GT5 location for the aftershock determined from a local seismic network (provided by R. Engdahl for the IASPEI Working Group). We see that the single-event confidence region is displaced by about 20 km from the GT location, and even the 98% confidence region does not include the GT location. This is expected since travel-time corrections were not applied to the AK135 travel-time tables that were used in the computations.

The other frames of Figure 3 show different versions of multiple-event confidence regions for the same Izmit aftershock. In each case, the event was located jointly with the 32 other events and the estimation of travel-time corrections at the roughly 640 stations in the data set. These other 32 events, which include the Izmit mainshock, play the role of calibration events. The different versions of multiple-event confidence regions have to do with

different GT constraints we used for the calibration events. The top/right frame assumed that the Izmit mainshock is a GT0 event. Thus, the mainshock was constrained to its local network solution while the other event epicenters were free to vary. The bottom/left frame also assumed the Izmit mainshock was the only GT event, but this time it was assumed to be GT5, i.e. its epicenter was constrained to be within 5 km of the local network solution. The bottom/right frame uses no GT constraints on any of the events. In each frame, the maximum-likelihood solution for the aftershock found by GMEL is in the center of the plot (at zero northing and easting) although it is not marked. In the top/right frame this is near the center of the confidence region, but this is not the case for the bottom two frames.

Comparing the top frames of Figure 3, we see that the multiple-event confidence region for the aftershock is much closer to its local network solution than was the case for the single-event confidence region. This is because the requirement that the event locations of all the events be self-consistent with the station travel-time corrections, combined with the GT0 constraint on the mainshock, removes much of the bias in the GMEL location that we saw in the single-event case. However, the local network solution (which might be in error by as much as 5 km) is a little outside the confidence regions at each confidence level. In the bottom/left frame, which assumed the mainshock was GT5, the confidence region for the aftershock is slightly larger, as expected, and comes closer to including the local network solution. In the bottom/right frame, we see that the multiple-event confidence region resulting from no GT constraints is much larger. This largely reflects the fact that, in small-aperture multiple-event location, there is a strong trade-off between the centroid of the cluster and the station corrections; i.e. absolute events locations cannot be determined without GT constraints. In the linear theory (Jordan and Sverdrup, 1981) this indeterminacy is total, and yet the confidence region in the bottom/right frame is finite. The probable explanation for this is that, for computational reasons, we limited the extent to which event locations could trade off with station travel-time corrections to 15 km. However, another reason might be that we imposed hard bounds on the station travel-time corrections, ±10 sec relative to AK135 times, which is a reasonable assumption. It may be that this constraint also has limited the size of the confidence regions in the bottom/right frame, and may also explain why they are not centered on the ones computed *with* a GT constraint on the mainshock.

These results, while preliminary, seem to support the validity of our implicit approach to modeling errors. Further, the results suggest the possibility that, even in this simplest of joint location/calibration problems, prior constraints on both reference event locations and travel-time discrepancies from global 1-D models might be an important element in location error assessment.

CONCLUSIONS AND RECOMMENDATIONS

We have developed a general theoretical and computational framework for characterizing the uncertainty in seismic event locations in the context of the joint inverse problem of multiple-event location and travel-time calibration. Like our earlier work on single-event location, our approach accommodates Gaussian and non-Gaussian assumptions about the picking errors in seismic arrival times, and avoids linearization of the forward travel-time problem. The most important new element of our approach is that it takes implicit account of the errors in travel-time forward models. This avoids a difficult task when the calibration and location problems are addressed separately, i.e. determining realistic uncertainty estimates in seismic calibration parameters, and then incorporating them into a single-event event location algorithm. However, our approach introduces a new difficulty in the fact that it is computationally intensive. We are investigating computational short cuts that will make our method more practical. Further, we are looking at how best to implement the approach with more general parameterizations of path corrections, including travel-time correction surfaces, so that the method is not restricted to small event clusters.

REFERENCES

Billings, S.D., M.S. Sambridge and B.L.N. Kennett, 1994. Errors in hypocenter location: picking, model and magnitude dependence, *Bull. Seism. Soc. Am., 84,* 1978–1990.

Engdahl, E.R. and E.A. Bergman, 2001, Validation and generation of reference events by cluster analysis, *Proceedings, 23rd Seismic Research Review: Worldwide Monitoring of Nuclear Explosions*, Jackson Hole, Wyoming.

Evernden, J.F., 1969. Precision of epicenters obtained by small numbers of worldwide stations, *Bull. Seism. Soc. Am., 59*, 1365–1398.

Flinn, E.A., 1965, Confidence regions and error determinations for seismic event location, *Rev. Geophys., 3*, 157–185.

Jordan, T.H. and K.A. Sverdrup, 1981, Teleseismic location techniques and their application to earthquake clusters in the south-central Pacific, *Bull. Seism. Soc. Am., 71*, 1105–1130.

Myers, S.C., and C.A. Schultz, 2000, Improving sparse network seismic locations with Bayesian kriging and teleseismically constrained calibration events, *Bull. Seism. Soc. Am., 90*, 199–211.

Rodi, W., E.R. Engdahl, E.A. Bergman, F. Waldhauser, G.L. Pavlis, H. Israelsson, J.W. Dewey and M.N. Toksöz, 2002, A new grid-search multiple-event location algorithm and a comparison of methods, *Proceedings, 24th Seismic Research Review - Nuclear Explosion Monitoring: Innovation and Integration*, Ponte Vedra Beach, Florida, 403–411.

Rodi, W., S.C. Myers and C.A. Schultz, 2003, Grid-search location methods for ground-truth collection from local and regional seismic networks, *Proceedings, 25th Seismic Research Review Nuclear Explosion Monitoring: Building the Knowledge Base*, Tucson, Arizona (this volume).

Rodi, W., and M.N. Toksöz, 2000, Grid-search techniques for seismic event location, *Proceedings, 22nd Annual DoD/DOE Seismic Research Symposium: Planning for Verification of and Compliance with the Comprehensive Nuclear-Test-Ban Treaty (CTBT)*, New Orleans, Defense Threat Reduction Agency (DTRA).

Rodi, W., and M.N. Toksöz, 2001, Uncertainty analysis in seismic event location, *Proceedings, Proceedings, 23rd Seismic Research Review: Worldwide Monitoring of Nuclear Explosions*, Jackson Hole, Wyoming.

Sambridge, M., 1999. Geophysical inversion with a neighborhood algorithm—1. Searching a parameter space, *Geophys. J. Int., 138*, 479–494.

Schultz, C.A., S.C. Myers, J. Hipp and C.J. Young, 1998, Nonstationary Bayesian kriging: a predictive technique to generate spatial corrections for seismic detection, location, and identification, *Bull. Seism. Soc. Am., 88*, 1275–1288.

GRID-SEARCH LOCATION METHODS FOR GROUND-TRUTH COLLECTION FROM LOCAL AND REGIONAL SEISMIC NETWORKS

William L. Rodi,[1] Stephen C. Myers,[2] and Craig A. Schultz[2]

Massachusetts Institute of Technology;[1] Lawrence Livermore National Laboratory[2]

Sponsored by National Nuclear Security Administration
Office of Nonproliferation Research and Engineering
Office of Defense Nuclear Nonproliferation

Contract No. DE-FC03-01SF22397[1] and W-7405-ENG-48[2]

ABSTRACT

The objective of this project is to develop improved seismic event location techniques that can be used to generate more and better quality reference events using data from local and regional seismic networks. Our approach is to extend existing methods of multiple-event location with more general models of the errors affecting seismic arrival time data, including picking errors and errors in model-based travel-times (path corrections). Toward this end, we are integrating a grid-search based algorithm for multiple-event location (GMEL) with a new parameterization of travel-time corrections and new kriging method for estimating the correction parameters from observed travel-time residuals. Like several other multiple-event location algorithms, GMEL currently assumes event-independent path corrections and is thus restricted to small event clusters. Our new parameterization assumes that travel-time corrections are a function of both the event and station location, and builds in source-receiver reciprocity and correlation between the corrections from proximate paths as constraints. Our new kriging method simultaneously interpolates travel-time residuals from multiple stations and events to estimate the correction parameters as functions of position. We are currently developing the algorithmic extensions to GMEL needed to combine the new parameterization and kriging method with the simultaneous location of events. The result will be a multiple-event location method that is applicable to non-clustered, spatially well-distributed events. We are applying the existing components of our new multiple-event location method to a dataset of regional and local arrival times from Nevada Test Site (NTS) explosions with known origin parameters. Preliminary results show the feasibility and potential benefits of combining our location and kriging techniques. We also show some preliminary work on generalization of the error model used in GMEL with the use of mixture-of-Gaussians probability distributions fit to observed travel-time residuals.

OBJECTIVE

Multiple-event location methods are enjoying increased popularity as tools for calibration and ground-truth collection (e.g. Engdahl and Bergman, 2001). The objective of this project is to develop improved multiple-event location techniques that can be used to increase the number and accuracy of reference events obtained from local and regional seismic networks. The limitations of existing methods can be primarily attributed to their parameterization of path travel-time corrections and the prior information allowed on these corrections. Typically, path corrections are assumed to be event-independent, which limits the location method to small event clusters, and unrelated between stations, which misses an important constraint when closely separated stations are involved. We are extending an existing multiple-event location algorithm (GMEL) to incorporate a more general model of path corrections and new procedures for estimating the corrections from multiple-station data. Further, existing event location methods are generally limited to Gaussian models of observational (picking) errors, therefore, we are investigating a more general error model parameterized with mixtures of Gaussians that can accommodate skewed and multi-modal error distributions.

RESEARCH ACCOMPLISHED

Approach

Multiple-event location problem

To describe our approach we consider the basic multiple-event location problem involving only first P arrival times observed for a subset of paths between m events (i=1,2…m) and n stations (j=1,2…n). This problem can be stated as

$$d_{ij} = t_i + T_j(\mathbf{x}_i) + c_{ij} + e_{ij} \quad (1)$$

where d_{ij} is the observed arrival time for the (i, j)th path; t_i and $\mathbf{x}_i$ are origin parameters (time and hypocenter, respectively) of the ith event; T_j is a model-based travel-time function for the jth station; c_{ij} is a correction to this function; and e_{ij} is an observational (picking) error in d_{ij}. The unknowns in this inverse problem are the event parameters, ($\mathbf{x}_i$,t_i), and the path corrections, c_{ij}. As part of the multiple-event location problem we may include appropriate prior constraints on the unknown parameters.

Path corrections

Multiple-event location methods (e.g., Dewey, 1971; Jordan and Sverdrup, 1981; Pavlis and Booker, 1983) have generally assumed that the path corrections are event-independent, i.e.

$$c_{ij} = a_j \quad (2)$$

where a_j is a time term associated with the jth station. This assumption is also made by GMEL. The inverse problem then becomes to solve simultaneously for the m event hypocenters ($\mathbf{x}_1$,t_1, $\mathbf{x}_2$,t_2…$\mathbf{x}_i$,t_i) and the n station time terms (a_1, a_2…a_j). GMEL accomplishes this with an iterative procedure for alternatively updating event hypocenters and station time terms, employing a grid-search technique for locating the events (see Rodi et al., 2002a). The use of a grid search makes it straightforward to constrain parameters within specified bounds, allowing the incorporation of ground-truth (GT) constraints on event locations.

The assumption of event-independent path corrections restricts our multiple-event location method to events with cluster sizes that are small compared to the cluster's distance to stations. This imposes a severe restriction on the event-station geometries that can be used in the multiple-event analysis, e.g. disallowing stations too close to the event cluster.

The more general parameterization of path corrections we are pursuing extends the idea of Schultz et al. (1998), which is to allow an explicit dependence on the location of an event, i.e.

$$c_{ij} = C_j(\mathbf{x}_i). \quad (3)$$

Our extension allows an explicit dependence on both the event *and* station locations. Denoting the latter as $\mathbf{y}_j$, for the *j* station, we have

$$c_{ij} = C(\mathbf{x}_i,\mathbf{y}_j). \tag{4}$$

The multiple-event location problem then becomes to solve simultaneously for the *m* event hypocenters and the function $C(\mathbf{x},\mathbf{y})$.

Since the function *C* has an infinite number of degrees of freedom, it is necessary to either restrict its functional form or invoke strong smoothness constraints on its spatial dependence, or both. To restrict the functional form of *C* we parameterize it in terms of one or more *universal parameter* functions, which are not specific to a particular event or station. The simplest such parameter function is a *time-term* function, *a*, which yields the correction for a path as

$$C(\mathbf{x},\mathbf{y}) = a(\mathbf{x}) + a(\mathbf{y}). \tag{5}$$

It is clear that the time-term function generates reciprocal travel-time corrections, since the event location **x** and station location **y** can be interchanged in equation (5). A more flexible parameterization, employed in the examples shown later, is a *mislocation-vector* function, $\mathbf{a}(\mathbf{x})$, for which

$$C(\mathbf{x},\mathbf{y}) = \mathbf{p}(\mathbf{x},\mathbf{y}) \cdot \mathbf{a}(\mathbf{x}) + \mathbf{q}(\mathbf{x},\mathbf{y}) \cdot \mathbf{a}(\mathbf{y}). \tag{6}$$

Here, **p** is the gradient of the model-based travel-time with respect to the event location, while **q** is the gradient with respect to the station location:

$$\mathbf{p} = \nabla_1 T(\mathbf{x},\mathbf{y}) \tag{7}$$
$$\mathbf{q} = \nabla_2 T(\mathbf{x},\mathbf{y}). \tag{8}$$

(∇_k means gradient with respect the *k*th argument of a function.) Each is a slowness vector pointed in the direction of the raypath, and each depends on both **x** and **y** since the raypath depends on the location of both its endpoints. The interpretation of **a** as a mislocation vector follows from the fact that equation (6) is the first order change in travel-time that results from perturbing the event location by $\mathbf{a}(\mathbf{x})$ and the station location by $\mathbf{a}(\mathbf{y})$.

Since *T* is a reciprocal function of its arguments, we have $\mathbf{p}(\mathbf{x},\mathbf{y}) = \mathbf{q}(\mathbf{y},\mathbf{x})$, which shows that the mislocation-vector parameterization also generates travel-time corrections that are source-receiver reciprocal.

We point out that station-specific correction functions of the type considered by Schultz et al. (1998) are easily defined in terms of universal parameter functions. In the case of the mislocation-vector parameterization:

$$a_j(\mathbf{x}) = \mathbf{p}(\mathbf{x},\mathbf{y}_j) \cdot \mathbf{a}(\mathbf{x}) + \mathbf{q}(\mathbf{x},\mathbf{y}_j) \cdot \mathbf{a}(\mathbf{y}_j). \tag{9}$$

This points up an important advantage of universal parameterizations such as those above. They define a correction function for a station at any location, whether or not the station has observed travel-time residuals to constrain the function. This is accomplished by allowing correlations between the corrections among stations and between stations and events.

We are developing an extension of GMEL that will solve simultaneously for *m* event locations and a universal parameter function that generates path corrections. The algorithm will alternate between two processes: locating events with the parameter functions fixed, and interpolating travel-time residuals with the event locations fixed. The latter process solves an interpolation problem that involves residuals from all the stations. To date, we have developed an algorithm, known as *multiple-station kriging*, to solve this interpolation problem but we have not yet integrated it with our multiple-event location algorithm.

Multiple-station kriging

We describe our new kriging algorithm for the simpler case of the time-term parameter function, $a(\mathbf{x})$, although the applications below use the mislocation-vector parameter, $\mathbf{a(x)}$, of equation (6).

For given event locations, we can define the set of residuals from the observed paths as

$$r_{ij} = d_{ij} - t_i - T_j(\mathbf{x}_i). \tag{10}$$

The interpolation problem for the time-term function then becomes

$$r_{ij} = a(\mathbf{x}_i) + a(\mathbf{y}_j) + e_{ij}. \tag{11}$$

This problem can be solved with geo-statistical constraints, as used in conventional kriging. However, we adopt a maximum-likelihood (ML) approach to the inverse problem, instead of the minimum-variance approach used in conventional kriging (e.g. Deutsch and Journel, 1998). For Gaussian data errors, the ML approach takes the solution of (11) to be the function a that minimizes the objective function given by

$$\Upsilon = \sum_{ij} | r_{ij} - a(\mathbf{x}_i) - a(\mathbf{y}_j) |^2 / \sigma_{ij}^2 + \int a(\mathbf{x})[Da](\mathbf{x})d\mathbf{x} \tag{12}$$

where σ_{ij} is the assigned standard deviation of e_{ij} and D is a specified differential operator. The maximum-likelihood inversion approach is equivalent to conventional kriging with a given correlation function when D is the *inverse* of the *covariance* operator that corresponds to the correlation function. That is, the covariance operator is the Green's function for the differential operator.

Currently we use the following operator for kriging in N spatial dimensions (N = 1, 2 or 3):

$$D = \frac{\text{const}}{\sigma_0^2}\left(\delta(\mathbf{x}) - \frac{1}{2\ell - N}\left(L_x^2\frac{\partial^2}{\partial x^2} + L_y^2\frac{\partial^2}{\partial y^2} + L_z^2\frac{\partial^2}{\partial z^2}\right)^{\ell}\right) \tag{13}$$

where σ_0^2 is a prior variance of the parameter function and L_x, L_y and L_z are correlation lengths in the x, y and z directions of a local Cartesian coordinate system. Various choices of the operator order, ℓ, correspond to correlation functions that are commonly used in conventional kriging, e.g. the *exponential* correlation function ($\ell = 1$ in 1-D, $\ell = 2$ in 3-D) and Gaussian correlation function $(\ell \to \infty)$. While we have expressed this operator in Cartesian coordinates, we have actually implemented it as a difference operator in a global, spherical coordinate system. We solve the ML criterion (Υ = minimum) for a sampled version of the function a on a latitude/longitude/depth grid. Numerically, the minimization is performed with a conjugate gradients technique.

Application to Nevada Test Site

We are applying our new approach to a dataset from the NTS explosions that have been assembled by Lawrence Livermore National Laboratory (LLNL) (Walter et al., 2003). The dataset comprises 74 nuclear explosions with known locations and origin times recorded at a network of regional and local stations. A LLNL analyst re-picked the phases and supplemented them with selected picks from the National Earthquake Information Center (NEIC) to produce a high quality dataset. The dataset has been used in studies of event location accuracy at LLNL (Myers et al., 2003) and we are using it to test our new approach to multiple-event location and kriging. The examples here use only the Pn picks from the dataset and we removed events with fewer than four Pn arrivals. The resulting subset comprises 674 arrivals from 71 events and 59 stations.

We applied the multiple-station kriging approach to the NTS data to estimate a universal parameter function of the mislocation-vector type. Depth dependence was not allowed since all the events are shallow. However, we note that the path travel-time corrections derived from the parameter function will be depth dependent owing to the depth-dependence of the slowness vectors in equation (6).

Multiple-station kriging

In these initial tests, we applied our kriging method to travel-time residuals using the IASP91 tables for model-based times and using the ground-truth locations of the events. We tried various values of the geo-statistical input parameters, as follows. In each case the order of the correlation operator (ℓ = 2, see equation (13)) was set to 2. In 2-D, this corresponds to a correlation function that is peaked at zero distance, but less peaked than a correlation function of the exponential type. We show the results for two combinations of the prior error on the mislocation function (s_0) and the correlation distance ($L = L_x = L_y$). Figure 1 shows the mislocation function obtained with s_0 = 5 km and L = 200 km, while Figure 2 shows the functions obtained with s_0 = 10 and L =100. The results are similar, but the smaller correlation distance and larger prior error (Figure 2) results in a rougher function with somewhat larger values, especially in the east component. This second case also fits the travel-time residuals better, yielding a 0.428 sec posterior RMS compared to 0.455 for the first case. The prior RMS of the residuals was 0.922 sec.

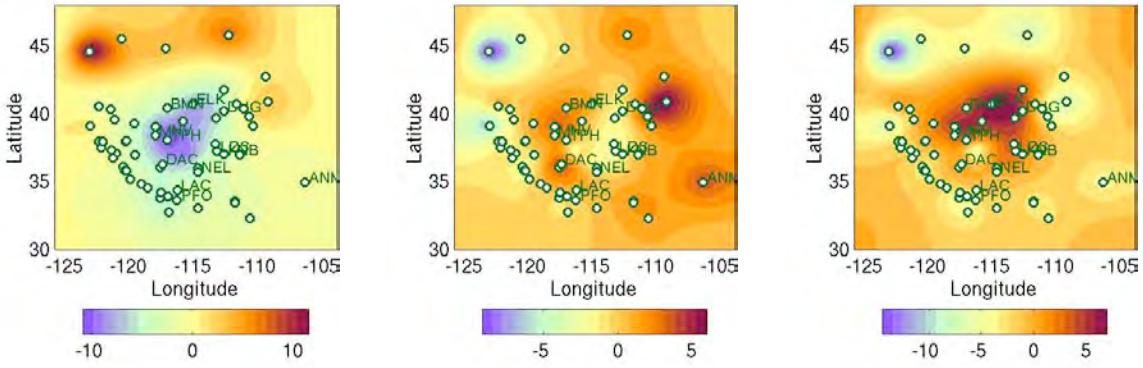


Figure 1: 2-D mislocation-vector parameter function for the region surrounding NTS: north, east and depth components (left, middle and right panels, respectively). This parameter function was derived by multiple-station kriging of Pn travel-time residuals, using 200 km for the correlation distance and 5 km for the prior error on the mislocation components. Station locations (some labeled) are marked with circles.

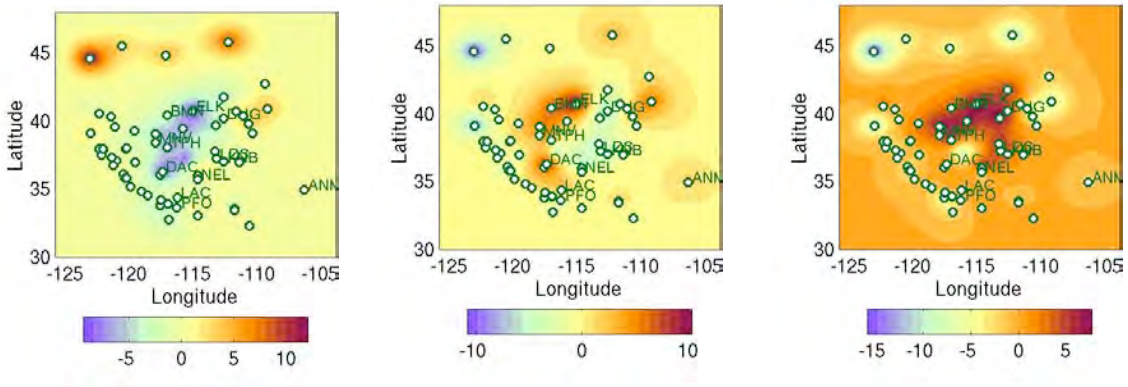


Figure 2: Same as Figure 1 but the mislocation-vector function was obtained using 100 km for the correlation distance and 10 km for the prior error on the mislocation components.

Next we show some travel-time correction functions generated from the second parameter function. Figure 3 shows the correction functions for stations ELK and BMN. These two stations are north of NTS and close to one another, and we see that their travel-time corrections are very similar (highly correlated). Figure 4 displays the correction functions for KNB, a station east of NTS, and LAC, south of NTS. Their pattern of corrections shows significant differences from each other and from the northern stations.

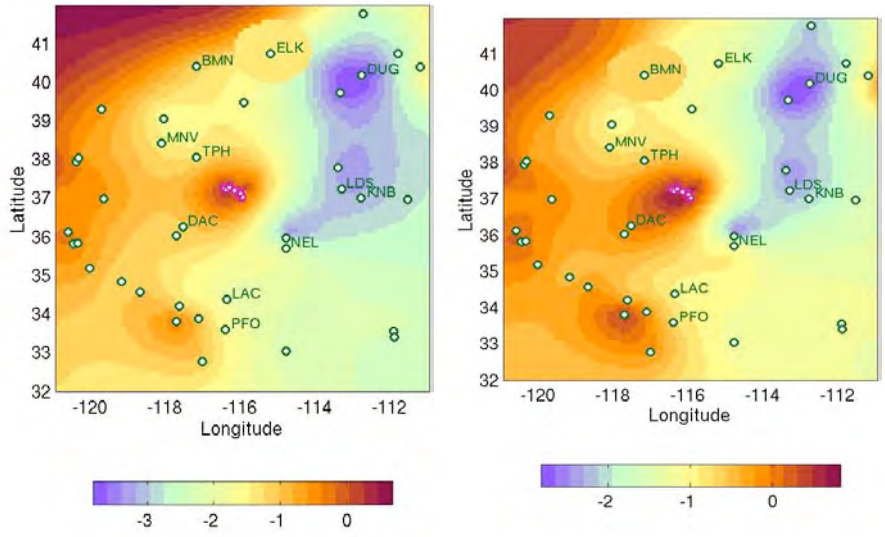


Figure 3: Travel-time correction functions for stations ELK (left) and BMN (right), generated from the 2-D mislocation-vector parameter function shown in Figure 2. The functions are displayed for zero event depth. Station locations (some labeled) are marked with circles, and the NTS events show as a small cluster of small white dots near the center of the plot.

Location experiments

We show some experiments with single-event and multiple-event location that compare the location accuracy achieved with various types of path corrections. First, we compare single-event location solutions using fixed path corrections, i.e. the events are located individually with no changes to the specified path corrections. Three cases of path corrections were used in this way:

1. Zero path corrections.
2. Station time-term corrections, obtained by averaging the residuals obtained using the ground-truth locations.
3. Travel-time correction functions obtained from the ground-truth residuals (examples are Figures 3 and 4).

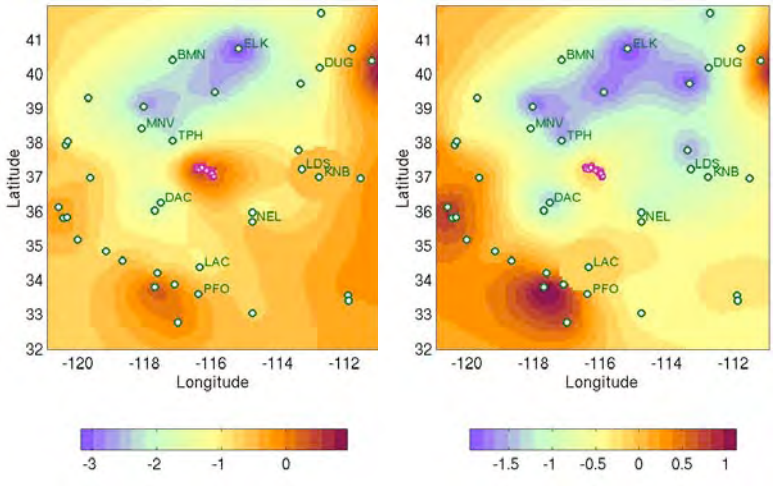


Figure 4: Travel-time correction functions for stations KNB (left) and LAC (right), generated from the 2-D mislocation-vector parameter function shown in Figure 2.

In each case, the dataset comprised 674 Pn arrivals from 71 events. Locations were run with depth bounded between 0 and 50 km.

Table 1 summarizes the location accuracy achieved with the various types of path corrections. The two versions obtained from kriged correction functions refer to the different correlation parameters used; A and B correspond to Figures 1 and 2, respectively. The table shows only epicenter mislocations, but we note that depth mislocations were often significant since only Pn arrivals were used. We see from the table that all versions of travel-time corrections improve location accuracy significantly, compared to zero corrections (line 1). The number of events with mislocations greater than 5 km drops from 15 to 3 when corrections are used in the location process. We also see that the mislocations obtained using kriged correction functions are somewhat better than those using station time terms. We point out that, in this application, the event aperture is small (approx. 50 km). Therefore, the main difference between correction terms and correction functions is that the latter allow for correlation between stations, based on their separation, while station terms are independent between stations regardless of their separation. Figure 5 shows the actual event locations obtained for two of the four cases in the table: zero corrections (line 1) and kriged corrections B (line 5).

Table 1. Location Accuracy of NTS Events: Comparison of Path Corrections.

Corrections Used	No. of Events vs. Misloc. <1	1–3	3–5	>5	Largest Misloc. (km)
None	4	38	14	15	10.4
station terms	27	38	3	3	9.8
kriged correction function (A)	36	29	3	3	9.4
kriged correction function (B)	40	26	2	3	9.1

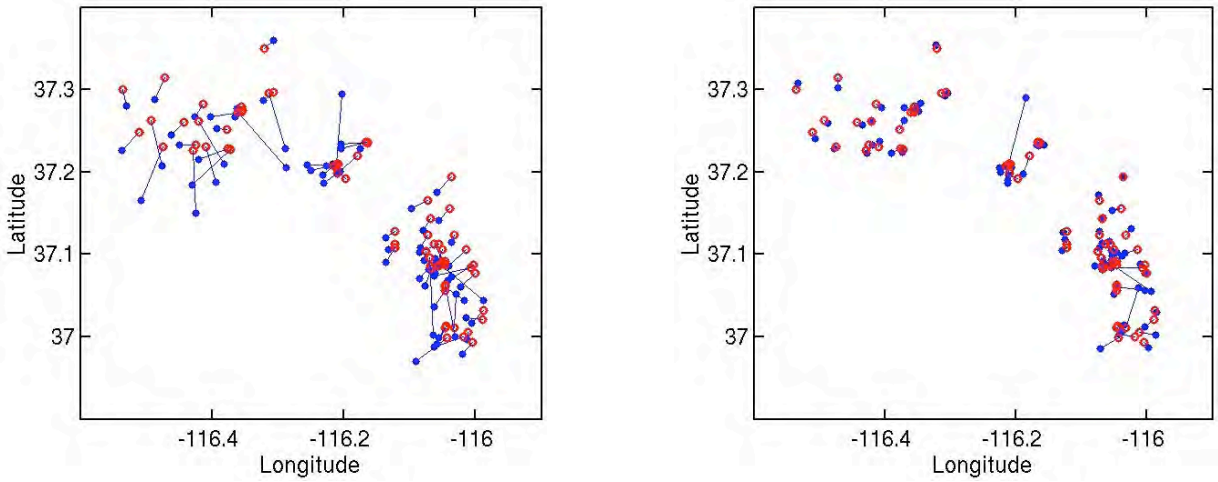


Figure 5: Locations and mislocations resulting from single-event location applied with no station corrections (left) and travel-time correction functions derived from multiple-station kriging, version B (right). In each panel, the filled (blue) circles are the solutions obtained with the location procedure and the unfilled (red) circles are ground-truth locations. A line connects the solution and GT location of each event.

We emphasize that both types of corrections just compared were derived from travel-time residuals computed using ground-truth locations for all the events, which is not realistic. In practice the corrections must be derived using limited ground-truth information. To see what difference this makes, Table 2 compares location results obtained with the ground-truth version of station terms (line 1) with those obtained using only one ground-truth location in a multiple-event location solution that solves simultaneously for the station time terms. (Note that line 1 of Table 2 repeats line 2 of Table 1.) We see from Table 2 that when there is only one ground-truth location (the best recorded event, at Rainier Mesa), the mislocations are increased, although it is mainly the smallest mislocations that get worse. The largest mislocations are similar.

Table 2. Location Accuracy of NTS Events: Single- vs. Multiple-Event Location.

	No. of Events vs. Misloc.				Largest
Loc. Method	<1	1–3	3–5	>5	Misloc. (km)
Single (with GT0 station terms)	27	38	3	3	9.8
Multiple (with one GT0 constraint)	12	46	11	2	8.9

Since we have not yet integrated our multiple-station kriging method into GMEL, we do not know how well correction functions will do when derived with limited ground-truth information. We do not expect a degration from those with station terms and correction functions will accommodate large event clusters, whereas the station term approach breaks down.

Extended Error Model

This aspect of our project addresses the complex error processes that affect arrival time measurements, as discussed in Rodi et al. (2002b). The error model now used in GMEL accepts non-Gaussian probability distributions for picking errors, but only of a restricted class (generalized Gaussian) that does not include asymmetrical (skewed) or multi-modal distributions. We are pursuing an alternative class of error distributions known as mixtures, or weighted sums, of Gaussian distributions having different means and variances.

We have developed an algorithm for fitting mixtures of Gaussians to an observed set of travel-time residuals. Given the number of terms in the mixture, *K*, the algorithm finds the weight, mean and variance of each component Gaussian distribution such that the sum provides the best fit to the histogram of observed residuals. Given the best fitting parameters for each *K*, the remaining task is to choose the smallest *K* that can explain, but not over fit, the data. Our algorithm for fitting the Gaussian parameters is a Markov-Chain Monte Carlo (MCMC) technique that optimizes the RMS misfit between the mixture distribution and the observed histogram.

Figure 6 shows an example of fitting mixtures-of-Gaussian distributions to observed residuals from the 1991 Racha earthquake sequence. The left panel shows a single Gaussian function fit to the observed histogram of residuals and the right panel is the best fitting mixture of five Gaussians, which is able to represent the multi-modal nature of the observations.

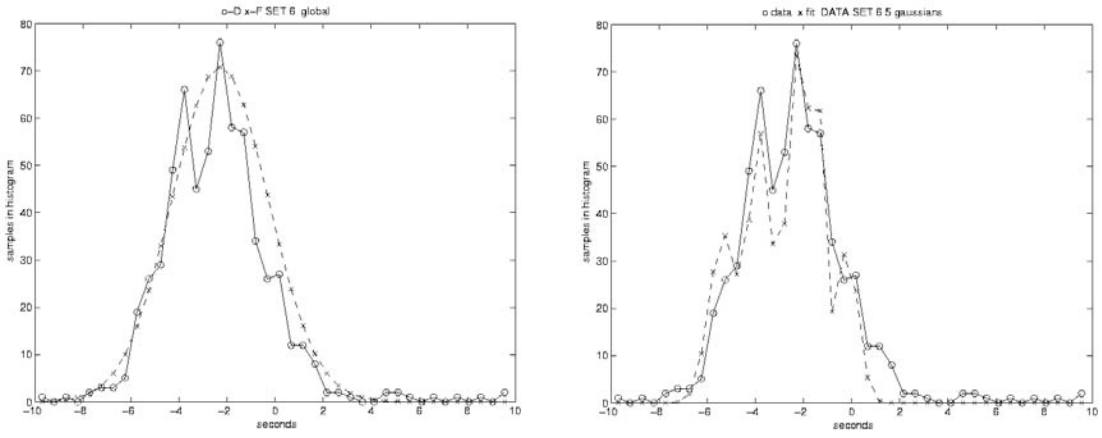


Figure 6: Probability distributions (dashed lines) fit to an observed histogram of travel-time residuals (solid line). The observed residuals are from the Racha earthquake sequence. *Left*: a single Gaussian distribution is fit to the data. *Right*: a mixture of five Gaussians is fit.

CONCLUSIONS AND RECOMMENDATIONS

We have developed and tested the key components of a new multiple-event location method that will allow the use of spatially well-distributed events and take into account correlations between the path travel-time corrections from proximate event-station paths, that are based on the spatial separation between their end-points. Preliminary tests of these components on a high quality dataset from NTS explosions, with known locations, indicate that our approach promises to improve location accuracy over single-event methods in more general station and event geometries than current methods of multiple-event location. Thus, our approach has the potential to provide more high quality reference events needed in calibration studies.

REFERENCES

Deutsch, C.V. and A.G. Journel (1998). *GSLIB: Geostatistical Software Library and User's Guide*, 2nd ed., Oxford University Press, Inc., New York, 369 pp.

Dewey, J.W. (1971). Seismicity studies with the method of joint hypocenter determination, *Ph.D. Thesis*, University of California, Berkeley.

Engdahl, E.R. and E.A. Bergman (2001), Validation and generation of reference events by cluster analysis, *Proceedings, 23rd Seismic Research Review: Worldwide Monitoring of Nuclear Explosions*, Jackson Hole, Wyoming.

Jordan, T.H. and K.A. Sverdrup (1981). Teleseismic location techniques and their application to earthquake clusters in the south-central Pacific, *Bull. Seism. Soc. Am., 71*, 1105-1130.

Myers, S.C., D.B. Harris, M.L. Anderson, W.R. Walter, M.P. Flanagan and F. Ryall (2003). LLNL location and detection research, *Proceedings of the 25th Seismic Research Review*, Tucson, Arizona, this volume.

Pavlis, G.L, and J.R. Booker (1983). Progressive multiple event location (PMEL), *Bull. Seism. Soc. Am. 73*, 1753-1777.

Rodi, W., E.R. Engdahl, E.A. Bergman, F. Waldhauser, G.L. Pavlis, H. Israelsson, J.W. Dewey and M.N. Toksöz (2002a). A new grid-search multiple-event location algorithm and a comparison of methods, "Proceedings of the 24th Seismic Research Review: Nuclear Explosion Monitoring: Innovation and Integration", 2002, Los Alamos National Laboratory *LA-UR-02-5048.*, Ponte Vedra Beach, Florida, 403-411.

Rodi, W., C.A. Schultz, W.G. Hanley, S. Sarkar and H.S. Kuleli (2002b). Grid-search location methods for ground-truth collection from local and regional seismic networks, "Proceedings of the 24th Seismic Research Review: Nuclear Explosion Monitoring: Innovation and Integration", 2002, Los Alamos National Laboratory *LA-UR-02-5048.* Ponte Vedra Beach, Florida, 394-402.

Schultz, C.A., S.C. Myers, J. Hipp and C.J. Young (1998). Nonstationary Bayesian kriging: a predictive technique to generate spatial corrections for seismic detection, location, and identification, *Bull. Seism. Soc. Am., 88*, 1275-1288.

Walter, W.R., K. D. Smith, J. L. O'Boyle, T. F. Hauk, F. Ryall, S.D. Ruppert, S.C. Myers, M. Anderson, and D.A. Dodge (2003), Improving the fundamental understanding of regional seismic signal processing with a unique western United States dataset, *Proceedings of the 25th Seismic Research Review*, Tucson, Arizona.

IMPROVED REGIONAL SEISMIC EVENT DEPTH ESTIMATION

Anca C. Rosca

Weston Geophysical Corporation

Sponsored by National Nuclear Security Administration
Office of Nonproliferation Research and Engineering
Office of Defense Nuclear Nonproliferation

DE-FG02-03ER83820

ABSTRACT

The primary objective of this research is to improve the accuracy of regional seismic depth estimation, which is essential to enhance national nuclear test monitoring capabilities. While the cepstral F-statistic, and other depth estimation techniques, have proved effective at teleseismic distances, regional depth estimation is still problematic. However, identifying regional secondary phases is necessary to accurately calculate the depth of small (3<mb<4) events recorded by only a few stations. To develop a reliable tool for depth phase detection and screening of small events recorded at regional arrays and sparse networks we test a preprocessing technique based on wavelet analysis and moveout corrections. The wavelet filtering method we propose, similar to de-noising, preserves and enhances the most prominent features from the waveform. With this method, it is possible to remove noise with little loss of details. We test thresholding criteria that preserve only a few large coefficients from the wavelet decomposition and enhance depth phase related features. Our test events show that the apparent velocity of the depth phase can differ significantly from the first arrival. We investigate an array of techniques to determine lag-times between phases. Applying moveout corrections enhances depth phase arrivals providing a better input for the depth estimation procedure. The processed waveforms are then input into a depth phase estimation algorithm, such as the cepstral F-statistic technique. This method improves the performance of regional depth estimation for our test events.

OBJECTIVE

Identifying regional secondary phases is critically important to accurately calculate the depth of small ($3<m_b<4$) events recorded by only a few stations. While the cepstral F-statistic, and other depth estimation techniques, have proved effective at teleseismic distances, regional depth estimation is still problematic. To continue our effort for improved depth estimation at regional distances we are developing a preprocessing technique based on wavelet analysis and moveout corrections. The preprocessed waveforms will be input into a depth phase estimation algorithm, such as the cepstral F-statistic technique. The preprocessing method we propose will improve the performance of regional depth estimation procedures.

RESEARCH ACCOMPLISHED

The starting date for this contract, in late July is after the paper submission date. Since research has not yet begun, we will review the motivation for this project.

Introduction

At regional distances depth phases are difficult to detect and identify in the complex coda of the first arrival. Over the past several years Weston Geophysical has been developing procedures that improved detection and identification of secondary phases. The cepstral F-statistic analysis method (Reiter and Shumway, 1999; Bonner *et al.*, 2000) was successfully used to detect depth phases from teleseismic recordings, but the results were mixed when the method was applied to regional events. At regional distances improper classification of cepstral F-statistic peaks sometimes results in depth miscalculations. This has led us to further investigate preprocessing methods that might enhance the success of the cepstral F-statistic depth phase detection method, specifically for regional arrays and sparse networks.

Technical Approach

Accurate determination of the focal depth of seismic events continues to be one of the most important monitoring problems. If the event hypocenter can be confidently found to be more than a few kilometers beneath the surface, the event can be ruled out as a nuclear explosion. Currently available techniques are not always robust, especially at regional distances. Using depth phase arrivals (*pP* and *sP*) becomes critically important to obtain precise locations for small events recorded by few stations (Reiter *et al.,* 2002).

Depth phases can be difficult to detect in seismic data due to path effects, focal mechanism and coda complexity. At regional distances, depth phases of interest are sometimes obscured by a multitude of arrivals. Furthermore, since *pPn* arrives with a different apparent velocity compared to the first arrival, the amplitude of this phase does not benefit from stacking. To compensate for these problems we propose a three-step procedure. First we use a wavelet analysis technique to enhance the important features in the waveforms, secondly we apply moveout corrections to better stack depth phases, and thirdly the resulting signal is input into the cepstral depth estimation method. The wavelet processing method we use, a version of the denoising procedure, preserves and enhances depth phase related features from the waveform. We will evaluate a cross-correlation technique to estimate moveout corrections for depth phases. The cepstral F-statistic method is our favored method for depth estimation, but we will evaluate other approaches as well (e.g., Murphy *et al*., 1999). The three steps outlined above - wavelet filtering, moveout corrections, and phase detection - are discussed below.

Wavelet Processing

We investigate the use of wavelet analysis to isolate depth phases in the P coda of regional array signals. This category of signal processing tools has been proved to be effective in seismic waveform processing (e.g., Anant and Dowla, 1997; Bear and Pavlis, 1999). A wavelet analysis technique that has proven very successful in other fields, such as image processing, is wavelet de-noising (Strang and Nguyen, 1996). We investigate its potential as a waveform preprocessing tool to aid in seismic depth phase detection. Wavelet de-noising is accomplished by calculating the Discrete Wavelet Transform (DWT) of a signal and then thresholding the resultant wavelet coefficients. To evaluate this technique, we analyzed ILAR waveforms for an event with a 31.8 km depth reported by the Alaska Earthquake Information Center (AEIC). The test thresholding criteria preserve only a few large coefficients from the wavelet decomposition details with most energy and the reconstructed waveform shows only a few prominent features most likely corresponding to phase arrivals (Figure 1).

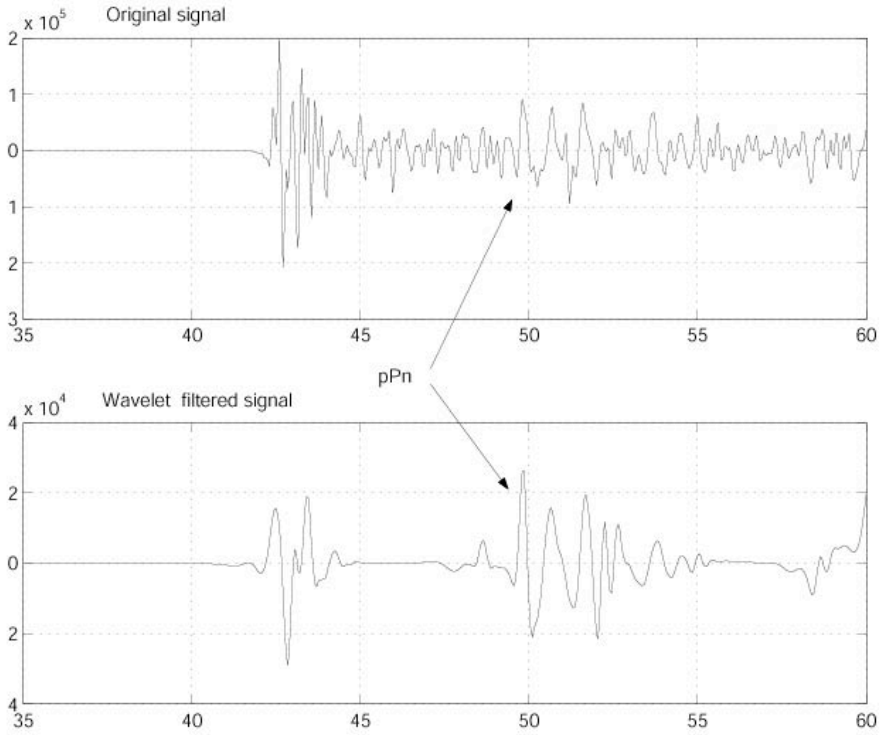


Figure 1. Waveform reconstructed from the most important wavelet coefficients compared to the original seismogram.

The reconstructed signal has properties that facilitate further processing. First, signal amplitude between phase arrivals is very low. This would allow us to "stretch" the seismogram for moveout correction by cutting and shifting a portion corresponding to the depth phase and inserting zeros for the missing values. Compared to time scale contraction (Woodgold, 1999) this procedure preserves the frequency content for each arrival. We will investigate if preserving the frequency content can aid with depth phase detection. Secondly, the consistency between peaks at different scales in the wavelet decomposition is an indication that a seismic phase is present. The most prominent features, those extracted for waveform reconstruction, are seen at multiple scales and correspond to phase arrivals. We will examine the use of this important characteristic of the wavelet decomposition method to select features based on a statistical evaluation of wavelet coefficients rather than the cepstral method. Thirdly, an analysis of the series of decomposition coefficients reveals that the frequency content of the first arrival, compared to later arrivals, is quite different for this event. Since the shapes of the various arrivals differ, cross-correlation would likely perform poorly on the original waveform but will work better with the wavelet-processed signal. We will investigate using cross-correlation of the wavelet-processed waveforms for lag time estimation.

Moveout Corrections

Theoretical IASPEI91 times calculated for the *Pn* and *pPn* phases across the 20 km array for this event, using the AEIC-reported depth, show differences in the individual element *pPn-Pn* lag times, leading to poor stacking of the depth phase. Such variation could explain why the cepstral F-statistic method developed for teleseismic distances can fail in its present form for regional cases in which the secondary arrivals of interest do not align. Applying moveout corrections may be a key component to improving the success of depth phase estimation methods such as the cepstral F statistic.

Lag time differences between the first arrival and the depth phase calculated from the array processing parameters in our test are on the order of 0.2 s. Correcting such differences may enhance the depth phases considerably, since it has been demonstrated that removing residuals as small as 0.02 s for local events (Bear and Pavlis, 1999) significantly improves the stack of the data for the first arrival. We will evaluate the range of moveout corrections

for regional distances and various array configurations. We will also investigate using the cross-correlation of wavelet coefficients or wavelet-processed waveforms to calculate these parameters. When the apparent velocity of the depth phase differs significantly from the first arrival, applying moveout corrections will enhance depth phase arrivals providing a better input for the depth estimation technique.

The Depth Phase Detector

We will first evaluate applying the cepstral F-statistic method for depth estimation (Reiter and Shumway, 1999; Bonner *et al*., 2000). This technique showed promising results at teleseismic distances, and we will evaluate its potential when used with the corrected regional waveforms. The cepstral F statistic attaches a statistical significance to peaks in the cepstrum through a signal-to-noise ratio computed from the beam cepstrum and the sum-stacked cepstrum. We estimate the cepstra from windows of data that contain the P arrival and its coda. The F-statistic is then formed by dividing the beam (mean) cepstrum by the error between the beam and the sum-stacked cepstra. Peaks associated with potential depth phase delay times appear in both the beam cepstrum and the F-statistic estimate. The three delay peaks with the highest confidence above a certain significance level are converted to candidate event depths using the IASPEI91 model. Multiple stations and arrays are then stacked to isolate the best network depth estimate. In addition to the cepstral F-statistic technique, we will test other methods, for example the network beamforming technique (Murphy *et al*., 1999), as possible candidates for extracting the depth phases from the preprocessed waveforms. We will develop a rigorous statistical framework to compare the success rate for each depth detector and determine the improvement after applying the proposed waveform preprocessing technique.

CONCLUSIONS AND RECOMMENDATIONS

Since this research will be funded starting in late July, no conclusions have yet been reached.

ACKNOWLEDGEMENTS

The author thanks James F. Lewkowicz, Delaine T. Reiter, Ileana Tibuleac, Jessie L. Bonner, Heather Hooper, and Robert H. Shumway for their help with this project.

REFERENCES

Anant, K. S. and F. U. Dowla, (1997), Wavelet transform methods for phase identification in three-component seismograms, *Bull. Seis. Soc. Am.*, **87**, 1598-1612

Bear L. K. and G. L. Pavlis, (1999), Multi-channel Estimation of Time Residuals from Broadband Seismic Data Using Multi-wavelets, *Bull. Seis. Soc. Am.*, **89**, 681-692.

Bonner, J.L., D.T. Reiter, R.H. Shumway, (2002), Application of a cepstral F statistic for improved depth estimation, *Bull. Seis. Soc. Am.*, **95**, 1675-1693.

Murphy J.R., R. W. Cook, and W.L. Rodi, (1999), Improved focal depth determination for use in CTBT monitoring, *Proceedings of the 21st Seismic Research Review: Technologies for Monitoring the Comprehensive Nuclear-Test-Ban Treaty*, Los Alamos National Laboratory, *LA-UR-99-4700*, **50-55**.

Reiter D. T., and R. H. Shumway, (1999), Improved seismic event depth estimation using cepstral analysis, *Proceedings of the 21st Seismic Research Review: Technologies for Monitoring the Comprehensive Nuclear-Test-Ban Treaty*, Los Alamos National Laboratory, *LA-UR-99-4700*, **599-606**.

Reiter, D., J. Bonner, C. Vincent, and J. Britton, (2002), Incorporating secondary phases in 3D regional seismic event location: Application to the sparse network problem, *Proceedings of the 24th Annual Seismic Research Review: Nuclear Explosion Monitoring: Innovation and Integration*, Los Alamos National Laboratory, *LA-UR-02-5048*, Vol. I, **375-384**.

Woodgold, C.R.D., (1999), Wide-aperture beamforming of depth phases by timescale contraction, *Bull. Seis. Soc. Am.*, **89**, 165-177.

GROUND TRUTH LOCATION USING A SYNERGY BETWEEN INSAR AND SEISMIC METHODS

Chandan K. Saikia[1], Rowena Lohman[2], Gene Ichinose[1] and Mark Simons[2]

URS Group, Inc.;[1] California Institute of Technology[2]

Sponsored by Air Force Research Laboratory

Contract No. DTRA01-01-C-0072

ABSTRACT

The objective of this study is to utilize Synthetic Aperture Radar Interferomtery (InSAR) to estimate accurate hypocenter locations for shallow and moderate-sized earthquakes in the Middle East and Eastern Asia. We have acquired different levels of Digital Terrain Elevation Data (DTED) from National Imagery and Mapping Agency for this region to improve the InSAR processing. Once surface deformation is identified in the InSAR signal and associated with an earthquake, the hypocenter location is estimated from a combination of geodetic and seismic modeling to provide accurate locations for regional velocity model calibration. One primary difficulty in the analysis of InSAR is the uncertainty in hypocenter location with the increasing earthquake size because of the increase of fault area with seismic moment. Another difficulty is the trade-off between fault area and fault slip and between focal mechanism and location because InSAR only measures the 3-components of surface deformation along a line of sight (e.g., Lohman et al., 2002).

Saikia et al. (2002) combined InSAR and seismic data modeling to estimate the location of the 1999/04/30 M_w 4.8 earthquake in Southern Iran. The focal depth is 4 km, which was estimated from modeling InSAR data. When we compared the Lg-waves at station RAYN between this event and a nearby 1998/11/13 earthquake (depth=9 km), the Lg-wave characteristics were similar indicating that both are shallow depth earthquakes. We performed a grid-search and inversion of the regional long-period waveforms and high-frequency P-waves to reaffirm this earthquake's shallow depth and help constrain the focal mechanism estimated from InSAR modeling. Using the accurate hypocenter location estimated from InSAR and seismic waveform modeling (probably now GT1), we obtained empirical SSSCs at regional stations between (0-30°) and relocated 11 other earthquakes ($4.4 < m_b < 5.7$) that occurred near this event. The SSSC significantly reduced the area of the error ellipse for these earthquakes.

In this study, we used InSAR data to examine additional events in Southern Iran. We examined the 1998/10/18 (m_b 4.2), 1997/05/05 (m_b 4.8), 1997/09/18 (m_b 4.7), and 1999/04/28 (m_b 4.8) earthquakes. The satellite radar data available for these events spanned a time interval that included several events making the association of the observed deformation field with each earthquake difficult. For example, radar data for events of 1997/05/05 and 1997/09/18 were obtained from track 478 /frame 3069, which spanned a time interval between April 1996 and April 1999. During this time interval, several events occurred within 50-80 km of the identified SAR signal locations. However, based on InSAR analysis, most of these events did not contribute to the radar signal as they were too small ($m_b<4.5$). Broadband waveforms from station RAYN were compiled for all events occurring during each time interval of the radar data and investigated for their high-frequency Lg-wave characteristics. We also modeled the teleseismic and regional P-waves and long-period waveforms. The following are a list of conclusions: 1). processing and modeling of InSAR data identifies four shallow earthquakes, 2). within the limits of resolution, seismic depths determined from the modeling of the long-period seismic waveform and far-regional broadband P waveforms are consistent with the depths determined by modeling the InSAR ground deformation, 3). the ISC depths are often poorly estimated, and 4). locations of small seismic events improve, when the SSSCs estimated using the location of events determined from the synergy of InSAR and seismic are applied during location.

OBJECTIVES

The goal of this ongoing study is to obtain reliable locations for moderate-sized earthquakes (M_w<5.5) in parts of Asia and Middle East. We will deliver accurate locations, associated waveforms, raw satellite synthetic radar interferometry (InSAR) images, processed InSAR phase maps and ground deformation maps to the Department of Energy knowledge database.

The study is divided into two parts: seismic and geodetic, which are concerned with identifying ground truth (GT) locations for reference events in regions of monitoring interest. The primary objective is to improve earthquake locations to within the GT10 or GT5 level of accuracy (i.e., events within 10 or 5 km accuracy in their epicentral locations, respectively) when they apparently satisfy the GT25 criteria (Yang and Romney, 1999). The other objective is to utilize geodetic data, including synthetic aperture radar interferometry (InSAR) to establish accurate locations for shallow and moderate-sized seismic events (M_w<5.2) to validate the ground truth (GT) results determined from seismic methods.

The final task of this study combines seismic and geodetic results to validate the GT locations. These locations determined from InSAR will be used to develop station-specific-source corrections (SSSCs) for the upper-mantle P-wave phase arrivals, which in turn will be used for relocating nearby earthquakes (M_w < 4.5).

RESEARCH ACCOMPLISHED

1999/04/30 Event

Radar images have been used by many authors to identify surface deformation generated by earthquakes and mine collapses in many parts of the world (Feigl *et al.*, 1995; Massonnet and Feigl, 1998; Foxall *et al.*, 1998; Akoi *et al.*, 1999; Rigo and Massonnet, 1999, Stromondo *et al.*, 1999; Myers *et al.*, 2002; Steck *et al.*, 2002; Lohman *et al.*, 2002). Saikia *et al.* (2002) studied a small earthquake that occurred in southern Iran on April 30, 1999 (M_w 4.8) and estimated its location by modeling the ground deformation identified from a geocoded interferograms (Figure 1), formed using radar images for track 20/frame 3051 (99/04/21-99/05-26) and for track 249,/frame 3051 (99/04/02-99/06/11), respectively. The radar images were processed by removing topography, filtering and unwrapping of the phase. Topography was removed by using digital elevation model (DEM) from the level 1 Digital Terrain Elevation Data (DTED). In Figure 1, the surface deformation generated by this earthquake is observed in the upper right of the image at location of 27.87°N and 53.610°E as two circular interferometric fringes. In our earlier report, we estimated a hypocenteral depth of less than 9 km based the characteristics of high frequency (f > 1 Hz) Lg-waves. These Lg-waves generated by this earthquake were compared to a co-located earthquake on November 13, 1998 (depth < 9 km) at a broadband station RAYN in Saudi Arabia (Δ=938 km, AZ=241°). By modeling the deformation determined from the InSAR images, we estimated its depth at 4 km. We also inverted for the centroid moment tensor using long-period regional-waves recorded at stations RAYN, GNI (Δ=1591 km, azimuth=332°) and ATD (Δ=2126 km, AZ=214°). Within the limits of resolution of the long-period waves, the centroid depth is resolved to within 2 to 10 km (Figure 2). The focal depth of 35 km, estimated by ISC, using the P travel times only, is poorly determined. Further, forward modeling of the broadband P wave displacements at stations ATD and KIV (Δ=18.3°) also yielded the hypocentral depth less than 5 km. In Figure 3, we present the move-out of pP and sP depth phases relative to the P onset. Both ATD and KIV are located within the range of upper-mantle discontinuity triplications but the modeling and data indicate that the depth phases have not separated from the P-wave onsets. Synthetics generated at a depth of 4 km show the best agreement with the recorded waveform. Table 1 presented in Saikia *et al.* (2002) shows a comparison of various locations that were available for this earthquake including the one determined using the synergy of the InSAR (epicentral location) and seismic data (depth and travel times of P waves). This way, we predict the most reliable origin time for this event. Note that the other locations are biased and the HRV (Harvard) location is the worst.

We used the location of the April 30, 1999 earthquake estimated by the synergy of InSAR and seismic methods to estimate Source Specific Station Corrections (SSSCs) for regional and teleseismic stations. About 11 other events occurred in the proximity of this earthquake. We applied these SSSCs and relocated these earthquakes (Table 2.). The applications of the empirical SSSCs have reduced the ellipse error area for seven events (based on the error ellipse estimated at a 90% confidence interval). The 1998/07/01 earthquake (m_b 3.9) and had a large azimuthal gap of 112° for its recording stations. With the application of the SSSCs, its error ellipse area has significantly

increased, but the error ellipse area decreased for events when the azimuthal gap was less than 35°.

Table 1. Location Parameters for 1999/04/30 Southern Iran Earthquake

Date d/m/y	Origin Time hr:mn:ss	Latitude (°N)	Longitude (°E)	Z (km)	ΔR (km)	Agency
04/30/99		27.870	53.610			INSAR
04/30/99	04:20:02.0	27.765	53.519	33.1	14.68	ISC (MOS)
04/30/99	04:20:22.5	27.837	53.538	35.0	7.0	USGS
04/30/99	04:19:59.6	27.748	53.553	4.0 (F)	14.6	URS
04/30/99	04:20:05.4	27.866	53.576	45.0	3.04	URS
04/30/99	04:20:12.5	27.74	52.960	44.9	65.65	HRV
04/30/99	04:20:00.1	27.870 (F)	53.610 (F)	4.0 (F)		Seis+INSAR

(F) - Fixed location or depth

Table 2. Relocation of Southern Iran earthquakes using 1999/04/30 as the Reference Event

Date	h:m:s	°N	°E	Z (km)	m_b	Gap	# Sta	ER(1)	ER(2)
96/05/24	06:35:56.30	27.80	53.576	3.3	4.4	28	162	38.3	25.61
96/05/25	17:00:54.70	27.82	53.554	3.2	4.8	40	109	32.2	30.43
98/06/13	02:23:42.70	27.86	53.745	8.3	4.6	45	102	32.5	45.99
98/07/01	21:36:31.70	27.79	53.688	12	3.9	112	12	1344.2	1632.5
98/11/13	13:01:07.80	27.75	53.672	2.8	5.3	28	257	14.4	11.59
98/11/14	10:37:20.50	27.89	53.633	10	4.6	42	102	51.2	75.58
98/12/10	14:21:49.80	27.89	53.581	10	4.7	63	98	39.9	58.23
98/12/27	04:10:39.30	27.84	53.688	8.9	4.7	63	116	42.1	32.51
99/04/28	18:11:41.50	27.83	53.595	3.9	4.5	34	134	34.4	25.32
99/05/06	23:00:50.20	29.49	51.971	3.3	5.7	28	289	32.2	8.41
99/05/06	23:13:24.40	29.57	51.954	10	5.2	35	217	27.1	42.96

(ER1) minor axis length of error ellipse, (ER2) major axis length of error ellipse

1997/05/05 and 1997/09/18 Events

We then examined the availability of the radar data for nearly 200 events in southern Iran. We requested radar data for 90 events from the European Space Agency based on the time span and baseline criteria. These events included mostly smaller magnitude earthquakes, and since the ISC depths and locations are often unreliable for such magnitudes, we decided to obtain waveform data for additional analysis. For example, Figure 4 shows a set of vertical component velocity seismograms recorded from many earthquakes in our study area in the magnitude range of $3.9 < m_b < 4.9$. These seismograms are all recorded at station RAYN from earthquakes nearly co-located at approximately 938 km to the northeast. The seismograms were filtered to frequencies above 1 Hz in order to examine their Lg-wave characteristics. The best characteristic of Lg-waves is their extended durations with decreasing focal depth. For each seismogram, we labeled the origin time (hour:min), peak amplitude (in counts), ISC magnitude (m_b) and ISC depth (km). In these waveforms, not only the Lg-waves, but also the onsets of the P waves are quite clear. We infer from the extended duration of the Lg-waves that these events have shallow depths.

Figure 5a shows interferograms constructed using radar data acquired from track 478/frame 3069 spanning the time period from April 1996 to April 1999 where signals for two events can be identified at 27.1345°N, 53.8842°E and 27.0886°N and 53.9412°E. The northern most deformation (event-N) has a lobe of subsidence and uplift, which is adjacent to and superimposed upon a smaller lobe of uplift (event-S). Modeling these deformations observed in the InSAR signal required two events at depths of 5.6 and 4 km with focal mechanism of δ=3°, λ=90°, φ=309° and δ=60°, λ=90°, φ=280° respectively (Figure 5b). We used Okada's (1992) formulation to compute three-component surface deformation at each grid point, rotated them along the line of sight (LOS) and multiplied by the LOS directional cosines used in processing the interferogram (Figure 5a). Modeling and fit was performed using Neighborhood Algorithm developed by Sambridge (1998). Figure 5c shows the residual between the observed and synthetic surface deformations.

By examining the ISC bulletins, we identified 22 events that occurred within 50 km of the first InSAR signal. Majority of these events have large location uncertainties because they were located using P-wave travel-times from only a sparse distribution of seismic stations, mostly beyond 10° (e.g., 2-3 stations within 6°), which does not provide an adequate azimuthal coverage. Of these, one event, which occurred on 1997/05/05 (15h:11m, m_b 4.8), is within 2 km of this InSAR signal. This earthquake was reported by 220 stations ($\Delta \geq 9.5°$) providing an azimuthal gap of 71°. According to the ISC, the 1997/05/05 event occurred at a depth of 47.5±9.4 km. The Harvard Centroid Moment Tensor catalog (HRV) lists a depth of 15 km with an M_w of 5.1.

We applied waveform modeling and inversion to estimate the centroid depth and focal mechanism for the 1997/05/05 and 1997/09/18 earthquakes. We inverted long-period regional waveforms recorded at RAYN to estimate the focal mechanism and centroid depth (Figure 6a) of event 1997/05/05. The source parameters for nodal plane #1 are δ=69°, λ=123°, φ=336°, M_w=4.94, z=16 km, which is different from the HRV solution for the most similar nodal plane (δ=52°, λ=128°, φ=296°, M_w=5.1). The centroid depth of 16 km is poorly resolved from the long-period regional-waves from a single station. For a better estimate and resolution of the centroid depth, we examined broadband regional P-waves. Using our focal mechanism, a suite of *f-k* synthetics were computed for stations ATD and KIV at depths ranging between 2 and 10 km in 2 km increments. The synthetics were compared them with the recorded P-waves. Based on this additional analysis, we found the depth of this event is shallower than 6 km.

A second event also occurred at a distance of 4.72 km from this InSAR signal on 1997/09/18 (m_b 4.7-5.2). This event was recorded by 184 stations globally with an azimuthal gap of 64°. We performed a moment tensor inversion on the long-period regional-waves recorded at stations RAYN, ABKT and GNI. We estimated source parameters of (Nodal Plane 1: δ=19°, λ=89°, φ=110°), (Nodal Plane 2: δ=71°, λ=90°, φ=292°) and (M_w=4.7-5.1, z=2-8 km). The ISC reported a depth at 55 km, but long-period modeling of recorded seismograms at these stations yielded its depth at 2-8 km (Figure 6b). The broadband regional P waveform at ATD indicates a shallow depth (about 2-4 km). A comparison of the Lg-waves in Figure 4 also indicated that these earthquakes are shallow. Note that both these events are located at 5.7 and 4.6 km from the second InSAR location in the interferogram (Figure 5). The 1997/09/18 event was reported by 181 stations, which provided an azimuthal gap of 71°, but lacked P-wave travel times from local stations. We can associate the 1997/05/05 event to the first InSAR signal because of its close proximity of the ISC location to the centroid location based on the modeling of the InSAR signal. The 1997/09/18 event is probably the second InSAR signal, as there is no occurrence of any other seismic events within this vicinity, which can contribute to the InSAR deformation signal.

Figure 7 shows an interferogram constructed from radar data acquired from track 13/frame 567 (time span between October 1997 and September 1999) which shows range deformation of about 1 cm at 28.6736°N, 54.2484°E. We were able to identify this event on multiple interferograms, thus reducing the possibility that it was caused by other sources of errors. During the time span between 10/97 and 9/99, 14 earthquakes with magnitudes (m_b) between 3.9 and 4.7 occurred within 100 km of this InSAR signal. Of these, two events on October 18, 1998 (28.5848°N, 54.2007°E; m_b 4.2) and on October 19, 1998 (28.4764°N, 54.4519°E; m_b 3.9) occurred within 50 km. Of the two events, the event of the 18th occurred 11 km from the location of InSAR signal. According to the ISC bulletin, the depth of this event is at 97.7 km and it is reported to have damaged sixty houses in Darab area, which is unlikely for an event of this size at such depth. The slightly smaller second event ($m_b < 3.9$) occurred about 29.5 km away along the southeast direction from the InSAR signal. It is too small of an event in magnitude to contribute to the InSAR signal.

CONCLUSIONS AND RECOMMENDATIONS

Estimating accurate ground truth locations for earthquakes is difficult in areas where seismic network stations are sparse or inaccessible. The addition of InSAR data can overcome this difficulty and provide accurate ground truth locations. Earthquakes that do not produce surface rupture may still generate measurable surface deformation observed from processed radar images acquired before and after the event. However, atmospheric noise or topographical uncertainty may have a correlation length smaller than the regular coherence estimation window, which may prevent retrieval of useful InSAR signals from processed interferograms. Nevertheless, when ground deformation is identified in interferograms, hypocenter locations of seismic events can be reliably estimated within the error of the fault dimensions (for M 5 earthquake this is about 1-2 km).

We have noted that events, which produced identifiable ground deformation within the Zagros of southern Iran, are estimated to have occurred at depths less than 15 km. Hypocenter depths estimated by ISC and HRV, which ranged from 15 to 90 km, are poorly resolved based on combined InSAR and seismic source depth modeling estimates. Moment tensor inversion or long-period regional-waves and broadband regional P-waves are more consistent with InSAR modeling (less than 6 to 10 km). Since the depths for many earthquakes in this region are mostly overestimated, then it is encouraging from the viewpoint that many deeper events may be suitable for this type of analysis. Since acquiring radar data is expensive, it is therefore necessary to assess their depths by carefully modeling the regional-wave long-period waveforms and regional broadband P-waves, especially the interaction of P with pP or sP depth phases recorded at regional station as we have demonstrated in Figure 6.

The following are a list of conclusions: 1). processing and modeling of InSAR data identifies four shallow earthquakes, 2). within the limits of resolution, seismic depths determined from the modeling of the long-period seismic waveform and far-regional broadband P waveforms are consistent with the depths determined by modeling the InSAR ground deformation, 3). the ISC depths are often poorly estimated, and 4). locations of small seismic events improve, when the SSSCs estimated using the location of events determined from the synergy of InSAR and seismic are applied during location.

In our continuing effort to improve radar data processing, we have acquired Digital Terrain Elevation Data (DTED) for different levels (e.g., from highest to lowest resolution: level 0, 1, and 2) to form high-resolution digital elevation models in countries including China, India, Pakistan, Afghanistan, Iran, Iraq, and Saudi Arabia. We applied DTED level 1 data in processing of radar data, which have greatly improved our processing capability. We found that the time span between the scenes of the pre- and post-seismic deformation must be small. Otherwise, several earthquakes may occur within the time span, as is the case in our investigation, which can contribute to the ground deformation that is discernable in the interferogram. In such situations, associating of a seismic event to the observed ground deformation becomes difficult.

The surface deformation caused by large earthquakes ($M > 6$) is of limited significance because the large source size makes it difficult to associate the observed deformation to a definite source rupture initiation (i.e., the hypocenter). The ambiguity between the location of surface deformation and epicenter location is reduced significantly for smaller magnitude earthquake. Because of the offset between locations of surface deformation and epicentral locations, ground deformation discernable in the differential InSAR must be analyzed in conjunction with the seismic data that can provide focal mechanism and event depth. It is also essential to perform error analysis to some degree of confidence limits of the epicentral locations.

REFERENCE

Akoi, S., M. Furuya, S. Kobayashi and S. Okubo (2002). Co-seismic crustal deformation of the 1996 Onikobe earthquakes, Japan, detected by InSAR, *Eos. Trans.* AGU 83(47), Fall Meeting Suppl. Abs G61B-0994.

Feigl, K. L., A. Sergent, and D. Jacq (1995). Estimation of an earthquake focal mechanism from satellite interferogram: Application to December 4, 1992 Landers aftershock, Geophys. Res. Lett, 9, 1037-104.

Foxall, B., J. J. Sweeny, and W. R. Walter (1998). Identification of mine collapses, explosions and earthquakes using InSAR: a preliminary investigation, in Proceed. 20th Annual Seismic Res. Symposium., Monitoring Comprehensive Test Ban Treaty, 21-23 September, 408-416.

Lohman, R. B., M. Simons and B. Savage (2002). Location and mechanism of the Little Skull Mountain earthquake as constrained by satellite radar interferometry and seismic waveform modeling, J. Geophys. Res., 107,10.1029/2001JB000627. ETG, 7-1 to 7-8.

Massonnet, D. and K. L. Feigl (1998). Radar interferometry and its application top changes in the Earth's surface , Rev. Geophys., Vol 36, No. 4, 441-500.

Myers, S., M. Flanagan, M. Pasyanos, W. Walter, P. Vincent and C. Shultz (2002). Location calibration in western Eurasia and North Africa: Ground truth improved earth models, Bayesian Kriging, regional analysis, location algorithms, array calibration and validation, 24th Seism. Res. Rev., Nuclear Explosion Monitoring: Innovation and Integration, Sept 17-19, 351-360.

Okada, Y. (1992). Internal deformation due to shear and tensile faults in a half-space, Bull. Seism. Soc. Am. 82, 1018-1040.

Rigo, A. and D. Massonnet (1999). Investigating the 1996 Pyrenean earthquake (France) with SAR interferograms heavily distorted by atmosphere, Geophys. Res. Lett., 26, 3217-3220.

Saikia, C. K., R. Lohman, G. Ichinose, D. Helmberger, M. Simons and P. Rosen (2002). Ground truth locations - A synergy of Seismic and Synthetic Aperture Radar Interferometric Methods, 24th Seism. Res. Rev., Nuclear Explosion Monitoring: Innovation and Integration, Sept 17-19, p420-429.

Sambridge, M. (1998). Geophysical inversion with a neighborhood algorithm - I, Searching a parameter space, Geophys. J. Int. 138, 479-494.

Steck, L. H. Hartse, C. Bradley, C. Aprea, A. Valesco, G. Randall, and J. Franks (2002). Regional location calibration in Asia, 24th Seism. Res. Rev., Nuclear Explosion Monitoring: Innovation and Integration, Sept 17-19,, p430-439.

Stramondo, S., M. Tesauro, P. Briole, E. Sansosti, S. Salvi, R. Lanari, M. Anzidei, P. Baldi, G. Fornaro, A. Avallone, M. Buongorno, G. Franceschetti, E. Boschi (1999). The September 26, 1997 Colfirito, Italy earthquakes: modeled coseismic surface displacement from SAR interferometry and GPS, Geophys. Res. Lett, 26. 883-886.

Yang, X. and C. Romney (1999). PIDC ground truth event (GT) database (revision 1), CMR Tech Rept, CMR-00/15.

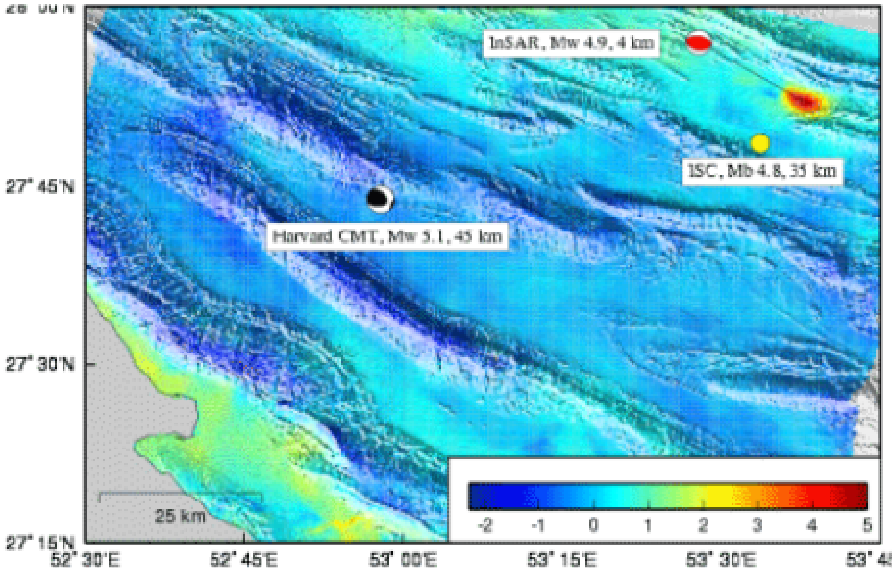


Figure 1. LOS displacement field from interferogram constructed from scenes acquired between 1999/04/21 and 1999/05/26. There is a lobe of uplift of about 5 cm observed in the InSAR that was modeled to estimate the focal mechanism shown in the upper-right. The ISC location for the 1999/04/30 event is shown and associated with this deformation. The thrust mechanism of the Harvard centroid moment tensor is consistent with the InSAR modeling yet the hypocenter and centroid depth for both ISC and HRV locations are in error by about 30 to 40 km.

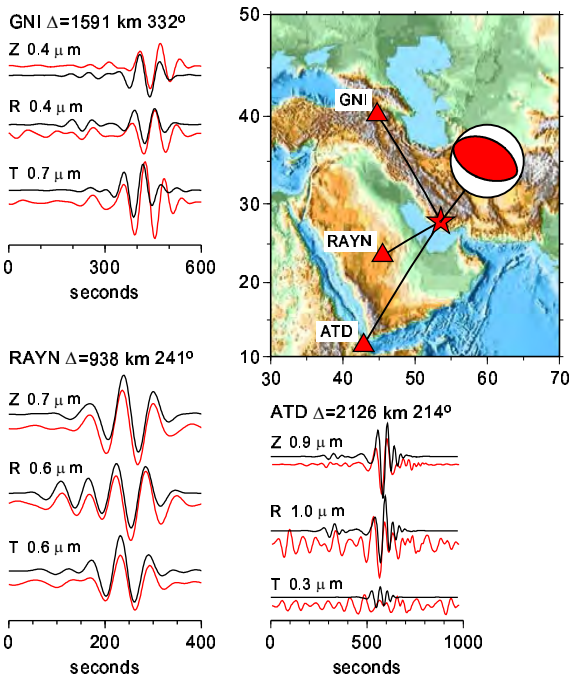


Figure 2. Observed and predicted regional-waves filtered to long-periods (100-50 sec) for the 1999/04/30 04:20 UTC event. The observed seismograms were used to invert for the Moment tensor.

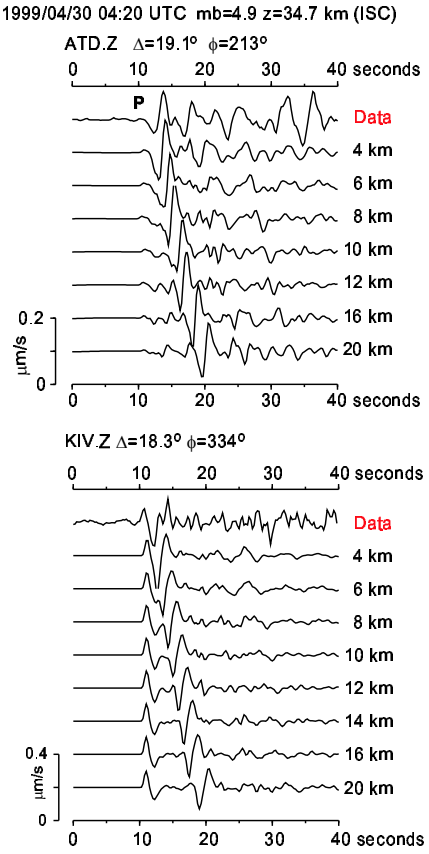


Figure 3. Modeling broadband far-regional P-waves for the 1999/04/30 04:20 UTC event. The P-waves from stations ATD and KIV are aligned and compared to synthetics computed at 2 km depth increments.

The depth phases and upper-mantle phases indicate that this event has a shallow depth of less than 6 km. We used the source parameters estimated from the long-period moment tensor inversion (Figure 2) to compute the synthetics.

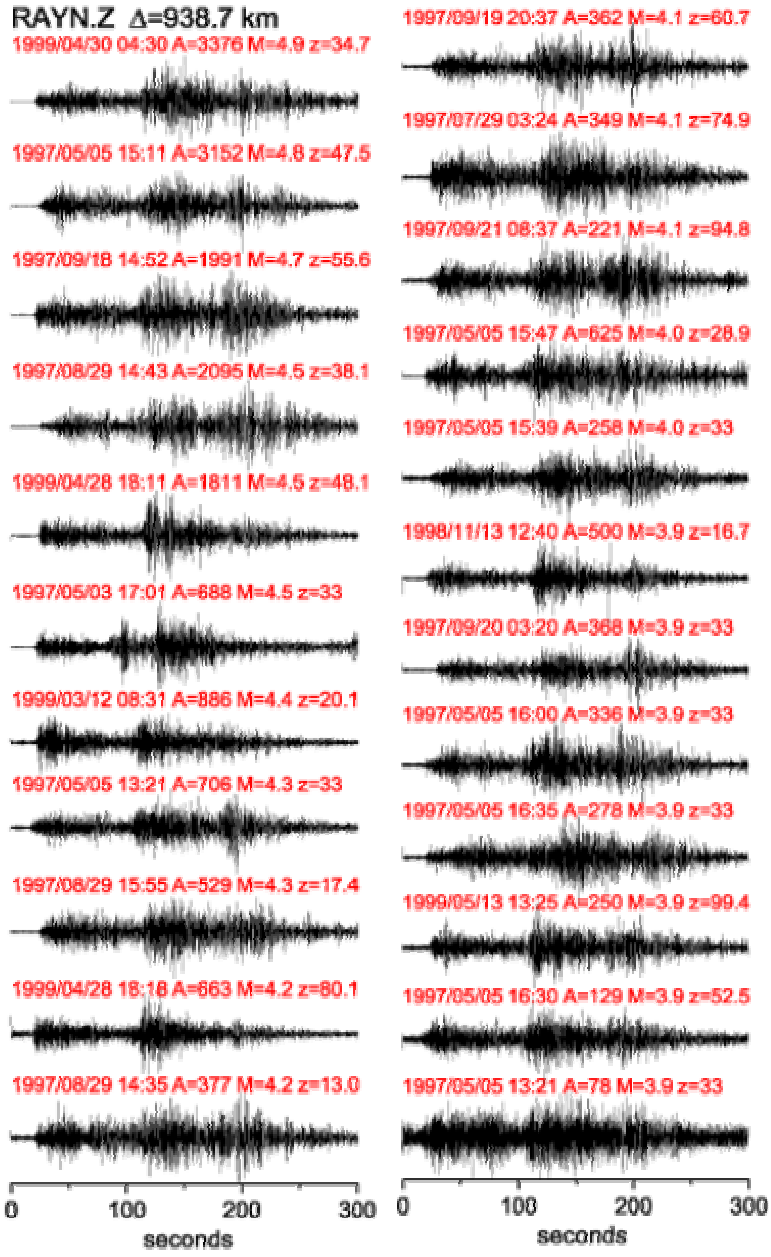


Figure 4. RAYN vertical component velocity seismograms high-pass filtered at 1 Hz.

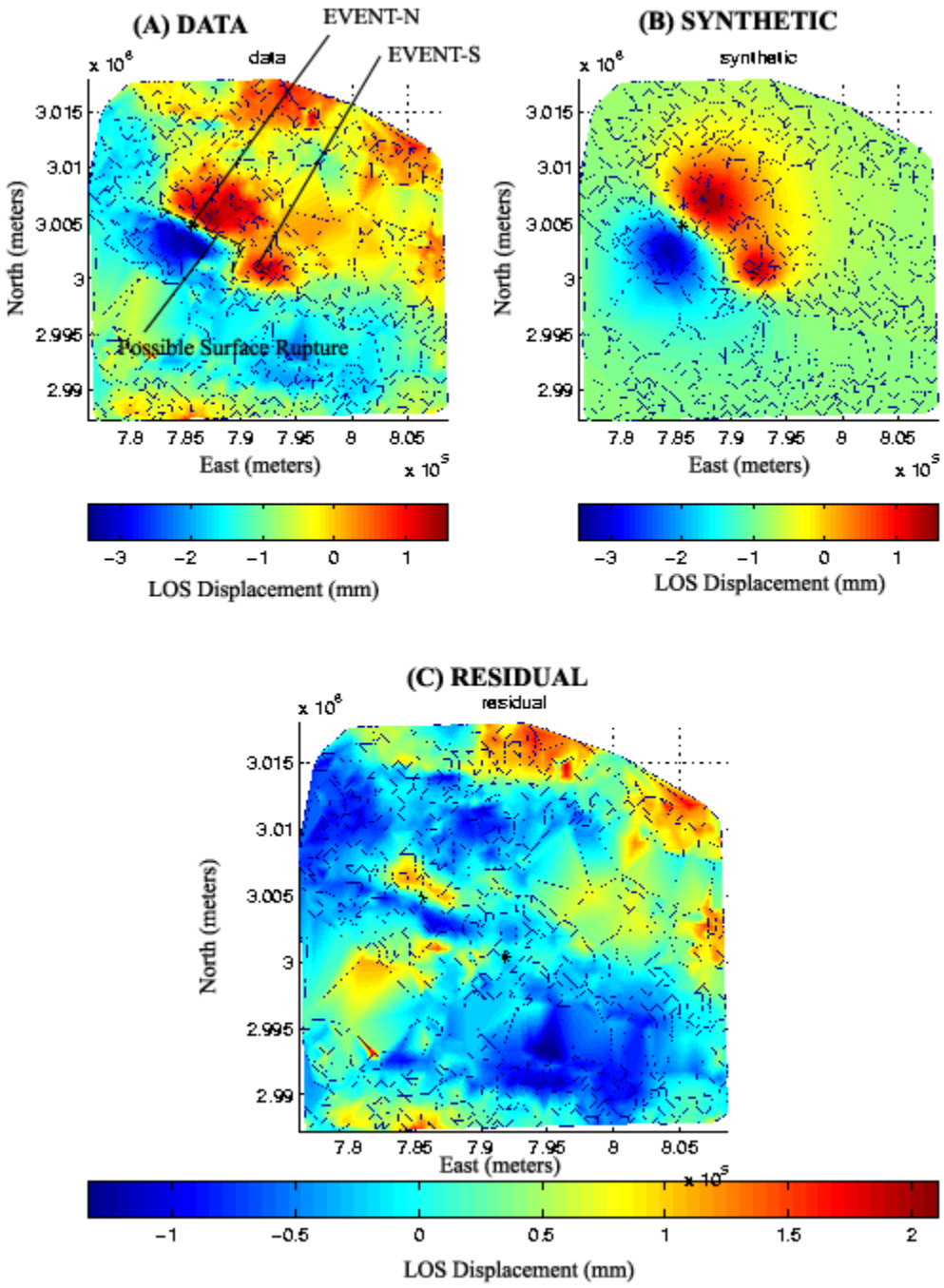


Figure 5 (a) observed InSAR Interferogram for event-N (1997/09/18) and event-S (1997/05/05), (b) synthetic surface displacements estimated from a grid-search inversion, and (c) residuals between observed and synthetics.

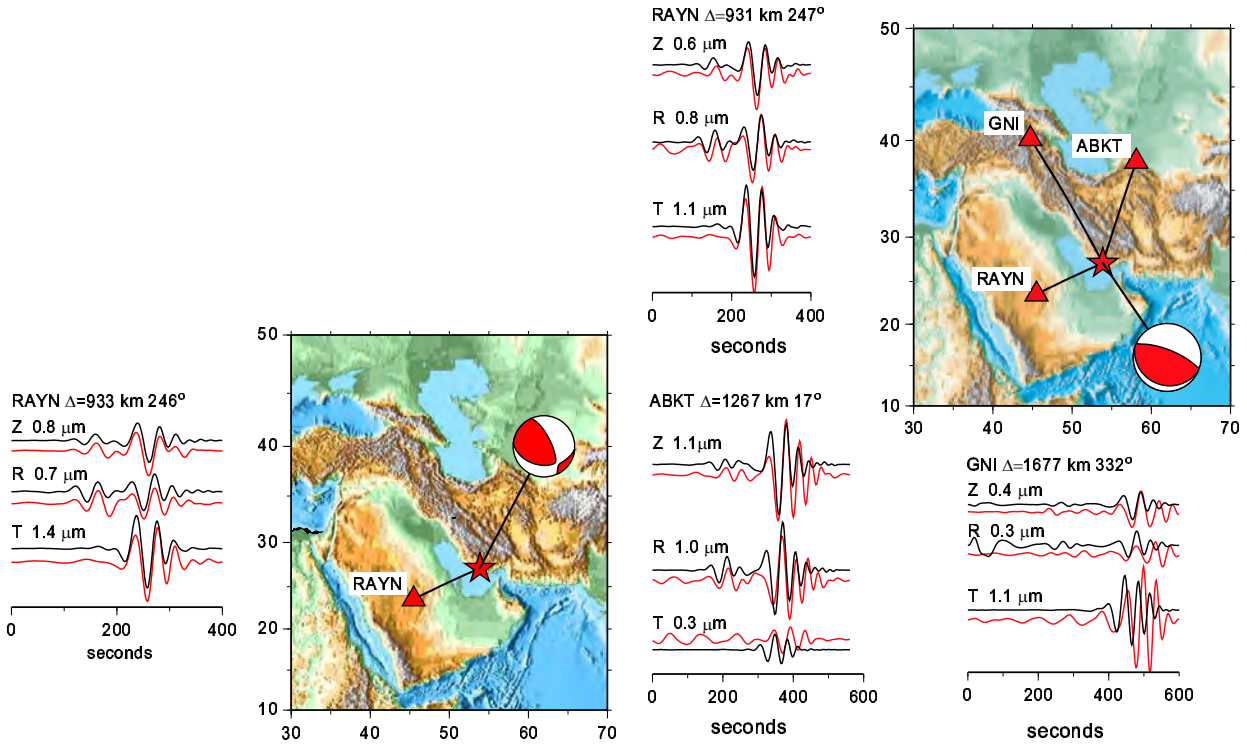


Figure 6. (A-Left) Regional-wave moment tensor inversion results for event 1997/05/05. (B-right) Regional-wave moment tensor inversion results for event 1997/09/18.

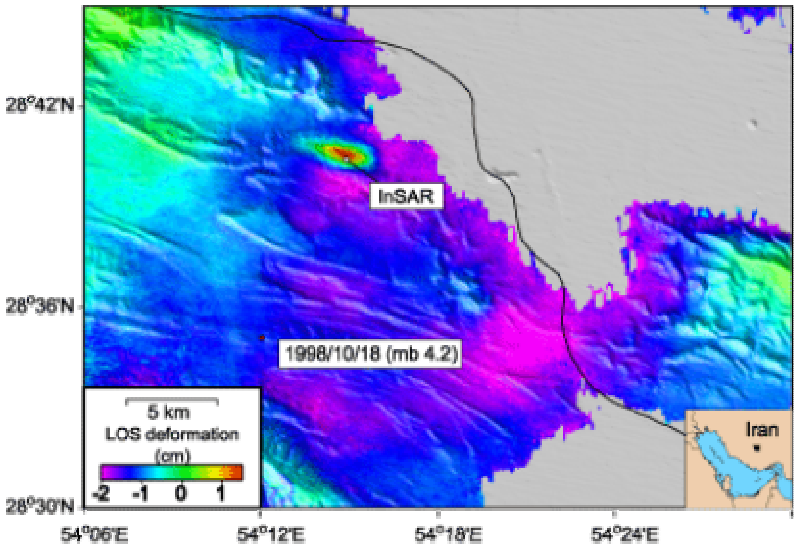


Figure 7. LOS displacement field from interferogram constructed from scenes acquired between 1997/10 and 1999/09 that a peak deformation of about 1 cm at 28.6736°N, 54.2484°E. This deformation may be associate with the 1998/10/18 event that the ISC estimates at mb 4.2. Unfortunately, to our knowledge, there is no available seismic waveform data for this event at stations RAYN or ATD for this date.

KARATAU, MAKANCHI, AND LOCATION IN WESTERN CHINA

Lee K. Steck, George E. Randall, Michael L. Begnaud, Charlotte A. Rowe, and Aaron A. Velasco

Los Alamos National Laboratory

Sponsored by National Nuclear Security Administration
Office of Nonproliferation Research and Engineering
Office of Defense Nuclear Nonproliferation

Contract No. W-7405-ENG-36

ABSTRACT

The introduction of the Karatau (KKAR) and Makanchi (MKAR) seismic arrays into central Asia is changing the nature of seismic event location in that region. This paper presents a preliminary look at location calibration issues associated with these stations. We are exploring the improvement in earthquake location in Central Asia made possible by data from the Karatau Array in Kazakhstan in conjunction with the Makanchi Array and Global Seismic Network (GSN) stations. Parts of central Asia are sparsely instrumented and we need to make the maximum possible use of all stations and arrays. The two arrays provide azimuth estimates to an event—in addition to seismic phase arrival times—thereby improving the location of small events recorded at only a few stations. The apparent velocity of an arrival across the arrays is also useful for confirming phase identification. Preliminary azimuth and slowness correction surfaces have been developed for both arrays and are being tested with the National Nuclear Security Administration's event location algorithms. At MKAR, azimuth corrections are of moderate size, with a standard deviation of about 7°, while slowness corrections have a standard deviation of about 0.028 sec/km. Azimuth and slowness corrections at KKAR are similar. Very preliminary travel time correction surfaces are also presented for MK31 and KK31, the broadband central stations at the arrays. These surfaces are much more sparsely populated than surfaces for azimuth and slowness due to tighter restrictions on event locations required for travel time data.

We believe that the Karatau seismic array frequently records useful Pg phases in cases where Pn is lost in the noise. Apparent velocity can substantiate the Pg identification and, if a correction surface can be formed, we may have an additional phase available at Karatau for locating some events. Examination of waveforms from a number of events at Karatau (and Makanchi) shows a clear error in some of the Reviewed Event Bulletin (REB) solutions, and we will add our phase picks and azimuth estimates to all available information to improve locations.

OBJECTIVES

The objective of this research is to improve seismic event location in western China using the Makanchi (MKAR) and Karatau (KKAR) seismic arrays.

RESEARCH ACCOMPLISHED

Azimuth and slowness corrections

We developed code to estimate the azimuth and apparent slowness for seismic phases arriving at a regional array. Using predicted values from a great circle path and an assumed earth model, the deviations of the estimates of azimuth and slowness, respectively, were used as residuals to derive the kriged correction surfaces. The derivations were performed in the Knowledge Base Calibration Integration Tool (KBCIT), using Modified Bayesian Kriging (*Schultz et al.*, 1998). We have also developed a procedure to estimate confidence bounds for the estimated azimuth and slowness (*Blandford*, 1974; *Shumway*, 1971).

We begin the procedure with an event at a regional distance from MKAR and/or KKAR and a published location. We specifically choose events large enough to be well located, so that we can expect to measure the errors in azimuth and slowness associated with the array analysis and not with an event mislocation. We identify and pick visible seismic phases or use appropriate group velocity windows for phases that are not readily selectable by a trained seismologist. For each phase we construct an energy surface of the simple delay and sum plane-wave beam for a grid of horizontal slownesses. We take the peak energy to be a first order estimate of the arrival and then define the region that is greater than a given fraction—for example, 70% of the peak beam energy. We normalize the beam energy surface for the region so that the total volume is 1, and treat the region and the normalized energy surface as defining a density function. We then compute the mean value and the second moments over the bounded slowness surface, treating the mean slowness as the refined estimate of the arrival and second moments as defining the confidence limits of the estimate of the arrival. The results are shown in the left panel of Figure 1, where the warmer colors (reds, yellows, oranges [i.e., lighter shades]) represent large beam energy and the white 'X' is the peak on the grid. The white elliptical region represents the border of the region used to define the density function. The right panel shows the time domain beam for the Pn-phase estimated azimuth and slowness and the time domain F-detector trace. The F detector exhibits a strong peak for the Pn arrival as shown in the red portion of the two waveforms (or the small/large amplitudes at the beginning of the beam/F-Detector waveforms, respectively). Unlike the beam, which has significant energy for later phases, the F detector shows much lower values for the later phases. This behavior is most probably caused by the poor coherence of later phases when beamed at the Pn slowness.

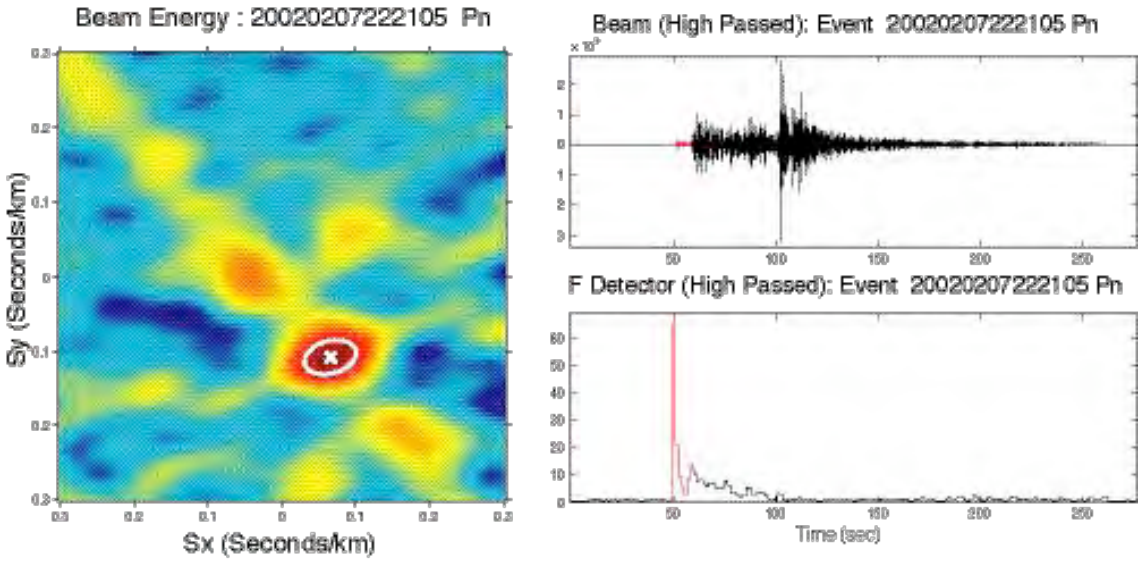


Figure 1. Seismogram, F-detection, and beam energy for an event seen at MKAR.

To produce azimuth and slowness correction surfaces, 234 events were processed for KKAR and 226 events were processed for MKAR. No ground-truth (GT) criteria were imposed to limit the data entered into KBCIT. However, events with bulletin depths greater than 51 km and, in the case for azimuth measurements, error standard deviations of greater than 15° were manually removed from the data. Following outlier removal, KKAR and MKAR azimuth pipelines consisted of 147 and 137 events, respectively. Conveniently, this process removed events close to the stations where mislocations could contribute signal to the residuals. Standard deviations of 6.5 and 7.0 degrees are observed at MKAR and KKAR. Slowness standard deviations are observed to be 0.028 and 0.022 s/km at MKAR and KKAR, respectively. It is possible that some deep events have remained in the event population used to form the surfaces, which could distort the corrections and will be investigated further. Figure 2 shows azimuth corrections for both MKAR and KKAR, and it is interesting to compare azimuth residuals for the two arrays from the west end of

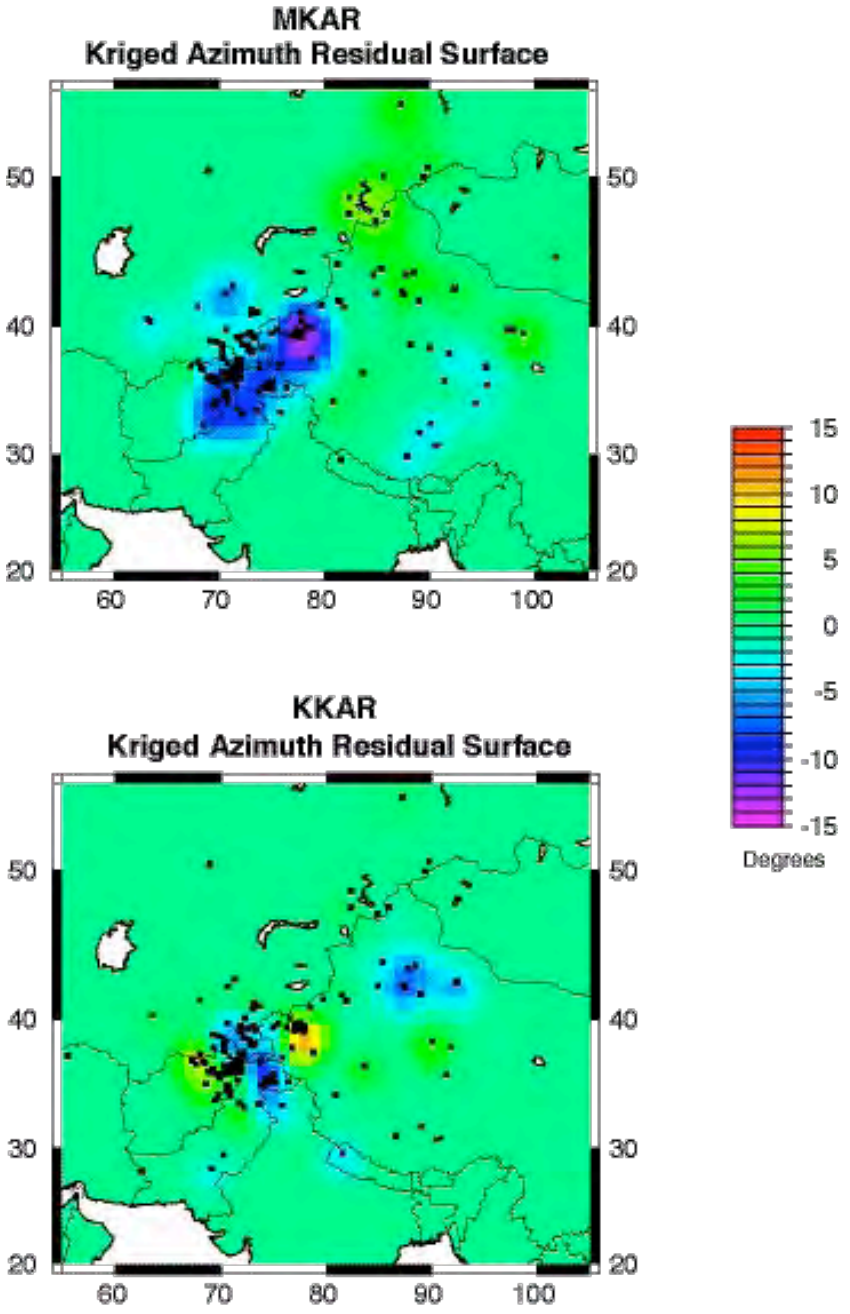


Figure 2. Kriged Pn azimuth correction surfaces for MKAR and KKAR.

the Tarim Basin, at about 40° latitude and about 78° longitude. It appears that the Tien Shan causes a defocusing effect for events from this location to the two arrays, which could be explained by thicker and slightly slower crust for this tectonic province compared to those surrounding it. Figure 3 shows slowness correction surfaces for the two arrays.

Travel time corrections

Preliminary travel-time correction surfaces are calculated for MK31 and KK31 using picks by Los Alamos National Laboratory (LANL) analysts. Ground-truth levels are required to be GT20 or better, based on the *Bondar et al.* (2003) criteria, and hence, fewer data are available for the construction of these surfaces than for those of slowness and azimuth.

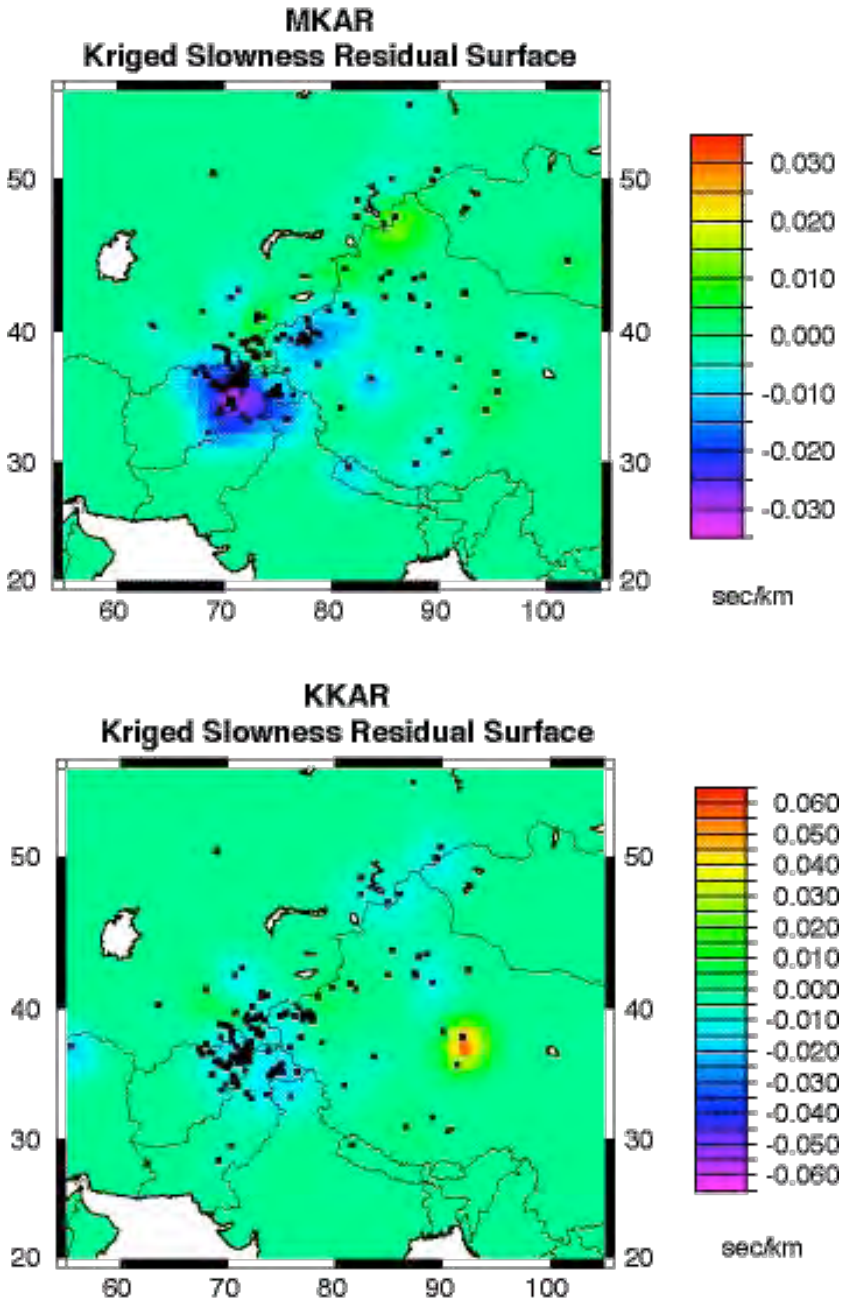


Figure 3. Kriged Pn slowness correction surfaces for MKAR and KKAR.

Data at KK31 were limited and only available for about a 5-month time period. Within this time frame, only 4 events had sufficient ground-truth quality to be included. Natural seismicity will eventually provide higher quality ground truth for this station. Figures 4 and 5 show kriged travel time correction surfaces. In Figure 5, the March 13,

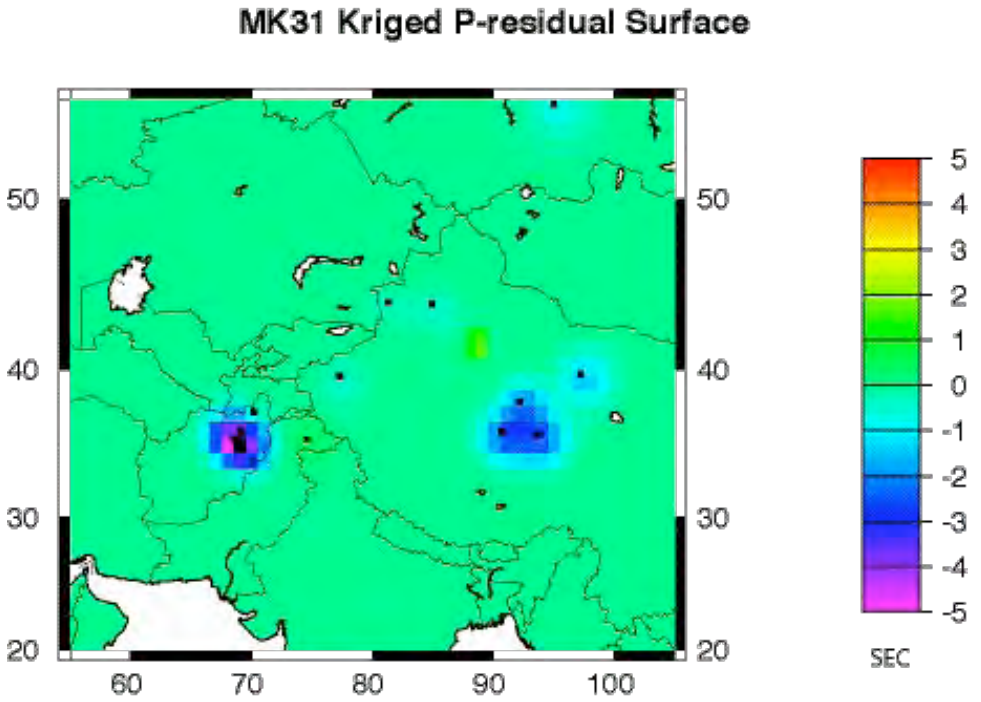


Figure 4. Kriged P travel-time correction surface for MK31.

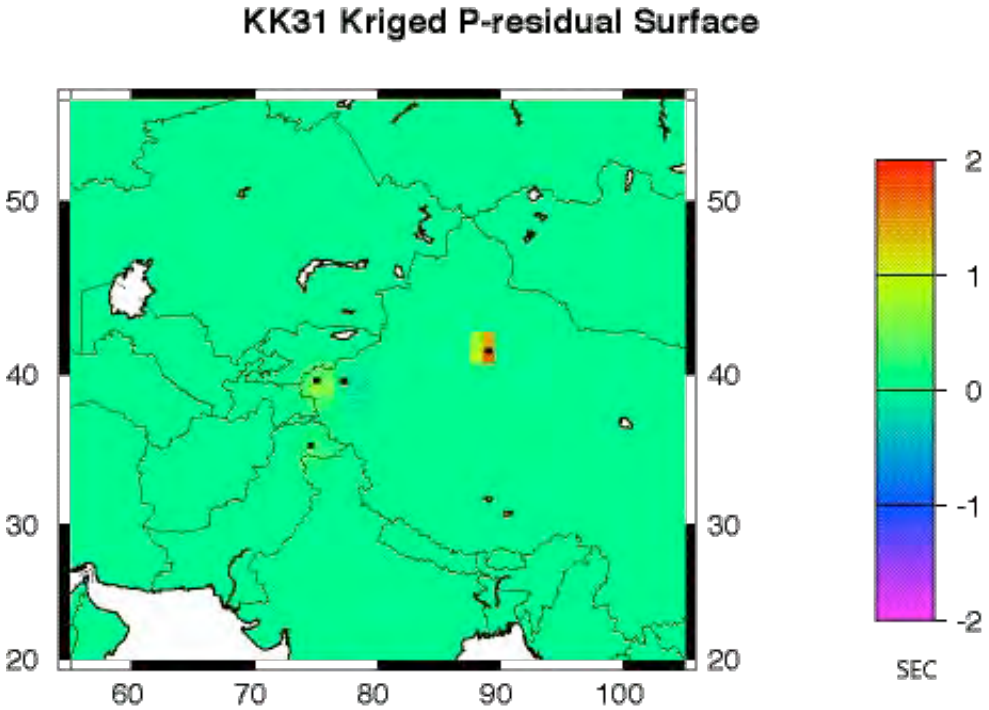


Figure 5. Kriged P travel time correction surface for KK31.

2003 earthquake near Lop Nor is the source of the “bright spot” at that location.

Phase detection at Karatau

We observe that the Karatau seismic array frequently records useful Pg phases in cases where Pn is lost in the noise. Apparent velocity can substantiate the Pg identification and, if a correction surface can be formed, we may have an additional phase available at Karatau for locating some events. To illustrate these phenomena, we use events from a mainshock/aftershock sequence near Kashgar in the Xinjiang province of China (Figure 6) that began on Feb 24, 2003. Figures 7 and 8 compare Pg propagation at MK31 and KK31—the broadband three-component stations of the MKAR and KKAR arrays. The Pg onset at KK31 is quite pronounced, particularly when compared to MK31. Figure 9 shows Pn disappearing into the noise at KK31, while Pg remains a prominent arrival. Adding KK31 Pg arrivals into our relocations where Pn is absent results in several additional convergent locations among the aftershock population. Examination of a number of events at Karatau (and Makanchi) shows a clear error in some of the REB solutions, and we add our phase picks and azimuth estimates to all available information to improve locations.

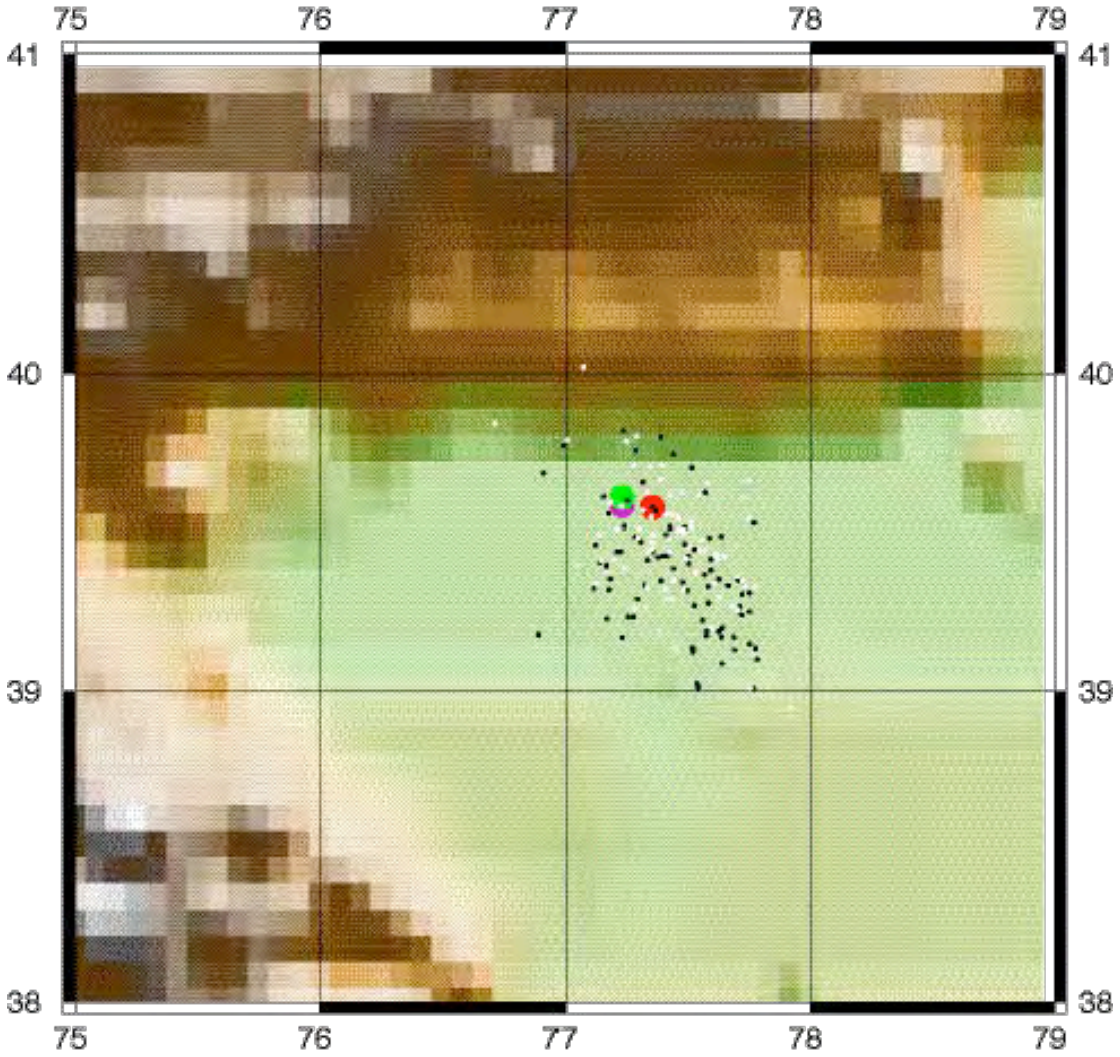


Figure 6. Mainshock/aftershock sequence in western China. Large dots are the mainshock locations from different sources: the rightmost (red or dark grey) dot is the REB solution, upper left (green or light gray) dot is the EDR Weekly solution, and lower left (purple or medium gray) dot is the LANL solution using a merged database. The small black dots are REB aftershocks and the small white dots are LANL relocations.

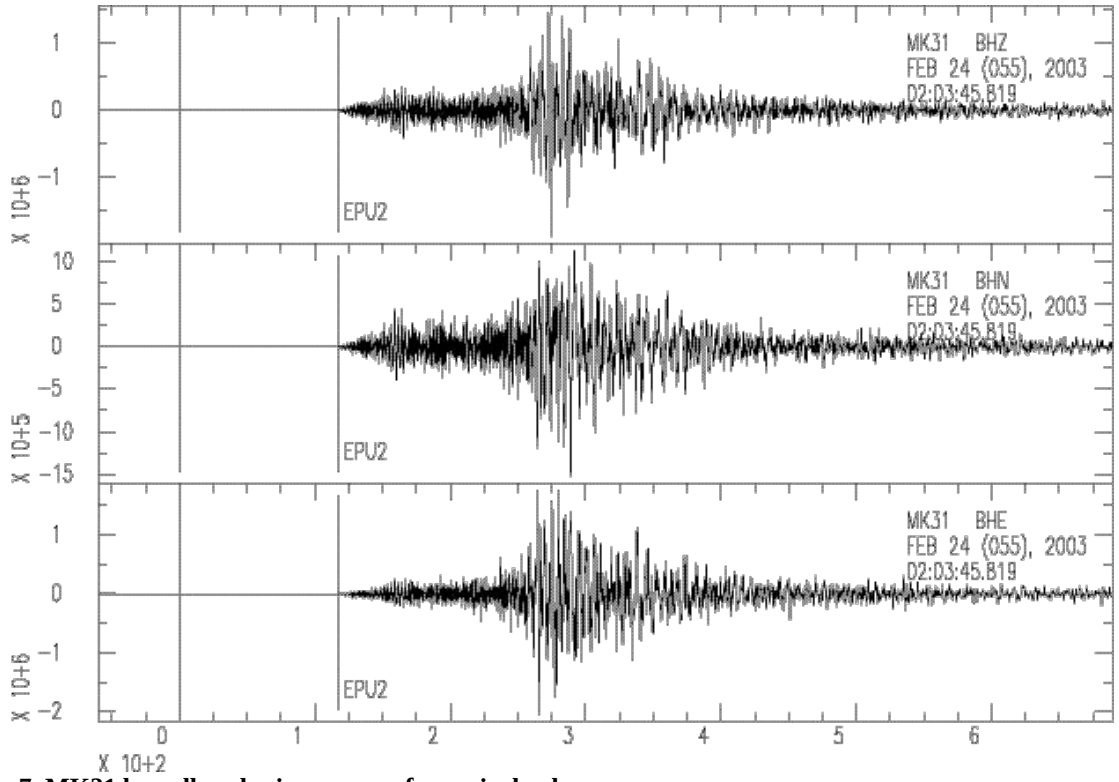


Figure 7. MK31 broadband seismograms for mainshock.

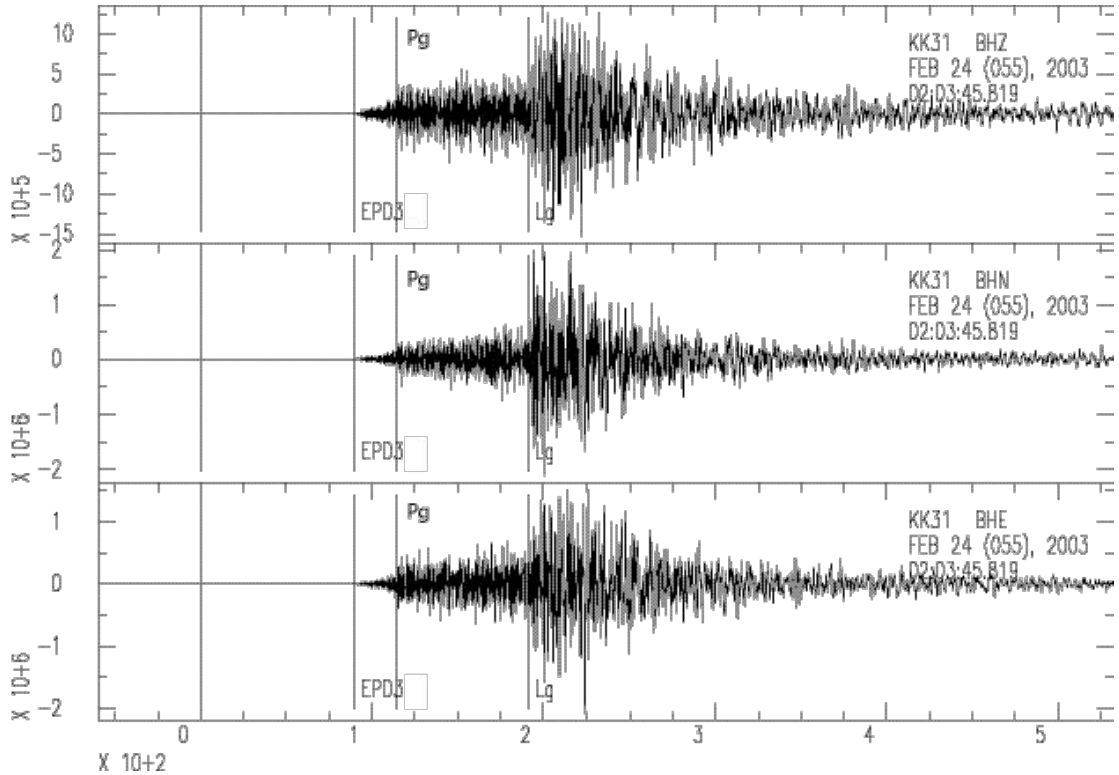


Figure 8. KK31 broadband seismograms for mainshock.

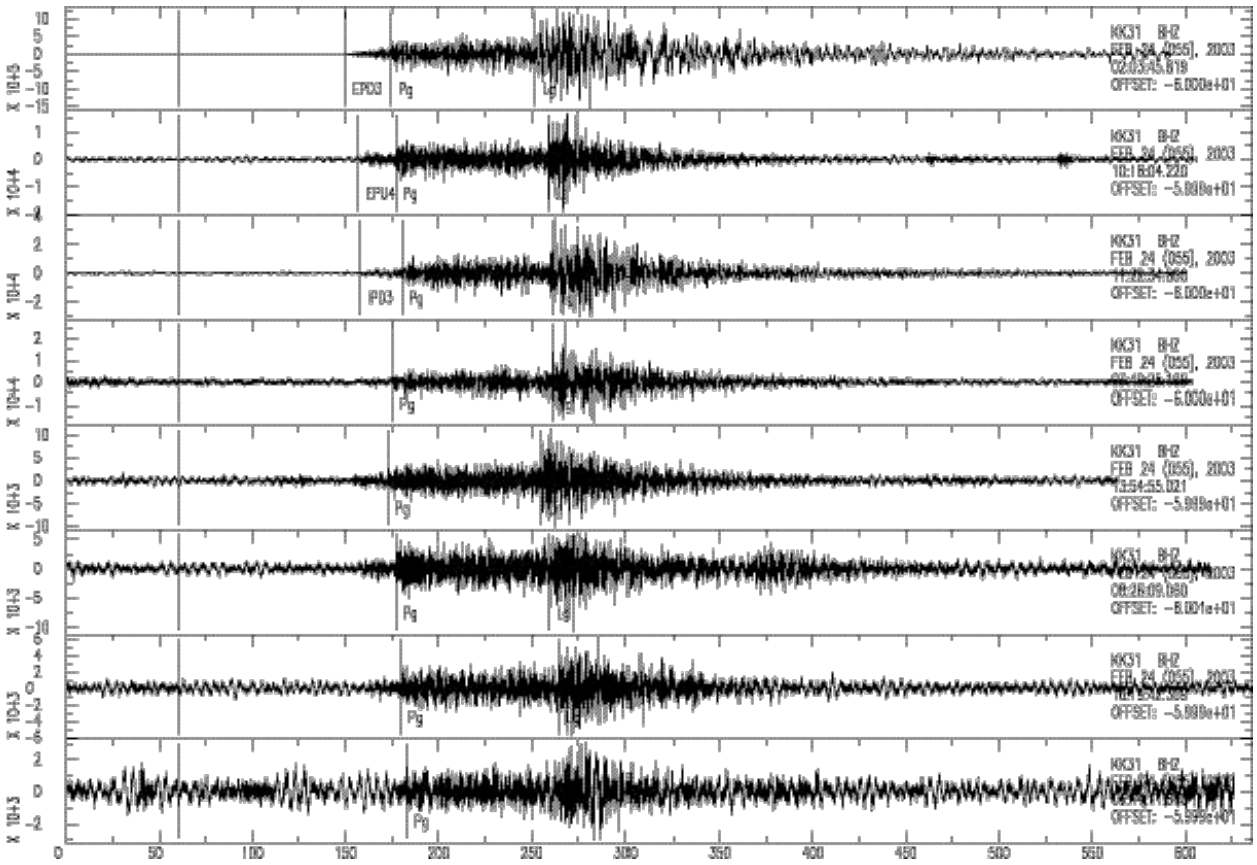


Figure 9. Mainshock (top) and selected aftershocks at KK31 showing Pn, Pg, and Lg phase picks.

CONCLUSIONS AND RECOMMENDATIONS

In our preliminary investigations, we find clear azimuth and slowness perturbations associated with regional arrivals seen at KKAR and MKAR. We will implement and test the effect of correcting for these perturbations, which should improve our location ability for smaller events. Travel-time data at KK31 are very sparse because of its short history. Over time, natural seismicity should rectify this shortcoming. Though station MK31 is more mature, secondary phases are also not plentiful. It is clear from regional wave propagation characteristics at these stations that correction surfaces for secondary phases—and here we use the term broadly to include all post-first-P arrivals—would be of great benefit to location efforts in this area.

REFERENCES

Blandford, R.R. (1974), An Automatic Event Detector at the Tonto Forest Seismic Observatory, *Geophysics* 39, 633-643.

Bondar, I., S.C. Myers, E.R. Engdahl, and E.A. Bergman (2003), Epicenter Accuracy Based on Seismic Network Criteria, submitted to *Geophysical Journal International*.

Schultz, C.A., S.C. Myers, J. Hipp, and C.J. Young (1998), Nonstationary Bayesian kriging: A predictive technique to generate spatial corrections for seismic detections, location, and identification, **Bull. Seis. Soc. Am**., 88, 1275-1288.

Shumway, R. H. (1971), On Detecting a Signal in N Stationarily Correlated Noise Signals, *Technometrics* 13, 499-519.

METHODS FOR IMPROVING SEISMIC EVENT LOCATION PROCESSING

Clifford H. Thurber, Wen-xuan Du, Haijiang Zhang, and William J. Lutter

University of Wisconsin-Madison

Sponsored by Air Force Research Laboratory

Contract No. DTRA01-01-C-0085

ABSTRACT

Our research program consists of four components, each involving some aspect of multiple-event analysis: (1) high-precision waveform cross-correlation (WCC) for arrival time estimation, (2) robust event clustering, (3) waveform decomposition and source wavelet deconvolution reshaping, (4) double-difference (DD) multiple-event location and tomography. Our research focused initially on the development and testing of these seismic analysis methods using "ground-truth" (GT) datasets at different scales (local and regional), and is being followed by the application of these methods to a "test-bed" regional-distance seismic dataset, including tests on real-time and simulated real-time data streams. Here we highlight some of the more significant project achievements from components 1, 2, and 4.

(1) Differential arrival times for pairs of seismic events observed at the same station are often calculated by WCC techniques. Researchers often choose the differential times to use based on the associated cross-correlation (CC) values exceeding a specified threshold. When two similar time series are corrupted by correlated noise, the time delay estimate calculated with the WCC technique may not be reliable. Thus the selection of a threshold value is important. If it is set too high, then only a limited number of very accurate differential time data are available to constrain the relative positions of earthquakes. If the threshold value is set too low, then many unreliable differential time estimates are used and they will negatively affect the final relocation results. The bispectrum method can suppress the correlated Gaussian noise sources in two similar time series and be used to obtain the relative time delay between them. We compute time delay estimates between the waveform pairs with the bispectrum method and use them to verify the WCC-determined one. This technique can provide quality control over the selected time delay estimates and potentially provide more differential travel time data for close events pairs, by verifying the reliability of differential times that might not meet the threshold criterion.

(2) We have tested a two-step event location technique with a California GT data set. In step 1, event locations are estimated via WCC of Hilbert-envelope waveforms. The Step 1 procedure accurately located the epicenters within 20 km (approximately 1 bin) of the NCSN catalog location for 16 of the 20 test events. However, depth estimates were poorly constrained. The Step 2 refinement based on WCC of the high-frequency P arrivals followed by DD relocation improved both epicenter and depth estimates. This two-step procedure offers advantages over conventional location techniques including a Step 1 event location not dependent on the accuracy of catalog picks and a Step 2 improvement in location accuracy using the high-accuracy DD technique.

(3) We have developed the new method of DD tomography. The inversion code tomoDD takes the double-difference location method (hypoDD) a step further to solve for 3D velocity structure simultaneously with hypocenter locations using both catalog picks and differential arrival times (WCC and catalog). Compared to conventional tomography, the result is a sharpening of the seismicity distribution equal in quality to hypoDD plus a sharpening of the velocity image due to removal of the majority of the location scatter. We have developed local- and regional-scale versions of tomoDD, and have applied each to synthetic and real datasets.

OBJECTIVE

Our research program consists of four components, each involving some aspect of multiple-event analysis: (1) high-precision waveform cross-correlation (WCC) for arrival time estimation, (2) robust event clustering, (3) waveform decomposition and source wavelet deconvolution reshaping, (4) double-difference (DD) multiple-event location and tomography. Our research focused initially on the development and testing of these seismic analysis methods using "ground-truth" (GT) datasets at different scales (local and regional), and is being followed by the application of these methods to a "test-bed" regional-distance seismic dataset, including tests on real-time and simulated real-time data streams. Here we highlight some of the more significant project achievements from components 1, 2, and 4.

RESEARCH ACCOMPLISHED

Bispectrum analysis

Differential arrival times for pairs of seismic events observed at the same station are often calculated by WCC techniques. These differential times (or adjusted picks derived from them) can be used to dramatically improve the earthquake relocation results (Got et al., 1994; Dodge et al., 1995; Shearer, 1997; Rubin et al., 1999; Waldhauser and Ellsworth, 2000; Schaff et al., 2002). Researchers often choose the differential times to use based on the associated CC values exceeding a specified threshold. For example, Schaff et al. (2002) only selected those time delays with CC values larger than 0.7 and mean coherences above 0.7. The selection of an "optimum" threshold value is important but difficult. If it is set too high, then only a limited number of very accurate differential time data are available to constrain the relative positions of earthquakes. On the other hand, if the threshold value is set too low, then many unreliable differential time estimates are used and will negatively affect the final relocation results. Also the time delay estimate calculated with the CC technique may not be reliable when the noise sources in the two time series are correlated.

The WCC approach and its variants work in the second-order spectral domain. When the underlying signal inside two similar time series can be regarded as a non-Gaussian process and the noise sources as zero-mean Gaussian processes, the similarities between the two time series can be better compared in the third-order or bispectrum domain (Nikias and Raghuveer, 1987; Nikias and Pan, 1988; Yung and Ikelle, 1997). This bispectrum method takes advantage of the fact, that for Gaussian processes only all spectra of order higher than two are identically zero. Thus the effect of correlated Gaussian noise is completely suppressed when we compare the two time series in the bispectrum domain, while it may make WCC techniques fail to work well. Noise at a station for different events can be expected to be partially correlated due to a combination of constant predominant noise sources with time-varying amplitude (microseisms, wind or cultural noise) and site response effects. Cycle skips are another potential WCC pitfall that bispectrum analysis may help detect.

Figure 1 demonstrates the application of the CC and bispectrum methods to the waveforms of two closely spaced M2.5 New Zealand earthquakes. The waveforms for these events recorded at nearby stations are highly similar, but the signal to noise ratios (SNRs) for the records at station MOW (epicentral distance of 93 km) are noticeably lower (Figures 1A and 1B). The two bispectrum-correlation series (Figures 1E and 1F) peak at lag 6 and 7 respectively, whereas the two CC series (Figures 1C and 1D) reach maxima at lags very different from each other and also from the two bispectrum-correlation series. Careful examination reveals that the two CC series reach local maxima at lag 7. They fail to become global maxima there, however, apparently due to the contamination of correlated noise. Figures 1G and 1H plot the stacked signals for both raw and band-pass filtered waveforms. In both cases the lower trace (the stacked signal obtained by shifting the waveform of the first event with bispectrum-determined lags) has a larger root-mean-square (RMS) amplitude than the upper trace, which is obtained after shifting the waveform of the first event with the CC-determined lags. The above example corroborates the findings of Nikias and Pan (1988) and Yung and Ikelle (1997) that the bispectrum method works better than CC techniques in getting relative time delay between two similar signals contaminated by correlated noise.

In our approach, we compute two more time delay estimates between the waveform pairs with the bispectrum method (the raw data and band-pass filtered data) and use them to verify the WCC-determined one using the band-pass filtered data. This technique can provide quality control over the selected time delay estimates and potentially provide more differential travel time data for close events pairs, by verifying the reliability of differential times that might not meet the threshold criterion.

The process of time delay calculation and bispectrum verification can be briefly described as follows. For the *k*-th mutual station that provides waveforms for two earthquakes *i* and *j*, we rely on the catalog phase (P or S) picks to

form the data windows used for time delay calculations. Then using the band-pass filtered waveforms, we calculate both the CC value CC_{ij}^{k} and the relative time delay in lag number $D_{ij}^{k(cc)}$ for the event pair. If the value of CC_{ij}^{k} is larger than a threshold CC^{sub}, we also perform sub-sample time delay calculation to get $D_{ij}^{k(sub)}$ by a weighted linear fitting of the cross spectrum phase (Poupinet et al., 1984). After we make the CC calculations for all the mutual stations between events *i* and *j*, we can obtain the maximum CC value CC_{ij}^{max} for the event pair. If CC_{ij}^{max} is larger than a second threshold CC^{bs}, we will perform bispectrum time delay estimation for each mutual station of the event pair. We obtain two estimates of time delay in lag number, i.e. $D_{ij}^{k(bs1)}$ using the band-pass filtered waveforms and $D_{ij}^{k(bs2)}$ with the raw waveforms. Thus depending on the extent of waveform similarity for an event pair, which is measured by the size of CC_{ij}^{max}, four possible time delay estimations are carried out at a mutual station for either P or S waves.

Besides the aforementioned threshold value that researchers often use to select time delay estimates, which we term CC^{lim1}, three other parameters CC^{lim2}, CC^{lim3} and D^{lim} control the bispectrum verification process. Generally $CC^{lim2} \geq CC^{lim1} \geq CC^{lim3}$. After we make the CC calculations across all the mutual stations of an event pair, we compare the maximum CC value CC_{ij}^{max} with CC^{lim2}. If CC_{ij}^{max} is larger than CC^{lim2}, we will verify the CC time delay estimates for those stations with CC_{ij}^{k} larger than CC^{lim3}. A CC time delay estimate $D_{ij}^{k(cc)}$ is trusted (or passes the verification) if its differences from both $D_{ij}^{k(bs1)}$ and $D_{ij}^{k(bs2)}$, the ones determined with the bispectrum method, do not exceed the tolerance limit D^{lim}. In other words, for an event pair with high CC_{ij}^{max} value we will select the CC time delay estimates as long as they pass the bispectrum verification, even though the CC values associated with some of them are smaller than CC^{lim1} and would not be used under the threshold criterion often adopted by other researchers. If $CC^{lim1} £ CCij^{max} < CC^{lim2}$, we will make the verifications only for those stations with CC_{ij}^{k} larger than CC^{lim1}. If CC_{ij}^{max} falls below CC^{lim1}, the CC time delays for the event pair are simply discarded.

As an example, we apply this technique to obtain bispectrum-verified WCC differential times for a set of New Zealand earthquakes, and relocate 521 of the events using the DD algorithm hypoDD (Waldhauser and Ellsworth, 2000). We find that the bispectrum-verified time delays provide more clustered earthquake relocation results with lower arrival time residuals compared to the threshold criterion. Figure 2 shows the relocation results for a subregion near Lake Wairarapa, New Zealand.

Generally for an earthquake, fewer S arrivals are available in the phase catalog than P arrivals because they are more difficult to select. We can obtain additional bispectrum-verified S differential times for those waveforms lacking catalog S picks, using the predicted S arrivals either from a velocity model (Shearer, 1997) or from the S-P time of a nearby event. Our work demonstrates that relocation results can be further improved with these additional time constraints.

Hierarchical clustering and location

We have implemented and tested a two-step location technique that offers several advantages over conventional techniques due to its use of WCC and DD location methods. Step 1 event location is based solely on high-quality GT event waveforms without use of catalog picks. Step 2 location estimates offer the same improvement in location accuracy as documented by the use of high-resolution DD techniques over standard techniques (Waldhauser and Ellsworth, 2000). We evaluated the technique using 640 events from N. California (magnitude range 4.3-5.3) using a 6°x 6° study region and 7 master stations from the UC Berkeley NCSN array (Fig. 3). In step 1, event locations are estimated via CC of Hilbert-envelope waveforms. A test event is cross-correlated against a suite of reference events binned by latitude, longitude, and depth. The step 1 location derived from the CC global maximum is then used as a starting location in the step 2 refinement using the DD relocation method (hypoDD).

All events were initially binned using the catalog locations into 0.1° latitude and longitude bins and 1.5 km depth bins. We selected the highest magnitude event per bin as a reference event. We assembled a suite of test events by selecting the second highest magnitude event from each multiple-event bin. After data quality considerations, this yielded 161 reference events and 19 test events for use in the step 1 waveform location technique with location accuracy limited to the binning interval.

Relocation with hypoDD using NCSN data from 25 Berkeley network stations provided GT hypocenter information for the test events. We explored 4 different parameter settings controlling the extent of clustering and residual outlier rejection. Average standard deviations of GT locations for the 19 test events indicate good control on latitude and longitude (±0.015° and ±0.02°) and moderate control on depth (±1.23 km). We chose GT solutions with a mean errors (absolute value) of 0.03°, 0.04°, and 1.26 km.

In the step 1 procedure, the entire seismogram was filtered and an eigenvector decomposition of the covariance matrix was applied to the 3-component data (Rowe et al., 2002) prior to the calculation of Hilbert-envelopes for the principal direction. Test event data for each of the master stations were cross-correlated against 161 GT events with the position of the CC global maximum determining the step 1 location (Fig. 3). The Step 1 procedure located 14 of 19 test events to within 20 km (approximately 1 bin) of the NCSN catalog location with location error for the remaining events ranging from 25-50 km. Errors in test-event depth were < 1.5 km (1 depth bin) for half of the events and on the order of 2.5-10 km for the remaining step 1 relocated events.

The step 2 procedure attempts to improve upon the step 1 epicentral and depth estimates based on the use of catalog and WCC differential times with hypoDD. For each test event, subsets of the catalog and WCC data are prepared for use in hypoDD with the step 1 location providing the initial test-event location.

We augmented the existing P and S picks from the network catalog using skew and kurtosis analysis followed by a manual evaluation. Many catalog P picks required manual adjustment. We then prepared WCC data based on 3- and 5-second P windows (Rowe et al., 2002). A subset of non-test event data (P and S NCSN phase catalog times and WCC P-pick adjustments) augmented with test event data allows clustering of the test event with adjacent reference events. Clustering parameters for hypoDD are chosen to improve vertical control by strongly weighting pick data from event pairs with larger separation distances and WCC data from event pairs with smaller separation distances (Waldhauser, 2001).

We evaluated various ways of constructing pick and WCC data subsets. Relocation results were not influenced by the choice of distance cutoff in the cluster analysis. We used a cutoff value of 1° (reference event to test event) in our construction of pick and WCC data subsets. Construction of WCC differential time data subsets also depended on quality information, absolute arrival-time difference cutoff (5-15 s) and the minimum CC value (0.7-0.9). Both arrival-time and WCC data were influenced by choice of clustering parameters.

We also experimented with the use of bispectrum-correlation (BC) values to validate WCC information with low CC values. An event was eligible for BC analysis if a station CC value was greater than a threshold value cutoff. Data from a subset of stations per event were selected for BC calculation based on a minimum CC value cutoff. If the BC and CC lag values were within a time-difference tolerance (0.25 s), BC data was allowed into the DD data set. The lowering of threshold value cutoffs (0.5-0.7) increased inclusion of BC data from 10% to 20% and led to a slight improvement in step 2 depth estimation over use of P pick WCC data with standard parameters (0.7 CC cutoff and maximum travel-time difference of 10 sec). Although we have not at this point adjusted catalog S picks, S-pick WCC data based on 30-s windowing were added to the P-pick WCC data as a final effort to improve depth estimation.

To test the stability of the step 2 procedure, locations were calculated using a range of starting depths (1.0, 2.5, 5.0, 10.0, 15.0, and 20.0 km) for each test event. Location mean and standard deviation values (Figure 4) show that depths are less constrained for events outside of the ring of master stations, in particular the test events positioned near 34.3°. This is indicated by the tendency of the mean locations to shift towards the center of the test depth range and by larger depth standard deviations. Average standard deviation values of latitude, longitude, and depth for test events near 34.3° are larger (0.027°, 0.019°, 4.6 km) than within station coverage (0.004°, 0.013°, and 2.35 km) suggesting tradeoff in latitude and depth for the outside events. We attempted to improve the stability of the outlier events by adjusting WCC P-window length, including BC data, and adjusting parameters that control the use of WCC and BC data. A 5-second P window with a 0.9 cross-correlation cutoff was used to produce the results shown in Figure 4. The use of the BC data or other WCC parameter settings yields similar results.

We included S-wave WCC data to calculate step 2 relocations displayed in Figure 5, as it slightly lowered relocation errors for some of the events outside station coverage (34.3° latitude). The hypoDD relocation improves both epicenter and depth estimates (Figure 5) both in resolution (GT error < bin intervals) and in accuracy. Seventeen of 19 test events have hypocenter location errors < 15 km, with 11 events relocated to within 5 km of GT. Depth errors for 16 events are within 2.5 km of GT. Mean latitude, longitude and depth errors (absolute value) for test events outside station coverage are larger (0.059°, 0.051°, and 2.5 km depth) by roughly a factor of 2 than mean errors within station coverage (0.028°, 0.031°, and 1.02 km depth). Step 2 location mean errors for events within station coverage are within the mean location error of the GT solution. Improvement of the S arrival-time picks over catalog times should lead to improved CC data and depth estimation. The accuracy of the relocation estimates even with coarse master station coverage suggests this approach could have broader application outside of this particular GT dataset study region.

Double-difference tomography

We have developed a new DD tomography method (Zhang and Thurber, 2003), which takes a step further of the DD location method (Waldhauser and Ellsworth, 2000) to solve for 3D velocity structure simultaneously with hypocenter locations using both catalog picks and differential arrival times (WCC and catalog). At the local scale (10s to 100s of kilometers), the earth can be represented with a flat model. We use the pseudo-bending ray-tracing algorithm (Um and Thurber, 1987) to find the rays and calculate the travel times between events and stations. The model is represented as a regular set of 3D nodes and the velocity values are interpolated by using the tri-linear interpolation method. The hypocentrer partial derivatives are calculated from the direction of the ray and the local velocity at the source. The ray path is divided into a set of segments and the model partial derivatives (calculated in terms of fractional slowness perturbation, so that the derivatives are related to path length) are evaluated by apportioning the derivative to its 8 surrounding nodes according to their interpolation weights on the segment midpoint (Thurber, 1983).

We have tested the local-scale version of DD tomography (tomoDD) with a synthetic dataset that was constructed on the basis of an idealized model of the velocity structure of the San Andreas Fault in central California (Kissling et al., 1994) shown in Figure 6. The events and stations used to construct the synthetic dataset are from the actual seismicity and USGS stations in the Loma Prieta region (Fig. 7). We added Gaussian random noise with zero mean and a standard deviation of 0.04 s to all the true arrival times. In addition, we also added a constant noise term to the arrivals at each station from a uniform distribution between –0.3 s and 0.3 s. This simulates the case that the systematic errors (model errors and pick bias) associated with the arrival times are larger than the random ones. We construct the pseudo "cross-correlation" data directly from the absolute arrival times by differencing the synthetic arrival times at common stations for events pairs within 20 km. As a result, the "cross-correlation" data are more accurate than the absolute data.

We first use the DD location algorithm *hypoDD* to relocate the events (Waldhauser, 2001). The 1D velocity model used is the Dietz and Ellsworth (1990) model, based on seismic refraction and earthquake data. We use both the residual weighting and distance weighting schemes in the inversion to control the large residuals, as did Waldhauser and Ellsworth (2000). The absolute differences between this set of event relocations and the true locations and their standard deviations are shown in Table 1. The results indicate that the event relocations from the DD location algorithm based on a 1D velocity model have a substantial bias (>1 km in each coordinate direction) from the true locations**.** This bias is caused by a difference between the velocity model (horizontal layers) used to calculate the DD locations and the true velocity model (vertical "sandwich") used to generate the data. The heterogeneity of the true velocity model makes path anomalies different for different events. However, the DD location method assumes that the path anomalies are location-independent, and this assumption introduces bias into event locations (Wolfe, 2002).

Next, we show the results of applying the standard tomography method to the relatively noisy absolute arrival times. The inversion starts from the same 1D velocity model as the DD location method. The X-Y nodes used to represent the velocity model are shown in Figure 7; in depth, nodes are positioned at 0, 3, 7, 11, and 16 km. The computational algorithm is identical to that for DD tomography, but the differential times are excluded. Both damping and smoothing (with weight 5.0 in both the horizontal and vertical directions) are applied to the inversion to make the solution more stable. Figure 8a shows horizontal slices through the velocity structure obtained from the standard tomography. The absolute difference between this velocity model and the true velocity model has a median value of 0.164 km/s, a mean value of 0.245 km/s and a standard deviation of 0.249 km/s. The main features of the true velocity model are evident in the depth slices. The event locations have smaller errors than those from the DD location method (Table 1).

DD tomography uses both the noisy absolute arrival times and more accurate differential times. We also apply damping and the smoothing constraints to stabilize the solution, with the residual weighting used to penalize the large residuals during the inversion. DD tomography starts with the same 1D velocity model and uses the same inversion grid as the standard tomography. Figure 8b shows the horizontal slices of the velocity structure from DD tomography. The absolute difference between this velocity structure and the true velocity structure has a median value of 0.136 km/s, a mean value of 0.178 km/s, and a standard deviation of 0.164 km/s. DD tomography characterizes well the low velocity zone of the true velocity model, especially at the depths of 3 km and 7 km. Subtracting the DD tomography solution and the standard tomography solution from the true model (Fig. 8c and d), we find that the velocity model from DD tomography has a more correct value in the low-velocity trough except at the depth of 0 km, where the ray paths from event pairs almost completely overlap and the accuracy of velocity

structure is mainly controlled by absolute catalog data. This indicates that DD tomography recovers better the low-velocity zone, and overall the velocity model is more accurate than the standard tomography. Compared with the standard tomography method, DD tomography also produces more accurate event locations (Table 1).

At the regional scale (100's to 1000's of km), however, the earth should not be treated as flat, but as a sphere. Some velocity discontinuities such as Conrad, Moho, and subducting slab boundary should also be taken into account. Finite-difference ray tracing algorithms developed by both Podvin and Lecomte (1991) and Hole and Zelt (1995) are able to accurately calculate first-arrival times in the presence of extremely severe, arbitrarily shaped velocity discontinuities. These algorithms solve a finite difference approximation to the Eikonal equation in the regularly gridded velocity structure through a systematic application of Huygens' principle. This procedure can explicitly take into account different propagation modes including transmitted and diffracted body waves, and head waves in addition to direct waves. The principle of reciprocity is utilized by placing the source point at the seismic station location and interpolating the travel times computed at the grid nodes to match the exact earthquake location (Flanagan et al., 1999).

To adapt the finite-difference algorithm to the regional scale, the curvature of the Earth must be taken into account. Earth flattening transformation is only valid for 1D velocity models and not for 3D velocity models. Following Flanagan et al. (2000), we solved this problem by parameterizing a spherical surface inside the Cartesian volume of grid nodes. The coordinate center was put at the surface of the Earth, positive X and Y-axes point to the direction of North and West, and positive Z-axis points downward, respectively. The grid nodes above the Earth surface (air nodes) are attributed to the true velocity values traveling in the air. As a result, all the rays travel inside the Earth. The regular uniform velocity (slowness) grid nodes used to calculate the travel time field using finite-difference algorithms are interpolated from the non-uniform inversion grid nodes through tri-linear interpolation. If an inversion grid node is 2 km above the Earth's surface, then it is treated as an air node and its value is fixed during the inversion. We treat each station as a source and calculate travel times to all velocity nodes in the volume. The travel time from a station to each earthquake is interpolated from its eight neighboring nodes through tri-linear interpolation. The ray path from the earthquake to the station is found iteratively with increments opposite to the travel time gradient. After these setups, DD tomography is adapted to the regional scale with ray paths and related partial derivatives calculated by the finite-difference method. We have tested the regional-scale version of DD tomography on data from the subduction zone beneath northern Honshu, Japan, and obtained the velocity structure with unprecedented resolution.

CONCLUSIONS AND RECOMMENDATIONS

(1) WCC is vulnerable to problems associated with correlated noise that can be overcome using bispectrum analysis. It is our recommendation that a verification approach comparable to that described here be adopted for earthquake location applications for which very high accuracy is essential.

(2) A hierarchical location approach, for “new” events relative to a set of reference events, that starts with CC of long records at low frequencies to identify the approximate source region based solely on waveform similarity and then switches to DD location using CC of short records at high frequencies works effectively for a regional dataset from California. This approach should next be tested in a real-time monitoring environment.

(3) Algorithms for DD tomography have been successfully developed for both local (10's to a few 100 km) and regional (100's to 1000's of km) scale. Synthetic tests show the method yields locations with greater accuracy than either DD location or standard tomography, and a velocity model that is closer to the true model than standard tomography. The DD tomography approach works with either waveform-based or catalog-based differential time data, and thus is applicable to any dataset to which standard tomography can be applied.

ACKNOWLEDGEMENTS

We thank Megan Flanagan for providing codes for the spherical earth finite-difference method.

REFERENCES

Dodge, D. A., G. C. Beroza, and W. L. Ellsworth (1995), Foreshock sequence of the 1992 Landers, California, earthquake and its implications for earthquake nucleation, *J. Geophys. Res.*, 100, 9865-9880.

Flanagan, M. P., S. C. Myers, C. A. Schultz, M. E. Pasyanos, and J. Bhattacharyya (2000), Three-dimensional a priori model constraints and uncertainties for improving seismic location, 22nd Seismic Research Symposium: Technologies for Monitoring the CTBT, New Orleans, LA, *UCRL-JC-138984*.

Flanagan, M.P., C. A. Schultz, and L. J. Hutchings (1999), Development of 3-D crust and upper mantle velocity models to improve seismic event location, AGU Fall meeting, San Francisco, CA, *EOS Trans. Am. Geophys. Un.*, 80, p. F656.

Got, J.-L., J. Fréchet, and F. W. Klein (1994), Deep fault plane geometry inferred from multiple relative relocation beneath the south flank of Kilauea, *J. Geophys. Res.*, 99, 15,375-15,386.

Hole, J. A., and B. C. Zelt (1995), 3-D finite-difference reflection traveltimes, *Geophys. J. Int.*, 121, 427-434.

Kissling, E., W. L. Ellsworth, D. Eberhart-Phillips, and U. Kradolfer (1994), Initial reference models in local earthquake tomography, *J. Geophy. Res.*, 99, 19.635-19,646.

Nikias, C. L., and M. R. Raghuveer (1987), Bispectrum estimation: A digital signal processing framework, *Proc. IEEE*, 75, 869-891.

Nikias, C. L., and R. Pan (1988), Time delay estimation in unknown Gaussian spatially correlated noise, *IEEE Trans. Acoust. Speech Signal Processing*, 36, 1706-1714.

Podvin, P., and I. Lecomte (1991), Finite difference computation of travel times in very contrasted velocity models: a massively parallel approach and its associated tools, *Geophys. J. Int.*, 105, 271-284.

Poupinet, G., W. L. Ellsworth, and J. Fréchet (1984), Monitoring velocity variations in the crust using earthquake doublets: an application to the Calaveras fault, California, *J. Geophys. Res.*, 89, 5719-5731.

Rowe, C.A., R.C. Aster, B. Borchers and C.J. Young (2002), An automatic, adaptive algorithm for refining phase picks in large seismic data sets, *Bull. Seismol. Soc. Am.*, 92, 1660.

Rubin, A. M., D. Gillard, and J.-L. Got, Streaks of microearthquakes along creeping faults (1999), *Nature*, 400, 635-641.

Schaff, D. P., G. H. R. Bokelmann, G. C. Beroza, F. Waldhauser, and W. L. Ellsworth (2002), High-resolution image of Calaveras Fault seismicity, *J. Geophys. Res.*, 107, 2186, doi:10.1029/2001JB000633.

Shearer, P. M. (1997), Improving local earthquake locations using the L1 norm and waveform cross correlation: Application to the Whittier Narrows, California, aftershock sequence, *J. Geophys. Res.*, 102, 8269-8283.

Thurber, C. H. (1983), Earthquake locations and three-dimensional crustal structure in the Coyote Lake area, central California, *J. Geophys. Res.*, 88, 8226-8236.

Um, J., and C. H. Thurber (1987), A fast algorithm for two-point seismic ray tracing, *Bull. Seism. Soc. Am.*, 77, 972-986.

Waldhauser, F. (2001), hypoDD: A computer program to compute double-difference hypocenter locations, *U.S. Geol. Surv. Open File Rep.*, 01-113, 25 pp.

Waldhauser, F., and W.L. Ellsworth (2000), A double-difference earthquake location algorithm: Method and application to the Northern Hayward Fault, California, *Bull. Seism. Soc. Am.*, 90, 1353-1368.

Wolfe, C. J. (2003), On the mathematics of using difference operators to relocate earthquakes, *Bull. Seism. Soc. Am.*, 92, 2879-2892.

Yung, S. K., and L. T. Ikelle (1997), An example of seismic time picking by third-order bicoherence, *Geophys.*, 62, 1947-1951.

Zhang, H., and C. H. Thurber (2003), Double-difference tomography: The method and its application to the Hayward fault, California, *Bull. Seism. Soc. Am.*, in press.

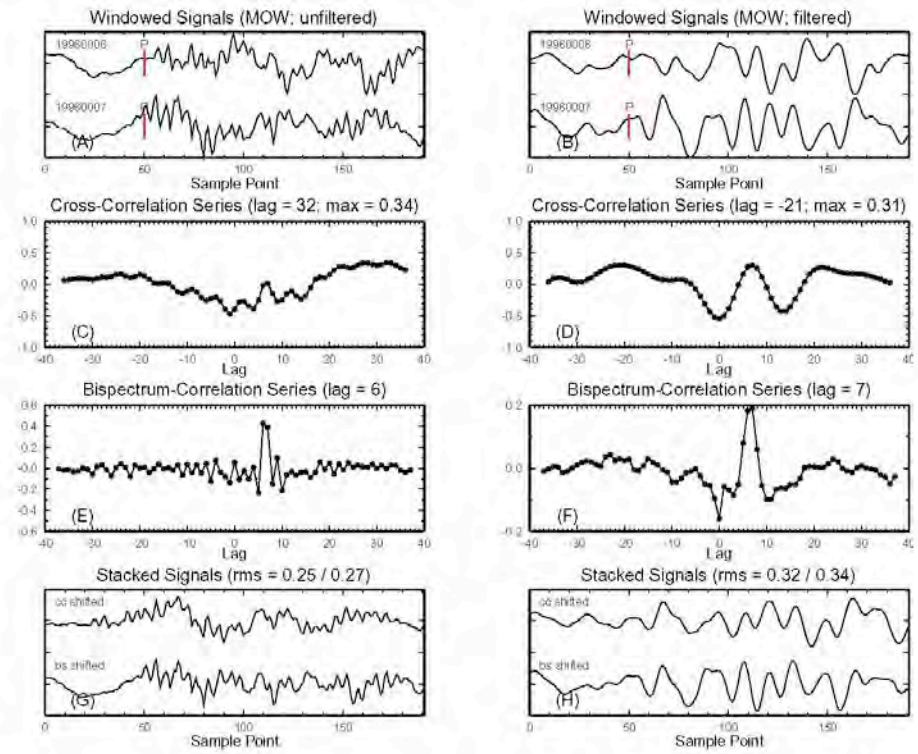


Figure 1. (A) Windowed waveforms (1 second before and 2.82 seconds after the catalog P pick) for two New Zealand earthquakes recorded at station MOW. The station sampling rate is 50 sample/sec and the signals are aligned by the P picks. (B) Windowed waveforms band-pass filtered between 1 and 6 Hz. (C, D) CC series for the (C) unfiltered (raw) and (D) filtered waveforms. (E,F) Bispectrum-correlation series for the(E) raw and (F) filtered waveforms. (G) Stacked raw waveforms. The upper trace is obtained by shifting the waveform of the first event with the CC determined lag relative to the second one, while the lower trace is computed after shifting the waveform of the first event with the lag calculated with the bispectrum method. The root-mean-square amplitudes for the two traces are 0.25 and 0.27 respectively. (H) Same as G for the stacked band-pass filtered waveforms. The root-mean-square amplitudes for the two traces are 0.32 and 0.34 respectively.

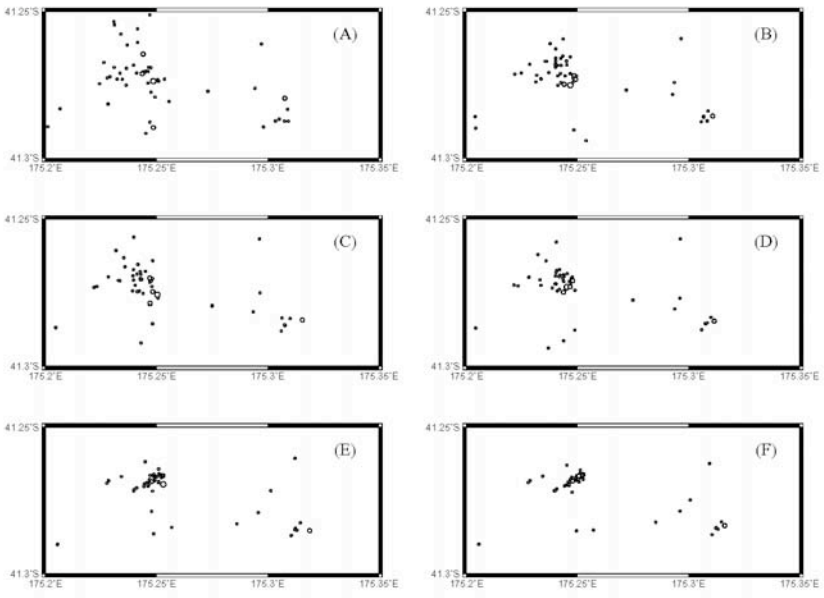


Figure 2. Locations of 53 earthquakes near lake Wairarapa, NZ. (A) Before relocation; (B) relocated with catalog differential travel times; (C) relocated with CC differential travel times chosen with the threshold criterion; (D) relocated with CC differential travel times verified with the bispectrum method; (E) relocated with both catalog and threshold-chosen CC differential travel times; (F) relocated with both catalog and bispectrum-verified CC differential travel times.

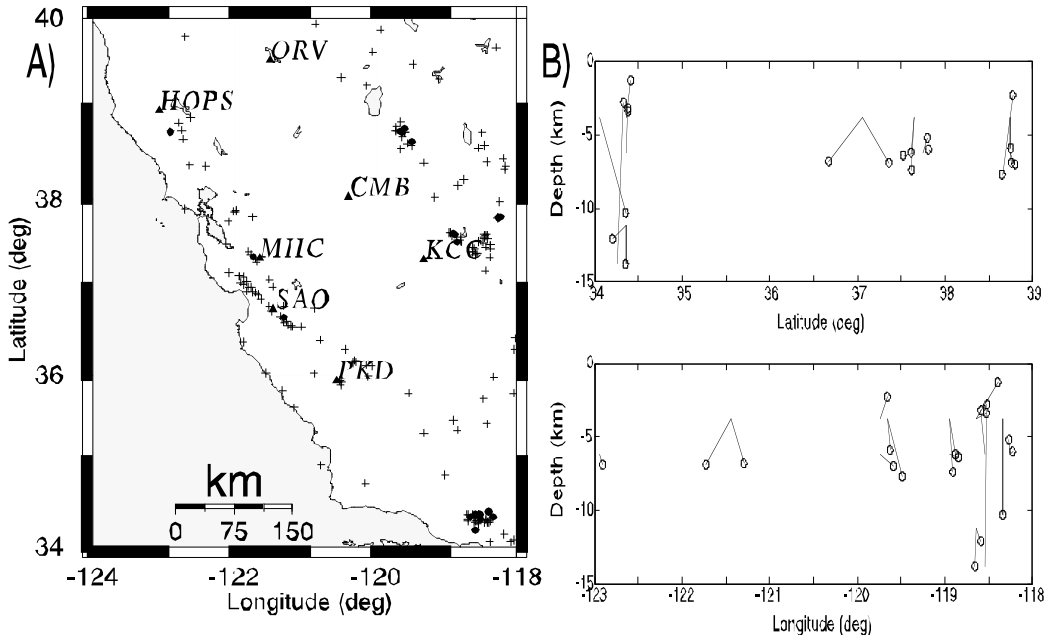


Figure 3. A) Map of study region showing the 7 master stations used in the step 1 procedure, 161 reference events, and 19 test events. Stations are indicated by triangles and labeled by their BK network station abbreviation. Test and reference events are indicated by '*' and '+' symbols respectively. Usage of hypoDD to construct GT for test events and in the step 2 relocation includes catalog data from 18 Berkeley network stations in addition to the 7 master stations for a total station range of .35.9° to 41.9° latitude and –119.3° to –124.07° longitude. B) Step 1 derived mislocation of hypocenter indicated by lines connecting the step 1 location with the hypoDD based GT location ('o' symbol). Events positioned outside master station coverage (near 34° latitude) have larger mislocation errors relative to GT than test events within the circumference of master station coverage.

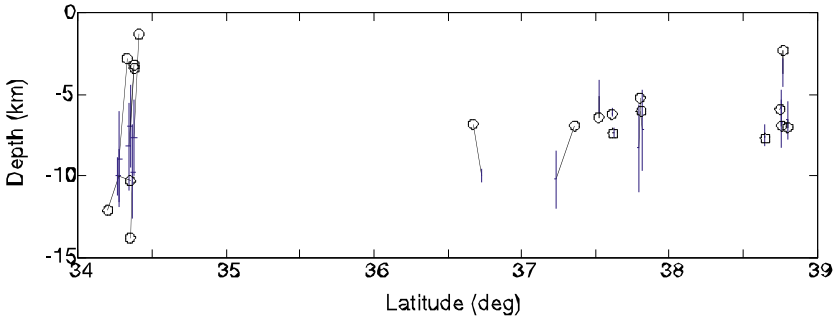


Figure 4. Stability test showing poorer depth constraint for events outside the set of master stations. The mislocation is indicated by solid line connecting the mean step 2 location with the hypoDD GT location ('o' symbol). The vertical and horizontal lines at the mean step 2 location indicate standard deviations of the step 2 estimates of depth and latitude.

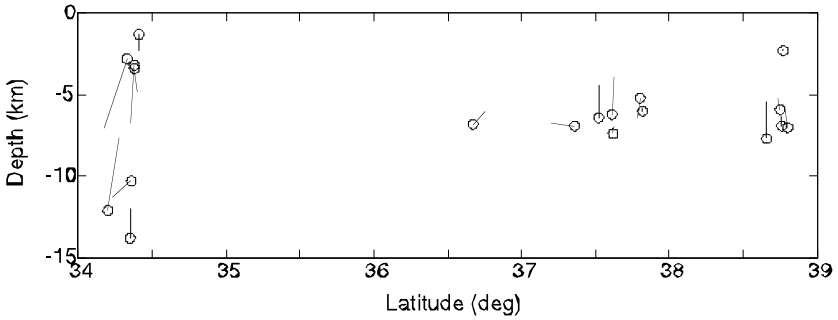


Figure 5. Step 2 mislocation of hypocenters indicated by lines connecting the step 2 location with the hypoDD based GT location ('o' symbol).

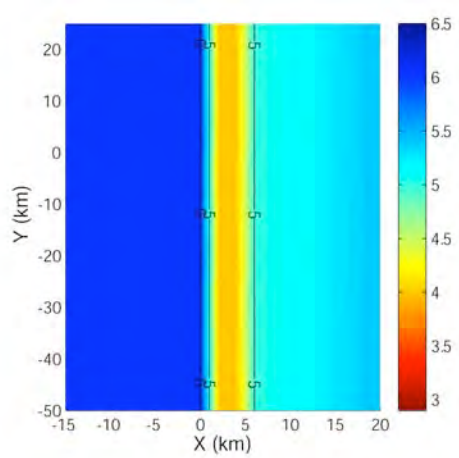


Figure 6. A horizontal slice through the true synthetic velocity model. The true velocity model in 3D is similar to a "vertical sandwich," with velocity constant with depth.

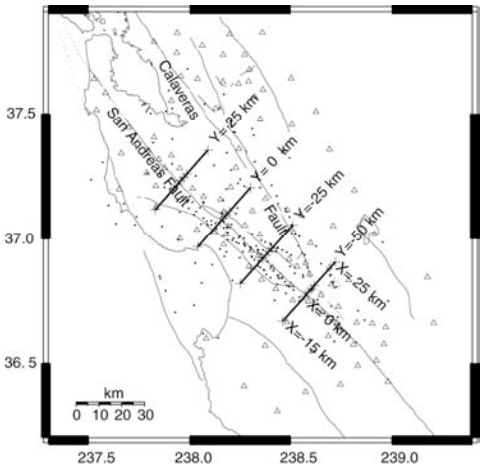


Figure 7. Event locations (filled circles) and stations (triangles) used for the synthetic data set. The inversion grid used in the standard and DD tomography solutions is shown as crosses. The inversion grid points are at X=-35, -15, 0, 2, 4, 6, 20, 35 km, at Y=-60, -40 –20, 0, 20, 40 km, and at Z=0, 3, 7, 11, 16 km.

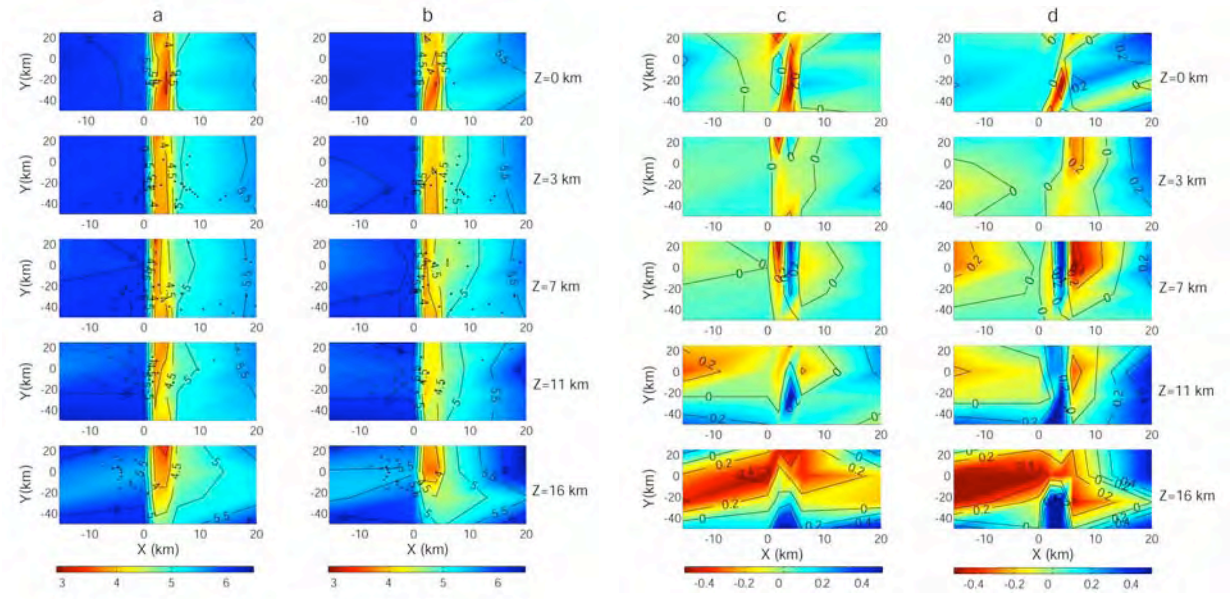


Figure 8. Horizontal slices through the velocity models from (a) standard tomography and (b) DD tomography, and the difference between (c) the DD tomography solution and the true model and (d) the standard tomography solution and the true model. Black dots indicate the earthquake hypocenters within half the grid-size of the slice.

Table 1. The absolute differences between the true locations and those from the DD location method based on 1D velocity model, standard tomography, and DD tomography.

	Median value (km)			Standard deviation (km)		
	Latitude	Longitude	Depth	Latitude	Longitude	Depth
DD location (1D)	1.131	1.235	1.123	0.976	0.941	1.658
Standard tomography	0.320	0.295	0.460	0.399	0.342	0.575
DD tomography	0.238	0.218	0.329	0.288	0.314	0.427

AUTOMATIC SECONDARY SEISMIC PHASE PICKING USING WAVELET TRANSFORMS

Ileana Madalina Tibuleac,[1] Eugene T. Herrin,[2] James M. Britton,[1] Robert Shumway,[3] and Anca C. Rosca[1]

Weston Geophysical Corporation;[1] Southern Methodist University;[2] University of California, Davis[3]

Sponsored by Defense Threat Reduction Agency

Contract No. DTRA01-02-P-0130

ABSTRACT

The primary objective of this study was to develop a new and innovative wavelet technique for accurate, reliable and semi-automatic arrival time determination, specifically for secondary phases in complex regional seismograms. For regional nuclear test monitoring applications, determining accurate locations for small-to-intermediate events ($2.5 < m_b < 4.0$) using sparse stations or arrays is an important and difficult problem. Since relatively few *P*-wave observations will be available for hypocenter location, secondary seismic phases, such as *Lg* and *Pg*, must be considered to improve location accuracy to the level required for nuclear test monitoring. For these events, single array or single station locations may be used to determine an epicenter for an event, based on estimates of back azimuth and epicentral distance. Because *Lg* propagates at a consistent group velocity of approximately 3.5±0.2 km/s, the distance estimates using the travel time difference between this arrival and primary phases (e.g., *Pn*, *Pg*) are often quite reliable. However, *Lg* is a very complicated phase and identifying its onset time on seismograms remains one of the most difficult problems encountered in regional seismology. We have tested an improved version of the *Lg* wavelet picker, WAVELET1.0, based on a method developed by Tibuleac and Herrin (1999, 2001), and compared it with two other phase picking algorithms: CUMSQ and AR. CUMSQ is a method based on the cumulative sum of squares of a statistic whose minimum indicates the detection (Inclan and Tiao, 1994; Der and Shumway, 1999). AR is an autoregressive algorithm that picks arrivals at the location of the minimum of a function called the Akaike Information Criterion (AIC) and was developed by Taylor *et al*. (1992). We tested the three methods on *Lg* and *Pg* (as secondary arrivals), from a data set of 97 shallow ($m_b < 4.0$) well-located mine explosions and collocated aftershocks recorded at the TXAR (Lajitas, Texas), NVAR (Mina, Nevada) and PDAR (Pinedale, Wyoming) seismic arrays. Based on a rigorous statistical evaluation, WAVELET1.0 estimates were more consistent for seven out of eight clusters located 300 to 700 km from three seismic arrays, and produced the lowest location sample standard deviations, in the 4.1 to 5.8 km range, while the other two methods had sample standard deviations well above 5.8 km. The 95% confidence intervals for location standard deviations were estimated as follows: standard deviation between 4.1 and 5.8 km for WAVELET1.0 picks, between 6.9 and 9.5 km for the analyst picks and between 5.8 and 8.0 km for CUMSQ picks. Our results show that WAVELET1.0 offers an improvement in semi-automatic secondary phase picking over the CUMSQ and AR algorithms and has the potential to be developed into a powerful and robust automatic tool for routine operations.

OBJECTIVES

The primary objective of this research was to develop a new and innovative semi-automatic wavelet technique (WAVELET1.0) for accurate and reliable arrival time determination, specifically for secondary phases in complex regional seismograms.

To accomplish this objective we have:

1) Improved the performance of an existing *Lg* wavelet picking technique by Tibuleac and Herrin (1999). Improvements to the method include: a more flexible use of the algorithm's parameters based on the frequency content of the waveforms, an empirically variable threshold, and implementation of an algorithm to separate emergent from impulsive arrivals.

2) Compared WAVELET1.0 to results from two other phase picking methods based on Fourier transforms: CUMSQ (Inclan and Tiao, 1994; Der and Shumway, 1999) and AR (Takanami, 1991; Taylor *et al*., 1992), to determine individual performance metrics. Each method was also compared to analyst picks to determine if any of the three methods offered more consistent picks than a trained analyst.

3) Developed a rigorous statistical framework to objectively evaluate the comparison. The phase picks from each method were used to estimate event locations and the 95% confidence intervals for the sample standard deviations of the location errors.

RESEARCH ACCOMPLISHED

Introduction

Different types of seismic phase pickers, in time or frequency domain, were previously developed (for a review, see Tibuleac and Herrin, 1999). However, most of these techniques were developed to pick first arrivals, and none has been demonstrated to be an optimal method for picking secondary phases. These methods pick phases based on changes in either amplitude or frequency of the signal. Most of the picking methods work well on first arriving impulsive *P* phases, but have difficulty picking later arrivals on regional seismograms. Also, all methods use windowing, and the length of the windows affects the precision of the picks.

Wavelet transforms are alternatives, rather than replacements for Fourier transforms. Their basis functions are short wavelets instead of cosine waves. As with any filtering technique, they have advantages and disadvantages. The advantage we exploit is that wavelet transforms are more local than Fourier transforms. When we deal with transient, *non-stationary* phases such as *Lg*, and we require computation speed, the wavelet transform represents the signal with a small number of rapidly computable base functions, localized in time and therefore better at extracting sharp features of the signal. To design and describe wavelets, we still use Fourier techniques. However, instead of transforming a pure "time description" into a pure "frequency description", the new methods find a good compromise: a time-frequency description that avoids the "blocking effect" at the edge of the time segments that is the nemesis of the Short Time Fourier Transform (Strang and Nguyen, 1996). In this study we use a class of wavelets that are orthogonal and are implemented using short digital filters (Daubechies, 1992).

Wavelet transform methods were used for *P* and *S* phase identification in three component seismograms by Anant and Dowla (1997), for detection and classification of seismic events (Gendron *et al*., 2000), for automatic *P* wave detection (Zhang *et al*., 2002) and for identification of secondary phases in seismograms (Yomogida, 1994). However, these studies did not address in detail the problem of picking complicated *Lg* arrivals.

The *Lg* phase is typically of lower frequency than the first arrivals, and the surrounding coda and noise, and represents a change in process on the seismogram, meaning a change in both frequency and amplitude. The wavelet transform (see Tibuleac and Herrin, 1999, 2001) is the most effective technique for identifying *Lg* because it can detect changes in both time and scale (inverse frequency). In contrast, Fourier transforms can only globally detect changes in frequency.

These properties led to the development of a phase picker (Tibuleac and Herrin, 1999, 2001) based on the ability of the wavelet transform to represent the signal in time-scale space and using data from one vertical component of a regional seismic array. For waveform examples, the reader is referred to the 1999 study by Tibuleac and Herrin. The study also shows that the coefficients at scale 16 of a continuous *db2* (Daubechies order 2) wavelet decomposition (corresponding to a range of frequencies of 0.9 to 2.1 Hz) were empirically chosen as best to be analyzed for all events. The reason was that this frequency band (centered on 1.5 Hz) is a band with significant energy in the *Lg* Fourier spectrum (Campillo *et. al*; 1985, Nuttli, 1986; Herrmann *et al*., 1997). In their 1999 and 2001 studies, Tibuleac and Herrin picked *Lg* arrival times by this semi-automatic method with a standard deviation of less than 1.5 seconds (less than 10 km location error) for explosions and earthquakes with high quality local to regional locations and for data recorded at three seismic arrays: TXAR (Lajitas, Texas), PDAR (Pinedale, Wyoming) and NVAR (Mina, Nevada).

We have developed an improved semi-automatic wavelet picking technique (which we have designated WAVELET1.0) based on the initial work of Tibuleac and Herrin (1999, 2001). The novelty of this technique is that it provides consistent arrival time picks of *Lg* phases previously identified and approximately picked by an analyst or by an automatic algorithm. Errors in *Lg* arrival time, when picked by an analyst, can be up to ten seconds. Our method ensures consistency of the measurements and we correct for the bias in each region.

We demonstrate in this study that the semi-automatic WAVELET1.0 outperforms the CUMSQ and AR methods as well as the analyst. It is important to note that we measured performance based on algorithm's capability to consistently pick the same phase feature for each event. We applied the three phase picking techniques on local to near-regional (100 to 700 km) array data for well-located, small (m_b<4.0) event clusters to compare algorithm performances.

Improved Wavelet Technique: WAVELET1.0

Pre-filtering. We have allowed more flexible use of the picking parameters in this study than in the initial version of the wavelet picker. Specific parameters such as the search window length, the Continuous Wavelet Transform (CWT) scale and the Discrete Wavelet Transform (DWT) *Haar approximation* were chosen by the analyst as a function of the particular characteristics of the waveforms. In the case of high signal-to-noise ratio (*snr)* events, the analyst chose whether to pre-filter the data.

Normalization. In WAVELET1.0, the time series in the search window is normalized to the maximum value of the *Lg* amplitude in the window to avoid considering possible localized and very large amplitudes later in the *Lg* signal. In the initial version, the waveforms were normalized to the maximum value in the window and the following five seconds of the signal.

Threshold. In the new version of the algorithm, WAVELET1.0, an empirical variable threshold was calculated after wavelet filtering for all *Lg* picks:

$$th = 10^{-0.02*snr-0.25} - 0.05$$

where *snr* (*dB*) is the ratio between the maximum value of the squared signal in a seven second window starting at the approximate pick and twice the sample standard deviation of the squared noise in a seven second window before the signal (Der and Shumway, 1999). This *snr* formula was chosen to compensate for short duration, very large amplitude pulses in the *Lg* signal. These large amplitudes were affecting the time picks for a waveform weighted to the maximum value of the signal in the search window. A second method used to eliminate these large amplitudes, before the threshold calculation, was to discard any amplitude maximum value larger than 3.5 times the standard deviation of the signal in the search window, and replace it with the second largest value.

We have observed that, by using squared waveforms after pre-filtering, WAVELET1.0 improves the *snr* more than the other techniques. In their study, Tibuleac and Herrin (1999) also showed that, in the same frequency range, the amplitude difference between the *Lg* signal and the coda before *Lg* is much less after Fourier pre-filtering than after wavelet pre-filtering.

Phase Picking. Finally, we have implemented an algorithm that separates and corrects for emergent arrivals. An arrival is considered impulsive when it exceeds the threshold plus 0.3 units within one second from the detection.

When the arrival is emergent, the algorithm picks the arrival time at the intersection of the threshold level with the line that fits the time series (L2 fit) in a four second window centered on the time pick. This procedure is a first step in improving the phase picks for emergent arrivals, before a completely automatic algorithm can be developed.

Phase Picker Comparison

Dataset. A dataset of 97 events was assembled for this study: two sequences of collocated aftershocks and five clusters of well-located mining explosions. We used data between 1995 and 2000 from elements of the TXAR (TX09), PDAR (PD03) and NVAR (NV08) seismic arrays in a distance range of 100 to 700 km to make the comparison between the different pickers. Events from this database (Table 1) have been described in detail in two previous studies by Tibuleac and Herrin (1999, 2001).

Table 1. The seismic event database used to compare different pickers

LOCATION	LATITUDE (DEGREES)	LONGITUDE (DEGREES)
Alpine, Texas (ALPINE)	30.3	-103.3
Minas des Hercules (Mexico) (HERCULES)	28.1	-103.8
MICARE Coal Mines (Mexico) (MICARE)	28.3	-100.5
Tyrone, New Mexico (TYRONE)	32.7	-108.4
Morenci, Arizona (MORENCI)	33.1	-109.4
Black Thunder, Wyoming (BTH)	43.7	-105.3
Scotty's Junction, Nevada (SCOTTY)	37.4	-117.0

The CUMSQ and AR Algorithms. To our knowledge, no generally accepted method for automatic phase picking has been developed. Therefore, we chose two methods to compare with WAVELET1.0 that were originally developed for first arrivals, and adapted them for secondary phase picking. Both methods were proven to be better than STA/LTA type pickers.

The first, developed by Der and Shumway (1999), from an initial version by Inclan and Tiao (1994), was based on the cumulative sum of squares (CUMSQ). The algorithm picks *Pn* onset time at regional distances by estimating the minimum of the cumulative sum of the squares of a test statistic (the absolute value of the trace amplitude). We chose from two versions of the algorithm developed by Der and Shumway (1999): CUMSQ and CUMSUM. CUMSQ is based on the accumulation of squares of amplitudes and a statistic whose minimum indicates the detection. CUMSUM is based on simulated annealing (randomized search) and the accumulation of amplitude absolute values. A Wiener pre-filter of order 15 was chosen over several other pre-filtering methods, e.g., a zero phase Butterworth 4 pole filter with a frequency range of 0.6 – 4.5 Hz, a S/N^2 filter (ratio of the spectral amplitude of the signal S divided by the power spectrum of the noise *N*) and a $(S+N)/N^2$ filter. The CUMSQ method with a Wiener pre-filter proved to be the most stable, had the lowest distance standard deviations and was therefore adapted to be used in this study for secondary arrival time detection. However, a shortcoming of this algorithm was that it picked emergent arrivals too late for low *snr* events.

A second comparison was made with an autoregressive method (AR). This method uses a stable and fast technique initially developed by Takanami (1991). Taylor *et al*. (1992) extended the modeling procedure to develop a signal detection algorithm (AR) that can analyze continuous single-component data. The AR algorithm is based on developing a model of the background noise for a segment of data (typically 8 seconds). This noise model is used to predict the next short segment of data (typically 2 seconds). The detection occurs when the predicted and observed time series are different. The AR algorithm picks arrivals at the location of the minimum of a function called the Akaike Information Criterion (AIC). This function weighs the prediction error in each window (noise versus signal) by the length of the window, and its minimum (the onset time of the signal) defines the time where the data segment is best fit by the two different models. We applied a Wiener filter and different order zero phase Butterworth filters as pre-filters for the AR method. Based on these results, we chose a 4 pole zero phase Butterworth filter with a frequency range of 0.6 – 4.5 Hz as the optimal filter. An optimal search window of 14 seconds, centered on the approximate pick, was applied for both the AR and the CUMSQ algorithms. A drawback of the AR algorithm (for smaller signals) is that in the absence of white noise the autoregressive process cannot reliably predict the data.

Analyst *Lg* picks were performed after comparison of raw and filtered data. We consider these picks to be equivalent to those of an experienced analyst since all phases were identified using their horizontal phase velocity and back azimuth, estimated with array processing methods.

WAVELET1.0 parameters

The WAVELET1.0 algorithm requires several input parameters that at this time are analyst options. The WAVELET1.0 parameters are: 10 or 12 second search window; the use of raw or filtered waveforms; the wavelet family; the CWT decomposition scale and the DWT decomposition *approximation* (depending on the frequency content of the signal). We have observed relatively small sensitivity (2 – 4 km variation) of sample standard deviation to the length of the search window and to the *Haar* DWT *approximation* level for most of the clusters. It also appears that WAVELET1.0 results are not significantly affected by the signal–to–noise ratio due in part to the proper choice of the threshold.

Results

Comparing the arrival time picks. We have observed that choosing the correct type of pre-filtering method, which is not especially important when picking first arrivals (Der and Shumway, 1999), is essential when picking secondary arrivals.

We have used the pre-filtering method for which we had the lowest distance standard deviations for each algorithm. In order to give each algorithm the best chance of succeeding, we used the same carefully chosen analyst picks as the initial approximate picks for each algorithm. In operational practice, the *Lg* phase would be identified by an existing detection algorithm such as SLA/LTA (see as an example the PIDC *Lg* automatic detection algorithms in 'IDC Processing of Seismic, Hydroacoustic and Infrasonic Data' at www.cmr.org). Automatic secondary phase identification is a complicated problem, already the subject of extensive research (Harris *et al*., 2001, Bai and Kennett, 2000) and was not addressed in this study. Our efforts were directed towards developing an automatic, consistent and reliable secondary phase picking method.

Table 2 shows that WAVELET1.0 has the lowest estimated location sample standard deviation in km in most of the clusters of the different tectonic regions we considered. The second best results are obtained using the CUMSQ algorithm. In fact, WAVELET1.0 and CUMSQ have similar results for clusters at distances less than 300 km, which is to be expected for local, larger *snr* events. However, for clusters between 300 and 700 km, the WAVELET1.0 algorithm performs best. The intrinsic WAVELET1.0 location error (see Tibuleac and Herrin, 2001) was calculated, taking into account the down-sampling when applying the *Haar* DWT decomposition. Both WAVELET1.0 and CUMSQ have lower variance than the analyst.

Given the number of failures (arrival time error more than 5 seconds) when using the AR algorithm, we considered only the CUMSQ and WAVELET1.0 methods for further analysis. It is important to mention that the AR algorithm and the analyst performed best for the high *SNR Pg* arrivals, even if they were secondary arrivals (with a small *Pn* in front of them) recorded at NVAR from Scotty's Junction. This was to be expected because the AR algorithm was developed for these types of phases.

Statistical Analyses

We define the error as the difference between the 'true' epicentral distance and the epicentral distance estimated using *P – Lg* arrival time differences and appropriate regional models. We are interested in the consistency of the picks for a certain cluster expressed by the sample standard deviation of the errors, since the location bias can be corrected by proper calibration. A plot of the location errors for the 113 samples (7 clusters) is presented in Figure 1. We designated the three methods: 1. Analyst, 2. CUMSQ, and 3. WAVELET1.0.

Note that all three methods have errors of varying degrees for some of the clusters. However, the analyst errors have the largest variance. Testing the hypothesis of equality of variances for the three methods (Table 3) leads to a strong rejection (P=.000) under the normality assumption by the Bartlett test (Snedecor and Cochran, 1989) and a weak rejection (P=.076) using Levene's test (Levene, 1960), which is more robust relative to distributional

departures from normality. This means that we can be 93% confident that the standard deviations obtained by WAVELET1.0 are lower than those obtained using CUMSQ.

After examining the results it is clear that WAVELET1.0 produces consistent distance estimates with lower variance for seven out of eight clusters studied. The method is shown to produce good results for three different arrays in three different tectonic regimes in the Western US. Both WAVELET1.0 and CUMSQ methods have low variance estimates at local distances (< 300 km) and lower variance of distance estimates than the analyst. With 95% confidence, the standard deviation of the location error for WAVELET1.0 is between 4.1 and 5.8 km, while for CUMSQ it is between 5.8 and 8.1 km. Examination of Table 3, as well as Figure 1, indicates that the WAVELET1.0 standard deviations are substantially smaller than those measured by the other two methods, with the analyst having the largest variance. These results demonstrate clearly that the semi-automatic WAVELET1.0 significantly outperforms the CUMSQ and AR as well as the analyst.

Table 2. Location standard deviation (km) obtained for each cluster, using each picking method. Bold numbers represent the lowest location sample standard deviation. Italics represent similar results of WAVELET1.0 and CUMSQ. The distance from clusters to arrays increases to the right. The numbers under the backslash (/) represent the number of arrival time errors larger than 5 seconds (picking failures).

Method	Sample Standard Deviation (km) for cluster: ALPINE	HERCULES	SCOTTY *Lg*	SCOTTY *Pg*	MICARE	BTH	TYRONE	MORENCI
ANALYST	2.5	7.3	4.6	considered true	14.7	7.4	2.2	9
CUMSQ Wiener	3.4	*5.7*	3.6	1.5	8.6	10.7	2.1	11.3
AR Butterworth	6.4 /1	5.6 /14	4.7/7	**1.2**	13/13	2.9 /1	-	-
WAVELET1.0	**2.5**	*5.8*	**2.7**	*1.6*	**6.8**	**2.5**	**1.8**	**4.9**
WAVELET 1.0 method location error (km)	0.9	0.5	0.6	0.4	0.7	0.7	1.4	0.7
Number of events	15	21	16	16	22	7	9	7
ARRAY	TXAR	TXAR	NVAR	NVAR	TXAR	PDAR	TXAR	TXAR
Epic. Dist. (km)	108	150	157	157	329	360	579	681

Table3. Estimated sample standard deviations (*S* in km) and 95% confidence intervals for each method.

Method	WAVELET1.0	CUMSQ	ANALYST
Estimated *S*	**4.9**	**6.7**	**7.9**
Confidence Interval	**(4.10, 5.79)**	**(5.80, 8.01)**	**(6.85, 9.45)**

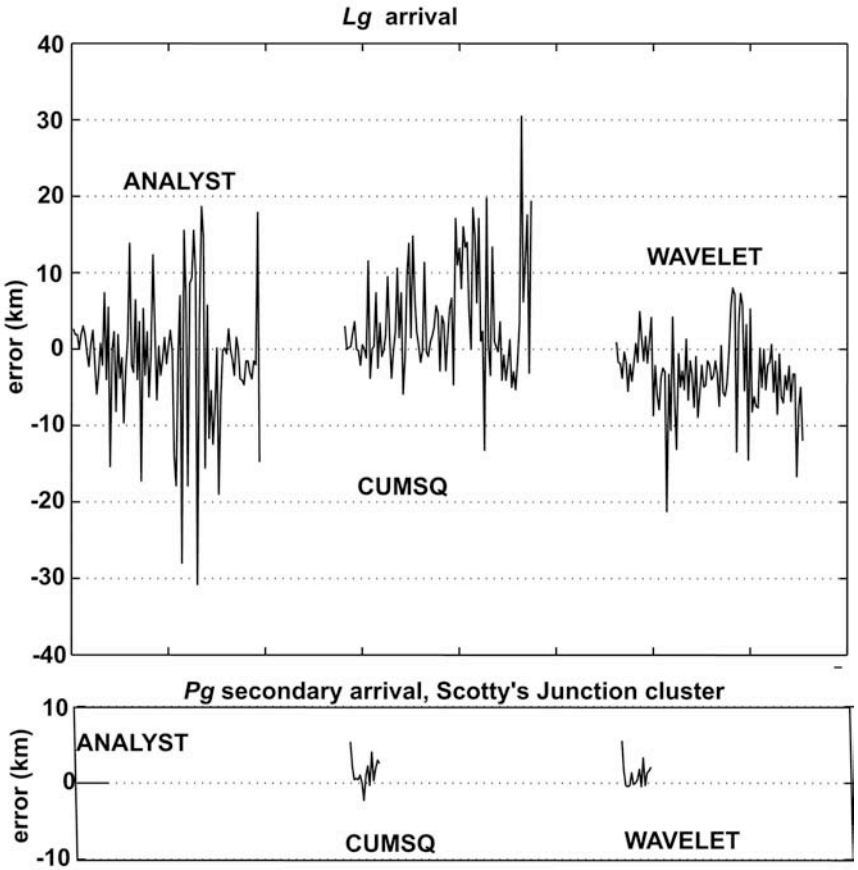


Figure 1. Errors in km from the three picking methods plotted by event number, in the same order of events for each method. Distance between clusters and arrays increase from left to right.

CONCLUSIONS AND RECOMMENDATIONS

We have improved the original wavelet picker (Tibuleac and Herrin, 1999) and developed a robust and consistent semi-automatic secondary phase picker designated WAVELET1.0. The improved version corrects for the delay of emergent arrivals. It empirically calculates a variable picking threshold based on the *snr* in the search window after wavelet pre-filtering. Although the success of this empirical threshold calculation method is encouraging, it remains to be determined by future research if the formula is transportable to different data sets or if it must be further modified. WAVELET1.0 was tested on a variety of events (earthquakes and commercial explosions) recorded at three arrays located within different tectonic regimes of the Western US. The results were compared to those obtained by applying two other techniques (CUMSQ and AR), which we modified to pick secondary arrivals for the same dataset. After considering the results, it is clear that WAVELET1.0 produces consistent distance estimates with lower variance for seven out of eight clusters of events studied. Both WAVELET1.0 and CUMSQ methods have low variance estimates at local distances (< 300 km) and lower variance of distance estimates than the analyst.

With 95 % confidence, the location standard deviation for WAVELET1.0 is between 4.1 and 5.8 km, while for CUMSQ it is between 5.8 and 8.1 km. The WAVELET1.0 distance standard deviation is smaller than the CUMSQ at a 93% confidence level. We therefore consider WAVELET1.0 to be a reliable and promising technique worth investigating in order to develop an entirely automatic phase picker.

ACKNOWLEDGEMENTS

We thank Mr. James Lewkowicz for tremendous help and support during the project. We should like to thank many people for their help and support on various aspects of this study: Jessie Bonner, Delaine Reiter, Heather Hooper and Sara Russell. We express our gratitude to Dr. Zoltan Der for help with software and for valuable scientific comments.

REFERENCES

Anant, K. S. and F. U. Dowla, (1997), Wavelet transform methods for phase identification in three-component seismograms, *Bull. Seis. Soc. Am.*, **87**, 1598-1612.

Bai, Chao-ying and B. L. N. Kennett, (2000), Automatic Phase – Detection and identification by full use of a single three component broadband seismogram, *Bull. Seis. Soc. Am*., **90**, 187-198.

Campillo, M., Plantet, J. L. and Bouchon, M., (1985), Frequency – dependent attenuation in the crust beneath Central France from *Lg* waves: Data Analysis and Numerical Modeling, *Bull. Seis. Soc. Am*., **75**, 1395-1411.

Daubechies, I, (1992), Ten lectures on wavelets, SIAM, New York, NY, 1992

Der, Z. A, and R. H. Shumway, (1999), Phase onset time estimation at regional distances using the CUMSUM algorithm, *Phys. Earth Planet. Int*., **113**, 227 –246.

Der, Z. and R. H. Shumway, (2000), Automatic interpretation of regional seismic signals using the CUMSUM-SA algorithms, *Proceedings* of the 21st Annual Seismic Research Symposium on Monitoring a Comprehensive Nuclear Test Ban Treaty, 21-24 September 1999, Las Vegas, Nevada, 393 – 403.

Gendron, P., J. Ebel and D. Manolachis, (2000), Rapid Joint Detection and Classification with Wavelet Bases via Bayes Theorem, *Bull. Seis. Soc. Am*, **90,** 764-774.

Harris, D. B, Walter, W. R., Rodgers, A. J., Sicherman, A., Myers, S. and C. Shultz, (2001), LLNL detection program: Broad area characterization of phase detectability and empirical detectors for specific sources, *Proceedings of the 23'rd Annual Seismic Research Symposium on Monitoring a Comprehensive Nuclear Test Ban Treaty*, Oct. 2-5 Jackson Hole, Wyoming,

Herrmann, R. B., Mokhtar, T. A., Raoof, M. and Ammon, C., (1997), Wave Propagation – 16 Hz to 60 sec, *Proceedings* of the 19'th Annual Seismic Research Symposium on Monitoring a Comprehensive Nuclear Test Ban Treaty, 23-25 September, 1997, 495-503.

Inclan, C. and G. C. Tiao, (1994), Use of cumulative sums of squares for retrospective detection in the changes in variance, *J. Amer. Statist. Assoc*., **89**, 913-923.

Levene, H. (1960), In Contributions to Probability and Statistics: Essays in Honor of Harold Hotelling, I. Olkin *et al.* eds., Stanford University Press, pp. 278-292.

Nuttli, O. W., (1986), Yield Estimates of Nevada Test Site explosions obtained from seismic *Lg* waves, *J. Geophys. Res*., **91**, 2137-2151.

Snedecor, G. W. and W. G. Cochran, (1989), *Statistical Methods*, Eighth Edition, Iowa State University Press, Ames, Iowa.

Strang, G. and T. Nquyen, (1996), Wavelets and Filter Banks, Wellesley-Cambridge Press, 81-82.

Takanami, T., (1991), A study of detection and extraction methods for microearthquake waves by autoregressive models, *J. Fac. Sci*., Hokkaido U., Ser. VII, 9, 67-196.

Taylor, D. W., Ghalib, H. A. and R. H. Kimmel, (1992), Autoregressive analysis for seismic signal detection and onset time estimation, ENSCO report, DCS-92-90.

Tibuleac, I. M. and E.T. Herrin, (1999), An automatic method for determination of *Lg* arrival times using wavelet methods, *Seism. Res. Lett*, **70**, 577–595.

Tibuleac, I. M. and E.T. Herrin, (2001), Location capability at NVAR (Mina, Nevada) seismic array for events on the Nevada Test Site, *Seism. Res. Lett.*, **72**, 97-107.

Zhang, H., C. Thurber and C. Rowe, (2002)Automatic P-wave Arrival Detection and Picking with Multiscale Wavelet Analysis for Single Component Recordings, , submitted to *Bull. Seis. Soc. Am.*

Yomogida, K, (1994), Detection of anomalous seismic phases by the wavelet transform, *Geophys. J. Int*, **116**, 119-130.

Seismic Identification and Source Characterization

PLANNING SOURCE PHENOMENOLOGY EXPERIMENTS IN ARIZONA

Jessie L. Bonner,[1] Brian W. Stump,[2] William R. Walter,[3] David C. Pearson,[4] Christopher T. Hayward,[2]
Aaron A. Velasco,[5] Diane F. Baker,[4] C.L. Edwards,[4] James F. Lewkowicz,[1] Steve Harder,[5]
Sara A. Russell,[1] Mark Leidig[1], and Stephen C. Myers[3]

Weston Geophysical Corporation;[1] Southern Methodist University;[2] Lawrence Livermore National Laboratory;[3]
Los Alamos National Laboratory;[4] and the University of Texas at El Paso[5]

Sponsored by National Nuclear Security Administration
Office of Nonproliferation Research and Engineering
Office of Defense Nuclear Nonproliferation

Contract No. DE-FC03-02SF22638/A000;[1,2,5] and W-7405-ENG-48;[3] W-7405-ENG-36[4]

ABSTRACT

Our consortium continues to plan a series of source phenomenology experiments at coal and copper mines in Arizona. The purposes of the experiments are to examine the source of single- and delay-fired explosion generated shear waves, to quantify the energy partitioning in regional seismic phases from different types of explosions, and to quantify the differences between contained single-fired chemical (a surrogate for nuclear tests) and delay-fired mining explosions in mines located in different lithologic and tectonic regimes.

During the first year of this project, we have planned the explosions to be conducted at each mine. Scaling relationships for single-fired explosions will be examined by detonating single-fired shots of 3.5- and 7-tons in confined and unconfined (i.e. blasting near a free face in the mine) settings. We will also examine the effects of scaled depth of burial by detonating confined 7-ton shots at depths of 20 and 40 meters. Additional tests, such as a 14-ton shot detonated during a delay-fired production shot, are also planned. In addition to shot planning, we have collected databases of near-source and regional waveforms for routine blasts at both mines. These data have been supplemented with shot records from the mine engineers and scaling relationships have been studied. Finally, we have designed the near-source, local, and regional station deployment configuration. The explosions will be recorded by near-source velocity of detonation recorders, videographic equipment, and an array of accelerometers optimally positioned for moment tensor inversion. At local and regional distances, the experiments will be recorded by a linear profile of 25 broadband seismic stations. The experiments are planned for August and September, 2003.

OBJECTIVES

Weston Geophysical, Southern Methodist University, Lawrence Livermore National Laboratory, Los Alamos National Laboratory, and the University of Texas at El Paso have formed a consortium to quantify the differences between contained single-fired chemical (a surrogate for nuclear tests) and delay-fired mining explosions in mines located in different lithologic and tectonic regimes. We have built upon ongoing cooperation with the US Mining Industry (Heuze *et al*., 1999) and previous studies (Bonner *et al*., 2003; Stump *et al.*, 2002) that have collected data from routine delay-fired explosions from mines across the US. In order to span the range of production mining techniques and *in situ* materials while maintaining a consistent set of regional stations, we have designed a series of single-fired explosions in the northeastern Arizona coal-mining district (cast blasting, parting, and coal shots) and in the southeastern Arizona copper mining district (hard rock fragmentation). The objectives of our shot designs include: 1) defining the fundamental source physics that govern energy partitioning among regional seismic phases, 2) identifying possible sources of *S*-wave generation for different types of explosions, 3) determining the effects of depth of burial, yield, and containment on the source function for contained chemical explosions, 4) performing discrimination between nuclear explosions, mining explosions, and earthquakes, 5) completing moment tensor inversions for source properties, and 6) determining whether regional signals from routine delay-fired explosions can be used to gauge anticipated signals from small nuclear explosions (Figure 1).

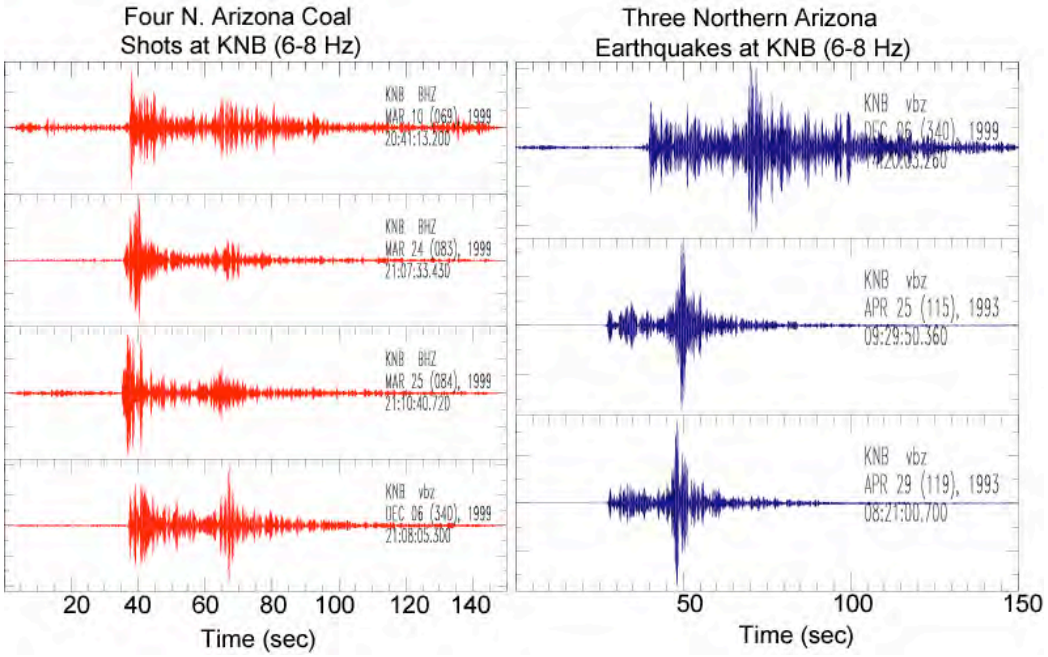


Figure 1. Examples of coal mining cast blasts and earthquakes in northern Arizona. An objective of the source phenomenology experiments is to examine mine blast and earthquake discrimination, in particular, the generation of *S*-waves from single- and delay-fired explosions.

During the initial year of this project, we have designed this series of explosions by 1) determining the characteristics of seismicity produced from routine production shots at both mines, 2) negotiating with mine engineers to design regionally recordable explosions that were within safety and production requirements at both mines, and 3) siting near-source, in-mine, and regional station arrays in order to record the data necessary to achieve the experiment objectives.

RESEARCH ACCOMPLISHED

Experiment Location

We proposed to conduct this source phenomenology experiment in Arizona (Figure 2) for multiple reasons. First,

the region. Second, by choosing copper and coal mines for the explosions, we could accomplish an objective of examining the differences in signals generated in hard and soft-rock settings, while maintaining a consistent set of regional stations. Finally, the two mines chosen also provide us with an understanding of the effects that different propagation paths may have on regional phase partitioning. At the request of the mining companies, we have withheld the mine names from this manuscript and refer to them as either Coal or Copper (as shown in Figure 2).

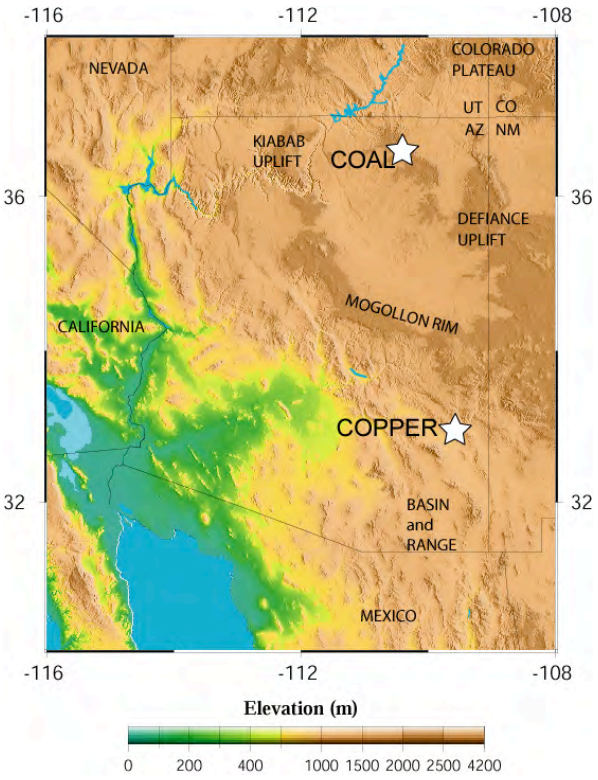


Figure 2. Topographic map of Arizona showing the locations for the proposed source phenomenology experiments. The soft rock coal mine is located in the structurally simple Colorado Plateau geophysical province, and the hard-rock copper mine is in the structurally complex southern extensions of the Basin and Range province.

Experiment Implications from Regional Seismograms of Routine Production Blasts

We have developed detailed shot databases for each mine that consist of local and regional seismic data, detailed blasting reports obtained from mine engineers, and in some cases videographic and ground-truth data. We have used the data to examine variations in routine blasting procedures and to predict the regional seismic amplitudes expected from the single-fired explosion series.

Copper. In the following paragraphs, we summarize some of the types of data and illustrate the effects of routine blasting practices on the regional seismograms from the copper mine (Figure 2). Two distinct types of delay patterns are currently used at the copper mine and are illustrated in Figure 3. Larger shots, over 250,000 lbs., utilize relatively long delay times between holes in a row (67 ms) and between rows (100 ms) resulting in long duration shots (Figure 3, left). Smaller shots utilize shorter delay times typically between 17 and 35 ms producing much shorter shot durations (Figure 3, right).

These time delays create additional complexity in the radiated seismic energy when compared to a contained, single-fired explosion. One simple way of modeling this complexity is with an impulse time series like that shown in Figure 3 (middle). At regional distances the seismic data are relatively band-limited by the earth filter, so it is important to look at the constructive and destructive interference introduced by the source delay times and total shot duration. The theoretical spectra from three explosion designs, two short delay time events (green and red) and one long delay shot (blue) are compared in the frequency domain in Figure 4.

In the 1 to 10 Hz band, typical of the regional data, the short delay time shots produce the largest amplitudes despite the fact that they have the smaller total charge size. This theoretical result is in strong contrast to that expected from single-fired explosions where models and data indicate consistent scaling relations between the total amount of explosives and peak amplitude of regional and teleseismic waves. Seismic instruments were deployed in the mine and at regional distances to document these blast-timing effects; these are discussed in the next two sections. These same instruments will be utilized in our source phenomenology experiments.

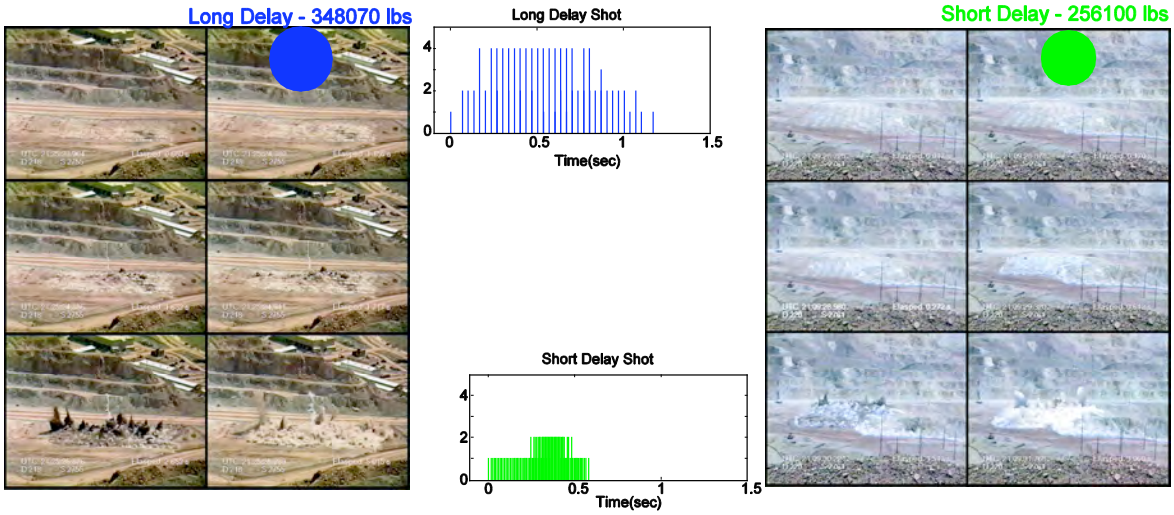


Figure 3. Two types of blasting are used in the mine. The first (top) are blasts with total explosive weights of over 250,000 lbs. and long time-delays between shots (67- 100 ms). The smaller shots (bottom) are detonated over a shorter total time interval with shorter delays (17-35 ms).

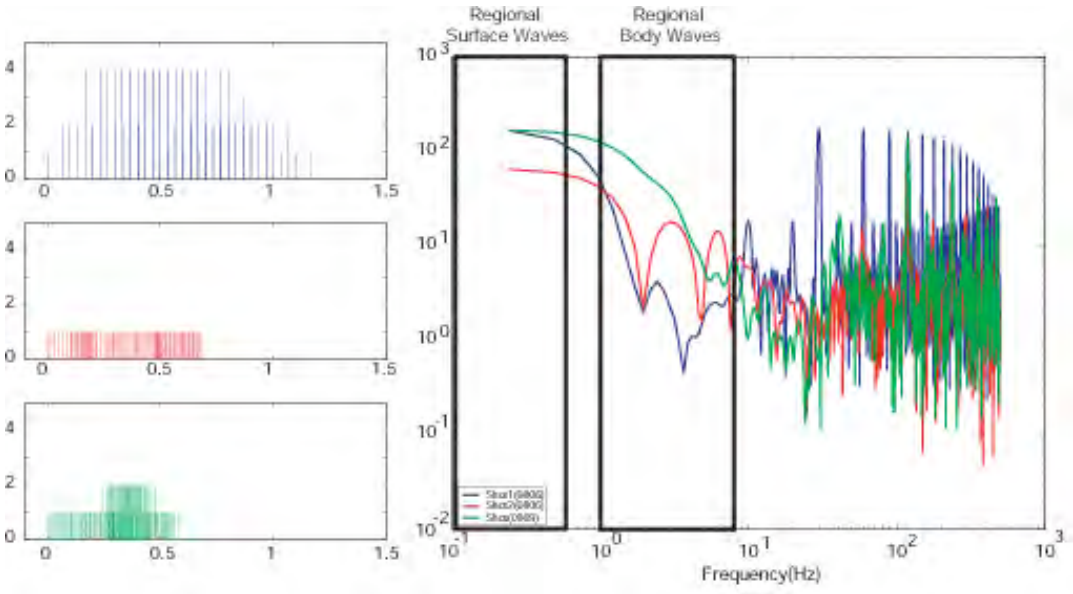


Figure 4. Comparison of predicted spectral levels from the impulse time series for a long-delay shot (blue) and two short delay shots (red and green). The long delay times result in substantial decrease in peak amplitudes in the 1-10 Hz band relative to the short delay shots.

Regional seismic stations high signal-to-noise ratio signals from typical mining explosions at this copper mine. For example, during July and August of 2001, nearly 1/3 of all events in the USGS Mining Database came from this mine. It is interesting to examine the events that appear in the USGS mining seismicity database. The vast majority

mine. It is interesting to examine the events that appear in the USGS mining seismicity database. The vast majority of events in this database are generated by short-delay shots, which close-in data suggests will produce the largest amplitudes at regional distances. This blasting practice effect is illustrated by comparing the total yield for the blast with the *P*, *Lg*, and surface wave amplitudes recorded at TUC (Figure 5). Variations in coupling and blasting delays for these explosions cause wide variations in the regional *P* and *Lg* amplitudes versus yields; however, the surface wave amplitudes generally increase with increasing yield. The blasts with the longer downhole delays (green stars), with yields of 350,000 and 500,000 lbs, have surface wave amplitudes typical of 150,000 and 100,000 lbs. short delay shots (red and yellow stars).

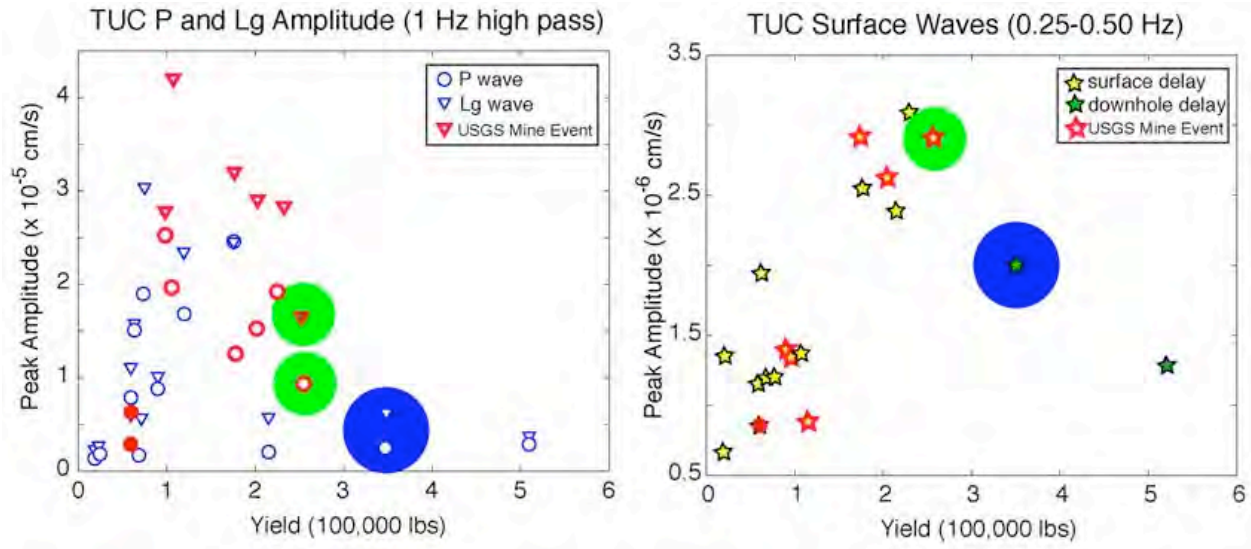


Figure 5. Comparison of observed regional *P* and *Lg* (left) and surface wave (right) amplitudes versus yield for short- and long-delayed copper mining explosions.

These in-mine and regional observations have been compiled in the shot database and have been used in the design of the source phenomenology experiments. For example, the strong effects of source timing on near-source and regional amplitudes and waveform complexity has led us to employ velocity of detonation recorders (VODRs) and electronic blasting detonation systems to better characterize the source. We also recognize that both *P* and *S* waves are observed in-mine thus helping us design our near-source seismic network. In addition, the regional data from these explosions suggest that we can reliably record the larger single-fired explosions at distances of 1000 km or less. Finally, the shot database highlights that the key to success for any study of mine blast seismicity is cooperation with the mining engineers and ground truth within the mine.

Coal. The shot database at the coal mine (Figure 2) consists of regional recordings of 22 routine blasts with blasting logs for each event. Our analysis of the data from these events has shown strong azimuthal surface wave radiation patterns from cast blasts (Bonner *et al.*, 2003) and variable relationships between yield and regional amplitudes for cast blasts and parting shots. The regional data in Figure 6 are plotted against the total yield of the explosion as well as the maximum amount of explosives that will detonate within an 8 millisecond (msec) time window. For cast blasts, which are designed to fragment and throw the overburden off coal seams, we determined power law increases in amplitude with yield (for both total and max per 8 msec), with correlation of at least 65%. However, for the parting shots, which are designed to fracture the material above coal seams, we do not observe similar scaling relationships. Further, we determined that the lowest total shot weight with measurable *P* and *Lg* amplitudes was 111,641 lbs (delay-fired) and the lowest yield per 8ms is1253 lbs. Therefore, all of the planned shots will have yields between 7,000 and 56,000 lbs of explosives.

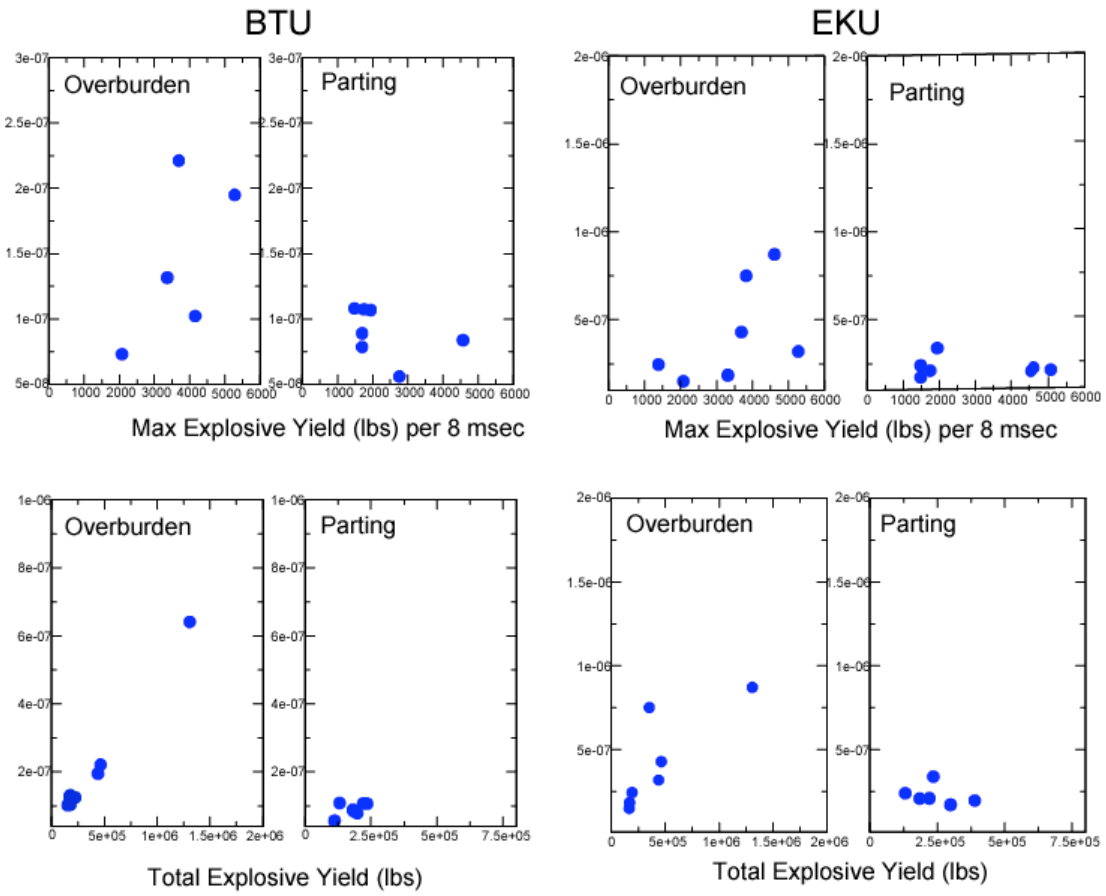


Figure 6. *P* amplitudes (BP 1 to 2 Hz) from coal cast and parting blasts measured at the regional seismic stations BTU (left) and EKU (right) as a function of maximum detonated yield per 8 msec as designed (upper) and total designed yield (lower).

Experiment Design: Explosions

We negotiated with mine engineers at the coal and copper mines to design the source phenomenology experiment explosions. Table 1 shows the planned single-fired shots that will be detonated at the mines in August and September 2003. The final explosion plan is currently being considered for compliance with the Office of Surface Mining (OSM) regulations.

Table 1. Planned Source Phenomenology Experiment Explosions

Shot Number	Tons[1]	Explanation
1	28	Shot to an open face with pre- and post-vibration monitoring
2	14	14 ton shot to start a cast blast
3	7	Single-fired at 40 meters depth
4	7	Single-fired at 20 meters depth
5	3.5	Shot to buffer
6	7	Shot to buffer
7	3.5	Shot to open face
8	7	Shot to open face

[1] Planned yield. Final yields to be determined based on in-mine vibration studies and OSM regulations.

Shots 1 and 2: Single-Fired Shots on an Open-Face of the Mine. One blast planned at the coal mine will be to detonate a single-fired shot to an open face of either 14 or 28 tons. The location of the shot will be on an active mine face. The blast cannot exceed acceptable ground vibration; thus, a pre- and post-blast survey of nearby structures in the mine will be required. The explosion yield may be reduced if damage to nearby structures is anticipated. Another blast will be a 14 or 28 ton single-fired blast during a routine cast blast to simulate the effects of sympathetic detonations on regional data, as well as to study the evasion scenario of hiding a nuclear explosion in a mine blast.

Shots 3 and 4: Depth of Burial Shots. At sites near the end of a production pit at the coal mine (Figure 7), we will detonate two single-fired shots of 7 tons (one shot at a depth of 20 meters and another at depth of 40 meters in confined rock). The location of these shots will be in a region that will not be mined in the future so that coal damage is not an issue. The planned location is within 300 to 400 yards of normal production shots at the mine. It is also at the required distance from uncontrolled structures such that pre- and post-blast surveys will not be required.

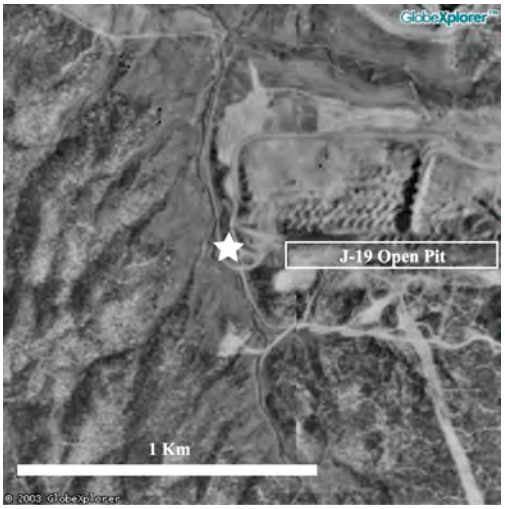


Figure 7. Proposed location of the depth of burial (DOB) shots (white star) near the J-19 pit of the coal mine.

Shots 5-8: Comparison of Confined and Unconfined Single-Fired Shots with Mine Blasts. At a location in a working pit (Figures 8 and 9), blasts of 3.5 and 7 tons will be detonated in the un-mined rock located at the base of the open pit. The blasts will be confined. Above these blasts, shots of 3.5 and 7 tons will be "shot to an open face" simulating unconfined conditions. Both shots will be located in pits where routine production shots occur thus allowing for an excellent comparison of the different types of explosions.

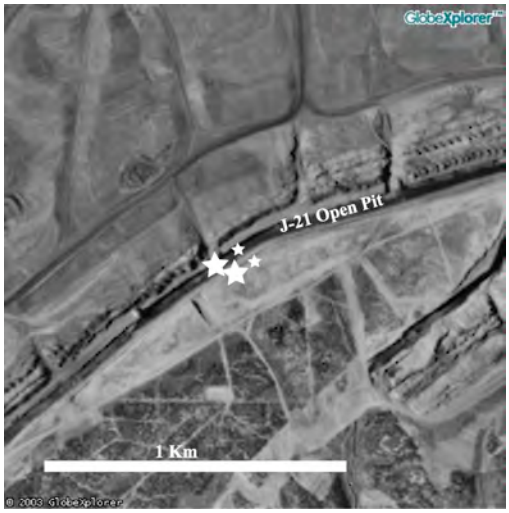


Figure 8. Proposed location of confined vs. unconfined single-fired shots in the J-21 pit of the coal mine. The blasts (stars) will be 3.5 and 7 tons single-fire shots.



Figure 9. The unconfined shots will be detonated in the light-colored rock (overburden) in the background, while the confined shots will be detonated in the rock (partings) comprising the lower level shown in this picture. The blastholes shown in this image are being shot to a buffer.

Predicting Regional Magnitudes. We used the Vergino and Mensing (1990) relationship:

$$\log_{10}(\text{Yield}) \sim 1.1\, m_b(Pn) \qquad (1)$$

to predict body wave magnitudes for the planned single-fired explosions. Our predictions are tied to the Non-Proliferation Experiment (NPE) shot (Denny *et al.*, 1997) of 1.07 kt that had an $m_b(Pn) = 4.14$. Since these relationships were developed for sources located in the Basin and Range, the predicted magnitudes (Table 2) will be most appropriate at the copper mine, located in the southern Basin and Range. Based on observations from the coal mine, we expect larger amplitudes for similar yield explosions as a result of more efficient propagation in the Colorado Plateau. The magnitudes may also vary with changes in confinement and different depths of burial.

Table 2. Predicted Magnitudes for the Source Phenomenology Experiment Explosions

Yield (tons)	$m_b(Pn)$
3.5	1.9
7	2.2
14	2.4
28	2.7

Experiment Design: Stations

There are three distinct station deployments that will be completed for the experiments: 1) in-mine arrays, 2) near-source arrays, and 3) a regional profile. First, five stations will be deployed for the experiment duration in various locations within each mine. These stations will consist of broadband sensors (STS-2 and Guralp CMG-3Ts) operated continuously at high (>100 sample/sec) sample rates. The in-mine array at the copper mine has been deployed previously. The planned in-mine array in the coal mine is also shown in Figure 10.

The second series of in-mine deployments will be a near-source array consisting of portable accelerometers within 200 meters of each shot. These sensors and systems, which will include Hi-8 videographic equipment with GPS timing, will be moved to the location of each single-fired or delay-fired explosion that we plan to instrument. Figure 11 shows the proposed configuration for the shots. The configurations were designed to achieve shot initiation data and to provide data for moment tensor inversions.

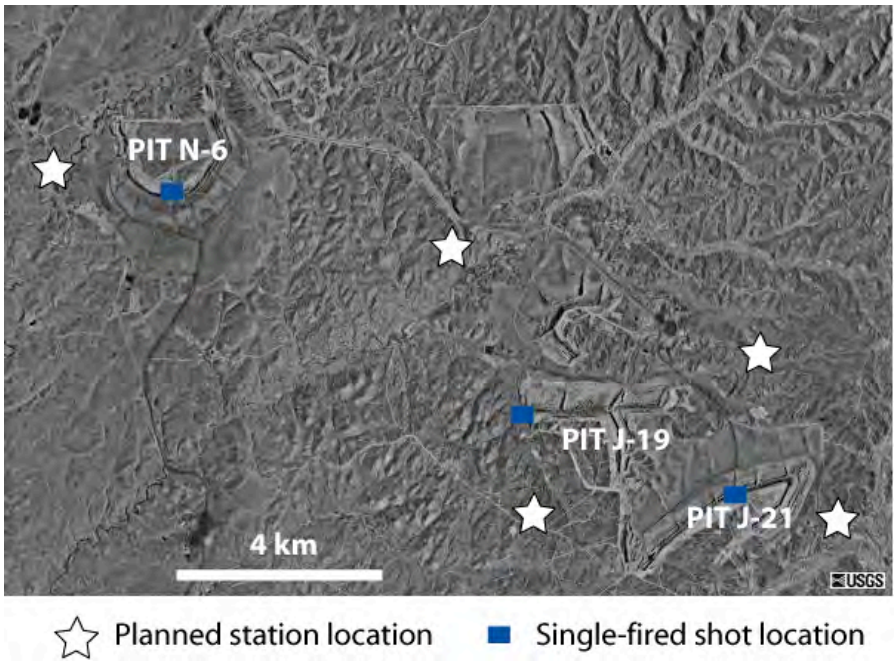


Figure 10. Planned in-mine seismic stations and experimental explosion locations at the coal mine.



Figure 11. Plan for near-source instrumentation.

The final deployment will consist of a regional profile of broadband stations (CMG-40Ts) that will be placed along a line between the coal and copper mines. The red triangles in Figure 12 are stations that will remain deployed throughout the experiments at both the coal and copper mines, while the blue triangles are sites that will only be deployed during experiments at each mine and then re-deployed.

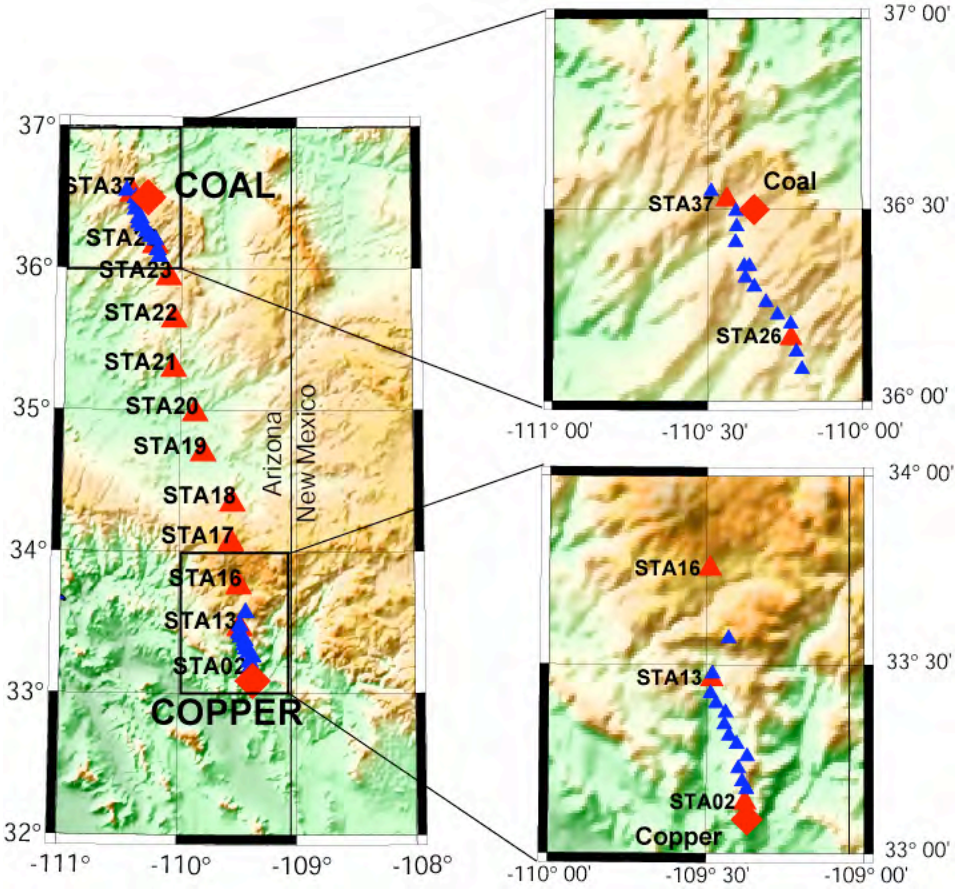


Figure 12. Stations for the regional profile between the coal and copper mines. The stations near the coal mine are located on Navajo reservation land are currently being negotiated.

CONCLUSIONS

We have designed a series of single-fired explosions at copper and coal mines in Arizona. The explosions will be conducted in August and September of 2003.

REFERENCES

Bonner, J., D. C. Pearson, and S. Blomberg, 2003, Azimuthal variation of surface wave energy from cast blasts in northern Arizona, *Bull. Seism. Soc. Am.*, 93, 724-726.

Denny, M. D., P. G. Goldstein, K. Mayeda, and W. R. Walter, 1997, Seismic results from DOE's Non-Proliferation Experiment: A comparison of chemical and nuclear explosions", In *Monitoring a Comprehensive Test Ban Treaty*, edited by E. S. Husebye and A. M. Dainty 355-364, Kluwer Academic Publishers.

Heuze, F., B. Stump, F. Chiappetta, R. Hopler, V. Hsu, B. Martin, D. Pearson, W. Walter, K. Zipf, 1999, Mine Seismicity and the Comprehensive Nuclear-Test-Ban Treaty, Report of a working group from Government, Industry, and National Laboratories, Sponsored by the U.S. Department of Energy Office of Nonproliferation and National Security, *LA-UR-99-384* and *UCRL-ID-132897*.

Stump, B.W., M.A.H. Hedlin, D.C. Pearson, and V. Hsu, 2002, Characterization of mining explosions at regional distances: implications with the international monitoring system, *Rev. Geophys*, 40RG000048.

Vergino, E.S. and R.W. Mensing, 1990, Yield estimation using regional m_b(*Pn*), Bull. Seism. Soc. Am., 80, 656-674.

ESTIMATING M_s FROM SHORT-PERIOD (< 10 SEC) RAYLEIGH WAVES

Jessie L. Bonner,[1] David G. Harkrider,[1] Mark Leidig,[1] Eugene Herrin,[2] Robert H. Shumway,[3]
Sara A. Russell,[1] Ileana Tibuleac,[1] and Delaine T. Reiter[1]

Weston Geophysical Corporation,[1] Southern Methodist University,[2] University of California, Davis[3]

Sponsored by Air Force Research Laboratory

Contract No. DTRA01-01-0080

ABSTRACT

Surface wave magnitude (M_s) estimation for small events recorded at near-regional distances will often require a magnitude scale designed for Rayleigh waves with periods less than 10 seconds. During the past year, we have examined the performance of applying two previously published M_s scales on 7-second Rayleigh waves recorded at regional distances. First, we modified the Marshall and Basham (1972) M_s scale, originally defined for periods greater than 10 seconds, which was developed to estimate surface wave magnitudes for short-period Rayleigh waves from earthquakes and explosions on or near the Nevada Test Site (NTS). We refer to this modification as M_s [M+B;7], and we have used short-period, high-quality dispersion curves to determine empirical path corrections for the 7-second Rayleigh waves at the stations MNV, LAC, ELK, and KNB. We have also examined the performance of the Rezapour and Pearce (1998) formula, developed using theoretical distance corrections and surface wave observations with periods greater than 10 seconds, for 7-second Rayleigh waves, M_s [R+P;7], recorded from the same dataset. The results demonstrate that both formulas can be used to estimate M_s for nuclear explosions and earthquakes over a wider magnitude distribution than is possible using conventional techniques developed for 20 second Rayleigh waves. These M_s(7) values scale consistently with other M_s studies at regional and teleseismic distances with the variance described by a constant offset; however, the offset for the M_s [M+B;7] estimates is over one magnitude unit closer to the teleseismic values than the M_s [R+P;7] values. Using our technique, it is possible to employ a near-regional single-station or sparse network to estimate surface wave magnitudes, thus allowing quantification of the size of both small earthquakes and explosions. Finally, we used a jackknife technique to determine the false alarm rates for the M_s [M+B;7]-m_b discriminant for this region, and found that the probability of misclassifying an earthquake as an explosion is 10% while the probability of classifying an explosion as an earthquake was determined to be 1.2%. The misclassification probabilities are slightly higher for the M_s [R+P;7] estimates.

We recently initiated a study aimed at examining the transportability of short-period M_s to the Lop Nor test site. We developed averaged dispersion curves from large (m_b>5.5) nuclear tests at Lop Nor to generate path corrections for the stations AAK, BRVK, KUR, MAK, and TLY. We then estimated short-period M_s for nuclear explosions and earthquakes at Lop Nor and determined that transportability of the M_s[M+B;7] -m_b discriminant is more complicated due to deeper earthquakes at Lop Nor than at NTS. However, by using the period of maximum amplitude, instead of restricting ourselves to 7-seconds, and by calibrating path corrections to periods less than 10 seconds, we were able to improve the separation between the earthquake and explosion populations at Lop Nor using non-conventional estimates.

OBJECTIVE

One of the most robust methods for discriminating between explosions and earthquakes is the relative difference between the body wave (m_b) and surface wave (M_s) magnitude for a seismic event. For a given m_b, earthquakes often generate substantially more surface wave energy than explosions and thus are characterized by a larger surface wave magnitude. Our research is aimed at determining if magnitudes obtained from surface waves recorded at near-regional distances and periods less than 10 seconds can be used to accurately characterize the size of a seismic source. The answer to this question is essential in determining our ability to discriminate lower yield events in the $3.5 < m_b < 4.5$ range. Levshin and Ritzwoller (2001) suggest this problem is difficult to answer because structural variations, which can alter short-period surface wave amplitudes by as much as 50%, have scales that cannot be resolved with current 3-D models, thus rendering path corrections difficult to determine. Also, short-period surface waves are more sensitive to high-frequency asymmetries in the shot cavity and spall. The fact remains, however, that at regional distances, surface wave trains are not well dispersed and explosions are often characterized by a pulse-like shape with dominant periods ranging from 5 to 12 seconds. Thus, it is difficult, and for small events often impossible, to determine an M_s as it was originally defined for 20-second Rayleigh waves. Either a path-corrected, spectral magnitude (e.g. Stevens and McLaughlin, 2001; Stevens and Murphy, 2001) or an M_s scale that can incorporate these shorter periods is required to examine the performance of the M_s-m_b discriminant for small events recorded at regional distances. The objective of this research is to present the results of applying two established and popular M_s formulas to regional Rayleigh-wave data with periods less than 10 seconds.

RESEARCH ACCOMPLISHED

Phase I: The Nevada Test Site

Data. We have estimated 7-second surface wave magnitudes for NTS explosions that occurred between December 1968 and September 1992. The primary research focus was on the 198 NTS explosions that were detonated after August 1979, for which digital data are available from the Lawrence Livermore Network (LNN) stations. Sixty-one (61) of these events have no LNN data available, are plagued by data dropouts and glitches, or are too small for measurable surface wave energy. We also analyzed 21 events prior to July 1979 that were digitized from analog records in order to compare these results with previous M_s studies for NTS events completed by Yacoub (1983), Marshall *et al*., (1979), and Stevens and Murphy (2001). Thus, this paper presents the results of our analyses of 158 NTS explosions including 51 events from Pahute Mesa, 13 from Rainier Mesa, and 94 explosions from the Yucca Flats. We have also tabulated the location of the events relative to the water table and the lithology in which the event was detonated.

We also estimated the M_s and m_b magnitudes for 40 earthquakes whose locations are shown in Figure 1. The earthquake data consisted of LNN seismograms for events tabulated in Patton (2001; Table A.1) that were within 2 degrees of the NTS. This allowed us to maintain similar azimuthal coverage and propagation paths for the NTS explosions in our dataset. The Patton (2001) earthquake database has no events beyond 1994, thus we also downloaded data recorded at station NV31 for events between January 1999 and June 2002. This earthquake dataset, while not as extensive as our explosion database, has $m_b(Pn)$ (Patton, 2001) values ranging from 2.98 to 5.84 and depths ranging from 0 to 17 km.

m_b Estimation. For our examination of the M_s-m_b discriminant performance for small events in the Western United States (WUS), we required both regional m_b and M_s magnitude scales. Fortunately, an m_b scale has already been developed and tested for the WUS. The Denny *et al.* (1987; 1989) body wave magnitude formula (referred to henceforth as the DTV m_b) was specifically developed for the WUS using an extensive database of earthquakes and nuclear explosions at or near the Nevada Test Site. Thus, all m_bs presented in this study are $m_b(Pn)$s estimated using the DTV equation and station constants. For most of the NTS explosions, we used the DTV m_b determined by Vergino and Mensing (1989), and we used the DTV m_b determined by Patton (2001) for most of the WUS earthquakes. For events in which no $m_b(Pn)$ was published, we used the DTV equation to calculate an average network $m_b(Pn)$ using the available LNN stations.

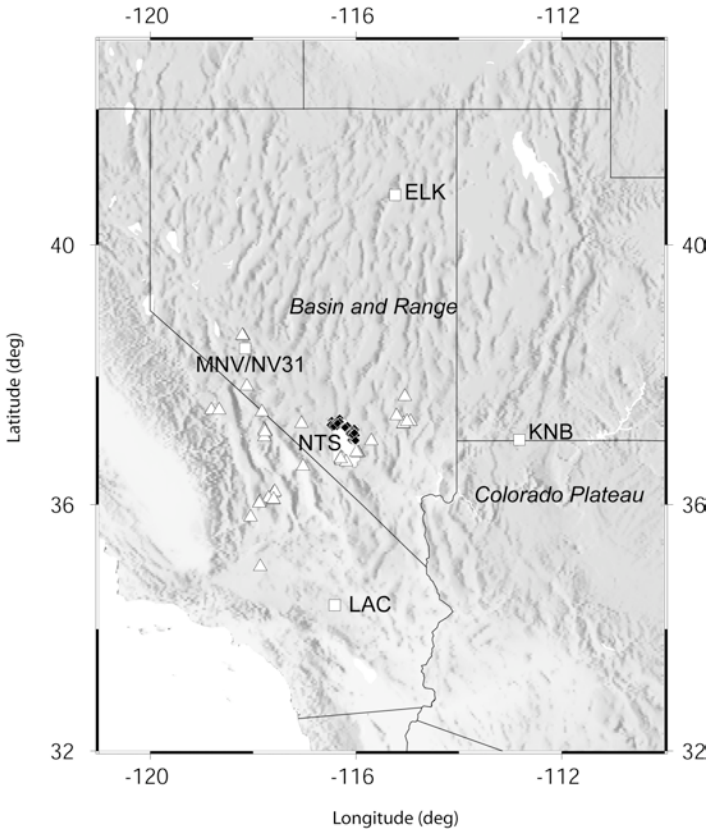


Figure 1. The locations of the four LNN stations (squared), as well as earthquakes (triangles) and explosions (diamonds on the NTS) used in this study.

***M*$_s$(7) from Marshall and Basham (1972).** Marshall and Basham (1972) reformulated the Prague formula (Vanek *et al.*, 1962) as:

$$M_s = \log_{10}(A) + B'(\Delta) + P(T) \quad (1)$$

where A is the Rayleigh wave amplitude (zero-to-peak in nm), B'(Δ) is an attenuation correction as a function of distance (Δ) in degrees, and P(T) is a path correction as a function of period T. There is an additional term of $0.008h$, where h is the depth of the event that can be included in Equation 1. Because depth is often difficult to determine for near-regional events, we did not apply a depth correction to the explosion and earthquake data in order to examine the discriminant performance assuming a surface focus. The distance corrections B'(Δ) used for this study are proportional to $0.8 \log_{10}(\Delta)$, as Basham (1971) showed this relation to be valid for earthquakes and explosions with an 8-14 second period at regional distances.

The path corrections listed in Table 2 of Marshall and Basham (1972) are not applicable to periods less than 10 seconds. The path correction P(T) is estimated from the amplitude of a group velocity (U) dispersion curve predicted by the method of stationary phase (Ewing *et al*., 1957) with the expression

$$\frac{U}{T^{3/2}\sqrt{\frac{dU}{dT}}}.$$

The P(T) corrections are normalized to a 20-second period in order to compare the short-period results with conventional M_s measurements. To generate the P(T) corrections, we used multiple filter analyses to generate group velocity dispersion curves for paths from NTS to MNV, ELK, KNB, and LAC. We averaged the dispersion curves for 8 NTS explosions with large Rayleigh-wave SNR (m_b > 5.2) between 5 and 20 seconds. We based our decision to make our surface wave measurements at a period of 7 seconds on two observations. First, a period of 7 seconds represents an average of the dominant periods for surface waves recorded at near-regional distances in the WUS.

Additionally, dispersion curves for paths in this region shows there is an inverse Airy phase (or a group velocity maximum) observable on the dispersion curves near approximately 9 seconds period, and it is best to retreat from the complications associated with this phenomenon when making amplitude measurements. As determined from the above expression, the P(T) corrections will become infinite at each Airy phase. We determined the P(7) corrections for each path, and the results are listed in Table 1. The P(7) corrections for paths to MNV, ELK, and LAC are essentially the same since these paths are all located within the Basin and Range tectonic province (Figure 1). The different dispersion curve for the path from NTS to KNB is caused by the thickening of the crust near the station associated with the transition from the Basin and Range to the Colorado Plateau (Keller *et al.*, 1976). We refer to our surface wave estimates for 7-second Rayleigh waves using Equation 1 and empirically calibrated path corrections as M_s [M+B;7].

Table 1. P(7) corrections for LNN Stations

Station	P(7)
MNV/NV31	-0.79
ELK	-0.79
KNB	-0.56
LAC	-0.73

***M*$_s$(7) from Rezapour and Pearce (1998).** Using the entire dataset from the International Seismic Center, Rezapour and Pearce (1998) developed a distance independent M_s defined as:

$$M_s = \log\frac{A}{T} + \frac{1}{3}\log_{10}(\Delta) + \frac{1}{2}\log_{10}(\sin(\Delta)) + 0.0046\Delta + 2.370 \qquad (2)$$

where A is the zero to peak amplitude in nm, T is the period in seconds, and Δ is the distance in degrees. Unlike the Marshall and Basham (1972) formula that used empirical distance and path corrections (Equation 1), the Rezapour and Pearce (1998) equation was developed using theoretical aspects of dispersion and geometrical spreading. The formula was adopted by the prototype International Data Center in 1998 for calculating surface wave magnitudes at distances between 20 and 100 degrees; however, it is now used by the International Data Center to determine an M_s for all surface waves recorded at distances less than 100 degrees (Stevens and McLaughlin, 2001). We note that the original Rezapour and Pearce (1998) paper presents no application of their formula at periods less than 10 seconds and at distances less than 20 degrees. For this study, we applied Equation 2 to short-period, near-regional data to determine M_s [R+P;7] estimates for the same dataset as used for the modified Marshall and Basham (1972) formula.

NTS Explosions. We measured the amplitude for 7-second period Rayleigh waves for 158 NTS events recorded at MNV, ELK, KNB, and LAC and estimated both M_s [M+B;7] and [R+P;7] for each event. We present a comparison of the network-averaged 7-second M_s for all measured NTS events versus the DTV network m_b(*Pn*) in Figure 2. Pahute Mesa, Rainier Mesa, and Yucca Flats events were analyzed and are presented as circles, stars, and triangles, respectively. We also denote the location of the water table, relative to each event, as either a solid symbol (events that were detonated above the water table) or an open symbol (events detonated below the water table). We regressed the [M+B;7] and [R+P;7] versus the DTV m_b(*Pn*), and the resulting equations and standard deviations for each NTS test area are shown. The primary goals of our research are to present the applicability of the M_s(7) scale, and to highlight the fact that using the short-period data allows us to estimate surface wave magnitudes for 45 explosions with $m_b < 4.5$, as compared to one in the original Marshall and Basham (1972) paper, two in the Rezapour and Pearce (1998) paper, and less than ten in Stevens and McLaughlin (2001). In addition, we have determined M_s(7) measurements for 9 events with $3.7 < m_b < 4.0$.

Comparison of the Near-Regional *M*$_s$(7) and Teleseismic *M*$_s$. Of course, estimating near-regional M_s(7) values for NTS events that can be calibrated to conventional M_s scales is of primary importance to our research as well. We compared our M_s [M+B;7] and M_s [R+P;7] estimates taken directly from the near-regional surface waves with the M_s measurements obtained from a modeling technique derived by Woods and Harkrider (1995). Their indirect method of estimating M_s consisted of modeling the surface waves recorded at regional distances, and then propagating the regional synthetics to distances of 40 degrees. At 40 degrees, the synthetics showed significant 20 second surface wave energy; thus Woods and Harkrider (1995) measured M_s from the synthetics. Figure 3 shows the comparison of our M_s [M+B;7] and M_s [R+P;7] with $\pm$ 1s plotted as the horizontal lines and the Woods and Harkrider (1995) indirect method (W+H) with $\pm$ 1s plotted as vertical lines. We performed a fixed-slope (slope=1)

linear regression to compare the $M_s(7)$ values with the Woods and Harkrider (1995) values and found a strong correlation. The offset shows that the M_s [M+B;7] and M_s [R+P;7] estimates are 0.20 m.u. lower and 0.95 m.u. higher, respectively, than the Woods and Harkrider (1995) estimates. Woods and Harkrider (1995) showed their measurements also correlated very well with conventional NTS M_s values from Marshall and Basham (1972), Marshall *et al*. (1979), and Yacoub (1983) with considerable variance in the offsets. We also compared the performance of M_s [M+B;7] and M_s [R+P;7] with Yacoub (1983). The results for the comparison with Yacoub (1983) are shown also in Figure 3 and indicate similar scaling relationships based on the fixed-slope regression analysis. In this case, our M_s [M+B;7] and M_s [R+P;7] values are offset from Yacoub's (1983) estimates by approximately +0.02 m.u. and +1.21 m.u., respectively. Differences in these absolute estimates result from the use of different M_s definitions, especially in the attenuation factors; however, these comparisons do show that our estimates are scaling similarly to other measurements of NTS surface wave magnitudes.

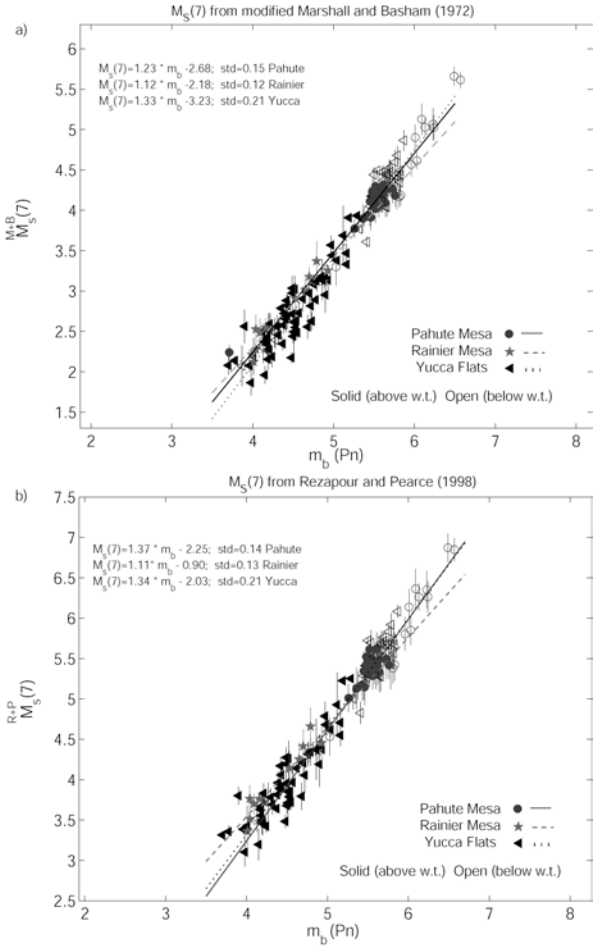


Figure 2. Network-averaged 7-second M_s estimates for 158 NTS events at Pahute Mesa, Rainier Mesa, and Yucca Flats regressed against m_b(*Pn*). The best-fitting regression lines are plotted as solid (Pahute), dashed (Rainier), and dotted (Yucca) lines. Solid symbols indicate events above the water table (w.t.) with open symbols showing events below the water table. The vertical lines represent one standard deviation for the M_s estimate.

The properties of Rayleigh wave propagation make it difficult to develop a single expression that gives consistent M_s values at both regional and teleseismic distances. Figure 4 presents the comparison of near-regional M_s estimates (i.e. M_s [M+B;7] and M_s [R+P;7]) with far-regional and teleseismic estimates of M_s using the same formulas (i.e. Marshall and Basham (1972) and Rezapour and Pearce (1998) formulas, respectively). Marshall *et al.* (1979) used the Marshall and Basham (1972) M_s formula for far-regional and teleseismic distance recordings of NTS events for Rayleigh waves with periods greater than 14 seconds. We determined that the near-regional M_s [M+B;7] estimates have a similar scaling relationship when using a fixed slope (slope = 1.00) regression analysis, but are consistently

0.35 m.u. higher than Marshall *et al*. (1979) for the 5 events in their dataset for which we had LNN data to analyze. We note that most of our near-regional estimates have better azimuthal coverage than Marshall *et al.* (1979) who mainly used Canadian data and thus may have strong azimuthal biases. This could be a possible source for the consistent difference. Another source could be the attenuation terms; however, we do not have data at a wide enough distance range in this study to verify the appropriateness of Basham (1971) as the correct attenuation model.

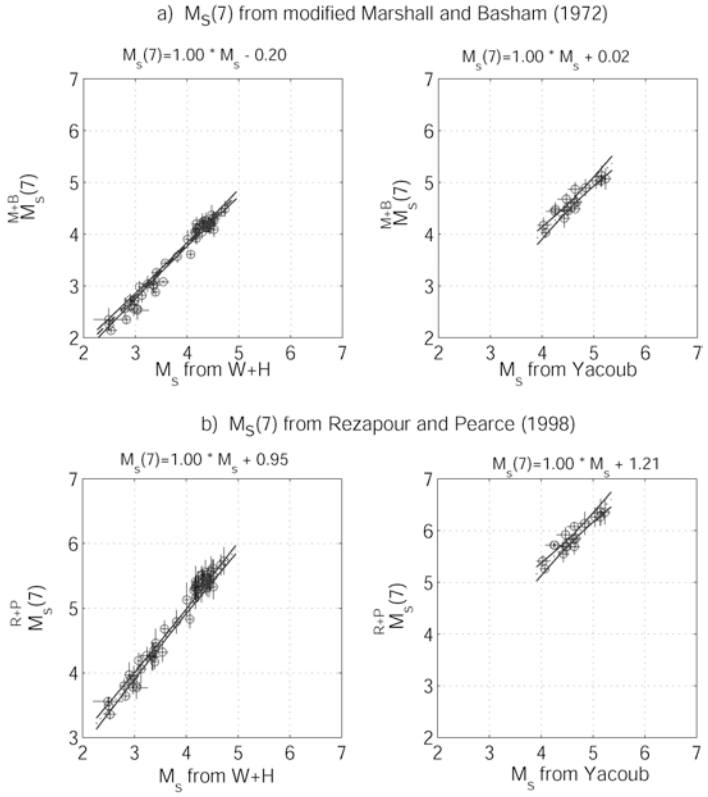


Figure 3. A comparison of our 7-second M_s estimates for NTS with the Woods and Harkrider (1995) indirect estimates (W+H; left) and Yacoub (1983; right). The best-fitting regression line, with a fixed slope = 1.0, is given by the dotted line running through the data points, and it is surrounded by the pointwise 95% confidence intervals plotted as two solid lines.

We observed that the M_s[R+P;7] estimates are on average 1.6 m.u. larger than the Marshall *et al.* (1979) teleseismic M_s values.

The Rezapour and Pearce (1998) formula has not been tested significantly at near-regional distances and short periods until this paper, and our results suggest there are considerable differences between the short-period, near-regional magnitudes and teleseismic magnitude estimates for NTS events. We regressed our M_s [R+P;7] estimates versus far-regional and teleseismic M_s estimates (Figure 4) determined by Stevens and Murphy (2001) using the Rezapour and Pearce (1998) formula. We note consistent scaling between the two estimates, however, there is an offset of +1.46 m.u. We note much better agreement between the Stevens and Murphy (2001) teleseismic M_s values and the 7-second modified Marshall and Basham (1972) estimates. Thus, we believe path corrections will be required for correct application of the Rezapour and Pearce (1998) formula at near-regional distances and periods less than 10 seconds.

Earthquakes and Discriminant Analysis. We measured the amplitude for 7-second period Rayleigh waves for 40 earthquakes (Figure 1) within 2 degrees of the NTS as recorded at MNV (or the collocated NV31), ELK, KNB, and LAC and estimated a M_s [M+B;7] and M_s [R+P;7] for each event. We then examined the performance of the modified Marshall and Basham (1972) and Rezapour and Pearce (1998) $M_s(7)$-m_b discriminants for earthquakes and explosions. The populations of earthquakes and explosions suggest that M_s and m_b will be fitted well by linear regressions, with approximately equal slopes assumed for the earthquake and explosion populations. Although we

did observe slightly different slopes in the regression analyses for the two populations, we believe that this is due to inadequate sampling of earthquakes at m_b magnitudes greater than 4.5. Our dataset does not present any evidence that the two populations are converging at smaller magnitudes, although other M_s-m_b studies (Stevens and McLaughlin, 2001) suggest that convergence does occur. Furthermore, it seems sensible to regard the M_s values as dependent variables, observed conditionally on fixed values for m_b, which are more accurately determined in the WUS when the DTV m_b (Denny *et al.*, 1987; 1989) formula is applied. This yields the following regression model:

$$M_s = a_i + b\, m_b + e \tag{3}$$

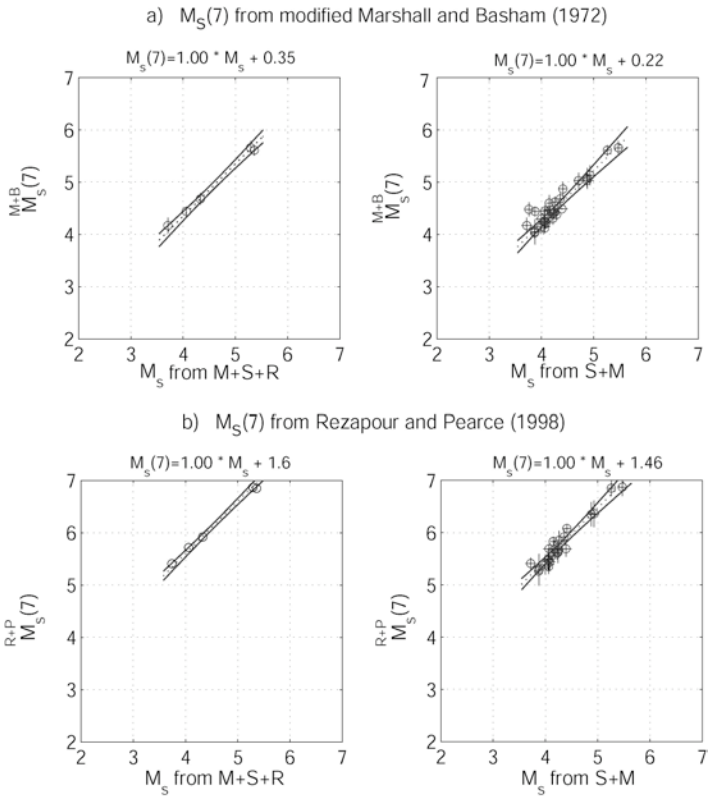


Figure 4. A comparison of our 7-second M_s estimates for NTS with the Marshall *et al.* (1979) estimates (M+S+R; left) and Stevens and Murphy (2001) estimates (S+M; right).

i=1,2 where the intercepts a_1 and a_2 correspond to the earthquake (Q) and explosion (X) populations respectively. Under this approach, the errors (e) are assumed to be independent and identically distributed normal variables. For determining the optimal discriminant functions, the parallel regression assumption with independent normal errors seems more sensible than the usual assumption of bivariate normality used to get the classification function. Hence, we proceed to use the linear function following from the conditional regression approach to discrimination. This leads to a discriminant function of the form:

$$d = M_s - \frac{1}{2}(a_1 + a_2) - b\, m_b. \tag{4}$$

With equal prior probabilities, we classify an event of unknown origin as an earthquake if d>0 and as an explosion otherwise. The classification criterion in the equal slope case is then applied with the values estimated from the data. We note first the result of applying the discriminant function, d, directly, as shown in Figure 5. Note the four misclassified earthquakes in the M_s[M+B;7]-m_b plot and the six misclassified earthquakes in the M_s[R+P;7]-m_b case. To estimate the performance of the discriminant function (Equation 4), we used a jackknifing technique where the observation to be classified is held out during the estimation of the slope and intercept procedure and then the discriminant function is applied to the observation to be classified using the estimated parameters. For the M_s[M+B;7] case, we misclassified 4 earthquakes as explosions (10%) while only classifying two explosions (1.2%)

as earthquakes. The misclassification rates are slightly higher for the M_s[R+P;7] estimates as we identified 6 earthquakes (16%) as explosions and 3 explosions (2%) as earthquakes.

Phase II: The Lop Nor Test Site Preliminary Results

Our next stage of the research project was to examine the applicability of short-period M_s scales on the Lop Nor Test site in western China. We followed the same procedures as outlined above and generated path corrections for Equation 1. We averaged the group velocity dispersion curves of four large Lop Nor nuclear explosions recorded at AAK, BRVK, MAK, KUR, and TLY and the results are shown in Figure 6. We then estimated the path corrections for these dispersion curves, and the results are also provided in Figure 6 in addition to the dashed line, which shows

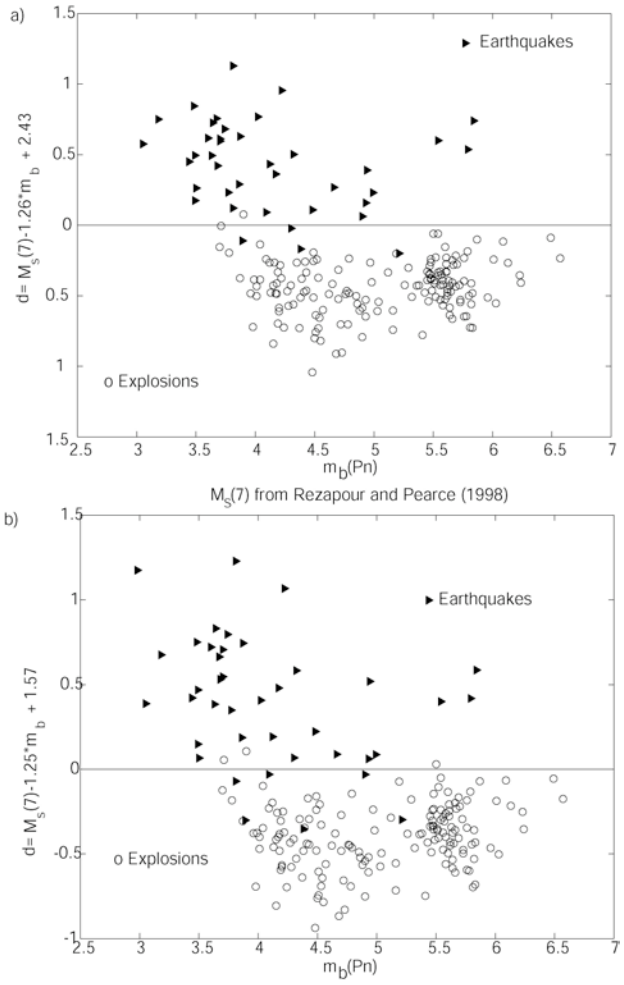


Figure 5. Discriminant functions for a) M_s[M+B;7] and b) M_s[R+P;7] for earthquakes and explosions considered in this study. The parameter *a* from Equation 4 represents the slope (1.26 and 1.25) of the m_b versus M_s populations and the decision line is determined from the means for both populations. Based upon our evaluation of the M_s[M+B;7] -m_b relationship for this region, we calculated the probability of misclassifying an earthquake as an explosion as 10% and the probability of classifying an explosion as an earthquake to be 1.2%. The results are slightly worse for M_s[R+P;7] -m_b , where 15% of the earthquakes are misclassified as to be explosions and 2% of the explosions labeled as earthquakes.

the path corrections for Marshall and Basham's (1972) "Eurasia". The variability in the dispersion curves and resulting path corrections highlight the need for improved regional calibration, which is being completed in China by Maceira and Taylor (2003). We then used these path corrections to determine M_s[M+B;7] for six explosions and for five earthquakes located on or near the Lop Nor test site. The results of plotting them versus USGS m_b are shown in Figure 7 and highlight the problems associated with restricting our analysis to 7-second Rayleigh waves.

While this formed a robust discriminant for events near NTS, we see that there is inadequate offset in the two populations for our current small dataset. Two of five earthquakes could not be statistically distinguished from the explosions. We believe the poor performance is related to the effect of source depth on 7-second Rayleigh wave generation. All five of these earthquakes have reported depths greater than 14 km resulting in reduced 7-second surface wave generation.

To improve the discrimination analysis, we returned to the original definition of the Marshall and Basham (1972) formula which stated that the period used to calculate M_s should be where the maximum amplitude in the surface wave train occurs. For these five explosions recorded at regional distances, the maximum amplitude occurred at periods between 8 and 10 seconds. Thus, we used the path corrections for the period of maximum amplitude and calculated M_s [M+B; Max], and unlike Marshall and Basham (1971), we did not limit ourselves to periods greater than 10 seconds. We recalculated the earthquake magnitudes in the same manner; however, the period of maximum amplitude ranged from 8 to 18 seconds. The results are also shown Figure 7, and in this case there is increased separation among the populations. We note that the recent (13 March 2003) event located near the Lop Nor test site falls within the earthquake population for both methods. We plan to add more earthquake and explosion data to this analysis within the next year to better understand short-period surface wave estimation at Lop Nor and elsewhere.

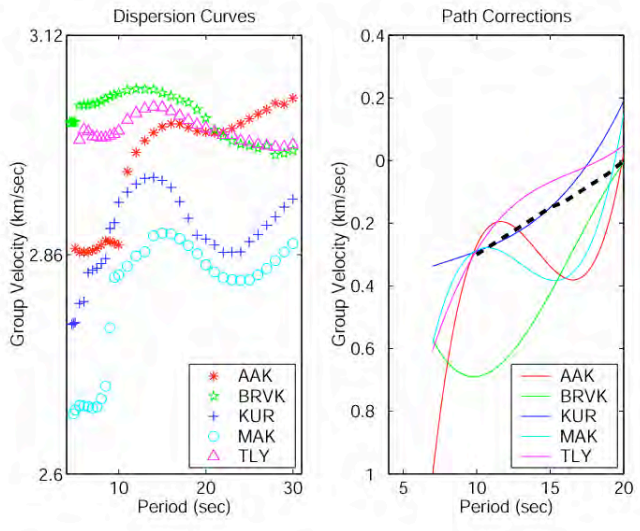


Figure 6. Left) Dispersion curves for paths from Lop Nor to regional stations. Right) Path corrections as a function of period.

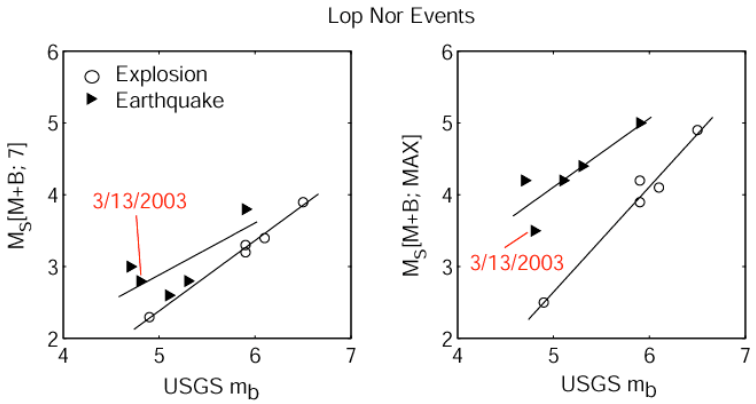


Figure 7. An examination of network averaged surface wave measurements for events on or near Lop Nor calculated with (left) 7-second Rayleigh waves and (right) the period (between 8 and 18 seconds) of the maximum Rayleigh wave amplitude.

CONCLUSIONS AND RECOMMENDATIONS

The M_s[M+B;7] -m_b and M_s[R+P;7] -m_b discriminants defined in this paper can now be used as tools to help screen explosions from earthquakes in the vicinity of the Nevada Test Site (NTS). The false classification rates for the method are small, and the method can be used in conjunction with other regional NTS discriminants, such as the phase and spectral ratios (Walter *et al*., 1995) and body wave and moment magnitude ratios (m_b-M_w) (Patton, 2001). Transportability of the M_s[M+B;7] -m_b discriminant to Lop Nor was complicated due to deeper events than at NTS. However, by using the period of maximum amplitude instead of 7-second only and by calibrating path corrections to periods less than 10 seconds, we were able to increase the separation between the earthquake and explosion populations at Lop Nor. There is important information related to source size and depth in short-period surface waves, and our work will continue to improve the regional path corrections required to improve the accuracy in magnitude estimation.

ACKNOWLEDGMENTS

We are indebted to Howard Patton for his assistance in database acquisition and his comments concerning various aspects of the research. We also wish to thank Bill Walter for help in acquiring the MNV dataset. We express our gratitude to Marv Denny, Jeff Stevens, Nazeih Yacoub, Steve Taylor, Nancy Cunningham, Shelly Johnson, and James Lewkowicz for insightful discussions about the manuscript and research.

REFERENCES

Basham, P.W. (1971), A new magnitude formula for short-period continental Rayleigh waves, *Geophys. J. R. Ast. Soc.*, **23**, 255.

Denny, M.D., S. R. Taylor, and E.S. Vergino (1987), Investigation of m_b and M_s formulas for the western United States and their impact on the M_s/m_b discriminant, *Bull. Seism. Soc. Am.*, **77**, 987-995.

Denny, M.D., S. R. Taylor, and E.S. Vergino (1989), Erratum: Investigation of m_b and M_s formulas for the western United States and their impact on the M_s/m_b discriminant, *Bull. Seism. Soc. Am.*, **79**, 230.

Ewing, W.M., F. Press, and W.S. Jardetzky (1957), *Elastic waves in layered media*, McGraw-Hill, New York.

Herrmann, R. B. (2002). Computer Programs in Seismology Version 3.15, St. Louis University.

Keller, G.R., R.B. Smith, L.W. Braile, R. Heaney, and D.H. Shurbet (1976), Upper crustal structure of the eastern Basin and Range, northern Colorado plateau, and middle Rocky Mountains from Rayleigh-wave dispersion, *Bull. Seism. Soc. Am.*, **67**, 869-876.

Levshin, A.L. and M.H. Ritzwoller (2001), Automated detection, extraction, and measurement of regional surface waves, *Pure Appl Geophys*, **158**, 1531 - 1545.

Maceira, M. and S. R. Taylor (2003), Short-period surface wave tomography in central Asia and its application to seismic discrimination, *Seism. Res. Letts*., 74, p 212.

Marshall, P.D. and P.W. Basham (1972), Discrimination between earthquakes and underground explosions employing an improved M_s scale, *Geophys. J. R. Astr. Soc.*, **29**, 431-458.

Marshall, P.D., Springer, D.L, and Rodean, H.C. (1979), Magnitude corrections for attenuation in the upper mantle, *Geophys. J. R. Astr. Soc.*, **57**, 609-638.

Patton, H. (2001), Regional magnitude scaling, transportability, and M_s-m_b discrimination at small magnitudes, in *Monitoring the Comprehensive Nuclear Test Ban Treaty: Source Processes and Explosion Yield Determination*, eds. Ekstrom, G., M. Denny, and J.R. Murphy, *Pure Appl. Geophys*., **158**, 1951-2015.

Rezapour, M., and R.G. Pearce (1998), Bias in surface-wave magnitude M_s due to inadequate distance correction, *Bull. Seism. Soc. Am.*, **88**, 43-61.

Stevens, J.L., D.A. Adams, and E. Baker (2001), Surface wave detection and measurement using a one-degree global dispersion grid, *SAIC Final Report SAIC-01/1085.*

Stevens, J. L. and K.L. McLaughlin (2001), Optimization of surface wave identification and measurement, in *Monitoring the Comprehensive Nuclear Test Ban Treaty: Surface Waves*, eds. Levshin, A. and M.H. Ritzwoller, *Pure Appl. Geophys.*, **158**, 1547-1582.

Stevens, J. L. and J.R. Murphy (2001),Yield Estimation from Surface-wave Amplitudes, in *Monitoring the Comprehensive Nuclear Test Ban Treaty: Surface Waves*: *Source Processes and Explosion Yield Determination*, eds. Ekstrom, G., M. Denny, and J.R. Murphy, *Pure Appl. Geophys*., **158**, 2227-2251.

Vanek, J., A. Zatopek, V. Karnik, Y.V. Riznichenko, E.F. Saverensky, S.L. Solov'ev, and N.V. Shebalin (1962), Standardization of magnitude scales, *Bull. (Izvest.) Acad. Sci. U.S.S.R., Geophys. Ser.*, **2**, 108.

Vergino, E.S. and Mensing, R.W. (1989), Yield estimation using regional m_b(*Pn*), *Lawrence Livermore National Laboratory Report UCID-101600.*

Walter, W. R., K.M. Mayeda, and H.J. Patton (1995), Phase and spectral ratio discrimination between NTS earthquakes and explosions. Part I. Empirical Observations. *Bull. Seism. Soc. Am*., **85**, 1050-1067.

Woods, B. and D.G. Harkrider (1995), Determining surface-wave magnitudes from regional Nevada Test Site data, *Geophys. J. Int.*, **120**, 474.

Yacoub, N.K. (1983), Instantaneous amplitudes: a new method to measure seismic magnitude, *Bull. Seism. Soc. Am.*, **73**, 1345-1355.

ASPECTS OF *Rg* AND *Lg* GENERATION FROM THE SHAGAN DEPTH OF BURIAL EXPLOSIONS

Jessie L. Bonner,[1] Howard J. Patton,[2] Anca C. Rosca,[1] Heather Hooper,[1] Jeffrey Orrey,[3]
Mark Leidig,[1] and Indra Gupta[4]

Weston Geophysical Corporation;[1] Los Alamos National Laboratory; [2] GeoVisual Tech; [3] and Multimax, Inc. [4]

Sponsored by National Nuclear Security Administration
Office of Nonproliferation Research and Engineering
Office of Defense Nuclear Nonproliferation

Contract No. DE-FG02-00ER83123

ABSTRACT

Regional *S*-wave amplitudes observed on recordings from the Depth of Burial (DOB) experiments conducted at the Shagan Test Site in August and September 1997 varied according to source depth (Phillips *et al*., 1998; Myers *et al*., 1999). Similar depth dependence was noted on nearfield recordings of *Rg* waves. These are significant observations in support of nearfield *Rg*-to-*S* scattering proposed by Gupta and co-workers in the early 90s (Gupta *et al*., 1992). Unfortunately, the importance of nearfield scattering relative to competing mechanisms of *S*-wave generation by underground explosions remains unresolved in part due to the need for a phenomenological model with which to predict *S*-wave amplitudes and their yield scaling as a function of source and material parameters. One of the goals of this project is to begin developing such a model by describing source mechanisms of *Rg* excitation using simple elastodynamic models for explosion sources, and by examining the effects of different source depths on *P*-to-*S* conversions at the free surface using two- and three- dimensional Generalized Fourier Methods.

Very little is known about *Rg* excitation by underground explosions. To fit observations of *Lg* spectral ratios, Patton and Taylor (1995) invoke *Rg*-to-*S* scattering and a linear superposition of spatially distributed sources to excite *Rg* waves: a pure point-source explosion (monopole) and a compensated linear vector dipole (CLVD) with shallower depth compared to the DOB. The CLVD source is believed to be associated with large deformations over the detonation point related to spallation, block motions, and dynamic rebound caused by the outgoing shock wave. This compound source model will be tested against nearfield and farfield recordings of the DOB chemical explosions. We extracted *Rg* waves from nearfield records and carried out spectral analysis to recover source amplitudes and phase. Significant differences between the recovered source spectra and spectra predicted for a monopole source suggest that the source of *Rg* waves for all three DOB explosions depart significantly from a pure point-source explosion. Modeling will be performed to investigate whether the addition of a CLVD source can explain the observations. Furthermore, comparisons between the absolute amplitudes predicted by source models and those observed for regional *S* waves will help characterize the scattering transfer function and the energetics of mode conversion.

We have completed a series of GFM2D simulations in order to examine *S*-waves generated from free surface reflections. We generated a model consisting of the shallow structure of the Shagan Test Site determined from *Rg* inversions overlying the eastern Kazakhstan model of Priestley *et al.* (1988). For this model, significant shear wave energy can be trapped in the crust from explosions at 300 and 550 m depth to form a regional *Lg* phase. Comparison of the synthetics to regional data shows that the different depths of burial for the two sources can account for much of the observed differences in 0.7-3 Hz *Lg* amplitudes at MAK. Additional models with random velocity heterogeneities and laterally varying structure are also being examined to further quantify the regional observations.

OBJECTIVES

The objectives of this research project are to create physically realistic models of short-period (0.2 to 12 seconds) surface wave generation from earthquakes, small chemical explosions and different classifications of mine blasts, and to understand the propagation characteristics of these surface waves, including mechanisms for explosion-generated *Lg*. To accomplish these objectives, we have:

- Examined whether a pure point-source explosion (monopole) and a compensated linear vector dipole (CLVD) with shallow depth can explain the *Rg* recorded at the Shagan Depth of Burial (DOB) experiments,

- Continued development of a numerical modeling package to generate short-period surface waves from different explosion sources and to propagate them through complex 3D and 2D media, and

- Compared preliminary numerical results to empirical data to aid in development of regional explosion discriminants based upon surface waves.

The preliminary results of modeling DOB *Rg* source spectra with the CLVD source, updates to the development of the 3D and 2D surface wave modeling program, and applications of the modeling package are presented in the following paper.

RESEARCH ACCOMPLISHED

CLVD Modeling for the Shagan DOB Explosions (*Patton, Gupta, and Bonner*)

Introduction. Local and regional seismic recordings of three 25-ton chemical explosions comprising the DOB experiment at the Shagan Test Site (Myers *et al*., 1999; Bonner *et al.*, 2001) offer a unique opportunity to investigate the excitation of near-field, short-period, fundamental-mode surface waves (*Rg*) and the relationships these *Rg* waves have with waves recorded at greater distances. Interest in these relationships has grown steadily in recent years as evidence accumulates that *Rg*-to-*S* scattering is an important mechanism for the generation of regional *S* waves by underground explosions. Due to the importance of *Lg* and *Lg* coda waves for discrimination and yield estimation, it is crucial that a physical model for the genesis of regional *S* waves is well understood for underground explosions. Unfortunately, there is much controversy over the causes of *S*-wave generation by explosions, and much of the evidence gathered to date in support of *Rg*-to-*S* scattering is only qualitative in nature. A physical model will be advanced significantly if observations relevant to *Rg*-to-*S* scattering can be put on firm quantitative footing.

Very little is known about the excitation of *Rg* waves by underground explosions. It has long been recognized that shallow sources in the Earth should excite *Rg* waves efficiently. However, the excitation of *Rg* waves by explosions may be very complex because real world explosions are usually not simple monopole (point isotropic) sources, but rather complex, anisotropic sources distributed in time and space. One model for the excitation of *Rg* waves invokes a compensated linear vector dipole (CLVD) to explain the frequency content of *Lg* spectra and spectral ratio observations for nuclear explosions (Patton and Taylor, 1995; Gupta *et al*, 1997). In this case, the CLVD is an elastodynamic equivalent of a conical source, with apex at the detonation point, extending to the free surface, and the material within the volume undergoes catastrophic shear failure. This source is believed to be associated with large deformations accompanying underground explosions in the form of spallation, tensile failures and block motions below the spalled layers, as well as dynamic rebound caused by the outgoing shock wave.

The objective of this study is to characterize *Rg* waves recorded within 20 km of three chemical explosions, all with the same yield, but buried at significantly different depths. Scaled depth of burials (sDOB) for these explosions span a wide range, and source phenomenologies accompanying these explosions are expected to exhibit great variability. Indeed, the shallowest explosion is known to have cratered, while the deepest explosion, with sDOB of ~1400 scale meters, was significantly over buried. Theoretically, the more over buried an explosion is, the more like a monopole it should behave. The spectral amplitude and the phase of *Rg* waves from the DOB explosions have been studied in light of the variant phenomenology, and source models are proposed to explain the observed source spectra. In particular, the CLVD source model has been tested. The preliminary results are presented in this paper.

New Velocity Models. Bonner *et. al.* (2001) presented averaged velocity structures for the upper 2.5 km at the Shagan Test Site (STS) for both the northeastern and southwestern sections. The structures were obtained by inversion of group velocity dispersion curves obtained from local recordings of the DOB experiment. For the present study, we conducted a new set of inversions for paths either completely or partially within the southwestern section of STS. The objective of the current study was to obtain additional information about the upper crust at depths deeper than 2.5 km (in some cases as deep as 10 km). The starting model for these inversions consisted of a combination of the averaged model for the southwestern test site (Bonner *et al*., 2001 Figure 11) and the Priestley *et al.* (1988) model for Eastern Kazakhstan (EK). For some paths, two-station phase velocity data at short periods were used to further constrain the inversions. We then performed least-squares inversions on both the phase and group velocity dispersion curves. The inversion resulted in a new set of models, called Shagan+EK, for each DOB source-station path of interest.

Processing. The first processing step completed was to identify *Rg* on the local seismic recordings of the DOB experiments. We used particle motion and arrival times predicted from the new velocity models to identify *Rg* on the waveforms. We found that particle motions were quite troublesome for certain stations, while they were generally well-behaved for others. The troublesome stations were S4, S6, and S9, all of which have paths for the three DOB shots that tend to cut across the grain of the "geologic fabric" more so than do the paths for S2, S3, S7, and S8. Waveforms also tend to be more complex for S4, S6, and S9, which is probably caused by signal-generated noise due to inhomogeneities along the path. We are also examining the possibility that there may be instrument problems at these stations (in fact, we are verifying the responses for all local stations), thus the results presented in this paper are focused on stations S2, S3, S7, and S8. Further processing steps included multiple-filter analyses and time variable filtering to extract the *Rg* from the complex seismograms.

Spectral Analyses. We completed spectral analyses of the signals and compared them with synthetic signals generated for a monopole explosion. Figure 1 summarizes *Rg* spectral amplitude and phase observations for the three DOB shots. Attenuation-corrected, weighted mean amplitude spectra are shown with their model spectra in the top panels of Figure 1. Note that the mean spectra were determined using stations S2, S3, S7, and S8 for the 50 m and 300 m shots, while the mean spectra for the 550 m shot are based on only S3, S7, and S8 since S2 was too close to the source. The M_o used for the model spectrum of the 50 m shot, $2.8*10^{13}$ Nm, was determined from Denny and Johnson's (1991) scaling relationships. Likewise, the M_o for the 300 m and 550 m explosions were determined to be $1.2*10^{13}$ Nm and $1.0*10^{13}$ Nm, respectively. Mean phase spectra are plotted on the bottom row of Figure 1, where the units are circles. Discontinuities in the observations for the 550 m explosion are caused by phase wraparound.

The observed *Rg* phase spectra results are very interesting in light of their associated amplitude spectra and model spectra. Both amplitudes and phases indicate that the simplest model of an explosion source, the pure monopole, is inadequate to explain the frequency content of nearfield *Rg* signals for all three explosions. Considering the sDOB of the 550 m explosion (~1400), this finding is remarkable. On the other hand, the ground-zero accelerometer record for this shot does show evidence of spall, so from a phenomenological standpoint, even this shot was probably not a point dilatational source. While the final phase spectrum for the 550 m explosion (solid line in third frame on the bottom) is somewhat noisy, it nevertheless shows different behavior compared to spectra from the other explosions. Likewise, there are differences in the spectral shapes of observed amplitude.

CLVD Source. CLVD models are a primary focus of this study and have been tested against the spectral observations, both amplitude and phase. The CLVD source, Mxx = -0.5, Myy = -0.5, Mzz = 1.0, Mij = 0 for i not equal to j, has a vertical axis of symmetry (extension). This source excites azimuthally-independent Rayleigh waves, and does not excite Love waves. Several interesting features characterize the theoretical Rayleigh-wave radiation from such a source, including excitation nulls (Figure 2), which occur in the frequency range of *Rg* waves for source depths in the upper 300 m of the crust. The precise location of these nulls depends on the velocity structure as well as source depth. We used the Shagan+EK model to generate the CLVD source amplitude spectra in Figure 2.

Another interesting feature of the CLVD radiation is the source phase. For frequencies below the null frequency, the source phase is -0.125 circles, and above the null frequency, it's 0.375 circles. This assumes a step function time history. Thus if a point CLVD source at 50 m depth is coincident in time and space (epicenter) with a pure monopole source, Rayleigh waves will experience destructive interference below 5 Hz and constructive interference above 5 Hz since the waves excited by the CLVD and monopole sources are perfectly out of phase and in phase on

either side of the null frequency. The source phase characteristics of these sources lead to very interesting interference patterns which show additional complexity as more realism is introduced into the source. For example, the origin of the CLVD should be time delayed relative to the origin of the monopole. We are attempting to model the nearfield *Rg* spectra using a compound source model composed of a linear superposition of monopole and CLVD sources.

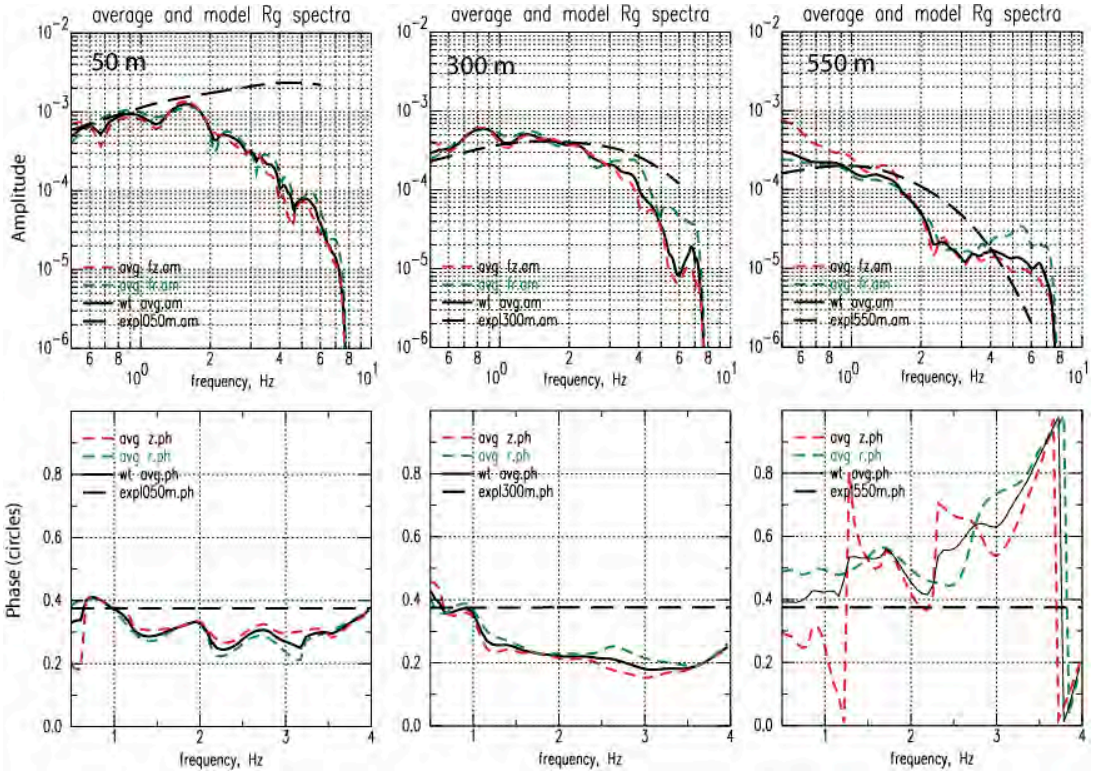


Figure 1. (Top) Amplitude *Rg* spectra for the sDOB explosions including the average vertical components (red dashed); averaged radial components (green dashed); the weighted average spectra (solid black); and the spectra for the pure monopole explosions (black dashed line). (Bottom) Phase spectra.

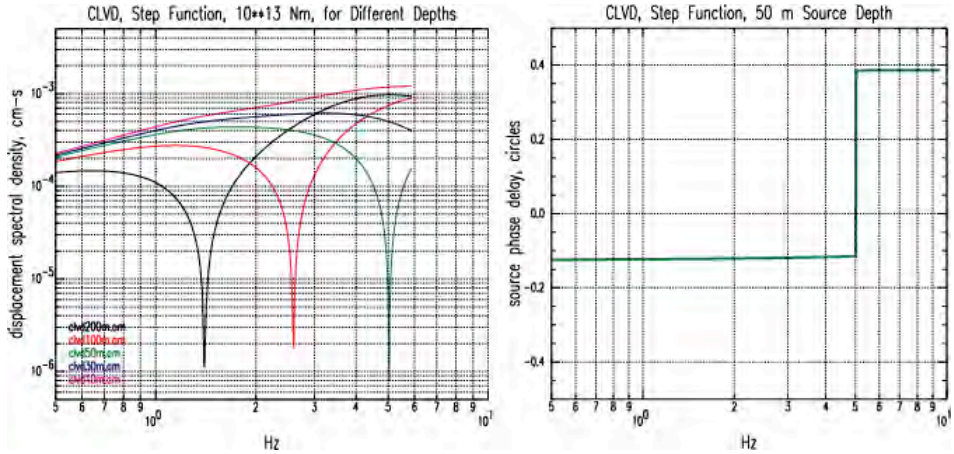


Figure 2. (Left) Theoretical *Rg* spectra for a CLVD source at depths of 200 m (black), 100 m (red), 50 m (green), 30 m (blue), and 10 m (magenta). Nulls in the amplitude spectra depend on source depth. *Rg* waves below the null frequency are exactly 180 degrees out of phase with *Rg* waves from a simultaneous, co-located monopole source with the same time history as the CLVD. Above the null frequency, they are in phase. (Right) A phase spectrum for 50 m depth is plotted in units of circles.

Advancements in 2D and 3D Modeling of *Rg* and *Lg* Using GFM (*Bonner, Rosca, Orrey, Hooper, and Leidig*)

Program Enhancements. We continue to improve the three-dimensional (3D) Generalized Fourier Method (GFM) developed by Orrey *et al*. (2003). GFM3D is a generalization of the standard Fourier pseudospectral method, in which the spatial approximations of the field variables are truncated Fourier series. During the past year, the GFM3D software package has been ported to a cluster of Linux workstations and tested for solution accuracy, reliability and optimal performance. The principal tasks involved in the porting phase have been 1) conversion of the software package's source code to a cross-platform version to incorporate the specifics of the Linux-based system compilers, 2) debugging of the new version to resolve differences in the MPI implementation on the Linux versus Cray architectures, 3) testing of the compiled system for a set of standard test problems, and 4) optimization of the code performance for the (currently) 9-node cluster. In addition, the code has been enhanced to work in 2D, and we have implemented the capability to convolve different source functions with the synthetics.

The final phase of the code implementation will involve addition of features to increase the range of geophysical problems that can be handled by the code. This includes a general Greens function convolution with different source functions and a non-uniform grid via a coordinate transformation from regular Cartesian coordinates. In addition, tests have indicated a problem with the implementation of anelasticity via the use of memory variables. The code will be completed by November 2003. Additional packages that have been developed for the software include a module that generates 2D profiles from the CRUST2 model (Bassin *et. al.*, 2000) and a *gfm2sac* conversion software.

GFM3D Modeling of the *Lg* and *Rg* Propagation in Pakistan. We completed a study to examine whether a GFM3D simulation for station NIL using the 3D CRUST2 model could be used to estimate *Lg* and *Rg* travel times for velocity model validation. We parameterized the model using a 5 km Cartesian grid spacing out to at least 1000 km in all directions from NIL and to a depth of 200 km. The resulting number of nodes for this simulation was 7.9 million and the time to simulate 400 seconds of data was 47 hours running on a nine-node parallel Linux cluster. We placed a point source at the NIL grid node and calculated full waveform synthetics for every other grid node. Two images of the surface velocities (bandpass filtered between 0.1 and 0.5 Hz) recorded 70 and 191 seconds after the initiation of the simulations are shown in Figure 3. Even though this is a point source simulating an explosion, there is abundant *S*-wave energy created by scattering processes within the 3D model. In addition, there is *Lg* energy propagating with significant spatial variations in group velocities (ranging between 3.2 and 3.7 km/sec) and amplitudes.

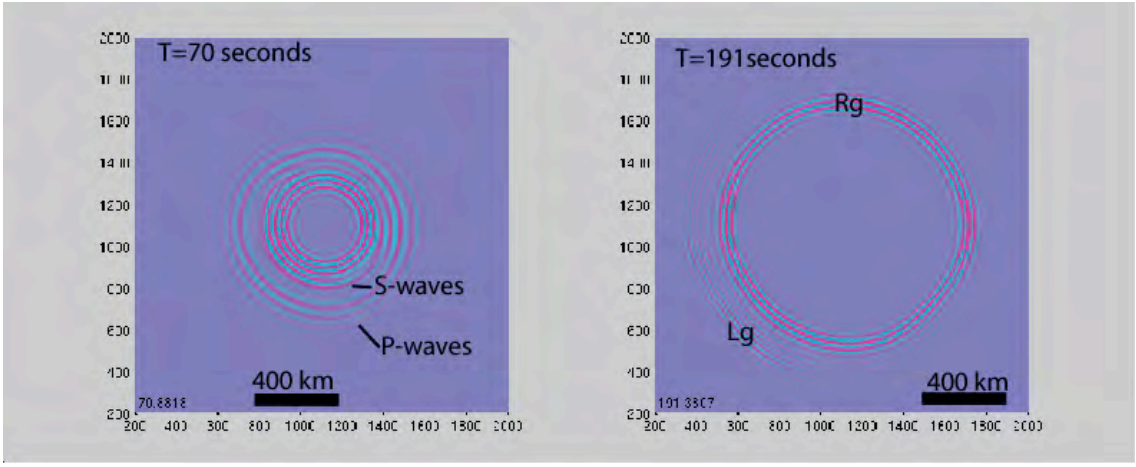


Figure 3. GFM3D snapshots of synthetic propagation at near-regional distances from station NIL using CRUST2 as the velocity model. The snapshots are of bandpass filtered data (0.1 to 0.5 Hz) at 70 and 191 seconds after initiation of a point source.

The next stage of the pilot study was to process each synthetic for an *Lg* arrival time. Given that there were over 33,000 stations for this simulation, we developed an automated algorithm that normalized the data to the maximum amplitude of the *Lg* data within a group velocity window between 3.2 and 4.0 km/sec. The algorithm then applied a

threshold detector within this window of synthetic data and determined the arrival time in which the amplitudes of the *Lg* reached 30% of the maximum amplitude in the window. We then divided this arrival time into the epicentral distance to get a node group velocity. The resulting image and randomly-picked synthetic seismograms at various locations within the model are shown in Figure 4. This is, to our knowledge, one of the first images of *Lg* group velocities synthesized from 3D full waveform modeling ever produced. We note slower *Lg* group velocities in the Katawaz, Tadjik, Tarim, and Indo-Gangetic basins and faster propagation in the Indian shield and other regions. We have completed similar maps for the *Rg* phase and intermediate-period Rayleigh waves and are in the process of using the 3D maps to validate the CRUST2 model in this region. We are also doing the same for the Weston Geophysical India and Pakistan 3D model (WINPAK3D).

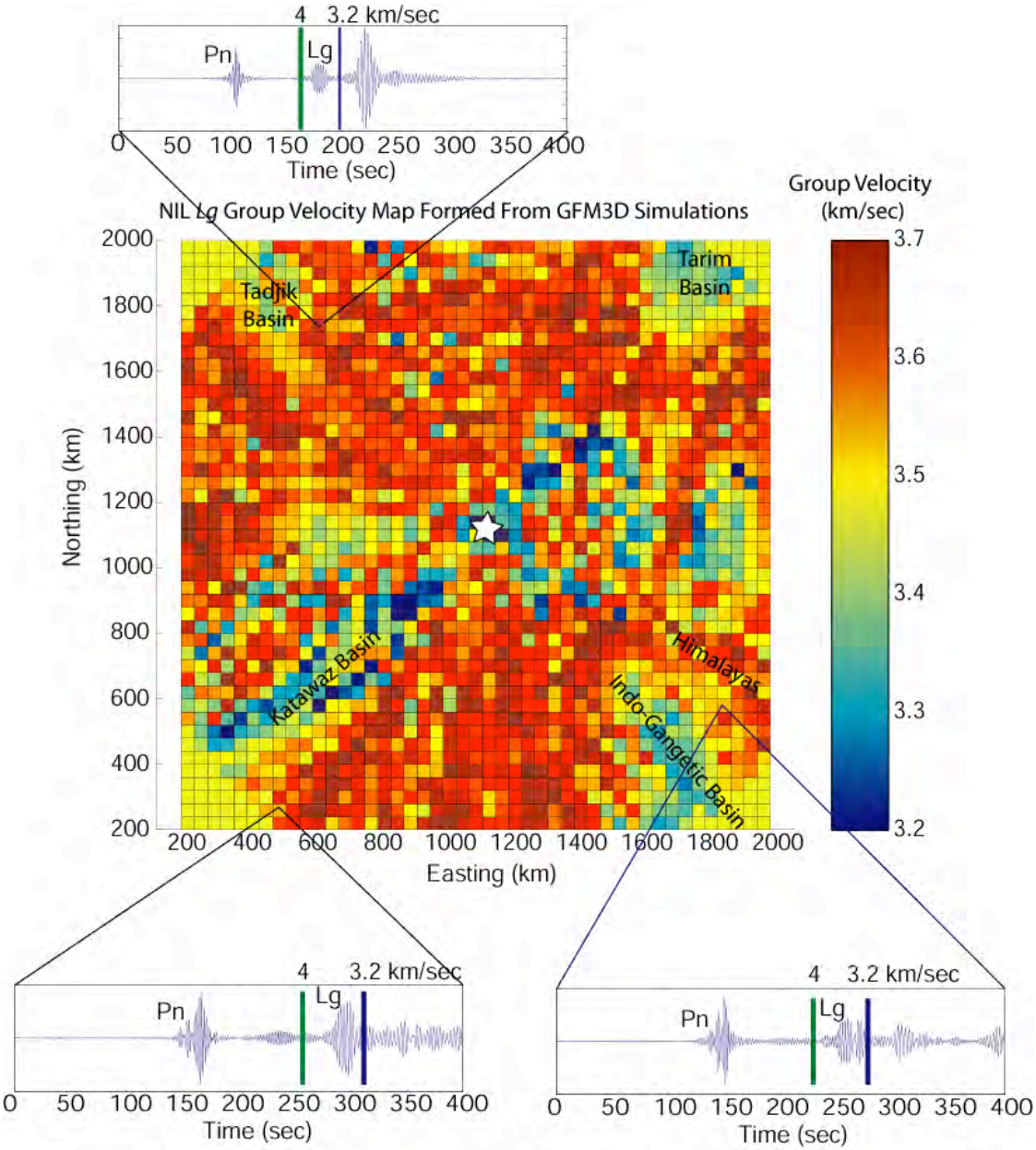


Figure 4. Results of *Lg* group velocity estimation from GFM3D synthetics for NIL. Example synthetics are shown for three randomly picked stations in the model. A group velocity window between 4 and 3.2 km/sec is shown. The *Lg* onset ranges from impulsive to emergent, which is similar to the phase as observed on regional seismograms.

GFM2D Modeling of the Effects of Basins on *Lg* and *Rg* Generation from Explosions. To study the effect of different tectonic features on the generation and propagation of surface waves and *Lg*, we generated synthetic waveforms using GFM2D for a range of models and source depths. For this component of the study, we used the EK model in which we embedded various elements such as basins, a rift and a crustal root. Some models included a thin low velocity layer at the top, with the *P*-wave velocity lower than the upper mantle *S*-wave velocity (termed Ekl). The simulations were performed in a 600x200 km 2D grid with 0.5 km node spacing. The parameters chosen for the basin were calculated as weighted averages of the parameters for soft and hard sediments in CRUST2. Using 20% soft sediments and 80% hard sediments, *P* velocity, *S* velocity and density are 3.7 km/s, 1.92 km/s and 2.34 g/cm^3 respectively. The same parameters were used for the uppermost low velocity layer when the feature was integrated in the model. Variations in Moho depth (referred to as "root" and "rift") were generated by lowering or raising the bottom two boundaries of the EK model crust. Each of the embedded structures extends 5 km in the z direction and 100 km laterally. The boundary of the first basin is at 10 km from the edge of the model and the sources were placed at 30 km from the model end. We performed simulations for sources placed within the basin at 1 and 2.5 km depth and below the basin at 5.5 km depth. All waveforms shown in this section were band-pass filtered between 0.001 and 1.0 Hz in order to avoid numerical artifacts for the synthetics. The effects of source depth, the presence of low velocity basins in the source region, and Moho depth variations are discussed below and shown in Figures 5 and 6.

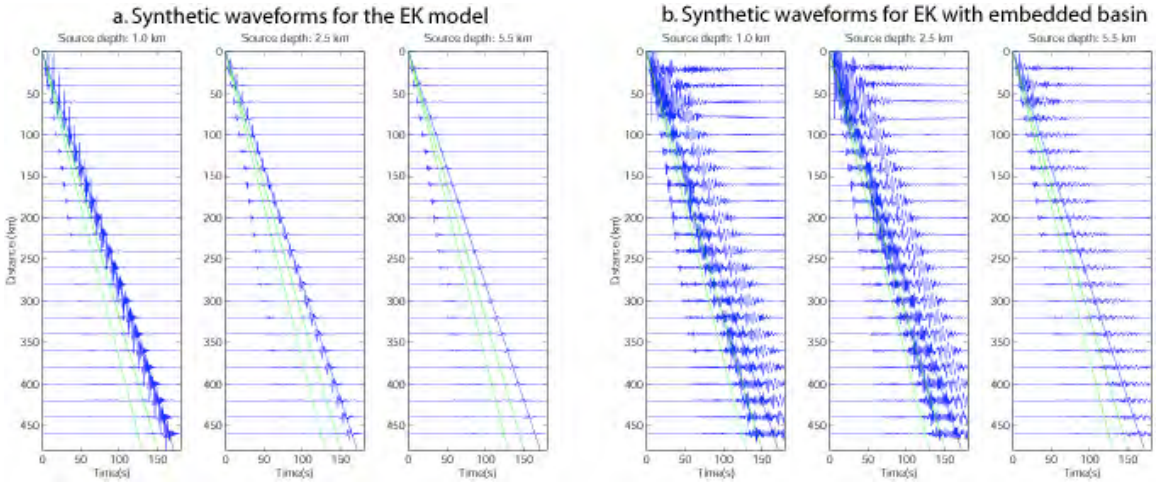


Figure 5. Synthetic seismograms generated for the EK model and a modified EK model with an embedded basin. Times corresponding to 3.7 km/s and 3.2 km/s are marked in green, 2.8 km/s in blue.

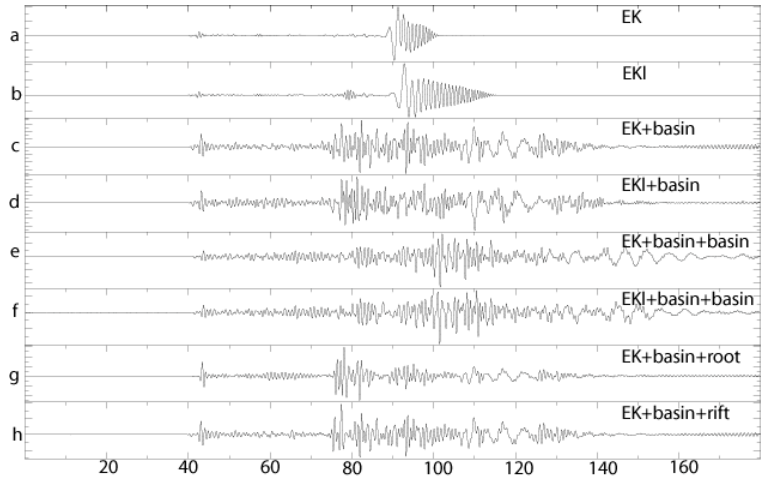


Figure 6. Vertical component synthetic seismograms generated for a range of models based on EK, recorded at 260 km from the source, filtered between 0.01 and 1.5 Hz.

Effect of source depth with an embedded basin. There was little difference in the arrival time characteristics generated for sources at different depths in the basin. However, the amplitude of the primary arrivals and, more drastically, of the *Lg* were increased significantly (Figure 5b) for sources at shallower depths within the basin. Adding more complexity to this structure had little contribution to the source-depth effect.

Effect of structure on generation and propagation. The large amplitude *Lg* generated for sources in the basin propagates beyond the extent of the low velocity structure (in the models used to create Figure 5b, the basin extends to 80 km from the source). There was little difference in the *Lg* window between waveforms generated for the simple EK model with embedded basin (Figure 6c) and the EK model with an uppermost low velocity layer and embedded basin (Figure 6d); however, in the *Rg* window low frequencies are delayed. When the source is placed underneath the basin the amplitudes of the surface waves are greatly reduced compared to those generated for shallow sources (Figure 5b); in this case the presence of a low velocity uppermost layer has a more notable effect. A crustal thickening next to the basin (Figure 6g) shifts more energy into the earlier part of the *Lg* window while the presence of a second basin below the receiver has the opposite effect (Figures 6e and 6f) . Thinning of the crust (Figure 6h) below the basin has little effect on generation and propagation. We will continue modeling the effects of common tectonic structures on the generation and propagation of *Rg* and *Lg*.

GFM2D Modeling of the Regional *Lg* from the DOB Explosions. We performed a final test of the capabilities of GFM2D by modeling the *Lg* generated from the DOB explosions at regional distances. Our initial model for this evaluation was the Eastern Kazakhstan (EK) model of Priestley *et al.* (1988), which was used in the Xie and Lay (1994) paper on *S*-wave generation using finite-difference modeling. The model was converted to GFM2D format and is 514 km long and 171 km deep, with a grid spacing of 0.5 km. It should be noted that the EK model has a *P*-wave velocity in the upper crust of 5.05 km/s, which was greater than the mantle-lid velocity of 4.57 km/s. Some authors (e.g., Frankel, 1989) have noted that for these *P*- and *S*-wave velocities, it is impossible to trap *S*-waves in the crust to form the *Lg* phase. Our synthetics from the EK model agree with this interpretation, as the energy in the *Lg* group velocity window was composed of very weak *S** arrivals.

To provide a comparison with the EK model, we then generated synthetics for the Shagan+EK model. The local *Rg* recorded at the Shagan test site for these explosions suggests that the near-surface *P*-wave velocities are less than 4.8 km/sec, which is the mantle-lid velocity in the EK model. Thus, in accordance with Frankel (1989) and Xie and Lay (1994), the Shagan+EK model should be suitable for trapping shear-waves in the crust with the appropriate *Lg* group velocity. The GFM2D synthetics in Figure 7 show significant energy in the *Lg* window for this model. For a grid spacing of 0.5 km, the *P*-waves are accurate up to ~6 Hz, the *S*-waves are accurate up to ~3 Hz, and the *Rg* is accurate to between 1 and 2 Hz. Figure 7 shows a comparison of both model runs for a single station at 288 km. Clearly, the Shagan+EK model traps more energy in the form of surface *P* to *S* conversions and subsequent multiple reflections than the EK model. The Shagan+EK model also spreads out the surface waves as a result of the low-velocity shallow layers; however, if intrinsic attenuation were considered in the GFM2D runs, these later-arriving higher-frequency surface waves would most likely be attenuated below the noise level.

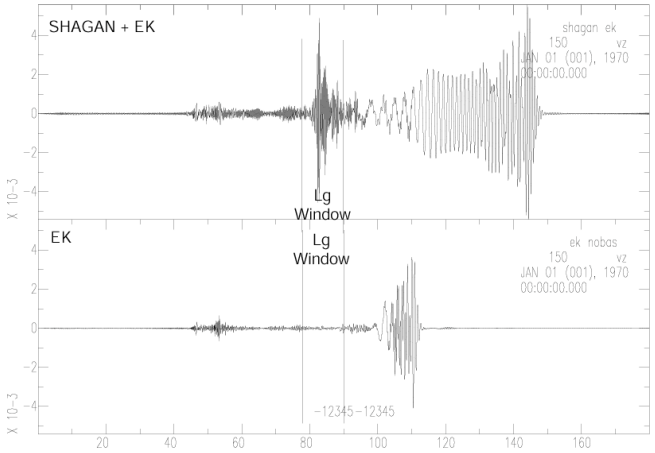


Figure 7. Comparison of SHAGAN+EK synthetics vs. EK only synthetics at X=288 km.

We used the Shagan+EK velocity model to synthesize the seismograms for the DOB explosions at station MAK. Explosion point sources were buried at 50 m, 300 m, and 550 m within the model. Then, GFM2D was employed to generate 200 seconds of data recorded at stations that were 421 km (MAK) from the sources. The synthetic data were then convolved with a Mueller-Murphy source (Mueller and Murphy, 1971) determined using the depth of each shot and the Shagan+EK model. A comparison of observed and synthetic *Lg* spectra is presented in Figure 8. Between 0.7-3 Hz, the relative *Lg* spectral amplitudes for the observed and synthetic data, as normalized to the 50 m explosion at 1 Hz, are similar, even when we consider the fact that the shallow explosion created a large crater. We observe that the shapes of the spectra have disparities. First, below 0.7 Hz, the observed data contains microseismic noise that boosts the amplitudes while the synthetic data is noiseless at these frequencies. The differences between the synthetic spectra at frequencies below 0.7 Hz are related to the addition of the Mueller-Murphy source component. Second, the synthetic spectral amplitudes decrease at a greater rate than the observed spectra between 1-3 Hz, possibly due to the large spectral null around 2.3 Hz. We see smaller nulls in the observed spectra for the DOB explosion followed by an increase in amplitudes. These results suggest that a significant proportion of the *Lg* amplitudes observed at station MAK may be explained as the effect that different source depths have on the amplitudes of the *P* to *S* surface reflection above the source. The remaining differences may be related to the effects of the CLVD source and near-source scattering of *Rg* to *S*. Figure 9 presents the *Pg/Lg* amplitude ratios for the synthetic and observed MAK data. For the observed data between 1 and 3 Hz, the 550 m explosion had the largest *Pg/Lg* ratio, followed by the 50 m explosion and the 300 m explosion. We observe the same order for the synthetic data, however there is a significant offset, possibly due to significant *Rg*-to-*P* scattering in the observed data (Gupta *et al*., 1991).

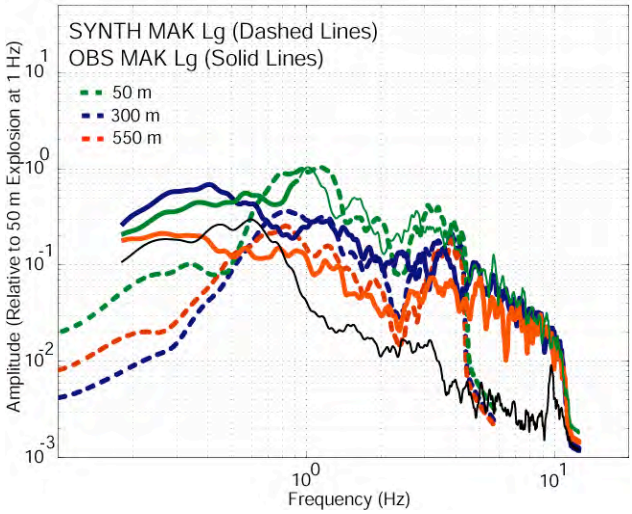


Figure 8. Displacement spectra for observed *Lg* (solid lines) and synthetic *Lg* for station MAK for the 50 m, 300 m, and 550 m DOB explosions at the Shagan Test Site. Also shown is the noise level at MAK (solid black line) for the same day that the 50 m explosion was detonated. The data have been normalized to the 1 Hz spectral amplitude of the 50 m explosion.

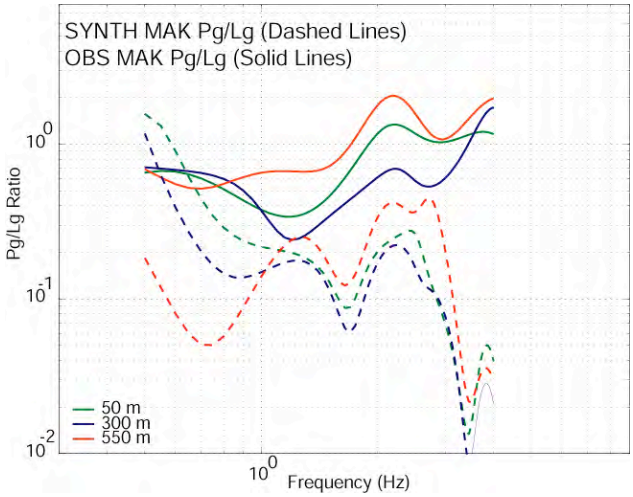


Figure 9. *Pg/Lg* ratios (observed=solid; synth=dashed) for the MAK DOB data.

CONCLUSIONS AND RECOMMENDATIONS

It is critical that a physical model for the genesis of regional *S* waves be well understood for underground explosions. One possible mechanism of generating *S* waves is by *Rg*-to-*S* scattering in which *Rg* waves are excited by a spatially-distributed source composed of the explosion and an inverted conical zone undergoing catastrophic shear failure above the dilatational point source. This conical source is equivalent to a compensated linear vector dipole (CLVD), which has been used to explain the frequency content of *Lg* spectra and spectral ratio observations for nuclear explosions (Patton and Taylor, 1995; Gupta *et al*, 1997). Observations of the *Rg* amplitude and phase spectra presented in this paper cannot be modeled adequately by a pure explosion monopole source for any DOB explosion, including the overburied 550 m explosion with sDOB of 1400. Thus, we are now examining whether a linear superposition of a monopole and a CLVD source can be used to improve the fit to the observed spectra.

We have observed that GFM modeling can provide improved understanding of the genesis of explosion-generated *S*-waves using 2D and 3D simulations. We have completed 3D simulations of *Lg* and *Rg* generation in 3D structures for NIL, and we have used the modeling to estimate the velocities for these phases. Additionally, we have used 2D GFM simulations to examine the effects of basins, crustal roots, and crustal thinning on the genesis of *Lg* and *Rg*. GFM simulations showed the EK model derived synthetics do not exhibit shear waves (e.g., *Sn* and *Lg*) similar to those observed from the Shagan Test Site DOB explosions; however, by attaching the shallow velocity structure determined from *Rg* inversions at the Shagan Test Site to the EK model, large amplitude shear-wave arrivals (both *Sn* and *Lg*) can be trapped within the crust. The arrivals in the *Lg* window consist of multiple-reflected *S*-waves resulting from the initial conversion of *P* to *S* at the free surface above the source. Synthetics generated by convolving GFM2D Green's functions with a Mueller-Murphy source at different depths can account for as much as 80% of the observed amplitude differences in the 1-3 Hz bandwidth at station MAK; however, differences in the shape of the spectra may result from the fact that the explosions were not pure monopoles. The *Pg/Lg* ratios observed from the MAK data are consistent with the synthetic data in terms of order as a function of DOB; however, the relative synthetic *Pg* amplitudes are smaller than the observed amplitudes.

REFERENCES

Bassin, C., G. Laske, and G. Masters (2000), Current limits of resolution for surface wave tomography in North America, *EOS Trans AGU*, **81**, F897.

Bonner, J.L., D.C. Pearson W.S. Phillips, and S.R. Taylor (2001), Shallow velocity structure at the Shagan Test Site in Kazakhstan, *Pure and Applied Geophysics*, 158, 2017-2039.

Denny, M.D. and L.R. Johnson (1991), The explosion seismic source function: models and scaling laws reviewed, in Taylor, S.R., H.J. Patton, and P.G. Richards, Eds. Explosion Source Phenomenology, American Geophysical Union Monograph 65, 1-24.

Frankel, A. (1989), Effects of source depth and crustal structure on the spectra of regional phases determined from synthetic seismograms, *DARPA/AFTAC Annual Seismic Research Review* FY 89, Air Force Technical Applications Center, Scientific Report, 97-118.

Gupta, I. N., W. Chan, and R. Wagner (1992), A comparison of regional phases from underground nuclear explosions at East Kazakh and Nevada Test Sites, *Bull. Seism. Soc. Am.* **82**, 352-382.

Gupta, I.N., T.R. Zhang, and R.A. Wagner (1997), Low frequency *Lg* from NTS and Kazakh nuclear explosions-observations and interpretation, *Bull. Seism. Soc. Am.* **87**, 1115-1125.

Meyers, S.C., W. R. Walter, K. Mayeda, and L. Glenn (1999), Observation in support of *Rg* scattering as a source of explosion S waves: regional and local recordings of the 1997 Kazakhstan depth of burial experiment, *Bull. Seism. Soc. Am*. **89**, 544-549.

Mueller, R.A., and J.R. Murphy (1971), Seismic characteristics of underground nuclear detonations, *Bull. Seism. Soc. Am*., **61**, 1675-1692.

Orrey, J. L., C. B. Archambeau and G. A. Frazier (2003), Complete Seismic Wave Field Synthesis with a Pseudospectral Method: The Generalized Fourier Method, revised manuscript submitted to *Geophys. J. Int*.

Patton, H.J., and S. R. Taylor (1995), Analysis of *Lg* spectral ratios from NTS explosions: implications for the source mechanisms of spall and the generation of *Lg* waves, *Bull. Seism. Soc. Am.* **85**, 220-236.

Priestley, K. F., G. Zandt, and G. E. Randall (1988), Crustal structure in Eastern Kazakh, USSR from teleseismic receiver functions, *Geophys. Res. Lett.*, **15**, 613-616.

Xie, X. and T. Lay (1994). The excitation of *Lg* waves by explosions: a finite-difference investigation, *Bull. Seism. Soc. Am*., **84**, 324-342.

ENERGY PARTITIONING FOR SEISMIC EVENTS IN FENNOSCANDIA AND NW RUSSIA

Hilmar Bungum,[1] Tormod Kvaerna,[1] Svein Mykkeltveit,[1] Michael Roth,[1], Ketil Astebol,[1]
David B. Harris,[2] and Shawn Larsen[2]

NORSAR[1] Lawrence Livermore National Laboratory[2]

Sponsored by National Nuclear Security Administration
Office of Nonproliferation Research and Engineering
Office of Defense Nuclear Nonproliferation

Contract No. DE-FC03-02SF22636/A000[1] and W-7405-ENG-48[2]

ABSTRACT

We have started a project to study the generation of seismic shear waves by explosions. The plan is to analyze data from close-in stations in mines to measure seismic waves within a few hundred meters of the explosions. We will combine these data with data from regional stations (out to several hundred kilometers) to characterize the mechanism of shear wave generation as a function of distance from the mine. Three-dimensional numerical (finite difference) simulations of wave propagation (full waveform) within the mines will be compared to the data taken in the mines as an aid to interpretation.

Cooperation has been established with the operators of the Pyhasalmi mine in Finland, where a new in-mine network of 16 sensors has been installed (4 three-component and 12 vertical-component geophones). For the 1500 m deep Pyhasalmi mine there exists comprehensive and detailed information on the mine geometry in digital form. This information has been utilized to build up a model of the mine, using the NORSAR 3D Model Builder. The result is a three-dimensional gridded model which includes the velocity and density characteristics of the ore bodies, mined-out voids, access tunnels and surrounding rocks. An initial three-dimensional finite-difference calculation has been performed for an explosive source in the mine model and, for comparison, similar calculations have been made for a homogeneous model. These preliminary results indicate that near-source heterogeneities, like voids from the mined out region and low velocity backfilled material, play an important role in shaping the seismic wavefield.

Since the installation of the Pyhasalmi in-mine network in November-December 2002, numerous microearthquakes and explosions have been recorded and located. NORSAR has obtained both bulletin and waveform data for these events, and we have started to investigate these data in more detail for the purpose of studying the development of the seismic shear waves.

A particularly interesting event occurred in the Pyhasalmi mine on 26 January 2003. This was a felt rockburst, with magnitude of about 1.0, which was also detected and located by the Finnish National Network operated by the University of Helsinki. Our plan is to use this event for validation of the wavefield modelling, as well as for more detailed analysis of the energy partitioning within the mine network, and at local and regional distances.

OBJECTIVE

The main objective of this project is to increase the (nuclear) explosion monitoring effectiveness through improved understanding of basic earthquake and explosion phenomenology. What this entails in essence is detailed characterization and understanding of how the seismic energy is generated from these phenomena (including simple and complex explosions, rockbursts, i.e. stress release in mines, and ordinary tectonic earthquakes, all at different depths and in different geological environments) and how this energy is partitioned between P and S waves.

Specific important questions here are:

- How is the generation and partitioning of seismic energy affected by properties such as source region medium and overburden, the local structure, and the surrounding tectonic structure?

- What are the significant measurable effects of the partitioning of the seismic energy into various regional P and S phases, especially at higher frequencies?

- What is the physical basis for a measurable property, such as magnitude, that can be directly related to the yield of a fully coupled explosion, and how emplacement conditions effect the observations?

RESEARCH ACCOMPLISHED

Introduction

This project is a three-year effort that started on 30 September 2002. The project is a collaboration that involves NORSAR (as the lead organization) and Lawrence Livermore National Laboratory (LLNL). This work addresses the generation of seismic shear waves by explosions. Example explosions at two mines, one in Sweden and the second in Finland, will be studied to determine where shear waves originate. The mines operate close-in stations that measure seismic waves within several hundred meters of the explosions. We will combine these data with data from regional stations (out to several hundred kilometers) to constrain the source of shear waves by range from the mine. Three-dimensional numerical (finite difference) simulations of wave propagation (full waveform) within the mines will be compared to the data taken in the mines as an aid to interpretation. These same calculations will be used as initial conditions for two-dimensional calculations. These secondary calculations will extend the numerical simulations to regional distance for comparison with more distant observations.

Mine model and 3-D finite difference calculations

Using the NORSAR 3-D Model Builder (Vinje et. al., 1999), we have completed an initial velocity model for the Pyhäsalmi mine in Central Finland, using a 4 meter equidistant grid. The three-dimensional model is visualized in Figure 1, where green represents copper ore, grey represents zinc ore, and purple and red represent backfilled material. Based on generally available information on typical seismic velocities of different rock types, combined with measurements of the rock densities, the properties given in Table 1 were initially assigned. For the surrounding rocks, having a density of about 2.8 g/cm^3, Gardners relation was used to estimate the P-velocity. The standard $\sqrt{3}$ P/S velocity ratio was then used for estimating the S-velocity.

The gridded mine model was provided to LLNL for 3-D finite-difference calculations of the seismic wavefield, and the data format used for model exchange worked well. Very preliminary results from the modelling (Larsen and Schultz, 1995) are shown in Figures 2-4, demonstrating that the modelling work at NORSAR and the wavefield simulations at LLNL now are ‘connected’, and that we now have the capability to do our required modelling.

The gridded model is represented by a 126x126x126 grid at 4 m spacing (i.e., 500 m on a side), with an explosive point source set near the center of the model. The source frequency is about 50 Hz (due to the coarseness of the model), and the simulation covers a duration of 0.25 s. The center of the gridded model is located in the middle of the zinc and copper ore bodies in the lower part of the mine, in the depth range 950 - 1450 meters (see Figure 1).

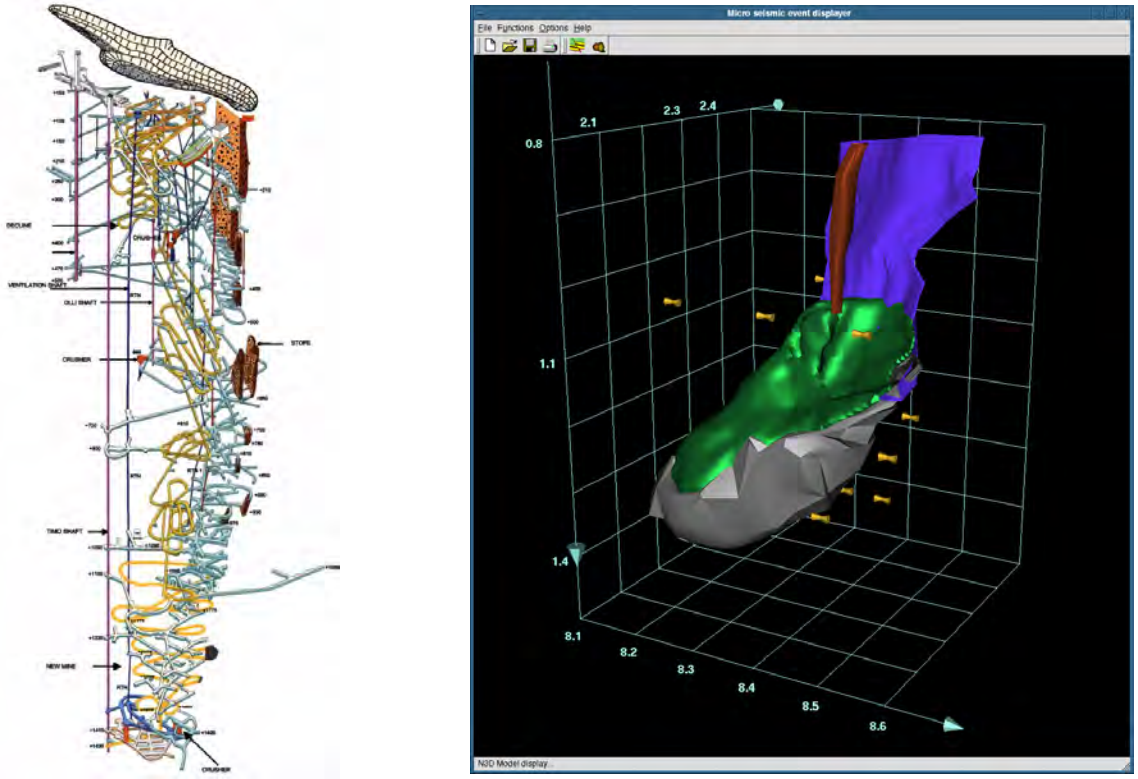


Figure 1. The left-hand part of the figure shows the shafts and access tunnels of the Pyhasalmi mine from the surface down to a depth of 1500 meters. The right-hand part of the figure shows a three-dimensional model of the mine, for the depth range 800 - 1500 meters. Green represents copper ore, grey represents zinc ore, and purple and red represent backfilled material. Material properties assigned to the different rock types are given in Table 1. The locations of the in-mine monitoring network are indicated by the yellow symbols.

Table 1: Initial material properties assigned to the Pyhäsalmi mine

Rock type	Density (g/cm^3)	P-velocity (km/s)	S-velocity (km/s)
Copper ore	4.6	7.39	4.59
Zinc ore	4.2	5.54	2.89
Backfill	1.8	2.66	1.54
Surrounding rocks	2.8	3.84	2.22
Voids, represented as water	1.0	1.48	0.00

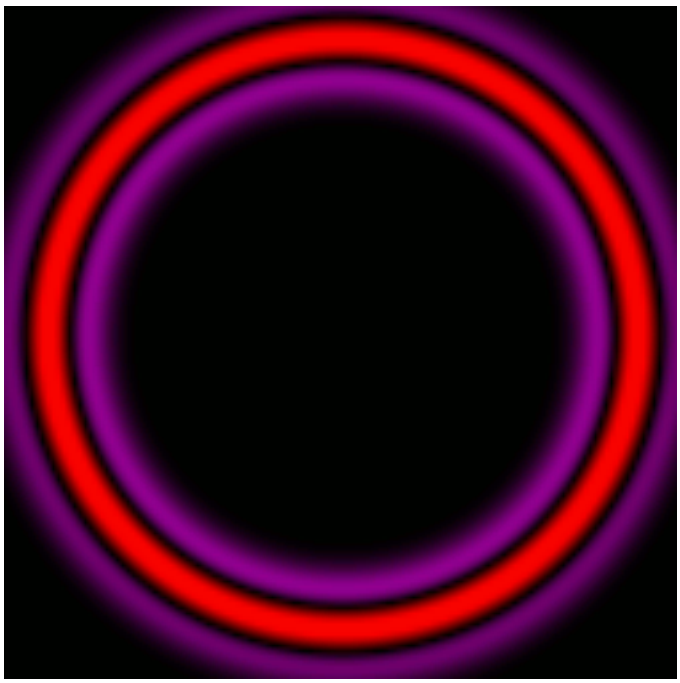


Figure. 2. The image shows a snap shot of the wave propagation in a vertical cross section cutting through the center of the model, using a homogeneous model, at a time of 0.0875 s. The red and blue-red colors represent compressional energy.

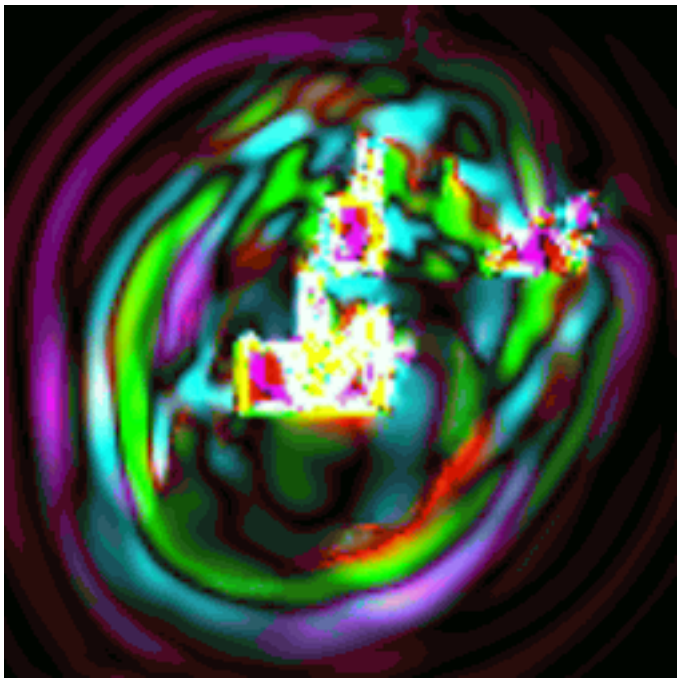


Figure 3. The image shows a snap shot of the wave propagation in the same vertical cross section as in Figure 2, but now calculated using the mine model. Again red and blue-red colors represent compressional energy, while green and blue-green colors mean shear energy.

When comparing the wavefield simulations in the mine model (Figure 3) with the simulations in the homogeneous model (Figure 2), we find that the simulated wave field is significantly perturbed when the mine model is included, and there is a significant conversion of compressional energy to shear energy in the near source region. As expected, the homogeneous model did not provide any shear energy for an explosive point source.

A different type of presentation of the modelling results is shown in Figure 4, where the vertical component of ground velocity and the shear potential for both simulations are shown at a point near the top of the model that is directly above the source. Again, the significant conversion of compressional energy to shear energy is observed.

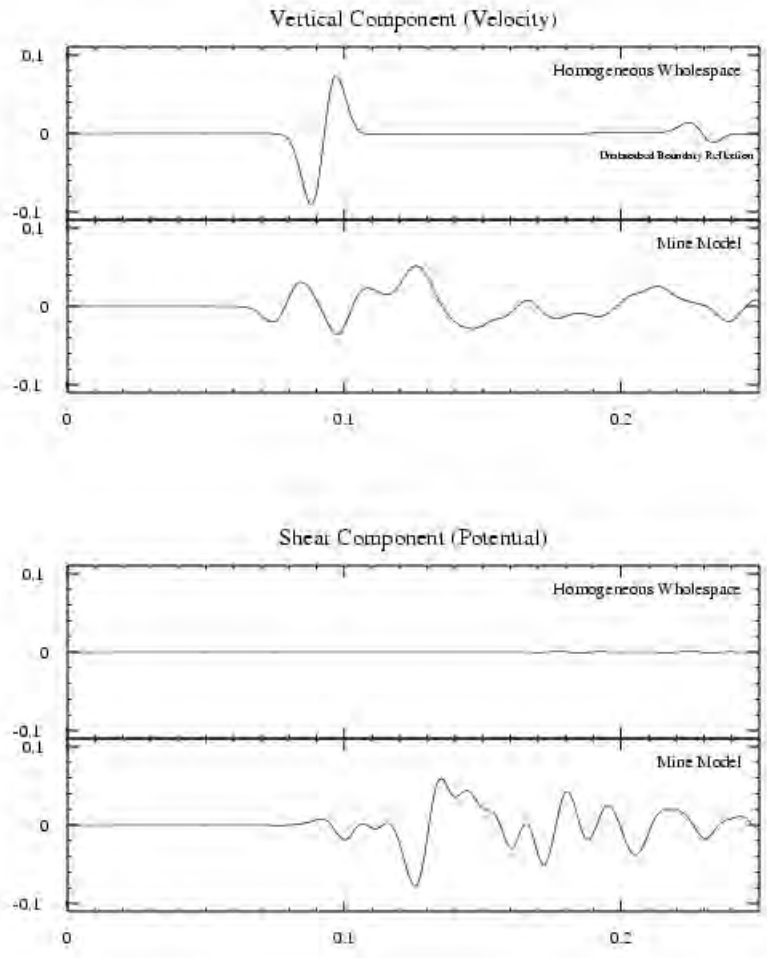


Figure 4. The top panel shows the vertical component of ground velocity for both simulations at a point near the top of the model that is directly above the source. The lower panel shows the corresponding shear potential at the same receiver point.

Collection and analysis of in-mine recordings

An in-mine seismic network became operational in the Pyhäsalmi mine during November-December 2002. The installed network is an ISS (Integrated Seismic System) system, manufactured in South Africa, consisting of 16 sensors, out of which 4 are three-component and 12 are single-component vertical.

At the end of each month we have received bulletin and waveform data for the microseismic events located by the ISS system in the Pyhäsalmi mine. In addition, we have for a couple of one-week intervals also received waveforms for all mining explosions (mainly ripple-fired). All waveforms have been converted to CSS 3.0 format at NORSAR.

In order to analyze the Pyhäsalmi in-mine data at NORSAR, we have extended our in-house microseismic monitoring software package, called MIMO, initially written for analysis of microseismic events in oil and gas reservoirs. The extensions include reading of CSS 3.0 format data, handling of a general network configuration with both three-component and single component data, as well as handling of variable sampling rate at the different sensors. All extensions are not yet completed, but functions for waveform display, phase detection, event association, onset time estimation, and polarization analysis are in place.

As an example, we show in Figure 5 waveforms and fully automatic processing results for a ripple-fired explosion in the mine. At this time, one three-component and one single-component sensor were disconnected from the Pyhäsalmi ISS system due to their proximity to ongoing mining activity. The left panel shows a time segment of about 8 seconds automatically stored by the ISS system. Signal detections and onset estimates of the P- and S-phases are marked by vertical bars. The results from polarization analysis of the P-phases are displayed in the two uppermost right plots (backazimuths and incidence angles). The three plots below show the automatically located hypocenters in a map view and two cross sections.

For more detailed analysis of these data in terms of energy partitioning, we plan to export the waveforms and associated processing results from the MIMO system in MATLAB format. MATLAB will then be used for measurements like amplitude spectra and spectral differences between P- and S-phases.

The microseismic activity recorded within the Pyhäsalmi mine have magnitudes usually ranging between -2.5 and 0, and thus they are not observable at other seismic stations in Finland. However, on 26 January 2003 a larger rockburst occurred in the mine, having an estimated magnitude of about 1. This felt event was caused by a pillar collapse and minor damages could be observed within the mine. The corresponding data from the in-mine ISS system is shown in Figure 6, together with the results from polarization analysis of the four three-component sensors. This event was also observed at the network operated by the University of Helsinki, Institute of Seismology, at receiver distances ranging between 92 and 275 km. The seismograms for these stations are shown in Figures 7 and 8. Notice the SNR increase by beamforming at the FINES array (Figure 8) compared to the center element FIA0 of the array.

The 26 January 2003 rockburst is the first event for which we have recordings both in the mine and at local and regional distances. We plan to use this event for validation of the wavefield modelling as well as for more detailed analysis of the energy partitioning.

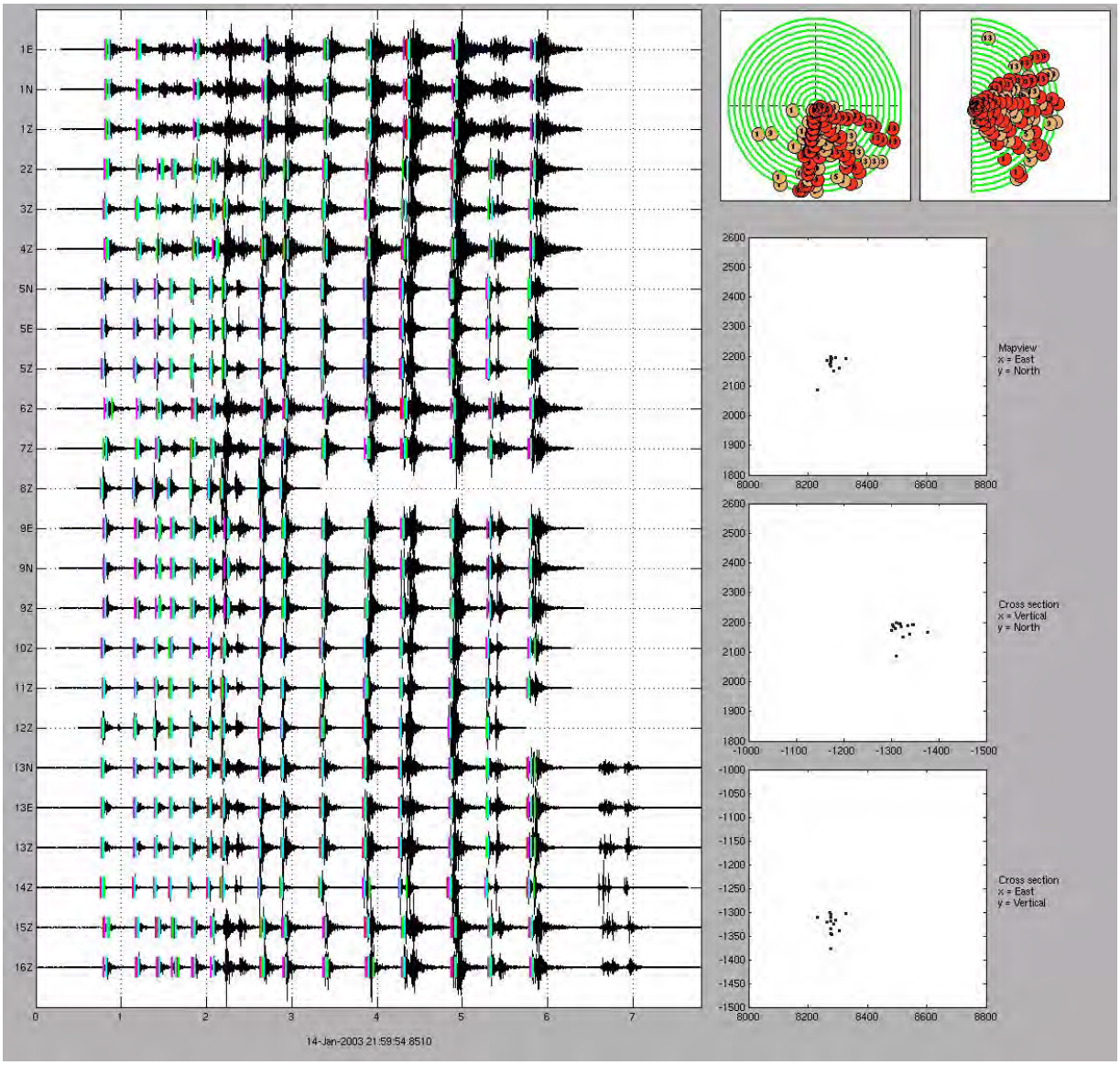


Figure 5. Waveforms and automatic processing results for a ripple-fired explosion in the Pyhäsalmi mine. The left panel shows a time segment of about 8 seconds automatically stored by the ISS system. Signal detections and onset estimates of the P- and S-phases are marked by vertical bars. The results from polarization analysis of the P-phases are displayed in the two uppermost right plots (backazimuths and incidence angles). The three plots below show the automatically located hypocenters in a map view and two cross sections.

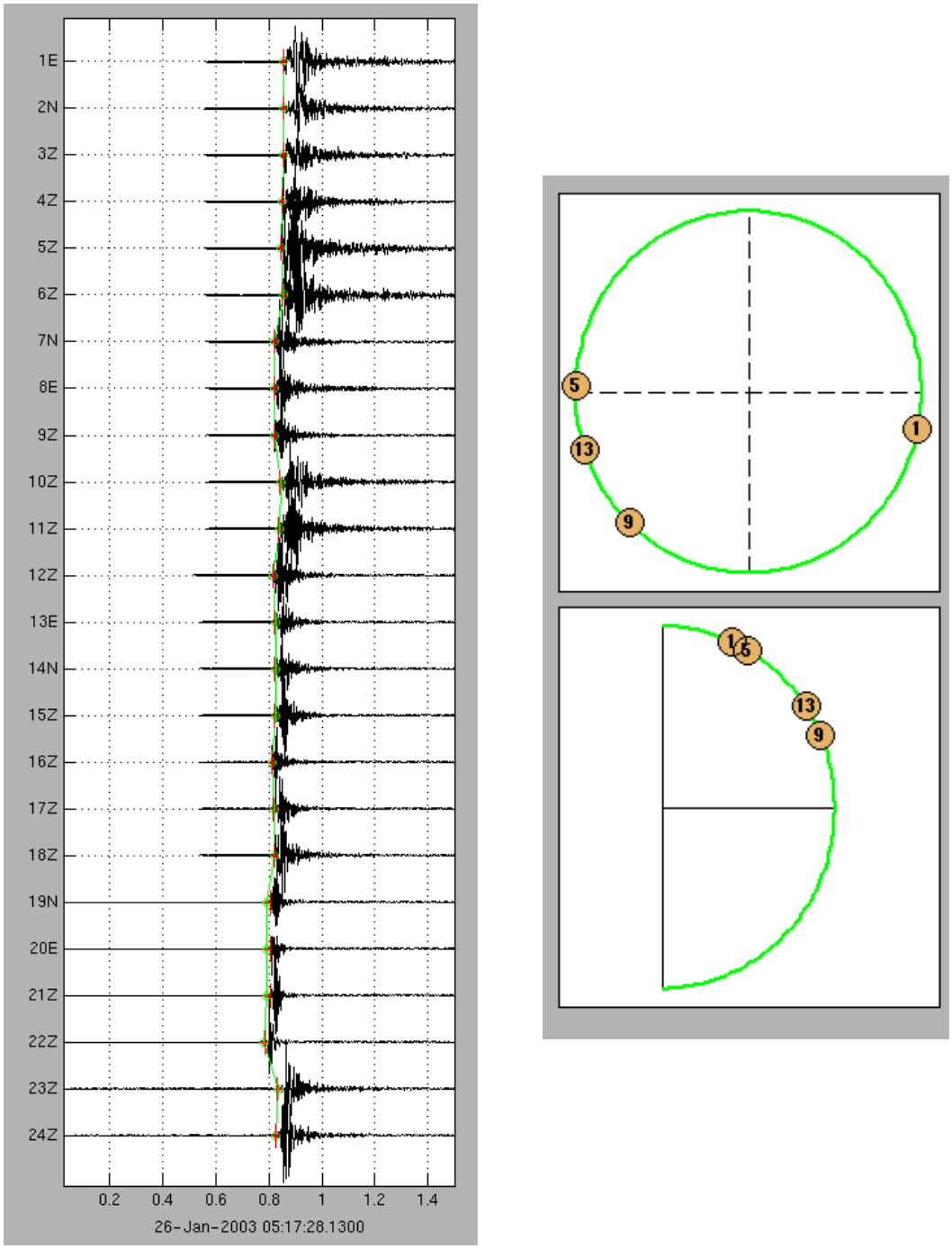


Figure 6. The left panel shows waveforms from all 24 channels of the Pyhäsalmi ISS system for the for 26 January 2003 rockburst. Receiver distances for this event range from 30 to 370 m. The upper plot to the right shows the backazimuth estimates for the four 3-C sensors, and the incidence angles are shown below. The 3-C sensors number 1, 5, 9 and 13 are associated with the channel numbers (1, 2, 3), (7, 8, 9), (13, 14, 15), and (19, 20, 21), respectively.

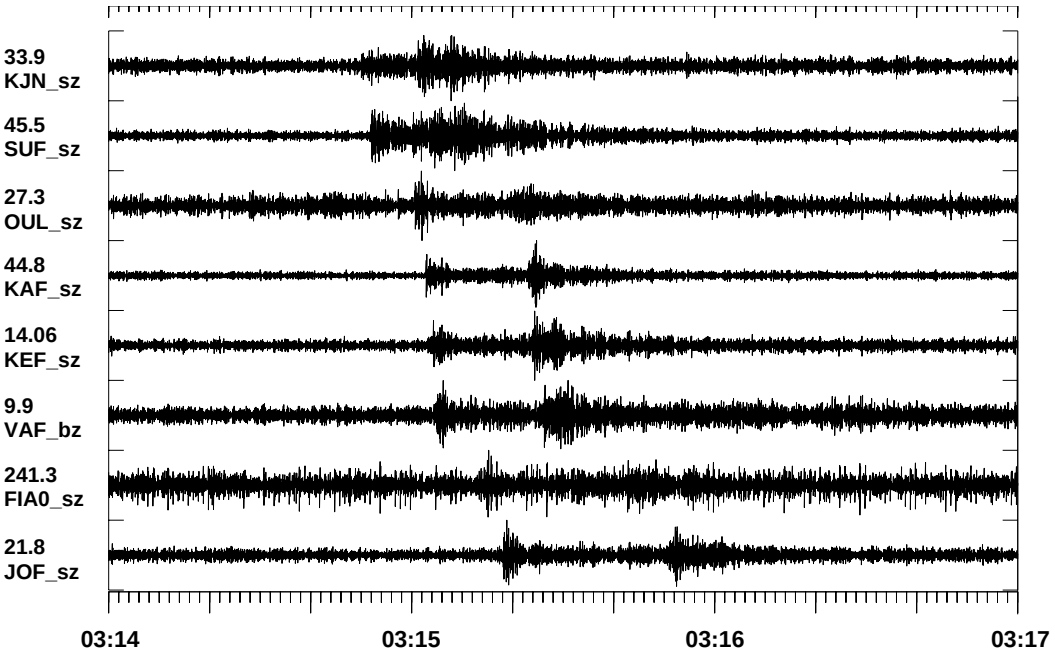


Figure 7. Vertical component recordings at the University of Helsinki network for the 26 January 2003 rockburst in the Pyhäsalmi mine. For KJN_sz the data are bandpass filtered between 6 and 12 Hz, whereas the other traces are filtered between 8 and 16 Hz. FIA0_sz is the center element of the FINES array.

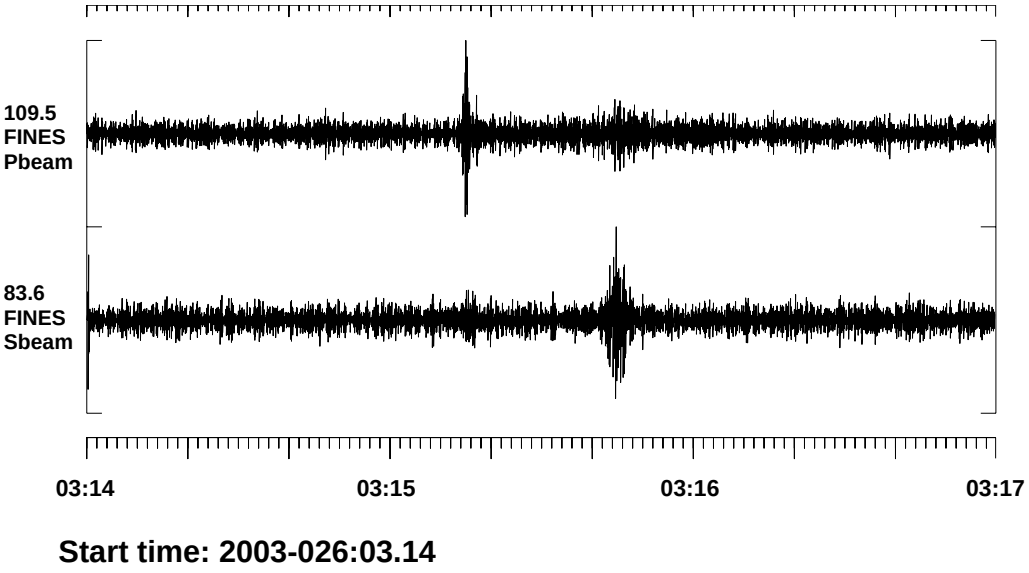


Figure 8. FINES P- and S-beams for the 26 January 2003 rockburst in the Pyhäsalmi mine. The P-beam (azimuth 0 degrees, apparent velocity 8 km/s) is filtered between 6 and 12 Hz, and the S-beam (azimuth 0 degrees, apparent velocity 4 km/s) is filtered between 4 and 8 Hz.

Collection of regional data from explosions and earthquakes

In order to study path effects on energy partitioning, we have, in addition to the 26 January 2003 rockburst, also collected waveform data from the Finnish National Network for five additional events in the Pyhäsalmi area. Information from the University of Helsinki bulletin for these events is shown in Table 2. The magnitude 1.8 event on 24 December 2001 was a large rockburst in the Pyhäsalmi mine that was felt over a large area around the mine.

Table 2: Recent seismic events in the area around Pyhäsalmi

Date	Origin time	Latitude	Longitude	Magnitude	Number of observing stations
1999/01/31	00:33:51.8	63.51	24.81	1.2	9
1999/01/31	08:58:33.5	62.75	26.26	1.2	10
2001/12/24	01:36:18.1	63.68	26.03	1.8	17
2002/04/23	12:18:49.6	64.23	24.81	1.2	9
2002/06/13	09:22:54.4	62.84	27.31	1.9	9
2003/01/26	03:14:34.9	63.67	26.09	0.5	9

CONCLUSIONS AND RECOMMENDATIONS

During the first nine months of the contract period significant resources have been used for data collection and interaction with the mine operators for the purpose of preparing data sets suitable for investigation of energy partitioning. Software tools for analysis of the in-mine data have been written, and we have started to investigate the characteristics of the P- and S-waves for the in-mine data. For the investigation of path effects on energy partitioning, regional data sets have also been collected. Specifically, we have:

- Collected waveform data and bulletin information of both microseismicity and blasts from the Zinkgruvan mine in Sweden for the time interval 1 October to 9 December 2002.

- Collected waveform data and bulletin information of both microseismicity and blasts from the Pyhäsalmi mine in Finland for the time interval 1 January to 30 June 2003.

- Extended and adapted existing software for analysis of waveform data from the Pyhäsalmi and Zinkgruvan mine.

- Identified and retrieved regional data from the stations of the Finnish National Network from events in the Pyhäsalmi area. In addition, NORSAR array data from a set of 11 local and regional events has been made available.

Through initial 3-D finite difference calculations in the Pyhäsalmi mine model, significant conversion of compressional energy to shear energy is found in the near source region. We have to emphasize that these results are very preliminary, and that we have to look more into details like the placement of the source relative to the voids, parameterization of the voids, and the sampling density of the model. However, the results indicate that the near-source heterogeneities, like voids from the mined out region and low velocity backfilled material, may play a significant role in the seismic wavefield.

Our next step will be to calculate the 3-D wavefield for the explosion and rockburst sources, and make comparisons to the in-mine three-component data. We will also take a closer look at the material properties of the mine model, and in particular the velocities of the surrounding rocks. Concerning the study of path effects on energy partitioning, we will analyze the P- and S-waves of the local/regional data sets. This will be accompanied with modelling of P-SV

conversions in 1-D lithospheric profiles using the reflectivity method (Müller, 1985) or 2-D finite difference schemes (e.g., Robertsson et. al., 1994).

REFERENCES

Larsen, S. C., and C. A. Schultz, ELAS3D: 2D/3D elastic finite-difference wave propagation code, *UCRL-MA-121792*, 18 p, 1995.

Müller, G. (1985): The reflectivity method: a tutorial. J. Geophys., 58, 153-174.

Robertsson, J. O. A., Blanch, J. O., Symes, W. W. (1994): Viscoelastic finite-difference modeling. *Geophysics*, 59, 1444-1456.

Vinje V., Astebøl K., Iversen E., and Gjoystdal H., 1999. 3-D ray modeling by wavefront construction in open models. Geophysics, 64, 1912-1919.

DISCRIMINATION STUDIES IN THE YUNNAN REGION, SOUTHWEST CHINA

Wenjie Jiao,[1] Winston Chan,[1] Robert Herrmann,[2] and Robert A. Wagner[1]

Multimax Inc., [1] St. Louis University[2]

Sponsored by Defense Threat Reduction Agency

Contract No. DTRA01-00-C-0068

ABSTRACT

The Lg/Pg ratio has been shown to improve in discriminant performance as the frequency content increases, with frequencies higher than 5 Hz leading to good separation of explosion and earthquake populations in most regions where it has been tested (National Research Council, 1997). Some further studies (e.g., Baumgardt and Schneider, 1997; Rodgers and Walter, 1997; Walter *et al.* 1997) have observed significant variability of regional phase ratios, such as Pn/Lg or Pg/Lg, which are generally powerful regional discriminants. Their characteristics vary significantly from one tectonic or geographic region to another and may also be strongly dependent on frequency (e.g. Baumgardt and Der, 1994). Southwestern China is known to have complex geology with large Q variations (e.g. Qin and Kan, 1986), so that several combinations of distinct source and receiver regions will need to be calibrated. It is important to understand and quantify these differences in order to accomplish improved regional discrimination in a region of complex geology, such as the Yunnan region in southwest China.

The Yunnan region is situated in a transitional tectonic region between the uplifted Tibetan plateau to the west and the Yangtze continental platform to the east. The region displays varying crustal thickness from 35 km to over 60 km with seismic activity strongly associated with the mapped active faults. The Yunnan region also has the strongest seismic zones in China. In this study, we built up a waveform database that consists of over 30,000 waveforms recorded at 23 broadband stations in the Yunnan provincial digital seismic network, as well as waveforms of earthquakes and explosions recorded by some portable arrays. Most of the waveform data have been reduced to absolute ground velocity in m/sec. The digital data so reduced are quality controlled, have their P and S-arrival times picked, and are filtered in narrow frequency bands. Then the spectral analysis is conducted in each frequency band. The scaling of the S energy is studied extensively for distance correction. Vertical component velocity seismograms are used to characterize high frequency S-wave propagation. The signals are processed to examine the peak ground motion and Fourier velocity spectra in the frequency range of 1-12 Hz. Analysis involves a two step process: first, modeling of peak S-wave motions in terms of EXCITATION, DISTANCE, and SITE; and is followed by a parameterization in terms of geometrical spreading, frequency dependent, Q and distance dependent duration. Observations are in the distance range of 30-700 km. The result has provided constraints on the amplitude-distance relation of 1-12 Hz high frequency ground motion in the distance range of 30-600 km in Yunnan, China, and surrounding provinces of China. The Pg/Lg ratio has been found to be a good discriminant in Yunnan region. As a test case of the process, we have successfully screened out an industry explosion with our discrimination analysis.

OBJECTIVE

Introduction

The Lg/Pg ratio has been shown to improve in discriminant performance as the frequency content increases, with frequencies higher than 5 Hz leading to good separation of explosion and earthquake populations in most regions where it has been tested (National Research Council, 1997). For example, in their study of discrimination between NTS explosions and earthquakes, Walter *et al*. (1995) noted improved performance at higher frequencies. Other examples are the regional discrimination study of explosions and earthquakes in the eastern United States and in southern Russia by Kim *et al*. (1993, 1997) who observed significantly improved discrimination capability of the amplitude ratio P/Lg in the 5-25 Hz band than in the lower frequency bands.

Several recent studies (e.g., Baumgardt and Schneider, 1997; Rodgers and Walter, 1997; Walter *et al.* 1997) have observed a significant variability of regional phase ratios, such as Pn/Lg or Pg/Lg that are generally powerful regional discriminants. Their characteristics vary significantly from one tectonic or geographic region to another, and may also be strongly dependent on frequency (e.g., Baumgardt and Der, 1994). Southwestern China is known to have complex geology with large Q variations (e.g., Qin and Kan, 1986), so that several combinations of distinct source and receiver regions will need to be calibrated. It is important to understand and quantify these differences in order to accomplish improved regional discrimination in a region of complex geology, such as southwestern China.

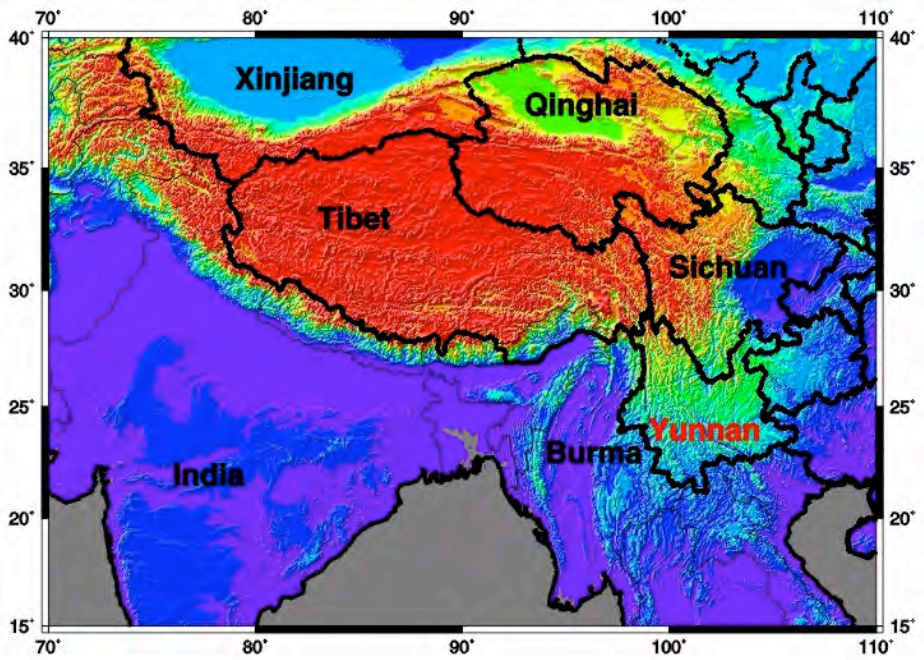


Figure 1. Yunnan and its surrounding area.

Yunnan Province is located at the south segment of the North-South Earthquake Zone in China, close to the Himalaya Orogenic Belt (Figure 1). Tectogenesis is strong in the region. Long and deep earthquake faults crisscross and spread over almost the entire region, and strong earthquakes occur frequently. As one of the most seismogenically active regions in China, western Yunnan is an earthquake prediction experiment field operated by the China Seismological Bureau. There is a well-developed seismic network in the region and a large volume of seismic data has been collected. Considerable efforts have been made on the study of the geological and geophysical features in the region. Wang, et al. (1994) investigated the 3-D velocity structure under Kunming seismic network and found an uplift of the Moho in central Yunnan. They also found that the Red River Fault cuts through the Moho discontinuity. Liu, et al. (1993) studied the 3-D crustal and upper mantle structure in Yunnan and the vicinity and found that there are strong correlation between the upper crustal structure and the topography in the region. Complex crustal velocity structures, including low velocity plume, low velocity layers were also revealed in the study. Lin, et al. (1993) found significant lateral heterogeneity in the crustal structure in western Yunnan based on several DSS profiles. They concluded that the velocity in the crust increases from south to north. Regional seismic characteristics in such an area are of high interest for discrimination studies.

Technical Objectives

The challenge for verification using the International Monitoring System will be to maintain reliable discrimination of small seismic events in diverse regions of the world by using sparsely distributed recording stations. At regional distances, Lg is often the largest seismic phase from both explosion and earthquake sources, and may sometimes be the only reliably observed phase from small events. The ratio of S- to P-wave energy (or Lg/Pn and Lg/Pg for regional data) has so far been found to be the most promising regional discriminant for earthquakes and explosions. Use of broadband data, whenever available, will allow us to investigate how low- and high-frequency data may be combined to enhance regional discrimination. The spectral characteristics of regional phases are known to vary drastically from one region to another. It is therefore important to investigate the variability of regional discriminants in a geologically complex region such as the southwest China. Results of the proposed research will lead to more effective and reliable discrimination of small events in various geological settings.

The objectives of this project include: 1) construction of a digital seismic waveform and ground truth database for southwest China; 2) regional discrimination studies, including location, spectral ratio, regional structure inversion, and structure tomography (combined with other projects); and 3) product delivery. This is the third year of this project. The waveform database has been built and is ready for delivery. A final report is in preparation. This paper is a brief summary of the three years' work. The tomography results are to be presented separately.

RESEARCH ACCOMPLISHED

The Waveform Database

We have constructed a database of digital waveforms recorded by both regional digital broadband network and the portable seismic arrays.

1) Data Recorded at the Regional Digital Broadband Network

There have been propositions from the Chinese central government that in their 1995 Five-Year-Modernization Plan efforts will be made to upgrade the Chinese Digital Seismic Network. Additionally, certain regional analog stations should be upgraded to digital recording format. The Chinese Digital Seismic Network consists of national digital seismic networks, regional digital seismic networks, portable digital seismic networks, regional seismic arrays, and digital strong earthquake networks. A regional digital seismic network has 30 digital broadband seismic stations, including telemetric ones. The bandwidth of the digital broadband seismograph is about 20 sec - 20 Hz (Figure 2). Each seismic station has digital broadband seismographs and short period seismographs with 16-bit data sampling board, data processing, and transfer facilities. The major specifications of the regional digital seismographs are: (1) sensitivity of $1\sim2\times10^{-8}$ m.s^{-1}/LSB; (2) dynamic range greater than 90dB; (3) resolution greater than 2^{-15}, 16-bit; (4) linearity greater than 10^{-3}; and (5) time error less than 1 ms. The center of the regional digital seismic network has the function of seismic data collection, storage, processing, and maintenance.

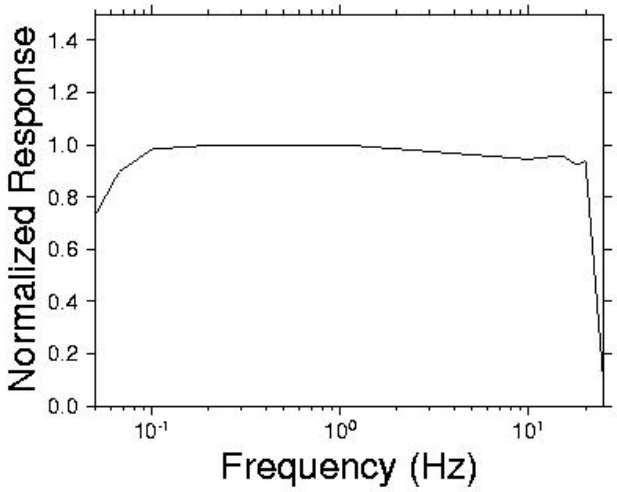


Figure 2. Instrument response of the digital broadband seismographs used in the regional digital seismic network in Yunnan, China.

Twenty-three digital broadband seismographs have been implemented in the Kunming regional digital seismic network in recent years (Figure 3). This network is the first fully functional, regional, digital seismic network in China that provides high-quality continuous 3-componant digital broadband waveform data. The seismographs are velocity recording with a 50-Hz sample rate and 16-bit sampling board. The network has been in operation since 1997 and a large volume of good quality digital seismic data have been collected. Multimax has obtained and examined the digital waveform data for over 900 seismic events recorded by the Yunnan regional digital seismic network. These data are the first time that the high-quality regional digital broadband waveform data from China are available to the U.S. seismologists. Figure 4 shows a comparison of the events recorded at this regional network with those reported by ISC, IDC, and IRIS DMC for the same period. Clearly, the regional network has a much better coverage of the regional seismic events, which are very important for regional seismic studies.

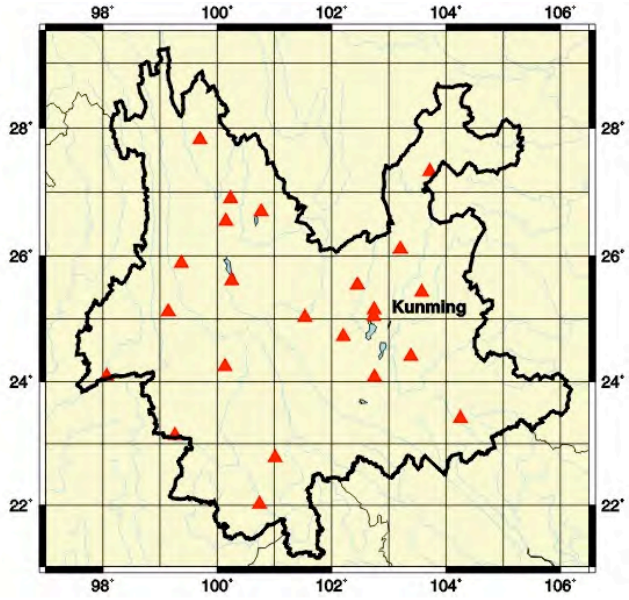


Figure 3. The digital broadband seismic network in Yunnan.

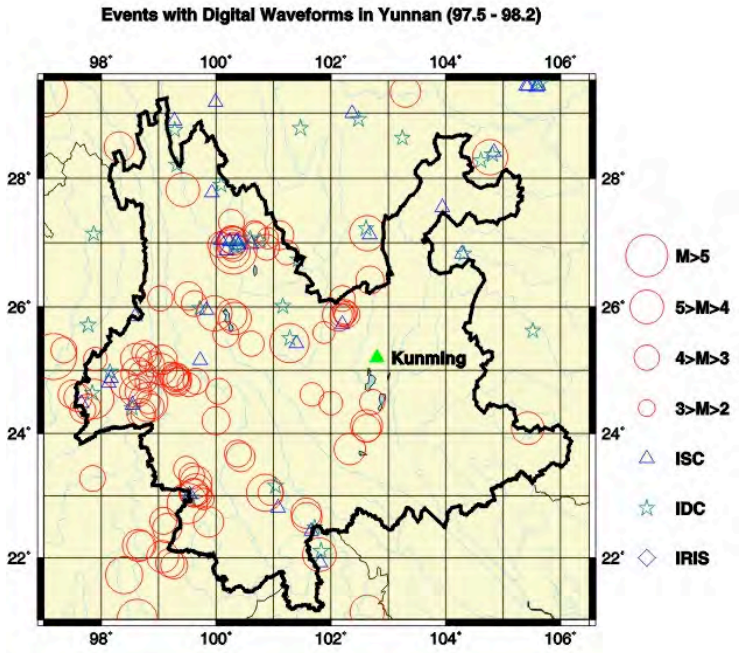


Figure 4. A comparison of the regional events recorded at the Yunnan digital network and those reported in several other global catalogs.

As an example, Figure 5 shows the vertical component of the waveforms recorded by the regional network for a M5.5 local earthquake. A typical 3-component waveform recording for a local event 110 km away is shown in Figure 6. We have established a data retrieval mechanism to access the digital broadband data from the regional digital seismic network through our Chinese collaborators. Over 30,000 waveforms with the same quality have been obtained in this project. There are an abundance of seismicity and mining activities in Yunnan, which provides a valuable data source for the study of regional seismic discriminants.

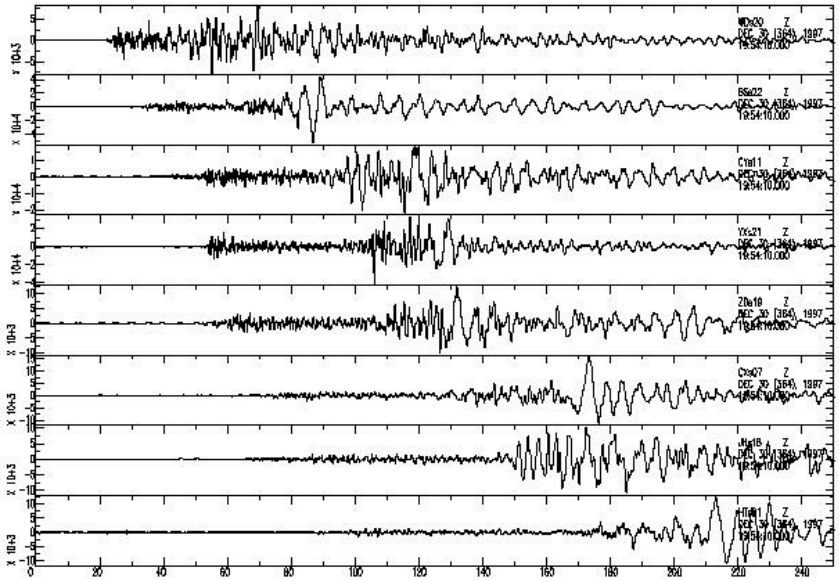


Figure 5. The vertical component of the waveforms of a M5.5 event recorded at the regional digital network.

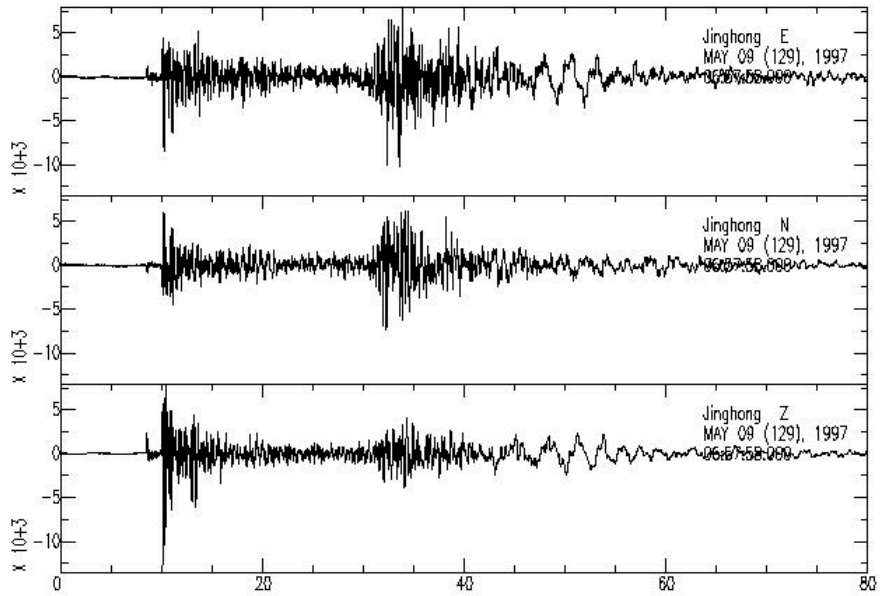


Figure 6. An example of 3 component waveforms of a local event (110 km away) recorded at one station of the regional digital network.

2) Data Recorded by Portable Broadband Arrays

We have also collected the waveform data recorded at 2 portable broadband seismic arrays for 7 underwater or underground explosions and 4 local earthquakes. All explosions are controlled ones in the southwest China, and of about 1,000 kg TNT. Figure 7 shows the waveform of one underwater explosion recorded at the portable broadband array. These

controlled explosion data are high quality ground-truth information. Figure 8 shows the waveform of a local earthquake recorded by a similar portable array in the same area of the explosions. Such data sets provide very good opportunities for discrimination studies.

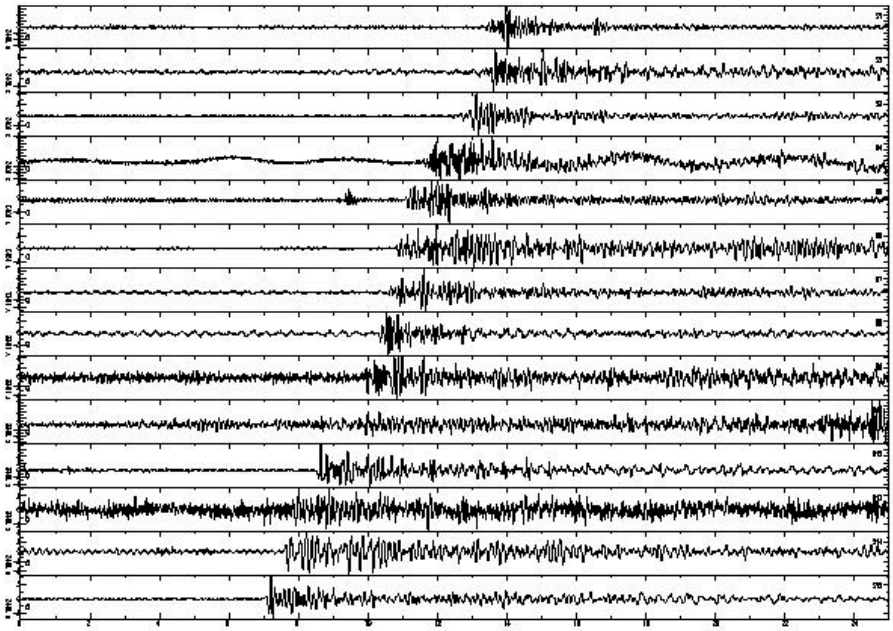


Figure 7. The vertical component of waveforms of an underwater explosion recorded by a portable broadband seismic array.

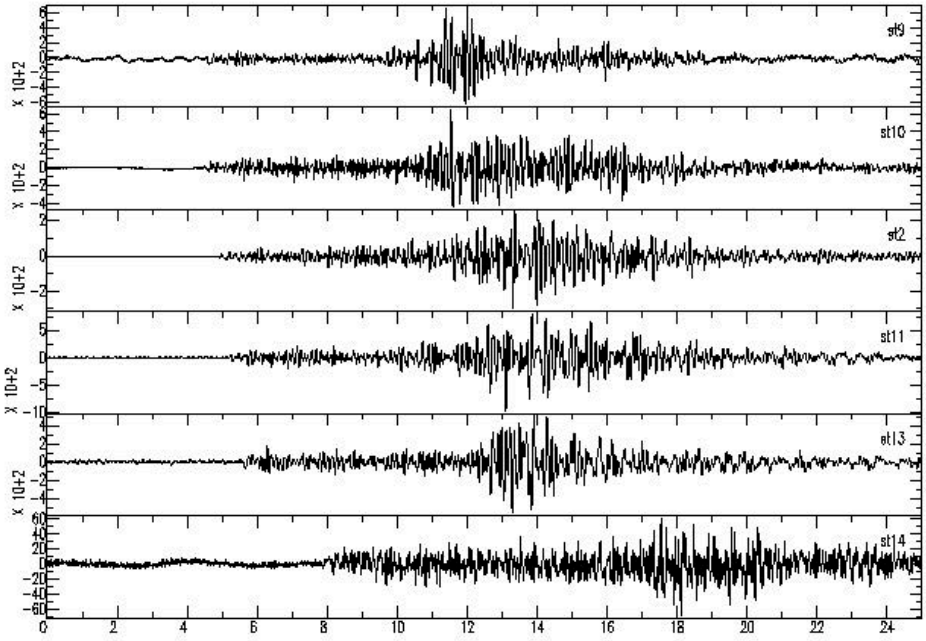


Figure 8. The vertical component of waveforms of an earthquake recorded by a portable broadband seismic array in the same area as the explosion shown in Figure 7.

The Spectral Ratio Analysis

Most of the waveform data have been reduced to absolute ground velocity in m/sec. The digital data so reduced are quality controlled, have their P and S-arrival times picked, and are filtered in narrow frequency bands. Then the spectral analysis is conducted in each frequency band. A table is finally created for further multivariate statistical analysis from each filtered

waveform that contains event–station information, peak filtered motion, smoothed Fourier velocity spectra, duration, and signal envelope information. To give an example of the spectral analysis, the spectral ratio for a local earthquake and a local explosion is shown in Figure 9 and Figure 10, respectively. All the phase picks are also assembled together with other data obtained by Multimax Inc. into a comprehensive bulletin for the region. Figure 11 gives the Pg/Lg spectral ratio for the explosions (red) and the earthquakes (black) recorded at the same array. The separation of the two groups is very good, with only one or two exceptions.

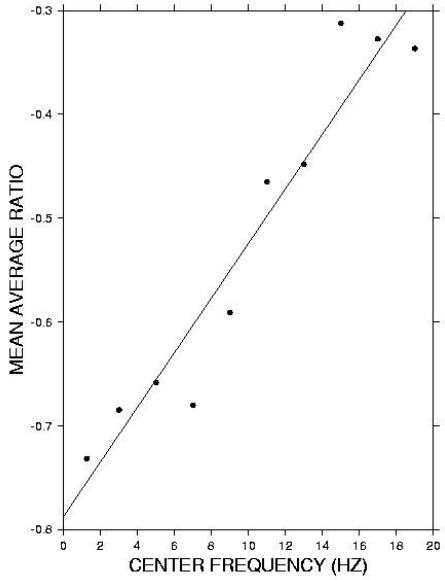


Figure 9. Spectral ratio of Pg/Lg for an earthquake.

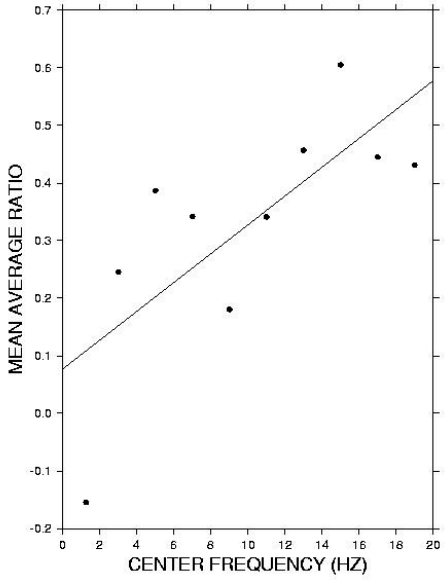


Figure 10. Spectral ratio of Pg/Lg for an underground explosion. Note the difference from the previous figure.

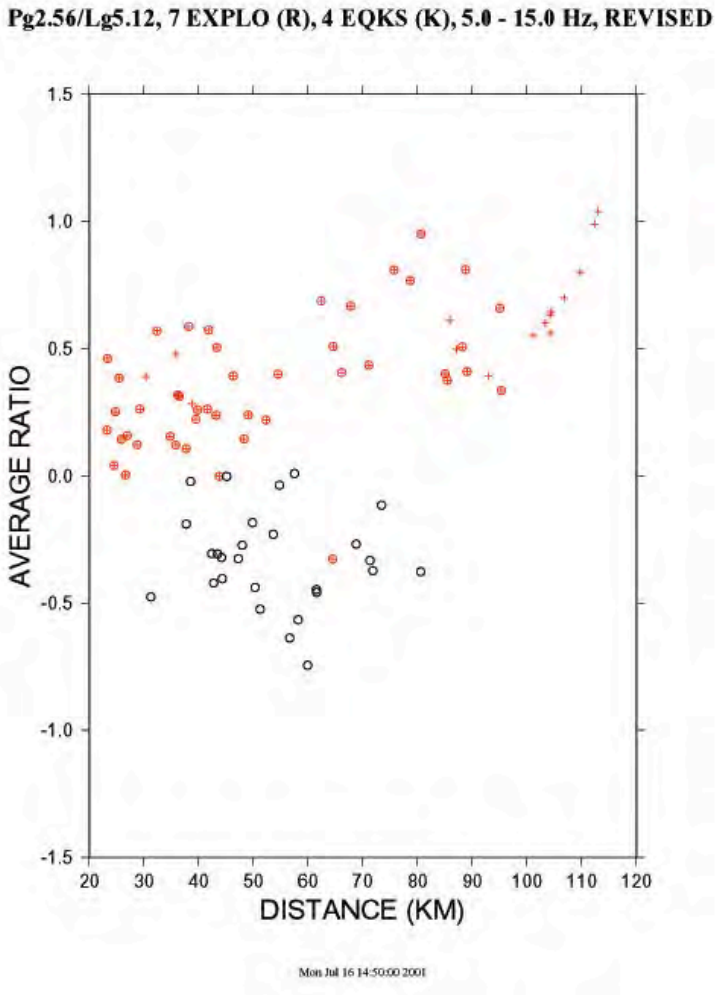


Figure 11. Spectral ratio of Pg/Lg averaged from 5–15 Hz for the explosions (red) vs. that for the earthquakes (black) recorded at the same array

High Frequency Ground Motion Scaling

Vertical component velocity seismograms from Yunnan digital seismic provincial network in Yunnan, China, are used to characterize high-frequency S-wave propagation. The signals are processed to examine the peak ground motion and Fourier velocity spectra in the frequency range of 1–12 Hz. Analysis involves a two-step process: first, modeling of peak S-wave motions in terms of EXCITATION, DISTANCE, and SITE terms; this step is followed by a parameterization in terms of geometrical spreading, frequency dependent Q and distance dependent duration. The data set from 05/97–02/98 and 02/99–01/00 consists of over 6,000 waveforms from 23 stations and 325events. Observations are in the distance range of 30–700km. The data are processed for purposes of defining the parameters needed for the application of Random Vibration Theory to predict high frequency earthquake motions. Figure 12 shows part of the regression results at 1.0 Hz using

$$\log A = D(r) + E(rref) + S$$

where A is observed motion, D(r) is distance term, E(rref) is the excitation term at the reference distance, and S is a site term. D(r) is a piecewise linear continuous function defined by distance nodes, whose frequency dependence is shown in Figure 13. The Fourier ground motion excitation fit is shown in Figure 14.

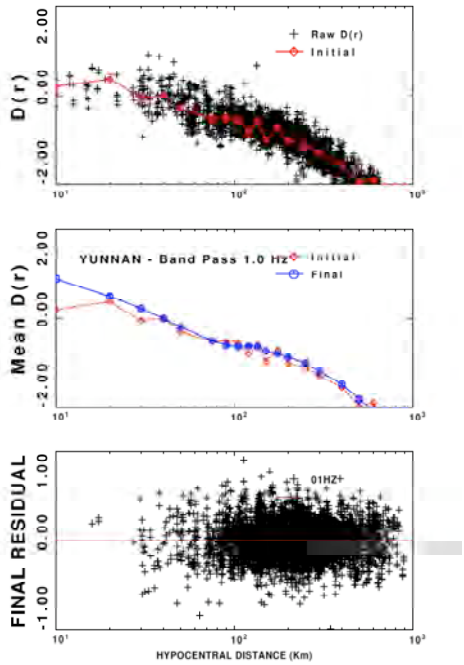


Figure 12. Regression results for processing the peak S motion at 1.0 Hz: Top) Estimate of the D(r) term using the coda normalization technique; Middle) Comparison of coda normalization (red) and regression (blue) results; Bottom) regression residuals as a function of distance. The uniform distribution of residuals and the lack of significant outliers indicate uniform calibration of instruments.

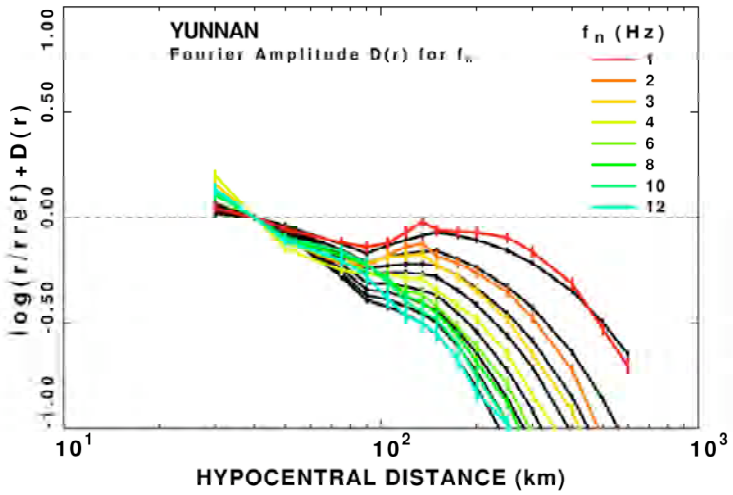


Figure 13. The frequency dependence of D(r).

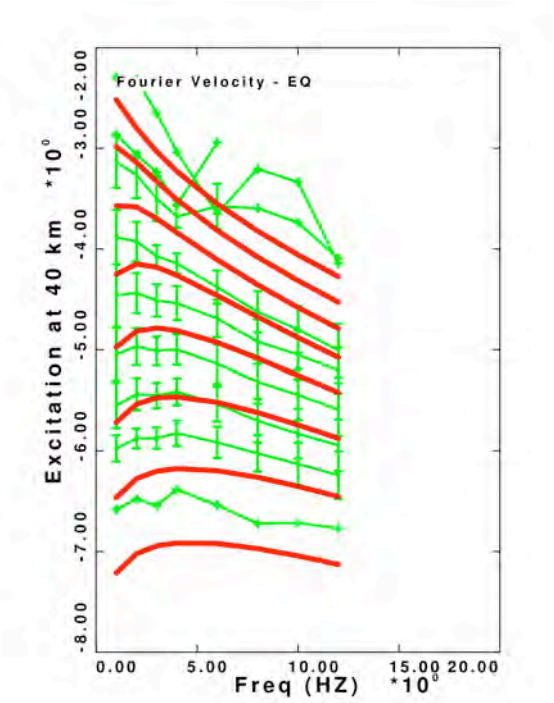


Figure 14. Comparison of model fit to the Fourier velocity excitation terms. The green curves are averages of the regression excitation terms into groups that are separated by 0.5 log units in level at 3.0 Hz. The red curves are the predicted excitation terms for the model for moment magnitudes of 2.0–5.5 at increments of 0.5 moment magnitude units. The high frequency level for small events is not a function of stress drop. The largest events in the data set had moment magnitudes of 5–5.5. Averages are used to be able to see the trends.

Inversion of Regional Structure

The waveform in the database have been used to inverse the regional structures. Two methods were conducted in our analysis: receiver function and surface wave dispersion. Figures 15 and 16 show one example of each method at one station, respectively. The results from the two methods are consistent. For example, both show a crust thickness of about 48 km under the station.

Screening the Outlier of Pg/Lg Spectral Ratio and Relocation

We tested Pg/Lg spectral ratio as a discriminant by screening for outliers. Figure 17 shows an example of a possible explosion recorded by 5 of our stations, which occurred on September 26, 2001, and was clearly recorded at Nanjian station. This event was not listed in the Chinese local catalog, so we searched for its waveforms recorded at some other stations. It turned out that it was recorded at five, with all positive first arrivals whenever it is clear enough to tell (Figure 17 a and b). Then we went further to do the Pg/Lg spectral ratio analysis and location of this event. The Pg/Lg spectral ratio of this event (the red plus signs in Figure 18) is close to the mean value of the ratio for all the events (a mixture of explosions and earthquakes) at low frequencies but well above the mean at high frequencies. This is a typical explosion pattern. Locating this event by LocSAT gives an initial time of 12h59m59.5s pm local time and a position at (100.2824E, 24.8783N). The initial time is almost on the hour, which is characteristic of industrial explosions in China. The location of this event is close to the on-going construction sites of two large dams and several highways. It is very likely that this event was a shot of one of these construction projects.

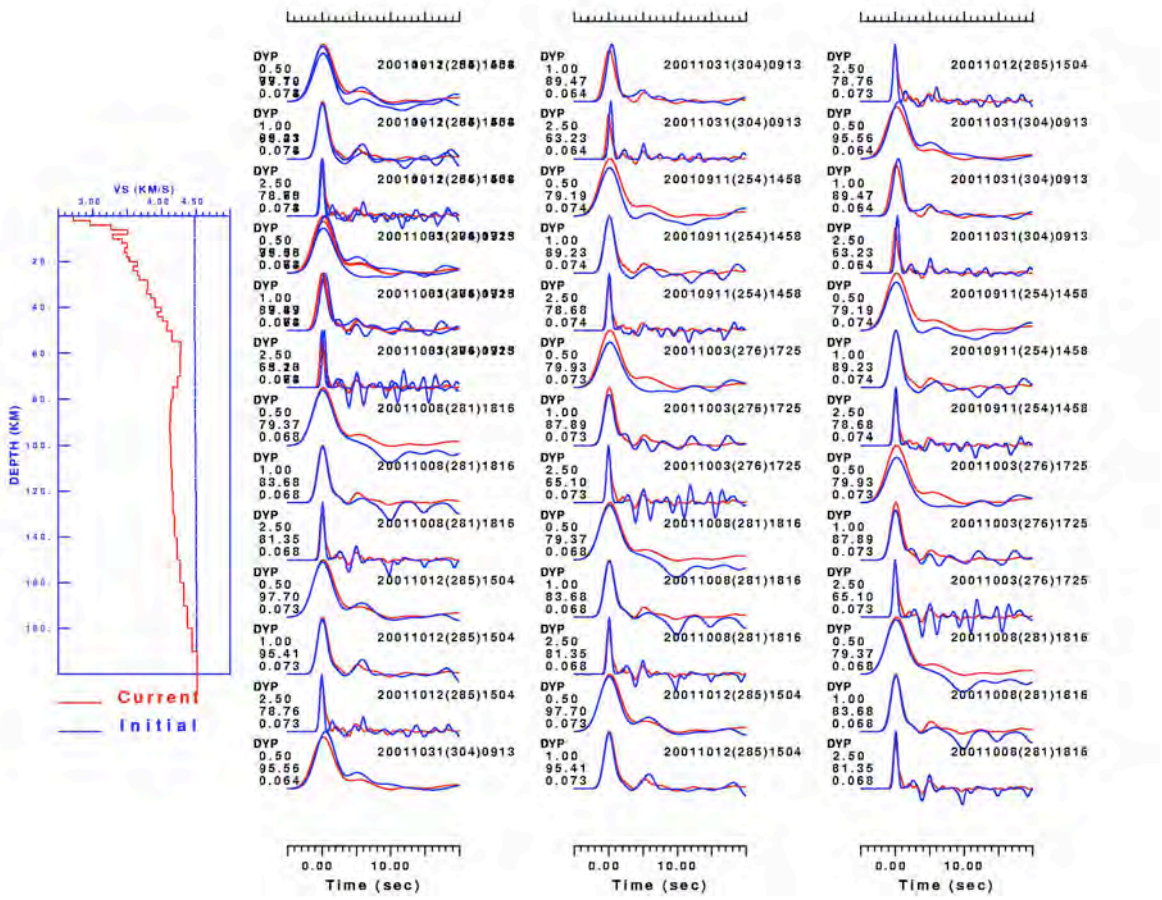


Figure 15. The receiver function inversion at Dayao station.

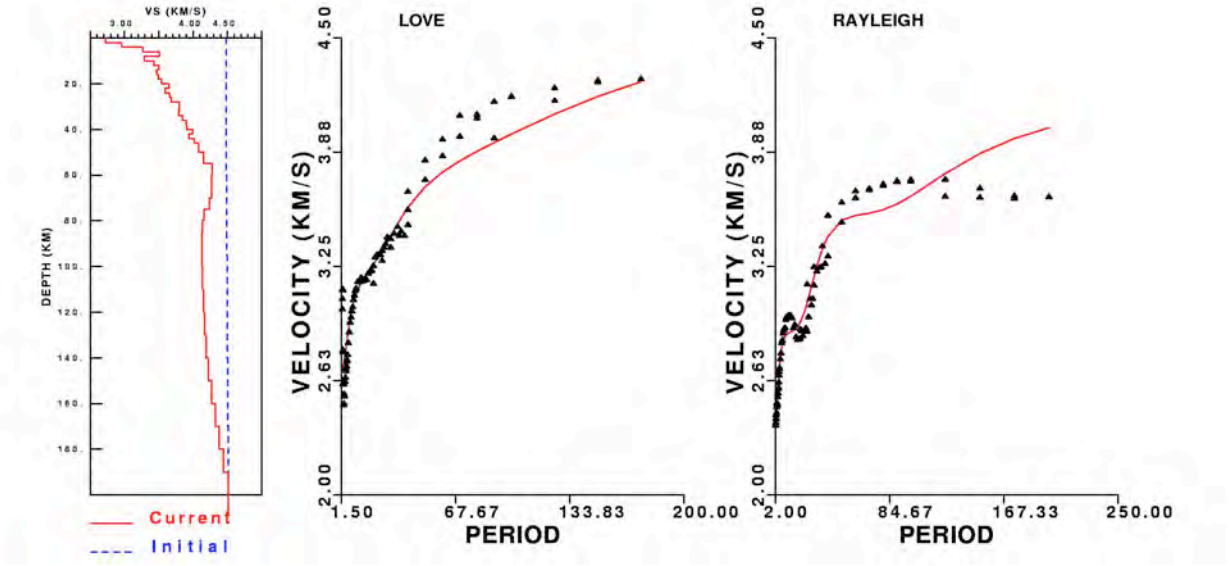


Figure 16. The surface wave dispersion analysis at Dayao station.

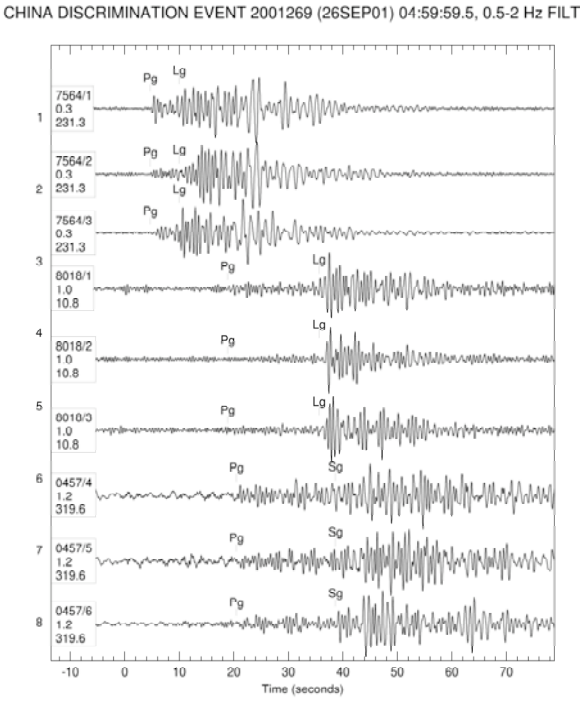


Figure 17a. The waveforms of an event on September 26, 2001, that is not in the Chinese catalog recorded at 5 stations in our network (part 1).

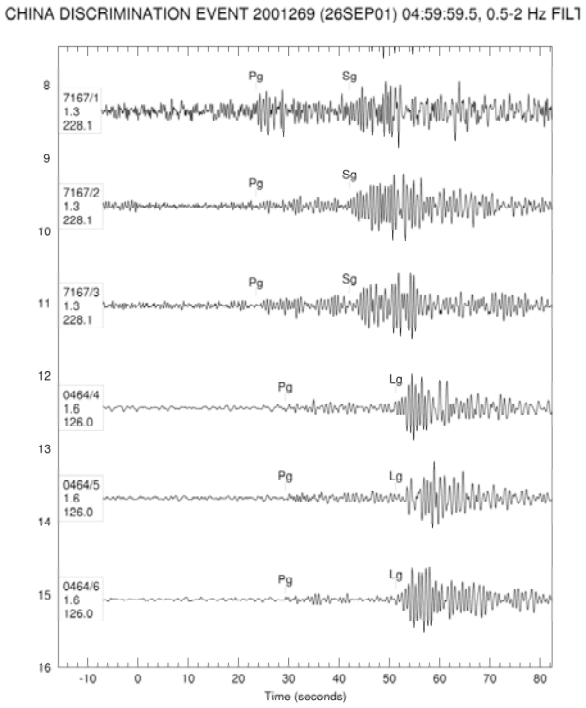


Figure 17b. The waveforms of an event on September 26, 2001, that is not in the Chinese catalog recorded at 5 stations in our network (part 2).

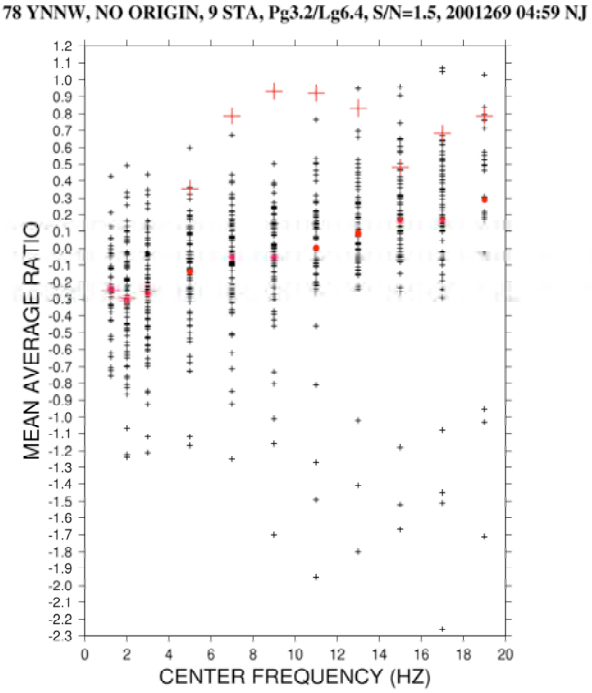


Figure 18. Pg/Lg spectral ratio for 78 events that are not in the Chinese catalog we have screened so far (black crosses). Red dots: the average Pg/Lg spectral ratio for all events. Red cross: the Pg/Lg spectral ratio for the event of September 26, 2001.

CONCLUSIONS

In summary, we have accomplished the following research of this project for studying the regional seismic characteristics in southwest China:

1. **Compiled a regional waveform database**. This is the first digital waveform database from China regional networks. Currently, over 30,000 waveforms reduced to the absolute ground velocity have been archived in the database. The database is ready for delivery.
2. **Assembled local bulletins with arrivals and phase picks**. Such bulletins have much better coverage than the national or global bulletins. They are very useful in relocation and tomography studies.
3. **Obtained ground-truth information for 7 local explosions**. These data contribute tremendously to the regional discrimination studies.
4. **Analyzed high frequency ground motion scaling**. The characteristics of the ground motion scaling were obtained through multivariate analyses. The results could be used for distance corrections.
5. **Inversed regional structures**. Both receiver function and surface wave dispersion analyses were conducted to inverse for the regional structures. The results are consistent from the two methods.
6. **Conducted Pg/Lg spectral ratio analysis**. Our analysis shows that Pg/Lg ratio is a good discriminant in the study area. As a test case, we have shown a successfully screened industry explosion.

REFERENCES

Aki, K. (1980), Attenuation of shear waves in the lithosphere for frequencies from 0.05 to 25 Hz, *Phys. Earth Planet. Inter*., 21, 50-60.

Baumgardt, D. R., and Z. A. Der (1994), Investigation of the transportability of the P/S ratio discriminant to different tectonic regions, PL-TR-94-2299, Phillips Laboratory, Hanscom Air Force Base, Massachusetts.

Baumgardt, D. R., and C. M. Schneider (1997), Multivariate canonical correlation of P/S ratios and propagation path parameters for Iran, *Proc. 19th Annual Seismic Research Symposium on Monitoring a Comprehensive Test Ban Treaty* (Editors: M. J. Shore, R. S. Jih, A. Dainty, and J. Erwin), Defense Special Weapons Agency, Alexandria, 14-23.

Boore, D. M. (1983), Stochastic simulation of high-frequency ground motions based on seismological models of the radiated spectra, *Bull. Seism. Soc. Am.* 73, 1865-1894.

Cartwright, D.E., and M. S. Longuet-Higgins (1956), The statistical distribution of the maxima of a random function, *Proc. Roy. Soc. London* Ser. A237**,** 212-232.

Chen, P. S., F. T. Liu, Q. Li, and J. Z. Qin (1991), The lateral inhomogeneity in Yunnan province. China, *Science in China (Series B)*, 34 (5), 630-640.

Cui, Z. Z., D. Y. Du, J. P. Chen, Z. Y. Zhang, and L. Y. Huang (1987), The Deep Structure and Tectonic Features of the Crust in Panxi Area, *Chinese J. Geophy*., 30(6): 566-580 (in Chinese).

Fan, G. and T. Lay (1998). Statistical analysis of irregular wave-guide influences on regional seismic discriminants in China, *Bull. Seism. Soc. Am.,* 88, 74-88.

Frankel, A., A. McGarr, J. Bicknell, J. Mori, L. Seeber, and E. Cranswick (1990), Attenuation of high-frequency shear waves in the crust: measurements from New York state, South Africa, and southern California, *J. Geophys. Res*., 95, 17,441-17,457.

Ge, B. R., and K. Y. Yang (1990), Mesozoic-Cenozoic Tectonic Features in Panzhihua-Xichang Area, *Chinese J. Geophy.*, 33(1): 64-69 (in Chinese).

Herrmann, R. B., and C. J. Ammon (1997). Faulting parameters of earthquakes in the New Madrid, Missouri region, *Engineering Geology* 46**,** 299-311.

Hu, H. X., et al. (1986), Explosion Investigation of the Crustal Structure in Western Yunnan Province. *Chinese J. Geophy*., 29(2), 133-144 (in Chinese).

Hu, H. X., Z. Y. Lin, Y. J. Bian, C. Y. Wang and L. B. Zhu (1996), Study on the Characteristics of Crust-Mantle Transition Zone in Western Yunnan Province, *Acta Seismologica Sinica*, 18 (4): 444-450 (in Chinese).

Kim, W. Y., D. W. Simpson, and P. G. Richards (1993), Discrimination of earthquakes and explosions in the eastern United States using regional high-frequency data, *Geophys. Res. Lett.* 20, 1507-1510.

Kim, W. Y., V. Aharonian, A. L. Lerner-Lam, and P. G. Richards (1997), Discrimination of earthquakes and explosions in southern Russia using regional high-frequency three-component data from the IRIS/JSP Caucasus Network, *Bull. Seism. Soc. Am.* 87, 569-588.

Lin, Z., et al. (1993), The Preliminary Interpretation of Deep Seismic Sounding in Western Yunnan, Acta Seismologica Sinica, 15 (4): 427-440 (in Chinese).

Liu, R. F., P. S. Chen, and Q. Li (1993), Three-Dimensional Velocity Images in Yunnan and Its Neibouring District, *Acta Seismologica Sinica*, 15 (1): 61-67 (in Chinese).

Liu, Z., R. B. Herrmann, J. Xie, and E. D. Cranswick (1991), Waveform characteristics and focal mechanisms of five aftershocks of the 1983 Goodnow, New York, earthquake by polarization analysis and waveform modeling, *Seism. Res. Letters*, 62, 123-133.

Malagnini, L. (1999), Ground Motion Scaling in Italy and Germany, *Ph. D. Dissertation*.

National Research Council (1997), Research Required to Support Comprehensive Test Ban Treaty Monitoring, National Academy Press, Washington, D.C.

Qin, J. Z., and R. J. Kan (1986), Q Values and Seismic Moments Estimates Using the Coda Waves of Near Earthquakes in the Kunming and Surrounding Regions, *Chinese J. Geophy*., 29(2): 145-155 (in Chinese).

Raoof, M., R. B. Herrmann, and L. Malagnini (1999), Attenuation and excitation of three-component ground motion in Southern California, *Bull. Seism. Soc. Am.* 89, (Aug. 99) preprint.

Rodgers, A. and W. Walter (1997), Regionalization and calibration of seismic discriminants, path effects, and signal-to-noise for station ABKT, *Proc. 19th Annual Seismic Research Symposium on Monitoring a Comprehensive Test Ban Treaty* (Editors: M. J. Shore, R. S. Jih, A. Dainty, and J. Erwin), Defense Special Weapons Agency, Alexandria, 143-151.

Sun, K. Z., J. W. Teng, D. M. Jin, and Y. Zheng (1987), Q-Value and Its Lateral Variations in Pan-xi Tectonic Belt, *Chinese J. Geophy*., 30(1): 101-104 (in Chinese).

Walter, W. R., K. M. Mayeda, and H. J. Patton (1995), Phase and spectral ratio discrimination between NTS earthquakes and explosions. Part1: empirical observations, *Bull. Seism. Soc. Am.* 85, 1050-1067.

Walter, W. R., D. B. Harris, and S. C. Myers (1997), Seismic discrimination between earthquakes and explosions in the Middle East and North Africa, *Proc. 19th Annual Seismic Research Symposium on Monitoring a Comprehensive Test Ban Treaty* (Editors: M. J. Shore, R. S. Jih, A. Dainty, and J. Erwin), Defense Special Weapons Agency, Alexandria, 459-468.

Wang, C. Y., X. L. Wang, and Q. Z. Yan (1994), Tree Dimensional Velocity Structure Beneath the Kunming Telemetered Seismic Network. Acta Seismologica Sinica, 1994, 16 (2): 167-175 (in Chinese).

Xiong, S. B., J. W. Teng, Z. X. Yin, M. H. Lai, and Y. P. Huang (1986), Explosion Seismological Study of the Structure of the Crust and Upper Mantle at Southern Part of the Panxi Tectonic, Belt, *Chinese J. Geophy*., 29(3), 235-244 (in Chinese).

Xiong, S. B., et al. (1993), The 2_D Structure and Its Tectonic Implications of the Crust in the Lijiang Panzhihua Zhehai Region, *Chinese J. Geophy*., 36(4), 434-444 (in Chinese).

Yazd, M. R. S. (1993), Ground motion studies in the Southern Great Basin of Nevada and California, *Ph. D. Dissertation*, Saint Louis University, 189p.

Zhu, P. D., Y. M. Li, L. M. Zhang, P. Y. Shu and S. H. Liang (1986), On the Study of the Seismic Telemetry Network in South Sichuan and North Yunnan Provinces, *Chinese J. Geophy*., 29(3), 245-254 (in Chinese).

MOMENT MAGNITUDE CALIBRATION FOR THE EASTERN MEDITERRANEAN REGION FROM BROADBAND REGIONAL CODA ENVELOPES

Kevin Mayeda,[1] Tuna Eken,[2] Abraham Hofstetter,[3] Niyazi Turkelli,[2] Jennifer O'Boyle,[1] Gonca Örgülü,[2] and Rengin Gok[1]

Lawrence Livermore National Laboratory,[1] Kandilli Observatory and Earthquake Research Institute,[2] Geophysical Institute of Israel[3]

Sponsored by National Nuclear Security Administration
Office of Nonproliferation Research and Engineering
Office of Defense Nuclear Nonproliferation

Contract No. W-7405-ENG-48;[1] DE-FC03-01SF22416;[2] and DE-FC03-01SF22417[3]

ABSTRACT

The following is an overview of results from ROA01-32 that focuses on an empirical method of calibrating stable seismic source moment-rate spectra derived from regional coda envelopes using broadband stations. The main goal was to develop a regional magnitude methodology that had the following properties: 1) it is tied to an absolute scale and is thus unbiased and transportable; 2) it can be tied seamlessly to the well-established teleseismic and regional catalogs; 3) it is applicable to small events using a sparse network of regional stations; 4) it is flexible enough to utilize S_n-coda, L_g-coda, or *P*-coda, whichever phase has the best signal-to-noise ratio. The results of this calibration yield source spectra and derived magnitudes that were more stable than any other direct-phase measure to date. Our empirical procedure accounted for all propagation, site, and *S*-to-coda transfer function effects. The resultant coda-derived moment-rate spectra were used to provide traditional band-limited magnitude (*e.g.*, M_L, m_b etc.) as well as an unbiased, unsaturated magnitude (moment magnitude, M_w) that is tied to a physical measure of earthquake size (*i.e.*, seismic moment). We validated our results by comparing our coda-derived moment estimates with those obtained from long-period waveform modeling. We first tested and validated the method using events distributed along the Dead Sea Rift (*e.g.*, Mayeda *et al*., 2003). Next, we tested the transportability of the method to earthquakes distributed across the entire country of Turkey and validated our results using seismic moments of over 50 events that had been previously waveform modeled using the method of Dreger and Helmberger, (1993). In both regions we demonstrated that the interstation magnitude scatter was significantly reduced when using the coda-based magnitudes (*i.e.*, M_w(coda) and m_b(coda)). Once calibrated, the coda-derived source spectra provided stable, unbiased magnitude estimates for events that were too small either to be reliably waveform modeled or to be seen at far-regional and teleseismic distances. In general coda-derived magnitudes are roughly a factor of 3 to 5 more stable than traditional regional magnitudes that use the direct-phases such as P_g and L_g. This appears to be a universal observation for all regions where the coda methodology has been applied.

OBJECTIVE

In this paper we review a method of calibrating a stable regional magnitude based on coda envelopes using a combination of International Monitoring System (IMS) and non-IMS seismic stations. The main goal was to develop a methodology for a universal regional magnitude that had the following properties: 1) it is tied to an absolute scale and is thus unbiased and transportable; 2) it can be tied seamlessly to the teleseismic catalog; 3) it is applicable to much smaller regional events using a sparse network of regional stations; 4) it is flexible enough to utilize S_n-coda, L_g-coda, or *P*-coda, whichever phase has the best signal-to-noise ratio.

In order to demonstrate and test the usefulness of our method, we chose the Eastern Mediterranean region as our study area. Our paper, keeping in mind the above-mentioned properties, has three main elements:

1) to prepare, outline and test our magnitude calibration procedure using a sub-region of the Eastern Mediterranean, specifically along the Dead Sea rift, as well as a portion of Eastern Turkey, using a variety of source types;
2) to extend and regionalize the procedure to IMS stations (*e.g.*, EIL, MRNI, KEG, GNI, KIV) throughout the broader, more complex regions of the Eastern Mediterranean using IMS and non-IMS data (*e.g.*, ISP, MALT, ISKB) for calibration;
3) to make the procedure and the code accessible for magnitude calibration of stations in any region.

For sparse local and regional seismic networks a stable magnitude is of utmost importance for establishing accurate seismicity catalogs and assessing seismic hazard potential. In the context of underground nuclear explosion monitoring, we need accurate magnitudes for construction of detection threshold curves, formation of discriminants and yield estimation. Unlike magnitudes such as M_L and m_b which are relative, narrowband measurements that often have regional biases, our approach can provide stable, absolute source spectra that are corrected for *S*-to-coda (or *P*-to-coda) transfer function, scattering, inelastic attenuation and site effects. In the small regions where this has been previously applied, we found that coda envelope amplitude measurements were not very sensitive to 3-D path heterogeneity and source radiation pattern. The resultant spectra were used to calculate stable moment estimates (and hence M_w), traditional short-period magnitudes (*i.e.*, m_b, M_L) and radiated seismic energy, E_R.

This research increases the IMS ability to compute stable magnitudes for small-to-moderate sized regional events using a sparse network and, consequently, contributes considerably to the improvement of seismic verification in the Eastern Mediterranean region. The resulting calibration methodology and software can be transferred to other observatories and groups of researchers to enhance the ability to monitor compliance with the Comprehensive Nuclear-Test-Ban Treaty (CTBT). This research was funded under ROA01-01 Topical Area 1.3 and 1.4 and is distinct from the DOE Base Program in a number of ways: 1) we are compiling non-IMS broadband waveforms to help calibrate IMS stations for regional magnitude from “in-country” networks which may otherwise be difficult to obtain; 2) we are testing the methodology over a much larger, more complex region using *P* and *S* coda envelopes; 3) we are studying a variety of seismic source types and depths to better understand the methods performance. The need for non-IMS stations is simple. There are significant trade-offs if we were to solely use IMS stations for the magnitude calibration. For example, non-IMS stations are more numerous, better distributed, and have closer-in data that can be used for independent moment estimation, determination of coda shape factors, velocity and attenuation. Furthermore, these non-IMS stations are likely to have been operational for a larger period of time and therefore have an archive of waveform recordings, whereas many of the IMS stations are relatively new (or currently non-existent). All three institutions bring regional seismological expertise to the project as well as waveform data that would otherwise be difficult to obtain.

RESEARCH ACCOMPLISHED

Dead Sea Rift Pilot Study:

In Mayeda *et al.* (2003) we described an empirical calibration method for obtaining stable seismic source moment-rate spectra derived from local and regional coda envelopes using broadband stations. This study was meant to be a pilot study to test the method in a small region using data essentially distributed along the strike of the Dead Sea fault. The results of applying this method provided source spectra that were more stable than any other direct-phase

measure to date. The procedure accounted for all propagation, site, and *S*-to-coda transfer function effects. The resultant coda-derived moment-rate spectra were then used to provide traditional band-limited magnitudes (*e.g.*, M_L, m_b etc.) as well as an unbiased, unsaturated magnitude (moment magnitude, M_w), which is tied to a physical measure of earthquake size (*i.e.*, seismic moment). We validated our results by comparing our coda-derived moment estimates with those obtained from long-period waveform modeling. Most importantly, we demonstrated that the interstation magnitude scatter was significantly reduced when using long-window-length coda (*i.e.*, M_w(coda) and m_b(coda)). However, when we used short-window coda measurements of 5 seconds in length taken after twice the direct wave travel time, the scatter remained large, comparable to direct waves. Once calibrated, the coda-derived source spectra provided stable, unbiased magnitude estimates for events that were too small either to be reliably waveform modeled or to be seen at far-regional and teleseismic distances. This property makes it ideal for sparse local or regional networks. We found that our source amplitude estimates were nearly insensitive to the expected source radiation pattern and exhibited roughly a factor of 3 to 5 less interstation scatter when compared against coda duration and conventional direct-phase measurements (*e.g.*, P_g, L_g). We also found that the coda stability, as measured by the interstation scatter for common events, reached a minimum value beyond a certain critical measurement window length. For example, at 6-8 Hz, the interstation standard deviation was less than 0.08 provided the coda measurement window was at least ~70 seconds in duration, whereas at 1.5-2.0 Hz the critical window length was ~90 seconds. For all frequency bands, as the coda window becomes shorter the standard deviation increases, asymptotically approaching the direct wave scatter. We defer the details of the calibration procedure to the paper of Mayeda *et al.* (2003) that describes in detail the methodology and addresses concerns related to choosing optimal measurement window lengths, estimating error, testing empirical path corrections, and tying coda amplitudes to an absolute scale.

Broad Area Calibration of Turkey:

To test the transportability of the coda method to a broader and more heterogeneous region we focused our attention to the country of Turkey. As of this writing, we have successfully transported the coda methodology to broadband data distributed over the entire region of Turkey using only three broadband stations and roughly 50 earthquakes ranging between $4.0 < M_w < 7.6$ (see Figure 1). After determining and applying distance corrections to the raw coda amplitudes for the frequencies 0.02 and 2.0 Hz, we looked at the consistency of the common events at stations ISP and ISKB for distance-corrected coda amplitude measurements. The interstation standard deviation of our distance-corrected coda amplitudes ranged between 0.07 and 0.2 (*e.g.*, see Figure 1). In addition to correcting coda amplitudes for distance, we also applied a grid search technique, which minimized the interstation scatter to the direct L_g waves in order to solve for the attenuation and geometrical spreading using the formulation of Street *et al.* (1975). We observed that the direct waves amplitudes showed scatter in the range of 0.27-0.45 for the same events. This proved that the interstation scatter results of distance-corrected coda amplitudes were remarkably 3-to-4 times lower than those obtained from distance-corrected direct wave amplitudes. Similarly, we observed that coda-based amplitudes between stations ISP and MALT had similar reduction in scatter when compared against direct waves. After all parameters were determined (*i.e.*, velocities, coda shape factors, and path corrections) we generated synthetic envelopes for a hypothetical source for a wide distance range. Considering the previous studies on coda waves (*e.g.*, Mayeda and Walter, 1996), the generation of the calibrated synthetics envelopes in this methodology represents a major change since they are purely empirical and do not depend on any assumption about the scattering mechanism and attenuation.

For the calibration of ISP-ISKB, we used independently derived seismic moment solutions of 39 earthquakes in the ISP-ISKB dataset to transform the coda amplitudes to absolute source spectra in dyne-cm. Seismic moment solutions were taken from Örgülü and Aktar (2001) as well as from the Harvard CMT (Centroid Moment Tensor) catalog. The magnitudes of these events ranged between M_w 4.0 and 7.6. These new coda-based source spectra obtained at two stations, ISP and ISKB showed a consistent behavior for almost all events (Figure 2). Coda-derived seismic moment values were determined by averaging the coda amplitudes for the two lowest frequencies. Coda-derived moment magnitudes, M_w(coda), were estimated from the equation developed by Kanamori and Hanks (1979), $M_w = 2/3\log_{10}(M_o) - 10.7$. The comparison made between M_w(coda) and waveform modeled moment magnitudes, M_W(waveform), showed excellent correspondence with a standard deviation of 0.2, comparable to results from the Dead Sea rift region (*e.g.*, Mayeda et al., 2003) and the western United States (*e.g.*, Mayeda and Walter, 1996). Figure 3 shows examples of coda-derived source spectra observed at ISP and ISKB and the relation between our M_w(coda) and M_w(waveform). Likewise, we calibrated the ISP-MALT station pair by using independently derived moment estimates of 49 earthquakes in the ISP-MALT dataset. Compared to 39 earthquakes

used for the calibration of ISP-ISKB station pair, these 49 earthquakes nearly sampled the entire region of Turkey. The magnitudes of these 49 earthquakes ranged between M_W 4.0 and 6.3. Following the same technique, we

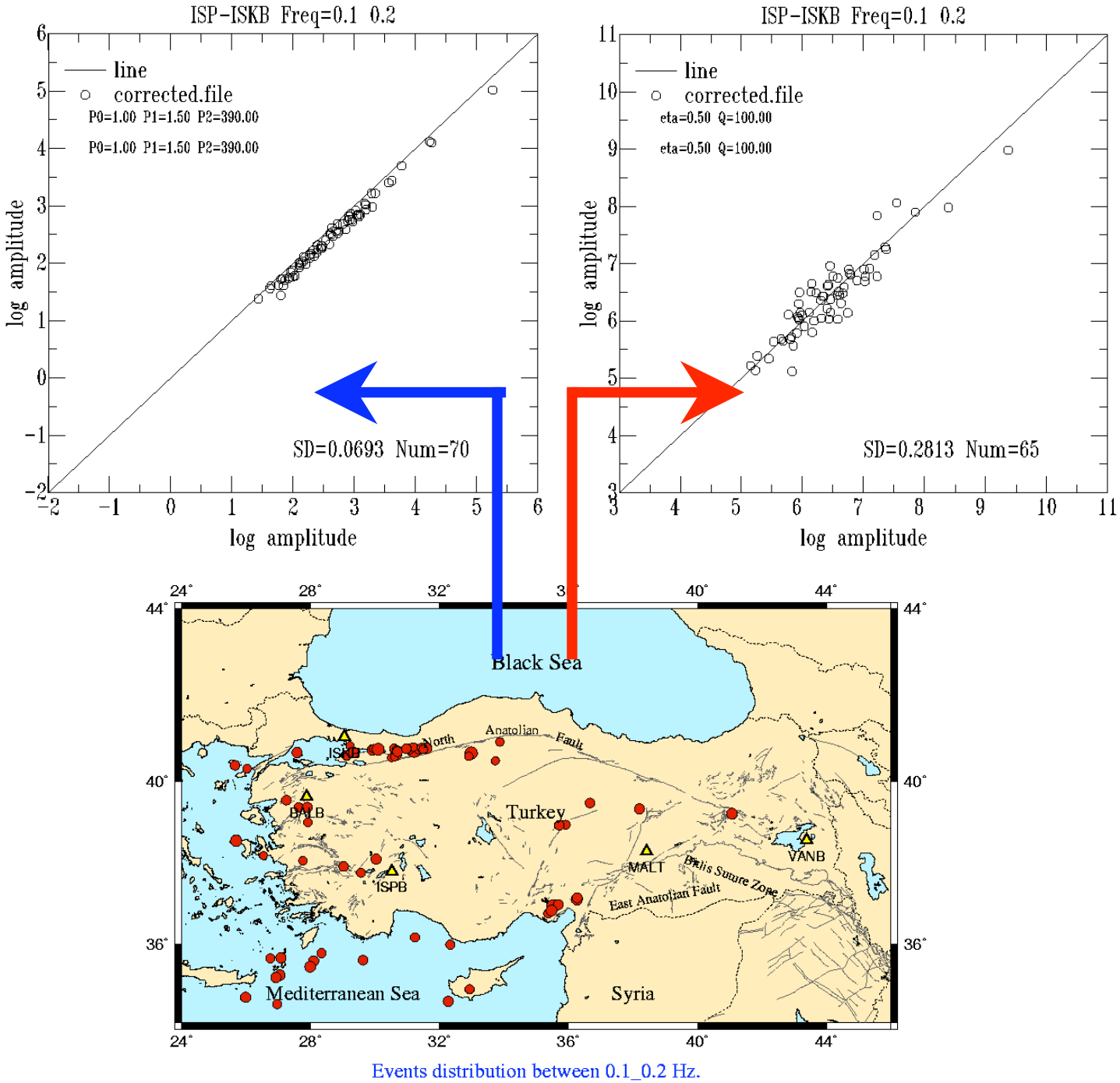


Figure 1. Comparison of distance-corrected coda amplitudes at 0.1-0.2 Hz with the amplitudes of direct L_g arrival for ISP-ISKB. Inter-station standard deviation results show that coda amplitudes at this frequency band are 4 times more stable than distance corrected direct waves for the common events whose locations are shown on the map.

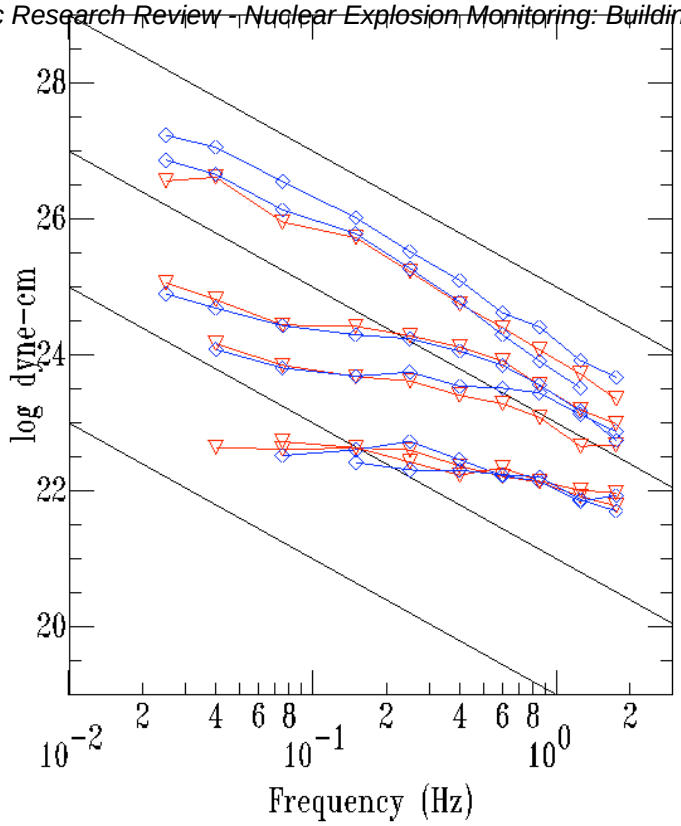


Figure 2. Example source spectra of common events from ISP (diamonds) and ISKB (triangles). Note that source spectra of each event are quite similar between the stations.

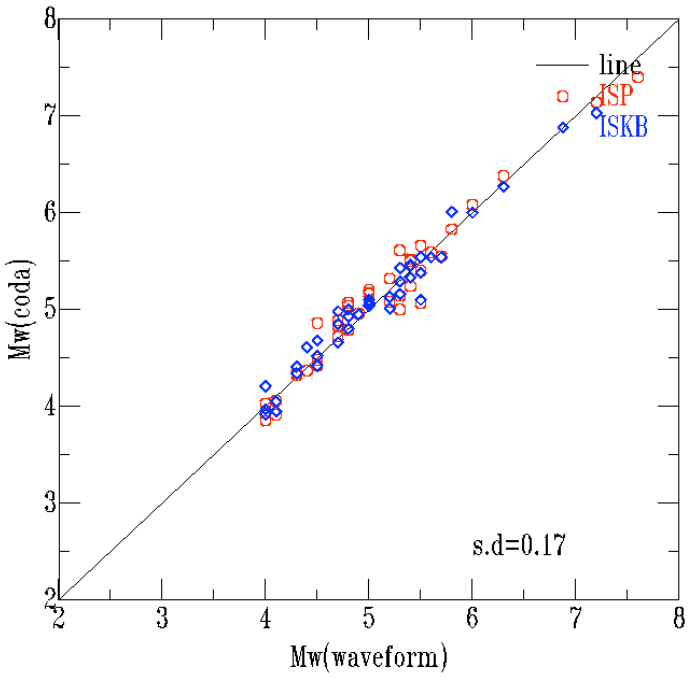


Figure 3. Comparison of M_W(coda) of 39 events estimated at stations ISP (circles) and ISKB (diamonds) with those obtained from long-period waveform modeling. There is a good correspondence with a standard deviation of 0.17 between two types of moment magnitude.

found the frequency dependent moment-rate constants for ISP-MALT station pair. After we applied these moment-rate constants to uncorrected coda amplitudes at each frequency, we observed that resultant coda-based moment rate spectra generated at each station for a given event showed good agreement. These source spectra, again, were then used to calculate M_w(coda) of the events for entire data set. Similar to the results from ISP-ISKB dataset, M_w(coda) estimated from the long-period levels of coda-derived source spectra indicated a consistent relation with independently derived M_w(waveform). Applying moment rate constants, we have computed coda-derived source spectra and then obtained M_w(coda) of some recent earthquakes, which we have not used during the calibration process without any knowledge of independently derived seismic moment, and moment magnitude. Some of the major earthquakes that have been recently studied are the Pülümür earthquake on January 27, 2003 with M_w(coda)~6.3, the Urla earthquake on April 14, 2003 with M_w(coda)~5.7, the Bingol earthquake on May 1, 2003 with M_w(coda)=6.4, and the Bandirma earthquake on June 9, 2003 with M_w(coda)=4.7. Our estimates again showed that the M_w(coda)'s found for these earthquakes were very consistent with moment magnitude estimates derived from long period waveform modeling.

CONCLUSIONS AND RECOMMENDATIONS

This paper reviews progress-to-date on ROA01-32 that focused on an empirical methodology to transform non-dimensional coda amplitudes into stable moment-rate spectra. The initial pilot study in the Dead Sea rift (Mayeda *et al*., 2003) showed unequivocally that the coda methodology provides the most stable estimates of the source spectra of any local or regional method to date. Once calibrated, the coda-derived spectra provide unbiased, absolute magnitude estimates for events that are too small either to be waveform-modeled or to be seen teleseismically. Our empirical path and site corrections were verified by comparing our seismic moment estimates against independent estimates from long-period waveform modeling. We found that source amplitude estimates were virtually insensitive to the source radiation pattern and exhibited roughly a factor of 3 to 5 less interstation scatter when compared against conventional direct-phase measurements (*e.g*., P_g, L_g) as well as coda duration. The typical interstation scatter ranged between 0.07 - 0.1 for the coda measurements for frequencies between 0.02 - 8.0 Hz. This means that a single coda amplitude measurement is equivalent to a 9- to 25-station network average of direct wave amplitudes. Results of our calibration procedure can be used as ASCII input into the latest version of SAC (Goldstein *et al*., 2002), which has a new command to produce coda-derived source spectra, energy, and moment.

In this study, an empirical regional calibration methodology was applied to two different datasets in Turkey consisting of earthquakes that occurred in a tectonically complex region with dominant lateral heterogeneities. During the calibration process two different datasets were compiled from three Turkish broadband stations (ISP, ISKB, and MALT) to obtain stable moment magnitude estimates. The events in the first dataset (ISP-ISKB) are distributed mostly over the western Anatolia region while the second dataset (ISP-MALT) samples the entire country. For both datasets, in a frequency range between 0.02 and 1.0 Hz, the interstation scatter of distance corrected-coda amplitudes varies from 0.07 to 0.15, in good agreement with results obtained from previous applications of the methodology to the western United States and Dead Sea Rift regions (*e.g*., Mayeda and Walter, 1996; Mayeda *et al*., 2003). This result is very encouraging because it demonstrates that the method can also be applied over larger and complex regions ranging between local and far-regional distances. As found in other regions, comparison to the direct waves (*i.e*., L_g , P_g, and surface waves), shows that the interstation scatter for the coda is a factor of 3 - 4 smaller. For this region, this appears to be a robust methodology for frequencies at least up to 1 Hz because the coda waves provide roughly 3 - 4 times more stable amplitude measurements relative to the direct waves. In other words, a single coda measurement is approximately equivalent to a 9 - 16 station network average using direct waves. Observational results with regard to the standard deviation between distance-corrected coda amplitude measurements at different pairs of stations also showed that even a single, frequency dependent coda attenuation function was enough to explain the coda envelope amplitude over the entire country. After correcting our coda amplitudes for propagation effects, we tied our non-dimensional measurements to an absolute scale using independently derived moments. In other words, we transformed distance corrected coda amplitudes into a source spectra by making frequency dependent corrections for both the site and *S*-to-coda transfer function effects. The validation of this empirical approach is proven by observing identical spectra for the same event at two stations separated by roughly 500 km. The stable source spectra also confirm that the coda is averaging over any source radiation pattern as well as any lateral crustal heterogeneity. As a final validation, these selected source spectra were used to estimate coda-derived moment magnitudes, M_W(coda). Upon comparing our M_W(coda)'s with those from long-period waveform modeling, M_W(waveform), we observed a standard deviation of 0.17 for ISP-ISKB and 0.14 for ISP-MALT. These observations prove the stability of coda waves at regional distances and furthermore can

be used for small events that cannot be reliably waveform modeled due to poor signal to noise ratio for long period surface waves.

In conclusion, we transported a newly developed regional magnitude methodology based on coda envelopes to estimate stable source spectra and hence moment magnitudes for earthquakes in Turkey. We calibrated the broadband stations ISKB, ISP and MALT and our results strongly suggest that they can be used to estimate M_W(coda) for waveforms that are clipped and/or too small to be waveform modeled. With the use of the calibration results, we successfully estimated M_W(coda)'s of three recent earthquakes, the January 27, 2003, Pülümür; the April 4, 2003, Urla; the May, 1, 2003, Bingöl; and the June 9, 2003 Bandirma; that occurred in Turkey. We also proved that; a) the application of the methodology is successful in a tectonically complex and laterally heterogeneous region, b) it is convenient for a sparse local and regional seismic networks, c) the magnitude estimation is unbiased, c) it is transportable and universal, d) it does not saturate, and e) it is insensitive to source radiation pattern. With the use of calibration results, we are now able to estimate M_W(coda) for events that are too small to be reliably waveform modeled.

REFERENCES

Aki, K. (1969). Analysis of seismic coda of local earthquakes as scattered waves, *J. Geophys. Res*., 74, 615-631.

Biswas, N. N. and K. Aki (1984). Characteristics of coda waves: Central and south central Alaska, *Bull. Seism. Soc. Am.*, 74, 493-507.

Dewey, J. F. and A.M.C. Sengör (1979). Aegean and surroundings regions: Complex multiplate and continuum tectonics in a convergent zone, *Geolog. Soc. Amer. Bull.*, 90, 84-92.

Dewey, J.F., M.R. Hempton, W.S.F. Kidd, F. Saroslu and A.M.C. Sengör (1986). Shortening of continental lithosphere: the neotectonics of Eastern Anatolia-a young collision zone, in *Collision Tectonics*, edited by M. P. Coward, and A.C. Ries, pp. 3-36, Geol. Soc. London, London.

Goldstein, P., D. Dodge and M. Firpo (2001). SAC2000: Signal processing and analysis tools for seismologists and engineers, UCRL-JC-135963, Invited contribution to the IASPEI, International Handbook of Earthquake and Engineering Seismology, Academic Press, London, U.K.

Mayeda, K. (1993). m_b(Lg Coda): A stable single station estimator of magnitude, *Bull. Seism. Soc. Am*., 83, 851-861.

Mayeda, K. and W. R. Walter (1996). Moment, energy, stress drop, and Source spectra of western United States earthquakes from regional coda envelopes, *J. Geophys. Res*., 101, 11195-11208.

Mayeda, K., A. Hofstetter, J. O'Boyle and W. R. Walter (2003). Stable and Transportable Regional Magnitudes Based on Coda-Derived Moment-Rate Spectra, *Bull. Seism. Soc. Am*., 93, 224-239.

McKenzie, D. P. (1972). Active tectonics of the Mediterranean region, *Geophy. J. Roy. Astr. Soc.*, 30, 109-185.

McKenzie, D. P. (1978). Active tectonics of the Alpine-Himalayan Belt: The Aegean Sea and surrounding regions, *Geophy. J. Roy. Astr. Soc*., 55, 217-254.

Örgülü, G. and M. Aktar (2001). Regional Moment Tensor Inversion for Strong Aftershocks of the August 17, 1999 Izmit Earthquake (M_W-7.4), 28, 371-374.

Reilinger, R.E., S.C. McClusky, M.B. Oral, R.W. King, M.N. Toksöz, A.A. Barka, I. Kinik, O. Lenk and I. Sanlı (1997). Global positioning system measurement at present-day crustal movements in the Arabia-Africa-Eurasia plate collision zone, *J. Geophys. Res.*, 94, 9983-9999.

Sengör, A.M.C. (1979). Northern Anatolian fault: Its age offset and tectonic significance, *J. Geol. Soc. London*, 136, 269-282.

Street, R. L., R. Herrmann and O. Nuttli (1975). Spectral characteristics of the Lg wave generated by central United States earthquakes, *Geophys. J. R. Astron. Soc*., 41, 51-63.

Taymaz, T., J. Jackson and D. McKenzie (1991). Active tectonics of the north and central Aegean Sea, *Geophy. J. Int.*, 106, 433-490.

IMPROVED FOCAL DEPTH DETERMINATION FOR USE IN NUCLEAR EXPLOSION MONITORING

John R. Murphy,[1] Brian W. Barker,[1] and William L. Rodi[2]

Science Applications International Corporation,[1] Massachusetts Institute of Technology[2]

Air Force Research Laboratory

Contract No. DTRA01-01-C-0056

ABSTRACT

Seismic event location remains as one of the important discriminants for separating natural tectonic and explosive events. In particular, high-confidence estimation of focal depths remains as an outstanding monitoring problem. Over the past several years, we have been pursuing a research program directed toward the development of improved detection and identification procedures for the depth phases pP and sP and the formulation of a new algorithm for computing more reliable confidence intervals on focal depth estimates. With regard to depth phase identification, we have investigated the utility of an automatic network stacking algorithm that maps post-P detection times at a station into candidate depth phases using the pP - P and sP - P delay times predicted by travel-time tables for that epicentral distance, and then combines the individual station results as a function of candidate source depth. This automatic algorithm has been applied to data from a large number of events in the Hindu Kush and in the Hokkaido and Honshu regions of Japan, as well as the region surrounding the Chinese Lop Nor test site. Prominent candidate pP and sP peaks have been identified in the resulting network detection stacks for many of these events, including some with m_b values as low as 3.7 and depths as shallow as 20 km. This algorithm has now been implemented in a software module that interacts directly with the standard Analyst Review Station (ARS) and is being evaluated and tested. While this algorithm promises to be a powerful tool for identifying candidate depth phases, the presence of a prominent peak on the network detection stack does not, by itself, constitute a positive identification that is confident enough to be used for purposes of event screening. Rather, it identifies possible depth phases that have to be validated by further review and testing. That is, since the positive identification of a depth phase with a time delay of greater than about 3 seconds with respect to P conclusively identifies an event as being to deep to be an explosion, it is important that this identification be made with a very high level of confidence. One tool that can be used to help characterize peaks on the network detection stacks is the F detector. The F detector operates on array station beam data and provides a quantitative measure of the probability that detections at a station have vector slownesses consistent with what would be expected for pP and sP phases arriving from the origin. This could provide a powerful means for eliminating false candidate peaks. We have collected a large amount of array data for events that have previously shown promising results during the depth phase stacking process, and are evaluating this F detector to see whether it provides any additional information to help us confirm depth phase identification. We are also continuing to investigate the applicability of calibrated regional S - P arrival time information to the estimation of independent event origin times for use as constraints in the hypocenter location process. Although the trade-off between focal depth and origin time can be complex in practical applications to small events for which few data of limited azimuthal distribution may be available, an ability to independently constrain origin time can often lead to significantly improved focal depth estimates. In particular, differences between origin times determined from regional S - P times and the corresponding origin times determined from standard hypocenter location codes with focal depths constrained to zero can be used to infer focal depth bounds which are useful for event discrimination purposes. We have collected regional seismic data recorded at selected the International Monitoring System (IMS) stations from samples of earthquakes with well determined focal depths located in the Hindu Kush and in Japan and have developed calibrated S - P travel time relations for use in the determination of independent origin times. The resulting regional S-P based origin times are being used in a preliminary hypothesis test, where they are statistically compared with origin time estimates obtained from constrained (h = 0) teleseismic solutions to assess whether the event focal depths are greater than 10 km at high confidence levels. Initial results suggest that this approach can consistently identify subcrustal events as being too deep to be explosions with a high degree of confidence. We are in the process of assessing the depth and distance dependent variations in the calibration constants and are attempting to establish a more statistically rigorous version of this test.

OBJECTIVES

The objectives of this research program are to determine more reliable estimates of the uncertainties associated with the different focal depth estimation procedures and to increase the number of events that can be identified as earthquakes on the basis of focal depth through the implementation of new and improved analysis tools. This is being accomplished through the development of improved procedures for identifying and using the teleseismic depth phases pP and sP, the incorporation of regional S-P based origin time constraints into an improved depth estimation algorithm, and the development of more robust statistical hypothesis tests for use in event discrimination. This effort includes the implementation and large-scale testing of these new algorithms on the Space and Missile Defense Command (SMDC) Research and Development Support System (RDSS).

RESEARCH ACCOMPLISHED

Seismic event location remains as one of the most important discriminants for separating natural tectonic and explosive events. Thus, for example, it has been estimated that approximately 80% of known global earthquakes have focal depths greater than 50 km or are located more than 25 km at sea. Since underwater nuclear explosions can be confidently identified to very low yields using hydroacoustic data, it follows that the vast majority of earthquakes can potentially be identified on the basis of location alone. This is an important observation, since global nuclear monitoring may require the screening of tens of thousands of seismic events per year and, in order to perform this function efficiently, it will be necessary to have simple and robust discriminants available that can be used to eliminate the vast majority of these events. However, in order to be useful for such discrimination purposes, the uncertainties associated with seismic locations must be well-defined and reliable; and this has proven to be difficult to accomplish to the required degree of accuracy. For example, during the GSETT-3 experiment, it was found that only about 50% of the event epicenters which have been well-constrained by local data reported to the National Data Centers (NDCs) fell within the corresponding 90% confidence ellipses published by the Prototype International Data Center (PIDC) in the Reviewed Event Bulletin (REB). This indicates that all of the sources of error have not been properly accounted for in the existing statistical location models.

More specifically, high confidence estimation of focal depths remains as an outstanding seismic monitoring problem. If accurate focal depths could be determined for the majority of earthquakes deeper than 5, or even 10 km, the event discrimination problem would be much easier. However, despite intensive efforts by well-trained and experienced analysts, more than two-thirds of the GSETT-3 REB events were assigned artificially constrained depths. Moreover, the cited accuracies of even those relatively few focal depth estimates is open to serious question, particularly in light of the evidence that the corresponding epicentral uncertainties appear to be significantly underestimated by the current hypocentral location algorithm. Thus, for example, Fisk et al (2000) found a number of cases in the GSETT-3 database where the cited uncertainties in the focal depths of earthquakes in particular areas had been consistently underestimated by the PIDC location program. Such discrepancies are frequently compensated for in a crude fashion by artificially inflating the input variance values until the associated confidence bounds encompass the required percentage of verified values. This was the interim approach taken by Fisk et al (2000) in their formulation of the focal depth discriminant for the experimental event screening system at the IDC. However, this is an ad hoc procedure that does not address the underlying deficiencies in the standard error model and can potentially lead to serious focal depth estimation errors under previously untested conditions. Clearly, improved focal depth estimation procedures are needed that can more fully utilize depth phase information and explicitly account for all sources of error in seismic arrival time data.

Reliable identification of the depth phases pP and sP provides one of the strongest pieces of evidence that a seismic event is a naturally occurring earthquake when the time delay between pP and direct P exceeds about three seconds, implying a focal depth of greater than 10 km. However, confident identification of such phases on actual recordings is not always a simple matter. That is, it is first necessary to unambiguously identify a phase onset in the P coda background; and it is then required to confirm that this phase is actually a depth phase and not some other P phase, such as PcP, which might have an expected arrival time within the time window being analyzed. Thus, with regard to identification of a detected secondary phase as a depth phase, it is generally further required that the subject arrival be detected at several stations at different epicentral distances and that the time interval between its onset time and the associated P onset time be an increasing function of epicentral distance. This distance dependence is commonly referred to as “step-out,” and the IASPEI 91 travel time tables used at the IDC predict step-outs between 30 and 90 degrees of approximately 0.4 seconds for a focal depth of 15 km, 4.4 seconds for a focal depth of 100 km

and 13.7 seconds for a focal depth of 300 km. Thus, even with high quality data for which it is possible to determine pP-P time of arrival differences with an accuracy of about 1 second, it is generally not possible to apply the step-out identification criterion to pP for events with focal depth less than about 50 km.

We have continued to focus on the development of improved tools for the detection and identification of the depth phases pP and sP and on the evaluation of the use of calibrated regional S-P time intervals to constrain event origin times for use in focal depth determination. With regard to depth phase identification, we have been attempting to improve the frequency and reliability of the identification of the depth phases, pP and sP, through the use of network beam-forming (Murphy *et al*, 2000). In our approach, post-P arrivals observed at each station for a given event are mapped from functions of delay times with respect to P to functions of source depth using the pP-P and sP-P delay times predicted by the IASPEI-91 travel-time tables for the various station distances. These functions of depth for all the stations in the detecting network are then added together to identify arrivals consistent with the predicted depth phase move-outs over the entire range of potential source depths. That is, the observed delay times of all post-P arrivals with respect to P are translated into equivalent focal depths under the hypothesis that they are either pP or sP arrivals. Those arrivals that are consistent with such hypotheses should then show up as peaks on a stacked network depth function. In the present application, difficulties associated with the variability of observed short-period signals between widely separated stations are avoided by stacking unit amplitude boxcar functions centered on the post-P detection times, which are automatically determined at each station by front end signal processing procedures. One advantage of this approach is that not only is it fully automatic, but it includes only signals that have triggered a detection, which should help to minimize the inclusion of questionable arrivals in the analysis. Figure 1 shows an example of the application of this algorithm to the automatic post-P detection times for three Central Honshu earthquakes. It can be seen that the network detection stacks in these cases show pronounced peaks at depths corresponding to the published REB depths for these events, indicating the presence of good candidate pP phases that should be further reviewed by the analyst. This automatic algorithm has now been applied to data from over 200 REB events located in the Hindu Kush, Lop Nor, Hokkaido and central Honshu regions. Prominent candidate pP and sP peaks have been identified in the resulting network detection stacks for a majority of these events, including some with mb values as low as 3.7 and depths as shallow as 20 km, indicating that this algorithm can provide the analyst with information useful for the confident identification of additional pP and sP phases. In order to make this depth phase stacking procedure available for large-scale testing and further evaluation,

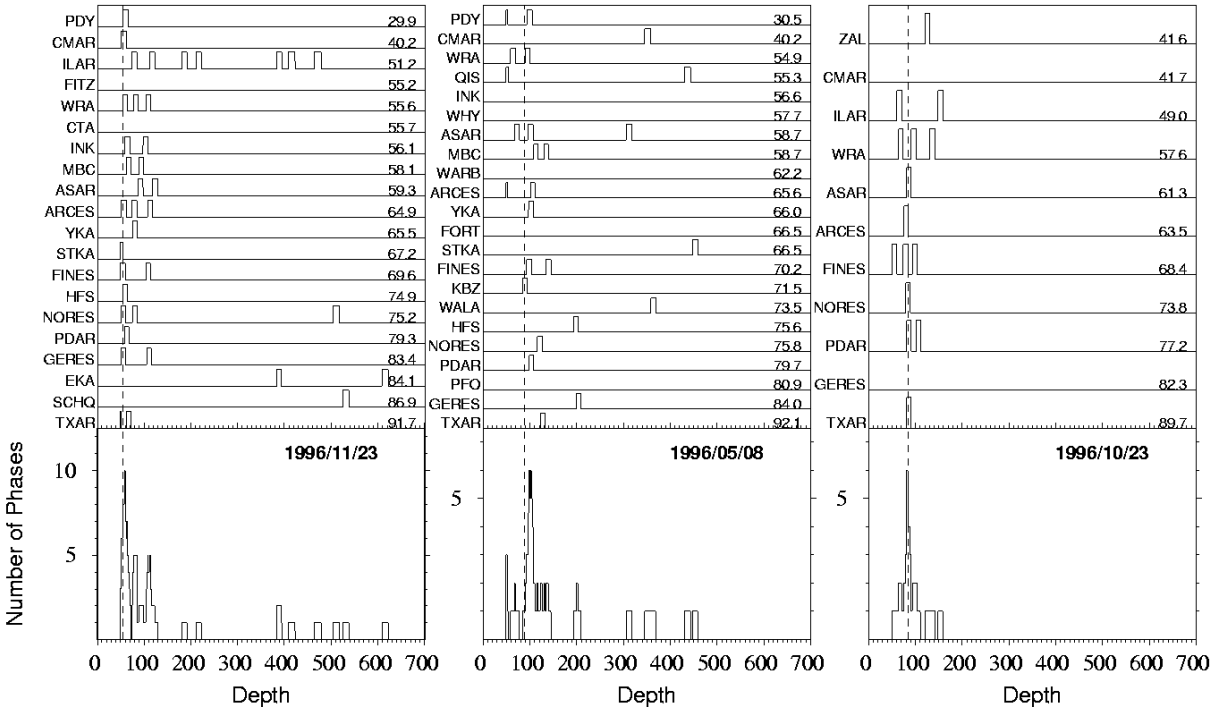


Figure 1. Network detection stacks of pP for the Central Honshu earthquakes of 1996/11/23 (m_b = 4.32), 1996/05/08 (m_b = 3.86) and 1996/10/23 (m_b = 3.79).

the algorithm described in Figure 1 has been integrated into the Analyst Review Station (ARS) software employed at the IDC and the USNDC. In this implementation, the analyst initiates a fully automatic process from the ARS that causes all of the post-P detection times for the current event to be recovered from the automatic detection files and passed to the depth phase stacking module, where they are converted into their corresponding depth traces, stacked, and presented back to the analyst in an X-Window display. Then, by clicking on a candidate peak with the mouse, the analyst initiates a process by which the corresponding waveforms are brought up in the standard ARS display with the data time aligned on the predicted pP times corresponding to the selected trial depth. These data can then be further processed using the bandpass filter routine or any of the other signal processing algorithms available in the ARS. This implementation will allow us to test the procedure at a large scale to determine whether it is powerful enough to be considered for incorporation into routine seismic analysis procedures such as those employed at the USNDC or the IDC.

The network beamforming algorithm described above is proving to be a powerful tool for identifying candidate depth phases. However, the presence of a prominent peak on the network detection stack does not, by itself, constitute a positive identification that is confident enough to be used for purposes of event screening. Rather, it identifies possible depth phases that would have to be validated by further review and testing. As a result, the development, implementation and testing of improved analyst tools and quantitative tests will play a key role in the completion of any new depth phase identification system. One tool that can be used in the characterization of prominent peaks on the network detection stacks is the F detector. The F detector (Blandford, 1974) operates on array station beam data and provides an output trace which is approximately equal to the time averaged power on the beam divided by N times the average variance of the individual channels and the beam, where N is the number of array stations. Its potential value for the present application is that it provides a quantitative, statistical means of assessing the likelihood that an arrival has the same vector slowness as the beam. Therefore, it provides a potential mechanism for evaluating whether particular detections at a station have vector slownesses that are consistent with what would be expected for pP and sP arrivals from the origin. This could provide a powerful means for eliminating false candidate peaks associated with source and receiver complexity or the presence of unidentified phases. We have implemented this algorithm and are evaluating its capabilities as a tool to assist in characterizing our depth phase stack peaks. Figure 2 shows the results of the F detector processing for an earthquake on July 9, 1997 located in the Honshu region of Japan and recorded at the YKA array in Canada. The top of the figure shows the beam trace steered to the location of the event and filtered between 0.5 and 3.0 Hz. The middle trace is the F-Trace, calculated using a 2 second moving window, and the bottom of the figure shows the ‘probability’ trace, which is derived from the F-Trace and is used to indicate the probability that a phase is arriving at the same vector-slowness that the beam was steered to. Also marked on the traces are the predicted pP and sP arrivals for the estimated REB depth of 71 km for this event. It can be seen from the beam trace that there is energy arriving near the time of the predicted pP phase for this event depth, and this energy also appears on the F–trace. The probability trace on the bottom indicates that there is a high probability that this energy represents a phase arriving with the same azimuth/slowness that the beam was steered to, giving us confidence that it might represent a true depth phase. The sP phase is not apparent on any of the traces, however. It may be that this phase is buried in the coda of another unknown phase arriving a few seconds earlier than the predicted sP time. Figure 3 shows an additional example of the application of the algorithm to the station YKA recordings of a shallow Lop Nor earthquake on 1999/01/27. Marked on this figure are the predicted pP and sP times for the REB assigned depth of 18 km. In this case, the traces show that there is evidence that our candidate depth phases are being generated at the event source and that they appear to correspond to the depth phases, pP and sP. A more specific application of the F detector, as a tool to provide confirmation of depth phase stacking results, is illustrated in Figure 4. In the top of this figure we show the depth phase stack results for an event in the Hindu Kush region. It indicates a pronounced peak at a depth of approximately 226 km that is in agreement with the REB depth shown by the dashed line, but also shows a number of prominent secondary peaks that need to be evaluated. We have calculated the F detector results for six of the array stations that contributed to this stack, and have used these results to weight the detections using the corresponding F probability traces. The weighted detections after this processing were then converted to depth and stacked to produce the new results shown in the bottom of this figure. The peak at 226 km has been retained, while secondary peaks have been greatly suppressed, which supports our initial interpretation of the stacking results. We are continuing with the development of a more general tool that will combine our depth phase stacking results with the F detector results to assist in the detection and validation of depth phases.

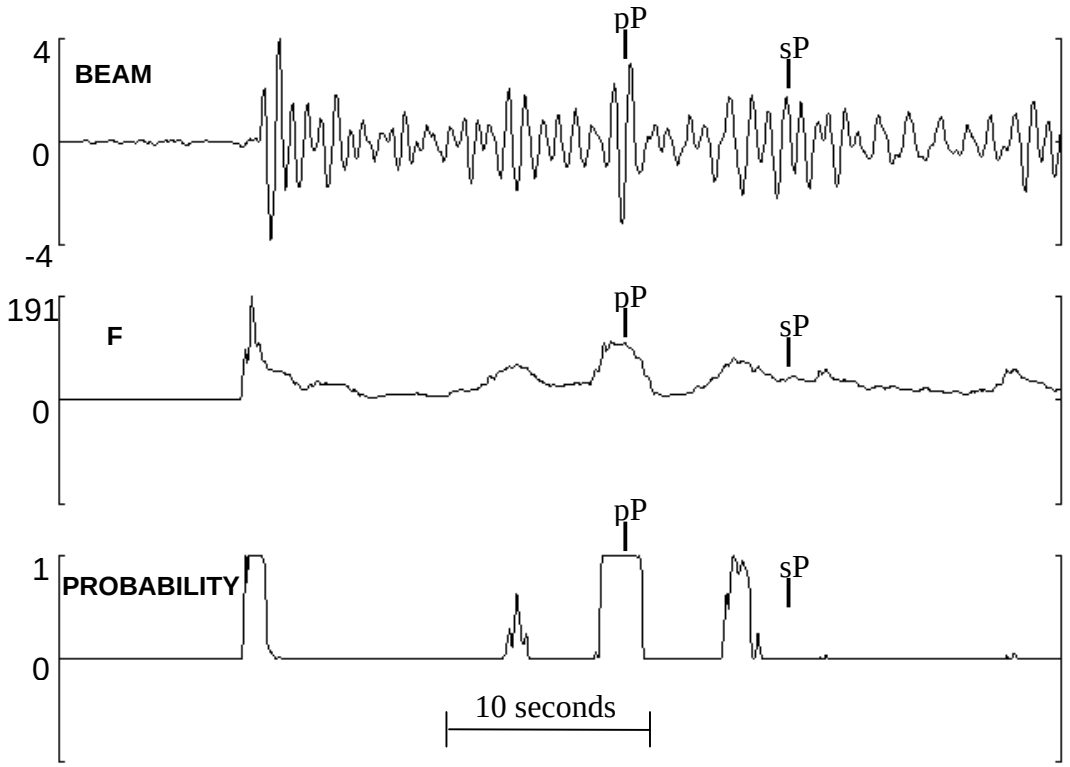


Figure 2. Best beam trace (top), F-trace (middle), and probability trace (bottom) for the Central Honshu earthquake of 1997/07/09, m_b = 3.94. The depth phase predictions are based on the REB depth of 71 km.

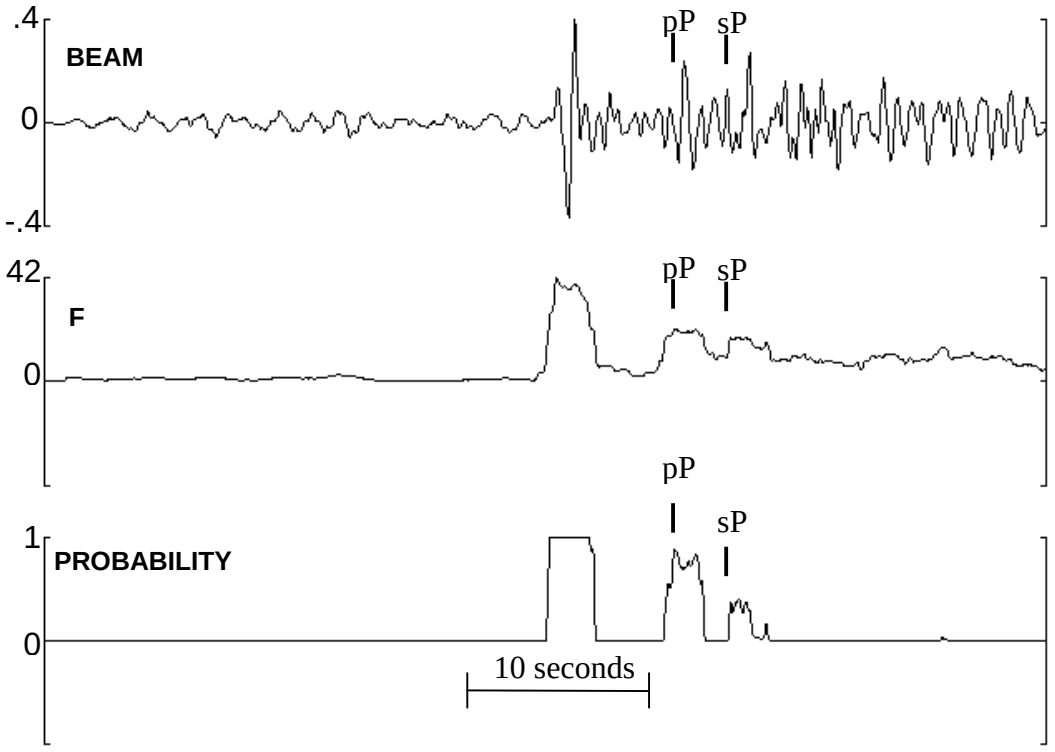


Figure 3. Beam trace (top), F-trace (middle), and probability trace (bottom) for the Lop Nor earthquake of 1999/01/27, m_b = 3.90. The depth phase predictions are based on the REB depth of 18 km.

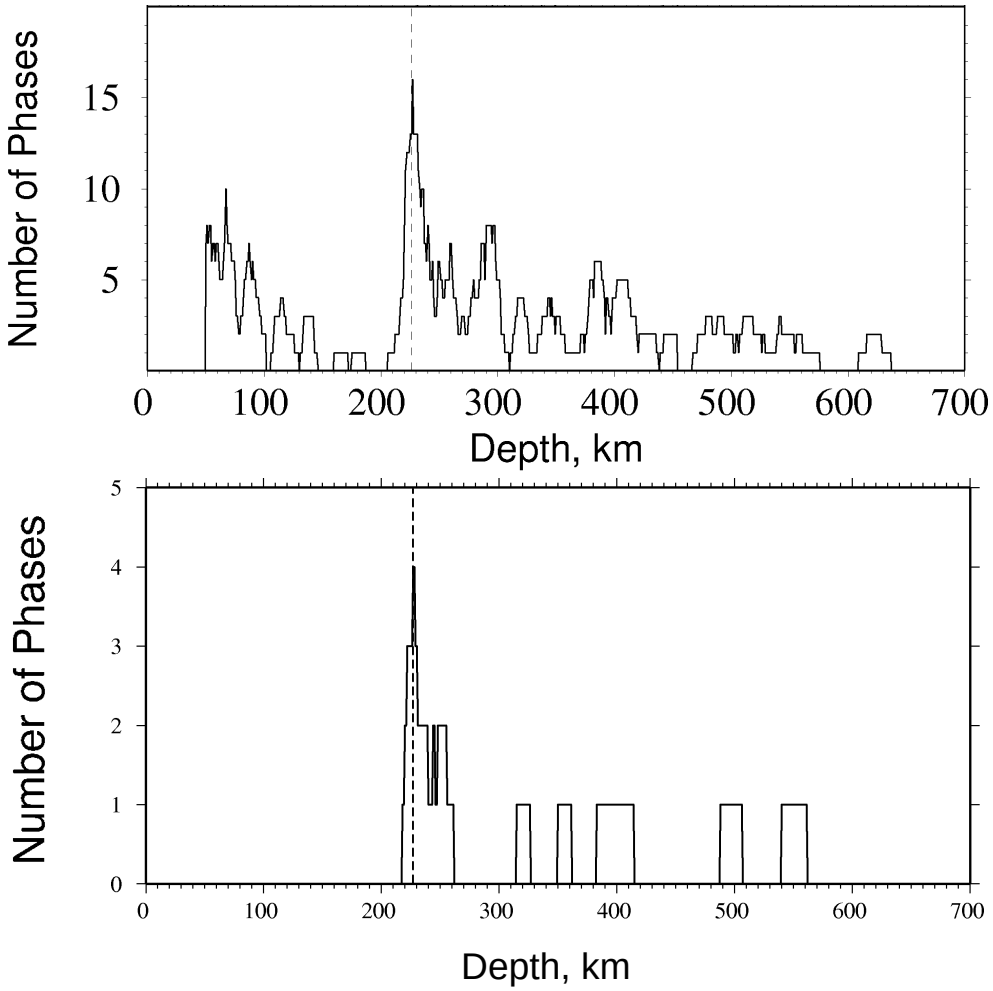


Figure 4. Network detection stack of pP for the Hindu Kush earthquake of 1998/02/14 (top). Array detection stack after confirmation by F detector results (bottom). The dashed vertical lines coincide with the REB depth estimate of 226 km.

It is important to recognize that, even if depth phase identification can be significantly improved by employing new analyses techniques such as those described above, there will still be many earthquakes for which focal depths can only be estimated through analyses of observed P wave first arrival times. Because of the well known tradeoff between event origin time and focal depth in the teleseismic distance range, teleseismic P wave first arrival times alone are not adequate for determining the focal depths of events with depths less than about 100 km with accuracy sufficient for confident event screening. In principal, this limitation can be overcome by incorporating P wave first arrival time observations at near-regional distances into the location procedure. However, as was documented by Murphy et al (2000), systematic biases in regional travel time data that are not well accounted for by the error models used in conventional seismic location algorithms, can lead to serious errors in focal depth determination which are not encompassed by the nominal uncertainty bounds on focal depth. One approach to resolving this ambiguity, which was originally proposed by Wadati some 75 years ago in his studies of deep Japanese earthquakes, is to independently constrain the event origin time using calibrated regional S-P travel time differences. That is, if t_o is the event origin time and t_s and t_p are the observed arrival times of P and S waves which traveled the same path to a station at distance D from the source, it follows that:

$$t_p = t_0 + \frac{D}{a}$$
$$t_s = t_0 + \frac{D}{b} \quad (1)$$

where a and b are the average P and S wave velocities along the path. It follows that the P wave travel time can be related to the observed S – P time as

$$t_p - t_0 = \frac{1}{\left(\frac{a}{b} - 1\right)}(t_s - t_p) \quad (2)$$

Thus, if the ratio a/b has been determined for a particular path the event origin time can be estimated from observed P and S arrival times through the simple relation

$$t_0 = t_p - \frac{1}{\left(\frac{a}{b} - 1\right)}(t_s - t_p) \quad (3)$$

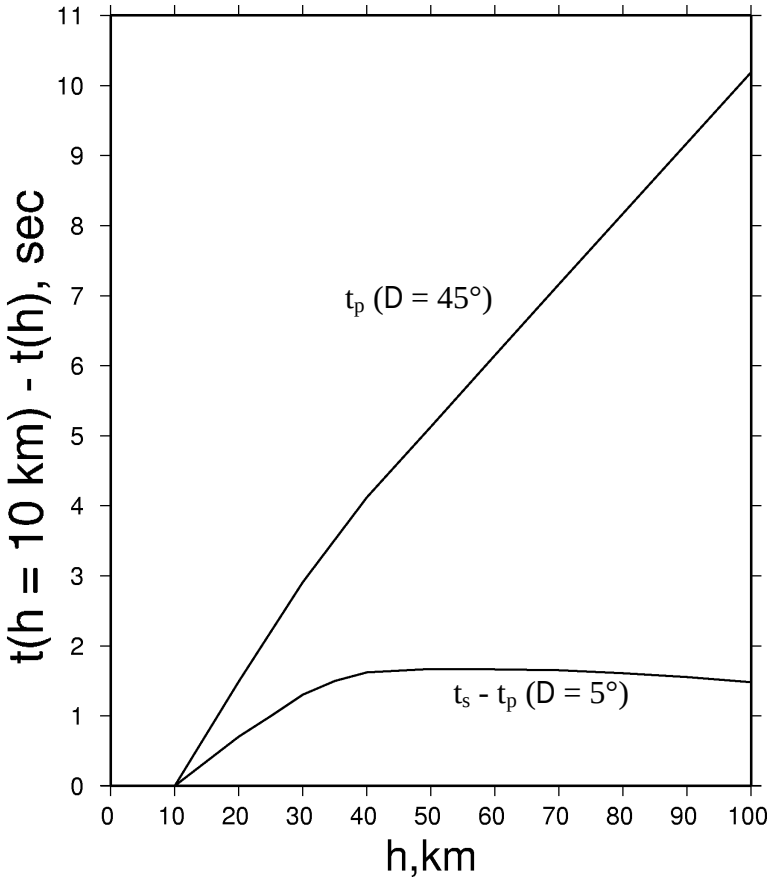


Figure 5. Comparison of $t_s - t_p$ variation as a function of focal depth predicted at a fixed near-regional distance of 5° by the IASPEI91 travel time tables with the corresponding predicted variation in P wave first arrival times at a nominal distance of 45°

The power of this approach is illustrated in Figure 5 which shows a comparison of $t_s - t_p$ variation as a function of focal depth between 10 and 100 km predicted at a fixed near-regional distance of 5° by the IASPEI91 travel time tables with the corresponding predicted variation in P wave first arrival times at a nominal teleseismic distance of 45°. Note that the predicted S-P times are virtually independent of focal depth between 30 and 100 km, while the teleseismic travel time decreases by more than 1 second for every 10 km increase in focal depth over that same range. Consequently, observed S-P times at regional distances can provide very robust constraints on event origin time which are largely independent of focal depth for depths less than about 100 km. This, of course, assumes that the S – P times are calibrated for the propagation paths of interest. As an example, Figure 6 shows such a calibration for a large sample of Honshu earthquakes recorded at the regional IMS station MJAR. This calibration has been used to estimate origin times from observed MJAR S – P times for a sample of 47 Honshu earthquakes that have accurate depth phase constrained focal depths in the range of 50 to 150 km. These origin time estimates were then used as constraints in determining focal depths of these events from P wave first arrival times alone, using a new event location algorithm which combines grid search location and Monte Carlo simulation algorithms to determine focal depths and associated rigorous uncertainty bounds (Rodi and Toksoz, 2000). An important aspect of this new algorithm is that it allows the analyst to specify precise bounds on the uncertainty in the origin time estimate, which is then properly accounted for in the focal depth determination process. The results of applying this new algorithm to the selected sample of 47 Honshu earthquakes are illustrated in Figure 7 where differences in estimated depths with respect to the "true", depth phase constrained values are compared for the solutions obtained with and without origin time constraints. It can be seen from this figure that the unconstrained depth differences show a significant average bias of 11.7 km and an associated standard deviation of over 32 km, while the corresponding S – P origin time constrained depth differences show a much reduced average bias of 3.7 km and a significantly smaller standard deviation of 8.0 km. These results indicate that earthquakes with depths greater than about 30 km in this region can be shown to be too deep to be explosions (i.e. h > 10 km) at a very high level of confidence if S – P constrained origin times are available. We are currently evaluating several candidate hypothesis tests using our generalized error model in order to determine which provides the most rigorous and powerful event screening procedure.

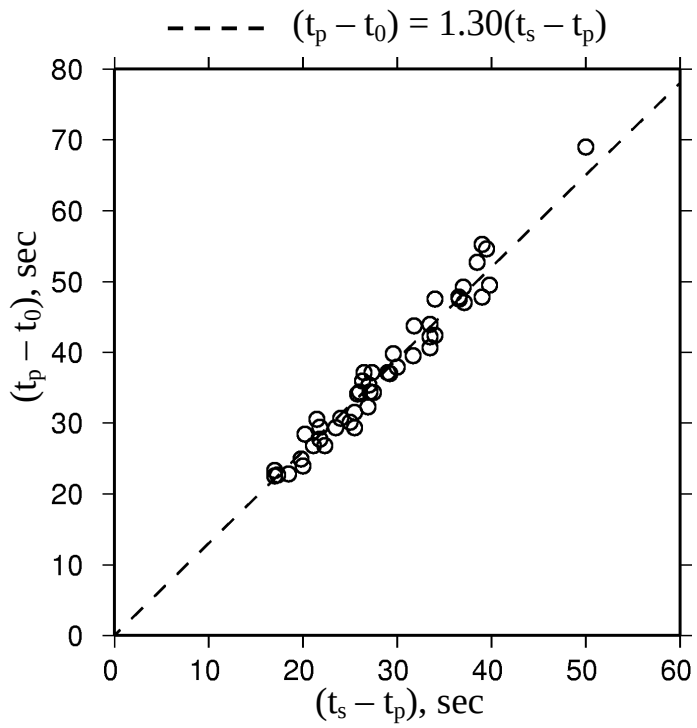


Figure 6. S – P travel time calibration results for a large sample of Honshu earthquakes at the regional station MJAR.

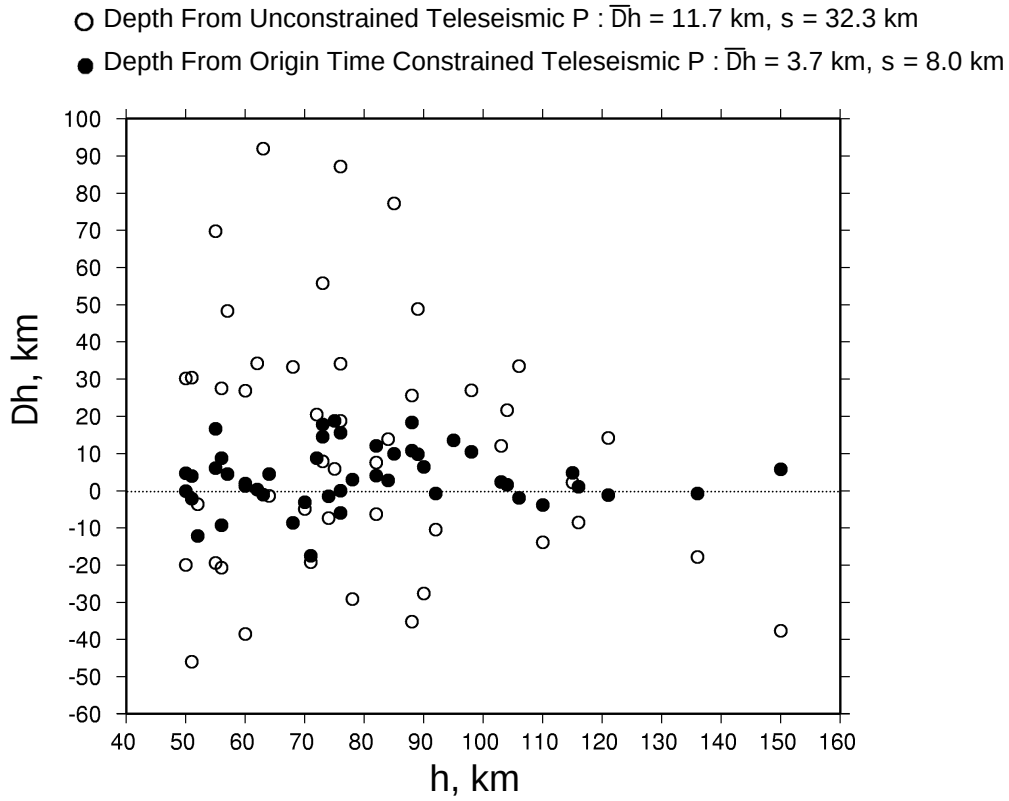


Figure 7. Differences in estimated depths with respect to the "true" depth phase constrained values.

CONCLUSIONS AND RECOMMENDATIONS

The second year of a three-year research investigation directed toward the development of improved focal depth estimates for use in event discrimination has now been completed. One result of this investigation has been the formulation and testing of an automated procedure for stacking raw P wave detection data to identify candidate pP and sP depth phases for further review by an analyst. This algorithm has been integrated into the Analyst Review Station (ARS) software employed at the IDC and U.S. NDC. We have also formulated a procedure that uses F detector output to weight the results of this depth stacking algorithm in order to suppress unwanted secondary peaks that do not originate from the source. This procedure shows promise as a tool that can be used by an analyst to assist in the detection and validation of depth phases. We are also continuing with the formulation of a depth hypothesis test based on the application of calibrated regional S – P travel time intervals to constrain event origin time. Results of application of this procedure to selected well located events in the Honshu region of Japan have indicated that it shows promise for use in event discrimination.

REFERENCES

Murphy, J. R., R. W. Cook, and W. L. Rodi (2000), Improved Focal Depth Determination for Use in Seismic Monitoring of Underground Nuclear Explosions, *Maxwell Technologies Final Report* MSD-DFR-00-16621.

Rodi, W., and M.N. Toksöz (2000). Grid-search techniques for seismic event location, *Proceedings*, 22nd Annual DoD/DOE Seismic Research Symposium, New Orleans, Defense Threat Reduction Agency (DTRA).

AUTOMATED BROAD AREA CALIBRATION FOR CODA BASED MAGNITUDE AND YIELD

W. Scott Phillips, Howard J. Patton, Claudia M. Aprea, Hans E. Hartse, George E. Randall and Steven R. Taylor

Los Alamos National Laboratory

Sponsored by National Nuclear Security Administration
Office of Nonproliferation Research and Engineering
Office of Defense Nuclear Nonproliferation

Contract No. W-7405-ENG-36

ABSTRACT

The stability of local (< 100 km) earthquake coda has been well established through observations that have shown coda amplitudes to be independent of distance, path details and azimuth with respect to the focal mechanism. This behavior is consistent with scattered energy models of coda and allows accurate measurement of relative amplitudes for use in source scaling or site effect studies. Furthermore, coda amplitudes can be measured to high precision because of the redundant information in adjacent time windows. Mayeda (2003) has recently extended coda wave techniques to regional distances, through the empirical calibration of distance-dependent coda shape. Using this technique, we apply coda analysis to a regional network (38 sites) covering China and central Asia. The analysis of large amounts of data is accomplished using automatic techniques to isolate coda, calibrate coda shape, obtain and apply path, site and coda generation corrections and shift to absolute level. The path and site corrections are obtained using amplitude difference tomography, which eliminates source terms from the inversion. For 13 bands between 0.03 and 8 Hz and datasets of up to 2250 multiple recorded events, residuals (RMS) are reduced to less than 0.1 log10 amplitude units. For 0.7 to 1 Hz data, variance reduction is 86% relative to the best fit uniform attenuation model. The resulting attenuation patterns closely follow regional geology. After calibration, we can directly compare scaling behavior of explosions across the region, which includes the Semipalatinsk and Lop Nor test sites. Ties can be made to parameters of monitoring interest, such as m_b. We can also directly compare spectra from a wide distribution of earthquakes, showing regional variations in source scaling that should be incorporated into event identification and coda calibration procedures.

OBJECTIVE

We calibrate coda wave behavior, including site and path effects, in order to isolate and study source phenomena and to determine magnitude and yield. Our objective is to develop a transportable methodology that can be used to characterize events to a small size threshold over broad areas. Because manual review of coda envelopes requires substantial time investment, we develop methods to process the data in an automated manner.

RESEARCH ACCOMPLISHED

The stability of coda waves has been well established through observations that have shown coda amplitudes to be independent of distance, path details and azimuth with respect to the focal mechanism (Aki, 1969). This behavior is consistent with the generation of coda by scattering and allows accurate measurement of relative amplitudes for use in source scaling (e.g. Aki and Chouet, 1975) or site effect (Phillips and Aki, 1986) studies. Furthermore, coda amplitudes can be measured to high precision because of the redundant information in adjacent time windows. This makes coda ideal for monitoring small, sparsely recorded events for purposes of discrimination (Hartse et al., 1995) and magnitude or yield estimation (Rautian et al., 1979; Mayeda, 1993) as the measurement stability is equivalent to that available from a multi-station network.

We apply the regional coda calibration methods developed by Mayeda et al. (2003) to obtain coda calibration parameters for China and central Asia stations. We processed 13,315 records from 157 nuclear tests, 28 chemical explosions and 5914 earthquakes recorded at 38 sites (Figure 1) for purposes of calibrating China and central Asia coda wave behavior. Including duplicate and surrogate stations in the list, these are: AAK, BJI, BJT, BRV, BRVK, CHTO, ENH, HIA, KMI, KKAR, KK31 KUR, KURK, LSA, LZH, MAK, MAKZ, MKAR, MK31, MDJ, NIL, NVS, PDY, QIZ, SSE, TKM2, TLG, TLY, ULHL, ULN, WMQ, WUS, XAN and ZAL, as well as Borovoye archive STsR-TSG instruments KS, KSM and KSVM (Richards et al., 1992; Kim and Ekstrom, 1996) and PASSCAL Tibetan Plateau Experiment stations AMDO, BUDO, ERDO, GANZ, LHSA, MAQI, SANG, TUNL, USHU, WNDO and XIGA (Owen et al., 1993).

Following instrument correction, data were reduced by band-passing in 13 bands, from 0.03-0.05 to 6.0-8.0 Hz, followed by Hilbert transform envelope and smoothing operations. Final envelopes were formed by averaging the two horizontal component envelopes. Exceptions are the vertical components at short-period arrays and Borovoye archive KSVM. MKAR and KKAR array envelopes were stacked without shifting, which reduced the scatter that typically rides on top of the envelope, allowing better detection of low signal-to-noise coda, especially in the higher frequency bands.

Coda analysis windows were determined by manual inspection for a subset of the China and central Asia envelope data that included all BRV(K), KKAR, MAK(Z), MKAR, NIL (BH), ULN, WMQ and Tibet Experiment records, all explosions, both nuclear and chemical, as well as all records of 44 earthquakes for which independently derived moments exist. The remaining data were analyzed using an automatic procedure to identify the coda window. This procedure was designed to stop short of secondary events or noise sources that can be present in the coda, as well as to extend the coda beyond poor, high estimates of noise level in cases where seismograms were triggered and little noise was available for measurement. Specifically, the method uses the expected coda shape to find the minimum amplitude point in the coda, and to project beyond that point until the envelope deviates too much from the model.

After manual review, we calibrated coda peak and shape parameters following the regional calibration procedure of Mayeda et al. (2003). First, we determined coda peaks by inspection of WMQ and NIL (BH) envelope data. In many cases, especially for low Q paths and high frequencies, peaks did not stand out; however a break in slope could be identified near the predicted Lg arrival. In some low Q path cases, the peak envelope occurred near the Sn arrival and no peak or break in slope could be identified near the Lg. Sn peaks were more commonly observed at NIL than at WMQ. Sn coda were used in the analysis if signal-to-noise were sufficient following the predicted Lg peak. The group velocities of the envelope peaks were calibrated by fitting (L_1) a flat Lg velocity along with a hyperbola with three adjustable parameters to describe the Sn velocity as a function of distance:

$$\mathbf{v_g} = \mathbf{v}_0 - \frac{\mathbf{v}_1}{\mathbf{v}_2 + \Delta}$$

where v_g is group velocity of the peak; v_0, v_1 and v_2 are adjustable parameters and Δ is distance in kilometers. Within scatter, Sn and Lg group velocities were the same for WMQ and NIL, so we applied the these calibration curves to all stations.

Coda shape was obtained by fitting the coda decay using:

$$\mathbf{a(t)} = \mathbf{a_0 \cdot t^{-\alpha} \cdot e^{\beta \cdot t}}$$

where *a(t)* is coda amplitude, *t* is time from the coda peak (taken as the smaller of the Lg and Sn velocities, see above), a_0 is the coda source factor, α is a spreading factor, set to 0.7 for all data and β is the coda decay parameter. The decay parameter was then calibrated as a function of distance by varying hyperbola parameters b_0, b_1 and b_2 to best fit (L_1) the coda envelope data:

$$\beta = \mathbf{b_0} - \frac{\mathbf{b_1}}{\mathbf{b_2} + \Delta}$$

The coda shape parameters were determined for various station groups. Well sampled stations, such as WMQ, were calibrated alone. Closely located stations, such as MAK, MAKZ, MKAR and MK31, or Kirgiz network stations, were grouped together. Poorly sampled stations were grouped by regional propagation characteristics (based on 2D amplitude tomography results, described below).

Using the calibrated envelope peak group velocity and coda shape factor, we obtain raw coda source factors, a_0 above, by fitting using the coda decay formula. These values must be corrected for path and site effects. We use 1D and 2D methods to do this. The 1D method follows Mayeda et al. (2003). We start with a rough source correction based on m_b (Taylor and Hartse, 1998) and fit (L_1) a spreading-attenuation model:

$$\mathbf{a(\Delta)} = \mathbf{s_0 \cdot \Delta^{-\alpha} \cdot e^{\frac{-\pi f \Delta}{Qc}}}$$

where *a* is m_b-corrected amplitude, s_0 represents the site effect, but contains other effects such as coda generation (media scattering strength), α is spreading, *f* is frequency, *Q* is the quality factor and *v* is velocity, to which we assign the nominal Lg velocity of 3.5 km/s. Spreading is set based on m_b-corrected coda amplitudes at distances under 100 km. These values are zero at low frequencies and increase (0.7 for the 6 - 8 Hz band) with frequency. These values reflect the shrinking range over which coda amplitude is observed to be independent of distance as frequency increases. Site and *Q* terms are varied to obtain the best fit. While appearing physical, this equation is only used for empirical fitting and fit parameters must not be overinterpreted. These site and Q values are used as the starting point for a second refinement step.

The site and Q terms are further refined using data only from events recorded at more than one station. This is done by adjusting the site and Q models simultaneously for all stations in order to fit station-to-station amplitude ratios. This removes the influence of a possibly biased m_b, which was used in the initial step to remove source effects (Mayeda et al., 2003). We implement this procedure using an L_1 criterion with direct search techniques (Press et al., 2001). We note that the heterogeneous seismicity pattern results in sampling over limited distance ranges for many stations, which makes extrapolation risky using the 1D results.

Our preferred path correction method employs tomography techniques to invert for a laterally varying (2D) Q and relative site terms (Phillips et al., 2000; Phillips et al., 2001; Phillips and Hartse, 2002). The inversion equations are the same as for the 1D case, above, with the addition of a sum over discretized path terms in place of 1/Q. We only use data from multiply recorded events, similar to the second, 1D path step, in order to eliminate source effects by fitting station-to-station amplitude ratios. We remove a small number of outliers (less than 1% of the data) based on the 1D results and use L_2 techniques in the inversion. Spreading is set as in the 1D calculations. Currently, the tomography treats the coda as a direct path, rather than an ellipsoidal area. This is most appropriate for short codas; however, misfits are low as RMS residuals fall below 0.1 log10 amplitude units for all bands. For data from 2250 multiply recorded events in the band 0.7 to 1 Hz, for example, residual variance is reduced 86% relative to the best

fit, uniform Q model. Q results follow regional geology well. We are confident in our ability to extrapolate path corrections into aseismic areas because of the more physical nature of the tomography model.

The final calibration steps adjust measurements between bands and shift to absolute units based on independently determined moments. Adjustments between bands are calculated in order to flatten earthquake spectra below their corners. Corner frequencies are estimated using scaling based on m_b (Taylor and Hartse, 1998). We start with earthquake data from bands less than 1/4 of the corner frequency in an L_1 simplex inversion to obtain the band corrections. For our dataset, this gives corrections for bands below 1 Hz. We assume an ω^2 model and allow data less than 1/2 the corner, and so on, to obtain corrections for the higher bands, which are spliced to the low frequency results. This approach was suggested by results of synthetic tests that showed that high frequency spectra can drift high by 0.1 to 0.2 $\log_{10}$ units, likely due to a slight curvature of earthquake spectra when using a liberal corner frequency cutoff.

We are fortunate to have data from 44 earthquakes for which moments have been independently determined using waveform matching techniques (Zhu et al., 1997; Patton, 1998; Ghose et al., 1998). An overall shift is obtained such that spectral data from bands less than 1/4 of the corner frequency, calculated as above, match the appropriate moment in a median sense. Spectra then carry units of N-m. Earthquake results become moment rate spectra and we refer to explosion results as apparent coda source spectra, the term apparent indicating possible near source effects, including near source path, on the spectra.

After correction, the scatter between coda and independently derived moments is 0.18 $\log_{10}$ units. We do not use CMT solutions in this step because of bias due to unaccounted for crustal thickness in this area (Patton, 1998). Additional independent moments will be needed in the future to further validate our results. A broad geographical distribution would help validate the broad area calibration. Moments for small events, perhaps obtained by applying spectral techniques to local network data, would help validate the results in higher bands.

Apparent source spectra for a well recorded Lop Nor nuclear event show good correspondence between stations (Figure 2). These spectra match especially well in the higher bands. Low frequency coda are less well studied, but are know to exhibit multipathing effects (Patton et al., 1985). Spectra from a suite of Degelen explosions show a marked scaling of the spectral peak (Figure 3). These spectral peaks occur in higher bands than has been observed for NTS explosions (Mayeda and Walter, 1996) and may reflect more competent emplacement material.

The earthquake results can be summarized by fitting a two-parameter ω^2 source model.We then calculate Mw and stress drop using standard formulae. Stress drop for network spectral fits show striking regional variation in China and central Asia (Figure 4). The patterns include low stress drop events (0.1 MPa) in areas of north-central Tibet and the North China Basin. A marked gradient in stress drop can be seen starting at the Tarim Basin-Tien Shan boundary where stress drops are uniformly about 1 MPa, then moving north into the Tien Shan where stress drops increase to above 10 MPa and finally approach 100 MPa. The stress drop patterns tend to be similar from station to station. Furthermore, for station WMQ and others, the low stress Tibet events lie along similar paths as more distant, higher stress events. This indicates unaccounted for path effects are not the cause of the variations. Such variations in scaling should be included in amplitude calibration efforts for both event identification and characterization work.

CONCLUSIONS AND RECOMMENDATIONS

Broad area calibration using tomographic imaging for path and site effects allows coda spectra to be displayed on a common basis throughout China and central Asia, for both earthquakes and explosions. Residuals from the tomographic inversions are remarkably low, on the order of 0.1 $\log_{10}$ units, demonstrating the internal consistency and precision of the amplitude data. Similar, two-dimensional patterns should be investigated in other coda calibration steps, including the group velocity of the peak envelope and coda shape effects.

The calibration steps are tied together by a single master script. This allows easy updating of results when methods are modified or new data or manual picks are added. This also allows synthetic tests to be run with minimal effort, which have given us insight into weaker links and generated upgrades in the calibration procedures. The critical

pieces of the automatic scheme are codes that determine the coda window, which have been designed to avoid secondary events and noise once the coda shapes are calibrated. Calibration is further aided by using robust, L_1, inversion methods wherever possible and by bootstrapping from starting models based on manually picked data.

The coda results show interesting scaling for both explosion and earthquake sources. Explosion spectra peak in bands higher than has been found for NTS, which may have implications for transportability of event identification and characterization techniques. Earthquakes also show systematic, regional variations in scaling through stress drop patterns, which could be included in event identification work (MDAC) to reduce scatter in earthquake populations of discriminants, as well as in the coda procedures, where emphasis on high stress drop events would be useful in obtaining spectral flattening corrections.

REFERENCES

Aki, K. (1969). Analysis of the seismic coda of local earthquakes as scattered waves, J. Geophys. Res., 74, 615-631.

Aki, K. and B. Chouet (1975). Origin of coda waves: attenuation, and scattering effects. J.Geophys.Res. 80, 3322-3342.

Ghose, S., M.W. Hamburger and C.J. Ammon (1998). Source parameters of moderate sized earthquakes in the Tien Shan, central Asia from regional moment tensor inversion, Geophys. Res. Lett., 25, 3181-3184.

Hartse, H.E., W.S. Phillips, M.C. Fehler and L.S. House (1995). Single-station spectral discrimination using coda waves, Bull. Seism. Soc. Am., 85, 1464-1474.

Kim, W-Y. and G. Ekstrom (1996). Instruments responses of digital seismographs at Borovoye, Kazakhstan, by inversion of transient calibration pulses. Bull. Seism. Soc. Am. 86, 191-203.

Mayeda, K.M. (1993). mb (Lg Coda): A stable single station estimator of magnitude, Bull. Seism. Soc. Am., 83, 851-861.

Mayeda, K.M., W.R. Walter (1996). Moment, energy, stress drop and source spectra of western United States earthquakes from regional coda envelopes, J. Geophys. Res., 101, 11195-11208.

Mayeda, K.M., A. Hofstetter, J.L. O Boyle, W.R. Walter (2003). Stable and transportable regional magnitudes based on coda-derived moment-rate spectra, Bull. Seism. Soc. Am., 93, 224-239.

Owens, T.J., G.E. Randall, F.T. Wu and R. Zeng (1993). PASCALL instrument performance during the Tibetan Plateau Passive Seismic Experiment, Bull. Seism. Soc. Am., 83, 1959-1970.

Patton, H.J., S.R. Taylor, D.B. Harris and J.M. Mills (1985). The utility of regional Chinese seismograms for source and path studies in central Asia, Geophys. J. Royal Astr. Soc., 81, 469-478.

Patton, H.J. (1998). Bias in the centroid moment tensor for central Asian earthquakes: Evidence from regional surface wave data, J. Geophys. Res., 103, 26963-26974.

Phillips, W.S. and K. Aki (1986). Site amplification of coda waves from local earthquakes in central California, Bull. Seism. Soc. Am., 76, 627-648.

Phillips, W.S., H.E. Hartse, S.R. Taylor and G.E. Randall (2000). 1 Hz Lg Q tomography in central Asia, Geophys. Res. Lett., 27, 3425-3428.

Phillips, W.S., H.E. Hartse, S.R. Taylor, A.A. Velasco and G.E. Randall (2001). Application of regional phase amplitude tomography to seismic verification, Pure Appl. Geophys., 158, 1189-1206.

Phillips, W.S. and H.E. Hartse (2002). Regional path calibration using multiple station amplitude tomography, Seism. Res. Lett., 73, 228.

Press, W.H., S.A. Teukolsky, W.T. Vetterling and B.P. Flannery (2001). Numerical Recipes in Fortran 77: The Art of Scientific Computing, Cambridge University Press, Cambridge, U.K.

Rautian, T.G., V.I. Khalturin, I.S. Shengelia, (1979). The coda envelopes and the determination of the magnitudes of Caucasus earthquakes, The Physics of the Earth, Acad. Sci. USSR, N6 22-29 (English translation of Russian original).

Richards, P.G., W.Y. Kim and G. Ekstrom (1992). The Borovoye Geophysical Observatory, Kazakhstan, EOS, 73, 201-206.

Taylor, S.R. and H.E. Hartse (1998). A procedure for estimation of source and propagation amplitude corrections for regional seismic discriminants, J. Geophys. Res., 103, 2781-2789.

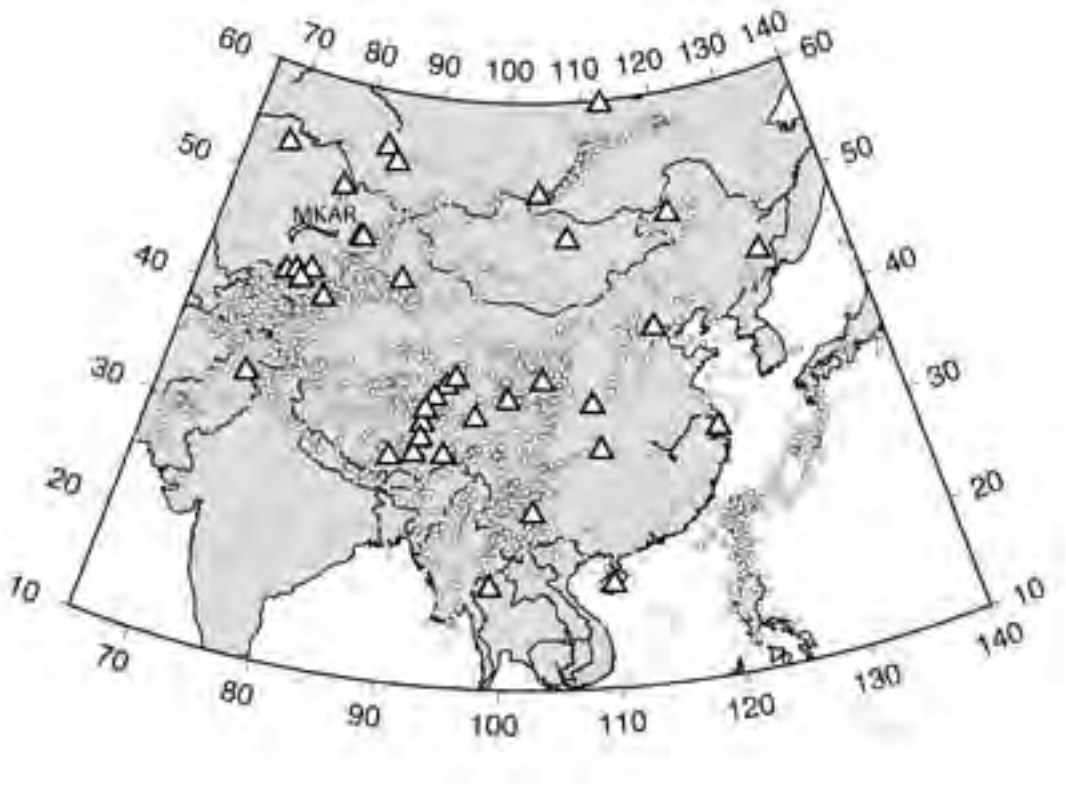


Figure 1. **Stations and events used in the coda wave study.**

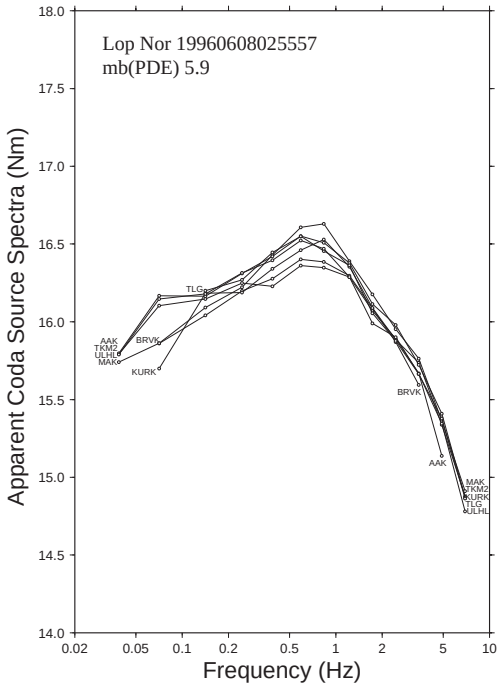


Figure 2. Apparent source spectra determined using coda wave data from seven stations for a Lop Nor test. Stations are indicated as spectra endpoints. The inter-station consistency is especially good for bands above 1 Hz.

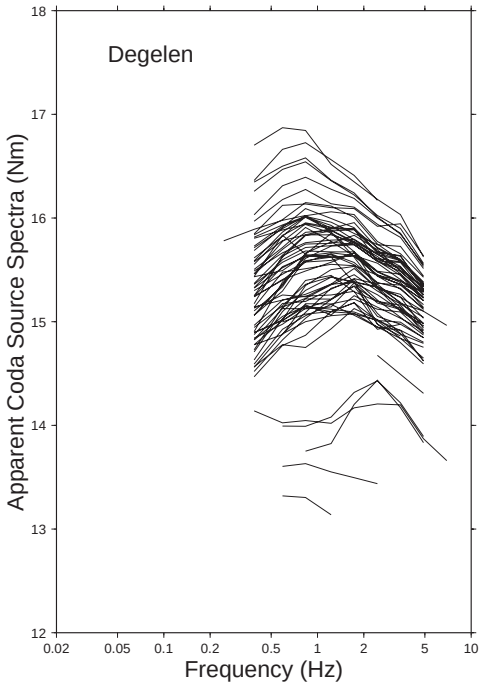


Figure 3. Apparent source spectra from coda for Degelen Mountain events, including the Omega series, 100 T chemical explosions.

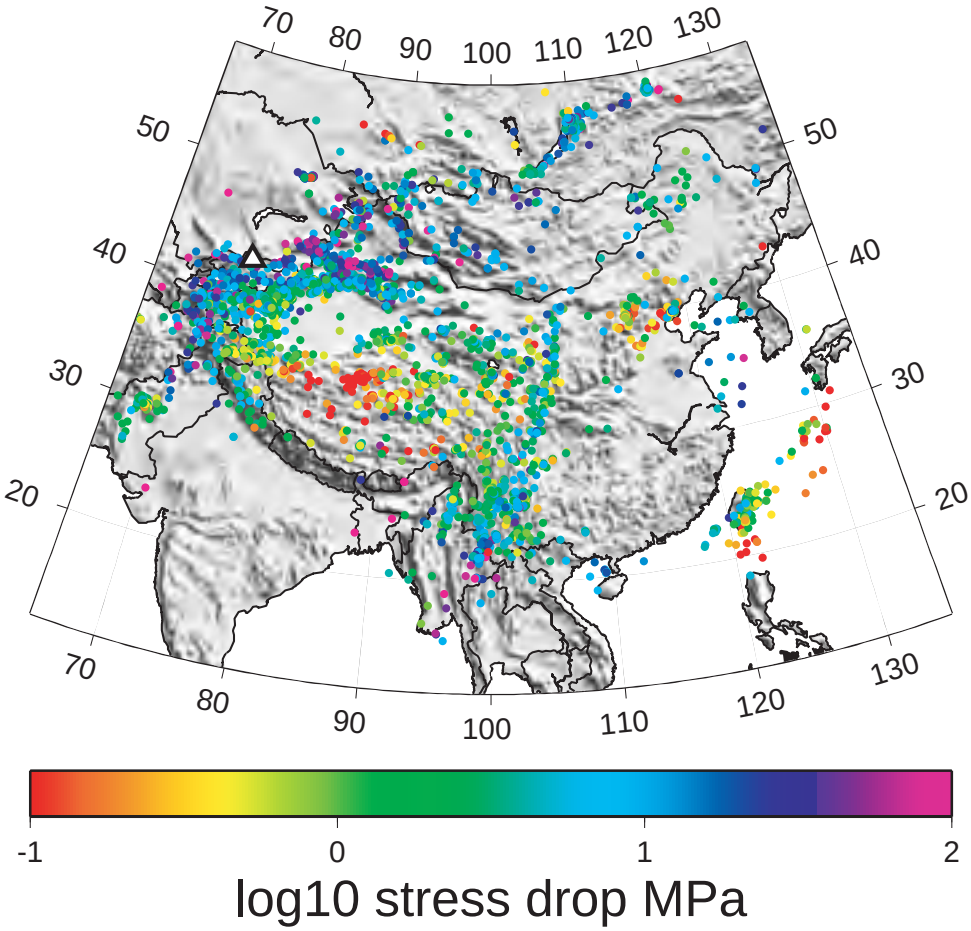


Figure 4. Network stress drop from coda spectra based on standard formulae.

SEISMIC SOURCE CHARACTERIZATION AND ENERGY PARTITIONING FROM IN-MINE AND REGIONAL BROADBAND DATA IN SOUTH AFRICA

Eliza Richardson,[1] Andrew A. Nyblade,[1] William R. Walter,[2] and Arthur J. Rodgers[2]

Penn State University[1] and Lawrence Livermore National Laboratory[2]

Sponsored by National Nuclear Security Administration
Office of Nonproliferation Research and Engineering
Office of Defense Nuclear Nonproliferation

Contract No. DE-FC03-02SF22673[1] and W-7405-ENG-48[2]

ABSTRACT

Mining-induced seismicity provides an important link between man-made and natural tectonic processes because it includes both fresh-fracturing events that are directly triggered by excavation and blasting, as well as events dominated by frictional slip which are analogous to tectonic earthquakes. These two types of events have distinguishable characteristics, such as different spatio-temporal clustering patterns, as well as different spectral signatures. Some previous studies using local in-mine data indicated that the fresh-fracturing events often have isotropic (explosional) moment tensors. Being able to differentiate the two types of events at regional and teleseismic distances is important for seismic verification studies.

We are studying a dataset of M > 2.5 mining-induced events that occurred between 1997 and 1999 in the Far West Rand gold-mining region of South Africa, approximately 80 km southwest of Johannesburg. The depth range of these events is 1.5 - 4 km, and they were recorded locally by four networks of 102 three-component geophones installed at depth throughout the active mining environment. These events were also recorded at regional distances by a two-year Passcal deployment of 80 broadband stations.

Using a spectral method, we have calculated source parameters for these events from the in-mine recordings, including seismic moment, stress drop, corner frequency, radiated energy, and apparent stress. Fresh-fracturing events have higher energy and larger stress drops than frictional events, although the latter generally have larger seismic moments. S/P wave amplitude ratios are lower for fracturing events as well, which can be an indication of isotropic components of the source.

INTRODUCTION

Mining-induced seismicity not only occurs at scales between those in the laboratory and those on tectonic faults but also can be recorded at the depth of seismic nucleation using in-mine seismometers, thus creating an excellent "natural laboratory" in which to study the physics of earthquake rupture. At present most gold mines in the Witwatersrand basin of South Africa use sophisticated underground arrays of geophones and accelerometers to record over 1,000 events per day. The extensive seismicity recorded at moment magnitude $M_w > 2$ provides a unique dataset to develop and test methods of discrimination between natural seismicity, mining tremors, and other industrially-related events such as chemical explosions. These $M_w > 2$ mining-induced events are large enough to be recorded on the in-mine arrays, as well as regionally by broadband seismometers. Therefore, locations, magnitudes, and focal mechanisms may be accurately determined from the high-frequency local data while regional phase propagation and energy partitioning may be studied via regional recordings. Another feature of this dataset is the variety of focal mechanisms as some mine events are purely double-couple shearing events whereas others have significant isotropic components (McGarr, 1992).

Background Information

The four adjacent mines of the Carletonville mining district in the Witwatersrand basin of South Africa, in which the events in this study were recorded, are the deepest in the world. They extract ore from two gold-bearing quartzite's, the Ventersdorp Contact Reef and the Carbon Leader Reef. These two units are separated by 900 m vertically, extend 2-4 km below the surface, and dip to the south at 21°. The mines contain old faults and dykes with two major trends: N 5° E and N 95° E. The interfaces between the faults, dykes, and host rock are planar discontinuities, many of which have been reactivated by the mining activities. It is these surfaces that provide the source region for the larger seismic events. The Witwatersrand basin itself is located in the Archean Kaapvaal cratonic province. This is not a tectonically active area. The seismicity recorded in this region is virtually all due to the strain energy accumulated over time by the mining processes of blasting and ore removal.

Figure 1 shows, in map view, the locations of the more than 100 3-component geophones installed at depth in the mines, together with epicenters of events for which we have determined source parameters (shown in Table 1). The geophones can sample at frequencies of 400-10,000 Hz. The station spacing underground is on the order of 100m in the active mining zones. Because there are two horizons being mined simultaneously, event depth is well-constrained by the geophones at different depths, especially compared to other mining-induced or borehole datasets in which the seismometers are usually situated on a single plane or in one line.

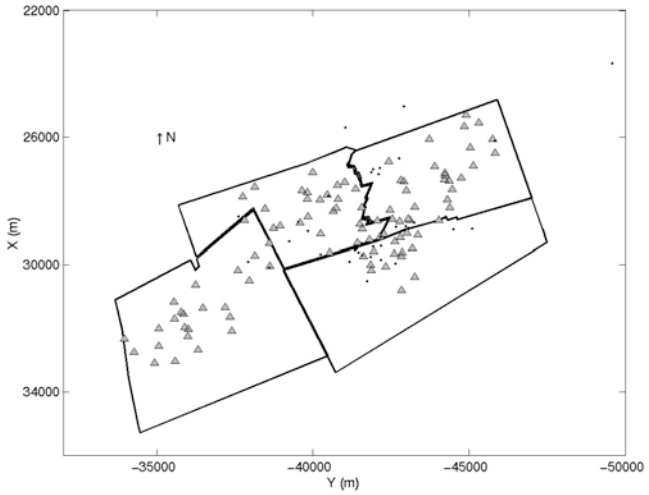


Figure 1. Map view of the lease areas of four mines in the Carletonville district (in mine coordinates). There are 102 three-component stations installed at depth (triangles). Dots represent the epicenters of large mining-induced events in this study.

Table 1. Preliminary Source Parameters of mining-induced events determined by in-mine array data*

Event	Lat	Lon	Depth	M_0	M_w	E	f_0	Ds
19980111144841	-26.401	27.411	2338	1.4e13	2.7	5.5e8	15.8	5.87
19980220050356	-26.429	27.430	3694	7.8e13	3.2	1.0e10	12.9	20.00
19980328134551	-26.437	27.417	2729	1.2e13	2.7	2.8e8	16.6	3.65
19980329051801	-26.435	27.422	2587	2.2e13	2.8	4.9e8	16.3	3.46
19980331135629	-26.439	27.380	2053	2.2e13	2.8	2.1e8	9.3	1.47
19980404190603	-26.430	27.399	2047	1.1e13	2.7	1.8e8	14.6	2.51
19980420170707	-26.395	27.430	2273	2.8e13	2.9	1.6e9	13.8	8.76
19980420194749	-26.412	27.422	1925	2.5e13	2.9	9.1e8	14.8	5.72
19980502123739	-26.414	27.419	1955	2.2e13	2.8	4.9e8	11.9	3.43
19980508103233	-26.440	27.427	2661	1.1e13	2.6	1.8e8	12.1	2.46
19980622162025	-26.439	27.423	2588	1.3e13	2.7	3.4e8	15.2	4.01
19980708212049	-26.434	27.416	2553	1.2e13	2.7	3.9e8	14.8	4.83
19980727135740	-26.427	27.419	2409	2.5e13	2.9	4.3e8	9.5	2.73
19981002194336	-26.432	27.423	2569	1.0e13	2.6	1.3e8	10.2	1.90
19981007192539	-26.420	27.406	3123	2.0e13	2.8	1.3e9	16.9	10.30
19981019200410	-26.436	27.416	2505	1.3e13	2.7	2.0e8	10.5	2.40
19981021044841	-26.434	27.420	2613	1.0e13	2.6	1.3e8	11.5	2.00
19981023160058	-26.437	27.420	2745	3.1e13	2.9	7.1e8	8.7	3.50
19981027090946	-26.426	27.377	2989	1.2e13	2.7	3.6e8	15.2	4.72
19981102163835	-26.427	27.434	2552	2.5e13	2.9	6.2e8	10.4	3.90
19981110172424	-26.404	27.459	2770	1.2e13	2.7	3.1e8	15.0	4.10
19981119170822	-26.414	27.422	2268	1.1e13	2.6	3.0e8	13.3	4.20
19981223093859	-26.433	27.393	3375	2.8e13	2.9	1.1e9	12.8	5.94
19990103155836	-26.412	27.420	1748	1.1e13	2.6	1.2e7	12.1	0.87
19990118213352	-26.409	27.429	2879	9.1e12	2.6	1.6e7	15.0	1.00
19990202123021	-26.435	27.415	2582	1.2e13	2.7	3.2e7	13.6	3.00
19990209195821	-26.401	27.418	1618	4.2e13	3.0	9.2e8	9.3	3.20
19990216053511	-26.429	27.432	3761	1.2e13	2.7	9.2e6	10.4	0.56
19990226143150	-26.397	27.387	1981	4.5e12	2.4	2.2e6	12.3	0.53
19990309161938	-26.435	27.415	2464	1.1e13	2.6	6.8e7	8.1	0.99
19990310023001	-26.429	27.428	2651	1.0e13	2.6	1.7e8	14.9	2.50
19990318193538	-26.428	27.396	395	4.6e13	3.1	1.5e9	11.5	5.20
19990703111216	-26.169	27.497	3099	2.2e13	2.9	1.8e8	18.5	10.60
19990709200228	-26.395	27.413	7235	5.5e13	3.1	9.7e8	8.7	4.00
19990718173016	-26.393	27.403	3823	7.0e13	3.2	1.2e9	8.6	4.80
19990907150924	-26.386	27.446	3634	4.0e13	3.0	2.7e9	13.0	10.90
19990923132820	-26.386	27.452	4028	4.1e13	3.0	1.5e9	13.3	10.30

*Event dates and times are listed as yyyymmddhhmmss, event locations are given by their latitude (°N), longitude (°E), and depth (meters below datum). It should be noted that event depths are referenced to the origin or "datum" of the Z-axis of the local mine coordinates. This datum is a reference point in Johannesburg, and is 250 m above ground level and about 1800 m above sea level in the Carletonville Mining District where these events occurred. Seismic moment M_0 is in Nm, magnitude M_w is moment magnitude (Hanks & Kanamori, 1979), energy E is given in Joules, corner frequency f_0 is in Hz, and static stress drop Ds is in MPa.

Preliminary Source Parameters

We have assembled a dataset of large (M_w > 2.5) mining-induced events from 4 gold mines in the Far West Rand region. The locations of these events were determined by operators at the mines via a ray-tracing algorithm based on body wave arrival times (Mendecki, 1993, 1997). This method incorporates a layered velocity model based on geologic units that have been determined by underground surveying and mapping as well as surface-based refraction

profiles and borehole log data. Since the wavespeeds and location procedures have been verified by test blasting, the location uncertainties are typically on the order of 10-20 m for events of $M_w > 2$.

Using the spectral method developed by Andrews (1986) and adapted by Richardson & Jordan (2002) for use with in-mine seismic recordings, we have calculated source parameters for 14 events that occurred in 1999 and 23 events from 1998 (see Table 1). Each of the events in this study was recorded by at least ten stations. In order to determine source parameters, we median-stacked each event's spectra and integrated the results up to the Nyquist frequency to determine S_D, the integral of the displacement power spectra (see Equation 6 of Andrews, 1986), S_V, the integral of the velocity power spectra (see Equation 7 of Andrews, 1986), and A^2, the acceleration power spectral level (see Equation 19 of Andrews, 1986). These are used to determine the source parameters radiated energy (E), seismic moment (M_0) , and static stress drop ($\Delta\sigma$) as follows:

$$E = 4\pi\rho v S_V$$

$$M_0 = \frac{8\pi\rho v^3 S_D^{(3/4)}}{\neg S_V^{(1/4)}}$$

$$\Delta\sigma = \frac{2\pi f_0 \rho A^2}{C\neg}$$

in which the corner frequency is found by

$$f_0 = \left(\sqrt{S_V / S_D}\right) / 2\pi.$$

In the previous equations, ρ is the rock density, which has been determined experimentally at the mines, v is wavespeed, $\neg$ is a constant based radiation pattern, and C is also a small constant. An advantage of this method is that the exponent of the spectral rolloff is not a fixed parameter as in the case of fitting spectra with a Brune-type curve. Because our data is band-limited, there is an upper limit to the radiated energy we can determine (Ide & Beroza, 2001). However, in practice the underestimation of energy for this dataset is very small (approximately 5%) since typical corner frequencies for the events in this study are generally 1/5 to 1/10 of the Nyquist frequency (Richardson & Jordan, 2002).

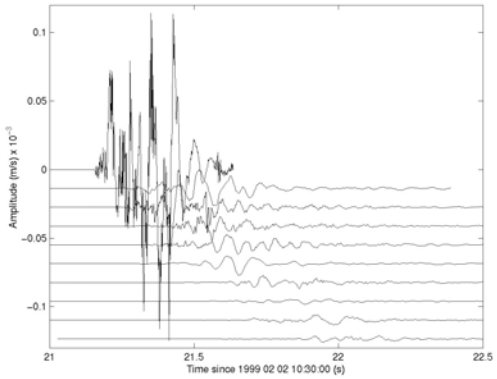


Figure 2. Vertical component velocity seismograms from nine stations of event 19990202123021 (see Table 1 for source parameters). The waveforms shown here were recorded at a range of 200 – 2500 m from the source.

CONCLUSIONS AND FUTURE WORK

To date, we have focused on producing a catalog of source parameters for several large mining-induced events. The next step is to determine focal mechanisms from waveform inversions of the near field in-mine data (see Figure 2) and then investigate the effect of energy partitioning on regional discriminants using regional broadband data.

Recent studies of mining-induced seismicity have suggested that radiated energy is a function of event size (Richardson & Jordan, 2002). However, it is not yet clear whether this property applies to natural as well as induced seismicity, nor has an adequate physical model been set forth that can account for all observations of source scaling parameters. Therefore, we intend to use this dataset to produce a catalog of regional discriminants specific to this mining region. Understanding how energy is partitioned in these events is important for basic research of the nucleation and rupture of small events as well as for increasing explosion monitoring effectiveness**.**

REFERENCES

Andrews, D. J., Objective determination of seismic source parameters and similarity of earthquakes of different size, in *Earthquake Source Mechanics*, S. Das, J. Boatwright, C.H. Scholz, eds, vol. 6 of Geophysical Monograph 37, pp. 259-267, Am. Geophys. Union, 1986.

Hanks, T.C. and H. Kanamori, A moment magnitude scale, *J. Geophys. Res*., **84**, pp. 2348-2350, 1979.

Ide, S. and G. C. Beroza, Does apparent stress vary with earthquake size?, *Geophys. Res. Lett.,* **28,** pp. 3349-3352, 2001.

Mendecki, A. J., ed., *Seismic Monitoring in Mines*, Chapman and Hall, 1997.

Mendecki, A. J., Real time quantitative seismology in mines, Keynote lecture in *Proc. 3rd Intl. Symp. on Rockbursts and Seismicity in Mines*, ed. By R. P. Young, Balkema, Rotterdam, pp. 1141-1144, 1993.

McGarr, A., Moment tensors of ten Witwatersrand mine tremors, *Pure Appl. Geophys.*, **139,** pp. 781-800, 1992.

Richardson, E. and T.H. Jordan, Seismicity in deep gold mines of South Africa: Implications for tectonic earthquakes, *Bull. Seism. Soc. Am.*, **92**, pp. 1766-1782, 2002.

SCALING LAWS FOR SECONDARY SEISMIC RADIATION GENERATED BY FRACTURE DAMAGE

Charles G. Sammis

University of Southern California

Sponsored by Air Force Research Laboratory

Contract No. DTRA01-01-C-0086

ABSTRACT

The non-linear source region of an underground explosion can be divided into a series of nested spherical shells, each characterized by a different deformation rheology. Between the detonation point and the cavity radius, r_c, rock is vaporized. Between r_c and the "failure radius", r_f, rock is fragmented. Between r_f and the "damage radius" r_d, new cracks are nucleated and grow, but rock is not fragmented. Between r_d and the "elastic radius" r_e, existing cracks slide, deformation is anelastic, but no new damage is generated. The micromechanical damage mechanics formulated by Ashby and Sammis (1990) allows us to quantify this model by calculating the bounding radii once the size and density of initial fractures in the rock is specified. Recently Johnson and Sammis (2001) and Sammis (2002) have shown that the integrated effect of the nucleation and growth of fracture damage in the non-linear source region between r_c and r_e can generate secondary seismic waves comparable to those generated by the source. We show here that the spectrum of this secondary radiation scales with the failure radius r_f, in the same way that the primary radiation has long been known to scale with the elastic radius r_e. This scaling is established using results from the Non-Proliferation Experiment (NPE) chemical explosion from Johnson and Sammis (2001) and near-field records from the PILEDRIVER nuclear explosion in granite.

OBJECTIVE

The objective of this research has been to identify and understand the nonlinear processes that contribute to the seismic signal radiated by underground explosions. Our specific focus is on crystalline rock where sliding on preexisting cracks and the nucleation and growth of new cracks contribute to the signal. In the past, in collaboration with Rimer and Stevens (Rimer *et al*., 1999; Stevens *et al*., 2002), we have shown that such processes provide a physical explanation for the "pulse broadening" observed in the near-field seismic records from the PILEDRIVER event. Our recent focus has been on the secondary radiation generated by these fracture processes, which we describe using micromechanical damage mechanics (Ashby and Sammis, 1990). Because this damage mechanics models the cracks, we are able to calculate the dilatational and shear moment tensors of each and sum their net effect over the entire source region. While the contribution of each crack is small and high-frequency, Johnson and Sammis (2001) have shown that the integrated signal is of comparable magnitude to the main pulse and in the seismic band. Because this higher frequency secondary radiation may contribute to regional phases currently being used to identify and characterize explosive sources, it is important that its scaling properties be understood. This report is a step in that direction.

RESEARCH ACCOMPLISHED

The source region of an underground explosion can be described by a nested set of concentric spheres, each characterized by a distinct rheology (Figure 1). Closest to the source, rock vaporizes and flows plastically to produce a cavity of radius r_c. At greater distances, the rock is driven to brittle failure, granulates, and may be further weakened by acoustic fluidization. Brittle failure extends to a radius r_f, which, for a given source model, may be calculated as the onset of failure in the Ashby and Sammis damage mechanics. At distances greater than r_f, radial cracks grow from preexisting flaws, but the rock does not fail and is not granulated. This process extends out to a distance r_d where stresses have fallen to the point where new cracks no longer nucleate from the preexisting ones. For a given source model, r_d is calculated using the nucleation condition in Ashby and Sammis (1990). At distances larger than r_d, sliding is still possible on the preexisting cracks, but new crack damage is not nucleated. The hysteresis associated with crack sliding results in an anelastic rheology, which extends out to the elastic radius r_e. The elastic radius may be estimated using the Couloumb friction criterion for sliding on a preexisting surface.

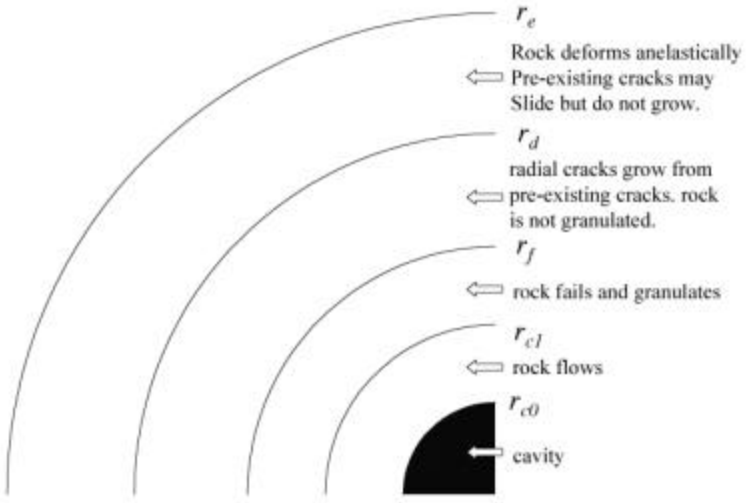


Figure 1. Rheological radii for the non-linear region of an explosion source

Johnson and Sammis (2001) used the Ashby and Sammis (1990) damage mechanics in a simple "equivalent source model" to calculated source radii r_c, r_f, and r_d, as well as the secondary radiation generated by the 1kt NPE explosion in tuff for a range of the two damage mechanics model parameters: a, the radius of the initial cracks in the source medium, and D_o, the initial damage in the source medium. D_o is defined as

$$D_o = \frac{4}{3}p\left(a\cos c\right)^3 N_v \qquad (1)$$

where N_v is the number of initial cracks per unit volume and $\boldsymbol{c}$ is a geometrical factor near one. These results were reported last year (Sammis, 2002), and are summarized here in Tables 1 and 2. Note that the initial crack size controls the nucleation radius r_d, while the initial damage controls the failure radius r_f.

Table 1. Effect of initial damage on source dimensions. (crack radius a =0.1 cm in all cases)

Initial damage D_o	Failure damage D_f	Failure radius r_f (m)	Damage radius r_d (m)	Maximum velocity at 450 m (cm/sec)
0.01	0.09	25	25	0.9
0.05	0.26	35	45	8.4
0.10	0.40	35	45	16.1
0.20	0.53	35	45	28.2
0.40	0.73	35	45	44.8
0.80	1.13	35	45	88.9

Table 2. Effect of initial crack radius on source dimensions. (initial damage $D_o = 0.1$ in all cases)

Crack radius a (cm)	Failure damage D_f	Failure radius r_f (m)	Damage radius r_d (m)	Maximum velocity at 450 m (cm/sec)
0.01	0.22	18	18	2.6
0.10	0.40	35	45	16.1
1.00	0.39	75	90	21.1
10.0	0.40	90	150	13.1

The question now is, what controls the peak frequency of the secondary radiation? In order to answer this question, we used Fast-Fourier analysis to find the peak frequency of the secondary radiation for the cases calculated by Johnson and Sammis (2002). Results are summarized in Table 3 where the various rheological radii and peak spectral frequencies are computed for $D_o = 0.1$ and a range of initial flaw sizes, a.

Table 3. Spectral analysis of NPE source.

	D_o	a (cm)	r_c (m)	r_f (m)	r_d (m)	$f_{\max}$ (Hz)
Explosion (observed)						9
Explosion (modeled)	0.1	0.1	15	35	45	6
Secondary P	0.1	0.01	15	18	18	31
	0.1	0.1	45	28.2		17
	0.1	1.0	45	44.8		12
	0.1	10.0	45	88.9		9
Secondary SH (Prestress)	0.1	0.1	15	35	45	7
Secondary SH (Preferred orientation)	0.1	0.1	15	35	45	7

When the peak frequency $f_{\max}$ was plotted as a function of the various radii, the following dependencies were found:

$$f_{\max} \propto r_f^{-1}, \qquad f_{\max} \propto r_d^{-1/2}, \qquad f_{\max} \propto \left(r_f - r_c\right)^{-1/2}, \qquad f_{\max} \propto \left(r_d - r_c\right)^{-1/3} \tag{2}$$

Only the first relation in equations (2) makes physical sense, and is the same scaling observed for the main pulse where the corner frequency in the spectrum f_c, scales with the elastic radius as (Denny and Johnson, 1991)

$$f_c = v / r_e \tag{3}$$

The scaling relation between the secondary radiation and the failure radius is shown in Figure 2. Note that $f_{\max}$ for the secondary SH waves are lower than for secondary P (at the same value of r_f) as expected from (3) above, but that the ratio $f_{\max}(P) / f_{\max}(SH) = 2.4$ while the ratio $v_P / v_S = 1.36$ in tuff. It may be that the frequency of the SH waves, being more sensitive to the sliding, scales with r_d. In that case, $(v_P / v_S)(r_d / r_f) = 1.75$, which is still less than 2.4. It may be that that the SH waves see the crack sliding all the way out to the elastic radius, while the P waves only see the major dilatation within the failure radius.

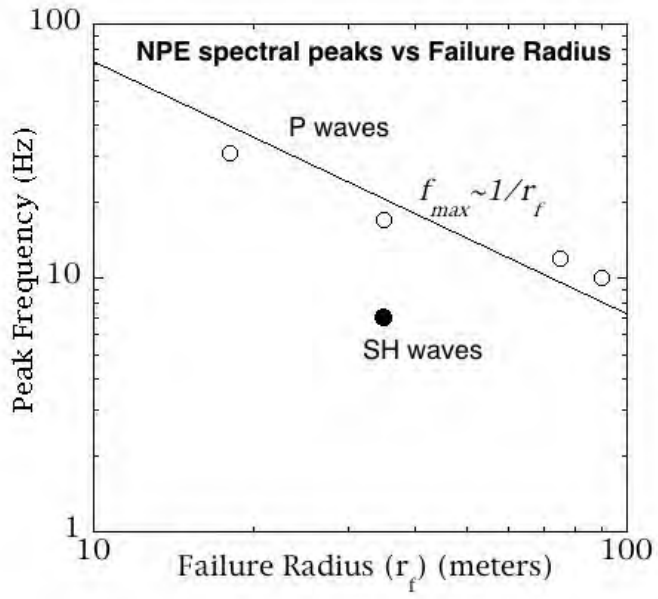


Figure 2. Peak frequency as a function of the failure radius. Note that the P waves frequency scales as $1/r_f$.

Finally, we compare these results with secondary radiation generated by the 61 kt PILEDRIVER event detonated in granodiorite.. Fourier analysis of the near-filed records (one of which is shown in Figure 3) reveals a high-frequency component with $f_{\max} \approx 25$ Hz. For granodiorite, $v_P \approx 5.5$ km/sec, so, the scaled frequency in the tuff ($v_P \approx 2.6$) is $f_{\max} = (2.6/5.5)25 = 12$ Hz. For the damage parameters used to construct Figure 2, this corresponds to $r_f \approx 70$ m, not an unreasonable value based on the post-shot core data (Borg, 1970). We are currently modeling the granite explosions PILEDRIVER, HARDHAT, and SHOAL to further quantify this result.

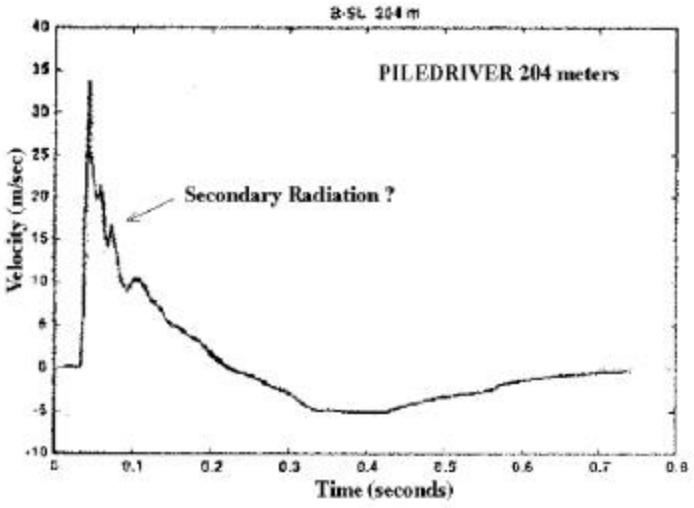


Figure 3. Velocity seismogram for PILEDRIVER at 204 m. (from Stevens et al., 2002).

CONCLUSIONS AND RECOMMENDATIONS

The frequency of secondary P wave radiation generated by fracture damage scales with the failure radius as $f_{\max} \propto v_P / r_f$. The frequency of secondary SH radiation appears to scale with the elastic radius as $f_{\max} \propto v_S / r_e$, possibly reflecting the fact that dilatation is most pronounced near failure while significant sliding on preexisting cracks occurs out to the elastic radius. We are currently exploring these scaling relations by modeling the nuclear explosions PILEDRIVE, HARDHAT, and SHOAL.

ACKNOWLEDGEMENTS

This work reflects an ongoing modeling collaboration with Lane R. Johnson at U.C. Berkeley.

REFERENCES

Ashby, M. F., S. and C. G. Sammis (1990), The Damage Mechanics of Brittle Solids in Compression, *Pure appl. Geophys*, 133, 489-521.

Borg, I. Y. (1970), Survey of Piledriver Results and Preliminary Interpretation of Three Postshot Cores in and Near the Cavity, Lawrence Radiation Laboratory Report UCRL-50865.

Denny, M. D. and L. R. Johnson (1991), The Explosion Seismic Source Function: Models and Scaling Laws Reviewed, in Explosion Source Phenomenology, Geophysical Monograph 65, edited by S. R. Taylor, H. J. Patton, and P. G. Richards, Am. Geophys. Union, pp. 1-24.

Johnson, L. R. and C. G. Sammis (2001), Effects of Rock Damage on Seismic Waves Generated by Explosions, *Pure appl. Geophys*, 158, 1869-1908.

Rimer, N., J. L. Stevens, J. R. Murphy, and G. G. Kocharyan (1999), Estimating Seismic Source Characteristics of Explosions in Hardrock Using a Micromechanical Damage Model, Maxwell Technologies Final Report MTSD-DFR-99-16423, July.

Sammis, C. G. (2002), Generation of High-Frequency P and S Wave Energy by Rock Fracture During a Buried Explosion: Its Effect on P/S Discriminants at Low Magnitude, Proceedings of the 24th Seismic Research Review – Nuclear Explosion Monitoring: Innovation and Integration, Sept. 17-19, 2002, Ponte Verde Beach, Florida, 542-551.

Stevens, J. L., N. Rimer, H. Xu, J. R. Murphy, G. E. Baker, G. G. Kocharyan, B. A. Ivanov, and S. M. Day (2002), Near Field and Regional Modeling of Explosions at the Degelen Test Site, Proceedings of the 24th Seismic Research Review – Nuclear Explosion Monitoring: Innovation and Integration, Sept. 17-19, 2002, Ponte Verde Beach, Florida, 562-571.

THE PHYSICAL BASIS OF Lg GENERATION BY EXPLOSION SOURCES

Jeffry L. Stevens,[1] G. Eli Baker,[1] Heming Xu,[1] Theron J. Bennett,[1] Norton Rimer,[1] Steven M. Day[2]

Science Applications International Corporation;[1] San Diego State University[2]

Sponsored by National Nuclear Security Administration
Office of Nonproliferation Research and Engineering
Office of Defense Nuclear Nonproliferation

Contract No. DE-FC03-02SF22676

ABSTRACT

The goal of the project is to develop a quantitative predictive capability for explosion-generated Lg phases with a sound and unambiguous physical basis. The research program consists of a theoretical investigation of explosion-generated Lg combined with an observational study. The specific question addressed by this research program is how the Lg phase is generated by underground nuclear explosions. This question is fundamental to how Lg phases are interpreted for use in explosion yield estimation and earthquake/explosion discrimination.

We have been looking initially at several explosion data sets - 1) Degelen Mountain explosions recorded at distances less than 100 km, and corresponding recordings at Borovoye at a distance of approximately 650 km; 2) recordings from Russian deep seismic sounding experiments; 3) Nevada Test Site (NTS) explosion sources including the Nonproliferation Experiment (NPE) and nuclear tests covering a range of source depths and media properties. A particularly interesting result from the Degelen explosion data is that:

a. The near regional data has small Sg phases, distinct from the strong Rg phase that persists out to at least 50 km.
b. At Borovoye, there are strong Sn and Lg phases.

Modeling of these data shows that both results are consistent with the signals from a shallow, axisymmetric compensated linear vector dipole (CLVD) source. This source has an S node in the horizontal direction, and therefore makes only a small direct S wave at the near regional stations, however it is a strong generator of S at takeoff angles corresponding to the crustal phases Lg and Sn. Synthetic seismograms generated using wavenumber integration are a very good match to the observed local Sg and regional Sn and Lg phases.

We are considering four candidate mechanisms for explosion-generated Lg:

1. Direct generation by the explosion source, where the explosion is modeled as a point compressional source.
2. Secondary generation by the explosion source, where Lg is generated primarily by the nonspherical parts of the explosion source, with strong influence from the free surface.
3. Rg scattering. The hypothesis is that the Rg phase is scattered as it travels away from the explosion and is converted to Lg.
4. P scattering. The hypothesis is that Lg is in a sense a variant on P coda containing converted P->S phases in the crust.

The observations discussed above favor explanation number 2. The spherically symmetric part of an explosion source in a high velocity medium generates very little Lg, and therefore does not explain the observations. However, the observed Lg waveforms and amplitudes can be explained by adding a CLVD, which is the lowest order non-spherical correction to the spherical source. That Rg persists to such large distances argues against explanation 3. We are in the process of performing a series of 2D nonlinear calculations of explosion sources. The main purpose of this work is to quantify the amount of seismic radiation generated by the non-spherical parts of a realistic explosion source. We have completed three calculations – a 2D nonlinear calculation modeled after the NPE source and structure, and two calculations of Degelen Mountain explosions. Lg calculated from the NPE calculation is consistent with an explosion plus a CLVD source with about half the strength of the explosion. However, because of the very low velocities at the NPE source location, the explosion generates substantial Lg directly and this alone may be sufficient to explain the Lg observations in this case. Since Degelen consists of a high velocity granite, little Lg is generated directly by the explosion, so the CLVD component is much more important.

OBJECTIVE

The objective of this project is to develop a quantitative predictive capability for explosion-generated Lg phases with a sound physical basis. The research program consists of a theoretical investigation of explosion-generated Lg combined with an observational study. The specific question addressed by this research program is how the Lg phase is generated by underground nuclear explosions. This question is fundamental to how Lg phases are interpreted for use in explosion yield estimation and earthquake/explosion discrimination.

RESEARCH ACCOMPLISHED

The importance of Lg to nuclear monitoring arises from Nuttli's (1986) remarkable results about the consistency of the Lg/yield relationship for explosions and from the application of the P/Lg discriminant (e.g. Bennett et al, 1997a, 1997b) and a variety of spectral ratio discriminants. Although Lg based discriminants have been widely used for regional earthquake/explosion discrimination, they are not completely satisfactory because regional variations are large enough that the discriminants cannot be regarded as reliable in uncalibrated regions. Because of this difficulty with transportability, it is very important to understand how Lg is generated in order to identify conditions under which the discriminants will fail and how to correct for those failures.

One of the peculiar properties of Lg is that it does not appear to be generated primarily by the explosion, even though it correlates very well with yield. That is, calculations based on point, spherical explosions in plane-layered media, which are generally satisfactory with minor corrections for predictions of other explosion-generated seismic phases, predict Lg that is both much smaller and more dependent on earth structure than the observations. Instead, Lg appears to be generated primarily by the non-spherical components of the explosion source including spall and other free surface effects. The most widely used explanation for Lg suggests that these non-spherical components can be modeled as a compensated linear vector dipole (CLVD) source, which generates Rg (regional fundamental mode surface waves), which then scatters into Lg (e.g. Gupta et al, 1997; Patton and Taylor, 1995; Patton, 2001). However, the non-spherical components of the source also generate Lg directly, so it may not be necessary to go through the intermediate Rg phase.

In this study, we are using numerical techniques coupled with observations of Lg and a review of observations from the literature to try to establish the physical mechanism for explosion-generated Lg. That is, we are looking at Lg data from explosions, performing numerical calculations of explosions, and comparing predictions with observations. Significant accomplishments to date include:

1. A detailed review of the literature on Lg generation, scattering, and related topics.
2. Nonlinear finite difference calculations of three explosions – the NPE and two Degelen Mt. explosions.
3. Collection and review of explosion-generated data from a variety of sources, including NTS data from LLNL stations, lines of stations that recorded Soviet deep seismic sounding (DSS) data, near field and near regional recordings of Degelen mountain explosions, and data from the same events recorded at Borovoye.

In this paper, we start by reviewing nonlinear modeling of explosion sources, and the calculations performed in the current study. Then we discuss the data that we are using for analysis, and finally compare results from the calculations with some of the observations.

The Nonlinear Explosion Source Near the Free Surface

The first approximation for an explosion is usually taken to be a point, spherically symmetric dilatational source. While this would be correct for an explosion in an infinite, uniform medium, the presence of the earth surface renders that description inadequate. The explosion source can be modeled more realistically using nonlinear finite difference calculations of explosions in a realistic earth model with gravity (Stevens et al., 1991). This approach models all near source effects including spall, cracking, and nonlinear deformation.

The seismic source generated by a realistic explosion can be described in various ways. Since a large part of the deformation is related to spallation of the surface layers, a natural characterization of the source is in terms of a horizontal tension crack at a shallower depth than the compressional source (Day and McLaughlin, 1991). The source can also be described by a multipolar expansion (e.g. Stevens, 1980), which for axisymmetric configurations includes a spherically symmetric term, a CLVD term, and higher order terms. Since the spherically symmetric term generates little Lg, it is reasonable to expect that the CLVD term would characterize the complex explosion source

for Lg. Patton and Taylor (1995) suggest that this is the case and that the CLVD source is more consistent with the data than the tensile crack source. Gupta and Wagner (1998) point to spectral nulls in Lg from NTS explosions as evidence that Lg is generated by Rg scattering from the CLVD source. It is puzzling, however, why the nulls are not filled in by Rg from the direct explosion, which generates a strong Rg phase as long as it is less than a wavelength deep.

In this study we have performed new nonlinear calculations in two very different types of structures: first, the Non-Proliferation Experiment (NPE), which was conducted at the Nevada Test Site (NTS) in a very low velocity medium; and second, a typical Degelen Mountain explosion which took place in a high velocity granite medium. Descriptions of these calculations follow.

NPE calculation

We performed a calculation of the Non-Proliferation Experiment (NPE) using detailed rock properties from Rimer et al. (1994). The NPE was a chemical explosion with yield equivalent to one kiloton of TNT. The material geology at the NPE site is based on that of the nearby Misty Echo event and consists of 4 layers (Figure 1a). Layers 1 and 4 are nonporous, and layers 2 and 3 have porosities of 3% and 0.5% respectively. The explosive is in a cylindrical cavity centered at 389 m depth, and is 7.7 m in radius (horizontally) and 5.2 m in height (vertically). We use a two-dimensional axisymmetric Lagrangian finite difference code to simulate nonlinear wave propagation from tamped underground explosions. The code has been used successfully for many ground motion calculations in our previous work. In Figure 1 (left) we show the extent of yielding and cracking from an HE source of 1.315kt of a 50/50 ANFO/emulsion mix. The region of nonlinear deformation near the explosion is approximately spherical, but elongated and slightly offset vertically. The region of cracking is confined to near the free surface. This explosion is deeply overburied, so there is less asymmetry than in a normally buried explosion.

We calculated full waveform synthetics from this calculation at a distance of 400 km. The synthetics are derived by saving the stresses and displacements on a monitoring surface outside the nonlinear region near the explosion and integrating with a Green's function calculated using wavenumber integration. Figure 1 (right) shows the synthetics together with synthetics from a point explosion and a CLVD source. Because this is a very low velocity structure, the crust effectively traps P->S converted waves from the explosion, so in this case the full waveform and in particular the Lg phase from the complex explosion source is modeled quite well by a point explosion source.

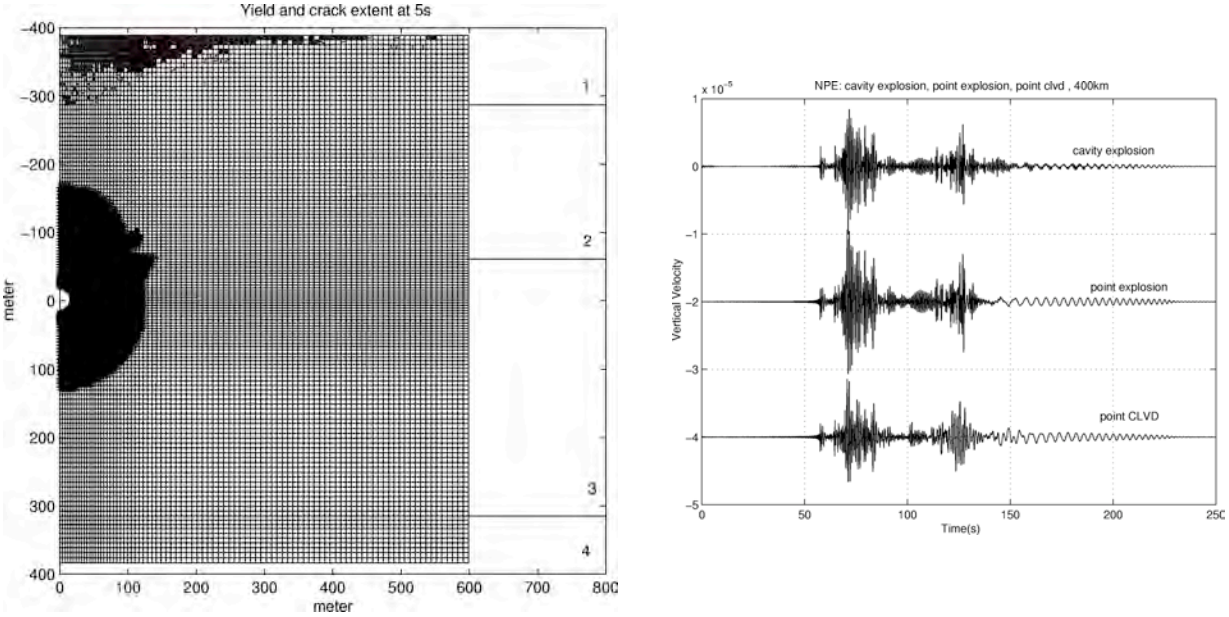


Figure 1. Region of nonlinear deformation and cracking from the NPE calculation (left). Vertical component synthetic seismograms at 400km from the HE explosion (right, top), and from a point explosion (right, middle) and point CLVD (right, bottom) in the same structure and at the same depth.

Degelen Mountain calculation

We performed two calculations for nuclear explosions at the Degelen Mountain test site. Material properties were taken from a detailed study of Degelen explosions (Stevens et al., 2003), and calculations were performed for the "wide pulse" and "narrow pulse" models described in that study. Figure 2 shows the results for the wide pulse model. The Degelen site consists of granite with a P-wave speed of 5.1km/s in the top 1.3km. In this calculation, the initial cavity is spherical, 7.3m in diameter, and its center is 300m deep. The "cavity" in this case corresponds to the region vaporized by the 62 kt nuclear explosion. The shape of the region of elastic deformation (Figure 2, left) is much different from the NPE and more typical of explosions at or above standard containment depth (Standard containment depth is approximately $122Y^{1/3}$ meters where Y is yield in kilotons (Murphy 1977), or 480 meters in this case). Note that the nonlinear region is more conical than spherical.

As before, full waveform synthetic seismograms were computed for this calculation and compared with synthetics from a point explosion source and a point CLVD source. In this case, synthetics were calculated at 650 km, the distance from Degelen to Borovoye. Figure 2 (right) shows the synthetics from the three sources. Because the Degelen test site is a high velocity structure, P->S converted waves are not trapped in the crust, so the point explosion generates only a small Lg phase, however the asymmetric part of the source which can be modeled approximately as a CLVD source generates shear waves directly, and therefore generates stronger Lg as well as a sharp Sn phase. It is clear from Figure 2 (right) that the CLVD source dominates the regional seismogram, and more detailed analysis shows that the complete source can be modeled quite well as a point explosion plus a CLVD with half the explosion moment.

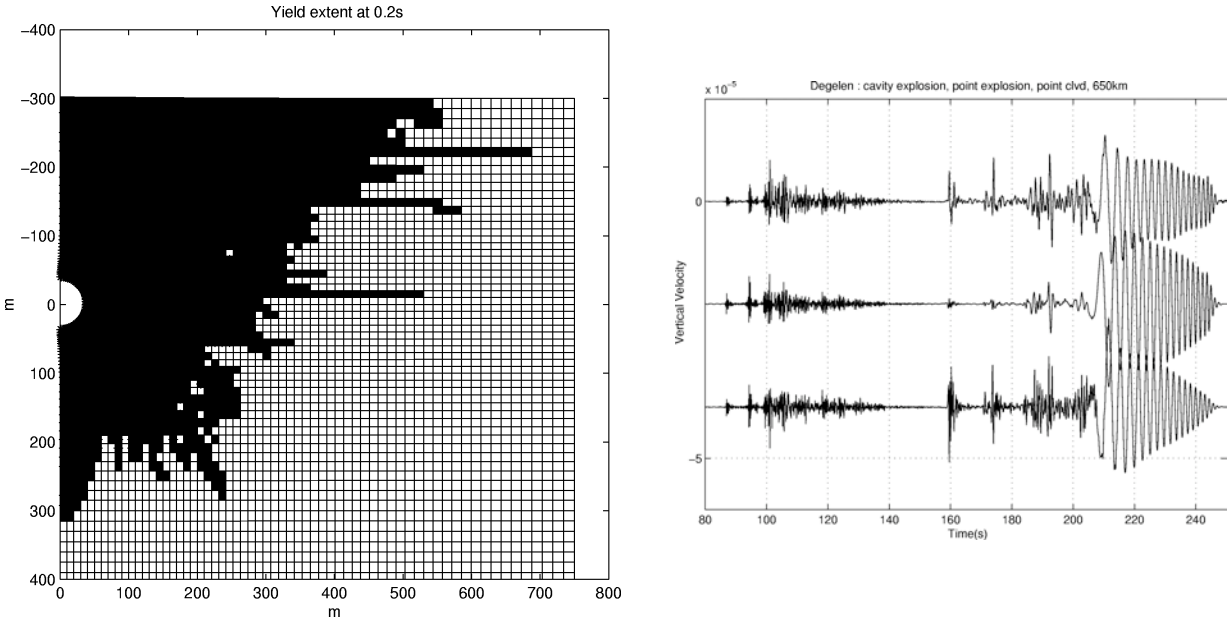


Figure 2. Region of nonlinear deformation from the Degelen Mountain calculation (left). Vertical component synthetic seismograms at 650km from the nuclear explosion (right, top), and from a point explosion (right, middle) and point CLVD in the same structure and at the same depth.

Data

We have collected several data sets that permit observation of the evolution of explosion shear wave phases from very near the source to regional distances.

1) Degelen-Borovoye: This dataset includes 19 radial and 14 vertical recordings at 7-57 km distance from 7 explosions at the Degelen test site, for which good 3-component records are also available from Borovoye (BOR), 650 km from Degelen.

Table 1. The number of local radial and vertical recordings extending past the predicted Sg time for Degelen events, for which there are also Borovoye seismic records. Where there are two depths of burial shown, the smaller indicates slant range to a free surface.

Date	Event Yield (Kt)	Depth of burial, m	Local Records No. Extending to Predicted Sg Time	Distance range, km
1971/12/15	1.5	115/145	5 radial, 4 vertical	7-33
1987/07/17	78	267	4 radial, 4 vertical	14-50
1987/12/20	3.2	105	2 radial	13-17
1988/04/22	2.3	124	1 radial	57
1988/10/18	2.5	125	2 radial, 1 vertical	11-17
1988/11/23	19	204	3 radial, 2 vertical	14-22
1989/10/04	1.8	94	4 radial, 3 vertical	16-42

2) Deep Seismic Sounding (DSS) PNEs: DSS records from IRIS (Morozov et al., 2001) for 6 PNEs in the former Soviet Union provide 3 component recordings every 10 to 15 km, from 100s of meters to 1000s of km from nuclear explosions in different media. We have performed extensive quality control and preliminary analyses on 4 of these data sets (Table 2).

Table 2. Quartz and Craton PNEs for which we have performed QC and preliminary analyses

Date	Time	Lat	Lon	Depth	Yield	Name
1984-Aug-11	19:00:00.20	65.05	55.10	759 m	8.5 Kt	Quartz-2
1984-Aug-25	19:00:00.33	61.90	72.10	726 m	8.5 Kt	Quartz-3
1984-Sept-17	21:00:00.0	55.87	87.446	557 m	10 Kt	Quartz-4
1978-Aug-24	18:00:00.0	66.60	86.21	-	22 Kt	Craton-2

3) Lop Nor: For the Chinese test site at Lop Nor, we have collected digital waveforms at regional stations 250 to 1900 km from 10 nuclear explosions, which range from m_b 4.7 to 6.4. We are reviewing these data to determine their quality and value for use in this project. Records from the same stations are available for earthquakes in the vicinity of Lop Nor for use in comparing excitation differences between source types.

4) NPE: This data set includes 3-component records at 4, 39, and 55 km, thirty-three 3-component regional seismograms from 200 to 1000 km and a range of azimuths (from IRIS, LLNL, and SNL), plus 3-component records from a line of regularly spaced instruments extending from 80 to 274 km eastward of the source (from Univ. of Az.).

5) NTS: We have high quality, 3-component records from LLNL stations at 190 to 400 km for 155 NTS nuclear explosions (Table 3). The explosions span the Yucca, Pahute, and Rainier test areas and a wide range in yield, mb, depth of burial, and porosity, enabling analyses of Lg generation sensitivity to source parameters. The Lg signals suggest differences between sources. To characterize the explosion Lg signals at these stations, we have been performing a variety of parametric measurements, including amplitude, spectral and filter processing.

Table 3. Summary of regional NTS events for which LLNL station data are being analyzed

NTS Source Areas	Number of Events	mb	Depths (m)	Distance range (km)
Yucca	100	3.7-5.8	200-701	220-400
Pahute	40	4.8-5.7	111-680	190-400
Rainier	15	4.0-5.0	261-400	200-400

Observations

There is a set of observations that hold for most of the Degelen and DSS explosion records analyzed thus far.

1) There are small but distinct Sg arrivals at less than 10 km to 10s of km from explosions. The Sg amplitude appears to increase with distance from the source.
2) At regional distances, there are large impulsive Sn arrivals.
3) At regional distances, there are large Lg arrivals.
4) At all distances, the tangential component S-wave phases are as large as those on the radial components.
5) The horizontal component Sn and Lg are much larger than their vertical component counterparts.
6) There is large high frequency Rg out to 100s of km distance.

Local radial and vertical records for a 1.5 Kt Degelen explosion, with the Rg phase included (left column) and with Rg cut off (right) show a small but distinct arrival on each record, marked by an S-wave pick (labeled ISUO) (Figure 3). The S minus P times are all consistent with the known velocity structure at Degelen, indicating that the Sg comes either directly from the source or is scattered almost instantly. The S-wave is minuscule at 7 km distance, and grows relative to P with distance. It is clearly a separate shear wave phase from the very large Rg phase. Recordings 645 km from the same explosion, at BOR, show impulsive Sn and large Lg on all three components (Figure 4).

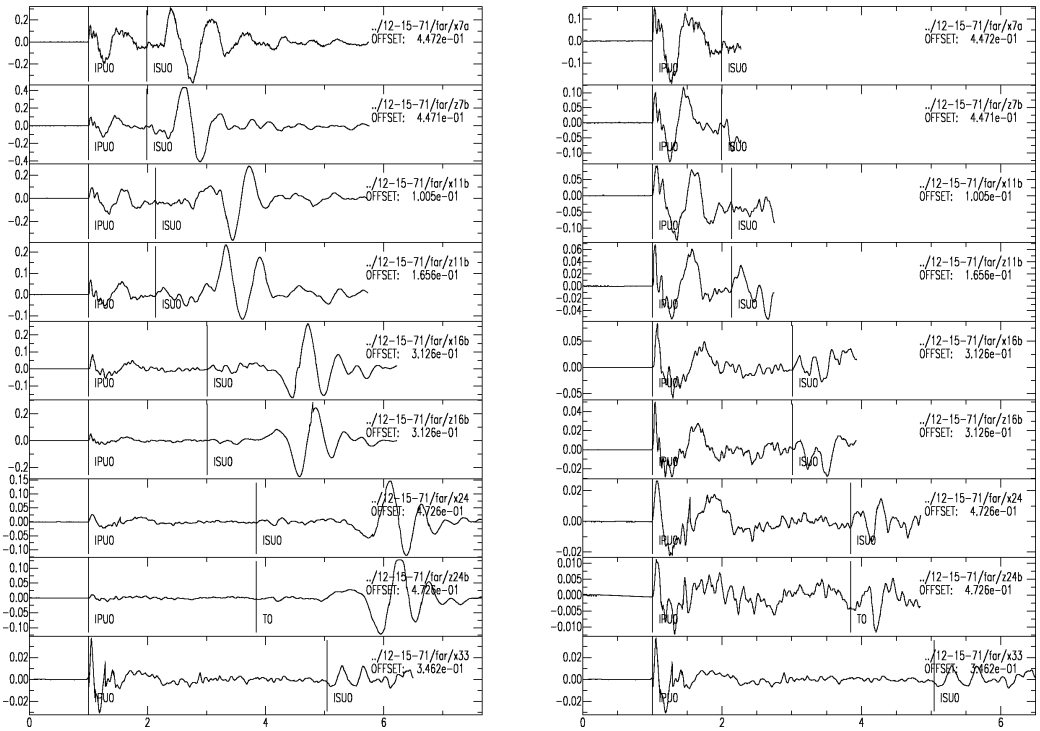


Figure 3: Local radial and vertical records for the 1.5 Kt, 12/15/71 Degelen explosion, aligned on the P-wave arrival, with the S-wave arrival marked (labeled ISUO). Rg is included on the left and excluded on the right. Distances and components are in the filenames, to the upper right of each trace, e.g. x is radial, z is vertical, the number is distance in km.

Seismograms recorded 597 km from Quartz-4 have much larger horizontal component shear wave amplitudes than their vertical counterparts (Figure 5). Sn and Lg are not visible in the vertical record filtered from 1 to 10 Hz (bottom trace of upper plot), but are apparent in the horizontals. Sn, arriving at ~4.1 km/s is visible only in the filtered data. Lg is most prominent in the records filtered from 0.5 to 1 Hz (lower 3 traces). This typical of DSS PNE records at all distances, as record sections (Figure 6) and spectrograms (Figure 7) of near regional records show.

The largest arrivals at the predicted Sg/Lg times on the spectrograms of records from 138 and 168 km east of Quartz-3 (Figure 7) are on the tangential components. The begin and end time of these phases on the tangential

components yield group velocities of 3.35 to 2.5 km/sec at 138 km and 3.3 to 2.9 at 168 km, consistent with earlier observations of late arriving Lg from shallow events. The radials also have large arrivals at the same time, but the phase is completely missing on the verticals. There are small arrivals on the verticals, at ~2.3 to 2.4 km/s, before the Rg but after the horizontal component arrivals. As with Quartz-4 (Figure 5), the shear waves, here Sg or Lg, are very large on the horizontal components and practically nonexistent on the verticals.

Analysis

The existence of a distinct pickable arrival at the predicted Sg time and its separation from Rg for the full range of local distances are inconsistent with its being scattered from Rg. The persistence of large Rg to 100s of kms (Figures 3 and 7) and the impulsiveness of Sn (Figure 4) also argue against gradual scattering of Rg to other S wave phases.

The lack of high frequency shear waves on vertical but not horizontal DSS records, and the substantial difference at lower frequency, casts doubt on much of what has been thought to be known about Lg, as nearly all previous work on Lg used only vertical component recordings.

The velocity structure at the Degelen test site is high velocity all the way to the surface. Using that structure, a CLVD source at 120 m depth reproduces the small, local Sg phases much more effectively than a pure explosion source of twice the CLVD source size (Figure 8). The synthetics are convolved with a 0.125 second wide source function (triangle).

The 120 m source depth is appropriate for most of the Degelen explosion source depths. Regional synthetics are surprisingly similar for the two source types at 120 m. The explosion and CLVD synthetics have comparable Lg amplitudes, and the explosion even produces a small Sn, although it is much smaller than that of the CLVD. Explosion amplitude is scaled to match observed initial P amplitude, and the CLVD is half the explosion size. Figure 9 shows vertical synthetic seismograms for the same model and sources at 120, 300, and 800 m depth, compared with the BOR vertical seismogram from the same 12-15-71 explosion.

The middle and right columns of Figure 9 show the effects of depth on the synthetics. The 300 m depth sources are slightly deeper than the largest Degelen explosion. The 300 m CLVD source produces slightly larger Lg and much larger Sn than the explosion source. The 800 m source depth is similar to the deeper DSS sources. At that source depth, the explosion Sn is minuscule and the Lg quite small, while those phases dominate the CLVD synthetics.

Another important factor not addressed here is the effect of the high velocity source structure of Degelen used in the 1-D modeling. The propagation path more typically has lower near surface velocities, which increase the Lg amplitude of the synthetics. That effect will be addressed in future work.

CONCLUSIONS AND RECOMMENDATIONS

The results to date suggest that Lg and Sn phases are generated by the explosion and interaction with the near surface media, without a significant contribution from secondary sources such as Rg scattering, and that these phases can be predicted fairly well with a realistic model of the explosion source that includes nonlinear effects and the free surface interaction. The observed persistence of Rg to large distances also argues against Rg scattering as a significant contributor to Lg. If the source-generated Lg hypothesis is correct, it allows some predictions to be made that will be considered further in the continuing project through comparison with observations. For example, the dependence of Lg on source media, source region structure, and depth should be predictable. As can be seen from the calculations for the NPE and Degelen, even explosions in dramatically different media and source regions generate significant Lg, but may have significantly different composition due to differences in modal structure and the relative excitation caused by explosion and CLVD components.

More difficult to explain is the observed presence of Lg on the tangential components. This cannot be modeled with an axisymmetric source, and must be due to either a non-axisymmetric source effect, or to polarization changes along the source to receiver path. If the former, then the tangential Lg should have an observable radiation pattern and is unlikely to correlate as well with yield as the vertical component. That tangential Sg is observed at quite close range favors the first explanation.

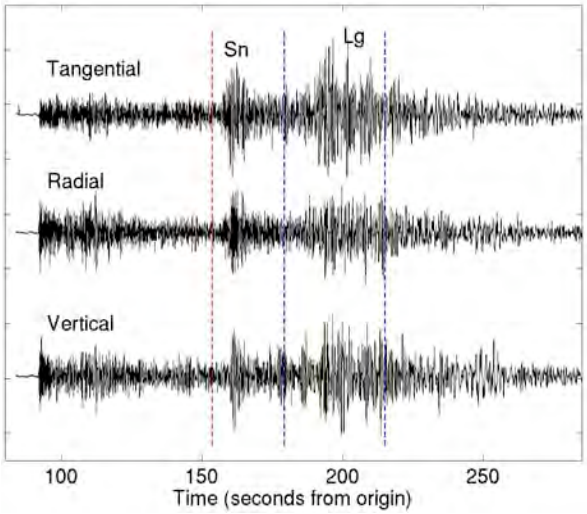


Figure 4: Tangential, radial, and vertical (from top down) records at BOR, 645 km from Degelen. The impulsive Sn arrives at ~4.1 km/s (1st line is at 4.2 km/s). The 2nd and 3rd lines, at 3.6 and 3.0 km/s, bracket the large Lg.

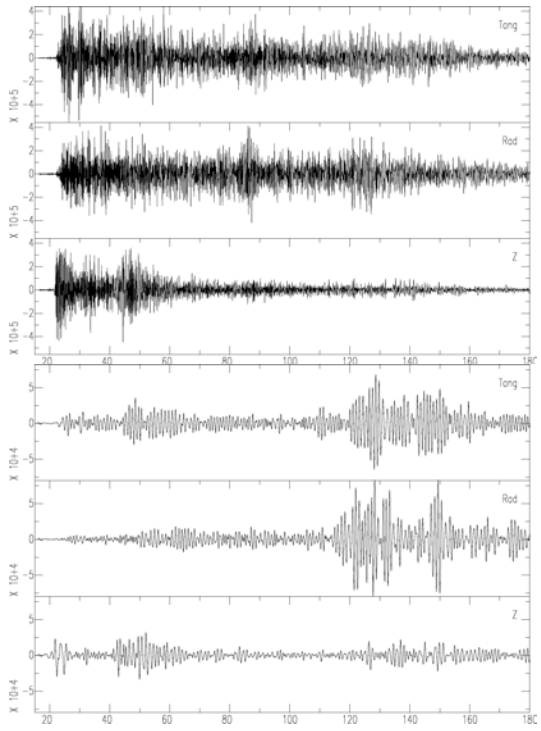


Figure 5: Tangential, radial, and vertical (from top down) records 597 km west of Quartz-4. The upper 3 traces are filtered from 1-10 Hz, and the lower 3 are filtered from 0.5-1 Hz. Time axis is reduced by range/10.

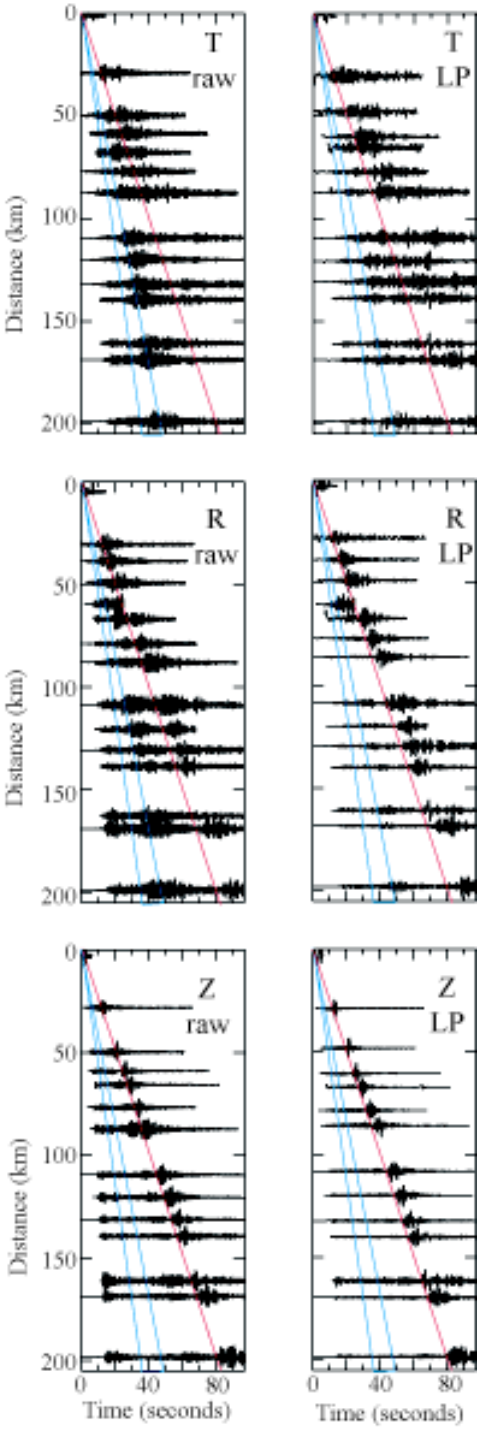


Figure 6: Tangential, radial, and vertical (from top down) record sections to 200 km east of Quartz-3. Raw traces are on the left and filtered (0.1-1.0 Hz) on the right. Amplitudes are scaled by the maximum of each trace. Blue lines are 3.6 to 3.0 km/s group velocity and red is 2.0 km/s. The time axis is reduced by range/10.

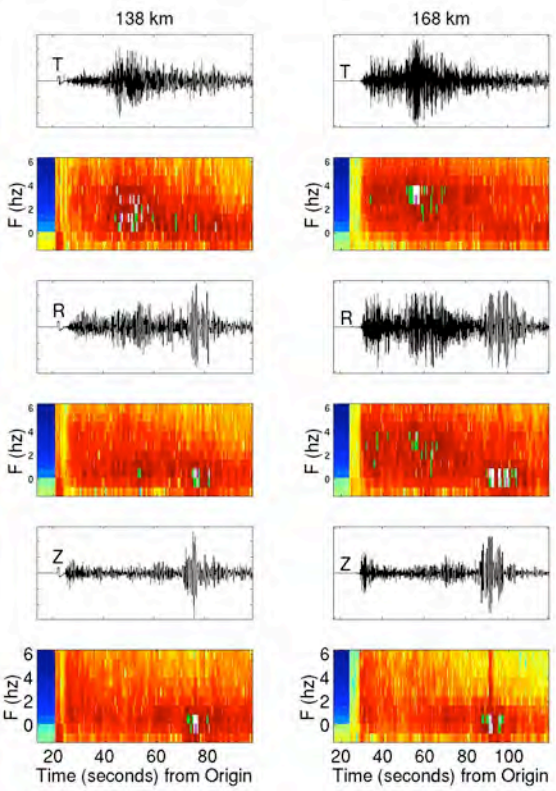


Figure 7: Spectrograms of the tangential, radial, and vertical records (from top down) 138 (left) and 168 (right) km east of Quartz 3.

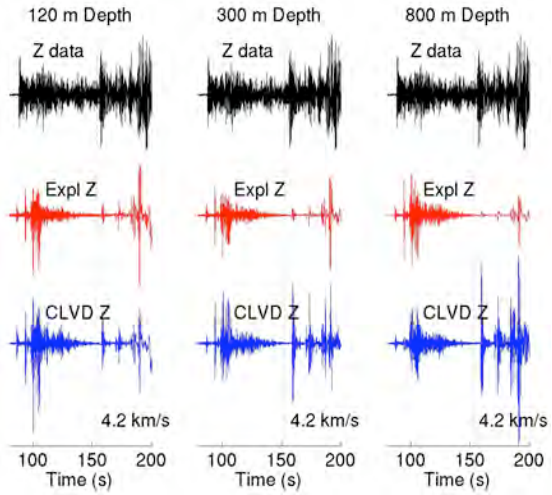


Figure 9. Vertical seismograms recorded at BOR for the 12-15-71 explosion (top), and explosion (middle) and CLVD (bottom) synthetics for source depths of 120 (left), 300 (middle), and 800 (right) m.

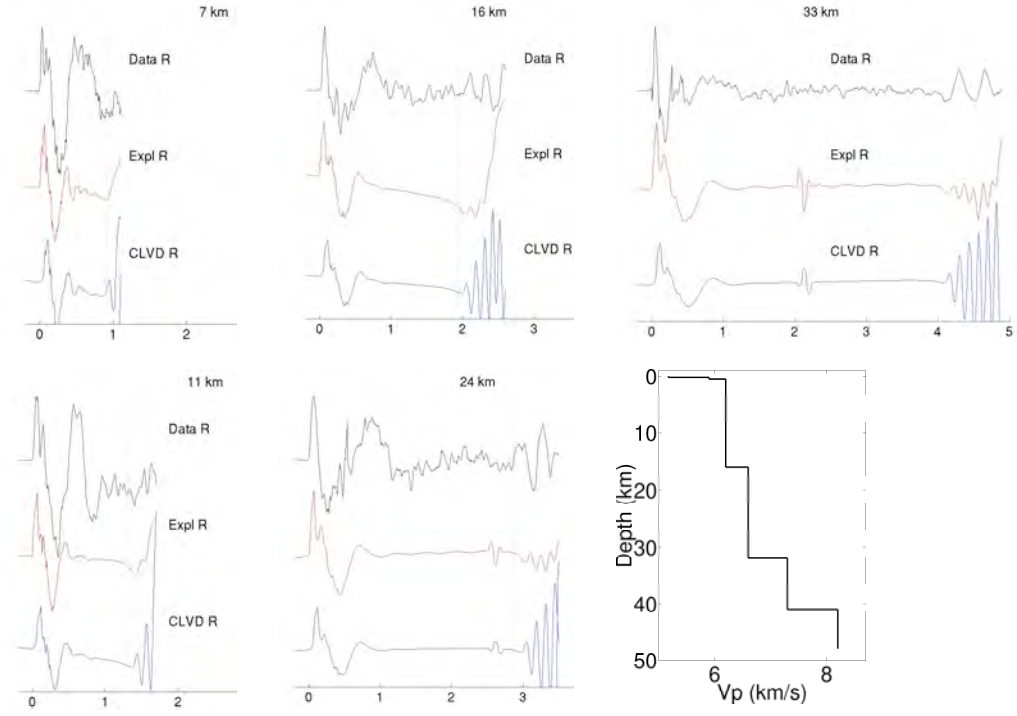


Figure 8: Radial data (top), explosion synthetics (middle), and CLVD synthetics (bottom) for the 12-15-71 Degelen explosion. Velocity structure used is shown in the lower right.

REFERENCES

Bennett, T. J., K. L. McLaughlin, M. Marshall, and J. L. Stevens (1997a), "The Physical Basis for the Lg/P discriminant: General Properties and Preliminary Modeling," PL-TR-97-2044, MFD-FR-97-15727.

Bennett, T. J., K. L. McLaughlin, R. Cook, and J. Carter (1997b), "The Physical Basis for the Lg/P Discriminant: Signal Characteristics and Modeling," PL-TR-97-2149, MFD-FR-97-15918.

Day, S. M., J. T. Cherry, N. Rimer and J. L. Stevens (1987), "Nonlinear model of tectonic release from underground explosions," Bull. Seism. Soc. Am, v. 77, pp. 996-1016.

Day, S. M. and K. L. McLaughlin (1991), "Seismic Source Representation for Spall," *Bull. Seism. Soc. Am.*, **81**, 191-201.

Gupta, I. N., T. Zhang, and R. Wagner (1997), "Low-frequency Lg from NTS and Kazakh nuclear explosions—Observations and interpretations," *Bull. Seism. Soc. Am.*, **87**, 1115-1125.

Gupta, I.N., and R.A. Wagner (1998), Study of low and high frequency Lg from explosions and its application to seismic monitoring of the CTBT, *Multimax Inc Final Report for AFRL-VS-HA-TR-98-0038.*

Morozov, I. B., S. B. Smithson, E. A. Morozova, and L. N. Solodilov (2001), A database of Deep Seismic Sounding Peaceful Nuclear Explosion recordings for seismic monitoring of northern Eurasia, *"23rd Seismic Research Review: Worldwide Monitoring of Nuclear Explosions"*, Jackson Hole, Wyoming.

Murphy, J. R. (1977), "Seismic coupling and magnitude/yield relations for underground nuclear detonations in salt, granite, tuff/rhyolite and shale emplacement media," Comput. Sci. Corp. Technical report CSC-TR-77-0004, December.

Nuttli, O. W. (1986), "Yield estimates of Nevada Test Site explosions obtained from Lg waves," J. Geophys. Res., 91, 2137-2151.

Patton, H. J. (2001). "Regional Magnitude Scaling, Transportability, and M_s:m_b Discrimination at Small Magnitudes," LA-UR-99-6705, PAGEOPH Special Volume on Monitoring CTBT: Source Processes, in press.

Patton H. and S. Taylor (1995), Analysis of Lg spectral ratios from NTS explosions: implications for the source mechanisms of spall and the generation of Lg waves, *Bull. Seism. Soc. Am.*, **85**, 220-236

Rimer, N., W. Proffer, E. Halda and R. Nilson (1994), "Containment related phenomenology from Chemical Kiloton," Maxwell Laboratories technical report to Defense Nuclear Agency, SSS-DTR-94-14405.

Stevens, J. L., T. G. Barker, S. M. Day, K. L. McLaughlin, N. Rimer, and B. Shkoller (1991), "Simulation of teleseismic body waves, regional seismograms, and Rayleigh wave phase shifts using two-dimensional nonlinear models of explosion sources," AGU Geophysical Monograph 65: Explosion Source Phenomenology, S. Taylor, H. Patton, P. Richards, editors, ISBN 0-87590-031-3, pp. 239-252.

Stevens, J. L. (1980), "Seismic radiation from the sudden creation of a spherical cavity in an arbitrarily prestressed elastic medium," Geophysical Journal of the Royal Astronomical Society, v. 61, pp 303-328.

Stevens, J. L., N. Rimer, H. Xu, G. E. Baker and S. M. Day (2003), "Near field and regional modeling of explosions at the Degelen Test Site," SAIC final report to DTRA, SAIC-02/2050, January.

ANALYSIS AND SIMULATION OF CAVITY-DECOUPLED CHEMICAL EXPLOSIONS

Jeffry L. Stevens,[1] Norton Rimer,[1] Heming Xu,[1] G. Eli Baker,[1] John R. Murphy,[1] Brian W. Barker,[1]
Conrad Lindholm,[2] Frode Ringdal,[2] Steven Gibbons,[2] Tormod Kvaerna,[2] and Ivan Kitov[3]

Science Applications International Corporation;[1] NORSAR;[2] Institute for the Dynamics of the Geospheres[3]

Sponsored by Air Force Research Laboratory

Contract No. DTRA01-01-C-0069

ABSTRACT

The objective of this project is to improve our capability to predict quantitatively the decoupling effectiveness of underground cavities in a variety of realistic configurations. This is being accomplished by expanding the existing decoupling data set with data that have recently become available from Russian and Swedish decoupled chemical explosions, and by performing data analysis and numerical modeling of this data set. This is a joint project of Science Application International Corporation (SAIC), the Russian Institute for the Dynamics of the Geospheres (IDG), and NORSAR.

NORSAR has obtained data from seven decoupled chemical explosions in Sweden. The explosions were conducted from 1987-2002 in Älvdalen, Sweden. The explosions were well recorded by the NORES, HAGFORS, and NORSAR arrays, except for the last explosion, which occurred shortly after NORES was damaged by lightning. NORSAR participated in the explosions during the summer of 2001 and 2002. They deployed a number of temporary instruments including one surface instrument for each event on site near the explosion. The last four explosions were conducted in a cavity 5 meters high by 10 m wide by 25 m long. The first three explosions were in smaller chambers. Explosive yields ranged from 2500 kg to 10,000 kg, with charges consisting of TNT, ANFO and ammunition shells. The rock overburden for each explosion was approximately 100 m. Spectral shape of decoupled explosion data is distinctly different from surface explosions in the same area. Variations in coupling depending on the size of the chamber are clearly observable. The smallest explosion in the largest chamber appears to be fully decoupled, while the other explosions are partially coupled. Near field data was recorded on pressure gauges in the chamber and adjacent tunnel, and on velocity gauges in boreholes at several locations near the chamber. We have completed some data analysis of waveforms and spectra at the arrays, and numerical modeling of some of the near field and regional data.

IDG has digitized a set of surface seismic data recorded from a series of Soviet high-explosive cavity decoupling tests conducted in a mine in Kirghizia in the summer of 1960. These decoupled tests were carried out in a variety of mined cavities in limestone with the objectives of assessing the dependence of cavity decoupling effectiveness on cavity volume, cavity shape, and charge emplacement geometry. In a previous study, Murphy et al (1997) conducted extensive analyses of free-field data recorded from these tests in the mine at distances on the order of 10-200 m. However, only limited waveform data were available from this regime, which made it difficult to determine the frequency dependence of the decoupling factors with a high degree of confidence. In the present study, seismic data recorded from a number of these tests on the surface at distances of 5 and 10 km from the source region have been recovered and digitized. We have analyzed the digitized 3-component seismic data that was recorded at surface stations located 5 and 10 km away, and compared these results with those obtained earlier from close-in data. High quality recordings are available from the 1 ton tamped and decoupled tests at the 5 km station, and the 6 ton tamped and decoupled tests at the 5 and 10 km stations. Results of detailed analyses of these data have proven to be generally quite consistent with those obtained from the previous analysis of the corresponding free-field data. In particular, all the decoupled tests conducted in the center of the cavities show low frequency chemical decoupling factors in the range 20-30, while that conducted 1 m from the wall of the 4.92 m radius cavity is about a factor of two smaller, indicating increased seismic coupling associated with nonlinear response of the cavity wall. The seismic signals observed from the 1 ton explosions conducted at the centers of the 2.88 m and 4.92 m radius cavities were found to be nearly identical, confirming that both of these tests were fully decoupled. These experimental results are currently being integrated with the results of theoretical simulation studies in an attempt to define scaling laws appropriate for decoupled explosions conducted in limestone cavities.

OBJECTIVE

The objective of this project is to improve our capability to predict quantitatively the decoupling effectiveness of underground cavities in a variety of realistic configurations. This will be accomplished by 1) expanding the existing decoupling data set using data that have recently become available from Russian and Swedish decoupled chemical explosions; 2) performing numerical simulations of these data and other decoupled data and then using the results to refine the material models used in the simulations; 3) performing numerical modeling of decoupled chemical explosions in nonspherical cavities for a variety of realistic material models and cavity geometries. This is a joint project between SAIC, the Russian Institute for the Dynamics of the Geospheres, and NORSAR.

RESEARCH ACCOMPLISHED

Although cavity decoupling has been the subject of extensive study over a period of nearly 40 years, there is still considerable quantitative uncertainty in the decoupling factor – the ratio of coupled to decoupled seismic signal that can be achieved under different conditions. This uncertainty comes from three sources – first, there is only a limited amount of decoupled data available; second, there is considerable uncertainty in the low pressure equation of state used in numerical modeling of decoupled explosions; and third, there has been only a limited investigation of the effectiveness of decoupling by nonspherical cavities. In this research project, we address all three of these issues. First, we expand on the existing data set using data that have recently become available from Russian and Swedish decoupled chemical explosions. Second, we perform numerical simulations of these data and then use the results to refine the material models used in the simulations. Third, we perform numerical modeling of decoupled chemical explosions in nonspherical cavities for a variety of realistic material models and cavity geometries.

NORSAR has been a participant in a series of recent Swedish decoupled chemical explosions, and has fielded a variety of instruments to record this data set. NORSAR is also gathering data from surface explosions and earthquakes for comparison with the decoupled explosion data. IDG has been reviewing and digitizing data from a series of Soviet high-explosive cavity decoupling tests conducted in a mine in Kirghizia in the summer of 1960. SAIC is performing numerical simulations of some of these explosions.

This paper is organized into three parts:
1. A description of the Swedish decoupling experiments
2. A description of the Kirghizia data and analysis
3. A brief review of cavity decoupling theory and description of numerical simulations.

Swedish Decoupled Explosions

At a site within Älvdalen Skjutfält in central Sweden, a number of decoupled chemical explosions have been carried out within underground cavities at a depth of approximately 100 meters. At Mossibränden, a site less than 20 kilometers from this chamber, outdated ammunition is routinely detonated at ground level by the Swedish Armed Forces. The seismic signals from both categories of explosions have been collected into a database and analyzed. The geographical location of the explosion sites is ideal for the purpose of comparison. The sites are in very close proximity to each other and are approximately equidistant from the seismic arrays HFS (Hagfors, Sweden), NRS (NORES, Norway), and the wide aperture NORSAR array (Figure 1). Figure 2 shows the location of the underground chamber relative to the surface and local instrumentation.

Table 1 Cavity decoupled explosions at the Älvdalen site. Origin times of the 1987-89 events were estimated from arrival times at NORES. Origin times of the 2000-2001 events were determined from a station at the explosion site.

Origin ID	Explosion origin time	Explosion charge (kg)	Explosive	Chamber Volume (m^3)	Charge/Volume (kg/m^3)
1987C146	1987-146:10.47.38.2	5000	ANFO	300	16.7
1987C259	1987-259:10.36.13.0	5000	ANFO	200	25.0
1989C263	1989-263:10.06.03.5	5000	ANFO	300	16.7
2000C348	2000-348:10.03.02.0	10000	TNT	1000	10
2001C150	2001-150:10.03.56.2	2500	TNT	1000	2.5
2001C186	2001-186:10.41.23.5	10000	Ammunition Shells	1000	10
2002C164	2002-164:08.59.25.1	10000	TNT/powder	1000	10

The seismic signals resulting from the three Älvdalen events from 1987 and 1989 have far higher amplitudes than the later events which probably reflects the differences in charge/cavity volume as displayed in Table 1. Despite the larger amounts of explosives used, the larger chamber size results in far weaker signals.

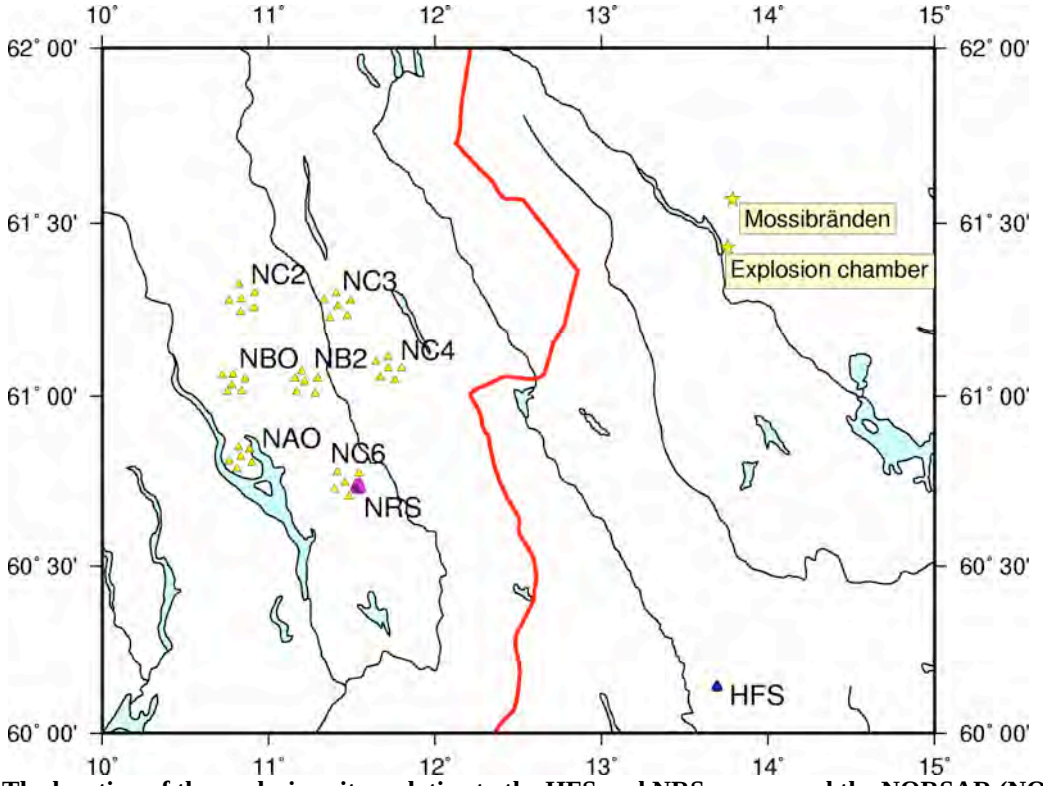


Figure 1. The location of the explosion sites relative to the HFS and NRS arrays and the NORSAR (NOA) sub-arrays. The solid red line is the Norway/Sweden national boundary.

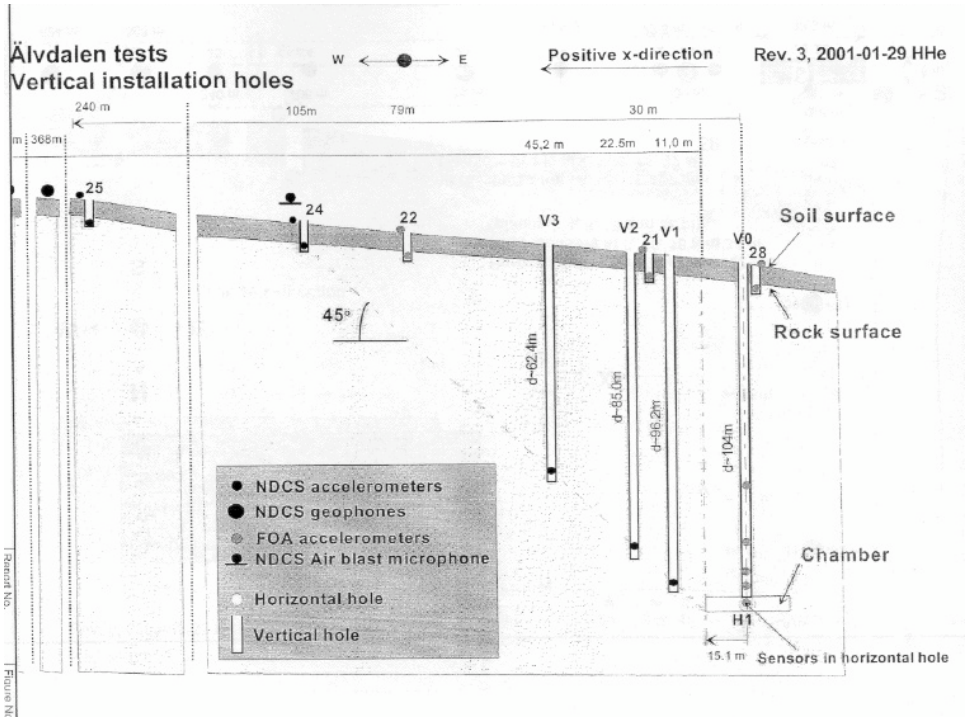


Figure 2. Location of chamber relative to the surface and local instrumentation.

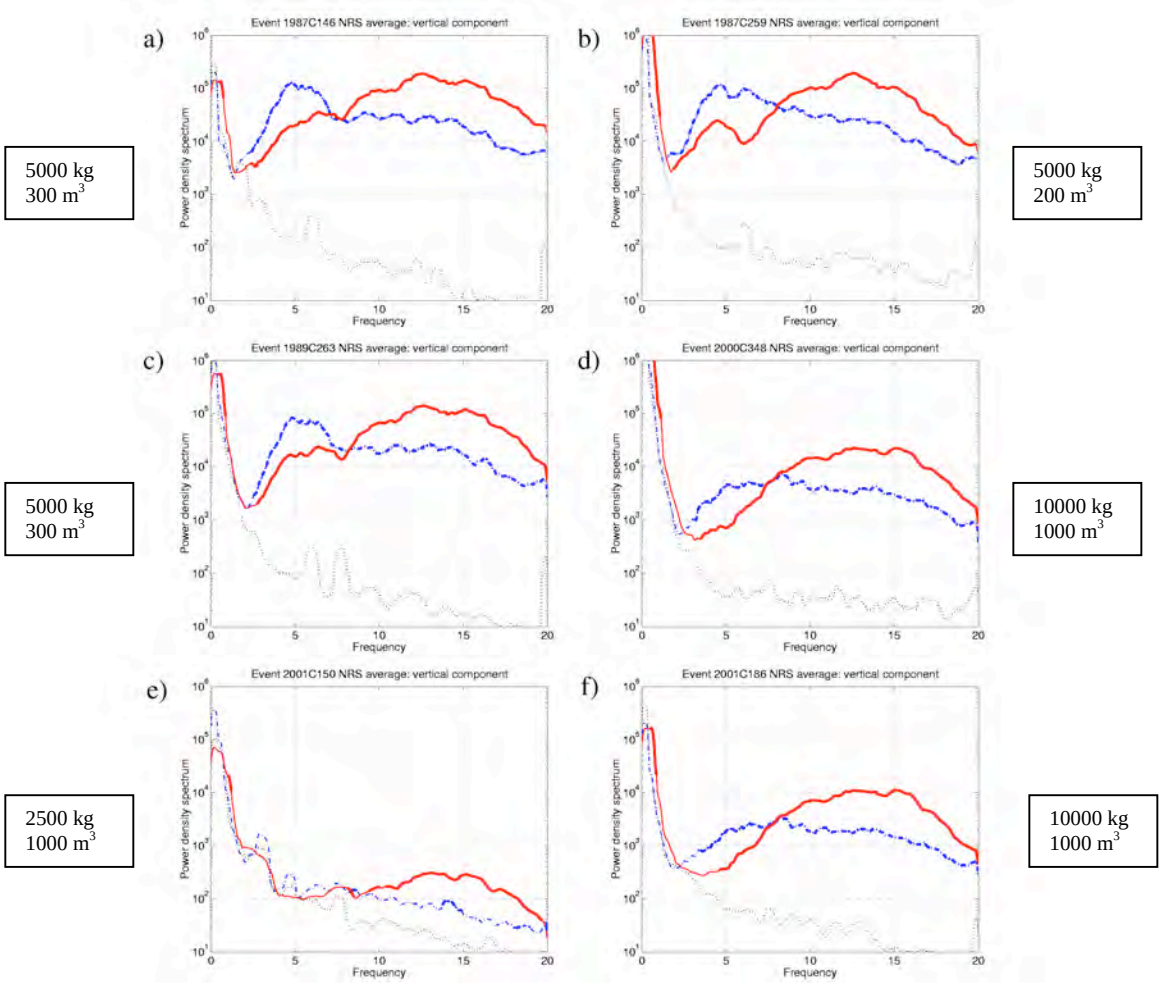


Figure 3. Average power density spectra (PDS) from NORES vertical component data for six decoupled explosions as indicated; all spectra are converted to HFS response. The solid red line indicates PDS for the P window, the dashed blue line indicates PDS for the S window and the dotted black line indicates PDS for the noise window. At frequencies where the PDS for the P or S window is less than 4.0 times that for the noise window, the signal spectrum is shown as a thin line.

In order to quantify the differences between these decoupled events, we examine the power density spectra. For each component, three time windows were defined corresponding to the P arrival, S arrival, and pre-event noise. A 5 second window of waveform data was extracted immediately after the P onset, and a 10 second window immediately after the S onset. A 10 second window ending 2 seconds before the P onset was defined in order to quantify the level of noise which is expected in the signal. A power density spectrum was calculated for each time window. In order to provide a common basis for comparison, we have converted all spectra to the characteristics of the HFS response. Unlike the NORES response, the HFS response is flat to velocity over the passband. Converted power density spectra, averaged over the vertical components of the NORES array, are shown in Figure 3 for the 6 explosions listed in Table 1 which were recorded by NORES, for frequencies up to the Nyquist frequency of 20 Hz. The results displayed in Figure 3 clearly show that the reduction in seismic energy is greater for the explosions in the larger chamber than those in the smaller chamber. This indicates that a greater decoupling is associated with the larger chamber.

NORSAR has also collected a large number of recordings from surface explosions for comparison with the decoupled data. A detailed analysis of this data is given in Stevens et al (2002). A characteristic difference between the two sets of events is that the surface explosions have more long period energy than the decoupled explosions (Figure 4). This difference is predictable because of the longer time duration of the surface source relative to the decoupled explosion.

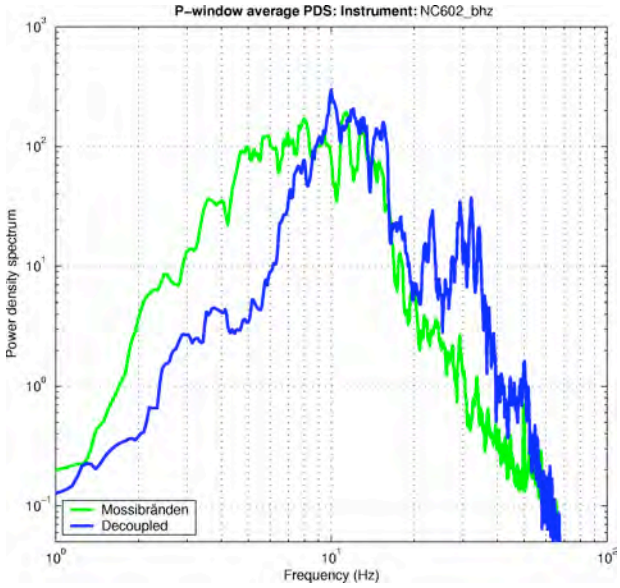


Figure 4. Power density spectra for the P arrival time window recorded on a high frequency GeoSys instrument with a 200 Hz sampling rate located at NORSAR. The blue line (first) corresponds to the 2001C186 decoupled explosion and the green line (second) is the average of 5 surface explosions.

Kirghizia Decoupled Explosions

During the summer of 1960, Soviet scientists carried out a series of high explosive (HE) cavity decoupling tests in a mine in the Tywya Mountains of Kirghizia. These included tests designed to evaluate the effects of cavity shape and charge geometry on decoupling effectiveness, in addition to conventional spherical cavity tests similar to those employed in the corresponding U.S. COWBOY test series. The Kirghizia test series was composed of 10 tamped and 12 decoupled explosions with yields of 0.1, 1.0 and 6.0 tons. For the cavity tests the explosives were suspended in the chambers and included cases in which the explosives were positioned off center, near the cavity walls. The configurations of the various cavity tests are graphically summarized in Figure 5 for each of the five test chambers.

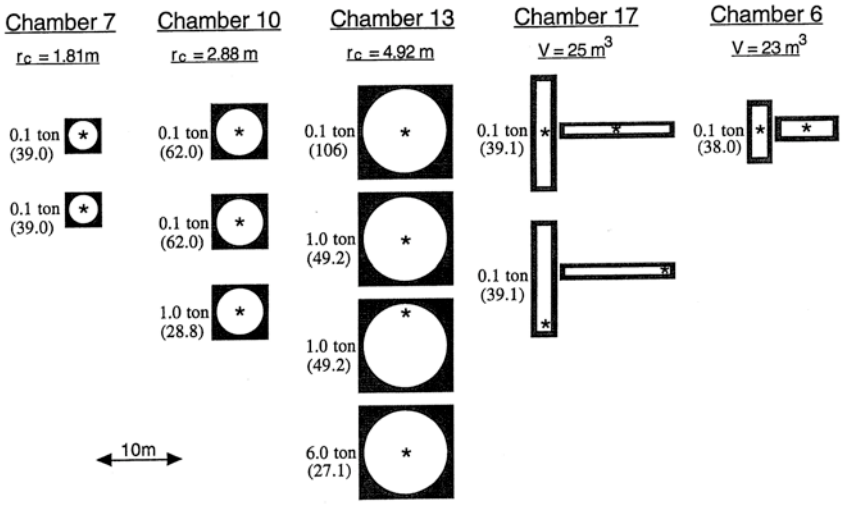


Figure 5. Graphical summary of the Kirghizia HE decoupling tests conducted in each of the excavated explosion chambers. The asterisk denotes the emplacement location of the charge within the chamber for each test. For the nonspherical cases, both horizontal (left) and vertical (right) sections through the chambers are displayed. The numerical values shown in parentheses below the yield values are the scaled radii in m/kt$^{1/3}$, with equivalent volume spherical cavity values listed for the nonspherical cases.

In our previous analysis of these tests (Murphy et al, 1997), we focused on free-field data recorded in the mine at distances on the order of 10 – 200 m. Unfortunately, only limited waveform data were available from this regime and, consequently, the analyses focused primarily on comparisons of peak amplitude values. While such comparisons provided a reasonable basis for comparing the relative decoupling effectiveness of different cavity configurations, they did not provide an adequate data set for confidently determining the frequency dependence of the absolute level of the decoupling factor. Consequently, under the current effort, we have recovered and digitized seismic data from these tests recorded at surface stations located at distances of 5 and 10 km. High quality recordings are available from the 1 ton tamped and decoupled tests at the 5 km station, and the 6 ton tamped and decoupled tests at the 10 km station. Results of detailed analyses of these data have proven to be generally quite consistent with those obtained from the previous analysis of the corresponding free-field data. Examples of these data are shown in Figure 6 which provides a comparison of vertical component recordings at the 5 km station from 1 ton tamped and decoupled explosions. In this case, the decoupled tests were conducted at the center of spherical cavities with radii of 4.92 and 2.88 m, and 1 m from the wall of the 4.92 radius cavity. It can be seen that the signal levels for the tests in the centers of the two different sized cavities are very comparable, indicating peak motion decoupling factors of about 20 and suggesting that both of these tests in different size cavities were fully decoupled. The signal level for the test near the cavity wall is about a factor of 2 larger, suggesting some significantly enhanced coupling associated with local nonlinear wall response.

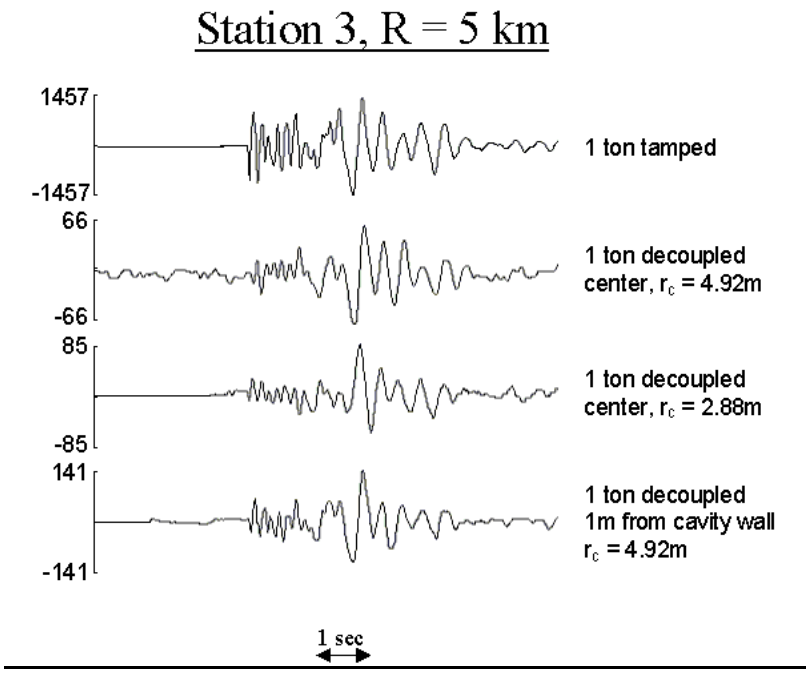


Figure 6. Vertical component recordings at the 5 km surface station from 1 ton tamped and decoupled explosions.

Recordings from the 6 ton tamped and decoupled explosions at the 10 km station are shown in Figure 7. In this case the decoupled explosion was detonated at the center of the 4.92 m radius spherical cavity. Again, the peak signal levels from the two tests shows a decoupling factor of a little more than 20, consistent with the results from the 5 km station and suggesting that this larger test was also fully decoupled. We have computed frequency-dependent decoupling factors between 1 and 4 Hz from these 5 and 10 km station recordings and the results are shown in Figure 8, where it can be seen that the decoupling factors for the two 1 ton tests in the centers of the different sized cavities over this frequency band are essentially identical and consistent with a low frequency decoupling factor in the range 20 - 30. This confirms that these explosions must have been essentially fully decoupled. The frequency dependent decoupling factor for the 1 ton test near the cavity wall is quite similar to the other two in shape, but lower by about a factor of 2, independent of frequency over this range. The results from the 6 ton test are in good agreement with those of the fully decoupled 1 ton tests, suggesting that it also was essentially fully decoupled. The decoupling factor for all of these fully decoupled tests over this frequency band is somewhere in the range of about 20 to 30. Also shown on this figure are the corresponding results at higher frequency (i.e. 10 – 200 Hz) obtained previously by Murphy et al (1997) using the limited free-field waveform data. It can be seen that the results from the

two distance regimes are generally quite consistent, confirming a low frequency decoupling factor in the range of 20 – 30 for these fully decoupled tests in limestone.

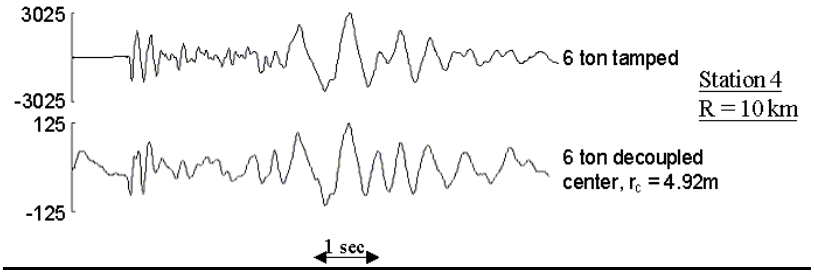


Figure 7. Vertical component recordings from the 6 ton tamped and decoupled tests at the 10 km station.

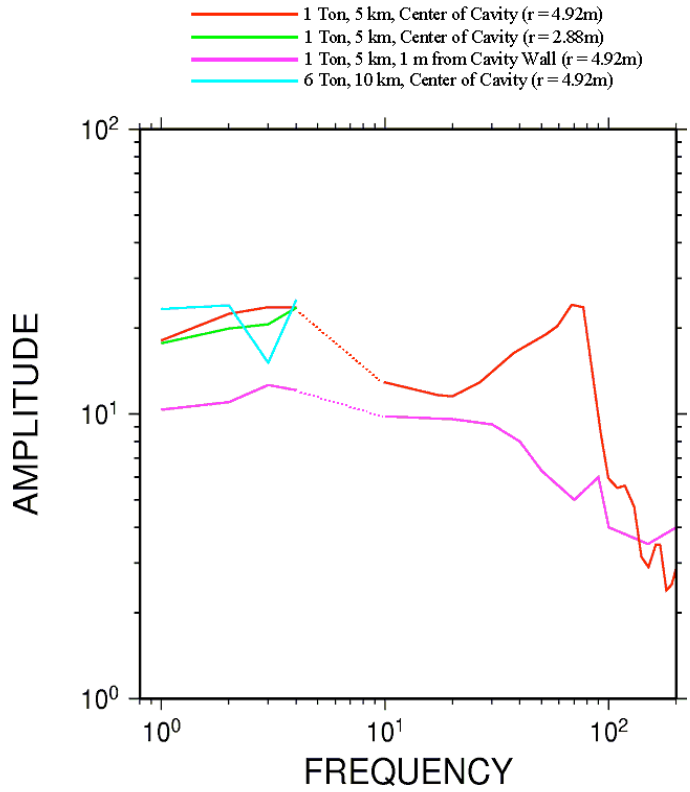


Figure 8. Frequency dependent decoupling factors for the 1 and 6 ton tests at the 5 and 10 km stations. Also shown are the corresponding results at higher frequency (i.e. 10 – 200 Hz) obtained previously by Murphy et al (1997) from the corresponding free-field data.

Cavity Decoupling Theory and Numerical Simulations

The source function for a fully decoupled explosion can be described as a pressure pulse applied to the wall of a cavity in an elastic medium. The actual physics is more complicated than this – there are reverberations in the cavity that cause high frequency spectral peaks, for example. However the simple model is useful for illustration and has most of the characteristics of a decoupled explosion.

The reduced velocity potential (RVP) for a pressure pulse $P(t)$ with derivative $\dot{P}(t)$ and corresponding Fourier transforms $P(w)$ and $\dot{P}(w)$ applied to the wall of a spherical cavity is (Stevens et al, 1991):

$$y(w) = P(w)\frac{R^3 w_0^2}{4m}\frac{e^{iw/w_0}}{w_0^2 + iww_0 - [(l+2m)/4m]w^2} \quad (1)$$

where $w_0 = a/R$, where R is the cavity radius, a is the compressional velocity of the external medium and l and m are the Lame constants of the external medium. For a step in pressure of magnitude P_0 applied at time $t = 0$, $P(w) = P_0$, and for this or any pressure pulse with static value P_0, in the low frequency limit, we have

$$y_. = P_0 R^3/4m \quad (2)$$

For an explosion in an air-filled cavity, the static value of the pressure is related to the yield W by

$$P_0 = \frac{(g-1)W}{V} \quad (3)$$

where g is the adiabatic expansion constant, which is approximately 1.2 for air and 1.3 for chemical explosion products, and V is the cavity volume.

The "decoupling factor" D is defined as the ratio of the fully coupled to decoupled source:

$$D = y_{tamped}/y_{decoupled} \quad (4)$$

The theoretical decoupling decreases with frequency. Figure 9 shows the coupled and decoupled source function and the frequency dependent decoupling factor obtained by taking the ratio of coupled to decoupled source. The decoupling factor decreases by an order of magnitude at high frequencies beginning at about 10 Hz, which is consistent with the observed differences between low and high frequencies in the Swedish explosions, as well as the observed frequency dependence in decoupling observed in the Kirghizia explosions (Figure 8).

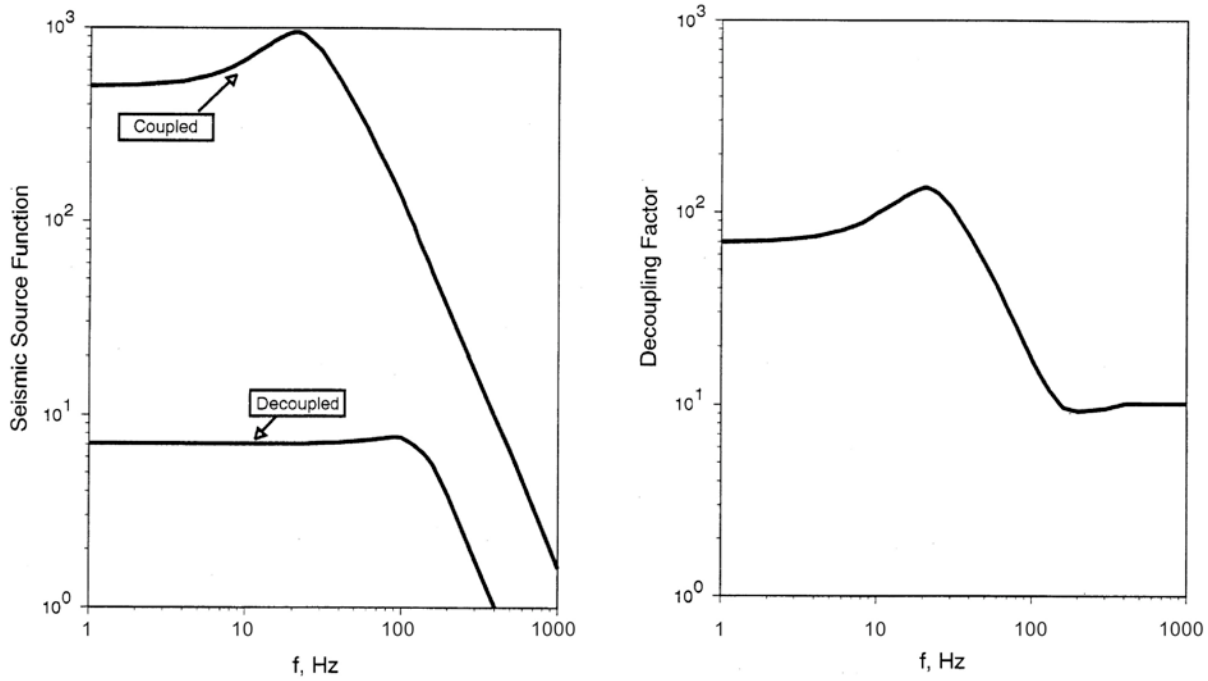


Figure 9. Source functions for fully coupled and fully decoupled 10-ton chemical explosions for a step pressure source in the cavity (left) and frequency dependent decoupling factor (right).

The criterion for full decoupling is usually expressed in terms of a requirement that the late-time, equilibrium pressure in the cavity be less than or equal to some constant, k, times the overburden pressure:

$$\frac{(g-1)W}{V} \pounds k\,rgh \quad (5)$$

where k is between 0.5 and 1.0, and rgh is the overburden pressure at depth h.

For the conditions of the Swedish chamber explosions which are at a depth of 100 meters depth in granite, the criteria for full decoupling is in the range of 1 kg/m^3 - 2 kg/m^3. Since these criteria were developed for spherical cavities, and nonspherical cavities bring the walls closer to the explosion where they experience a stronger shock, we expect some nonlinear behavior at lower yields. So referring to Table 1, the Swedish explosions cover a range from almost fully decoupled (2500 kg in 1000 m^3 chamber) to being overdriven beyond full decoupling by about a factor of 20. When the explosion yield is increased above the yield required for full decoupling, the coupling increases slowly at first, then changes rapidly and eventually reaches tamped coupling. However, there have been relatively few observations of partial decoupling, and the observations have been quite variable. The Swedish explosions therefore add some valuable new data points to help constrain this effect.

Figure 10 shows a comparison between the "observed" decoupling factors for the Swedish explosions and decoupling factors for a series of calculations of chemical explosions in a cavity in granite. "Observed" is in quotes because we do not have data from a tamped explosion for comparison. Instead, we scaled the decoupling factor of the most decoupled explosion to 100 to agree with the calculation for a fully decoupled explosion. The figure shows that the explosions remain almost fully decoupled until the charge/volume is approximately equal to 10, after which increases in yield cause a rapid decrease in decoupling. The calculation also shows this effect of nearly constant decoupling followed by a rapid decline. In the calculation the decline occurs at a higher charge/volume, most likely because the material used in the calculation was a stronger granite model, and because the Swedish cavities are not spherical, which increases coupling. Further calculations are now being done for more appropriate granite models, as well as calculations in two and three dimensional geometries.

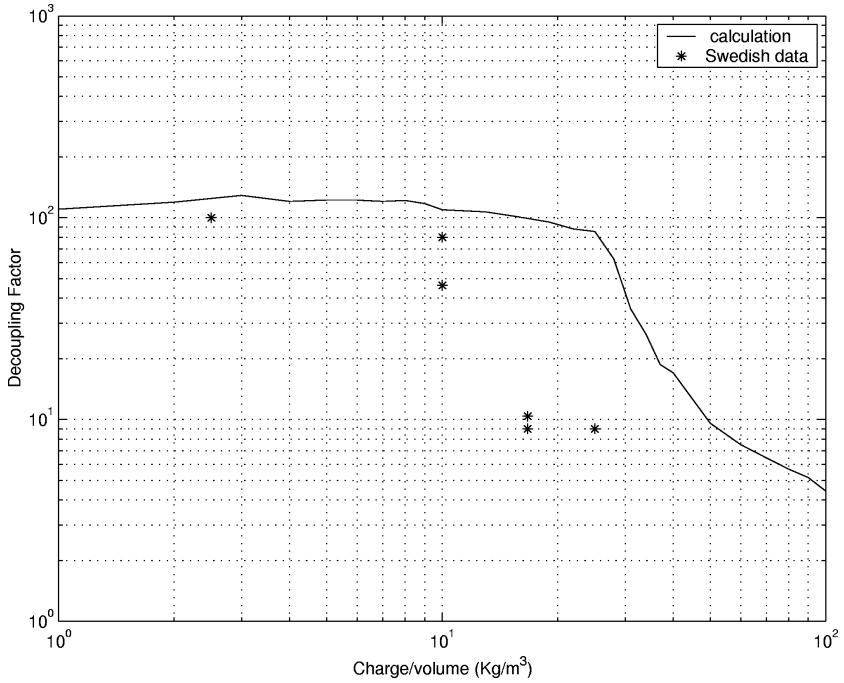


Figure 10. Observed and predicted decoupling factor for Swedish explosions. Calculations were for a chemical explosion in a 6.3 meter spherical cavity in hard (non-weakening) granite. The decoupling factor contains an unknown scale factor. The horizontal axis corresponds approximately to the overdrive factor above full decoupling.

CONCLUSIONS AND RECOMMENDATIONS

We are in the second year of a project to evaluate the decoupling effectiveness of underground cavities in a variety of configurations. New datasets have been provided by NORSAR and IDG that help to constrain the problem, particularly for the important partially coupled regime. Over the next year, the data set will continue to increase, and we will continue analysis of the data using empirical data analysis and numerical modeling of the chemical explosion data.

Following is a summary of some of the results achieved to date on this project.

Kirghizia Mine explosions provided by IDG:

- New data recorded on the surface at distances of 5 and 10 km have been analyzed and the results have been found to be generally consistent with previous results obtained from more limited free-field data, confirming low frequency decoupling factors in the range of 20-30 for fully decoupled HE tests in limestone.
- An explosion close to a cavity wall increases coupling by about a factor of 2.
- Decoupling in this data set is insensitive to cavity shape.

Swedish decoupled explosions provided by NORSAR:

- This new data set covers a range of yields overdriven beyond full decoupling by factors of approximately 2-20.
- The explosions in the smaller chambers produced far stronger signals despite significantly lower yields, consistent with expectations for partially coupled explosions.
- The resulting seismic signals from the Älvdalen cavity explosions display a low ratio of low frequency (2-6 Hz) energy to high frequency (8-16 Hz) energy. This ratio was lower for 10000 kg explosions in a 1000 m^3 chamber than for 5000 kg explosions in chambers of 200 m^3 and 300 m^3.

REFERENCES

Murphy, J. R., I. O. Kitov, N. Rimer, V. V. Adushkin and B. W. Barker (1997), "Seismic Characteristics of Cavity Decoupled Explosions in Limestone: An Analysis of Soviet High Explosive Test Data," *Journal of Geophysical Research,* **102**, B12, pp. 27, 393-27, 405.

Stevens, J. L., J. R. Murphy and N. Rimer (1991), "Seismic Source Characteristics of Cavity Decoupled Explosions in Salt and Tuff," *Bull. Seism. Soc. Am.*, **81**, pp. 1272-1291.

Stevens, Jeffry L., Norton Rimer, Heming Xu, G. Eli Baker, John R. Murphy, Brian W. Barker, Conrad Lindholm, Frode Ringdal, Steven Gibbons, Tormod Kvaerna and Ivan Kitov (2002), “Analysis and Simulation of Cavity-Decoupled Chemical Explosions,” SAIC Annual Report No. 1 submitted to the Defense Threat Reduction Agency, SAIC-02/2046, October 2002.

REGIONAL EVENT IDENTIFICATION RESEARCH IN EASTERN ASIA

Steven R. Taylor, Xiaoning (David) Yang, W. Scott Phillips, Howard J. Patton, Monica Maceira, Hans E. Hartse, and George E. Randall

Los Alamos National Laboratory

Sponsored by National Nuclear Security Administration
Office of Nonproliferation Research and Engineering
Office of Defense Nuclear Nonproliferation

Contract No. W-7405-ENG-36

ABSTRACT

We describe ongoing studies of broad-area regional-event identification in Eastern Asia. The goal of our work is to provide a framework that allows for accurate identification, operational transparency and clear reporting to non-technical decision makers. The underlying methodologies need to have a clear physical basis packaged in a sound statistical framework having proper uncertainty estimates.

The Magnitude and Distance Amplitude Correction (MDAC) methodology is used to correct regional seismic amplitudes for propagation effects and earthquake source scaling. We correct amplitudes rather than predefining various phase ratios because all information is retained from which to construct discriminants. Because signals from explosions are highly dependent on near-source material properties and emplacement conditions, it is difficult to *a priori* select discriminants from un-calibrated regions. The MDAC approach adds much flexibility to the problem and allows for construction of numerous combinations of discriminants in a multivariate setting using Gaussian statistics. The MDAC parameters are specified using an earthquake source model that allows for non-constant stress drop and variable P and S wave corner frequency scaling. Because the earthquake model is inappropriate for explosions it is assumed that a poor fit will be obtained for explosions and allow for their identification. MDAC calibration parameters for a region are updated when corresponding geophysical information is available. Seismic moments and earthquake source scaling are computed from coda M_w values and attenuation corrections are from regional phase tomography. The MDAC parameters can be used rapidly in an operational setting.

We are also developing regional surface wave discriminants (e.g. m_b - M_s). These studies involve validation of existing surface slowness tomographic models and refining where appropriate (Yang *et al.*, 2002). Tomographic models at shorter periods are being developed and refined in selected regions. These studies lower detection thresholds and allow for discrimination at lower magnitudes. Surface-wave attenuation maps are also being developed using a Bayesian approach. *A priori* tomographic models are constructed using two-station amplitude-ratio measurements. Single-station measurements are then inverted for higher resolution maps. In order to isolate and enhance the surface-wave signal, we apply a phase-matched filter constructed from surface-wave group-velocity maps before making the spectral-amplitude measurement. The filtering eliminates, or greatly reduces the ambiguity due to multi-pathing and improves the fidelity of our measurements. We also use the theoretical source spectra to guide the measurement and gauge the quality of the data. We found general correlation between the two-station attenuation map and geological provinces of the region. Preliminary results also indicate that attenuation models are not highly dependent on the source of event parameters (CMT or recent regional studies) that we use to correct the amplitudes.

OBJECTIVE

The objective of this work is to provide methodologies and calibration for robust event identification at reduced monitoring magnitude thresholds.

RESEARCH ACCOMPLISHED

Magnitude and Amplitude Distance Corrections (MDAC)

A fundamental problem associated with event identification lies in deriving corrections that remove path and earthquake source effects on regional phase amplitudes used to construct discriminants. Our goal is to derive a set of physically based corrections that are independent of magnitude and distance, and amenable to multivariate discrimination by extending the technique described in Taylor and Hartse (1998) and Taylor *et al.* (2002). The MDAC procedure for correcting regional seismic amplitudes for seismic event identification has been modified to include more realistic earthquake source models and source scaling (MDAC2; Walter and Taylor, 2002).

To model and understand regional seismic spectra, we need to break down the observations into their component parts. The observed instrument-corrected regional phase spectra can be thought of as a convolution between the source and the path. In the frequency domain we can write this out as a cascading multiplication:

$$A_o(\omega, R) = S(\omega)G(R)P(\omega)B(\omega, R), \quad (1)$$

where ω is the angular frequency; R is the distance and:

$S(\omega)$ is the source spectrum;
$G(R)$ is the geometrical spreading;
$P(\omega)$ is the frequency dependent site effect;
$B(\omega, R)$ is the apparent attenuation.

Here we have split the path effect into three pieces: 1) a frequency-independent geometrical-spreading component, 2) a distance-independent and frequency-dependent site-effect component, and 3) an apparent attenuation component.

The MDAC2 prediction of the observed, instrument-corrected spectra is then given by the same equation except now we estimate each of the components:

$$A_m(\omega, R) = S(\omega)G(R)P(\omega)B(\omega, R). \quad (2)$$

We linearize equation (2) by taking the logarithm of both sides:

$$\log A_m(\omega, R) = \log S(\omega) + \log G(R) + \log P(\omega) + \log B(\omega, R). \quad (3)$$

To remove the data trends with distance and magnitude, we correct the observed spectrum, $A_o(\omega, R)$, by subtracting the log of the MDAC2 spectrum in equation (3):

$$\log A_c(\omega, R) = \log A_o(\omega, R) - \log A_m(\omega, R). \quad (4)$$

These corrected spectra or residuals can then be kriged to further reduce un-modeled path effects (e.g. Schultz *et al.*, 1998).

For a given station and source region, a number of well-recorded earthquakes are used to estimate source and path corrections. In the MDAC2 formulation, we generalize the Brune (1970) earthquake source model with a more physical apparent-stress model that can represent non-constant stress-drop scaling. We also include a parameter that allows for variable P-wave and S-wave corner frequency scaling. The discrimination power in using corrected

amplitudes lies in the assumption that the earthquake model will provide a poor fit to the signals from an explosion. The propagation model consists of a frequency-independent geometrical spreading and frequency-dependent power-law Q. We incorporate regional phase attenuation tomographic models to replace a constant Q_0 model (Phillips *et al.*, 2000; Taylor *et al.*, 2003).

A grid search is performed simultaneously at each station for all recorded regional phases over stress-drop, geometrical spreading, and frequency-dependent Q to find a suite of good-fitting models that remove the dependence on M_w and distance. Very stable moment magnitude measures from regional coda wave envelopes that have been tied to independently derived regional seismic moments are incorporated. We also solve for frequency-dependent site/phase excitation terms. Once a set of corrections is derived, effects of source scaling and distance as a function of frequency are applied to amplitudes from new events prior to forming discrimination ratios. Thus, all the corrections are tied to M_w and distance and can be applied very rapidly in an operational setting. Moreover, phase-amplitude residuals as a function of frequency can be spatially interpolated (e.g., using kriging) and used to construct a correction surface for each phase and frequency. The spatial corrections from the correction surfaces can then be applied to the corrected amplitudes based only on the event location. The correction parameters and correction surfaces can be developed offline and entered into an online database for pipeline processing providing multivariate-normal corrected amplitudes for event identification (Figure 1).

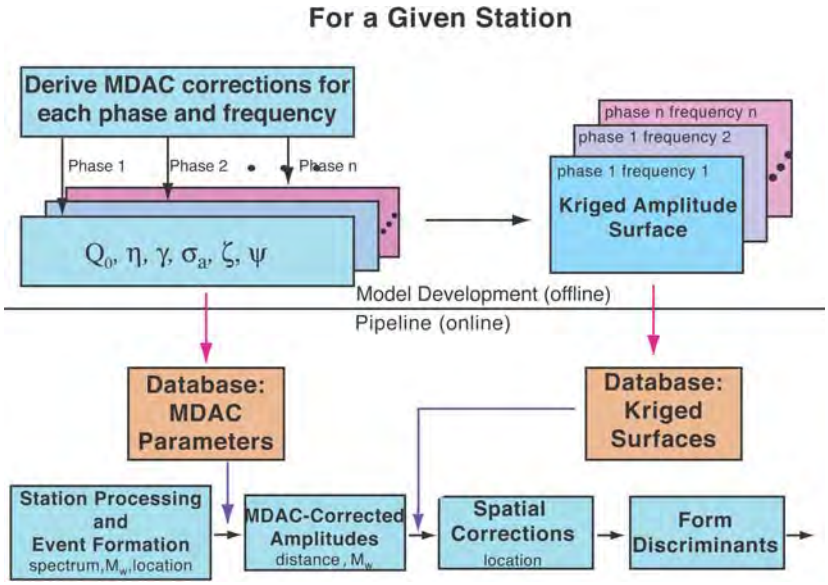


Figure 1. Example flowchart illustrating how the MDAC method can be combined with spatial interpolation (e.g., kriging) to develop database parameters to provide amplitude corrections for regional event identification in near-real time. These parameters can easily be incorporated into an operational pipeline to correct amplitudes from a new event for identification purposes.

As an illustration of the MDAC methodology, we present results from the IRIS (Incorporated Research Institutes for Seismology) GSN (Global Seismic Network) station MAKZ (Makanchi, Kazakhstan). The data are from four Lop Nor nuclear explosions and 412 earthquakes located in a region around Lop Nor extending between 35° and 50° N latitude and 80° and 100° E longitude. We corrected all amplitudes that passed the signal-to-noise cutoff of 1 using pre-phase noise including the four Lop Nor nuclear explosions. Figure 2 shows the corrected log amplitudes for each phase as a function of frequency for all four phases. We have also identified four earthquakes occurring within 50 km of the Lop Nor test site. As is expected, the corrected amplitudes for the earthquakes are very close to zero mean, and χ^2 goodness-of-fit tests show most frequency bands are normally distributed. The explosions show a significantly different pattern than the earthquakes. This is not unexpected, since we are using an earthquake model to fit the data. The misfit is particularly severe for Pn as can be seen by the high residuals at intermediate and high frequencies. As will be further illustrated below, the plot in Figure 2 is interesting in that it can be used as a guide in selecting individual discriminants that provide good separation between earthquakes and explosions. For example, it can be seen that a high frequency Pn to low-frequency Sn or Lg cross-spectral ratio will give excellent separation

between the earthquakes and explosions (as noted by Hartse *et al*., 1997). Additionally, a Pn, Pg, or possibly even an Sn spectral ratio will provide good separation. These observations reinforce our earlier comments about the potential restrictions on discrimination performance by *a priori* selecting ratios.

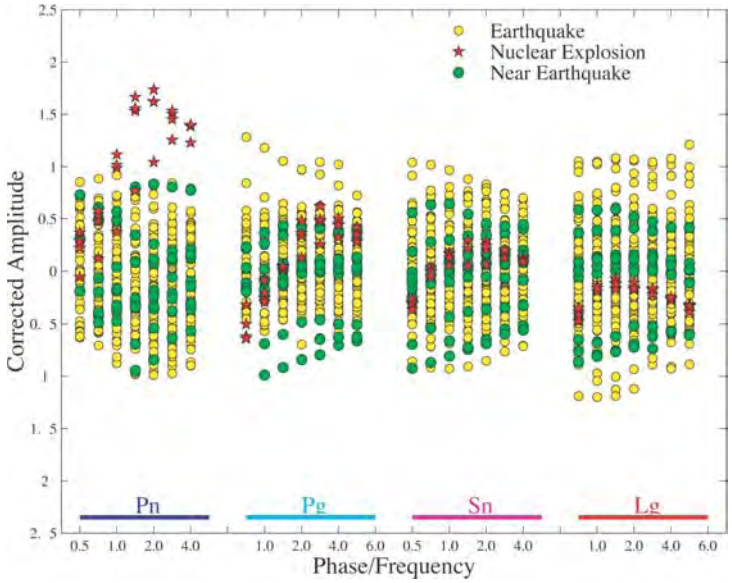


Figure 2. MDAC-corrections in log amplitudes for each phase as a function of frequency at MAK/MAKZ including the 4 Lop Nor nuclear explosions. Four earthquakes within 50 km of Lop Nor are also identified. Each amplitude is normalized by the lowest-frequency Lg amplitude (0.5-1 Hz).

At this point we can directly make traditional discrimination plots from the corrected amplitudes shown in Figure 2 by simply taking differences (log ratios) using any combination of phases and frequencies. Examples of four discriminants were discussed in Taylor, et al. (2002). The separation between the earthquakes and explosions is quite good (including the Lop Nor earthquakes). Note that in all cases the discrimination performance is excellent and trends are removed with magnitude. The separation between the Lop Nor explosions and earthquakes is very good indicating that the discriminants are based on source or very near-source differences between the two different source types. Thus, utility of the MDAC procedure allows us to retain all amplitude information as a function of phase and frequency.

Short-Period Rayleigh-Wave Group-Velocity Tomography

Short-period, high-resolution surface-wave slowness tomographic maps are necessary to lower detection thresholds and allow for discrimination at lower magnitudes. We focus on the region between 70° and 95° E longitude and 35° and 50° N latitude. We used the PDE catalog to guide the collection of earthquake data from IRIS DMC. We retrieved broadband waveform data from more than 1,100 events that occurred in the area between January 1997 and May 2002. Waveforms were obtained from four different networks (IRIS/USGS, IRIS/IDA, CDSN, and Geoscope) comprising 13 individual stations. Using multiple-filter analysis (Dziewonski *et al*., 1969; Herrmann, 1973) and phase-matched filter (Herrin and Goforth, 1977) techniques, we measured the dispersion characteristics of the signals between 5 and 30 seconds. These Rayleigh-wave group velocity dispersion curves were used to compute high-resolution (0.5° cell) slowness tomographic maps for each period.

We have adopted a Bayesian tomography method (Tarantola, 1987; Taylor *et al*., 2003) to solve the equation that relates the travel-time data with the velocity structure

$$\mathbf{d} = \mathbf{G}\mathbf{m}, \qquad (5)$$

where **G** represents the matrix containing path-length elements; **m** is the vector of unknown block slowness, and **d** is the data vector. The Bayesian solution of equation (5) is

$$\mathbf{m} = \mathbf{m}_0 + (\mathbf{G}^T\mathbf{C}_d^{-1}\mathbf{G} + \mathbf{C}_{m0}^{-1})^{-1}\mathbf{G}^T\mathbf{C}_d^{-1}(\mathbf{d} - \mathbf{G}\mathbf{m}_0), \quad (6)$$

where $\mathbf{m}_0$ is the *a priori* model, and $\mathbf{C}_d$ and $\mathbf{C}_{m0}$ are the data and *a priori* model covariance matrices respectively. Within the Bayesian framework, statistical characteristics of the data and the *a priori* information are utilized in the inversion to constrain the results and their uncertainty.

We used a declustering technique to remove the effect of event clusters. Instead of taking the average of the measurements in a cluster, we retain all the measurements, but down-weight each measurement with a weighting factor that is inversely proportional to the number of events that fall within the same cluster (Isaaks and Srivastava, 1989). The weighting factor is incorporated in the data covariance matrix $\mathbf{C}_d$. Global and regional 1° group-velocity maps are available from previous studies (Levshin *et al*., 2001; Ritzwoller and Levshin, 1998; Stevens *et al*., 2001). These maps were evaluated (Yang *et al*., 2002) and proved to be effective to construct an *a priori* model for the region of interest.

The slowness tomographic map for 10s is shown in Figure 3 as an example. The inverted model is similar, to some extent, to the *a priori* model, but it shows more structure and it is of higher resolution (0.5° cell compared to 1° cell for the *a priori* model). The tomographic patterns correlate really well with known geologic and tectonic features in the area. Accumulations of relatively young sediments across Eurasia are greater than on any other continent due to the continuing rapid uplift across central Asia because of the collision between the Eurasian plate and the Indian plate. The tomography maps display low velocities associated with the known sedimentary basins – Tarim, Junggar and Quaidam basins - in the area of central Asia under study. On the other hand, high velocities appear associated with mountainous tectonic features such as the Tien Shan Mountains. These improved high-resolution, short-period tomography maps can be used to lower the M_s detection thresholds to be used for construction of regional $m_b - M_s$ discriminants.

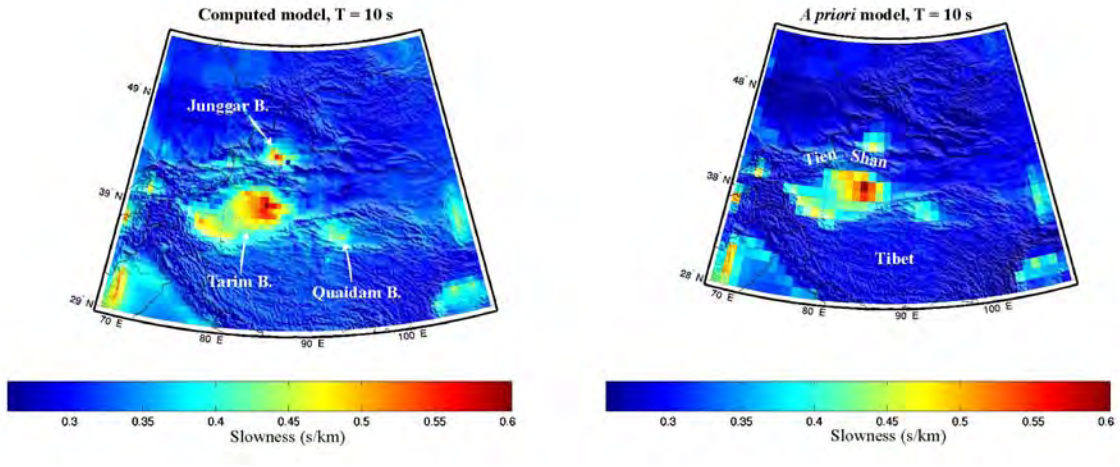


Figure 3. A comparison between the inverted Rayleigh-wave slowness tomographic map at 10 second and the *a priori* model. Warm colors represent low group velocities and cool colors indicate high velocities.

20-sec Rayleigh-Wave Attenuation Tomography

The $m_b - M_s$ relationship has proven to be an effective teleseismic discriminant. In order to extend its applicability to regional distances, lateral heterogeneity in the crust and upper mantle needs to be accounted for. We are mapping out another aspect of these heterogeneities by developing 20-sec Rayleigh-wave attenuation models for central Asia (15° - 65° N; 70° - 130° E). We take two steps in developing the attenuation model. First, we use two-station amplitude-ratio measurements, which are less affected by source-parameter error than single-station amplitude measurements, to obtain a coarse-grid (5° cell) model with a tomographic inversion. We then invert for the final model (2° cell) with single-station measurements, which have much better path coverage. We have adopted the

Bayesian approach discussed in last section for the tomography as well (equation (6)). The coarse-grid model is used as the *a priori* model in the final inversion.

The attenuation term $B(\omega, R)$ in equation (1) for surface waves can be expressed as $B(\omega, R) = \exp(-\lambda(\omega)R)$, where λ is the attenuation coefficient. An equivalent of equation (3) for surface waves, after geometrical-spreading correction, then becomes

$$\ln A(\omega, R) = \ln S(\omega) + \ln P(\omega) - \lambda(\omega)R. \qquad (7)$$

If two seismic stations lie on the same great-circle path that goes through an earthquake source, the geometrical-spreading corrected amplitude ratio between the two stations is

$$\frac{A(\omega, R_1)}{A(\omega, R_2)} = \frac{P_1(\omega)}{P_2(\omega)} e^{-\lambda(\omega)(R_2 - R_1)},$$

or in the logarithm domain as

$$\ln \frac{A(\omega, R_1)}{A(\omega, R_2)} = \ln P_1(\omega) - \ln P_2(\omega) - \lambda(\omega)(R_2 - R_1), \qquad (8)$$

where λ is the average attenuation coefficient of the medium between the two stations. In the tomographic inversion, we discretize the last term in equations (7) and (8) and group multiple observations together. In a matrix form, the problem is expressed as equation (5). Using 20-sec Rayleigh-wave spectral amplitudes, we solve for the model **m**, which contains discretized attenuation coefficients, site-effect and source-effect terms, with equation (6).

Surface-wave generation and propagation are affected by many factors such as source mechanism and location, path heterogeneity and site response (e.g., Mitchell, 1995). In order to reduce the error in the amplitude measurements caused by these factors or their uncertainties, especially the path heterogeneity, we designed a measuring tool that makes use of phase-matched filters and other source and path information available to achieve reliable measurements. We use Rayleigh-wave group-velocity models developed by Levshin *et al.* (2002), Ritzwoller and Levshin (1998) and Stevens *et al.* (2001) to construct phase-matched filters. We then calculate the cross-correlation between the instrument-corrected data and the phase-matched filter for the same path and window the cross-correlation around the peak associated with the main arrival. In many cases, this technique effectively isolates the direct arrival from multi-pathing, thus reduces the error introduced by off-great-circle propagation and focusing. Using source parameters from the Harvard CMT catalog, we also plot source radiation patterns and theoretical source spectra along with great-circle paths and data spectra to help guide our measurement and gauge the quality of the data. Figure 4 gives an example of the effectiveness of the phase-matched filters in extracting clean amplitude spectra.

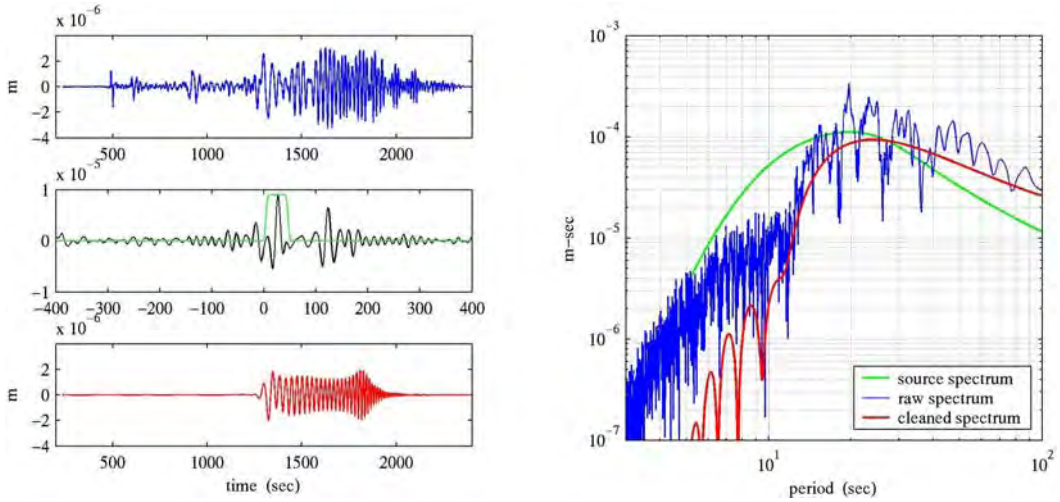


Figure 4. An example showing the phase-match filtering technique. The data are from an event in south RyuKyu Islands southeast of China and recorded at station Hyderabad in India. On the left, the top plot shows the original seismogram. Cross-correlation between the seismogram and the phase-matched filter for this path is plotted in the middle along with a window isolating the direct arrival. The cross-correlation clearly shows a second arrival indicating multi-pathing. The lower plot on the left is the cleaned seismogram. The plot on the right shows the theoretical source spectrum, the raw-data spectrum and the cleaned data spectrum. The cleaned spectrum is smooth and has a similar shape as the theoretical spectrum. The gentler roll-off of the theoretical spectrum toward lower periods is probably due to the fact that no attenuation was included in its calculation.

With the criterion that the azimuth difference between the two stations in a station pair is less than or equal to 2°, we have made 890 two-station amplitude-ratio measurements for 206 inter-station paths. Figure 5a shows the path coverage of the measurements and Figure 5b plots the geometrical-spreading corrected amplitude ratio as a function of inter-station distance.

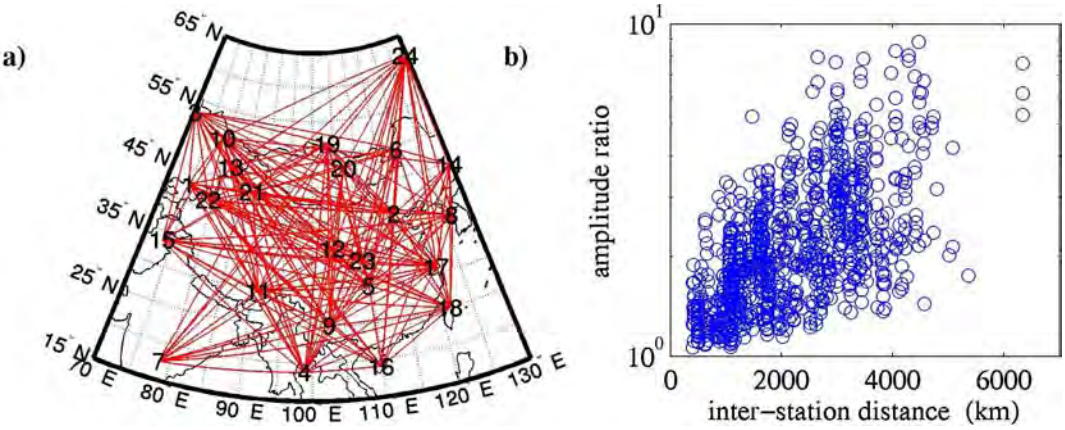


Figure 5. a) Path coverage of the two-station amplitude-ratio measurements. Station locations are marked by numbers. Grid lines define the discretization of the region for the first-step, coarse-grid inversion. b) Amplitude ratio as a function of inter-station distance. The logarithms of the ratios exhibit a linear trend as is expected.

For the two-station amplitude-ratio inversion, we assumed that the data are independent of each other. We then used a quality factor that we assigned to the data when we made the measurements to construct the diagonal elements of the data variance matrix $\mathbf{C}_d$. Because we usually have multiple measurements for each inter-station path, we down-weighted each measurement according to the number of measurements for that path by a weighting factor

incorporated in $\mathbf{C}_d$. We also used a diagonal matrix for the *a priori* model covariance and conducted a grid search to select reasonable values for the *a priori* model and its variance based on the behavior of data residuals. Figure 6 displays the inverted attenuation coefficient model and site-effect terms for 20-sec Rayleigh waves. The estimated attenuation coefficients span a range that corresponds to *Q* values from about 120 to about 785. Some of the broad correlation between the attenuation model and the geological and tectonic provinces of the region include high attenuation in western China, Tibetan Plateau, Sichuan Basin, Bay of Bengal, east China seas and Baikal Rift, and low attenuation in India and North China Platform. Due to the relatively sparse path coverage, there could be spurious features in the model. We believe that the single-station inversion will reduce the error in this *a priori* model and produce more accurate results.

CONCLUSIONS AND RECOMMENDATIONS

Event identification studies in eastern Asia involve development of algorithms for constructing discriminants as well as applying the algorithms for station calibration. Our research outlined in this paper has focused on regional seismic discrimination using MDAC corrected amplitudes and regional $m_b - M_s$ discriminants.

Our ongoing work in the surface-wave attenuation tomography is to make single-station spectral amplitude measurements and prepare for the final model inversion. Preliminary trial inversions with single-station amplitude data indicates that correcting the amplitudes with source parameters from different catalogs (CMT and recent regional studies) has minor effects on the resulting attenuation model (< 10%). We are also investigating the issue of constructing more realistic data and model covariance matrices with non-zero off-diagonal elements based on covariance models.

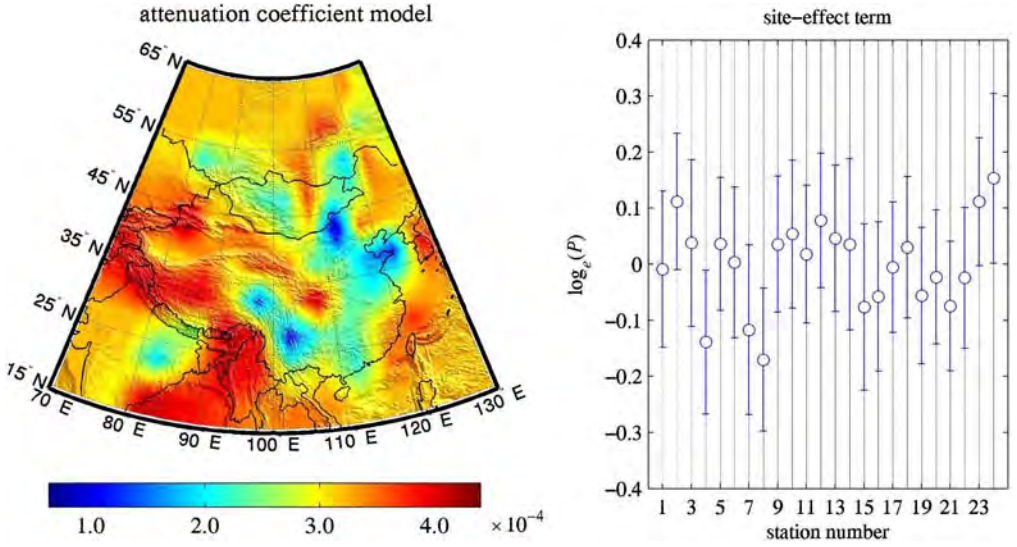


Figure 6. Estimated 20-sec Rayleigh-wave attenuation-coefficient and site-effect model from the two-station amplitude-ratio inversion. Site effects are displayed along with the error estimates. Station numbers correspond to those in Figure 5a.

ACKNOWLEDGEMENTS

We thank Anatoli Levshin and Michael Ritzwoller at University of Colorado at Boulder, and Jeffry Stevens at Science Applications International Corporation (SAIC) for providing us with their surface-wave group-velocity models.

REFERENCES

Brune, J. N. (1970), Tectonic stress and spectra of seismic shear waves from earthquakes, *J. Geophys. Res.*, 75, 4997-5009.

Dziewonski, A. M., S. Bloch, and M. Landisman (1969), A technique for the analysis of transient seismic signals, *Bull. Seism. Soc. Am.*, 59, 427-444.

Hartse, H. E., S. R. Taylor, W. S. Phillips, and G. E. Randall (1997), Regional event discrimination in central Asia with emphasis on western China, *Bull. Seism. Soc. Am.*, 87, 551-568.

Herrin, E. T. and T. T. Goforth (1977), Phase matched filters: application to the study of Rayleigh waves, *Bull. Seism. Soc. Am.*, 67, 1259-1275.

Herrmann, R. B. (1973), Some aspects of band-pass filtering of surface waves, *Bull. Seism. Soc. Am*., 63, 663-671.

Isaaks, E. H., and R. M. Srivastava (1989), *An Introduction to Applied Geostatistics*, Oxford University Press, New York, 561pp.

Levshin, A. L., J. L. Stevens, M. H. Ritzwoller and D. A. Adams (September 2002), Short-period (7-s to 15-s) group velocity measurements and maps in central Asia, in *Proceedings of the 24th Seismic Research Review: Nuclear Explosion Monitoring: Innovation and Integration, 2002*, LA-UR-02-5048, Vol. I, 97-106.

Mitchell, B. J., Y. Pan, J. Xie, and L. Cong (1997), Lg coda Q variation across Eurasia and its relation to crustal evolution, *J. Geophys. Res.*, 102, 22,767-22,779.

Mitchell, B. J. (1995), Anelastic structure and evolution of the continental crust and upper mantle from seismic surface wave attenuation, *Rev. of Geophys.*, 33, 441-462.

Phillips, W. S, H. E. Hartse, S. R. Taylor (2000), 1 Hz Lg Q tomography in central Asia, *Geophys. Res. Lett.*, 20, 3425-3428.

Ritzwoller, M. H. and A. L. Levshin (1998), Eurasian Surface Wave Tomography: Group Velocities, *J. Geophys. Res.* 103, 4839-4878.

Schultz, C. A., S. C. Myers, J. Hipp, and C. Young (1998), Nonstationaly Bayesian Kriging: A predictive technique to generate spatial corrections for seismic detection, location, and identification, *Bull. Seism. Soc. Am.*, 88, 1275-1288.

Stevens, J. L., D. A. Adams, and G. E. Baker (September 2001), Improved Surface Wave Detection and measurement Using Phase-Matched Filtering with a Global One-Degree Dispersion Model, in *Proceedings of the 23rd Seismic Research Review: Worldwide Monitoring of Nuclear Explosions, 2001*, LA-UR-01-4454, Vol. I, 420-430.

Tarantola, A. (1987), *Inverse Problem Theory*, Elsevier Science, Amsterdam, The Netherlands, 630pp.

Taylor, S. R., and H. E. Hartse (1998), A procedure for estimation of source and propagation amplitude corrections for regional seismic discriminants, *J. Geophys. Res.*, 103, 2781-2789.

Taylor, S. R., A. A. Velasco, H. E. Hartse, W. S. Phillips, W. R. Walter, and A. J. Rodgers (2002), Amplitude corrections for regional seismic discriminants, *Pure. App. Geophys.* 159, 623-650.

Taylor, S. R., X. Yang, and W. S. Phillips (2003), Bayesian Lg attenuation tomography applied to eastern Asia, *Bull. Seism. Soc. Am.*, 93 795-803.

Walter, W. R. and S. R. Taylor (2002), A revised Magnitude and Distance Amplitude Correction (MDAC2) procedure for regional seismic discriminants: Theory and testing at NTS, *Los Alamos National Laboratory*, LA-UR-02-1008, 15pp.

Yang, X., S. R. Taylor, H. J. Patton, M. Maceira and A. A. Velasco (September 2002), Evaluation of intermediate-period (10- to 30-sec) Rayleigh-wave group-velocity maps for central Asia, in *Proceedings of the 24th Seismic Research Review: Nuclear Explosion Monitoring: Innovation and Integration, 2002*, LA-UR-02-5048, Vol. I, 609-617.

IMPROVING THE FUNDAMENTAL UNDERSTANDING OF REGIONAL SEISMIC SIGNAL PROCESSING WITH A UNIQUE WESTERN UNITED STATES DATASET

William R. Walter,[1] Kenneth D. Smith,[2] Jennifer L. O'Boyle,[1] Teresa F. Hauk,[1] Flori Ryall,[1] Stanley D. Ruppert,[1] Stephen C. Myers,[1] Megan L. Anderson,[1] and Douglas A. Dodge[1]

Lawrence Livermore National Laboratory;[1] University of Nevada, Reno[2]

Sponsored by National Nuclear Security Administration
Office of Nonproliferation Research and Engineering
Office of Defense Nuclear Nonproliferation

Contract No. W-7405-ENG-48[1] and DE-FC03-01SF22419[2]

ABSTRACT

This project has built a unique historic database of regional distance nuclear explosion, earthquake, and mine-related digital broadband seismograms for the western United States (US). The emphasis is on data from Lawrence Livermore National Laboratory (LLNL)-managed stations MNA, ELK, KNB and LAC that recorded many nuclear tests and nearby earthquakes in broadband digital form since 1980, along with a small number of earlier events that were digitized from tapes. Through the generous cooperation of Sandia National Laboratories (SNL) we have also included waveforms from their Leo Brady network (BMN, DWN, LDS, NEL,TON). In addition we include data from other open broadband stations in the western US with long operating histories and/or ties to the International Monitoring System (e.g. PFO, YKA, CMB, NEW, DUG, ANMO, TUC). These waveforms are associated with a reconciled catalog of events and station response information to facilitate analysis. The goal is to create a high-quality database that can be used in the future to analyze fundamental regional monitoring issues such as detection, location, magnitude, and discrimination.

In the first stage of the project, we collected six different regional network catalogs from the University of Nevada, Reno, to provide accurate independent location information for events on the Nevada Test Site and in the surrounding region. We have used National Nuclear Security Administration (NNSA)-developed software to reconcile these catalogs with each other and to incorporate them into a set of larger continental scale (CNSS, see http://www.cnss.org; USGS mining catalog compiled by Jim Dewey) and global scale (PDE, REB, and ISC) catalogs. Finally, we incorporate the best catalogs of NTS nuclear event locations and source properties (Springer et al. 2002). The result is a single catalog of preferred origins, source information, and station information. Concurrently, we collected continuous seismic data from open stations and recovered and reformatted old event segmented data from the LLNL and SNL managed stations for past nuclear tests and earthquakes. We then used the preferred origin catalog to extract waveforms from continuous data and associate event segmented waveforms within the database. The result is a well-organized regional western US dataset with hundreds of nuclear tests, thousands of mining explosions and hundreds of thousands of earthquakes.

In the second stage of the project we have chosen a subset of approximately 125 events that are well located and cover a range of magnitudes, source types, and locations. Ms. Flori Ryall, an experienced seismic analyst is reviewing this dataset. She is picking all arrival onsets with quantitative uncertainties and making note of data problems (timing errors, glitches, dropouts) and issues. The resulting arrivals and comments will then be loaded into the database for future researcher use. During the summer of 2003 we will be carrying out some analysis and quality control on this subset. It is anticipated that this set of consistently picked, independently located data will provide an effective test set for regional sparse station location algorithms. In addition, because the set will include nuclear tests, earthquakes, and mine-related events, each with related source parameters, it will provide a valuable test set for regional discrimination and magnitude estimation as well. A final relational database of these approximately 125 events in the high quality subset will be put onto a CD-ROM and distributed for other researchers to use in benchmarking regional algorithms after the conclusion of the project.

OBJECTIVE

The objective of this project is to build a historic western U.S. database of regional distance nuclear explosion, earthquake, and mine-related digital broadband seismograms with their associated parameters (origin's times and location, instrument response, etc.). Although the original title of the project remains unchanged, its scope has been reduced to match the level of funding awarded. Therefore we focus on a subset of this data to undergo careful quality control, to provide independent regional network ground-truth location and to perform quantitative regional phase picking. This subset will be released as a CD-ROM at the conclusion of the project and provide source type and location ground-truth data for monitoring researchers to make use of in benchmarking regional algorithms.

RESEARCH ACCOMPLISHED

Seismic nuclear monitoring research is data driven. The number of digital seismic records of underground nuclear tests at regional distances is quite restricted both in number and geographical location. Consequently, the finite number of existing regional nuclear test records are a unique resource that needs to be thoroughly exploited to create the best verification system possible. We believe that this exploitation is incomplete for the extensive Nevada Test Site (NTS) nuclear explosion records. Therefore in this project our goal is to build the largest, most complete, and best-documented database of explosions, earthquakes, mine blasts and mine tremors in the Western U.S. Once completed we believe this database will provide a well-organized and highly efficient way to conduct fundamental monitoring research on regional seismic event detection, location and identification.

Building a Comprehensive Western U.S. Database

The process of building this new database involves a series of steps, which include:

1. Collecting local, regional and global seismicity catalogs from the NTS and the western U.S.
2. Reconciling catalogs into a single table of events with preferred origin information
3. Compiling event parameter information (e.g. yield, material properties, focal mechanisms, etc.)
4. Collecting continuous data from selected stations
5. Compiling station site and instrument response information
6. Extracting event waveforms from continuous data and loading into database with ties to the reconciled catalog
7. Selecting a high quality data subset to analyze
8. Quantitatively analyzing the data subset and loading timing picks and uncertainties into database
9. Distributing data subset and maintaining database for use in nuclear explosion monitoring research

At the time of this writing we have completed steps 1-7 and are working on steps 8-9. Here we briefly describe the research accomplished on this project so far.

We have attempted to obtain as complete of a list, as possible, of catalogs in the vicinity of the NTS and the western U.S. Springer et al. (2002) have compiled the most complete listing of dates, locations and working point parameters (e.g. depth, working point density, velocity, gas porosity) for U.S. underground nuclear tests. These parameters affect seismic frequency content and discriminants (e.g. Walter et al., 1995). The University of Nevada Reno (UNR) runs regional seismic networks in southern and northern Nevada that provide the most complete and accurate lists of earthquakes for this region. We have worked with UNR to obtain, the most complete a set of catalogs for the state of Nevada. We believe these local networks can be used to obtain independent high quality ground-truth location and depth information.

In addition to Nevada and NTS catalogs, we have also collected a number of regional and global scale catalogs. A U.S. seismicity catalog is compiled regularly by the University of California at Berkeley from most of the regional seismic network operator's catalogs in the country as part of the Council of National Seismic Stations (see http://www.cnss.org). Although this catalog contains a very large number of events, it does not capture all of the events in the local UNR catalogs listed above. We have also collected the United States Geological Survey (USGS) mine explosion listing that is compiled by Jim Dewey. Finally, we include the standard global catalogs from the

USGS Preliminary Determination of Epicenters (PDE), the International Seismological Commission (ISC) and the International Monitoring System (IMS) Reviewed Event Bulletin(REB).

We have gained much experience in building large reconciled databases over the past several years (see O'Boyle et al, this volume) and we make full use of these tools and procedures in this project. We assign each of these catalogs a rank order for reconciliation. The catalogs are then parsed, and locations and origin times are compared. Events in common are assigned to one unique event identification number and the highest-ranking catalog's origin information then becomes the preferred one. The other origin information is retained as well. In this way we build up a single listing of events that can be used to extract waveforms from continuous data or tie to event-segmented data. For a more complete discussion of the catalog reconciliation process see O'Boyle et al. (this volume).

Table 1. Seismicity Catalogs Collected, Parsed and Reconciled for this Project

Date Range	Source Types	Catalog Name	Comments and References
1946-1992	Nuclear tests	Springer catalog	Below surface tests, Springer et al (2002)
1978-2000	Earthquakes	UNR_SGB_merged	Covers Southern Great Basin (SGB) only
1992-2000	Earthquakes	UNR_SGB_relocated	Covers Southern Great Basin (SGB) only. Smith et al. (2002)
1868-2000	Earthquakes	YMP_PSHA	Yucca Mountain Project (YMP) Probability of Seismic Hazard Assessment (contains a composite of many catalogs within 300 km of YM)
1978-1999	Earthquakes	UNR_NN_consolidated	Covers Northern Nevada (NN) area only
2000-2001	Earthquakes	UNR_2000-2001	University of Nevada Reno networks catalog
2002-2003	Earthquakes	UNR_2002present	University of Nevada Reno networks catalog
1850-1998	Earthquakes	Nevada historic catalog	Compiled by Depolo and Depolo (1999)
1898-2002	Earthquakes	CNSS	Council of National Seismic Stations - a partially reconciled catalog of western US seismicity compiled by UC Berkeley
1920-2002	Earthquakes, explosion and mine tremors	USGS Monthly PDE	Preliminary Determination of Epicenters (PDE)
1964-1999	Earthquakes	ISC	International Seismological Commission (ISC)
1995-2000	Earthquakes	IMS REB	Comprehensive nuclear-Test-Ban Treaty International Monitoring System (IMS) Reviewed Event Bulletin (REB)
1997-2003	Mine Blasts	USGS Dewey catalog	A catalog of mining explosions compiled by Jim Dewey at the U.S. Geological Survey

A major emphasis of this project is on regional seismic waveforms from the four LLNL seismic stations operated by the Livermore NTS Network (LNN). These stations, all digital since about 1980, have recorded more than 120 underground nuclear tests during that time. In addition, there are a number of waveforms that were digitized from analog records that are of a more uncertain quality. We have identified the LNN waveforms from approximately 300 nuclear tests to review for quality control and to include in the database. Another large database of regional nuclear seismic waveforms was recorded on the Leo Brady Seismic Network (stations BMN, DAC, LDS, MVU, TPH) that is operated by Sandia National Laboratories (Lee, 2001). Through the generous cooperation of Sandia personnel we have included this dataset in the database as well. Both of these networks have recorded hundreds of

regional earthquakes, many in close proximity to prior nuclear tests and make an excellent dataset for studying the physical basis of regional seismic discrimination.

In addition to the national laboratory-managed networks, we have collected data from other broadband open seismic stations that are archived by the Incorporated Research Institutes for Seismology Data Management Center (IRIS DMC.) We have selected a subset of these stations with emphasis on stations that have long operating histories, stations that are part of the IMS network and stations that are spread throughout the western U.S. Table 2 below gives a list of the stations for which we have collected data to be included in the database.

Table 2. Seismic Station Data Retrieved for Event Waveform Extraction to Database

Data Type and Period	Station code	Location and comments
Continuous 1988-2001	PFO	Pinion Flat, California (IMS Auxiliary station)
Continuous 1989-2001	COR	Corvalis, Oregon
Continuous 1989-2001	ANMO	Albuquerque, New Mexico (IMS Auxiliary station)
Continuous 1992-2001	CMB	Columbia, California
Continuous 1992-2001	TUC	Tucson, Arizona
Continuous 1993-2001	YBH	Yreka, California (IMS Auxiliary station)
Continuous 1997-2001	DUG	Dugway, Utah
Continuous 1997-2001	TPNV	Topapah Springs, Nevada
Continuous 1997-2001	NEW	Newport, Washington (IMS Auxiliary station)
Continuous 1992-2002 Event segments 1968-1992	ELK	Elko, Nevada (IMS Auxiliary station)
Continuous 1992-2002 Event segments 1968-1992	KNB	Kanab, Utah
Continuous 1992-2002 Event segments 1968-1992	MNV	Mina, Nevada (IMS Primary array element)
Continuous 1992-1998 Event segments 1968-1992	LAC	Landers, California (closed in 1999)
Event segments	BMN	Battle Mountain, Nevada
Event segments	DAC	Darwin, California
Event segments	LDS	Leeds, Utah
Event segments	TPH	Tonopah, Nevada
Event segments	MVU	Marysvale, Utah

Additional event-segmented data that was collected over a limited time (for other projects) has been included in this database (e.g. WUAZ, SRU, GSC, ISA, NEE, NVAR, PDAR) for long-term storage and analysis.

In Figure 1 we show a map of the region with the locations of stations (Table 2) for which we are archiving seismic data and the locations of the reconciled events from 1997 to the middle of 2002. We selected 1997 as the starting point for this plot because that is when the Dewey catalog of mine seismicity starts. The reconciled catalog goes back to 1852. Figure 1 shows more than 8000 earthquakes and 1600 mining events (mainly explosions) in our reconciled catalog with magnitudes (mb, Mw or ML) greater than or equal to 2.5. The catalog does include events of all magnitudes and in some locations where the UNR network is dense there are magnitudes of -1 or smaller.

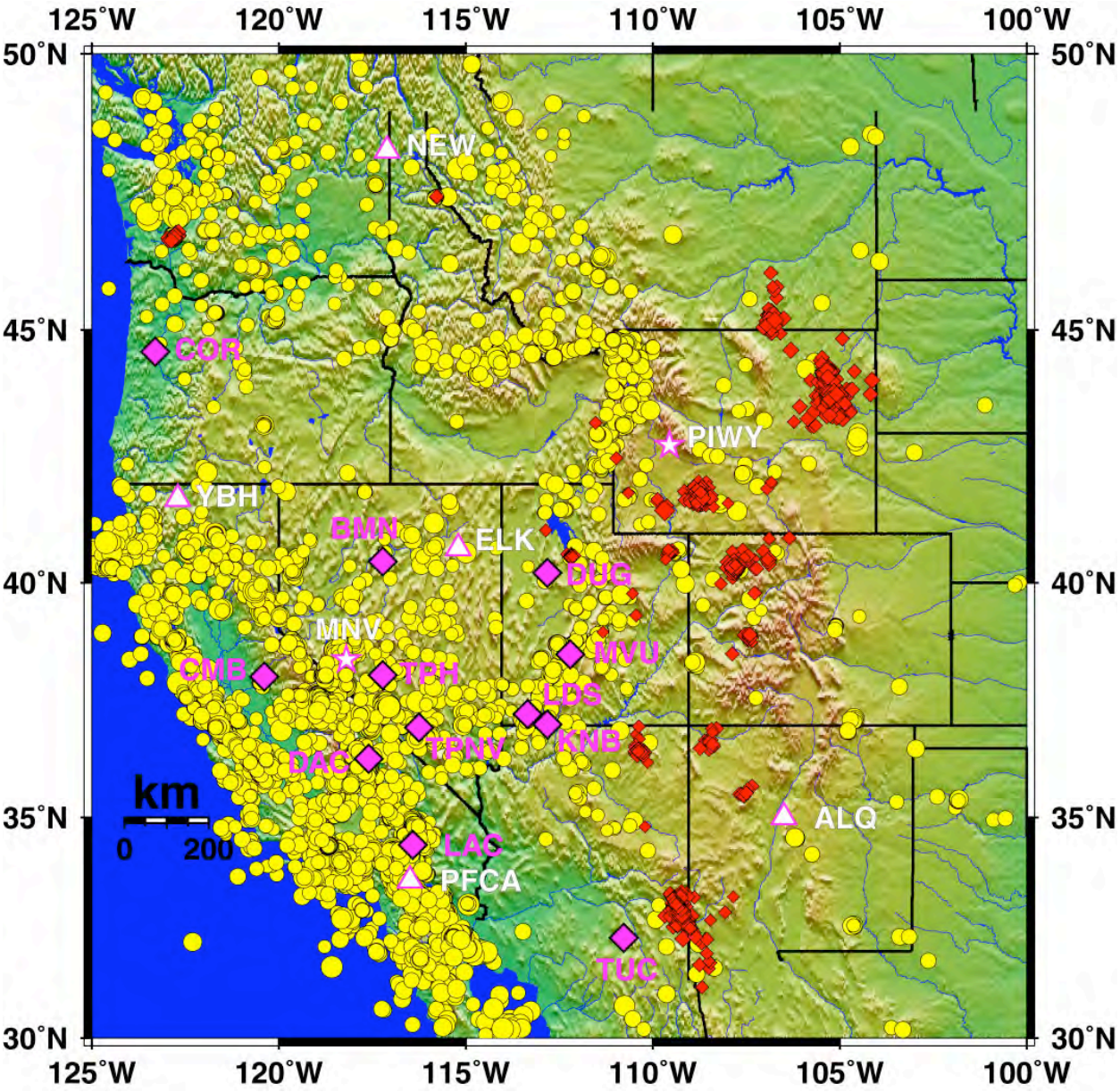


Figure 1. A shaded relief map showing the locations of seismic stations and select events in this project. Stations are listed in Table 2 and the events are drawn from a reconciled composite catalog created from the catalogs listed in Table 1. IMS primary stations are plotted as white stars. IMS auxiliary stations are plotted as white triangles and other broadband stations are plotted as pink diamonds. Seismic stations are labeled by name. Earthquakes are plotted as yellow circles and mine seismicity as small red diamonds. Seismic event symbols are scaled by magnitude.

Overall the western U. S. database contains 9.5 million waveforms from 360,000 events and occupies 1.2 terabytes of storage space in the LLNL Seismic Research Data Base (SRDB) (O'Boyle et al., this volume). A database of this size represents a significant resource for nuclear explosion monitoring research, but is impractical to distribute and will be maintained at LLNL. For both quality control purposes and to make a useful subset of this database for the broader research community, we are developing a high quality subset of this data for distribution on CD-ROM at the conclusion of this project.

High Quality Data Subset

For this subset we have selected approximately 125 events for detailed analysis. These events include 74 NTS controlled nuclear explosions, the 1993 NPE (Non Proliferation Experiment) chemical kiloton explosion, 30 earthquakes located on or near NTS, 20 earthquakes located in the broader western U.S., and 10 mining explosions from two mining districts in Arizona. This dataset is being analyzed by Ms. Flori Ryall, a seismic analyst with decades of experience. Flori will pick all arrival onsets with quality designations that can be mapped to quantitative uncertainties and make note of data problems (timing errors, glitches, dropouts) and other issues. These picks will then be loaded back into the database for researcher use. This effort has been ongoing this year and several thousand picks have been made so far. We anticipate completion of this task by the end of summer.

As an example of these picks we show the Pn, Pg and Lg picks with a high quality designation from the 74 NTS explosions shown in Figure 2. These events have a very precise location and timing (GT0) giving an excellent set of travel time curves for the basin and range. In the lower part of this figure we focus on the reduced Pn travel times for each station. First we note that none of the stations have good picks for all 74 events, due to station down time. Because nuclear testing at NTS ended in 1992, many of the open station networks (shown in red) have a very limited number of picks. In contrast, the two regional networks maintained by LLNL and SNL have a very large number of picks for the nuclear tests making them quite valuable for regional research. Looking at quality control, we note that a number of NTS events at the LLNL stations during the 1982-1983 time frame (Atrisco, Borrego) appear to have network clock problems of a couple of seconds. There also appear to be both network and individual station clock errors ranging from a couple seconds to tenths of seconds. Clock errors that are less than one second are very difficult to distinguish from picking errors. Despite these events with clock errors the dataset is large enough that after removing outliers we are able to obtain a very tight fit to linear travel time curves.

One goal for this high quality subset is to choose events with excellent ground-truth hypocenters from the regional networks for use in location research. The NTS explosions are clearly the best dataset for this purpose. These data and their picks are currently being used in relative regional relocation research (see location paper by Myers et al., this volume). For the earthquakes on or near the NTS we obtained the local UNR network data and re-picked these to allow high-quality local network locations to provide ground-truth independent of that based on the regional stations. We believe the high quality picks at local, near and far regional distances when combined with the independent ground truth will be useful in testing and benchmarking sparse station location algorithms.

We have also selected the high quality dataset with an eye towards discrimination research. Therefore, in addition to excellent ground truth locations, we also chose events that have well documented source properties. For explosions this means working point source medium properties such as density, P-velocity, and gas porosity. We have selected explosions that span a wide range of these properties. There are also a small number of explosions with announced yields and we use these events to facilitate yield estimation research. Finally we try to span the full range of magnitudes and depths to include a few of the larger explosions that were conducted prior to the 150 kt Threshold Test Ban Treaty of 1974. For earthquakes we want to select events that cover a range of magnitudes, depths and locations in the western U.S. For this reason we have picked events with some aftershock sequences (e.g. 1992 Little Skull Mountain, 1999 Scotty's Junction, 1999 Hector Mine, 1993 Eureka Valley, 1993 Cataract Creek). We also want focal mechanism information for as many of the earthquakes as possible. The impact of variations in focal mechanism and depth on regional discriminants are the subjects of current research (e.g. Zhang et al., 2002).

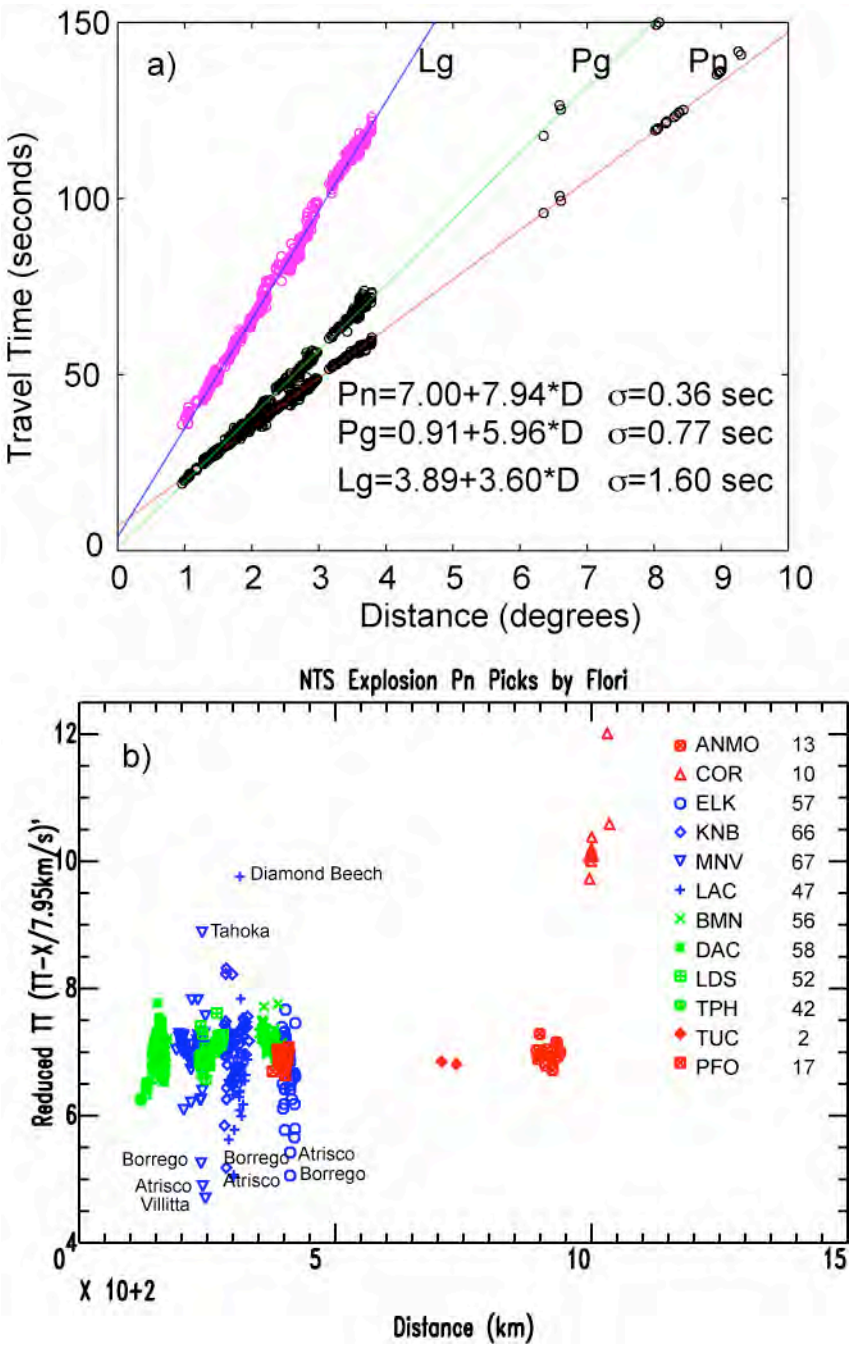


Figure 2. Travel time picks from 74 NTS nuclear tests recorded at regional stations and analyzed by Ryall are shown. Top plot (a) shows picks and linear travel time fits after removing three sigma outliers. Bottom plot (b) shows an expanded view of the reduced Pn picks listed by station along with the total number of Pn picks available. Some obvious outliers due to clock problems are labeled by the event names.

In Figure 3 we show 50 of the high quality subset events around the Nevada Test Site. The high level of natural earthquake activity since the 1992 Landers earthquake provides a nice dataset to contrast with the nuclear tests that ended in 1992. Recently a number of studies have been done that investigate the details of this seismicity (e.g. Smith et al, 2003; Ichinose, 2003). We use these studies to provide additional ground-truth about these events such as focal mechanisms and depth.

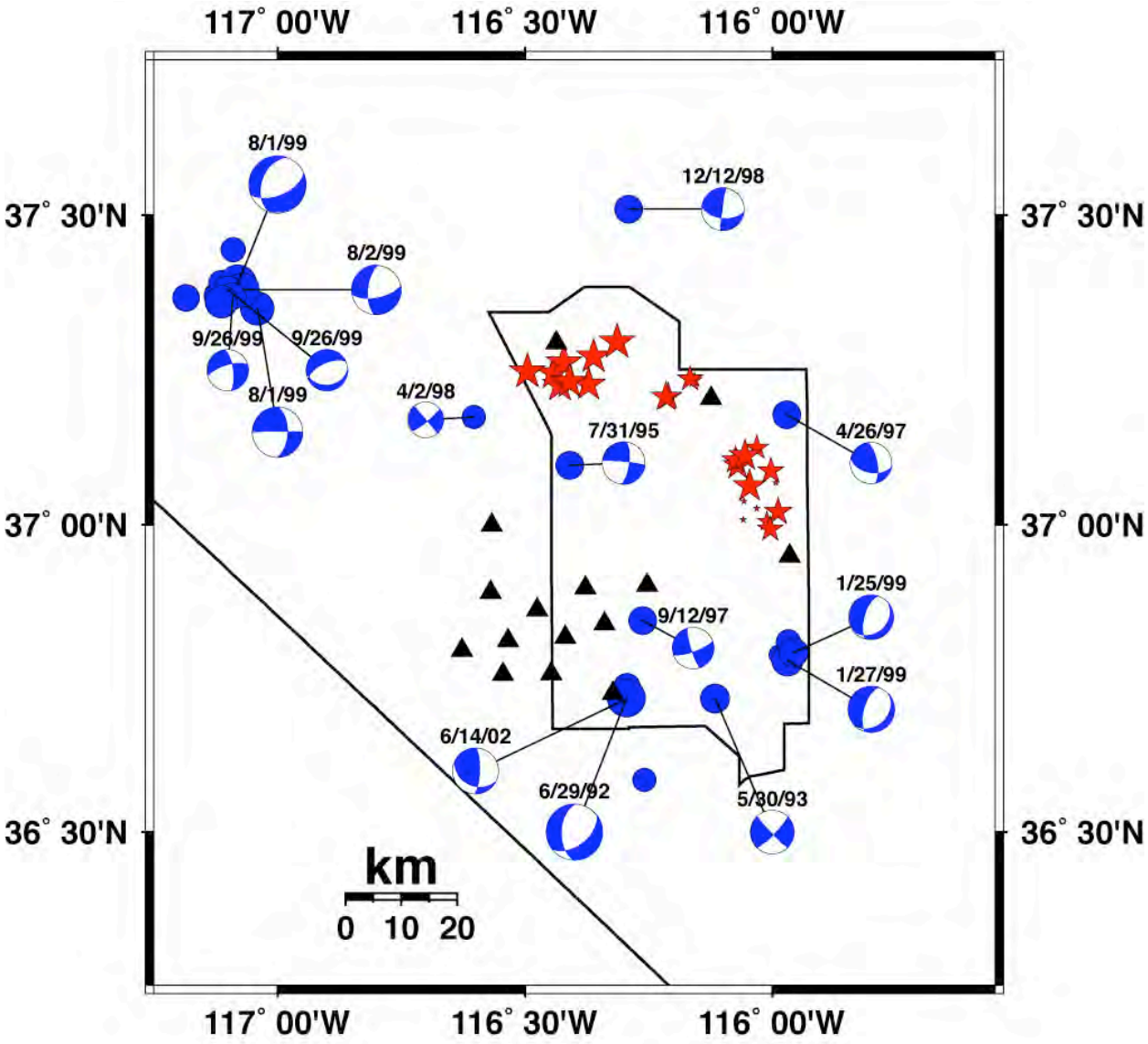


Figure 3. A map showing 25 earthquakes (blue circles) and 25 explosions (red stars) from 1989-2002 near NTS that are included in the high quality data subset. The map shows the boundaries of NTS and the locations of some of the UNR run Southern Great Basin network which can provide excellent ground truth hypocenter information for many of these events. Also shown are focal mechanisms for about 15 of these earthquakes drawn from regional studies by Smith et al (2002), Ichinose et al (2002) and the U.C. Berkeley moment tensor catalog. These earthquakes cover most of the seismicity in this region with magnitudes greater than about 3.5. The nuclear explosions cover the most recent 25 events when seismic network coverage is most complete and cover all three main testing areas at NTS (Pahute Mesa, Rainier Mesa and Yucca Flat). The explosions also cover a fairly full range of magnitude, depths and source material properties.

At the conclusion of this project we plan to put the high quality subset of approximately 125 events, along with associated parameters (time picks, focal mechanisms, source media properties, etc.) on a CD-ROM in Knowledge Base (KB) schema compatible database format for release to interested monitoring researchers. We hope this well-organized and compact set of data will prove useful in both researching and benchmarking seismic monitoring algorithms in detection, location, identification and magnitude yield estimation.

CONCLUSIONS AND RECOMMENDATIONS

We are finishing this ROA project to build the most complete and best-documented database of regional distance nuclear explosion, earthquake, and mine-related digital broadband seismograms in the western U.S. We have selected and marked phase onset times for a high quality subset of this data, which will be distributed at the conclusion of this project. We believe this set of consistently picked, independently located data will provide an effective test set for regional sparse station location algorithms. In addition because the set will include nuclear tests, earthquakes, and mine-related events, each with related source parameters, it will provide a valuable test set for regional discrimination and magnitude/yield estimation as well.

REFERENCES

dePolo, D.M and C. M. dePolo, (1999).Earthquakes in Nevada, Nevada Bureau of Mines and Geology, Map 119.

Ichinose, G.A., J. G. Anderson, and K.D. Smith (2003). Source parameters of eastern California and western Nevada earthquakes from regional moment tensor inversion, *Bull. Seism. Soc. Am.* (submitted in 2002).

Lee, J. W., (2001). A new seismic data system for determining nuclear test yields at the Nevada Test Site, Sandia National Laboratory Report, SAND2001-3373.

Smith, K. D., D. von Seggern, D. Depolo, (2003). Seismicity in the vicinity of Yucca Mountain 1992-2000 and regional tectonic process, *Bull. Seism. Soc. Am*. (submitted in 2002).

Springer, D. L., G. A. Pawloski, J. L. Ricca, R. F. Rohrer and D. K. Smith, (2002). Seismic source summary for all U. S. below surface nuclear explosions, *Bull. Seism. Soc. Am., 92*, 1806-1846, 2002.

Walter, W. R., K. Mayeda, and H. J. Patton (1995). Phase and spectral ratio discrimination between NTS earthquakes and explosions Part 1: Empirical observations, *Bull. Seism. Soc. Am.,* **85**., 1050-1067.

Zhang, J. T. Lay, J. Zaslow and W. R. Walter (2002), Source effects on regional seismic discriminant measurements, *Bull. Seism. Soc. Am. 92*, 2926-2945.

REGIONAL BODY-WAVE CORRECTIONS AND SURFACE-WAVE TOMOGRAPHY MODELS TO IMPROVE DISCRIMINATION

William R. Walter, Michael E. Pasyanos, Arthur J. Rodgers, Kevin M. Mayeda, and Alan Sicherman

Lawrence Livermore National Laboratory

Sponsored by National Nuclear Security Administration
Office of Nonproliferation Research and Engineering
Office of Defense Nuclear Nonproliferation

Contract No. W-7405-ENG-48

ABSTRACT

Our identification research for the past several years has focused on the problem of correctly discriminating small-magnitude explosions from a background of earthquakes, mining tremors, and other events. Small magnitudes lead to an emphasis on regional waveforms. The goal is to reduce the variance within the population of each type of event, while increasing the separation between the explosions and the other event types. We address this problem for both broad categories of seismic waves, body waves, and surface waves. First, we map out the effects of propagation and source size in advance so that they can be accounted for and removed from observed events. This can dramatically reduce the population variance. Second, we try to optimize the measurement process to improve the separation between population types.

For body waves we focus on the identification power of the short-period regional phases Pn, Pg, Sn and Lg, and coda that can often be detected down to very small magnitudes. It is now well established that particular ratios of these phases, such as 6- to 8-Hz Pn/Lg, can effectively discriminate between closely located explosions and earthquakes. To extend this discrimination power over broad areas, we developed a revised Magnitude and Distance Amplitude Correction (MDAC2) procedure (Walter and Taylor, 2002). This joint source and path model fits the observed spectra and removes magnitude and distance trends from the data. It allows for the possibility of variable apparent stress scaling in earthquakes, an unresolved issue that is the subject of investigation under separate funding. The MDAC2 procedure makes use of the extremely stable coda estimates of Mw for source magnitude and can also use independent Q tomography to help reduce trade-offs in fitting spectra. We can then apply the kriging operation to the MDAC2 residuals to provide full 2-D path corrections by phase and frequency band. These corrections allow the exploration of all possible ratios and multivariate combinations of ratios for their discrimination power. We also make use of the MDAC2 spectra and the noise spectra to determine the expected signal-to-noise value of each phase and use that to optimize the multivariate discriminants as a function of location. We quantify the discrimination power using the misidentified event trade-off curves and an equi-probable measure. In addition to the traditional phases, we are also exploring the application of coda amplitudes in discrimination. Coda-derived spectra can be peaked due to Rg-to-coda scattering, which can indicate an unusually shallow source.

For surface waves we have a new high-resolution regional Rayleigh-Wave tomography for the Yellow Sea and Korean Peninsula Region, based on measuring thousands of seismograms. We also continue to make new measurements for our regional Rayleigh and Love wave group velocity tomography models of Western Eurasia and North Africa. These tomography models provide high-resolution maps of group velocity from 10- to 100-s period. The maps also provide estimates of the expected phase spectra of new events that can be used in phase-match filters to compress the expected signals and improve the signal-to-noise ratio on surface wave magnitude (Ms) estimates. Phase match filters in combination with regional Ms formulas can significantly lower the threshold at which Ms can be measured, extending the Ms-mb discriminant. We have measured Ms in western Eurasia for thousands of events at tens of stations, with and without phase match filtering, and found a marked improvement in discrimination. Here we start to quantify the improvement to both discrimination performance and the Ms threshold reduction. The group velocity models also provide constraints on velocity structure, particularly in low seismicity regions. For example we are working with Dr. Bob Herrmann and Dr. Charles Ammon to combine tomography derived group velocity curves with station based receiver functions in joint inversions to estimate structure.

OBJECTIVE

Monitoring the world for potential nuclear explosions requires characterizing seismic events and discriminating between natural and man-made seismic events, such as earthquakes, mining activities, and nuclear weapons testing. We continue developing, testing, and refining size-, distance-, and location-based regional seismic amplitude corrections to facilitate the comparison of all events that are recorded at a particular seismic station. These corrections, calibrated for each station, reduce amplitude measurement scatter and improve discrimination performance. We test the methods on well-known (ground-truth) datasets in the U.S. and then apply them to the uncalibrated stations in Eurasia, Africa, and other regions to improve underground nuclear test monitoring capability.

RESEARCH ACCOMPLISHED

As part of the overall National Nuclear Security Administration Ground-based Nuclear Explosion Monitoring (GNEM) Research and Engineering (R&E) program, we continue to pursue a comprehensive research effort to improve our capabilities to seismically characterize and discriminate underground nuclear tests from other natural and man-made sources of seismicity. To reduce the monitoring magnitude threshold, we make use of regional body- and surface-wave data to calibrate each seismic station. Our goals are to reduce the variance and improve the separation between earthquakes and explosion populations by accounting for the effects of propagation and differential source size.

Body Wave Corrections

Effective earthquake-explosion discrimination has been demonstrated in a broad variety of studies using ratios of regional amplitudes in high-frequency (primarily 1- to 20-Hz) bands (e.g., Walter et al., 1995, Taylor, 1996, Rodgers and Walter, 2002, Taylor et al., 2002 and many others). When similar-sized earthquakes and explosions are nearly collocated, we can understand the observed seismic contrasts, such as the relative P-to-S wave excitation, in terms of depth, material property, focal mechanism, and source time function differences. For example in Figure 1 the top two Nevada Test Site (NTS) traces compare an earthquake and explosion of similar size and location and recorded at a common station. The traces have been high-frequency band passed at 6–8 Hz and show the characteristic discrimination difference, where the explosion has larger P wave (Pn, Pg) amplitudes relative to the S waves (Lg) when compared to the earthquake. However the third trace in Figure 1 shows another earthquake, a Hector Mine aftershock, located about 200 km farther away from the station, and it is clear that the P/S values look much more similar to those of the explosion. In reality the source P and S amplitudes for these earthquakes are nearly identical, but the farther distance the Hector Mine earthquake seismic waves have to travel to the station changes the P/S values, since the attenuation for Lg is stronger than for Pn. Clearly, if we want to discriminate between earthquakes and explosions using regional body-wave ratios, we need to account for such effects.

The availability of reference events, particularly nuclear tests, to compare to a new event in question is highly nonuniform and limited. Therefore, in many monitoring cases, we are comparing events that are not collocated, not the same size, and may have been recorded at different stations. In order to make sure any observed differences between a new event in question and the reference events (or models) are not a result of differences in path or magnitude, we must correct for these effects. In addition in order to optimally combine several different measurements to improve discrimination, we need to remove means and trends from our data. For the past several years, we have been working with our colleagues at Los Alamos National Laboratory (LANL) on the best ways to model and remove magnitude and distance trends from regional amplitudes. Last year we completed a description of the MDAC2[*] (a revised Magnitude and Distance Amplitude Correction) procedure that involved estimating and removing a simple theoretical earthquake spectrum from the data to remove any magnitude and distance trends in the regional phase amplitudes and any discriminants formed from those amplitudes (Walter and Taylor, 2002).

The MDAC2 model uses a more generalized version of the Brune (1970) earthquake source spectrum that allows nonconstant stress drop scaling and differential P/S corner frequency effects. We require the different phases for the same event recorded at the same station to have the same moment and apparent stress (or stress drop) values, and

[*] Subsequent references to calculations by MDAC in this paper were performed with MDAC2.

other source parameters, such as corner frequencies, to be related to each other. While such models of source spectra are certainly oversimplified, they have proven track records of providing good first-order fits to real earthquakes. In addition they also provide simple theoretical models to use in aseismic areas.

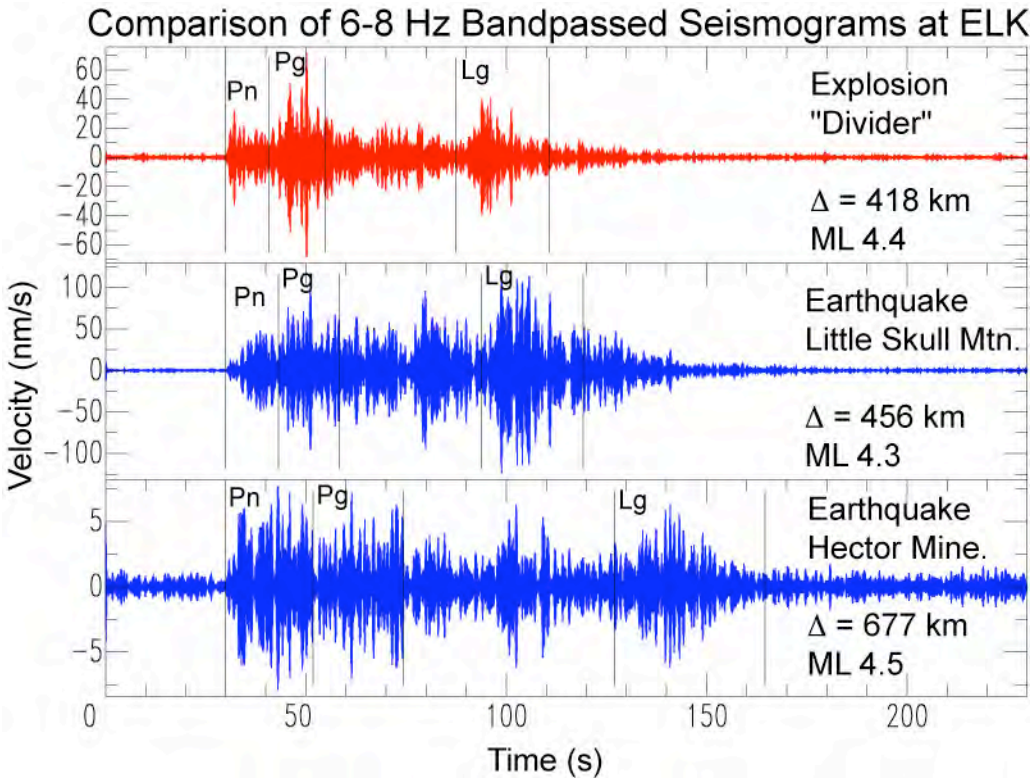


Figure 1. High-frequency (6–8 Hz band pass) seismograms of an explosion (top red) and two earthquakes (middle and bottom, blue) with similar magnitudes at auxiliary station ELK. The top two traces, both from NTS, show relative P-to-S wave amplitude differences that allow discrimination between the two source types. The bottom trace earthquake is located farther away and differential attenuation makes its P/Lg values look more like the explosion.

The details of the MDAC2 formulation are given in Walter and Taylor (2002). The predicted spectrum is a convolution of the generalized source term, geometrical spreading, site, and apparent attenuation terms. We can write the log of the MDAC2 predicted spectrum as (Walter and Taylor, 2002)

$$\log P(f,R) = \log(S_o) - \log\left[1+\left(\frac{w}{w_c}\right)^2\right] + \log G(R) + Site(f) - \frac{pR}{Q_o c} f^{(1-g)} \log(e) \qquad (1)$$

for a regional phase with velocity c. Here S_o is the source low-frequency spectral level and w_c is the source corner frequency. These terms are set by the input moment (we use the stable coda measures, see Mayeda et al, this volume), the apparent stress scaling, and material property terms. Apparent stress, geometrical spreading ($G(R)$), site effect, and attenuation (Q_o, g) terms are typically solved for using a grid search technique that simultaneously minimizes the spectral fit residual and residual magnitude and distance trends. In this way *a priori* information such as previous studies on geometrical spreading or Q-tomography results can be easily incorporated.

In Figure 2 we show a comparison of the observed regional phase spectra (Pn, Pg, and Lg) for some regional earthquakes recorded at station ELK with the model spectra. The calibrated MDAC Q parameters for this path are also given in this figure. For this figure we used an apparent stress scaling of $s \sim M^{0.1}$, which is less than the scaling exponent of 1/4 that we found previously in the Western U.S. (Mayeda and Walter, 1996), but more than the constant stress drop value of zero. In general we find that including some apparent stress scaling improves the

regional spectral fits. The issue of whether earthquake apparent stress really increases with moment and the implications for earthquake physics remains controversial (e.g., Ide and Beroza, 2001). In a separate project, under Lawrence Livermore National Laboratory (LLNL) Laboratory Directed Research and Development (LDRD) funding, we are directly investigating apparent stress scaling using MDAC and regional coda envelope techniques. We expect those results to help the MDAC fitting process for stations in regions with low seismicity.

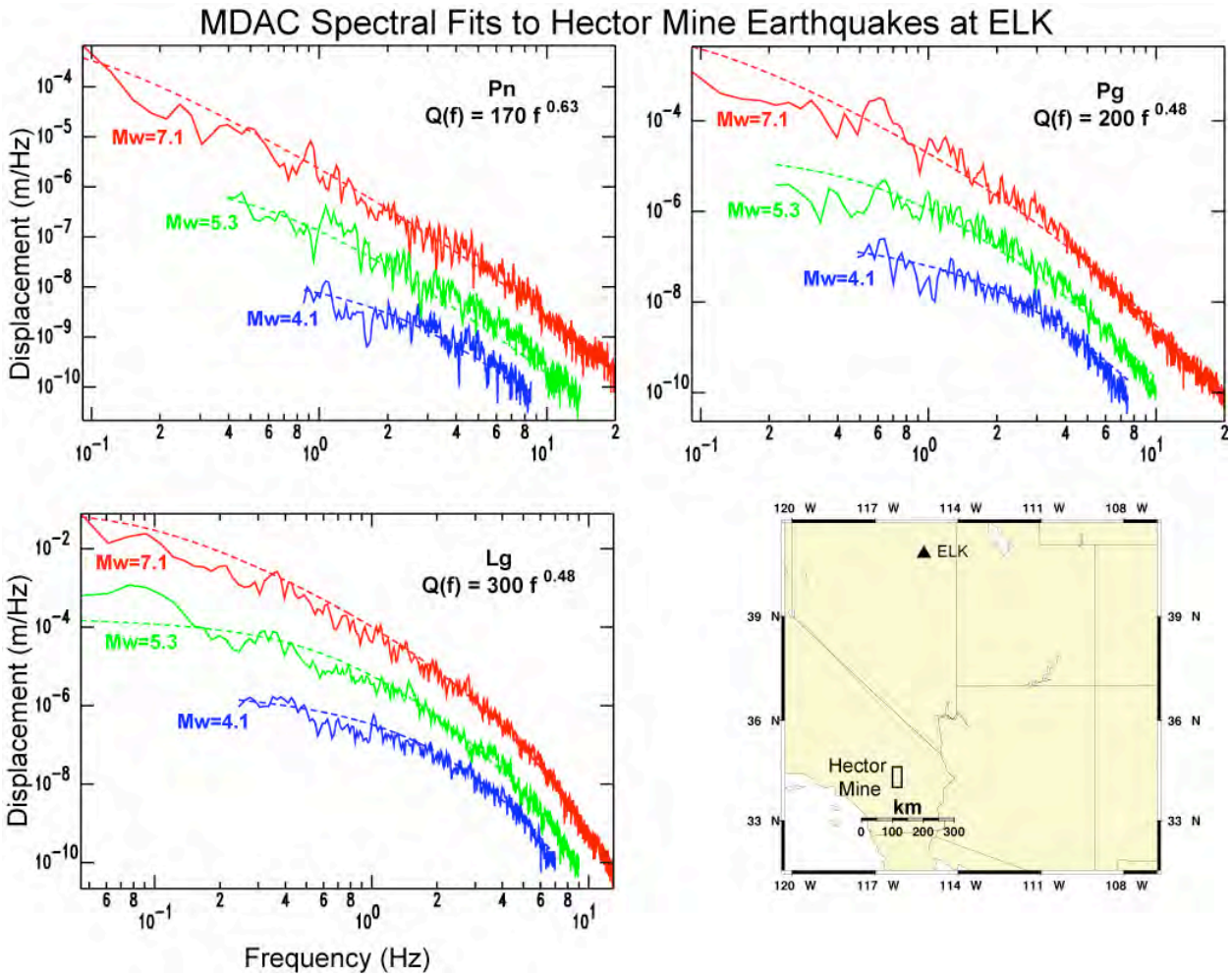


Figure 2. Comparison of the observed (solid) and MDAC2 model (dashed) spectra for the 1999 Hector Mine mainshock and two aftershocks recorded at ELK. Location map at bottom right.

For regional discrimination we can subtract these model spectra to essentially normalize the observations for effects of source, 1-D path and site. However 3-D path effects remain in the residuals. We can further reduce the MDAC2 residual amplitude variance by using the Bayesian kriging method of Schultz et al (1998) on the results. For each phase and frequency band we create kriged residual surfaces. These surfaces can then be used to create any discriminant measurement of choice. For example we can make phase, spectral, and cross-spectral ratio measurements between any phase and frequency combination. In practice it is found that the best discriminant performance comes from combining several different ratio measurements (e.g., Taylor, 1996). The MDAC (and MDAC+kriged) residuals are zero mean and roughly normally distributed, enhancing our ability to create optimized multivariate discriminant combinations using Linear Discriminant Analysis (LDA) or other techniques.

As an example of the power of combining measurements, we show in Figure 3 multivariate results (Sicherman et al., unpublished data) for some ratios at station MNV based on our earlier NTS study (Walter et al, 1995). The metric of performance we use is the equiprobable point, which provides a measure of the overlap of the earthquake and explosion populations. It is the point on an error rate receiver-operator tradeoff curve (ROC) where the error

rates are equal. For example, an equiprobable measure of 0.1 implies that 10% of the earthquakes are misclassified as explosions. In practice one might choose a decision line with unequal error rates, such as by picking a low probability of misclassifying an explosion. The equiprobable point provides a single numerical measure of performance that is much more intuitive than other measures such as Mahalanobis distance, though it can be related to that measure. From this plot we can see that multivariate combinations of measures can provide improvement over the best single measure. Equally important we can see that combining two mediocre measures (6–8 Hz Pg/Lg and 1–2/6-8 Hz Lg Coda) results in a very good discriminant. This result is important because the best single discriminant may not always be available because of phase detectability. In practice one needs to look at phase and frequency combinations with good expected signal-to-noise for the monitored region, and use those to form optimal multivariate discriminants.

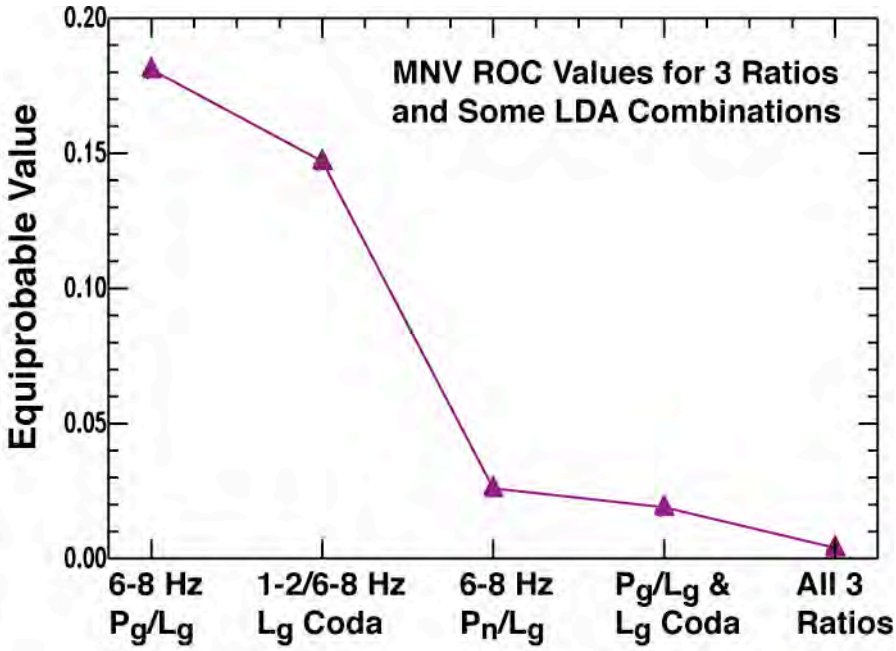


Figure 3. Discriminant performance at MNV for three individual ratio measures and two optimal LDA combinations based on data from Walter et al. (1995).

This issue of phase detectability is often overlooked in regional discrimination studies, but it is of critical importance. A great discriminant measure based on training data that is not detectable for all the magnitude, phase, and frequencies is of limited use. In order to truly evaluate discriminant performance, we need to map out ahead of time the expected signal-to-noise values as a function of magnitude, phase, and frequency. Fortunately the calibrated MDAC curves provide a straightforward means to do this mapping for earthquakes. In Figure 4 we show the expected 6–8 Hz RMS (root mean square) displacement amplitudes for an Mw 4.0 earthquake recorded at station ELK for the calibrated MDAC parameters discussed in Figure 2. For events within approximately 800 km of ELK, the Lg phase has the largest amplitude and beyond this distance, the P phases (Pn and Pg) dominate. We also put an average noise level for ELK on the plot, making it immediately apparent that there will be detectability issues for Lg beyond about 1,000 km and for Pn and Pg beyond about 1,200 km at 6–8 Hz for a Mw 4.0 and smaller earthquakes. If we were interested in using ELK to discriminate such small magnitude events at distances larger than about 1,000 km, then we need to choose different discriminant measures than those shown in Figure 3. In practice the picture is complicated further by 2-D effects, which we have ignored so far. In data rich areas we can use the kriging results to modify the curves by region; in data poor areas we can use Q tomography models. For optimal regional discrimination we calibrate the MDAC parameters for each station and use them both to determine the detectable phases we have to work with and the normalized measures to combine with multivariate techniques.

Finally in Figure 4 we can also easily ratio any of predicted amplitude curves to show the expected behavior of particular discriminant ratios as functions of distance, magnitude, or frequency. Here we show the P/Lg ratios with their strong distance dependence. From the figure we expect about a factor of 2 difference in the P/Lg ratios for the events at 450 km versus 680 km, consistent with what we saw in the data in Figure 1.

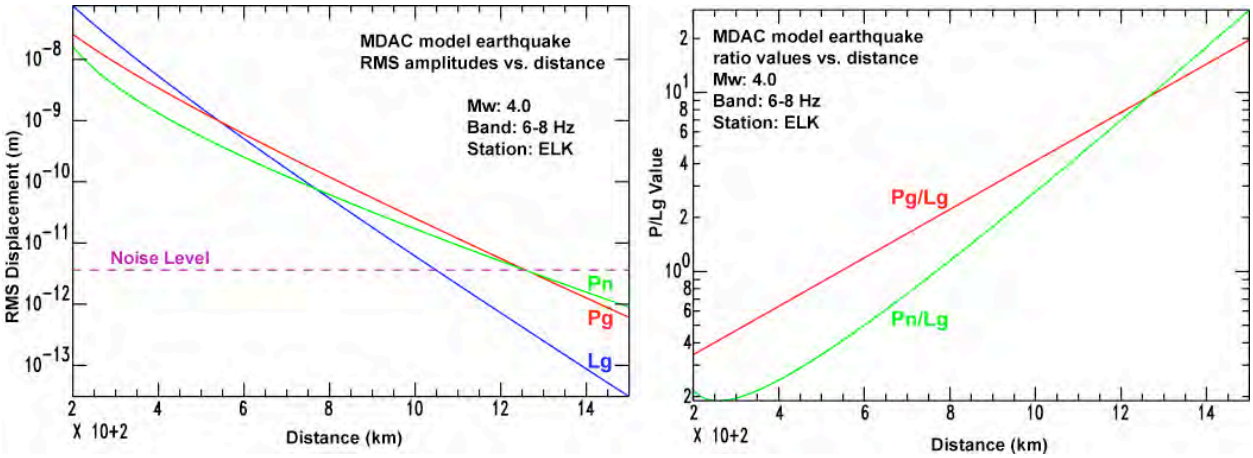


Figure 4. Predicted MDAC earthquake regional phase values as functions of distance from ELK. The calculations are done for an Mw 4.0 event at 6-8 Hz using attenuation parameters from Figure 2. Left-hand side shows RMS amplitude versus distance; right-hand side shows P/Lg ratio values versus distance.

Surface Wave Corrections

The teleseismic magnitude ratio M_S:m_b is one of the best-understood and most effective discriminants known (e.g., Stevens and Day, 1985). Several studies have also shown that it appears to be effective down to as small magnitudes as can be measured regionally (e.g., Denny et al., 1987). The problem is that the 20-second surface-wave amplitude on which M_S is based can be below the noise even at regional distances. We are researching several ways to allow M_S measurements on smaller magnitude events to be made and used to improve discrimination. One way is to allow regional M_S measurements at periods between 10 and 20 s where the regional Airy phase produces the largest amplitudes (e.g., Denny et al., 1987). Additionally we can improve signal-to-noise by making use of phase-match filters (e.g., Herrin and Goforth, 1977). This use of phase-match filters is particularly attractive because in addition to reducing the noise level in the signal, it can provide an accurate maximum M_S estimate even on a very noisy trace. For small explosions that have reduced M_S excitation to start with and may not have observable surface waves, this method can still provide some discrimination power relative to earthquakes of the same m_b that do have measurable M_S.

For the past several years we have been making systematic measurements of Rayleigh and Love wave group velocities in Western Eurasia and North Africa (WENA) with the goal of creating high-resolution tomography models (Pasyanos et al., 2001). We follow the guidelines for measurements laid out in the 1998 surface-wave workshop (Walter and Ritzwoller, 1998), and we have exchanged group velocity curves with other groups. We have incorporated more than 3,000 path measurements from the University of Colorado (Ritzwoller, written communication) and SAIC/Maxwell (Stevens, written communication). We have used the software code PGSWMFA developed by Dr. Charles Ammon to measure thousands of seismograms from the LLNL Seismic Research database (see O'Boyle et al., this volume) over the past several years. The tomography maps that we have created are formed from both our own regional measurements and the broader measurements provided by those two groups. We have also benefited from IRIS (Incorporated Research Institutions in Seismology) PASSCAL (Program for the Array Seismic Studies of the Continental Lithosphere) deployments in Africa and Arabia to supplement the (IMS) International Monitoring System, IRIS Global Seismic Network (GSN) and other open stations.

Overall, in the WENA region we have examined more than 25,000 seismograms and made more than 15,500 Rayleigh wave measurements and 10,000 Love wave measurements at periods from 8–150 seconds. These measurements are an increase of about 5,000 Rayleigh and Love measures each over our tomography models from last year. These numbers apply to the middle period range and the number of good measurements decreases at the

shorter and longer periods. In Figure 5 we show the WENA tomography results for Rayleigh waves at one period, 20 seconds. At this period crustal thickness differences between oceanic and continental crust are clear. Deep sedimentary basins (e.g., Caspian depression, Mesopotamian foredeep) also stand out as very slow areas. For reference we also show the path map with earthquake and station locations. Overall the coverage is quite good, although the lack of stations and seismicity in Western Africa and Northern Russia remains a challenge.

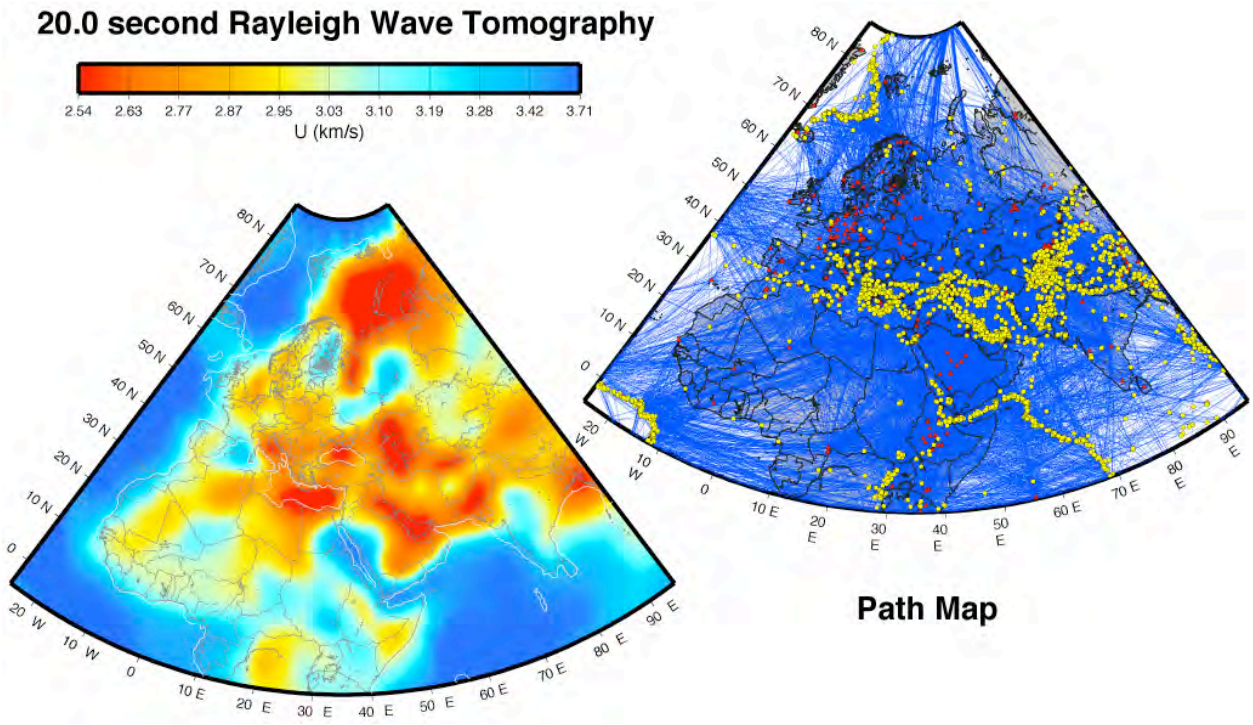


Figure 5. Rayleigh wave group velocity tomography and path map at 20-seconds period for the WENA region.

Last year we demonstrated the improvement provided by phase-match filtering on M_s-m_b in Western Eurasia (Walter et al. 2002). For that test we measured M_s using the formula of Rezapour and Pearce (1998). The maximum likelihood M_s was measured both by traditional band pass filtering and after phase-match filtering using the high-resolution tomography model. We tried a variety of tests in which we varied the signal-to-noise ration (SNR) or number of stations. We found that in almost all cases phase-match filtering improves the M_s-m_b discrimination by approximately a factor of two. We also estimate that phase match filtering is able to lower the M_s detection measurement threshold by roughly 0.3 magnitude units or a factor of two. Both these effects, improved discrimination performance and lower M_s measurement thresholds, indicate that using phase-match filtering for the M_s measurement can significantly improve discrimination performance.

Recently we have started making surface-wave dispersion measurements in the Yellow Sea—Korean Peninsula (YSKP) area in order to make a high-resolution tomography model for that region as well. Again we have greatly benefited from IRIS PASSCAL deployments in China and North Korea, as well as from the South Korean regional seismic network data (B. Herrmann, written communication). So far we have examined about 6,500 seismograms and made 5,000 Rayleigh wave measurements. In Figure 6 we show the group-velocity tomography results and the path map for 20-second period Rayleigh waves. We have used a new variable-grid smoothing algorithm in this result. As in the WENA tomography, the oceanic regions of the Sea of Japan and the Pacific show up as relatively fast velocities. Again deep sedimentary basis such as the Bohai in the northwest part of the Yellow Sea are slow. However path coverage remains poor outside of the Yellow Sea, Korean Peninsula and Sea of Japan. As we continue to make measurements, we expect to be able to combine these two separate tomographies into a single

large-scale tomography of Eurasia and Africa that will provide very good coverage of nearly the entire continental region.

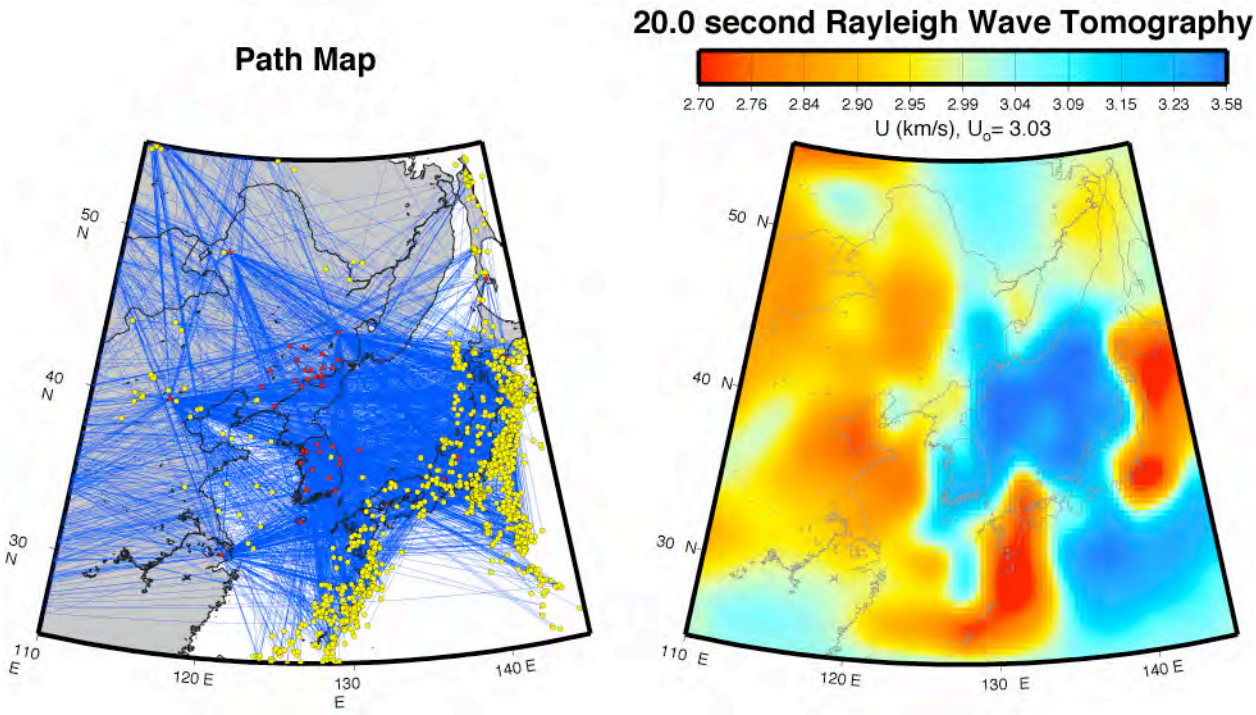


Figure 6. Rayleigh wave path map and group velocity tomography map at 20 seconds period for the YSKP region.

Finally the surface wave tomographies shown in Figures 5 and 6 provide information about the underlying velocity structure that may prove useful for location calibration, particularly in aseismic regions. We have used the WENA tomography to test an LLNL *a priori* model (see Pasyanos et al., this volume). We are currently using the surface wave tomography model in conjunction with receiver functions to estimate velocity structure in Western Eurasia (see Ammon et al., this volume) and the YSKP region with Dr. Bob Herrmann.

CONCLUSIONS AND RECOMMENDATIONS

Regional discrimination algorithms require calibration at each seismic station to be used for nuclear explosion monitoring. We have developed a revised Magnitude and Distance Amplitude Correction procedure to remove source size and path effects from regional body-wave phases. This procedure allows the comparison of any new regional events recorded at a calibrated station with all available reference data and models. It also facilitates the combination of individual measures to form multivariate discriminants that can have significantly better performance. We have also developed surface-wave group velocity maps and correction surfaces for phase-match filtering to improve Ms-mb discrimination and lower its effective threshold. Calibrating seismic stations to monitor for nuclear testing is a challenging task that will require processing large amounts of data, and collaboration with government, academic and industry researchers and incorporation of the extensive R&D results both within and outside of NNSA.

ACKNOWLEDGEMENTS

We thank Steve Taylor at LANL for many discussions on the topics of MDAC and regional discrimination. We thank Mike Ritzwoller and Jeff Stevens for generously sharing their group velocity measures. We thank Maggie

Benoit for making many new East Africa dispersion measurements this summer. We thank the many scientists for their efforts in providing open station data from PASSCAL, GSN and IMS, and other networks.

REFERENCES

Brune, J. N. (1970). Tectonic stress and seismic shear waves from earthquakes , *J. Geophys. Res.* **75**, 4997-5009.

Denny, M. D., S. R. Taylor, and E. S. Vergino (1987). Investigation of mb and Ms formulas for the western United States and their impact on the Ms/mb discriminant, *Bull. Seism. Soc. Am., 77*, 987-995.

Herrin, E. and T. Goforth (1977). Phase-matched filters: Applications to the study of Rayleigh waves, *Bull. Seism. Soc. Amer., 67*, 1259-1275.

Ide, S. and G. C. Beroza (2001). Does apparent stress vary with earthquake size?, *Geophys. Res. Lett.* **28**, 3349-3352.

Mayeda, K. M. and W. R. Walter, (1996). Moment, energy, stress drop and source spectra of Western U.S. earthquakes from regional coda envelopes, *J. Geophys. Res*., **10***1*, 11,195-11,208.

Pasyanos, M. E., W. R. Walter and S. E. Hazler (2001). A surface wave dispersion study of the Middle East and North Africa for monitoring the comprehensive nuclear-test-ban treaty, *Pure. Appl. Geophys*., 158, 1145-1474.

Rezapour, M. and R. G. Pearce (1998). Bias in surface wave magnitude Ms due to inadequate distance corrections, Bull. Seism. Soc. Am., 88, 43-61.

Rodgers, A. J. and W. R. Walter, (2002). Seismic Discrimination of the May 11, 1998 Indian Nuclear Test with Short-Period Regional Data From Station NIL (Nilore, Pakistan), *Pure Appl. Geophys.* 159, 679-700.

Schultz, C, S. Myers, J. Hipp, and C. Young (1998). Nonstationary Bayesian kriging: a predictive technique to generate corrections for detection, location and discrimination, *Bull. Seism. Soc. Am., 88* 1275-1288.

Stevens, J. L. and S. M. Day (1985). The physical basis of mb:Ms and variable frequency magnitude methods for earthquakes and explosion discrimination, *J. Geophys. Res., 90*, 3009-3020.

Taylor, S., (1996). Analysis of high-frequency Pg/Lg ratios from NTS explosions and Western U.S. earthquakes, *Bull. Seism. Soc. Am., 86*, 1042-1053.

Taylor, S., A. Velasco, H. Hartse, W. S. Philips, W. R. Walter, and A. Rodgers, (2002). Amplitude corrections for regional discrimination, *Pure. App. Geophys.* 159, 623-650.

Walter, W. R., K. Mayeda, and H. J. Patton, (1995). Phase and spectral ratio discrimination between NTS earthquakes and explosions Part 1: Empirical observations, *Bull. Seism. Soc. Am.*, **85**., 1050-1067.

Walter, W. R. and M. Ritzwoller, (1998). Summary report of the workshop on the U.S. use of surface waves for monitoring the CTBT, Lawrence Livermore National Laboratory *UCRL-ID-131835*, 16 pp.

Walter, W. R. and S. R. Taylor (2002), A revised Magnitude and Distance Amplitude Correction (MDAC2) procedure for regional seismic discriminants, Lawrence Livermore National Laboratory *UCRL-ID-146882.*

Walter, W. A. Rodgers, M. Pasyanos, K. Mayeda, and A. Sichermann, (2002). "Identification in western Eurasia: Regional body-wave corrections and surface-wave tomography models to improve discrimination," in "Proceedings of the 24th Seismic Research Review: Nuclear Explosion Monitoring: Innovation and Integration," Los Alamos National Laboratory, *LA-UR-02-5048.*

NETWORK INSTALLATION IN THE YANQING-HUAILAI BASIN AND PRELIMINARY STUDY OF NATURAL AND MAN-INDUCED EVENTS

Rong-Mao Zhou,[1] Brian W. Stump,[1] Yun-Tai Chen,[2] Christopher T. Hayward,[1] Zhi-Xian Yang,[2]
Mary Templeton,[3] Xiang-Wei Yu, [2] Shi-Yu Bai, [2] and Xiang-Tong Xu[2]

Southern Methodist University; [1] Institute of Geophysics; [2] IRIS-Passcal Instrument Center[3]

Sponsored by Air Force Research Laboratory

Contract No. DTRA01-02-C-0003

ABSTRACT

Southern Methodist University and the Institute of Geophysics of the China Seismological Bureau are carrying out "a comparative study of natural and man-induced seismicity in the Yanqing-Huailai basin and the Haicheng area". The geographic focus of this investigation is in the Yanqing-Huailai Basin, 120 km northwest of Beijing. Within the Yanqing-Huailai Basin, earthquake risk and propagation path assessments are important because of the basin's historical seismicity and Beijing's large population. Numerous underground mines in the region regularly experience rock bursts and collapses resulting in the disruption of mining operations, injury and occasionally death. The objectives of this project are to develop a dataset of near-source and regional waveforms that may be used to study natural and man-induced seismicity as well as regional wave propagation and source characterization constraints. The instrumentation deployed consists of four stations around and within the basin for source location and characterization, four stations at near-regional and seven stations at regional distances. IRIS (Incorporated Research Institutes for Seismology) PASSCAL Seismological Instrumentation Center provided STS-2 broadband seismometers and the new Quanterra Q330 digitizer and PB14 Baler recording systems. Each station includes two hand-dug vaults in hard rock; one for the STS-2 seismometer and one for the Quanterra system, power supply, and batteries. In the fall of 2002, five stations were deployed in and around the basin followed in the spring of 2003 by eight stations at regional distances. Two additional stations are planned in the summer of 2003. The data from the first five stations has been collected and exchanged between SMU and IGCSB. Local network bulletins for the Huailai Basin and the adjoining region indicates that this area has had active seismicity since installation. Two mine blasts at close distance, a regional event from a 1.3-kiloton mine explosion, and a teleseismic event from southwest Alaska are used to illustrate data quality.

OBJECTIVES

The goals of this collaborative study between Southern Methodist University (SMU) and the Institute of Geophysics, China Seismological Bureau (IGCSB) are to develop an earthquake and man-induced event database to refine event locations in Yanqing-Huailai Basin, to understand source characterization of natural and man-induced events, and to separate source and propagation path effects at regional distances. These goals contribute to earthquake risk assessments and mine safety issues, and this synergy motivated the collaborative empirical study (Stump et al., 2002). The region of focus is the Yanqing-Huailai Basin near Beijing.

The purpose of this experimental study is to compare natural and man-induced seismicity in the Yanqing-Huailai Basin, NW of Beijing (Figure 1). It is a region of historical natural and man-induced seismicity as well as a seismic hazard for Beijing. A broadband seismic network has been designed to provide near-source and regional coverage. Four seismic stations have been installed in the immediate vicinity of the basin (XJYAO, BAKOU, AYPU, and CJPU). Four near-regional stations surround the basin (ZSPO, YFANG, MJPU, and IGCSB). The seven additional stations are at regional distances. The first five stations were installed in Nov. 2002. Seismic events (dots) for the time period 20 Nov. 2002 through 05 May 2003 are superimposed on the map and illustrate the activity in this region. Triangle denotes the station that will be installed in the summer of 2003.

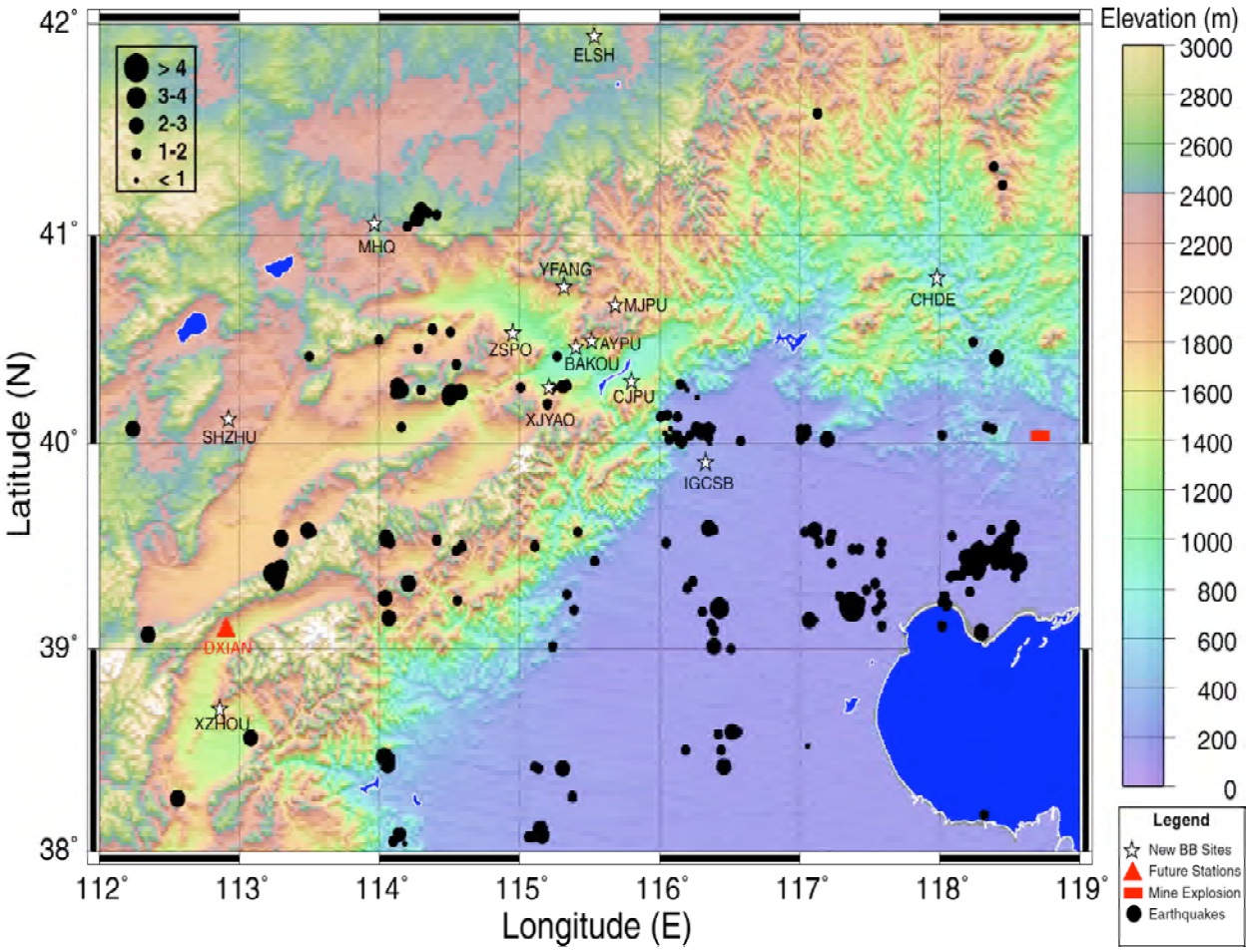


Figure 1. Topographic map of study area with the geographic distribution of 13 broadband seismic stations (stars) superimposed with regional seismicity (dots, magnitude 0.4 to 4.3) for time period of 20 Nov. 2002 and 5 May 2003. The triangle is the station that will be installed and the rectangle is location of the mine explosion used to illustrate data quality.

RESEARCH ACCOMPLISHED

Station Instrumentation, Design and Installation

Station Instrumentation

A joint SMU/IGCSB/IRIS team designed the station vaults, tested the new equipment (Summer 2002), and did the initial station installation in November 2002. IRIS PASSCAL provided STS-2 seismometers, Quanterra Q330 data acquisition systems, and Quanterra PB14 Packet Balers for this experiment (Figure 2). This is the first field deployment of these systems. The Quanterra Q330 includes ultra-low-power delta-sigma 24-bit A/D with DSP, 8 Mb RAM, a GPS receiver, power management, sensor control, and telemetry management. As a data recording system, Quanterra PB14 Packet Baler stores up to 20 Gb of data in miniSEED format.



Figure 2. STS-2's, Quanterra 330's and Baler PB14's during huddle test in Beijing, China.

Station Design and Installation

The seismic vaults were designed to house both the seismometer and data acquisition equipment. The vault was designed to reduce tilts at long periods, to provide temperature stabilization, and to isolate the equipment from water, dust, and dirt. Each installation consisted of two hand-dug 1-m ¥ 1-m ¥ 1-m vaults; one for the seismometer and one for the data acquisition system (Figure 3 and 4). The vaults were all in hard rock and were connected by a conduit for cabling. The seismometer was covered with a 10-cm-thick foam box for additional temperature stabilization. Figure 3 documents the installation at AYPU. Figure 4 is the overview of the XJYAO and BAKOU stations.



Figure 3. Left: Vault for STS-2 (upper) and Quanterra (Lower); Right: The installation team at work at AYPU



Figure 4. Overview of BAKOU (Left) and XJYAO (Right) station including two vaults for STS-2 and Quanterra system, solar panel for power supply.

Data is archived locally at each site. Periodic visits to the sites provide the opportunity to retrieve the data where it is stored on a Sun Ultra 10 at IGCSB; Beijing. Data is transferred to SMU by ftp and disk exchange.

Data

Local, regional, and teleseismic signals recorded by the first five stations illustrate the operation of the new network and instruments. These examples include a range of natural and man-induced events.

Local Events

Around the Yanqing-Huailai basin, frequent industrial explosions and rock bursts occur in numerous above and underground mines. Figure 5 is an example of two events separated by 37 seconds, and both were identified as mining explosions. Figure 6 is the superposition of the two seismograms at BAKOU from the two repeated events and their nearly identical spectra. Although the nearly identical waveforms indicate a common location and source, the spectra show a slight size difference between events. These events from the same location are well recorded by our network and occur approximately once a day. The signal-to-noise ratio is a factor of 100 from 1–20 Hz. The good signal-to-noise ratio from these repeated events will help us to understand the source and local propagation path characteristics over a broad frequency range. This example illustrates the high frequency response of the STS-2 and Quanterra recording system.

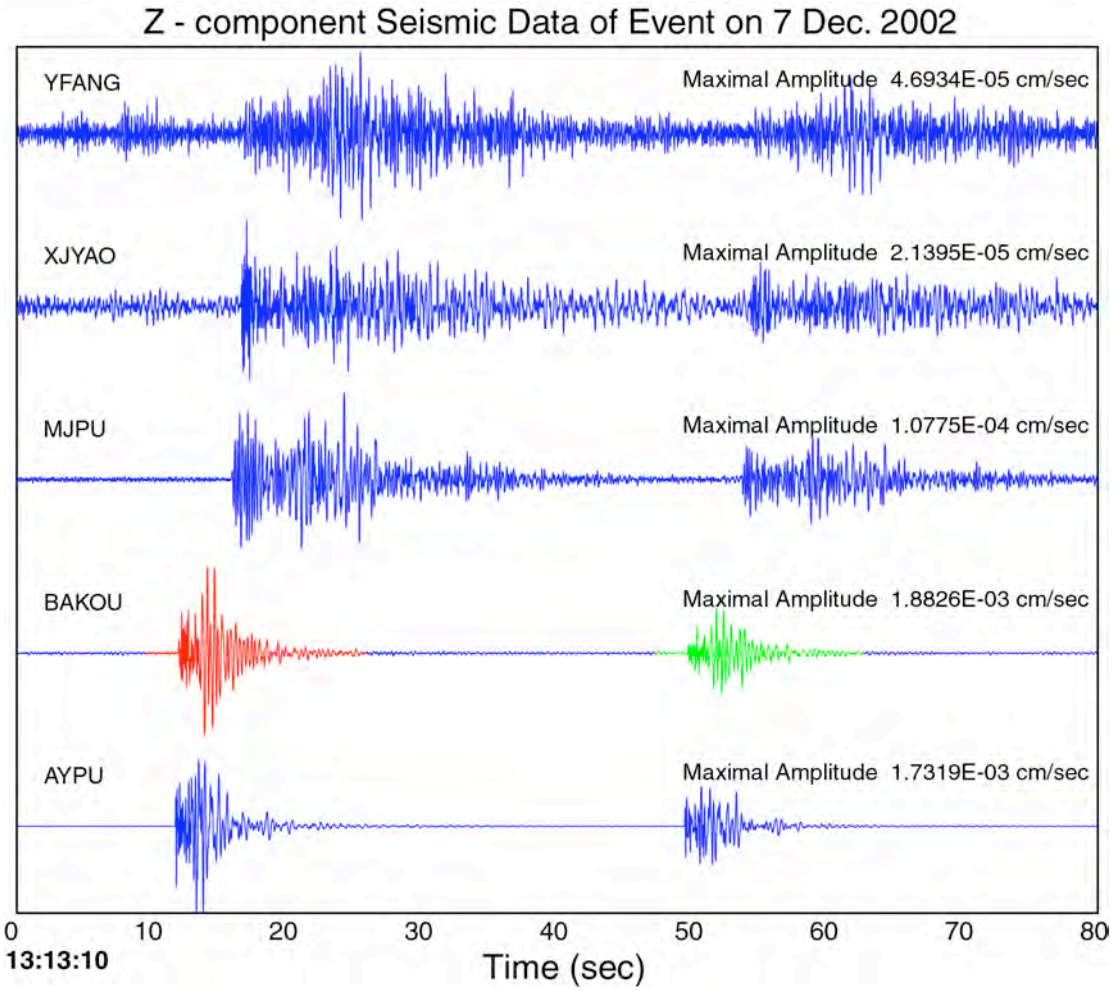


Figure 5. Z-component seismograms from the mining explosions.

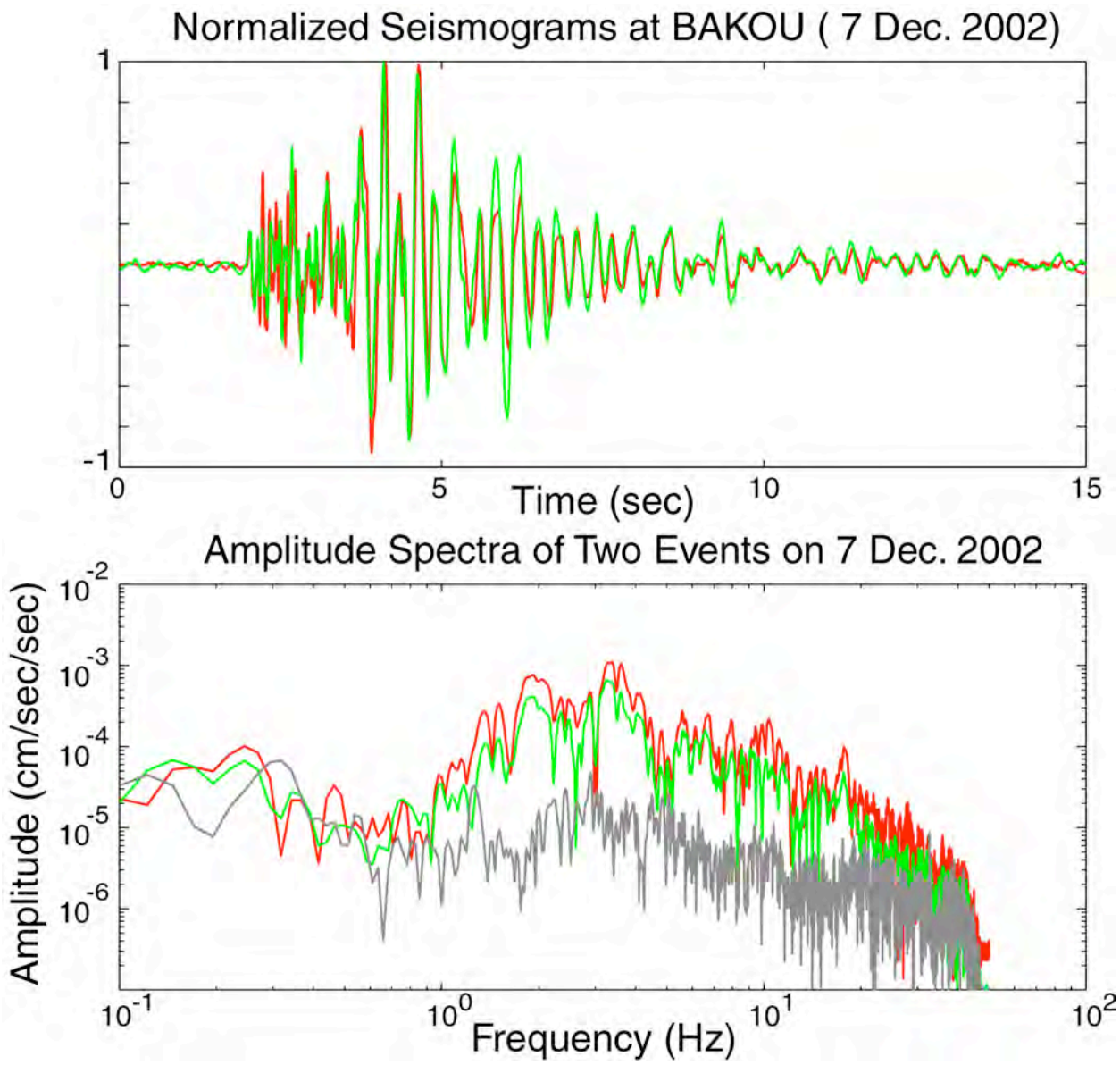


Figure 6. Upper: superposition of two events recorded at station BAKOU. Lower: spectra of two events (red and green) and noise (gray).

Regional Event

Eastday reported (*http://news.eastday.com/epublish/gb/paper148/20021230/class014800003/hwz854971.htm*) a 1.3-KT yield explosion (Figure 7, upper) fired on 29 Dec. 2002, at an iron mine in QianAn (the largest open-pit iron mine in Asia from *http://www.qian-an.gov.cn/qasgk/dlhj.htm*), 270 km southeast of Huailai Basin (red rectangle in Figure 1). This explosion is the largest engineering explosion in China for the last decade. The duration of the pattern was reported to be 1.3 seconds. The USGS NEIC reported the magnitude of m_b 3.5. The seismograms at four stations from our network are reproduced in Figure 7 (lower). XJYAO had an outage for this event. The signals are rich in high-frequency body waves and intermediate-period surface waves. The bandpass filtered data (Figure 8) quantifies the frequency characteristics of the P wave, Lg wave, and surface wave.



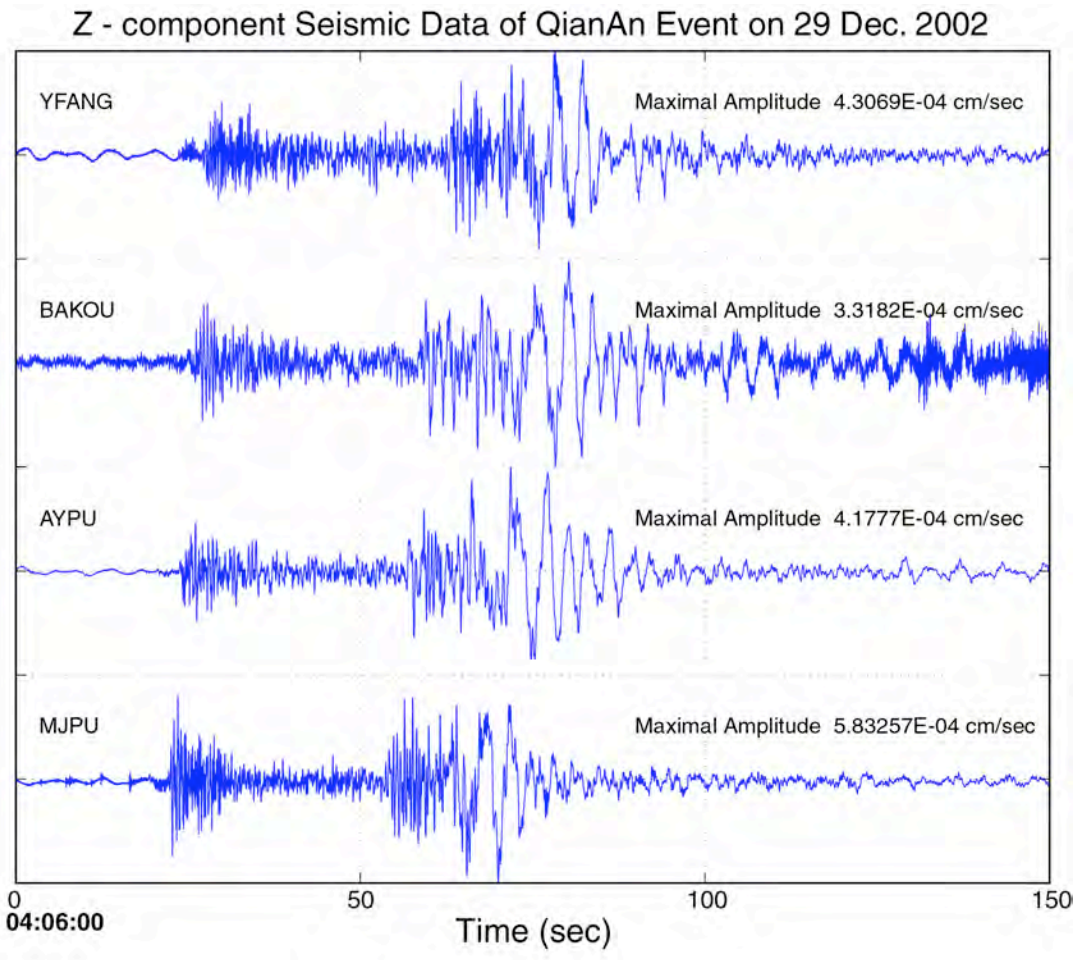


Figure 7. Top: Photo from media showing the explosion on 29 Dec. 2002. Bottom: Seismograms from the explosion at four stations

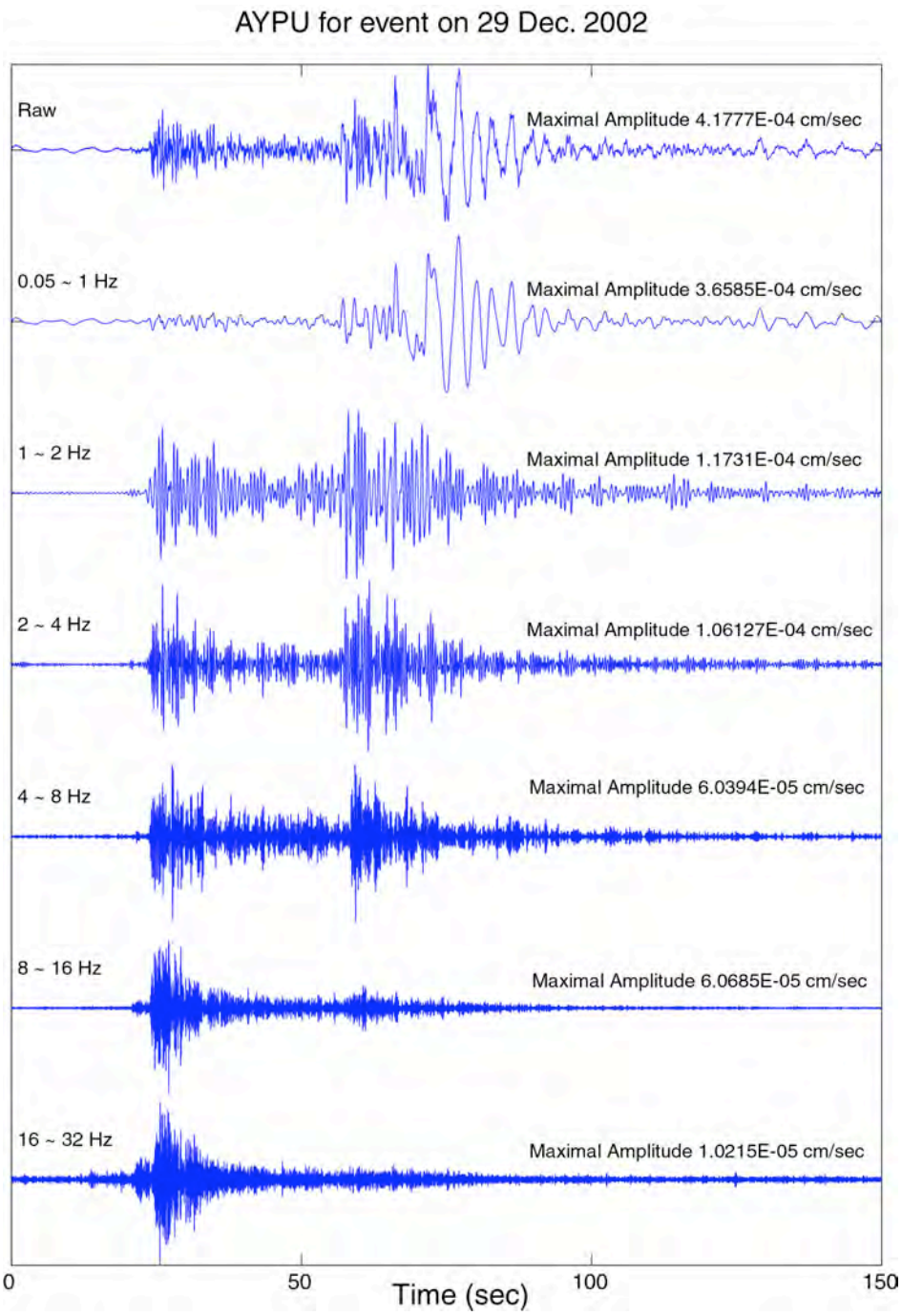


Figure 8. Spectral composition of QianAn event on 29 Dec. 2002 recorded at AYPU.

Teleseismic Event

A magnitude 5.9 earthquake at 51.465°N, 173.537°W, southwest of Alaska, on 26 Nov. 2002 (USGS NEIC), was the first large earthquake recorded by our network. The epicentral distance to the network was about 48 degrees, and the seismograms are displayed in Figure 9. The signal-to-noise ratio for the P-wave and surface-wave at AYPU are presented in Figure 10. The signal (red) to noise (gray) ratios are a factor of 100 over the period range of 1–30 sec and 10–100 sec for P-wave (Figure 10, upper) and surface-wave (Figure 10, lower), respectively.

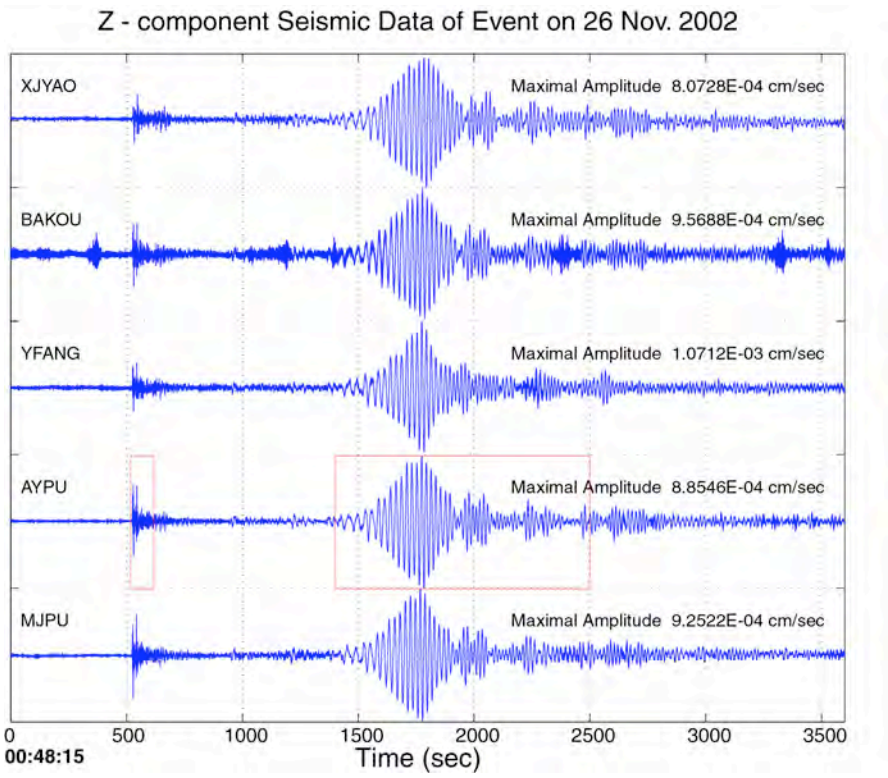


Figure 9. Seismograms from a teleseismic event occurred at southwest of Alaska on 26 Nov. 2002 with a magnitude 5.9.

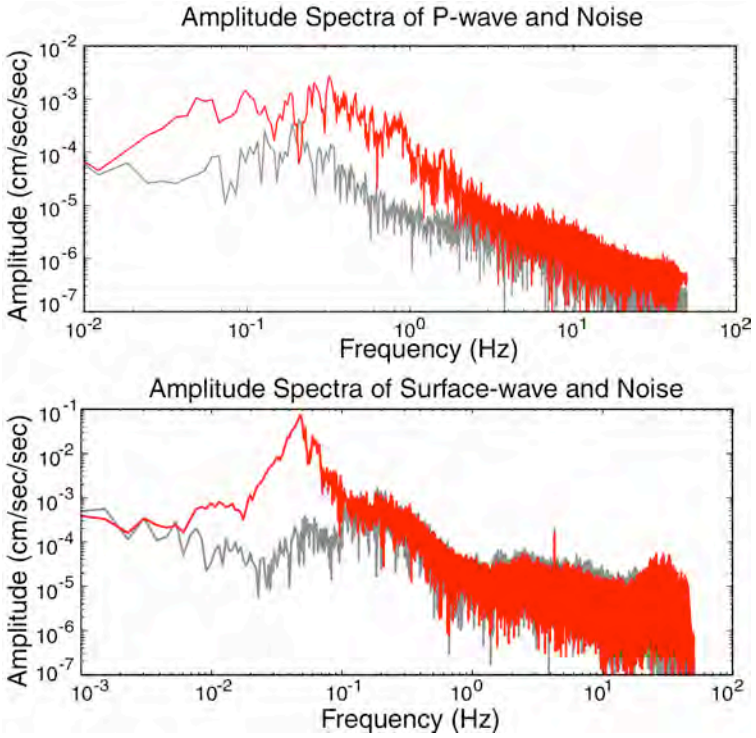


Figure 10. Top: Signal-to-noise ratio for P-wave (red: signal; gray: noise) Bottom: Signal-to-noise ratio for surface wave (red: signal; gray: noise)

CONCLUSIONS AND RECOMMENDATIONS

As the first field deployment of Quanterra system, the initial operation has highlighted several problems. During testing at SMU and prior to installation, data in the Baler could not be displayed and downloaded completely. A software update solved the problem. The Baler has had some outages at stations YFANG and XJYAO. We will change the cable connecting Quanterra Q330 and Baler and test at IGCSB. The outbreak of SARS in Beijing has slowed the deployment.

We will complete the installation of two final stations during the summer of 2003. The data, which is recorded in miniSEED format, will be converted into SEED format. Using the data collected by our network, we will begin locating earthquakes in the Huailai Basin and develop propagation effects for the basin, as well as model waveforms for source characterization. The assessment of intermediate-period surface waves from regional events such as that illustrated in Figure 7 will be used to constrain the crustal structure in the study area.

ACKNOWLEDGEMENTS

This work could not have been done without help from the Huailai Seismic Station, Hebei Province, China. Particularly, we acknowledge the contributions of Director Hai-xiao Li and Mr. Chang-hui Zhang.

REFERENCE

Stump, B., C. Hayward and R. -M. Zhou (2002). A comparative study of natural and man-induced seismicity in the Yanqing-Huailai basin and the Haicheng area, *24th Seismic Research Review—Nuclear Explosion Monitoring: Innovation and Integration*, 192-199.

Proceedings of the
25th Seismic Research Review --
Nuclear Explosion Monitoring:
Building the Knowledge Base

September 23-25, 2003

Tucson, Arizona

Volume II

Hydroacoustic Monitoring
Radionuclide Monitoring
Infrasound Monitoring
Data Processing and Analysis

Approved for Public Release; further dissemination unlimited.

National Nuclear Security Administration

LA-UR-03-6029

Proceedings of the 25th Seismic Research Review -- Nuclear Explosion Monitoring:
Building the Knowledge Base

To view these Proceedings online, visit
https://www.nemre.nnsa.doe.gov/review2003.

Vol. II

Table of Contents - Volume II

5. Hydroacoustic Monitoring 515

5-01 **Blackman, D., J. Mercer, R. Andrew, C. de Groot-Hedlin, and P. Harben**
Indian Ocean Calibration Tests: Cape Town-Cocos Keeling 2003 517

5-02 **Harben, P., E. Matzel, Z. Upton, and J. Pulli**
Hydroacoustic Blockage Calibration for Discrimination 524

6. Radionuclide Monitoring 531

6-01 **Ely, J., C. Aalseth, J. Hayes, T. Heimbigner, J. McIntyre, H. Miley, M. Panisko, and M. Ripplinger**
Novel Beta-Gamma Coincidence Measurements Using Phoswich Detectors 533

6-02 **Foltz Biegalski, K. and S. Biegalski**
Deconvolution of Three-Dimensional Beta-Gamma Coincidence Spectra from Xenon Sampling and Measurement Units 542

6-03 **Penn, D.**
Status of the United States International Monitoring System Radionuclide Monitoring Stations 552

6-04 **Rynes, J., D. Robbins, and M. Erickson**
Radionuclide Software Installation at the United States National Data Center 568

7. Infrasound Monitoring 575

7-01 **Bass, H., M. Garces, M. Hedlin, G. D'Spain, J. Olson, C. Wilson, D. Osborne, G. Herrin, P. Golden, R. Whitaker, D. Revelle, and J. Bhattacharyya**
Infrasound Monitoring of Atmospheric Events 577

7-02 **Bhattacharyya, J., H. Bass, D. Drob, R. Whitaker, D. Revelle, and T. Sandoval**
Description and Analysis of Infrasound and Seismic Signals Recorded from the Watusi Explosive Experiment, September 2002 587

7-03 **Chael, E. and R. Whitaker**
Infrasound Signal Library 597

7-04 **Drob, D.**
Detailed Specifications of the Atmosphere for Infrasound Propagation Modeling 605

7-05 **Garces, M. and C. Hetzer**
Optimizing the Progressive Multi-Channel Correlation Detector for the Discrimination of Infrasonic Sources 617

7-06 **Garces, M., C. Hetzer, M. Willis, and S. Businger**
Integration of Infrasonic Models with Ocean Wave Spectra and Atmospheric Specifications to Produce Global Estimates of Microbarom Signal Levels 628

7-07 **Gibson, R. and D. Norris**
Integration of Inframap with Near-Real-Time Atmospheric Characterizations and Applications to Infrasound Modeling 638

7-08 **Whitaker, R., T. Sandoval, and J. Mutschlecner**
Recent Infrasound Analysis 646

8. Data Processing and Analysis

655

8-01 **Aguilar-Chang, J. and M. Begnaud**
Data Warehouses in Support of Nuclear Explosion Monitoring Research 657

8-02 **Bowman, J., R. Cordova, W. Fox, and D. Lovell**
Wide Area Testing of CD-1.1 Reliable Multicasting 664

8-03 **Carr, D., J. Harris, L. Wilkening, C. Young, M. Chown, B. Merchant, and J. Hipp**
Assembling the Knowledge Base 671

8-04 **Hipp, J., R. Simons, and L. Jensen**
The 2003 Parametric Grid Software Suite for Ground-Based Nuclear Explosion Monitoring Research & Engineering 681

8-05 **Kromer, R., J. Harris, and T. Townsend**
Gurlap Seismic Instrumentation Component Evaluation 691

8-06 **Kvaerna, T., E. Hicks, J. Schweitzer, and F. Ringdal**
Regional Seismic Threshold Monitoring 701

8-07 **Langston, C., C. Chiu, I. Rabak, and D. Kang**
The Central Asia Regional Waveform Analysis Knowledge Base 712

8-08 **Merchant, B., E. Chael, and C. Young**
MatSeis and the GNEM R&E Regional Seismic Analysis Tools 721

8-09 **O'Boyle, J., S. Ruppert, T. Hauk, D. Dodge, M. Ganzberger, and F. Ryall**
Middle East, North Africa and Western Eurasia Seismic Research Database 729

8-10 **Rivers, W., R. Wagner, E. Siu, J. Chen, C. Schultz, D. Dodge, and G. Pope**
Efficient Integration of Old and New Research Tools for Automating the Identification and Analysis of Seismic Reference Events 738

Hydroacoustic Monitoring

INDIAN OCEAN CALIBRATION TESTS: CAPE TOWN-COCOS KEELING 2003

Donna K. Blackman,[1] James A. Mercer,[2] Rex Andrew,[2] Catherine D. de Groot-Hedlin,[1] and Philip E. Harben[3]

University of California at San Diego, (Scripps/IGPP);[1] University of Washington;[2]
Lawrence Livermore National Laboratory[3]

Sponsored by National Nuclear Security Administration
Office of Nonproliferation Research and Engineering
Office of Defense Nuclear Nonproliferation

Contract No. DE-FC03-01SF22356[1,2] and W-7405-ENG-48[3]

ABSTRACT

A series of hydroacoustic calibration shots were conducted in the Indian Ocean during a research cruise in May/June, 2003. The shots were distributed along an approximate great-circle track from the southern tip of South Africa to Cocos Keeling Island, in the northeast Indian Ocean. The acoustic signals propagated basin-wide in several cases and were recorded at the International Monitoring System (IMS) hydrophone stations off Isles Crozet, Diego Garcia, and Cape Leeuwin. Two-pound Signals, Underwater Sound (SUS) charges were fired at depths of ~600 m and ~900 m and imploding glass spheres were triggered at ~700 m water depth. Single-sphere glass imploders and 5-sphere imploders were each deployed at four stations. Often, both SUS and glass spheres were deployed at the same location so that a comparison of the signals received at each IMS hydrophone station could be made for a constant source-receiver path. The attenuation along most of each path is quite low as the signal travels within the oceanic sound channel. However, a number of shallow bathymetric features that protrude up into the channel do cause significant signal loss: Walters Shoal, the ridges where plate spreading is centered, the Ninety East Ridge, and the slope around Cocos-Keeling Island. The nature of the signal attenuation due to interaction with the seafloor varies, as expected, with the character of a given bathymetric feature and with the depth of the source in the sound channel. We analyze such effects in terms of variations in frequency content of the recorded signals as well as shifts in the position of peak amplitude within the wavetrain. Initial processing to assess the accuracy with which our small sources can be located using IMS recordings indicates that azimuth estimates can be within 2° in many cases. Thus far, we have only worked with the Diego Garcia and Cape Leeuwin data. Complete determination of IMS location capabilities for small sources in the Indian Ocean awaits the availability of data from Crozet.

OBJECTIVE

The hydrophone stations that comprise the International Monitoring System (IMS) within the Indian Ocean basin have recently become fully operational. The completion of stations off Crozet (H04) in early 2003 makes it possible to document the event detection and location capabilities of the full system using small man-made sources with well-known origin time and location. The present study builds on the results from a similar cruise undertaken in 2001 where a large airgun array and several glass sphere shots were recorded at Diego Garcia (H08) and Cape Leeuwin (H01). The intent of our work during the 2003 R/V Melville cruise was to test additional types of calibration sources, to test source-receiver paths from a different ship track than had been followed in 2001, and to provide some of the first well known signals for assessment of performance at the Crozet hydrophones. By firing each source within the sound channel, long-distance propagation was achieved. However, regions of shallow seafloor within the basin resulted in variable signal loss. Since each source-receiver paths were characterized by distinct bathymetry, the amount of interaction with the seafloor ranged from paths that were completely unblocked, to paths containing some features that caused diffraction and some attenuation, to paths with total blockage for one or both arms of a station. One goal of this study is to document regions within the Indian Ocean basin that result in more (or less) attenuation or blockage than is expected based on typically employed elevation and propagation models.

RESEARCH ACCOMPLISHED

The three source types that were planned for the 2003 Melville experiment were an electroacoustic projector system, imploding glass spheres, and small explosive depth charges. The receivers were permanently installed hydrophones that are part of the International Monitoring System that is overseen by the Comprehensive Nuclear-Test-Ban Treaty Organization (CTBTO) of the United Nations. During the cruise, source information was sent to colleagues onshore and at the CTBTO and they checked the IMS data and reported detections, or lack thereof, back to the ship via emails. At the time of this report, we have begun systematic analysis of the Diego Garcia and Cape Leeuwin data. Initial findings are discussed below. Data from Crozet is still in a test phase due to the very recent installation of that station. We are in the process of working with the CTBTO to determine whether access to those data will be granted for short time periods on either side of our calibration shots. For the September 2003, meeting we expect to report the results based on a more detailed analysis.

Source Information

The SUS charges used were model MK94 with 1.8 lb explosive. For our experiment, the shear disks that triggered detonation were set to 610 m (2000 feet) or 915 m (3000 feet). At these detonation depths, the peak energy density of the source is at about 100 Hz at a level of about 270 dB, re 1mPa at 1-meter range (Urick, 1967). Scott Jenkins, Indian Head Division, US Navy, oversaw the manufacture and deployment of the SUS. Twelve each of the 610 m and 915 m charges were used. The time required for the charges to sink after deployment was ~2 minutes for 610 m charges and ~3 minutes for 915 m charges. The ship held position during this time so the Global Positioning Satellite (GPS) fix is a valid source location, accurate to within 10 m.

Two versions of the Lawrence Livermore National Laboratory (LLNL) imploding glass sphere system were used — a single-sphere device and a 5-sphere device (Harben *et al*., 2000; 2001). The single sphere device uses a 22-liter glass sphere and a piston driven smashing system that causes sphere failure at a pre-determined depth through failure of a ruptured disk. The 5-sphere device uses the same piston driven smashing system as the 1-sphere device. The remaining 4 spheres fail as a direct result of the first one. The spheres imploded quite reliably although there was some variation in the depth (690-731 m) at which the discs ruptured. Prior near-source recordings indicate that the peak output (250-270 dB re mPa at 1 meter range) of the imploding spheres was in the 300-500 Hz band, however several shots recorded at the IMS hydroacoustic stations in 2001 showed that signal-to-noise ratio (SNR) of the arrivals is sufficient for it to be seen above the noise at 40-125 Hz (Blackman *et al*., 2003). As for the SUS deployments, ship GPS fixes were used to determine the location of each glass sphere implosion since the instruments were lowered on a winch line while the ship held position.

Our intent was to operate the University of Washington, Applied Physics Lab (APL) electroacoustic projector system at several stations during the cruise, with depths ranging from 1300-300 m, so as to generate signal within the 40-100 Hz band with an output level of 195 dB re mPa at 1 meter. A self-contained winch was designed and

built by APL so that the system can be used on any vessel with enough deck space to accommodate a standard container van centered on an A-frame. The electroacoustic source is fundamentally the same as those used previously for acoustic thermometry (ATOC) experiments (ATOC Consortium, 1998; ATOC Instrumentation Group, 1995; Dushaw *et al*., 1999). Following a series of deck tests the system was deployed to 1300 m depth during our cruise. Unfortunately, the attempt to pressurize the source at depth was not successful. In this state, the system failed upon receiving a command to begin generating a series of test signals to calibrate the program that would drive the source. The reason for the failed pressurization was determined immediately upon recovery of the instrument. After a series of tests with the system open, it was determined that one ceramic stave needed to be replaced (an operation that was not possible at sea). Thus, it is expected that the source will be repaired and that it will be operational for future use, but we were not able to use it during our 2003 experiment.

Accurate source times were determined from recordings made with a portable hydrophone deployed over the side of the ship. This hydrophone was intended for use with the electroacoustic source so its sensitivity was too great for useful waveform recording of the SUS and glass sphere shots, most of which were clipped. However, the onset of the arrivals can be picked with accuracy to within 0.002 seconds. GPS time was integrated with the recording of the near-source hydrophone and these data were sampled at 3000 Hz then low-passed by a filter with corner at 500 Hz. Local seawater velocity was determined from a CTD cast (conductivity, temperature, depth measurements in the water column) to 1000 m depth in the vicinity of each acoustic source deployment. The source time was determined by correcting the arrival time for the sound travel between the source (whose trigger depth was known to within 2-3 m for the glass spheres, and 6-9 m for the SUS) and the hydrophone. Table 1 lists the location and time of all the calibration shots.

Table 1. Acoustic source times, locations and initial IMS detections (H04S/N, H08N/S, H01).

Source	Time jd hr:mn:sec	Latitude S	Longitude E	Z (m)	4S	4N	8N	8S	1
A1 sph1	140 13:26:23.33	34°03.381'	40°30.159'	710					
A1 sus3	140 13:55:09.15	34 03.382	40 30.157	915					
A1 sus2	140 14:04:59.23	34 03.384	40 30.156	610					
A2 sus3	142 13:35:02	32 51.157	47 44.150	915			+		
A2 sus2	142 13:39:47.39	32 51.142	47 44.139	610			+		
A3 sph1	143 13:47:29.06	31 49.640	52 36.594	690					
A4 sph5	144 10:23:11.56	30 52.227	56 19.051	715					
A4 sus3	144 10:54:57.77	30 52.227	56 19.046	915		+	+	+	
A4 sus2	144 10:59:49.04	30 52.223	56 19.049	610		+	+	+	
A5 sph5	146 06:18:34	28 44.111	63 24.094	726					
A5 sus3	146 06:48:38	28 44.104	63 24.095	915				m	+
A5 sus2	146 06:52:38	28 44.115	63 24.097	610				+	~
A6 sus3	149 04:20:21.90	22 05.089	72 44.529	915	+	+		+	+
A6 sus2	149 04:25:51.21	22 05.089	72 44.529	610	+	+		+	~
A7 sph5	151 04:20:17.85	18 26.050	80 55.093	713		~		+	~
A7 sus3	151 11:52:11.75	18 26.045	80 55.091	915			+	+	+
A7 sus2	151 11:58:15.81	18 26.045	80 55.091	610			+	+	+
A8 sph1	152 08:46:44.89	17 10.552	83 40.514	725					
A8 sus2	152 09:13:59.37	17 10.555	83 40.506	610	+	+	~	+	+
A8 sus2	152 09:19:59.23	17 10.555	83 40.506	610	+	+	~	+	+
A9 sus3	156 10:48:48.10	13 29.673	91 41.316	915	?	?		+	+
A10sus3	158 03:55:21.68	12 12.799	96 47.799	915	?	?		+	+
A11 sus	160 00:37:33.83	13 11.878	104 41.661	915	?	?		+	+
A11sph5	160 01:37:39.90	13 11.875	104 41.665	731					

sph1/5 is glass implosion (1/5 sphere); sus2/3 is SUS 2000'/3000' charge. Z is source depth. + indicates signal detected; ~ indicates a weak but apparent signal; m indicates that another signal masked the arrival. Blank means no signal was detected. ? indicates that we have not yet received word one-way or the other.

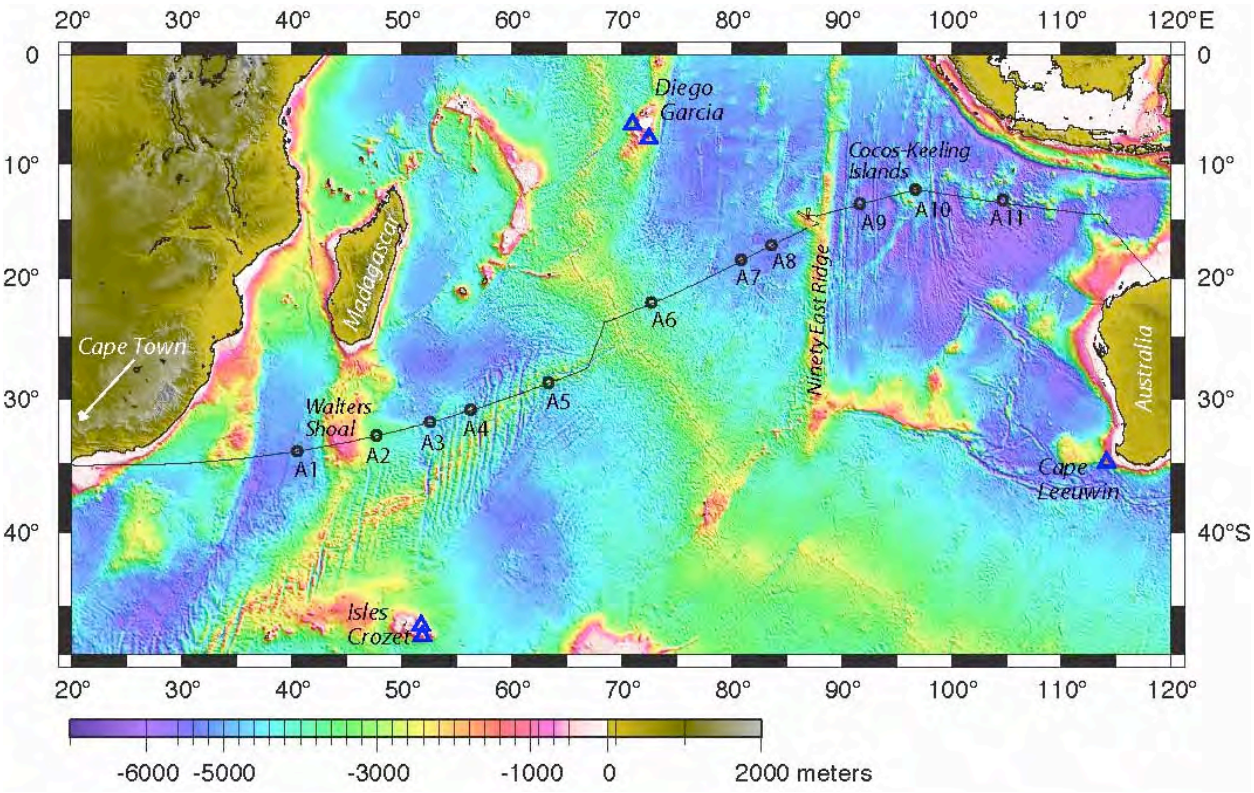


Figure 1. Track of the R/V Melville cruise in May/June 2003 overlain on shaded bathymetry of the Indian Ocean basin. IMS hydrophone stations are shown by triangles (individual tripartite arms). Source locations are shown by circles and corresponding labels identify the sites as listed in Table 1.

IMS Recordings of Calibration Shots

Each arm of the IMS hydrophone stations consists of 3 sensors, spaced 1-2 km apart. Both Diego Garcia and Crozet stations are comprised of a north and south arm (Figure 1). Cape Leeuwin has a single tripartite layout. Data for the IMS hydrophone stations is archived at 250 samples per second and instrument response is essentially flat in the 5-115 Hz band.

Based on the predicted range for each source-receiver pair the expected arrival time for the calibration shots was computed using a sound speed velocity of 1.49 km/s. Sections of data, ten minutes either side of the expected arrival, have been analyzed thus far. Background noise levels vary both between stations and with time during the cruise so at this stage we simply discuss how the recorded signals compare to concurrent noise. In general, the SUS recordings had energy in the 40-120 Hz band, with the weaker signals typically lacking in the lower 40 Hz of this band. Initial analyses indicate that the recorded signal for the 915 m SUS recordings was commonly somewhat stronger than that of the 610 m SUS shot. This is sensible in view of the fact that at most source sites, the axis of the sound channel were at 1000-1200 m depth. The difference in frequency content of signals from the different SUS depths does not appear, under initial analysis, to be consistent. This probably reflects a combination of variable bathymetric losses as well as the fact that the bubble pulse frequency for charge depths that we had were at the upper end, or just above, that of the IMS hydrophone recording range. Figure 2 illustrates how the SUS signal can vary as a function of charge depth as well as source-receiver path. The case shown is for site A6 to Diego Garcia, south, and Cape Leeuwin. The 915 m SUS signal at H08S has peak energy early in the arrival whereas at H01 the peak is at the end of the arrival. Frequency content and amplitudes for the 915 m and 610 m signals are similar at H08S, though somewhat more energy occurs in the 30-50 Hz band for the shallower charge. In contrast, at Cape Leeuwin, the signal for the two depths differs markedly. Whereas the 915 m signal is quite clear in the 40-120 Hz band, only a faint signal is apparent in the 60-110 Hz range for the 610 m charge.

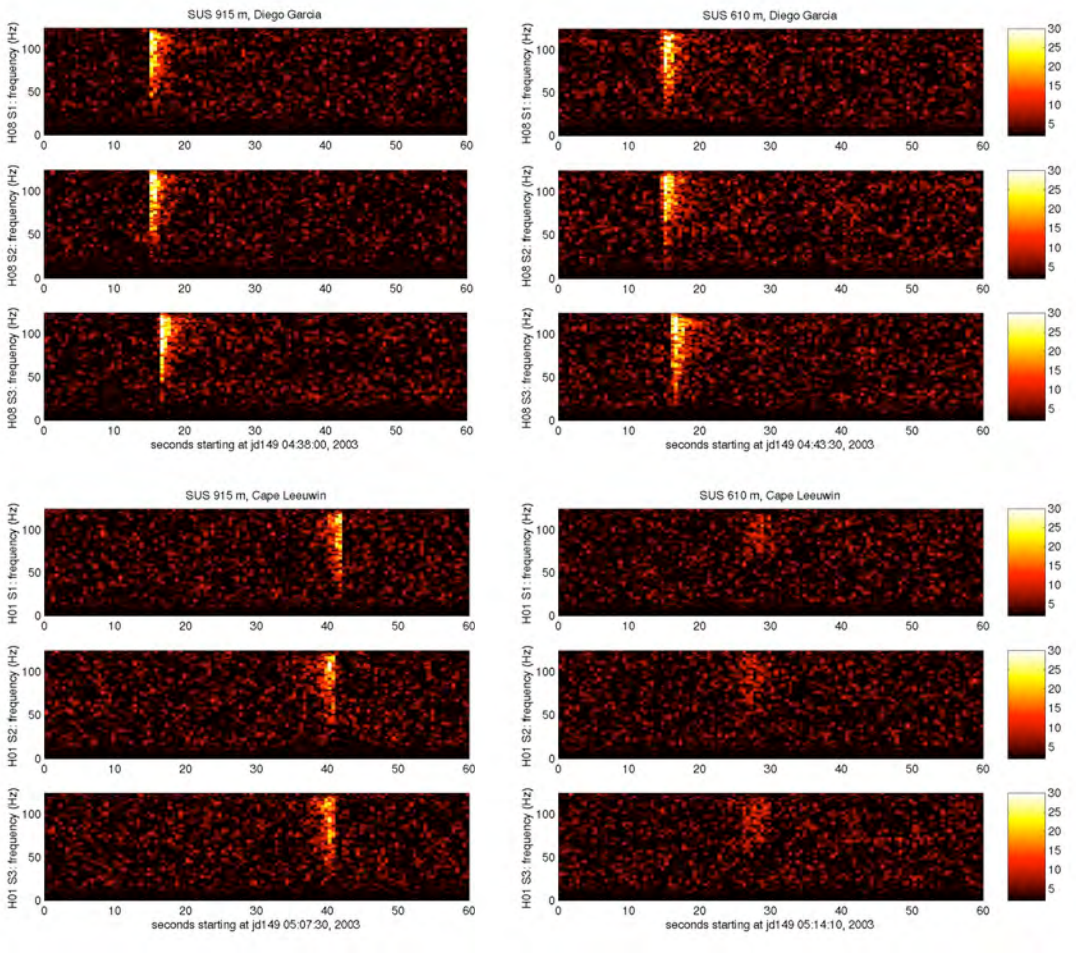


Figure 2. Spectragrams illustrate SUS signals recorded by IMS hydrophone stations in the Indian Ocean. The location of the shots (A6) is listed in Table 1 and shown in Figure 1. Mean (background) spectral level at each frequency, for each time section, has been subtracted so that signal relative to noise is shown in deciBels. Color scale is the same for all panels. Top panels show data from Diego Garcia, south arm (H08S), sensors 1-3; lower panels are for Cape Leeuwin sensors (H01). Left panels show the signal generated by a SUS charge at depth 915 m; right panels show SUS charge at 610 m depth. Significant attenuation occurs for the latter at Cape Leeuwin. In contrast, at Diego Garcia the 610 m SUS arrival has slightly more energy at lower frequencies (30-50 Hz) than does the signal from the deeper SUS. Source-receiver range to H08 is 1608 km; to H01 it is 4259 km.

Most of the glass sphere implosions were not detected. This contrasts with our findings in 2001 when both 5-sphere shots were observed at range greater than 4000 km and single-sphere shots were detected at ranges on the order of 1000 km (Blackman *et al*., 2003). One sphere shot that was detected is shown in Figure 3, where the source-receiver range was 1510 km to H08S, 1724 to H08N, and 3750 km to H01. Blockage to the north arm of Diego Garcia clearly stripped a lot of the energy, but some signal is apparent in the 80-100 Hz band. Signal-to-noise ratio in the Cape Leeuwin recording is only about a factor of two and the loss, relative to Diego Garcia, south, is probably due to attenuation at the Ninety East Ridge. Our 1500 km and greater source-receiver ranges may have precluded detection of the single sphere shots. Instrumental factors probably played a role in the reduced detectability of the 5-sphere shots, compared with 2001. The 5-sphere frame degraded significantly with each use due to the impact suffered during the implosions. A number of welding fixes were required and at one site, the frame had bent far enough out of shape that the lower sphere was able to move out of the way of the piston-triggered ram, rather than be shattered by it. Minor modifications allowed for successful firing at the next site but these experiences suggest that the 5-sphere signal may not have been as coherent as it was in the 2001 shots, when the frame was new. Upgrades of this system are currently being discussed at Lawrence Livermore National Laboratory.

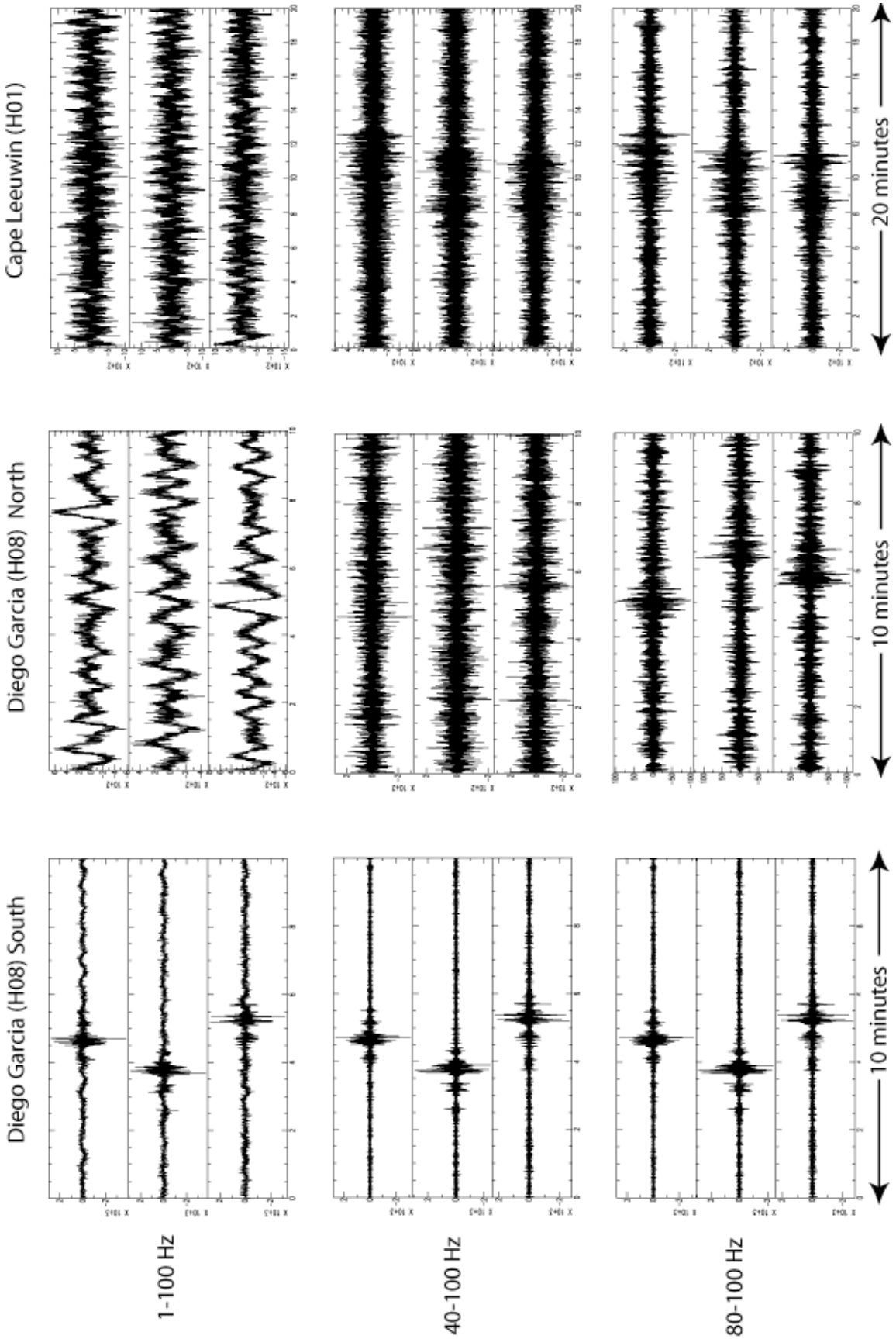


Figure 3. Recordings of the 5-sphere glass implosion at site A7. Each group of 3 panels shows data for the 3 sensors of a single arm of an IMS station (labeled at top). Band pass applied to the data varies from top to bottom (labeled at left).

CONCLUSIONS AND RECOMMENDATIONS

The calibration shots that we produced will be useful for assessing IMS location capabilities for small sources with energy in the 40-120 Hz range. One of the shots produced notable energy in the 10-20 Hz band, as well as at higher frequencies, so this may provide useful tests of discrimination algorithms. Our initial results are sufficiently interesting that complete analysis of the data is warranted and we plan to achieve this in the coming 6 months. A variety of topographic losses were encountered along the series of paths between our shots and the IMS hydrophones. Characterization of these losses, as a function of frequency and topographic roughness, should provide constraints on the resolution at which propagation models need to incorporate bathymetry in order to obtain loss predictions within the desired accuracy.

ACKNOWLEDGEMENTS

We thank the crew and science party aboard the R/V Melville for their willing and cheerful support throughout the cruise. Martin Lawrence and Andrew Forbes provided advice during the planning stages of the cruise. Patrick Grenard, Spiro Spilioupoulous, and John Newton were quite responsive via email during the cruise and they informed us of which signals they could and could not detect in the IMS station data.

REFERENCES

ATOC Consortium (A.B. Baggeroer, T. G. Birdsall, C. Clark, J.A. Colosi, B.D. Cornuelle, D., Costa, B.D. Dushaw, M. Dzieciuch, A.M.G. Forbes, C. Hill, B.M. Howe, J. Marshall, D. Menemenlis, J.A. Mercer, K. Metzger, W. Munk, R.C. Spindel, D. Stammer, P.F., Worcester and C. Wunsch). (1998), Ocean climate change: Comparison of acoustic tomography, satellite altimetry, and modeling. *Science 281*, 1327-1332.

ATOC Instrumentation Group: B.M. Howe, S. G. Anderson, A.B. Baggeroer, J.A. Colosi, K.R. Hardy, D. Horwitt, F.W. Karig, S. Leach, J.A. Mercer, K. Metzger, L.O. Olson, D.A. Peckham, D.A. Reddaway, R.R. Ryan, R.P. Stein, K. von der Heydt, J.D. Watson, S.L. Weslander & P.F. Worcester. (1995), Instrumentation for the Acoustic Thermometry of Ocean Climate (ATOC) prototype Pacific Ocean network, *OCEANS 95 MTS/IEEE Proceedings*, 1483-1500.

Blackman, D.K., de Groot-Hedlin, C., Harben, P., Sauter, A., Orcutt, J.A. (in review, 2003), Testing LF/VLF acoustic sources for basin-wide propagation in the Indian Ocean, *J. Acoust. Soc. Amer.*

Dushaw, B. D., Howe, B. M., Mercer, J. A. & Spindel, R. C. & the ATOC Group. (1999) Multimegameter-range acoustic data obtained by bottom-mounted hydrophone arrays for measurement of ocean temperature, *IEEE Journal of Oceanic Engineering 24*(2), 202-214.

Harben P.E., Boro, C., Dorman, L., Pulli, J. (2000), Use of imploding spheres: an alternative to explosives as acoustic sources at mid-latitude SOFAR channel depths, *University of California Pub*. UCRL-ID-139032.

Harben, P.E. and Boro, C. (2001), Implosion source development and Diego Garcia reflections, *Proc. 23rd Seismic Research Review: Worldwide Monitoring of Nuclear Explosions*, 23-31.

Urick, R.J. (1967) *Principles of underwater sound*, McGraw-Hill, New York.

HYDROACOUSTIC BLOCKAGE CALIBRATION FOR DISCRIMINATION

Philip E. Harben,[1] Eric Matzel,[1] Zachary Upton,[2] and Jay J. Pulli[2]

Lawrence Livermore National Laboratory,[1] BBN Technologies[2]

Sponsored by National Nuclear Security Administration
Office of Nonproliferation Research and Engineering
Office of Defense Nuclear Nonproliferation

Contract No. W-7405-ENG-48[1] and DE-AC03-02SF22560[2]

ABSTRACT

The core focus of this hydroacoustic research is to develop a better understanding of hydroacoustic blockage to better predict those stations that can be used in discrimination analysis for any particular event. The research involves two approaches: 1) model-based assessment of blockage and 2) ground-truth data-based assessment of blockage. The goal is to reliably determine all hydroacoustic stations that can be brought to bear on a discrimination analysis from any event location in the world's oceans. An important aspect of this capability is to include reflected T-phases where they reliably occur since reflected T-phases can allow station utilization when the direct path is otherwise completely blocked. We have conceptually designed an approach to automate assessment procedures that will allow both model-based and data-based methodologies to be utilized and in the future, integrated. We have modified the HydroCAM model-based network assessment code to include variable density bathymetry grids. This will improve the reliability of model-based blockage assessment as dense bathymetry grids are added to the bathymetry database where available and needed. We are also running the HydroCAM code to produce blockage grids in the Indian Ocean for many different blockage criteria. We have been building the database necessary to begin the data driven assessment of blockage. At present, the database is accumulating earthquake events within the Indian Ocean basin as recorded at Diego Garcia and Cape Leeuwin. Over 130 events from 2001 and 2002 have been loaded. Now earthquake event data is automatically loaded into the Lawrence Livermore National Laboratory database at 1-hour record lengths to accommodate future reflection phase analysis. Future work will focus on the utilization of reflected T-phases, the automated use of model-based blockage grids, and the enhancement and use of the data-based method for blockage assessment in the Indian Ocean. The analysis methodology will then be applied to other ocean basins to eventually include all ocean basins for a full worldwide blockage assessment capability.

OBJECTIVE

The ultimate objective of this research is to enhance discrimination capabilities for events located in the world's oceans. Two research and development efforts are needed to achieve the stated objective: 1) improvement in discrimination algorithms and their joint statistical application to events and 2) development of an automated and accurate blockage prediction capability that will identify all stations and phases (direct and reflected) from a given event that will have adequate signal to be used in a discrimination analysis. More emphasis will be put on the first R&D need in the future. This paper will focus on the progress made on the 2nd R&D need.

The strategy for improving blockage prediction in the world's oceans is to improve model-based prediction of blockage and to develop a ground-truth database of reference events to assess blockage. This two-pronged approach emulates the approach taken in seismic monitoring and to the extent that seismic tools and know-how can be utilized in hydroacoustic blockage assessment, they will. Improving model-based blockage prediction entails, first and foremost, improving resolution of the bathymetry databases used in blockage calculations. The BBN Inc. developed code, HydroCAM (Hydroacoustic Coverage Assessment Model), is in use at the National Data Center (NDC) and is the basis for all model-based grid file calculations. Improving HydroCAM's blockage modeling capability starts with improving the bathymetry databases the blockage calculations are based upon. Research has focused on developing the capability in HydroCAM to utilize variable resolution bathymetry data and hence incorporate high-resolution "spotlight" bathymetry databases into the overall bathymetry data utilized in blockage calculations.

Research has also focused on specifying the form and function of the blockage assessment software tool. The software tool is envisioned to develop into a sophisticated and unifying package that optimally and automatically assesses both model-based and data-based blockage predictions in all ocean basins and for all NDC stations. The tool development begins in FY03 by developing the model-based element of the tool. The model-based software tool effort focuses on the Diego Garcia station in the Indian Ocean and uses a suite of blockage grids produced by HydroCAM to assess blockage.

The ground-truth element of blockage assessment has begun with the assembly and delivery of an earthquake event database recorded at Diego Garcia Station in the Indian Ocean and implementation of an automated event-loading schema. The assembly of a database test bed will be the focus of this component through FY03 and into FY04. Future plans call for integration of the database element with the blockage assessment software tool. An important issue in building ground-truth databases is the understanding of ground-truth sources and the limitations of each in providing broadband blockage information and accurate source locations. For example, earthquakes will be the dominant component of database events but their limited bandwidth (nominally 1-15 Hz) and fundamental location difficulties (de Groot-Hedlin, 2001) require another class of events to fill the bandwidth and location accuracy gaps. The database will seek to include sources of all types to span the monitoring bandwidth.

RESEARCH ACCOMPLISHED

The primary research focus in FY03 was on implementing a basic model-based blockage calibration capability at Diego Garcia and developing the database for a future data-based blockage capability. This section outlines the accomplishments on both the model-based and data-based approaches.

The model-based research and development has focused on extending the modeling capability of HydroCAM and on developing a basic software tool that can be used to access a suite of blockage grid files (based on different blockage criteria) produced by HydroCAM. The critical shortcoming in current HydroCAM blockage modeling accuracy can be blamed on the coarseness of the present-day worldwide bathymetry databases. The nominal wavelengths in the hydroacoustic-monitoring band are about 15 meters to 1.5 km whereas the current average resolution of the ocean surface slope and topography with satellite altimetry is 24 km (Smith and Sandwell, 1997). It would seem unlikely that worldwide bathymetry databases will be at the resolution needed for accurate hydroacoustic model-based blockage prediction anytime soon. The prospect for improving bathymetry databases, however, is not so grim. The vast majority of the world's ocean basin area is at depths well below the sound channel and consequently poor bathymetry resolution is not a factor in blockage prediction. Instead, accurate blockage prediction hinges on augmenting the worldwide database with high-resolution (nominally 200 meters from ship soundings) bathymetry in "spotlight regions" like island arcs, atolls, and ridges. Such data has been collected in many spotlight regions making the task one of integrating variable resolution databases and modifying HydroCAM to work with variable density meshes. During FY03 HydroCAM was modified to work with variable density meshes as shown in Figure 1. The fundamental modifications in the code algorithms have been completed and, as of this writing, testing is underway with a high-resolution database in the vicinity of Wake Island.

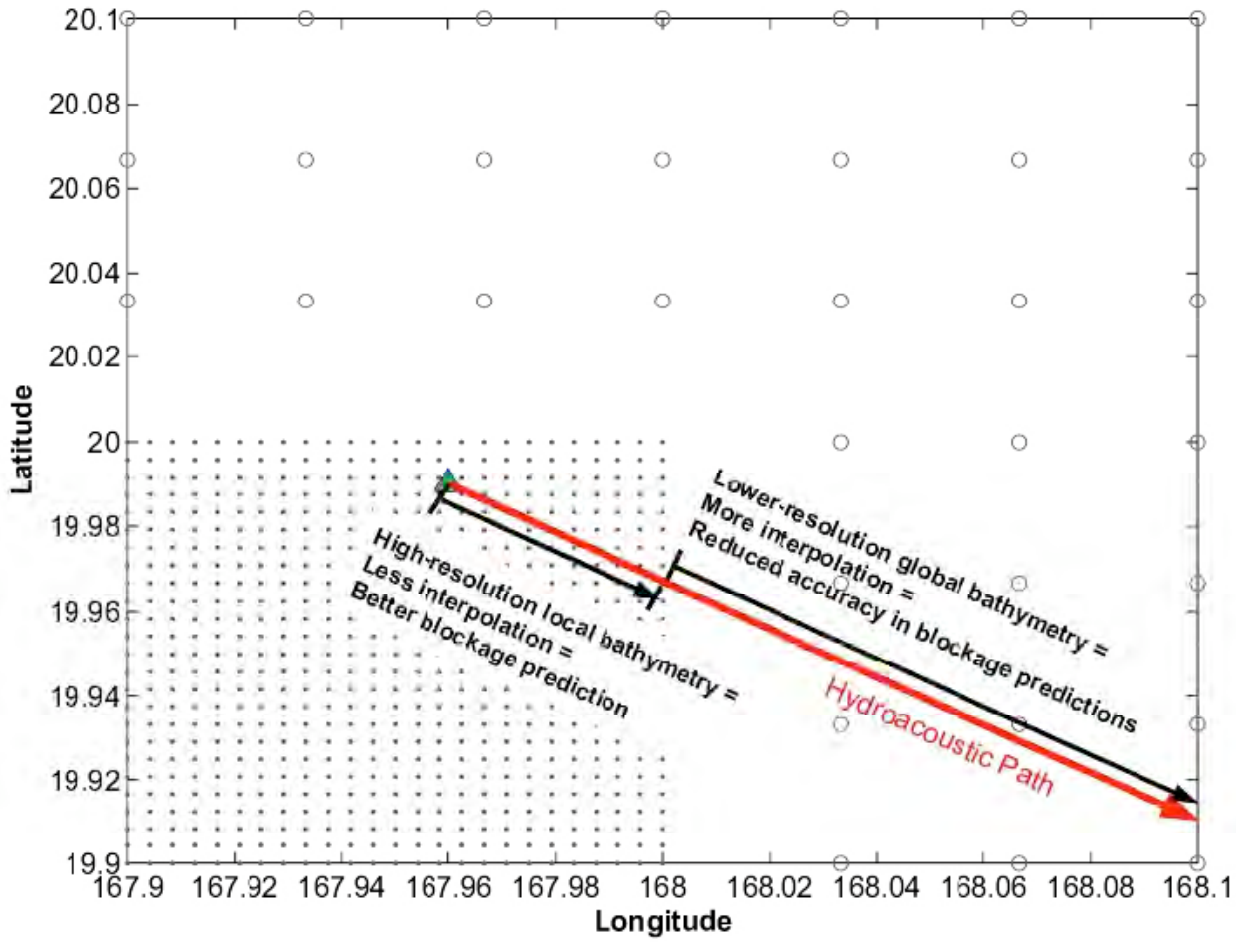


Figure 1. An illustration of the variably density grid concept with high-density grid "spotlight" areas.

The form and function of the blockage assessment tool has been specified through several generations of development. The ultimate goal of the tool will be automated assemblage of data windows containing all unblocked event phases at all stations for any given event location. The windowed phases will then be ready for analyst post-processing and discrimination analysis. A block diagram of the tool functionality is shown in Figure 2. The analysis of blockage will rely on a model component and a data component. The model component will be based on blockage grid files produced by HydroCAM. The blockage grids will be modeled using the highest resolution bathymetry database available (Smith and Sandwell) and will be recalculated whenever significant changes in relevant HydroCAM analysis algorithms or bathymetry databases occur. The data component will be based on an event database containing ground-truth source events recorded at hydroacoustic stations. The database will primarily contain earthquake source events but every attempt will be made to include as many explosive and higher frequency content events as possible. As part of the database, measurement tools will be developed that analyze the recordings to determine arrival time, back azimuth, S/N, coherence, and duration. Such measurements will be made for direct and consistent reflected phases (Pulli, 2000). Using an approach that emulates the seismic monitoring methodology to optimally make use of model and ground-truth data, the blockage assessment tool will draw on both model predictions and the database of source events. The tool will ultimately be set up for all ocean basins and all hydroacoustic monitoring station of interest.

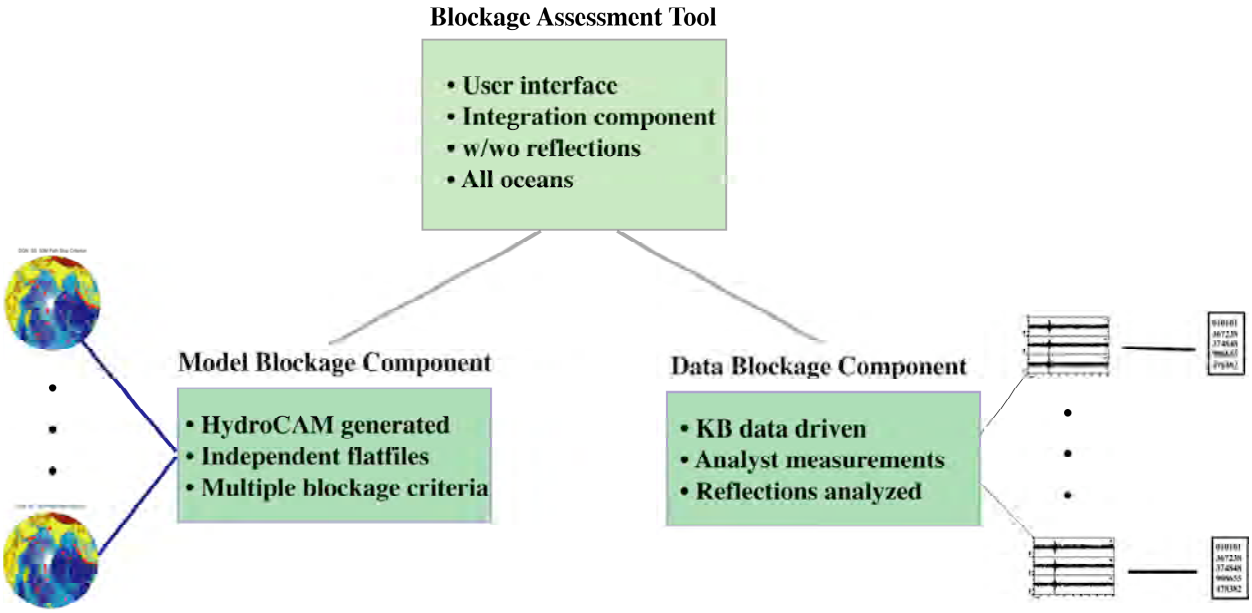


Figure 2. The conceptual flow and functionality of the blockage assessment tool.

A research database of hydroacoustic events has been developed that currently consists of 132 Indian Ocean area events recorded at Diego Garcia and at Cape Leeuwin. The waveform records are 1-hour in duration to accommodate future processing and analysis of reflected phases. Figure 3 maps the distribution of events compiled to present; all are earthquakes. Clearly the database is of adequate event density in the region of Java and Sumatra to begin to be useful in defining blockage to Diego Garcia from those areas. Although it is straightforward to accumulate and automate earthquake source events into a database and, in time, build a dense event dataset, the shortcomings of an earthquake ground-truth database are clear. For one, the location of the origin of the T-phase associated with the event is uncertain in two ways: 1) in the earthquake bulletin itself and 2) in where on the ocean floor the seismic energy converts to acoustic energy. The other problem with earthquake source events is that the signal bandwidth is about 1-15 Hz but the monitoring band is 1-100 Hz. Consequently, blockage mapping at higher frequencies, if different, will not be accounted for. It will be important to include accurately located high frequency events in the database to better understand the conditions under which earthquake-based event blockage predictions become unreliable for mapping high frequency event blockage. A major challenge will be to populate the database

with higher frequency source events. Imploding spheres (Harben, 2000) and Navy explosive charges used in the 2001 Indian Ocean cruise and in the 2003 Indian Ocean cruise have been identified and will be loaded into the database.

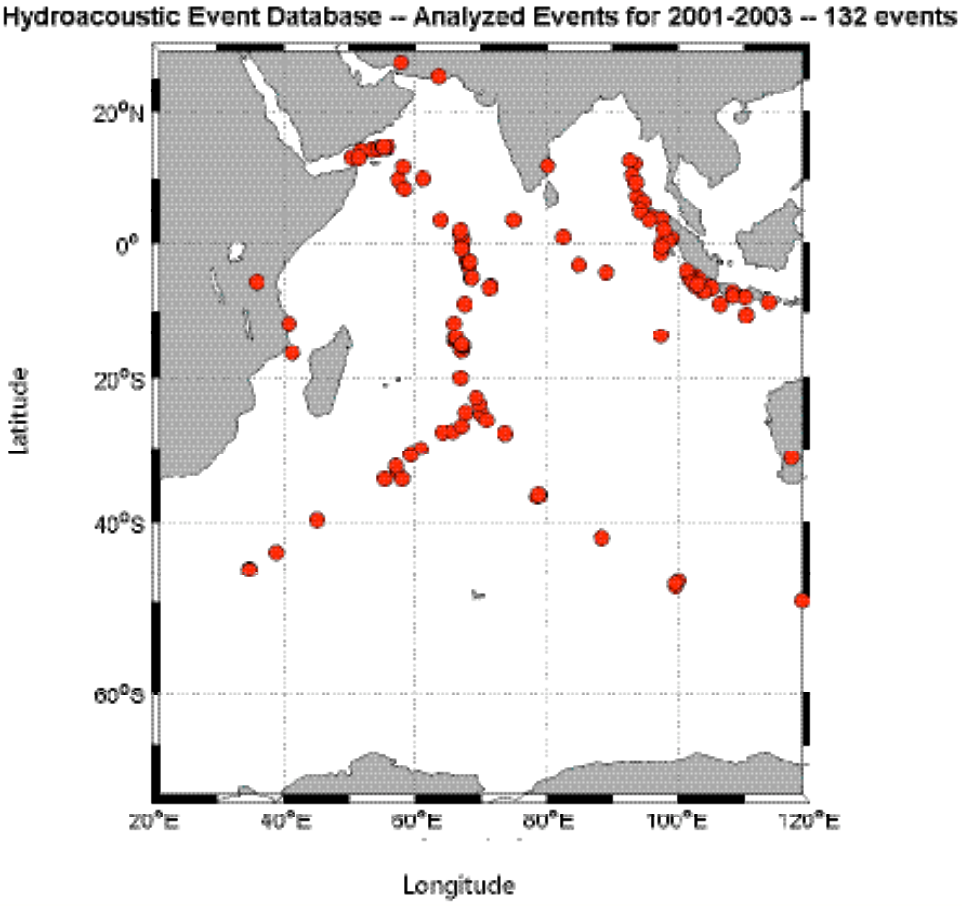


Figure 3. Research database of events in the Indian Ocean recorded at Diego Garcia and Cape Leeuwin

Although the database mapped in the previous figure was manually selected and loaded, future earthquake events will be loaded automatically as part of the overall development and growth of the LLNL seismic (and hydroacoustic) event database. An initial region has been specified for trial use and is currently being evaluated. The region is shown in Figure 4. All earthquake magnitudes greater than 4.5 and within the bounds of the Figure will be loaded and become part of the hydroacoustic event database. Earthquakes of that size and greater have reliably resulted in relatively high S/N direct-path T-phases. In the Java trench region the minimum magnitude was chosen as 5.0 to limit events from this very high-seismicity region. All records include an hour record starting shortly before the predicted T-phase arrival time. This is to include a time record long enough to record most reflected phases also. Reflected phases will ultimately be measured in identical ways to the direct T-phase arrival.

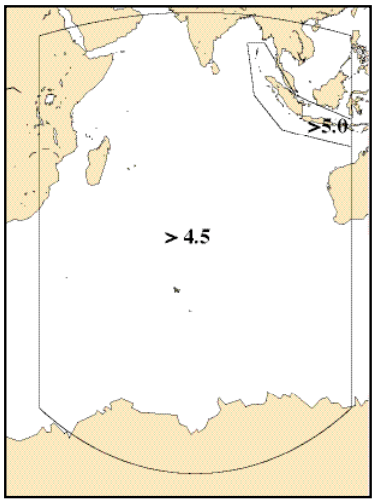


Figure 4. All events greater than magnitude 4.5 in the Indian Ocean and greater than 5.0 in the Java trench region (to limit event numbers in this high-seismicity area) will be automatically loaded into the LLNL research database.

CONCLUSIONS AND RECOMMENDATIONS

Blockage is not an on-off phenomenon. Rather, it is a frequency dependent loss of S/N and coherency due primarily to bathymetric obstacles in the source-receiver transmission path. Accurate assessment of blockage requires either a very sophisticated model prediction capability or an extremely rich ground-truth database. We have neither. Consequently, the research focus is on using crude modeling and a sparse ground-truth database in an optimal way, while steadily improving both capabilities. The focus in FY03 has been on the development of a basic software tool to analyze blockage using blockage grid files produced by HydroCAM and a suite of blockage criteria. Work has also focused on populating a ground truth database in the Indian Ocean. Future work will build on this, expanding model-based analysis and ground truth database development to all ocean basins while developing an integrated software tool that provides an optimal blockage predictive capability given the model and database limitations.

Hydroacoustic monitoring is generally considered secondary to seismic monitoring for meeting current requirements. Hydroacoustic monitoring can be exploited in new ways when used in synergy with other technologies for special types of events and has an important and unique niche to fill in the big event monitoring picture. Research in new analysis, processing and utilization of hydroacoustic assets (such as the new International Monitoring System hydroacoustic triads) should lead, not lag, new requirements.

REFERENCES

de Groot-Hedlin, C.D. and J.A. Orcutt (2001), Excitation of T-phases by Seafloor Scattering, J. Acoust. Soc. Am. 109, 1944-54.

Harben, P.E., C. Boro, L. Dorman, and J. Pulli (2000), Use of Imploding Spheres: An Alternative to Explosives as Acoustic Sources at Mid-Latitude SOFAR Channel Depths, UCRL-ID-139032.

Pulli, J.J., Z. Upton, R. Gibson, J. Angell, T. Farrell, and R. Nadel (2000), Characterization of Reflected Arrivals and Implications for Hydroacoustic Test-Ban-Treaty Monitoring, BBN Tech. Memor. W1380.

Smith, W.H.F. and D.T. Sandwell (1997), Global Seafloor Topography from Satellite Altimetry and Ship Soundings, Science 277, 1956-1962.

Radionuclide Monitoring

NOVEL BETA-GAMMA COINCIDENCE MEASUREMENTS USING PHOSWICH DETECTORS

James H. Ely, Craig E. Aalseth, James C. Hayes, Tom R. Heimbigner, Justin I. McIntyre, Harry S. Miley, Mark E. Panisko, and Mike Ripplinger

Pacific Northwest National Laboratory

Sponsored by National Nuclear Security Administration
Office of Nonproliferation Research and Engineering
Office of Defense Nuclear Nonproliferation

Contract No. DE-AC06-76RLO1830

ABSTRACT

The Pacific Northwest National Laboratory developed an Automated Radio-xenon Sampler/Analyzer (ARSA) for the Comprehensive Nuclear-Test-Ban Treaty (CTBT) to measure four radio-xenon isotopes, ^{131m}Xe, ^{133m}Xe, ^{133}Xe, and ^{135}Xe, originally using a beta-gamma coincidence counting detector. Betas and conversion electrons are detected in a cylindrical plastic scintillation cell and gammas and x-rays are detected in a surrounding NaI(Tl) scintillation detector. This paper reports investigations into a novel method to measure beta-gamma coincidences using a phoswich detector with state-of-the-art pulse shape discrimination techniques. A thin CaF_2(Eu) and thick NaI(Tl) crystal phoswich detector, with the use of pulse shape discrimination, is able to separate gamma and beta responses in a single detector unit. A single detector allows for simplification of the hardware and calibration needed for the counting system. In addition to identifying radio-xenon, the phoswich detector has the potential for detection of other radioactive noble gas species, such as radon, via daughter gamma and direct alpha emission, allowing more information to be gleaned from a single sample. The experimental configuration and results of a phoswich beta-gamma measurement will be presented.

OBJECTIVE

Of all the fission products produced in an underground nuclear explosion, only noble gases with relatively low-interaction cross-sections are likely to escape. Noble gases like xenon are, therefore, the isotopes used to detect clandestine nuclear explosions, and are part of the Comprehensive Nuclear-Test-Ban Treaty (CTBT) detection task assigned to the International Monitoring System (IMS). The IMS has been mandated to establish a worldwide network of detector systems capable of detecting the four radioxenons: ^{131m}Xe, ^{133g}Xe, ^{133m}Xe, and ^{135g}Xe. The proposed detection systems need to be sensitive to very low concentrations of radioxenon and be automated for remote operation. These four radioxenon isotopes each have unique, though overlapping, signatures that can be exploited using beta-gamma coincidence techniques. Table 1 lists the half-life, fission yield, prominent gamma rays, x-rays, beta endpoint energy, and dominant conversion electrons (CE) for ^{131m}Xe, ^{133g}Xe, ^{133m}Xe, and ^{135}Xe (Browne and Firestone (1986), ENDF/B-VI). Pacific Northwest National Lab (PNNL) has developed an Automated Radioxenon Sampler/Analyzer (ARSA) to detect these four radioxenon fission products. The ARSA is designed to be an automated system that separates and concentrates the ambient xenon (0.087 ppm in air) from the air, and uses a beta-gamma coincidence counting system to determine the concentrations of these four radioxenon isotopes as described in detail in Reeder *et al* (1998) and Reeder and Bowyer (1998). The detection system of the ARSA consists of four separate cylindrical gas cells used on a rotational basis to provide continuous monitoring. The walls of the gas cells are made from 1.2-mm thick plastic scintillator (Bicron BC-404) and are 5-cm-long hollow cylinders with a diameter of 1.25 cm (see Figure 1) so that in addition to containing the gas, the cells are also beta detectors. The scintillating light produced in the cell walls is collected at each end of the cell through two small photomultiplier tubes (PMT). The gamma detector consists of two optically separated 5-in. by 8 in. NaI(Tl) crystals that surround the four beta cells (see Figure 2). Each NaI(Tl) crystal is viewed by two 3" sideways looking PMTs. The output signals are added in coincident circuits to reduce PMT dark noise and to select out the beta-gamma coincidence signals. For the ARSA configuration, the gas responses in each cell are viewed by at least four PMTs requiring numerous electronic circuits and configuration time to gain-match and calibrate each PMT.

In order to reduce the required amount of hardware and maintenance overhead, we have investigated an alternate system of viewing the beta-gamma coincident signals. This novel system uses a phoswich detector to investigate differences between beta, gamma, and beta-gamma coincident pulses, and to separate the beta and gamma contribution from a single beta-gamma coincidence pulse.

Table 1. Half-lives, fission yields, principal radiation, and abundances of xenon fission products.

Nuclide	^{131m}Xe	^{133m}Xe	^{133g}Xe	^{135g}Xe
Half-life	11.93 d	2.19 d	5.25 d	9.14 h
Fission yield				
Independent (%)	2.41×10^{-7}	4.23×10^{-3}	1.46×10^{-3}	1.20×10^{-1}
Cumulative (%)	4.51×10^{-2}	1.98×10^{-1}	6.72×10^{0}	6.60×10^{0}
Gamma-rays				
Energy (keV)	163.9	233.2	81.0	249.8
Abundance (%)	1.96	10.3	37.0	90.0
X-rays (K-shell)				
Energy (keV)	30.	30.	31.	31.
Abundance (%)	54.1	56.3	48.9	5.2
Beta Spectrum				
Max. Energy (keV)			346.	905.
Abundance (%)			99.	97.
CE (K-shell)				
Energy (keV)	129.	199.	45.	214.
Abundance (%)	60.7	63.1	54.1	5.7

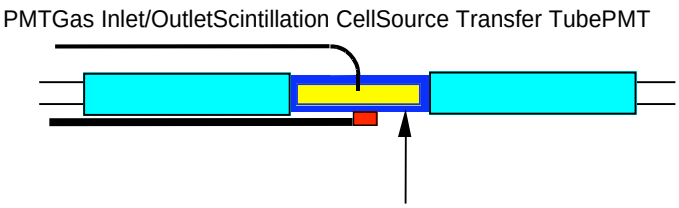


Figure 1. Schematic of the ARSA gas cell illustrating the dual PMT readout.

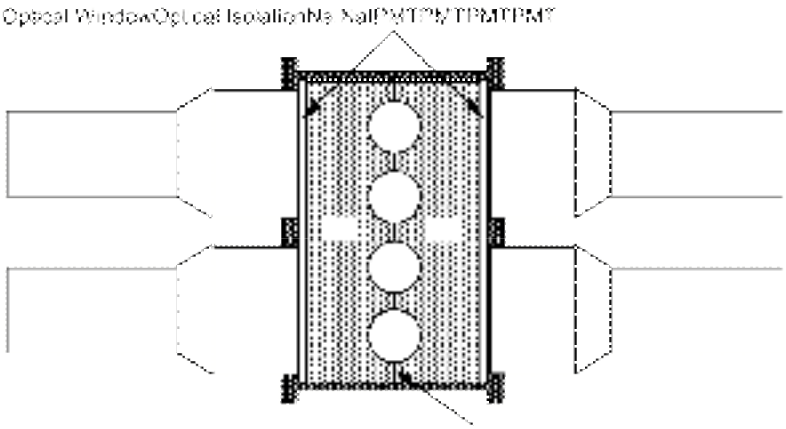


Figure 2. Schematic of the NaI(Tl) crystal of the ARSA detector.

RESEARCH ACCOMPLISHED

Phoswich Detector and Experimental Setup

The phoswich detector arose from the idea of combining two different phosphorous materials together in a sandwich that was viewed by a single light detection system. The term phosphorous sandwich was shortened to phoswich and is presently used to describe any dual scintillating material system viewed by a single light sensitive device. The two detector materials respond differently to incoming radiation and these different responses can be separated electronically. In practice, a material with a fast decay-time is used together with a slow decay-time material, both of which are read out by a single light sensitive device, such as a PMT. A pulse produced in the slow decay-time material will have a distinctively different shape than a pulse of the same amplitude produced in the fast decay-time material. The separation of the two responses is carried out in a post-processing phase. Typically integrating the pulses for a specific amount of time, and comparing the integrated pulse heights with the total pulse heights accomplish this separation. With the advent of fast digital processing, more sophisticated approaches to the separation process can be used. In addition, it may be possible to separate the gamma and beta contributions of a single beta-gamma coincident pulse. If this is possible, a single detector could be used to select individual beta-gamma pulses and perform isotopic identification based on the separated gamma and beta energies.

A phoswich detector for this investigation was custom built by Saint-Gobain Crystals and Detectors from a 2x2 inch NaI(Tl) cylindrical crystal with a 0.04-inch-thick window of calcium fluoride (CaF_2(Eu)) on one end. The NaI(Tl) crystal was separated from the CaF_2(Eu) crystal by a quartz optical window of 0.25-inch thickness as a result of the hydroscopic nature of the NaI(Tl). Pulses from a Na(Tl) crystal have typical rise-times of 250 ns (250ns decay-time of the NaI(Tl) material), while the response of the CaF_2(Eu) is somewhat slower, with typical rise-times of 940 ns. On the other end of the NaI(Tl) crystal, an ETI 9266 PMT was attached with a standard tube base mount. The crystals and PMT were packaged in an aluminum housing, which was threaded on the viewing end for the attachment of a gas cell. The gas cell was a short hollow cylinder fabricated at PNNL out of aluminum with inside dimensions of approximately 2-inch diameter by 1-inch depth. A gas-tight fitting was added on the end to allow filling of the cell. The PMT base used was an ORTEC 276 single-unit PMT base with preamp. The preamp power, PMT high voltage, and signals were connected to modules in a NIM crate. The pulses were collected and

processed by an XIA DGF4C digital pulse processor. Finally, the individual digitized pulses were sent to a computer for display and storage.

Initial testing of the detector system involved known calibration sources to ensure the normal response of the detector and to optimize the parameters of the XIA unit for resolution. The gamma radiation will, for the most part, transverse the CaF_2(Eu) window and deposit energy in the NaI(Tl) crystal that will produce a fast rising pulse in the electronic circuitry. Low-energy photons may, however, deposit some energy in the CaF_2(Eu), resulting in a slow rising pulse. The CaF_2(Eu) window is thick enough that any beta radiation should be completely deposited, forming a slow rising signal in the PMT. An example of the two distinct pulses is shown in Figure 3.

A ^{137}Cs source was used initially to view the detector response to photons, as well as to optimize the bias voltage of the PMT and the parameters of the XIA module. We observed that the resolution of the 662 keV peak from the ^{137}Cs source was maximized at a PMT bias voltage of 1,000V. Several parameters were optimized on the XIA module to ensure maximal resolution of the 662 keV peak of the ^{137}Cs source. The peaking time was adjusted to 4 µs, while the gap time was set to 2 µs. The lower-level discriminator threshold level was set to 8 (XIA units) to reduce background noise. After optimization, an energy spectrum of the ^{137}Cs source was produced (see Figure 4) that exhibits 7% resolution for the 662 keV peak.

To check the detector's response to beta particles, a ^{99}Tc source was placed directly in front of the detector with the gas cell removed. The detector responds to beta particles in a normal fashion, although the energy spectrum also contains the gamma signature from background radiation (see Figure 5). Although not performed in this investigation, the calibration sources can be used to convert the channels of energy into a common unit such as electron volts (eV).

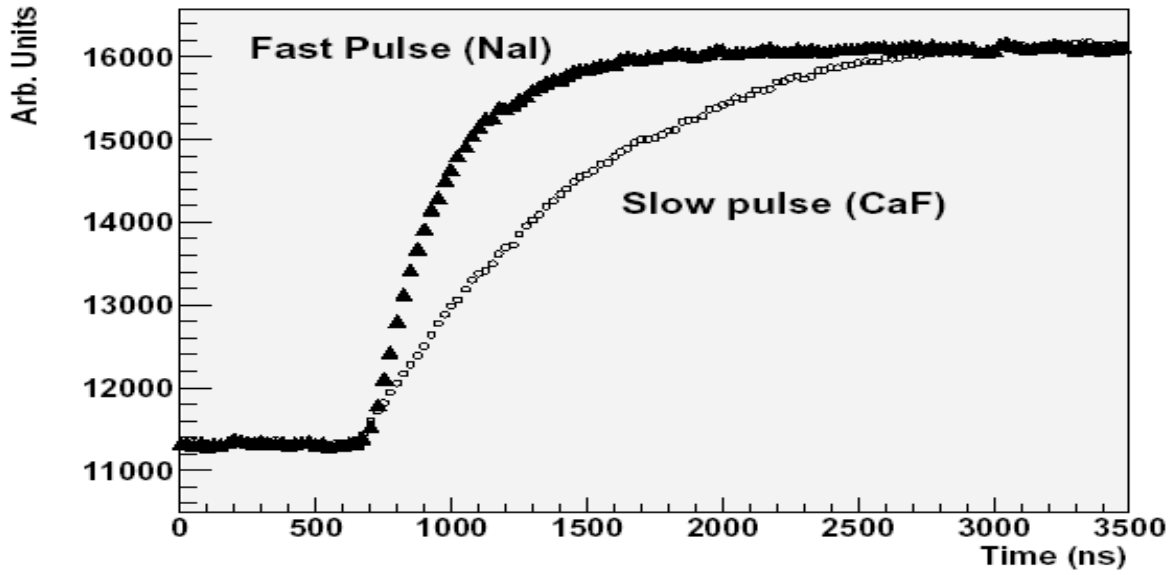


Figure 3. Example of the fast and slow rising pulses from the phoswich detector. The plot is obtained from the digitized XIA pulses.

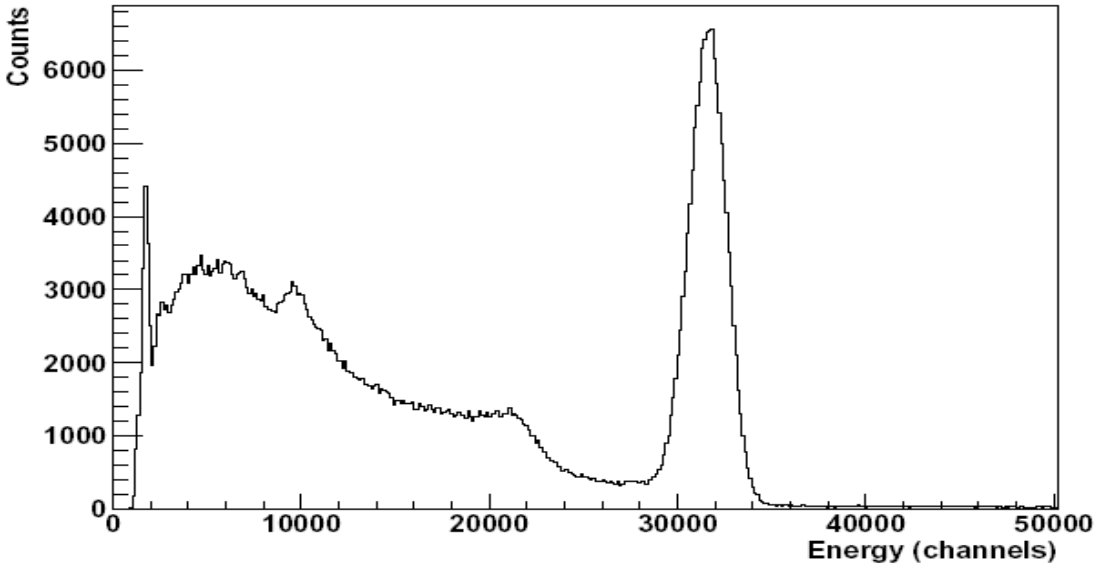


Figure 4. Energy spectrum of the phoswich detector when exposed to a ^{137}Cs calibration source.

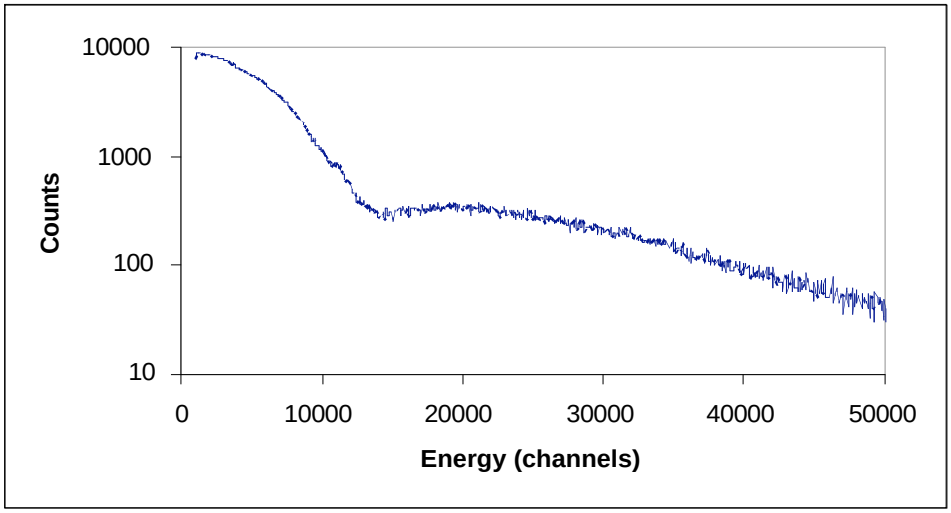


Figure 5. Energy spectrum of the phoswich detector from a ^{99}Tc calibration source. Both the beta response and gamma signature from background radiation are collected.

Xenon Analysis and Discussion

After the initial check of the detector and optimization for energy resolution, the gas cell was re-attached to the phoswich detector and xenon gas injected. Data were collected from the phoswich detector for xenon gas over a period of approximately 4 hours and yielding approximately 2.5 million pulses for analysis. The XIA module to a binary file recorded the digitized pulses. A program developed for a similar analysis was used to read and manipulate the data using the framework of the data analysis package ROOT as described in Brun and Rademakers (1997).

The data were first sorted according to the amount of time the pulses took to develop from 10% to 90% of the full pulse height, and also with respect to energy. The results are plotted in the 2-D histogram of Figure 6. The fast and slow rising pulses can be separated into two distinct distributions. An energy spectrum of pulses with rise-times less than 1,000 ns is compared to longer pulses in Figure 7, illustrating different energy distributions for

slow and fast pulses. It appears that this detector system can differentiate between pulses formed in the NaI(Tl) from pulses originating in the CaF_2(Eu) window.

As illustrated in Figure 6, there are also a significant number of pulses with rise-times in-between the two distinct distributions. In particular, there are several clusters of these pulses with rise-times in the middle region that appear as ridges. These ridges are most prominent near the fast rise-time distribution and decreasing in number toward the slow rise-time distribution. In addition, the pulses in these ridges increase in energy as the rise-time increases. This behavior is similar to what would be expected from beta-gamma coincident pulses in a phoswich detector. The gamma in a beta-gamma coincidence has a single energy, while the beta has a range of energies. Therefore, one would expect a peak in the fast rise-time distribution, with a ridge of longer rise-times and increasing energy as the variable-energy beta pulse is combined with the gamma pulse in the PMT of the phoswich detector. Also, since the beta distribution is peaked at low energy, the pulses in this 2-D plot should decrease in number as the rise-time increases. The pulses in the middle rise-time region forming the ridges of Figure 6 are promising candidates for beta-gamma coincident pulses. In order to illustrate these candidate pulses in another way, the energy distributions for the fast rise-time pulses (less than 800 ns) were compared to pulses with slightly longer rise-times (800-1200 ns) and displayed in Figure 8. In the fast rise-time energy spectrum there are three dominant peaks that are mimicked in the medium rise-time energy distribution. In addition, the peaks of the medium rise-time distribution are all at higher energy, which corresponds with the expectation of a beta response added to the gamma pulse.

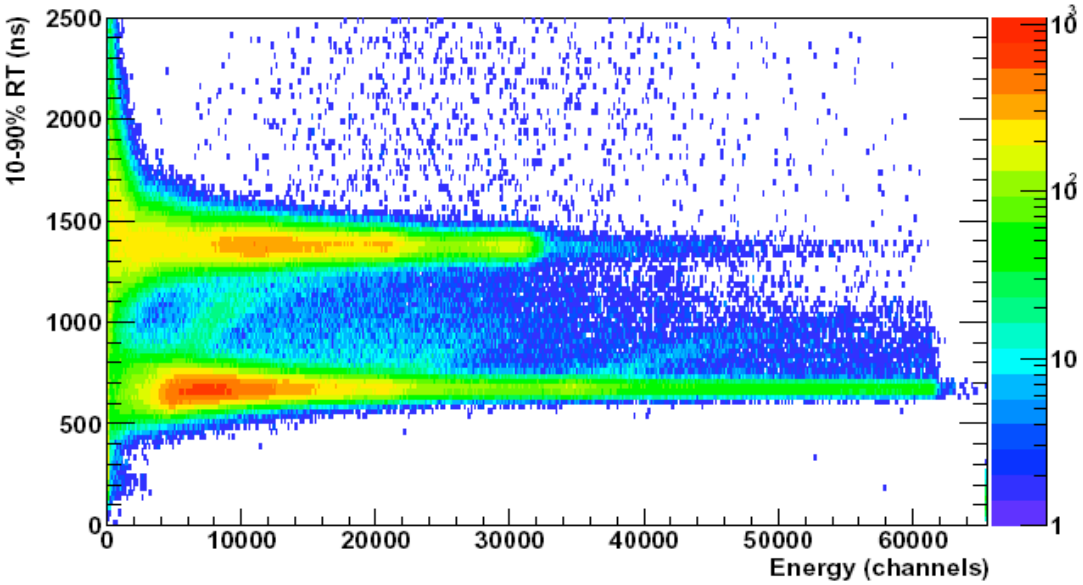


Figure 6. Rise-time (10-90%) versus energy for the xenon pulses in the phoswich detector.

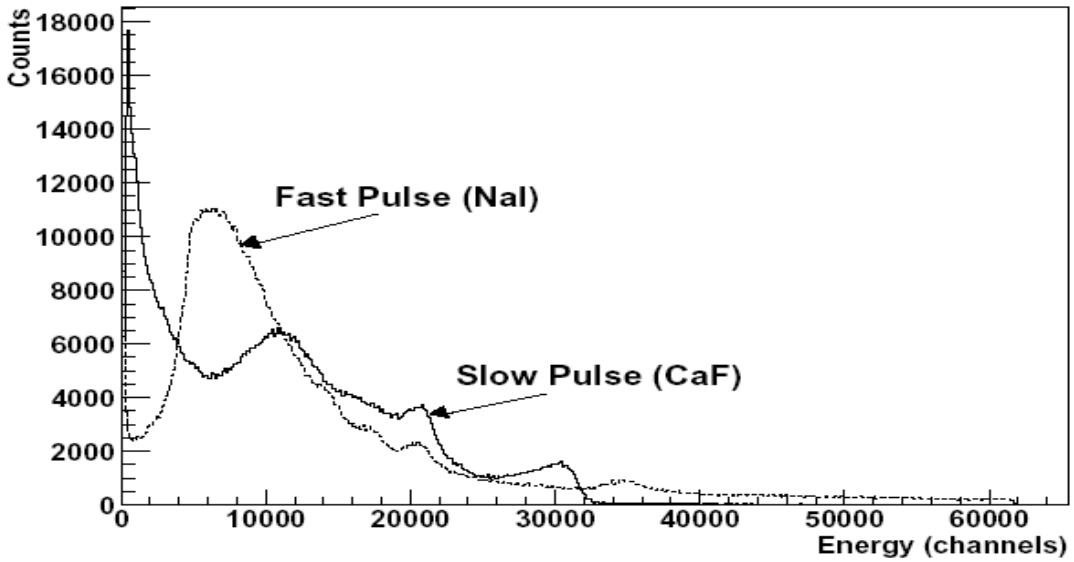


Figure 7. Energy spectra for the fast and slow rise-time pulses of xenon produced in the phoswich detector.

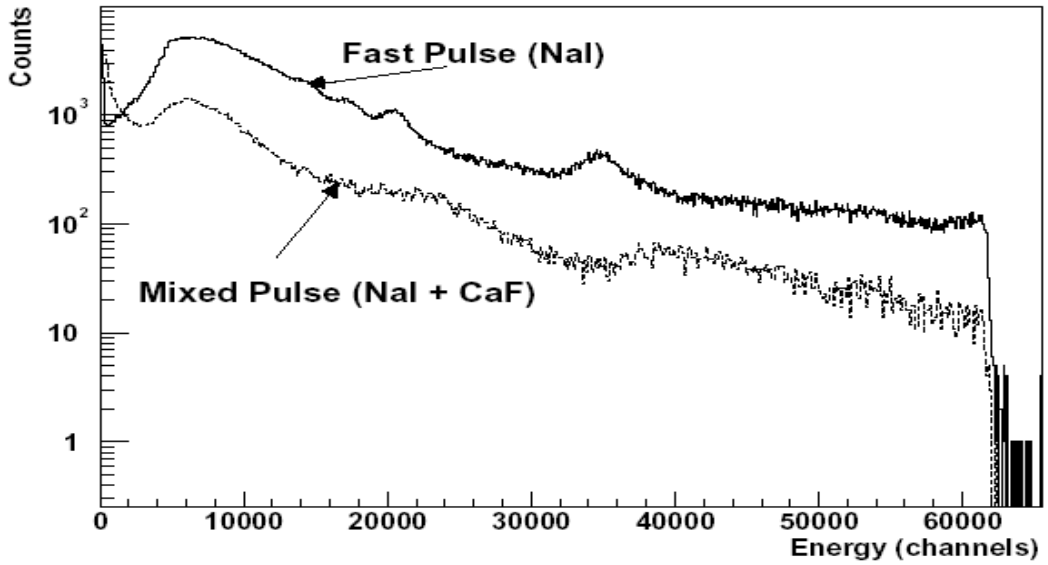


Figure 8. Energy distribution of xenon pulses with fast and medium rise-times from the phoswich detector system.

The pulses with medium rise-times are candidates for beta-gamma coincident pulses, but must be distinguished from either a single gamma or beta pulse. In addition, for the intended use of the phoswich, the beta-gamma coincident pulses must be separated into constituent pieces. This aspect of separating out the gamma and beta contributions of an individual pulse is quite different from the normal phoswich use where single particle pulses are sorted by rise-times. Generally, we can describe a pulse produced by a single particle as a single exponential with the rise-time characterized by a single parameter. For a pulse arising from two particles in a phoswich detector, the shape should be described by two exponentials and two rise-times. The difference in the rise-times should result in a pulse with an initial fast-rising shape, followed by a slow-rising tail. This difference would be distinct from a fast pulse with both a fast initial piece and tail or a slow pulse with a slow initial piece and tail. To investigate this expectation for beta-gamma coincident

pulses, the initial rise-time of the pulse (10-50%) is plotted against the final rise-time of the pulse (50-90%), for pulses with energies between 4,000–14,000 channels (see Figure 9). The energy constraint is used to ensure pulses have similar total pulse height. Two peaks, corresponding to the fast and slow pulses, are shown in Figure 9 with a relatively smooth connecting distribution. No other peak, which would correspond to anticipated fast initial pieces and slow tails, is observed. The data of Figure 9 indicate this technique does not identify beta-gamma coincident pulses. A further investigation to develop an appropriate method of identifying and selecting beta-gamma coincident pulses is required.

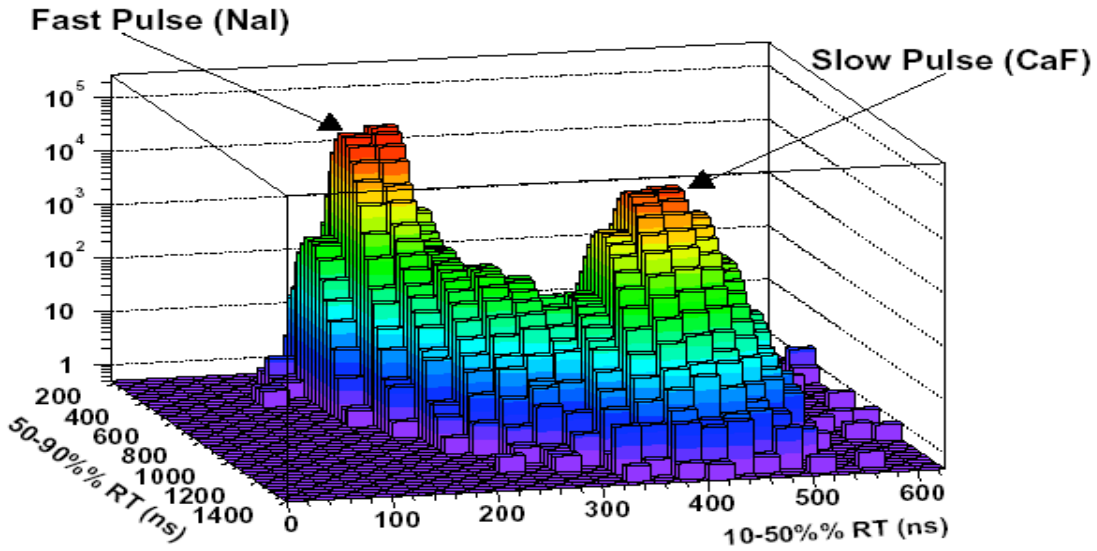


Figure 9. Distribution of the initial (10-50%) versus final (50-90%) rise-time of the xenon pulses in the energy range of 4000 – 14000 channels.

CONCLUSIONS AND RECOMMENDATIONS

A NaI(Tl) and CaF_2(Eu) phoswich detector system was built and responds to both gamma and beta radiation sources. It is possible to effectively discriminate between pulses created by either a gamma or beta particle with this system. It appears, however, that the discrimination of pulses resulting from by both a gamma and beta response in a beta-gamma coincidence event is not straightforward. There are indications that beta-gamma coincident events can be identified, and more investigation is warranted to develop an algorithm with better discriminating power than was used in this preliminary investigation. For example, a technique to fit each individual digitized pulse with an appropriate two-parameter function may be useful. In addition, different detector materials may provide a better differentiation than the choice of NaI(Tl) and CaF_2(Eu) and should be investigated. Finally, although the beta-gamma coincident events may ultimately be separable from single gamma or beta events, it may be challenging to separate the individual gamma and beta contributions of a single pulse with any precision.

ACKNOWLEDGEMENTS

We would like to acknowledge the United States Department of Energy, the Office of Nonproliferation Research and Engineering, and the Office of Research and Development for sponsorship of this work.

REFERENCES

Browne E. and R. B. Firestone (1986), *Table of Radioactive Isotopes*, John Wiley and Sons, Inc., New York.

ENDF/B-VI, National Nuclear Data Center, Brookhaven, NY.

Reeder P. L., T. W. Bowyer, and R. W. Perkins (1998), *J. Radioanal. Nucl. Chem.* 235, 89.

Reeder P. L. and T. W. Bowyer (1998), *Nucl. Instr. Meth. in Phys. Res. A* 408, 582.

Brun R. and F. Rademakers (1997), *Nucl. Instr. Meth. in Phys. Res. A* 389, 81.

DECONVOLUTION OF THREE-DIMENSIONAL BETA-GAMMA COINCIDENCE SPECTRA FROM XENON SAMPLING AND MEASUREMENT UNITS

Kendra M. Foltz Biegalski[1] and Steven R. Biegalski[2]

Veridian;[1] University of Texas at Austin[2]

Sponsored by the Army Space and Missile Defense Command

Contract No. DTRA01-99-C-0031

ABSTRACT

Because radioxenon isotopes may be all that is released from nuclear weapons tests performed deep underground or underwater, environmental xenon sampling and measurement units are used in nuclear weapons test monitoring networks. Some environmental xenon sampling and measurement units, like the Automated Radioxenon Sampler-Analyzer (ARSA) developed by Pacific Northwest National Laboratory (PNNL) and the Swedish Automated Noble Gas Unit (SAUNA) developed by the Swedish National Defense Research Establishment (FOI), use b-g coincidence detectors that are energy dispersive on both the g and b axes. Signals from four radioxenon isotopes (^{131m}Xe, ^{133}Xe, ^{133m}Xe, ^{135}Xe) comprise a sample spectrum. Under poor operating conditions, a few radon daughters (^{214}Pb, ^{214}Bi) may interfere with the sample spectrum. Applying conventional region-of-interest (ROI) spectrum analysis algorithms to such 3-D spectra results in relatively high minimum detectable concentrations (MDCs) due to the subtractive process of determining net counts in the ROI. Deconvolving the 3-D sample spectra into the most probable combination of signals using non-negative least-squares results in a better ability to resolve spectral interferences. In addition, this method utilizes the entire signal from each radionuclide and consequently improves the signal to noise ratio. This paper describes the multiple isotope component analysis (MICA) algorithm developed for analysis of 3-D b-g spectra from xenon sampling and measurement units, which comprises activity concentration and MDC calculations as well as nuclide identification methodology.

OBJECTIVE

There are two acceptable noble gas monitoring measurement modes for Comprehensive Nuclear-Test-Ban Treaty (CTBT) verification purposes as defined in CTBT/WGB/TL-11/5/Rev.8 (2000). These are 1) beta-gamma (β-γ) coincidence counting and 2) high-resolution γ-spectrometry. Two out of the three β-γ coincidence systems designed for this purpose acquire energy dispersive data on both the electron energy and photon energy axes: these systems are the ARSA (Bowyer et al., 1998) developed by PNNL and produced by EG&G Ortec, and the SAUNA (Weiss et al., 2000) developed by FOI in Stockholm, Sweden. The current software used by the CTBT organization in Vienna, Austria and the United States (US) National Data Center in Satellite Beach, Florida to analyze such data is *rms_xanalyze* (Dompierre et al., 2001; Donohoe et al., 2001). This algorithm was developed by the US Defense Threat Reduction Agency through a contract with Veridian. It is based on a Region of Interest (ROI) approach not dissimilar from most high-resolution gamma spectroscopy algorithms, but applied in two dimensions (Biegalski and Magyar, 2001). The main problem arising with the *rms_xanalyze* algorithm is that not all the physics of the problem are taken into account (such as ^{135}Xe contributions in the E_γ = 30 keV region), which can result in negative net counts or higher than necessary false positive detection rates for some radioxenons. To improve the data processing for such β-γ coincidence data, work has begun on a new software algorithm that takes into account all known physics and reduces the uncertainties involved in the results. This new software is called the Multiple Isotope Comparison Analysis (MICA) algorithm.

RESEARCH ACCOMPLISHED

MICA involves the deconvolution of a sample signal into the contributions from each isotope. Detector-specific responses for each possible isotope are used in the deconvolution. The responses can be generated using actual radioisotope sources counted on the detector, or they can be created using modeling techniques like the Monte Carlo N-Particle Extended (MCNPX) code (LA-CP-02-408 and LA-CP-02-2607, 2002). The geometry and materials of the detector must be known to produce good response files. Because only five different isotopes are detected in xenon samples, deconvolving a sample is not highly complex. Deconvolution of nuclear spectroscopy data is not a new concept (Meng and Ramsden, 2000; Guttormsen et al., 1996; Prettyman et al., 1995). What makes MICA unique is that this methodology is applied to 3-D β-γ coincidence data.

Required Input Data

The format of the data sent by β-γ coincidence detectors in the International Monitoring System network is described in IDC3.4.1rev3, "Formats and Protocols for Messages" (Salzberg et al., 2001). It is the sample histogram that will be deconvolved into individual isotopic responses using the MICA concept to determine atmospheric activity concentrations for each radioxenon of interest. To do this, however, we must have calibrated histograms of all the possible individual signals that can make up a sample histogram. Therefore, we need the following detector response matrices with their associated activities:

$$\left[{}^{131m}Xe\right]_{255\ x255}\ ,\ \left[{}^{133m}Xe\right]_{255\ x255}\ ,\ \left[{}^{133}Xe\right]_{255\ x255}\ ,\ \left[{}^{135}Xe\right]_{255\ x255}\ ,\ \left[{}^{214}Pb\right]_{255\ x255}\ ,\ \text{and}\ \left[DETBKG\right]_{255\ x255}.$$

These histograms should have the same size and calibration characteristics as the sample histogram in addition to good counting statistics; however, MICA is designed to be able to handle changes in the γ or β-ECR. Changes in the RER or EER require new detector response histograms to be acquired. Unique weight matrices can be used with each, but these should be designed a priori, be the same size as the detector response matrices, and not change over time.

Each detector response histogram can be generated using a detector modeling program like MCNPX or acquired by counting a calibration source on the detector. Since the ARSA has four beta detector cells, the above detector response histograms would need to be generated or acquired for each beta cell. In addition, the energy, resolution, and efficiency calibrations have to be determined for each beta cell. Weight matrices are also detector-specific since the calibration can differ between detectors. Calibration information should be supplied in the beginning part of the PHD message. With all of this information at hand, and knowing in which detector cell the sample was counted, the MICA algorithm can be applied to a sample for determining the atmospheric radioxenon concentrations.

MICA Concentration Calculation

First, it must be checked that the sample histogram has the same energy vs. channel calibration characteristics on both the g and b axes as the detector response histograms. If this is not the case, the sample histogram must be mapped into the energy vs. channel space of the detector response histograms. The details of this operation will not be described in this paper due to space considerations.

As mentioned previously, we then have the following matrices as input to the deconvolution problem:

$$\left[{}^{131m}Xe\right]_{255\ x255},\ \left[{}^{133m}Xe\right]_{255\ x255},\ \left[{}^{133}Xe\right]_{255\ x255},\ \left[{}^{135}Xe\right]_{255\ x255},\ \left[{}^{214}Pb\right]_{255\ x255},\ \text{and}\ \left[DETBKG\right]_{255\ x255}.$$

These all have the same calibration characteristics and size. These matrices can be weighted so that noise is filtered out. This requires the following predefined detector-specific weight matrices:

$$\left[W_{131m}\right]_{255\ x255},\left[W_{133m}\right]_{255\ x255},\left[W_{133}\right]_{255\ x255},\left[W_{135}\right]_{255\ x255},\left[W_{214}\right]_{255\ x255},\left[W_{S}\right]_{255\ x255}.$$

Elements in the weight matrices are binary, i.e., either 0 or 1. The last weight matrix listed, $[W_S]_{255x255}$, is used for weighting both the SAMPLEPHD and the DETBKPHD histograms. $[W_S]_{255x255}$ is determined by combining the isotopic weight matrices listed above. Essentially, if element i,j in any of the isotopic weight matrices is 1, then this element in $[W_S]_{255x255}$ is assigned 1. Otherwise, it is zero.

To weight the input matrices, they are array-multiplied (.*) with the appropriate weight matrix. Array multiplication entails multiplying two matrices element by element and is different than matrix multiplication (i.e., [A]X[B]):

$$\left[{}^{131m}Xe\right]_{255\ x255}.*\ \left[W_{131m}\right]_{255\ x255}=\left[{}^{131m}Xe\right]'_{255\ x255},$$

$$\left[{}^{133m}Xe\right]_{255\ x255}.*\ \left[W_{133m}\right]_{255\ x255}=\left[{}^{133m}Xe\right]'_{255\ x255},$$

$$\left[{}^{135}Xe\right]_{255\ x255}.*\ \left[W_{135}\right]_{255\ x255}=\left[{}^{135}Xe\right]'_{255\ x255},$$

$$\left[{}^{214}Pb\right]_{255\ x255}.*\ \left[W_{214}\right]_{255\ x255}=\left[{}^{214}Pb\right]'_{255\ x255},$$

$$\left[DETBKG\right]_{255\ x255}.*\ \left[W_{S}\right]_{255\ x255}=\left[DETBKG\right]'_{255\ x255},$$

$$\left[SAMPLE\right]_{255\ x255}.*\ \left[W_{S}\right]_{255\ x255}=\left[SAMPLE\right]'_{255\ x255}.$$

The weighted detector response histograms and sample histogram are then vectorized, i.e., the 255x255 matrices are converted into column vectors of dimension 65025x1. This is done by appending each histogram row onto one another, and then transposing the resulting row matrix, i.e.,

$$\left[{}^{131m}Xe\right]'_{255\ x255}\rightarrow\left[{}^{131m}Xe\right]_{65025\ x1},$$

$$\left[{}^{133m}Xe\right]'_{255\ x255}\rightarrow\left[{}^{133m}Xe\right]_{65025\ x1},$$

$$\left[{}^{133}Xe\right]'_{255\ x255}\rightarrow\left[{}^{133}Xe\right]_{65025\ x1},$$

$$\left[{}^{135}Xe\right]'_{255\ x255}\rightarrow\left[{}^{135}Xe\right]_{65025\ x1},$$

$$\left[{}^{214}Pb\right]'_{255\ x255}\rightarrow\left[{}^{214}Pb\right]_{65025\ x1},$$

$$\left[DETBKG\right]'_{255\ x255}\rightarrow\left[DETBKG\right]_{65025\ x1},$$

$$\left[SAMPLE\right]'_{255\ x255}\rightarrow\left[SAMPLE\right]_{65025\ x1}.$$

The vectorized weighted detector response histograms are then assembled into a response matrix like so:

$$\left[\left[{}^{131m}Xe\right]_{65025\ x1}\ \left[{}^{133m}Xe\right]_{62025\ x1}\ \left[{}^{133}Xe\right]_{62025\ x1}\ \left[{}^{135}Xe\right]_{62025\ x1}\ \left[{}^{214}Pb\right]_{62025\ x1}\ \left[DETBKG\right]_{62025\ x1}\right]_{62025\ x6}$$

This results in a two-dimensional matrix with 65,025 rows and six columns, i.e.,

$$[\mathrm{Re}\,sponse]_{65025x6} = \begin{bmatrix} X & X & X & X & P & D \\ e & e & e & e & b & E \\ 1 & 1 & 1 & 1 & 2 & T \\ 3 & 3 & 3 & 3 & 1 & B \\ 1 & 3 & 3 & 5 & 4 & K \\ m & m & & & & G \end{bmatrix}_{65025x6}$$

The response matrix is related to the vectorized sample histogram by the following equation:

$$[\mathrm{Re}\,sponse]_{65025x6} \quad [Coefficients]_{6x1} = [Sample]_{65025x1}$$

The coefficient matrix holds the multipliers, x_i, needed for multiplying the activities associated with each of the detector response histogram to obtain the sample activities for each isotope in the sample. This is a classic over-determined system of equations. The non-negative least squares solution is used to solve for $[Coefficients]_{6x1}$ in this problem. This method was chosen over the standard least squares solution since all the components of the $[Coefficients]_{6x1}$ matrix should be greater than or equal to zero.

Once the response coefficients, x_i, are known, the activity concentration of the radionuclides without parents (^{131m}Xe, ^{133m}Xe, and ^{135}Xe) may be calculated as:

$$Q_{Sample_i} = \frac{A_{std_i} y}{V_{Xe}} \frac{x_{Sample_i}\left(1 - e^{-\lambda_i t_{a_{std}}}\right) - x_{GB_i}\left(1 - e^{-\lambda_i t_{a_{std}}}\right) e^{-\lambda_i t_{d_{(GB-Sample)}}}}{\left(e^{-\lambda_i t_{d-Sample}}\right)\left(1 - e^{-\lambda_i t_{a-Sample}}\right)\left(1 - e^{-\lambda_i t_{a-GB}}\right)\left(1 - e^{-\lambda_i t_{c-Sample}}\right)}$$

where Q_{Sample_i} is the activity concentration of radioisotope *i* in the sample, A_{std_i} is the activity of radioisotope *i* in the calibration standard used to obtain the detector response matrix for that radioisotope, y is the concentration of elemental Xe in air (i.e., 0.087 cm^3/m^3), V_{Xe} is the sample volume of elemental Xe in cm^3, x_{Sample_i} is the response coefficient of radioisotope *i* in the sample, x_{GB_i} is the response coefficient of radioisotope *i* in the gas background, λ_i is the decay constant of radioisotope *i*, $t_{a_{std}}$ is the acquisition time of the detector response matrix, $t_{a-Sample}$ is the acquisition time of the gas background histogram, $t_{d_{(GB-Sample)}}$ is the difference in time between the start of the gas background histogram acquisition and the start of the sample histogram acquisition, $t_{d-Sample}$ is the decay time between the end of the sample collection and the start of the sample histogram acquisition, and $t_{c-Sample}$ is the collection time of the sample histogram.

Assuming that the uncertainties of the decay constants and the times are negligible, the uncertainty of the activity concentration for the radionuclides without parents (^{131m}Xe, ^{133m}Xe, and ^{135}Xe) may be calculated as:

$$s_{Q_{Sample_i}} = Q_{Sample-i}\sqrt{\left(\frac{s_{A_{std_i}}}{A_{std_i}}\right)^2 + \left(\frac{s_{V_{Xe}}}{V_{Xe}}\right)^2 + \left(\frac{s_y}{y}\right)^2 + \left(\frac{s_{x_{Sample_i}}\left(1 - e^{-\lambda_i t_{a_{std}}}\right) + s_{x_{GB_i}}\left(1 - e^{-\lambda_i t_{a_{std}}}\right)}{x_{Sample_i}\left(1 - e^{-\lambda_i t_{a-Sample}}\right) - x_{GB_i}\left(1 - e^{-\lambda_i t_{a-GB}}\right) e^{-\lambda_i t_{d_{(GB-Sample)}}}}\right)^2}$$

^{133}Xe poses a particular complication due to the possibility of a parent-daughter relationship existing in the sample. In cases where ^{133m}Xe is present, our sample histogram indicates ^{133}Xe decays representing ^{133m}Xe that was collected in the atmosphere. Therefore, for ^{133}Xe the following must be utilized to calculate the atmospheric aerosol concentration:

$$Q_{Xe133}^{Sample} = \frac{A - C - D - E}{\frac{F}{\lambda_{Xe133}^2}\left(1 - e^{-\lambda_{Xe133} t_c}\right)\left(e^{-\lambda_{Xe133} t_d}\right)\left(1 - e^{-\lambda_{Xe133} t_a}\right)}$$

where

$$A = \frac{A_{o_{Xe133}}^{std}}{\lambda_{Xe133}}\left(1 - e^{-\lambda_{Xe133} t_a^{std}}\right) x_{Xe133}^{sample},$$

$$C = \left[\frac{A_{o_{Xe133}}^{GB} e^{-\lambda_{Xe133} t_a^{GB}}}{\lambda_{Xe133}} + \frac{A_{o_{Xe133}}^{GB} \lambda_{Xe133}}{\lambda_{Xe133m} - \lambda_{Xe133}}\left(\frac{e^{-\lambda_{Xe133m} t_d^{GBS}}}{\lambda_{Xe133m}}\left(1 - e^{-\lambda_{Xe133m} t_a^{GB}}\right) - \frac{e^{-\lambda_{Xe133} t_d^{GBS}}}{\lambda_{Xe133}}\left(1 - e^{-\lambda_{Xe133} t_a^{GB}}\right)\right)\right],$$

$$A_{o_{Xe133}}^{GB} = \frac{\frac{A_{o_{Xe133}}^{std}}{\lambda_{Xe133}}\left(1 - e^{-\lambda_{Xe133} t_a^{std}}\right) x_{Xe133}^{GB} - A_{o_{Xe133m}}^{GB}\frac{\lambda_{Xe133}}{\lambda_{Xe133m} - \lambda_{Xe133}}\left(e^{-\lambda_{Xe133m} t_a^{GB}} - e^{-\lambda_{Xe133} t_a^{GB}}\right)}{\left(1 - e^{-\lambda_{Xe133} t_a^{GB}}\right)},$$

$$A_{o_{Xe133m}}^{GB} = \frac{A_{o_{Xe133m}}^{std}\left(1 - e^{-\lambda_{Xe133m} t_a^{std}}\right)}{\left(1 - e^{-\lambda_{Xe133m} t_a^{GB}}\right)} x_{Xe133m}^{GB},$$

$$D = \frac{Q_{Xe133m} F}{\lambda_{Xe133m}\lambda_{Xe133}}\left[\frac{\lambda_{Xe133m}\left(1 - e^{-\lambda_{Xe133} t_c}\right) - \lambda_{Xe133}\left(1 - e^{-\lambda_{Xe133m} t_c}\right)}{\lambda_{Xe133m} - \lambda_{Xe133}}\right]\left(e^{-\lambda_{Xe133} t_d}\right)\left(1 - e^{-\lambda_{Xe133} t_a}\right),$$

$$E = \frac{\lambda_{Xe133} Q_{Xe133m} F}{\lambda_{Xe133m}\left(\lambda_{Xe133} - \lambda_{Xe133m}\right)}\left(1 - e^{-\lambda_{Xe133m} t_c}\right)\left[\frac{e^{-\lambda_{Xe133m} t_d}}{\lambda_{Xe133m}}\left(1 - e^{-\lambda_{Xe133m} t_a}\right) - \frac{e^{-\lambda_{Xe133} t_d}}{\lambda_{Xe133}}\left(1 - e^{-\lambda_{Xe133} t_a}\right)\right],$$

$F = \frac{y}{V_{Xe}}$, Q_{Xe133}^{Sample} is the concentration of ^{133}Xe in the sampled air, Q_{Xe133m} is the concentration of ^{133m}Xe in the sampled air, $A_{o_{Xe133}}^{std}$ is the activity of ^{133}Xe in the standard used to create the detector response matrix, $A_{o_{Xe133m}}^{std}$ is the activity of ^{133m}Xe in the standard used to create the detector response matrix, $A_{o_{Xe133}}^{GB}$ is the activity of ^{133}Xe in the gas background at the start of the gas background histogram acquisition, $A_{o_{Xe133m}}^{GB}$ is the activity of ^{133m}Xe in the gas background at the start of the gas background histogram acquisition, x_{Xe133}^{sample} is the detector response coefficient for ^{133}Xe in the sample histogram, x_{Xe133}^{GB} is the detector response coefficient for ^{133}Xe in the gas background histogram, x_{Xe133m}^{GB} is the detector response coefficient for ^{133m}Xe in the gas background histogram, λ_{Xe133} is the decay constant for ^{133}Xe, λ_{Xe133m} is the decay constant for ^{133m}Xe, t_a is the acquisition time of the sample histogram, t_a^{std} is the acquisition time of the detector response matrix, t_a^{GB} is the acquisition time of the gas background histogram, t_d is the decay time between sample collection and the start of the sample histogram acquisition, t_d^{GBS} is the decay time between the start of the sample background acquisition and the start of the sample acquisition, and t_c is the sample collection time. All other variables have been previously defined. The uncertainty of the ^{133}Xe atmospheric concentration is also very complicated and is not addressed in this paper due to space considerations.

Detection Limit Calculation

To determine an MDC, the nuclide-specific detection limit (L_D) must be calculated. This section includes the derivation of L_D for each radioxenon of interest according to the MICA algorithm requirements. The MDC calculation is based on the L_D derivation as described in Foltz Biegalski and Biegalski (2001). The nuclide-specific L_D is utilized to calculate an MDC as shown below.

$$MDC = \frac{L_D}{\frac{\varepsilon_b \varepsilon_g I_b I_g F}{\lambda^2}\left(1 - e^{-\lambda t_c}\right)\left(e^{-\lambda t_d}\right)\left(1 - e^{-\lambda t_r}\right)}$$

where ε_g is the energy-dependent detection system photon efficiency, ε_b is the energy-dependent detection system electron efficiency, I_g is the photon intensity, I_b is the intensity of the β particle or conversion electron in coincidence with the photon, F is the sampling flow rate, t_c is the sample collection time, t_d is the sample decay time, t_r is the sample acquisition real time, and λ is the nuclide decay constant.

The L_D is the true net signal level that may be *a priori* expected to lead to detection (Currie, 1968). The detection limit is considered the minimum level at which a signal can be reliably quantified. It is a function of the critical level (L_C): the level at which a net signal may not be reliably detected. Both the L_D and L_C may be calculated for nuclides not found in a spectrum, as well as for those found (Canberra, 1995). The detection limit is defined as

$$L_D = L_C + k_b \sigma_D$$

where $L_C = k_a \sigma_o$, k_a and k_b are abscissas of the Normal distribution, σ_D is the standard deviation of the net signal when its real value is equal to L_D, and σ_o is the standard deviation of the observed net signal. Nominally, the acceptable probabilities for errors of the first and second kind are set equal, i.e., $\alpha = \beta$ and $k_a = k_b = k$. For a 95% confidence level, $\alpha = \beta = 0.05$ and k = 1.645 (Currie, 1968).

In the case of β-γ coincidence detectors, the observed gross signal (*G*) is a function of the counts from the nuclide of interest (*S*), the counts from interference radionuclides (*I*), and the counts from nuclides adsorbed onto the walls of the detection chamber from the previous sample (*M*). There is no interference from Compton for this analytical method (i.e., MICA) since the Compton counts are part of the nuclide signal. In addition, there are no radioxenon isotopes in the detector background signal that need to be counted as interferences. The observed net signal is then

$$S = G - I - M$$

and the signal variance is

$$\sigma_S^2 = \sigma_G^2 + \sigma_I^2 + \sigma_M^2$$

where σ_G^2, σ_I^2, and σ_M^2 are the variances of *G*, *I*, and *M*, respectively. It is assumed that background interferences are included in M.

Because the gross signal may be assumed Poisson distributed (Currie, 1968), the variance of the gross signal can be approximated by the "true" mean gross signal, μ_G. Therefore,

$$\sigma_S^2 = \mu_G + \sigma_I^2 + \sigma_M^2$$

or

$$\sigma_S^2 = \mu_S + \mu_I + \mu_M + \sigma_I^2 + \sigma_M^2$$

where μ_S, μ_I, μ_M, and μ_B are the "true" mean net counts for *S*, *I*, and *M*, respectively. If the net signal is null (*i.e.*, $\mu_S = 0$), then the variance of the net signal becomes

$$\sigma_O^2 = \mu_I + \mu_M + \sigma_I^2 + \sigma_M^2$$

When the true net signal is equal to the detection limit (*i.e.*, $\mu_S = L_D$), then the net signal variance becomes

$$\sigma_D^2 = L_D + \mu_I + \mu_M + \sigma_I^2 + \sigma_M^2 .$$

Inserting the definitions of L_D and L_C and setting $k_a = k_b = k$ yields

$$L_D = L_C + k\sqrt{L_D + \mu_I + \mu_M + \sigma_I^2 + \sigma_M^2}$$

and

$$L_C = k\sigma_O = k\sqrt{\mu_I + \mu_M + \sigma_I^2 + \sigma_M^2} .$$

Solving for L_D yields

$$L_D = k^2 + 2L_C .$$

Xenon-133

In a β-γ coincidence detector, the primary ^{133}Xe signal is the γ-line at 81 keV in coincidence with a β^- particle of maximum energy equal to 346.4 keV. Interference with this signal occurs from radon daughters, primarily ^{214}Pb. The ^{133}Xe signal in the 30 keV X-ray region (from coincidence with beta particles) has interference from ^{131m}Xe,

^{133m}Xe, and a small amount from ^{135}Xe The detection limit for ^{133}Xe is calculated by first determining the critical level, L_C:

$$L_C^{Xe\text{-}133} = k\sqrt{m_I^{Xe\text{-}133} + m_M^{Xe\text{-}133} + (s_I^{Xe\text{-}133})^2 + (s_M^{Xe\text{-}133})^2}$$

The ^{133}Xe interference term is simply the difference between the gross number of ^{133}Xe counts in the sample histogram and the number of counts attributed to ^{133}Xe by the spectral deconvolution fit of the sample, or

$$m_I^{Xe\text{-}133} = m_G^{Xe\text{-}133} - m_{G\,fit}^{Xe\text{-}133}$$

where $m_G^{Xe\text{-}133}$ is the gross counts in the sample spectrum in the channels that have counts attributed to ^{133}Xe and $m_{G\,fit}^{Xe\text{-}133}$ is the gross ounts attributed to ^{133}Xe by the spectral deconvolution fit. Following from the Poisson distribution assumption, the following equality can be assumed:

$$\left(s_I^{Xe\text{-}133}\right)^2 = m_I^{Xe\text{-}133}$$

The memory effect, *M*, is caused by the adsorption of a small fraction of atoms from the previous sample on the detector cell wall. This fraction depends on the amount of atoms in the previous sample as well as the chemical characteristics of the element. For the Automated Radioxenon Sampler-Analyzer (ARSA), the residual count rate from the memory effect can range up to 10% of the previous sample count rate (Reeder, Bowyer, Abel, 1997). The expressions for the signal and variance due to the memory effect are derived as

$$m_M^{Xe133} = e_{Xe133} g_{Xe133} \left[\frac{A_o^{Xe133} e^{-\lambda_{Xe133} t_d}}{\lambda_{Xe133}} \left(1 - e^{-\lambda_{Xe133} t_a}\right) + \frac{A_o^{Xe133m} \lambda_{Xe133}}{\lambda_{Xe133m} - \lambda_{Xe133}} \left[\frac{e^{-\lambda_{Xe133m} t_d}}{\lambda_{Xe133m}} \left(1 - e^{-\lambda_{Xe133m} t_a}\right) - \frac{e^{-\lambda_{Xe133} t_d}}{\lambda_{Xe133}} \left(1 - e^{-\lambda_{Xe133} t_a}\right) \right] \right]$$

where $A_o^{Xe133} = \dfrac{\dfrac{m_{GB}^{Xe133}}{e_{Xe133} g_{Xe133}} - A_o^{Xe133m} \dfrac{\lambda_{Xe133}}{\lambda_{Xe133m} - \lambda_{Xe133}} \left(e^{-\lambda_{Xe133m} t_{GB}} - e^{-\lambda_{Xe133} t_{GB}}\right)}{\left(1 - e^{-\lambda_{Xe133} t_{GB}}\right)}$, the ^{133}Xe activity at the start of the gas background count; $A_o^{Xe133m} = \dfrac{m_{GB}^{Xe133m}}{e_{Xe133} g_{Xe133} \left(1 - e^{-\lambda_{Xe133m} t_{GB}}\right)}$, the ^{133m}Xe activity at the start of the GB count; m_M^{Xe133} is the signal (gross counts) from ^{133}Xe in the sample count from the cell memory effect; m_{GB}^{Xe133} is the signal (gross counts) from ^{133}Xe in the gas background count; m_{GB}^{Xe133m} is the signal (gross counts) from ^{133m}Xe in the gas background count; ε_{Xe133} is the total detector efficiency for ^{133}Xe; ε_{Xe133m} is the total detector efficiency for ^{133m}Xe; γ_{Xe133} is the β-γ coincidence yield for ^{133}Xe; and t_{GB} is the acquisition time for the gas background count. The gas background count occurs after the detector cell has been purged of the previous sample and before the next sample acquisition. All other parameters have been previously defined.

Xenon-135

A similar derivation can be performed for ^{135}Xe. This radioxenon has a primary γ-line at 249.8 keV in coincidence with a beta particle of E_{max} = 908.2 keV. Interference with this signal occurs primarily from ^{214}Pb. The detection limit for ^{135}Xe is calculated by first determining the critical level, L_C:

$$L_C^{Xe\text{-}135} = k\sqrt{m_I^{Xe\text{-}135} + m_M^{Xe\text{-}135} + (s_I^{Xe\text{-}135})^2 + (s_M^{Xe\text{-}135})^2}.$$

Expression for the interference signal is:

$$m_I^{Xe\text{-}135} = m_G^{Xe\text{-}135} - m_{G\,fit}^{Xe\text{-}135}$$

where $m_G^{Xe\text{-}135}$ is the gross counts in the sample spectrum in the channels that have counts attributed to ^{135}Xe and $m_{G\,fit}^{Xe\text{-}135}$ is the gross ounts attributed to ^{135}Xe by the spectral deconvolution fit. As before, the variance of the interference signal is assumed equivalent to m, i.e.,

$$\left(s_I^{Xe\text{-}135}\right)^2 = m_I^{Xe\text{-}135}.$$

Expressions for the signal and the variance from the memory effect are derived as

$$m_M^{Xe\text{-}135} = \frac{\left(m_{GB\,\mathrm{fit}}^{Xe\text{-}135}\right)}{(1 - e^{-\lambda_{Xe\text{-}135} t_{GB}})} \; e^{-\lambda_{Xe\text{-}135} t_{GB}} \; (1 - e^{-\lambda_{Xe\text{-}135} t_r})$$

and

$$\left(s_M^{Xe\text{-}135}\right)^2 = \left[\frac{e^{-\lambda_{Xe\text{-}135} t_{GB}} \; (1 - e^{-\lambda_{Xe\text{-}135} t_r})}{(1 - e^{-\lambda_{Xe\text{-}135} t_{GB}})} \; s\left(m_{GB\,\mathrm{fit}}^{Xe\text{-}135}\right)\right]^2$$

where $\left(m_{GB\,\mathrm{fit}}^{Xe\text{-}135}\right)$ is the ^{135}Xe counts in the GB count and $\lambda_{Xe\text{-}135}$ is the decay constant for ^{135}Xe. The other parameters have been previously defined.

Xenon-131m

The ^{131m}Xe signal is produced between the coincidence of one of several ~30 keV X-rays in coincidence with a conversion electron at 129.4 keV. Interference with this signature occurs from ^{133}Xe. The detection limit for ^{131m}Xe is calculated by first determining the critical level, L_C:

$$L_C^{Xe\text{-}131m} = k\sqrt{m_I^{Xe\text{-}131m} + m_M^{Xe\text{-}131m} + (s_I^{Xe\text{-}131m})^2 + (s_M^{Xe\text{-}131m})^2}.$$

Expressions for the interference signal and variance are similar to those of the other xenon radioisotopes. The expression for the interference signal is:

$$m_I^{Xe\text{-}131m} = m_G^{Xe\text{-}131m} - m_{G\,\mathrm{fit}}^{Xe\text{-}131m}$$

where $m_G^{Xe\text{-}131m}$ is the gross count in the sample spectrum in the channels that have counts attributed to ^{131m}Xe and $m_{G\,fit}^{Xe\text{-}131m}$ is the gross ounts attributed to ^{131m}Xe by the spectral deconvolution fit. Following from the Poisson distribution assumption, the following equality is assumed:

$$\left(s_I^{Xe\text{-}131m}\right)^2 = m_I^{Xe\text{-}131m}.$$

The signal and variance of the memory effect for ^{131m}Xe are derived as

$$m_M^{Xe\text{-}131m} = \frac{\left(m_{GB\,\mathrm{fit}}^{Xe\text{-}131m}\right)}{(1 - e^{-\lambda_{Xe\text{-}131m} t_{GB}})} \; e^{-\lambda_{Xe\text{-}131m} t_{GB}} \; (1 - e^{-\lambda_{Xe\text{-}131m} t_r})$$

and

$$\left(s_M^{Xe\text{-}131m}\right)^2 = \left[\frac{e^{-\lambda_{Xe\text{-}131m} t_{GB}} \; (1 - e^{-\lambda_{Xe\text{-}131m} t_r})}{(1 - e^{-\lambda_{Xe\text{-}131m} t_{GB}})} \; s\left(m_{GB\,\mathrm{fit}}^{Xe\text{-}131m}\right)\right]^2$$

where $\left(m_{GB\,\mathrm{fit}}^{Xe\text{-}131m}\right)$ is the ^{131m}Xe counts calculated for the gas background count and $\lambda_{Xe\text{-}131m}$ is the decay constant for ^{131m}Xe.

Xenon-133m

^{133m}Xe is detected through one of several ~30 keV X-rays in coincidence with a conversion electron at 198 keV. Interference with this signature occurs from ^{133}Xe. The detection limit for ^{133m}Xe is calculated by first determining the critical level, L_C:

$$L_C^{Xe\text{-}133m} = k\sqrt{m_I^{Xe\text{-}133m} + m_M^{Xe\text{-}133m} + (s_I^{Xe\text{-}133m})^2 + (s_M^{Xe\text{-}133m})^2}.$$

The interference signal and variance are derived as

$$m_I^{Xe\text{-}133m} = m_G^{Xe\text{-}133m} - m_{G\,\mathrm{fit}}^{Xe\text{-}133m}$$

where $m_G^{Xe\text{-}133m}$ is the gross counts in the sample spectrum in the channels that have counts attributed to ^{133m}Xe and $m_{G\ fit}^{Xe\text{-}133m}$ is the gross ounts attributed to ^{133m}Xe by the spectral deconvolution fit. Following from the Poisson distribution assumption, the following equality can be assumed:

$$\left(s_I^{Xe\text{-}133m}\right)^2 = m_I^{Xe\text{-}133m}.$$

The signal and variance of the memory effect for ^{133m}Xe are derived as

$$m_M^{\text{Xe-131m}} = \frac{\left(m_{GB\,\text{fit}}^{Xe\text{-}133m}\right)}{(1 - e^{-l_{Xe\text{-}131m}t_{GB}})}\ e^{-l_{Xe\text{-}131m}t_{GB}}\ (1 - e^{-l_{Xe\text{-}131m}t_r})$$

and

$$\left(s_M^{\text{Xe-131m}}\right)^2 = \left(\frac{e^{-l_{Xe\text{-}131m}t_{GB}}\ (1 - e^{-l_{Xe\text{-}131m}t_r})}{(1 - e^{-l_{Xe\text{-}131m}t_{GB}})}\right)^2 s\left(m_{GB\,\text{fit}}^{Xe\text{-}133m}\right)^2.$$

where $\left(m_{GB\,\text{fit}}^{Xe\text{-}133m}\right)$ is the ^{133m}Xe counts calculated for the gas background count and $l_{Xe\text{-}133m}$ is the decay constant for ^{133m}Xe.

Nuclide Identification

The counts attributed to each radionuclide are compared against L_c to determine if the radionuclide is present. The counts for each radionuclide are determined from:

$$Counts_i = x_i \sum_{j=1}^{n} \sum_{k=1}^{m} m_i(j,k)$$

where $Counts_i$ is a scalar combined by adding up all the counts in the detector response matrix, x_i is the detector response coefficient for radionuclide *i*, and $m_i(j,k)$ is the detector response matrix for radionuclide *i*. If $Counts_i$ is greater than L_C for radionuclide *i*, it is considered a positive detection and the radionuclide is identified as present in the sample.

CONCLUSIONS AND RECOMMENDATIONS

This method allows for an increase in the utilized signal size by incorporating the entire detector response in the analysis algorithm. This equates to improved detection limits. However, such improvements are dependent on other radionuclide signals present in the sample spectrum and the quality of the detector response histograms used in the analysis. From applying the MICA algorithm to simulated and real sample data using simulated detector response histograms, it was found that the algorithm works very well. However, some error was introduced into the real sample data analysis by non-ideal simulated detector response histograms.

The work incorporated in this paper demonstrates the feasibility of using the spectral deconvolution concept for analysis of 3-D b-g coincidence data. The next phase of this work will be to improve the detector response histograms utilized in the analysis and to allow for energy calibration matching between the sample histogram and the detector response histograms. The detector response histograms will be improved by a combination of MCNPX modeling and direct radioxenon calibration measurements on a b-g coincidence detector. The algorithm will then be tested with a large quantity of real sample data.

REFERENCES

Preparatory Commission for the Comprehensive Nuclear-Test-Ban Treaty Organization (2000), *Operational Manual for Radionuclide Monitoring and the International Exchange of Radionuclide Data*, CTBT/WGB/TL-11/5/Rev.8.

Bowyer, T.W. et al. (1998), "Xe Radionuclides, Atmospheric: Monitoring" in *Encyclopedia of Environmental Analysis and Remediation*, editor: R. A. Meyers, John Wiley & Sons, Inc.

Weiss, W. et al. (2000), "International Program to Test and Evaluate CTBT/IMS Noble Gas Equipment", *Abstracts of Papers of the American Chemical Society*, 220: 103-NUCL Part 2.

Dompierre, D. et al. (2001), *Radionuclide Software Design*, IDC7.1.10rev2, Veridian.

Donohoe, P. et al. (2001), *Radionuclide Software User Manual*, IDC6.5.10rev2, Veridian.

Biegalski, K. and H. Magyar (2001), *IDC Processing of Radionuclide Data*, IDC5.2.2rev2, Veridian.

Los Alamos National Laboratory (2002), *MCNPX 2.4.0 User's Manual*, LA-CP-02-408.

Los Alamos National Laboratory (2002), *MCNPX 2.3.0 User's Guide*, LA-CP-02-2607.

Meng, L.J. and D. Ramsden (2000), *IEEE Transactions on Nuclear Science*, 47(4), 1329-1336.

Guttormsen, M. et al. (1996), *Nuclear Instruments and Methods in Physics Research A*, 374, 371-376.

Prettyman, T.H., R. A. Cole, R. J. Estep, G. A. Sheppard (1995), *Nuclear Instruments and Methods in Physics Research A*, 356, 470-475.

Salzberg, D. et al. (2001), *Formats and Protocols for Messages*, IDC3.4.1rev3, SAIC and Veridian.

Foltz Biegalski, K.M. and S. Biegalski (2001), *J. Radioanalytical & Nucl. Chem.*, Vol. 248, No. 3, 673-682.

L.A.Currie, *Anal. Chem.*, 40 (1968) No. 3, 586.

Canberra Industries Inc. (1995), *Model S400 Genie-PC Spectroscopy System: Basic Operation*, Meriden CT.

Reeder, P. L. T.W. Bowyer, K.H. Abel (1997), *Analysis of Beta-Gated Gamma Spectra for the PNNL ARSA and Estimate of Minimum Detectable Activities for (^{133g}Xe+^{133m}Xe), ^{133g}Xe, and ^{135g}Xe*, PNNL-11784, PNNL, Richland.

Penn, D. and S. Biegalski (2002), "Monte Carlo Simulations of Prototype Radioxenon Beta-Gamma Counting Systems," *AIP Conference Proceedings, Unattended Radiation Sensor Systems for Remote Applications*, Washington, DC, Vol. 632, 17-27.

Foltz Biegalski, K. M. (2001), *J. Radioanalytical Nucl. Chem.*, 248(3), 663-672.

STATUS OF THE UNITED STATES INTERNATIONAL MONITORING SYSTEM RADIONUCLIDE MONITORING STATIONS

David Penn

Veridian Systems Division

Sponsored by Army Space and Missile Defense Command

Contract No. DTRA01-99-C-0031

ABSTRACT

Veridian Systems Division (Veridian) is engaged in the development and upgrade of the 11 designated U.S. International Monitoring System (IMS) radionuclide monitoring stations. The U.S. IMS stations are planned to contain the Automated Radioxenon Sampler/Analyzer (ARSA) and the Radionuclide Aerosol Sampler/Analyzer (RASA). Initially prototyped by Pacific Northwest National Laboratory (PNNL) and for the past two years undergoing a field re-engineering and enhancement R&D program by Space Missile Defense Command (SMDC)/Veridian the ARSA system is designed to continuously sample the atmosphere and concentrate atmospheric xenon on cooled, activated charcoal traps. After collection the xenon sample is transferred to an electron-photon coincidence radiation detector for inspection and the data is transmitted to a data center. The RASA systems operate in a similar manner but collect aerosol samples on filter material for inspection with an HPGe radiation detector. Currently, these two pieces of equipment are at different levels of maturity: RASA systems are commercially available that meet IMS specifications, and those RASA systems already installed are in the process of being upgraded by Veridian. The manufacturing prototype ARSA system is currently being constructed and is scheduled for government review later in 2003. Several modifications were incorporated into the engineering prototype currently deployed in Guangzhou, China to improve its performance and reliability. This paper will focus on the current state of the ARSA and issues associated with the development of a first article, as well as progress to date for the ARSA in the International Noble Gas Experiment.

OBJECTIVE

The objective of the ARSA program is to support nuclear test-ban-treaty monitoring. The ARSA was designed as a continuous automated monitoring system for concentrating xenon gases and collecting the radiation spectrum for identification of four primary xenon nuclides (^{131m}Xe, ^{133m}Xe, ^{133}Xe, ^{135}Xe). The ARSA design is currently in a transitional phase between prototyping and low rate production. The data collected and lessons learned from operating the engineering prototype within the U.S. and its current location in Guangzhou, China are being utilized to implement design improvements to a manufacturing prototype currently in production. The following sections provide detail on the installation process, and performance of the ARSA with regards to the International Noble Gas Experiment and the current status of the manufacturing prototype.

Pre-Installation

The ARSA system was prepared for shipping on 20 August - 6 September 2002. The system was disassembled and the equipment, including spares, tools, and consumables, were inventoried and crated for shipment. Although the hardware was ready to be delivered to Guangzhou, the actual shipping was delayed while a request for a tariff free import was processed and the method of remotely communicating with the system was resolved. The tariff free import was resolved quickly but the method of remote communications took some time.

The Chinese requested that the system not transmit data anywhere but directly to the International Data Center (IDC) and that remote access be limited. To accomplish this Veridian proposed using a commercial data router at CN22 that could control the access to the machine by time, protocol, or IP address. A commercial router, the Cisco 806, was selected, procured, and would be hand carried to Guangzhou for the installation by Veridian. Once the communication issue was resolved the equipment was cleared for shipment to Guangzhou on 28 October 2002. The equipment arrived at the Canton airport in Guangzhou on 11 November 2002. Unfortunately, somewhere along the route the U.S. Department of Agriculture certification that the wood crating had been heat treated, as required by Chinese customs, had been misplaced, most likely while in transit through Hong Kong. This caused a concern and for the equipment to be released from customs it would have to be unpacked and the crates burned or an original certification of heat treatment would need to be provided. Veridian contacted the Department of Agriculture to obtain a duplicate certification and it was hand carried to China and delivered to the Chinese Customs on the day of arrival. Once Chinese customs received the certification, the equipment was released and delivered to the GERC on 18 November 2002.

On 19 November the Guangzhou Heavy Lifting Company was contracted to fabricate a lifting mechanism to hoist the equipment crates through the stairwell to the CN22 laboratory on the seventh floor of the building. The lifting mechanism was comprised of a truck mounted, gas powered, winch, with a cable running to a pulley in the stairwell at the ground floor. The cable was then routed up the stairwell to another pulley fastened to a beam system on the ninth floor. The cable was routed back down the stairwell and attached to the individual crates for hoisting. Figures 1 through 5 show the construction and operation of the hoisting mechanism.

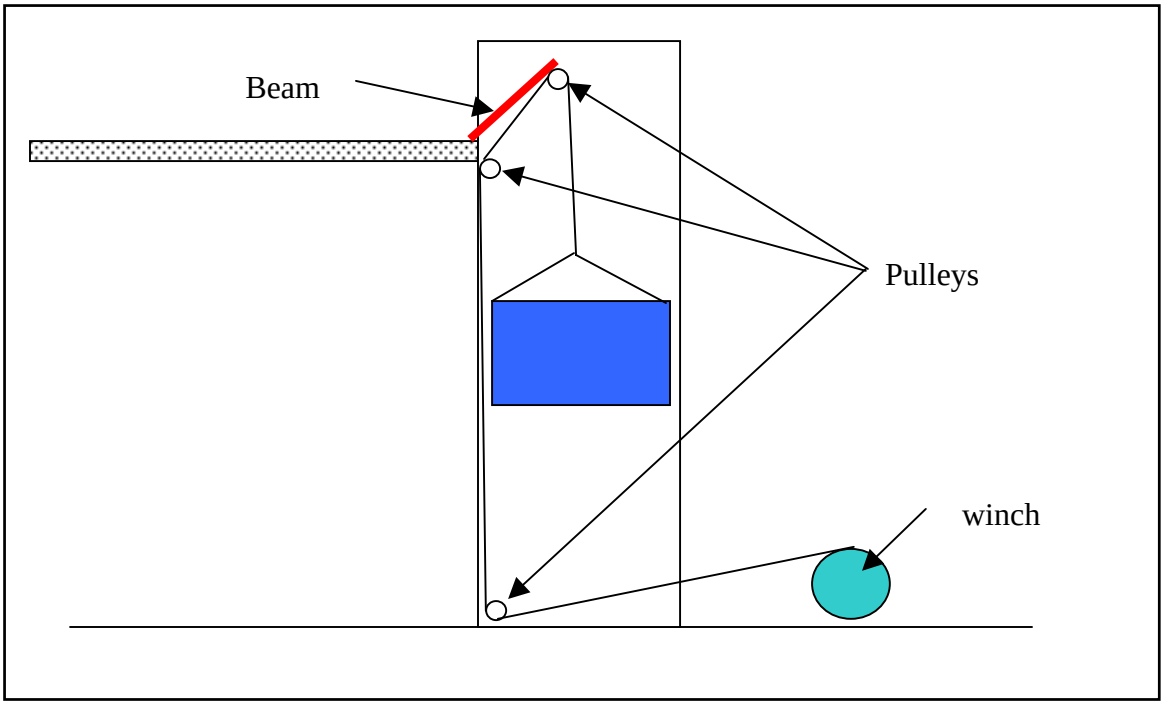


Figure 1. Hoisting mechanism design



Figure 2. Transferring the equipment from the delivery truck to the CN22 building



Figure 3. Truck mounted, gas powered winch and lifting cable



Figure 4. Beam assembly and upper cable pulleys



Figure 5. ARSA main crate arriving at the 8th floor

The crates were lifted to the seventh floor one by one starting with the lightest crate and going up in weight with each lift. Figure 5 shows the heaviest crate, approximately 900 kg containing the ARSA main assembly, arriving at the seventh floor. All of the crates except for the final crate were small enough to fit through the doorways and could be placed in the CN22 laboratory immediately. It was necessary to remove the main frame from the final crate and install a temporary wheel system allowing the ARSA to be transferred into the laboratory. Figure 6 shows the ARSA with the wheel assembly attached.



Figure 6. ARSA mainframe in CN22 laboratory with temporary wheels

Installation

Kickoff Meeting

The installation of the ARSA at CN22 began on 15 November 2002 with a kickoff meeting attended by representatives of Veridian, Gunagdong Environmental Radiation Research and Monitoring Center (GERC), PTS, Northwest Institute of Nuclear Technology (China), and the Chinese Ministry of Defense, see Figure 7.



Figure 7. Attendees at ARSA kickoff meeting

During the coordination meeting the state of the infrastructure and the list of action items from the coordination meeting, held in April 2002, were reviewed. It was found that all of the action items from the coordination meeting had been completed or an alternative solution was reached. It was also agreed that for remote access the data router

would be configured to allow scheduled FTP and telnet sessions. The remote access would be controlled by programming the data router to open the specific ports assigned to FTP and telnet every Monday, Wednesday, and Friday from 12:30 to 13:00 UTC.

Establishment of Operation

The Establishment Of Operation (EOO) for CNX22 began on the 20 November 2002. There were five GERC technicians and engineers on hand during the installation period to help with the work. Each morning the install team and the representatives from the GERC would congregate to discuss the itinerary for the day as well as review the work that was done the prior day. At the conclusion of the daily review session at least one training session pertinent to the days work was conducted.

On the First day the ARSA system was positioned in place in the laboratory and set on vibration dampening pads to minimize dynamic coupling to the HPGe detector in the adjacent room, a manual particulate monitoring system. It was also necessary to position the ARSA with the lead shielding for the detector directly above a main support beam for the floor.

Individual ARSA system components were then installed including an air pump, cryogenic cooler, and electron-photon coincidence detector system, see Figure 8. The power was connected to the ARSA along with an individual ground cable to the ARSA framing.

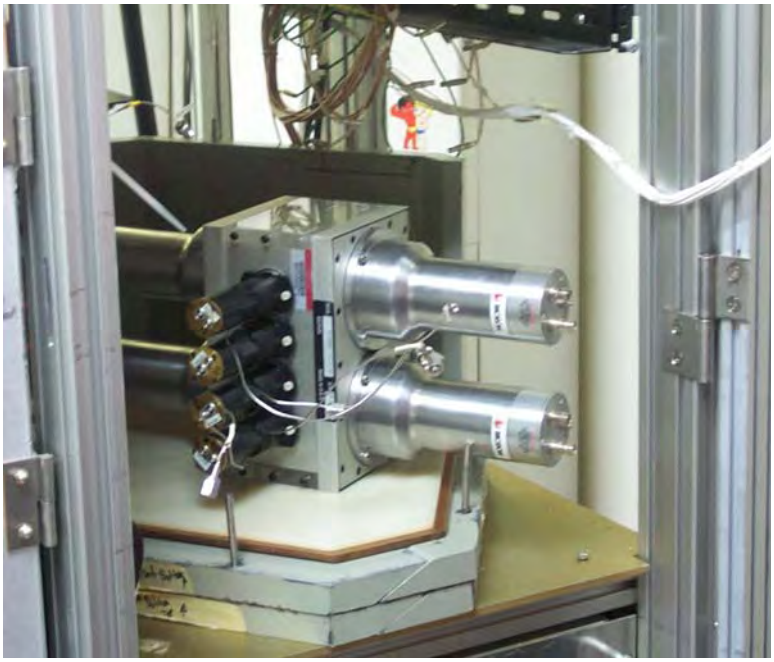


Figure 8. Installing the electron-photon coincidence detector

On the second day of the EOO the remainder of the mechanical hardware was installed on the system. The software on the station computer was installed, a GUI to control the system and view the instrumentation outputs in real time as well as a detector data viewer and a viewer for looking at the instrumentation history or State-of-Health (SOH). The system was then temporarily connected to the communications interface (ADSL modem).

Power was applied to the system but on initial startup a misconnected temperature sensor (on the cryogenic cooler motor) caused the system to shutdown after approximately five minutes. Because of the misconnection it appeared that the cooler compressor temperature was beyond the preset safety limit and the system shut down automatically. Once the misconnection was corrected the system was restarted and ran over-night in bypass mode where the

process flow is diverted away from the gas processing section but does generate SOH data from all sensors and allows the operator to manually control the system.

On the third day of the EOO the system was leak tested, Veridian trained the local operators on how to leak test the system and oversaw the local operators as they performed the actual tests, see figure 10. Also on the third day, the nitrogen carrier gas was connected to the system, see figure 11 and a few sample spectra were collected to be sure the detector was functioning.



Figure 9. Leak testing the ARSA gas process deck



Figure 10. Nitrogen carrier gas supply

Over the weekend the system had stopped running, apparently after a power outage and it was found to have stopped even though the power was on at the station. The fault was traced to the main power wiring where a commercial connector had failed. The failed connector was removed and the replaced, see figure 12, with twisted pairs and commercial wire nuts and the system was restarted.

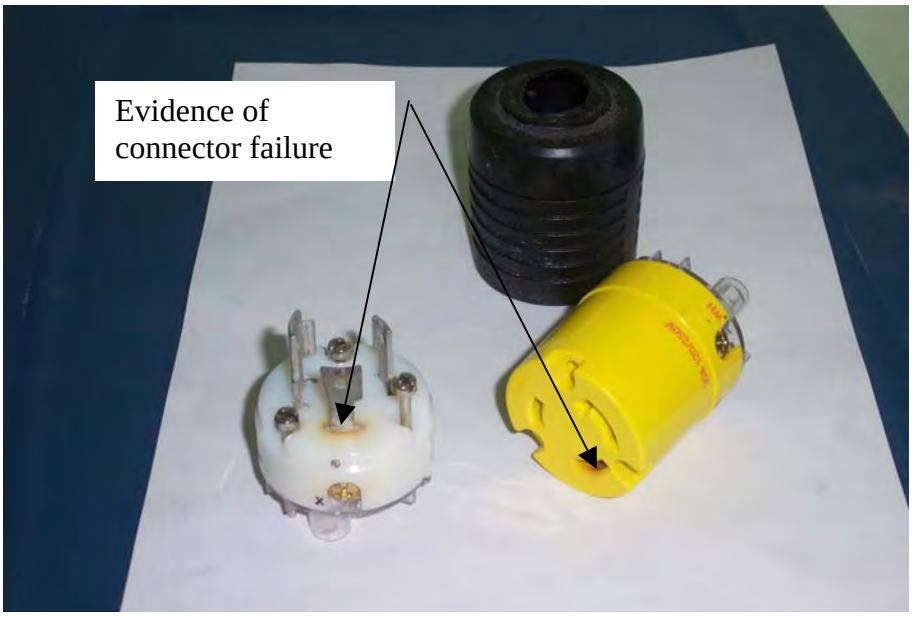


Figure 11. Failed main power connector

Communications

During the second week of the installation the software and communications were configured and the system operation was monitored closely. The ARSA was configured to communicate over the internet through a Linksys broadband router and ADSL modem. Because of the inconvenience of remote access, the ARSA SOH messages were modified, as requested by the PTS, to include approximately 140 process sensors in the SOH message process sensor block. CNX22 was also configured to transmit data to the IDC only. Since the installation, the SOH message size has been reduced per the request of the PTS, to 40 sensors, to reduce the amount of data delivered.

Tuning

During 10 March 2003 through 14 March 2003 a second trip to Guangzhou was made to complete the tuning of the system. It was decided to wait several weeks before performing the tuning to operate the system for some time at a specific location and allow it to stabilize and see if any optimizations are required. For instance, in Guangzhou, the radon levels appear to be much higher than what was seen during operation in Charlottesville, Virginia. This resulted in an elevated radon level in the spectra and an increased MDC. To compensate for the increased radon levels the gas processing parameters needed to be adjusted, i.e. adjusting some of the processing temperatures and flow rates. All of the gas processing parameters were adjusted remotely and took approximately one month to optimize the settings. Once the system was optimized remotely we went to the site for further optimization, mainly increasing insulation on the gas processing lines. All of these actions contributed to a reduced radon level, Figure 13 shows the improvement in radon rejection in the spectra for cell 3.

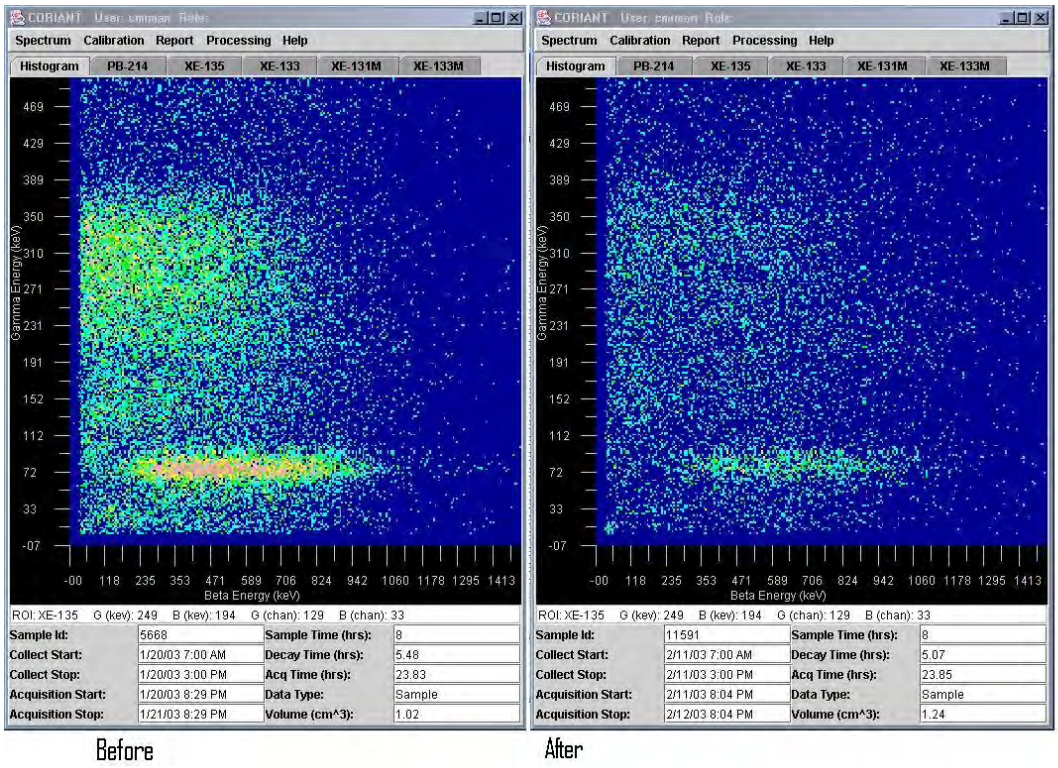


Figure 12. Radon improvement in cell 3 after optimization

All of the ARSA instrumentation was calibrated during the tuning trip including the gas quantification system which is composed of two instruments. The first instrument, a pressure sensor for measuring the sample absolute pressure, was calibrated with a mechanical, class 4A, pressure gauge. The second instrument, a Thermal Conductivity Detector (TCD) that determines the amount of xenon in the collected sample, was calibrated by passing known mixtures of nitrogen and carbon dioxide gas through the detector. The carbon dioxide gas interferes with the xenon measurement; therefore known levels of CO2 will appear as a proportional value of xenon. The instrument's zero reference point for both xenon and CO2 is calibrated by backfilling the instrument with 100% dry nitrogen. The span value for xenon is calibrated by backfilling with 100% CO2, this represents a xenon concentration of 28%. The CO2 span value was calibrated by backfilling the detector with a mixture of 30% CO2 and 70% dry nitrogen. Table 1 shows the results of the gas quantification procedure.

Table 1. Gas quantification calibration

Gas mixture	Xe reading	CO2 reading
100% nitrogen	-0.4%	-2.5%
100% CO2	27.2%	
30% CO2 + 70% nitrogen		31.3%

The radiation detector was calibrated using a combination of Eu-152 and Cs-137 sources placed directly on top of the beta cells and inside the gamma detector. The Eu-152 source provides multiple lines for checking the gamma energy calibration. The beta cell energy calibration was checked using the Cs-137 source. The 662 keV gamma ray from Cs-137 will create coincident events in the detector assembly through Compton scattering in the sodium iodide and Compton electrons produced in one of the plastic scintillators.

A particular item of interest in the Cs-137 coincidence spectrum is a line that can be seen where the sum of the photon and electron energy is 662 keV, equal to the original photon energy. If this line is extended to intersect both axes it will cross at the 662 keV point, indicating that the full energy of the photon would have been deposited in a single detector volume. Another area of interest in the spectrum is at the photon energy 184 keV. This energy

represents the photon backscatter detected in the sodium iodide block. Also there is a concentration of events with an electron energy at approximately 480 keV that corresponds to the Compton edge in the plastic scintillator spectra. See figure 14 for a spectrum taken from cell 1.

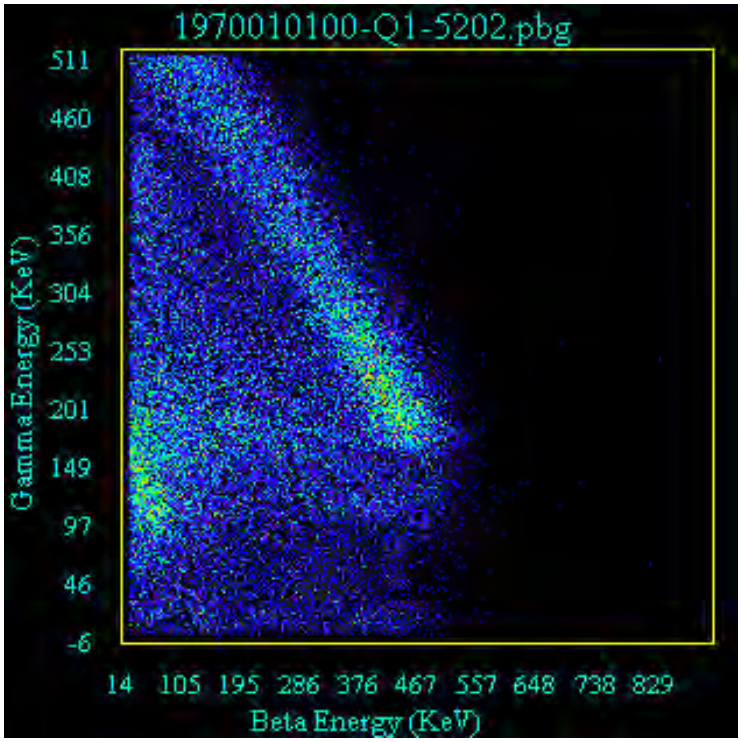


Figure 13. Typical calibration spectrum from cell 1

On-Site Training

The CN22 local operators were trained through hands-on interaction with the ARSA as well as several formal presentations throughout the establishment of operation and tuning phases of the installation. The local operators received training on the topics in Table 2.

Table 2. CN22 operator training topics

Topic	Method
ARSA Introduction	Presentation
ARSA Process Flow	Presentation
ARSA Control Software	Presentation
ARSA Safety Features	Presentation
ARSA Scheduled Maintenance	Presentation
ARSA QNX Operating System	Presentation
ARSA Normal Operational Parameters	Presentation
IDC Radionuclide Data Products	Presentation
Radionuclide Review	Presentation
Xe Processing	Presentation
System Leak Testing	Hands - on
Replacing Consumables	Hands – on
IDS operation	Hands – on
TCD Calibration	Hands – on
Control and Sensor Hardware	Hands – on
System Configuration Files	Hands – on
PHD, SOH, and Alert Message Format	Hands – on



Figure 15. Hands – on training of operators for replacing air pump consumables

Performance Testing

The goal of the performance testing period was to show that the ARSA system is functioning in a similar manner as when it was installed in Charlottesville. In general, the ARSA installed at CNX22 had been operating reliably since November 2002 with the exception of four issues that have affected the system.

1. The system shutdown automatically at the end of December due to faulty read of one of the temperature sensors. The system was restarted without problem
2. The TCD wiring harness became disconnected resulting in an elemental xenon volume of zero being reported. The connector was secured with no real affect on system operation.
3. During March the system shut down automatically due to a reported temperature for the main air pump. The resistance thermal device (RTD) used to monitor the pump motor temperature became loose. The local operators repaired the connector and the system was restarted.
4. During April the system shut down due to an excessive temperature being reported on the final charcoal trap. The fault was intermittent and took some time to repair. In the end it was found that the system had a faulty thermocouple where the electrical insulation was damaged causing erroneous readings.

Other than during the times above the system had operated well and commensurate with it's performance before being shipped to CN22. Data from CNX22 is given below from the period of 29 March 2003 to 11 April 2003 and is compared to test data while in Charlottesville and provided in the pre-shipment test report. Table 3 lists the performance requirements for IMS radioxenon sampling systems.

Table 3. IMS requirements for radioxenon sampling systems

Requirement	Characteristics	Minimum requirements
1	Air flow	0.4 m^3 h^{-1}
2	Total volume of sample	10 m^3
3	Collection time	≤ 24 h
4	Measurement time	≤ 24 h
5	Time before reporting	≤ 48 h
6	Reporting frequency	Daily
7	Isotopes measured	^{131m}Xe, ^{133m}Xe, ^{133}Xe, ^{135}Xe
8	Measurement mode	Beta-gamma coincidence or high resolution gamma spectroscopy
9	Minimum detectable concentration	1 mBq m^{-3} for ^{133}Xe

1. The total airflow produced by the system during the pre-shipment testing period and performance test can be seen in figure 16. The mean values are 5.94 and 7.24 m^3 h^{-1} for the pre-shipment and performance test periods respectively.

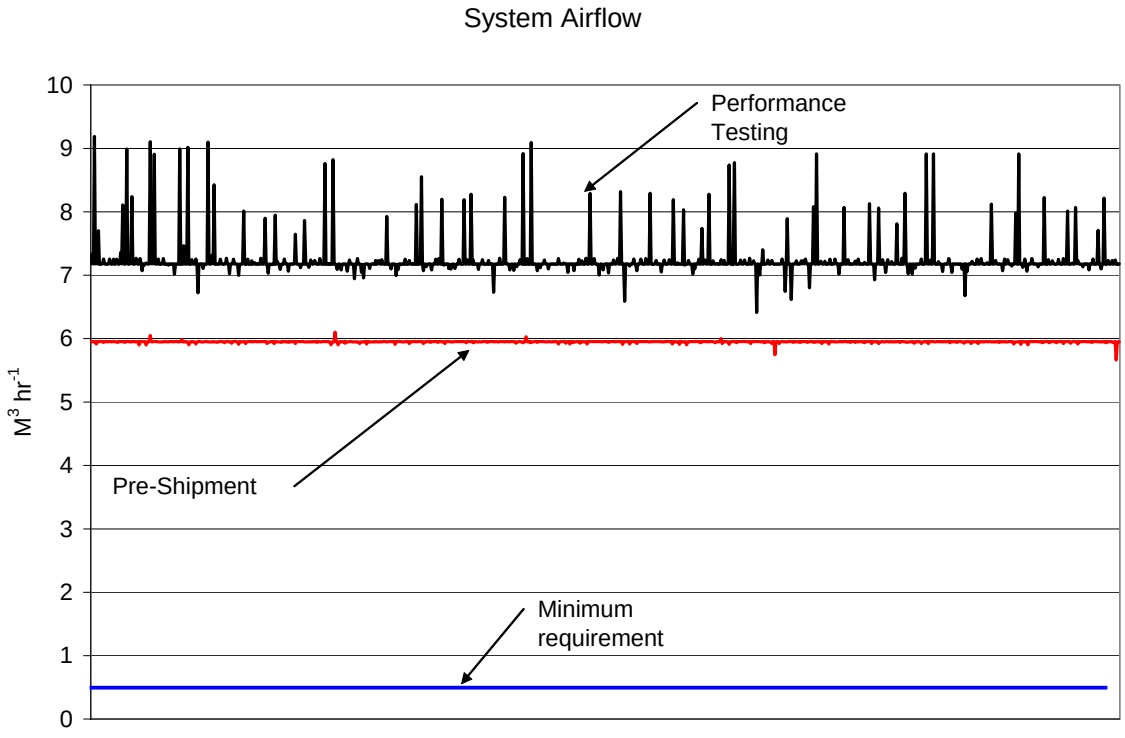


Figure 16. Total airflow through system during pre-shipment testing

2. The total volume of each sample during the pre-shipment and performance testing periods are shown in Figure 17. The mean values are 17.11 and 16.47 m^3 for the pre-shipment and performance tests respectively.

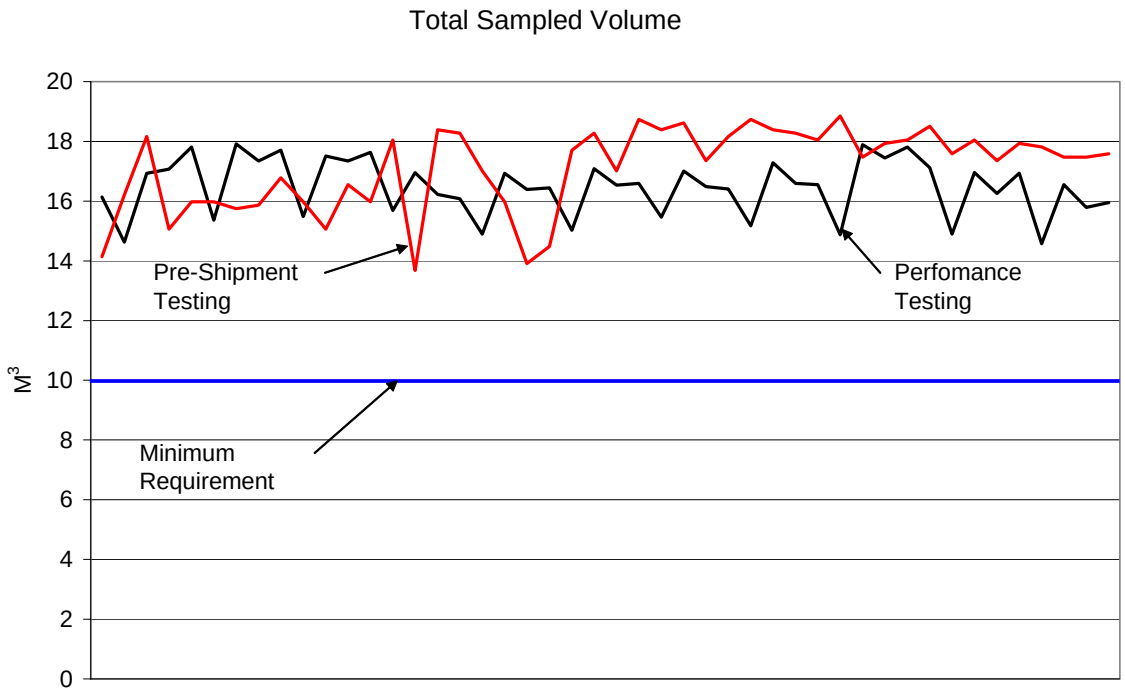


Figure 17. Total air volume sampled

3. The collection time for each sample for both the pre-shipment and performance test periods is eight hours plus or minus ten minutes. The collection time was determined by calculating the amount of time the process flow control valve was open for each collection side.

4. The mean measurement time for the gas samples during the pre-shipment and performance tests is 24.00 hours with a standard deviation of 0.01 hours. The mean measurement time for the gas background measurements is 7.36 hours with a standard deviation of 0.01 hours.

5. The time before reporting data was examined by comparing the dates a sample acquisition stopped and the date the data was transmitted. In all cases the dates were the same indicating no more than 24 hours passed before the data was reported.

6. During the testing periods the gas sample data was consistently reported three times per day.

7. Figure 18 displays the spectra measured for a sample collected on the 10th of April. The data is visualized using the software package Coriant. The outlined boxes are indicative of the regions of interest for the four isotopes of interest (^{131m}Xe, ^{133m}Xe, ^{133}Xe, ^{135}Xe). The abscissa and ordinate represent the beta and gamma measurement energy range which provides evidence of the measurement mode, beta-gamma coincidence. Note that this sample appears to have a small amount of ^{131m}Xe in the spectrum.

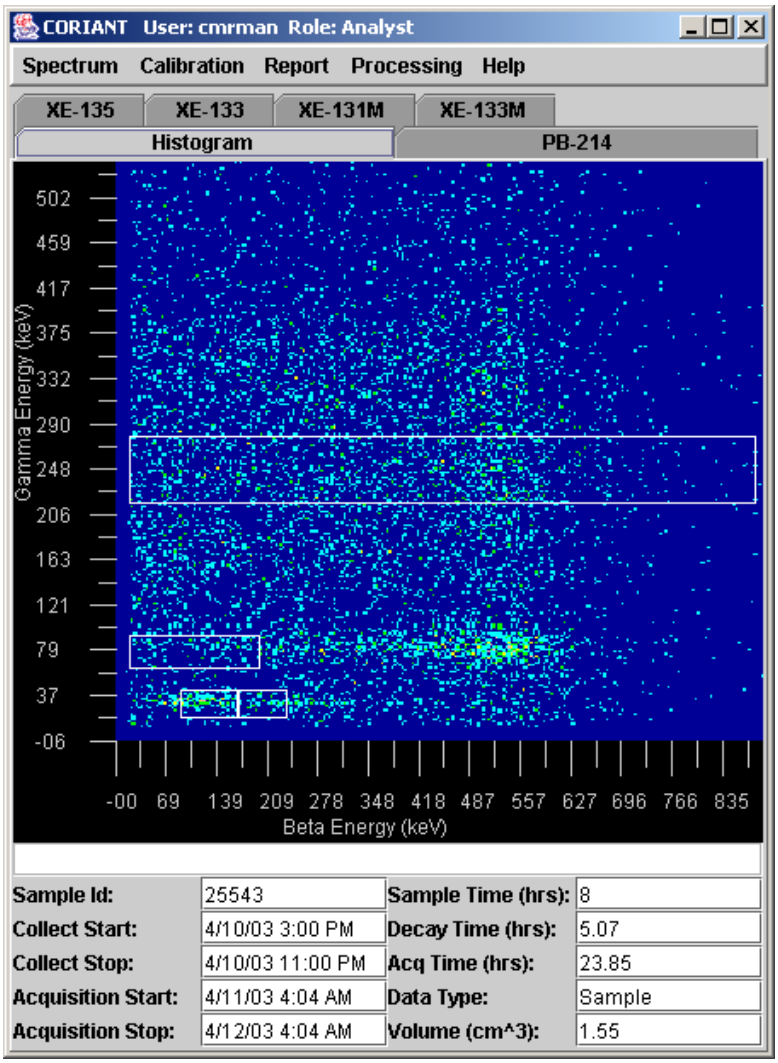


Figure 18. Sample beta-gamma coincidence data

8. The minimum detectable concentration for the testing periods was consistently below the 1 mBq m^{-3} limit for ^{133}Xe. The mean values for each of the sample cells are reported in table 4.

Table 4. Mean ^{133}Xe MDC (mBq m^{-3})

Detector Cell	*Pre-shipment MDC*	*Performance Testing MDC*
1	0.60	0.63
2	0.43	0.40
3	0.56	0.51
4	0.52	0.47

Post Initial Testing

Since completing the initial testing period, early April 2003, the ARSA has experienced two failures that have accumulated a significant amount of downtime. The first failure, due to a thermocouple grounding out intermittently and picking up stray current caused a temperature safety switch to trigger an automatic shutdown of the system. Unfortunately this failure was not a hard fault and at times the system would run for weeks without the fault occurring, other times it would run for hours. The fault initially appeared near the end of April and was not diagnosed for certain until the beginning of July.

The second failure occurred between April and July where a valve failed in the gas processing section of the system. The failure was not immediately evident to the operators and the data quality was severely affected for approximately one week. Typically when a valve fails on the system the flow rate or pressure will be adversely affected that initiates an automatic shutdown. In this case the system ran for several days before the problem was noticed. The valve failure affected the gas processing in the system which caused an exceptionally high level of radon to be in the spectra. The system was diagnosed by examining the SOH data and performing diagnostic procedures remotely. Once the problem was identified the local operators were able to replace the failed valve.

During July 2003 representatives from Veridian traveled to Guangzhou to replace the failed thermocouples and perform any required maintenance on the system. Since the system had seen two failures that created a significant amount of downtime, Veridian found it necessary to perform an inspection of the system. At the time of writing this paper the maintenance visit is scheduled but has not been performed. The system should be repaired within a couple weeks and ready to begin the International Noble Gas Experiment Phase IIIB. During Phase IIIB the system performance and reliability will be scrutinized and compared to the three other systems in the experiment, the French SPALAX, Swedish Sauna, and the Russian ARIX.

First Article, Manufacturing Prototype

In July 2002, Veridian performed a commercial review for possible manufacturing partners for the ARSA system. During this review 17 vendors were contacted of which 4 were requested to submit proposals. The companies were reviewed based on cost, past performance, relevant work within and outside of atmospheric sampling and radiation measurements, as well as manufacturing and management capacity. The AMETEK Corporation, (formerly ORTEC) in Oak Ridge, TN was selected to build the ARSA systems. Currently AMETEK is in the process of building the manufacturing prototype with the guidance of Veridian. Lessons learned during the operation of the ARSA in Virginia and China have been integrated into the baseline package. The first article is scheduled for delivery to the IMS station RN75 in Charlottesville, Virginia in November 2004. Once installed the system will be subjected to a requirements Validation test to be performed by representatives from Sandia National Laboratories. The requirements for the first article are drafted but have not been finalized and are currently being reviewed by U.S. and International experts. Once the first article is found to be acceptable and meet all requirements agreed upon the system drawings and documentation will be updated and the system will be ready to begin low rate production. The development of the ARSA is being managed through a Technical Program Plan that has been developed based on the SMDC version of the DOD 5000 acquisition model.

CONCLUSIONS AND RECOMMENDATIONS

The Automated Radioxenon Sampler Analyzer has been installed in Guangzhou, China since November 2002. The system ran reliably for approximately 6 months before suffering from an intermittent problem related to a failing thermocouple. The only other hard fault seen with the system was a failed valve in the gas processing section. After the system was initially installed it was allowed to run for over a month to determine how the local environment would affect performance. It was found that the radon levels in Guangzhou were significantly greater than in Charlottesville, Virginia, where the system was initially tested. The gas processing portion was optimized remotely by adjusting the timing and temperatures and the radon level was reduced significantly. After remote optimizations were performed a team traveled to Guangzhou to perform on-site tuning activities. Once the tuning was completed the system performance met or exceeded the performance level set in Charlottesville. A short while after the tuning trip was completed the system has not operated reliably due to an intermittent failure and a hard failure. The system is scheduled for repair in late July 2003. Once the system has shown that it is running well and reliably it will enter into the International Noble Gas Experiment Phase IIIB. The experiment will compare the performance of the four systems participating to determine applicability to the International Monitoring System network.

RADIONUCLIDE SOFTWARE INSTALLATION AT THE UNITED STATES NATIONAL DATA CENTER

Joel C. Rynes, Daniel J. Robbins, and Mark Erickson

Veridian

Sponsored by Army Space and Missile Defense Center

Contract No. DTRA01-99-C-0031

ABSTRACT

The United States (US) Army Space and Missile Defense Command (SMDC) has contracted Veridian to develop, test, and install Version 5.1 of the Radionuclide Monitoring System (RMS) software at the US National Data Center (NDC) located at the Air Force Technical Applications Center (AFTAC). The NDC currently uses RMS 5.0 to store and analyze atmospheric radionuclide data received at their facility. Veridian installed this version of software in August 2002. RMS 5.1 is scheduled to be installed in the fall of 2003. This paper describes the improvements and additions included in RMS 5.1. These enhancements can be grouped into three categories and include:

- Data Analysis Tools
  - The **Coriant** software used in the interactive analysis of three-dimensional beta-gamma coincidence data (*e.g.*, ARSA) was matured and hardened to increase usability and functionality of the software. The most notable modifications were the addition of three-dimensional graphing capability, noncoincidence graphing capabilities, and a help menu.
  - Software was added to automatically and interactively process data from the Russian ARIX xenon detection system.
  - The **Radionuclide Ratio Analysis Tool** (RRAT) was enhanced to allow calculations of estimated concentrations for fission products among nuclides that should be present in a sample given a concentration of any single nuclide, a date range, or a scenario.
- Data Management
  - An algorithm was placed at the front end of the RMS software pipeline to only assign samples that meet some intelligent criteria to analysts.
  - The error tracking of the RMS data pipeline was consolidated into a single log allowing pipeline engineers to find and resolve problems more efficiently.
  - A database archiving utility was built to reduce the volume of information stored in the database and to move relative and historic data off-line to a backup system.
  - The **Quality Assurance Tool** (QAT) was added to facilitate the quality control of reviewed radionuclide samples.
- State-of-Health (SOH) Tools
  - The **SOH Viewer** was added to allow users to read and to graphically and tabularly display raw (flat file) SOH data. The **SOH Viewer** can be used either in the field by a station operator or at a data center.
  - **Trendvue** was enhanced to display radioxenon detection system SOH data and to display reports generated at other data centers and received at the NDC (*e.g.*, IDC data). **Trendvue** is used to analyze trends in raw and processed data.
  - A utility was added to automatically and periodically generate and distribute HTML-based reports describing the SOH of the radionuclide component of the International Monitoring System (IMS).
  - A utility was added to automatically and periodically generate and distribute HTML-based reports describing discrepancies between the NDC and the International Data Center (IDC) analysis results.

OBJECTIVE

This paper describes Version 5.1 of the Radionuclide Monitoring System (RMS) software developed at Veridian's Nuclear and Radiological Technology Department that is scheduled to be installed at the Air Force Technical Applications Center (AFTAC) in October 2003. RMS 5.1 contains many improvements to the previous version currently in use at the data center. The enhancements to the RMS software include improvements and additions to many tools plus an expansion of Cascade Summing Correction (CSC) software and additional functions in the Forensic Event Tools (FET) that were added to the RMS suite with version 5.0 (Robbins et al., 2002). In the following sections the new components of the RMS software will be described and the differences between the R5.0 and R5.1 software will be summarized. To keep this paper within the limits for this seminar the functions of the software will be discussed only at a high level.

RESEARCH ACCOMPLISHED

Data Analysis Tools

Coriant is the software application that analyzes coincidence β-γ spectra collected by the Atmospheric Radioxenon Sampler/Analyzer (ARSA). Additional functions were added that make the tool easier to use for analysts. The analysts can now add general comments about samples, view the sample log, and access a help page on the 2-d graph commands. These additional functions will allow more efficient and timely processing of samples. Other capabilities that were added include:

- Capability to review non-coincidence data
- The ability for an analyst to concurrently review data related to a sample histogram
  - Gas background
  - Detector background
  - Most recent prior result
- Capability to calculate gross, net, and critical level counts from a configurable region-of-interest
- Spectrum manipulation commands were improved and documented
- Three-dimensional graphing capability for beta energy versus gamma energy, shown in Figure 1.
- An Open Sample window that displays pertinent, configurable, and sort capable data

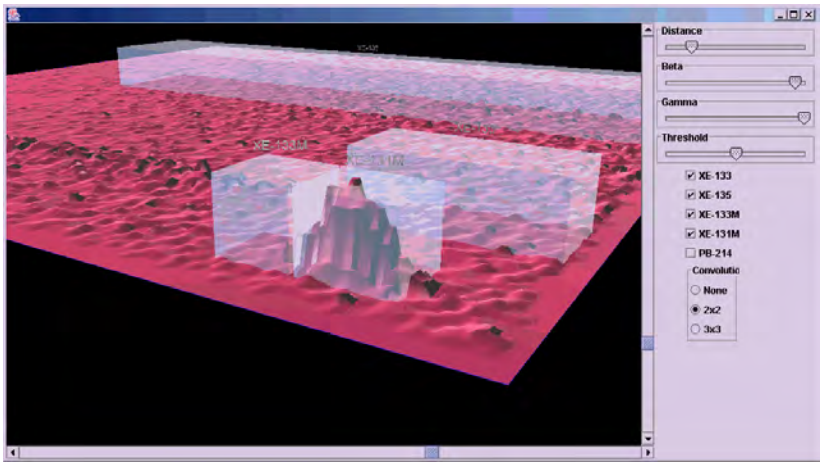


Figure 1. Three dimensional ß-γ plot generated by Coriant.

The ability to remove identification flags from nuclides from analysis results was also added. Certain conditions cause the automatic analysis program to falsely identify xenon isotopes as present in a spectrum. The analyst has been given the ability to manually change the flag on selected isotopes to 0, not identified.

ARIX Data Processing

The Russian designed and built radioxenon sampling and measuring system known as ARIX will soon go into service and that data needs to be analyzed. Vladimir Popov and Sergei Bogachev from the Khlopin Radium Institute in St. Petersburg, Russia, visited the Space and Missile Defense Center for Monitoring Research (SMDCMR) from 23 July to 23 October 2002 as part of the visiting scientist program. During their visit, Popov and Bogachev developed, tested, and documented the automatic and interactive data processing software for the ARIX noble gas detection system (Popov and Bogachhev, 2002). This software was integrated into the RMS software, installed at the SMDCMR, and will be delivered to both the Russian NDC and the data center.

The Radioxenon Detection Software (*rms_arix_DataBase*) begins by reading the processing parameters and 2-D spectral data for a FULL sample spectrum and its corresponding background and preliminary (PREL) spectra. Each spectrum is divided into regions of interest (ROIs) defined by the γ-ray energies. The gross counts in each ROI are calculated by summing the counts per channel. The net counts are calculated by correcting the gross counts for the effects of the Compton continuum background or detector background and interference from other nuclides. The calculated air concentration and minimum detectable concentration (MDC) for each nuclide are determined using the net counts and the processing parameters.

The results of the analysis are stored in the Radionuclide Monitoring System (RMS) database for later use by the Radioxenon characterization software and by interactive tools such as the ARIX graphical user interface (GUI). The analysis results and errors are also written to a log file located on the UNIX file system. Analysts can view this log file or query the database to determine the status of the analysis.

Coincidence Summing Correction

The **Coincidence Summing Correction** (CSC) corrects for the phenomena in which two photons with different energy and from the same source enter the detector and are counted as one photon with the sum of their energies. The algorithm requires a total efficiency calibration for the detector being used. Because it is often difficult to measure the total efficiency of a deployed detector system, the software allows the use of modeled values inserted into the database. Included in RMS 5.0 were modeled values of a generic HPGe detector. RMS 5.1 will include Monte Carlo N-Particle (MCNP) modeled total efficiency calibrations of deployed RASA systems.

In addition, the IDC uses a technique for calculating CSC correction somewhat different than the technique designed for the data center. This technique requires modeled coefficients that will be distributed by the IDC when they get deployed into IDC operations. The options of using the IDC method, the data center method, or no CSC correction now exist as a choice for the user. Results of the various methods may then be compared.

Radionuclide Ratio Analysis Tool

The **Radionuclide Ratio Analysis Tool** (RRAT) is a tool that aids analysis of fission products detected in environmental samples. It uses the ratio of isotopes as evidence for whether the fission products originated in nuclear reactor processes or in the detonation of a nuclear weapon. It was formerly called the Ratio – Source Discrimination Tool.

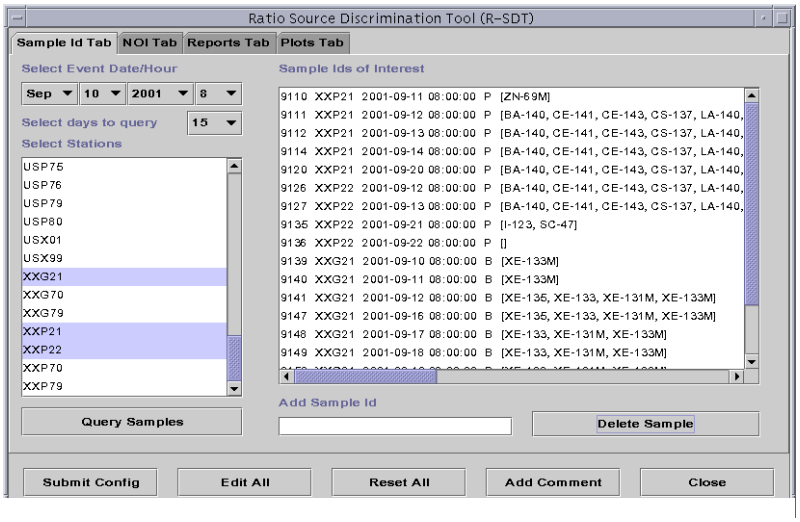


Figure 2. RRAT Sample selection tab

The RRAT (GUI shown in Figure 2) was enhanced to allow the calculation of estimated concentrations for fission products among nuclides that should be present in a sample given a concentration of any single nuclide, a date range, and a production scenario.

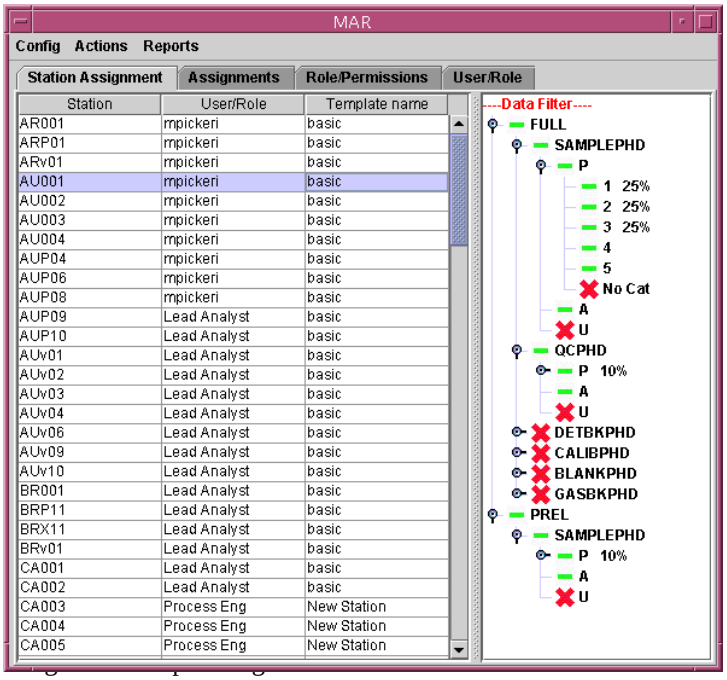
Experience has shown that sometimes, one or two fission product isotopes are found in one or more environmental samples. Either a nuclear explosion or large scale release of radionuclides from a nuclear reactor are expected to result in environmental samples with several isotopes present. The discovery of one or two isotopes immediately raises the question of what other isotopes ought to be in the sample above the minimum detectable concentration (MDC) given the presence of those seen.

The additional function in the RRAT allows the user to select an origin date and time, a period in days after this date and time to search for samples and execute the calculation, and stations in the International Monitoring System

(IMS) network. The tool will produce a list of all samples from these stations during the specified period that contained one or more fission products. If only one or two fission products appear in one or more samples, the user may select one or both of these fission products, a production scenario from a list (plutonium fueled bomb, uranium fueled bomb, light-water reactor operated for one year, and light-water reactor operated for less than a month), and a set of radionuclide ratios. The tool will then perform a simple equation, multiplying the isotope concentrations in the samples by the applicable ratios to find what the concentration of the other isotopes should be in the sample given the selected production scenario. The user can then compare these expected concentrations to the MDCs. While one cannot prove a negative, the lack of multiple fission products in environmental samples when analysis indicates that they should be measured strengthens the argument against the analyzed scenario having occurred. The new tool added to the RRAT allows this analysis to be conducted much more quickly.

Data Management Tools

SmartMAR



The Multiple Analyst Review (MAR) tool (sample assignment tree shown in Figure 3) allows the management of sample analysis through the assignment of spectra to analysts. The version in RMS 5.0 has been improved and renamed the **SmartMAR** in RMS 5.1. The capability to custom configures parameters for sample assignment was added. This allows samples to be assigned:

- Based on sample status, spectral qualifier, data type and auto categorization;
- Based on stations of interest; and
- Randomly for quality control purposes.

Pipeline Diagnostics

Pipeline diagnostics were added to the data processing software. The input processing errors for data files that fail to process are now stored in the database for easier retrieval. Previous input logs are consolidated into one log file, rms. log, with improved error messaging, timestamp, and process identification listings. The pipeline upgrades will allow the pipeline engineer to find and resolve problems more quickly, easily, and efficiently.

Quality Assurance Tool



Figure 4. QAT manual review GUI window.

The **Quality Assurance Tool** (QAT) was added to facilitate the quality control of reviewed radionuclide samples (GUI shown in Figure 4). The QAT is the primary facilitator of quality control (QC) review of radionuclide samples. The QAT provides the Review Officer (RO), the Unit Head (UH), and other users the ability to manually review information about reviewed samples ready for release prior to their release. The QAT is broken into three components:

- **QAT GUI**: Provides the ability to manually review information about samples that have been released by the analyst but have not been released by the QAT Auto Tool. Notification messages can be sent to

selected recipients during the QC review. During this process, samples can be reassigned to the "Processed" status, which reinserts the sample back into the reviewing analyst's assignment queue. This facilitates the RO in executing his oversight responsibility and streamlines the review process

- **QAT Auto**: The QAT Auto automatically releases samples that fall under the categories that do not need to be reviewed by the RO or UH.

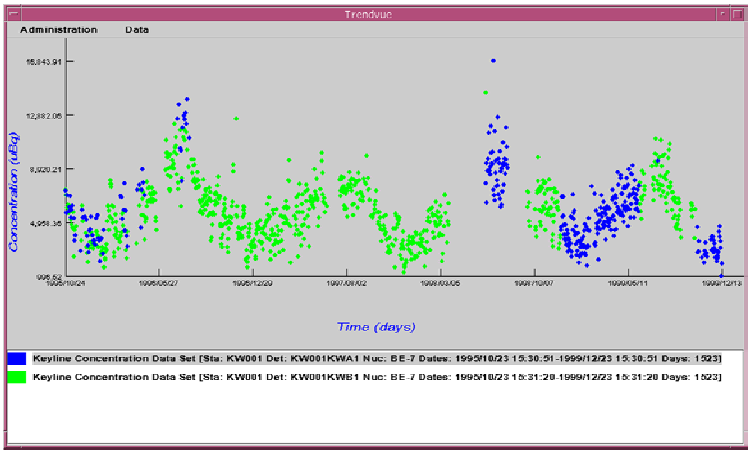
- **QAT Report**: The QAT reports the RO and UH actions. It automates the record keeping process, ensuring accurate records of the QC review process.

State-of-Health (SOH) Tools

SOH Viewer

The **SOH Viewer** opens and reads flat files containing SOH data for Radionuclide Aerosol Sampler/Analyzer (RASA) and ARSA machines. It sorts the data in the files, plots the data on graphs, and performs statistical analysis of the data selected by the user. The SOH Viewer gives scientists and technicians the capability to monitor performance of RASA and ARSA machines during installation, routine operation, and maintenance. It facilitates the prediction and identification of component failures, speeding repairs and improving system reliability. Message data may be reviewed and tabulated or plotted to reveal trends or significant events in the operating history of the RASA or ARSA.

Trendvue



Trendvue is a program that allows the user to sort and plot various sample and SOH data from IMS stations. An example of data plotted on Trendvue is shown in Figure 5. Trendvue was enhanced as follows:

Figure 5. Example of Trendvue data plot.

- Added the ability to simultaneously process, analyze and plot data from multiple detectors at the same station (for example, in the case of an ARSA which has 4 detectors per station)
- Added the ability to view Automated Radionuclide Reports (ARR) and Reviewed Radionuclide Reports (RRR) report data from other data centers.
- Added a Sensor plot to capture the process sensors block in ARSA SOH messages. This graphical tool allows an analyst to more quickly review the data and diagnose problems as well as identify peculiar trends and anomalies**.**

SOH Report

The **SOH Report** tool provides the capability to automatically and periodically send HTML formatted reports, shown in Figure 6, based on the status of the radionuclide network.

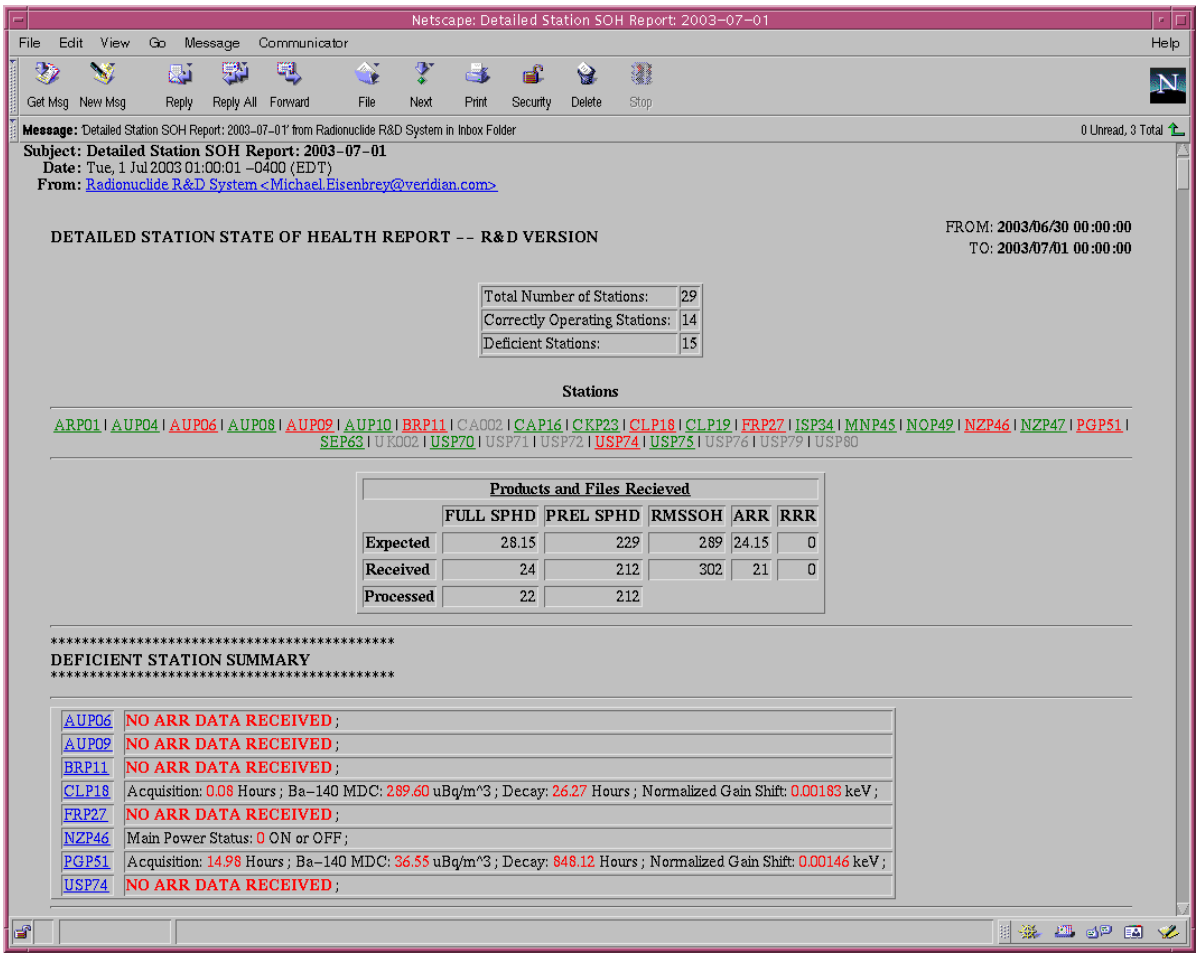


Figure 6. First page of Detailed SOH Report.

The properties of the report include:

- Displays station performance status as 'PASS' or 'FAIL' depending on tests performed on SOH messages and Sample Reports received from each station.
- Report can be generated and sent to subscribers
- Report can be generated based on sample and state of health data

The International Data Center (IDC) and the data center review the same spectra using the same software tools. The RRR and ARR from the two centers should be nearly identical, the only differences occurring due to small variations in calibration parameters used by them. The **SOH report comparison** tool provides the capability to automate comparison of the IDC and US data center RRRs and ARRs, comparing multiple parameters.

CONCLUSIONS AND RECOMMENDATIONS

The software suites described are effective and robust. It is recommended that the software suites enter into operational use at the data center, and that work continue on developing further capabilities and applications for the tools.

REFERENCES

Radionuclide Software Installation at the U.S. National Data Center, D.J. Robbins, J. Rynes, and K.F. Biegalski, *24th Seismic Research Review - Nuclear Explosion Monitoring: Innovation and Integration*, 2002, Ponte Vedra, FL.

Automatic and Interactive Data Processing Software for the ARIX Noble Gas Detection System, V. Popov and S. Bogachev, Space and Missile Defense Center for Monitoring Research, 2002

Infrasound Monitoring

INFRASOUND MONITORING OF ATMOSPHERIC EVENTS

Henry E. Bass,[1] Milton A. Garces,[2] Michael A. Hedlin,[3] Gerald L. D'Spain,[3] John V. Olson,[4] Charles Wilson,[4] Dan Osborne,[4] Eugene T. Herrin,[5] Paul W. Golden,[5] Rodney W. Whitaker,[6] Douglas O. ReVelle,[6] and Joydeep Bhattacharyya[7]

University of Mississippi;[1] University of Hawaii, Manoa;[2] University of California, San Diego;[3] University of Alaska, Fairbanks;[4] Southern Methodist University;[5] Los Alamos National Laboratory;[6] and Science Applications International Corporation[7]

Sponsored by Army Space and Missile Defense Command

Contract No. DASG60-99-C-0018

ABSTRACT

In the second half of the twentieth century there was an intense international effort to establish a global seismic observing system that could reveal the Earth's inner structure and reduce hazards posed by earthquakes. The recent addition of International Monitoring System (IMS) infrasound stations around the globe to complement existing arrays provides an opportunity to perceive with unprecedented fidelity energetic events that take place in our atmosphere as well as dynamic processes in the atmospheric shell that we inhabit. An update on the status of the United States and international infrasound stations will be given. In addition to an increasing number of stations, the quality of stations is also improving with the adoption of modern electronics and large spatial wind filters. This sometimes complicates the comparison of new data with data collected in past decades. Empirical relations developed based upon less capable stations must now be revalidated or modified if required. Some examples will be given. Much of the data is going to a few centralized locations where researchers interested in treaty monitoring, source physics, or propagation can access these well-documented high quality data. Natural infrasonic signals are known to be generated by meteors, volcanic eruptions, earthquakes, landslides, avalanches, glacier calvings, hurricanes, tornadoes, auroral storms, thunderstorms, sprites, littoral processes, and ocean wave fields. A host of human activities add to infrasound in the environment. For the treaty monitoring community these sources represent potential false alarms that severely complicate interpretation of infrasound data. A few examples of alternative uses of the infrasound data will be included. From a purely scientific point of view, infrasound from these sources will provide the basis for better physical modeling and understanding of processes not readily observable by other means. Most infrasound signals recorded by the expanding global system of stations are unexplained. Many of these unexplained events are, no doubt, the result of local or regional human activity but there remains the possibility that this large network will detect events from sources not yet envisioned. Several stations in the expanding infrasound array are co-located with seismic stations providing a new opportunity for data fusion.

OBJECTIVES

This paper describes the current status of the United States infrasound stations that are part of the International Monitoring System. In addition, some signals recorded at these stations will be summarized.

RESEARCH ACCOMPLISHED

The U. S. has responsibility for eight infrasound stations that are to be a part of the IMS. Those stations are:

- I-53US Fairbanks, AK
- I-54US Palmer Station, Ant.
- I-55US Windless Bight, Ant.
- I-56US Newport, WA
- I-57US Pinon Flat, CA
- I-58US Midway Islands
- I-59US Hawaii, HI
- I-60US Wake Island

In addition, the U. S. infrasound team has recently installed I-52GB at Diego Garcia. As these stations are installed, recorded signals are analyzed to gain a better insight into regional noise and false alarms. Many of the false alarms are of scientific interest for reasons unrelated to treaty monitoring.

Fairbanks, AK

The Fairbanks station is an eight-element, outer pentagon, inner triangle array. Each element has a 96 port low impedance pipe noise reducing systems with approximately 1.0 km spacing of the outer elements and 100 meter spacing of the inner elements, from the center of the array. The array is located near the University of Alaska at Fairbanks. Installation of the equipment was completed in early December 2002. Data has been transmitted to the Center for Monitoring Research (now SMDC Monitoring Research) and the IMS since that time.



Figure 1. View of I53 at Fairbanks, AK

The trees and surrounding mountains provide a relatively low wind noise environment so it was a surprise to note that when the array first began to provide data, low frequency signals historically associated with wind flow over mountains (mountain associated waves) and waves generated by aurora were not observed. The problem was traced to the phase response of the Chaparral 5.0 sensors. Changing the leak tube at the backside of the capacitance transducer corrected the problem. The station is now providing low frequency signals of unprecedented fidelity allowing for the study of pulsating aurora.

Palmer Station, Antarctica

The plan is to build a four to eight element array with spacing as allowed by the small islands in the bay.



Figure 2. Unloading equipment during the site survey at Palmer station

Windless Bight, Antarctica

The station consists of an eight-element outer pentagon, inner triangle array each with a 96 drilled matched impedance port pipe noise reduction system with approximately 1.0 km spacing of the outer five elements and 100 meter spacing of the inner elements. The station was installed in February 2001 and has been transmitting data continuously since then. The primary problem with this station has been to get data out through the restricted bandwidth available to the National Science Foundation (NSF).



Figure 3. Photo of the infrasound station at Windless Bight with Mt. Erebus in the background.

Windless Bight derives its name from the absence of wind during most of the season. The absence of wind provides a very low noise floor allowing the installation to take full advantage of the very large dynamic range and noise floor of the Chaparral 5.0 microbaragraph. Mt. Erebus seen in the background of the picture above provides frequent signals to allow for the study of volcanoes and to verify system performance.

Newport, WA

I56US is a four-element array with approximately 1 km spacing. The array was installed in August of 2002 with connection to Vienna in February 2003. The station is located in and near national forest land protected from wind by a very well developed forest. This station has not been transmitting data long enough to determine regional noise sources.



Figure 4. Certification visit at Newport. Note mature forest in background and wind noise filter inlets in foreground.

Pinon Flat, CA

The configuration at Pinon Flat is an eight-element array with 0.15-2 km spacing, one triangle inside a large one. The station has been certified since August 2002. Located in the mountains above Palm Springs, this station is often subject to significant winds. Those winds coupled with very sparse foliage give rise to high wind noise much of the time. For this reason Pinon has been used extensively to test new wind noise reduction approaches. Results of those tests have been reported separately.

Midway Islands

The configuration planned for Midway Islands is an eight-element array with 0.15-2 km spacing. Current plans are to install this station starting in June of 2004.

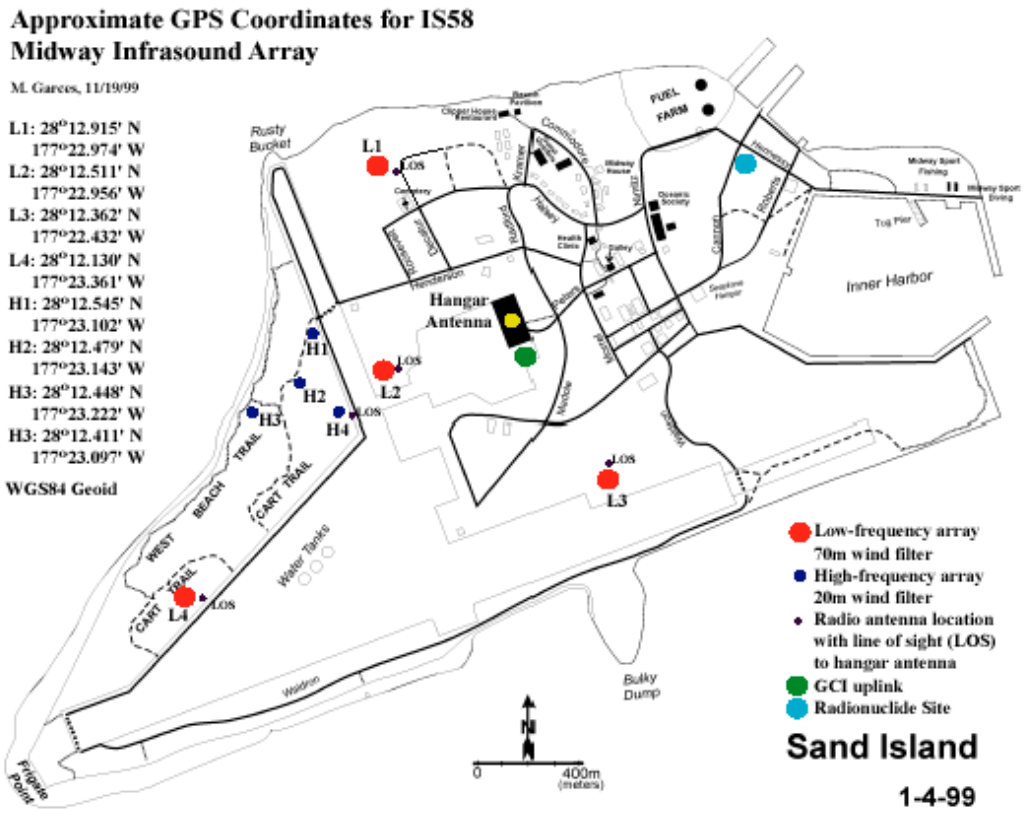


Figure 5. Midway Islands showing planned infrasound array.



Figure 6. Midway Islands is home to the endangered Albatross shown here. Plans for the installation must protect the birds and their environment.

Hawaii

The station near Kona, Hawaii was the first U. S. IMS infrasound station installed and certified (December 2001). The station is installed in an old dense forest on the leeward side of the island. Most of the time there is little or no wind on that side of the island giving rise to a very quiet station. Since the beginning of operations, substantial effort has gone into the characterization of the ambient sound field (Garces and Hetzer, 2002). Most recently, data recorded at this station has been used to better understand microbaroms, which are a major source of background noise in the 0.1 to 0.3 Hz band of the acoustic spectrum.

Wake Island

The Wake Island station is now under construction by Southern Methodist University. The plan is to use an eight-element array with approximate 1 km maximum separation. The installation should be complete by the end of the year.



Figure 7. View towards the Wake Island infrasound station.

The shortage of land, which stays dry, and the lack of foliage were instrumental in the design and location of the array.



Figure 8. Foliage available on Wake Island.

Data Exploitation at I59US

Microbaroms provide a continuous source of infrasound over the entire globe in the frequency range near 0.2 Hz. Automatic detection of nuclear explosions must exclude these continuous signals from consideration and analysis of data should exclude these signals without rejecting information about events of interest. The fact that microbaroms are almost always present might prove useful for infrasound tomography of the atmosphere.

Microbaroms are believed to be generated by the nonlinear interaction of ocean waves (Kibblewhite and Wu, 1996). The theory for predicting the frequency and magnitude of microbaroms (Arendt and Fritz, 2000) has been developed and tested, at least for a few cases (Garces *et al*, 2002b and this issue). With the installation of the infrasound array in Hawaii, data is now available over an extended period of time. In addition, sophisticated models of wave motion in the oceans such as shown in Figure 9 provide the input required to predict the location and magnitude of microbaroms. With that input, the global pressure field as a function of frequency can be computed and cannot be compared to measurements.

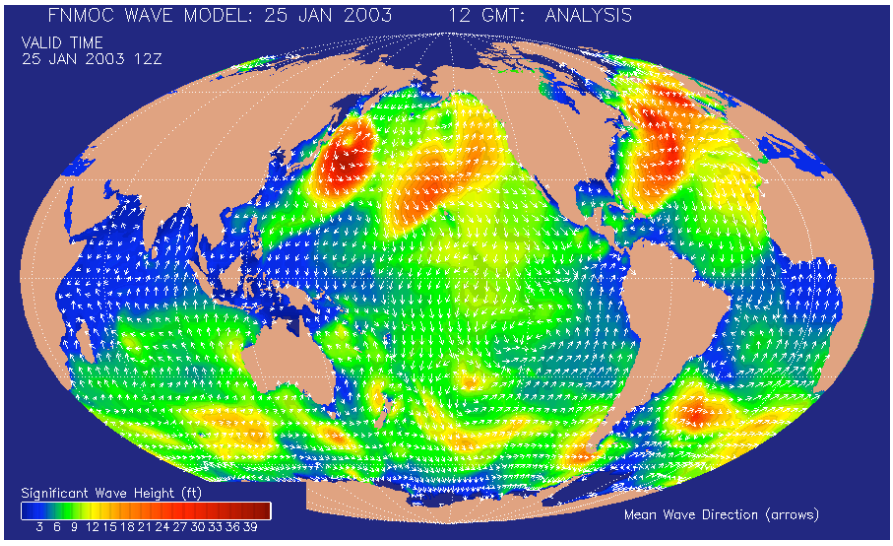


Figure 9. Calculation of wave motion globally.

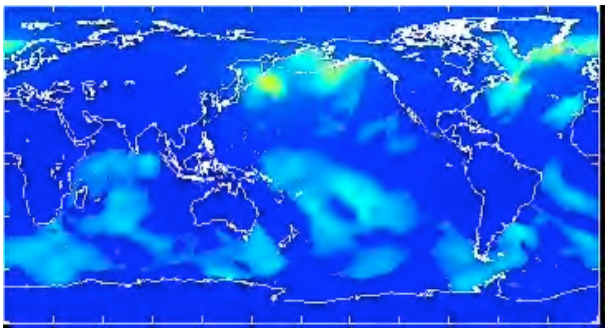


Figure 10. Predicted pressure field at a fixed frequency from microbaroms generated by the wave model in Figure 9.

In the coming months, as more stations come on line to allow better location of the microbaroms, these calculations will be compared to the experimental observations to determine how accurately the microbaroms can be located from independent measurements and removed from event lists to reduce false alarms.

Ground-Truth Data Base

The sensitive and high fidelity infrasound arrays that are a part of the International Monitoring System require data from similar arrays to build a database of events that will allow an analyst or automatic detection system to identify events of interest. Since new IMS stations have been coming into operation, events of different types have been identified from observations other than infrasound. The infrasound recordings from stations in the area have been analyzed, and the part of the signal associated with the known event have been cataloged. Over time, this database will include regional as well as global sources. The events that have been added to the SMDC Monitoring Research database are shown in Figure 11.

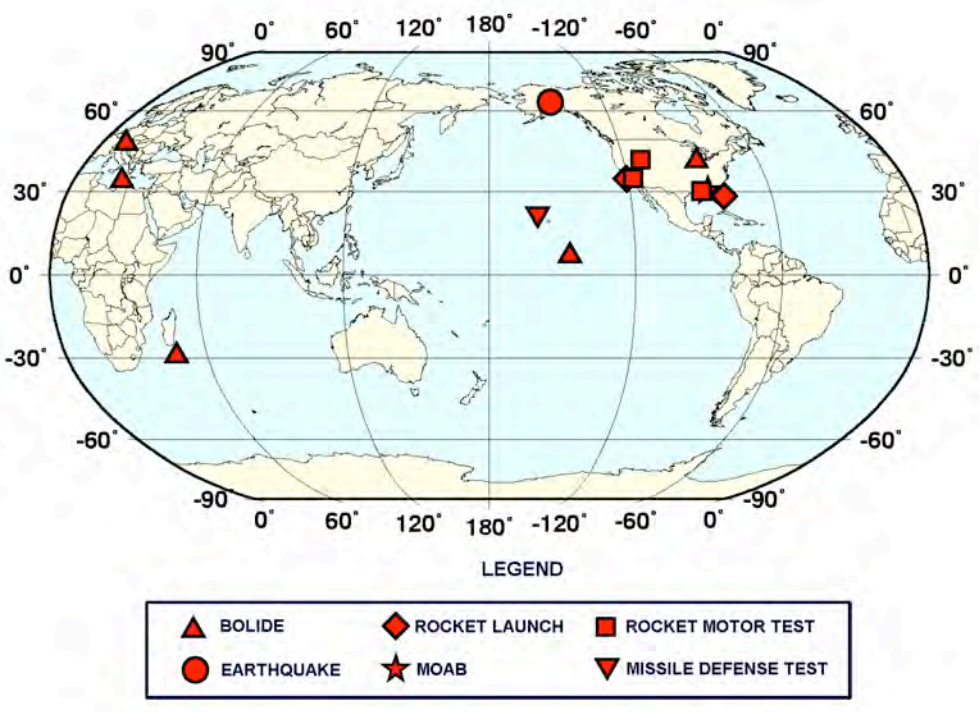


Figure 11. Recent infrasound events collected at SMDC Monitoring Research

Table 1. Ground Truth Data Base Additions

Event Type	Event Information	Detecting Stations						
Bolide	March9_2002	I57US	IS10	I59US	PDIAR	SGAR		
	April6_2002	IS26	DIA					
	June6_2002	IS26						
	July25_2002	I33MG						
	March28_2003	I10CA	Blossom Point					
Shuttle	Columbia_breakup	TXIAR	SGAR	I10CA	PDIAR			
Earthquake	November3_02	I53US	SGAR					
Hawaii Missile Defense Tests	January27_2002	I59US						
	June14_2002	I59US						
	November21_2002	I59US						
Bomb Drop	MOAB	Null observation						
Rocket Launches	November20_2002 (Cape Canaveral)	IS10	TXIAR					
	October14_2002 (Vandenberg)							
Rocket Motor Test	Thiokol (January23_2003)	NVIAR	DLIAR	I57US	TXIAR	I56US		
Chemical Explosion	Watusi (September28_2002)	NTS	NVIAR	SGAR	PDIAR	IS10	DLIAR	LSAR
	Billy-Berclau (March27_2003)	DBN	IS26					

CONCLUSIONS AND RECOMMENDATIONS

The growing number of high quality infrasound stations around the globe provide a unique opportunity to explore the capabilities of this technology for nuclear test monitoring, signal to noise improvement, development of useful automatic detection approaches, and document naturally occurring and man made sources. This global network of stations will also allow scientific applications, potential for early warning of natural events (volcano plume warning for example), and verification of future treaties.

ACKNOWLEDGEMENTS

Dr. Joydeep Bhattacharyya as part of the SMDC Monitoring Research provided most of the ground-truth information along with Figure 11. More information on accessing this database can be obtained from Dr. Bhattacharyya.

REFERENCES

Arendt, S. and D. Fritts (2000), Acoustic Radiation by Ocean Surface Waves, *J. Fluid Mech*, 415, 1-21.

Garces, M. and C. Hetzer, Evaluation of Infrasonic Detection Algorithms, *Proceedings from the 24th Seismic Research Review - Nuclear Explosion Monitoring: Innovation and Integration*, Ponte Vedra, FL, 17-19 September 2002a, LA-UR-02-5048.

Garces, M., C. Hetzer, S. Businger, and M. Willis, Modeling of Microbarom Signals in the Pacific, *Proceedings from the 24th Seismic Research Review - Nuclear Explosion Monitoring: Innovation and Integration*, Ponte Vedra, FL, 17-19 September 2002b, LA-UR-02-5048.

Kibblewhite, A. and Cheng Y. Wu (1996), Wave Interactions as a Seismo-Acoustic Source, *Lecture Notes in Earth Sciences*, Springer-Verlag, Berlin.

DESCRIPTION AND ANALYSIS OF INFRASOUND AND SEISMIC SIGNALS RECORDED FROM THE WATUSI EXPLOSIVE EXPERIMENT, SEPTEMBER 2002

Joydeep Bhattacharyya,[1] Henry E. Bass,[2] Douglas P. Drob,[3] Rodney W. Whitaker,[4]
Douglas O. Revelle,[4] and Thomas D. Sandoval[4]

Science Applications International Corporation;[1] National Center for Physical Acoustics;[2]
Naval Research Laboratory;[3] Los Alamos National Laboratory[4]

Sponsored by Army Space and Missile Defense Command and
National Nuclear Security Administration
Office of Nonproliferation Research and Engineering
Office of Defense Nuclear Nonproliferation

Contract No. DASG60-03-0009[1,2,3] and W-7405-ENG-36[4]

ABSTRACT

The Watusi test was conducted at 21:25 UTC on 28 September 2002 at the Nevada Test Site (NTS). At that time, 19 tons of TNT equivalent were detonated in a cylindrical container that was partially above ground level. The resulting infrasound signal was recorded clearly at seven infrasound stations from nearby station NTS to the International Monitoring System (IMS) station I10CA located 2165 km from the test. No observations were made at two stations closer to the event than I10CA, i.e., TXIAR and I57US, suggesting significant variations in atmospheric conditions and/or station noise levels. The seismic observations were limited to distances less than 250 km though we do not note any significant azimuthal variation of detection in this dataset. Such a distance limitation makes infrasound technology better suited to detect small surface explosions. For each infrasound array, we estimate the arrival time and duration, dominant period and the peak-to-peak amplitude of the detected signals. For the array analysis, the window length and the overlap between consecutive windows and the frequency range of the analysis were adjusted depending on the nature of the signal, the signal-to-noise ratio (*SNR*) and to a certain extent, the distance from the source. The signal duration scales approximately with distance, though we observe no clear relationship between distance and the dominant period of the signal. We undertake forward modeling exercises to verify the ability of atmospheric propagation models to predict the travel times and amplitudes of the infrasound signals. Following ray tracing using realistic atmospheric models, we note that the travel times are slightly better predicted by a real-time environmental model like *G2SRT* compared to a climatological model like *HWM/MSISE-00*, though due to limitations in our modeling tool, we could only use range independent profiles in the former case. Based on the predicted travel times of various infrasound phases, we note that most of our observations are of thermospheric paths. Using time independent parabolic equation calculations we could qualitatively verify the lateral variation of observed amplitudes. The variation of wind corrected amplitude with distance range is consistent with those from large-scale explosions carried out at the White Sands Missile Range. We hope the Watusi data, which has been distributed publicly to the infrasound community will provide a framework for testing theoretical predictions using realistic conditions.

OBJECTIVES

This paper presents the Watusi explosion data and analysis that augments Whitaker *et al*. (2002) with additional infrasound and seismic observations, forward modeling that tests our ability to predict the infrasound signals, and a preliminary analysis of the amplitudes of these observations.

RESEARCH ACCOMPLISHED

The Watusi explosion was detonated at 21:25:17 UTC on of September 28, 2002 at the Nevada Test Site (NTS) (37.099º N, 116.092º W). A cylindrical container that was partially above ground level held the 38,000 pounds (0.019 kT) of TNT equivalent. The acoustic wave was recorded clearly at seven infrasound stations at distances ranging from 45 km (station NTS) to 2,165 km (IMS station I10CA). Signals were not detected at stations I57US at a distance of 390 km and TXIAR at a distance of 1,440 km; both south of the source (Table 1, Figure 1).

Table 1. Infrasound stations used in the analysis.

Station	Location (º)	Distance (km)	Signal Detected	Observed Azimuth(º)
NTS	36.7056 N, 115.9631 W	45	Yes	352.77
SGAR	37.0153 N, 113.6153 W	219	Yes	277.27
NVIAR	38.4296 N, 118.3030 W	244	Yes	128.99
I57US	33.6058 N, 116.4532 W	390	No	
PDIAR	42.7663 N, 109.5939 W	838	Yes	218.06
LSAR	35.8670 N, 106.3340 W	883	Yes	294.08
DLIAR	35.8670 N, 106.3340 W	883	Yes	285.64
TXIAR	29.3338 N, 103.6670 W	1,440	No	
I10CA	50.2010 N, 96.0270 W	2,165	Yes	230.44

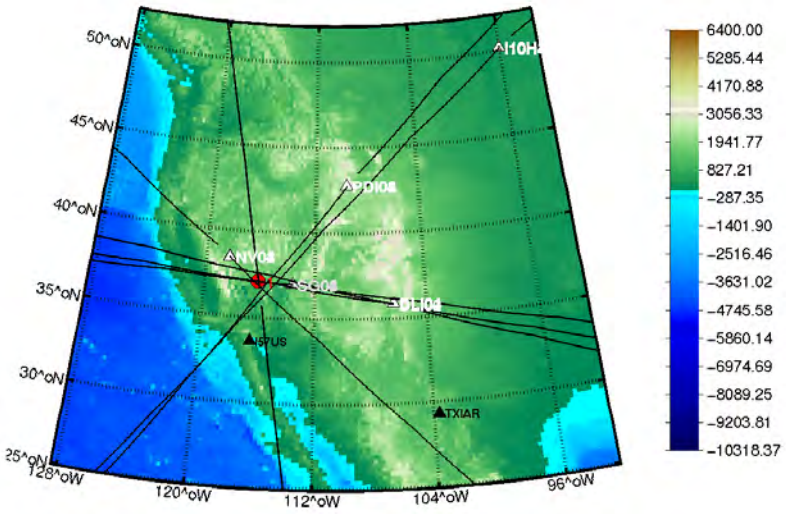


Figure 1. Infrasound stations, the Watusi explosion, and observed azimuths. Elevations are in meters. I57US and TXIAR did not detect Watusi.

Observed Waveforms

Array processing results and samples of the observed waveforms for the nearest (NTS) and furthest (I10CA) stations that clearly recorded signals from the Watusi event are shown in Figure 2. The top panel shows the F-statistic (*Fstat*), which is a measure of the presence of the coherent signal. The second and third panels show the observed signal velocity across the array and the observed back-azimuth to the source. Consistent velocities and back-azimuth estimates, coupled with distinctly higher *Fstat* values identify the start and duration of the detections that are shown as shaded regions in the top three panels. The bottom panel shows examples of filtered waveforms.

The array analysis parameters (window lengths, overlaps, and frequency ranges) were adjusted for optimal results. Typically, the data were filtered between 0.5–3.0 Hz using a 20-s window and a 50% overlap. For the nearby NVIAR and NTS stations, the data were filtered between 1–3 Hz, and for the distant I10CA station, the frequency band was 0.5–2 Hz and a 100-s window was used.

Stations LSAR and DLIAR are nearly co-located (within a few hundred meters of each other) at a distance of 883 km from the source. The energy incident on the two arrays from the explosion was assumed to be the same, but the waveforms at LSAR had higher amplitudes than those at DLIAR did. The LSAR array is smaller than the DLIAR array; so lower correlation values are expected (and observed) for frequencies above 1.5 Hz at DLIAR. The duration of the explosion signal for these two stations was similar.

The explosion signal lasts only a few seconds at NTS (Figure 2) but the duration of the explosion signal at I10CA is several minutes. Longer duration signals are expected at larger distances because acoustic energy is returned to the receiver from different layers of the atmosphere. Although the trace velocities and *Fstat values* were not always stable, the azimuths were reasonably constant and crossed near the source location for each station (Figure 1).

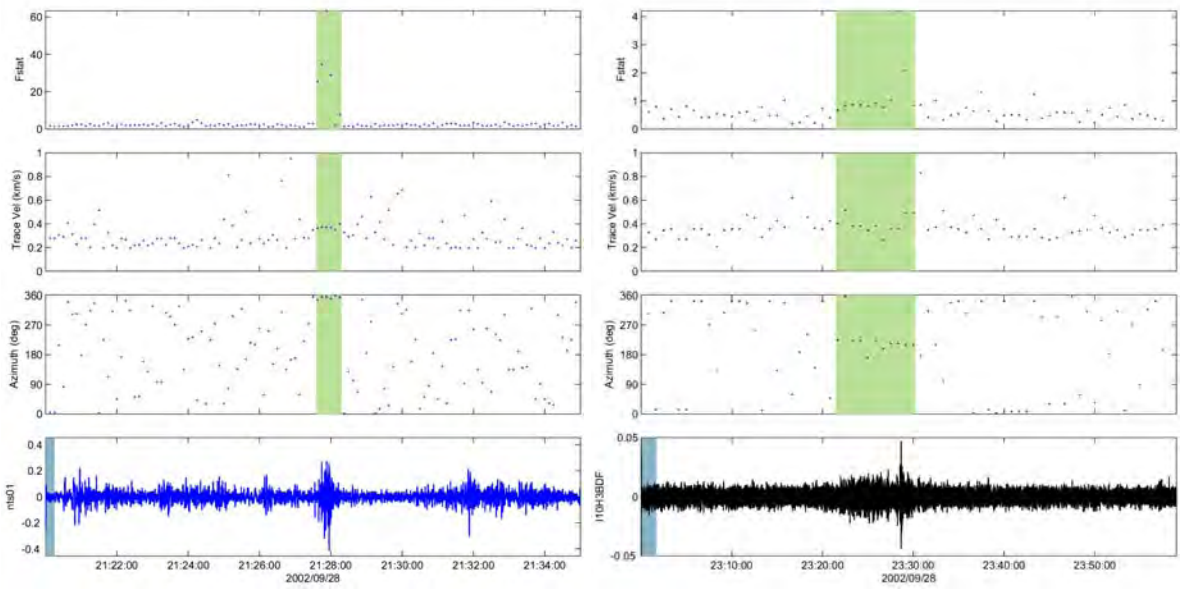


Figure 2. Acoustic signals from the Watusi explosion as recorded at NTS (45 km from the source, left panels) and I10CA (2,165 km from the source, right panels). The NTS data were filtered between 0.5–3.0 Hz and the signal amplitude is in volts. The I10CA data were filtered between 0.5–2.0 Hz and the signal amplitude is in Pascals. The shaded box indicates the detected infrasound signal.

Table 2 gives the maximum single-cycle peak-to-peak signal amplitude measured at each station. The amplitudes from all the sensors at a single station were averaged to determine the amplitudes reported. At PDIAR the signal amplitude from two of the sensors were up to 40% larger than the remaining two sensors. It is not clear if this was caused by different local meteorological conditions or poor calibration. The amplitude estimates from PDIAR are less reliable than the other estimates.

Table 2. Measured and wind-corrected amplitudes for acoustic waveforms.

Station	Measured Amplitude (μbar)	Wind (m/s)	Wind Corrected Amplitude (μbar)	Distance from Source (km)
NTS	3.20			45
SGAR	4.10	11.6	1.60	219
NVIAR	0.35	–6.6	0.62	244
PDIAR	0.44	31.0	0.78	838
LSAR	0.60	11.1	0.24	883
DLIAR	0.70	11.1	0.24	883
I10CA	0.82	27.8	0.13	2,165
TXIAR	-	–4.7	0.06	1,440
I57US	-	–10.0	0.28	390

Table 2 also shows an estimate of the wind-corrected amplitude. Whitaker (1995) developed an empirical expression that relates acoustic pressure, P, in Pascals to the yield, W, in kT, distance, R, in km, and wind velocity, v, in m/sec,

$$\log(P) = 3.37 + 0.68 \log(W) - 1.36 \log(R) + 0.019\, v \qquad (1)$$

The vector wind velocity shown in Table 2 was computed from wind profiles and is the wind in the direction of propagation at 50-km elevation. Figure 3 shows wind-corrected amplitudes as a function of scaled range. The pressure values are given as the maximum peak-to-peak amplitude divided by $10^{(0.019v)}$. The scaled range is given by (*distance*/√(2×*yield*)), where the *yield* for the Watusi explosion is 0.019 kT.

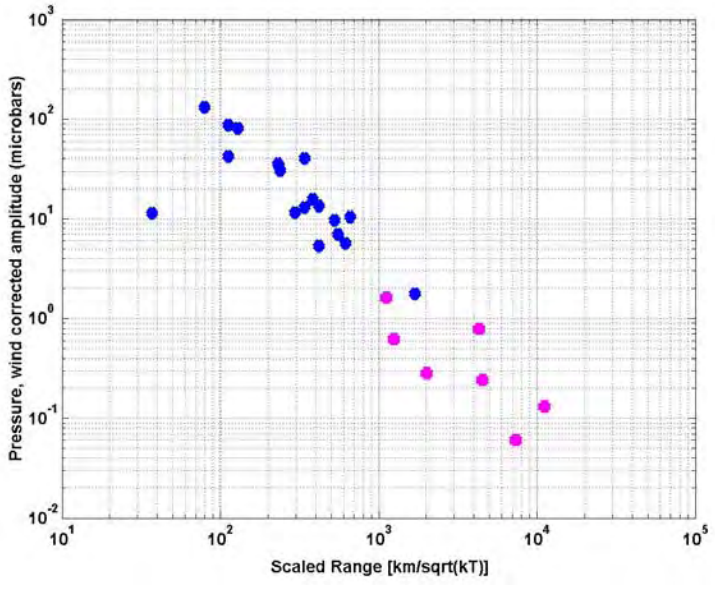


Figure 3. Wind-corrected amplitudes for Watusi (light symbols) and other explosive tests (dark symbols).

The dark symbols in Figure 3 were obtained from Davidson and Whitaker (1992) and from a series of large-scale explosive tests at White Sands Missile Range. The range of infrasonic measurements for those events was from 250 km to 5,300 km. The values for the Watusi experiment are shown by the light symbols.

The Watusi explosion measurements follow the trend of the data from the other explosions plotted in Figure 3. However, the maximum peak-to-peak amplitudes used for this comparison may not be an adequate measure. As the signal propagates it is dispersed by multiple paths and frequency dependent velocity and absorption. The acoustic energy received at any location might be represented well by an integral over the entire waveform.

Meteorological Modeling

Acoustic signal travel times and amplitudes are functions of the meteorological conditions. Near the source, most of the acoustic energy is along a direct path near the ground. At greater distances, however, signals propagate into the stratosphere or thermosphere (or both) and return to the surface if the meteorological conditions are favorable. Accurate travel time prediction requires knowledge of the atmospheric conditions along the propagation path.

Table 3 lists the observed travel time and signal duration as well as travel times computed using different atmospheric models. The predicted travel times were calculated using a ray trace routine (Gibson and Norris, 2002). Two different atmospheric profiles were tested: the Mass Spectrometer and Incoherent Scatter Radar empirical model (NRLMSISE-00) combined with the Horizontal Wind Model (HWM-93), and the Naval Research Laboratory Ground to Space (NRL-G2S) semi-empirical spectral model (Drob *et al*., 2003). For the NRL-G2S calculation, the range-averaged effective sound speed was used. The G column contains the travel times predicted for a wave propagating near the surface (the ground wave). The travel times of these waves are the great circle distance divided by the nominal speed of sound near the surface. The columns labeled S and T are the travel times predicted for returns from the stratosphere and thermosphere, respectively. Two entries for thermospheric arrivals imply that two ray paths are predicted.

Table 3. Observed and predicted acoustic travel times for the Watusi event.

Station	Observed (time, duration)		Predicted (HWM-93/NRLMSISE-00) G	S	T		Predicted (NRL-G2S) G	S	T
NTS	160 s	25 s	136	-	-		113	-	-
SGAR	776 s	35 s	663	-	793		643	-	777
NVIAR	841 s	30 s	740	-	1,153		717		1,146
PDIAR	2,691 s	220 s	2,539	-	3,052		2,445	-	2,805
DLIAR	2,886 s	115 s	2,676	-	3,215	3,668	2,597	*	3,223
LSAR	2,893 s	110 s	2,676	-	3,215	3,668	2,597	*	3,223
I10CA	7,390 s	500 s	6,560	-	7,459	8,197	6,395	-	7,047

* Stratospheric arrivals are seen with less stringent eigen-ray conditions.

Wind and temperature as a function of altitude were predicted along the great circle path (GCP) from source to receiver using both HWM-93/NRLMSISE-00 and NRL-G2S models. Temperature and wind profiles computed from the NRL-G2S model are shown in Figure 4 for the path from Watusi to PDIAR. Atmospheric profiles were computed at ten equally spaced points from the source to the receiver. These profiles were then averaged to produce range-independent profiles for the forward calculations. Average values were used for the NRL-G2S model because the modeling software was limited to range-independent profiles for models other than HWM-93/NRLMSISE-00. The HWM-93/NRLMSISE-00 ray simulations were range-dependent by default.

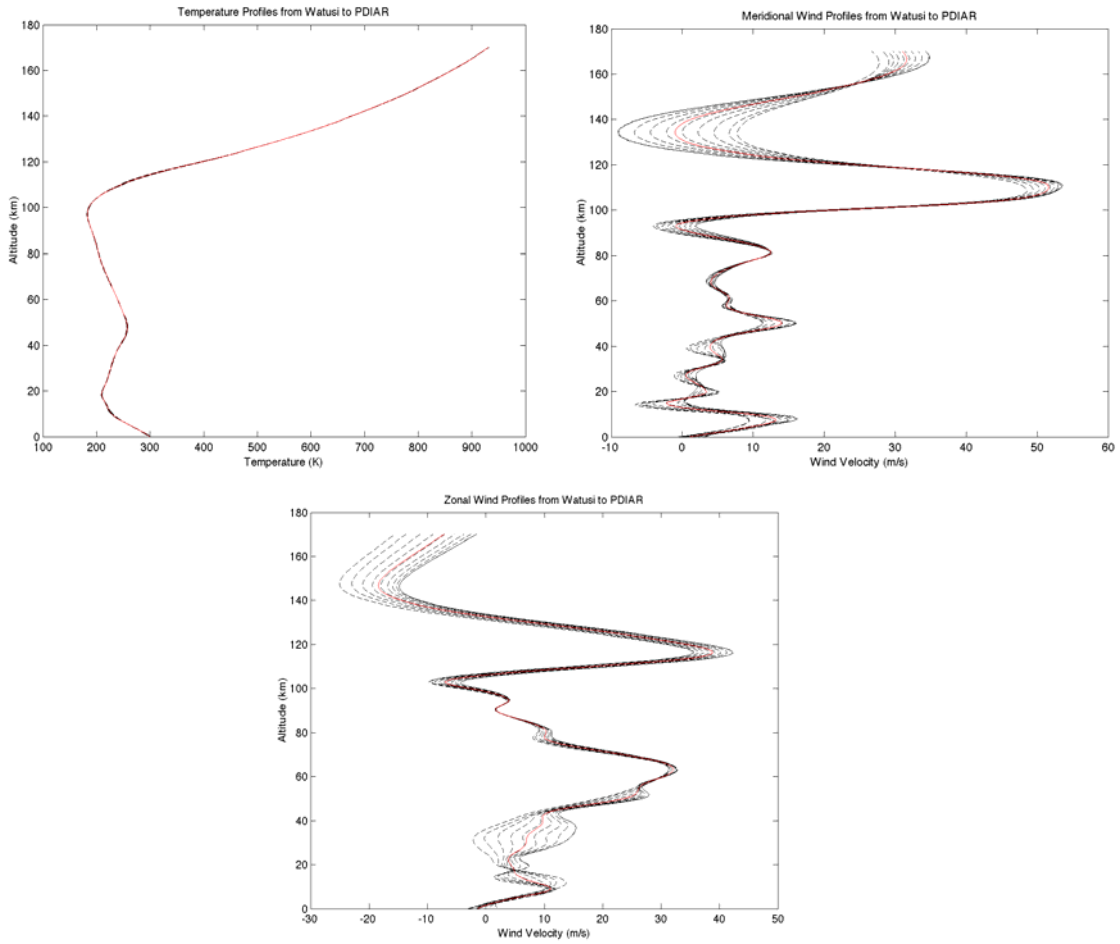


Figure 4. Temperature (upper left), meridional wind speed (upper right), and zonal wind speed (bottom) for ten vertical profiles along the great circle path from source to receiver from model NRL-G2S.

A range-independent approach is questionable because ray-path deviations close to the source can have a significant effect on the travel time. Thus, the calculations based upon range-independent profiles using NRL-G2S are considered preliminary.

The temperature profile from the source to PDIAR does not change dramatically along the great circle path but the winds do (Figure 4). This is common. The wind profiles are largely responsible for the variation in propagation conditions on time scales of several hours to several days. These effects are observed in daily measurements of Concorde bow shock arrivals (Le Pichon *et al.*, 2002). Several detailed theoretical studies have investigated the importance of wind variability on infrasound propagation (Garces *et. al.*, 1999, 2002; Drob *et al.*, 2003).

For the HWM-93 model the predicted meridional wind component below 60 km is zero. This is because climatologically, the average meridional wind velocity *is* near zero. A monthly average is a poor approximation compared to daily data. For example, the HWM model would not predict a tropospheric or stratospheric duct in a predominantly meridional direction. Above 75 km the NRL-G2S and HWM/MSISE specifications are virtually identical.

Signal Amplitudes

The measured amplitudes are reasonably well predicted by the LANL empirical relation (Whitaker, 1995). The amplitude at the receiver can also be predicted from calculations that include full wave effects. The signal loss from a reference point to the measurement point is predicted by Parabolic Equation solutions (Figure 5).

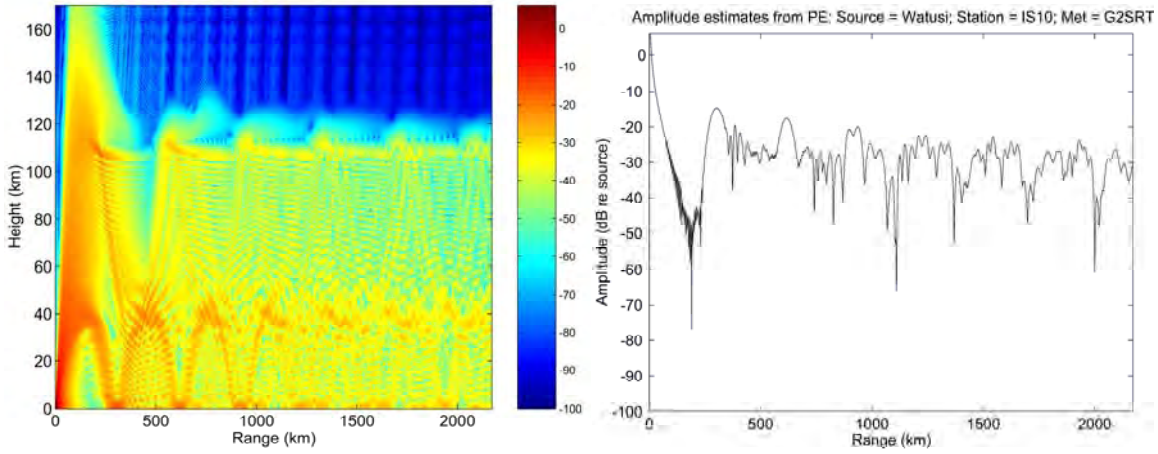


Figure 5. The acoustic field predicted by the PE calculation as a function of height and at the surface. The amplitude units are in dB relative to the amplitude at 10 km from the source. Model NRL-G2S was used for the calculations.

The predicted surface amplitudes qualitatively agree with the observation. Beyond 700 km the amplitude decreases with range very slowly, but inside of 200 km the amplitude decreases dramatically with distance. The interference dip near 200 predicts reduced amplitudes due to turbulence, but the measured signal amplitude at SGAR (219 km) is a little larger than that measured at NTS (45 km). At a range of about 800 km, there are fluctuations with range that are larger than the mean difference between signal amplitudes predicted at ranges of 800 km and 2,200 km. These fluctuations explain the relative amplitudes observed at PDIAR, DLIAR, and I10CA. The measured signal amplitude is smaller at PDIAR than at DLIAR, even though PDIAR is nearer to the event, and the signal amplitude at I10CA is greater than either PDIAR or DLIAR.

Single Station Estimates of Range Using Seismic and Infrasound Data

The IMS infrasound network is sparse. For events with source sizes comparable to Watusi, only one IMS infrasound station will possibly detect the signal. Combining seismic and infrasound data from the same event can improve location estimates when a single infrasound station detects the event.

The Watusi explosion was a relatively small event. The only co-located seismic and infrasound array stations that both recorded signals associated with the explosion were in Mina, Nevada (seismic station NVAR and infrasound station NVIAR). The back-azimuth estimates from the two datasets were consistent. Using t_a as the travel time for the infrasound energy, t_P as the travel time for the seismic P wave, V_a as the velocity of the acoustic wave (300 m/s), and V_P as the average speed of the P wave, the distance from source to receiver is given by equation (2):

$$D = V_a t_a = V_P t_P. \quad (2)$$

The value of V_P used was 6.18 km/s. Although D and t_P were used to estimate V_P in this case, the average seismic velocity near Mina could have been obtained from independent data recordings of nearby earthquakes. The distance to the event is insensitive to the average P-wave velocity (an error of 0.5 km/s would change the distance by about 1 km) so the use of an exact P-wave velocity does not alter the conclusions. The travel-time difference between the P-wave and the acoustic wave, $t_a - t_P$, measured at NVAR was 784 s. Solving for D gives 247.4 km; close to the correct value of 244.5 km. This example illustrates how combined seismic and acoustic sensor technologies can be used to locate (with back-azimuth estimates obtained from infrasound data) relatively small events recorded by a sparse network.

Analysis of Seismic Data

Seismic data from six western US seismic stations were analyzed for the Watusi explosion. Table 4 lists observations from the seismic stations that recorded arrivals from Watusi. Figure 6 shows the geographical distribution of these stations. Seismic arrivals were observed for stations up to about 250 km from the source. Unlike the infrasound observations, there is no clear azimuthal dependence of the seismic observations. Figure 6 shows the seismic arrival at the closest station, TPNV.

Table 4. Observations from the seismic stations recording Watusi.

Station	Lat., Long. (deg)	Arrival Time (GMT)	Dist (km)	BAZ (deg)	V (km/s)	Site
TPNV	36.9488 –116.2495	21:25:22.671	21.8	39.9	3.49	Topopah Spring Nevada
SHP	36.5055 –115.1602	21:25:36.639	106.6	308.7	5.42	Sheep Range, Nevada
TPH	38.0750 –117.2225	21:25:44.138	147.3	136.9	5.42	Tonopah, Nevada
MPM	36.0580 –117.4890	21:25:47.312	169.7	46.8	5.61	Manuel Prospect Mine, California
NEN (Pn)	35.6495 –114.8433	21:25:53.049	196.4	325.3	5.44	Nelson, Southern Nevada
NEN (Sn)	35.6495 –114.8433	21:26:16.739	196.4	325.3	3.28	Nelson, Southern Nevada
NVAR (Pn)	38.4296 –118.3036	21:25:56.572	244.5	126.5	6.18	Mina Array, Nevada
NVAR (Sn)	38.4296 –118.3036	21:26:30.497	244.5	126.5	3.32	Mina Array, Nevada

Of the six seismic stations, NVAR is the only array and the arrivals can be clearly associated to the Watusi event. For the other 3-component stations, the arrival-times and back-azimuths are consistent with Watusi. The group velocity increases with distance because the seismic wave detected at the farther stations has sampled deeper regions of the Earth. The Sn waveform is clearly observable only at the farthest two stations. From this limited sampling, the (V_p/V_s) ratio varies significantly for paths to the north and south of Watusi. Conversely, the Pn travel time can be anomalously early at NVAR

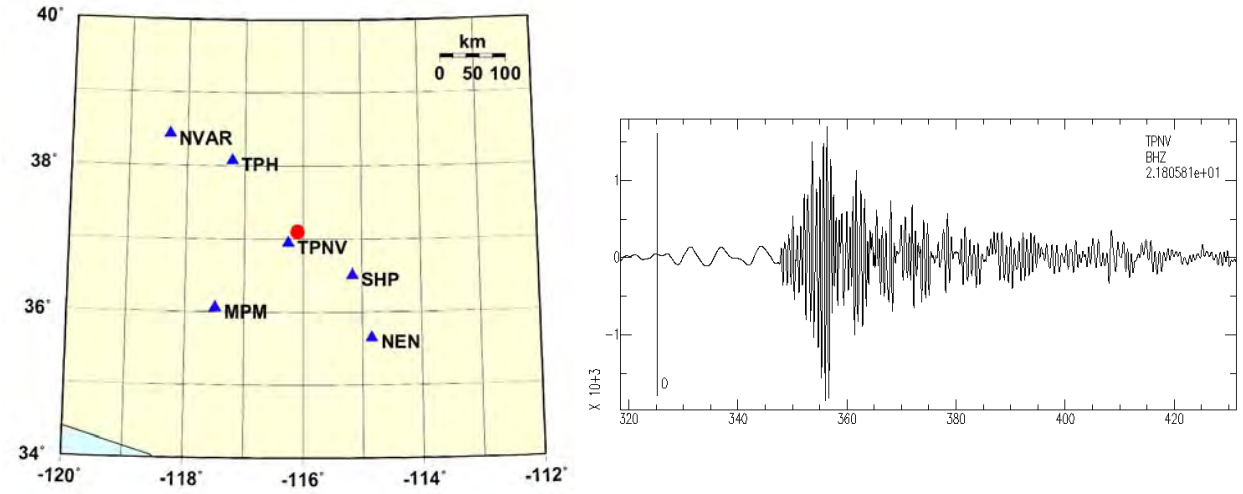


Figure 6. Locations of seismic stations that detected the Watusi event (circle) and an example waveform from station TPNV (21.8 km from the event).

CONCLUSIONS AND RECOMMENDATIONS

The waveform data, well-estimated meteorological profiles, and the ground-truth information make Watusi one of the best-characterized infrasound events available. The tools available to model the signal are not sufficient. For example, the amplitude cannot be predicted other than with an empirical relation. Travel times are only qualitative because the basis for the predicted values, raytracing, makes assumptions that are not fulfilled in this case. Hopefully, the Watusi data will provide an experimental dataset that can be used to test theoretical predictions of more realistic simulations.

Estimating source size

Prior investigators found that the period of the recorded acoustic wave in the far field scales with the size of the charge. Specifically, ReVelle (1980) finds that the observed period at maximum signal amplitude in seconds (T) for stratospheric returns is related to the known source energy (E in kT of TNT) by:

$$\log (E/2) = 3.34 \log (T) - 2.58 \quad (3)$$

For the Watusi data, zero crossings were counted to determine periods of 1 s for SGAR, 1.1 s for PDIAR, 1.2–2 s for NVIAR, and 1.1–1.9 s for I10CA for the un-filtered data. The average period was about 1.35 s, which gives an estimated yield of 0.014 kT. The range of yields varied between 0.0097 and 0.053 kT. The average was close to the true yield but the large variation suggests that result might simply be fortuitous.

Using normal mode calculations to predict infrasonic arrivals

A preliminary analysis of signal propagation using normal mode codes was performed with encouraging results. These codes predict both arrival times and signal amplitudes. A significant improvement in the predicted travel times was obtained using the Pierce normal mode code. However, the observed amplitudes were poorly predicted by the calculations. Research on this topic will benefit from the data produced by the Watusi experiment.

Null observation of Watusi at I57US

The location of the Watusi event was less than 400 km from I57US (Figure 1), which was less than the distance to several of the stations that detected the event. One possible reason for the null observation at I57US is that the wind patterns were not favorable for stratospheric or thermospheric propagation. The noise levels at the station might also have contributed to the null observation. Figure 7 shows the noise spectrum at I57US for the time window between 21:15 and 21:45 on the day of the event. This time window brackets the expected arrival time of the acoustic signal. Between 0.5–3.0 Hz the noise level is about 0.1 Pascal or 1 mbar. The predicted amplitude at I57US is much smaller than 1 mbar (see Table 2), so the absence of the signal for the Watusi explosion at I57US is expected.

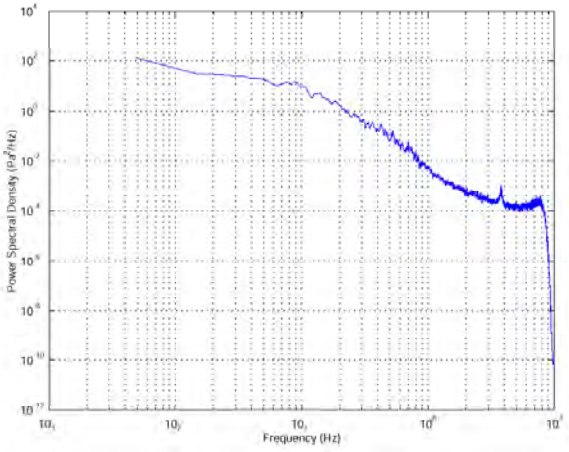


Figure 7. Noise levels at station I57US during the time of Watusi.

Ability of automatic infrasound processing algorithms to detect Watusi

Automated processing routinely analyzes waveforms recorded at SGAR, PDIAR, DLIAR and I10CA stations but only detected the signals at SGAR (even though the signals related to Watusi were clear at all of these stations). This suggests that improvements are needed in the automated detection parameters or their methods. Despite this detection failure, it is encouraging that an explosion with an equivalent yield of only 0.019 kT provided a clearly observable signal at a distance of 2,165 km. With reliable detections at this distance relatively small surface explosions like Watusi can be monitored with a sparse infrasound network.

ACKNOWLEDGEMENTS

Michael Hedlin performed the I57US noise analysis. We thank Bob North and Bob Woodward for comments on this report, Victoria Oancea and Paul Piraino for their help in obtaining both the infrasound and seismic datasets respectively, and Alysa Gorham for formatting the manuscript. Discussions with David Norris and Rob Gibson improved on this analysis.

REFERENCES

Davidson, M. and R. W. Whitaker (1992), "Miser's Gold", LA-12074-MS (available at http://lib-www.lanl.gov/cgi-bin/getfile?00818199.pdf).

Drob, D. P., J.M. Picone, and M.A. Garces (2003), The spatiotemporal variability of infrasound path partitioning, *J. Geophys. Res.*, accepted for publication.

Garces, M., D.P. Drob, and J.M. Picone (2002), A theoretical study of the effects of geomagnetic fluctuations and solar tides on the propagation of infrasonic waves in the upper atmosphere, *Geophys. J. Int.*, 148, 77–87.

Garcés, M., R. Hansen, K. Lindquist, D. Drob, and M. Picone (1999), Variability of the lower atmosphere and its effect on the propagation of infrasonic waves, Proceedings of the 21st, Annual Research Symposium on Monitoring a Comprehensive Test Ban Treaty, US Government Printing Office.

Gibson, R. and D. Norris (Oct 2002), Development of an Infrasound Propagation Modeling Tool Kit, Defense Threat Reduction Agency Technical Report, DTRA-TR-99-47, Ft. Belvoir, VA.

Le Pichon, A., M. Garcés, E. Blanc, M. Barthélémy, and D. Drob, (2002), Acoustic propagation and atmosphere characteristics derived from infrasonic waves generated by the Concorde, *J. Acoust. Soc. Am.*, 111 (1), 629–641.

Picone, J.M., A.E. Hedin, D.P. Drob, and A.C. Aikin (2002), NRLMSISE-00 Empirical model of the atmosphere: statistical comparisons and scientific issues, *J. Geophys. Res.*, 107 (A12): art. no. 1468.

Revelle, D.O. (1980), Interaction of Large Bodies with the Earth's Atmosphere, in *IAU Symposium #90 Solid Particles in the Solar Syste*m, edited by I. Halliday and B.A. McIntosh, D. Reidel Pub Co., Dordrecht, 185–198.

Whitaker, R. (1995), Infrasonic Monitoring, Proceedings of the 17th Annual Seismic Research Symposium in Scottsdale, AZ, September 12–15, 997-1000.

Whitaker, R.W., T.D. Sandoval, and D.O. Revelle (2002), Infrasonic observations of the Watusi explosive test, Infrasound Technology Workshop, De Bilt, The Netherlands.

INFRASOUND SIGNAL LIBRARY

Eric P. Chael[1] and Rodney W. Whitaker[2]

Sandia National Laboratories[1] and Los Alamos National Laboratory[2]

Sponsored by National Nuclear Security Administration
Office of Nonproliferation Research and Engineering
Office of Defense Nuclear Nonproliferation

Contract No. DE-AC04-94AL85000[1] and W-7405-ENG-36[2]

ABSTRACT

The United States conducted over 100 atmospheric nuclear tests at the Nevada Test Site (NTS) from 1951-1962. Beginning with Operation Buster, Sandia National Laboratories (SNL) deployed infrasound sensors to record the air waves across the southwestern United States. In addition, some tests in the South Pacific were monitored, as well as numerous chemical explosions. A typical test was recorded at about a dozen stations from the Control Point on the Nevada Test Site (NTS) to as far away as Pasadena, California. The strip charts registered signals in the frequency band from 0.05 to 30 Hz, and the paper tapes of this data were eventually stored in the archives at Sandia. The NTS atmospheric shots ranged in yield from below 1 ton to 74 kilotons; source altitudes varied from near ground level (including some cratering experiments) to as high as 11 km. More recently, Los Alamos National Laboratory (LANL) has operated infrasound stations in New Mexico and Utah for many years. Over that time, they recorded explosions at White Sands Missile Range and elsewhere, as well as several bolides. The LANL stations provide continuous digital signals, with the earlier data from them recorded on 9-track magnetic tapes. The SNL and LANL archives contain a wealth of information on the source function, yield scaling, weather effects, and regional propagation of infrasound signals from atmospheric explosions. International interest in infrasonic monitoring for the Comprehensive Nuclear-Test-Ban Treaty (CTBT) verification has prompted us to explore these collections and retrieve and digitize numerous recordings. For the NTS events, our initial focus has been on yield scaling and altitude effects. We have selected several low-altitude NTS tests spanning a wide range in yield, as well as the few available high-altitude shots. We will attempt to read the LANL magnetic tapes and transfer their contents to CD-ROM. Once the various signals are in a usable digital form, we will convert them to the established NNSA schema, along with relevant event and station information. The resulting database tables and binary waveform files will be made available to the research community. Where appropriate, the information will be included in the Knowledge Base (KB) under development by the National Nuclear Security Administration (NNSA).

OBJECTIVE

The International Monitoring System (IMS) under construction for the verification of the Comprehensive Nuclear-Test-Ban Treaty includes a network of infrasound stations designed to detect atmospheric explosions. An increasing number of infrasound stations around the world are collecting pressure signals from a wide assortment of atmospheric events and phenomena. However, relatively few records are available for kiloton-size atmospheric explosions, the yield range of greatest concern for CTBT monitoring, because atmospheric testing was discontinued in the early 1960's. Sandia Corporation (subsequently Sandia National Laboratories) recorded pressure signals from most of the atmospheric tests conducted by the United States prior to the Limited Test Ban Treaty, primarily to determine the potential for off-site property damage. The signals at several stations across the Southwest were recorded on strip charts. The paper charts were subsequently stored in Sandia's archives. We have initiated an effort to retrieve many of these records, digitize them, and assemble a 'ground-truth' collection of digital infrasound waveforms from atmospheric nuclear tests of known location, time and size. In addition to this collection, Los Alamos National Laboratory (LANL) will provide infrasound data on a variety of events recorded by their stations since the 1980's. These stations have recorded acoustic signals from several underground tests at the Nevada Test Site (NTS), conventional explosions at White Sands Missile Range, regional earthquakes and bolides. The LANL data include both paper records and 9-track digital tapes. The set of recordings that we assemble will be converted to a standard format and made available to the infrasound research community.

RESEARCH ACCOMPLISHED

Atmospheric Testing at NTS

The U.S. began nuclear testing at the NTS in January 1951. Until the Limited Nuclear Test Ban Treaty (LTBT) outlawed atmospheric testing in 1963, the majority of shots at NTS were conducted above ground. The Department of Energy's list of 'Announced United States Nuclear Events' includes over 100 tests detonated on or above the ground surface. Figure 1a shows the number of such events by year, and Figure 1b shows the number by month. The announced yields of these tests ranged from below 1 ton (*e.g.*, LASSEN) up to 74 kt (HOOD).

The Blast Prediction Unit at Sandia

Atmospheric nuclear tests at NTS in the early 1950's occasionally resulted in the damage to some buildings in Las Vegas and other surrounding communities. Most of the early damage claims filed against the Atomic Energy Commission involved broken windows and cracked plaster. Even this relatively minor damage was unexpected, based on anticipated pressures for the yields and distances involved. Such effects in Las Vegas jeopardized continued operations at NTS. A Blast Prediction Unit (BPU) was formed at Sandia in 1951, and tasked with collecting pressure data from subsequent tests, determining the cause of the damaging pressures, and improving predictions of pressure amplitudes (Reed, 1974).

The first step for the BPU was to develop an infrasound recording system, or microbarograph, suitable for recording a very wide range of overpressures and operating in a variety of environments (Sandia Corp., 1953). The resulting system employed a twisted Bourdon tube pressure sensor, with an adjustable bleed plug for controlling the low-frequency response. As with modern infrasound stations, an array of porous hoses helped to reduce noise from localized turbulence. An adjustable amplifier boosted the sensor signal, then a variable bandpass filter removed noise outside the desired frequency band. The low-frequency cutoff could be set at 0.01, 0.03, 0.1 or 0.3 Hz, and the high-frequency cutoff at 1, 3, 10 or 30 Hz. The filter output went in parallel to two more amplifiers, which resulted in high-gain and low-gain signals with an amplitude ratio of 4. Finally, a strip-chart recorder wrote the signals onto paper tape, along with a timing code. This chart usually ran at 25 mm/sec; pressure at full deflection of the pen (±20 mm) varied from 4 mb to 48 mb, depending on the amplifier setting. Under optimal conditions, the designers believed the system could detect pressure signals as small as 1 mb.

For a typical NTS atmospheric shot in the fifties, the BPU operated approximately 12 infrasound stations in Nevada, Utah and California (Figure 2). Six of these were 'dual stations' with 2 sensors separated by about 1 mile along a line from NTS. These stations measured phase velocities of the wavefronts. This helped in identifying arrivals and provided information on the structure of the upper atmosphere. Several tests in the South Pacific were monitored as well. These were generally larger than the NTS events, so the stations would be installed at greater ranges. All

stations were manned during the tests. One-ton chemical explosions were detonated 1-2 hours prior to each test, to check on the actual propagation conditions and assist the selection of gains. Recording began prior to the shot time, and extended for several minutes past the time of the first arrival. The resulting paper tapes were many meters in length, so they were cumbersome to reproduce. Because of this, the original tapes are the only existing copies of the raw data from these operations.

During the 1960's, and particularly after signing of the LTBT in 1963, acoustic signals from a wider variety of sources were investigated. The BPU recorded many of the larger underground tests. The Plowshare program conducted numerous cratering experiments, using both nuclear and chemical explosions. Studies of sonic booms from aircraft were conducted for National Aeronautics and Space Administration (NASA) and the Air Force, and of signals from underwater high-explosive (HE) explosions for the Navy. HE shots were also used to improve the understanding of source altitude effects, upper atmosphere propagation and surface reflections. In 1974, all available microbarograph records entered the permanent retention archives at Sandia. Reed (1974) provides an overview of the archive contents along with brief comments on the various experiments that were conducted.

Infrasound Data Collected by Los Alamos

Over the duration of the LANL infrasound program a few unique datasets have been collected with direct relevance to explosion monitoring. To date, these datasets have had limited utility due to their format (paper records and/or magnetic tapes with archaic formats). We have selected three of these datasets as candidates for conversion to a standard digital format.

The old AFTAC infrasound network was in operation from 1950-1974 and consisted of 12-25 stations, depending on the recording date. In addition to atmospheric explosions, the network recorded many other types of events, including bolides. Bolides represent the most important impulsive natural event for infrasound, and such events may not be detected by other technologies. Approximately 20 years ago LANL acquired from AFTAC a set of bolide recordings from a limited number of network stations. In all, there are about 100 records. Unfortunately, these recordings are on paper strip charts (digital recording technology was not available) so their utility has been limited. As with the Sandia BPU data, we propose to digitize these records and convert them to established NNSA schema to make them available for analysis and for comparison with events recorded by the IMS infrasound network.

A second LANL dataset of direct use for explosion monitoring is a set of infrasound observations from large-scale explosive tests sponsored by the Defense Nuclear Agency (DNA). These tests used ammonium nitrate and fuel oil (ANFO) as the charge, covered charge weights of 24 – 4,880 tons of ANFO, and were executed from 1981-1993 at White Sands Missile Range (WSMR) in southern New Mexico. The recordings are from permanent stations at Los Alamos, NM, St. George, UT and the NTS, including 2 - 4 mobile stations per event. These recordings represent recent infrasound measurements of kiloton size explosions, and would be similar to the source size of interest in the current era of nonproliferation monitoring. Regrettably, due to the older computer platforms, these data are not in an easily recoverable electronic form. Fortunately, paper records are available for all of the events and these could be digitized and converted to established NNSA schema using the same methods and technology discussed below.

Finally, LANL also has a large number of the data collection tapes from the higher frequency infrasound arrays at St. George and Los Alamos. These tapes hold continuous recordings, not triggered or segmented and so they contain an unknown number and variety of events. In this case electronic media is available, but as 9-track magnetic tapes that are becoming increasingly difficult to read. Fortunately, we believe that Sandia still has the equipment to read these 9-track tapes and will extract the data. We plan to pull from this collection the tapes that would have data on specific events of interest: ANFO events, earthquakes, bolides, underground tests and other impulsive events.

Digitizing the Signals

In preliminary efforts to retrieve pressure signals from the SNL archives, we assessed the quality of the recordings and put together a digitizing system capable of effectively handling them. In general, the archived strip charts are in excellent condition, and have neither faded nor become brittle in the 40+ years since they were produced. Each of the nearly 15,000 tapes was annotated with the shot, station and channel names, along with information on the system gain and filter settings. Every tape includes both high- and low-gain signals, along with a timing signal with 1-second intervals. Reference timing pulses were added to the signals at the shot time and at 5-minute intervals until

the end of the recording, so the locally-generated 1-sec time code can be calibrated with reasonable accuracy. Most of the charts used a recording speed of 25 mm/sec. All began recording before the shot time and the most distant stations in California and Utah continued until about 1200-sec after the shot, in order to capture signals returned from the thermosphere. Individual charts were as long as 30 m, making them inconvenient either to reproduce or to digitize on a standard digitizing table. Instead, we are using a digitizing system originally developed for use with well logs. It employs a continuous-feed gray-scale scanner, which generates a digital image of each chart. Figure 3 shows a portion of the scanned image of a record from the station in Indian Springs, NV for the NTS shot HORNET on March 12, 1955. In this case, the high-gain signal (top trace) clipped at the beginning of the first arrival, while the low-gain trace remained on-scale. Also evident in the figure is the curvature of the amplitude axis caused by the 70-mm length of the pen arm, and we will correct the final digitized signals for the effects of this curvature.

Once a scanned image of a chart is available on the computer, we digitize the signals using a commercial software package from Neuralog, Inc. This program can correct for skewed axes as well as both minor warping and drift along the time axis. The user first defines the time and amplitude axis for the program, then initiates digitization of a trace by clicking on a few points at its beginning. After this, the software attempts to automatically follow the signal along the graph. In general, this process works quite well and saves considerable time. However, it occasionally wanders off the signal, a problem most frequently encountered with faint or high frequency traces. Because of this, the operator must diligently monitor the digitizing process, and occasionally intervene to assist the software through troublesome portions of the record. The software includes some tools to scan the digitized trace and mark certain types of potential errors, such as spikes or inconsistent timing. Once the signals have been satisfactorily digitized, time and amplitude values are written to a file using a specified sampling rate, along with header information and comments entered by the operator. Finally, we will convert the data in these text files to standard binary '.w' files with associated wfdisc database records, as used by the NNSA Knowledge Base.

Representative Data

Initial efforts with the Sandia data on NTS atmospheric tests are focused on providing information on yield scaling and altitude effects. For the first of these, we are digitizing pressure signals from several shots which cover a wide range in source size, as given in the Department of Energy's list of 'Announced United States Nuclear Events'. The selected events were primarily detonated atop a tower, typically 300-500 ft off the ground. Yields range from below 1 ton (LASSEN, 6/5/57) to 43 kt (TURK, 3/7/55). To minimize the effects of seasonal winds, we will concentrate on the events conducted during the spring for this set of data. In addition, the closer stations (*e.g.*, the Control Point (CP) on NTS and Mercury, NV) should be less affected by variations in atmospheric conditions, so these may prove most useful for establishing yield scaling over the available range. Figure 4 shows a record section constructed from the digitized signals from HORNET, 3/12/55. Peak overpressures range from 7.5 mb at CP to 0.1 mb at Las Vegas, NV. Note in the figure that the stations in California and Utah, at distances beyond 200 km, observed stronger arrivals than the Nevada stations approximately 150 km from the source. This is consistent with standard models of acoustic velocity *vs.* altitude, which predict a 'first bounce' return from the stratosphere at a distance of approximately 200 km (see Gutenberg, 1951, Fig. 14).

To address the effects of source altitude on the acoustic arrivals at surface stations, we will retrieve as much data as we can from the few high-altitude NTS tests. The highest of these was HA, 4/6/55, a 3-kt test at an altitude of 36,600 ft. Other NTS tests were detonated at altitudes of 20,000 ft (JOHN) and 1500 ft (several). If feasible, we will also digitize the signals from high-altitude tests over the Pacific, most notably YUCCA at 86,000 ft. The signals from these events should provide useful information for constraining the equivalent yields of bolides and large meteors that sometimes catastrophically disintegrate high in the atmosphere thus, behaving somewhat like concentrated explosions (Chyba *et al.*, 1993). Bolides are likely to represent one of the more common types of impulsive events recorded by the IMS infrasound network, and pose some concern as sources of false alarms.

CONCLUSIONS AND RECOMMENDATIONS

The SNL and LANL collections of pressure signals can provide valuable data for addressing some current research issues in infrasonic monitoring. They contain records from a wide variety of atmospheric events, including nuclear tests, conventional explosions, sonic booms, and bolides. The signals span a similar frequency band to that of the IMS infrasound network. We are digitizing some of the old paper records and we will attempt to extract the available digital data from the magnetic tapes. The data we collect will be converted to a common format, then distributed to the monitoring research community.

REFERENCES

Chyba, C. F., P. J. Thomas and K. J. Zahnle (1993), The 1908 Tunguska explosion: atmospheric disruption of a stony asteroid, *Nature*, 361, 40-44.

Cox, E. F. and J. W. Reed (1957), Long-distance blast predictions, microbarometric measurements, and upper-atmosphere meteorological observations for operations Upshot-Knothole, Castle, and Teapot, *Report* WT-9003, Sandia Corporation, Albuquerque, NM.

Gutenberg, B. (1951), Sound propagation in the atmosphere, in *Compendium of Meteorology*, T. F. Malone (ed.), American Meteorological Society.

Reed, J. W. (1974), Archiving guide to microbarograph records of nuclear and chemical explosion tests, *Report* SLA-74-0210, Sandia Laboratories, Albuquerque, NM.

Sandia Corp. (1953), Microbarograph evaluation report, *Report* SC-2990 (TR), Sandia Corporation, Albuquerque, NM.

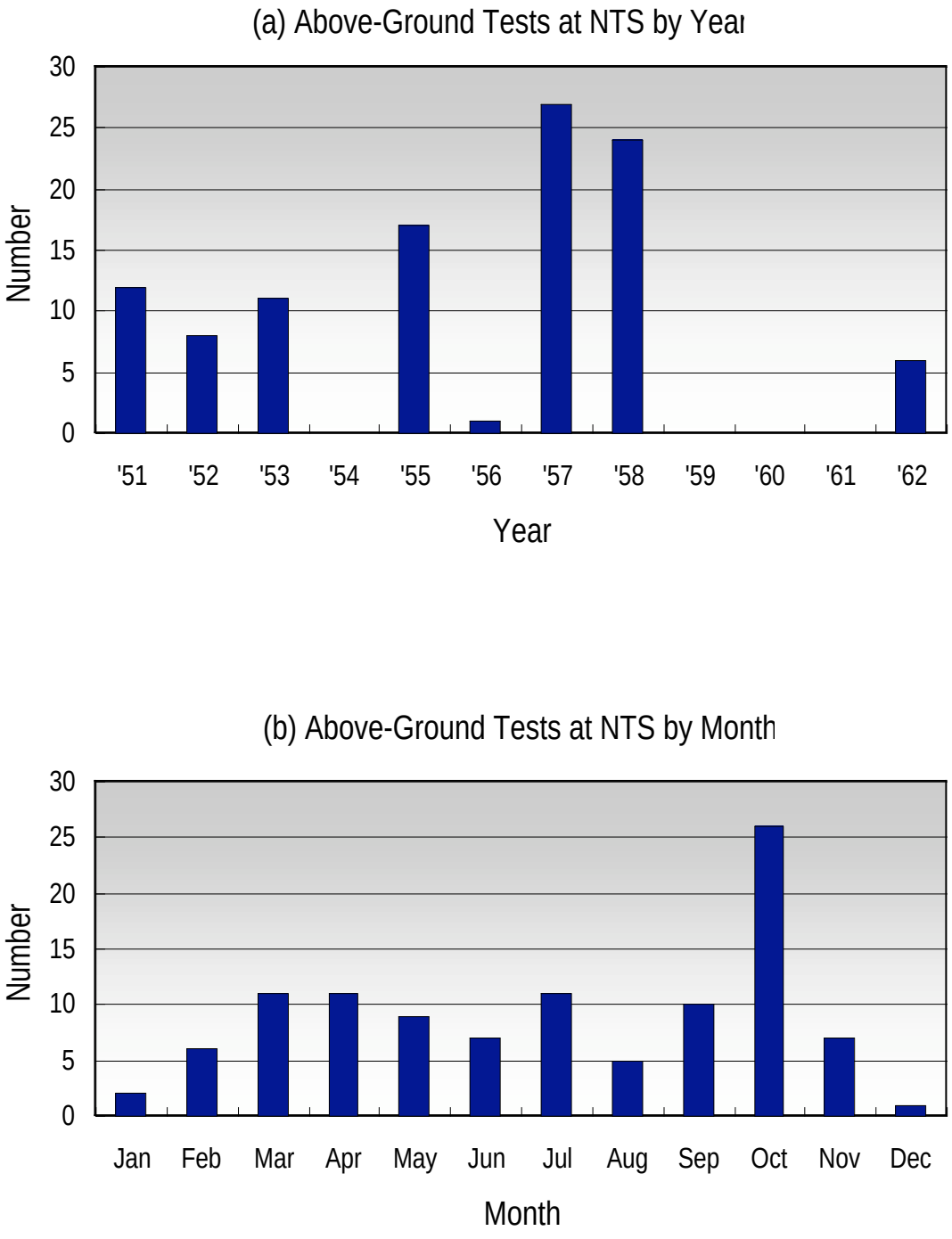


Figure 1. Distributions of announced NTS above-ground tests by year (a) and month (b).

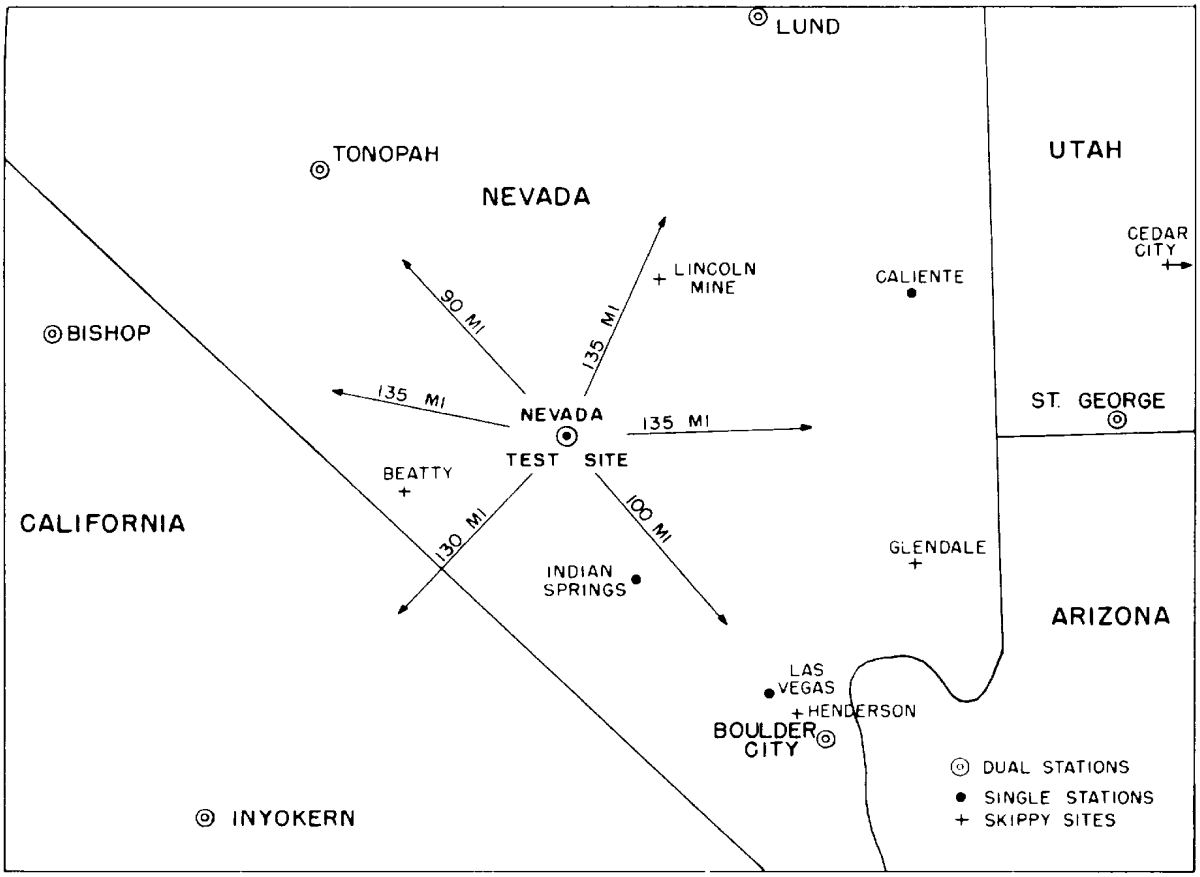


Figure 2. Map of microbarograph station locations used during 1955 (Cox and Reed, 1957).

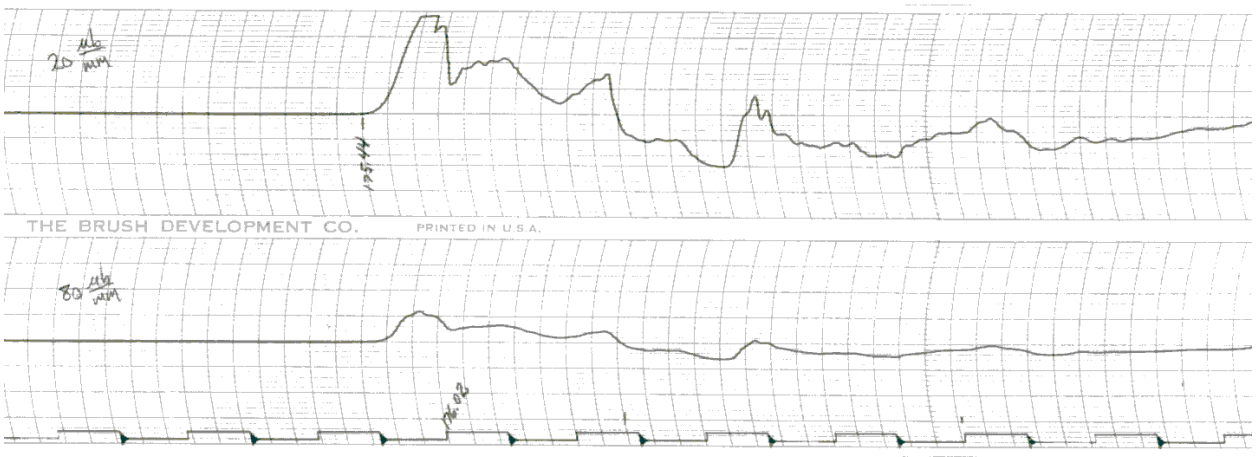


Figure 3. A portion of the strip chart from Indian Springs, NV for the NTS test HORNET, 3/12/1955.

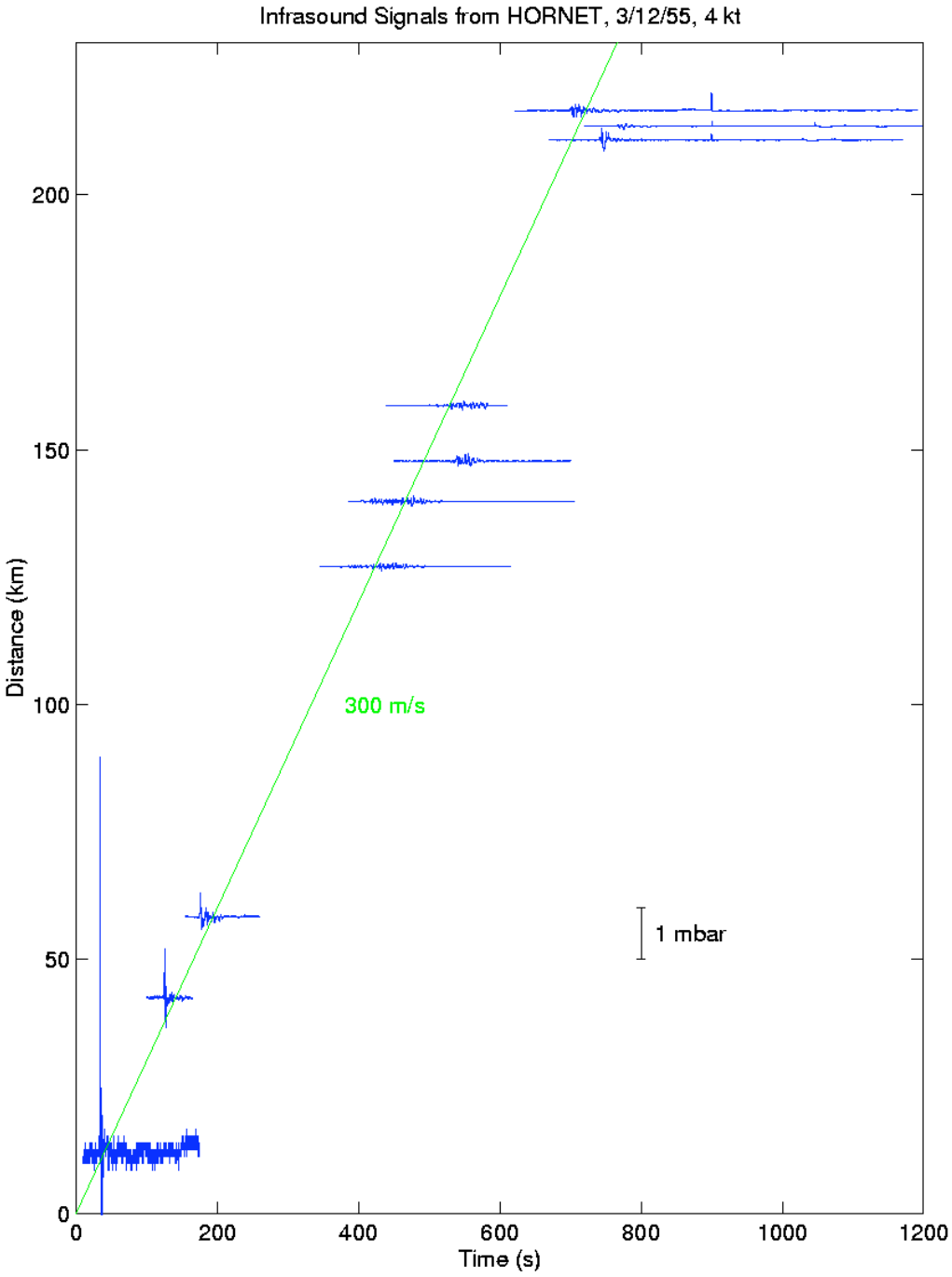


Figure 4. Record section of the pressure signals from HORNET.

DETAILED SPECIFICATIONS OF THE ATMOSPHERE FOR INFRASOUND PROPAGATION MODELING

Douglas P. Drob

Naval Research Laboratory

Sponsored by Defense Threat Reduction Agency

Contract No. DTRA-MIPR-02-2317

ABSTRACT

To model infrasound propagation accurately, detailed knowledge of the background atmospheric state variables—regional wind, temperature, pressure, and density fields from the ground to approximately 170 km—is required. Providing these specifications is a difficult problem, partially because the atmosphere is a complex medium, which varies on time scales from several hours to several months, and over horizontal scales of about 750 km. Several government agencies (e.g., NOAA, NASA, USAF, etc.) build and maintain operational networks of ground-based weather stations and satellites to monitor the lower atmosphere. Using the combination of rigorous statistics and geophysical fluid dynamics, these observations are continuously assimilated into numerical models to produce detailed numerical weather specifications and predications (NWP). These NWP products are typically updated several times daily, have spatial resolutions exceeding 1ºx 1º, and can range from the surface to near 55 km. For the middle and upper atmosphere (>55 km), however, there are currently no operational measurements or NWP products available. Fortunately, sparse and sporadic scientific data have often been available. From these data, reliable empirical atmospheric models can be constructed. Two such models are the Naval Research Laboratory, Mass Spectrometer and Incoherent Scatter Radar (MSIS) model and the Horizontal Wind Model (HWM). The crux of the problem in providing detailed specifications of atmosphere for infrasound propagation modeling lies in combining the various pieces of available information into a single coherent specification which can be applied to an arbitrary time, location, and altitude. To meet this challenge a unique atmospheric specification system is being developed. The Naval Research Laboratory, Ground to Space semi-empirical spectral model (NRL-G2S) produces high-resolution global atmospheric specifications ranging from 0 to 170 km that are seamless and self-consistent. The specifications are currently being produced on a case-by-case basis for ground-truth events, as well as every 6 hours in near real-time. These new specifications introduce a great deal of complexity into infrasound propagation modeling results. This complexity arises from the highly structured spatial and temporal variability of the atmosphere as specified by the historical and near-real-time operational data. It is asserted that it is both necessary and possible to account for this complexity. This is demonstrated with global maps of local ducting fractions calculated from the HWM/MSIS and NRL-G2S models. The resulting information provides a comprehensive picture of the variability and coupling of atmospheric regions as it relates to infrasonic signal propagation. In operational event detection and location applications, these novel calculations might potentially provide a means to assess possible propagation paths quickly.

OBJECTIVES

The objective of this work is to provide detailed specifications of the atmosphere from the ground to space for nuclear explosion monitoring. Infrasound propagation calculations require specifications of the atmospheric state variables U, V, T, *r* and P (the wind components, temperature, mass density, and pressure) from the surface to approximately 170 km. In addition, these specifications are needed in near real-time for operational processing and on a case-by-case basis for the analysis of historical events. These specifications should be global in nature and have enough temporal and spatial resolution to provide a meaningful advantage over the existing climatological models in use. Compared to static propagation mediums, the complexity of the atmosphere seems daunting. It requires a concerted effort to understand, manage, and utilize the required information effectively. In addition, the complexity of this information tends to increase when integrated into propagation codes and monitoring systems. These atmospheric specifications should obviously be robust, self-consistent, and as accurate as possible. One problem is that this information can easily be called into question because the uncertainties needed to qualify the information are often even more complex. An additional general requirement is that the software tools for working with atmospheric specifications be simple, functional, and reliable. Extraneous environmental information may overburden operational monitoring systems or even unduly alter the interpretation of a suspected event.

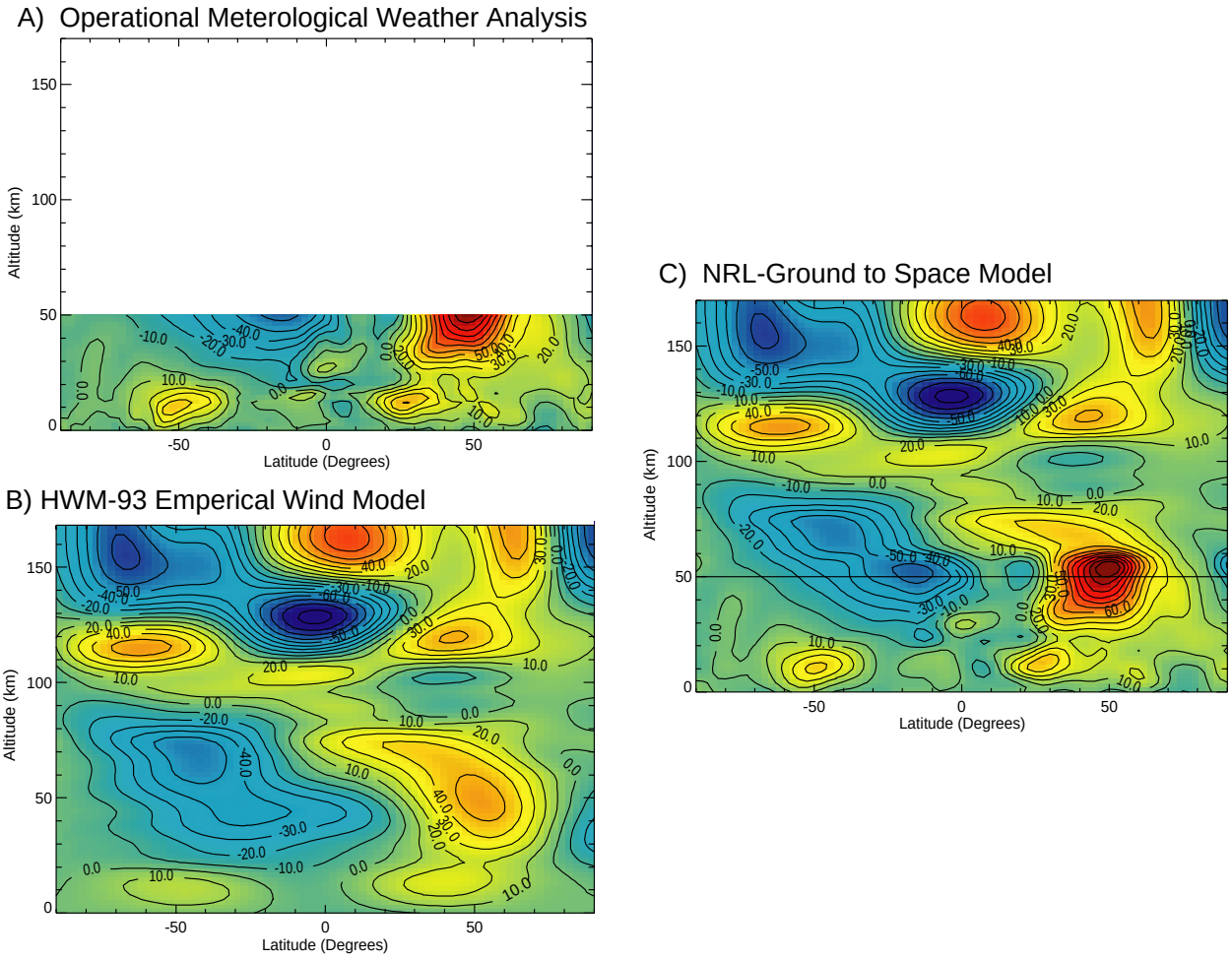


Figure 1. Three typical atmospheric specifications of the eastward wind velocity component (zonal) at 120º E on January 31, 1999, at 12:00 UTC; A) Numerical Weather Predication analysis products (e.g., NOAA-NCEP), B) the HWM-93 empirical wind model, and C) the NRL Ground to Space (G2S) semi-empirical spectral model.

RESEARCH ACCOMPLISHED

To meet these objectives a next-generation atmospheric specification system that fuses state-of-the-art empirical models with operational meteorological analysis products has been developed. The system produces a global current-time specification that is seamless, physically self-consistent, and easy to use. Special care is taken to ensure that no spurious artifacts are introduced into the atmospheric specifications during the data fusion process.

Data Fusion System

Figure 1 illustrates the current state of affairs with respect to available atmospheric data. It shows three different data based specifications for the zonal (eastward) velocity component of the wind as a function of altitude and latitude, at 120º E, for January 31, 1999, 1200 UTC. The zonal wind-field is an important factor in determining whether tropospheric, stratospheric, or thermospheric ducting of infrasound signals occurs. Panel A shows a typical near real-time meteorological analysis specification, here provided by the NASA Global Modeling and Assimilation Office. The near real-time aspect and fidelity of the data is certainly desirable for improving the accuracy of nuclear detections through infrasound. Unfortunately, the specification does not extend to thermospheric altitudes. Panel B shows the most common ground-to-space specification available—the HWM-93 empirical/climatological model (Hedin et al., 1996). While extending over the entire domain, many of the details of the atmospheric state, captured by the near real-time specification, are missing from the climatological model. Panel C shows how the G2S system preserves and extrapolates the details of the meteorological analysis to higher altitudes using the context provided by HWM, while simultaneously combining the two parameter sets into a coherent seamless global field. The salient features of both specifications are discernable in the fused G2S specification results. Our methodology represents an extension of the meteorological specifications into space, or alternatively an assimilation of meteorological data into the empirical models. The G2S system is also capable of assimilating raw observations not yet incorporated into the meteorological specifications or upper atmospheric models. In future versions geophysical fluid dynamic constraints can be applied during the fusion processes to improve the accuracy of the results.

The underlying mathematical formulation of the G2S model is as follows. Depending on the region and nature of available data, the horizontal variations of the state-variables are decomposed into spherical and vector spherical harmonics (SH/VSH). These data fields are typically the meteorological specifications and correspondingly gridded empirical model output fields from the HWM-93/NRLMSISE-00 models (Hedin et al., 1996, Picone et al., 2003). Where we have regularly spaced input data, Fourier transform methods are used to determine the SH/VSH coefficients. Were unevenly sampled ground- and/or satellite- observations available, direct linear-matrix inversion methods could be used to estimate the spectral coefficients. This method includes the use of error weighting and sidesteps the need to interpolate different types of observations having different granularity.

Our system can go one step further in that the thermospheric temperature and density output fields from the NRLMSISE-00 model can be dynamically tuned to agree with historical and operational UV satellite imaging and limb-scanning observations. At a centralized location, information from near real-time UV observations can be used to generate epoch dependent MSIS model correction factors. These factors dynamically renormalize the internal global temperature distribution and output densities of the models. Data from the DMSP-SSULI and SSUSI instruments, to be launched later this year, will be used to implement and validate this technique.

Once the SH/VSH harmonics coefficients are determined at all levels throughout the atmosphere, each spectral coefficient (n,m) is fit with rational B-splines in the vertical direction using an error-weighted least-squares estimation procedure. We perform these operations in a vertical pressure coordinate system. It is easier to impose dynamical constraints during the data assimilation process in this coordinate system. Available meteorological fields are also distributed on pressure surfaces for the same reason. For nuclear monitoring applications, however, the G2S specifications are needed in altitude coordinates rather than on pressure surfaces. This is a minor problem overlooked by operational meteorological centers. To map subsequent results from pressure surfaces to geometric altitude an extra atmospheric state variable is needed. Geopotential height specifies the altitude at which a given pressure level occurs over a given location.

Sample results of the vertical SH/VSH fitting stage, for the single harmonic order (n,m) = (1,3) are shown in Figure 2. Here B_r (1,3) and C_r (1,3) are the real parts of the rotational and solenoidal VSH coefficients of the vector wind fields. T_a (1,3) and Z_a (1,3) are the real parts of the SH coefficients for the temperature and geopotential height

fields, respectively. Once the rational B-spline coefficients have been estimated for all the SH/VSH harmonics out to some spectral order, the coefficient sets are archived and distributed by the NRL assimilation system. The maximum spectral order is ultimately limited by the effective resolution of the raw data sets. Different model resolutions are also used to optimize G2S data storage and transmission requirements.

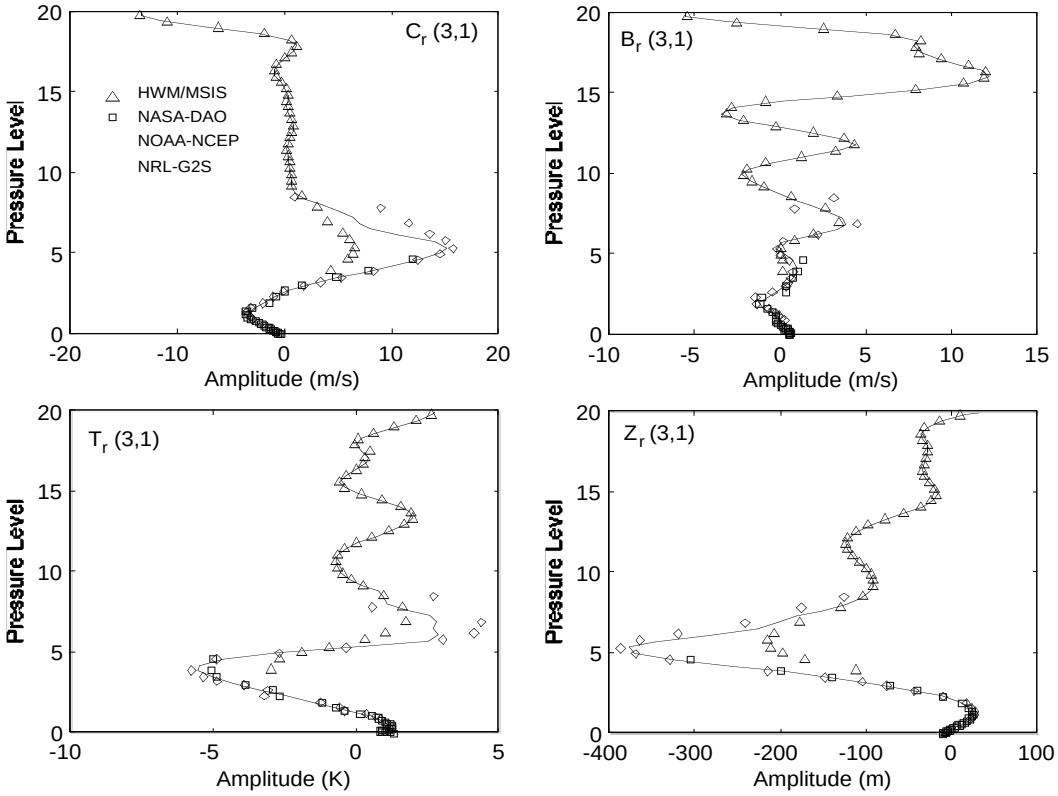


Figure 2. Examples of vertical SH/VSH fitting stage for (n=3, m=1) using transformed January 1, 2003, 12:00 UT data. The raw data sources are from the; NOAA/NCEP reanalysis products extending from 1,000 to 10 mb (0–35 km) (squares), NASA-DAO analysis from 400 to 1 mb (10–50 km) (circles), and the HWM-93 and MSISE-90 empirical models >10 mb (triangles). B_r and C_r are the real parts of the rotational and solenoidal VSH coefficients of the wind field. T_r and Z_r are the real parts for the temperature and geopotential height fields SH coefficients.

Client-Side Software

A set of precompiled software routines that perform the appropriate inverse spectral transforms needed to generate atmospheric specifications from the splined coefficients are provided to G2S model users. Here emphasis has been placed on developing the core environmental data processing routines, rather than graphical user interfaces, as there are several commercial and open source software tools available for visualizing complex 2- and 3-D global data sets. The BBN InfraMAP tool kit is one such example with particular relevance to nuclear monitoring (Gibson and Norris, 2002).

For a given event, or in near real time, individual G2S coefficient files are generated by the assimilation system at NRL-DC and distributed accordingly. A single G2S coefficient file encapsulates all of the information needed to reconstruct the temperature, pressure, total mass density, and the two components of the horizontal wind from 0 to 200 km anywhere over the globe for a given time. The G2S binary data files are also platform independent. This methodology encapsulates and compresses the information providing a very efficient way to store, transmit, and reconstruct large global volumes of environmental data.

The current client software has been optimized to provide vertical atmospheric profiles anywhere over the globe. From within MATLAB, the user first calls an external function library to load a specific G2S coefficient set into shared memory. Then given the input arguments of a spectral truncation and the global coordinates (lat,lon), the routines return vertical profiles of temperature, winds, pressure, and total mass density. From these fields the effective sound speed in the direction of wave propagation can be calculated as; $C_{eff} = sqrt(g*P/r) + V_x*cos(q) + V_y*sin(q)$. Here q is the direction of propagation, V_x is eastward (zonal) wind component, and V_y in the northward (meridional) wind component, g = 1.4 is the approximate ratio of specific heats, P is pressure, and r is the total mass density. Figure 3 shows a sample output from the G2S specification system. The default vertical resolution of the nominal profiles is 1 km and ranges from 0–170 km. Multiple function calls can easily be made to construct 2- and 3-D fields. Precompiled binary libraries - G2Slib.a (Solaris) and G2Sclient.lib (Windows) have also been built for use with FORTRAN and C/C++ source codes.

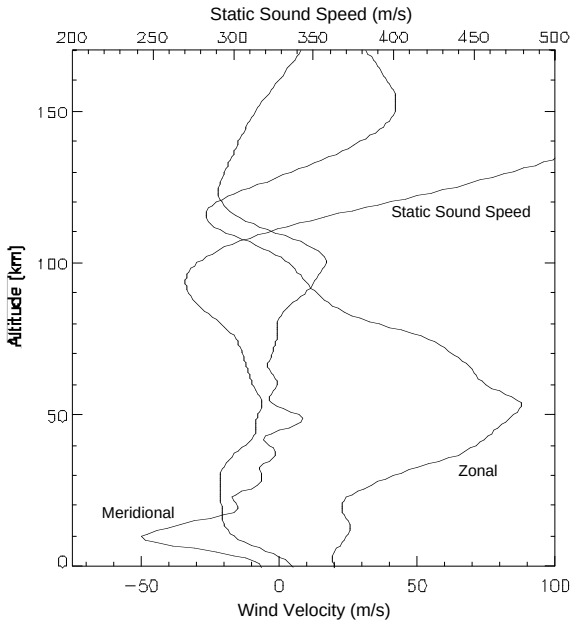


Figure 3. An example output from the G2S specification system outputs.

Additional features of the G2S client software include estimates of the surface altitude relative to mean sea level, i.e., a topographical model. From the client software, it is possible to obtain the corresponding HWM/MSIS model outputs for direct model comparisons. Information on internal G2S file content, such as time stamping and system version numbers can also be accessed with the software. A programmers guide and example codes are also available. Version 1.1 of the client software has been successfully integrated into both the Windows and Solaris versions the Tau9 (Garcés et al. 2002) infrasound propagation software package. The G2S client software is also being integrated into the BBN InfraMAP tool kit (Gibson et al. 2002). Several other institutions have also utilized the G2S client software as a stand-alone package in their research. These efforts will complement existing work to integrate near real-time environmental model capabilities into infrasound propagation modeling calculations.

G2S-E and G2S-RT

For interactive event analysis, we found that it is important to generate a G2S coefficient set that corresponds as closely as possible to the estimated event time. These files are referred to as G2S-E files (E for event). For a variety of different infrasonic ground-truth events covering 1998 to the present, a significant number of G2S-E coefficient files have been generated. G2S-E files are generated for ground-truth events as early as 1992. In special circumstances, it is even possible to go as far back as 1960. The quality of the archived meteorological data, however, is slightly limited relative to recent standards. To investigate ground-truth events such as volcanoes, or analyze signals having travel times greater than a couple hours, a series of files can also be generated. It was found that when providing and working with these G2S coefficient files a triangularly truncated spectral order of 120 (T-

120) is sufficient for infrasound propagation modeling. This spectral resolution translates into a horizontal spatial resolution of 1.5º. At this spectral order, each G2S coefficient file is approximately 20 MB in size.

In addition to the event driven generation of G2S coefficient files, we have developed a prototype operational processing system (G2S-RT) that produces near real-time specifications every 6 hours. The spectral resolution of these files is T-64, having an approximate global spatial resolution of 3º. Each of these G2S-RT data files is roughly 5 MB in size. We have been successfully operating this system since September 2002. The resulting G2S-RT files are pushed to the user's FTP site every 6 hours with a 48-hour delay. Automatically forwarding the data in an operational capacity requires a formal memorandum of agreement with the recipient.

Every 6 hours the G2S system autonomously obtains and archives the operation numerical weather analyses from the NOAA National Centers for Environmental Prediction (NCEP, http://www.ncep.noaa.gov). The NOAA-NCEP specification is generated from all available NOAA, DoD, and international weather monitoring network measurements and provides a detailed snapshot of the state of the entire atmosphere below 35 km at 1ºx1º resolution. A similar operational estimate can be obtained from the Navy's Fleet Numerical Meteorological and Oceanography Center (FNMOC, http://www.fnoc.navy.mil) that runs the Navy Operational Global Atmospheric Prediction System (NOGAPS). The G2S system also collects global pseudo-operational estimates of the stratosphere (10–55 km) from the NASA Global Modeling and Assimilation Office (GMAO, http://polar.gsfc.nasa.gov). This data is available for research purposes on a 24-hour delay. As with the NOAA and NOGAPS specifications, the NASA-GMAO specifications represent a synthesis of measurements from available NOAA, DoD, and NASA sensors. Finally, daily bulletins containing the measured solar 10.7 cm-1 radio flux ($F_{10.7}$) and geomagnetic activity parameters (A_p) are obtain from the NOAA/USAF Space Environment Center (SEC, http://www.sec.noaa.gov). These parameters are crucial inputs into the NRLMSISE-00 and HWM-93 portion of the G2S-RT specifications.

Model Validation Studies

Several infrasonic validation studies of the G2S model have been performed (e.g., Bhattacharyya et al., 2003) and several are ongoing. It is important that these studies cover a wide range of atmospheric configurations. In some cases the instantaneous atmospheric state will be close to its climatological state, and no differences in infrasound propagation characteristics (e.g., travel times) will be observed between calculations made with climatological models and those made from more detailed specifications. In other instances, things will be quite different.

In this symposium paper, the importance of accounting for topography and including a detailed lower atmosphere is illustrated by means of two simple comparative calculations. In the first calculation, the percentage of infrasonic energy (or ray surface area) emitted by a point source, which is transmitted though the various ducts, is calculated for the G2S and standard HWM/MSIS atmospheric specifications.

Figure 4 shows the ray turning height (z_{max}) for a hemispherical set of acoustics rays as a function of initial launch azimuth and elevation. The source was located at the surface and the atmospheric specifications shown in Figure 3 were used. Four distinct propagation modes are evident; those rays ducted in the troposphere below about 16 km (dark blue), those ducted in the stratosphere around 40–55 km (light blue), those ducted in the lower thermosphere around 110–160 km (orange), and those escaping (transparent). A local energy partitioning fraction for each of the atmospheric ducts can be defined as the total surface area of each subgroup or duct. In this example, 7.7 % of the radiated infrasound energy propagates in the troposphere, 13.2 % in the stratosphere, 61.6 % in the thermosphere, and 17.5 % escapes into the upper thermosphere. The boundaries of the four ducts are defined as; $z_{max} < 20$ km (tropospheric), 20 km $< z_{max} < 70$ km (stratospheric), $70 < z_{max} < 165$ km (thermospheric), $z_{max} > 165$ (escape) where the altitude z is defined as true geodetic altitude, relative to mean sea level.

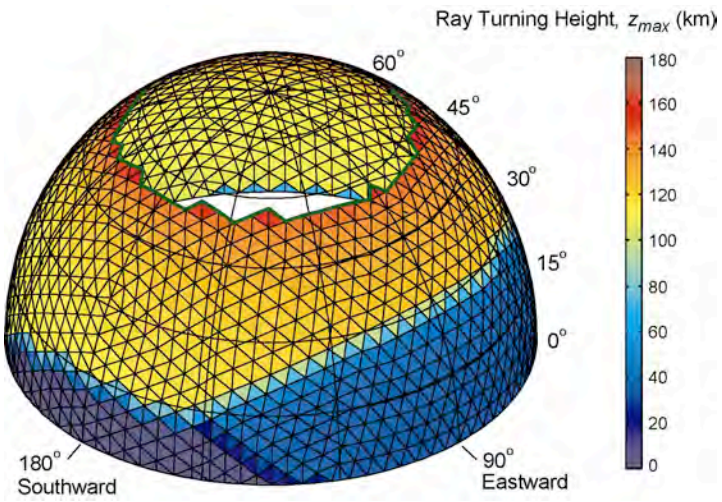


Figure 4. The turning height (z_{max}) of 2592 infrasound ray elements from an idealized isotropically radiating surface source. The ray turning heights are displayed as a function of the initial launch azimuth and elevation. The source origin is located at the center of the tessellated sphere.

Having now defined a local partitioning fraction, the calculations are preformed over a global ensemble of idealized sources to produce morphological global maps of these fractions. These maps indicate regions where tropospheric and stratospheric ducting is occurring. Figure 5 shows the global tropospheric, stratospheric, and thermospheric ducting fractions for February 27, 2000 made using; (a) the HWM-93/NRLMSISE-00 models without topography, (b) the HWM/MSIS models accounting for topography, and (c) the complete G2S atmospheric specifications including topography. A separate color scale for each duct has been defined.

While, the HWM/MSIS and NRL-G2S calculations are qualitatively similar on a global scale, there are appreciable differences on regional scales, particularly in the tropospheric ducting fractions. For all cases, the ducting fractions calculated through the HWM/MSIS models indicates that minimal tropospheric ducting exists (< 2%) in stark contrast to the G2S results. This is no surprise. The meteorological phenomenon responsible for tropospheric ducting tends toward zero when averaged over the spatiotemporal scales of the empirical models (see for example figure 7). Similar differences exist in the amounts of stratospheric ducting predicted. This difference is important because the net propagation speeds (celerity) in the tropospheric and stratospheric ducts can be significantly faster than for the thermospheric ducts. Improper phase identification would lead to errors in source locations through erroneous travel time estimates and could overwhelm operational monitoring systems with false detections.

Additionally, the meteorological specifications (e.g., NOAA-NCEP), and the HWM/MSIS and NRL-G2S models typically provide output fields at altitudes relative to mean sea level that may actually be situated below the surface of the earth. When performing infrasound propagation calculations, it is important to avoid using this part of the specifications. Relative to the calculations in Figure 5(a), the resulting ducting fractions in (b) and (c) show that infrasound originating on the Tibetan Plateau, Antarctica, and Greenland exhibits much more lower atmospheric ducting than in surrounding regions. This is especially true over Antarctica.

For high-yield events where signals travel halfway around the globe, the differences between the climatological and near real-time models may be negligible; however, for low-yield events where propagation is limited to isolated regions, the differences discussed above become important. A comprehensive discussion of the global morphology of infrasound propagation can be found in Drob et al. (2003).

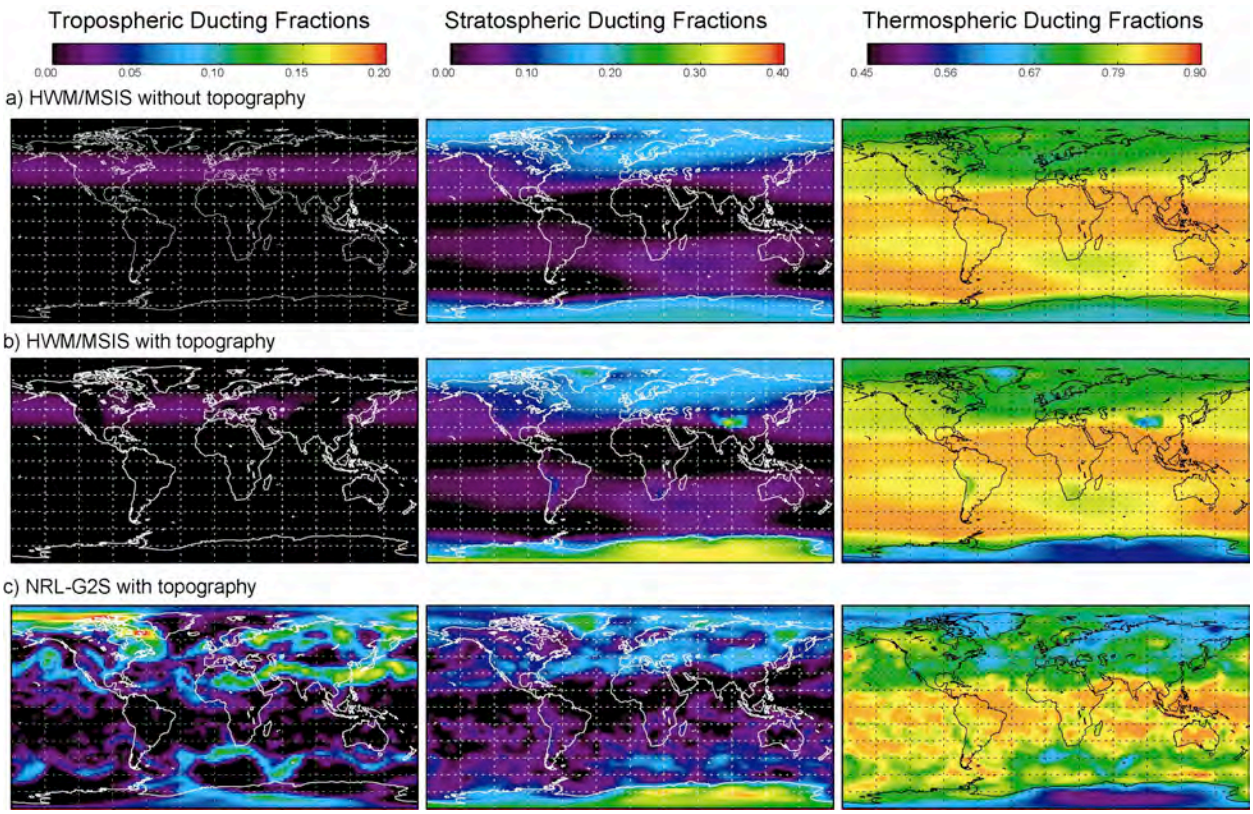


Figure 5. The February 27, 2000, 06:00 UTC tropospheric, stratospheric and thermospheric ducting fractions for a global ensemble of idealized isotropically radiating surface sources using various model assumptions. The first row (a) shows the ducting fractions calculated using the HWM/MSIS empirical model without topography. The second row (b) shows the fractions calculated using the HWM/MSIS empirical model accounting for topography. The last row (c) shows the fractions calculated using the NRL-G2S model including for topography.

A second series of calculations was performed to illustrate the behavior of infrasound propagation characteristics resulting from the day-to-day variability of the lower atmosphere as shown earlier by Garcés et al., (1999) and Le Pichon (2002). Acoustic ray-turning heights, single skip travel times, ranges, and celerity were calculated with a simple ray-tracing code (Drob et al., 2003) using both the HWM-93/NRLMSISE-00 and G2S models. The calculations were done for the first 25 days of January 2003 (00:00 UT) for an infrasound array arbitrarily located in the Southwest United States. Results from two arrival azimuths are presented in Figures 6 and 7. Figure 6 shows the corresponding HWM and G2S zonal wind profiles, derived ray-turning heights, and the effective celerity for eastward propagating infrasound signals. Figure 7 shows the corresponding HWM-93 and G2S meridional winds, ray-turning heights, and celerity for northward propagating infrasound signals.

Note the differences between the HWM/MSIS and G2S derived celerity curves. These differences are primarily caused by differences in the background wind component along the direction of propagation. For northward propagation, the calculated monthly average propagation characteristics are generally similar for both the empirical and G2S models, but some differences exist. For example, the empirical models do not predict the occasional occurrence of a northward stratospheric duct. Additional calculations are needed to quantify this. The estimated variances are, however, obviously different. For the eastward propagating waves, the estimated monthly average celerity curves also appear to be slightly different. On the other hand, the estimated variances are very different. These calculations highlight the importance of accounting for the day-to-day variability of the lower atmosphere. As a first step to account for this in current operational monitoring systems, the estimated monthly variances from the G2S calculations shown here could be used in conjunction with static climatologically derived static travel-time tables. Ultimately, near real-time G2S specification derived travel-time tables should be used operationally.

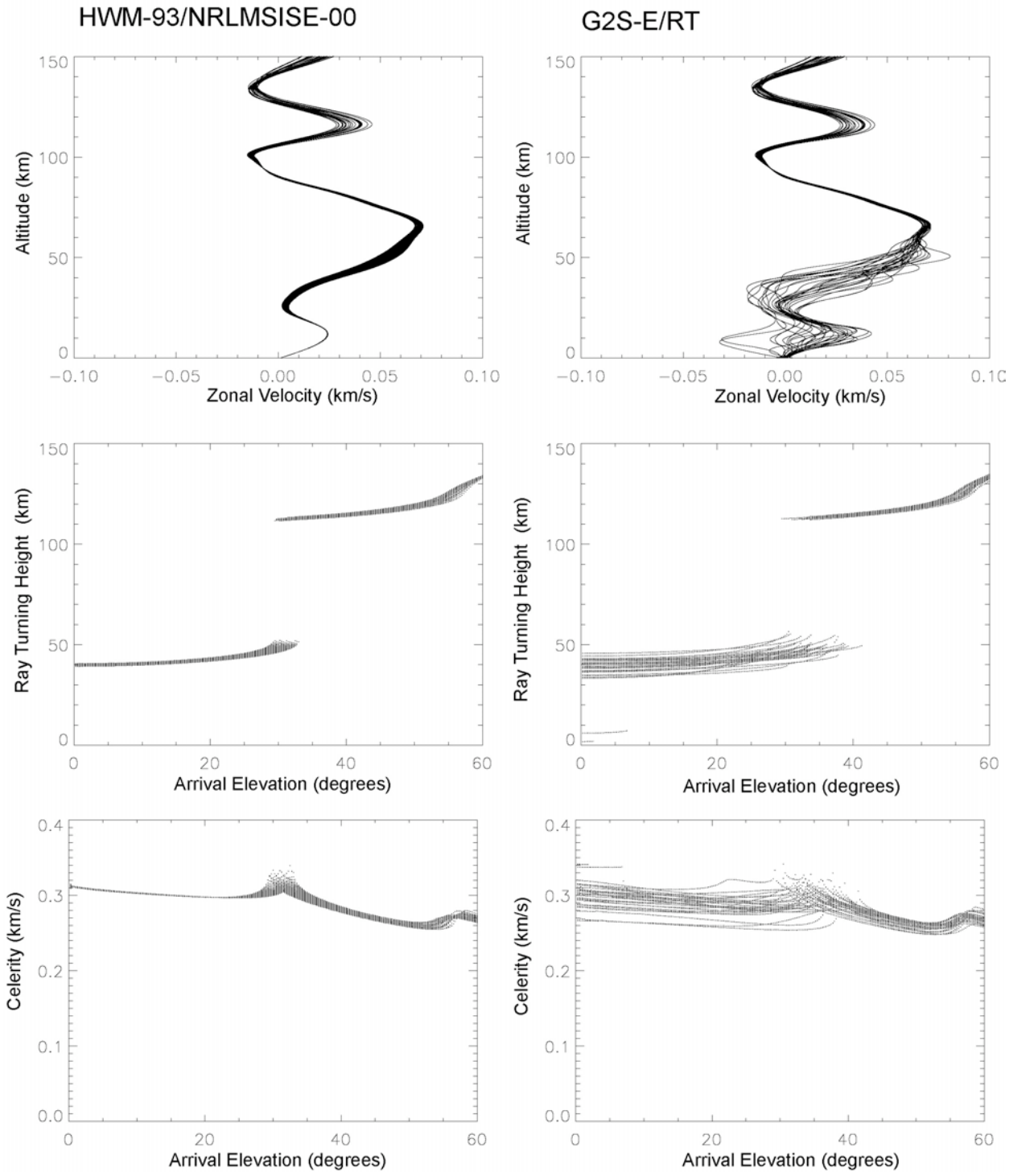


Figure 6. The HWM-93/NRLMSISE-00 (left column) and G2S (right column) zonal wind profiles (first row), derived ray turning heights (second row), and the effective celerity (third row) for infrasound signals propagating eastward. The results represent an ensemble of 00:00 UT calculations for the first 25 days in January 2003 for an infrasound array arbitrarily located in the Southwest United States.

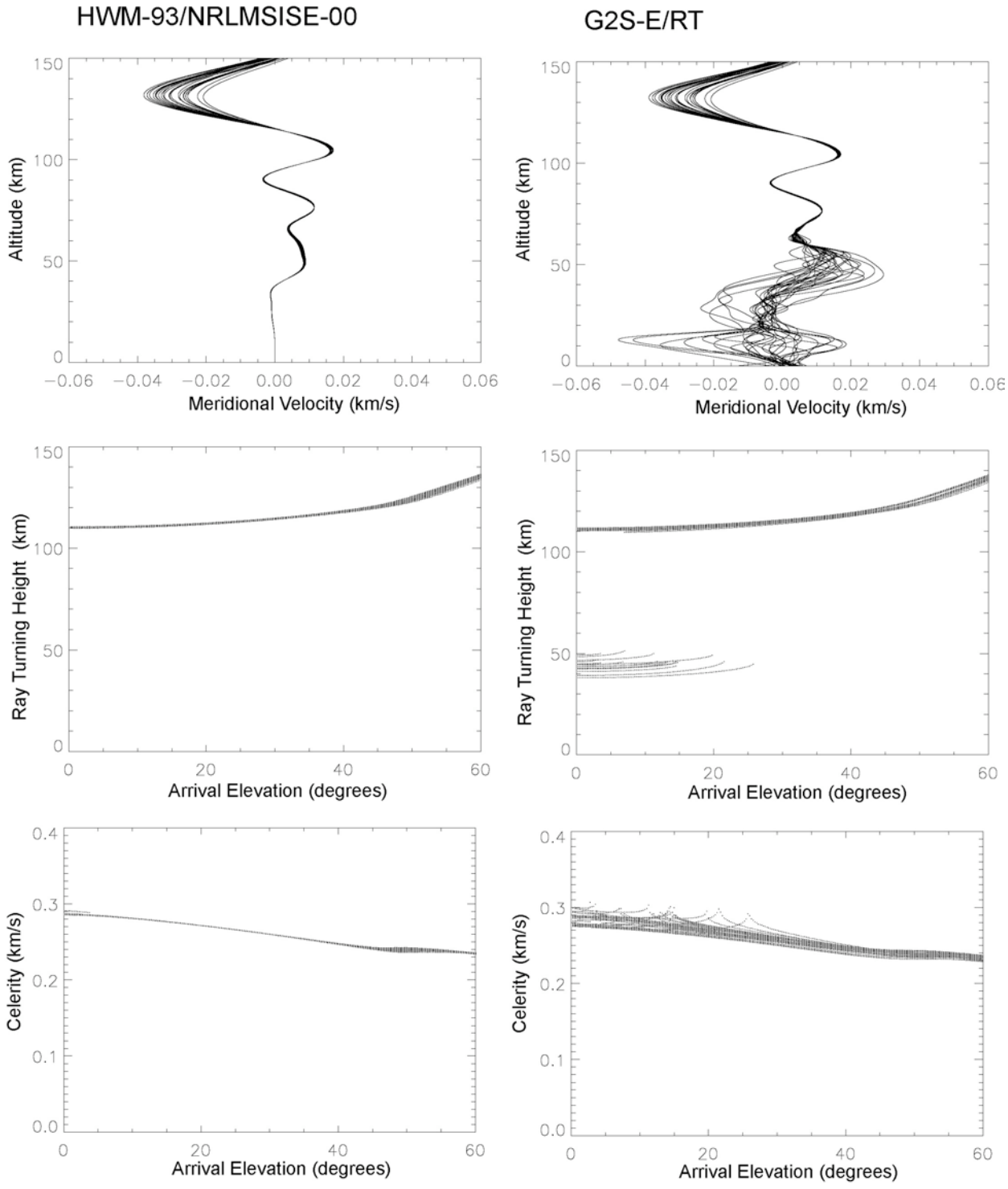


Figure 7. Same as figure 6, but for infrasound signals propagating northward.

CONCLUSIONS AND RECOMMENDATIONS

This work seeks to demonstrate the importance of having accurate atmospheric specifications, starting at the source level for nuclear monitoring. If the initial conditions (e.g., improperly specified source altitude and surface conditions) or the intervening atmospheric profiles are inaccurate, then inaccurate estimates of ducting heights, travel times, and source locations will result. Therefore, in order to accurately relate regional infrasound propagation calculations to microbarograph observations, the use of detailed atmospheric specifications and topography is highly recommended.

In shifting away from climatologically based atmospheric profiles, however, a great deal of complexity is introduced into the problem of infrasound propagation modeling. This complexity arises from the natural variability of the atmosphere across all levels. It has time scales from several hours to several months and horizontal scales of roughly 750 km. We have demonstrated with a simple model that it is now possible to account for this complexity.

The NRL-Ground to Space G2S semi-empirical spectral model seeks to combine numerous sparse datasets in a self-consistent manner to specify the details of the entire atmosphere for infrasound propagation calculations and specifically nuclear explosion monitoring. This new model includes important latitudinal, longitudinal, and daily variability as given by historical and near-real-time operational data. The system seeks to encapsulate and compress the available information, providing a very efficient way to store, transmit, and reconstruct large global volumes of environmental data.

For infrasound applications, G2S is meant to replace the HWM-93/NRLMSISE-00 models as the next generation semi-empirical atmospheric specification tool. There are some known issues regarding the tidal amplitudes and phases of empirical models during certain times of the year that the current version of G2S model does not address (Drob and Picone, 2000). These tidal phases strongly influence the behavior of thermospheric phases. In the absence of G2S specifications, the underestimation of the lower and middle atmospheric wind jets by the empirical models is also of importance to infrasound propagation modeling (Drob and Picone, 2000). The adjustment or updating of the current HWM-93/NRLMSISE-00 internal model coefficients thus remains a top priority. The empirical models serve as the backbone of the G2S model, are easy to use, and adequate for some monitoring applications.

Finally, no measurement or model is perfect, especially when considered individually. While the meteorological specifications and empirical atmospheric models used in the study have been validated in numerous ways, the ultimate substantiation of the conclusions, and future work, should involve the analysis of infrasonic ground-truth events observed by infrasound monitoring networks. It is also felt that it is important to continue this evaluation with a host of different propagation models such as normal modes, ray tracing, and parabolic equations. Furthermore, side-by-side comparison of specifications of the BBN InfraMAP method of combining NOGAPS specification with the HWM-93/NRLMSISE-00 model will be important.

ACKNOWLEDGEMENTS

User feedback and beta testing was provided by Claus Hertzer and Milton Garces of ISLA, and Galina Rovner and Gerald D'Spain of UCSD. Additional ideas, model application, and feedback were also provided Joydeep Bhattacharyya and others at CMR/SAIC. Discussions with Rob Gibson and David Norris of BBN technologies on defining the G2S external library programming interface and G2S output fields were also helpful. Everyone's efforts and contributions are greatly appreciated. I would also like to thank the NASA Goddard Space Flight Center, Global Modeling and Assimilation Office (GSFC-GMAO), and the NOAA National Centers for Environmental Predication (NCEP) for making their meteorological products available for this research.

REFERENCES

Bhattacharyya, J., H. Bass, D.P. Drob, R.W. Whitaker, D.O. ReVelle, and T. Sandoval (2003), Description and Analysis of Infrasound and Seismic Signals Recorded from the Watusi Explosive Experiment on September 28, 2002, *Current Proceedings.*

Drob, D. P., J.M. Picone, and M.A. Garcés (2003), The Global Morphology of Infrasound Propagation, *J. Geophys. Res.*, in press.

Drob D.P., and J.M. Picone, Statistical Performance Measures of the HWM-93 And MSISE-90 Empirical Atmospheric Models and the Relation to Infrasonic CTBT Monitoring (2000), *Proceedings of the 22nd Annual DoD/DOE Seismic Research Symposium: Planning for Verification of and Compliance with the Comprehensive Nuclear-Test-Ban Treaty (CTBT)*, New Orleans, LA, no.07-03, 8 pages.

Garcés, M., R. Hansen, K. Lindquist, D. Drob, and M. Picone (1999), Variability of the Lower Atmosphere and Its Effect on the Propagation of Infrasonic Waves, Proceedings of the 21st, Annual Research Symposium on Monitoring a Comprehensive Test Ban Treaty, Los Alamos National Laboratory - LA-UR-99-4700, 105-111.

Garcés, M., C. Hetzer, K. Lindquist, and D. Drob (2002), Source Location Algorithm for Infrasonic Monitoring, *Proceedings of the 24th Seismic Research Review – Nuclear Explosion Monitoring: Innovation and Integration*, Ponte Vedra, FL, Los Alamos National Laboratory - LA-UR-02-5048, 755-765.

Gibson, G.G. and D.E. Norris, Integration of Near-Real-Time Atmospheric Models with InfraMAP and Applications to Modeling Infrasound from Rockets (2002), *Proceedings of the 24th Seismic Research Review – Nuclear Explosion Monitoring: Innovation and Integration*, Ponte Vedra, FL, Los Alamos National Laboratory - LA-UR-02-5048, 775-782.

Hedin, A. E, E. L. Fleming, A. H. Manson, F. J. Schmidlin, S. K. Avery, R. R. Clark, S. J. Franke, G. J. Fraser, T. Tsuda, F. Vial, and R. A. Vincent (1996), Empirical wind model for the upper, middle, and lower atmosphere, *J. Atmos. Terr. Phys*., 58, 1421-1447.

Le Pichon, A., M. Garces, E. Blanc, M. Barthélémy, and D. Drob, (2002), Acoustic propagation and atmosphere characteristics derived from infrasonic waves generated by the Concorde, *J. Acoust. Soc. Am.*, 111 (1), 629-641.

Picone, J.M., A.E. Hedin, D.P. Drob, and A.C. Aikin (2002), NRLMSISE-00 Empirical model of the atmosphere: statistical comparisons and scientific issues, *J. Geophys. Res.*, 107 (A12): art. no. 1468.

OPTIMIZING THE PROGRESSIVE MULTI-CHANNEL CORRELATION DETECTOR FOR THE DISCRIMINATION OF INFRASONIC SOURCES

Milton A. Garcés and Claus H. Hetzer

University of Hawaii, Manoa

Sponsored by Defense Threat Reduction Agency

Contract No. DTRA01-00-C-0106

ABSTRACT

We use the Progressive Multi-Channel Correlation (PMCC) detector to define the temporal and spectral characteristics of various infrasonic sources observed by diverse infrasonic array configurations. Previous work demonstrated the PMCC was not as vulnerable to aliasing as frequency-domain detectors, and it allowed recognition of coherent signals with signal to noise levels close to unity. PMCC is presently used to produce automatic bulletins of signals detected by the International Monitoring System (IMS) station I59US in Hawaii. We show the detection parameters and features for storm systems, volcanic eruptions, meteors, aircraft, and the Columbia STS-107 reentry as observed by various array geometries and locations, and describe how these detection features can be used for event discrimination. Future work will concentrate on the development of an automatic, intelligent event identification algorithm that can screen the large amount of events picked by automatic detectors.

OBJECTIVE

The aim of this paper is to illustrate the performance of the PMCC feature extraction algorithm (Cansi, 1995; Cansi and Klinger, 1997) when applied to different signals and array configurations.

RESEARCH ACCOMPLISHED

Introduction

The ambient infrasound field for frequencies above 0.1 Hz has been well characterized at I59US, Hawaii, by analyzing PMCC detections with fixed trigger setting for over a year. The PMCC algorithm and the automatic detection setting used at I59US are described in Garcés and Hetzer (2002). This paper consists largely of figures giving examples of the kind of signal features that can be extracted with PMCC for different kinds of infrasonic sources. The fist part of the paper discusses various signals observed in Hawaii and introduced in Garcés and Hetzer (2002). The second part of the paper discusses the forensic acoustic analysis of the tragic Columbia space shuttle reentry of February 1, 2003.

Microbarom Arrivals

Microbarom signals are believed to be generated by ocean swells, and source mechanisms are discussed in Garcés et al. (this issue, 2002). The upper panel of Figure 1 shows all the automatic microbarom detections at I59US for year 2002. The large mountains adjacent to the array appear to cause acoustic shadow zones for energy arriving close to the horizontal. The variation in azimuth shows the seasonal trends for storm systems in the Pacific, with N and NW swells dominating in winter and trade (E) and south swells predominant in summer. There was no obvious seasonal trend in the amplitude of the signal. The lower panel of Figure 1 shows the character of microbarom detections at I59US. Although the microbarom oscillations are continuous, most of the time they are uncorrelated across the array. This may be due to the relatively large aperture and low number of elements (4) at I59US. However, distinct microbarom bursts produce detection triggers on the order of hundreds per day, with a detection azimuth that is highly variable. Under some circumstances it may be desirable to preserve the coherence of the microbaroms, as it may then be easier to remove this contribution from a signal of interest.

Surf Arrivals

Some of the surf arrivals at I59US are believed to be produced by ocean waves trapped within specific bays along the coast of the Big Island. However, during periods of high surf, the western coast of the island is acoustically illuminated. A four-element portable array with an aperture of ~100m was deployed between the coastline and the airport in January-February 2002, concurrent with an epic episode of high swell. Figure 2 shows the detection azimuths and pressure amplitudes observed by the array as a swell started arriving on the coast. The swell height correlates directly with the acoustic pressure, opening possibilities for infrasonic surf monitoring. Gaps in the detections corresponded to periods of high wind. The PMCC detection parameters were similar to those used for automatic high frequency detections at I59US, as described in Garcés and Hetzer (2002).

Volcanic Arrivals

Although some tentative correlations have been found between infrasonic events at I59US and peaks of thermal activity in the Pu'u 'O'o crater, no unambiguous detections have been made. To assess the character of the infrasonic signals that could be expected from Kilauea volcano, we performed temporary array deployments ~2 km and ~13 km from the active vent. These deployments revealed a continuous vibration of the atmosphere, known as tremor, that may correspond to the resonance of the lave tube system that carries lava from the vent to the ocean (Figure 3). At a range of 13 km the signal was significantly reduced, thereby explaining why we do not observe infrasound from Kilauea at I59US, which is at a range of ~90km and blocked by Mauna Loa. Except for extension of the frequency band to 20 Hz, the PMCC detection parameters were as in the previous section.

Signals from above

Bolides, aircraft, and spacecraft may generate infrasound during flight. Two possible bolide signals are shown in Figure 4. The June 23, 2003 bolide was observed visually and by satellites, but the June 30 signal remains unconfirmed. The upper panel of Figure 5 shows the infrasonic signal for an aircraft takeoff observed by a temporary array deployed within 2 km of Keahole International Airport in Kona. This type of signal is periodically observed by I59US at a range of ~20 km. The lower panel of Figure 5 shows the takeoff pattern to the NW of the array as a function of time and apparent speed. Although these sources are above the array, the arrival angles appear

close to the horizontal. The PMCC detection parameters were similar to those used for automatic high frequency detections at I59US.

Columbia reentry of February 1, 2003

The tragic reentry of Shuttle flight STS-107 was recorded by most of the stations in the North American infrasound network except for Hawaii and Alaska. Data was analyzed from the International Monitoring System (IMS) arrays located in Pinon Flat, CA, Fairbanks, AK, Kona, HI, Newport, WA, and Lac du Bonnet, Manitoba, from experimental infrasonic arrays operated by Los Alamos National Laboratory (Department of Energy) at St George (UT), Los Alamos (NM) and Pinedale (WY), from arrays operated by Southern Methodist University at Mina, NV and Lajitas, TX, a NOAA array located near Boulder, Colorado, and a temporary array at White Sands Missile Range operated by the Army Research Laboratory (Bass, 2003). ISLA personnel used PMCC to analyze all available data to look for anomalous signals during the reentry. We experimented with various PMCC settings, starting varying from 30s to ~5s windows. The latter settings enhanced the detection of short duration bursts. We also had the hope of finding a signal feature set that could trigger a detection at the Hawaii and Alaska stations. Despite multiple reanalyses, these two stations did not yield any signals associated with the reentry.

Figure 6 shows the Columbia detections at TXIAR , Texas, the station closest to the final moments of the Shuttle. Note that the pattern of the azimuth plots in Figure 5 and Figure 6 look similar, although the plane is moving west to east while the Columbia was moving east to west. Since supersonic objects move faster than the acoustic propagation speed, the temporal order of the signal arrivals is reversed with respect to a subsonic source. The infrasonic signal at TXIAR consisted of a series of high-amplitude pulses followed by signals that corresponded to the approach trajectory. Although there is a substantial scatter in the azimuth plot of Figure 6, we can look at short windows around the peak pulses to extract their main features. Table 1 provides the onset time, azimuth of the main arrival and the group, peak pressure of the dominant pulse, and peak period of the dominant pulse. Table 2 provides the detection parameters used for this analysis. Thus it appears that the main pulses appear to originate from a similar region, a remarkable observation for a source that is moving at Mach 19. Herrin (personal communication, June 2003) hypothesized that a tire might have exploded at that stage of the trajectory. For an unloaded inflation pressure at STP of 2.2 MPa, the equivalent explosive yield of a tire burst may range from a few pounds to tens of pounds of TNT, depending on the temperature of the gas in the tire and the external pressure inside the wing.

Figure 7 shows the PMCC detections at SGAR, Utah, for STS-107 and STS-78, both with orbital inclination angles of 39 degrees. Many of the features appear similar, except that for STS-107 the late arrivals come in from the west whereas for STS-78 most of the late energy arrives from the east, illustrating the effects of the predominant winds in winter (STS-107, February 1) and summer (STS-78, July 7). The coda of the STS-107 signal lasts almost an hour and deflects well south of the expected trajectory, suggesting contamination from the ambient infrasonic clutter. Analysis of all the available infrasound data did not yield any obvious signs of distress except during its final moments and helped eliminate hypotheses that bolides or lightning might have damaged the shuttle.

Table 1. Time, azimuth, pressure, and period for the main pulses observed at TXIAR

Pulse Onset Time (GMT)	Azimuth, Deg (Group)	Peak Pressure, Pa (- /+)	PP Pressure, Pa	Peak Period (s)
14:29:30	14.5 (16.4)	-0.1622, 0.1315	0.2937	5
14:29:50	17.4 (19.0)	-0.4032, 0.4595	0.8627	3
14:30:30	18.0	-0.1980, 0.2784	0.4764	1
14:31:13	18.6 (19.4)	-0.7146, 0.5537	1.2683	3.5-5
14:31:54	17.0 (17.7)	-0.4209, 0.6799	1.1008	4.5
14:33:32	17.0 (16.3)	-0.2903, 0.5683	0.8585	6

Table 2. PMCC detection parameters and array apertures for the analyses at TXIAR and SGAR shown in Figures 6 and 7

Station (Event)	Frequency Band (Hz)	Window Length (sec)	Window Overlap (sec)	Max Consistency (sec)	Trace Velocity Limits (km/s)	Maximum Aperture (km)
TXIAR (STS-107)	1-5	10	8	1	0.2-0.7	1.6
SGAR (STS-107)	1-4	5	4	1	0.2-2	0.2
SGAR (STS-78)	1-4	5	4	1	0.2-1	0.2

CONCLUSIONS AND RECOMMENDATIONS

The PMCC feature extraction algorithm is used automatically at I59US to produce updated bulletins every four hours. With thousands of automatic detections per month at I59US, it is necessary to develop intelligent event classification algorithms. PMCC also performed well when exposed to different signals and array configurations, demonstrating that this algorithm is robust, flexible, and well suited for infrasonic applications.

ACKNOWLEDGEMENTS

S. Tenney, J. Noble, R. Gibson, D. Norris, J. Bhattacharyya, I. Bondar, H. Israelsson, R. North, M. Skov, R. Woodward, X. Yang, R. Whitaker, T. Sandoval, D. ReVelle, A. Bedard, R. Nishiyama, A. Gasiewski, D. Drob, M. Hedlin, G. D'Spain and E. Herrin contributed data and analyses for the Columbia report. Many thanks to S. Rowland for bringing the June 23 bolide to our attention.

REFERENCES

Bass, H., (2003). Report to the Department of Defense on Infrasonic Re-Entry Signals from the Space Shuttle Columbia (STS-107), Revision 3, March 30, 2003.

Cansi, Y. (1995), An Automatic Seismic Event Processing for Detection and Location: The P.M.C.C. Method, *Geophysical Research Letters* 22, 1021-1024.

Cansi, Y., and Y. Klinger (1997), An Automated Data Processing Method for Mini-Arrays, *Newsletter of the European-Mediterranean Seismological Center* 11, 2-4.

Garcés, M. and C. Hetzer (2002), Evaluation of Infrasonic Detection Algorithms, 24th Annual DTRA/NNSA Seismic Research Review, Ponte Vedra, FL, 17-19 September 2002.

Garcés, M., C. Hetzer, S. Businger, and M. Willis (2002), Modeling of Microbarom Signals in the Pacific. 24th Annual DTRA/NNSA Seismic Research Review, Ponte Vedra, FL, 17-19 September 2002.

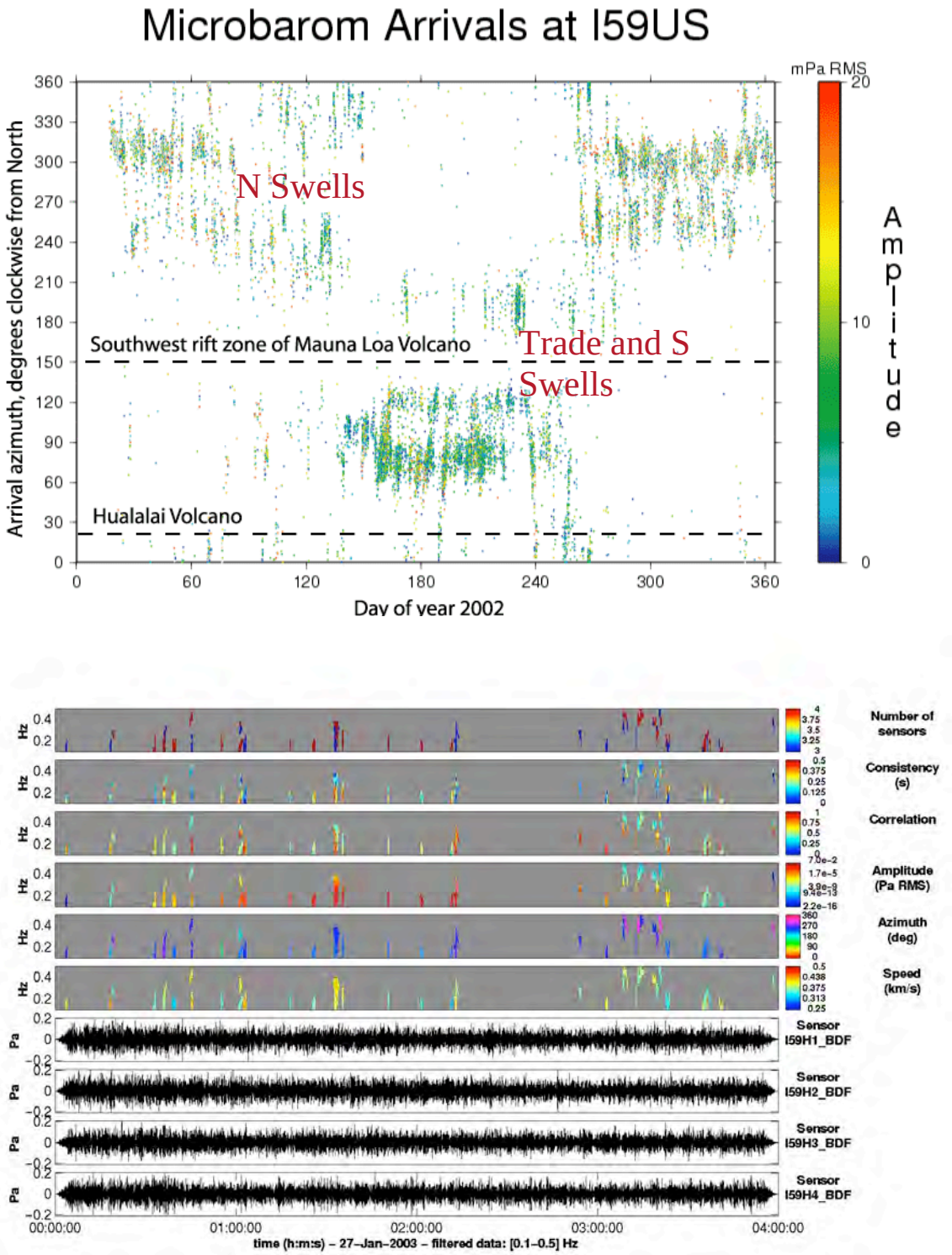


Figure 1. Microbarom detections for 2002, showing blocking by mountains and seasonal pattern. The lower panel shows typical microbarom bursts observed at I59US.

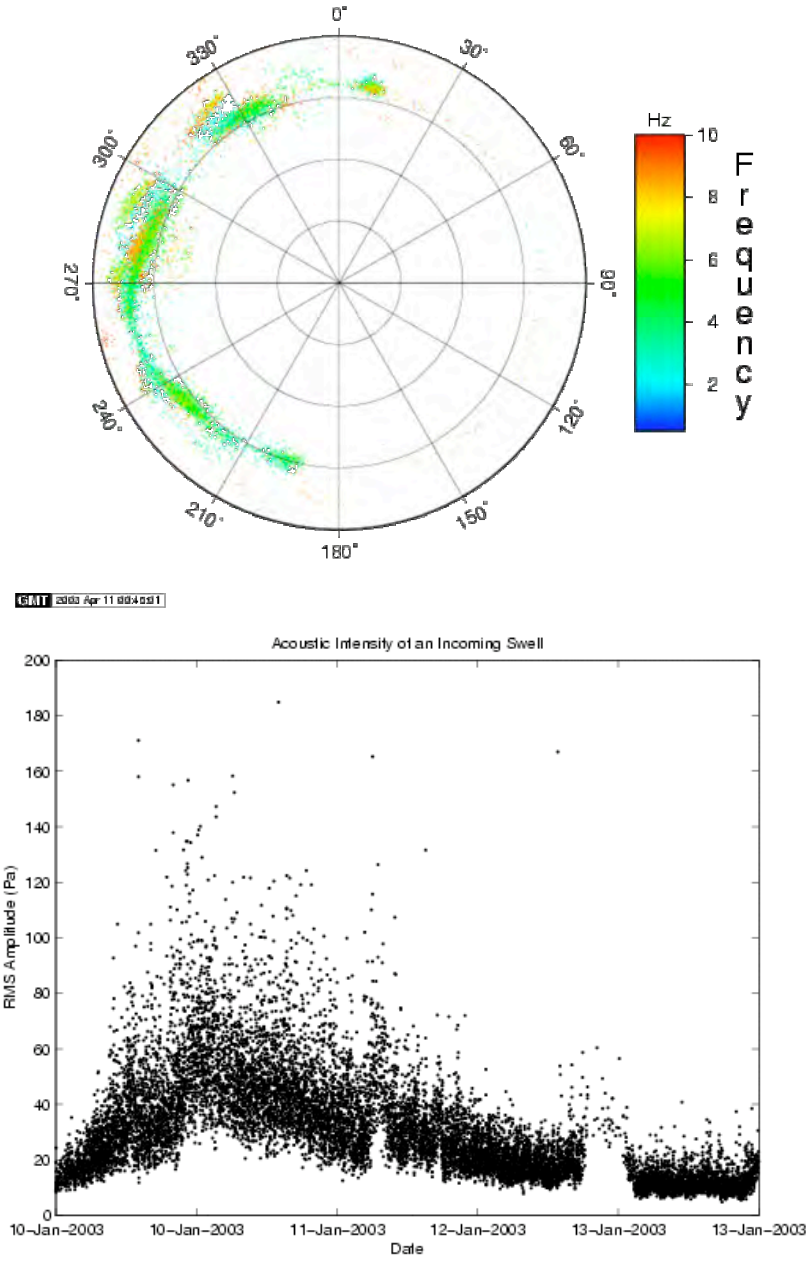
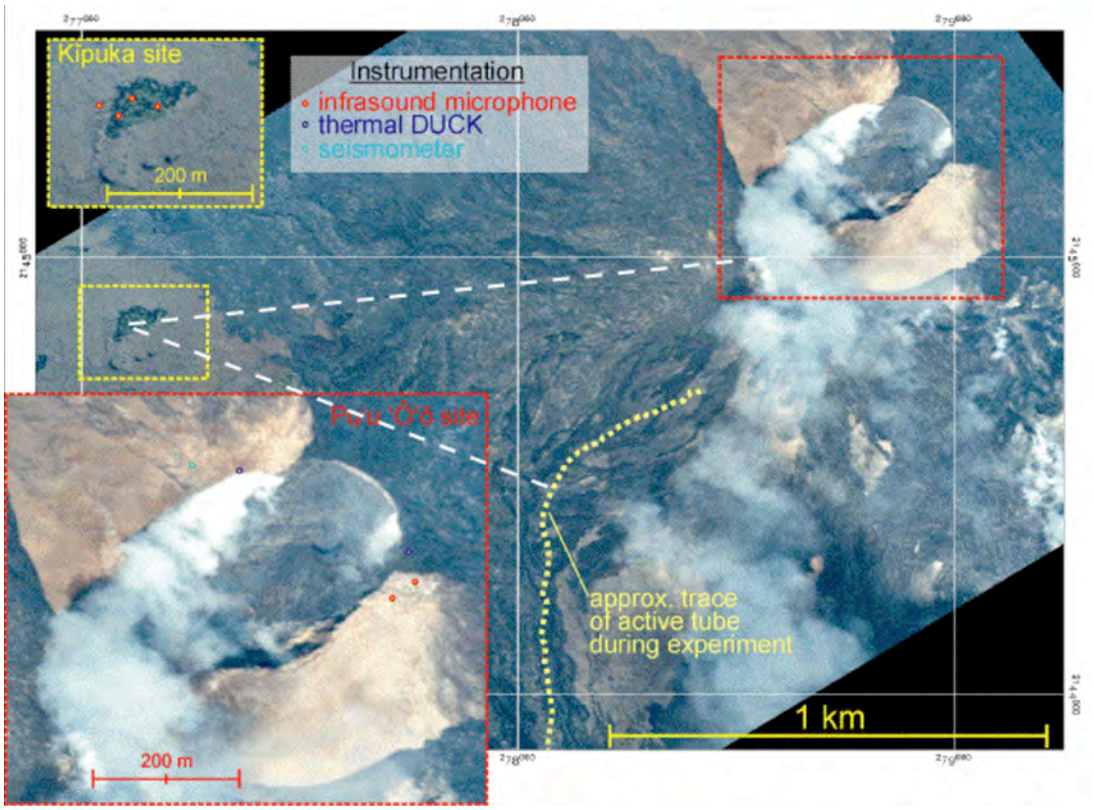


Figure 2. Surf detections and pressure amplitude (mPa) captured by a portable array near the coastline, January 10-13 2003.



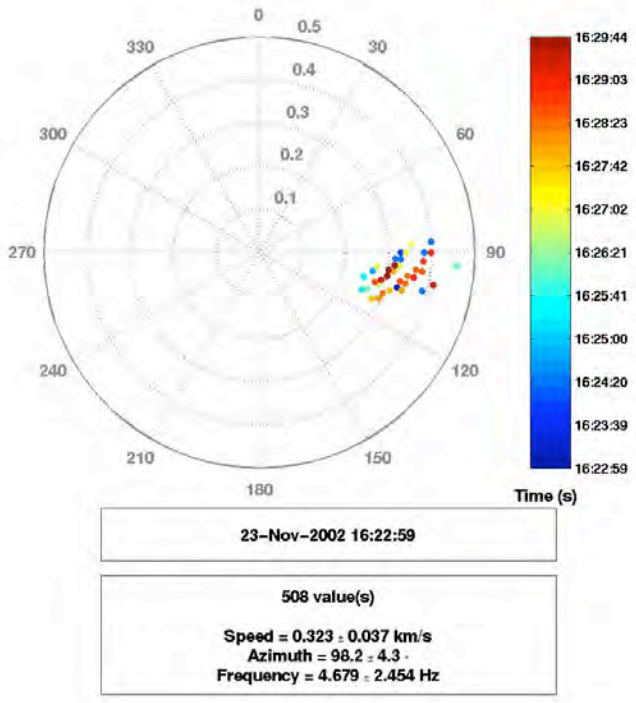


Figure 3. Volcanic tremor at Kilauea volcano, Hawaii, observed by a small-aperture array approximately 2 km from the active vent of Pu'u O'o.

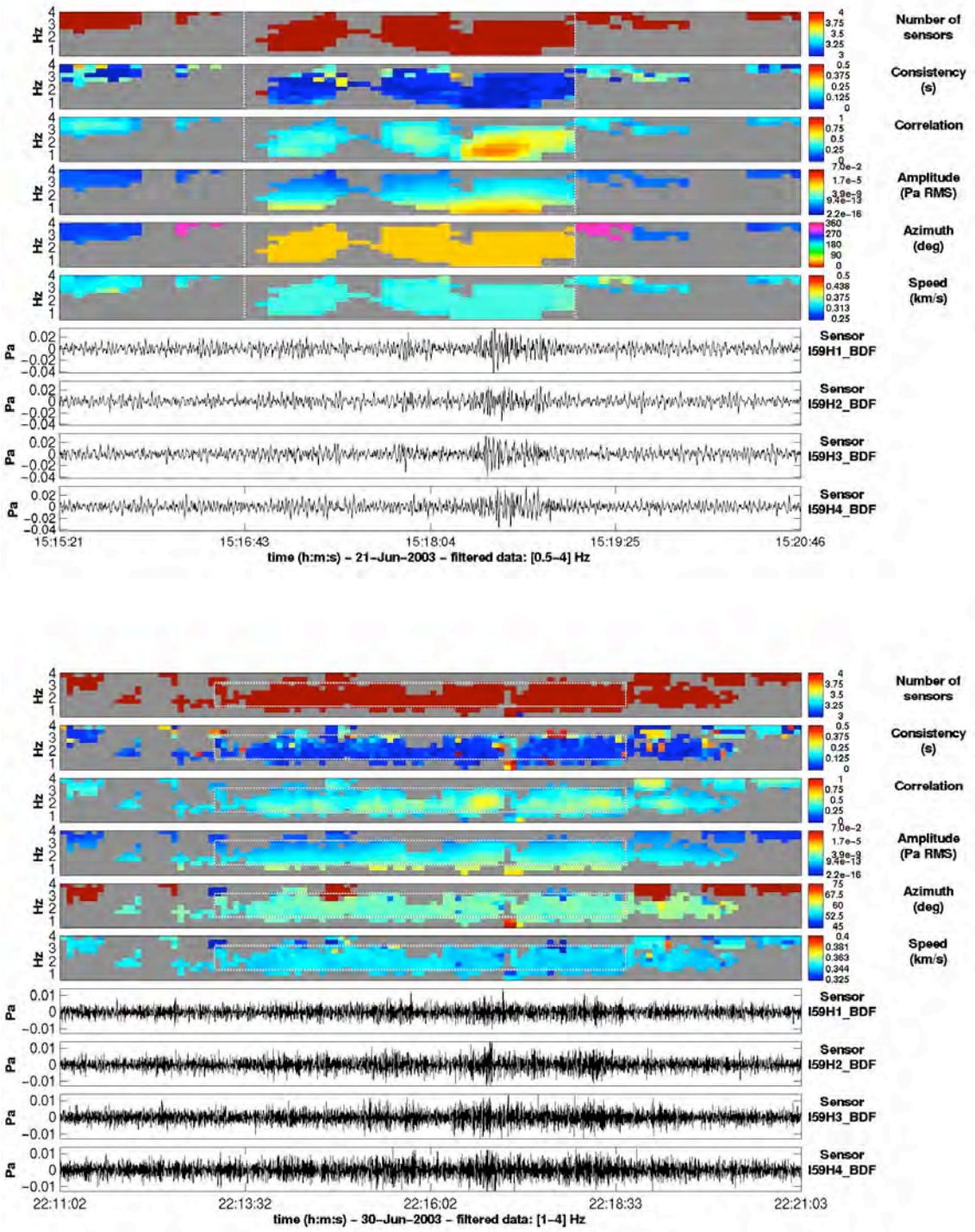


Figure 4. Possible bolides observed at I59US but outside the detection range of other IMS stations. The June 21 bolide was observed visually and by the DOD/DOE satellite monitoring system.

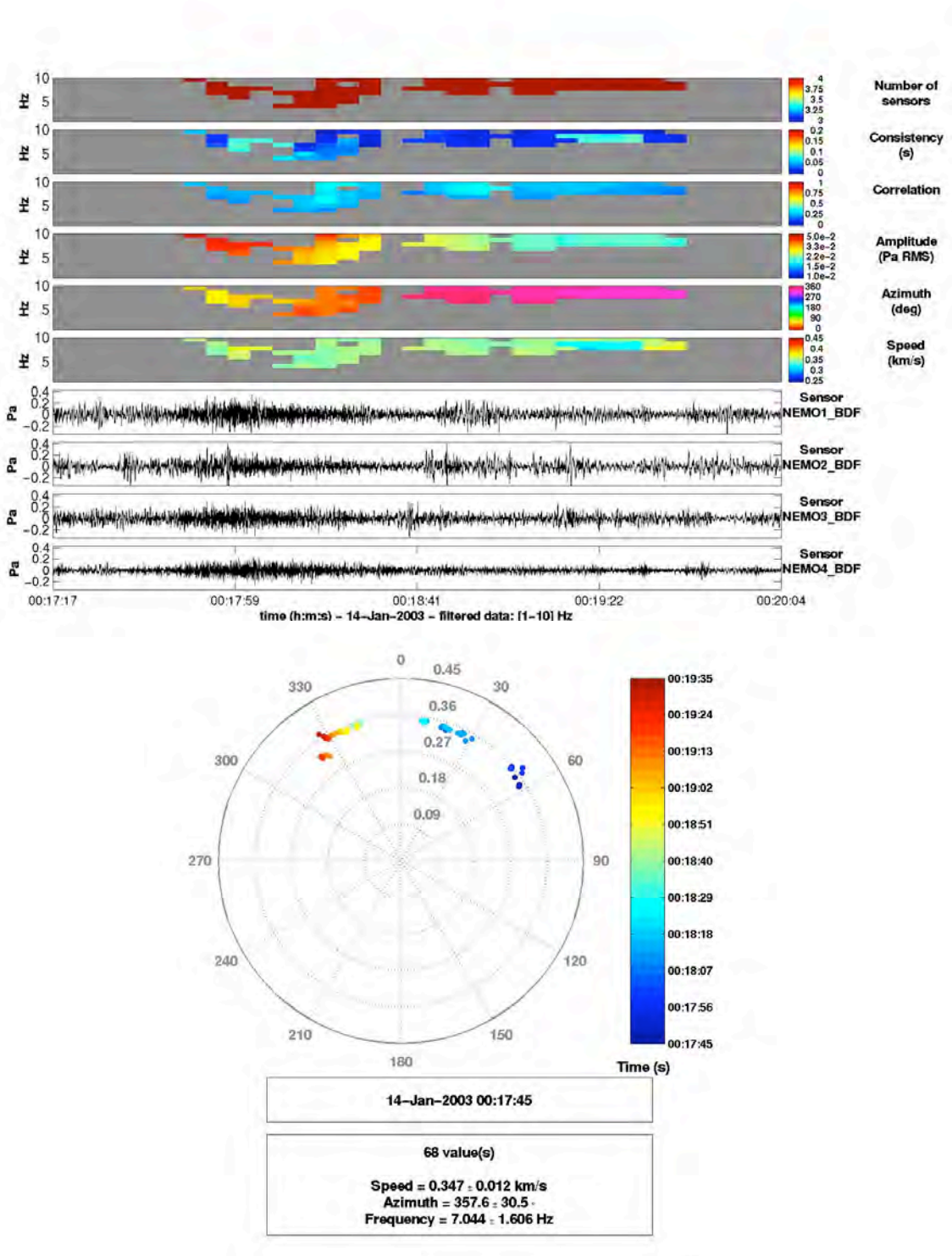


Figure 5. Aircraft takeoff observed by a portable array near Keahole International Airport.

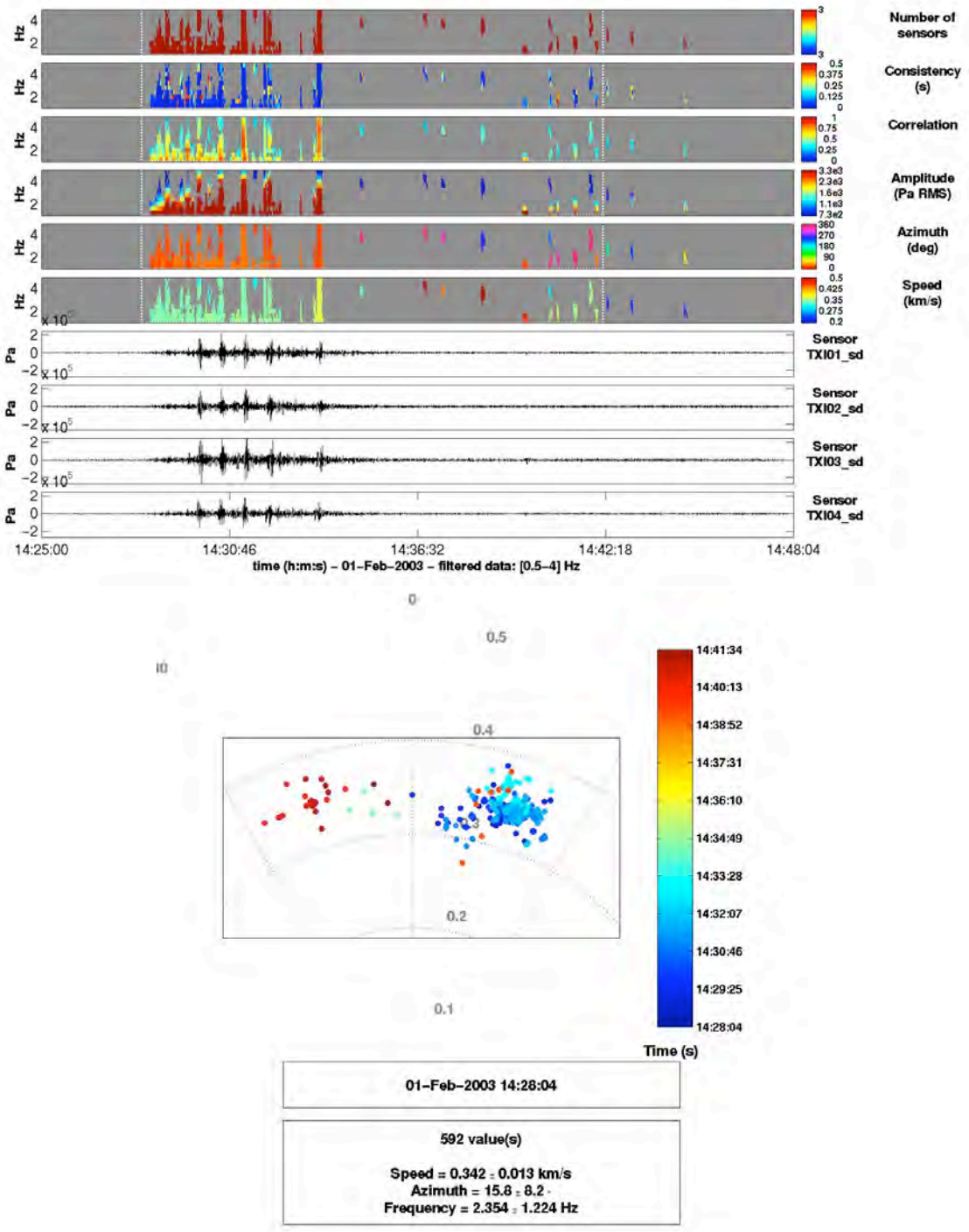


Figure 6. Columbia reentry observed at TXIAR, Lajitas, Texas.

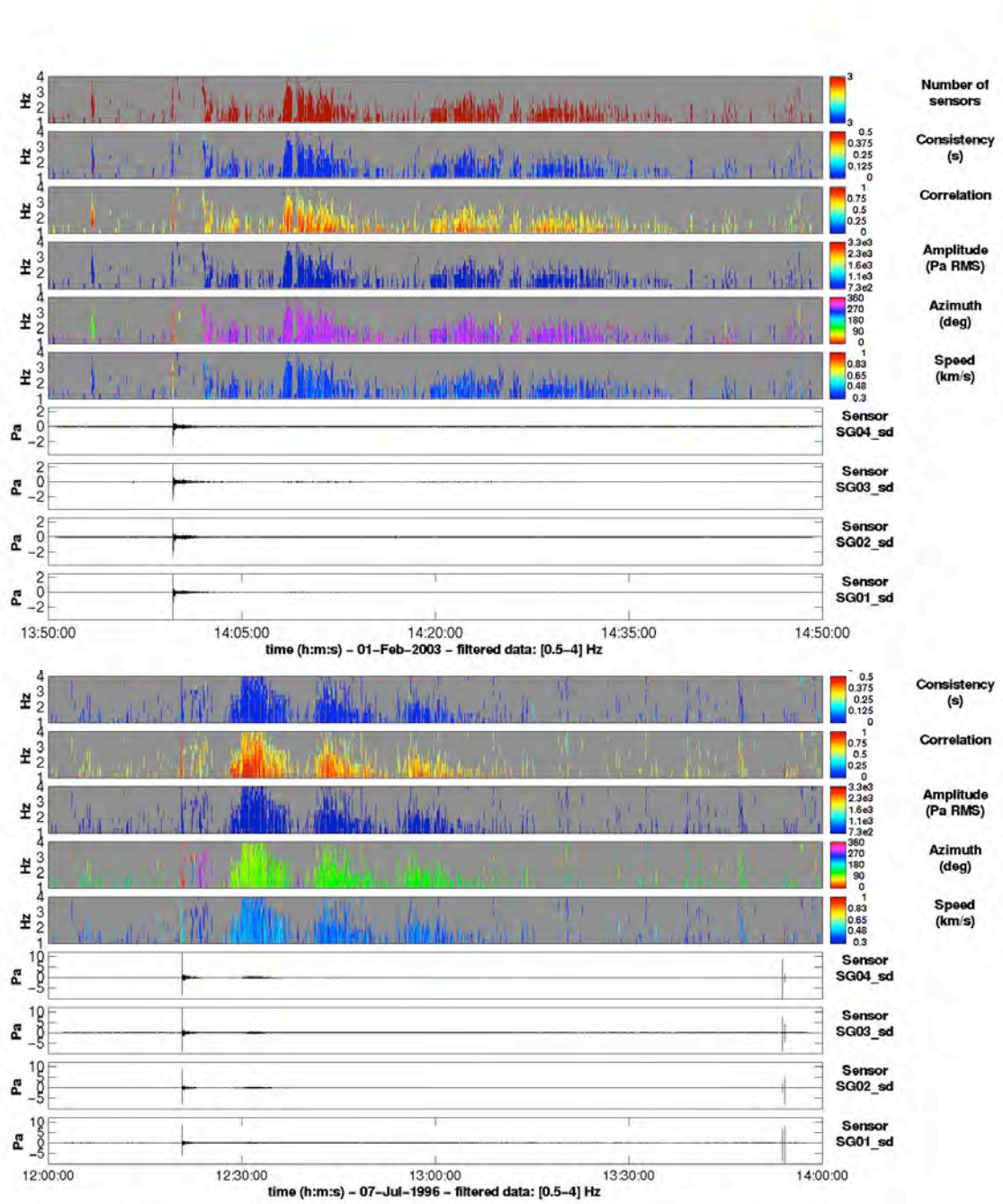


Figure 7. Reentries for shuttlesSTS-107 (upper panel) and STS-78 (lower panel) recorded at SGAR, Utah.

INTEGRATION OF INFRASONIC MODELS WITH OCEAN WAVE SPECTRA AND ATMOSPHERIC SPECIFICATIONS TO PRODUCE GLOBAL ESTIMATES OF MICROBAROM SIGNAL LEVELS

Milton A. Garcés, Claus H. Hetzer, Mark Willis, and Steven Businger

University of Hawaii, Manoa

Sponsored by Defense Threat Reduction Agency

Contract No. DTRA01-01-C-0077

ABSTRACT

Severe weather in the ocean generates infrasonic signals in the 0.1-0.5 Hz frequency band that can propagate for thousands of kilometers. The source generation mechanism for these microbarom signals is attributed to the nonlinear interaction of surface ocean waves, which are predicted to radiate acoustically only if the swells are almost opposite in direction and of a near identical frequency. We study the statistics of microbarom signals detected at International Monitoring System (IMS) station I59US, Hawaii, to identify features that may be used to assess array performance in the microbarom range. For selected storm systems, we use the global ocean wave estimates produced by National Oceanic and Atmospheric Administration's (NOAA's) Wavewatch 3 (WW3) to estimate the spatial and temporal distribution of the acoustic source spectra induced by nonlinear ocean wave interactions. We then use empirical amplitude scaling relationships to predict microbarom signal levels and peak frequencies. Results are presented with a view toward applications in storm and sea-state evolution and how these affect infrasonic detection thresholds in the microbarom frequency band.

OBJECTIVE

The aim of this work is to characterize microbarom signals observed in the Pacific and model the source processes that generate these signals, with the aim of determining infrasonic detection thresholds in the microbarom frequency range.

RESEARCH ACCOMPLISHED

1. Introduction

Microbaroms consist of atmospheric pressure oscillations with energy between 0.1 and 1 Hz and a peak at ~0.2 Hz, and they can appear as coherent energy bursts or as a continuous oscillation. For infrasonic stations near the ocean, microbarom clutter often defines the low-wind noise floor, and thus detection thresholds, in that band. Like their seismic and hydroacoustic counterpart (microseisms), microbaroms are associated with severe weather in the ocean (Benioff and Gutenberg, 1939; Rind, 1980), and more specifically, to the ocean swells generated during storms (Posmentier, 1967; Kibblewhite and Wu, 1996, Garcés et al, 2002). We use the theoretical microbarom generation model of Arendt and Fritts (2000) with the third-generation Wavewatch 3 (WW3) ocean wave model of Tolman et al (2002) to try to reproduce our observations of microbarom signals at I59US.

2. Observations and theoretical background

Infrasound array I59US, Hawaii, has four elements and a baseline of ~2km. It was believed that microbaroms would be incoherent across this larger aperture. Although in general the continuous microbarom noise is indeed uncorrelated, distinct microbarom packets can be clearly detected in Hawaii. When designing an array it would perhaps be useful to retain the coherence of microbaroms, as then it may be possible to remove this contribution from a signal of interest.

The microbarom field at I59US varies seasonally and generally follows the yearly pattern for severe weather in the Pacific. In summer most of the microbaroms appear to come from the east and south, and in winter they arrive from the north and west. Statistics for microbarom signals for year 2002 are discussed in Garcés and Hetzer 2002. According to theory (e.g. Arendt and Fritts, 2000), microbaroms can be generated by ocean surface waves propagating with nearly the same period and the opposite direction. However, a real developed sea consists of multiple frequency and direction components, and on any given point in the central Pacific there may be between 4 and 7 swells interacting with each other. We choose to use the WW3 model of Tolman et al. (2003) because it provides reliable estimates of the ocean wave field directional spectrum that we can use as an excitation function for our microbarom amplitude estimates.

2.1. Ocean wave spectrum

The WW3 model outputs the variance density, F, of the surface wave field as a function of frequency, f, and propagation direction, θ, at each node of a global 1 degree grid. At each point of that grid, the variance density can be integrated over angle and frequency to provide the total wave energy E,

$$E = \int_0^{2\pi} d\theta \int_0^{\infty} df\, F(f,\theta). \quad (1)$$

The significant wave height is defined as

$$H_s = 4\sqrt{E}\,. \quad (2)$$

And thus the variance density has units of m^2/(rad*Hz) and it is a measure of the energy in the surface wave field. The phase of each wave component is assumed to be random. Figure 1 shows an example of the significant wave height and dominant period of the global surface wave field. However, these plots show the average of the ocean wave field after integration over frequency and angle, whereas we need the variance density itself to produce estimates of the microbarom pressure field.

Arendt and Fritz (2000) start with a prescribed amplitude spectrum of the ocean surface wave field given by the cosine Fourier transform

$$g(x,y,t) = \int_{-\infty}^{\infty} dk_x \int_{-\infty}^{\infty} dk_y A(k_x,k_y)\cos(\omega t - k_x x - k_y y + \phi) \tag{3}$$

$$= \int_{-\infty}^{\infty} dk_x \int_{-\infty}^{\infty} dk_y A(k_x,k_y)\cos(\omega t - k_x x - k_y y + \phi)$$

Thus we wish to find a functional relationship between the variance density *F* (also known as the directional spectrum) and the Fourier coefficient *A*, which has to have units of m^3.

From Kinsman (1965), Eq. (8.3:1)

$$g(x,y,t) = \int_0^{\infty} \int_{-\pi}^{\pi} \cos(\omega t - k_x x - k_y y + \phi)\sqrt{F(\omega,\theta)d\theta d\omega} \tag{4}$$

This integral representation reminds us that we are dealing with a Gaussian process, and is the subject of a detailed discussion by Kinsman. Since the WW3 model is defined in a grid of frequencies and azimuths, we estimate our wavenumber spectrum as:

$$g(x,y,t) \approx \int_0^{\infty} \int_{-\pi}^{\pi} \cos(\omega t - k_x x - k_y y + \phi)\sqrt{\frac{F(\omega,\theta)}{\Delta\theta\Delta\omega}}d\theta d\omega$$

The first transformation only concerns the change of variables from frequency to wavenumber,

$$g(x,y,t) \approx \int_0^{\infty} \int_{-\pi}^{\pi} \cos(\omega t - k_x x - k_y y + \phi)\frac{d\omega}{dk}\sqrt{\frac{F(\omega,\theta)}{\Delta\theta\Delta\omega}}d\theta dk \tag{5}$$

$$g(x,y,t) \approx \int_0^{\infty} \int_{-\pi}^{\pi} \cos(\omega t - k_x x - k_y y + \phi)c_g\sqrt{\frac{F(\omega,\theta)}{\Delta\theta\Delta\omega}}d\theta dk$$

where c_g is the group velocity. The second transformation involves a change of coordinates in wavenumber space from polar to rectangular,

$$g(x,y,t) \approx \int_{-\infty}^{\infty} dk_x \int_{-\infty}^{\infty} dk_y \cos(\omega t - k_x x - k_y y + \phi)\frac{c_g}{k}\sqrt{\frac{F(\omega,\theta)}{\Delta\theta\Delta\omega}} \tag{6}$$

For short-period waves, the phase velocity c_s and group velocity c_g are given as

$$c_s = \frac{\omega}{k} = \sqrt{\frac{g}{k}} = \frac{g}{\omega}, \quad c_g = \frac{1}{2}c_s, \tag{7}$$

and the dispersion relation is $\omega^2 = gk$. Comparison of Eq.(6) with Eq.(3) yields

$$A(k_x,k_y) = \frac{c_g}{k}\sqrt{\frac{F(k_x,k_y)}{\Delta\theta\Delta\omega}} \tag{8}$$

Since the variables in the radical have units of (m s), we see that *A* has units of m^3, as desired.

2.2. Acoustic spectrum

From Arendt and Fritts (2000) the pressure field radiated by a three dimensional surface wave field into an isotropic half space may be expressed as

$$p_m(x,y,z,t) = \int_{-\infty}^{\infty} dK_x \int_{-\infty}^{\infty} dK_y \int_{0}^{\infty} dK_z P_k(K_x, K_y, K_z) \exp\left(\omega_m t - \vec{K} \bullet \vec{R} + \phi\right) \tag{9}$$

where K is the acoustic wavenumber, ω_m is the angular frequency for the sound field, and R is the spherical radius from the source location to the receiver. The spectrum P_k is given by

$$P_k = \frac{\rho c^6}{64 g^2} K_z K^4 \int_0^{2\pi} A(k_x, k_y) A(k'_x, k'_y) d\theta_\xi \tag{10}$$

where k and k' correspond to the second order, propagating solutions of interacting wave fields with near equal angular frequencies ω and ω' and opposite directions, and

$$\begin{aligned} K^2 &= K_x^2 + K_y^2 + K_z^2 \\ K_x &= k_x + k'_x,\ \xi_x = k_x - k'_x \\ K_y &= k_y + k'_y,\ \xi_y = k_y - k'_y \\ K_z &= \sqrt{\left(\frac{\omega + \omega'}{c}\right)^2 - K_x^2 - K_y^2}\ . \end{aligned} \tag{11}$$

The highest spectral amplitude will occur when $K_x = K_y = 0$, or $k' = -k$, and $\omega = \omega'$, and

$$P_k^0 = \frac{\rho c^6}{64 g^2} K^5 \int_0^{2\pi} A(k_x, k_y) A(-k_x, -k_y) d\theta \tag{12}$$

$$\begin{aligned} \xi_x &= 2k_x \\ \xi_y &= 2k_y \\ K = K_z &= \frac{2\omega}{c} = \frac{\omega_m}{c}. \end{aligned} \tag{13}$$

Where θ is now the directional angle for k specified in equation (1). Using Equations (6) and (8), as well as $\omega_m = 2\omega$,

$$A(k_x, k_y) A(-k_x, -k_y) = \left(\frac{c_g}{k}\right)^2 \frac{\sqrt{F(k_x, k_y) F(-k_x, -k_y)}}{\Delta\theta \Delta\omega} = \left(\frac{4g^2}{\omega_m^3}\right)^2 \frac{\sqrt{F(k_x, k_y) F(-k_x, -k_y)}}{\Delta\theta \Delta\omega}\ . \tag{14}$$

The peak microbarom source spectrum amplitude then becomes

$$P_k^0 = \frac{\rho c g^2}{4\omega_m \Delta\theta \Delta\omega} \left[\int_0^{2\pi} \sqrt{F(k_x, k_y) F(-k_x, -k_y)} d\theta \right] = \frac{\rho c g^2}{4\omega_m (\Delta\theta \Delta\omega)} Q_m^0 \tag{15}$$

$$Q_m^0 = \int_0^{2\pi} \sqrt{F(k_x, k_y) F(-k_x, -k_y)} d\theta = 2 \int_0^{\pi} \sqrt{F(f, \theta) F(f, \theta + \pi)} d\theta \tag{16}$$

The integral can be readily evaluated through either the trapezoidal rule or the parabolic rule. For an even number of intervals n (odd number of discrete points x_j, $j = 0,n$), the parabolic rule states

$$\int_a^b f(x)dx \approx \frac{h}{3}\left[f(x_0) + 4f(x_1) + 2f(x_2) + \ldots + 4f(x_{n-1}) + f(x_n)\right], \tag{17}$$

where $h = (b-a)/n$. If n is an odd number (even number of points), we can use the trapezoidal rule

$$\int_a^b f(x)dx \approx \frac{h}{2}\left[f(x_0) + 2f(x_1) + 2f(x_2) + \ldots + 2f(x_{n-1}) + f(x_n)\right]. \tag{18}$$

After this integration is complete, we have completed the transformation from ocean to sound waves. For the evaluation of the sound field it is practical to use the acoustic microbarom angular frequency $\omega_m = 2\omega$.

2.3. Pressure scaling with range, including the effects of the stratospheric winds

The atmosphere is a complex propagation medium, and for the purpose of microbarom amplitude determinations it behooves us to start with a simple amplitude scaling relationship that will allow us to estimate relative acoustic levels at a receiver. Stevens et al (2002) provide an evaluation of various scaling laws that have been derived from nuclear tests, and we use the expression that provided the best fit:

$$P = \frac{P_{ref}}{R^{1.36}} 10^{0.019v} \tag{19}$$

where the reference pressure P_{ref} is relative to the source location, the range R is in km, and the stratospheric wind speed v at 50 km along the propagation direction is given in m/s. For our initial tests we ignore the stratospheric winds, which will be eventually incorporated using Naval Research Laboratory (NRL) ground-to-space (G2S) atmospheric specifications. A source magnitude may be defined as

$$M_I = log_{10}(P_{ref}), \tag{20}$$

and used to plot the microbarom source spectrum amplitude as a function of global location.

3. Implementation and Results

Figure 2 shows a graphical user interface developed for the computation of the infrasonic field generated by a specified ocean wavefield. The upper panel shows the microbarom source pressure corresponding to the swell plots in Figure 1 at a microbarom frequency of 0.2 Hz, which corresponds to an ocean wave frequency of 0.1 Hz. As noted earlier, the significant wave height plots are derived from an integral over all angles and frequencies (Equations 1 and 2), although the WW3 model output provides the directional spectrum of the ocean wavefield at each grid point. Thus the upper panel of Figure 2 was produced by taking the base 10 logarithm of Equation 15, which yields a frequency dependent source pressure spectrum at each grid point. To propagate the sound field, we need to specify a threshold magnitude below which we ignore source contributions. We also specify a range mask, after which we do not propagate the source point any further. To compute the lower panel of Figure 2, we ignored source points with magnitudes lower than –1 and propagated to 180 degrees away from the source, or to the antipode. To compute the propagated field shown in the lower panel of Figure 2, we compute the distance from each source point with a magnitude greater than –1 and within 180 degrees to the receiver. A dual processor SunBlade workstation takes ~8 hours to run this model. For this algorithm, the speed of computation depends on the source threshold that is used. A more realistic (and computationally expensive) model would also produce a propagation time from the source to the receiver, so that for each time step of the wave model there would actually be a series of time-lagged acoustic solutions. When we include the stratospheric winds as well as attenuation, we need to consider in more detail each source-receiver path. Time dependence and integration with atmospheric models will be incorporated into later generations of the computational algorithm.

Figure 2 only shows the results at a microbarom frequency of 0.2 Hz. It is also possible to look at the peak pressure and peak frequency of the source and received field, as shown in Figure 3. We see that the received field is richer in lower frequencies, and that higher microbarom noise levels are expected in sites that are close to the ocean. At each

grid point we can extract the acoustic source and received fields, and Figure 4 shows the spectra for a grid point at 20N, 160W. Comparison with the observed spectrum at I59US (lower panel of Figure 4) shows that despite our sweeping assumptions and generalizations, we have a reasonable match between theory and observation. The predicted peak frequency appears lower than the observed frequency, and this discrepancy may be corrected by accounting for the acoustic radiation pattern of the ocean wave interactions. Adding a viscous attenuation term may reduce the higher frequency components. These promising results encourage further development of the computational algorithm.

CONCLUSIONS AND RECOMMENDATIONS

The algorithm described in this paper is designed to produce a proof of concept integration of oceanographic and acoustic models, and the next level of detail should incorporate atmospheric specifications as well as more accurate acoustic radiation and propagation models. However, these improvements will require far more computational power than can be presently provided by desktop computers. During the next stage of the project, we would port the WW3 model to the Maui High Performance Computing Center Linux Supercluster. The acoustic propagation algorithm should include the atmospheric winds, attenuation, and the propagation time of the signals. The microbarom source mechanism needs to incorporate the radiation pattern of the microbarom source instead of considering only the peak power. The WW3 model needs to be modified so as to include reflections at coastlines and bathymetry changes, and could also be extended into a lower frequency. Our preliminary results are encouraging, and should eventually permit the generation of temporally and spatially dependent microbarom noise levels that may be used to compute more realistic global detection thresholds for IMS infrasound stations. Conversely, infrasonic observations may be used to refine ocean wave models in regions of poor coverage.

REFERENCES

Arendt, S. and D. Fritts (2000), Acoustic Radiation by Ocean Surface Waves, *Journal of Fluid Mechanics* 415, 1-21.

Benioff, H. and B. Gutenberg (1939), Waves and Currents Recorded by Electromagnetic Barographs, *Bulletin of the American Meteorological Society* 20, 421.

Garcés, M. and C. Hetzer (2003). Optimizing the Progressive Multi-Channel Correlation Detector for the Discrimination of Infrasonic Sources, 25th Seismic Research Review, this proceedings.

Garcés, M. and C. Hetzer (2002), "Evaluation of infrasonic detection algorithms," in "Proceedings of the 24th Seismic Research Review, Nuclear Explosion Monitoring: Innovation and Integration," (Ponte Vedra, FL) Los Alamos National Laboratory document LA-UR-02-5048 (September 2002).

Garcés, M., C. Hetzer, S. Businger, and M. Willis, "Modeling of microbarom signals in the pacific," in "Proceedings of the 24th Seismic Research Review, Nuclear Explosion Monitoring: Innovation and Integration," (Ponte Vedra, FL) Los Alamos National Laboratory document LA-UR-02-5048 (September 2002).

Kibblewhite, A., and C. Y. Wu (1996), Wave Interactions as a Seismo-Acoustic Source *Lecture Notes in Earth Sciences*, Springer-Verlag, Berlin.

Kinsman, B. (1965), *Wind Waves*, Prentice Hall, N.J., USA.

Posmentier, E. (1967), A Theory of Microbaroms, *Geophysical Journal of the Royal Astronomical Society* 13, 487.

Rind, D. (1980), Microseisms and Palisades 3. Microseisms and Microbaroms, *Journal of Geophysical Research* 85, 4854.

Stevens, J., I. Divnov, D. Adams, J. Murphy, and V. Bourchik (2002), Constraints on Infrasound Scaling and Attenuation Relations from Soviet Explosion Data, *Pure and Applied Geophysics* 159, 1045-1062.

Tolman, H., B. Balasubramaniyan, L. Burroughs, D. Chalikov, Y. Chao, H. Chen, and V. Gerald (2002), Development and Implementation of Ocean Surface Wave Models at NCEP, *Weather and Forecasting*, 17, 311-333.

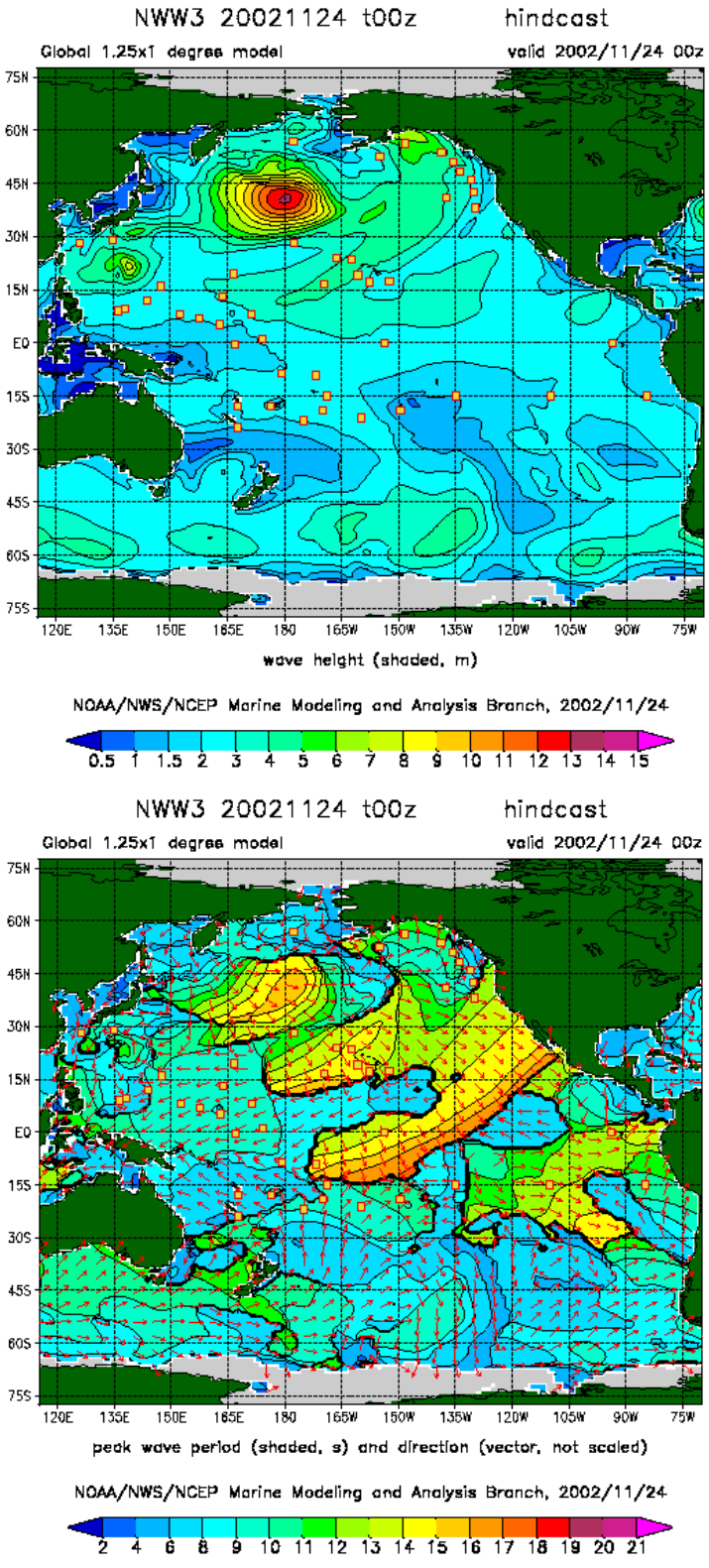


Figure 1. Significant wave height (upper panel) and dominant period and propagation direction for the global surface wave field on November 24, 2002 as predicted by WW3.

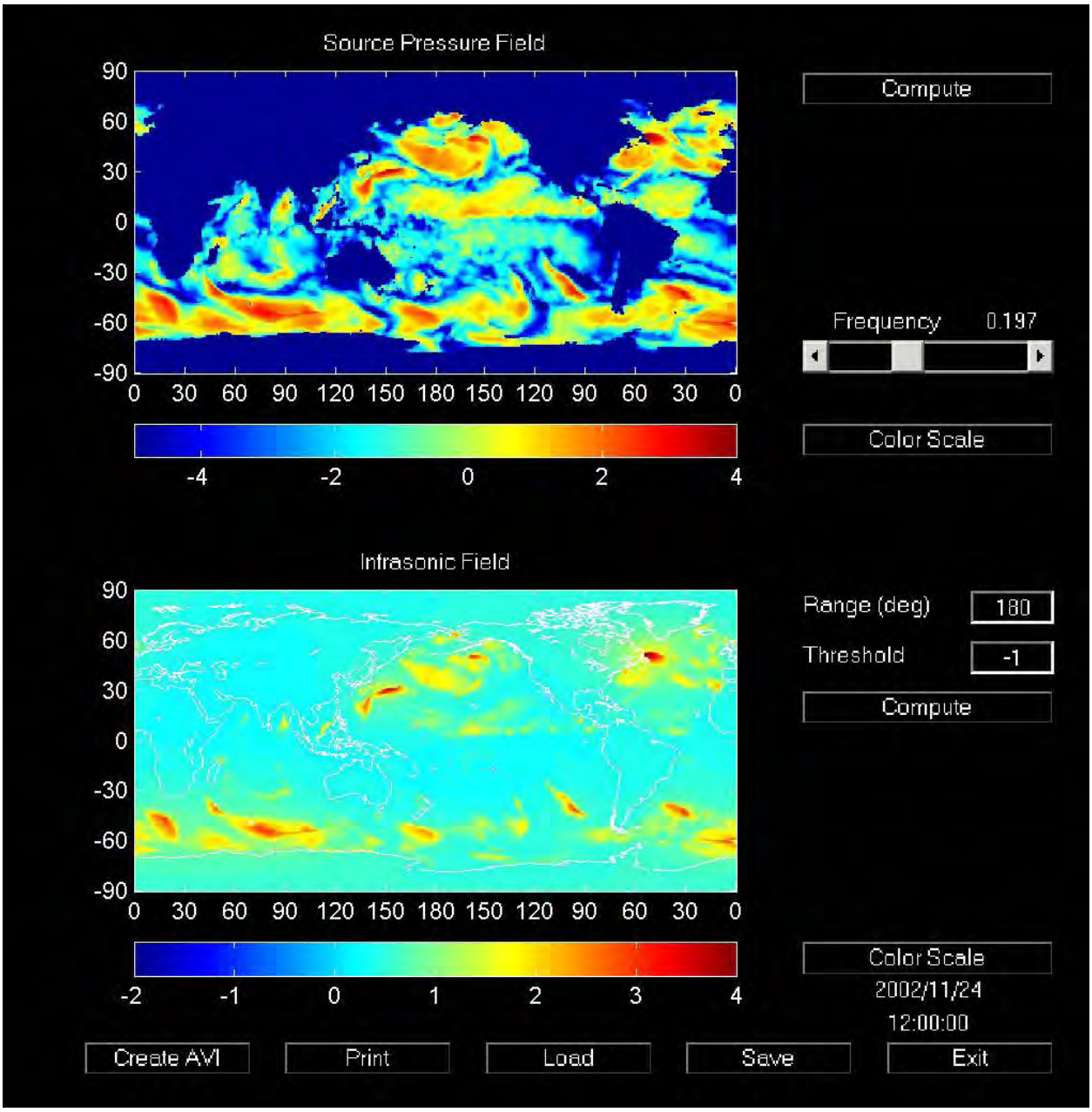


Figure 2. GUI panels showing the predicted source pressure field (top panel) and resultant infrasonic field (bottom panel) at a microbarom frequency of 0.2 Hz, as calculated from the output of WW3 for November 24, 2002. The infrasonic field results from a propagation limit of 180 degrees and a source magnitude cutoff of –1.

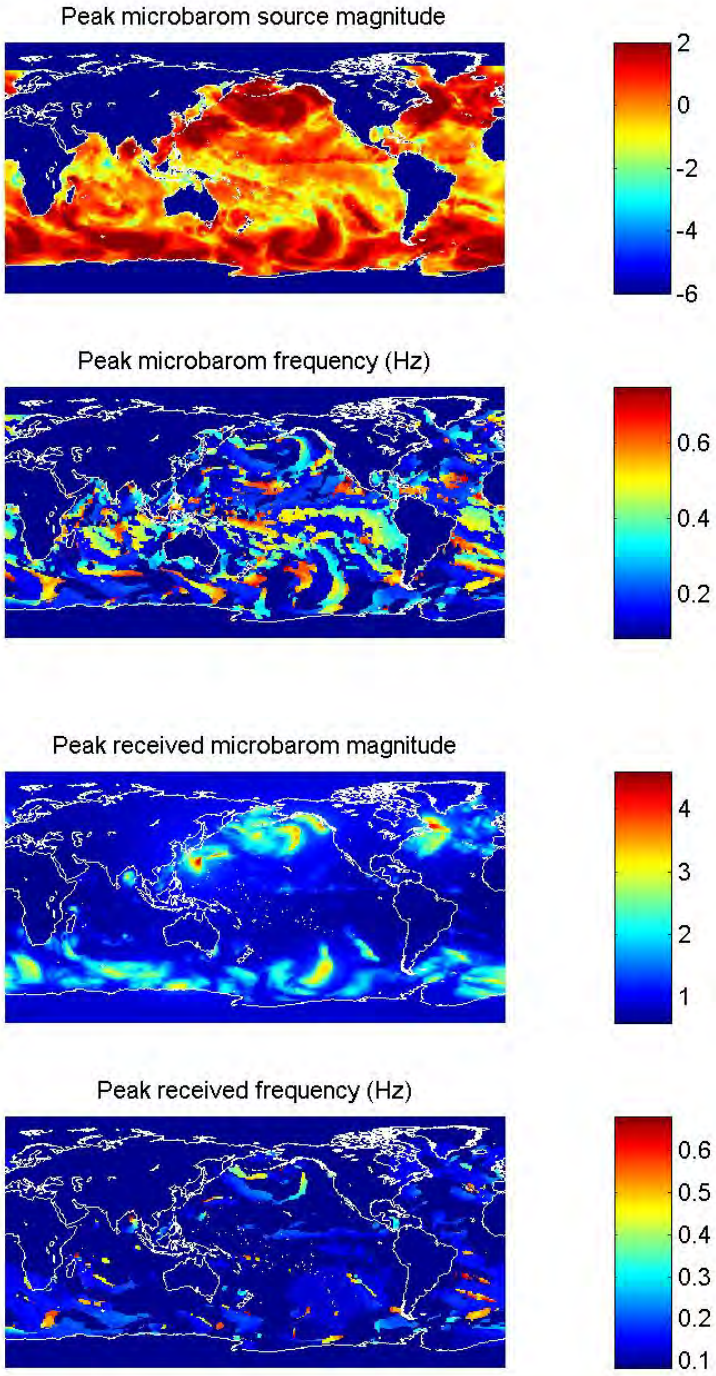


Figure 3. Panels showing peak source magnitude (top), the frequency at which the source peak magnitude occurs (second), peak received magnitude (third), and the frequency at which the received peak occurs (bottom) based on the results of WW3 for November 24, 2002.

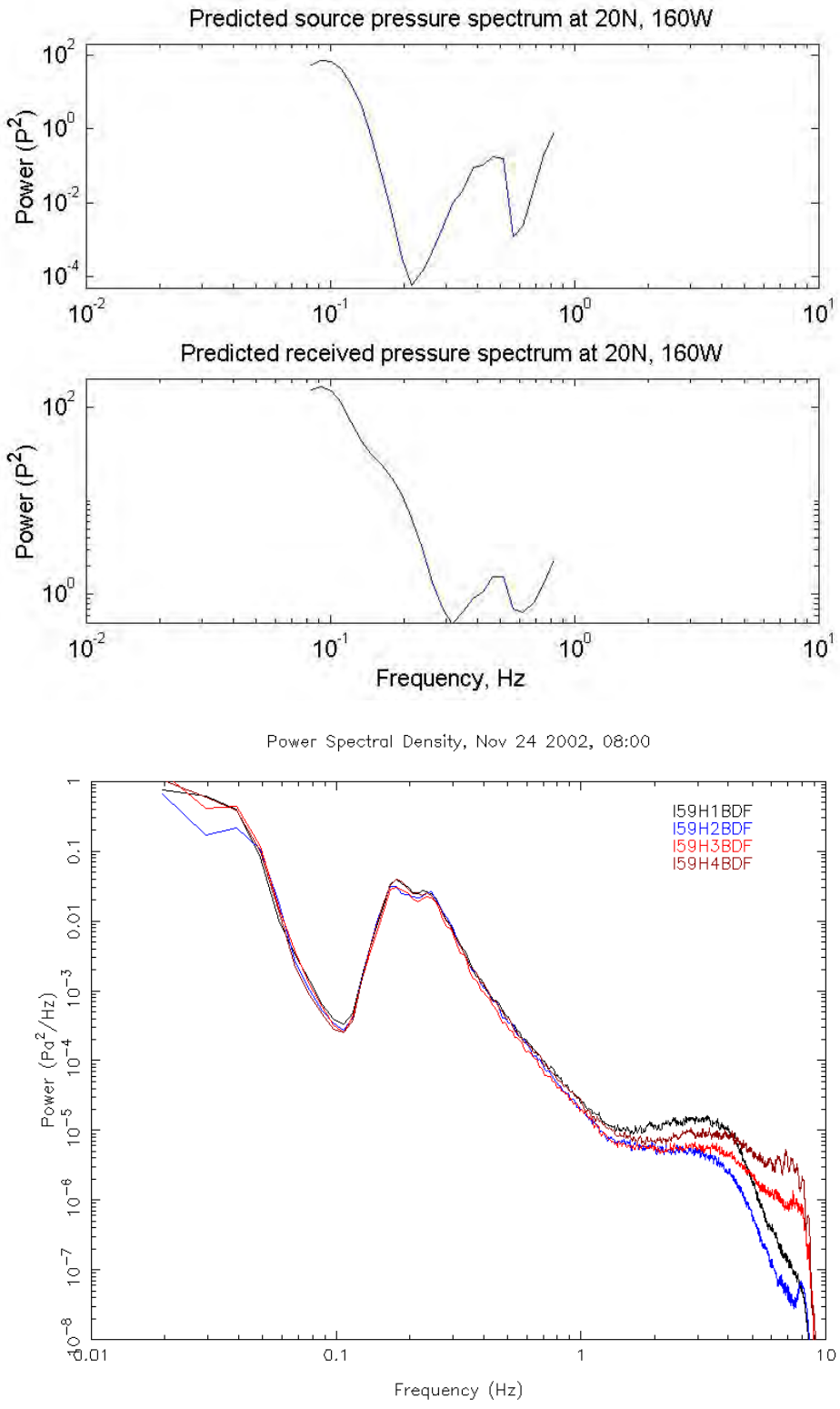


Figure 4. Predicted source pressure spectrum (top), predicted received pressure spectrum (middle) and observed pressure spectrum (bottom) for the Hawaii (20°N, 160°W) region on November 24, 2002.

INTEGRATION OF INFRAMAP WITH NEAR-REAL-TIME ATMOSPHERIC CHARACTERIZATIONS AND APPLICATIONS TO INFRASOUND MODELING

Robert G. Gibson and David E. Norris

BBN Technologies

Sponsored by Air Force Research Laboratory

Contract No. DTRA01-01-C-0084

ABSTRACT

Predicting the long-range propagation of infrasound relies on characterization of the propagation medium, namely the global atmosphere from the ground to altitudes above 100 km. The ability to realistically model infrasound propagation depends on the fidelity of the atmospheric characterization. The analysis tool kit InfraMAP (*Infra*sound *M*odeling of *A*tmospheric *P*ropagation) offers a range of options for specifying the propagation environment. The baseline capability utilizes global climatological models of temperature, wind and air composition. Of particular interest herein is the recently developed capability to incorporate near-real-time atmospheric updates, such as the output from numerical weather prediction models, to supplement climatological characterization of the environment.

New InfraMAP modules support integration of propagation models (ray-tracing, parabolic equation) with two versions of near-real-time atmospheric characterizations. First, output from the Navy's synoptic model NOGAPS (Navy Operational Global Atmospheric Prediction System) can be imported into InfraMAP and merged with the baseline climatological models, HWM-93 and NRL-MSISE-00. NOGAPS generates global grids of temperature and wind, several times per day, on a one-degree grid over 27 isobaric surfaces. The corresponding altitudes are not sufficiently high to characterize the entire region of interest for infrasound propagation; therefore, NOGAPS output is merged with climatology within InfraMAP at the higher altitudes to cover the full propagation domain. Second, output from the NRL-G2S (Naval Research Laboratory Ground to Space) specification can be imported and used to characterize the entire propagation environment. NRL-G2S is a semi-empirical spectral model that fuses climatological models with output from operational numerical weather prediction models. These new capabilities extend the ability of infrasound researchers to investigate critical propagation phenomena and to conduct sensitivity studies.

Validation efforts are essential to build confidence in the modeling procedures and are used to assess the value of potential improvements to the atmospheric specification. Observed infrasound events with known ground-truth represent valuable sources of opportunity for use in validating propagation modeling techniques. InfraMAP has been used to model long-range propagation of infrasound originating from the space shuttle and other sources. Predictions of infrasound arrival times and azimuths resulting from three-dimensional ray tracing through various environments are compared with observed data.

OBJECTIVES

The primary objective of this research effort is the development of an enhanced InfraMAP software tool kit that enables higher-fidelity infrasound propagation modeling by incorporating near-real-time atmospheric characterizations. This effort is intended to support improved event localization and phase identification. A validation effort is also being undertaken, using a diverse set of observations and ground-truth, in order to improve confidence in the modeling techniques and provide calibration in support of operational needs. Anticipated uses of the software include: in-depth analysis of events and scenarios of particular monitoring interest; sensitivity analyses; and detailed infrasound localization and detection studies.

RESEARCH ACCOMPLISHED

Near-Real-Time Environmental Updates to InfraMAP

The InfraMAP software tool kit is composed of research-grade propagation models (3-D ray tracing, normal modes and parabolic equation) and upper-atmospheric characterizations, integrated to allow for user-friendly model execution and data visualization. InfraMAP can be applied to predict travel times, bearings, and amplitudes from potential event locations worldwide. Such predictions can be used to identify infrasound phases and to define travel-time and bearing corrections, which can improve localization performance (Gibson and Norris, 2002a). Recently introduced InfraMAP modules allow for analysis of propagation variability due to environmental effects, calculation of source location using measurements and model predictions, and prediction of network localization performance (Norris and Gibson, 2002).

Range-dependent characterizations of temperature, wind and air composition are incorporated into the propagation models to account for temporal and spatial variability of the atmosphere. The baseline atmospheric characterizations in InfraMAP are two empirical models: the horizontal wind model, HWM-93 (Hedin *et al.*, 1996), and the mass spectrometer-incoherent scatter radar extended model, NRLMSISE-00, which provides temperature and air composition (http://uap-www.nrl.navy.mil/models_web/msis/msis_home.htm). The integration of the NRLMSISE-00 model into InfraMAP is a recent upgrade from the earlier baseline temperature model, MSISE-90 (Picone *et al.*, 1997). Using these characterizations, wind, temperature, and molecular densities are modeled from the surface into the thermosphere and include spatial, diurnal, and seasonal effects. The models are climatological in that they predict the mean environmental profiles based on assimilation of multiple years of data.

The HWM and MSISE models were chosen for use in InfraMAP due to their high fidelity over a wide range of altitudes and temporal scales, their global domain, and the relative ease of software integration. Validation studies conducted to date using InfraMAP with the HWM and MSISE characterizations indicate generally good agreement between modeled propagation paths and infrasound measurements. However, there exist cases in which measured infrasound phases are not adequately predicted using the baseline InfraMAP. Global climatological models such as HWM and MSISE that are based solely on historical data do not capture fine-scale temporal and spatial atmospheric structure. The current effort addresses the incorporation of appropriate near-real-time sources of atmospheric information to improve the estimate of the infrasound propagation environment.

Classes of near-real-time atmospheric updates include:

- *in situ* observations, such as measured profiles from radiosondes, and
- physics-based synoptic models that assimilate observations from a number of sources.

Models generally produce gridded output, whereas observed profiles (e.g., radiosondes) are not gridded, i.e., the observations are not uniformly sampled geographically or in altitude. InfraMAP allows for integration of *in situ* data sources with range-independent propagation modeling by providing an option for manually importing user-defined atmospheric profiles. The focus of activity during this effort has been on the integration of output from synoptic models with InfraMAP.

New InfraMAP modules have been developed to incorporate output from NOGAPS, which provides near-real-time global grids of temperature and wind over three spatial dimensions (Bayler and Lewit, 1992). NOGAPS, originated by the Navy's Fleet Numerical Meteorology and Oceanography Center (FNMOC), is a numerical weather prediction system that utilizes not only profiles measured by radiosondes, but also an extensive data set of ship-based, land-

based and satellite measurements. It provides temperature and wind speed, several times per day, on a one-degree grid over 27 isobaric surfaces. Output data from NOGAPS are readily available from the ground up to the 10 mb pressure surface (approx. 30-35 km).

Figures 1a and 1b show examples of temperatures along a slice of the atmosphere between the South Pole and the North Pole, at a constant longitude, from NRLMSISE-00 and NOGAPS, respectively, for a particular day and time. The large-scale temperature features are similar between the climatology and the near-real-time characterization, but the fine-scale structure is different. It can also be observed that the NOGAPS grid is non-uniform in altitude, due to the use of pressure surfaces rather than constant altitude surfaces. The upper boundary of the NOGAPS grid can be seen, varying between approximately 27 and 33 km in this case.

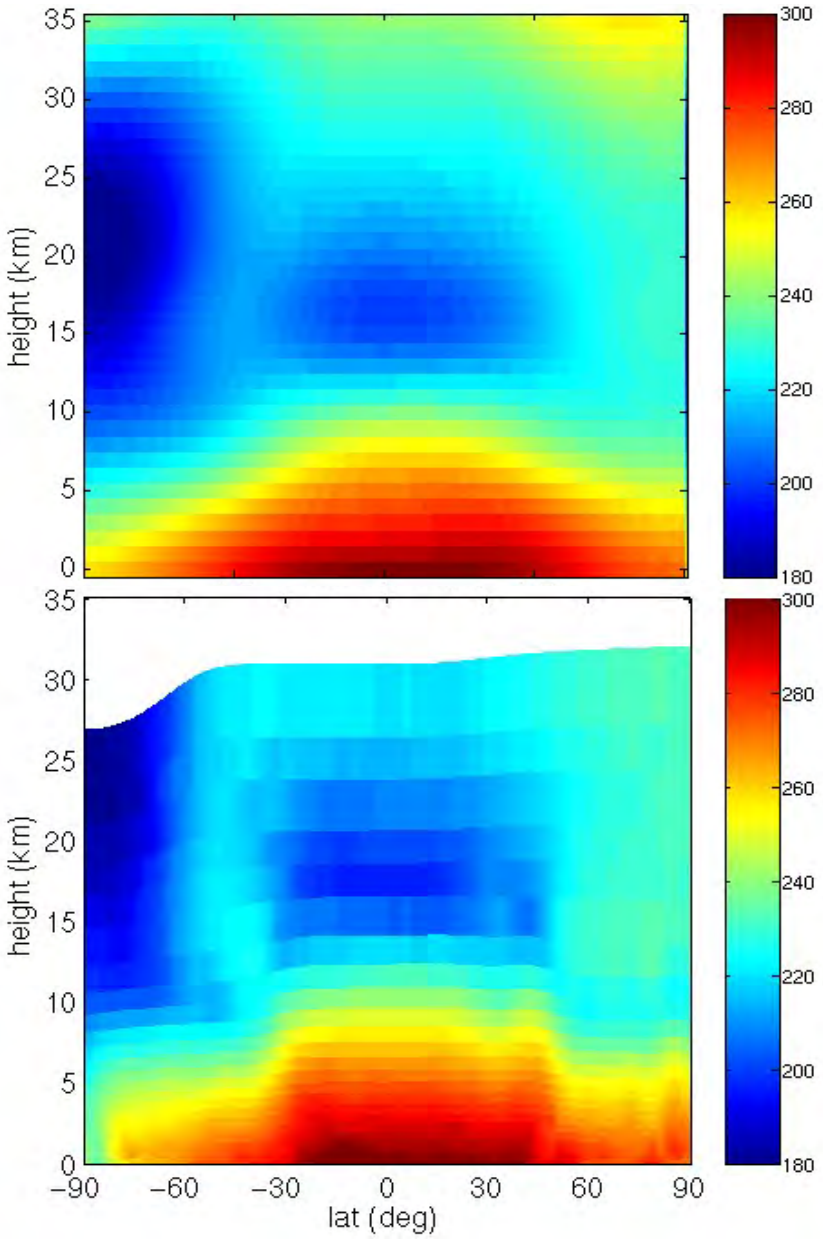


Figure 1a (above) and 1b (below). Temperatures (in degrees K) from NRLMSISE-00 climatology (above) and NOGAPS numerical weather prediction model (below), along a slice of the atmosphere at constant longitude of 60 degrees W, for year 1999, day 206, 0 UT.

An additional example is presented in Figures 2a and 2b, which show zonal winds over a region between the equator and the North Pole (in a Mercator-style projection), from HWM-93 and NOGAPS, respectively, for a particular day and time (29 September 2002). In the HWM figure, winds are shown at a constant altitude of 30 km. In the NOGAPS figure, winds are shown at the 10 mb constant pressure surface, which is at a slowly varying altitude of approximately 30 km throughout the region. The large-scale features are similar in the two figures, showing a shift in wind direction with increasing latitude. However, there is considerably more fine-scale structure in the NOGAPS characterization.

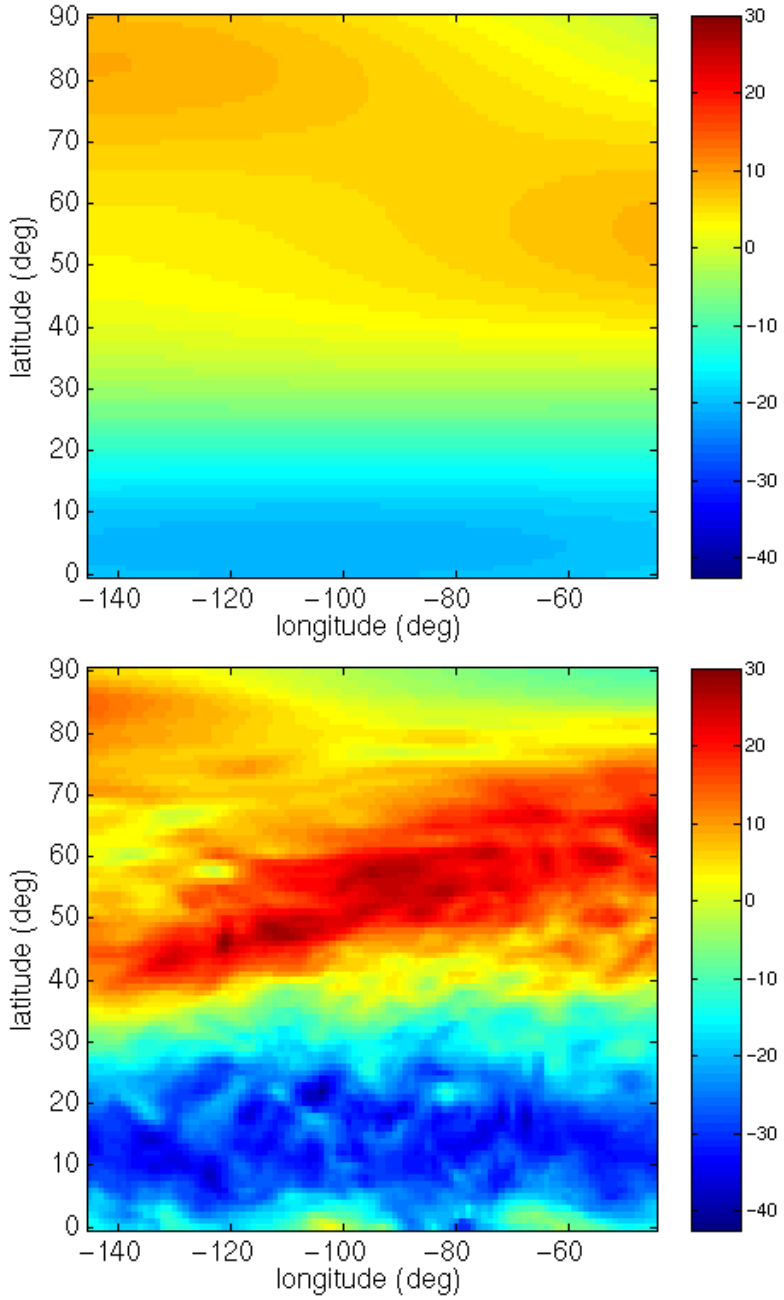


Figure 2a (above) and 2b (below). Zonal winds (in meters per second) from HWM-93 climatology (above) and NOGAPS numerical weather prediction model (below), above a region of the northern hemisphere at constant altitude of 30 km (above) and constant pressure surface of 10 mb (below), for year 2002, day 272, 0 UT.

NOGAPS is a promising environmental characterization for use with infrasound propagation models due to its global domain, frequent updates, and relatively high altitude coverage. However, infrasound propagation modeling requires information well into the thermosphere (approx. 120 km). Therefore, climatological models remain an essential tool for estimating the environment, particularly at high altitudes. Techniques have been developed within InfraMAP to merge NOGAPS grids at lower altitudes with climatological models at higher altitudes.

Links have been implemented to archives of NOGAPS grids, and modules have been developed to import and decode the files for use in InfraMAP. A user then selects a subset of the global grid (i.e., a range of latitude and longitude cells) for use in a propagation scenario of interest. Within the region of interest, NOGAPS output is used in conjunction with the HWM and MSISE characterizations to define the propagation environment. A user specifies the thickness of the transition layer above NOGAPS. A cubic interpolation algorithm that matches the values and their derivatives at the boundaries is employed to join NOGAPS temperatures, zonal winds and meridional winds with the climatologies. This approach results in smooth first derivatives and continuous second derivatives, which ensures that non-physical behavior is not introduced in the ray path predictions. Examples of resulting temperature profiles are shown in Figure 3. Four profiles are shown for locations at the corners of a specified region. The transition region in this case is 10 km in thickness.

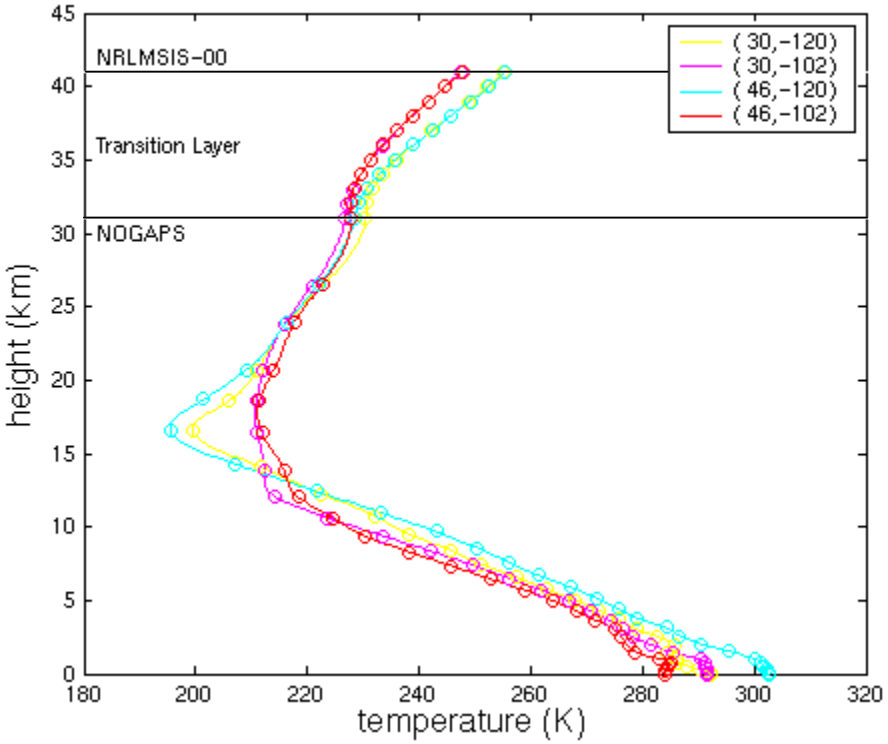


Figure 3. Temperature profiles (in degrees K) at four locations over North America, from InfraMAP. NOGAPS numerical weather prediction model is used at lower altitudes and NRLMSISE-00 climatology is used at higher altitudes, with a transition region between. Year 2002, day 272, 0 UT.

NOGAPS characterizations can be viewed in InfraMAP's environmental menu and can be used in propagation modeling. In order to accommodate an environment defined by a gridded database such as NOGAPS, modifications have been made to InfraMAP's interface between propagation codes and environmental characterizations, particularly in order to allow range dependence. To propagate three-dimensional rays through gridded data, wind and temperature values and their spatial derivatives must be estimated at each point along a ray path. Because ray models are highly sensitive to sharp changes in sound speed, the estimation approach must avoid introducing gradient variability that is not inherent in the original data grid.

InfraMAP is also being upgraded to incorporate an additional near-real-time atmospheric characterization. Output from the NRL-G2S (Naval Research Laboratory Ground to Space) specification can be used to characterize the entire propagation environment. NRL-G2S is a semi-empirical spectral model that fuses climatological models with output from operational numerical weather prediction models (Drob and Garces, 2002). Upper atmospheric characterizations are based on NRLMSISE-00 and HWM-93. Lower atmospheric characterizations are based not only on NOGAPS but also on output of other prediction systems and other relevant global data sets. NRL-G2S employs vector spherical harmonics in the data assimilation process to produce a set of model coefficients for each day and time of interest. Coefficient sets can then be used to reconstruct fields of each atmospheric state variable as well as spatial derivatives. An InfraMAP user can access coefficient sets from a data repository, import the coefficients, and utilize the resulting NRL-G2S specifications within InfraMAP to define a propagation environment.

Supplementing the baseline climatological models with available near-real-time updates is likely to yield improved infrasound predictions, particularly for propagation paths that dwell primarily in the lower and middle atmosphere, where updated data are more readily available.

Other Enhancements to Environmental Specifications in InfraMAP

In addition to the incorporation of NRLMSISE-00, NOGAPS and NRL-G2S specifications, a number of other enhancements have been introduced in InfraMAP to improve the fidelity of the environmental characterization. They include:

- Integrated archive of solar and geomagnetic parameters;
- Incorporation of variable molecular weight in sound velocity calculations;
- Incorporation of variable specific heat ratio in sound velocity calculations.

These are primarily intended to improve characterization of the thermosphere.

Solar flux and geomagnetic disturbances from solar activity influence the modeled atmospheric temperature and winds above 100 km and have been shown to affect the modeled propagation of thermospheric infrasound (Gibson and Norris, 2002a). The variables F10.7, F10.7A, and A_P are used as input to the HWM and MSISE models, and entry of values for these parameters allows their effects to be modeled in InfraMAP.

- A_P is the planetary equivalent amplitude of daily geomagnetic disturbance,
- F10.7 is the daily solar radio flux at 10.7 cm wavelength, and
- F10.7A is the 81 day average of F10.7 values, centered on the day of interest.

Archives of historical values, obtained from the National Geophysical Data Center (NGDC), have been integrated in InfraMAP, and appropriate daily values are automatically selected as defaults in a propagation run. Daily values of the parameter A_P for the year 2001 are shown in Figure 4a. Temperatures from MSISE, calculated for a range of thermospheric altitudes above the North Pole, are shown in Figure 4b for a representative range of A_P values.

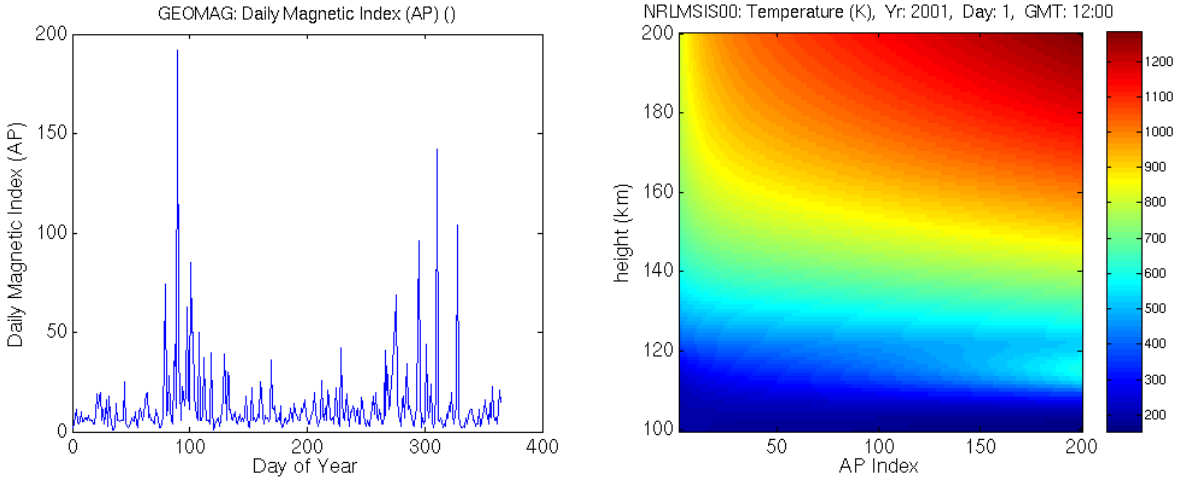


Figure 4a (left) and 4b (right). Daily values of geomagnetic disturbance parameter A_P for year 2001 (left) and thermospheric temperatures above the North Pole for a range of A_P, using NRLMSISE-00 (right).

The values of the average molecular weight and the specific heat ratio (the ratio of heat capacity at constant pressure to heat capacity at constant volume), both of which depend on air composition, have effects on calculations of sound velocity and acoustic absorption. The determination of these quantities using NRLMSISE-00 has recently been included in InfraMAP calculations. This will improve fidelity of the modeling of thermospheric infrasound at little or no computational cost. Examples of typical ranges of these parameters over the annual cycle, as predicted from MSISE, are shown in Figures 5a and 5b.

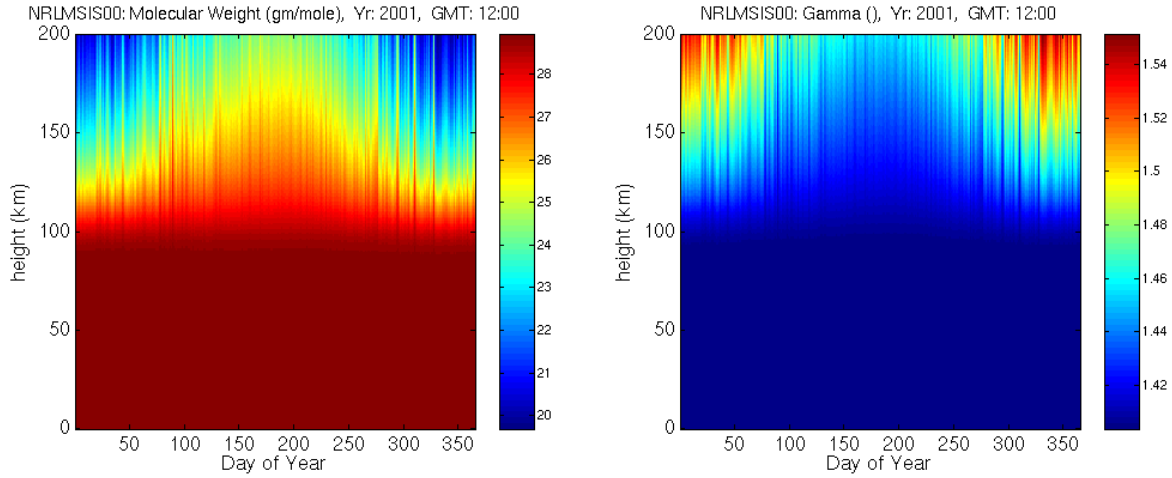


Figure 5a (left) and 5b (right). Modeled values of average molecular weight (in grams/mole, at left) and specific heat ratio (dimensionless, at right) at a range of altitudes above the North Pole, calculated using NRLMSISE-00 over the annual cycle. The "spiky" features result from incorporation of the solar and geomagnetic measurements for the year 2001 (as shown in Figure 4a).

Software Integration

The near-real-time update capabilities developed to date and other environmental enhancements have been integrated into the InfraMAP software tool kit, and graphical user interfaces have been developed. User manual development and software beta testing are in progress. The most recent software release, InfraMAP 3.0, developed under a parallel effort (Norris and Gibson, 2002), will be upgraded in a subsequent release as part of this effort.

Model Validation Efforts

Validation efforts are essential to build confidence in the modeling procedures and to identify areas where further refinements are required. Where ground-truth is available, validation results support event localization, phase identification and calibration efforts.

Validation activities during this effort have focused on infrasound from rocket launches. Space shuttle launches from Cape Kennedy, FL have been frequently observed at infrasound arrays at Los Alamos, NM (DLIAR prototype array), at Lac du Bonnet, Canada (IS10 array), and at other locations in the eastern US. Reasonably good agreement in both travel time and azimuth has been obtained between ray tracing model results using InfraMAP and observed infrasound, and biases have been quantified for individual events (Gibson and Norris, 2002b). Components of infrasound signals have been associated with both the ascending orbiter and the descending solid rocket boosters. More recently, analyses have been conducted of annual trends in observability, travel time and azimuth of infrasound signals from space shuttle launches (Gibson and Norris, 2002c). Preliminary investigations have also been conducted into the improvements in model fidelity that are achievable using NOGAPS environmental updates. These investigations are ongoing and will focus on first establishing a baseline and then documenting the modeling improvements achievable with near-real-time updates as compared to climatology.

Based on the successful model results previously obtained for space shuttle launches, the authors participated in the Department of Defense Columbia Investigation Support Team (DCIST) Infrasound Working Group (ed. Bass, 2003). InfraMAP was used to model infrasound from the reentry and approach of the space shuttle Columbia up to the point of its untimely breakup. During this investigation, the NRL-G2S specifications were used to characterize the propagation environment. Range-independent propagation modeling was conducted from a large number of points along the reentry trajectory to the locations of those infrasound arrays in the western US and Canada that observed the event. Ray tracing model predictions of arrival time, azimuth and elevation angle were generally in good agreement with the observations.

CONCLUSIONS AND RECOMMENDATIONS

The InfraMAP tool kit is used to predict the critical propagation characteristics that affect infrasound localization and detection. Adequate atmospheric characterization is necessary to correct for biases in travel time and azimuth that result from the propagation environment in order to avoid large location errors. *In situ* observations of winds and temperature can be used in InfraMAP for range-independent propagation modeling. Techniques have been developed to integrate output from the NOGAPS numerical weather prediction model with climatology for use in range-dependent propagation models. The NRL-G2S atmospheric specifications can also be used within InfraMAP. InfraMAP's integrated set of models will allow for higher fidelity propagation modeling than has previously been available to the infrasound monitoring community. As new high-fidelity environmental characterizations become available, they should be considered for integration into an enhanced version of the InfraMAP software.

Rocket launches and reentries generate infrasound signals for use in model validation studies. Comparisons of measured and modeled arrival times and azimuths suggest that baseline infrasound modeling techniques are good but that higher fidelity predictions would likely be obtained with the use of near-real-time wind and temperature characterizations. Further modeling of a large set of observed events, using updated atmospheric characterizations, should continue in order to quantify the improvements in travel time and azimuth predictions that are achievable.

REFERENCES

Bayler, G. and H. Lewit (1992), The Navy Operational Global and Regional Atmospheric Prediction System at the Fleet Numerical Oceanography Center, *Weather and Forecasting*, Vol. 7, No. 2.

Drob, D. P. and M. Garces (2002), The spatiotemporal variability of infrasound path partitioning, *Proceedings of the Infrasound Technology Workshop*, De Bilt, NL.

Gibson, R. and D. Norris (2002a), Development of an Infrasound Propagation Modeling Tool Kit, DTRA-TR-99-47.

Gibson, R. G. and D. E. Norris (2002b), Integration of near-real-time atmospheric models with InfraMAP and applications to modeling infrasound from rockets, *Proceedings of the 24th Seismic Research Review - Nuclear Explosion Monitoring: Innovation and Integration*, Ponte Vedra Beach.

Gibson, R. G. and D. E. Norris (2002c), Long-range infrasound propagation modeling using updated atmospheric characterizations, *J. Acoust. Soc. Am.*, **112**, No. 5, Pt. 2, 2380.

Hedin, A. E, E. L. Fleming, A. H. Manson, F. J. Schmidlin, S. K. Avery, R. R. Clark, S. J. Franke, G. J. Fraser, T. Tsuda, F. Vial, and R. A. Vincent (1996), Empirical wind model for the upper, middle, and lower atmosphere, *J. Atmos. Terr. Phys*., **58**, 1421-1447.

Norris, D. E. and R. G. Gibson (2002), InfraMAP enhancements: environmental/propagation variability and localization accuracy of infrasonic networks, *Proceedings of the 24th Seismic Research Review - Nuclear Explosion Monitoring: Innovation and Integration*, Ponte Vedra Beach.

Picone, J. M., A. E. Hedin, S. L. Coffey, J. Lean, D. P. Drob, H. Neal, D. J. Melendez-Alvira, R. R. Meier, and J. T. Mariska (1997), The Naval Research Laboratory program on empirical models of the neutral upper atmosphere, in *Astrodynamics: Advances in the Astronautical Sciences*, Vol. 97, edited by F. R. Hoots, B. Kaufman, P. J. Cefola, and D. B. Spencer, American Astronautical Society, San Diego, Ca.

Report to the Department of Defense on Infrasonic Re-Entry Signals from the Space Shuttle Columbia (STS-107) (2003), ed. by H. Bass, National Center of Physical Acoustics, University of Mississippi.

RECENT INFRASOUND ANALYSIS

Rodney W. Whitaker, Thomas D. Sandoval and J. Paul Mutschlecner

Los Alamos National Laboratory

Sponsored by National Nuclear Security Administration
Office of Nonproliferation Research and Engineering
Office of Defense Nuclear Nonproliferation

Contract No. W-7405-ENG-36

ABSTRACT

We will discuss analysis of several fairly recent events using the Matseis package, Infra_Tool. The events include a recent explosive test, Watusi at the Nevada Test Site (NTS), recent earthquakes, a recent bolide, and the tragic return of the shuttle Columbia. Watusi, with a charge weight of 19 tons, was recorded at four Los Alamos National Laboratory/Department of Energy (LANL/DOE) infrasound arrays. Summary results will be presented and followed by a comparison to other HE (high explosive) data recorded by LANL arrays. Analysis of moderate earthquakes (m_b < 5.0) has continued and results are beginning to suggest that larger (km) sized arrays do not see these events as well as smaller (100 m) arrays, which is good for monitoring applications. For Columbia, the LANL arrays were close to the flight path and recorded N wave records, which will be presented. We will illustrate the new location software in Matseis, which utilizes simple travel time curves for three infrasound phases. This new software performs the same type of location as LocSat but can be run separately from the LibLoc library.

OBJECTIVE

We will discuss the analysis of infrasound data from several recent events. We used Infra_Tool to perform the primary analysis; this tool is part of the Sandia National Laboratory (SNL) analysis software, Matseis.

RESEARCH ACCOMPLISHED



Watusi was a high-explosive (HE) test executed at the Nevada Test Site (NTS) on 9/28/02 at 2:25 pm PDT (21:25 UTC) with an explosive force of 38,000 lbs of TNT equivalent yield. The configuration was a cylindrical container, which was partially above ground level. Group EES-8 (now EES-2) made infrasonic measurements at four arrays: NTS; St. George, UT, (SGAR); and two arrays in Los Alamos, LSAR and DLIAR. The coordinates of the arrays are listed in Table 1. Data were collected at all four arrays. The geographical coordinates of the test were: 37˚.099 N and 116˚.092 W in Area 4 of the NTS. The Los Alamos National Laboratory (LANL) Dynamic Experimentation Division (DX) planned and executed the test.

Table 1. Coordinates of the Watusi test.

Array Name	Latitude (degrees)	Longitude (degrees)
NTS	36.7056	-115.9631
SGAR	37.0153	-113.6153
LSAR	35.867	-106.334
DLIAR	35.867	-106.334

Each of the arrays has four microphones in rectangular or triangular configurations. The first three arrays have sensors spaced approximately 100 m apart, while the last array, DLIAR, is a larger array with 1.2 km baseline. LSAR sits inside the area of the DLIAR array, and for purposes here, has essentially the same location. Sampling rates were 20 samples per second (sps) for the first three and 10 sps for DLIAR. Sensors in the first three arrays are Chaparral Physics Model 2 microphones with a nominal frequency range of 0.1–100 Hz; however, only data below 10 Hz are used for the current sample rate. DLIAR uses the Chaparral Physics model 5 microphone with a frequency range of 0.02–100 Hz, but only data below 4 Hz are used with its current sample rate. Distances of the arrays from the event were: NTS, at 45 km; SGAR, at 219 km; and LSAR and DLIAR, at 883 km.

Data processing was performed with the SNL analysis package Matseis; a general package for waveform analysis built around MATLAB. Matseis allows easy processing of array data for correlation analysis, spectrograms, power spectral density (PSD), waveform display, and amplitude measurements.

For amplitude data, we took the peak-to-peak values of the largest single-cycle feature in the region of peak correlation. This measure of amplitude follows our practice for other tests we have measured since the early 1980s. For each array, the average of the four channels was found and converted to microbars. The results are given below in Table 2:

Table 2. Conversion of each array into microbars.

Array	Amplitude (microbars)
NTS	3.2
SGAR	4.07
LSAR	0.58
DLIAR	0.53

As used in airblast measurements, scaled ranges are used to make amplitude comparisons for events of different yields. For the HE data, we use the charge weight in kilotons, including a factor of two for being on the surface, raised to the 0.5 power. This formulation follows from traditional scaling relations where equal pressures are found at scaled ranges. The use of 0.5, rather than the near-field value of 1/3, is to account for the long range of our measurements.

The waveform data are presented in Figure 1 for all four arrays.

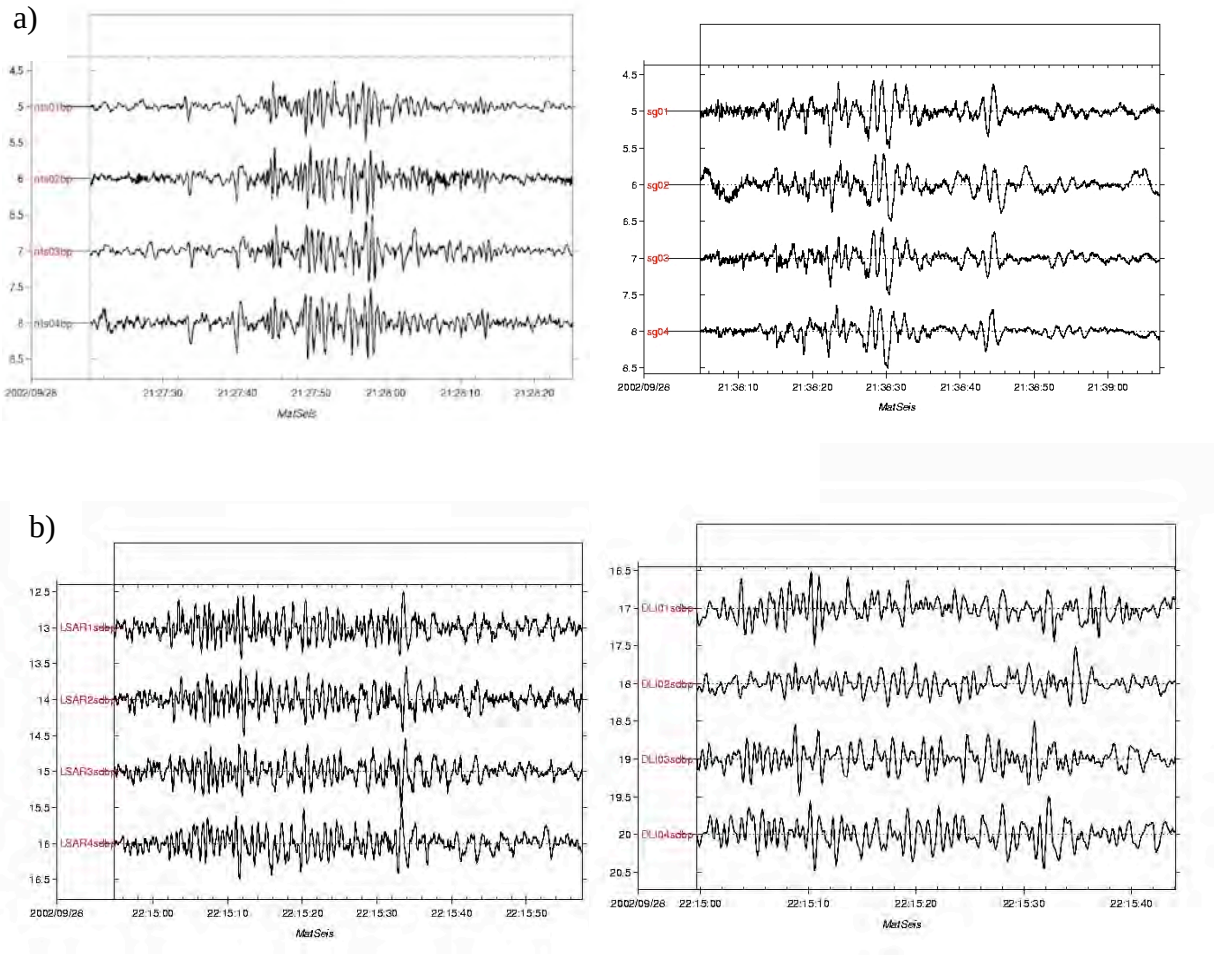


Figure 1. Waveforms (normalized amplitude versus time) are shown in a) above from the NTS array, left, and St George array, right. In b) we show waveforms for LSAR, left, and DLIAR, right. All plots are around the time of peak correlation.

Figure 2 shows the Watusi data for St. George and Los Alamos (squares) on the plot for the eight Defense Nuclear Agency (DNA) events. Here we plot the wind corrected amplitudes as a function of scaled range. The wind correction (or normalization) adjusts for the effects of atmospheric winds at 50 km (Mutschlecner et al. (1999)). Dr. Douglas Drob, Navel Research Laboratory (NRL), provided the wind profiles for the time of the event (Drob, 2003), and through the combination of observations and models gives a value of 12 m/s for the zonal wind at 50 km. This value gives normalized amplitudes at St. George and Los Alamos of 2.48 and 0.353 microbars. For scaled ranges we used two times the charge weight in kilotons raised to the 0.5 power.

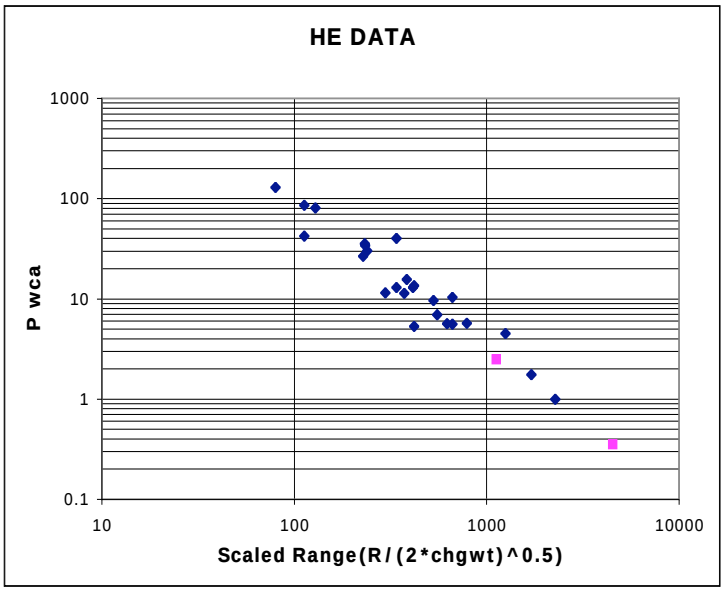


Figure 2. Wind corrected amplitude vs scaled range for USMR 9 (diamonds) and Watusi (squares) data.

The other events in Figure 2 (diamonds) are from a series of, then DNA, large-scale explosive tests at White Sands Missile Range (WSMR). There were eight tests from 1981 to 1993 ranging from 24–4,880 tons of ammonium nitrate and fuel oil (ANFO). The ranges of infrasonic measurements were from 250–5,300 km. The Watusi data are in good agreement with the Watusi data. We did not include NTS, as this station was close enough to the event to see different propagation paths. LSAR and DLIAR are collocated but LSAR uses a sampling rate of 20 sps, whereas DLIAR uses 10 sps. The LSAR sensors are the same type used in the earlier measurements, so we used the LSAR data in Figure 2. With the addition of the Watusi data, our relation now spans almost two orders of magnitude in scaled range. The least squares regression of the data yields:

$$P = 59457*(SR)^{-1.4072} \text{ with an } R^2 \text{ of } 0.93$$

In this relation, P is wind corrected amplitude and SR is scaled range.

Next we show results for some recent earthquake infrasound signals, which will also illustrate some of the newer features of the Matseis Infra_Tool (Figure 3). First is an earthquake from 10/16/1999, at 9:46:44 UT, with a magnitude of 7.0 located at 33.6˚ N and 116.27˚ W. The Infra_Tool plot given below shows correlation, trace velocity (km/s), azimuth (degrees), and a channel of raw or bandpassed data. In the current Infra_Tool, one can cycle through all the channels selected in the Matseis data window, switch between correlation and Fstat, change parameters of processing and do a quick update in Infra_Tool, and get standard deviations for the three plotted variables that fall within the vertical green averaging window. Features from earlier versions remain in the newest version.

This event shows a strong seismic surface-wave arrival, about 09:50 UT, before the main acoustic arrival, just after 10:30 UT. The surface wave amplitude is larger than the acoustic arrival amplitude, which is not always the case for infrasound data. Also we should note that the back azimuths from the acoustic signals for earthquakes might not always be on the epicenter as that may not be the region of greatest ground motion.

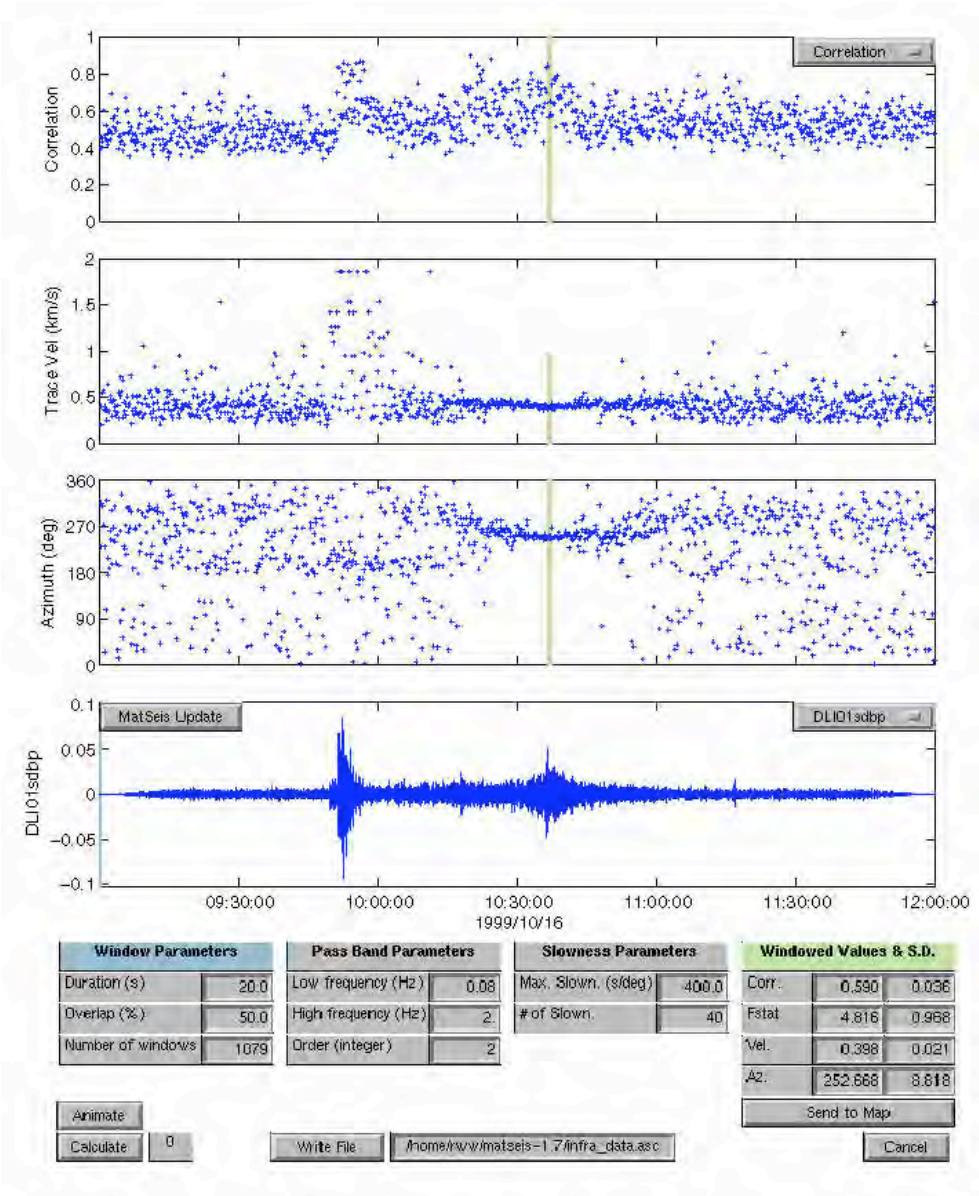


Figure 3. Infra_Tool analysis for the 10/16/1999 earthquake.

In Figure 4 we show selected results for the 11/03/2002 Alaska earthquake, which was a magnitude 8.5 event with epicenter of 63.52˚ N and 147.44˚ W at 22:12:41 UT. An impressive surface wave arrives at DLIAR (4,133 km distance) at 22:32 UT and lasts for over four minutes. The main acoustic arrival follows at 01:50 on 11/04. Figure 4 shows the raw channel data for the surface wave as recorded on DLIAR. The larger amplitude part of this signal has a peak Fstat over 2,500, in a band of 0.02—2.0 Hz.

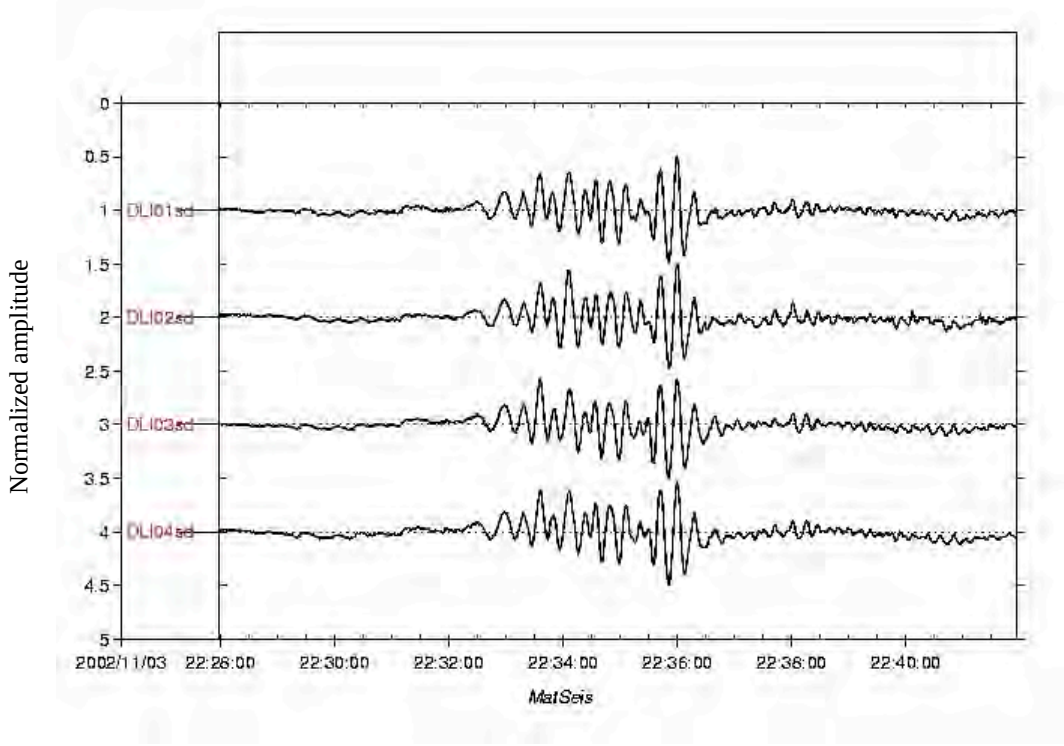
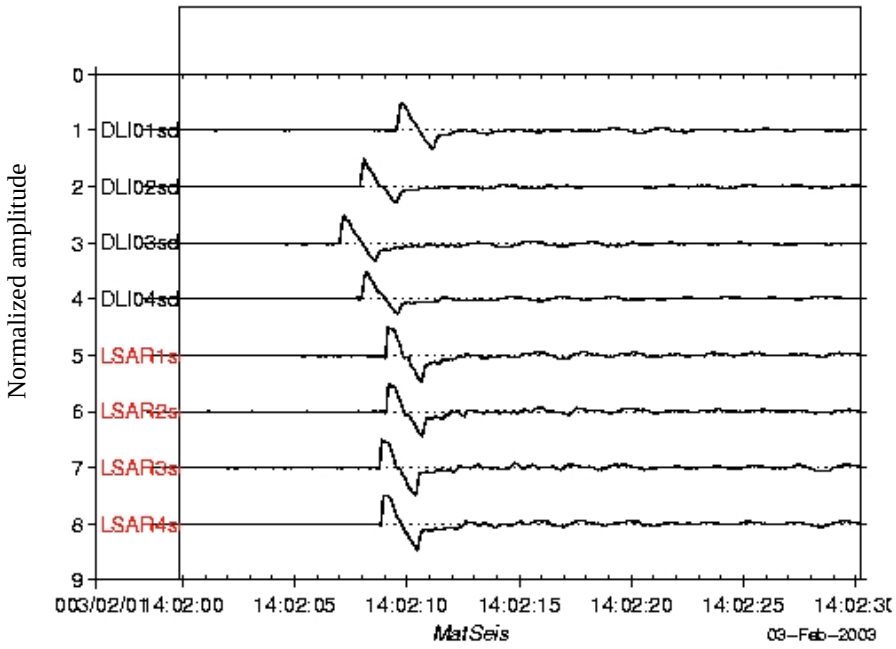


Figure 4. The seismic surface wave recorded at DLIAR for the 11/03/2002 earthquake.

Other recent efforts on earthquake analysis have concentrated on searching for signals from smaller regional events that might be detected by our arrays in the Southwest United States. In earlier Seismic Research Review (SRR) meetings, we have shown data from our earthquake detections, generally from events above magnitude 5.0. Now we are concentrating on events below 5.0. Our work is just beginning and we are not seeing as many of the lower magnitude events as we might have expected. Vertical ground motion is necessary to generate the infrasound signal, and smaller magnitude events may not have significant vertical motion. As we continue our analysis, we can begin to look at which events have some good ground motion data that may shed light on the source issues. In addition we can also approach this issue from a modeling perspective using a code that calculates the near-field acoustic signal from a source of ground motion by doing a numerical integration of the Rayleigh integral over the ground motion area. This approach could help bound expected near-field signal levels for different ground motion models. The modeling coupled with the observations should bring a better understanding of the infrasonic earthquake signal generation.

Several infrasound stations observed the tragic re-entry of space shuttle Columbia, STS 107, on 2/1/2003. LANL arrays were close to the ground track and obtained excellent data from the hypersonic shock wave and data from other parts of the trajectory. Such data illustrate the wide variety of man-made and geophysical signals that can be recorded by infrasound arrays. In Figure 5 (below) we show the raw channel plots of the N wave signals from the re-entry of the space shuttle, Columbia recorded on four LANL arrays: NTS, SGAR, DLIAR and LSAR.

a.



b.

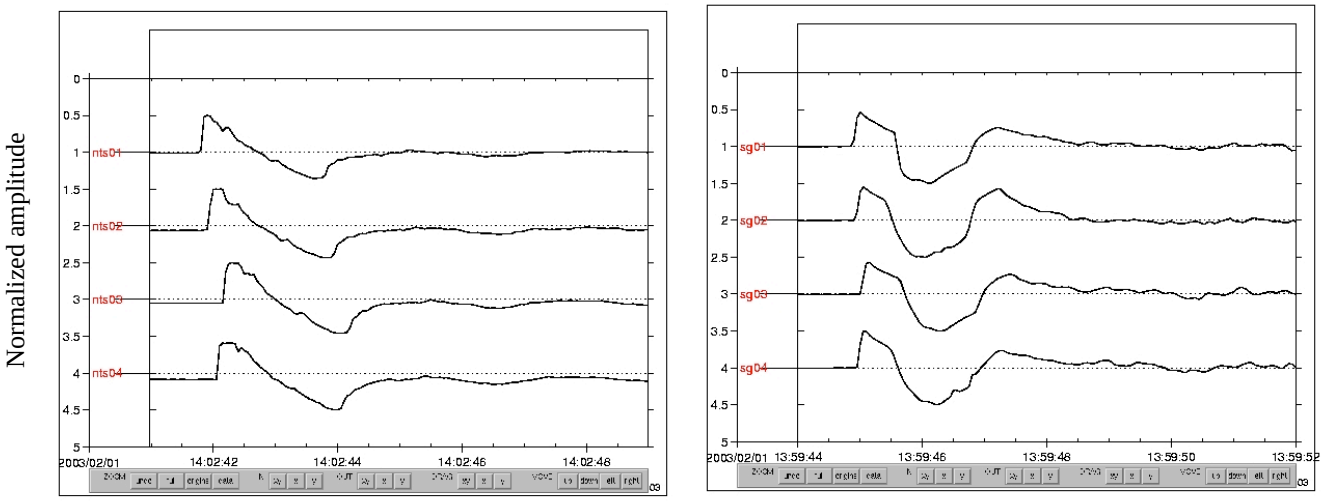


Figure 5. (a) N waves recorded by DLIAR and LSAR, (b) for NTS on the left and SG on the right.

The peak-to-peak amplitudes were: NTS 37.6, SG 36.9, DLIAR 94.4, and LSAR 93.3, all in microbars. While there is some structure in the post-peak N wave data, the cause of that structure probably is related to propagation effects.

Another event was the March 9, 2002, Pacific bolide recorded by several infrasound stations (Figure 6). There was an official announced position, 6.9 N and 147.3 W, with an energy estimate of about 1.1 kt. Figure 6 also shows results of analysis with Matseis for the International Monitoring Systems (IMS) stations I10CA, I57US, I59US, and the LANL array at St. George, UT. The plot gives the back azimuths from the Infra_Tool processing for each station and the announced rough location shown as the circle. No propagation corrections have been applied to the bearings.

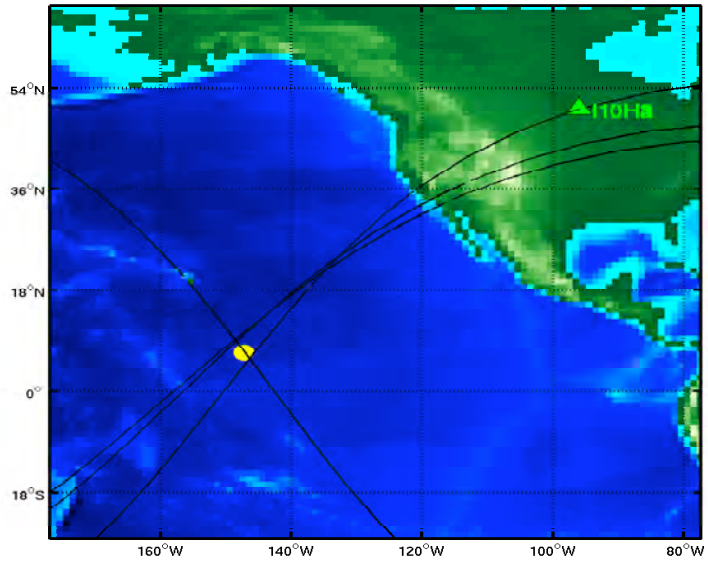


Figure 6. March 9, 2002, Pacific bolide recorded by several infrasound stations.

Figure 7 shows the results of a simple application of the new Matsies MS Locator Tool using just the I59US station and the NTS array. Normal Infra_Tool processing is done for each station getting back azimuths of 143.46 for I59US and 231.9 for NTS. We input average travel-time curves for stratospheric paths (constant velocity) and pick arrivals where the travel-time curves cross the waveforms. We defined time and azimuth location with sigmas of 30s in time and three degrees in azimuth (nominal rough values). The locator tool achieved a solution in four iterations. The four-pointed star is the announced position, and the circle is the iterated location. The back azimuths are the white lines, and the error ellipse is shown as well. This error ellipse is based on nominal estimates for the uncertainty in time and azimuth. The MS Locator Tool uses the same algorithm as used in LocSat but is a stand alone dot M file, avoiding platform dependent LibLoc problems.

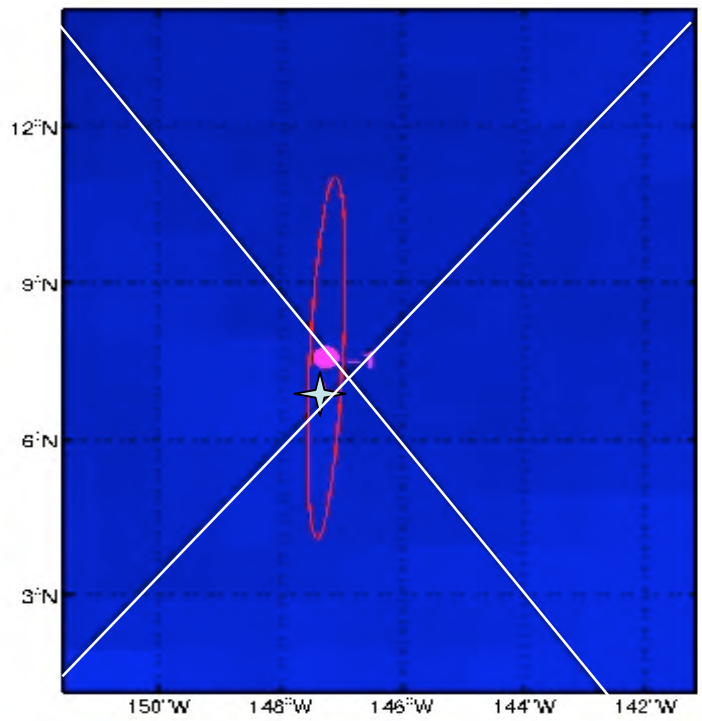


Figure 7. MS Locator Tool results for the 3/9/02 Pacific bolide.

CONCLUSIONS AND RECOMMENDATIONS

We have shown interesting results for recent events. The overall agreement of the Watusi measurements with the earlier tests at WSMR is quite impressive and pleasing. New features have been added to Infra_Tool enhancing its functionality. The new location software in Matseis was exercised using travel times and azimuths for two stations; however, more could be added. The main point is that this is all working well.

ACKNOWLEDGEMENTS

We thank Dr. Douglas Drob of NRL for providing the wind data for the time of the Watusi event.

REFERENCES

Drob, Douglas (2003), personal communication.

Mutschlecner, J.P., R.W. Whitaker and L.H. Auer, (1999), An Empirical Study of Infrasonic Propagation, LA-13620-MS, Los Alamos National Laboratory.

Data Processing and Analysis

DATA WAREHOUSES IN SUPPORT OF NUCLEAR EXPLOSION MONITORING RESEARCH

Julio Aguilar-Chang and Michael L. Begnaud

Los Alamos National Laboratory

Sponsored by National Nuclear Security Administration
Office of Nonproliferation Research and Engineering
Office of Defense Nuclear Nonproliferation

Contract No. W-7405-ENG-36

ABSTRACT

For the past six years, the Ground-based Nuclear Explosion Monitoring Research & Engineering (GNEM R&E) program has created and maintained an Oracle data warehouse at Los Alamos National Laboratory (LANL) to store and manipulate global and regional seismic research data. The LANL regional data holdings have focused on Eastern Asia. This data warehouse supports LANL scientists in their daily research efforts towards improving event location, discrimination, and characterization. It is also instrumental in providing data for research in focused areas of interest in Eastern Asia.

This paper will present a brief overview of how the LANL seismic research data warehouse has been used by researchers to achieve their goals of improving nuclear monitoring capabilities.

LANL's GNEM R&E seismic data warehouse uses Oracle's relational database management system (RDBMS) technology to store collections of global and regional seismic data that have been collected over the last six years from various sources, such as open global bulletins, academic colleagues, private contacts, and contractor collaborations. Two of the most challenging tasks of maintaining a functional data warehouse are the constant population of the database tables with the most up-to-date seismic information, and the care needed to integrate all the data sources into a cohesive database. We have received, and continue to receive, seismic bulletins from open sources such as the International Data Center (IDC) Reviewed Event Bulletin (REB), United States Geological Survey (USGS) Earthquake Data Reports (EDR), and International Seismic Centre (ISC) event bulletins. The event location solutions reported in these bulletins, corresponding phase arrivals, and network and station magnitude information are reconciled into single events; thus, researchers are able to compare bulletin information as reported by different organizations for a given event.

The reconciled database tables assist researchers working in event relocations by making available to them a merged set of phase arrivals and ground-truth information from global and regional sources. The location effort has, in fact, created its own location data warehouse by combining all available phase arrival information and manipulating the database tables to create consistent arrivals and improve event relocations.

The data warehouse is also important for event identification, discrimination, and characterization work because it provides consistent location information needed in the seismic analysis code (SAC) headers in the waveform data file. We use in-house programs—primarily written in Perl—to query database tables for preferred event location solutions, and to imbed these solutions into the SAC headers. The event discrimination and characterization work makes extensive use of the SAC headers to correctly tie measurements to events. The ability to store amplitude measurements in the research data warehouse, and to use those measurements in MDAC (Magnitude and Distance Amplitude Corrections) and coda magnitude work, provide us the means to tie all these results to specific events. The source information and resulting measurements are kept in a consistent and integrated framework.

OBJECTIVE

This paper will present an overview of the LANL seismic research data warehouse, and how LANL researchers use it to help them calibrate seismic stations used by the United States government in their mission of monitoring for clandestine nuclear explosions.

RESEARCH ACCOMPLISHED

Introduction to the Data Warehouse

For the past six years, the Ground-based Nuclear Explosion Monitoring Research & Engineering (GNEM R&E) program has created and maintained an ORACLE data warehouse at LANL to store and manipulate global and regional seismic research data. The LANL regional data holdings have focused primarily in Eastern Asia. This data warehouse supports LANL scientists in their daily research efforts towards improving algorithms and seismic models for event location, discrimination, and characterization. The data warehouse maintained at LANL uses the same technology as the data warehouses at the two other National Nuclear Security Administration (NNSA) laboratories that are part of the GNEM R&E program, as well as at the Air Force Technical Applications Center (AFTAC), the ultimate customer of our research efforts. The three NNSA laboratories and AFTAC use ORACLE's relational database management system (RDBMS) technology. The laboratories have maintained close contact with AFTAC to ensure that we are using the same version of the database server, thus allowing for easy exchange of data. Likewise, the design of the database tables is uniform throughout the GNEM R&E program, which helps to ease collaboration between researchers and guarantees consistency in the presentation of the final results to the user. The current agreed upon format for database tables is documented in *National Nuclear Security Administration Knowledge Base Core Table Schema Document* [Carr].

Contents of the Data Warehouse

The LANL GNEM R&E seismic data warehouse stores global and regional seismic data that have been collected over the last six years from various sources such as open global bulletins, academic colleagues, private contacts, and contractor collaborations. Our data warehouse holds over 114 gigabytes of data and provides direct access to over 160,000 seismic waveforms. We have received, and continue to receive, seismic bulletins from open sources such as the International Data Center (IDC) Reviewed Event Bulletin (REB), United States Geological Survey (USGS) Earthquake Data Reports (EDR), and the International Seismic Centre (ISC). Over the years, the number of distinct event locations and phase arrivals available from the global bulletins has increased at an amazing rate. Figure 1 below shows the cumulative number of event origins collected from global and other bulletins per year. Similarly, Figure 2 shows the cumulative number of collected phase arrival picks from available catalogs per year, and the number of reporting stations.

Two of the most challenging tasks of maintaining a functional data warehouse are the constant population of the database tables with the most up-to-date seismic information and the care needed to integrate all the data sources into a cohesive database. We follow various steps of collecting and integrating seismic data into the LANL GNEM R&E data warehouse depending on the source of the data. We electronically collect weekly and monthly bulletin reports from the USGS EDR, and daily event bulletins from the IDC REB. Once a week and once a month we run a program to query the USGS EDR web site for new bulletins. Likewise, once a day we query the IDC data source for new events. The bulletins are sent to LANL through electronic mail and stored on a disk as ASCII flat files. We then run Perl programs, written at LANL, to parse the information from the native bulletin format and transform them into KB schema format flat files. The EDR and REB Perl parsers look at the contents of the database tables to determine if events already exist and will make the appropriate connection to match newly collected EDR and REB events to existing ones. This process also assigns the preferred location solution for an event through the use of an origin-location-author ranking list. This list was created at LANL to establish the rank of origin location authors when an event has more than one location contributed by different sources. This ranking list was created based on prior knowledge of the data catalogs that we have received, and on years of researcher experience in dealing with origin locations from diverse sources. The LANL EDR and REB Perl parsers create new *event* KB schema flat files with updated preferred origin authors, as well as *origin*, *origerr*, *assoc*, *arrival*, *netmag*, and *stamag* ASCII text files. The data in these files are merged with existing data in the database tables and are immediately made available to LANL researchers. We also use built-in ORACLE database server functionality to ensure quality control of these new data so that duplicate information is not inserted into the existing tables.

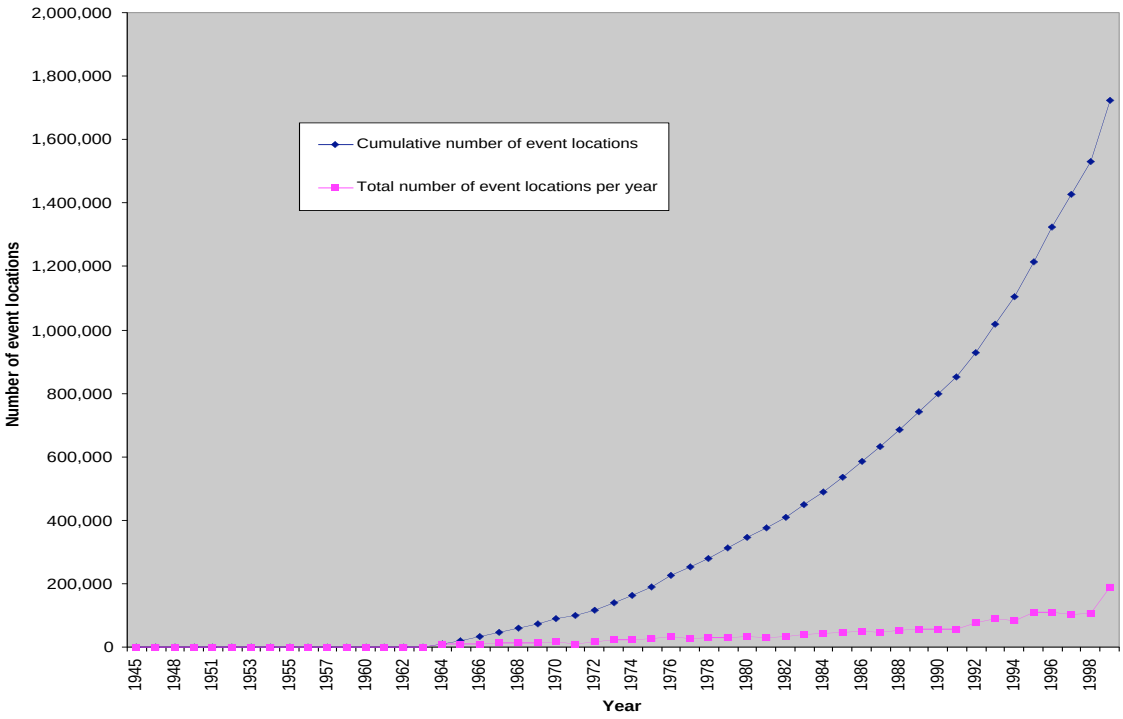


Figure 1. Total and cumulative number of reported event location solutions.

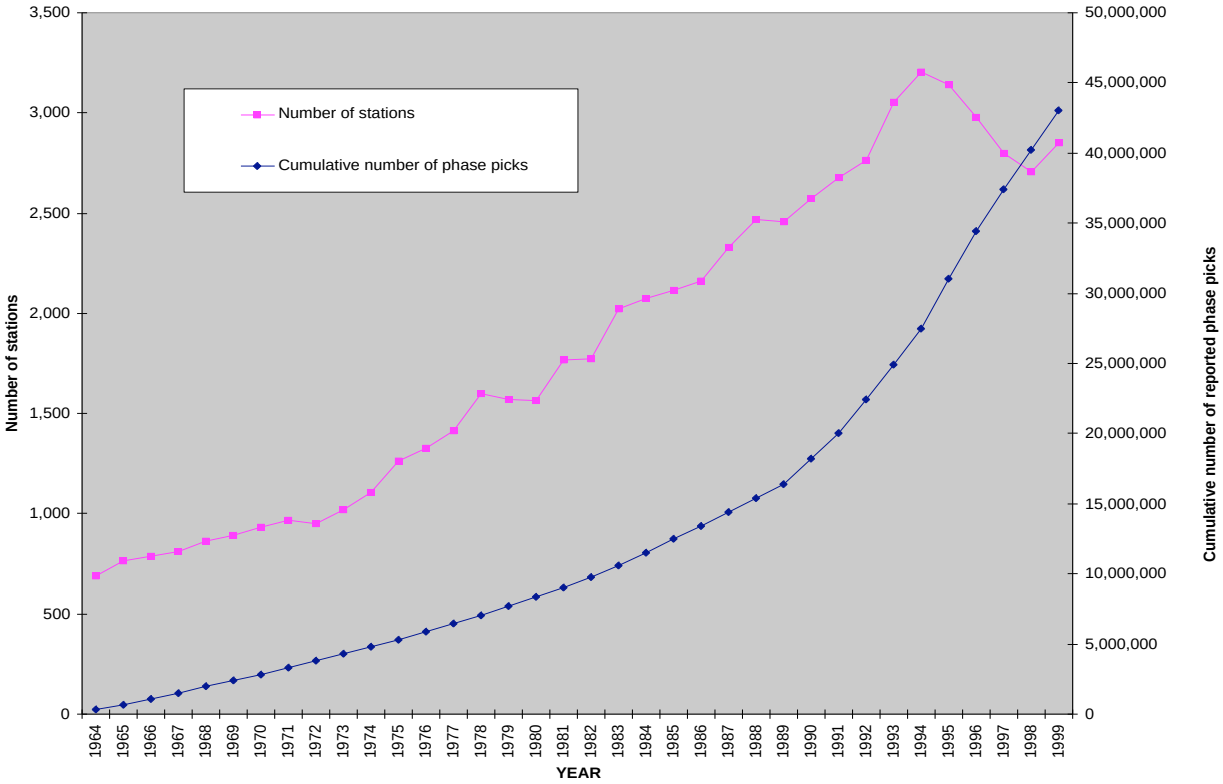


Figure 2. Cumulative number of stations and reported phase picks.

We follow a similar process to collect data from the ISC seismic bulletins and update our data warehouse. However, we use the program ORLOADER created at Lawrence Livermore National Laboratory LLNL to parse, load, and reconcile the information in the native ISC bulletin format with the existing data in the database tables. Similar to the parsing and loading of EDR and REB bulletins, the origin-author ranking table is also used by ORLOADER to update the preferred origin assigned to an existing event when loading ISC data.

Periodically we collect binary waveform files in seed format from organizations such as the Incorporated Research Institutions for Seismology (IRIS) Data Center. These data are transformed at LANL into SAC format waveforms. The data warehouse is used to populate the SAC headers with event, origin, and waveform identification information, which tie a particular binary waveform file to an event and preferred origin location in the data warehouse. Once the SAC headers have the correct identification information, our researchers make body-wave phase picks. These LANL-generated phase arrival data are merged and reconciled with existing data in the data warehouse and made available to the event location researchers to use in their relocation efforts. The SAC waveforms are also available for amplitude processing, which is used later on in event discrimination research. Figure 3 shows a graph depicting the total cumulative number of waveforms at LANL per year and the total cumulative number of phase picks made by our researchers. Figure 4 shows the cumulative number of raw amplitude measurements and amplitude corrections measured at LANL over the years for most of our waveform holdings.

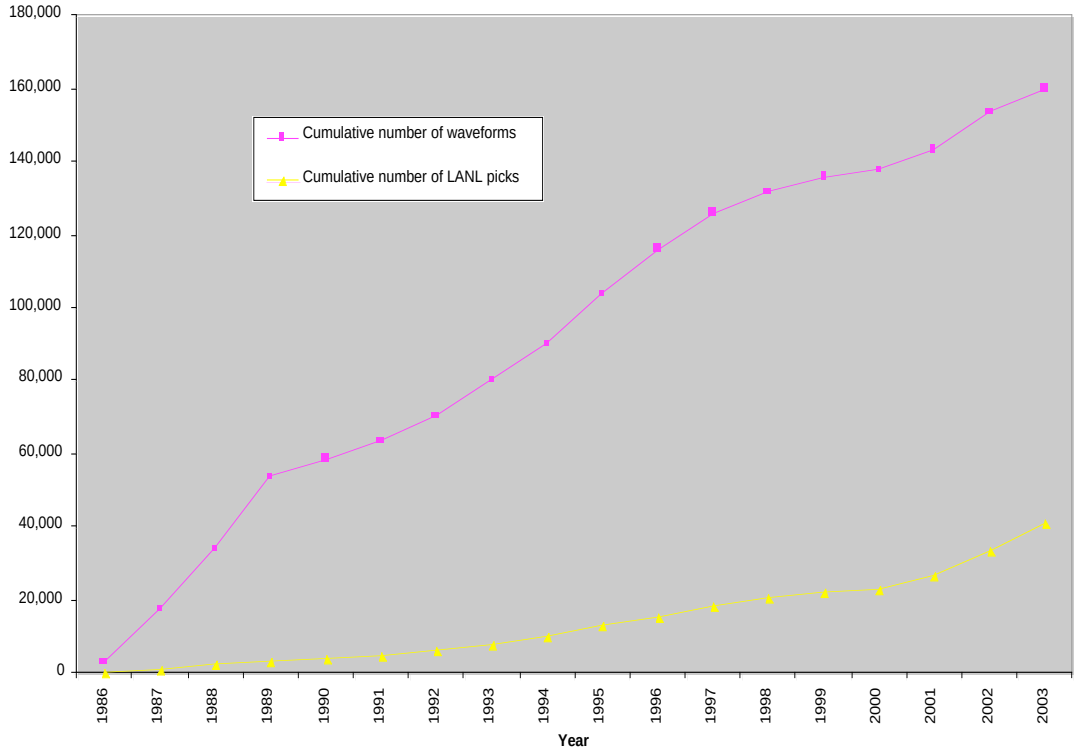


Figure 3. Cumulative number of waveforms (top line) and LANL picks (lower line).

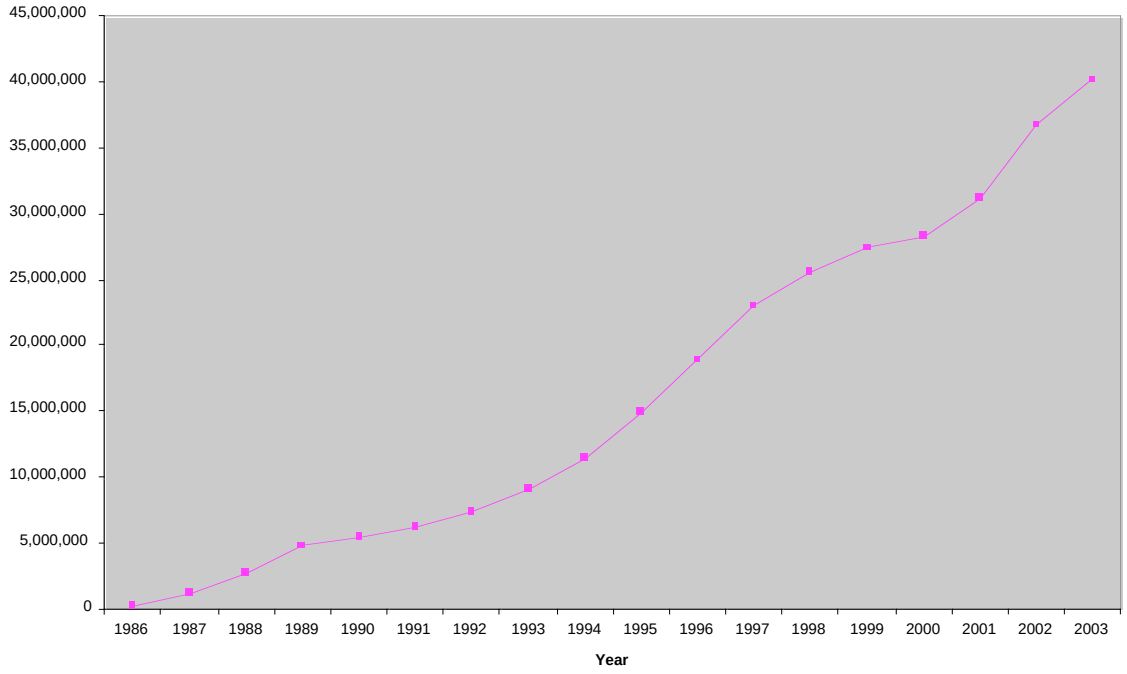


Figure 4. Cumulative number of amplitude measurements.

Using the Data Warehouse for Event Location Research

Merged global and regional phase arrival and ground-truth source data is available in our research data warehouse to assist researchers in their event location efforts. The location effort has, in fact, created its own database tables by combining all available phase arrival information and manipulating it to create consistent arrivals and improve event relocations that lead to better correction surfaces. Researchers use the reconciled database tables that contain global and regional bulletin information, as well as LANL-generated phase arrival and waveform data, to create new *arrival* and *assoc* tables specific for relocation purposes. When working with the location-specific database tables, the *assoc* table contains only the phase arrivals associated with the preferred origin location for a given event based on a pre-determined LANL-generated ranking table. One event can have one or more origin locations, and each origin location corresponds to a different author, i.e., the USGS EDR, IDC REB. This *assoc* table also contains all phase arrival picks made at LANL. Seismic phases in the *arrival* table are renamed so that all phases associated with a given event have unique descriptive names, which is a requirement of the EvLoc program used in location tasks. The renaming of the seismic phases follows a pre-determined ranking scheme, in which LANL picks are ranked highest and phase names remain unchanged. An example is shown in Table 1.

Table 1: Example of phase renaming

Phase pick author	Rank	Original phase			Renamed phase		
		time 1	time 2	time 3	time 1	time 2	time 3
LANL	1	Pn	Pg		P	Pg	
REB	2	Pg	P	Pn	Pg2	P2	Pn
EDR	3	Pn	P	Pg	Pn2	P3	Pg3

The phase renaming process is necessary to provide the best distinct phase arrival times to the programs used in location. By doing this process, we are compiling a database with the best distinct seismic phase arrivals, so that for a given event at a given station there is only one of each P, Pg, and Pn phase arrival.

Using the Data Warehouse for Event Discrimination Research

The event discrimination and magnitude research conducted at LANL benefits directly and indirectly from the data warehouse. The event discrimination work uses data stored in database tables as input for processing, while magnitude work uses the data contained in the headers of the SAC-format waveform files that are populated using data in the database. The final products of the event discrimination work are MDAC (Magnitude and Distance Amplitude Corrections) correction parameters for given event/station paths and amplitude corrections for raw amplitude measurements. One of the final products of the magnitude research work is the computation of network and station coda moment magnitudes.

As a first step, the event and station location information, magnitude estimates, and reporting catalog name contained in the headers of the SAC-format waveform files are compared against data in the database tables. When a match is found, the waveform headers are updated with the event, origin, and waveform identification numbers that tie a particular waveform to a specific event and location solution in the database. The researcher uses this header information, together with the waveform file, to make the calculations needed to estimate network and station coda moment magnitudes for a particular event. These results are inserted into the database tables' *netmag* and *stamag* that contain network and station event magnitudes respectively. At the same time, raw amplitude measurements are made on the waveforms for a variety of phases and frequency bands, and the results are then incorporated into the appropriate database tables. These amplitude measurements, as well as the magnitude estimates, are tied through a unique origin identification number to the corresponding event origin solution. At this point, the waveforms, phase arrivals, associated preferred event location, amplitude measurements, and magnitude estimates are all tied together through the event and origin identification numbers; thus, we are taking advantage of the relational nature of these data by storing them in a relational database server. We use programs written in Perl that query the database tables for event locations, magnitudes, and raw amplitude measurements, and the output is a set of ASCII flat files that are used in in-house written Matlab codes to perform the actual computations of MDAC parameters and amplitude corrections. The resulting MDAC amplitude corrections are then inserted back into the corresponding database tables and tied to existing raw amplitude measurements by using the event and origin identifiers.

Integration and Reconciliation of Data for Knowledge Base Deliverables

A large portion of the research results is stored in database tables in our data warehouse. New event location solutions from event relocation work are stored in KB schema *origin, origerr*, and *assoc* tables. The coda moment magnitudes computed for selected events are stored in KB schema *netmag* and *stamag* tables. The raw amplitude measurements and amplitude corrections are stored in custom tables *nnsa_amp_descript* and *nnsa_amplitude*. Finally, the results of MDAC research are stored in custom tables *mdac_fi* and *mdac_fd*. These research results are most useful to our customer as part of an integrated KB. An integrated KB gives the final user centralized access to all research results associated with the GNEM R&E program. The research results produced at LANL are integrated as part of a station-centric approach; this approach gives the user tremendous flexibility to view and access the data in various forms. Graphical user interface (GUI)-based tools have been developed to access these data, which makes the mining of the KB extremely efficient.

The database tables containing our research results are integrated and reconciled with those from other NNSA laboratories to accomplish the goals described above. LANL's research products are delivered to the customer through KB deliveries. There are two documents that describe in detail the procedures followed to compile and create a KB deliverable. These are the *Knowledge Base Contributor's Guide* [Carr], and *The Integration Process for Incorporating Nuclear Explosion Monitoring Research Results into the National Nuclear Security Administration Knowledge Base* [Gallegos, et. al]. The step-by-step description of the steps that the NNSA laboratories follow to meet the requirements for delivering research products to the KB is beyond the scope of this paper. The two documents mentioned above, as well as other papers in this conference, describe these steps in detail.

CONCLUSIONS AND RECOMMENDATIONS

The bulletins maintained in our warehouse report information such as event location solutions, phase arrival times, and network and station magnitudes. These data are reconciled into single events, and researchers are able to compare the information obtained from many bulletins as reported by different organizations for a given event, giving them the ability to quickly evaluate which information is most appropriate for the event. For example, for an

event a researcher may choose to use the location as reported from organization A and the network magnitude as reported from organization B. This choice is made possible by using the relational power of the data warehouse management system.

The reconciled database tables help researchers working on event location problems achieve improved event relocations by making available a merged set of global and regional phase arrivals and ground-truth information. The location effort has, in fact, created its own location database by combining all available phase arrival information.

The data warehouse is also instrumental in the event identification, discrimination, and characterization work because it provides consistent location information needed to populate the headers in the SAC-formatted waveform data files. The event discrimination and characterization work makes extensive use of the SAC headers to correctly tie measurements to events. The ability to store amplitude measurements in the data warehouse, and use those measurements in MDAC (Magnitude and Distance Amplitude Corrections) computations, provides researchers the means to tie all their results to specific events. The source information and resulting measurements are kept in a consistent and integrated framework.

ACKNOWLEDGEMENTS

The people who contribute to and maintain the Los Alamos National Laboratory research data warehouse are: Julio C. Aguilar-Chang, Michael L. Begnaud, Hans E. Hartse, Steven R. Taylor, W. Scott Phillips, George E. Randall, Richard J. Stead, Thomas L. Riggs, and Diane F. Baker.

REFERENCES

Carr, D. (09/02), *Knowledge Base Contributor's Guide*, Sandia National Laboratories report SAND2002-2771 (available at https://www.nemre.nnsa.doe.gov/cgi-bin/prod/nemre/index.cgi?Page=Knowledge+Base).

Carr, D. (09/02), *National Nuclear Security Administration Knowledge Base Core Table Schema Document*, Sandia National Laboratories report SAND2002-3055 (available at https://www.nemre.nnsa.doe.gov/cgi-bin/prod/nemre/index.cgi?Page=Knowledge+Base).

Gallegos, D. et. al. (09/02), *The Integration Process for Incorporating Nuclear Explosion Monitoring Research Results into the National Nuclear Security Administration Knowledge Base*, Sandia National Laboratories report SAND2002-2772 (available at https://www.nemre.nnsa.doe.gov/cgi-bin/prod/nemre/index.cgi?Page=Knowledge+Base).

WIDE AREA TESTING OF CD-1.1 RELIABLE MULTICASTING

J. Roger Bowman, Ray Cordova, Warren Fox, and Dale Lovell

Science Applications International Corporation

Sponsored by Army Space and Missile Defense Command

Contract No. DASG60-03-C-0009

ABSTRACT

New software for reliable multicasting of sensor data has been successfully tested over a wide-area network between an International Monitoring System (IMS) infrasound station in Newport, Washington (I56US) and the Science Applications International Corporation (SAIC) testbeds in San Diego, California and Arlington, Virginia, and an Air Force Technical Applications (AFTAC) testbed in Satellite Beach, Florida. Multicast communication is a group communication mechanism that provides one-to-many (or many-to-many) communication. Multicasting is not an inherently reliable communication mechanism, so applications requiring reliable data transmission must provide their own reliability mechanism. The reliable multicasting application software uses the formats and protocols for continuous data (CD-1.1). CD-1.1 was designed for reliable and secure transmission of data from data providers, which are generally stations of the IMS or other sensor networks, to data consumers, which are generally data centers. The initial, unicast software implementation of the CD-1.1 formats and protocols was designed for point-to-point transmission and relied on TCP/IP (Transmission Control Protocol/Internet Protocol) for data transmission and data packet reliability, ordering and flow control. The unicast version of the Continuous Data Subsystem (CDS) CD-1.1 has proven to be reliable and secure for transmission of data. It is currently in use transmitting data from five data providers distributed globally to three data consumers.

IP multicasting can overcome two inherent drawbacks of unicast data transmission. Unicasting is inefficient for transmission of data to multiple data consumers, because data packets are duplicated for transmission to each consumer. In contrast, multicasting simultaneously transmits data packets to multiple data consumers using multicasting features of network routers to duplicate packets only when necessary to service all members of a multicast group. The reliability of the unicast implementation is limited by dependence on intermediate data forwarding sites, which are potential single points of failure. In contrast the CD-1.1 reliable multicasting system multicasts data packets to all data consumers simultaneously and relies on packet retransmission directly from the data provider to all data consumers to provide the principal reliability service. Thus, under both normal and somewhat degraded conditions, CD-1.1 with reliable multicasting provides a stream of data to all data consumers independent of any intermediate forwarding center. In addition, the CDS CD-1.1 with reliable multicasting provides an additional level of reliability with a unicast catch-up mechanism.

We implemented a multicast version of the CDS CD-1.1 application software. This version could not rely on the services of TCP/IP, which is strictly a point-to-point protocol, and therefore uses the Universal Datagram Protocol (UDP) over IP. Services such as data packet-level reliability, ordering and flow control were incorporated in the application software.

We tested the CD-1.1 reliable multicasting system in three phases progressing from a local testbed environment toward a configuration resembling the target environment. The first phase was conducted using a simulated data provider on SAIC's San Diego testbed, with data consumers on the San Diego testbed and a testbed in Arlington. In the second phase, the I56US infrasound station in Newport was used as the data provider with data consumers in San Diego and Arlington, while the third phase added a data consumer on a testbed at AFTAC. The *mrouted* application was used to tunnel multicast packets through the public Internet, which did not have routers configured for our multicast use. Some of the capabilities tested were: basic multicast transmission, recovery from multicast connectivity failure, acceptable multicast layer network usage, change of multicast group address, gap notification and unicast catch-up, and acceptable data timeliness. The CD-1.1 reliable multicasting system performed well during testing, providing a reliable, timely, and secure stream of data to data consumers. The wide-area tests demonstrated the feasibility of using this system in an operational setting to address US requirements for data reliability and security. Several minor anomalies identified during testing were resolved with software or configuration changes or were logged in a defect database for future action.

OBJECTIVE

The objective of this research is to develop and demonstrate prototype software for multicasting sensor data simultaneously from stations of the US Atomic Energy Detection System (AEDS) and the International Monitoring System (IMS) to more than one data consumer (center). An important application of this research would be to transmit data from stations to both the U.S. National Data Center (NDC) and the alternate NDC, which would simplify the transfer of the test-monitoring mission between the two data centers.

IP multicasting can overcome two inherent drawbacks of unicast data transmission. First, unicasting is inefficient for transmission of data to multiple data consumers, because packets are duplicated for transmission to each consumer. In contrast, multicasting simultaneously transmits data packets to multiple data consumers using multicasting features of network routers to duplicate packets only when necessary to service all members of a multicast group. Second, the reliability of the unicast implementation is limited by dependence on intermediate data forwarding sites, which are potential single points of failure. In contrast the CD-1.1 reliable multicasting system multicasts data packets to all data consumers simultaneously and relies on packet retransmission directly from the data provider via multicast to all data consumers to provide the principal reliability service. Thus, under both normal and somewhat degraded conditions, CD-1.1 with reliable multicasting provides a stream of data to all data consumers independent of any intermediate forwarding center.

RESEARCH ACCOMPLISHED

Introduction

Multicast communication is a group communication mechanism that provides one-to-many or many-to-many communication. For transmission of data from sensors to data centers, only the one-to-many capability of multicast is utilized. Figure 1 shows unicast and multicast data flows, contrasting the duplication of data for all paths between a data provider and data consumers in the unicast case, and the lack of duplication until the last multicast router before two members of a multicast group in the multicast case. Multicasting is not inherently a reliable communication mechanism, so applications requiring reliable data transmission must provide their own reliability mechanism.

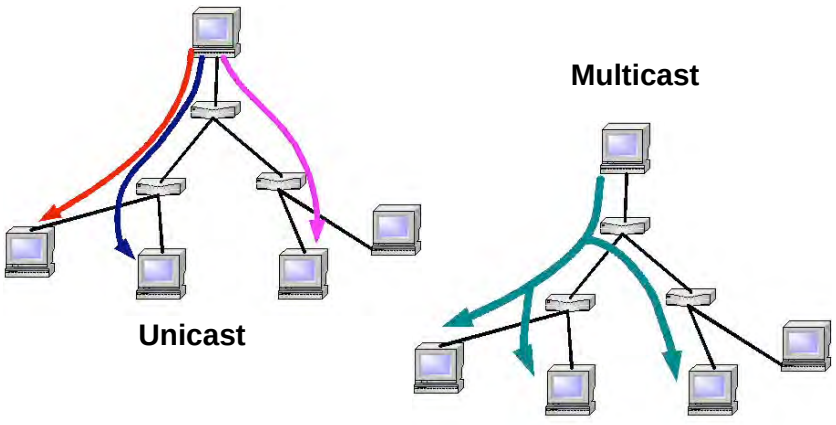


Figure 1. Comparison of unicast and multicast data flows.

SAIC has designed, developed and tested prototype software for reliably multicasting sensor data from monitoring stations to data centers. The reliable multicasting application software uses the formats and protocols for continuous data (CD-1.1) (SAIC, 2003b). Multicasting required minor extensions to the CD-1.1 formats and protocols that were originally defined for unicasting (SAIC, 2001; IDC, 2002). The application software that implements the CD-1.1 formats and protocols is called the Continuous Data Subsystem (CDS) CD-1.1. The CDS CD-1.1 for multicasting is an extension of the CDS CD-1.1 for unicasting.

The CD-1.1 formats and protocols were designed for reliable and secure transmission of data from data providers, which are generally stations of the US AEDS, IMS or other sensor networks, to data consumers, which are generally data centers. The initial, unicast software implementation of the CD-1.1 formats and protocols was designed for point-to-point transmission and relied on TCP/IP (Transmission Control Protocol/ Internet Protocol) for data transmission and data packet reliability, ordering and flow control. The unicast version of the CDS CD-1.1 has proven to be reliable and secure for transmission of data. It is currently in use for transmitting data from five data providers (e.g., AKASG, I56US, and I57US) and for receiving data at three data consumers (US NDC, SAIC-

Arlington, and the International Data Center). Independent and reliable delivery to multiple data consumers makes CD-1.1 reliable multicasting well suited for transmitting data to both the U.S. NDC and the alternate U.S. NDC.

Different multicast data transmission modes provide distinct levels of reliability, as illustrated in Table 1. Application-level Error Correction (AEC) is a critical reliability mechanism, determining which data have been sent and received, and retransmitting missing data as necessary (Saltzer et al., 1984). CD-1.1 reliable multicasting has Application-level Error Correction for both data packets, which are fragmented from CD-1.1 Data Frames, and for Data Frames.

Table 1: Services Provided by Various Modes of Multicast Data Transmission

Transmission Mode	Definition	Service
Multicast	Group delivery mechanism.	Best-effort delivery.
Reliable multicast	Group delivery with packet-level AEC.	Reliable delivery of data packets absent major failure modes (better best effort).
CD-1.1 reliable multicast	Group delivery with packet-level AEC and individual delivery with frame-level AEC.	Reliable delivery of Data Frames, even with major failure modes.

Software Design and Development

We designed and implemented a multicast version of the CDS CD-1.1 application software (SAIC, 2003a). This version of the CDS could not rely on services of TCP/IP, which is strictly a point-to-point protocol, and therefore uses the Universal Datagram Protocol (UDP) over IP. Services such as data packet-level reliability, ordering and flow control were incorporated in the application software. The design was constrained by several factors. First, we applied all CD-1.1 unicast requirements to reliable multicasting, most notably the requirement for 99.99% reliability of transport of Data Frames. Second, we minimized changes to the CD-1.1 formats and protocols (SAIC, 2003b) to preserve compatibility with unicast implementations. Third, we designed CDS CD-1.1 software components to operate in either multicast or unicast mode, according to parameter settings.

Multicasting functions used in normal operation have been separated from unicast functions used during catchup operation in two largely independent subsystems. Normal operation has at most short outages and modest network congestion. During normal operation, data are multicast to all data consumers, as illustrated in Figure 2. Data Frames are the minimum unit of data transmitted from a station and generally contain 10-30 s of data from all sites and channels of a station, digital signatures for each data channel, and a digital signature for the frame itself. In general, Data Frame sizes exceed the Maximum Transmission Unit (MTU) of communications networks. Mechanisms are provided in the CDS CD-1.1 application software to fragment CD-1.1 Data Frames into smaller data packets that can be transmitted using UDP, to control the packet transmission rate, to re-assemble packets into Data Frames upon receipt, to identify and request re-transmission of missing data packets, and to re-multicast missing data packets.

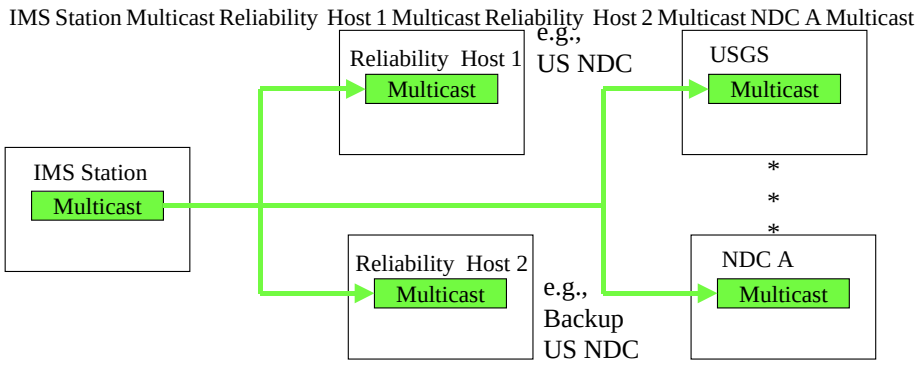


Figure 2. Data flow for CD-1.1 reliable multicast during normal operation.

Catch-up operation occurs after long outages or periods of high network congestion. Long outages are those exceeding the configurable, but relatively short, buffer of the multicast subsystem. Long outages might result from failure of hardware or communications circuits at a station or a data consumer. The design of the catchup subsystem employs reliability hosts, one of which is collocated with a station and the other(s) located at one or more locations of convenience. The reliability host provides re-transmission of Data Frames after those outages exceeding the multicast subsystem's buffer. During catchup operation, illustrated in Figure 3, point-to-point connections are first established between a data consumer and a reliability host. The data consumer requests Data Frames that were missed during the outage and the reliability host unicasts these Data Frames to the requesting data consumer. Catchup processing uses the frame-level reliability mechanisms of CD-1.1 and provides a higher level of reliability than can be provided by the packet-level reliability mechanisms of reliable multicasting. Note that it is not practical for all data consumers to interact directly with the reliability host at a station. This approach would not scale well to multiple data consumers in circumstances in which the bandwidth of the communications link to the station is limited. In case of an outage of the station or the tail circuit to the station, which is often vulnerable to outages, all data consumers would request their missing data at a similar time, resulting in contention for the limited available bandwidth. Our design includes one or more reliability hosts remote from the station at sites with broad bandwidth communication links and optionally with communications and other infrastructure that is more reliable than that for an individual station. Key design features of the multicasting subsystem of the CD-1.1 reliable multicast software are (SAIC 2003a):

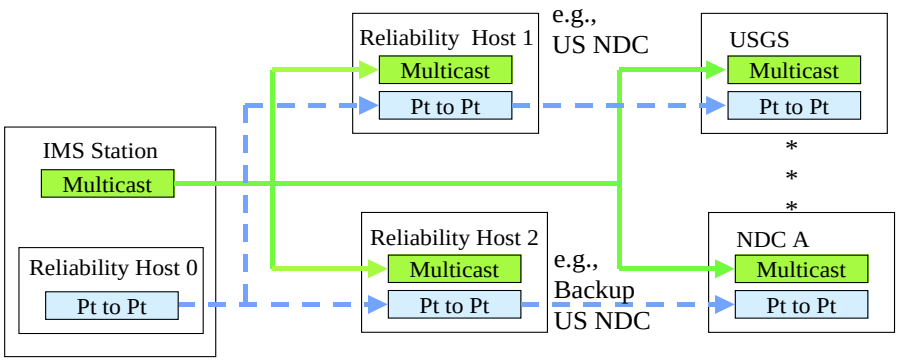


Figure 3. Data flow for CD-1.1 reliable multicast during catchup operation after an outage.

- Allows up to 20 data consumers in a single multicast group.
- A data provider is not limited in its sending by the absence or presence of any specific data consumer.
- A support increases and decreases in the size of the multicast group without the need to restart the sending activity of the data provider.
- A data consumer can enter or leave a multicast group without negatively impacting other group members.
- Transmission rates are constant and configurable to mitigate network congestion.
- The size of multicast data packets is configurable to support small MTU (Maximum Transmission Unit) networks (frames broken into packets).
- Missing multicast data packets of an active multicast session can be identified, requested, and resent, availability limited by configurable data buffer size.
- A data provider transmits frames in the order in which they were written to its CD-1.1 frame set, (except retransmissions). A multicast data provider can begin delivery at the current time or a configurable lookback time less than 10 minutes prior to the current time to prevent gaps in the stream caused by short data provider outages.

Key design features of the unicast catchup subsystem of the CD-1.1 reliable multicast software are (SAIC 2003a):

- Uses sequence numbers to detect Data Frames not received by a data consumer via multicast.
- Provides reliable delivery to a data consumer of frames not received via multicast.

The CD-1.1 reliable multicast software was written in C and C++. Maximum reuse was made of existing components of the Continuous Data Subsystem CD-1.1.

Testing Configurations

We followed the test plan for the CD-1.1 reliable multicasting system of Lovell and Bowman (2003). This plan defined configurations for hardware, communications, and application software, and defined test cases for four phases (Table 2). The first phase of testing was local area network testing in San Diego, California. Wide-area testing of the system consisted of three phases progressing toward a configuration resembling the target environment (Table 2). The first phase of wide-area testing (Phase 2) was conducted using a simulated data provider on SAIC's San Diego testbed, with data consumers on the San Diego testbed and a testbed in Arlington, Virginia. In the second phase of wide-area testing (Phase 3), the I56US infrasound station in Newport was used as the data provider with data consumers in San Diego and Arlington, while the third phase of wide-area testing (Phase 4) added a data consumer on a testbed at AFTAC in Satellite Beach, Florida. The IP multicast routing daemon *(mrouted)* application (Deering, 1989, Xerox, 2003) was used to tunnel multicast packets through the public Internet, which does not have routers configured for our multicast use.

Table 2: Test Phases for CD-1.1 Reliable Multicasting

Phase	Title	Data Provider	Network	Data Consumers
1	Local Area Network Testing on the San Diego Testbed	San Diego testbed (synthetic source)	LAN	San Diego testbed (two Consumers)
2	San Diego to Arlington Wide-Area Testing	San Diego testbed (synthetic source)	Internet	Arlington testbed; San Diego testbed
3	I56US to Arlington and San Diego Wide-Area Testing	I56US	Internet	Arlington testbed; San Diego testbed
4	I56US to AFTAC, Arlington, and San Diego Wide-Area Testing	I56US	Internet	AFTAC, Arlington testbed; San Diego testbed

Local-Area Tests

We extensively tested the CD-1.1 reliable multicast application software during Phase 1 using a Local Area Network on a testbed in San Diego. Because this paper focuses on wide-area testing, here we only enumerate the test results achieved during Phase 1. The test cases demonstrated:

- The ability to establish and maintain a multicast group (a data provider and one or more data consumers).
- The ability to do an orderly, commanded shutdown of a multicast group via an Alert Frame sent by the data provider.
- The ability to receive and store CD-1.1 multicast data Frames at a data consumer.
- That the multicast software enforces the configured upper limit on network bandwidth usage.
- The ability to request re-transmission of a packet.
- That the addition of a new data consumer to a multicasting group does not alter the ability to provide a flow of data packets to existing group members.
- That the data Frame auditing process can determine when unicast catchup needs to take place.
- That data Frame auditing produces an accurate list of frame sequence number gaps.
- That a unicast catchup connection can be established.
- That during a unicast catchup connection, frames specified by a requesting data consumer are sent to that data consumer.
- That reliable multicast makes efficient use of host computer CPU and memory.
- That reliable multicast occurs within reasonable transport network utilization constraints.
- Timely delivery of data to data consumers.
- Complete delivery of data to data consumers.
- The ability to recover from a data provider reboot.
- The ability to recover from a data consumer reboot.

Wide-Area Tests

Figure 4 shows the topology of the wide-area tests of CD-1.1 reliable multicasting. Phase 2 used a simulated data provider on SAIC's San Diego testbed and data consumers on SAIC's Arlington testbed as well as on the San Diego testbed. Phase 3 used an IMS station in Newport, Washington as a data provider and used data consumers San Diego and Arlington. Phase 4 added a data consumer at AFTAC.

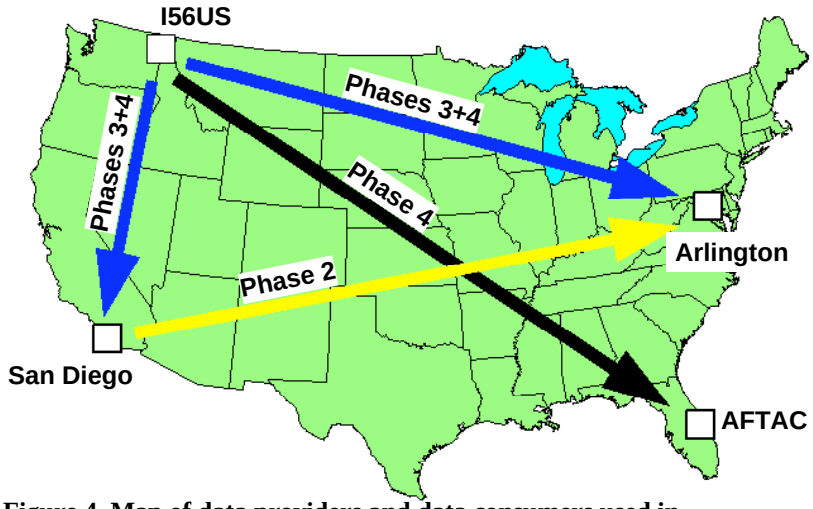


Figure 4. Map of data providers and data consumers used in wide-area testing.

Table 3 summarizes test results for Phases 2 and 3. Several minor anomalies identified during testing were resolved with software or configuration changes during testing or were logged in a defect database for future action. For example, heavy load on the link from I56US caused a high rate of packet loss, which was resolved by adjusting transmission control parameters. Initially, firewall and router network address translation at I56US prevented correct connection for unicast catchup. This was resolved by modifying the application software to specify the external IP address. Detailed test results are reported by Cordova and Lovell (2003).

Table 3: Results of Phase 2 and 3 testing.

Test Case	Purpose	Expected Result	Actual Result
Multicast data transmission	Demonstrate that Data Frames are successfully transmitted and stored.	Data Frames will be successfully transmitted to data consumer and stored in Frame Store.	As expected.
Gap notification and unicast catchup	Demonstrate that catchup connection is established if gaps are detected and that missing Data Frames are supplied.	Data Frames originally listed as missing will be stored in Frame Store.	As expected.
Change of multicast group address	Demonstrate that a data consumer can change group address at which it receives data following change of address by data provider.	Data will be successfully transmitted to data consumers using new multicast address and destination port.	As expected.
Multicast layer network usage	Determine bandwidth used in transmission of data from data providers to data consumers.	Average throughput will be less than configured value.	As expected.
Data timeliness	Demonstrate that average data latency is within specifications.	Maximum latency for test period will not exceed 3 minutes.	As expected.
Multicasting connectivity fails	Demonstrate proper behavior when multicast connectivity fails.	Multicast data transmission should stop and catchup processing should fill in gap when connectivity is restored.	As expected.

Figure 5 shows the configuration for Phase 4 testing. A testbed was established at AFTAC during June 2003. Hardware was designated for testing, and the firewall and application software were configured. Phase 4 testing will be performed during July and August using a subset of test procedures from Phase 3 testing. Therefore, we expect the testing to complete the successful demonstration of the capabilities of CD-1.1 reliable multicasting.

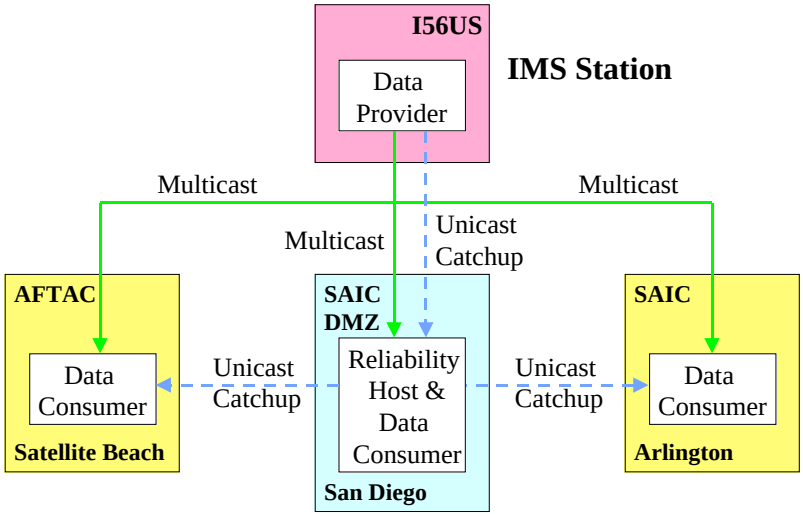


Figure 5. Configuration used in Phase 4 wide-area multicast tests.

CONCLUSIONS AND RECOMMENDATIONS

Wide-area tests of CD-1.1 reliable multicasting have demonstrated the feasibility of using a multicast system in an operational setting to address US requirements for data reliability and security. We recommend that CD-1.1 reliable multicasting be completed as an operational product and then be deployed at selected stations, at the US National Data Center, and at the alternate National Data Center.

ACKNOWLEDGEMENTS

We thank Jim Burns and Brian Coan of Telcordia Technologies for valuable suggestions on the design and testing of the CD-1.1 reliable multicast software, Jon Berger, Michael Hedlin and Clint Coon of UCSD for use of the I56US infrasound station as a multicast data provider, Victor Oancea of SAIC for supporting Arlington tests, Bruce Varnum, Dan Harvala and Richard Baumstark of AFTAC for coordinating wide area tests that included AFTAC, and Deb Agarwal of Lawrence Berkeley Laboratory for contributing to plans for wide-area testing.

REFERENCES

Cordova, R. and D. Lovell (2003). Test Report for Continuous Data Subsystem CD-1.1 Reliable Multicasting, SAIC Technical Report SAIC-03/3014.

Deering, S. (1989), IP multicast routing daemon, Stanford University.

IDC (2002), IDC Software documentation Formats and Protocols for Continuous Data CD-1.1 Revision 0.3, IDC3.4.3Rev. 0.3.

Lovell, D. and R. Bowman (2003), Plan for Wide Area Network Testing of Continuous Data Subsystem CD-1.1 Reliable Multicasting, SAIC Technical Report 03/3013.

SAIC (Science Applications International Corporation) (2001), Formats and Protocols for Continuous Data CD-1.1 Revision 0.2.

SAIC (Science Applications International Corporation) (2003a), Continuous Data Subsystem CD-1.1, Revision 1, SAIC-03/3000, 2003a.

SAIC (Science Applications International Corporation) (2003b), Formats and Protocols for Continuous Data CD-1.1, Draft revision to SAIC-01/3027 Rev. 1.0.

Saltzer, J.H., D.P. Reed, and D.D. Clark (1984), End-to-end arguments in system design, ACM Transaction on Computer Systems, 2, 277-288.

Xerox Corp. (2003), ftp://ftp.parc.xerox.com/pub/net-research/ipmulti/mrouted3.8-sparc-solaris2.tar.gz.

ASSEMBLING THE KNOWLEDGE BASE

Dorthe B. Carr, J. Mark Harris, Lisa K. Wilkening, Christopher J. Young, Matthew N. Chown, B. John Merchant, and James R. Hipp

Sandia National Laboratories

Sponsored by National Nuclear Security Administration
Office of Nonproliferation Research and Engineering
Office of Defense Nuclear Nonproliferation

Contract No. DE-AC04-94AL8500

ABSTRACT

The National Nuclear Security Administration (NNSA) Knowledge Base (KB) is a combination of the information content, database storage framework, and interface applications needed to provide integrated research products in a form that will allow the United States National Data Center (USNDC) to meet its monitoring objectives. To build a successful Knowledge Base, all the different pieces must be validated, integrated, tested, and organized to make a seamless, high-quality product, which is effective and easy to use. Sandia National Laboratories (SNL), as the KB Integrator, is responsible for accomplishing this.

Component integrated research products were delivered to the KB Integrator by KB Contributors for the latest release of the KB. These products were made up of a combination of one or more related datasets. Requirements for the datasets and the accompanying documentation were established early in the process by the KB Working Groups and given to all contributors. At the KB Integrator, the integrated research products were organized into five categories, based on their format, and then processed. The five categories are event data, parametric grid data, contextual data, research tools and supplemental information. For event data, the format is Oracle database tables (which follow the established NNSA Knowledge Base schema) and complete integration was achieved using the Lawrence Livermore National Laboratory (LLNL) program Orloader, and various SQL scripts. For parametric grid information, the format is a custom database format known as a PG database, and no further processing was needed as integration of the various PG databases was not a goal. For contextual data, the formats are shapefile (vector) or imagery (raster), and some processing was required to tailor the geographic extents of the data and to make it all accessible from a single custom ArcView GIS (Geographical Information System) Project. For research tools – i.e. software used to help create and access other integrated research products – there is no standard format; a researcher can use the language of their choice, as long as they provide instructions for compiling the program and information about the environment under which the tool was developed. Most of the integration work was accomplished during the development process for the tools because tool designers worked with the KB Integrator throughout the process to make sure the required hardware and software needed to run the tool would be available at the customer's site. Finally, for the supplemental information (white papers) the established format was PDF (portable document format) documents, and the only processing needed was to convert the original format to PDF if necessary.

Once the products were all processed, they were then organized and indexed for ease of access and the validation process began, using a new process that was developed for this release cycle. The integrated research products were divided among a dozen "Validators" at SNL. Each Validator was tasked to make sure all the components of the integrated research product had been delivered and to run a functional test on the product provided by the researcher. The functional tests were done twice. The first time was as a stand-alone test on the product before it had been integrated with other products in the Knowledge Base. The tests were run a second time after the products had been integrated to insure that nothing had been altered during the integration process. Once integration and validation had been accomplished, an interface to the Knowledge Base was created using the KB Navigator, a new piece of software developed by the KB Integrator specifically for this purpose. The KB Navigator allows users to find products, check geographical extents, access standard GIS datasets, view metadata and launch the research tools. The Navigator is supported by a custom database schema, which contains details about every product in the NNSA KB. As a final test that the NNSA Knowledge Base had been successfully built, the KB Navigator was then used to browse and examine all the delivered integrated research products.

OBJECTIVE

The National Nuclear Security Administration (NNSA) Knowledge Base (KB) is a combination of the information content, database storage framework, and interface applications needed to provide integrated research products in a form that will allow the United States National Data Center (USNDC) to meet its monitoring objectives. To build a successful Knowledge Base, all the different pieces must be validated, integrated, tested, and organized to make a seamless, high-quality product, which is effective and easy to use. Sandia National Laboratories (SNL), as the KB Integrator, is responsible for accomplishing this. In this paper, we describe the process used by the KB Integrator to put together the latest release of the NNSA Knowledge Base.

RESEARCH ACCOMPLISHED

Preparing for Integration

The KB Integrator, as defined in Gallegos et al. (2002), is a group of individuals in the Ground-based Nuclear Event Monitoring Research and Engineering (GNEM R&E) program at SNL, who combine Information Products (IPs) into the NNSA Knowledge Base. The process involves verifying and functionally validating all the documentation and products that are submitted, integrating them together and organizing the information so that it is easy to access and use. During prior releases, two or three people at SNL were designated to do the verification and functional validation of the submitted integrated research products. This did not work well, because the total number of submitted integrated research products ranged between 70 and 80, and it was very difficult for such a small group of people to do both verification and functional validation in the time allotted for that process.

For the latest release of the KB, researchers, known as Scientific Integrators, were given approximately ten months to create their integrated research products and write draft documentation, before it was due to the KB Integrator. The KB Integrator then had two months to verify, functionally validate and integrate the products into the KB. Because of the problems that had occurred in integrating prior KB releases, SNL redefined the internal process of how integration of the KB was done. The first was to name one person within the KB Integrator to coordinate the integration and be the point-of-contact for the Scientific Integrators.

Four months before the integrated research products were due to the KB Integrator, we defined a directory structure and database accounts to hold the integrated research products. The directory structure that was developed consisted of three major directories: Documents, Tools and Products. The Documents directory was designed to hold the IP documents. The Tools directory was designed to hold the research tool products. It provides a framework that facilitates code maintenance while enabling extensibility and allows different tools to share codes and libraries. The Products directory grouped integrated research products by IP. This is a convenient way to keep track of the individual integrated research products during integration. For the research tool products, we planned to have the products reside in the Tools directory, with appropriate links back to the Products directory. Once the directory structure was finalized on the unclassified server at SNL, it was replicated in the SNL vault and at the customer site, the Air Force Technical Applications Center (AFTAC).

We also decided that we needed to get more people involved in the verification and functional validation of individual integrated research products. Each expected integrated research product was assigned to a Validator at SNL, who was tasked with verifying and functionally validating that product. There were a total of 67 expected products and fourteen SNL Validators. Most Validators were assigned three or four products, and we tried not to match products to “experts” at SNL. Our goal was to try and catch problems that an inexperienced user might find. The first thing the Validator did was to make sure that all the entities (files, database tables, etc.) that comprise a product made it to SNL. The second was to run a test provided by the Scientific Integrator to make sure that the integrated research product could be accessed and used as the Scientific Integrator intended. This was not a test to look at the scientific validation of the product; instead it was considered to be a functional validation test. The Validator was to functionally validate the product first as a stand-alone product, and then run the same test again after all the products had been integrated. The KB Integrator coordinator would track the progress of all Validators and provide support wherever needed.

Six weeks before the integrated research products were due at SNL, the Scientific Integrators were required to submit the “Files” and “Installation Testing Procedure” sections from the integrated research product

documentation. We requested all Scientific Integrators to make these two sections as complete as possible. The "Files" section contained a complete description of all the entities that made up the product. The "Installation Testing Procedures" section described the test the Validator was to run to make sure the product could be accessed and used correctly. Scientific Integrators were encouraged to send test data and their results so that the Validator could compare the results of the test done at SNL to the results of the test done by the Scientific Integrator. The Validator reviewed the two sections for the products to which they had been assigned. If they found any problems or did not understand the testing procedures, they contacted the Scientific Integrator and worked with them over the six-week period before the products were due to make sure problems were resolved.

Integration

Products arrived at SNL on January 21, 2003 and the integration process began (see Figure 1). The KB Integrator coordinator received the products and put the data into the appropriate place in the Products directory. If the product was unclassified it was put onto the unclassified server at SNL; if it was classified, it was put directly into the vault. Once a product was in place, the Validator was notified that his product was ready. If there were files or database tables the Validator could not find, he first went to the KB Integrator coordinator to make sure that all the information delivered for a product had been put in the correct place, or to make sure they were looking at the correct database account. If it was determined that not all the files listed in the "Files" section arrived at SNL, the Validator contacted the Scientific Integrator to get the additional files delivered to SNL. In some cases, there were additional files delivered in an integrated research product that had not been described in the "Files" section of the documentation. In these cases, the Validator contacted the Scientific Integrator to determine if these files were part of the product.

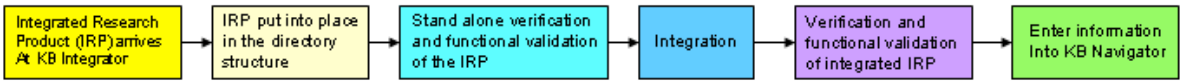


Figure 1. The process of assembling the Knowledge Base

Once the product had been verified, the Validator ran the installation test on the product. The first step was to do unit testing on the product, i.e. testing it as a stand-alone product. If the Validator had problems running the unit test, they contacted the Scientific Integrator for the product to try and resolve the problems. Most of the problems the Validators ran into with the installation tests were because the test was not well-defined, well-documented or the test sets that were to be used to verify the results of the test were not supplied to the KB Integrator. A README file was started by the Validator for each integrated research product that described how the test was run and any changes the Validator had to make from the Installation Test Procedures provided by the Scientific Integrator to get the test to run correctly.

As soon as an integrated research product had been both verified and functionally validated by the Validator, he informed the KB Integrator coordinator that the product was ready for integration and the KB Integrator coordinator moved the product into the SNL Vault (classified products were installed directly in the vault). The integration of an integrated research product depends on the format of the product. There are five different formats, depending on the kind of information – event data, which is stored in Oracle database tables, parametric grid information, which is stored in a custom database format, contextual data which is stored as shapefiles or imagery, research tools, which had no standard format, and white papers stored in PDF format. The bulk of the integration done by the KB Integrator was for event data and contextual data. Details on the integration process for each of these are given below.

Event Data Integrated Research Products

All event data is stored in Oracle database tables, with associated instrument response files and waveform files. We use the NNSA core table schema (Carr, 2002) for the basic information and the NNSA custom table schema for

storing additional event parameters. The NNSA core tables separate into two groups: Lookup and Primary. The Lookup tables change infrequently and are used for auxiliary information used by the processing. The Primary tables are dynamic and consist of information that can be used in automatic and interactive processing. The integration of the event data fell into four categories: Lookup tables, Primary tables-catalogs, Primary tables-waveforms, and custom tables. We use the convention in the following paragraphs that table names are in **bold** and column names from the tables are in *italics*.

The Lookup tables consist of six tables that describe station parameters (**site**, **sitechan**, **instrument**, **sensor**, **network** and **affiliation**) plus the instrument response files (Figure 2). Most of the information on the station parameters came from Lawrence Livermore National Laboratory (LLNL), but both Los Alamos National Laboratory (LANL) and the AFTAC also provided station parameter information. At SNL there were some diagnostics run on the station parameter information to check for consistency problems, such as stations without responses, bad calibration periods (calper), etc. Problems found were resolved through communication with the information sources. The LLNL information was loaded in as the basic information, and changes to that information were only made when it was deemed that the LANL or AFTAC information was better. Then the station parameter information was changed from the NNSA convention to the convention used at AFTAC. The major changes involved making sure the networks, channel names and stations names matched the names used at AFTAC. At SNL, all the instrument response files were converted to frequency-amplitude-phase (FAP) format, which was the format requested by AFTAC. For each response file that was converted, we made sure that instrumentation calibration information (calibration factor and calibration period) were correct, and matched the calibration information in the waveform table (**wfdisc**).

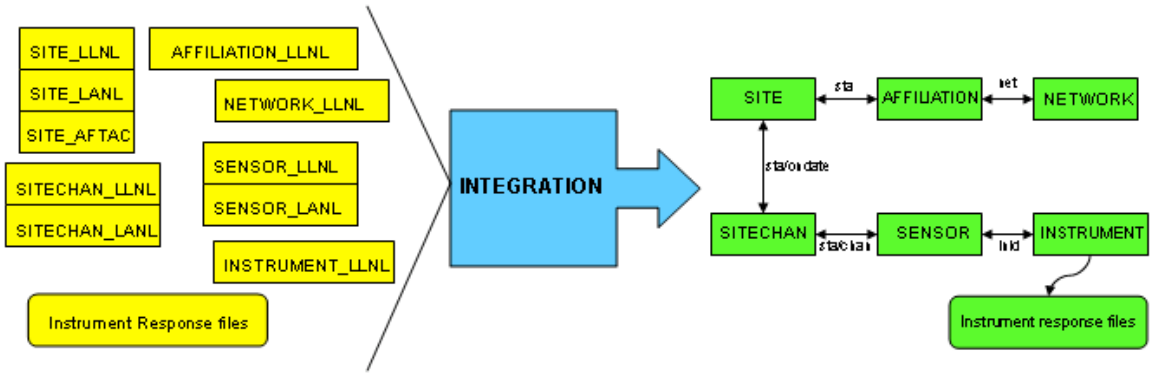


Figure 2. Integration of the Lookup tables

There are seven Primary tables that contain earthquake catalog type information: **origin**, **event**, **origerr**, **arrival**, **assoc**, **netmag** and **stamag**. LLNL and LANL provided global, regional and local earthquake catalogs to SNL as flat files or database tables. For AFTAC's use, it is essential that these catalogs be merged to a single set of tables and corresponding events in each be tied together. The catalogs were merged together by the KB Integrator using a program developed at LLNL called Orloader. As each catalog is merged (Figure 3), event locations common to multiple catalogs are assigned a common event identifier (*evid*) and unique origin identifiers (*orid*) in the **origin** table. The **event** table lists the preferred origin for each event based on a user-specified author preference table (**origin_authors_rank**) that ranks the catalogs so that catalogs that provide the best location are ranked higher. Any information from the catalogs that fit into the **origerr**, **arrival**, **assoc**, **netmag** and **stamag** tables are put into the appropriate tables. A **remap** table is created in the process of merging the catalogs that lists the *orids* and *evids* in the origin table and maps them to the original values (*origorid*, *origevid*). SNL started the merging process in December, 2002 with the global catalogs. Once the merging of global information was completed, the regional and local catalogs were merged into the tables. The entire process of merging all the earthquake catalogs took approximately two months to complete. All available catalog information as of January 21, 2003 was merged into the KB tables.

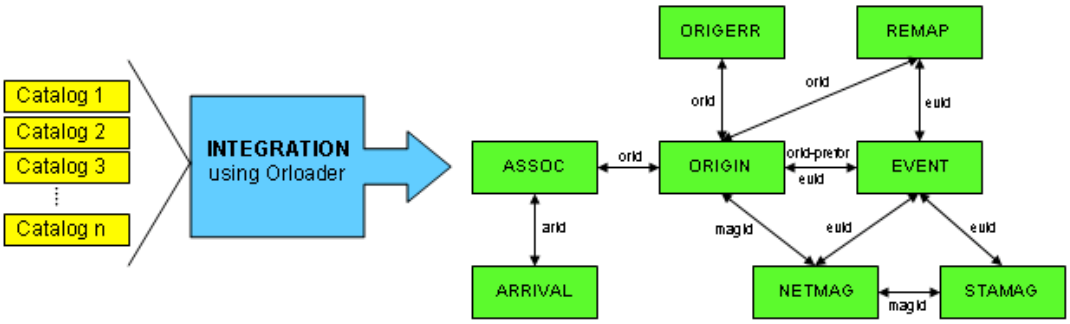


Figure 3. Integration of the Primary tables that contain earthquake information

The **wfdisc** and **wftag** Primary core tables contain information about the waveforms. The waveforms themselves must be in one of several supported binary formats. Both LANL and LLNL delivered **wfdisc** and **wftag** tables with their associated waveforms. To merge the information from the two laboratories, we first compared the two **wfdisc** tables to see if there were any identical waveforms (see Figure 4). There turned out to be 8 identical segments (out of ~282,000) and the labs were contacted to determine which information should be used for those segments. Then the waveform identifiers (*wfids*) in each table were remapped to the KB numbering scheme, using the **remap_wfids** table created by the KB Integrator. Once the *wfids* were changed the two **wfdisc** tables from the laboratories, were combined to make the KB **wfdisc** table. The same remapping of wfids was done in the two **wftag** tables from the laboratories. In addition, the column *tagid* in the wftag tables needed to be remapped. The *tagid* in the wftag tables for the KB are always *evids*. Using the remap table created in the process of merging catalogs, the *tagids* were remapped to the *evids* for the KB. Once the *wfids* and *tagids* were changed in both tables, the two wftag tables from the laboratories were combined to make the KB wftag table.

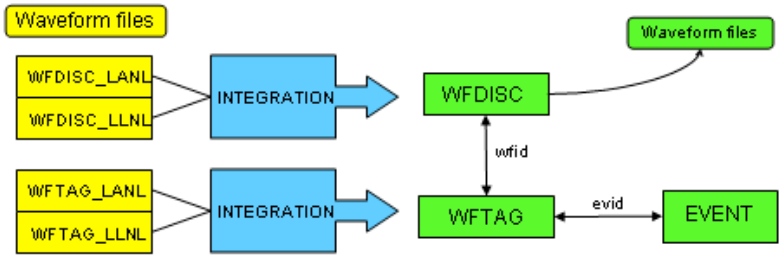


Figure 4. Merging the wfdisc and wftag tables from the two laboratories

For this release of the KB, there were 32 custom database tables. Five of these tables had one or both of the columns *orid* and *evid* that needed to be remapped to match the ids in the merged catalog tables. There were three tables we used to remap the *orids* and *evids*: the **remap** table created when merging the catalogs with Orloader, and the **remap_lanl_events** and **remap_llnl_events** tables which we had to create by hand using the merged **origin** table and origin tables sent from LANL and LLNL, **origin_lanl** and **origin_llnl**. The **remap** table created when merging the catalogs with Orloader could be used to remap *orids* and *evids* for the origins that came from the regional catalogs that were sent to SNL as database tables, because the *origorid* and *origevid* values in the **remap** table could directly be related to *orids* and *evids* in the origin information delivered from the laboratories. However, for the origins from the global catalogs and the regional catalogs that were merged from flat file information, the *origorid* and *origevid* values in the **remap** table related to the flat file numbering and not the numbering in either the **origin_lanl** or **origin_llnl** tables. To remap the origins from those catalogs, we created the tables

remap_lanl_events and **remap_llnl_events** that mapped the *orids* and *evids* from the merged **origin** table to the *orids* and *evids* in either the **origin_lanl** or **origin_llnl** table where the origin information (*lat*, *lon*, *depth*, *time*, *auth*) matched. Once the **remap**, **remap_lanl_events** and **remap_llnl_events** tables were in place, the *orids* and *evids* were changed in the **discrim_data**, **gttable**, **magnitude**, **nnsa_amplitude** and **nnsa_amp_descript** tables using simple update SQL commands.

In addition to remapping *orids* and *evids*, there were two tables where the column *arid* needed to be remapped and one table where the column *wfid* needed to be remapped. To remap the *wfids* in the **nnsa_amp_descript** table, we used the **remap_wfids** table that had been created for remapping *wfids* in the **wfdisc** and **wftag** tables, and changed the *wfids* using a simple SQL command. Remapping the *arids* was a little more complicated. All the arids that needed to be remapped came from LANL. Using the **arrival_lanl** table that LANL provided, we created the **remap_arids** table that mapped the *arid* from the merged **arrival** table to the *arid* in the **arrival_lanl** table by matching the arrival information (*sta*, *time*, *iphase*, *auth*). Again, a simple update SQL statement changed the *arids* in the **nnsa_amplitude** and **nnsa_amp_descript** tables to the KB numbering scheme.

The final remapping that needed to be done concerned identifiers only found in the custom tables: *fdid*, *corrid*, *paramsetid*, and *windowid*. We needed to make sure that before we combined tables from both laboratories that these identifiers did not overlap. If they did overlap, we added a constant to one laboratories numbers and then combined the information into single tables. The tables combined in this manner were **mdac_fd**, **mdac_fi**, **discrim_param** and **discrim_data**.

Once the integration was completed, all the database tables were put into a single database account and primary keys and indexes were set on the tables in consultation with AFTAC. The README files for the integrated research products that contained event data were updated to reflect the name of the database account.

Parametric Grid Data Integrated Research Products

The parametric grid (PG) data format is an NNSA custom format developed to store a wide variety of types of geophysical information that is not handled well by any single existing system: travel time tables, kriged correction surfaces, tessellated correction surfaces, layered Earth models, etc. PG data is stored as a set of binary files, which we refer to as a PG database. The PG software provides the functionality to store and retrieve PG objects from the database in a generalized manner, and is used by many of the software tools delivered with the KB. Each object stored in the database is decomposed into a Meta-Data Key (MDK) and a Serialized Binary Stream (SBS). The MDK is used to contain summary information about the object including its object type (class name), date of creation, location in the database of the associated SBS, pertinent attributes (station, phase, base model, frequency, etc.), a description string, and a unique 16 byte (128 bit) hash string, called the Key String Identifier (KSI). The KSI uniquely identifies an object's MDK for which it was created. Additionally, the MDK contains all dependency KSIs that are required to build the object associated with the MDK. All MDK objects are loaded from the database immediately after connecting to a database platform. More information about PG can be found in Hipp et al. 2002.

NNSA developed the Data Manager (DM) package to browse and merge PG databases created by Scientific Integrators, but for this KB release no merging of PG databases was done. From a software perspective, the merging is straightforward so we were able to code it into DM, but from a scientific perspective, it raises many troubling questions. For example, if travel correction surfaces are developed for the same station and phase by each lab, and their geographic extents overlap, what should happen in the region of overlap? The NNSA researchers collectively decided that such issues should be worked out before the PG databases were created, with the labs working together to create a single correction surface whenever there was an overlap. Thus, when the products were delivered to SNL, there were no regions of overlap, so merging was not needed. We kept the component PG databases from each lab and delivered them as such. The various PG databases were placed in the directories for the corresponding integrated research products.

Contextual Data Integrated Research Products

Contextual data are generally stored in one of two models, vector and raster. For the purposes of the KB, vector data are stored in ESRI shapefile format for use with the ArcView Global Project, the KB's geographic information system (GIS). The vector data are made up of a series of features with explicit geometry. Examples of vector data

in the KB include political boundaries (polygons), mine locations (points), road and railroad networks (lines), geologic provinces (polygons), and seismic station networks (points). Raster data are represented as cells of a uniform size, each containing a single numeric value. Most raster data are stored in some imagery format, such as TIFF, JPEG, etc. The KB also supports the use of ESRI Grid format raster data, which are generally used to represent surfaces, such as topography, bathymetry, or correction surfaces, models, etc., derived from integrated research products submitted to the KB. Although each dataset is unique, the processing of these data is similar. The general steps taken to process the data are described here and depicted in Figure 5.

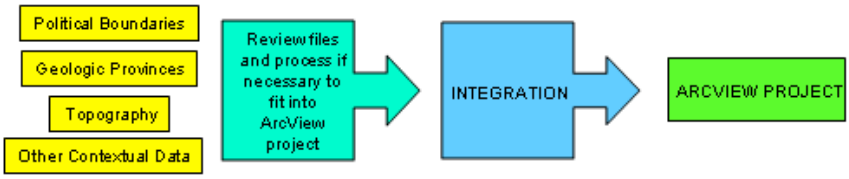


Figure 5. Integration process for Contextual Data

In most cases, the contextual data has been preprocessed before it reaches the KB Integrator. For example, the original source (shapefile, report with latitude and longitude coordinates, etc.) for a mining dataset may have covered more geographic area than is of interest to the submitting laboratory or customer. The Scientific Integrator will have clipped out the appropriate portions and submitted this subset to the KB Integrator. The Scientific Integrator will also have submitted an accompanying ArcView legend file, which is used by the ArcView software as a guide for symbolizing the dataset when it is displayed in the ArcView project. The same may be true for raster data, with the exception of imagery, for which ArcView does not support the use of customized legend files.

Once the KB Integrator receives the contextual data, a two-step process is performed. First, the Integrator reviews the data itself, checking that the files are not corrupted or missing, that they can be viewed in the ArcView application, that a legend file has been provided, and that the dataset and its attributes are consistent with the documentation describing the data. In some cases, the data must be processed further in order to conform to the ArcView project. This may involve the removal of attributes or inconsistent features from the dataset, “clipping” the data to correspond to specified geographic regions, or modifications to the legend file.

Second, the KB Integrator must incorporate the contextual data into the ArcView Global Project. This project is a customized application built specifically for the customer. It incorporates all contextual data submitted to the KB, as well as customized tools, functionality, maps, specialized database query tools, and custom interprocess communication procedures for communicating with other KB tools. The new datasets must be folded into this project in such a manner that it is both easily accessed by the user and complements the function of the project as a whole.

For inclusion in the ArcView Global Project, the data must be incorporated into a custom menuing system. The data are organized into specific locations on disk based on their function and geographic location, which is mirrored in the ArcView project. Rather than rely on a continuous connection to a relational database, data are organized into a lookup table that is stored within the project. The lookup table stores information about the dataset, including its location on disk, the location of its metadata, symbology information, and keys used by ArcView to facilitate access to the data itself. The table is utilized by the menuing system to access the data on disk, load the data into a View (or Map) in the project, and pull in any associated information stored with the data in the table record. In addition, the data may also be accessed by certain custom tools in the ArcView project. In all cases, however, the data, its symbology, and its metadata must be reviewed in the context of using the ArcView Global Project in order for the GIS as a whole to be tested. Once this process is concluded, the contextual data and the ArcView Global Project are considered complete and ready for submission.

Research Tool Integrated Research Products

There is no standard format for research tool integrated research products. The tool designers could pick any format they wanted, but the KB Integrator required that during development the designers needed to work with SNL to make sure that the required hardware and software to run the tool would be available at AFTAC for integration and testing. In past deliveries, tools were treated as autonomous packages despite the fact that many of them share libraries or even call one another directly, and this led to problems with the delivery and testing (duplication of files and general confusion). For this release, all SNL tools were installed as sub-directories into a directory called GNEM_Tool_Root. Links to executables for each tool were placed in a common bin directory also under GNEM_Tool_Root, and links to all of the libraries were placed in a common lib directory. This structure was very successful; it made it easier for the SNL tool developers to develop their products, it made the overall tool delivery more space efficient, and it also made it much easier to configure and test the tools after delivery. We integrated fourteen research tool products.

White Paper Integrated Research Products

The established format for the White Paper integrated research products was PDF. The Scientific Integrator sent to SNL papers either in PDF, or in the original format. For those that came in the original format, we changed the cover page to match the standard created for the KB, and then we converted the document to PDF. If the paper came in PDF, then we sent a copy of the standard cover page to the Scientific Integrator and asked him to include it in the document and resubmit the document in PDF with the new cover page attached. The various White Papers were placed in the directories for the corresponding integrated research products. There were six white papers in the KB.

Post Integration and Organization

As soon as an integrated research product was integrated into the entire KB, the KB Integrator coordinator informed the Validator so that he could verify and functionally validate the integrated product. By this point the verification was a fairly simple process; the goal was to make sure that all the entities associated with the product had been successfully integrated into the KB. The functional validation was again done by running the installation test that the Scientific Integrator provided. The goal was to make sure that the integration process did not corrupt the product so that the installation test could not be run successfully. If there were problems with the installation test, the Validator first worked with the KB Integrator coordinator to make sure they did not arise because of the integration and hopefully resolved them. If they could not resolve the problems, the Validator then went back to the Scientific Integrator for help to determine the solution.

For the latest release of the KB, the KB Integrator designed a graphical interface to easily organize and access the information in the KB. This tool is called KB Navigator. It is a “window” into the KB that allows a user to find the integrated research products, check geographic extents, access standard GIS datasets, view metadata and launch the research tools. An Oracle database schema was designed for the KB Navigator to hold all the pertinent information about the products. As Validators were verifying and functionally validating the integrated research products, the KB Navigator developers were entering information into the schema.

Nodes in the Navigator were created for each integrated research product and their associated datasets following the directory structure that had been set up prior to the start of integration. There were two distinct kinds of nodes – tool nodes and dataset nodes. Tool nodes were for the different tools that could be used to access information in the KB. The required information for a tool node included the startup information and the communication protocol. Dataset nodes represented a variety of files, dataset types, database queries (SQL) and research tools - all the contents of the KB as best as could be captured with one tool. Each dataset node included as much descriptive information as possible: proper name and version, location of the data on disk, dataset type, descriptive keyword information and the tool that should be used for access. A load date and the name of the author of the dataset node information were also included to keep track of when and who entered the information. The descriptive keyword information and the geographic extent of an integrated research product were taken from the documentation supplied by the Scientific Integrator for the product. There could be any number of keywords that describe an integrated research product. Most keywords were common words or phrases that could be used to describe the subject of the integrated research product. In addition, keywords could be a geographic name of the location covered by the integrated research product.

Displaying the data directly in Navigator itself only worked well for the Contextual Data integrated research products and Event Data integrated research products where we could define specific database queries and show the results. For most of the other products, configuration files were set up to display data using the appropriate tool for the integrated research products. Tools were configured to be launched from the KB Navigator using shell scripts that execute simple commands from the Navigator.

Descriptive information on the contents of the KB Navigator nodes and how to display or use the dataset was included in the README file started by the Validator for each integrated research product. If the integrated research product was not yet viewable with the KB Navigator, the information about where the dataset was located, why it was not viewable in the KB Navigator and the time frame for when it would be included was discussed in the README file. Every README file was added as a node in the KB Navigator so that a user would be able to easily see this information.

The final step in the integration process was to make sure that each integrated research product could be accessed and used through the KB Navigator. (Figure 6). This step ensured that the KB Navigator schema had been set up correctly, and again verified that no problems in accessing or using the integrated research product occurred during integration. This process also allowed the KB Integrator to assess the functional weaknesses of some of the products in the KB. It was difficult in some cases to determine exactly how products were intended to be used and what their format should be if they could not be run using one of the research tools, queried from the database or even highlighted in the document.

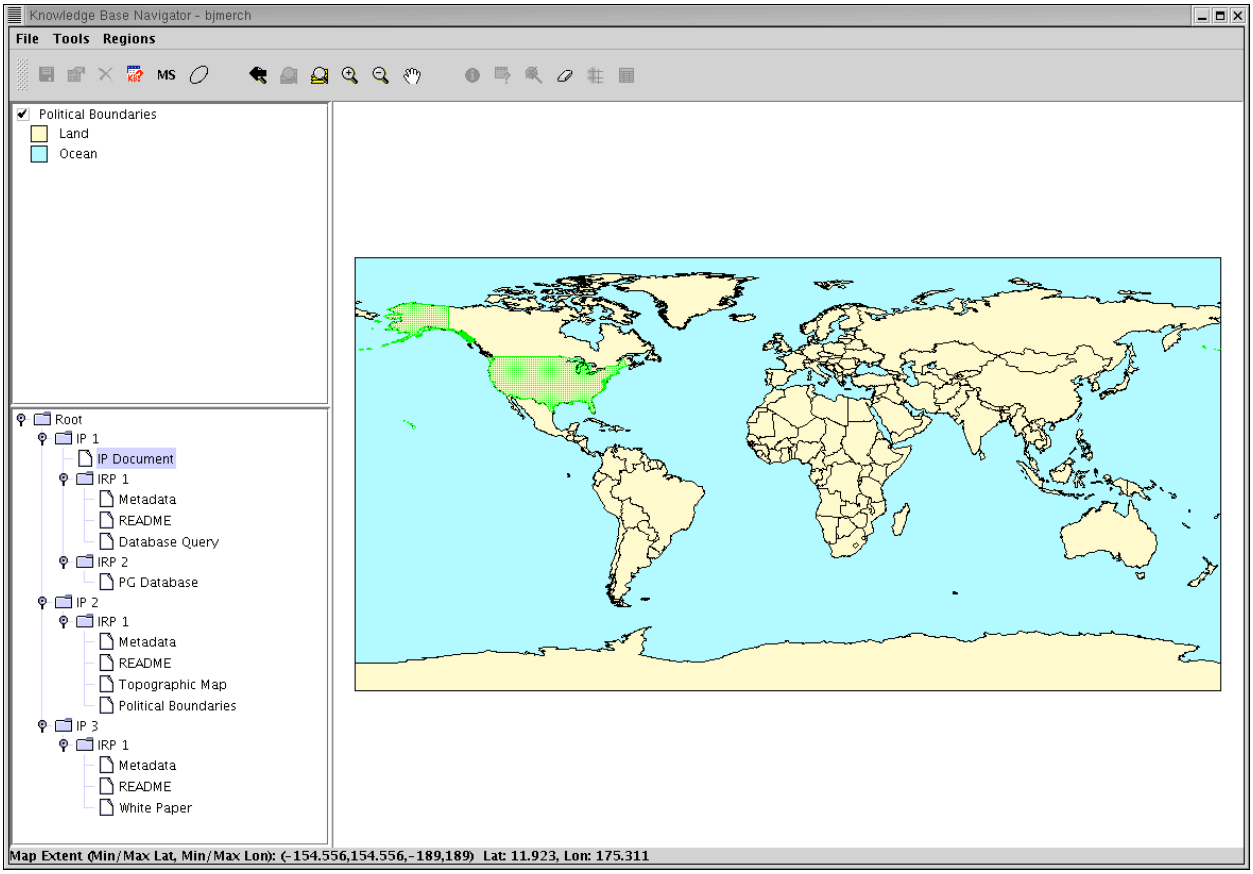


Figure 6. KB Navigator

Documentation

Documentation is also an important part of the KB. The main documents are the IP documents. The core of the IP document is the integrated research product descriptions written by the individual Scientific Integrators. The introduction section contains the overall purpose of the IP, summarizes the changes from previous versions, lists members of the working group that created the IP and provides an overview of the products in the IP. This section is written by the administrative points of contacts for the working group assigned to that IP. Each IP document was also assigned an editor to help put the introduction and integrated research product descriptions together and do final formatting and editing.

Scientific Integrators were required to get final descriptions for their integrated research product to the KB Integrator six weeks after the products themselves arrived at SNL. The editors came to SNL at that point and began compiling the integrated research product descriptions into the composite IP document. The editor also worked with administrative points of contact in getting the introduction written and into the document. The final documents were converted into PDF and placed in the Documents directory. All the IP documents were entered as dataset nodes in the KB Navigator so that users could easily access them.

CONCLUSIONS AND RECOMMENDATIONS

A well-defined process is needed when integrating products into the KB to make sure the result is a high-quality seamless product. Involving more people in the process of verifying and functionally validating integrated research products allowed the KB Integrator to take the time needed to really make sure a product could be accessed and used in the most appropriate manner. Running the Installation Test Procedures both before and after a product was integrated was important to let the KB Integrator know if any problems had been introduced due to integration. Finally, the use of the KB Navigator as a final test of the KB was inordinately valuable. SNL was very confident that we knew exactly what was in this release of the KB, and what the weaknesses were.

REFERENCES

Carr, D. (2002), National Nuclear Security Administration Knowledge Base Core Table Schema Document, Sandia National Laboratories, SAND2002-3005 (available at http://www.nemre.nn.doe.gov).

Gallegos, D. P., D. B. Carr, P. B. Herrington, J. M. Harris, C. L. Edwards, S. R. Taylor, J. J. Zucca, D. B. Harris, N. A. Wogman, D. N. Anderson and L. A. Casey (2002), The Integration Process for Incorporating Nuclear Explosion Monitoring Research Results into the National Nuclear Security Administration Knowledge Base, SAND2002-2772 (available at http://www.nemre.nn.doe.gov).

Hipp, J.R., R.W. Simons, L. Jensen, L. A. Lindsey and M. N. Chown (2002), The GNEM R&E Parametric Grid Data Software Suite: Tools for Creation, Access, Management, Viewing, and Export, *"Proceedings of the 24th Seismic Research Review: Nuclear Explosion Monitoring: Innovation and Integration"*, 2002, Los Alamos National Laboratory *LA-UR-02-5048.*

THE 2003 PARAMETRIC GRID SOFTWARE SUITE FOR GROUND-BASED NUCLEAR EXPLOSION MONITORING RESEARCH & ENGINEERING

James R. Hipp, Randall W. Simons, and Lee A. Jensen

Sandia National Laboratories

Sponsored by National Nuclear Security Administration
Office of Nonproliferation Research and Engineering
Office of Defense Nuclear Nonproliferation

Contract No. DE-AC04-94AL85000

ABSTRACT

One of most important types of data in the National Nuclear Security Administration (NNSA) Ground-Based Nuclear Explosion Monitoring Research and Engineering (GNEM R&E) Knowledge Base (KB) is Parametric Grid (PG) data. PG data can be used to improve signal detection, signal association, and event discrimination, but so far its greatest use has been for improving event location by providing ground-truth-based corrections to travel-time base models. In this presentation we will discuss the latest versions of the suite of GNEM R&E tools developed by NNSA to create, access, manage, and view PG data.

The primary PG population tool is the Knowledge Base Calibration Integration Tool (KBCIT). KBCIT is an interactive computer application whose goal is to produce interpolated calibration-based information that can be used to improve monitoring performance by improving precision of model predictions and by providing proper characterizations of uncertainty. It is used to analyze raw data and produce kriged correction surfaces that can be included in the Knowledge Base. KBCIT not only produces the surfaces but also records all steps in the analysis for later review and possible revision. New features in KBCIT include: support for 3D travel time models; auto-generation of polygon transition boundaries; enhanced decimation of complex region boundaries; and a new detailed tutorial providing step-by-step instructions for most functionality.

The Parametric Grid Library (PGL) provides the interface to access the data and models stored in a PGL file database. The PGL represents the core software library used by GNEM R&E tools that read or write PGL data (e.g., KBCIT). The PGL also provides a common access interface, the Run-Time Object Manager, for many of the United States National Data Center codes. The library provides data representations and software models to support accurate and efficient seismic phase association and event location. The PGL currently provides direct support for travel-time, slowness, azimuth, and amplitude data, as well as for generalized geophysical model data. PGL stores all of its data and model representations as Serialized Binary Stream Objects (SBSOs) that can be conveniently accessed using a set of database key objects. The key objects contain the SBSOs' descriptive meta-data information. Because PGL supports the KBCIT and Data Management Tool (DMT), some new features in those tools required corresponding modifications to PGL.

The DMT provides access to PG data for purposes of managing the organization of the generated PGL file database, or for perusing the data for visualization and informational purposes. It is written as a Graphical User Interface that can access the key file associated with any PGL file database and display it in an easily interpreted visual format. The format allows a user to view the entire object reference and dependency hierarchy, to remove objects from a database, copy objects from one database to another, or create new minimal PGL file databases that use a subset of one or more existing PGL file databases. The DMT also provides a mechanism to textually or visually display the content of any SBSO in a PGL file database. It provides a means to locate and remove redundancy and to evaluate the overall storage efficiency of each type of supported SBSO. Most of the objects supported by the PGL lend themselves to visualization. Each PGL object that can be visualized has a visualization interface that can be launched from the DMT. Some visualization interfaces have data export capabilities providing data formatted for use by other analysis tools. New features in DMT include import/export of ASCII representations of travel time, azimuth, and slowness base models (2D and 3D), as well as site information and ellipticity corrections.

OBJECTIVE

Monitoring sensor data for possible nuclear explosions involves four fundamental tasks: signal detection, signal association, event location, and event identification. For all but the first of these, the task is accomplished by minimizing the misfit between observations and theoretical predictions, which in turn are dependent on the model of the Earth used. Thus, improving the quality of the Earth model used for monitoring is of critical importance and this is why it is a primary focus of the GNEM R&E efforts.

Having a better Earth model, is not enough, however; if the model is to be maintained and used for operational monitoring, we need a cohesive set of software tools to leverage the improved model's benefits. Population tools are needed to make it easy to process the data into the proper format, and to update the model when new data becomes available. The Earth model must be designed and defined into an integrated and extensible software system. An interface is needed around the model to serve predictions to various applications. An efficient, extensible storage format is needed to archive the model on disk. Finally, some sort of data management and viewing utility is needed to easily allow users to browse through the model to better understand it, and to make simple edits (deletions, insertions) as needed.

Researchers at Sandia Labs have been working to meet these needs by developing an integrated suite of tools collectively expressed as the Parametric Grid Software Suite (PGSS).

RESEARCH ACCOMPLISHED

The PGSS consists of the primary data population tool, KBCIT, the low level storage, representation, and model library, PGL, the database management tool, DMT, and the viewing and export tool, VExTool. We briefly describe each tool below accompanied by new enhancements incorporated over the previous year. See Hipp et al. (2002) for more information concerning the basic operation of each tool.

Knowledge Base Calibration Integration Tool (KBCIT)

The Knowledge Base Calibration Integration Tool (KBCIT) is an interactive computer application whose goal is to produce interpolated calibration-based information that can be used to improve monitoring performance by improving precision of model predictions and by providing proper characterizations of uncertainty. It is used to analyze raw data and produce kriged correction surfaces that can be included in the Knowledge Base. KBCIT not only produces the surfaces, but also records all steps in the analysis for later review and possible revision.

KBCIT allows the user to define the boundaries of regions, where the data in each region can be treated differently, including using different base models, trend removals, outlier limits, and variograms in each region (See Figure 1). KBCIT allows the user to set parameters for blending functions to apply across region boundaries to avoid discontinuities. A declustering operation is available to reduce data-set size by removing redundancy, and stabilize kriging by averaging values close to one another.

KBCIT uses the Parametric Grid Library, described below, to implement both stationary and non-stationary Bayesian kriging for interpolation of empirical data with uncertainties (See Figure 2). The results of kriging can be cross-validated by comparing empirical values with interpolated predictions based on a kriged surface formed using all but the values to be compared.

To provide a faster alternative to interpolating a kriged surface, the user can specify a tessellation on which KBCIT will pre-compute kriged values. Any combination of kriged and tessellated surfaces can be summed or differenced and viewed with an interactive 3D viewer (See Figure 3). Kriged and tessellated surfaces can be saved in a Parametric Grid database for use by other programs such as those doing event location.

New features added to KBCIT this year (2003) include:

1. Azimuth and Slowness Data and Models – Added the ability to generate surfaces for azimuth and slowness observations, and created new base models to allow the computation of residuals.

2. 3D Travel-Time Models – Added support for base models with parameters (latitude, longitude, depth), allowing residuals to be computed relative to 3D models.

3. Multi-Polygon Regions – Added support for kriging regions made up of many polygons, to allow complex continental and oceanic regions.

4. Default Transition Boundaries - Added decimation of complex region boundaries, and auto-generation of transition bounds with user-specified width.

5. User-Interface Improvements – Allow selection of observations on the map to highlight corresponding rows in the observation list; zoom-in on the variogram plot and limit the portion used for auto-fit; improve default variogram values for amplitude data; load a single kriging set from a project.

6. Documentation - Added a 40-page tutorial, giving step-by-step instructions for most functions KBCIT can perform.

7. Travel-Time Tables - Updated standard IASPEI 91 and AK135 travel-time tables to match what the Air Force Technical Application Center is using in the operational system.

8. Project-Specific Configuration Files – Added the option to allow configuration for a project to override a user's configuration.

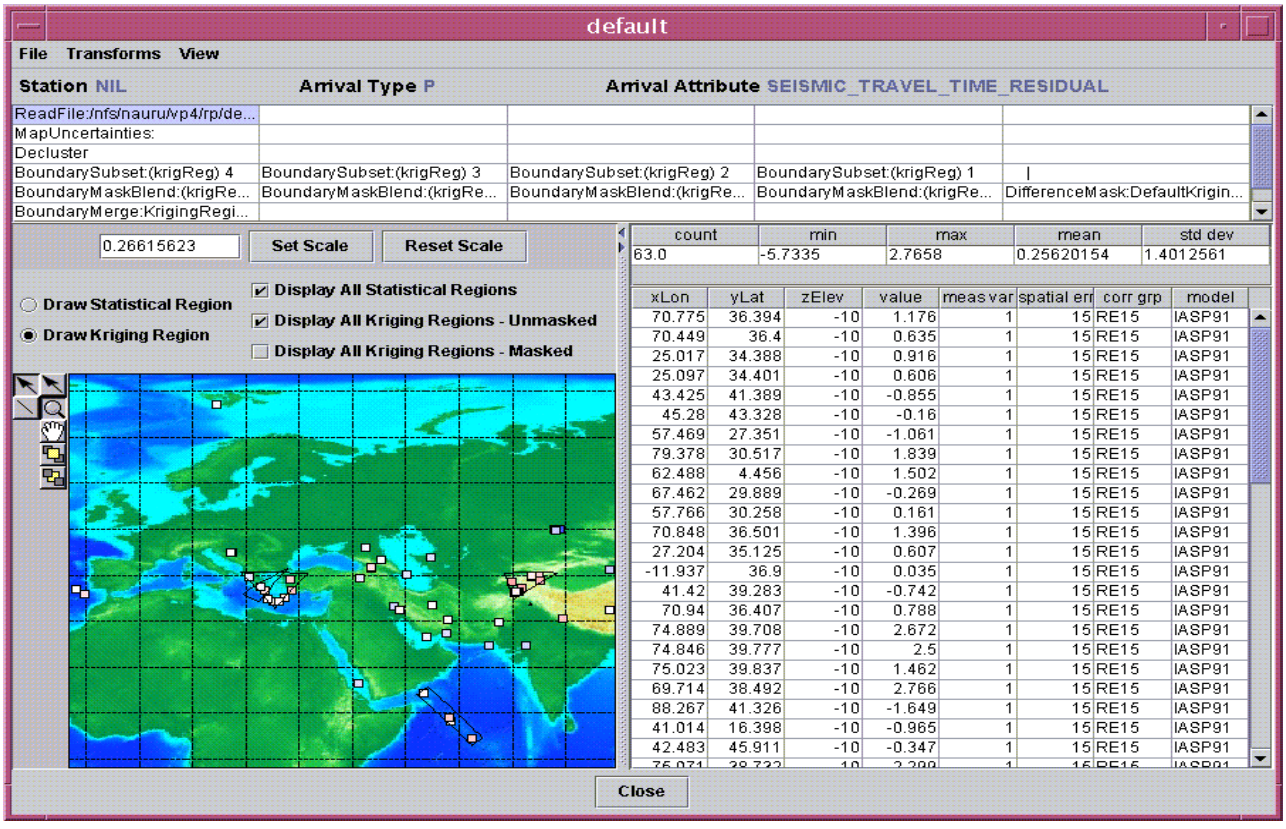


Figure 1. Kriging set window in KBCIT

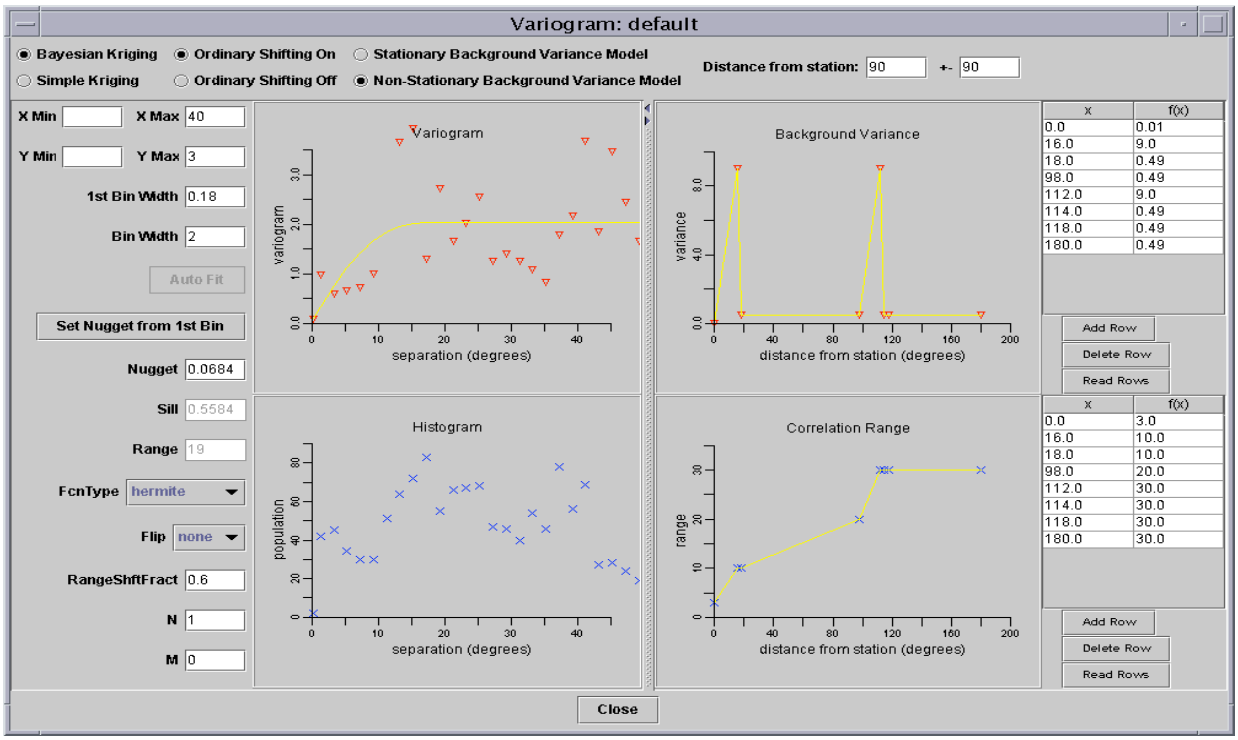


Figure 2. Variogram window in KBCIT

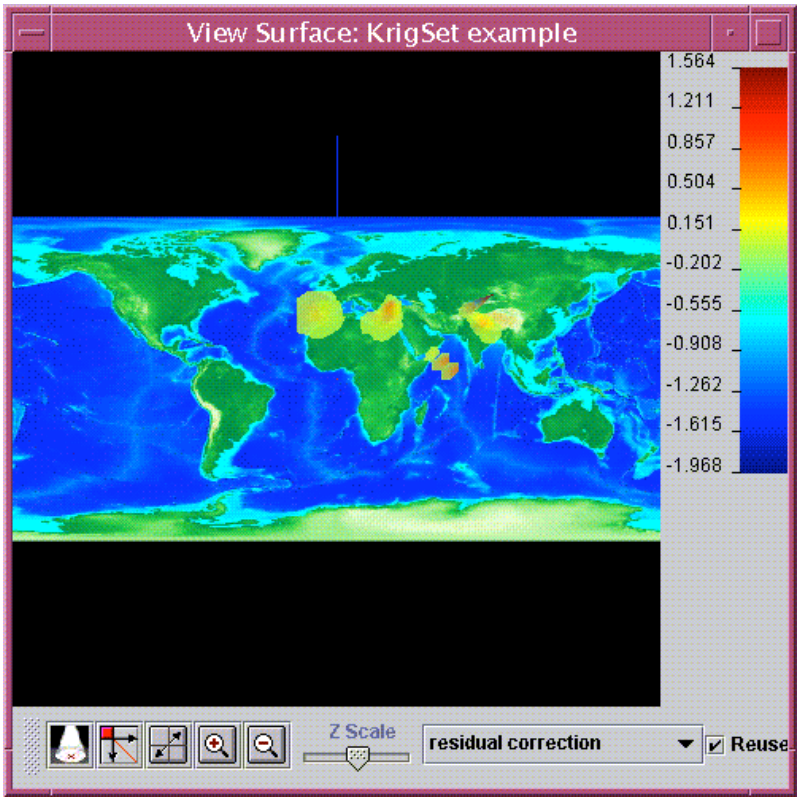


Figure 3. View surface window in KBCIT

Parametric Grid Library (PGL)

The Parametric Grid Library (PGL) provides the internal representation and client interfaces to access the data and models utilized by GNEM R&E tools. This includes tools that provide a means of populating the PGL (e.g., KBCIT described above) and those that require access to its data or models (e.g., U.S. National Data Center codes). The library can be divided into several distinct functional groups that provide necessary library capability. These groups include:

1) A physical-models group that supports basic and complex seismic modeling, Bayesian kriging for providing enhanced path corrections to the seismic models, and multi-region polygonal representations to provide a means for smoothly transitioning from discrete models defined in different tectonic regions;
2) A geometry group that provides the interface and representation functionality to support a variety of 1D, 2D, and 3D representation schemes; these include parametric and tessellated curve, surface, and volume representations, and a 2D point location facility;
3) A tessellation group that provides a means of generating and subsequently representing tessellated data for purposes of data interpolation and spatial searching;
4) A database group that defines the means to store and access arbitrary object data in a rapid manner;
5) An interfaces group that provides a Run-Time Type Identification (RTTI) facility for creating, managing, and destroying all database object types, and various client Application Programming Interfaces (APIs) for interfacing directly with the PGL functionality; and finally
6) A general utility group for providing other types of PGL requirements such as geometric vector support, memory management, and core-level base-class definitions.

Figure 4 depicts the structure of the various PGL groups outlined above.

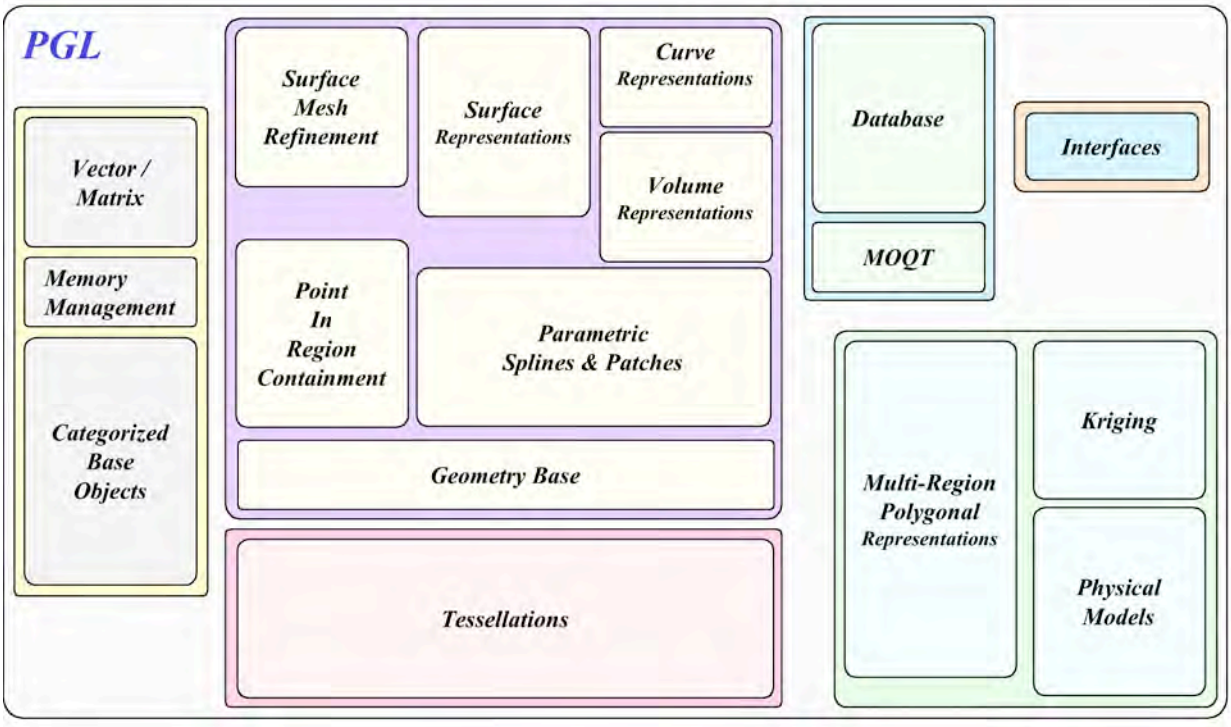


Figure 4. The six major groups of the PG software library and various subcomponents of each group

This year (2003) several new features were added to the PGL interface including:

1. Added a new exception logging service. The new service tracks all errors/warnings that occur in any function of the PGL interface and reports those messages immediately to calling clients. Additionally, clients can access the message queue programmatically or dump the queue to an ASCII file at any time during the PGL execution phase.

2. Produced a new Date/Time facility. This object was initially constructed by Sandy Ballard for the LocOO tool but was seen to have broader applicability across GNEM tools and was modified and moved to PGL in late 2002. The Date/Time object is used in PGL to set station activity and positions as a function of the stations operational history. In this way event location codes (e.g., LocOO, LocSAT, EvLoc, etc.) can set the time for which an arrival is detected at a station and guarantee that the proper historical station position coordinates are used.

3. Added a new results access interface to the PGL API. The new interface provides a common data access blueprint through which any output-centric PGL object can be mapped. This mapping simplifies results access by providing a common set of results access functionality regardless of the internal structure and implementation of the PGL object.

4. A new directory structure for seismic base-data objects and support of import/export functionality. Supported seismic base-data objects include travel-time, azimuth, slowness, and amplitude models, base models, and 3D regional model representations. The new directory structure provides for three different client initiated data access modes including accessing existing seismic base data in a default directory structure; retrieving, copying, or merging from one seismic base-data directory into another; or accessing new data that is currently not contained in any seismic base-data directory. The DM software now supports a graphical user interface (GUI) driven import/export functional interface for manipulating the new seismic base-data structure. The new interface can extract a seismic base-data directory from any PGL File Database (FDB) and write the extraction as an ASCII seismic base-data directory. Conversely, the new interface can also read an ASCII seismic base-data directory and export the entire directory as a PGL FDB.

5. Added a new crustal depth model (Laske, Masters, and Reif from Bassin et al. 2000). The crustal model is used to fade path corrections, which are developed for events occurring in the crust, to zero as the event location deepens beyond the local crustal depth. This avoids incorrectly adding path-corrections to events that are beyond the depth for which the path corrections were developed. The crustal depth is modeled as an internal parametric surface using the 2 x 2 degree spacing specified in the model. If path-corrections are present the crustal depth is interpolated from its defining parametric surface and compared to the depth at which the path correction is being requested. If the requested depth is less than the computed crustal depth the correction is returned un-altered. If the requested depth is greater than the crustal depth by some user defined fraction then zero is returned for the path correction. A smoothly varying weight (between 1 and zero) is used to multiply the path correction for requested depths that are greater than the crustal depth but less than the crustal depth plus the user-specified fraction. In this way the path correction can vary smoothly with depth, from its nominal value for event locations that are shallower than the crustal depth, to zero for requested depths that are much deeper than the crustal thickness.

In addition to the new PGL modifications mentioned above, a new PGL graphics interface is currently undergoing development using the Visualization Toolkit (VTK) software (Schroeder et al. 2003). The new interface, and its high-level Java driver and GUI, will be used to provide DMT (see below) and the new GNEM Knowledge Base Navigator tool (KB Navigator) with visualization capability for visualizing 1D, 2D, 3D, and layered volume PGL objects. This functionality is discussed in greater detail in the next section.

Data Management Tool (DMT)

The Data Management Tool (DMT) provides access to the PG data for purposes of managing the organization of the generated PG database, and for perusing the data for visualization and information purposes. The tool is written in Java providing a GUI front end and a JNI interface into PGL. The visualization component is primarily handled by the VExTool application, which is the topic of the next section.

The database management facilities of the DMT include a means for inspecting the entire object reference and dependency hierarchy for any object in multiple databases simultaneously. These facilities provide mechanisms to copy or move objects and their dependents from one database to another or to simply remove them from their containing database entirely. These services allow a user to construct new databases from existing databases that use a subset of the objects contained in any of the existing databases. This functionality provides a means for users to build databases that are tailored for spatially interesting regions or that contain objects that are specific for certain types of problems (e.g., seismic location). Figure 5, below illustrates a typical hierarchical dependency view of a database including object Meta Data Key (MDK) listings and their dependents.

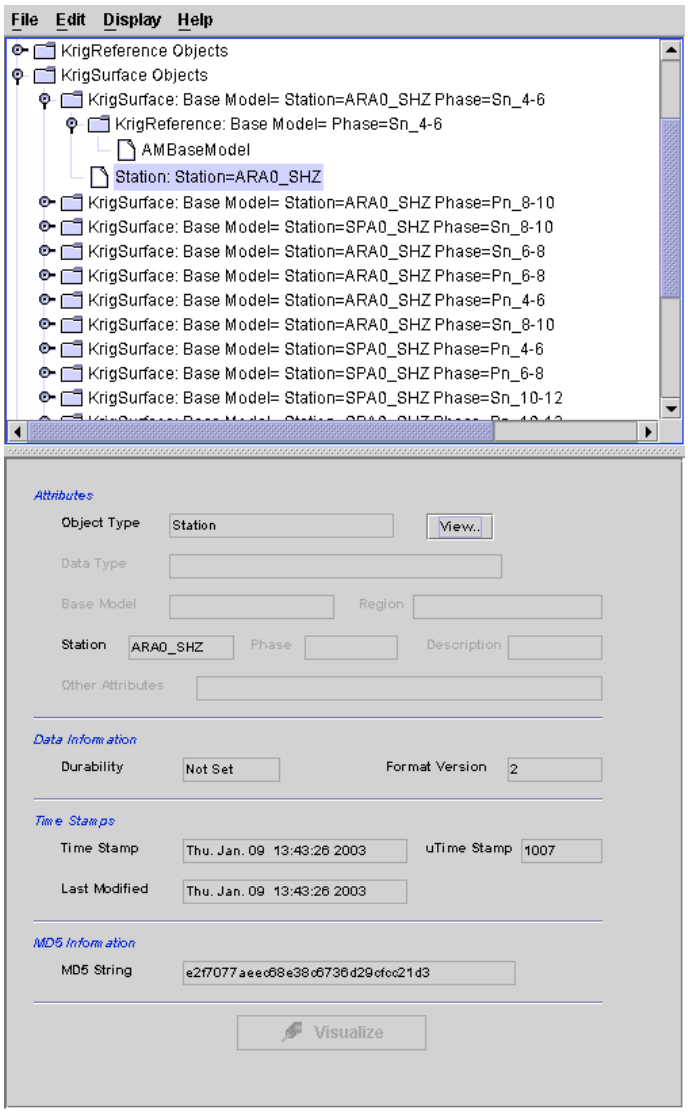


Figure 5. A typical screen shot of the DMT GUI displaying a hierarchical view of the database objects and their dependents.

In addition to database object construction, the DMT also provides services for managing MDK modifications. These services permit a database administrator to correct errors or deficiencies in an MDK object in the database. Obviously, some of the MDK data cannot be changed such as object type, location of the Serialized Binary Stream Object (SBSO) in the database, dependent object Key String Identifiers (KSIs), etc. However, attribute and descriptive data can by modified and replaced back into the database without harming the overall database structure. This service is a key feature for performing routine maintenance on existing PG databases.

Another maintenance service involves generic searching facilities. Searching allows a user to discover specific patterns of data within the database. Search requests are formulated by supplying a generic search MDK object with the attributes of interest filled with desired patterns, and unimportant or irrelevant patterns left blank. All matches are returned to the user for inspection.

Finally, the database can be inspected for duplicate binaries. These are objects that have two or more MDKs that all point to SBSOs that are duplicates of one-another. This duplication can happened when identical objects are created at different times producing new MDKs with a different KSIs. These duplicates can be discovered and all but one may be removed. The DMT automatically updates the database dependency hierarchy to reflect the changes.

Aside from these features the DMT can also load individual SBSOs for examining the contents in a textual format. This data is not available for change, as only a population tool is capable of modifying the data, but it does provide a means for a researcher or analyst to examine the defining data from which the object is composed. Also, as mentioned above, the DMT can request a visual inspection of an SBSO by calling the primary VExTool visualization service. This is described in more detail in the next section.

Viewing and Export Tool (VExTool)

The primary role of the VExTool is to visualize the properties of any geometric object in a PG database, regardless of the object's type or dimension. It is also used to export interpolated model data to a number of third-party tools utilized by GNEM researchers. The VExTool interface was written in Java and provides a user friendly GUI for manipulating complex objects graphically. The tool utilizes a JNI interface for accessing the PG data and models directly through the PGL CGI object described above.

VExTool can display an individual property of an object in 1, 2, or 3 dimensions or a range of properties as a set of curves or surfaces. Additionally, VExTool can display multiple views of the same object simultaneously. Figure 6 illustrates a typical VExTool screen dump where a property of a layered volume object is displayed simultaneously with a 2D cross-section and a 1D positional borehole.

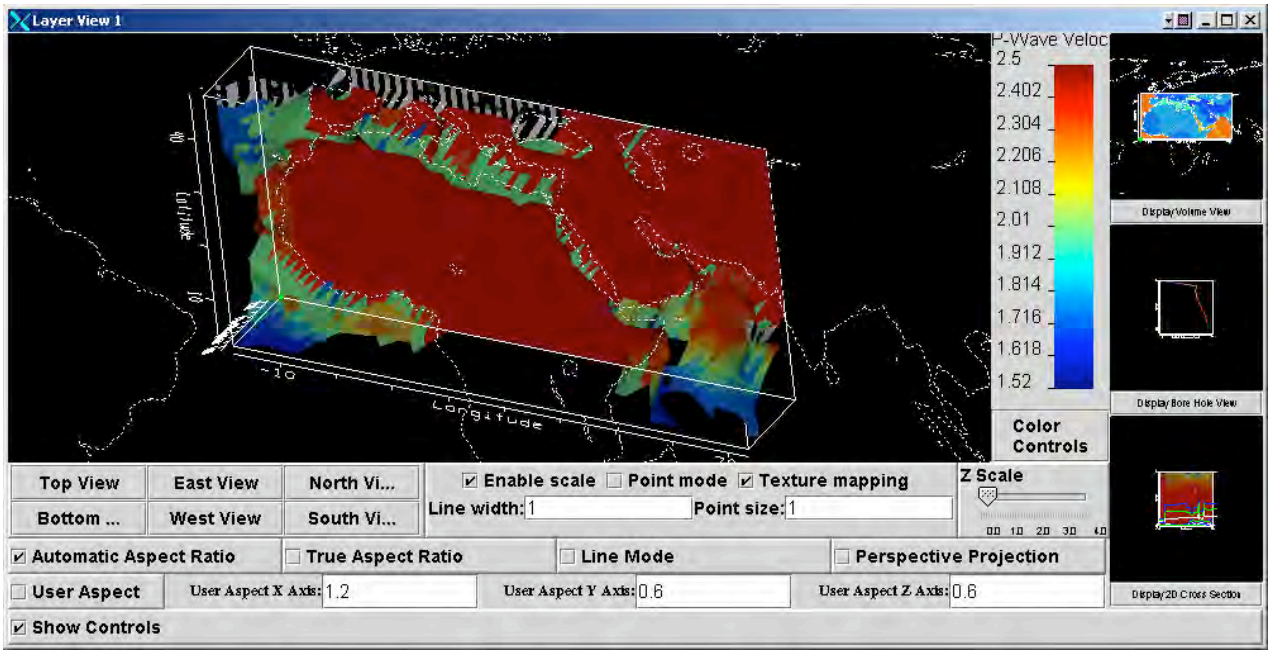


Figure 6. A typical VExTool screen shot where a 3 dimensional layered volume object is shown displaying various geophysical properties in 3D, 2D cross-section, and 1D bore hole depictions.

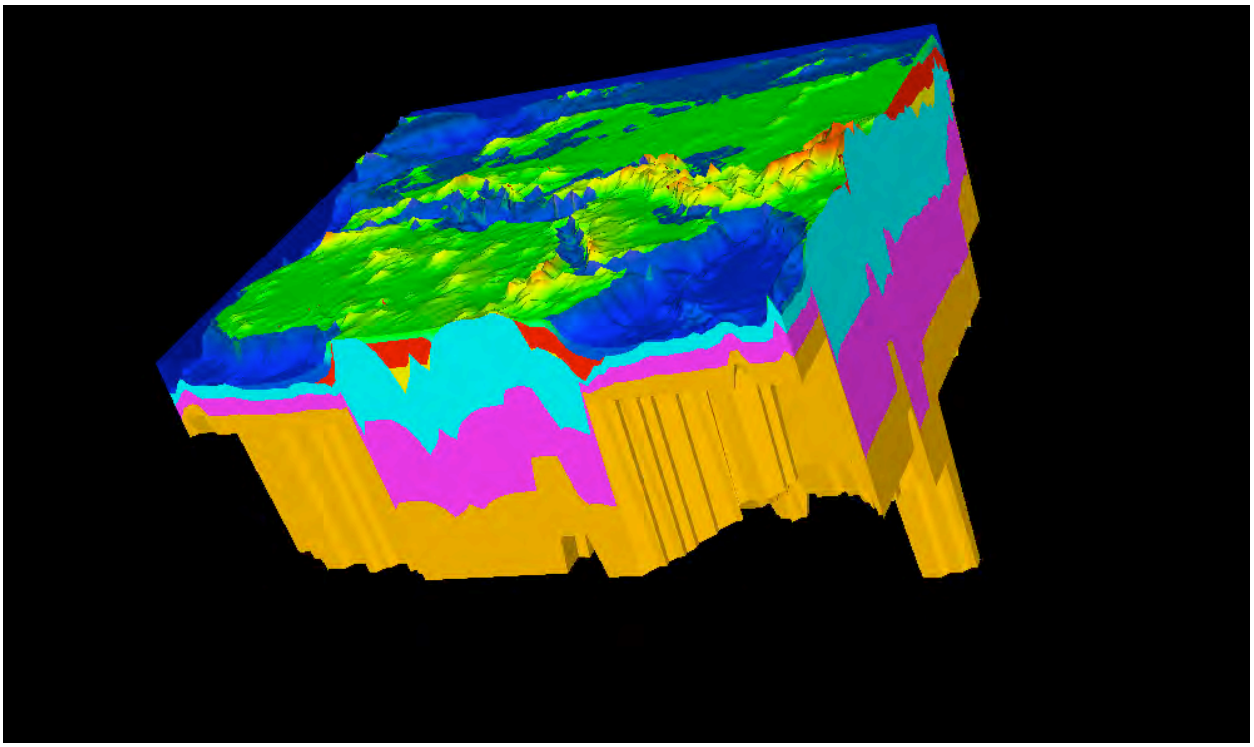


Figure 7. A screen shot of VTK graphics being incorporated into the VExTool.

CONCLUSIONS AND RECOMMENDATIONS

In this paper, researchers at Sandia National Laboratories have described a set of integrated software tools and their associated enhancements over the past year. The tools were developed to take advantage of the improvements in the new GNEM R&E Earth model. This integrated set of software, known as the Parametric Grid Software Suite, consists of data population, storage, modeling, and data management and viewing tools.

The population tool, KBCIT, provides interpolated calibration-based information that can be used to improve monitoring performance by improving precision of model predictions and by providing proper characterizations of uncertainty. The underlying software representation of the GNEM R&E improved Earth model is provided by the PGL. The PGL also provides a generalized object database for storing model data and a set of API interfaces utilized by the population, data management, and viewing tools. The PG data-management facilities are handled by the DMT. The DMT is primarily responsible for maintaining and validating PG databases and for creating subset databases from existing ones. Finally, all model object-viewing and data-export facilities are provided by VExTool.

REFERENCES

Bassin, C., Laske, G. and Masters, G., (2000), The Current Limits of Resolution for Surface Wave Tomography in North America, EOS Trans AGU, 81, F897, 2000.

Hipp, J.R., Simons, R.W., Jensen, L.A., (2002), The GNEM R&E Parametric Grid Data Software Suite: Tools for Creation, Access, Management, Viewing, and Export, "Proceedings of the 24th Seismic Research Review - Nuclear Explosion Monitoring: Innovation and Integration," *LA-UR-02-5048*.

Schroeder, W., Martin, K., Lorensen B., (2003), The Visualization Toolkit, 3rd Edition, Kitware, Inc., February 2003, ISBN: 1930934076

GURALP SEISMIC INSTRUMENTATION COMPONENT EVALUATION

Richard P. Kromer, J. Mark Harris and Toby O. Townsend

Sandia National Laboratories

Sponsored by National Nuclear Security Administration
Office of Nonproliferation Research and Engineering
Office of Defense Nuclear Nonproliferation

Contract No. DE-AC04-94AL85000

ABSTRACT

Sandia National Laboratories have tested and evaluated seismic instrumentation from Guralp Systems Limited (GSL), Aldermaston, Reading, United Kingdom. Components evaluated include the DM24-B1 single channel borehole digitizer and the CMG-3V single component short-period vertical borehole seismometer. These two components were then integrated into two subsystems along with the CMG-AM borehole data authenticator modules.

GSL DM24-B1 tests included a response to static and dynamic input signals, data time-tag accuracy and seismic application performance. Configurations tested include:

- DM24 1-channel 40 samples per second GSL CMG3-V short-period seismometer gain
- DM24 1-channel 1 sample per second GSL CMG3-T broadband seismometer gain

The GSL CMG-3V tests included side-by-side testing to determine sensor self noise, seismometer response, seismometer sensitivity, and calibration capability. Dual subsystem installation using Sandia FACT site 'shotgun' boreholes was demonstrated. CMG-AM data streams were connected via the Internet to the Air Force Technical Applications Center (AFTAC) at Patrick Air Force Base in Melbourne, Florida.

The GSL equipment was evaluated for use in the International Monitoring System (IMS). In these cases, IMS data surety requirements and guidelines must be met for station certification. GSL CMG-AM data surety was tested to verify correct operation in the station environment and to ensure that data surety requirements are met. These tests included data authentication (CD-1.1 format), intrusion monitoring, remote command authentication, and remote key management operations. Connections to the AFTAC Operation and Maintenance Subsystem (OMS) were demonstrated.

This paper describes the evaluation of the GSL seismometer, digitizer, authenticator/formatter components and performance within the subsystem.

OBJECTIVES

Introduction

AFTAC is tasked with monitoring the compliance of existing and future nuclear test treaties. To perform this mission, AFTAC uses several different monitoring techniques to sense and monitor nuclear explosions, each designed to monitor a specific physical domain (e.g. space, atmosphere, underground, oceans, etc.). Together these monitoring systems, equipment and methods, form the United States Atomic Energy Detection System (USAEDS). Some USAEDS seismic stations may be included in the International Monitoring System (IMS).

Sandia National Laboratories tested and evaluated seismic instrumentation from Guralp Systems Limited (GSL) including the DM24-B1 single channel borehole digitizer and the CMG-3V single component short-period vertical borehole seismometer. These two components were then integrated into two subsystems along with the CMG-AM borehole data authenticator modules. The GSL equipment was evaluated for use in the International Monitoring System.

Evaluations Performed

Sandia evaluated the overall technical performance of the GSL DM24-B1 borehole digitizer component of the Guralp instrumentation. Distortions introduced by the high-resolution digitizers were measured. The results of these evaluations were compared to relevant IMS application requirements or specifications.

Sandia evaluated the overall technical performance of the GSL CMG-3V short-period vertical borehole seismometer component of the Guralp instrumentation. GSL CMG-3V tests included side-by-side testing to determine sensor self noise, seismometer response, seismometer sensitivity, and calibration capability. The results of these evaluations were compared to relevant AFTAC and IMS application requirements or specifications.

Sandia will evaluate the data surety performance of the GSL CMG-AM authenticator module component of the Guralp instrumentation. GSL CMG-AM data surety will be tested to verify correct operation in the station environment and to ensure that data surety requirements are met. These tests will include data authentication (CD-1.1 format), intrusion monitoring, remote command authentication, and remote key management. These tests are intended to verify correct operation of the CMG-AM and the OMS in an IMS station environment.

RESEARCH ACCOMPLISHED

Guralp DM24-B1 Borehole Digitizer

The DM24-B1 borehole digitizer was manufactured by Guralp Systems Limited. The input to the digitizer is single-ended with an input impedance of 3,000 ohms. GSL provided two DM24-B1 digitizers to be part of a 2-element demonstration system that will include two CMG-3V seismometers and a CMG-AM data authenticator/ communications modules. The DM24-B1's were configured to acquire data at 40 samples per second and 1 sample per second concurrently. GSL provided 'Scream' data acquisition software for each DM24-B1 digitizer. Scream is operated on a PC laptop computer and communicates with the DM24-B1s through a direct-connect serial connection. Data were acquired in Guralp Compressed Format (GCF) flat-file records. Selected tests were performed at 1 sample per second to demonstrate that capability.

Testing was performed at the SNL Facility for Acceptance, Calibration and Testing (FACT) site (Figure 1).

Two DM24-B1s were tested:

1. DM24-B1 S/N DA62, 1-channel, 40/1 samples per second, CMG-3V [1]
2. DM24-B1 S/N DA63, 1-channel, 40/1 samples per second, CMG-3V [1]

This paper presents a sampling of the test results from these configurations.

DM24-B1 Digitizer Performance Tests and Results

The following tests were conducted on the DM24-B1. This is a subset of tests as outlined in the Sandia Ground-based Monitoring R and E Technology Report [2].

Static Performance Tests

Input Terminated Noise (ITN) test: Measure the input terminated noise of the DM24-B1.

ITN test results: Figure 2 indicates that the DM24-B1/DA 62 has < 0.87 count RMS noise at 40 sps. Figure 3 indicates that the DM24-B1/DA 62 has < 0.34 count RMS noise at 1 sps.

Maximum Potential Dynamic Range (MPDR) test: Compute maximum potential dynamic range using data from the ITN test.

Table 1. DM24-B1 MPDR

DM24-B1 Serial No.	RMS Noise µV 0.033 to 20 Hz	RMS Full-Scale Volts	MPDR
DA62	1.624	7.07	132.8 dB
DA63	1.642	7.07	132.7 dB

MPDR test results: Table 1 indicates that the DM24-B1 40 sps maximum potential dynamic range was greater than 132.7 dB.

Tonal dynamic performance tests:

Total Harmonic Distortion (THD) test: Measure the linearity of the DM24-B1 digitizers using total harmonic distortion.

Table 2. DM24-B1 THD

DM24-B1 Serial No.	THD
DA62	-116.4 dB
DA63	-114.2 dB

THD test results: Figure 4 and Table 2 indicate that the DM24-B1 total harmonic distortion was better than –114.2 dB.

Timing tests:

Time-Tag Accuracy (TTA) test: Determine the accuracy of the time-tags of the DM24-B1 data samples.

TTA test results: Figures 5 and 6 indicate that the DM24-B1 can time tag data samples to within 148 microseconds with a jitter standard deviation of 0.61 microseconds.

Time-tag accuracy drift

Time-tag Drift (TTD) test: Determine the impact of GPS loss on the ability of the DM24-B1 to correctly time-tag data samples.

TTD test results: Figure 7 indicates that the DM24-B1 time-base/clock drifts at a rate of approximately 76 microseconds per hour when GPS is lost and recovers at 49 microseconds per hour after GPS restoration.

Broadband Dynamic Performance Tests

Seismic Application Tests

Seismic System Noise (SSN) test: Determine ability of the DM24-B1 to resolve the expected seismic background using a CMG-3V seismometer.

SSN test result: Figure 8 indicates that the noise of the DM24-B1 digitizer was at least 8 dB below the USGS New Low Earth Noise Model (NLNM) between 0.033 and 18 Hz when used with a CMG-3V seismometer. Digitizer noise was at least 3 dB under the CMG-3T (the CMG-3V noise model is not available yet) sensor self-noise.

Guralp CMG-3V Short-period Vertical Borehole Seismometer

The GSL CMG-3V short-period vertical borehole seismometer was manufactured by Guralp Systems Limited. The sensor has a flat response from 30 seconds to 50 Hertz. GSL provided two CMG-3V seismometers for evaluation.

Testing is being performed at the SNL Facility for Acceptance, Calibration and Testing site (Figure 9).

Sandia will evaluate the overall technical performance of the GSL CMG-3V short-period vertical borehole seismometer component of the Guralp instrumentation. GSL CMG-3V tests include side-by-side testing to determine sensor self noise, seismometer response, seismometer sensitivity, and calibration capability. The results of these evaluations will be compared to relevant AFTAC and IMS application requirements or specifications.

Data Surety

Data Surety Requirements

The Provisional Technical Secretariat (PTS) has developed requirements to ensure that data from IMS stations is reliable and authentic. These requirements cover data surety aspects of the station, including data authentication, command authentication, key management operations, and intrusion monitoring. Our tests are intended to verify correct operation of the GSL CMG-AM equipment in an IMS station environment. IMS station data surety requirements, summarized from PTS documents [3], are listed here.

(1) All IMS data must be signed at the sensor sites.
(2) Data must be digitized and signed within a secure (tamper-detecting) environment.
(3) Signature must be calculated within a dedicated, tamper-indicating hardware authentication device.
(4) Data must be formatted for signing as specified by an approved protocol.
(5) DSS (DSA with SHA-1) must be used with 1024-bit public key.
(6) Signature device must generate DSA keys internally.
(7) Signature device must provide public key components to user.
(8) Signature device must not disclose private key directly to user or leak private key during operation.
(9) Commands originating remote from the station must be signed by the originator and verified at the station.
(10) A remote key change command must be supported for each authentication device; the authentication device must securely generate a new key pair and securely transmit the new public key.

Also, the PTS strongly recommends that a PC card device, certified to FIPS 140-1 Level 2, be used for DSA operations and private key storage.

Test Configuration

Testing of the GSL equipment will be performed during July and August 2003. The following test environment will be assembled at the Sandia National Laboratories in Albuquerque, NM.

The DC Simulator is a computer at SNL that is configured with software to parse the "Frame Store" files. It displays the CD-1.1 data format in a readable format, checks the validity of the format, and verifies authentication signatures using the *authd* program.

Data Surety Tests

System Design Review
Determine that the GSL CMG-AM, as part of the station environment, is designed to meet IMS surety guidelines; that system security, data authentication, and command authentication are incorporated in the equipment design and meet the minimal criteria.

Data Authentication
Determine that the GSL CMG-AM correctly calculates DSA signatures for sensor data in CD-1.1 format; that the station equipment transmits signed data that can be verified using the public key retrieved from the station.

Intrusion Monitoring
Determine that intrusion detection hardware is monitored correctly by the GSL CMG-AM; that the GSL CMG-AM sets the appropriate intrusion flags in the signed data; that the data transmitted from the station has these flags set correctly.

Remote Key Change Command
Determine that the key change operation works correctly on the GSL CMG-AM.

Remote Command Authentication
Determine that all commands issued remote from the station are signed at the remote location and verified at the station.

CONCLUSIONS AND RECOMMENDATIONS

DM24-B1 Digitizer Performance Tests

Table 3. DM24-B1/CMG-3V SP digitizer evaluation summary

	II. Minimum requirements for station specifications		
	Table 3. Specifications for primary and auxiliary seismic stations		
	Characteristics	**Minimum Requirements**	**Guralp DM24-B1-CMG-3V/USGS LNM**
1	***Array Pass Band***	SP: 0.5-16Hz	SP: 0.5-18Hz
2	***Seismometer noise***	<= 10 dB below minimum-earth noise at the site over the pass band	For CMG-3T sensor noise model: below the LNM minimum-earth noise model between 0.5 and 12 Hz; above the LNM minimum-earth noise model between 12 and 18 Hz
3	***Calibration***	within 5% in amplitude and 5 degrees in phase over the pass band	DC accuracy errors were within 0.4% for nominal and full-scale; -4% for over-scale
4	***Resolution***	18 dB below the minimum local seismic noise	Hz for calib (resolution) = 0.0148 nm/count @ 1 sec; resolution > -17 dB for 0.5 to 16 Hz.
5	***System noise***	<= 10 dB below the noise of the seismometer over the pass band.	<8 dB below the USGS LNM between 0.5 and 16 Hz; <4 dB below the CMG-3T seismometer noise
6	***Dynamic range***	>= 120 dB	better than 132.7 dB
7	***Relative timing accuracy***	<+ 1 ms between array elements	better than 146 microseconds

The DM24-B1 digitizer met IMS requirements as defined in Table 3.

CMG-3V Seismometer Performance Tests

At the time of this writing, the seismometer performance tests have not been completed. We expect to complete testing of the seismometers by September 2003.

Data Surety Tests

At the time of this writing, data surety tests have not been completed. Hardware, software, and documentation are needed to complete the evaluation.

REFERENCES

Evaluation of the Guralp DM24-B1 Borehole Digitizer for CMG-3V Application, Ground-based Monitoring R and E Technology Report, June 19, 2003.

Test Plan for the Evaluation of Digitizing Waveform Recorder Subsystems for Ground-based Geophysical Monitoring, Ground-based Monitoring R and E Technology Report, February 26, 2002.

Implementation Plan for IMS Authentication, CTBT/PTS/INF.100/Rev.1, 4 February 1999.



Figure 1. DM24-B1 Testing at FACT site

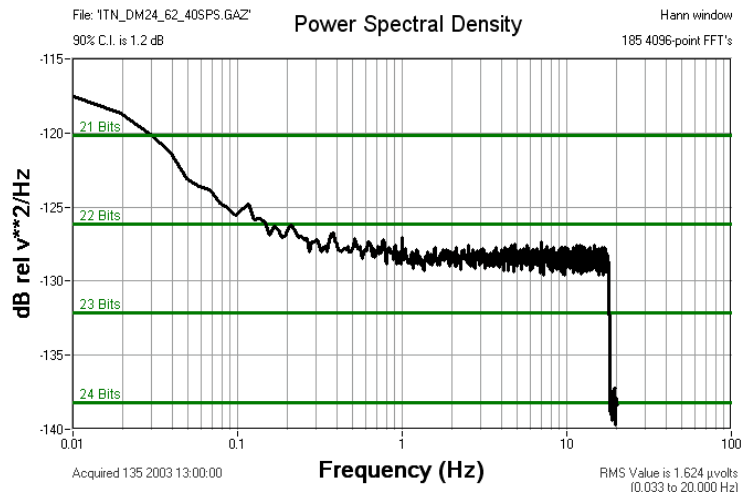


Figure 2. DM24-B1/DA 62 40 SPS input terminated noise

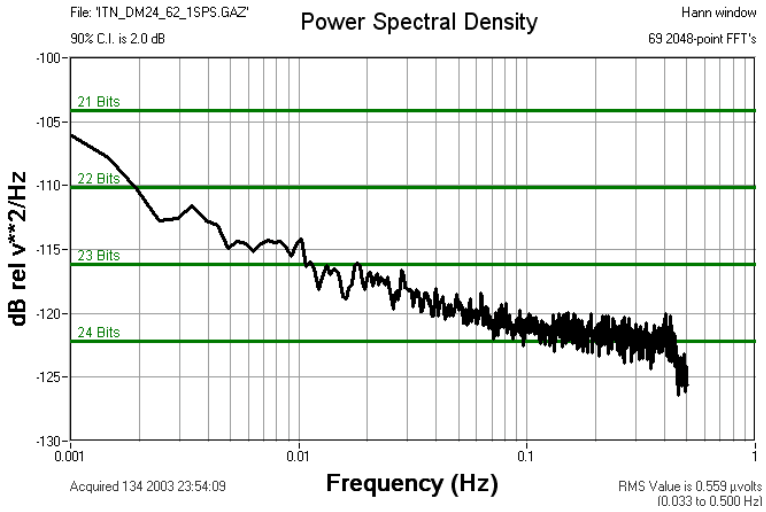


Figure 3. DM24-B1/DA 62 1 SPS input terminated noise

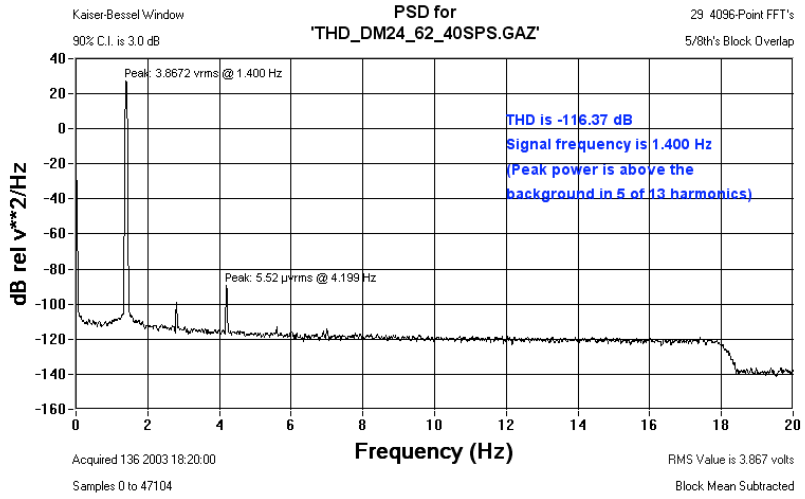


Figure 4. DM24-B1/DA62 Total harmonic distortion

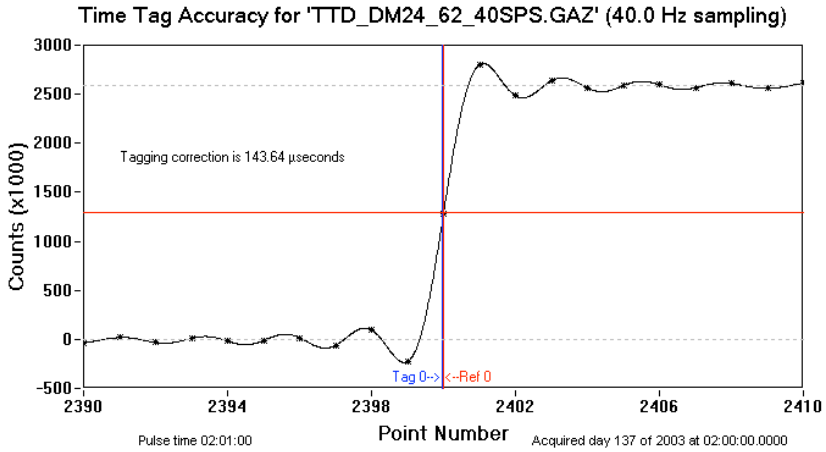


Figure 5. DM24-B1/DA62 Time-tag accuracy

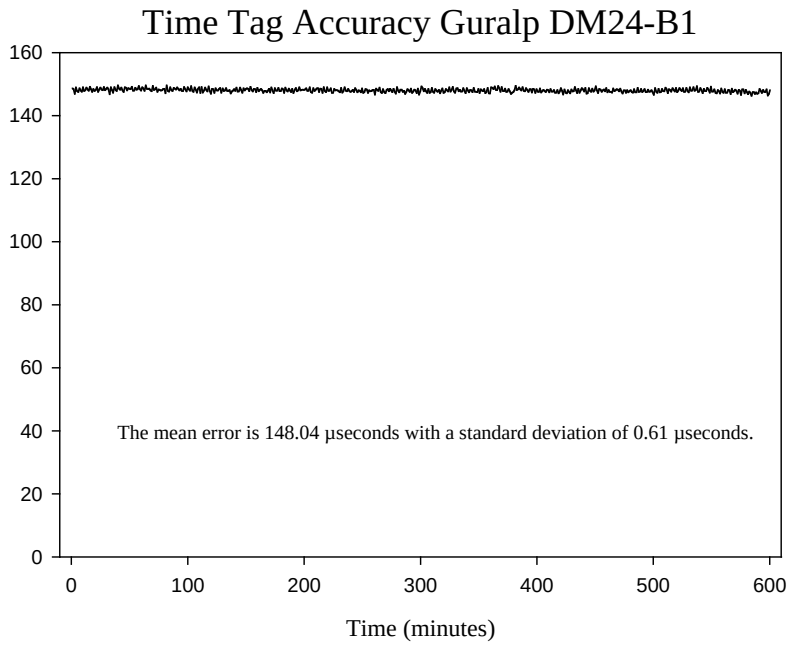


Figure 6. DM24-B1/DA62 Time-tag accuracy stability

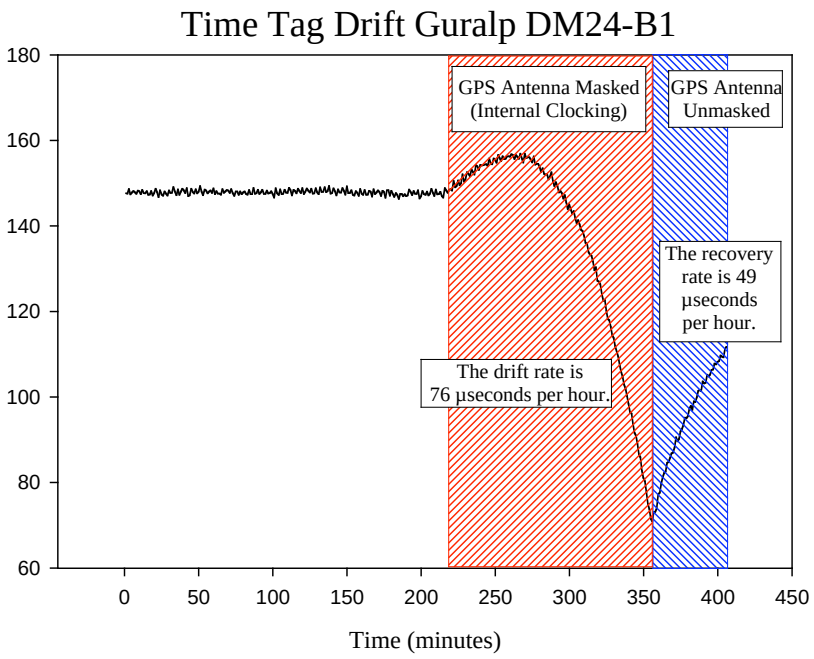


Figure 7. DM24-B1/DA62 Time-tag accuracy drift

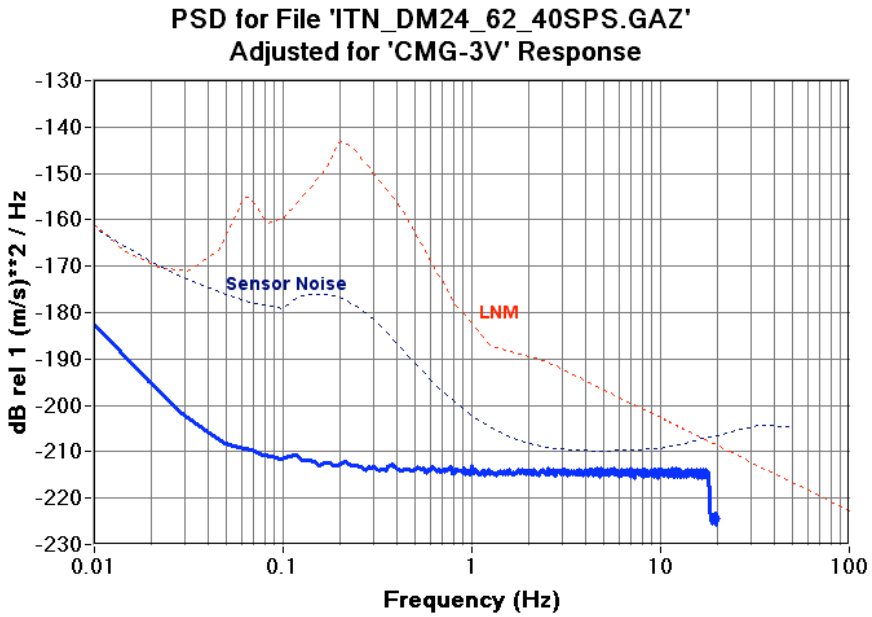


Figure 8. DM24-B1/DA 62 seismic system noise



Figure 9. CMG-3V testing at FACT site

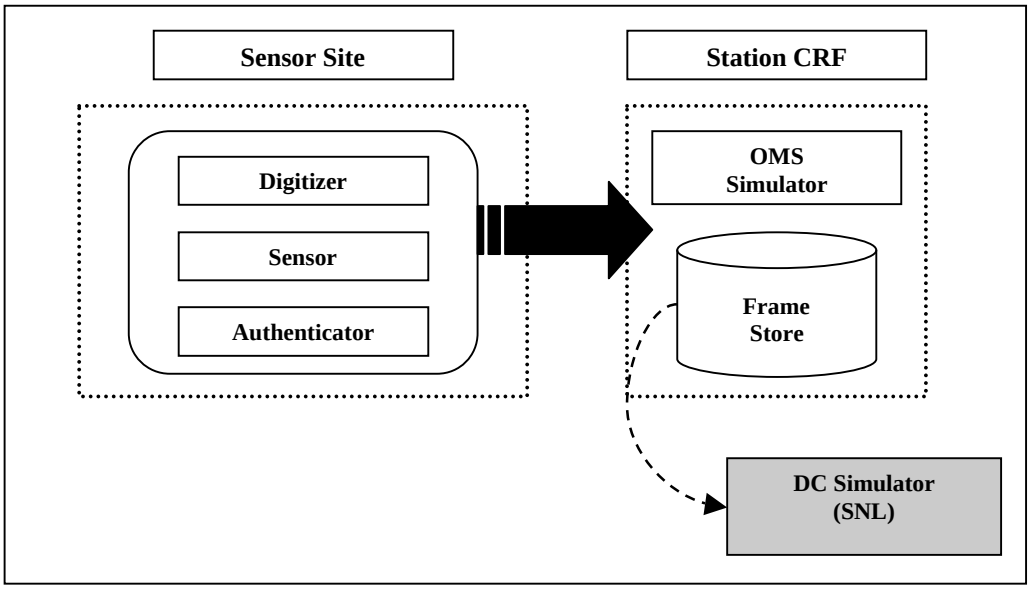


Figure 10. FACT site test configuration

REGIONAL SEISMIC THRESHOLD MONITORING

Tormod Kvaerna, Erik Hicks, Johannes Schweitzer, and Frode Ringdal

NORSAR

Sponsored by Defense Threat Reduction Agency

Contract No. DTRA01-00-C-0107

ABSTRACT

This three-year project was completed by the end of March 2003, and has resulted in a Final Scientific Report and software with documentation. The work has focused on the development and testing of a method for optimized, regional seismic monitoring, using a sparse network of regional arrays and three-component stations. Specifically, the following topics have been addressed during the project period:

- An experimental application of the threshold monitoring method to a small region of the Barents Sea, surrounding the accident site of the Russian submarine Kursk in August 2000. This study demonstrated how a number of small underwater explosions in the area following the accident have been detected using the threshold monitoring technique.

- A preliminary study of Pn amplitude attenuation relationships for the Barents Sea and adjacent regions. In particular, this work provided information on the expected spatial variability of the Pn amplitudes for regions of different extents.

- Compilation and analysis of a database of 45 seismic events, selected to provide the best possible ray path coverage of the Barents Sea and adjacent areas. This analysis was different from that in the standard analyst reviewed bulletin, in that we required that all discernible phases should be timed, regardless of whether or not they provide a good fit in the event location process. The readings were used for a mapping of phases observable for the different propagation paths, and for an assessment of the travel-time models applicable to this region.

- A detailed attenuation and inversion study, using the compiled database, aimed at obtaining attenuation relations for each of the major regional phases (Pn, Pg, Sn, Lg). We showed that these new attenuation relations represented an improvement relative to previously available relations, and that they provided consistent magnitude estimates based on different phase amplitudes. However, some significant blockage features in the Barents Sea and adjacent regions were noted.

- A regional threshold monitoring (TM) case study for the Novaya Zemlya region, which illustrated the performance of the regional threshold monitoring method using different combinations of monitoring stations. Using as an example a small seismic event about 100 km from the Novaya Zemlya test site, we made a special study addressing the trade-off between the beam radius and the beam focusing sharpness (noting the desire to have a single beam represent the largest possible area with no significant loss in performance).

- A regional threshold monitoring case study focusing on the Kola Peninsula. This study gave us the opportunity to obtain an impression of the potential TM performance in a case where a local network is available. Not unexpectedly, the monitoring thresholds turned out to be much lower than for the case of Novaya Zemlya.

- Development and delivery of software for Regional Seismic Threshold Monitoring, including a manual with descriptions of the programs and the basic operational procedures.

For the Novaya Zemlya region we have shown that for a threshold monitoring target region with radius as large as 100 km, the variations in threshold magnitudes are all within 0.2 magnitude units. For the investigated station geometry, it will therefore be meaningful to represent the monitoring threshold of the entire Novaya Zemlya region with the values of a single target point, together with *a priori* determined uncertainty bounds. For areas with larger variations in threshold magnitudes, like in the vicinity of the arrays or when local networks are available, denser deployment of the target regions is required for complete coverage.

OBJECTIVE

The main objective of this research is to develop and test a new, advanced method for applying regional seismic array technology to the field of nuclear test ban monitoring. To that end, we address the development and testing of a method for optimized seismic monitoring of an extended geographical region, using a sparse network of regional arrays and three-component stations. Our earlier work on optimized site-specific threshold monitoring serves as a basis for the development of this new method. Emphasis of the research is on algorithms that can be efficiently applied in a real-time monitoring environment, which are using primarily automated processing, and which can be readily implemented in an operational Comprehensive Nuclear-Test-Ban Treaty (CTBT) monitoring system.

RESEARCH ACCOMPLISHED

As described in the abstract, several sub-tasks have been addressed during this project. The results from most of these studies have been presented at earlier Seismic Research Reviews, but we will in this paper present some new results from a regional threshold monitoring study of the Kola Peninsula of northwestern Russia with its active mining regions. In addition, the conclusions and recommendations from the work on this contract will be provided at the end of the paper.

Regional Threshold Monitoring - A Kola Peninsula Case Study

As a case study of the performance of regional threshold monitoring, we have selected the mining areas in the Kola Peninsula, Russia. Figure 1 shows the location of the major mines in this area, together with the location of the two seismic arrays ARC and APA. Both the primary International Monitoring System (IMS) array ARC and the non-IMS station APA record high-SNR observations of all important regional phases at a range up to at least 500 km, which is the maximum distance range being considered in this case study. Furthermore, for the more distant recordings, these phases are well-separated in time.



Figure 1. Map of the Kola Peninsula with the main mining areas. Also shown are the locations of the ARCES and Apatity arrays.

Under a separate project funded by DoE, an effort is being undertaken to collect ground truth information, and explosion and rockburst observations for mines of the Kola peninsula. Such information is regularly collected from the mine operators by the Kola Regional Seismological Center (KRSC), and will serve as a reference set for our study. The mining areas comprise Khibiny, Olenegorsk, Kovdor and Zapolyarnyi.

In particular, the mines of the Khibiny Massif provide a natural laboratory for examining and contrasting the signals generated by different types of mining explosions and rockbursts. Of the five mines in the Massif, three have both underground operations and surface pits. Underground shots range in size from very small (~2 tons) with only a few delays and durations on the order of a few hundred milliseconds, to very large (400 tons) with many delays and durations approaching a half second (Ringdal et al., 1996). Shots above ground range from 0.5 tons to 400 tons with a wide range of delays and durations. Induced seismicity is frequent and triggered rockbursts accompany a significant fraction of the underground explosions (Kremenetskaya and Trjapitsin, 1995).

A grid system with a spacing of 0.2 degrees was used in this study. For computing the threshold traces, magnitudes based on the attenuation of Pg and Lg amplitudes were used for grid point to station distances within 2 degrees, while magnitudes for distances above 2 degrees are based on Pn and Sn attenuation (see Table 1). This is in accordance with the distances at which these phases are observable in the actual region. The frequency band used in the study was 3-6 Hz for all phases, except for Lg for which we used 2-4 Hz. Software to extract peak and mean threshold magnitudes for each grid point within a given time segment was used to analyze the TM results.

Table 1: Parameters used for regional threshold monitoring of the Kola mining areas

Travel time model	'barey' - Schweitzer and Kennett, 2002
Attenuation model	Hicks et al., 2002
Grid Spacing	0.2 degrees
Pg distance range	0 - 2 degrees
Pn distance range	2 - 20 degrees
Lg distance range	0 - 2 degrees
Sn distance range	2 - 20 degrees
Pg frequency band	3 - 6 Hz
Pn frequency band	3 - 6 Hz
Lg frequency band	2 - 4 Hz
Sn frequency band	3 - 6 Hz

Processing example 1

Figure 2 shows mean threshold magnitudes for each grid point for a 1-hour time segment starting at 2002-102:06.30. Even if this time interval is not without seismic events, this figure is representative of the combined TM capabilities of ARC and APA during typical noise conditions. In this and other similar plots, the individual TM grid points have been resampled onto a continuous grid using a minimum curvature surface fitting algorithm. As seen from the figure, the monitoring capability is between 0.5 and 1.0 mb units for the mining sites (marked as black squares).

Figure 3 shows the peak network magnitude thresholds with mean subtracted for the same 1-hour time interval as shown in Figure 2. This essentially shows the height of the highest peak above the background level within the time interval for each grid point. Note that an event in the Khibiny mine KH5 (see also Figure 4) creates a significant threshold peak in almost the entire region.

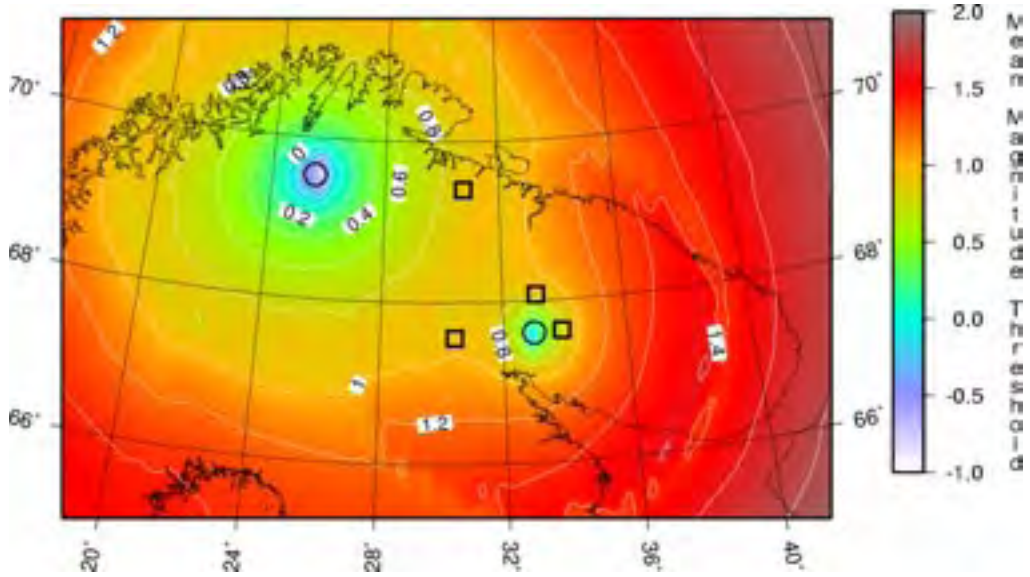


Figure 2. Mean network magnitude thresholds for a 1-hour time interval starting 2002-102:06.30, using the ARCES and Apatity arrays (black circles). The locations of the mining areas Khibiny, Olenegorsk, Kovdor and Zapoljarny (see Figure 1) are shown by black squares.

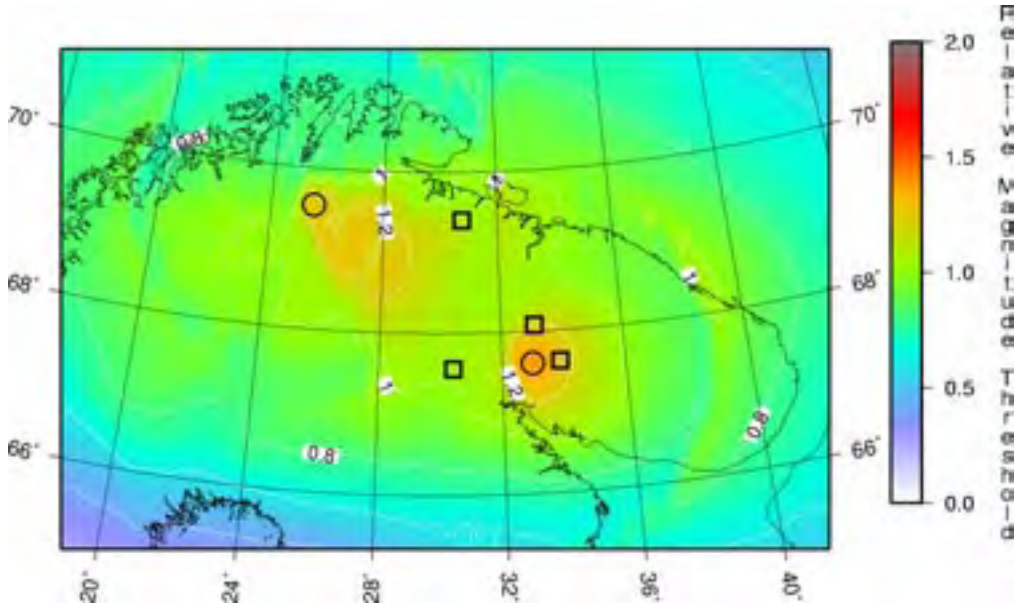


Figure 3. Peak network magnitude thresholds with mean subtracted for the same 1-hour time interval as shown in Figure 2.

Figure 4 shows the threshold time traces for a two hour interval surrounding the interval described previously. We have plotted the threshold trace of the grid point closest to the actual mine for each of the four major mining sites.

There is one large mining explosion (mine 5 of the Khibiny group) during this time interval, and this explosion causes a peak for each beam. Otherwise, the typical background threshold is between 0.5 and 1.0 mb units, consistent with Figure 2.

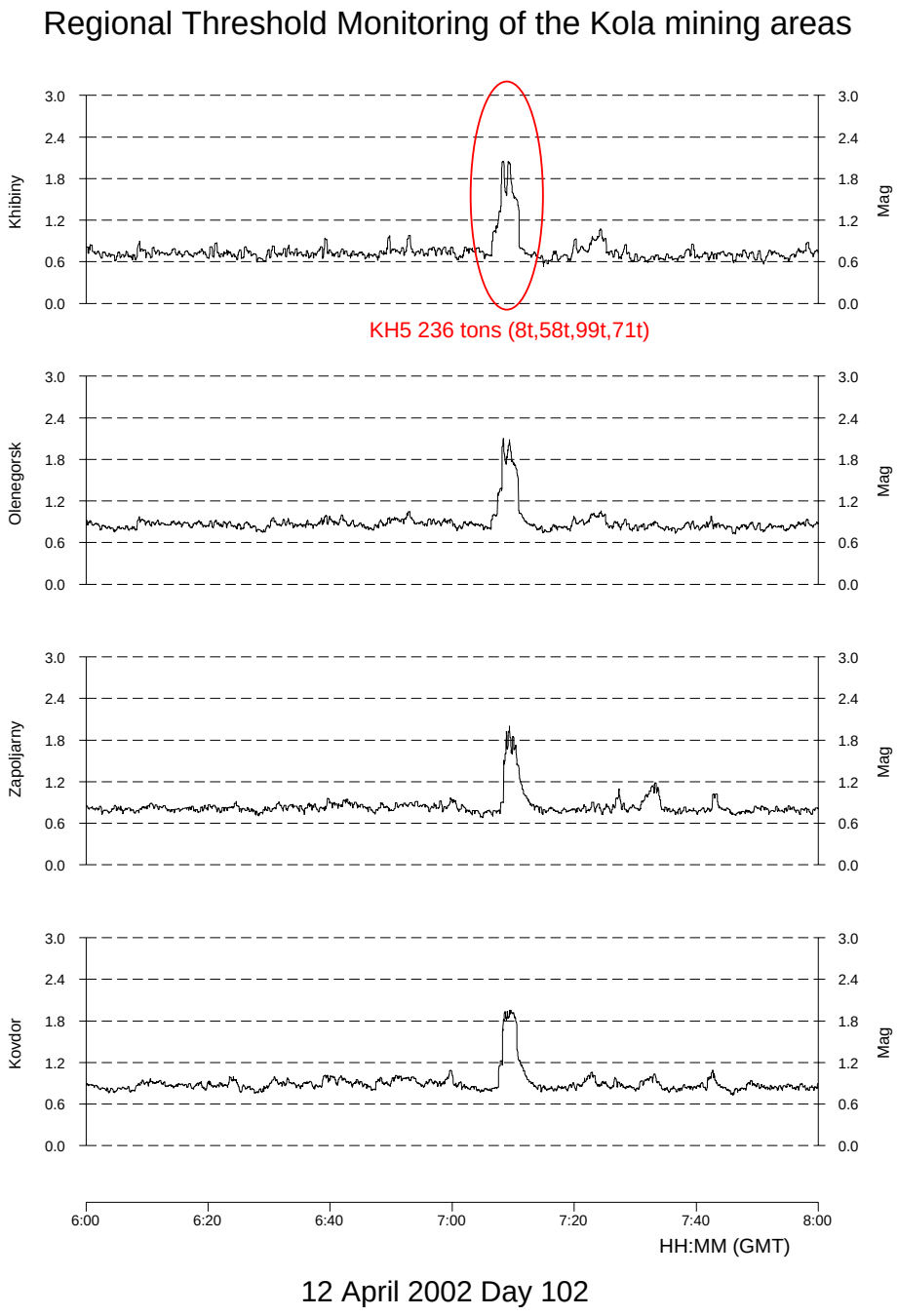


Figure 4. Network magnitude thresholds for the grid points closest to the four mining areas shown in Figure 1, for the 2-hour time interval starting 2002-102:06.00. The threshold peak corresponds to an explosion in the open mine Koashva (KH5) located in the Khibiny area. The total yield of the ripple-fired explosion was reported to be 236 tons, and consisted of 4 smaller explosions with yields of 8, 58, 99 and 71 tons.

Processing example 2

Figures 5-7 show a second example of a threshold plots, similar to the plots shown in Figures 2-4. In this second case, the time interval processed is a two-hour interval starting at 2002-102:10.00, i.e. some hours later during the same day. The mean magnitude thresholds (Figure 5) are almost identical to the mean thresholds for the first interval (Figure 2), which shows that the background noise level is stable. The peak network threshold magnitudes with the mean subtracted (Figure 6) are quite similar to those in Figure 3.

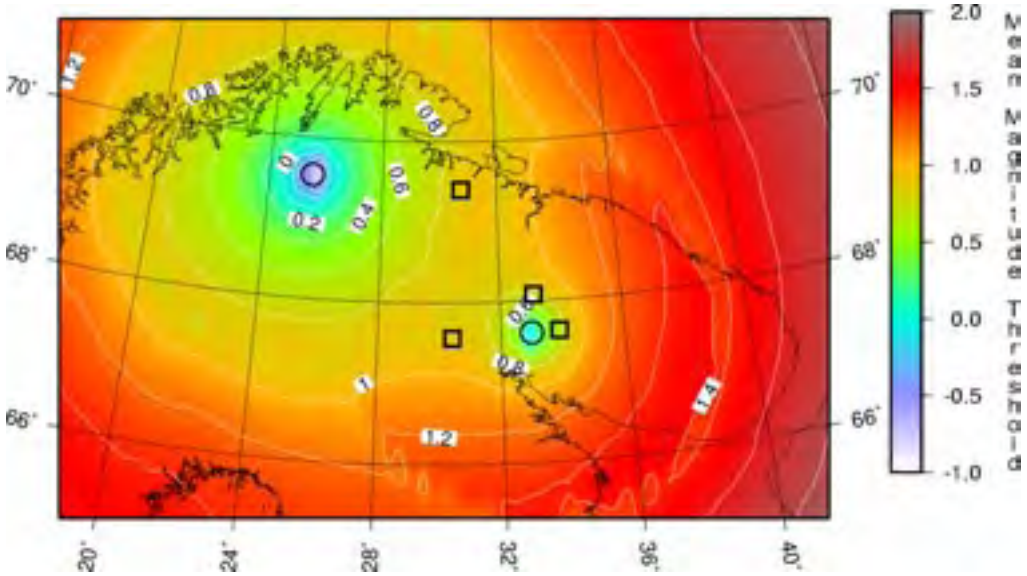


Figure 5. Mean network magnitude thresholds for a 2-hour time interval starting 2002-102:10:00.

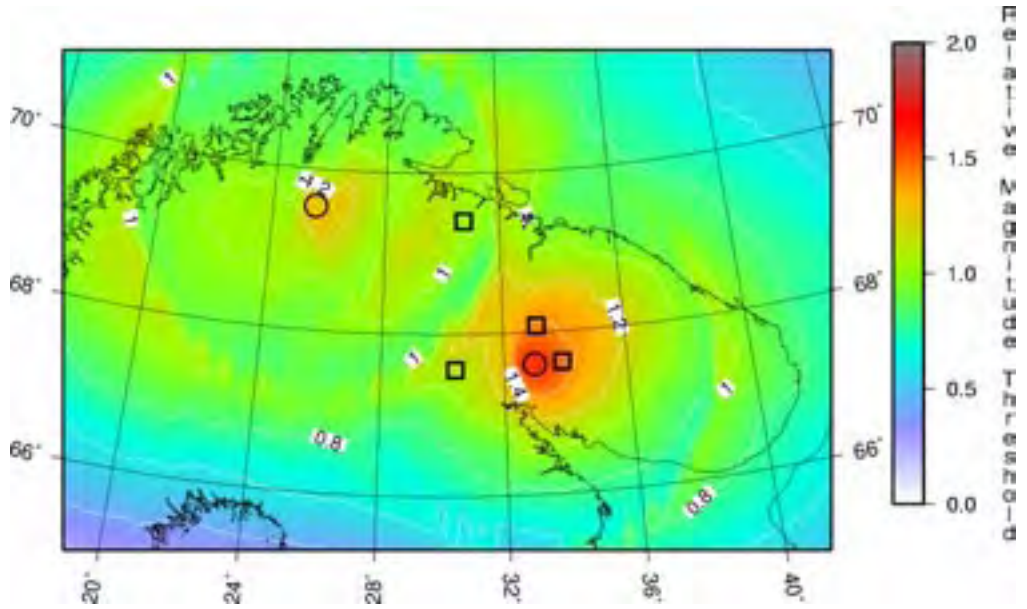


Figure 6. Peak network magnitude thresholds with mean subtracted for the same 2-hour time interval as shown in Figure 5. This essentially shows the height of the highest peak above the background level within the time interval for each grid point. The five events occurring in the region during this time interval create significant threshold peaks in the entire region.

The individual time traces for each of the four mining sites (Figure 7) show a quite significant activity during these two hours, with confirmed mining explosions both at Khibiny, Olenegorsk and Zapolyarnyi. As expected, there is a corresponding threshold increase on all the traces for each mine explosion, but in each case the increase in threshold level is greatest for the actual site of the explosion. There is also an unknown event (perhaps a small earthquake) that is located outside of the mining areas.

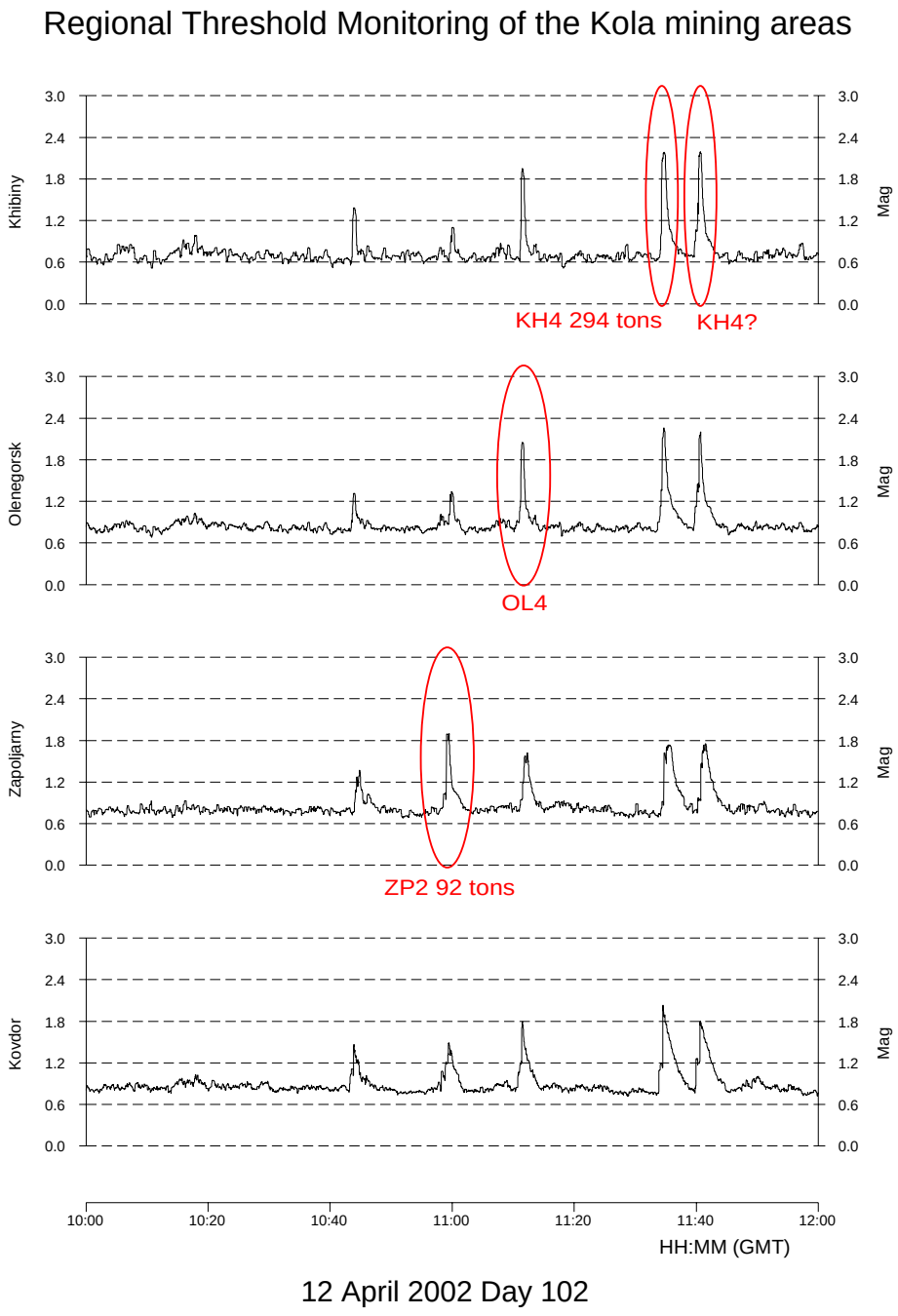


Figure 7. Network magnitude thresholds for the grid points closest to the four mining areas shown in Figure 1, for the 2-hour time interval starting 2002-102:10.00. Five significant threshold peaks are seen during this time interval, of which three are mining explosions reported by the KRSC. The last peak at 11:40 is believed to be an additional explosion at the Central Khibiny mine KH4. The first peak at 10:44 is caused by an event located approximately 70 km south-west of the Apatity array.

Processing a 24 hour interval

Figure 8 shows network magnitude thresholds for the grid points closest to the four mining areas Khibiny, Olenegorsk, Zapoljarny and Kovdor for the entire day 12 April 2002. This is the same day from which the two previous time segments were extracted. During this day 10 events are found which are located in three of these mining areas, of which 6 are confirmed by KRSC. The corresponding mines and threshold peaks are indicated by red arrows.

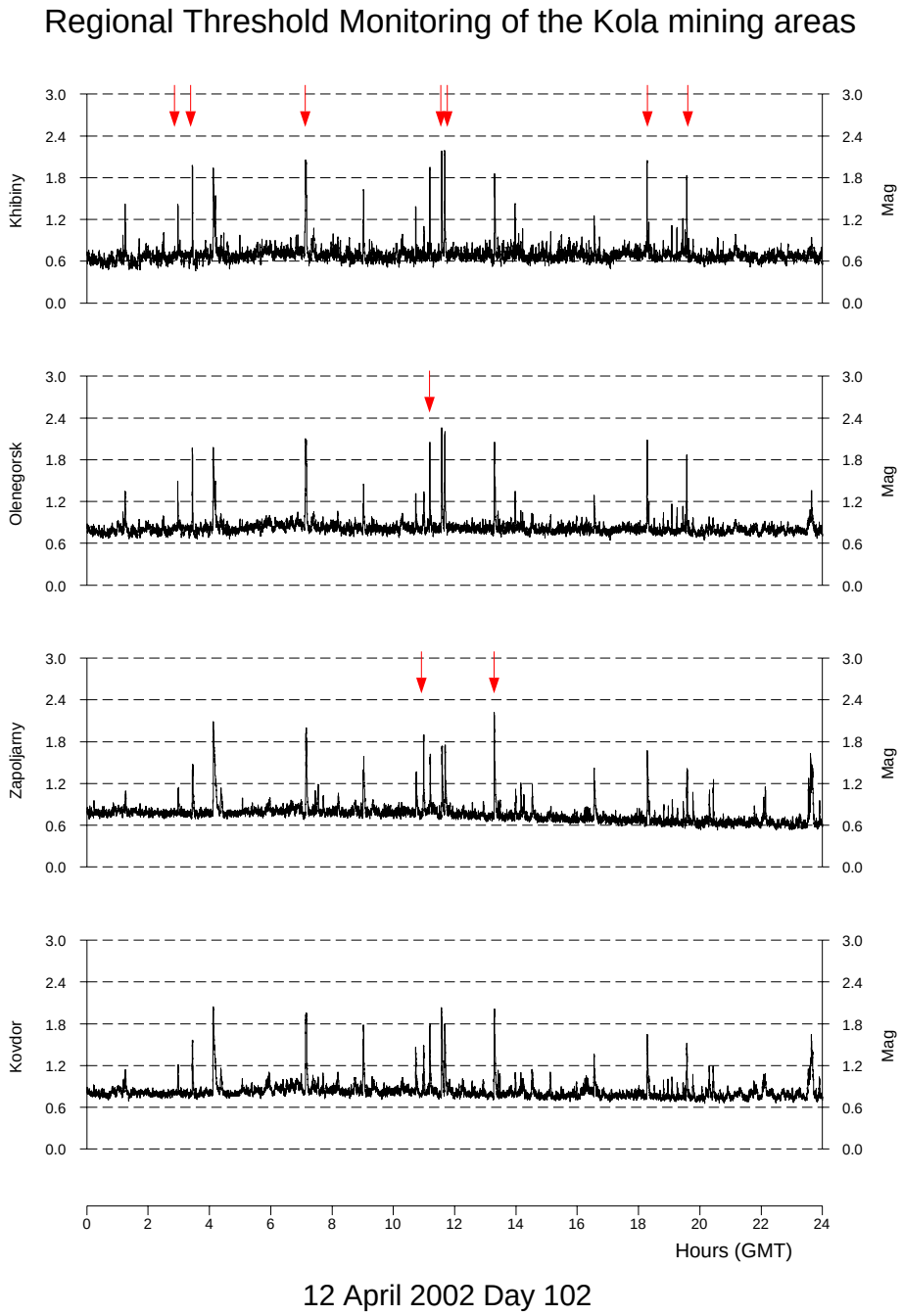


Figure 8. Network magnitude thresholds for the grid points closest to the four mining areas Khibiny, Olenegorsk, Zapoljarny and Kovdor for 12 April 2002. During this day 10 events are found which are located in three of these mining areas, of which 6 are confirmed by KRSC. The corresponding mines and threshold peaks are indicated by (red) arrows.

CONCLUSIONS

This section contains the main conclusions from the work on all the sub-tasks associated with this contract. The results from the Regional Threshold Monitoring of the Kola Peninsula are given at the end of this section.

Regional Database and Attenuation Relations

A database comprising 45 seismic events, selected to provide the best possible ray path coverage of the Barents Sea and adjacent areas, has been compiled and reanalyzed in a consistent manner. This has resulted in new regional attenuation relations for Pn, Sn, Pg and Lg, together with a preferred average velocity model to be used for predicting the travel times of regional phases. We have applied these attenuation relations to develop and assess a regional threshold monitoring scheme for selected subregions of the European Arctic (Hicks et al., in press).

Amplitude inversion has been used in this study to resolve new attenuation coefficients and station corrections for estimating magnitudes from STA amplitude observations for Pn, Pg, Sn and Lg phases in the Barents Sea region. The distance range for observations on which the Pg and Lg relations are based is limited; a future study using a greater number of continental events could most likely provide a relation for STA based Lg magnitudes that is applicable at larger distances, albeit limited to paths within Fennoscandia.

The pattern of Lg arrivals and associated amplitudes supports the previously published indications that the deep sediment basins and Moho topography under the Barents Sea efficiently block Lg wave energy from crossing. From this, it is clear that Pn and Sn are the most useful phases for calculating stable and consistent magnitudes for events in the Barents Sea.

The BAREY model from Schweitzer and Kennett (2002), based on a model for the Barents Sea area from Kremenetskaya et al. (2001), provides the smallest overall travel-time residuals when locating events within the vicinity of the Barents- and Kara Seas.

The seismic station in Amderma can be tied in to the regional network in Fennoscandia and on the Svalbard archipelago using an appropriate crustal model, and is able to provide important information regarding the location of events in the eastern parts of the Barents Sea and the Kara Sea (Schweitzer and Kennett, 2002). Magnitudes calculated at this station are on the whole consistent with the other observations.

The attenuation in the Barents Sea region differs somewhat from that observed in other stable tectonic regions, as evidenced by the fact that the coefficients given by Jenkins et al. (1998) for such regions do not give consistent magnitudes across frequencies, phases and stations for our amplitude observations from the events in the Barents Sea region.

Regional Threshold Monitoring

We have successfully developed a methodology and associated software for regional seismic threshold monitoring, and applied it to distinct regions of different sizes in the Barents Sea, Novaya Zemlya and the Kola Peninsula.

The Kursk accident on 12 August 2000 and subsequent underwater explosions occurring during the fall and winter of 2000 provided an excellent opportunity to test and evaluate the usefulness of the threshold monitoring method. By tuning the processing parameters using the recordings of the Kursk accident, we were able to consistently monitor the numerous underwater explosions in the area around the accident site down to magnitude 1.5. The study demonstrated that the threshold traces steered to the accident site also provided excellent results for the underwater explosions that occurred in a relatively small geographical area (some tens of kilometers across) surrounding the accident site.

An initial grid system with an approximately 100-km grid spacing has been deployed to cover the entire Barents Sea region, and the observations at the arrays, ARCES, SPITS, FINES and NORES have been used for calculating threshold magnitudes for each of the grid points. During an interval without seismic signals, the threshold magnitudes showed large variations over the region, and, in particular, in the vicinity of each array. However, for the region around the island of Novaya Zemlya the variations are modest, varying around a mean of magnitude 2.1-2.2, when using this array network.

In order to investigate in more detail the variations in threshold magnitudes for the Novaya Zemlya region, we have deployed a dense grid with an areal extent of about 500 x 500 km around the former Novaya Zemlya nuclear test site. For each of the grid nodes, we calculated magnitude thresholds for the two-hour time interval 00:00 - 02:00 on 23. February 2002. At 01:21:12.1 there was an event with a magnitude of about 3, located about 100 km northeast of the former nuclear test site.

Regions of different sizes have been constructed by selecting grid points within different radii from the former nuclear test site. Average, minimum and maximum threshold magnitudes have been compared for circular regions with radii of 20, 50, 100 and 200 km, respectively. The most important result is that even for a target region with radius as large as 100 km, the variations in threshold magnitudes are all within 0.2 magnitude units. This applies both for the time interval with the event and for background noise conditions. For the investigated station geometry, it will therefore be meaningful to represent the monitoring threshold of the entire Novaya Zemlya region with the values of a single target point, together with the priori determined uncertainty bounds.

For areas with larger variations in threshold magnitudes, like in the vicinity of the arrays, a 100-km radius target region will obviously show larger differences between the maximum and minimum values. Examples illustrating this point have been shown.

In cases when data from the Amderma station can be retrieved we find significant variations in threshold magnitudes over the island of Novaya Zemlya, ranging from 1.4 at the southern tip to 2.2 at the northern tip during noise conditions. This applies to the time interval immediately preceding the event on 23 February 2002. During this time interval, the monitoring capability for the former nuclear test site is lowered by about 0.3 magnitude units to about 1.9. This implies that a regional threshold monitoring scheme for the NZ region has to be divided into geographical subregions having similar threshold magnitudes during background noise conditions.

Using data from the ARCES and Apatity arrays, we have implemented a regional threshold monitoring scheme focusing on the Kola Peninsula. For the most active mining areas in this region (Khibiny, Olenegorsk, Zapoljarny and Kovdor), the magnitude thresholds during normal noise conditions vary between 0.7 and 1.0 magnitude units. During the studied time interval (12 April 2002), 10 out of 18 peaks exceeding threshold magnitude 1.2 at any of the mining areas were caused by events in the actual mining areas. However, the spatial resolution of the threshold traces when using the ARCES and Apatity arrays is quite low. In fact, each mining event created significant threshold peaks not only for the threshold trace associated with the actual mine, but also for the traces for the other mining areas.

This implies that for a regional threshold monitoring scheme for the Kola Peninsula it will be sufficient to deploy a set of targets for the most active mining areas. When a threshold peak is found at any of these targets, the peaks have to be associated with seismic events as outlined for the Kursk study.

RECOMMENDATIONS

We recommend that the work with amplitude attenuation relations for regional phases in Fennoscandia and adjacent areas be continued and extended to broader regions. The development of consistent regional magnitude scales is an important problem which still is far from a solution, but the results obtained in this study are encouraging.

The software which has been developed for this project should be considered for operational implementation. The necessary procedures and parameters for such implementation are provided in the final report of the project.

The automatic explanation facility for peaks on the threshold traces provided in the final report of the project assumes that a reasonably accurate on-line seismic detection bulletin is available. The joint development of combined threshold monitoring and reliable automatic detection bulletins is a future priority area.

The application of the regional threshold monitoring technique to other regions of monitoring interest should be considered. It would be particularly useful to investigate the benefits of adding local (non-IMS) stations to the IMS Primary and Auxiliary networks in such applications.

REFERENCES

Hicks, E.C., Kv rna, T., Mykkeltveit, S., Schweitzer, J. and Ringdal, F. (in press), Travel-times and attenuation relations for regional phases in the Barents Sea region, Pure and Applied Geophysics, in press.

Jenkins, R.D., T.J. Sereno, and D.A. Brumbaugh (1998), Regional attenuation at PIDC stations and the transportability of the S/P discriminant. AFRL-VS-HA-TR-98-0046, Science Applications International Corporation, San Diego, CA, USA.

Kremenetskaya, E.O. and V.M.Trjapitsin (1995): Induced seismicity in the Khibiny Massif (Kola Peninsula), Pure and Applied Geophysics, 145(1), 29-37.

Kremenetskaya, E., Asming, V., and Ringdal, F. (2001). Seismic location calibration of the European Arctic, Pure Appl. Geophys. 158, 117-128.

Ringdal F., E.Kremenetskaya, V.Asming, I.Kuzmin, S.Evtuhin, V.Kovalenko (1996): Study of the calibration explosion on 29 September 1996 in the Khibiny Massif, Kola Peninsula. Semiannual Technical Summary 1 April - 30 September 1996, NORSAR Sci. Rep. 1-96/97, Kjeller, Norway.

Schweitzer, J., and Kennett, B.L.N. (2002), Comparison of location procedures - the Kara Sea event 16 August 1997, Semiannual Technical Summary, 1 July - 31 December 2001, NORSAR Sci. Rep. 2-2001/2002, Kjeller, Norway, 97-114.

THE CENTRAL ASIA REGIONAL WAVEFORM ANALYSIS KNOWLEDGE BASE

Charles A. Langston, Christy Chiu, Ivan Rabak, and Daejin Kang

University of Memphis

Sponsored by National Nuclear Security Administration
Office of Nonproliferation Research and Engineering
Office of Defense Nuclear Nonproliferation

Contract No. DE-FC04-2002AL68280

ABSTRACT

A knowledge base of event source parameters, earth structure models, regional and teleseismic waveforms, modeling tutorials and regional phase attributes is being constructed that will be accessible using standard web browsers. Teleseismic source models are now being constructed for a catalog of 73 earthquakes larger than a magnitude 5.5 located within central Asia. These teleseismic models constrain event source depth, time function, and source mechanism so that broadband regional and local waveforms can be modeled. Of interest is the nature of broadband, regional seismic wave propagation for predicting relative amplitudes, complexity, and arrival times of major regional seismic phases that propagate within central Asia. Using a variety of regional waveform modeling techniques (e.g., surface wave dispersion and “phase-time” inversion) 1D regional crust and upper mantle models are being developed that predict the observed waveforms. The learned experience in building these models and geophysical parameters derived from the waveform modeling are then incorporated into a knowledge base. The knowledge base can be browsed by seismic analysts who may be interested in learning about wave propagation in a particular region, seismic source characteristics, or attributes of past-observed seismograms that may be used to understand future unknown events. The web system is being constructed using the mySQL database manager as event data and event analyses become available. The final system will consist of a series of web pages, for each event, with text and graphics describing basic data, derived parameters, earth structure models, the modeling process, phase characteristics, etc. In addition, the original binary data and resulting synthetic seismograms will be accessible through a Java application, called kseis, that performs many of the same functions as Lawrence Livermore National Laboratory’s Seismic Analysis Code but is machine-independent.

OBJECTIVES

The overall objectives of this 2-year research program are to:

1) Determine waveform characteristics of earthquakes and explosions over a broad frequency band that can be used to locate and identify small seismic sources in central Asia;

2) Construct a waveform and source parameter database to be used to understand local/regional wave propagation in central Asia and to identify sources;

3) Construct an earth structure database for models of the crust and upper mantle that accurately predicts the waveforms for seismic sources in central Asia;

4) Construct a knowledge base system that links data, data-derived source models, data-derived structure models, and educational tutorials for understanding sources, structure, and wave propagation in central Asia.

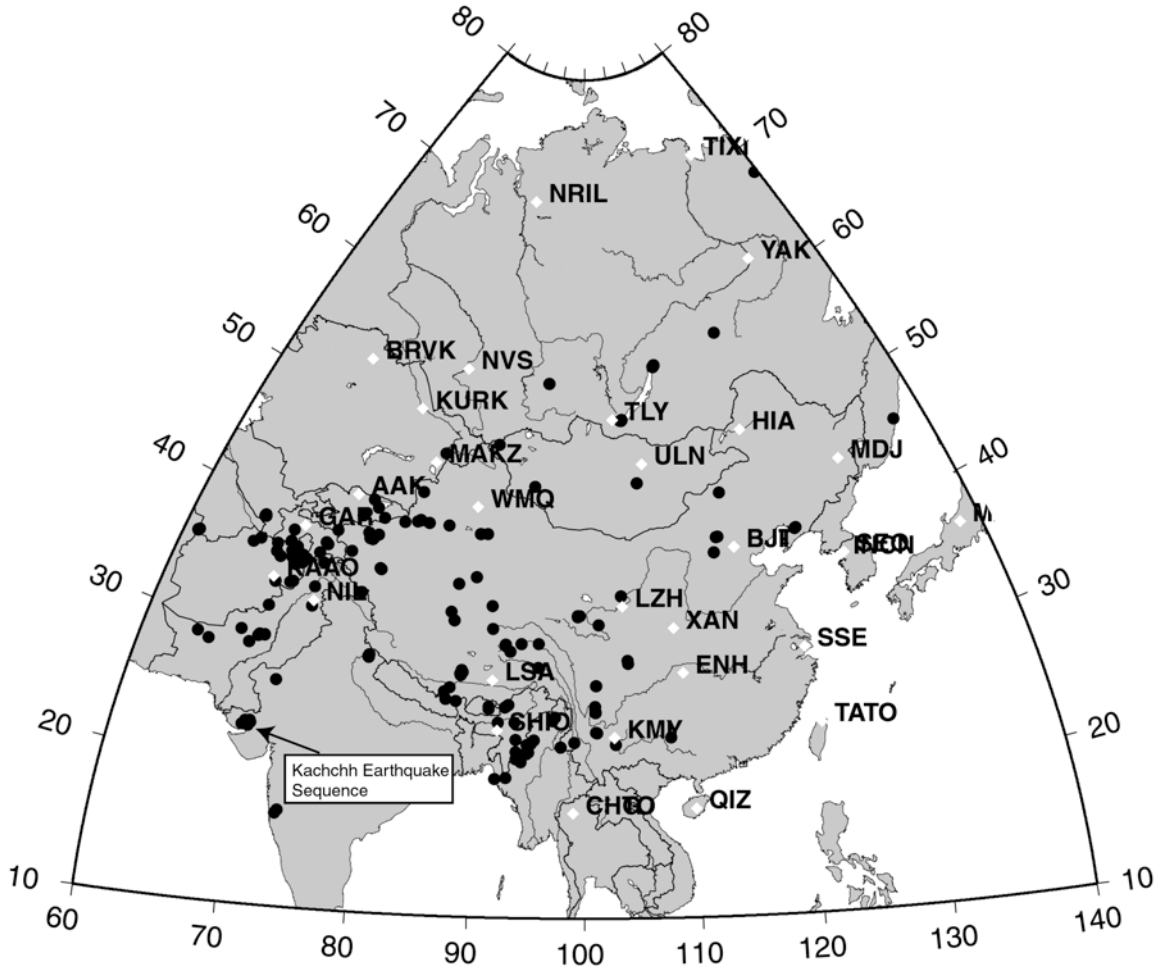


Figure 1. Map of central Asia showing station locations of the GSN and 375 earthquake events of mb greater than 5.0 from 1/01/98 to 6/01/01. The recent Kachchh earthquake sequence is annotated.

RESEARCH ACCOMPLISHED

Introduction

Work on this project can be usefully divided into two parts: “Scientific” and “Knowledge System”.

The “scientific” work involves the collection, processing, and modeling of seismological waveform data for earthquake and explosion sources in central Asia. There are numerous technical issues that must be addressed to obtain accurate source parameters (such as source depth, focal mechanism, moment tensor, and time function) from teleseismic waveforms that can then be used to understand and model regional waveforms. The ultimate scientific product will be a set of one-dimensional (1D) earth structure models that can accurately predict the time and amplitude of major regional phases seen on seismograms from stations in central Asia. These regional models will allow insight on how regional waves propagate and lead to predictive hypotheses of what expected seismograms should look like for future events in the region.

The “knowledge system” work involves the manipulation of event catalog data, map displays, derived source parameters, derived earth structure parameters, graphical displays of data and synthetic seismograms, text-based tutorials, and relational databases in an html format that can be accessed by standard web browsers. In a very real sense, the knowledge system will be an interactive book that incorporates the data, scientific results, and scientific methods used to obtain those results. An interested seismic analyst or student can learn about particular earthquakes, particular regional earth structures, seismological techniques, wave propagation theory, or characteristics of observed seismograms. The knowledge system will integrate the scientific results of the project and be a self-teaching tool for use in the verification environment.

Effort in these two areas have natural separations but ultimately, the structure of the scientific problem defines how the knowledge system is to be constructed. The first year of work was spent in developing the tools for addressing the seismological analysis and also in developing the structure of the web-based “knowledge system”.

Scientific Work Progress

The premises of the seismological study can be examined by considering a single earthquake event. Suppose an event occurs in central Asia, possibly in an area that is under suspicion for possible clandestine nuclear tests. Are there attributes of the regional seismic phases that can be used to determine the depth of the source or whether it is an explosion or an earthquake? Because it is likely that such events will be relatively small and not be observable at teleseismic distances, the only data that may be available will come from regional seismic stations at distances of hundreds to a thousand kilometers from the event. Thus, it is critical to know what regional seismic phases may be useful in estimating the possible source parameters and how those waves propagate in the region of interest. The well-known source/structure duality in seismology comes into play since the only way to infer the seismic source is to know the wave response of the structure.

The problem of regional seismic phase propagation has been around for many years mainly because large distances geographically separate earthquake sources and recording stations. It has been difficult to infer the earth structure wave response since the structure response has been masked by the (usually) unknown source excitation. Earthquake parameters, in particular, have been difficult to obtain since standard location procedures often cannot define source depth accurately enough and because there may be too few stations to infer a focal mechanism solution.

However, recent work with moderate earthquakes has shown that when the accurate source parameters are available, these source parameters may be effectively used to construct synthetic seismograms that accurately match observed regional seismograms. In a recent study of regional waves in Tanzania (Langston et al 2002), it was shown that a very simple crust and mantle structure could explain broadband regional waveforms out to distances of 900 km from the source. The timing of the regional phases yielded strong constraints on the average velocity structure of the crust and mantle and their amplitude and frequency content on the exact nature of the wave propagation. For example, the data showed clear multiple Sn phases associated with multiple S reverberations within the crust. Furthermore, the nature of the velocity gradient inferred in the crust and timing of the multiple S reverberations

yielded a precise understanding into the nature of the Lg phase as high amplitude, high phase velocity turning waves in the crust. The relative timing of other phases, such as sPmP phases yielded estimates of source depth.

The key to understanding regional wave propagation is obtaining accurate source parameters for the regional events. In this research, we are concentrating first on examining moderate earthquakes (M5 and greater) within central Asia because it is possible to constrain source parameters with proven teleseismic body wave modeling techniques. Events of this size can be observed at teleseismic distances so that the source depth can be estimated accurately using the differential travel times of the direct wave and free-surface reflections and source mechanism from the waveform. In addition, the teleseismic P and S waveforms yield an important estimate of the far-field source time function that will be applicable to understanding the regional waveforms.

Using these source-constrained larger events, we will then be able to infer the physical mechanisms of regional wave propagation through analysis with synthetic seismograms as done in our previous African work. Using a variety of events with different source mechanisms and source depths, we expect to be able to characterize the crustal and upper mantle structure for many propagation paths in central Asia. These models will then be used to predict ground motions and model the source characteristics of smaller events in the same region.

During the first year's work, we have constructed several earthquake catalogs for events in central Asia. Shown in Figure 2 is a catalog of 73 events of M5.5 and greater from 1999-2003. Christy Chiu, the CERI seismic analyst working on this project, has produced an automated procedure to request data from all broadband stations within 90 degrees distance of the source that are archived by the Incorporated Research Institutes for Seismology (IRIS) Data Management Center. Data from these 73 events have been obtained and are archived on our SUN Microsystems computer network.

The data are transmitted to the Center for Earthquake Research and Information (CERI) by ftp and undergo a series of processing steps before analysis. A series of UNIX Cshell scripts are used to unpack the waveform data from the SEED volumes, correct individual broadband channels for instrument response (using Lawrence Livermore National Laboratory's (LLNL's) seismic analysis code (SAC)), rename channel files to a less cumbersome name, and rotate the horizontal component data into the theoretical backazimuth to the event to obtain radial and transverse ground motions. Christy Chiu also manually examines the data from each station to determine if a signal exists above the noise or if there are any other anomalous problems with the data. Acceptable data are then copied to separate UNIX file system directories for ground displacements and ground velocities. In addition, the data are segregated into a "teleseismic" directory for teleseismic waveform analysis and a "regional" directory for regional/local waveform analysis.

Once that data have been quality-checked and processed, a standard CSS3.0 schema database is built using the IRIS Datascope seismic database package. This software builds "flat" database files (simple ASCII files) that are incorporated into further seismic processing and modeling. Further processing for teleseismic waveform modeling includes calculating P and S wave arrival times and placing a marker into each waveform file for the particular arrival time. This is done using a short script and incorporates recent Java-based software provided by the University of South Carolina (the "TauP" travel-time package). The teleseismic P and S waveforms are then windowed from the three component data and modeled to determine the source depth, focal mechanism, moment tensor, and time function. Synthetic seismograms are computed using a Thompson-Haskell formulation for a point source in plane-layered media that incorporates teleseismic geometrical spreading for an appropriate whole-earth model, such as IASPEI91, and separate three-component receiver functions for each receiver.

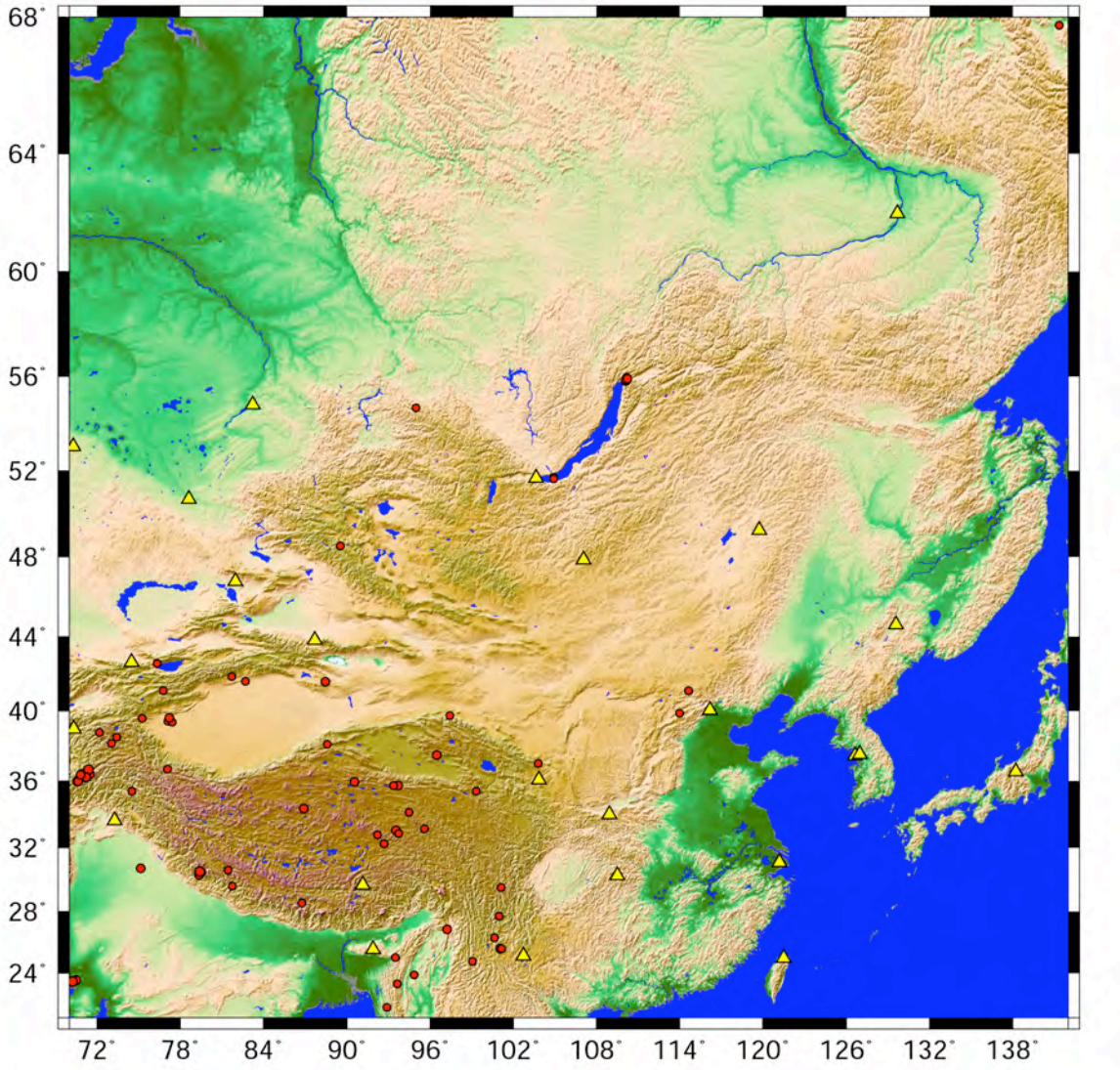


Figure 2. Map of central Asia showing the epicenters of 73 events of M5.5 or greater. The catalog search was for the time interval of 1/01/1999 to 5/31/2003.

Each of the events has 1 to approximately 10 stations that record the event within a regional or local distance. An examination of a few of these broadband waveforms shows that the regional wave propagation in much of central Asia seems similar to propagation in the Tanzanian craton. There are distinct, clear regional phases, such as PnL, Sn, and S multiples along with well dispersed surface waves for the shallow events. The surface waves afford a straightforward probe into average crustal structure through analysis and inversion of group velocity dispersion. The clear regional phases lend themselves to the newly developed "phase time" inversion where a simply-parameterized structure model is used to model the times and amplitudes of observed seismic phases through computation of accurate wave number synthetic seismograms.

Knowledge System Work Progress

Perhaps one of the most challenging parts of this project is the construction of the knowledge system that will bring the scientific results together into a unified framework. This system will ultimately consist of databases of source parameters, structure models, interactive graphical displays, and tutorials linked together in html format that can be accessed with common web browsers. In addition to the series of web pages there will be a facility where the

broadband data and synthetics can be accessed through a Java program called “kseis” so that simple seismic analysis functions can be performed on the archived data independent of the type of computer used.

Work on the web page system has progressed such that we have solved the technical problems of linking diverse databases, text, and graphical objects. At the start of this project two of CERI’s web designers, Kathy Tucker and Tanya Broadbent, suggested design ideas and web site structure. However, in January 2003, Ivan Rabak, a recent CERI master’s graduate, joined the project half time to do the necessary programming to implement the system. His solution consists of using the openly available mySQL database management software with associated tools to create GUI’s and scripts to incorporate seismic database results into the web page format.

The input and results of the scientific work will consist of

(1) event catalogs (location, date, origin time, and magnitude)
(2) station catalogs (location, and info)
(3) event source parameters (source depth, time function, mechanism, and errors)
(4) teleseismic event data and synthetic wave form graphics
(5) regional wave form data and synthetics graphics
(6) crustal and upper mantle structure models, tabular data, and graphics
(7) text tutorials (with graphics) on source modeling, structure modeling, and seismic phase results

The basic entry to the web system will be map based. Earthquake locations, station locations, and regional path results will be accessible, among other links, from a clickable base map. For example, Figure 3 shows the current rendition of the source map where each earthquake source can be accessed by the cursor and the source catalog data shown in a scroll box below the map. Buttons are available to zoom into the high resolution GTOPO5 map to pick an event epicenter. Each source point on the map and each entry in the catalog table are linked to other web pages that describe source modeling results. A similar page is available to describe seismic stations (represented as *yellow* triangles). Paths between sources and regional receivers will also be shown for individual regional sources. Clicking on a path will bring up the pertinent information on earth structure and regional waveform modeling that went into that path structure.

The database management software allows all and any of the data to be accessed either directly, as in the table example, or as links to other files, html documents, or graphic images. Currently we are incorporating the flat database files from the CSS3.0 database schema used in Datascope into the mySQL database manager through appropriate scripts so that the event results can be automatically converted into html format and a set of event web pages.

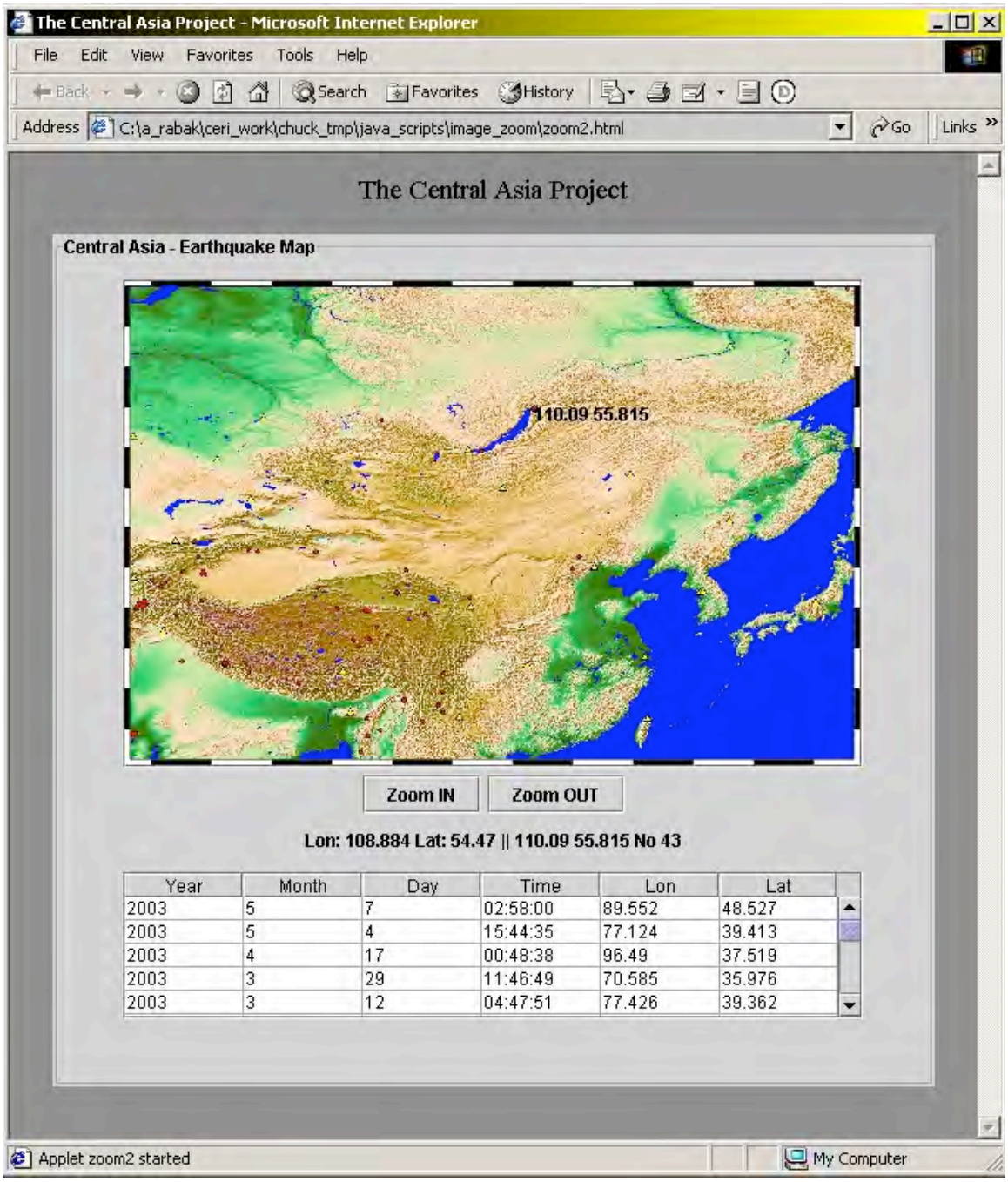


Figure 3. Example of the map interface used for accessing regional seismic sources.

Kseis Java Program

Daejin Kang has written a universal seismic data viewer that will be incorporated into the final knowledge system. This program, named "kseis", is written in Java and can be run on any machine with Java installed. This program can access SAC (LLNL seismic analysis code) binary file seismic data in either little endian or big endian byte format, display the data in a window, and perform various amplitude scaling, time picking, filtering operations, and particle motion analyses through button menus. Figure 4 shows an example of a PC-Linux system screen capture of the kseis waveform and seismogram information window. Shown are three components of broadband data, from the TIXI station in northern Siberia, from a central Asian event. The data waveforms can be examined by choosing a

box around any phase to zoom in or out. Buttons along the top can be pushed to increase or decrease amplitude, move the seismograms in time, or expand/compress the time scale. Simple filtering operations, time differentiation, and time integration may also be chosen and there is a facility for removing instrument responses.

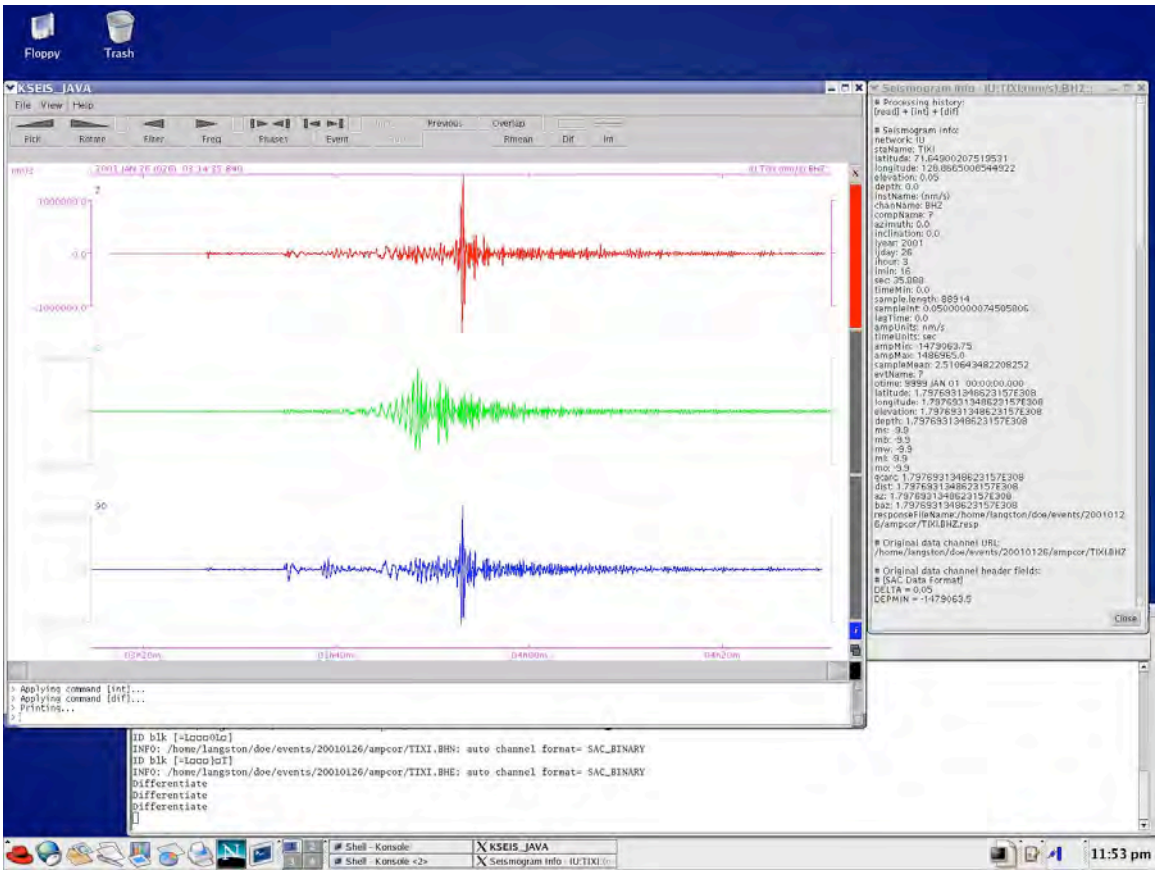


Figure 4. Screen capture jpeg showing the kseis seismogram analysis window and a pop-up window with the seismogram header information.

Figure 5 shows the particle motion plot where a perspective view is given for the three-component particle motion. The mouse can move this view for other perspectives, and time windows can be chosen for any sections of the seismogram. There is also a "movie" facility showing how a particle moves along the trajectory in time.

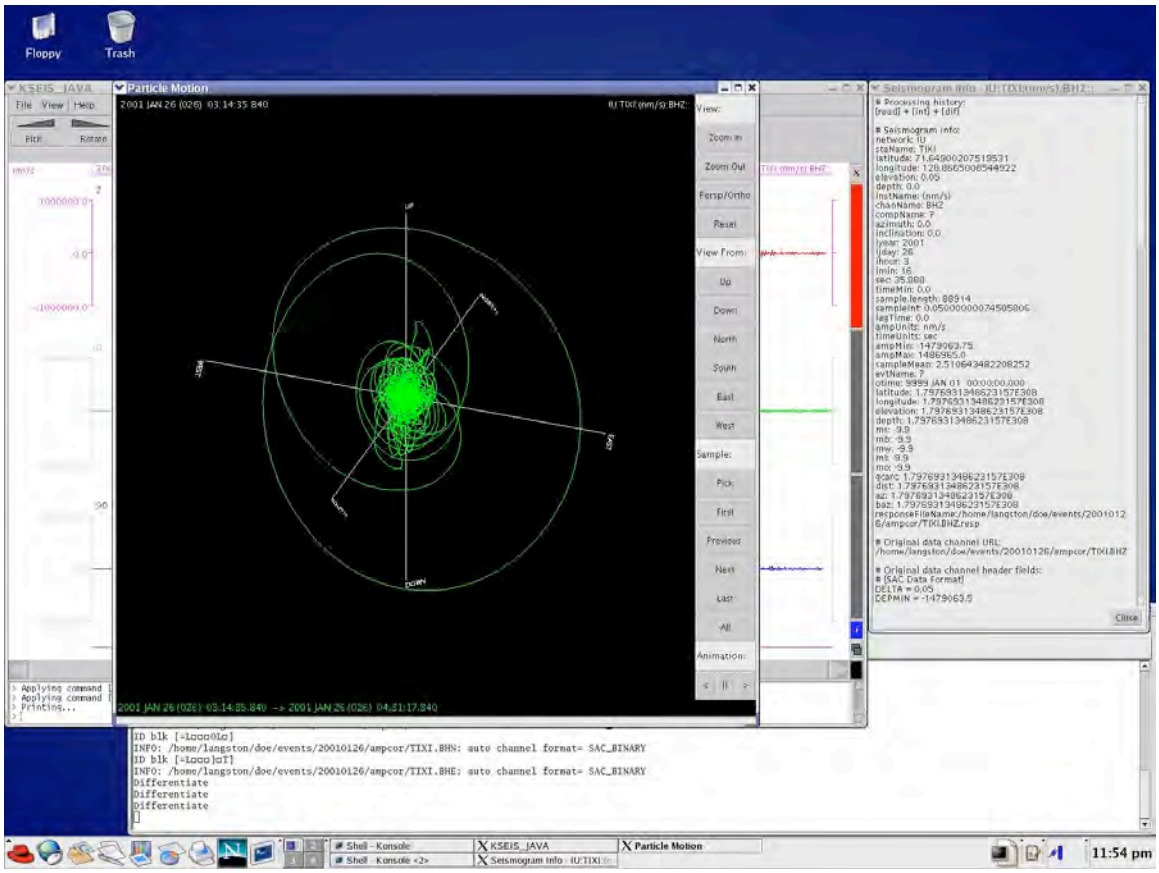


Figure 5. Screen capture showing the particle motion function in kseis.

Kseis is a natural utility to include with the knowledge base system for seismic analysts who want to examine the original seismogram data or any processed data or synthetic waveform. It is our intention to make the original waveform data available through the knowledge system with the kseis interface.

CONCLUSIONS AND RECOMMENDATIONS

Melding of scientific results and web-page presentation style should produce a useful research and information tool for the seismic analyst to use in understanding seismic sources in central Asia.

REFERENCE

Langston, C. A., A. A. Nyblade, and T. J. Owens (2002), Regional wave propagation in Tanzania, East Africa, *Jour. Geophys. Jour. Res.*, 107.

MATSEIS AND THE GNEM R&E REGIONAL SEISMIC ANALYSIS TOOLS

B. John Merchant, Eric P. Chael, Darren Hart, and Christopher J. Young

Sandia National Laboratories

Sponsored by National Nuclear Security Administration
Office of Nonproliferation Research and Engineering
Office of Defense Nuclear Nonproliferation

Contract No. DE-AC04-94AL85000

ABSTRACT

To improve the nuclear event monitoring capability of the United States (US), the National Nuclear Security Administration (NNSA) Ground-based Nuclear Explosion Monitoring Research & Engineering (GNEM R&E) program has been developing a collection of products known as the Knowledge Base (KB). Though much of the focus for the KB has been on the development of calibration data, we have also developed numerous software tools for various purposes. The Matlab-based MatSeis package and the associated suite of regional seismic analysis tools were developed to aid in the testing and evaluation of some Knowledge Base products for which existing applications were either not available or ill-suited. This presentation will highlight new features in this year's versions of MatSeis and the regional analysis tools.

New MatSeis features include: support for the United States National Data Center (USNDC) 2003 database schema, backwards compatibility with the previous database schema, a full-featured locator written entirely in Matlab code (compiled libraries not required), an interface to LocOO (a new Object-Oriented locator written in C++), communication with KBNavigator (a new Knowledge Base GIS application), and an updated user's manual with expanded feature descriptions and tutorials.

The Regional Seismic Tools include CodaMag Tool, EventID Tool, PhaseMatch Tool, and Dendro Tool. New CodaMag Tool features include: more informative output records and the use of kriged correction surfaces. New EventID Tool features include: a plot of Ms vs m_b and processing parameters obtained from the database. New PhaseMatch Tool features include an interface to display a dispersion curve for any desired path. New Dendro Tool features include: expanded capabilities to automatically add/re-pick arrivals based on the picked arrivals for similar events; integrated use of Measure Tool to manually adjust arrival times; expanded multi-window processing parameters (filter banks, different sized windows and filters); and Principle Component Analysis/Factor Analysis capabilities.

OBJECTIVE

MatSeis continues to provide an excellent prototyping environment in which promising seismic analysis techniques can be implemented and evaluated quickly and with relatively little effort. Sandia has used the package to build a set of prototypes for various regional analysis tasks: PhaseMatch Tool for phase match filtering, CodaMag Tool for regional magnitude calculations, EventID Tool for phase ratio discrimination, and Dendro Tool for event clustering using waveform correlation. These products are now all fairly mature, but development on them continues in response to the research results from our co-workers at LANL and LLNL and to feedback from our users at AFTAC. In addition to the changes to the tools, we also continue to make changes to MatSeis itself, particularly in fixing bugs and adding in missing basic features.

RESEARCH ACCOMPLISHED

The following sections describe the latest versions (1.7) of MatSeis, and the four regional seismic analysis tools. The important new features are highlighted for each.

MatSeis

The main MatSeis graphical window is a standard time vs. epicentral distance plot that can display waveforms, arrivals, origins, and travel time curves. The user can interact with this display by clicking directly on the displayed objects, by using the buttons along the bottom, by using the menus along the top, or by typing commands at the Matlab prompt. MatSeis is predominantly written as Matlab m-file functions, which are organized in a set of directories according to the general purpose of each. However, the package also includes a set of compiled C functions linked to the m-files via the Matlab cmex utility. Typically the C functions are introduced where performance of an m-file is too slow (e.g. FK calculations).

Data IO

MatSeis can read US NDC format data from either an Oracle database, or flatfiles. Output is restricted to flatfiles only. The number of tables used by MatSeis has steadily expanded and now includes: *affiliation, amplitude, arrival, assoc, event, instrument, nextid, netmag, network, origerr, origin, remark, sensor, site, sitechan, stamag, wfdisc,* and *wftag*. In Version 1.7, flatfile data reads have been greatly sped up, making it practical to work with larger data sets than has been the case in the past. In order to allow the user to better control the data read into MatSeis, Version 1.7 has an extensive set of filters for both origins (*lat, lon, magnitude, etype, auth*) and arrivals (*sta, chan, phase, auth, orid*). These filters have been expanded to support querying for lists of several parameters (i.e. multiple station names). In the origin read popup, *evid* is now displayed, which makes it more convenient to work with multiple origins for the same event. The origins across the top of the main MatSeis window are now displayed with both *orid* and *evid*.

Location

MatSeis-1.7 includes two new options for performing locations. The first option is a fully-featured locator written entirely in Matlab (Figure 1). The advantage of this new locator is that there are no binaries to compile or proprietary libraries to reference. So, this locator will be able to run on any platform that is supported by Matlab.

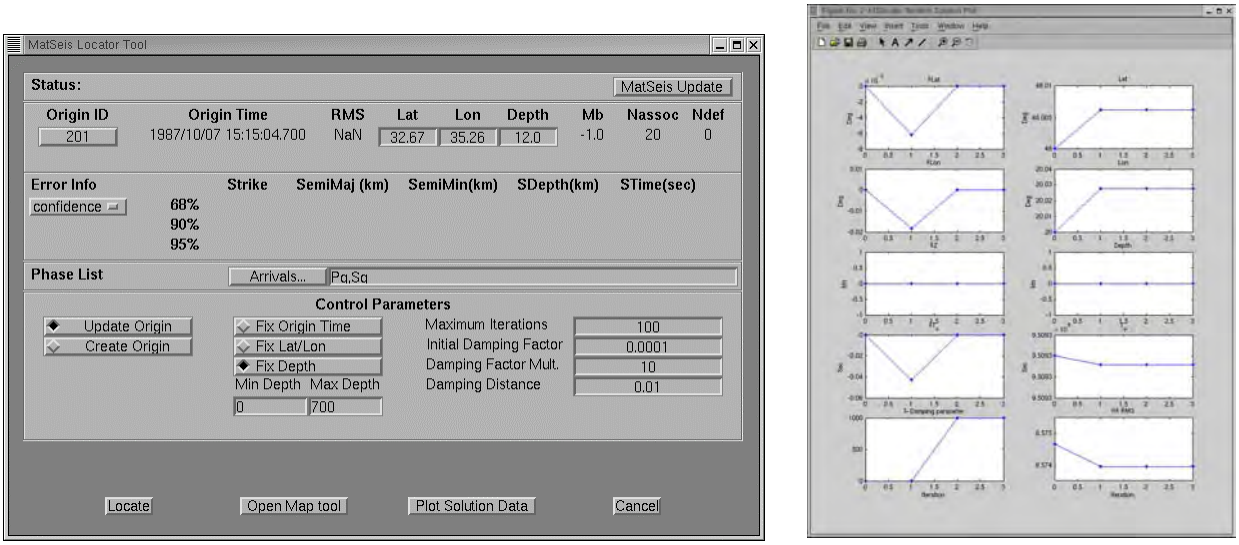


Figure 1. The MatSeis Locator (left) is written entirely in Matlab. The iterative solution data is also shown (right).

The second new locator option (not included in the standard release) is a MatSeis interface to LocOO (Figure 2). LocOO is an extensible Object Oriented locator written in C++ that provides the capability for developers to add their own solvers (Ballard, 2002). The interface allows the user to review and edit various control parameters, locate the event, and then review the results.

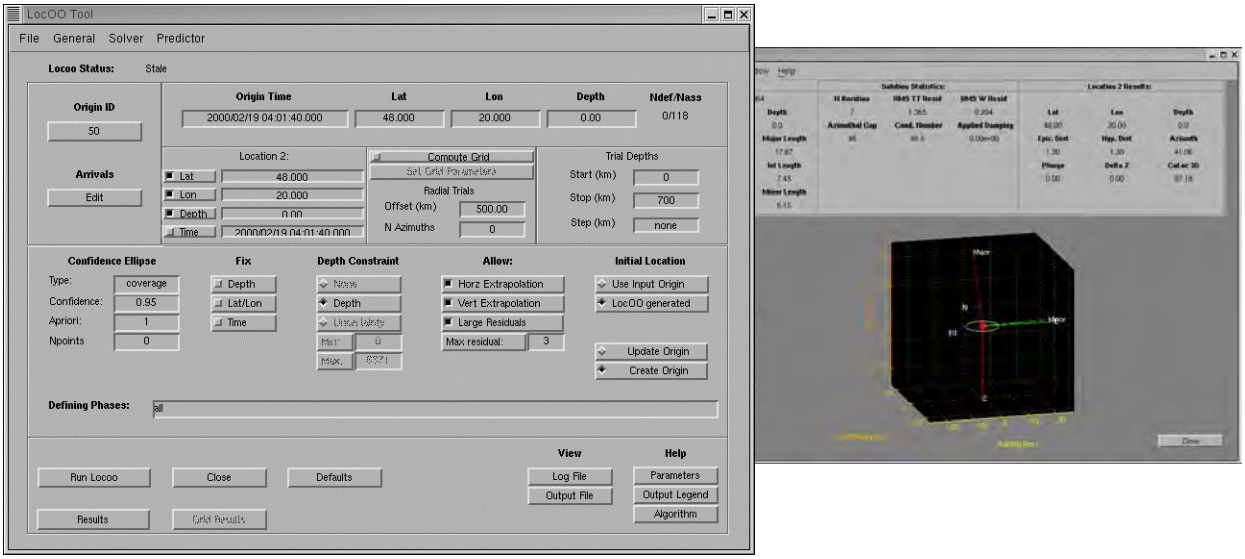


Figure 2. The MatSeis interface to LocOO (left) and the 3D location results (right).

In addition to graphical controls for the various parameters needed to run LocOO, the interface also provides innovative graphical presentations of the solution location and the calculated uncertainties which can aid in interpreting the event.

Regional Seismic Analysis Tools

Phase Match Tool

PhaseMatch Tool is a waveform analysis interface launched from MatSeis that allows the user to calculate the predicted surface wave dispersion for a given source to receiver path by ray tracing through a model, and then use the model dispersion to generate and apply a matched filter (Herrin and Goforth, 1977). The tool allows the user to view the observed waveform, the model dispersion, the predicted waveform, the cross-correlation of the predicted and observed waveforms, and the match-filtered waveform. The user can control the frequency range of the model dispersion used, as well as the time limit of the portion of the cross-correlated waveform from which the match-filtered waveform is taken. Once a satisfactory filtering has been achieved, the user can send either the observed waveform or the filtered waveform to Measure Tool to measure surface wave amplitudes, which can then be used to determine event magnitude.

The new feature for Version 1.7 is an option to display a dispersion curve for any desired path by entering the start and end points of the path (Figure 3).

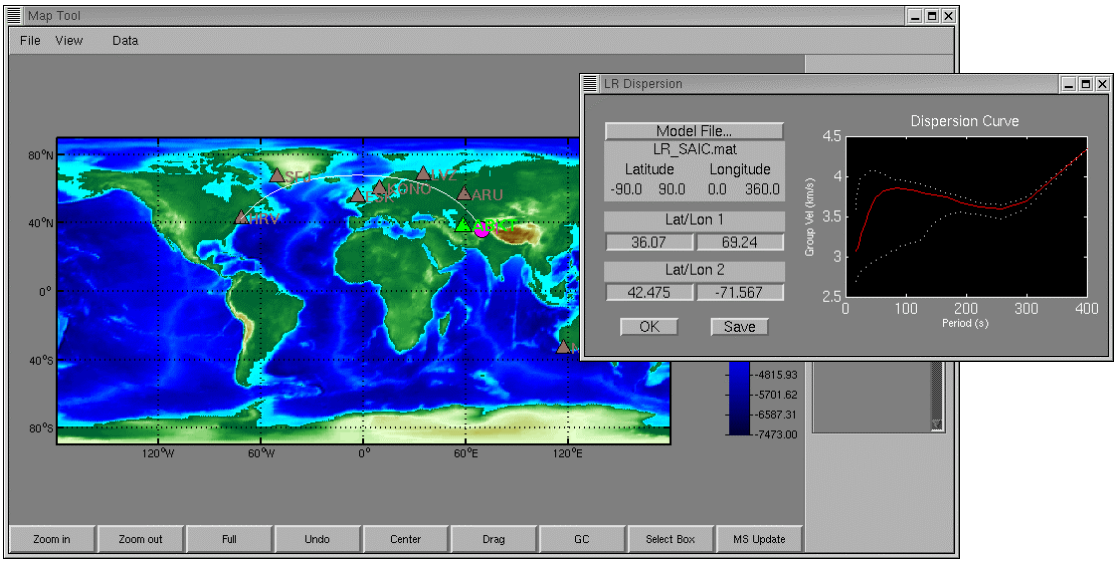


Figure 3. Phase Match Tool now allows the user to compute a dispersion curve for any path.

Coda Magnitude Tool

CodaMag Tool is a waveform analysis interface launched from MatSeis that allows the user to calculate magnitudes and source spectra for an event of interest by fitting empirical decay functions to narrow-band coda envelopes of a given phase (currently Lg). The technique was developed by Mayeda and has been described in detail in several papers (Mayeda, 1993; Mayeda and Walter, 1996; Mayeda, et al., 1999). The tool consists of two displays. The main one shows the calculated moment spectrum and the derived magnitudes. The second display shows how the spectrum was derived. The user can adjust the Lg arrival window, examine the fit between the observed and synthetic envelopes, and control which frequency bands are used for the magnitude calculations. The various required parameters (frequency bands, groups velocity windows, decay curves, etc.) are read from parameter files unique to each station.

Important new features in Version 1.7 include more informative output data records and the ability to make use of kriged correction surfaces.

Event Identification Tool

EventID Tool is a waveform analysis interface launched from MatSeis that allows the user to identify an event of interest (i.e. explosion or earthquake) using spectral ratios of standard regional arrivals (see Hartse et al., 1997; Walter et al., 1999). The tool consists of three displays. The main display plots the phase ratio for the current event against a backdrop of the same ratio for archived events that have already been identified. The user can choose different phases and/or frequency bands to ratio to try to improve the separation of the earthquake and explosion

populations, and the display will immediately update. A second display shows the user a plot of an "MDACogram" (i.e. the MDAC corrected measurements at all of the phase/frequency combinations) for the current event along with all of the archived events. This can be useful in deciding which ratio will yield the best separation. If there are questions about the amplitude measurements themselves, a third display can be brought up, and the user can easily examine group velocity windows for the phases and change them if necessary. If they are changed, the measurements will automatically be re-made and the ratios updated in the main display.

Version 1.7 has several new features including a plot of Ms vs m_b and storage of the processing parameters within a custom database table.

Dendrogram Tool

Dendro Tool provides a tool to perform waveform correlation-based cluster analysis techniques on seismic data. The purpose of Dendro Tool is quite simple: to allow a user to quickly and efficiently determine whether a waveform of interest matches any in the available archives. By arranging the correlations in a hierarchical dendrogram, rather than just determining the most similar waveform, the user gets a much more complete picture of how the current event fits with the archived events. For example, in regions with repeated mining explosions, the mines are often easily identified as distinct clusters, and new mining events can be readily identified as such by association with those clusters.

Dendro Tool consists of many interfaces to help the user assess the effectiveness of the clustering and to use the clusters to identify the events. The main display shows the dendrogram (Figure 4), along with a set of metrics that can be used to determine the correlation level to use to identify the families of events. Once a level has been chosen, the families are assigned separate, distinct colors to make them easier to see. Parameters controlling filtering and windowing of the waveforms, the method used to build the dendrogram, etc. can be set using another display, and the dendrogram will then be updated. The color-coded waveforms for any or all of the families in the dendrogram display can be sent to a variety of tools for further analysis: Free Plot for displaying waveforms, Map Tool for event locations, histograms for time analysis.

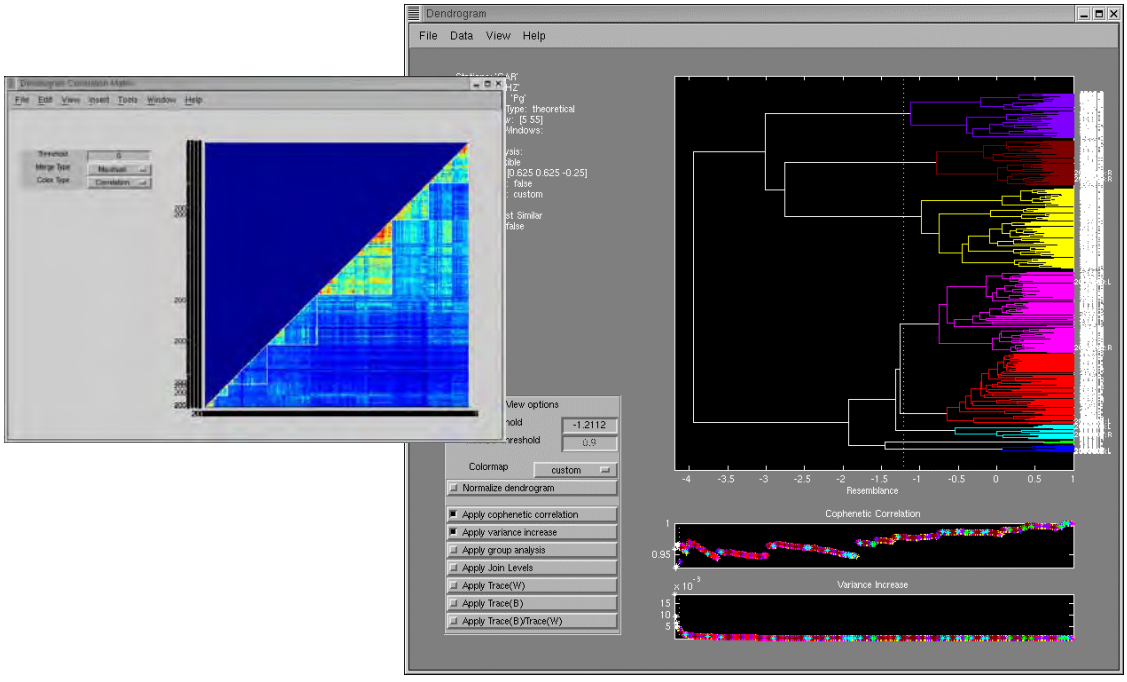


Figure 4. The Dendrogram Tool (right) employs hierarchical cluster analysis to group similar waveforms. The correlation matrix (left) can be displayed to help validate the relationships defined in the dendrogram.

Dendro Tool can form dendrograms based on a single-phase window for a single station, or the user can choose to use multiple windows and/or multiple stations. The method of combining the multiple correlations (minimum, maximum, mean, median) is user controlled.

The significant new features for Version 1.7 are related to verifying the families, and using the families to automate the task of re-timing arrivals. To verify the families, we provide a plot of the correlation matrix from which the dendrogram was derived (Figure 4). The ordering of the events is the same as in the dendrogram, so one can easily evaluate from this plot the strength of the intracorrelations within groups and the intercorrelations between groups. Factor Analysis provides another method to evaluate the families assigned from the dendrogram (Figure 5). The eigen-vectors of the correlation matrix are computed to consolidate the observed variance in the correlations in as few dimensions as possible. The resulting coordinates from the eigen-vector decomposition are then displayed in a scatter plot, with the events having the same color-coding as in the dendrogram.

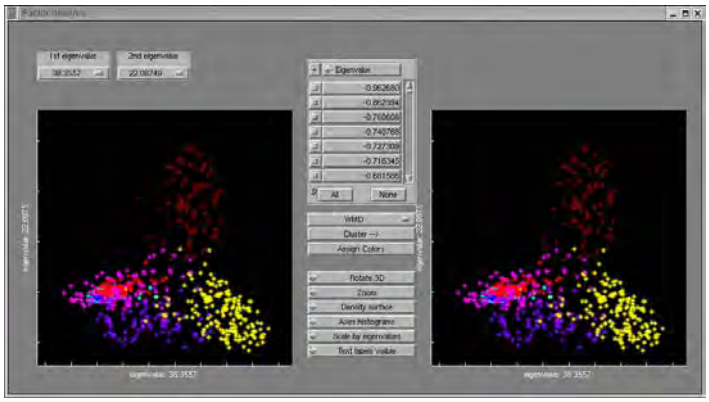


Figure 5. The Factor Analysis figure displays a color-coded scatter plot of the events from the Dendrogram Tool.

For re-timing arrivals, the solution method has been improved to compute the least-squared solution for a group of waveforms (Rowe et al, 2002). Also, the re-timing interface has been integrated with Measure Tool to allow for easy adjustments to the reference arrivals (Figure 6).

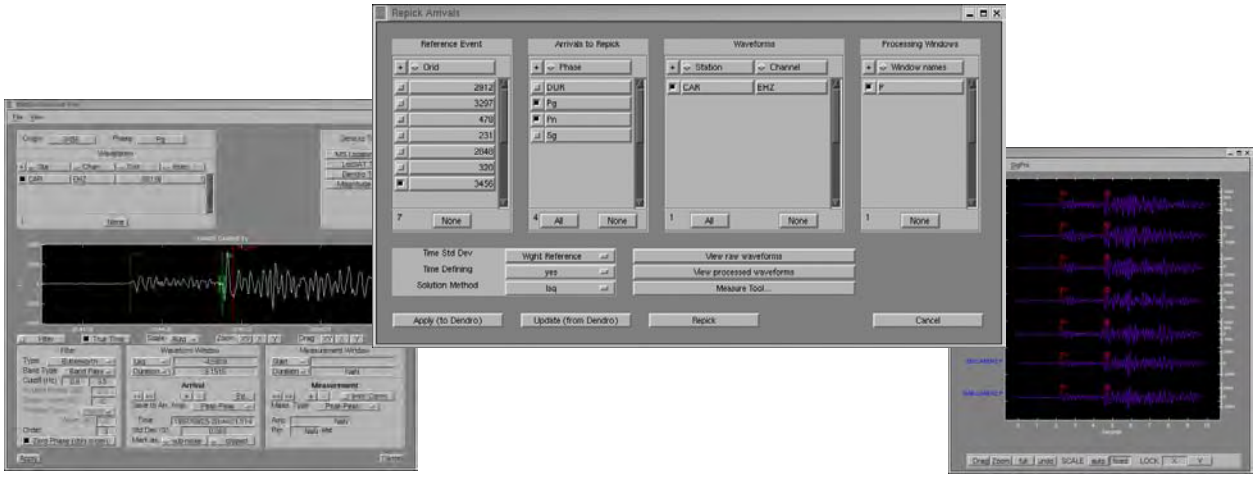


Figure 6. The Dendrogram Repicking interface (center) allows the user to control the operation of the repicking process, provides integration with Measure Tool (left) to manually adjust the arrival timing for the reference waveform, and can display the waveforms and their arrivals in Freeplot (right).

With the new interface, the user can quickly review the waveforms from a given family to choose a reference, decide which phase(s) to re-time, choose which events to include in the re-timing, execute the process, and review the results. The waveform processing parameters have been generalized to allow for greater control over how the processing windows are computed (Figure 7). These generalized parameters will allow analysis techniques such as multiple processing windows with different lengths or filter banks to analyze a variety of frequency bands.

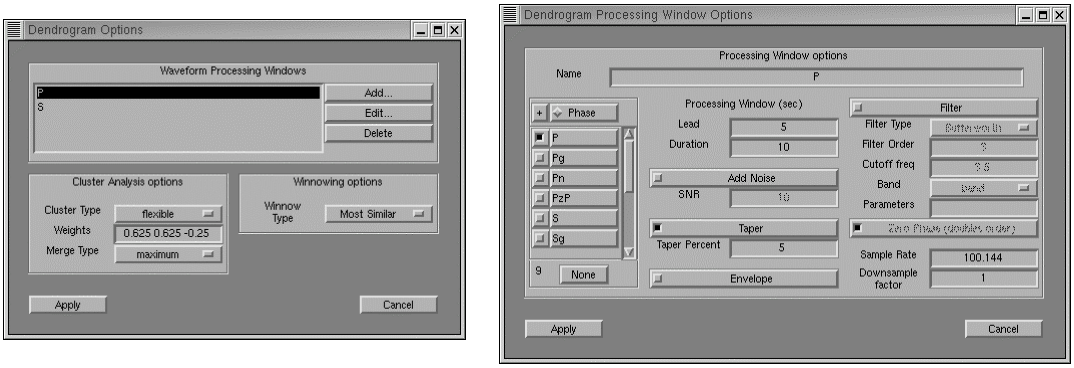


Figure 7. The Dendrogram Tool can provide any number of processing windows (left). Each processing window can be defined independently of any other processing window (right).

CONCLUSIONS AND RECOMMENDATIONS

In this paper, we have highlighted some of the more significant changes from the past year to MatSeis and the MatSeis-based regional seismic analysis tools -- Phase Match Tool, Codamag Tool, EventID Tool, and Dendro Tool. These tools will continue to evolve in response to user needs. We also recognize that there are still many other useful research algorithms that could be used by AFTAC, and we will look for good candidates to add into the MatSeis tool suite. We believe that MatSeis continues to offer one of the best, if not the best, platforms to prototype analysis tools.

The official 1.7 version of the basic MatSeis package is available to all from the GNEM R&E web site: https://www.nemre.nnsa.doe.gov/cgi-bin/prod/nemre/matseis.cgi

Matlab and the Signal Processing Toolbox are required to run MatSeis. Version 6.0 of Matlab or later is required. MatSeis will run on Sun workstations, Windows PC's, and Linux PC's. It should run on other supported Matlab platforms as well, but the C code will need to be re-compiled.

Some of the regional seismic analysis tools may be available to researchers for event monitoring research. Requests should be made though the AFRL/NNSA contracting officer to the NNSA sponsor.

ACKNOWLEDGEMENTS

We thank all of the MatSeis users who have helped us to debug and improve the software, particularly our colleagues at LANL and LLNL.

REFERENCES

Ballard, Sanford (2002). Seismic Event Location Using Levenberg-Marquardt Least Squares Inversion, *SNL Report SAND2002-3083*.

Everitt, B. S. (2001). Cluster analysis, Arnold, London.

Hartse, H. E., Taylor, S. R., Phillips, W. S., and G. E. Randall (1997). A preliminary study of regional seismic discrimination in central Asia with emphasis on western China, *Bull. Seism. Soc. Am.*, 87, 551-568.

Herrin, E. and T. Goforth (1977). Phase-matched filters: application to the study of rayleigh waves, *Bull. Seism. Soc. Am.*, 67, 1259-1275.

Mayeda, K. (1993). Mb(LgCoda): a stable single station estimator of magnitude, *Bull. Seism. Soc. Am*., 83, 851-861.

Mayeda, K. and W. R. Walter (1996). Moment, energy, stress drop, and source spectra of western United States earthquakes from regional coda envelopes, *J. Geophys. Res.*, 101, 11,195-11,208.

Mayeda, K., R. Hofstetter, A. J. Rodgers and W. R. Walter (1999). Applying coda envelope measurements to local and regional waveforms for stable estimates of magnitude, source spectra, and energy, *21st Annual Seismic Research Symposium on Monitoring a CTBT*, Vol I, 527-533.

Ringdal, F. (1976). Maximum-likelihood estimation of seismic magnitude, *Bull. Seism. Soc. Am*., 66, 789-802.

Rowe, C. A., R.C. Aster, B. Borchers, and C. J. Young (2002). An Automatic, Adaptive Algorithm for Refining Phase Picks in Large Seismic Data Sets, *Bull. Seism. Soc. Am.*, 92, 1660-1674.

Walter, W. R., A. J. Rodgers, A. Sicherman, W. Hanley, K. Mayeda, S. C. Myers and M. Pasyanos (1999). LLNL's regional seismic monitoring research, *21st Annual Seismic Research Symposium on Monitoring a CTBT*, Vol I, 294-302.

MIDDLE EAST, NORTH AFRICA AND WESTERN EURASIA SEISMIC RESEARCH DATABASE

Jennifer L. O'Boyle, Stanley D. Ruppert, Teresa F. Hauk, Douglas A. Dodge,
Michael D. Ganzberger, and Flori Ryall

Lawrence Livermore National Laboratory

Sponsored by National Nuclear Security Administration
Office of Nonproliferation Research and Engineering
Office of Defense Nuclear Nonproliferation

Contract No. W-7405-ENG-48

ABSTRACT

The National Nuclear Security Administration (NNSA) Ground-Based Nuclear Explosion Monitoring Research and Engineering (GNEM R&E) Program at Lawrence Livermore National Laboratory (LLNL) has made significant progress populating a comprehensive Seismic Research Database (SRDB) used for deriving seismic calibration parameters for the Middle East, North Africa and Western Eurasia (ME/NA/WE) regions. In addition to an overview of select individual information products, we present an overview of our visualization, integration, validation, and organizational processes. Development of these processes and the LLNL SRDB was necessitated by both the very large amount of data and information involved (over 15 terabytes) and the varied data and research result formats utilized. The LLNL SRDB allows for the collection of raw and contextual seismic data used in research, provides an interface for researchers to access data, provides a framework to store research results and integrate datasets, and supports assembly, integration and dissemination of datasets to the NNSA Knowledge Base (KB).

The LLNL SRDB is a flexible and extensible framework consisting of a relational database (RDB), Geographical Information System (GIS), and associated product/data visualization and data management tools. This framework is designed to accommodate large volumes of data in diverse formats from many sources (both in-house-derived research and integrated contractor products), in addition to maintaining detailed quality control and metadata. In order to efficiently organize information within the LLNL SRDB, it was necessary to automate procedures needed to create and update database tables, but a large effort is still required by technicians and scientists to load special datasets, review results of automated processing and resolve quality issues. The LLNL SRDB currently has 3 million reconciled event origins and arrivals from several global, regional and local seismic bulletins and 30 million waveforms from 570,000 seismic events. We also use the LLNL SRDB for integration and have developed procedures, algorithms, and tools, organized as a tool set called KBITS, which permits datasets to be merged and dataset quality control to be maintained. KBITS can be used to integrate waveform and bulletin data into unified datasets. This suite of tools is now being used by LLNL for content development and by Sandia National Laboratory to assist in creation of the KB. It enables inclusion of data from contractors, universities, and NNSA collaborators for content development and to provide coherent, reconciled and integrated results to the NNSA KB. The SRDB integration framework also supports and facilitates NNSA ROA and BAA projects.

The LLNL SRDB provides the basis for synergistic development of all LLNL GNEM R&E Program research. It is not only a coherent framework in which to store and organize very large volumes of collected seismic waveforms, associated event parameter information, and spatial contextual data, but also provides an efficient data processing/research environment for deriving a wide range of information products required to support the ME/NA/WE regionalization program. Products assembled, integrated and validated using the LLNL SRDB are grouped into five main categories: reference and contextual information, detection data, calibration and ground-truth data, event location products and event identification products. Using the LLNL SRDB, we are combining travel-time observations, event characterization studies, and regional tectonic models to assemble a library of ground-truth information and phenomenology (e.g. travel-time and amplitude) correction surfaces. Corrections and parameters distilled from the LLNL SRDB provide essential contributions to the NNSA KB for the ME/NA/WE region and facilitate calibration of seismic monitoring stations, thereby improving capabilities for underground nuclear explosion monitoring.

OBJECTIVE

The primary objective of the LLNL SRDB is to facilitate development of information products for the Ground-Based Nuclear Explosion Monitoring Research and Engineering (GNEM R&E) Middle East, North Africa and Western Eurasia (ME/NA/WE) regionalization program. The database provides efficient access to, and organization of, millions of seismic events and associated waveforms, while also providing the framework to store, organize, integrate and disseminate information products for delivery into the National Nuclear Security Administration Knowledge Base (NNSA KB).

The LLNL SRDB provides a unified framework for all seismic data and information products as outlined in Figure 1. This requires the reconciliation and merging of data derived from different sources and methods and of varying quality, along with the ranking of the datasets based on relative quality. Integration occurs on many levels in order to generate data, datasets, databases or knowledge bases. This database also allows for the integration of research with contractor research products and other available datasets. In order to efficiently organize information within the LLNL SRDB, it was necessary to automate procedures needed to create and update database tables, but a large effort is still required by technicians and scientists to load special datasets, review results of automated processing and resolve quality issues. Sufficient metadata (including measurement procedures, codes, comments and measurement errors) are stored at each step in the data creation and analysis process to allow re-creation or verification of results at any stage in the processing flow.

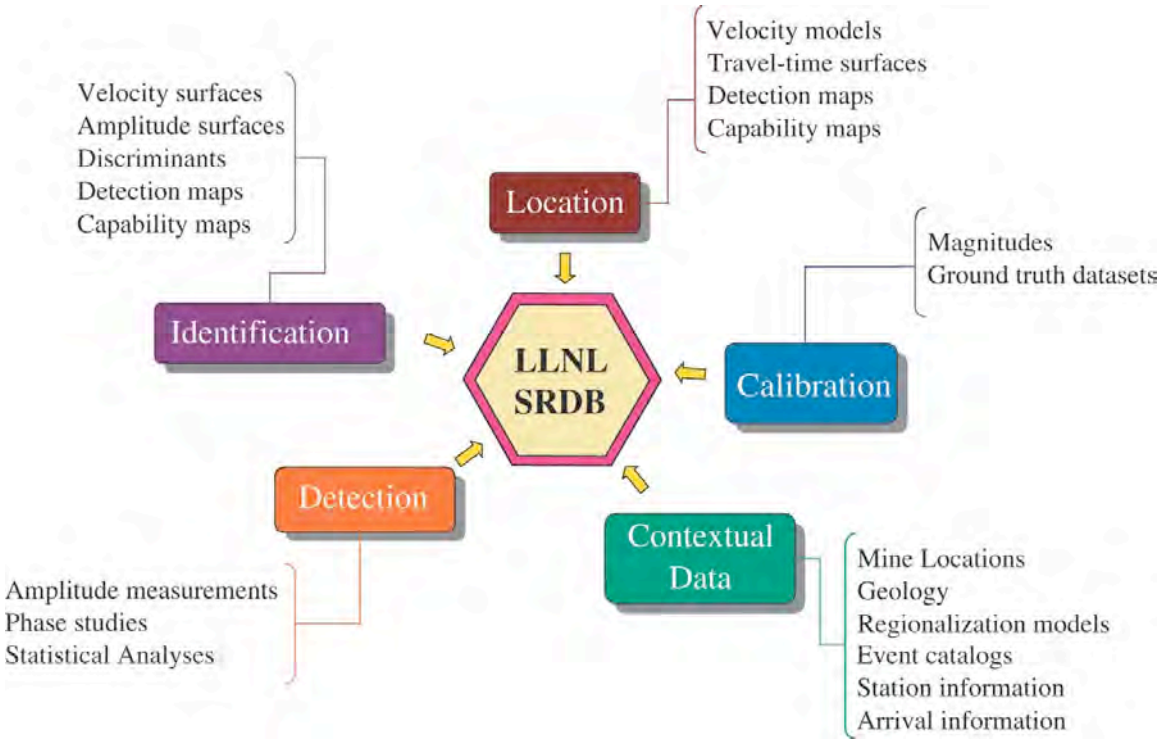


Figure 1. The LLNL SRDB provides a unified framework for contextual/reference data and information products. The database provides efficient access to, and organization of, thousands of seismic events and associated waveforms, while also providing the framework to store, organize, integrate and disseminate information products for delivery into the NNSA KB.

Information products created using the LLNL SRDB may be grouped under two major categories: primary data products and derived products. The primary products are those developed in the process of collecting the raw materials for calibration: ground-truth data, waveform data, event catalogs, phase pick information, regional station information and instrument responses. The derived products (distilled from the organized raw seismological data)

are models and corrections that improve detection, location and identification functions. In order to calibrate seismic monitoring stations, our database must incorporate and organize the following categories of primary and derived measurements, data and metadata:

Contextual and Raw Data
- station parameters and instrument responses
- global and regional earthquake catalogs
- selected calibration events
- event waveform data
- Geologic/geophysical datasets
- geophysical background model

Measurements and Research Results
- phase picks
- travel-time and velocity models
- Rayleigh and Love surface wave group velocity measurements
- phase amplitude measurements and magnitude calibrations
- detection and discrimination parameters

Corrections and parameters distilled from the database provide needed contributions to the NNSA KB for the ME/NA/WE region and will improve capabilities for underground nuclear explosion monitoring. The contributions support critical functions in detection, location, feature extraction, discrimination, and analyst review. Figure 2 outlines the processes of data collection, research and integration that result in contributions to the KB.

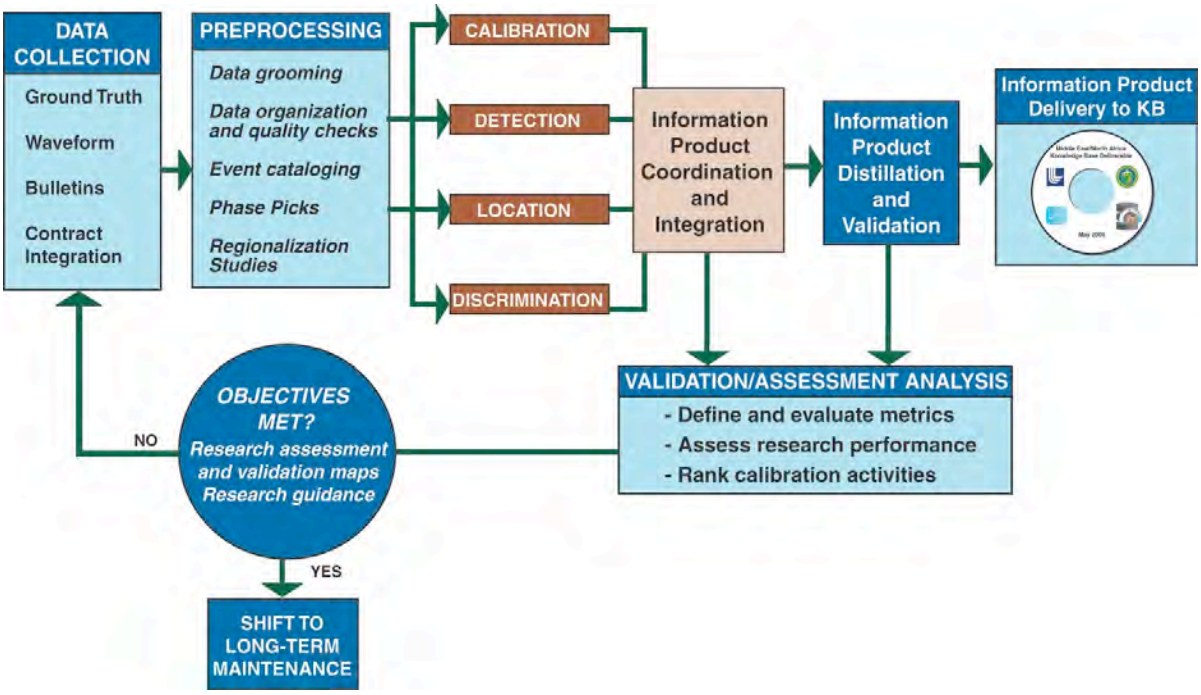


Figure 2. LLNL Seismic Research Database process flow. The database is the framework that supports development of information products related to seismic calibration research. Integration and synergy of data and research and visualization tools are made possible through this database.

RESEARCH ACCOMPLISHED

The LLNL SRDB is a framework consisting of an ORACLE relational database (RDB), Geographical Information System (GIS), and associated product/data visualization and data management tools. This database is necessary for the storage and organization of very large volumes of collected seismic waveforms, associated event parameter information, and spatial contextual data. It also provides an efficient data processing/research environment for deriving location and discrimination correction surfaces. Figure 3 outlines the interaction between all components of the LLNL SRDB. The relational database is organized using the NNSA schema comprised of CSS 3.0 with custom extensions. NNSA schema provides parameter defined tables for different elements of seismic data, such as event and station information, as well as allowing for customized tables to be developed for specific research needs or results and the compatibility with other organizations.

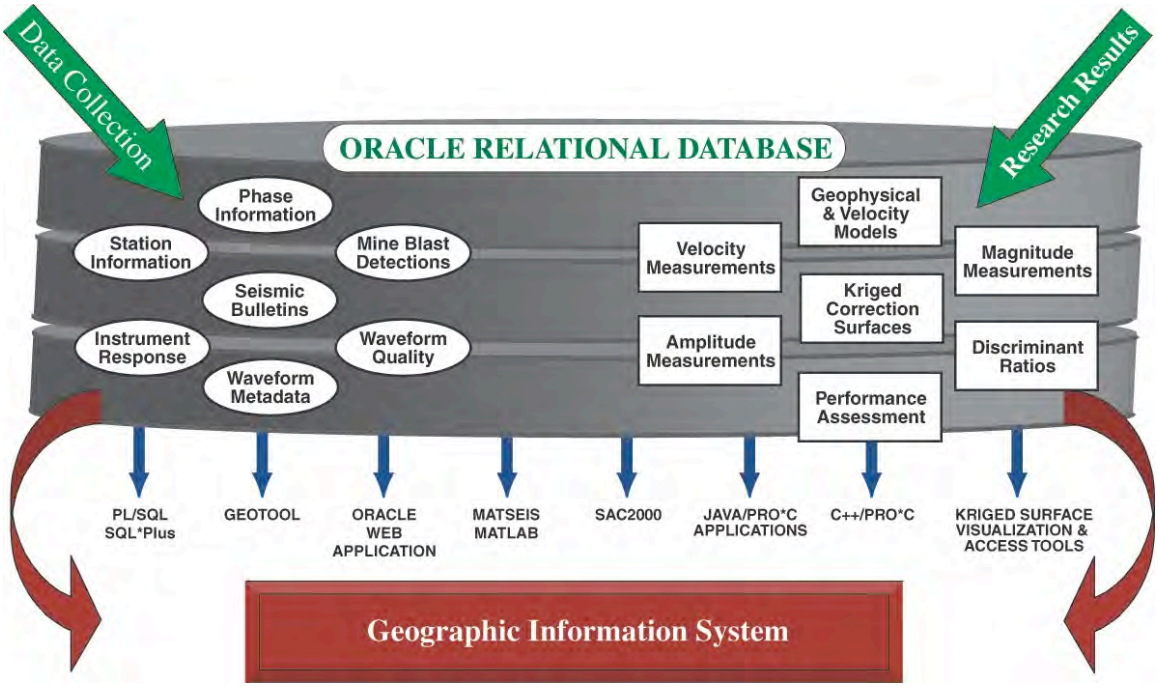


Figure 3. The LLNL SRDB integrates a relational database, a GIS and visualization/data management processes. Many aspects of GNEM R&E are contained within the database and can be accessed using a wide variety of tools.

The first tier of the LLNL SRDB development is largely the collection of catalogs and waveform data, parsing, conversion and extraction of data and database entry. What make these tasks challenging are the multitude of catalog and waveform data formats, and the sheer volume of the data. LLNL has succeeded in automating many of the collection, parsing, reconciliation and extraction tasks, individually. We are currently working towards a more integrated system so that much of this first tier of the database development will be almost completely facilitated by automated processes.

Currently, the automated procedures are organized into a tool set called KBITS, which uses modern object-oriented and database programming practices to combine a number of tools and libraries that incorporate automation where possible to streamline the data set loading, reconciliation, and integration processes. This framework also provides the primary mechanism for merging and reconciling derived calibration data from contractors, individual researchers, and NNSA laboratories into a single product. There are six main classes of products that require integration effort and four main reconciliation issues for each class summarized below:

Data set Class	Reconciliation Issue
Core tables / Core files (e.g. velocity models)	Initial merge
Catalogs	Updating
Waveforms	Validation
Derived products (internal and external)	Back propagation / synchronization
Spatial/Contextual information	
Assembled databases / Knowledge bases	

To assist us in the integration and reconciliation tasks related to calibration research, we have written a set of 130 C++ classes designed primarily as components of computer programs for use by the GNEM R&E program. A class is a software abstraction of an entity from the problem domain, which combines all of the attributes and actions of a single entity into one data type. This allows programmers to work at a higher level of abstraction, thus improving productivity and software maintainability. Of the classes we designed, about 10 are service classes with no specific seismological capability, *e.g.* time class, architecture class, etc. All the remaining classes are specialized to some degree for use in seismological applications. All of the collection classes have database-aware specializations as well, since most of the programs developed with the classes interact extensively with the LLNL SRDB database. The class library has built-in support for the CSS3.0, SAC, GSE2.0, and PC-SUDS data formats. Using the class library has proven to be an effective means of building the utility programs required to support the LLNL SRDB as described in the following paragraphs.

We have developed an automated method/tool (Orloader) to load various seismic bulletins of different formats into native-format database tables, which retain many of the fields provided in the original bulletin, as well as assign a unique origin identifier (*orid*) to each event. Individual bulletins are then merged into a single CSS3.0 **origin** table retaining the author of the original bulletin. The native tables are linked to the origin and event tables created by Orloader through a remap table. Using the remap table, any origin in the target CSS3.0 table can be uniquely associated with the corresponding native origin. Because the same event may often be reported by different organizations, there will be instances in which new origins correspond to origins that are already in the database. A space-time correlation algorithm is used to reconcile events between individual catalogs. Events common to multiple bulletins will be assigned common event identifiers (*evid*) while retaining unique *orid*s. The **event** table stores the preferred origin for each event based on a ranked list of catalog preferences. Phase arrivals provided with native catalogs are loaded into the **assoc** and **arrival** tables.

To generate the event waveforms for our database we have developed automated methods/tools (Ddload, UpdateMrg) for extracting event waveforms from continuous data and inserting them into the appropriate database tables. Event selection can be restricted by time, location, event magnitude or a specific list of *evids*. Ddload extracts waveforms from continuous data in the native format, converts the data to CSS3.0 format and creates entries in staging tables (**wfdisc**, **wftag**). The **wfdisc** table contains pointers to the waveform files and the **wftag** table associates the waveform file with the *evid* used in the extraction. Currently, we can perform waveform extraction on data in SAC, SEED, CSS, SEGY and GSE formats. The UpdateMrg program is used to insert the staged **wfdisc** and **wftag** records into the target tables. During the insertion process, UpdateMrg checks waveforms for poor or missing signals, which are then recorded in a metadata table. If waveforms for a specific event are segmented, the segments will be merged together; if a gap exists between segments, the space will be filled with zero-value data points. If two segments that are being inserted overlap or a segment for an overlapping time period already exists in the target tables, a correlation test is done before the two segments are joined.

Also included in KBITS are a suite of consistency tests and related updating/repair procedures (DBcheck / DBfix) to assist both the data set loading staff and researchers in maintaining the highest quality collection of data possible. These test procedures consist of PL/SQL stored procedures used for identifying and resolving inconsistencies between datasets (core tables and measurement tables) to be integrated as well as maintaining consistency in the final LLNL SRDB and products to be delivered.

The second tier of LLNL SRDB development activities, the development of correction surfaces and other calibrations, is less susceptible to complete automation as these activities require the judgement of scientists skilled in the interpretation of often highly unpredictable event observations. However, development of proper tools to extract observations and parameter data from the database and to make thousands to millions of waveform

measurements can significantly increase the efficiency of the scientists who construct and validate integrated calibration surfaces. This trend is likely to continue and even accelerate leading ultimately to larger investments in enabling technologies offset by declining expenditures on the routine construction of calibrations. The first tool to be developed is a prototype body wave amplitude measurement tool. The tool is written in Java and incorporates a GUI and GIS system for project management and event selection with a semi-automated, interactive measurement window picker. Development of this tool has produced a number of reusable classes that we expect will be helpful in further automation efforts.

The LLNL SRDB also provides the framework to perform end-to-end process validation and testing of research results. Validation and assessment tasks include the definition and evaluation of specific metrics, analysis and use of metrics to define the stopping criteria for particular location and identification tasks, and ranking and performance evaluation of calibration activities. Success and efficient implementation of validation and assessment tasks require a framework that ties research results to data and measurements used to create each calibration product and that also supports statistical and visualization tools for performing the validation tasks. The metadata inherent in the LLNL SRDB allow multiple realizations of calibration products, created with different processes and assumptions, to be created, stored, and compared with one another. Thus our database facilitates the distillation, documentation, and delivery of information products.

Contextual and Raw Data

Station Parameters

Seismic station information is a metadata requirement needed to support all stages of seismic waveform analysis. These metadata include such parameters as station operation dates, location and elevation, type of channels and instruments, sampling rates, and instrument responses. Our main source of this information is Incorporated Research Institutes for Seismology (IRIS) “dataless” SEED files, which are provided by each of the networks affiliated with IRIS. Other station information has been obtained through Internet station books and AutoDRM systems. CSS3.0 **site** and **sitechan** table entries (listing station location, available channels, sensor orientations, operation dates, etc.) were created for almost all IRIS affiliated networks as well as many other stations with waveforms in the LLNL SRDB. All station parameters are reviewed among existing information sources, and conflicts must be resolved between sources and in reference to waveforms available before database tables are updated. Over 2400 station and array element table entries have been updated, but reliable parameter data do not exist for some stations if only minimal or inconsistent information is available. **Instrument** and **sensor** tables are used to document instrument type and response for each station and channel. The Seismic Analysis Code (SAC) has been modified to interpret response information in RESP or FAP format for use in performing instrument response corrections on waveform data by using the EVALRESP software library available from IRIS.

Event Bulletins

Reference event locations and origin time information are necessary in most stages of our seismic processing and research. Bulletin information from many global, local, and regional earthquake catalogs has been incorporated into the LLNL SRDB and provides a much larger source for event selection. This combined and reconciled source facilitates comparison of event parameters provided by multiple networks with different degrees of location accuracy and provides a wider range of magnitudes and event types. The global catalogs include: United States Geological Survey (USGS) Monthly (Final) Preliminary Determination of Epicenters (PDE) catalog and Earthquake Data Report (EDR) catalog, Bulletin of the International Seismological Centre (ISC), Harvard Centroid Moment Tensor (CMT) catalog, and the International Data Centre Reviewed Event Bulletin (REB). We have also compiled numerous regional and local catalogs for the ME/NA/WE region, including Jordan, Israel, Scandinavia/European Arctic and the Kola Peninsula. Figure 5 shows a map of the event location coverage provided by several of the bulletins in the ME/NA/WE region. We have established a number of collaborative agreements with countries and institutes in our study region to obtain both local seismic catalogs and ground-truth information as well as seismic waveform data.

Waveforms

We are collecting seismic data from IMS primary and auxiliary stations, as well as surrogate stations (for IMS stations not yet installed) and other stations needed to support calibration in the region of study. We have obtained over 10 years of continuous data for important ME/NA/WE stations from IRIS, Institut de Physique du Globe de

Paris GEOSCOPE program, the GEO-Forschungs Zentrum/Potsdam, Germany GEOFON program and other data centers. Data for particular events has been obtained from the prototype International Data Center (PIDC) and the United States National Data Center (US NDC). The Center for Monitoring Research (CMR) and NORSAR have provided waveforms for special regions/events, such as the Novaya Zemlya test site. Stations in the ME/NA/WE region with event waveforms stored in the LLNL SRDB are shown in Figure 4.

Most of the archived waveforms in the LLNL SRDB are from events located within the ME/NA/WE region and occurring between 1976 and 2002. Although the continuous data remain archived on tapes, data segments for seismic events are extracted from the continuous waveforms. The number of waveforms in the LLNL SRDB is now almost 30 million, which represents 570,000 seismic events. The events with waveforms in the LLNL SRDB are shown in Figure 5.

Other Reference and Ground-truth Datasets

Projects to develop reference datasets include waveform correlation and subspace detectors to provide statistics on mining activity and a regionalization model based on *a priori* geophysical knowledge used as a reference model for model-based correction surfaces. Collaborations with Cornell University, USGS and other organizations allow us to obtain reference datasets useful as background and supporting information for research. Most of these datasets are provided as Geographic Information System (GIS) products, which allow us to integrate them with our datasets. The datasets include geographic, geopolitical, mining industry, geologic and tectonic information for the ME/NA/WE region. We also collect photographs and satellite imagery to support ground-truth determination.

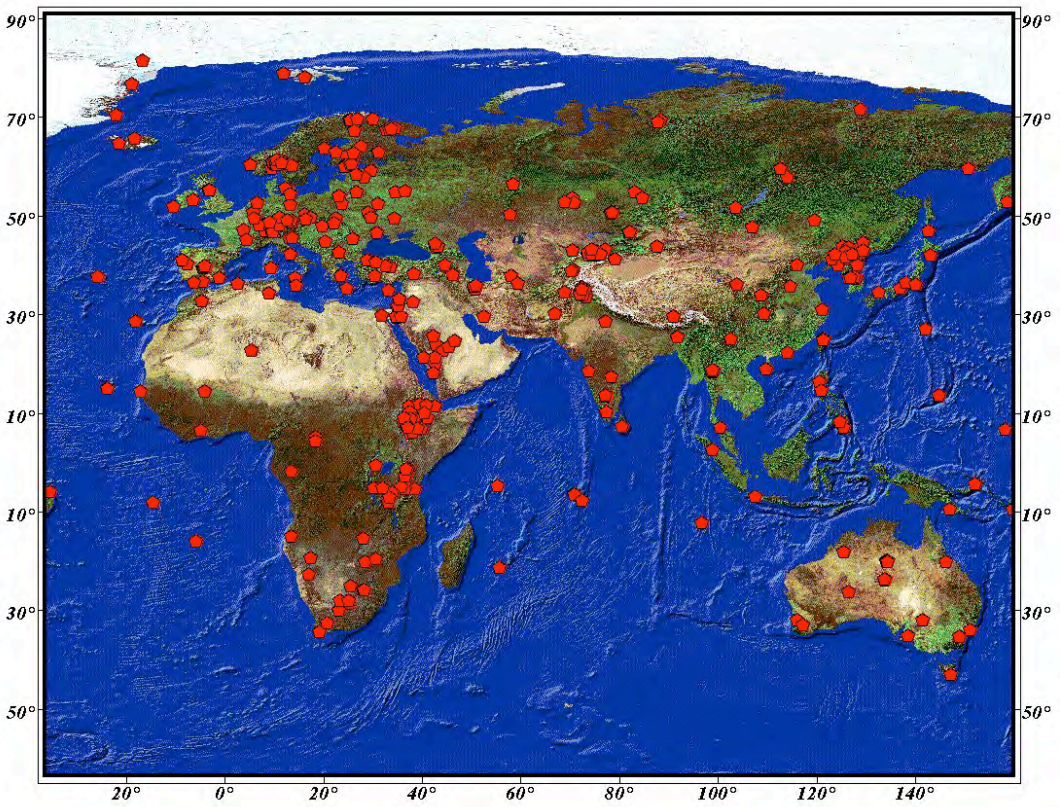


Figure 4. Seismic stations in the ME/NA/WE region with event waveforms stored in the LLNL SRDB.

Measurements and Research

Phase Information

LLNL researchers and analysts have made phase picks for over 1700 events to yield over 24,500 travel-time observations available to the research team for location and discrimination projects. Phase information is recorded

in the **arrival** and **assoc** tables, along with pick and waveform quality and other comments that are recorded in a **remark** table. Augmenting the picks, we added 36 million ISC phase arrival measurements, 2 million REB arrivals and 12 million EDR arrivals along with picks from several regional bulletins to be used for travel-time correction studies.

Seismic Location Research

Seismic location researchers utilize event catalogs (especially ground-truth), waveforms and phase picks to develop travel-time corrections. Improvement in seismic location is accomplished by combining model-based and empirical travel-time corrections. After a calibration model is applied, empirical corrections are calculated using Modified Bayesian Kriging algorithm with travel-time residuals for suitably well located calibration events. The travel-time and velocity models developed through this research are an important part of the LLNL SRDB. See the LLNL Location and Detection Research (Myers *et al*., 2003 this Proceedings) paper for more details about these aspects of the GNEM R&E research.

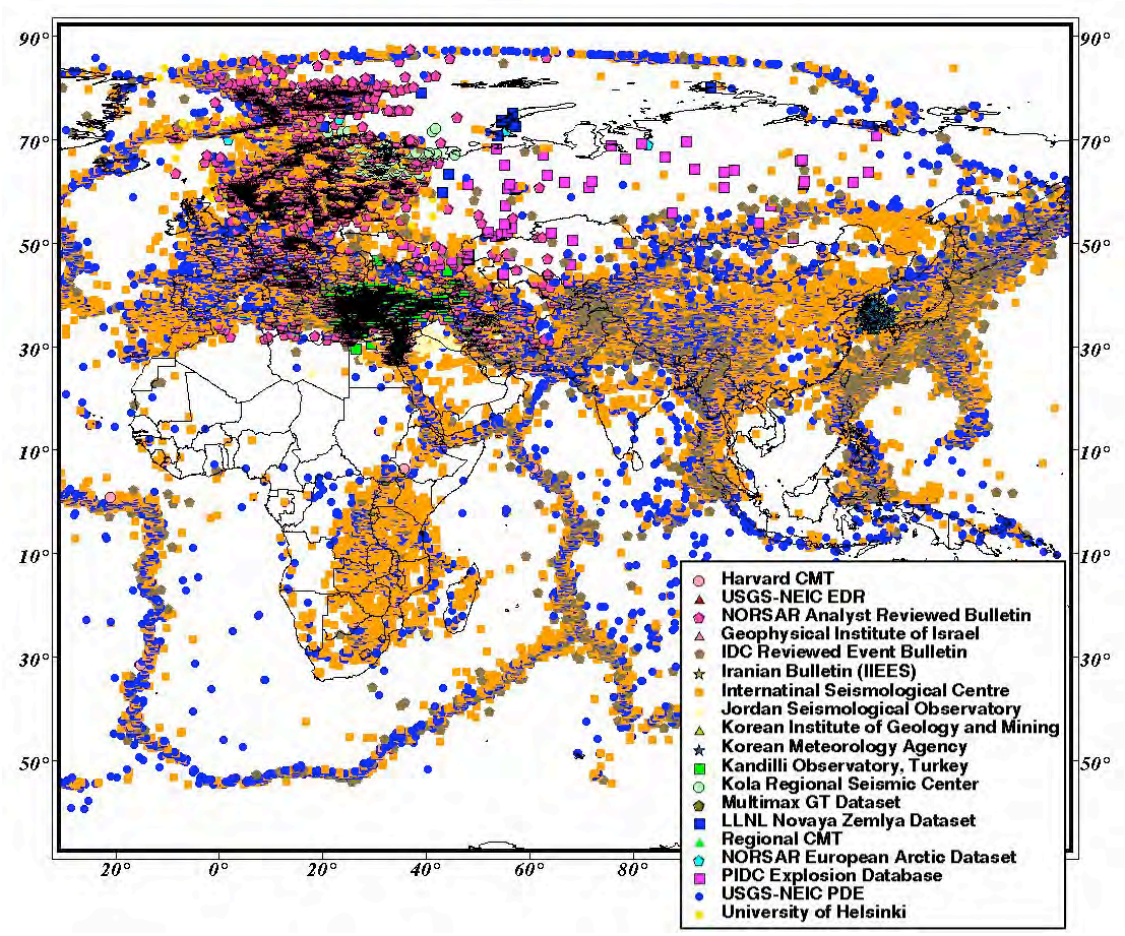


Figure 5. Plot of seismic events in the ME/NA/WE region with waveforms in the SRDB. The LLNL SRDB contains multiple seismic event catalogs that have been reconciled into one database table. These catalogs range in scope from global to regional to special ground-truth datasets and provide a much broader range of event magnitudes and event types than any single catalog.

Event Identification and Magnitude Research

The event identification researchers also use event catalogs, waveforms and phase picks to develop products that provide seismological information to improve the ability to identify underground nuclear explosions, by discriminating them from the background of earthquakes. The magnitude research results in calibration products and magnitudes for 1-Hz regional phases, broadband coda waves, and long-period surface waves. This provides the

necessary calibration information for regional data in order to calculate seismic magnitudes for use by nuclear monitoring functions (detection, location, identification, and characterization). Custom tables in the LLNL SRDB database store measurements and related parameters for surface wave group velocities, body wave amplitudes and magnitudes. See the Regional Body-Wave Corrections and Surface-Wave Tomography Models to Improve Discrimination (Walter *et al*., 2003 this Proceedings) paper for more details about these aspects of the GNEM R&E research.

Data Access

Different researcher needs for data and metadata require that subsets of data be provided in a format easily accessible to many diverse types of software and analysis tools. Therefore, the LLNL SRDB access tools have been designed to utilize the power of the relational database to facilitate efficient queries and data retrieval. The SAC software used by researchers provides direct access to database table information and waveforms and uses the response files to perform instrument response corrections. For spatial queries and organization, we have adopted a GIS, which provides a framework to store and manipulate spatially defined data. The GIS is linked with the ORACLE database to provide joint spatial and relational queries. We have integrated a large number of our research and contextual datasets into the GIS products in conjunction with other datasets, including contractor products. Researchers can use the GIS to browse many of their research datasets combined with integrated datasets, and also perform basic comparisons, queries, and analyses.

Given the large quantity of data now managed by the LLNL SRDB, the need arose to create the efficient "production" level seismic data selection, processing and visualization tools necessary to meet programmatic and NNSA KB needs. These tools, along with data browsers to allow visualization and quick access to both data and delivered information products, were developed in collaboration with Sandia National Laboratories. The tools provide such functionality as deriving location corrections, making amplitude and magnitude measurements, and developing discriminants.

CONCLUSIONS AND RECOMMENDATIONS

We have made a major effort to provide a product development environment that encourages the natural synergies between each of the separate research efforts of the GNEM R&E researchers. The derivation of reference and ground-truth datasets and location and identification products takes place in an integrated environment with changes and improvements in one area being used to facilitate development of the remaining areas. We utilize the LLNL SRDB as an integrating framework to provide the basis for synergistic development of all GNEM R&E. By combining travel-time observations, event characterization studies, and regional wave-propagation studies for ground-truth and regional events, we have assembled a substantial library of ground-truth information (origin times, locations, depths, magnitudes), mine explosion statistics, tomographic models and travel-time and body-wave correction surfaces.

The LLNL SRDB allows for the collection of raw and contextual seismic data to be used in research, provides an interface for the researchers to access data, provides a framework to store research results and integrate datasets, and supports assembly and dissemination of datasets to the NNSA KB. A wide range of information products required to support the ME/NA/WE regionalization program are being derived from waveforms, station parameters, and event origin information contained in this database. Corrections and parameters derived, assembled, integrated and validated using this database provide essential contributions to the Knowledge Base for the ME/NA/WE region and will improve capabilities for underground nuclear explosion monitoring by supporting critical functions in detection, location, feature extraction, identification, and analyst review in the Middle East, North Africa and Western Eurasia.

REFERENCES

Myers, S., D. Harris, M. Anderson, W. Walter, M. Flanagan, F. Ryall (2003), LLNL Location and Detection Research, *Proceedings of the 25th Seismic Research Review: Nuclear Explosion Monitoring: Building the Knowledge Base.*

Walter, W., M. Pasyanos, A. Rodgers, K. Mayeda, A. Sicherman (2003), Regional Body-Wave Corrections and Surface-Wave Tomography Models to Improve Discrimination, *Proceedings of the 25th Seismic Research Review: Nuclear Explosion Monitoring: Building the Knowledge Base.*

EFFICIENT INTEGRATION OF OLD AND NEW RESEARCH TOOLS FOR AUTOMATING THE IDENTIFICATION AND ANALYSIS OF SEISMIC REFERENCE EVENTS

Wilmer Rivers,[1] Robert A. Wagner,[1] Eric Siu,[1] Joey Chen,[1] Craig A. Schultz,[2]
Douglas A. Dodge,[2] and Gregory Pope[2]

Multimax, Inc.;[1] Lawrence Livermore National Laboratory[2]

Sponsored by National Nuclear Security Administration
Office of Nonproliferation Research and Engineering
Office of Defense Nuclear Nonproliferation

Contract No. DE-FG02-01ER83218[1] and W-7405-ENG-48[2]

ABSTRACT

The selection and study of reference events for inclusion in the National Nuclear Security Administration (NNSA) Knowledge Base requires the application of a much broader suite of seismic analysis software than does either the routine production of a seismic bulletin or the subsequent preliminary screening of those bulletin events to conduct nuclear monitoring. For either of those latter applications, a large program designed explicitly for that single purpose can be applied to the many events that will be processed daily, but to study the much smaller number of reference events in adequate detail it is necessary to use many separate specialized programs. These individual programs must communicate with one another in an efficient and flexible manner, so that a scientist can select which programs to run and in what order, thereby improvising a data-processing pipeline of programs passing their results from one to the next. The scientist may in fact wish to develop new software to perform specific analyses on the particular events under examination, and this new software must work in tandem with the existing software.

We have therefore explored the use of a distributed programming environment as the architecture for a reference event analysis system. This environment was chosen so that specialized analysis tools could be developed independently of one another and then integrated with existing programs. The specialized tools would remain separate from the existing software, however, and they could in fact run on different platforms, communicating with the other software across a local network or even the Internet. A distributed processing environment allows an expanded system to be built from stand-alone software components that can easily be added to or removed from the existing system by re-directing the data communications without requiring fundamental changes to the existing software. A particular advantage to this approach is that a researcher who wishes to design and test a particular algorithm for seismic analysis can construct a software component that performs only that algorithm, and then existing software systems can be used to provide data input and graphics display capabilities for testing that component. It will thus not be necessary to include those capabilities within the component under development nor to make changes to the existing software systems that could introduce harmful software "side effects" to them.

In the first phase of this project, we investigated implementing this system architecture using the large seismic analysis package *geotool* as a client program that invoked services from distributed components via the Common Object Request Broker Architecture (CORBA) as the data communications platform and the Internet Inter-ORB Protocol (IIOP) as the wire protocol for Internet transmission. CORBA is software architecture for binary data communications, and it was designed in the 1990s primarily for client-server computing within a single enterprise. Because the data transmissions are binary, CORBA cannot be used to invoke services across a firewall. Within the last two years there has emerged a new software standard for distributed computing, especially among different enterprises communicating across the Internet, that is based on ASCII messages (encoded using XML) rather than binary transmissions. This standard, known as Simple Object Access Protocol (SOAP), allows components to operate as "Web services" that can be called using HTTP as the wire protocol and that can thus operate across firewalls. In our recent work we have replaced CORBA with SOAP as the basis for our distributed data processing. Because Web services are becoming an important aspect of electronic commerce, most modern software development systems on the UNIX, Java, and Windows platforms all include tools that facilitate the construction of Web services, and since the data are transmitted as ASCII messages rather than binary code, software components on these different platforms can operate together as a single data processing system. This inter-platform distribution of components is likely to become a key aspect of most newly developed large data analysis systems.

OBJECTIVE

Scientists use a variety of stand-alone computer programs to analyze and identify seismic events for nuclear explosion monitoring, and an especially wide selection of software tools is needed for the detection and intensive study of reference events that will be included in the NNSA Knowledge Base for use in future event comparisons. Some of these stand-alone programs are large software packages that offer many tools for routine seismic analysis, but they are difficult to modify to include additional tools for specialized tasks. Others of these stand-alone programs offer the capability of performing only specific operations, and they must be used in conjunction with other programs such as interactive waveform graphics displays that offer more general analysis capabilities. In most cases neither the large software packages nor the specialized analysis programs can communicate adequately from one to another without the tedious creation and input of temporary data files and other awkward techniques. Since the stand-alone programs cannot exchange data easily, it is difficult to use them in a data-processing pipeline that could add new capabilities to those offered by the large software packages or that could allow the specialized analysis programs to rely on other software for tasks such as graphics displays.

A reference event analysis system should therefore be built by using a system architecture that facilitates data flow among these stand-alone programs, including any new programs that will be developed in the course of future research and that may be especially valuable for the identification and characterization of reference events. This new architecture should allow the results of one program to be sent easily to another one, as chosen on a case-by-case basis by the seismic analyst, without the creation of temporary files and database tables. Because many of the stand-alone seismic analysis programs that need to communicate with one another are written in different computer languages, and many are written for use under different operating systems, it will be important for this architecture to be as nearly platform-independent as possible. Furthermore, the communications among the separate programs should allow access to remote resources for data retrieval or specialized computations. The reference event analysis system should therefore be constructed as a distributed system of individual software components rather than as a single large software package. The first objective of our study is to examine software architectures and communications protocols that will allow existing and newly developed programs to be used as the components in this distributed system. Our next objective is to select and modify those programs so that they can be integrated into a reference event analysis system using that distributed system architecture.

RESEARCH ACCOMPLISHED

It is our intention to use the familiar seismic analysis program *geotool* as the cornerstone, at least initially, of the reference event system because it offers a wide suite of graphics tools and processing routines. The *geotool* routines will first be supplemented and eventually be replaced by other processing routines that will operate remotely, and finally the core graphics will also be replaced by a dedicated user interface program. We have therefore undertaken tasks to augment *geotool* with new functionality and with an up-to-date description of its processing, especially in the form of metadata files, and we have undertaken tasks to implement a distributed processing architecture based on XML SOAP messages passed between *geotool* and seismic processing routines running as Web services, possibly on different computers and different operating systems.

Software Requirements for a Reference Event Characterization Tool

We have undertaken an extensive review of the operational capabilities, limitations, problems, and deficiencies of the stand-alone seismic analysis program *geotool*. The program itself (Henson, 1993) is now ten-years old, and although it has continued to evolve throughout its software life cycle, its most recent publicly distributed documentation (Coyne and Henson, 1995) is eight-years old. We have written a documentation update describing the program's current operations, and we have constructed a software requirements specification detailing the changes to the program that will be necessary if it is to be used as a central component of the reference event analysis system. We have also categorized the current operations of *geotool* in terms of a metadata description of the results of the processing, as will be described below.

Change in System Architecture

In our previous work (Rivers et al., 2002) we investigated the use of CORBA as the backbone architecture for data processing communications between *geotool* and remote programs. In our current work we have replaced CORBA

with XML SOAP Web services as the backbone of the distributed processing. There are several benefits motivating this change, but there are also certain costs associated with it. Within a single computer, it may be preferable to implement inter-thread communications using direct socket connections for remote procedure calls (RPCs), and, within a client/server LAN, it may be preferable to use a binary protocol such as CORBA, as has been done throughout the 1990s to connect PCs to mainframes. For business-to-business commerce, however, it is preferable to invoke RPCs and transmit data using ASCII messages sent across the Internet through HTTP, a format that can work even if the client and server operate inside separate firewalls. It is for this reason that XML SOAP Web services are rapidly becoming the industry standard, and we feel that a reference event analysis system can make use of this loosely coupled system by swapping newly developed software into and out of it. Moving from sockets to CORBA to SOAP results in a gain of flexibility by moving to increasingly higher levels of software abstraction within the TCP/IP stack, but it comes at the cost of decreased efficiency, as direct binary communications are replaced by ASCII messages. We nevertheless believe this loss in efficiency is offset by the decrease in development time, and especially by the decrease in software maintenance time, required for the implementation of such a loosely coupled system of independently developed components rather than a large single program or a tightly coupled client/server system. Another advantage is that whereas CORBA permits communication among the UNIX, Linux, and Java platforms, SOAP Web services permit these platforms to communicate easily with the Windows 2000 platform.

Our investigations of the use of XML SOAP for distributed seismic processing will be illustrated by a Web service that computes the short-term average (STA) of a time series. This routine is a C++ program running within the Microsoft .NET software platform under Windows 2000 (not as a program running on the Java platform within Windows). Figure 1 shows the Web Services Description Language (WSDL) interface that this program presents to the Internet. In this case the WSDL file was generated automatically by the Microsoft Visual Studio software development tool when the C++ program was installed within the *Inetpub/wwwroot* directory of the Web server, so the programmer does not need to write the WSDL description. Figure 2 shows the format of the SOAP message that should be used by a client program such as *geotool* that has need of this particular Web service. The Microsoft.NET development environment automatically generates this SOAP format tool, and SOAP messages in that format can then be used by a program running under Linux (like *geotool*) to communicate with this Windows program.

In our description of the work that we performed using CORBA as the middleware platform for distributed processing (Rivers et al., 2002), we presented a number of screenshots showing the transmission of waveforms between the C-language program *geotool* running under Linux and a Java program running within Windows. We shall not show a similar sequence of screenshots herein, since externally the distributed processing appears the same whether CORBA or Web services are used as the architecture. We do show in Figure 3 how to establish a routing to that same Java program, now accepting SOAP messages rather than CORBA transmissions to invoke its operations, and at the bottom of the figure we show that a *geotool* menu item is being used to receive the results of the processing performed by that remote application.

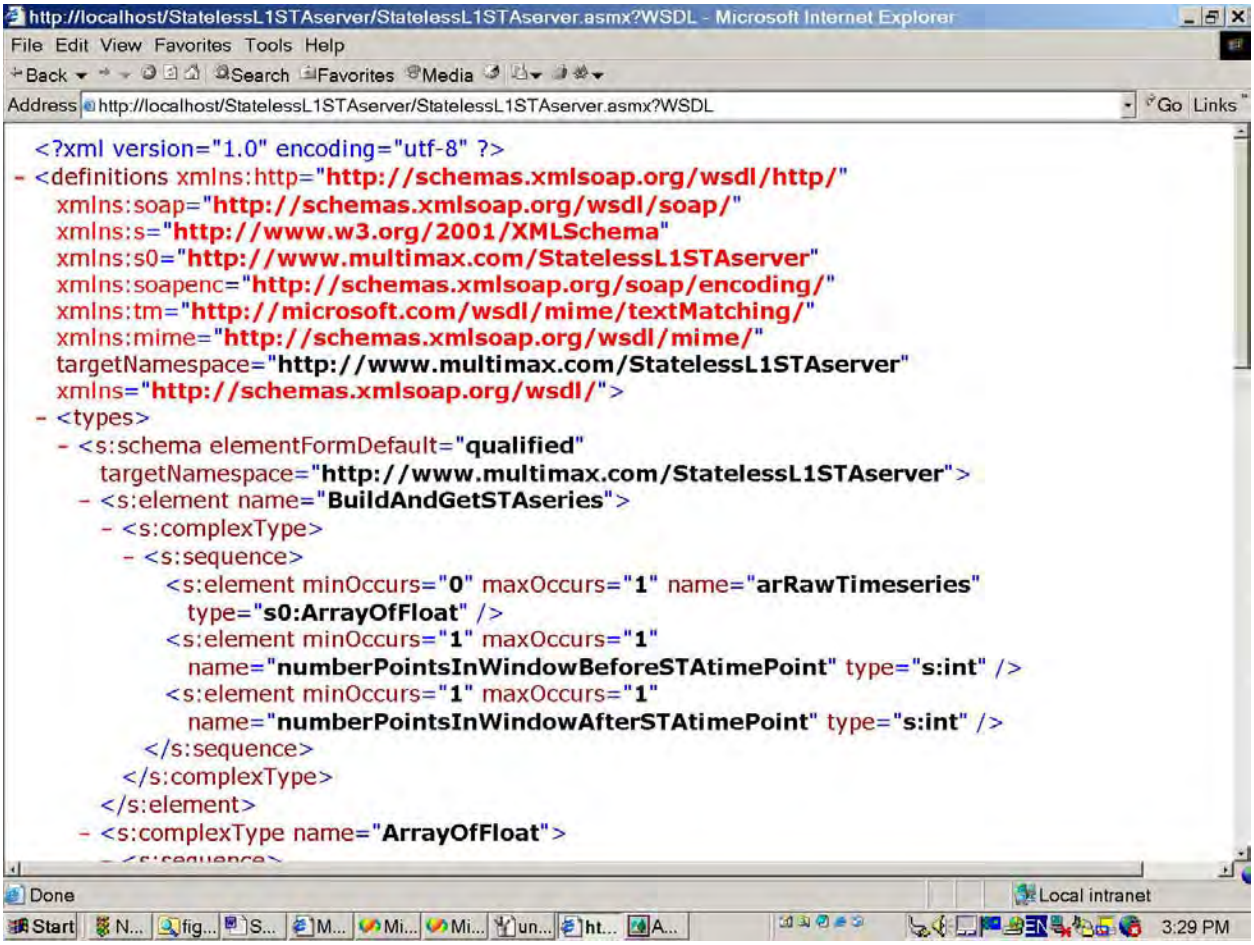
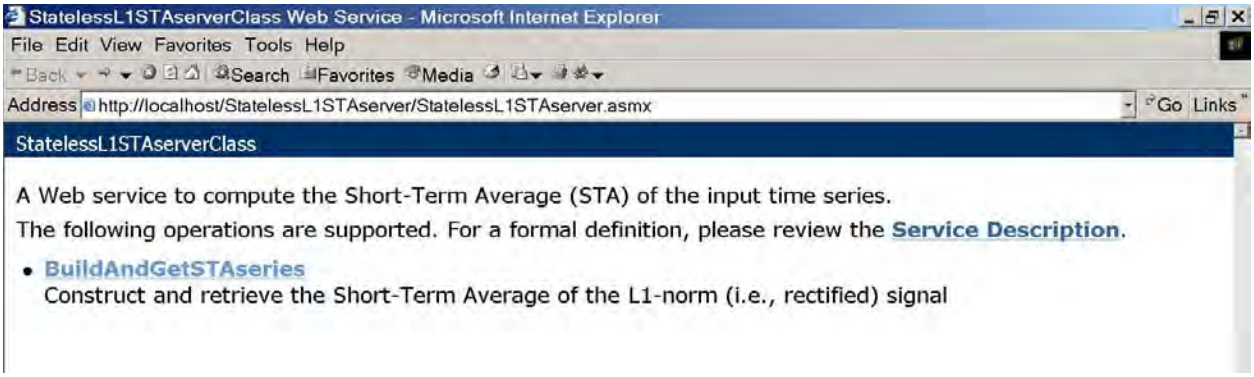


Figure 1. Screenshot of a browser window displaying the WSDL (Web Services Description Language) interface to the Web service *StatelessL1STAserver*, which computes the short-term average (STA) of a time series, using the L1 (*i.e.*, absolute value) norm to rectify the data. *StatelessL1STAserver* is a C++ class operating as a Web service within the Microsoft .NET software platform under the Windows 2000 operating system. The WSDL interface shows the input values (namely the array of data points that make up the time series, along with a couple of integers describing the desired STA time window) that can be used by *geotool* (or any other program needing the service of this STA algorithm) to access this Web service, as well as the output values (namely, a new array of data points) that this service will return to the calling program. The application that needs this service will call a local proxy object that has the same interface as is shown in this WSDL file, and the proxy will transmit the request via the Web server (within the local host, or across the Intranet or Internet, as directed by the URL for the Web service) and will receive the response. Because WSDL and SOAP are XML vocabularies, it does not matter that *geotool* and *StatelessL1STAserver* are written in different programming languages and run on different operating systems.



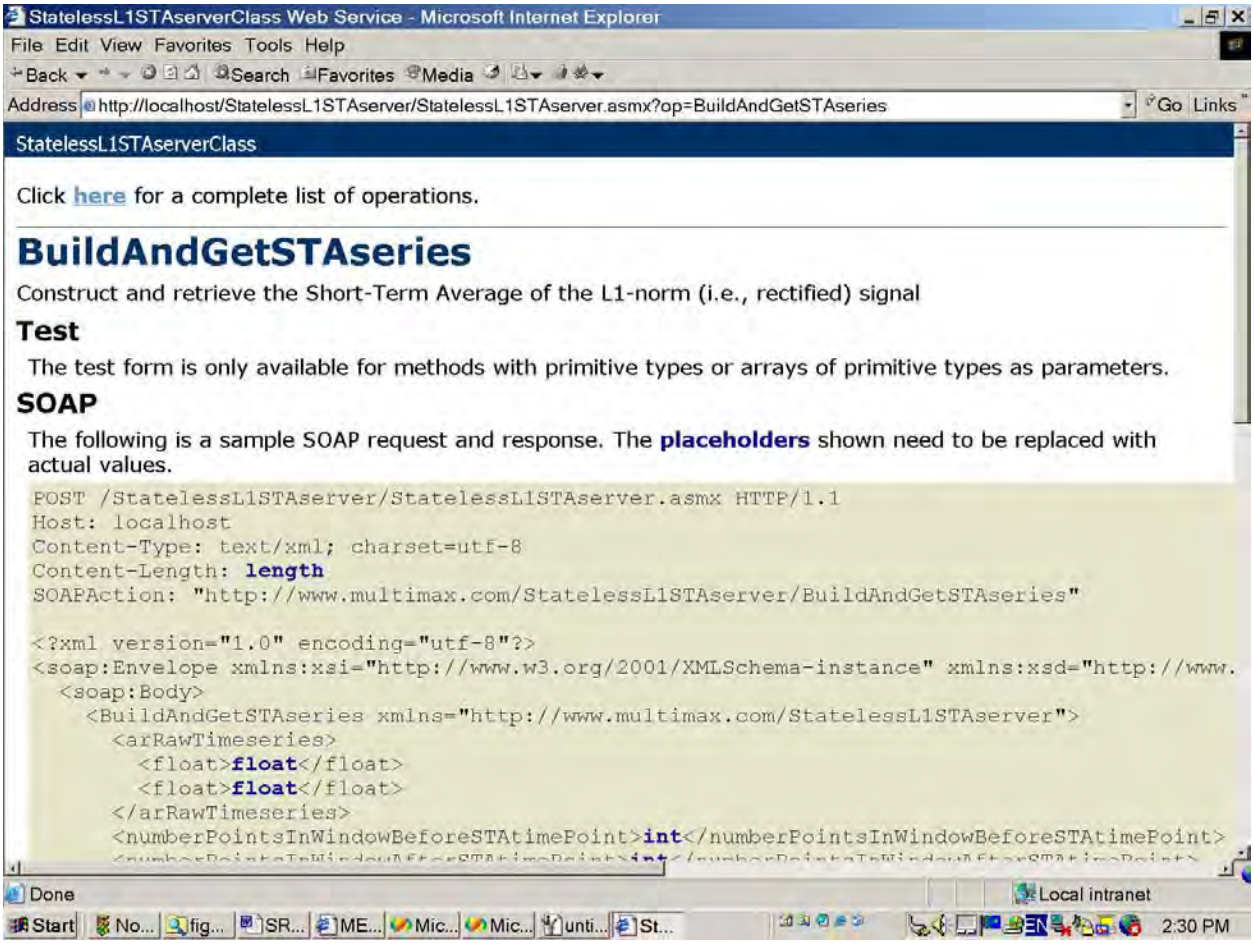


Figure 2. (Top) Screenshot showing a browser window that exposes the *StatelessL1STAserver* Web service to examination by a potential user of this service. The hyperlink to the "Service Description" exposes the WSDL file shown in Figure 1 that can be used to construct the interface to the proxy object. (Bottom) Screenshot showing that the hyperlink to the *BuildAndGetSTAseries* method of the C++ class exposes a template of the Simple Object Access Protocol (SOAP) message that will be sent to the Web service via HTTP when the calling program, such as *geotool*, makes a call to the *BuildAndSetSTAseries* method of the proxy object.

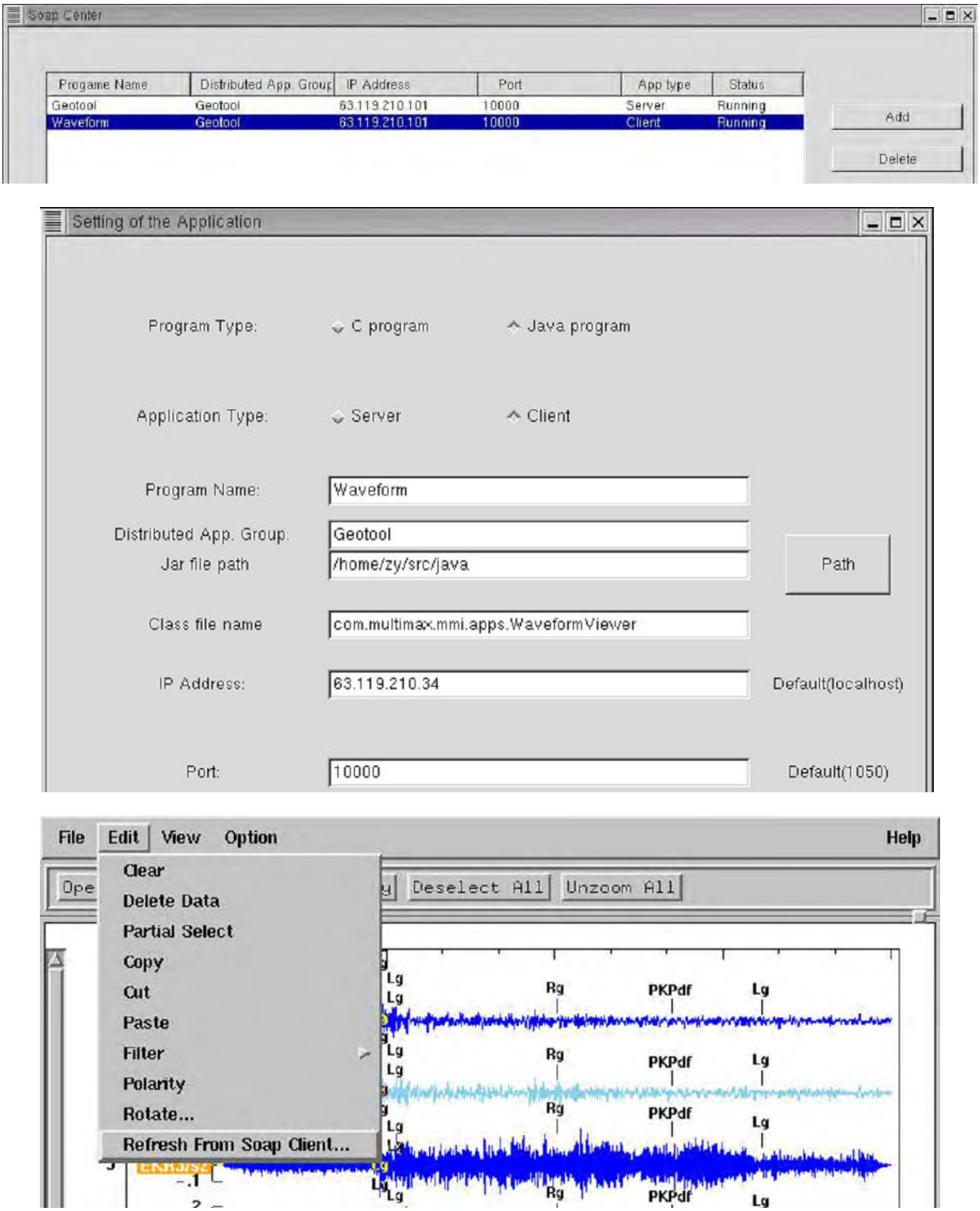


Figure 3. (Top and middle) Windows that set up a SOAP RPC connection from the C-language program *geotool* to the Java program *Waveform*. Although in this instance both programs are running on the same computer, this need not be the case. (Bottom) A window showing the menu item to refresh the selected waveform in the *geotool* display using data modified within the *Waveform* program.

Metadata Requirements

In seismic data analysis the issue of metadata is always an important one, since before the data can be entered into the Knowledge Base and the events can be located, parameterized, and classified it is necessary to know such things as how the raw data were obtained, how reliable were the measurements, what automatic and interactive processing were applied to the data, and the thresholds beyond which the processing results are invalid . This need for a thorough description of the metadata is even more nearly critical for a distributed processing system than for a single large seismic analysis package, since in our reference event system the client program such as *geotool* will treat the independent analysis programs as black boxes. It will send them data and receive results back, but the internal operations of these remote services must be regarded as unknown. It is therefore essential that the servers return to the clients not only the output of their algorithms but a thorough metadata description of all the values it returns and how they were derived. We have therefore undertaken the design of metadata records for all the processing routines within *geotool*, and we are extending that design to include external processing that will communicate with *geotool*. XML is becoming the software industry standard to use for categorizing metadata, and this format is especially beneficial to us since it can be passed back and forth between clients and Web services through HTTP, along with the XML SOAP RPC messages that instigate the data processing. Because ORACLE and other RDBMS vendors are enabling their products to manage XML metadata records along with relational tables, we shall be able to store on the server the contents of the passed metadata files. Figure 4 shows the XML markup for a metadata file describing the waveform processing applied by *geotool*. Because the XML markup tags are by definition extensible, we must define the tags that will be used in all instances of waveform processing, and the schema for these tags (itself an XML document) is shown on the right-hand side of the figure. The design of this particular schema is illustrated in Figure 5. Although the XML markup is intended to be read, principally by the data processing software, it can be presented in a form readily accessible by the *geotool* user, as is shown in Figure 6. The stylesheet that transforms the XML file into a presentation format is yet another XML document, and it is shown on the right-hand side of that figure.

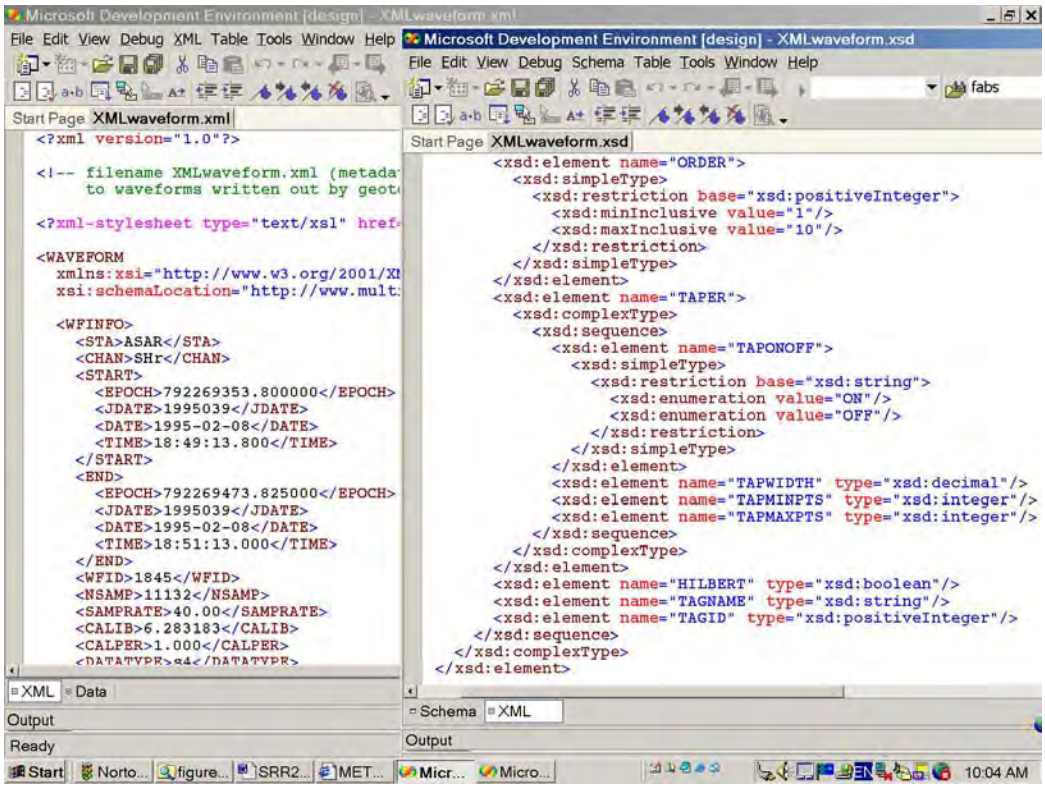


Figure 4. The XML markup describing a waveform (characterized by a CMR-format *.wfdisc* database record) that has undergone interactive processing by geotool is shown in the window on the left-hand side of the screenshot. The XML schema that was used for this metadata file is shown in the window on the right-hand side of the screenshot.

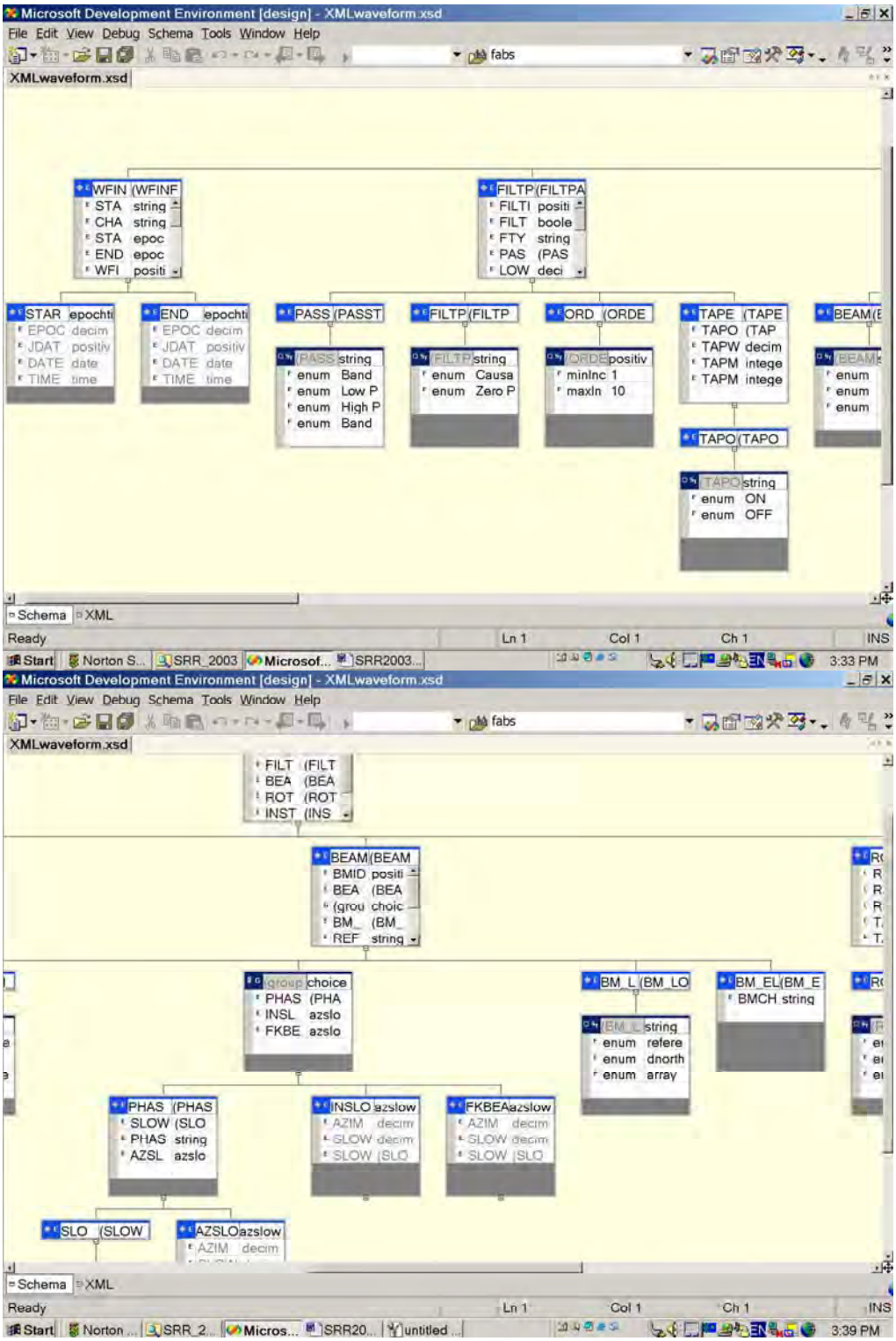


Figure 5. (Top and bottom) Two selected excerpts from the design layout of the waveform metadata XML schema that was shown in the window on the right-hand side of the screenshot in Figure 4.

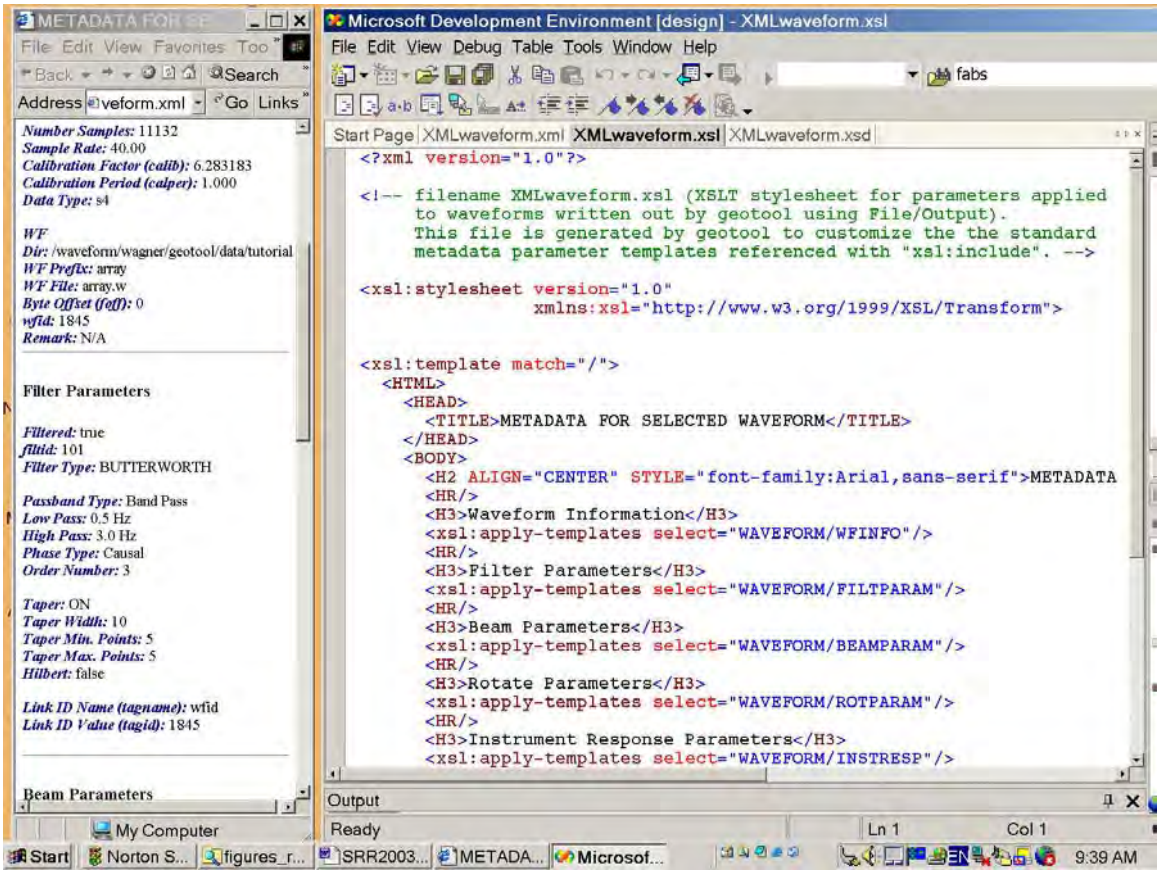


Figure 6. The browser window on the left-hand side of the screenshot shows, in a format that can readily be understood by the *geotool* operator, the contents of the waveform metadata file that were shown in XML format in the window on the left-hand side of the screenshot in Figure 4. To the right of the browser window there is shown another window that displays the XSLT (Extensible Stylesheet Language – Transformation) file that was used to transform the XML metadata file into the visual presentation form that is shown in the browser window.

CONCLUSIONS AND RECOMMENDATIONS

Even if it were feasible to construct an expanded version of *geotool* that offered all the capabilities needed by a scientist to characterize fully the seismic reference events that will be included in the Knowledge Base, such a program would suffer from inflexibility to change in the face of new requirements or the development of new seismic data analysis techniques. We have therefore examined the use of a system architecture that is based on independent software components that may be located on a single computer or distributed across a network (possibly the Internet). We have found the design and construction of such a system architecture to be possible using the modern software technology which is employed in commercial applications such as business-to-business commerce. Although our initial investigations demonstrated that CORBA technology is suitable for that purpose, our work within the last year has shown that the technology of XML SOAP Web services can also serve as the foundation for a reference event analysis system. In such a system a graphically intensive application such as *geotool* can act as the user interface, dispatching data and commands to independent software components that may be written in different programming languages and that may run under different operating systems. It is our recommendation that XML Web services rather than CORBA be used as the foundation for the reference event analysis system, since this appears to be the prevalent trend in the software industry and since it is much easier to communicate with applications running under the Windows operating system from applications running on different platforms by means of XML and SOAP than it is by means of a software bridge between CORBA and Windows.

In a distributed data processing system, the generating, transmitting, and archiving of files of metadata describing the seismic analysis process is even more important than in a stand-alone application used for analysis. We have therefore conducted a detailed analysis of the metadata that describe the output of *geotool*, and we have examined how XML can be used as the format for describing those metadata. We recommend that XML metadata files, schemas, and stylesheets be designed for all software components that will be used within the reference event analysis system.

We envision that a reference event analysis system will consist of a graphical presentation tier running on a desktop computer or workstation for user interactions, a data tier that can run on a dedicated database server, and an applications tier that may run on the same computer as the user interface or that may be distributed across multiple computing platforms. Although initially *geotool* will be used for both the graphical presentation tier and the applications tier, the creation of new applications software as well as the incorporation of legacy seismic analysis programs into the applications tier will eventually reduce the need for the analysis capabilities of *geotool*. We anticipate that *geotool* will then be replaced by a user interface program written using an object-oriented design that will be easier to maintain throughout the remainder of the system's software lifecycle than is the design of a huge C-language program like *geotool*.

ACKNOWLEDGEMENTS

We are indebted to Floriana Ryall for her many extensive and insightful contributions to the evaluation of problems with the operation of *geotool* and the identification of useful and important extensions to its current capabilities.

REFERENCES

Coyne, J.M. and I. Henson (1995), *Geotool* Sourcebook: User's Manual, Phillips Laboratory report PL-TR-96-2021.

Henson, I. (1993), The *Geotool* Seismic Analysis System, in: Proceedings of the 15th Annual Seismic Research Symposium 8-10 September 1993, Phillips Laboratory report PL-TR-93-2160.

Rivers, D.W., C.A. Schultz, and D.A. Dodge (2002), Efficient Integration of Old and New Research Tools for Automating the Identification and Analysis of Seismic Reference Events, in: Proceedings of the 24th Seismic Research Review, Los Alamos National Laboratory report LA-UR-02-5048, 882-891 (available at http://www.nemre.nn.doe.gov/review2002/CD/screen/07-05.pdf).

Acknowledgements

The National Nuclear Security Administration (NNSA) and the Air Force Research Laboratory (AFRL) gratefully acknowledge the important contributions of the following people for their work on the ***Proceedings of the 25th Seismic Research Review – Nuclear Explosion Monitoring: Building the Knowledge Base.***

Authors of papers for excellent research, good technical content and willing cooperation in electronic submission.

Dr. Anton M. Dainty, Air Force Research Laboratory (AFRL)/Defense Threat Reduction Agency (DTRA), for review and clearance of abstracts and papers related to AFRL and DTRA contracts.

Dr. Fredrick R. Schult, Air Force Technical Applications Center (AFTAC)/AFRL, for review and clearance of abstracts and papers related to AFTAC contracts.

Dr. Stanley D. Ruppert, Lawrence Livermore National Laboratory (LLNL), for burning, labeling, jacketing, and delivering the CD ROMs.

Ms. Francesca C. Chavez, Los Alamos National Laboratory (LANL), for technical editing of abstracts and papers.

Ms. E. Louise Mendius, LANL, for technical editing of abstracts and papers.

Mr. Michael C. Pankratz, LANL, for classification review of compiled papers.

Ms. Ruth N. Robichaud, LANL, for design and artwork of the CD label.

Ms. Leslie A Casey, NNSA, for review and clearance of abstracts and papers related to NNSA contracts and for providing financial support for the Proceedings.

Mr. Marvin D. Denny, NNSA, for technical review of abstracts and papers.

Dr. Christine M. Wehlburg, NNSA, for technical review of abstracts and papers.

Dr. Joseph C. Wehlburg, NNSA, for technical review of abstracts and papers.

Mr. William L. Andre, Space and Missile Defense Command (SMDC), for review and clearance of abstracts and papers related to SMDC contracts.

Ms. Mary L. Girven, Sandia National Laboratories (SNL), for making everyone's job easier with web-based technology for abstract and paper submission, on-line review and approval tools, and creation of the master files for the hardcopy and CD versions of the Proceedings.

Ms. Guadalupe (Lupe) Massoth, SNL, for providing assistance to Mary Girven on troubleshooting web related problems.

Dr. David B. Harris, LLNL; ***Dr. John J. Zucca,*** LLNL; ***Dr. CL Edwards,*** LANL; ***Dr. Steven R. Taylor,*** LANL; ***Dr. Dale N. Anderson***, Pacific Northwest National Laboratory (PNNL); ***Dr. Harry S. Miley,*** PNNL; ***Mr. J. Mark Harris,*** SNL; ***Mr. Preston B. Herrington,*** SNL; for a myriad of internal management and technical reviews of NNSA abstracts and papers.